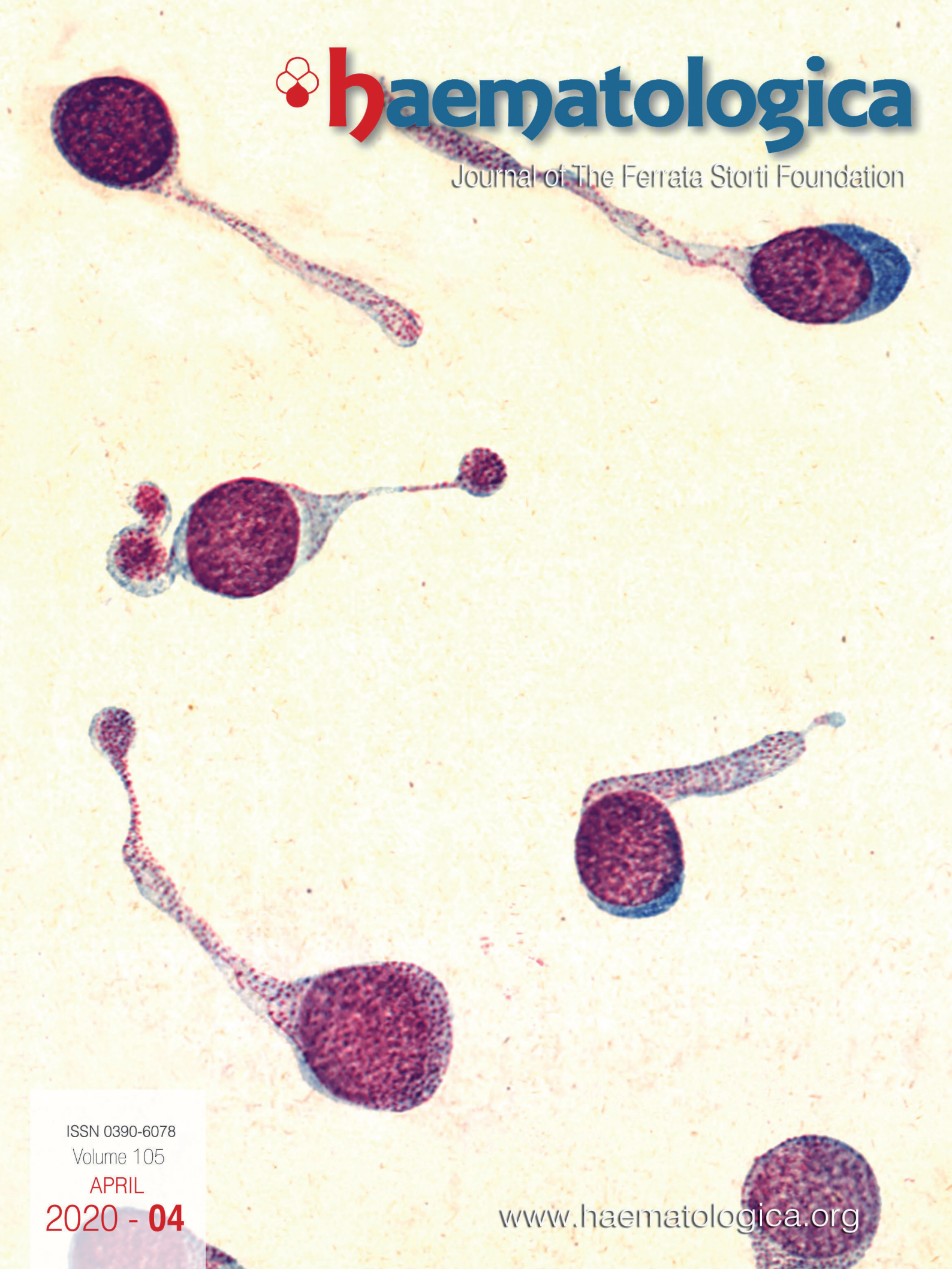

haematologica

Journal of The Ferrata Storti Foundation

ISSN 0390-6078
Volume 105
APRIL
2020 - 04

www.haematologica.org

haematologica
Journal of the Ferrata Storti Foundation

haematologica
Journal of the Ferrata Storti Foundation

Information for readers, authors and subscribers

Haematologica (print edition, pISSN 0390-6078, eISSN 1592-8721) publishes peer-reviewed papers on all areas of experimental and clinical hematology. The journal is owned by a non-profit organization, the Ferrata Storti Foundation, and serves the scientific community following the recommendations of the World Association of Medical Editors (www.wame.org) and the International Committee of Medical Journal Editors (www.icmje.org).

Haematologica publishes editorials, research articles, review articles, guideline articles and letters. Manuscripts should be prepared according to our guidelines (www.haematologica.org/information-for-authors), and the Uniform Requirements for Manuscripts Submitted to Biomedical Journals, prepared by the International Committee of Medical Journal Editors (www.icmje.org).

Manuscripts should be submitted online at http://www.haematologica.org/.

Conflict of interests. According to the International Committee of Medical Journal Editors (http://www.icmje.org/#conflicts), "Public trust in the peer review process and the credibility of published articles depend in part on how well conflict of interest is handled during writing, peer review, and editorial decision making". The ad hoc journal's policy is reported in detail online (www.haematologica.org/content/policies).

Transfer of Copyright and Permission to Reproduce Parts of Published Papers. Authors will grant copyright of their articles to the Ferrata Storti Foundation. No formal permission will be required to reproduce parts (tables or illustrations) of published papers, provided the source is quoted appropriately and reproduction has no commercial intent. Reproductions with commercial intent will require written permission and payment of royalties.

Detailed information about subscriptions is available online at www.haematologica.org. Haematologica is an open access journal. Access to the online journal is free. Use of the Haematologica App (available on the App Store and on Google Play) is free.
For subscriptions to the printed issue of the journal, please contact: Haematologica Office, via Giuseppe Belli 4, 27100 Pavia, Italy (phone +39.0382.27129, fax +39.0382.394705, E-mail: info@haematologica.org).

Rates of the International edition for the year 2019 are as following:

	Institutional	*Personal*
Print edition	*Euro 700*	*Euro 170*

Advertisements. Contact the Advertising Manager, Haematologica Office, via Giuseppe Belli 4, 27100 Pavia, Italy (phone +39.0382.27129, fax +39.0382.394705, e-mail: marketing@haematologica.org).

Disclaimer. Whilst every effort is made by the publishers and the editorial board to see that no inaccurate or misleading data, opinion or statement appears in this journal, they wish to make it clear that the data and opinions appearing in the articles or advertisements herein are the responsibility of the contributor or advisor concerned. Accordingly, the publisher, the editorial board and their respective employees, officers and agents accept no liability whatsoever for the consequences of any inaccurate or misleading data, opinion or statement. Whilst all due care is taken to ensure that drug doses and other quantities are presented accurately, readers are advised that new methods and techniques involving drug usage, and described within this journal, should only be followed in conjunction with the drug manufacturer's own published literature.

Direttore responsabile: Prof. Carlo Balduini; Autorizzazione del Tribunale di Pavia n. 63 del 5 marzo 1955.
Printing: Press Up, zona Via Cassia Km 36, 300 Zona Ind.le Settevene - 01036 Nepi (VT)

Associated with USPI, Unione Stampa Periodica Italiana.
Premiato per l'alto valore culturale dal Ministero dei Beni Culturali ed Ambientali

haematologica
Journal of the Ferrata Storti Foundation

Table of Contents

Volume 105, Issue 4: April 2020

About the cover

Editorials

Perspective Article

Review Articles

Articles

Hematopoiesis

Red Cell Biology & its Disorders

haematologica
Journal of the Ferrata Storti Foundation

haematologica
Journal of the Ferrata Storti Foundation

Errata Corrige

Letters to the Editor

Letters are available online only at www.haematologica.org/content/105/4.toc

haematologica
Journal of the Ferrata Storti Foundation

Case Reports

Case Reports are available online only at www.haematologica.org/content/105/4.toc

100-year-old Haematologica images: acute histiocytemic syndrome or blastic plasmocytoid dendritic cell neoplasm

Carlo L. Balduini

Ferrata-Storti Foundation, Pavia, Italy

E-mail: CARLO L. BALDUINI - carlo.balduini@unipv.it

doi:10.3324/haematol.2020.249912

At the beginning of the last century, the nature of leukemia was still the subject of heated discussion. Some authors were convinced that leukemias were neoplastic diseases, while others claimed them to be hyperplastic, reactive illnesses.[1] Despite this uncertainty, the availability of new methods for staining blood cells and better microscopes stimulated many researchers to try to classify leukemias on a morphological basis.

The two previous covers of Haematologica this year have been dedicated to the articles published in this journal in 1927 and 1928 by Alder and Di Guglielmo who identified by clinical and morphological criteria two 'new' disorders: acute promyelocytic leukemia and pure erythroid leukemia, respectively.[2,3] The cover image of this issue was taken from one of the figures (Figure 1) illustrating the paper by Ferrata and Reitano entitled 'Sindromi istiocitemiche' (Histiocytemic syndromes) published in Haematologica in 1923.[4] Based on blood film evaluation of leukemic patients, the authors identified a rare form characterized by the presence of 'tennis racket' cells and a rapidly fatal course. They were inclined to believe that these elements derived directly from very early progenitor cells, which at the time were named hemohistioblasts or Ferrata's cells.[5] The authors tentatively proposed the name acute histiocytemic syndrome for this new form of leukemia. In 1966, Rappaport introduced the term malignant histiocytosis for this disorder,[6] which is currently classified as blastic plasmacytoid dendritic cell neoplasm since it has been shown to derive from transformation of precursors of plasmocytoid dendritic cells.[7]

Figure 2 allows us to compare the 'tennis racket' cells described by Ferrata and Reitano with those reported in the chapter blastic plasmacytoid dendritic cell neoplasm of the Haematologic Atlas of Hematologic Cytology published this year by the Ferrata-Storti Foundation.[8]

The close similarity between the cells of Figures 1 and 2 is obvious. So, we suggest that the merit of having been the first to identify this disorder should go to Ferrata and Reitano.

Figure 1. Hand-drawn color plate illustrating the Ferrata and Reitano paper on 'acute histiocytemic syndrome' published in Haematologica in 1923. From the original caption of this figure: 'Leukocytoid cells of histioid origin. Typical cells in the shape of a 'tennis racket'. These cells were observed in the peripheral blood of a patient with an aggressive form of leukemia. The authors concluded that he was affected by a new form they named 'histiocytemic syndrome'.

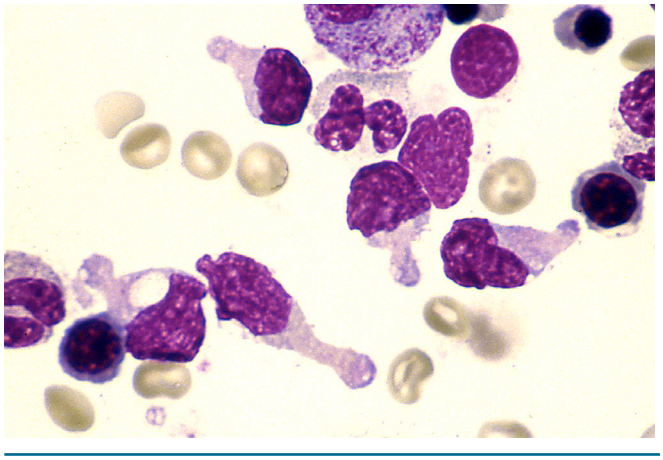

Figure 2. Image with 'tennis racket' cells from a patient with blastic plasmacytoid dendritic cell neoplasm published in the Haematologic Atlas of Hematologic Cytology.[8]

References

1. Mazzarello P. One hundred years of Haematologica. Haematologica. 2020;105(1):12-21.
2. Balduini CL. 100-year-old Haematologica images: Acute promyelocytic leukemia. Haematologica 2020;105(2):245.
3. Balduini CL. 100-year-old Haematologica images: Di Guglielmo disease or pure erythroid leukemia. Haematologica 2020;105(3):525.
4. Ferrata A, Reitano D. [Sindromi istiocitemiche (emoistioblastiche)]. Haematologica. 1923;4:385-393.
5. Baserga A, Zavagli G. Ferrata's stem cells: an historical review on hemocytoblasts and hemohistioblasts. Blood Cells. 1981;7(3):537-545.
6. Rappaport H. Tumors of the hemopoietic system, in Atlas of Tumor Pathology, p 49. Armed Forces Institute of Pathology, Washington, DC, 1996.
7. Facchetti F, Petrella T, Pileri SA. Blastic plasmacytoid dendritic cell neoplasm. In: Swerdlow SH, Campo E, Harris NL et al (Eds). WHO Classification of Tumors of Hematopoietic and Lymphoid tissues (Revised 4th edition). IARC: Lyon; 2017.
8. Invernizzi R. Blastic plasmacytoid dendritic cell neoplasm. Haematologica. 2020;105(Supplement n° 1):120-121.

GATA1 gets personal

Anna Rita Migliaccio

Dipartimento di Scienze Biomediche e NeuroMotorie, Alma Mater Studiorum - Università di Bologna, Bologna and Tisch Cancer Institute, Ichan School of Medicine at Mount Sinai, New York, NY, USA

E-mail: ANNA RITA MIGLIACCIO - annarita.migliaccio@unibo.it or annarita.migliaccio@mssm.edu

doi:10.3324/haematol.2019.246355

Until the beginning of the 20th century, physicians had very few drugs at their disposal to assist them in their fight against disease. The blooming of chemistry into the new field of pharmacology completely revolutionized the concept of "treatment" in medicine. Pharmacology made a large array of chemicals available to physicians and this greatly improved their ability to treat or at least to halt the progression of numerous diseases. The synthesis of new effective chemical entities drove an optimistic belief that it would soon be possible to produce a "compound" to specifically cure every "disease". This belief has been tamed by the fact that, in recent years, the rate of discovery of new effective drugs has greatly decreased. The current consensus in the field is that pharmacology has exhausted its potential, and that any further progress in our ability to cure will be driven by being able to match the "treatments" with the "driver genetic lesions" and/or by personalizing the "treatment modality", including optimization of the supportive treatments, to the "genetic and life-style" profile of the patient. This awareness has given rise to the development of the novel fields of precision[1] and/or personalized[2-4] medicine.

One of the most common consequences of the chemotherapy used to treat cancer is a severe and potentially lethal anemia which is treatable by blood transfusion, which represents an essential part of modern patient care. Transfusion has become a safe and widely available therapy thanks to the discovery of the major blood types by Karl Landsteiner, who received the Nobel price in 1930, and by the establishment of national and international blood banks in the 1940-1950s.[5] Blood, however, is a limited human resource, and although in western countries the blood supply is currently sufficient, in developing countries, the supply rarely meets existing needs.[6] Furthermore, changes in human demographics predict a progressive increase in the population >60 years of age, restricting the pool of eligible donors, and increasing the blood requirements needed to support advanced surgical procedures and medical treatments in older individuals. This means that, even in industrialized countries, by as early as 2050, the blood supply may no longer be adequate.[7] Additional challenges are presented by the outbreaks of novel infective diseases that increase the numbers of tests a transfusion product must undergo before it can be considered safe and by the awareness that the shelf-life of blood products may be much shorter than previously foreseen, which increases the number that go to waste. These challenges are posing an exponential burden to the economic and social costs of producing blood. The transfusion medicine community is aware of these challenges and the need to ensure an adequate blood supply that is safe and affordable in order to meet the clinical needs of the 21st century. More stringent and personalized criteria are, therefore, being implemented to define the patient populations in need of transfusion. These criteria are essential for evidence-based calculations of the blood products required at any given time, to reduce waste, and, therefore, the availability and costs of this therapy.

Human populations vary enormously in the number and biophysical properties of the red blood cells (RBC) present in the circulation and in the ability to recover from blood loss. The genetic basis of this variability has been the subject of several Genome Wide Association Studies (GWAS). These have identified several single nucleotide polymorphisms (SNP). These are regions of the DNA which do not affect the coding sequence of a gene, but rather the efficiency of its mRNA transcription and/or translation, and ultimately regulate the final protein content which predicts, among other factors, the genetic basis of RBC variability. Most of the SNP associated with inherited erythroid traits identified so far are located in the putative regulatory regions of *cKIT*, the gene which encodes the receptor for stem cell factor, the growth factor which, in combination with erythropoietin, regulates RBC production. These SNP lie close to a prominent DNase hypersensitive region approximately 115 kb upstream of *cKIT* and are associated with the variability in RBC counts, mean RBC volume, and mean RBC hemoglobin content observed in the normal population.[8,9] However, so far these studies have failed to drive personalized medicine strategies, for example, by identifying biomarkers for risk stratification of patients subjected to erythroid-related therapies. Surprisingly, these studies did not recognize SNP associated with GATA1.

GATA1 is a transcription factor which regulates the maturation of erythroid cells in a concentration-specific fashion. It is encoded by a gene, *GATA1*, located both in mice and men on the non-autosomal region of the X chromosome.[10] Therefore, males are hemizygote for the maternal GATA1 allele while, due to the Lyonization effect, the hematopoietic stem cells of females are a mosaic of cells carrying either the maternal or the paternal allele in an active configuration. *GATA1* is so important for erythropoiesis that mice lacking this gene die *in utero* from severe anemia and thrombocytopenia. Genetic alterations leading to a dysfunctional GATA1 protein have been identified in several diseases:[10] (i) point mutations in the coding sequences of the gene impairing, directly or indirectly, the DNA binding ability of the protein were detected in X-linked disorders associated with erythroid and/or megakaryocyte/neutrophil phenotype; (ii) deletions of the regulatory regions of the gene that eliminate a transcription start site required for the transcription of the mRNA encoding the full length form of the protein, making the cells hypomorphic for GATA1 protein, are associated with

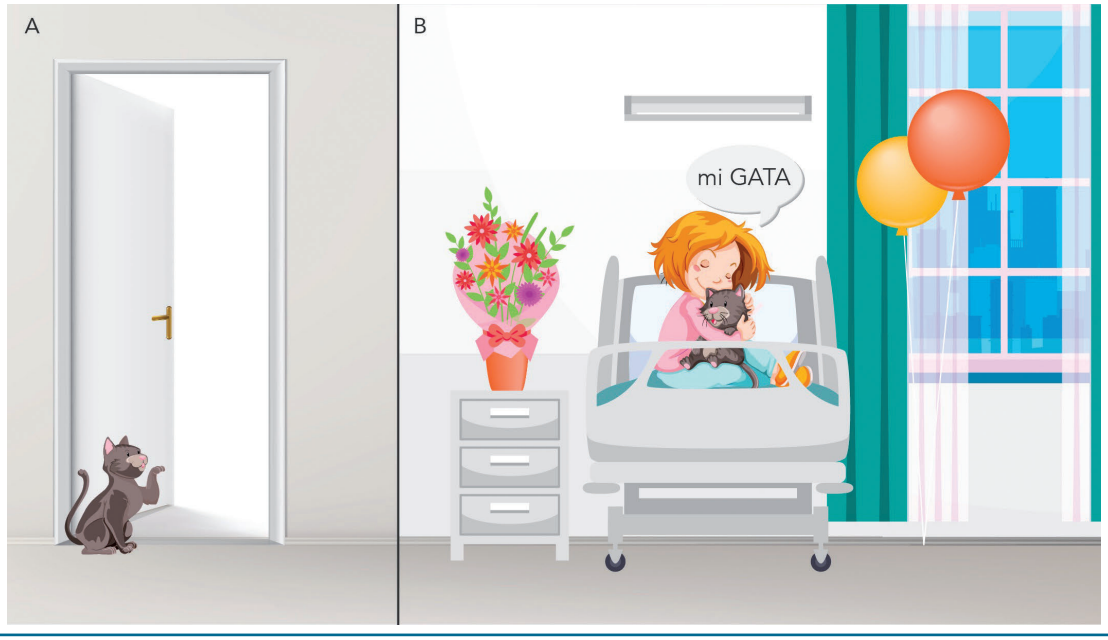

Figure 1. (A) A single nucleotide polymorphism hampering a binding site for the transcription factor GATA1 may predict whether children with acute lymphoblastic leukemia will need transfusion after chemotherapy. (B) This concept is reflected by the image of a little girl in a hospital thanking her GATA site (mi GATA in Spanish) for not having to undergo transfusion.

megakaryocyte leukemia in children with Down Syndrome and in sporadic forms of acute megakaryocyte leukemia in adults. These mutations are also detected in some patients with the inherited Diamond Blackfan anemia. Furthermore, in this disease, hypomorphic levels of GATA1 may result also from mutations in the gene encoding the ribosome protein RSP14 that impairs the ribosome ability to bind and translate *GATA1* mRNA. In addition, progression of benevolent forms of myeloproliferative neoplasms to their fatal myelofibrosis state is associated with a RSP14 signature that makes megakaryocytes of the patients hypomorphic for GATA1.[11] This knowledge has prompted studies that have targeted GATA1 for clinical purposes as pharmacological rescue of GATA1 has been shown to be an effective treatment for myelofibrosis.[12] However, surprisingly, GWAS studies have not yet identified clinically relevant correlations between SNP located either in the regulatory regions of *GATA1* or in GATA1-DNA binding sites, and variability of erythroid traits. One of the few exceptions is an old study which identified a SNP in the GATA1-binding site of the gene encoding the truncated form of the stem cell kinase receptor that determines the susceptibility to develop polycythemia in response to infection with the Friend virus in mice.[13]

In this issue of Haematologica, the paper by Xie *et al.* identifies by whole genome sequencing a single nucleotide polymorphism (SNP) in the intron of a gene (*ARHGEF12*) encoding a RhoA guanine nucleotide exchange factor which predicts whether children with acute lymphoblastic leukemia (ALL) will require multiple transfusions after chemotherapy.[14] On the basis of the assumption that chemotherapy hampers RBC production, and that the requirement for transfusion after this treatment depends on the efficiency with which the patient activates the stress erythropoiesis pathway necessary to overcome anemia, the authors hypothesized that *ARHGEF12* encodes a protein that plays an important role in the control of terminal erythroid maturation and that this function is affected by the SNP. To test this hypothesis, Xie *et al.* carefully determined that the SNP is located in a regulatory site disrupting a functional binding site for GATA1 and that, at the homozygous state, it reduces the gene transcription rates by 60%. Loss-of-function studies of *ARHGEF12* in animal models indicated that the gene regulates erythropoiesis at the proerythroblast level and studies in cell lines indicated that ARHGEF12 is upstream of a rhoA-p38 signaling pathway, the forced activation of which rescued impaired erythropoiesis induced by ARHGEF12 deficiency in animal models.

This study is important because it provides information on many levels. (1) It identifies a new signaling pathway, ARHGEF12/rhoA/p-38, which regulates the progression of proerythroblasts toward terminal maturation. Although the ligand which activates this pathway has not yet been identified, it is conceivable that it may represent a novel erythroid-stimulating agent other than erythropoietin which may have clinical value in the treatment of anemia. (2) It identified an SNP which is associated with the requirement for blood transfusion in children with ALL undergoing chemotherapy. If this association is validated by additional prospective studies on children with ALL, and possibly in other cancers, genetic testing for this SNP may represent a biomarker to stratify cancer patients at risk of anemia, allowing the blood supply necessary to support these patients during therapy to be calculated from the data base. (3) Last but not least, it suggests that GWAS studies designed on the basis of well-characterized patient cohorts may be more informative for devising precision/medicine

strategies than studies based on large numbers of healthy donors which may be flawed by the great level of noise in the signals generated with this strategy.

Funding

Supported by grants from the National Cancer (P01-CA108671), Heart, Lung and Blood (1R01-HL134684) Institute, Associazione Italiana Ricerca Cancro (AIRC IG23525)

References

1. Dzau VJ, Ginsburg GS. Realizing the Full Potential of Precision Medicine in Health and Health Care. JAMA. 2016;316(16):1659-1660.
2. Vogenberg FR, Isaacson Barash C, Pursel M. Personalized medicine: part 1: evolution and development into theranostics. P T. 2010;35(10):560-576.
3. Vogenberg FR, Barash CI, Pursel M. Personalized medicine: part 2: ethical, legal, and regulatory issues. P T. 2010;35(11):624-642.
4. Vogenberg FR, Barash CI, Pursel M. Personalized medicine: part 3: challenges facing health care plans in implementing coverage policies for pharmacogenomic and genetic testing. P T. 2010;35(12):670-675.
5. Alter HJ, Klein HG. The hazards of blood transfusion in historical perspective. Blood. 2008;112(7):2617-2626.
6. Report of the US Department of Health and Human Services. The 2009 National Blood Collection and Utilization Survey Report. Washington, DC: Services, T.U.D.o.H.a.H; 2010.
7. 3. Ali A, Auvinen MK, Rautonen J. The aging population poses a global challenge for blood services. Transfusion. 2010;50(3):584-588.
8. Kamatani Y, Matsuda K, Okada Y, et al. Genome-wide association study of hematological and biochemical traits in a Japanese population. Nat Genet. 2010;42(3):210-215.
9. van der Harst P, Zhang W, Mateo Leach I, et al. Seventy-five genetic loci influencing the human red blood cell. Nature. 2012;492:369-375.
10. Crispino JD, Horwitz MS. GATA factor mutations in hematologic disease. Blood. 2017;129(15):2103-2110.
11. Ling T, Crispino JD, Zingariello M, Martelli F, Migliaccio AR. GATA1 insufficiencies in primary myelofibrosis and other hematopoietic disorders: consequences for therapy. Expert Rev Hematol. 2018;11(3):169-184.
12. Gangat N, Marinaccio C, Swords R, et al. Aurora Kinase A Inhibition Provides Clinical Benefit, Normalizes Megakaryocytes, and Reduces Bone Marrow Fibrosis in Patients with Myelofibrosis: A Phase I Trial. Clin Cancer Res. 2019;25(16):4898-4906.
13. Persons DA, Paulson RF, Loyd MR, et al. Fv2 encodes a truncated form of the Stk receptor tyrosine kinase. Nat Genet. 1999;23(2):159-165.
14. Xie Y, Gao L, Xu C, et al. ARHGEF12 regulates erythropoiesis and is involved in erythroid regeneration after chemotherapy in acute lymphoblastic leukemia patients. Haematologica. 2020;105(4):925-936.

Genomic profiling of histiocytic sarcoma: new insights into pathogenesis and subclassification

Jonathan Said

Department of Pathology and Laboratory Medicine, UCLA Medical Center and David Geffen School of Medicine, Los Angeles, CA, USA

E-mail: JONATHAN SAID - jsaid@mednet.ucla.edu

doi:10.3324/haematol.2019.246314

A revised classification of histiocytoses and their neoplasms was long overdue when members of the Histiocyte Society suggested dividing them into five groups, designated L (Langerhans cell), C (Cutaneous), M (Malignant), R (Rosai-Dorfman), and H (Hemophagocytic) (Figure 1).[1] As an example, the L group, which includes Langerhans cell histiocytosis and Erdheim Chester disease, is characterized by mutations in the MAPK pathway and BRAF V600E. In contrast histiocytic sarcomas in the M group remain an elusive category. These rare and highly malignant neoplasms occur at all ages, and frequently involve extranodal sites including skin, soft tissues, and the gastrointestinal tract. There are few objective criteria for diagnosis other than expression of histiocyte markers (CD68, CD163, CD4, lysozyme, CD21, CD35, S100) and exclusion of other tumors by a panel of antibodies including, but not limited to, S100, keratins, EMA, Melan-A, HMB45, and B- and T-lymphoid markers.[2] Further complications arise in the apparent plasticity between histiocytic sarcomas and other malignancies, such as follicular lymphomas, demonstrated by translocations, immunoglobulin gene rearrangements, or mutational analysis.[3] Because of these pitfalls, histiocytic sarcoma has been vastly over diagnosed, with mimics including T-cell and other lymphomas with histiocyte-rich backgrounds, and, in particular, CD30 positive anaplastic large cell lymphomas. Clearly, any progress in diagnosing and treating these aggressive neoplasms will depend on identifying specific molecular and other markers for their accurate diagnosis.

Until recently, molecular analysis of histiocytic sarcomas has given confusing results, and there have been no consistent cytogenetic abnormalities. Mutations involving the RAS-MAPK signaling pathway, BRAF V600E mutations, as activation of PI3K and the tumor suppressor gene CDKN2A[4] have been most frequently reported, and there have been no reports of ALK translocations. Some cases, particularly in patients with associated B-cell lymphomas, have demonstrated immunoglobulin heavy or light chain gene rearrangements.

In this issue of Haematologica, Egan *et al.* performed genomic profiling of 21 primary histiocytic sarcomas, and in addition to confirming frequent alterations in the RAS/MAPK pathway, identified a novel intra-chromosomal transcript between exon 12 of TTYH3 and exon 8 of BRAF on chromosome 7. Moreover, differential expression analysis identified two distinct molecular subgroups with distinct molecular profiles and associated clinical characteristics based on the presence or absence of NF1/PTP11 mutations.[5] Cases that had NF1/PTPN11

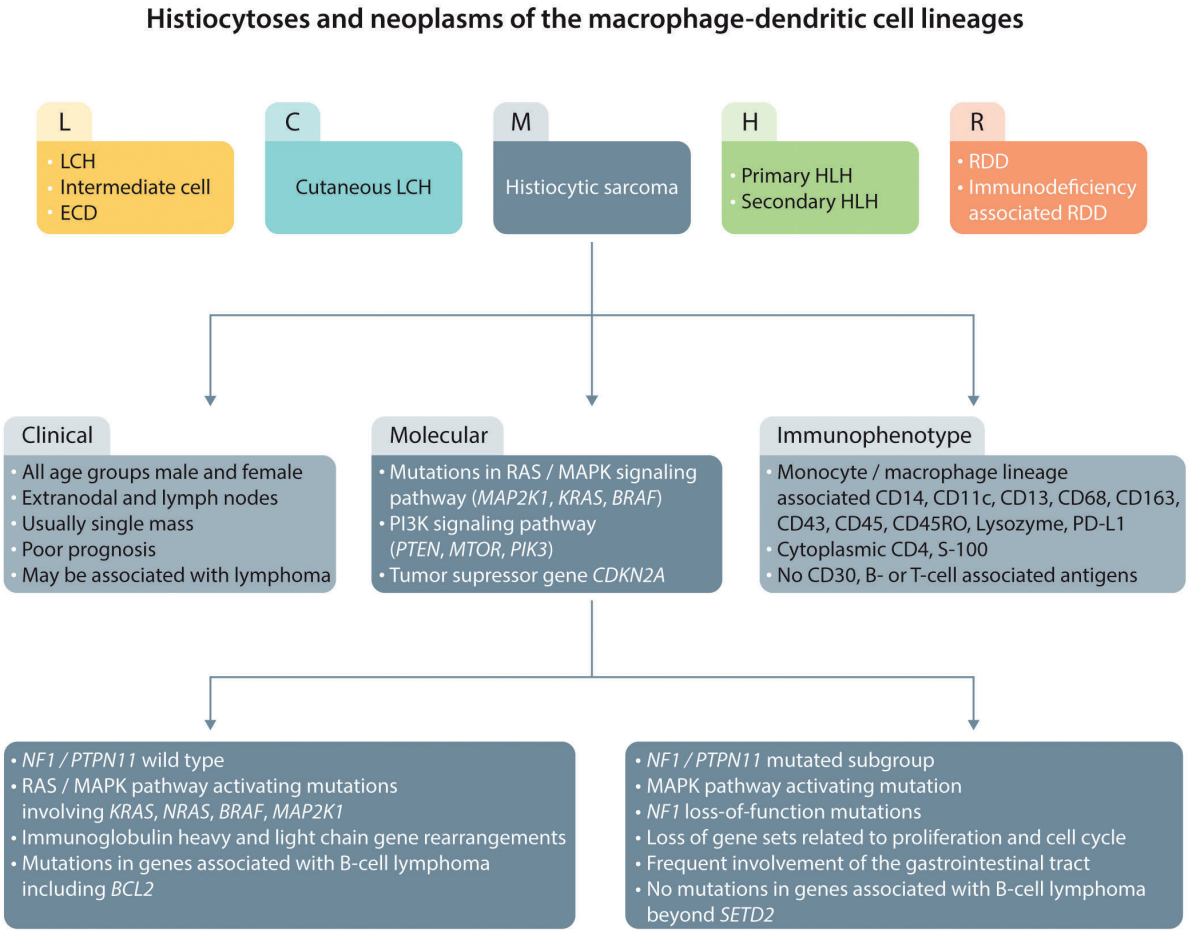

Figure 1. Clinical, immunophenotypic, and molecular changes in histiocytic sarcoma and relation to other histiocytoses. LCH: Langerhans cell histiocytosis; HLH: hemophagocytic lymphohistiocytosis; RDD: Rosai Dorfman Disease; ECD: Erdheim-Chester disease.

mutations had a predilection for gastrointestinal tract involvement. This group was characterized by loss of gene sets related to cellular proliferation and the cell cycle. Further data suggest that a subset of these cases involve co-occurring NF1 and PTPN11 mutations, suggesting that activating mutations of PTPN11 may synergize with NF1 mutations to potentiate oncogenesis. None of these cases had abnormalities in genes associated with B-cell lymphomas, besides SETD2, or had B-cell-related gene rearrangements.

In contrast, cases with wild-type NF1/PTP11 had RAS/MAPK pathway activating mutations, and were unrelated to site of presentation, and had activating mutations involving KRAS, NRAS, BRAF, and MAP2K1. This group alone demonstrated an association with immunoglobulin gene rearrangements and genes associated with B-cell lymphomas, including BCL2 rearrangement. This molecular profile offers an intriguing insight into the relationship between histiocytic sarcoma and B-cell lymphoma. The ability to identify subsets of histiocytic sarcoma according to their molecular profiles offers a potential for improvement in the diagnosis and targeted therapy of these neoplasms that has so far foiled conventional pathological examination.

References

1. Emile JF, Abla O, Fraitag S, et al. Revised classification of histiocytoses and neoplasms of the macrophage-dendritic cell lineages. Blood. 2016;127(22):2672-2681.
2. Pileri SA, Grogan TM, Harris NL, et al. Tumours of histiocytes and accessory dendritic cells: an immunohistochemical approach to classification from the International Lymphoma Study Group based on 61 cases. Histopathology. 2002;41(1):1-29.
3. Feldman AL, Arber DA, Pittaluga S, et al. Clonally related follicular lymphomas and histiocytic/dendritic cell sarcomas: evidence for transdifferentiation of the follicular lymphoma clone. Blood. 2008;111(12):5433-5439.
4. Shanmugam V, Griffin GK, Jacobsen ED, Fletcher CDM, Sholl LM, Hornick JL. Identification of diverse activating mutations of the RAS-MAPK pathway in histiocytic sarcoma. Mod Pathol. 2019;32(6):830-843.
5. Egan C, Nicolae A, Lack J, et al. Genomic profiling of primary histiocytic sarcoma reveals two molecular subgroups. Haematologica. 2020;105(4):951-960.

HIF-1α: a potential treatment target in chronic lymphocytic leukemia

Martina Seiffert

Molecular Genetics, German Cancer Research Center (DKFZ), Heidelberg, Germany

E-mail: MARTINA SEIFFERT - m.seiffert@dkfz.de

doi:10.3324/haematol.2019.246330

In 2019, William Kaelin Jr., Peter J. Ratcliffe and Gregg L. Semenza were jointly awarded the Nobel Prize in Physiology or Medicine for their work in elucidating how the transcription factor Hypoxia-inducible factor 1 (HIF-1) senses oxygen availability and adapts cellular response accordingly.[1] HIF-1 is a heterodimeric protein complex that consists of two proteins: a constitutively expressed HIF-1β subunit and an inducible HIF-1α subunit. During hypoxia, HIF-1α hydroxylation is reduced, preventing its proteasomal degradation, and the stabilized HIF-1 complex comprised of HIF1α and HIF-1β is transported to the nucleus where it regulates the expression of several hundred genes to counter the lack of oxygen.

In solid cancer, hypoxia is widely involved in tumor biology. Overexpression of HIF-1α is associated with aggressive cancer cell behavior and is correlated with poor overall patient survival. Tumor cells react to low oxygen levels by inducing HIF-1α expression, which results in an activation of many crucial cancer hallmarks, such as angiogenesis, glucose metabolism, cell proliferation/viability, invasion and metastasis.[2] Even though hypoxia was initially identified as a driver of HIF-1α expression, it has become clear in recent years that its overexpression in cancer can be also driven by genetic alterations, such as gain-of-function mutations in oncogenes or loss-of-function mutations in tumor-suppressor genes.

In this issue of *Haematologica*, Griggio *et al.* report that disrupting mutations in the tumor-suppressor gene *TP53* are associated with higher HIF-1α levels and activity in patients with chronic lymphocytic leukemia (CLL).[3] They further show that elevated HIF-1α levels are due to an increased transcription as well as a decreased protein degradation of HIF-1α. Evidence for both regulatory mechanisms have already been described in CLL and are summarized in Figure 1.

A constitutively higher expression and activity of HIF-1α in CLL cells compared to normal B cells was suggested to be due to reduced levels of the von Hippel-Lindau gene product (pVHL), which is responsible for HIF-1α degradation. Downregulation of pVHL was attributed to the inhibitory activity of miR-155, a highly abundant microRNA in CLL which is suggested to contribute to increased HIF-1α stability in CLL cells.[4] As pVHL expression levels were lower in CLL patients with disrupted *TP53* compared to wild-type *TP53* cases, Griggio *et al.* suggest that the observed accumulation of HIF-1α protein in *TP53*-disrupted CLL might be partially explained by an increased stability of HIF-1α.

It has recently been suggested that the mutant forms of FBXW7 contribute to HIF-1α stability in CLL cells.[5] FBXW7 is known to target proto-oncoproteins including HIF-1α for proteasomal degradation. *In silico* modeling predicted that mutations in FBXW7 that recurrently occur in CLL change the binding of protein substrates including HIF-1α and are therefore involved in the increased stability of HIF-1α in patients with these mutations.

HIF-1α has been suggested to be transcriptionally regulated in CLL cells *via* signals delivered by the microenvironment. In oxygenated blood, circulating CLL cells were shown to be primed for hypoxia and to undergo a rapid induction of HIF-1α activity when entering lymphoid tissues.[6] In these tissues, CLL cells are in constant interaction with accessory cells which deliver essential signals for survival and proliferation of CLL cells and contribute to resistance to drug-induced apoptosis.[7] The contact of CLL cells with stromal cells induces HIF-1α expression *via* induction of phosphatidylinositol 3-kinase (PI3K) and ERK mitogen-activated protein kinase (MAPK) signaling. In addition, hypoxia in lymphoid tissues was shown to modify central metabolic pathways in CLL cells, including increased adenosine generation and signaling *via* the A2A adenosine receptor.[8] Inhibiting the A2A receptor has been shown to counteract the effects of hypoxia in CLL and accessory cells, and to increase their susceptibility to pharmacological agents.

In line with this, Griggio *et al.* observed increased expression of HIF-1α in CLL cells upon co-culture with stromal cells to a level that is comparable to hypoxic conditions.[3] They further showed that HIF-1α transcript levels of primary CLL cells positively correlate with CLL cell survival in culture. This is likely related to the observation that HIF-1α critically regulates the interaction of CLL cells with their microenvironment. It has previously been shown that HIF-1α induces an upregulation of chemokine receptors, such as CXCR4, and cell adhesion molecules that control the interaction of leukemic cells with bone marrow (BM) and lymphoid microenvironments.[9] In line with this, inactivation of HIF-1α was shown to impair chemotaxis and cell adhesion to stroma, reduce BM and spleen colonization in xenograft and allograft CLL mouse models, and prolong survival of these mice. In support of a modulation of CLL cell motility, HIF-1α transcript levels were shown to correlate with the expression of CXCR4 and other target genes in CLL patient samples.

Further evidence for stroma-induced activation of HIF-1α in CLL comes from a comparative transcriptome analysis of primary CLL cells co-cultured or not with protective BM stromal cells which revealed that oxidative phosphorylation, mitochondrial function and hypoxic signaling are the most significantly deregulated functions in non-protected CLL cells.[10] These relevant transcriptomic changes were compared to the Connectivity Map database,[11] which contains transcriptomic responses of cell lines to treatment with small molecules. This comparison identified drugs that act by repressing HIF-1α and disturbing intracellular redox homeostasis as potential compounds blocking stroma-mediated support of CLL cells.

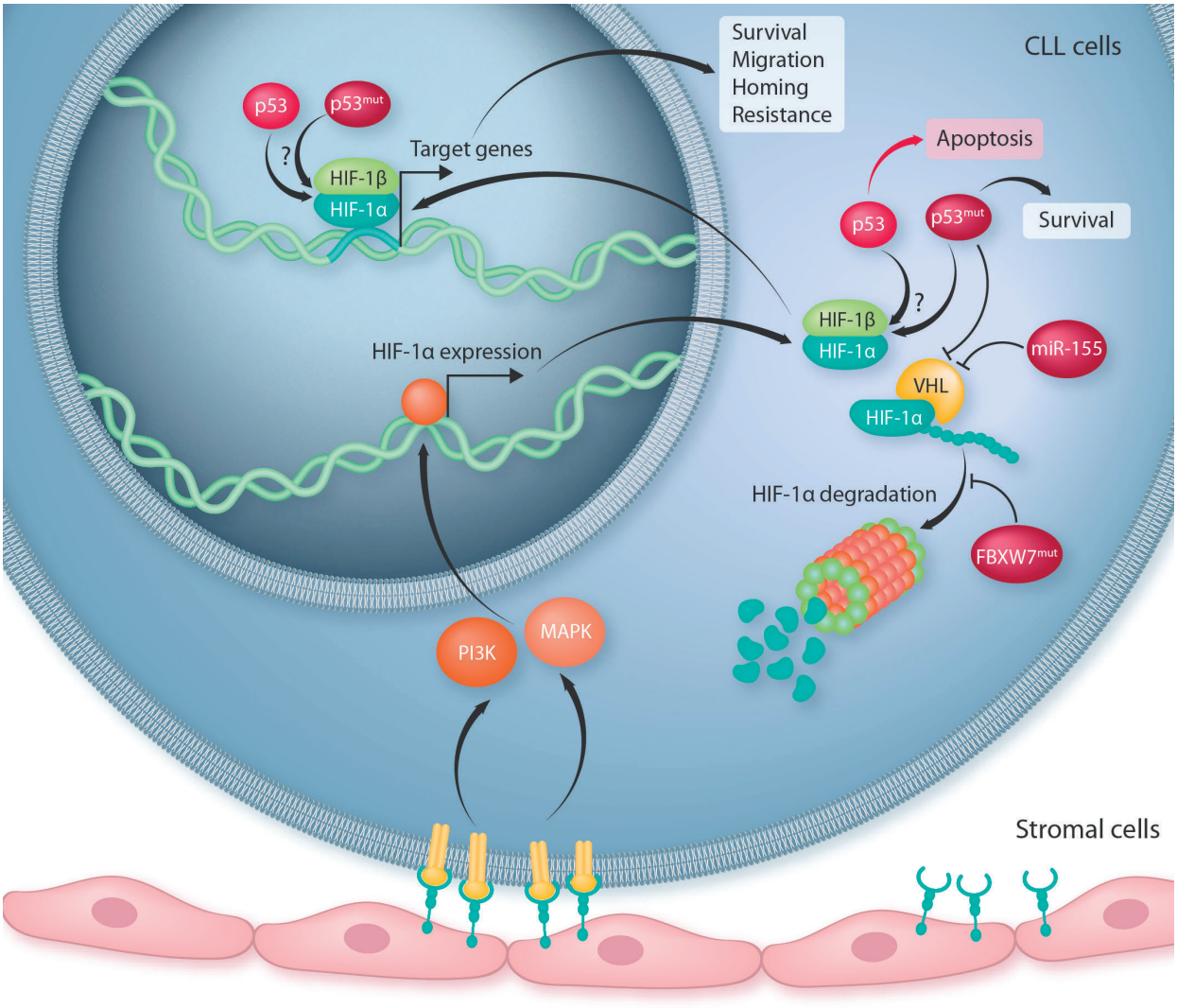

Figure 1. Schematic summary of mechanisms regulating HIF-1α in chronic lymphocytic leukemia (CLL). Contact of CLL cells with stromal cells induces transcriptional upregulation of HIF-1α *via* PI3K- or MAPK-signaling. Stability of HIF-1α is tightly connected to von Hippel-Lindau (VHL) tumor suppressor protein which triggers proteasomal degration of HIF-1α. In CLL, high levels of miR-155, disrupted p53, and mutant FBXW7 were connected to reduced HIF-1α degradation. Whether direct binding of p53 to HIF-1α is involved in the stability or transcriptional activity of HIF-1α in CLL remains unclear.

Under hypoxic conditions, the tumor suppressor protein p53 plays an important role in sensing stress and inducing apoptosis in cells. It was suggested that hypoxia in tumors represents a selection pressure for loss of functional p53 to avoid cell death.[12] p53 directly interacts with HIF-1α as an unfolded protein, but the biological implications of this interaction have not been completely clarified.[13] Recent work showed that hypoxia-induced HIF-1α leads to *TP53* expression, where the resulting p53 protein has a reduced capacity to modulate transcription of target genes but is abundantly available for protein-protein interactions.[14] Interestingly, both wild-type and mutant p53 proteins were shown to bind and chaperone HIF-1α to stabilize its binding to DNA response elements and therefore impact on HIF-1α transcriptional activity. Whether direct interactions of p53 with HIF-1α play a role in CLL, or whether CLL cells with disrupted *TP53* merely have a selective advantage in the hypoxic lymphoid microenvironment is still not clear.

Based on its role and function in cancer, HIF-1 is a promising target for the treatment of many tumor entities, and a multitude of small molecules of diverse chemical composition and promising biological potency have been identified as inhibiting HIF-1 activity.[15] Most of these substances are, however, only indirect inhibitors of HIF-1 and exhibit off-target effects by affecting other pathways as well, such as cell signaling, cell division, and DNA replication. To date, no HIF-1 inhibitor has been clinically approved.

The potential of targeting HIF-1α in CLL has previously been tested in immunocompromised mice that were transplanted with the CLL cell line MEC-1, as well as in the syngeneic *Eμ*-TCL1 adoptive transfer mouse model of CLL.[9] Camptothecin-11 (EZN-2208), a cytotoxic topoiso-

merase I inhibitor that also inhibits HIF-1α, was used for treatment of these mice which affected homing and retention of CLL cells in protective microenvironments, as shown by reduced spleen weight and decreased colonization of spleen and/or BM with CLL cells, and prolonged survival of mice. As knockdown of HIF-1α did not cause apoptosis of CLL cells *in vitro* or *in vivo*, the authors suggested that the pro-apoptotic effect of EZN-2208 towards CLL cells *in vivo* may be caused by mechanisms that do not depend on HIF-1α inhibition.

To further explore the potential of HIF-1α targeting in CLL, Griggio *et al*. used the previously described HIF-1α inhibitor BAY 87-2243 which acts by inhibiting mitochondrial complex I activity and hypoxia-induced mitochondrial reactive oxygen species production, thus achieving reduction of HIF-1α level with relatively higher specificity than other drugs.[16] BAY 87-2243 was shown to suppress hypoxia-induced HIF-1 target gene expression *in vitro* at low nanomolar concentrations and to harbor anti-tumor efficacy in xenograft mouse models of lung carcinoma and melanoma.[16,17] Pharmacological inhibition of HIF-1α with BAY87-2243 in primary CLL cells induced cell death *in vitro*, regardless of the *TP53* mutational status, with a generally weaker effect under hypoxia or in co-culture with stromal cells.[3] Pre-clinical testing of this drug in the *Eμ*-TCL1 adoptive transfer model of CLL resulted in lower numbers of malignant B cells in the BM and among them a higher frequency of apoptotic cells. In all other organs that are affected by CLL, including spleen and blood where the majority of leukemia cells accumulate, HIF-1α inhibition had no effect. Combination treatment of BAY87-2243 with fludarabine or ibrutinib showed higher rates of CLL cell death *in vitro* compared to monotherapy, which was independent of functional *TP53*. Therefore, the authors suggest that HIF-1α inhibition renders *TP53*-disrupted CLL cells sensitive to fludarabine treatment.

Even though treatment options for CLL have improved tremendously within the last decade, dysfunctional *TP53* is still associated with inferior patient outcome.[18] The development of novel treatment strategies is, therefore, extremely important for this patient group, as well as in the light of overcoming or avoiding therapy resistance to novel targeted therapies due to clonal evolution and/or selection of clones with aggressive phenotype, including disrupted *TP53* status.

Acknowledgment

I would like to thank Daniel Mertens, Deyan Yosifov, and Michaela Reichenzeller for their critical review and helpful comments on the manuscript.

References

1. The Nobel Prize in Physiology or Medicine 2019. NobelPrize.org. Nobel Media AB 2020. Wed. 12 Feb 2020. <https://www.nobelprize.org/prizes/medicine/2019/press-release/>
2. Semenza GL. Targeting HIF-1 for cancer therapy. Nat Rev Cancer. 2003;3(10):721-732.
3. Griggio V, Vitale C, Todaro M, et al. HIF-1α is overexpressed in leukemic cells from TP53-disrupted patients and is a promising therapeutic target in chronic lymphocytic leukemia. Haematologica. 2019;105(4):1042-1054.
4. Ghosh AK, Shanafelt TD, Cimmino A, et al. Aberrant regulation of pVHL levels by microRNA promotes the HIF/VEGF axis in CLL B cells. Blood. 2009;113(22):5568-5574.
5. Close V, Close W, Kugler SJ, et al. FBXW7 mutations reduce binding of NOTCH1, leading to cleaved NOTCH1 accumulation and target gene activation in CLL. Blood. 2019;133(8):830-839.
6. Koczula KM, Ludwig C, Hayden R, et al. Metabolic plasticity in CLL: adaptation to the hypoxic niche. Leukemia. 2016;30(1):65-73.
7. Hanna BS, Öztürk S, Seiffert M. Beyond bystanders: Myeloid cells in chronic lymphocytic leukemia. Mol Immunol. 2019;110:77-87.
8. Serra S, Vaisitti T, Audrito V, et al. Adenosine signaling mediates hypoxic responses in the chronic lymphocytic leukemia microenvironment. Blood Adv. 2016;1(1):47-61.
9. Valsecchi R, Coltella N, Belloni D, et al. HIF-1α regulates the interaction of chronic lymphocytic leukemia cells with the tumor microenvironment. Blood. 2016;127(16):1987-1997.
10. Yosifov DY, Idler I, Bhattacharya N, et al. Oxidative stress as candidate therapeutic target to overcome microenvironmental protection of CLL. Leukemia. 2020;34(1):115-127.
11. Lamb J, Crawford ED, Peck D, et al. The Connectivity Map: Using Gene-Expression Signatures to Connect Small Molecules, Genes, and Disease. Science. 2006;313(5795):1929-1935.
12. Hammond EM, Giaccia AJ. The role of p53 in hypoxia-induced apoptosis. Biochem Biophys Res Commun. 2005;331(3):718-725.
13. Sánchez-Puig N, Veprintsev DB, Fersht AR. Binding of Natively Unfolded HIF-1α ODD Domain to p53. Mol Cell. 2005;17(1):11-21.
14. Madan E, Parker TM, Pelham CJ, et al. HIF-transcribed p53 chaperones HIF-1α. Nucleic Acids Res. 2019;47(19):10212-10234.
15. Bhattarai D, Xu X, Lee K. Hypoxia-inducible factor-1 (HIF-1) inhibitors from the last decade (2007 to 2016): A "structure–activity relationship" perspective. Med Res Rev. 2018;38(4):1404-1442.
16. Ellinghaus P, Heisler I, Unterschemmann K, et al. BAY 87-2243, a highly potent and selective inhibitor of hypoxia-induced gene activation has antitumor activities by inhibition of mitochondrial complex I. Cancer Med. 2013;2(5):611-624.
17. Schöckel L, Glasauer A, Basit F, et al. Targeting mitochondrial complex I using BAY 87-2243 reduces melanoma tumor growth. Cancer Metab. 2015;3:11.
18. Tausch E, Beck P, Schlenk RF, et al. Prognostic and predictive role of gene mutations in chronic lymphocytic leukemia: results from the pivotal phase III study COMPLEMENT1. Haematologica. 2020 Jan 9. [Epub ahead of print]

Prevention of bone disease and early detection of impending fractures in multiple myeloma patients can reduce morbidity and mortality: the necessity of interdisciplinary state-of-the-art treatment

Georg W. Herget,[1,2] Ralph Wäsch,[2,3] Lukas Klein,[1,2] Hagen Schmal,[1,2] Evangelos Terpos[4] and Monika Engelhardt[2,3]

[1]Department of Orthopaedics and Trauma Surgery, Medical Center, University of Freiburg, Faculty of Medicine, Freiburg, Germany; [2]Comprehensive Cancer Center Freiburg (CCCF), Medical Center University of Freiburg, Freiburg, Germany; [3]Department of Medicine I Hematology and Oncology, Medical Center, University of Freiburg, Faculty of Medicine, Freiburg, Germany and [4]Department of Clinical Therapeutics, University of Athens School of Medicine, Alexandra General Hospital, Athens, Greece

E-mail: GEORG W. HERGET - georg.herget@uniklinik-freiburg.de

doi:10.3324/haematol.2019.245423

Multiple myeloma (MM), the second most common hematologic cancer, is an indolent B-cell malignancy characterized by clonal expansion of terminally differentiated, immunoglobulin-producing, transformed plasma cells in the bone marrow.[1] In spite of the substantial improvement in overall survival (OS) seen in in MM over the last decades, it accounts for approximately 20% of hematologic malignancy-related deaths and for 2% of all cancer deaths.[2-4] Although causes of cancer-related deaths often include the underlying disease, infections and organ dysfunction, one essential complication in MM throughout the disease course are skeletal-related events (SRE). SRE, including pathological bone fractures, spinal cord compression, the need for radiation, and the need for surgical intervention on bones, are the leading symptom and feared complication in MM.[5,6]

At the time of MM diagnosis, the majority of patients present various skeletal abnormalities: osteolytic lesions, osteopenia and (secondary) osteoporosis, or a combination of these. Moreover, during the course of the disease, up to 90% of MM patients develop osteolytic lesions.[7] The cause of bone disease lies in the interaction between malignant plasma cells and the bone microenvironment, which leads to osteoclastic bone destruction, reduced osteoblast function, and blocking of bone repair.[8]

Bisphosphonates are the current mainstay of treatment of bone disease in MM, as they reduce SRE and bone pain.[9-12] Newer drugs, such as the anti-RANKL monoclonal antibody denosumab, have already been approved in MM.[13] Bone anabolic agents such as romosozumab, licensed for the treatment of post-menopausal osteoporosis, are currently under investigation and may represent further promising tools in the treatment.[14] However, even after appropriate treatment with anti-myeloma agents and osteoclast-targeting therapy with bisphosphonates, denosumab or others given at initial diagnosis, pathological bone fractures frequently occur during the course of the disease. Indeed, in a recent study, the authors found SRE in newly diagnosed MM patients who very frequently had osteolytic disease: two-thirds of patients had an SRE before study enrolment, an additional 44% had at least one on-study SRE, with 60% of all first SRE occurring within the first three months, and 81% occurring within the first six months.[13]

While pathological fractures can occur in almost every bone (but most commonly vertebras), the long bones (femur and humerus) and the ribs are often affected. However, their impact on patients' mobility depends on their location, with fractures of the long bones along with vertebral fractures, especially in combination with spinal cord compression, being the most harmful. Figure 1 illustrates different manifestations and locations of osteolyses in MM patients, including operative treatment options.

As a consequence, the detection of bone lesions is crucial for the investigation and subsequent treatment of MM. SRE-prevention and treatment in MM is aimed at avoiding or minimizing such events. However, these are often present at initial diagnosis and upon relapse, and, therefore, often drive treatment decisions, i.e. of systemic and/or operative and radiation treatment, as well as of additional supportive measures.[10,11,15]

In this issue of the journal, Thorsteinsdottir *et al.* report results of their large retrospective population-based study "Fractures and Survival in Multiple Myeloma".[16] They used data from 14,013 MM patients diagnosed in Sweden in the years 1990-2013, who had been identified by the Cancer Registry. Information on date of birth, MM diagnosis, fractures, and death were collected from central registries. Their aim was to compare survival in patients with and without fractures at MM diagnosis, including certain subtypes of fractures. Furthermore, the authors compared the effect of fractures on survival in MM before and after the introduction of novel agents that have generally improved OS in MM patients.

In their impressive study, the authors show that MM patients with a fracture at the time of diagnosis had an inferior survival rate compared to those without a fracture at diagnosis. Moreover, patients who developed a fracture during the course of the disease had a 2-fold risk of death compared to those that did not develop a fracture. This risk of death was significantly increased in nearly all subtypes of fractures except for ankle fractures: e.g. for vertebral fractures [hazard ratio (HR)=1.74; 95% confidence interval (CI): 1.61-1.87], hip fractures (1.99; 95%CI: 1.82-2.18), humerus fractures (2.57; 95%CI: 2.31-2.85) and femoral fractures (2.62; 95%CI: 2.32-2.98). Furthermore, the risk of death for elderly MM patients ≥70 years of age at the time of MM diagnosis with a fracture was significantly increased compared to those without.[16] Results from other studies are in line with these and these authors observed that pathological fractures increase the risk of death by 20-40%.[17]

Underlying causes for the observations of Thorsteinsdottir *et al.* are plentiful, the most likely being that SRE may hamper intensified systemic anti-MM treatment and impair patient constitution/fitness levels.[2] Moreover, cancer patients may indeed have a better outcome when impending pathological fractures are prevent-

Figure 1. Different manifestations and locations of osteolyses in multiple myeloma patients. (A) Pathological fracture of the femur, stabilized by an LISS (less invasive stabilization system) plate. (B) Almost complete destruction of the sixth cervical vertebral with spinal cord compression followed by vertebral body replacement. (C) Osteolysis of the left femoral neck which threatens stability. Prophylactic stabilization by total hip replacement. (D) Extended osteolysis of the left ilium stabilized by pelvic bone cementoplasty.

ed (i.e. by surgical intervention) than patients with actual pathological fractures. Substantial differences were observed with less average blood loss, shorter hospital stays, greater likelihood of discharge, and greater likelihood of resuming support-free ambulation.[6,18,19]

If pathological fractures do occur, they are mainly treated surgically to stabilize the fractured bones and to improve patients' quality of life *via* pain relief and restoration of function and mobility.[20] Palliation, not cure, is usually the surgical objective of treatment of MM-related bone disease.

The findings of Thorsteinsdottir *et al.* deserve the interest of interdisciplinary teams of MM experts. However, further investigations are needed to corroborate and better understand these findings, i.e. that the risk of death after suffering a fracture has not significantly decreased compared to patients who do not develop a fracture after the introduction of more effective treatment agents in MM. Moreover, subsequent analyses should study the risk of death after fracture in MM patients compared to patients without cancer. This is of particular importance since elderly patients in general have a higher morbidity and mortality after fractures.

As a consequence of Thorsteinsdottir *et al.'s* and previous findings, the early recognition of an impending fracture remains highly relevant in MM and other cancer patients. This includes taking a detailed general medical history, especially if aggravating or novel pain occurs or reoccurs. The following questions should be asked: "Is there any new onset of pain?" "Is there pain at night?" "Is pain independent of movement?" etc. In addition, radiographic imaging, such as low-dose whole-body computed tomography (WB-CT) is mandatory as part of the diagnostic process to detect possible osteolyses that may threaten stability. Moreover, during the course of the disease follow up, when symptoms occur or reoccur, imaging may be required to guide changes in therapy and disease management that may prevent or delay the onset of clinically significant morbidity and mortality as a result of SRE.[15]

Most importantly, optimal treatment strategies for fractures or impending fractures as part of SRE are achieved by discussion of patients' history of disease and image scans in interdisciplinary tumor boards, taking into consideration the actual status of the disease, prognosis, and background of the individual patient.[21] This interdisciplinary approach should involve a team of MM specialists in hematology-oncology, radiology, radiotherapy, orthopedics, pathology/molecular scientists, and other specialized disciplines if required (i.e. nephrologists, cardiologists, neurologists).[22] We are happy and fortunate that a highly-skilled interdisciplinary team of this kind is well established at our institution.

References

1. Panaroni C, Yee AJ, Raje NS. Myeloma and Bone Disease. Curr Osteoporos Rep. 2017;15(5):483-498.
2. Engelhardt M, Domm AS, Dold SM, et al. A concise revised Myeloma Comorbidity Index as a valid prognostic instrument in a

large cohort of 801 multiple myeloma patients. Haematologica. 2017;102(5):910-921.
3. Palumbo A, Anderson K. Multiple myeloma. N Engl J Med. 2011;364:1046-1060.
4. Zweegman S, Engelhardt M, Larocca A, EHA SWG on 'Aging and Hematology'. Elderly patients with multiple myeloma: towards a frailty approach? Curr Opin Oncol. 2017;29(5):315-321.
5. O'Donnell EK, Raje NS. Myeloma bone disease: pathogenesis and treatment. Clin Adv Hematol Oncol. 2017;15(4):285-295.
6. Kimura T. Multidisciplinary Approach for Bone Metastasis: A Review. Cancers. 2018;24;10(6).
7. Kyriakou C, Molloy S, Vrionis F, et al. The role of cement augmentation with percutaneous vertebroplasty and balloon kyphoplasty for the treatment of vertebral compression fractures in multiple myeloma: a consensus statement from the International Myeloma Working Group (IMWG). Blood Cancer J. 2019;9(3):27.
8. Terpos E, Ntanasis-Stathopoulos I, Gavriatopoulou M, Dimopoulos MA. Pathogenesis of bone disease in multiple myeloma: from bench to bedside. Blood Cancer J. 2018;8(1):7.
9. Engelhardt M, Herget GW, Graziani G, et al. Osteoprotective medication in the era of novel agents: a European perspective on values, risks and future solutions. Haematologica. 2018;103(5):755-758.
10. Terpos E, Kleber M, Engelhardt M, et al. European Myeloma Network guidelines for the management of multiple myeloma-related complications. Haematologica. 2015;100(10):1254-1266.
11. Terpos E, Ntanasis-Stathopoulos I, Dimopoulos MA. Myeloma bone disease: from biology findings to treatment approaches. Blood. 2019;133(14):1534-1539.
12. Mhaskar R, Kumar A, Miladinovic B, Djulbegovic B. Bisphosphonates in multiple myeloma: an updated network meta-analysis. Cochrane Database Syst Rev. 2017;12:CD003188.
13. Raje N, Terpos E, Willenbacher W, et al. Denosumab versus zoledronic acid in bone disease treatment of newly diagnosed multiple myeloma: an international, double-blind, double-dummy, randomised, controlled, phase 3 study. Lancet Oncol. 2018;19(3):370-381.
14. Toscani D, Bolzoni M, Ferretti M, Palumbo C, Giuliani N. Role of Osteocytes in Myeloma Bone Disease: Anti-sclerostin Antibody as New Therapeutic Strategy. Front Immunol. 2018;9:2467.
15. Hillengass J, Usmani S, Rajkumar SV, et al. International myeloma working group consensus recommendations on imaging in monoclonal plasma cell disorders. Lancet Oncol. 2019;20(6):e302-e312.
16. Thorsteinsdottir S, Gislason G, Aspelund T, et al. Fractures and survival in multiple myeloma: results from a population-based study. Haematologica. 2019;105(4):1067-1073.
17. Yee AJ, Raje NS. Denosumab for the treatment of bone disease in solid tumors and multiple myeloma. Future Oncol. 2018;14(3):195-203.
18. Johnson SK, Knobf MT. Surgical interventions for cancer patients with impending or actual pathologic fractures. Orthop Nurs. 2008;27:160–171.
19. Ward WG, Holsenbeck S, Dorey FJ, Spang J, Howe D. Metastatic disease of the femur: Surgical treatment. Clin Orthop Relat Res. 2003;415:230-244.
20. Bryson DJ, Wicks L, Ashford RU. The investigation and management of suspected malignant pathological fractures: a review for the general orthopaedic surgeon. Injury. 2015 Oct;46(10):1891-1899.
21. Engelhardt M, Selder R, Pandurevic M, et al. [Multidisciplinary Tumor Boards: Facts and Satisfaction Analysis of an Indispensable Comprehensive Cancer Center Instrument]. Dtsch Med Wochenschr. 2017;142(9):e51-e60.
22. Sakellariou VI, Mavrogenis AF, Savvidou O, Sim FH, Papagelopoulos PJ. Reconstruction of multiple myeloma lesions around the pelvis and acetabulum. Eur J Orthop Surg Traumatol. 2015;25(4):643-653.

Animal models of thrombotic thrombocytopenic purpura: the tales from zebrafish

Paul Coppo[1] and Bernhard Lämmle[2,3,4]

[1]Service d'Hématologie, Centre de Référence des Microangiopathies Thrombotiques, AP-HP.6, Paris, France; [2]Department of Hematology and Central Hematology Laboratory, Inselspital, Bern University Hospital, University of Bern, Bern Switzerland; [3]Center for Thrombosis and Hemostasis, University Medical Center Mainz, Mainz, Germany and [4]Haemostasis Research Unit, University College London, London, United Kingdom

E-mail: PAUL COPPO - paul.coppo@aphp.fr or BERNHARD LÄMMLE - Bernhard.laemmle@uni-mainz.de

doi:10.3324/haematol.2019.245043

Thrombotic thrombocytopenic purpura (TTP) results from systemic microvascular von Willebrand factor (VWF)-induced clumping of platelets causing thrombocytopenia, microangiopathic hemolysis, and ischemia in the brain, kidneys, heart, and other organs.[1] The identification of a severe deficiency of the specific VWF-cleaving protease, now denoted as ADAMTS13,[1] by Furlan *et al.*[2] and Tsai and Lian,[3] provided an explanation for the accumulation of extremely adhesive, unusually large VWF multimers in the plasma of patients with chronic relapsing TTP first reported by Moake *et al.* in the 1980s.[4,5] Severe deficiency of ADAMTS13 activity, caused by biallelic mutations of the encoding *ADAMTS13* gene[6-8] or, more commonly, by autoantibodies directed against various epitopes of the metalloprotease resulting in functional inhibition of the enzyme and/or the formation of immune complexes and enhanced clearance of ADAMTS13[2,3,9] underlies congenital (cTTP) and acquired, autoimmune TTP (iTTP), respectively.[10]

The novel insights into disease mechanisms identified in the laboratory during the past two decades were rapidly and successfully integrated into the clinical management, to the benefit of patients.[11] Targeted therapies were thereby progressively associated with the historical treatment empirically introduced in the 1970s-1980s, based on repeated plasma exchange, replacement of the deficient protease through fresh-frozen plasma, and corticosteroids, which had already dramatically improved the prognosis of patients with this previously mostly fatal disease.[12] The successful story of these newly introduced therapeutic approaches include B-cell-depleting monoclonal antibodies that inhibit autoantibody production,[13] and nanobodies that bind to the VWF A1 domain and inhibit the VWF-platelet glycoprotein Ib interaction.[14,15] Recently, a recombinant form of human ADAMTS13 was successfully tested in a pharmacokinetics and safety study in 15 patients with cTTP[16] and is expected to facilitate the management of cTTP and possibly iTTP in the near future. This ongoing development illustrates the strength of translational medicine when basic science and clinical research combine efficiently. This approach allowed TTP to fully enter the exciting era of targeted therapies and personalized medicine.

A crucial advance in TTP pathophysiology was the demonstration of the direct role of ADAMTS13 deficiency

in the occurrence of the disease, an insight that was strongly supported by the development of animal models of cTTP and iTTP.

Mouse models of thrombotic thrombocytopenic purpura

Several groups have generated ADAMTS13-deficient (*ADAMTS13*$^{-/-}$) mice via gene targeting using a mixed-strain C57BL/6J-129X1/SvJ genetic background.[17-19] The conclusion from evaluation of these models was that *ADAMTS13*$^{-/-}$ is not, *per se*, sufficient to produce the typical symptoms and signs of TTP in these strains of mice which also had normal survival.[17] Interestingly, however, when these *ADAMTS13*$^{-/-}$ mice were backcrossed into the CASA/Rk genetic background resulting in substantially higher plasma VWF levels, the resulting *ADAMTS13*$^{-/-}$ mice had unusually large VWF multimers, a lower average platelet count and decreased survival, with some mice developing spontaneous TTP manifestations.[17] Moreover, when these *ADAMTS13*$^{-/-}$ mice of C57BL/6J-129X1/SvJ mixed strain that had been backcrossed into the CASA/Rk background were injected with a strong trigger, i.e. shiga-toxin, they developed classic features of acute TTP with severe thrombocytopenia, anemia with schistocytes, increased levels of lactate dehydrogenase (LDH), reflecting both hemolysis and tissue damage, and microthrombi in several organs, especially the heart.[17] Using very high doses of intravenous recombinant human (rh) VWF (2000 U/kg of body weight) as a trigger, even the mixed strain C57BL/6J-129X1/SvJ *ADAMTS13*$^{-/-}$ mice developed acute TTP with severe thrombocytopenia, schistocytic anemia, elevated LDH and myocardial necrosis.[19] Interestingly, the prophylactic administration of rhADAMTS13 (200 U/kg) protected the mice from acute TTP and even the therapeutic infusion of rhADAMTS13 (320 U/kg), given within 1.5 h after a challenge with rhVWF, could reduce the severity of TTP findings, demonstrating that this model was useful for investigating the efficacy of prophylaxis and treatment of cTTP.[19]

Thereafter, murine monoclonal antibodies raised in *ADAMTS13*$^{-/-}$ mice against murine ADAMTS13 were used to generate a mouse model of immune-mediated TTP.[20] Injecting a combination of two inhibitory monoclonal antibodies into *Adamts13*$^{+/+}$ mice resulted in complete and prolonged inhibition of ADAMTS13 activity for more than 7 days, leading to the appearance of ultralarge VWF multimers in the plasma. In line with the above-mentioned murine cTTP models, TTP-like symptoms in this murine iTTP model did not occur and could only be induced when rhVWF was injected as an additional trigger.[20]

Baboon model of thrombotic thrombocytopenic purpura

To get closer to man, a non-human primate model of immune-mediated TTP was developed in the baboon (*Papio ursinus*).[21] An inhibitory murine anti-human ADAMTS13 monoclonal antibody was administered intravenously to baboons. In contrast to the mouse models of congenital and immune-mediated TTP discussed above, the monoclonal antibody-mediated complete inhibition of ADAMTS13 in the baboon for 4 days resulted in severe thrombocytopenia, microangiopathic hemolytic anemia with increased LDH levels and VWF-rich microthrombi in most organs without the need for an additional trigger. Nevertheless, none of the animals developed severe organ failure or died during the study.[21] Hence, this model represents early-stage iTTP, and a second hit or prolonged ADAMTS13 inhibition might be needed to induce full-blown TTP with organ failure and death in these baboons.

The baboon iTTP model provided useful data on the feasibility, efficacy and tolerance of new therapeutic strategies for iTTP.[22,23] Thus, it could be established that injection of a monoclonal antibody blocking the VWF A1 - glycoprotein Ib interaction was a safe and effective means to prevent and treat the early symptoms of iTTP,[22] whereas the therapeutic application of N-acetylcysteine was unable to resolve established TTP manifestations such as thrombocytopenia, hemolytic anemia and organ damage due to failed resolution of microvascular thrombosis.[23]

These animal TTP models demonstrated that a complete deficiency of ADAMTS13 activity, at least in mice, is not sufficient to produce the typical manifestations of acute TTP which may also depend on the quantity and quality of VWF.[24] Several authors have postulated that a "second hit" besides severely deficient ADAMTS13 activity may be needed to bring about acute TTP.[25-27] Such second hits triggering the release of VWF from Weibel-Palade bodies in endothelial cells may include extracellular DNA, histones, e.g. resulting from neutrophil extracellular traps, as well as neutrophil peptides 1-3 (α-defensins) or complement activation products such as sC5b-9 which are generated during infections and inflammation.[25-27] Importantly, however, no direct evidence is available to date to support the causative role of these inflammatory mediators in the pathogenesis of TTP. In this regard, more experimental research using additional models is needed to further unravel the pathophysiology and natural course of TTP and to probe new prophylactic and therapeutic interventions for this rare and severe disease.

What the *ADAMTS13*$^{-/-}$ zebrafish reveals about thrombotic thrombocytopenic purpura

The zebrafish (*Danio rerio*) was reported to be a relevant research tool for studying hemostasis and thrombosis, as it displays a high degree of genetic and functional conservation of hemostatic factors including the key functions of VWF, and its nucleated platelets (thrombocytes) seem to have properties comparable to those of human platelets.[28] The advantages of this vertebrate model include high fecundity, rapid and external embryonic development, and conservation of virtually all hemostatic factors in the zebrafish genome.

In this issue of *Haematologica*, Zheng *et al.*[29] report a new model of cTTP in zebrafish with interesting experiments showing the indispensable role of VWF in the occurrence of TTP and the role of a specific histone as an endothelial activator triggering acute severe disease in the context of severe ADAMTS13 deficiency. The authors took advantage of a double transgenic zebrafish line (*gata-1*/dsRed and *Fli-1*/eGFP), which expresses a red fluorescent protein under the gata-1 promoter in erythrocytes and immature thrombocytes and a green fluorescent protein under the fli-1 promoter in the entire vasculature and thrombocytes.

Using CRISPR/cas9, they created zebrafish lines carrying a null mutation in *Adamts13*, in *VWF*, and in both genes. *Adamts13*$^{-/-}$ zebrafish have higher plasma levels of VWF antigen, larger VWF multimers, and an increased ability of thrombocytes in anticoagulated zebrafish blood to adhere to a fibrillar collagen-coated surface under arterial flow. The *Adamts13*$^{-/-}$ zebrafish also show an accelerated rate of developing occlusive thrombi in the caudal venules after injury by iron chloride ($FeCl_3$), consistent with a prothrombotic phenotype.[29] *Adamts13*$^{-/-}$ zebrafish have a reduced number of mature and immature thrombocytes with increased erythrocyte fragmentation, suggesting a mild TTP phenotype in the basal state. The administration of a lysine-rich histone resulted in more severe and persistent thrombocytopenia and a mortality rate of 30% in *ADAMTS13*$^{-/-}$ *versus* 10% in *ADAMTS13*$^{+/+}$ zebrafish. Both spontaneous and histone-induced TTP phenotypes in *Adamts13*$^{-/-}$ zebrafish were completely prevented when *VWF* was genetically deleted, proving that the pathophysiological consequence of severe ADAMTS13 deficiency depends entirely on the presence of VWF. On the basis of these results, the zebrafish model developed by Zheng's research team clearly recapitulates the most meaningful features of TTP, which makes this model a promising tool for in-depth exploration of the interrelations between microbes or other environmental influences and the endothelium. Besides a better understanding of the natural history of human TTP, it should also facilitate the assessment of novel therapeutics for TTP and possibly for other arterial thrombotic disorders. One potential limitation of this model is the phylogenetic distance between zebrafish and the human species, raising the question of whether all aspects of hemostasis involving ADAMTS13 will be completely transposable to human physiology and pathology. This new zebrafish TTP model should reveal exciting and still unreported tales of TTP pathophysiology.

References

1. Kremer Hovinga JA, Coppo P, Lammle B, Moake JL, Miyata T, Vanhoorelbeke K. Thrombotic thrombocytopenic purpura. Nat Rev Dis Primers. 2017;3:17020.
2. Furlan M, Robles R, Galbusera M, et al. von Willebrand factor-cleaving protease in thrombotic thrombocytopenic purpura and the hemolytic-uremic syndrome. N Engl J Med. 1998;339(22):1578-1584.
3. Tsai HM, Lian EC. Antibodies to von Willebrand factor-cleaving protease in acute thrombotic thrombocytopenic purpura. N Engl J Med. 1998;339(22):1585-1594.
4. Moake JL, Rudy CK, Troll JH, et al. Unusually large plasma factor VIII:von Willebrand factor multimers in chronic relapsing thrombotic thrombocytopenic purpura. N Engl J Med. 1982;307(23):1432-1435.
5. Moake JL, Turner NA, Stathopoulos NA, Nolasco LH, Hellums JD. Involvement of large plasma von Willebrand factor (vWF) multimers and unusually large vWF forms derived from endothelial cells in shear stress-induced platelet aggregation. J Clin Invest. 1986;78(6):1456-1461.
6. Levy GG, Nichols WC, Lian EC, et al. Mutations in a member of the ADAMTS gene family cause thrombotic thrombocytopenic purpura. Nature. 2001;413(6855):488-494.
7. Joly BS, Boisseau P, Roose E, et al. ADAMTS13 Gene mutations influence ADAMTS13 conformation and disease age-onset in the French cohort of upshaw-Schulman syndrome. Thromb Haemost. 2018;118(11):1902-1917.
8. van Dorland HA, Taleghani MM, Sakai K, et al. The International Hereditary Thrombotic Thrombocytopenic Purpura Registry: key findings at enrollment until 2017. Haematologica. 2019;104(10):2107-2115.
9. Alwan F, Vendramin C, Vanhoorelbeke K, et al. Presenting ADAMTS13 antibody and antigen levels predict prognosis in immune-mediated thrombotic thrombocytopenic purpura. Blood. 2017;130(4):466-471.
10. Scully M, Cataland S, Coppo P, et al. Consensus on the standardization of terminology in thrombotic thrombocytopenic purpura and related thrombotic microangiopathies. J Thromb Haemost. 2017;15(2):312-322.
11. Coppo P, Cuker A, George JN. Thrombotic thrombocytopenic purpura: toward targeted therapy and precision medicine. Res Pract Thromb Haemost. 2018;3(1):26-37.
12. Rock GA, Shumak KH, Buskard NA, et al. Comparison of plasma exchange with plasma infusion in the treatment of thrombotic thrombocytopenic purpura. Canadian Apheresis Study Group. N Engl J Med. 1991;325(6):393-397.
13. Hie M, Gay J, Galicier L, et al. Preemptive rituximab infusions after remission efficiently prevent relapses in acquired thrombotic thrombocytopenic purpura. Blood. 2014;124(2):204-210.
14. Peyvandi F, Scully M, Kremer Hovinga JA, et al. Caplacizumab for acquired thrombotic thrombocytopenic purpura. N Engl J Med. 2016;374(6):511-522.
15. Scully M, Cataland SR, Peyvandi F, et al. Caplacizumab treatment for acquired thrombotic thrombocytopenic purpura. N Engl J Med. 2019;380(4):335-346.
16. Scully M, Knobl P, Kentouche K, et al. Recombinant ADAMTS-13: first-in-human pharmacokinetics and safety in congenital thrombotic thrombocytopenic purpura. Blood. 2017;130(19):2055-2063.
17. Motto DG, Chauhan AK, Zhu G, et al. Shigatoxin triggers thrombotic thrombocytopenic purpura in genetically susceptible ADAMTS13-deficient mice. J Clin Invest. 2005;115(10):2752-2761.
18. Banno F, Kokame K, Okuda T, et al. Complete deficiency in ADAMTS13 is prothrombotic, but it alone is not sufficient to cause thrombotic thrombocytopenic purpura. Blood. 2006;107(8):3161-3166.
19. Schiviz A, Wuersch K, Piskernik C, et al. A new mouse model mimicking thrombotic thrombocytopenic purpura: correction of symptoms by recombinant human ADAMTS13. Blood. 2012;119(25):6128-6135.
20. Deforche L, Tersteeg C, Roose E, et al. Generation of anti-murine ADAMTS13 antibodies and their application in a mouse model for acquired thrombotic thrombocytopenic purpura. PLoS One. 2016;11(8):e0160388.
21. Feys HB, Roodt J, Vandeputte N, et al. Thrombotic thrombocytopenic purpura directly linked with ADAMTS13 inhibition in the baboon (Papio ursinus). Blood. 2010;116(12):2005-2010.
22. Feys HB, Roodt J, Vandeputte N, et al. Inhibition of von Willebrand factor-platelet glycoprotein Ib interaction prevents and reverses symptoms of acute acquired thrombotic thrombocytopenic purpura in baboons. Blood. 2012;120(17):3611-3614.
23. Tersteeg C, Roodt J, Van Rensburg WJ, et al. N-acetylcysteine in preclinical mouse and baboon models of thrombotic thrombocytopenic purpura. Blood. 2017;129(8):1030-1038.
24. Vanhoorelbeke K, De Meyer SF. Animal models for thrombotic thrombocytopenic purpura. J Thromb Haemost. 2013;11 (Suppl 1):2-10.
25. Fuchs TA, Kremer Hovinga JA, Schatzberg D, Wagner DD, Lammle B. Circulating DNA and myeloperoxidase indicate disease activity in patients with thrombotic microangiopathies. Blood. 2012;120(6):1157-1164.
26. Miyata T, Fan X. A second hit for TMA. Blood. 2012;120(6):1152-1154.
27. Staley EM, Cao W, Pham HP, et al. Clinical factors and biomarkers predict outcome in patients with immune-mediated thrombotic thrombocytopenic purpura. Haematologica. 2019;104(1):166-175.
28. Weyand AC, Shavit JA. Zebrafish as a model system for the study of hemostasis and thrombosis. Curr Opin Hematol. 2014;21(5):418-422.
29. Zheng L, Abdelgawwad MS, Zhang D, et al. Histone-induced thrombotic thrombocytopenic purpura in adamts13-/- zebrafish depends on von Willebrand factor. Haematologica. 2020;105105(4):1107-1119.

Ferrata Storti Foundation

Myelodysplastic syndrome patient-derived xenografts: from no options to many

Christophe Côme,[1,2,3] Alexander Balhuizen,[1,2,3] Dominique Bonnet[4] and Bo T. Porse[1,2,3]

[1]The Finsen Laboratory, Rigshospitalet, Faculty of Health Sciences, University of Copenhagen, Denmark; [2]Biotech Research and Innovation Center (BRIC), University of Copenhagen, Copenhagen, Denmark; [3]Danish Stem Cell Center (DanStem), Faculty of Health Sciences, University of Copenhagen, Denmark and [4]Haematopoietic Stem Cell Laboratory, The Francis Crick Institute, London, UK

Haematologica 2020
Volume 105(4):864-869

Correspondence:

BO T. PORSE
bo.porse@finsenlab.dk

Received: October 9, 2019.

Accepted: November 27, 2019.

Pre-published: March 19, 2020.

doi:10.3324/haematol.2019.233320

Check the online version for the most updated information on this article, online supplements, and information on authorship & disclosures: www.haematologica.org/content/105/4/864

Introduction

According to the recently updated tumor classification by the World Health Organization, myelodysplastic syndrome (MDS) constitutes a heterogeneous group of blood disorders characterized by cytopenia and dysplasia in at least one of the myeloid lineages.[1] MDS is most common in the elderly and is caused by inefficient hematopoiesis and increased apoptosis within the bone marrow (BM). It is a genetically heterogeneous disorder and individual cases generally harbor two to three mutations in one of approximately 30 driver genes which are recurrently mutated in MDS.[2,3] Of importance, many of these genes have also been found to be mutated in acute myeloid leukemia (AML), with frequencies of mutations differing between the two diseases.[2,4] The spectrum of survival of patients with MDS is broad and high-risk MDS is associated with an increased propensity to progression to AML.[5]

There has been considerable emphasis on the development of genetically engineered mouse models in attempts to study MDS. These include strains harboring lesions in the most commonly mutated genes in MDS, such as *SF3B1*,[6] *TET2*,[7,8] *ASXL1*[9] and *SRSF2*.[10] The phenotypic properties of these models have been reviewed in detail previously[11-13] and although they all present with several phenotypic features of MDS, they clearly have some limitations with respect to their abilities to recapitulate human MDS biology. As an example, *Sf3b1*^{K700E} mutant mice develop anemia and display expansion of the long-term hematopoietic stem cell compartment, consistent with an MDS phenotype. However, the *Sf3b1*^{K700E} mutant line fails to present with ring sideroblasts which are normally found in patients with *SF3B1* mutations.[14] Another likely contributor to the inability of current genetically engineered mouse model lines to fully recapitulate the phenotypic spectrum of MDS is the fact that most models typically harbor one genetic lesion and, therefore, not the full mutational complement observed in MDS patients. Thus, there is a clear need for better models of MDS biology, including patient-derived xenografts (PDX), in order to recapitulate the disease's biology and complexity better.

The history of myelodysplastic syndrome patient-derived xenografts

The first PDX models of AML were established more than 40 years ago by subcutaneously engrafting patient material into immune-deprived mice.[15] More physiologically relevant models were developed over the next decade via the use of tail vein injection and improved immune-deficient strains.[16,17] In contrast, it was not until the beginning of this millennium that cells from MDS patients were demonstrated to engraft functionally in immune-compromised mice.[18-20] However, only cells from a limited number of patients could be engrafted and a study with a large number of patients demonstrated that engraftment was sustained by residual normal cells and not by the MDS clone(s).[21] During the last decade, several laboratories have published a number of complementary approaches for the generation of MDS PDX.[22-34] Importantly, these combined efforts have demonstrated the engraftment capacity of most MDS subtypes,[23-28,34] that the expanded cells retain the genetic and phenotypic features of the primary tumor,[24-27,29,30,32,34] that these PDX models also sustain engraftment in secondary recipients[24,27,29,34] and that they allow evaluation of new therapies.[32,33] Nevertheless, as summarized in Table 1 and Figure 1, these models are quite heterogeneous. Specifically, several immune-compromised murine strains have been used (NOG, NSG, NSG-S or MISTRG) and injected at different ages (from newborn pups to adult animals). Moreover, a number of different cell

Table 1. Summary of published patient-derived xenograft models from myelodysplastic syndrome patients.

Year	Reference	Mice				MDS patient cells			MSC co-injected?	Patients tested	Expansion time (weeks)
		Strain	Age	Irradiation?	Injection route	MDS subtype / features	Injected cells	Cell numbers			
2002	Nilsson *et al.*[18]	NOD/LtSz-SCID or NOD/LtSz-SCID β2m$^{-/-}$	8-12 weeks	yes, 350-375 cGy	tail vein	trisomy 8+	BM CD34$^+$ BM CD34$^+$ CD38$^-$	1.68-5 x10^5 1-1.4x10^4	No No	3	6 - 8 weeks
2003	Benito *et al.*[21]	NOD/SCID	6-8 weeks	300-350-375 cGy	tail i.v or i.p	15 RA, 11 RAEB, 6 RAEBt, 5 RARS	BM cells	0.4-3.5x10^7	No	37	n.s
2004	Thanopoulou *et al.*[20]	NOD/-SCID β2m$^{-/-}$ or NOD/-SCID β2m-/-3/GM/SF	8-10 weeks	yes, 350 cGy	tail vein or i.p	1 RA, 1 RARS, 2 RAEB, 3 RAEBT, 4 CMML	BM cells	4-17x10^6	No	11	5-23 weeks
2004	Kerbauy *et al.*[19]	NOD/-SCID β2m$^{-/-}$	n.s	n.s	intrafemoral	n.s	BM MNC + MSC cell lines HS5 & HS27a	10^7 MNC + 10^5 HS5 & HS27a	yes, HS5 & HS27a	6	4-17 weeks
2010	Martin *et al.*[37]	NSG	n.s	yes, 250 cGy	i.v. (retro-orbital) or intra-tibial i.v. (retro-orbital)	low risk	BM cells BM cells T cells depleted BM cells CD34$^+$	5x10^5-5x10^6 1.8-5x10^6 5x10^5/2x10^6	No	5 5 3	7-12 weeks
2011	Muguruma *et al.*[22]	NOG	n.s	yes, 250 cGy	intrafemoral	3 RA, 3 RAEB, 5 RAEB-T	BM CD34$^+$	1.4-5x10^5	Yes	6	n.s
2013	Pang *et al.*[23]	NSG	P0-P3 newborn pups	sublethal (100 rads)	anterior facial vein	low risk (monosomy 7)	HSC-like (Lin$^-$CD34$^+$ CD38$^-$CD90$^+$ CD45RA$^-$)	1.5-3x10^3	No	4	16
2014	Medyouf *et al.*[24]	NSG or NSG-S	6-8 weeks	yes, 200 cGy	intrabone	low or intermediate risk	BM CD34$^+$ + BM MSC	10^5	Yes	20	16-28 weeks
2015	Mian *et al.*[25]	NSG (females)	8-12 weeks	yes, 375 cGy	intra-BM (tibia)	RARS	BM CD34$^+$	0.65-2 10^5	No	4	18-20 weeks
2017	Rouault-Pierre *et al.*[26]	NSG or NSG-S	n.s	yes, 330-375 cGy	intra-BM (tibia)	8 RCMD, 3 RCMD-RS, 7 RAEB, 6 RARS, 1 MDS/MPN, 3 CMML	CD34$^+$ BM cells +/- BM MSC CD3$^-$ BM cells +/- BM MSC (2:1 for CD3$^-$)	1-2x10^5 (1:1 for MSC) 10^6 CD3- (2:1 for MSC)	Yes Yes	28	12-18 weeks
2017	Yoshimi *et al.*[27]	NSG-S	6-10 weeks	yes, 200-250 cGy	intrafemoral tail i.v	CMML JMML	BM CD34$^+$ BM or PB MNC	0.2-1.18x10^6 2.2-4x10^6 (BM) or 1.3-2x10^6 (PB)	No No	8 4	3-11 weeks 2-7 weeks
2017	Zhang *et al.*[28]	NSG or NSG-S	6-8 weeks	yes, 250 cGy	i.v. (retro-orbital)	CMML	BM or PB CD34$^+$	3x10^4-1.2x10^6	No	16	10-16 weeks
2018	Krevvata *et al.*[29]	NSG or NSG-S	6-8 weeks	yes, 250cGy	intrafemoral	3 low-risk, 4 high-risk	BM MNC +/- BM MSC	10^6 BM MNC +/- 10^5 BM MSC	Yes	7	8-32 weeks
2018	Meunier *et al.*[30]	NSG	8-12 weeks	no, 25mg/kg busulfan d-1 i.p	intra-BM (tibia)	1 RAEB, 2 RAEB1, 1 RARS	CD34$^+$ BM cells + BM MSC	5x10^5 CD34$^+$ & 1.5x10^6 MSC (1:3)	Yes	4	6 months
2018	Shastri *et al.*[31]	NSG	n.s	yes, 200cGy	tail i.v	2 int-2 risk, 1 high-risk, 1 MPN	BM/PB MNC	2-5x10^6	No	4	3 weeks
2018	Stevens *et al.*[32]	NSG-S	n.s	no, 25mg/kg busulfan d-1	tail i.v	8 high-risk	BM MNC	0.8-1x10^6	No	4	6-10 weeks
2019	Smith *et al.*[33]	NSG	n.s	yes, 200cGy	tail i.v	U2AF1 mutants	BM MNC	2-5x10^6	No	2	3 weeks

continued on the next page

continued from the previous page

2019	Song *et al.*[34]	MISTRG or NSG	1-3 days	yes, 2x150cGy (MISTRG) or 1x100cGy (NSG)	intrahepatically	1 del(5q), 3 MLD, 2 RS-SLD, 1 RS-MLD, 1 MPN-RS-T, 3 EB-1, 3 EB-2	BM CD34+	0.2-2.75x10^5	No	22	12-31 weeks
						1 MLD, 2 EB-1, 1 EB-2	BM CD3-	1.15-6x10^5	No	4	13-15 weeks

The main characteristics of the protocols published to generate patient-derived xenograft (PDX) models from patients with myelodysplastic syndromes (MDS) are presented. NOD/SCID: non-obese diabetic mice with *Prkdc*^{scid} mutation; β2m$^{-/-}$: beta2-microglobulin null; 3/GM/SF: constitutive expression of human interleukin-3 (IL-3), granulocyte-macrophage colony-stimulating factor (GM-CSF) and stem cell factor (SF); NOG: NOD/Shi-scid *Il2rg*^{null}; NSG: NOD.Cg- *Prkdc*^{scid} *Il2rg*^{null}-; NSG-S: NSG with human IL-3, GM-CSF and SF constitutive expression; MISTRG: humanized macrophage colony-stimulating factor, IL-3/GM-CSF, SIRP alpha and thrombopoietin combined with Rag2$^{-/-}$, IL2Rγ$^{-/-}$; i.v.: intravenous injection; i.p: intraperitoneal injection; cGy: centigray; BM: bone marrow; PB: peripheral blood; MNC: mononuclear cells; MSC: mesenchymal stromal cells; HSC: hematopoietic stem cells; Lin-: lineage negative; RA: refractory anemia; RAEB: refractory anemia with excess blasts; RAEB-I: RAEB type 1; RAEB-II: RAEB type 2; RAEBt: RAEB in transformation; RARS: refractory anemia with ringed sideroblasts; RARS-T: RARS with thrombocytosis; RS: ringed sideroblasts; RCMD: refractory cytopenia with multilineage dysplasia; RCMD-RS: RCMD and ringed sideroblasts; del(5q): MDS associated with isolated deletion of chromosome 5q; MDS/MPN: myelodysplastic/myeloproliferative neoplasms; CMML: chronic myelomonocytic leukemia; JMML: juvenile myelomonocytic leukemia; MLD: multilineage dysplasia; SLD: single lineage dysplasia; EB: excess blasts; MDS/MPN-RS-T: MDS/MPN with ring sideroblasts and thrombocytosis; n.s.: not specified.

sources have been employed (BM or peripheral blood mononuclear cells, CD3-depleted BM cells, CD34+ BM cells) which were injected in different quantities, in the presence or absence of BM-derived mesenchymal stromal cells (MSC) and in different anatomical locations (intravenous, intrafemoral, intrahepatic). Not surprisingly, this resulted in very different disease latencies (from 3 to 32 weeks post-injection). A number of conclusions can be drawn from this extensive work:

(i) With respect to selection of the recipient strain, an immunodeficient background is necessary. The most commonly used recipient for the generation of PDX is the NSG strain which harbors mutations in *Prkdc* and *Il2g* leading to the absence of B, T and NK cells.[35] The constitutive expression of the human cytokines interleukin-3 (Il-3), granulocyte-macrophage colony-stimulating factor (GM-CSF) and stem cell factor (SCF) on this background (NSG-S, also designated NSG-SGM3) does not lead to enhanced engraftment of most MDS subtypes, except for chronic myelomonocytic leukemia,[28] in contrast to the situation in AML.[24,26,29,36] On the other hand, the recently developed MISTRG strain, expressing human macrophage colony-stimulating factor (M-CSF), IL-3, GM-CSF, signal regulatory protein alpha (SIRPα) and thrombopoietin at physiological levels on a different immunodeficient background (Rag2$^{-/-}$, IL2Rγ$^{-/-}$), was recently demonstrated to be a promising host for engraftment of MDS patients' material.[34] Not only could cells from patients with various subtypes of MDS be expanded in this line, but the levels of engraftment were increased, with a higher percentage of CD33+ myeloid cells than in NSG mice. Moreover, long-term engraftment of these myeloid cells was also improved in this strain as CD33+ cells constituted more than 80% of the hCD45+ compartment in secondary recipients, compared to 30% in NSG mice. Additionally, MDS cells engrafted in MISTRG mice generated erythroid and megakaryocytic lineages at a higher frequency than in the NSG counterpart.[34]

(ii) T-cell depletion of the primary MDS tumor, either by treatment with a human CD3 antibody or by physical separation, is a prerequisite to limit graft-*versus*-host disease.[26,34,36-38] Indeed, one of the first attempts to generate MDS PDX failed mainly because of the predominant growth of human CD3+ T cells, leading to graft-*versus*-host disease in most of the recipient animals.[37]

(iii) Intrafemoral injections result in better engraftment in NSG mice compared to an intravenous route of injection.

(iv) Co-injection of MSC leads to variable results in terms of promoting the engraftment of MDS samples, with some laboratories reporting some enhancement,[22-24] whereas others have not found this effect.[26,29] The underlying reasons for this variation are not clear. However, as human MSC only survive for 2-4 weeks in the murine BM,[24,26] this variation could potentially reflect patient-specific differences in the ability of MSC to promote the initial seeding and engraftment of MDS cells in the murine BM.

(v) Engraftment capacity does not seem to be related to MDS subtypes, but rather appears to be specific to the individual samples, as indicated in studies with large numbers of patients.[24,26,34]

Alternative strategies

Despite extensive efforts in several laboratories, this cumulative work has only produced a total of approximately 100 MDS PDX so far. There is, therefore, a strong need for alternative systems that could enhance the generation of MDS PDX. Interestingly, descriptions of a number of humanized bone marrow-like structure (hBMLS) models have been published recently. These models enable the expansion of AML patients' cells that failed to engraft with conventional methods.[39-41] They are all based on the use of BM MSC and can be separated into two categories. In the first category, which we will define as "scaffold" models, *in vitro*-expanded MSC are seeded in a gelatin sponge and cultured for a couple of days. Next, human leukemic cells are injected into the sponge which is subsequently introduced subcutaneously into non-irradiated immunocompromised mice[41] (Figure 1). In the second approach, BM MSC are first mixed with Matrigel and introduced subcutaneously into immune-deficient mice in which they develop a so-called "ossicle" after 2-3 months, which constitutes an exterior bone structure surrounding a hematopoietic core. Following sublethal irradiation, human leukemic cells are injected into the ossicle where they expand[39] (Figure 1). Another ossicle-like approach combines osteogenic priming of MSC with a physical support consisting of two or three biphasic calcium phosphate particles, prior to subcutaneous insertion into mice and subsequent ossicle development.[40] Importantly, up to four hBMLS per animal can be introduced,[39-41] and Reinisch *et al.* have elegantly demonstrated that tumor cells can cir-

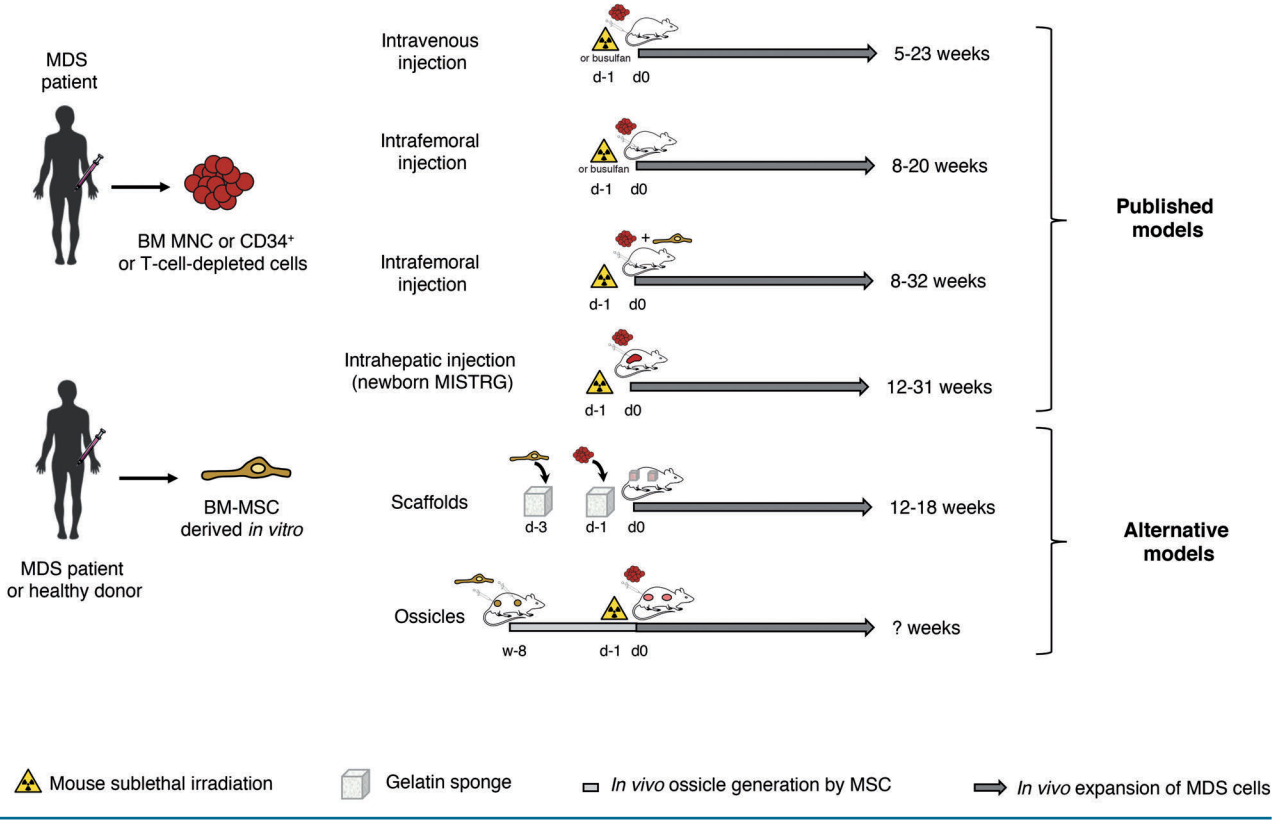

Figure 1. Key features of published and alternative patient-derived xenograft models of myelodysplastic syndrome. The left panel depicts the sources of cells from patients with myelodysplastic syndrome (MDS) which are injected to generate MDS patient-derived xenografts. Tumor cells (red circles) are constituted of bone marrow (BM) cells, mononuclear cells (MNC), or CD34+ purified or T-cell depleted BM cells. Supporting cells (yellow) are BM-derived mesenchymal stromal cells (MSC) derived from patients or healthy donors. The time periods for ossicle development and engraftment of MDS cells are illustrated by light and dark gray bars, respectively. The time of conditioning of the animal, by either irradiation or busulfan treatment is indicated, and the injection route is illustrated by a syringe.

culate between ossicles leading to engraftment of leukemic cells in non-injected hBMLS, thereby allowing for increased expansion of the original material from patients.[39]

In the previously described MDS PDX models, engraftment and expansion of the MDS material occur mainly in the recipient BM. In contrast, the hBMLS approaches exploit a humanized version of the BM niche, since at least bone, cartilage and MSC present in the niche are of human origin.[42] Of note, these hBMLS constitute a preferential homing niche for leukemic cells when compared to murine BM because leukemic cells injected intravenously expand earlier and at higher frequency in hBMLS than in the BM of mice.[39,40] Moreover, as the BM microenvironment has been reported to play an important role in the onset and development of MDS as well as the response to therapy, these hBMLS models are likely to be superior in mimicking key disease parameters.[43,44]

Is a standardized approach possible?

As discussed above, a plethora of approaches has been or could be used to generate PDX from MDS patients (Table 1 and Figure 1). However, these approaches are quite heterogeneous, and use different murine strains, injection sites, types and numbers of cells injected. In order to facilitate a comparison between different studies, it would be helpful if the field could agree on a more limited set of robust experimental protocols. In our opinion, two options are quite attractive. Our first candidate is the MISTRG model which has been demonstrated to mediate the engraftment of material from patients with different subtypes of MDS and appears relatively simple to implement. Moreover, in the published research, in which patients' cells have been injected intrahepatically into irradiated pups, this line appears to be superior to NSG in terms of engraftment frequency and myeloid percentages.[34] One note of caution is the reported development of anemia in this strain, which is also a characteristic of human MDS.[45,46] This may potentially make it complicated to determine whether the anemia observed in MDS PDX is caused by defects in MDS hematopoietic stem cells or by the intrinsic phenotype of the MISTRG strain. Moreover, the intrahepatic route of injection in newborn pups may not only raise some logistic challenges, but could also potentially influence tumor behavior, because this system constitutes a "young" niche, in contrast to the BM niche of elderly MDS patients. It is to be hoped that further generation of AML/MDS PDX with this mouse model by additional laboratories will strengthen the relevance of this model.

Even though the ossicle strategy is extremely seducing as it allows engraftment of patients' cells into a mature humanized BM-like environment, our own experience indicates that a very high proportion of MSC batches fail to sustain ossicle development (11/12, *unpublished observa-*

tions). Moreover, to our knowledge, AML PDX models based on this approach have only been described by one laboratory so far.[39,42] Therefore, our second proposed model is hBMLS based on gelatin scaffolds. This technique is quite simple and, as for ossicles, up to four scaffolds can be inserted per animal. Moreover, this strategy does not involve a long period of *in vivo* incubation in order to generate ossicles and, importantly, does not require pre-conditioning with irradiation.[41] Using this technique, we have succeeded in generating MDS PDX models covering several MDS subtypes in both our laboratories. A limitation of this approach, as for other hBMLS models, is the use of BM-derived MSC because these MSC have various alterations compared to those derived from healthy donors, such as DNA methylation status[47,48] and *in vitro* proliferation/differentiation capacity.[47] There is therefore a risk that the use of healthy allogeneic MSC may affect the behavior of the MDS clone(s) *in vivo*. Encouragingly, the few studies that have compared the use of healthy and patient-specific MSC have not suggested a major impact of the MSC origin on the engraftment levels of MDS in immunocompromised mice receiving intra-femoral injections.[26,29] Nevertheless, MDS-derived BM MSC do have an impact on the survival and differentiation capacities of CD34$^+$ hematopoietic stem and progenitor cells *in vitro* and *in vivo*,[47,49] and they can also respond favorably to the hypomethylating agent azacytidine, the current treatment regimen for high-risk MDS.[49] Consequently, investigation are needed to determine whether autologous MDS-BM MSC would be better at recapitulating the complexity of the disease in this model rather than BM MSC from healthy donors.

A major unresolved issue for the hBMLS approaches is that MSC display significant donor-to-donor variations and it would therefore be extremely useful to have a standardized source of MSC, i.e. in the form of BM MSC lines. Importantly, such cell lines have been generated recently and it would be of paramount importance to determine whether they retain their capacity to generate hBMLS *in vivo*[50] and whether MDS material could engraft and expand in these structures. As MDS MSC have been shown to have a strong impact on the *in vivo* potential of CD34$^+$ hematopoietic stem and progenitor cells, notably by showing altered extracellular signaling such as reduced CXCL12 expression,[48,49] such a cell line should either retain the features of MDS MSC or be receptive to "education" by MDS cells. However, if a MSC cell line that robustly retains these features could be obtained, this would provide an experimental platform for genetic manipulation of niche-derived cells, thereby facilitating studies into niche-MDS cell interactions.

Conclusions and perspectives

MDS is a very heterogeneous group of blood disorders, associated with lesions in dozens of driver genes.[2,3] Genetically engineered mouse models harboring mutations in the most common MDS driver genes display several characteristics of MDS[11-13] but remain imperfect as an experimental tool since they generally only recapitulate a subset of the phenotypes associated with human MDS. During the past few decades, in particular during the past 5 years, we have seen several improvements in the toolbox available for the generation of MDS PDX.[18-20,22-27,29,31,34] Moreover, various alternative methods, especially hBMLS models, appear to be extremely promising in terms of facilitating a more robust generation of MDS PDX.[39-41] This is important since an increase in the number of MDS PDX models will allow us to cover the broad genetic and phenotypic spectra of human MDS more comprehensively and provide tools to address key aspects of MDS biology.

Despite the recent developments in MDS PDX, these models may be further improved by incorporating additional human niche cells, such as endothelial cells. Indeed, these cells are functional in hBMLS settings[51,52] and endothelial cells from low-risk MDS patients influence hematopoietic stem cell behavior *in vitro*.[53] However, the recent developments of hBMLS models already provide an excellent opportunity to characterize the interaction between MDS tumor cells and their microenvironment better. As indicated above, the tumor microenvironment plays a key role in the pathogenesis of MDS and if we could manipulate MSC in the hBMLS models, we would have a precise tool to discern the biological importance of the niche. Finally, the increasing armory of MDS PDX also holds great promise as preclinical translational models for the development and validation of novel therapies as well as for personalized medicine along the lines already occurring in solid cancers.

Acknowledgement

Work in the Porse laboratory was supported through a center grant from the Novo Nordisk Foundation (Novo Nordisk Foundation Center for Stem Cell Biology, DanStem; Grant Number NNF17CC0027852). The present work is also part of the Danish Research Center for Precision Medicine in Blood Cancers funded by the Danish Cancer Society (grant n. R223-A13071) and Greater Copenhagen Health Science Partners. Work in the Bonnet laboratory was supported by the Francis Crick Institute, which receives its core funding from Cancer Research UK (FC001045), The UK Medical Research Council (FC001045) and the Wellcome Trust (FC001045).

References

1. Arber DA, Orazi A, Hasserjian R. The 2016 revision to the World Health Organization classification of myeloid neoplasms and acute leukemia . 2016;127(20):2391-2405.
2. Papaemmanuil E, Gerstung M, Malcovati L, et al. Clinical and biological implications of driver mutations in myelodysplastic syndromes. Blood. 2013;122(22):3616-3627.
3. Haferlach T, Nagata Y, Grossmann V, et al. Landscape of genetic lesions in 944 patients with myelodysplastic syndromes. Leukemia. 2014;28(2):241-247.
4. Papaemmanuil E, Gerstung M, Bullinger L, et al. Genomic classification and prognosis in acute myeloid leukemia. N Engl J Med. 2016;374(23):2209-2221.
5. Strupp C, Nachtkamp K, Hildebrandt B, et al. New proposals of the WHO working group (2016) for the diagnosis of myelodysplastic syndromes (MDS): Characteristics of refined MDS types. Leuk Res. 2017;57:78-84.
6. Obeng EA, Chappell RJ, Seiler M, et al. Physiologic expression of Sf3b1K700E causes impaired erythropoiesis, aberrant splicing, and sensitivity to therapeutic spliceosome modulation. Cancer Cell. 2016;30(3):404-417.
7. Moran-Crusio K, Reavie L, Shih A, et al. Tet2 loss leads to increased hematopoietic stem cell self-renewal and myeloid transformation. Cancer Cell. 2011;20(1):11-24.
8. Hasegawa N, Oshima M, Sashida G, et al. Impact of combinatorial dysfunctions of Tet2 and Ezh2 on the epigenome in the pathogenesis of myelodysplastic syndrome. Leukemia. 2017;31(4):861-871.
9. Wang J, Li Z, He Y, et al. Loss of Asxl1 leads to myelodysplastic syndrome–like disease in

mice. Blood. 2014;123(4):541-553.
10. Kim E, Ilagan JO, Liang Y, et al. SRSF2 mutations contribute to myelodysplasia by mutant-specific effects on exon recognition. Cancer Cell. 2015;27(5):617-630.
11. Beachy SH, Aplan PD. Mouse models of myelodysplastic syndromes. Hematol Oncol Clin North Am. 2010;24(2):361-375.
12. Beurlet S, Chomienne C, Padua RA. Engineering mouse models with myelodysplastic syndrome human candidate genes; how relevant are they? Haematologica. 2012;98(1):10-22.
13. Zhou T, Kinney MC, Scott LM, et al. Revisiting the case for genetically engineered mouse models in human myelodysplastic syndrome research. Blood. 2015;126(9):1057-1068.
14. Malcovati L, Papaemmanuil E, Bowen DT, et al. Clinical significance of SF3B1 mutations in myelodysplastic syndromes and myelodysplastic/myeloproliferative neoplasms. Blood. 2011;118(24):6239-6246.
15. Franks CR, Bishop D, Balkwill FR, et al. Growth of acute myeloid leukaemia as discrete subcutaneous tumours in immune-deprived mice. Br J Cancer. 1977;35(5):697-700.
16. Lapidot T, Sirard C, Vormoor J, et al. A cell initiating human acute myeloid leukaemia after transplantation into SCID mice. Nature. 1994;367(6464):645-648.
17. Bonnet D, Dick JE. Human acute myeloid leukemia is organized as a hierarchy that originates from a primitive hematopoietic cell. Nat Med. 1997;3(7):730-737.
18. Nilsson L, Åstrand-Grundström I, Anderson K, et al. Involvement and functional impairment of the CD34(+)CD38(-)Thy-1(+) hematopoietic stem cell pool in myelodysplastic syndromes with trisomy 8. Blood. 2002;100(1):259-267.
19. Kerbauy DM, Lesnikov V, Torok-Storb B, et al. Engraftment of distinct clonal MDS-derived hematopoietic precursors in NOD/SCID-beta2-microglobulin-deficient mice after intramedullary transplantation of hematopoietic and stromal cells. Blood. 2004;104(7):2202-2203.
20. Thanopoulou E, Cashman J, Kakagianne T, et al. Engraftment of NOD/SCID- 2 microglobulin null mice with multilineage neoplastic cells from patients with myelodysplastic syndrome. Blood. 2004;103 (11):4285-4293.
21. Benito AI, Bryant E, Loken MR, et al. NOD/SCID mice transplanted with marrow from patients with myelodysplastic syndrome (MDS) show long-term propagation of normal but not clonal human precursors. Leuk Res. 2003;27(5):425-436.
22. Muguruma Y, Matsushita H, Yahata T, et al. Establishment of a xenograft model of human myelodysplastic syndromes. Haematologica. 2011;96(4):543-551.
23. Pang WW, Pluvinage JV, Price EA, et al. Hematopoietic stem cell and progenitor cell mechanisms in myelodysplastic syndromes. Proc Natl Acad Sci U S A. 2013;110(8):3011-3016.
24. Medyouf H, Mossner M, Jann J-C, et al. Myelodysplastic cells in patients reprogram mesenchymal stromal cells to establish a transplantable stem cell niche disease unit. Cell Stem Cell. 2014;14(6):824-837.
25. Mian SA, Rouault-Pierre K, Smith AE, et al. SF3B1 mutant MDS-initiating cells may arise from the haematopoietic stem cell compartment. Nature Commun. 2015;6: 10004.
26. Rouault-Pierre K, Mian SA, Goulard M, et al. Preclinical modeling of myelodysplastic syndromes. Leukemia. 2017;31(12):2702-2708.
27. Yoshimi A, Balasis ME, Vedder A, et al. Robust patient-derived xenografts of MDS/MPN overlap syndromes capture the unique characteristics of CMML and JMML. Blood. 2017;130(4):397-407.
28. Zhang Y, He L, Selimoglu-Buet D, et al. Engraftment of chronic myelomonocytic leukemia cells in immunocompromised mice supports disease dependency on cytokines. Blood Adv. 2017;1(14):972-979.
29. Krevvata M, Shan X, Zhou C, et al. Cytokines increase engraftment of human acute myeloid leukemia cells in immunocompromised mice but not engraftment of human myelodysplastic syndrome cells. Haematologica. 2018;103(6):959-971.
30. Meunier M, Dussiau C, Mauz N, et al. Molecular dissection of engraftment in a xenograft model of myelodysplastic syndromes. Oncotarget. 2018;9(19):14993-15000.
31. Shastri A, Choudhary G, Teixeira M, et al. Antisense STAT3 inhibitor decreases viability of myelodysplastic and leukemic stem cells. J Clin Invest. 2018;128(12):5479-5488.
32. Stevens BM, Khan N, D'Alessandro A, et al. Characterization and targeting of malignant stem cells in patients with advanced myelodysplastic syndromes. Nature Commun. 2018;9(1):3694.
33. Smith MA, Choudhary GS, Pellagatti A, et al. U2AF1 mutations induce oncogenic IRAK4 isoforms and activate innate immune pathways in myeloid malignancies. Nat Cell Biol. 2019;21(5):640-650.
34. Song Y, Rongvaux A, Taylor A, et al. A highly efficient and faithful MDS patient-derived xenotransplantation model for pre-clinical studies. Nature Commun. 2019;10(1):366.
35. Shultz LD, Lyons BL, Burzenski LM, et al. Human lymphoid and myeloid cell development in NOD/LtSz-scid IL2R null mice engrafted with mobilized human hemopoietic stem cells. J Immunol. 2005;174(10): 6477-6489.
36. Wunderlich M, Chou F-S, Link KA, et al. AML xenograft efficiency is significantly improved in NOD![sol]SCID-IL2RG mice constitutively expressing human SCF, GM-CSF and IL-3. Leukemia. 2010;24(10):1785-1788.
37. Martin MG, Welch JS, Uy GL, et al. Limited engraftment of low-risk myelodysplastic syndrome cells in NOD/SCID gamma-C chain knockout mice. Leukemia. 2010;24(9): 1662-1664.
38. Wunderlich M, Brooks RA, Panchal R, et al. OKT3 prevents xenogeneic GVHD and allows reliable xenograft initiation from unfractionated human hematopoietic tissues. Blood. 2014;123(24):e134-e144.
39. Reinisch A, Thomas D, Corces MR, et al. A humanized bone marrow ossicle xenotransplantation model enables improved engraftment of healthy and leukemic human hematopoietic cells. Nat Med. 2016;22(7): 812-821.
40. Antonelli A, Noort WA, Jaques J, et al. Establishing human leukemia xenograft mouse models by implanting human bone marrow–like scaffold-based niches. Blood. 2016;128(25):2949-2959.
41. Abarrategi A, Foster K, Hamilton A, et al. Versatile humanized niche model enables study of normal and malignant human hematopoiesis. J Clin Invest. 2017;127(2): 543-548.
42. Reinisch A, Hernandez DC, Schallmoser K, et al. Generation and use of a humanized bone-marrow-ossicle niche for hematopoietic xenotransplantation into mice. Nat Protoc. 2017;12(10):2169-2188.
43. Li AJ, Calvi LM. The microenvironment in myelodysplastic syndromes: niche-mediated disease initiation and progression. Exp Hematol. 2017;55:3-18.
44. Pronk E, Raaijmakers MHGP. The mesenchymal niche in MDS. Blood. 2019;133 (10):1031-1038.
45. Rongvaux A, Willinger T, Martinek J, et al. Development and function of human innate immune cells in a humanized mouse model. Nat Biotechnol. 2014;32(4):364-372.
46. Herndler-Brandstetter D, Shan L, Yao Y, et al. Humanized mouse model supports development, function, and tissue residency of human natural killer cells. Proc Natl Acad Sci U S A. 2017;114(45):E9626-E9634.
47. Geyh S, Oz S, Cadeddu RP, et al. Insufficient stromal support in MDS results from molecular and functional deficits of mesenchymal stromal cells. Leukemia. 2013;27(9):1841-1851.
48. Schroeder T, Geyh S, Germing U, et al. Mesenchymal stromal cells in myeloid malignancies. Blood Res. 2016;51(4):225-232.
49. Poon Z, Dighe N, Venkatesan SS, et al. Bone marrow MSCs in MDS: contribution towards dysfunctional hematopoiesis and potential targets for disease response to hypomethylating therapy. Leukemia. 2019;33(6):1487-1500.
50. James S, Fox J, Afsari F, et al. Multiparameter Analysis of human bone marrow stromal cells identifies distinct immunomodulatory and differentiation-competent subtypes. Stem Cell Reports. 2015;4(6):1004-1015.
51. Chen Y, Jacamo R, Shi YX, et al. Human extramedullary bone marrow in mice: a novel in vivo model of genetically controlled hematopoietic microenvironment. Blood. 2012;119(21):4971-4980.
52. Passaro D, Abarrategi A, Foster K, et al. Bioengineering of humanized bone marrow microenvironments in mouse and their visualization by live imaging. J Vis Exp. 2017;(126). e55914.
53. Teofili L, Martini M, Nuzzolo ER, et al. Endothelial progenitor cell dysfunction in myelodysplastic syndromes: possible contribution of a defective vascular niche to myelodysplasia. Neoplasia. 2015;17(5):401-409.

REVIEW ARTICLE

Ferrata Storti Foundation

Haematologica 2020
Volume 105(4):870-887

How I curate: applying American Society of Hematology-Clinical Genome Resource Myeloid Malignancy Variant Curation Expert Panel rules for *RUNX1* variant curation for germline predisposition to myeloid malignancies

David Wu,[1,*] Xi Luo,[2*] Simone Feurstein,[3] Chimene Kesserwan,[4] Shruthi Mohan,[5] Daniel E. Pineda-Alvarez,[6] and Lucy A. Godley[3,7] on behalf of the collaborative group of the American Society of Hematology - Clinical Genome Resource Myeloid Malignancy Variant Curation Expert Panel[#]

[1]Department of Laboratory Medicine, University of Washington, Seattle, WA; [2]Department of Pediatrics/Hematology-Oncology, Baylor College of Medicine, Houston, TX; [3]Section of Hematology/Oncology, Department of Medicine, and The University of Chicago Comprehensive Cancer Center, Chicago, IL; [4]Albert Einstein College of Medicine, Department of Pathology, New York, NY; [5]Department of Genetics, University of North Carolina School of Medicine, Chapel Hill, NC; [6]Invitae, San Francisco, CA and [7]Department of Human Genetics, The University of Chicago, Chicago, IL, USA

DW and XL contributed equally to this work.

[#]*Members of this Clinical Genome Resource Variant Curation Expert Panel are listed in the Acknowledgments.*

ABSTRACT

The broad use of next-generation sequencing and microarray platforms in research and clinical laboratories has led to an increasing appreciation of the role of germline mutations in genes involved in hematopoiesis and lineage differentiation that contribute to myeloid neoplasms. Despite implementation of the American College of Medical Genetics and Genomics and Association for Molecular Pathology 2015 guidelines for sequence variant interpretation, the number of variants deposited in ClinVar, a genomic repository of genotype and phenotype data, and classified as having uncertain significance or being discordantly classified among clinical laboratories remains elevated and contributes to indeterminate or inconsistent patient care. In 2018, the American Society of Hematology and the Clinical Genome Resource co-sponsored the Myeloid Malignancy Variant Curation Expert Panel to develop rules for classifying gene variants associated with germline predisposition to myeloid neoplasia. Herein, we demonstrate application of our rules developed for the *RUNX1* gene to variants in six examples to show how we would classify them within the proposed framework.

Correspondence:

DAVID WU
dwu2@uw.edu

LUCY A. GODLEY
lgodley@medicine.bsd.uchicago.edu

Received: July 16, 2019.

Accepted: October 21, 2019.

Pre-published: March 12, 2020

doi:10.3324/haematol.2018.214221

Check the online version for the most updated information on this article, online supplements, and information on authorship & disclosures: www.haematologica.org/content/105/4/870

Introduction

Germline mutations in genes involved in hematopoiesis and lineage differentiation predispose patients to myeloid neoplasia with or without thrombocytopenia. The broad adoption of next-generation sequencing and microarrays in the clinical laboratory has expanded our knowledge of germline contribution to myeloid neoplasia. Drazer *et al.* reported that in six of 24 patients with myeloid neoplasia, presumed somatic variants in *DDX41*, *GATA2* and *TP53* were of germline origin.[1] Similarly, Churpek *et al.* showed that 29% of acute myeloid leukemia (AML)/myelodysplastic syndrome (MDS) kindreds with a positive family history carried a variant in one of 12 genes associated with germline predisposition to hematopoietic malignancies, including *FANCA*, *GATA2*, *RUNX1*, and *SBDS*.[2] To date, more than 65 genes have been associated with a predisposition to hematologic malignancies.[3] Recognizing the contribution of germline variation toward myeloid neoplasia, the 'WHO classification of Tumors of Hematopoietic and

Lymphoid Tissues' incorporated the classification of myeloid neoplasia with germline predisposition in their 2016 revised edition.[4,5]

In parallel, clinical laboratories are increasingly offering broad next-generation sequencing-based tests for patients with myeloid neoplasia for somatic testing, and will readily detect germline variants, if present in a patient. While there is increased clinical awareness of the potential for these germline variants to contribute to a patient's disease, there are often insufficient data in the literature to definitively classify whether a detected variant is contributing to the patient's phenotype.[6,7] For example, familial platelet disorder with predisposition to AML (FPD/AML) is an autosomal dominant disorder in which germline mutations in *RUNX1* result in thrombocytopenia, platelet functional and/or ultrastructural defects, and/or susceptibility to hematologic malignancies commonly including MDS, AML, and other malignancies[8-11] (Table 1). ClinVar (*https://www.ncbi.nlm.nih.gov/clinvar/*) is a database repository of clinically actionable genomic variants[12,13] that currently lists 325 germline *RUNX1* variants deposited by clinical laboratories. More than half of these variants are currently reported as being of uncertain significance.

Worldwide, most clinical laboratories follow the 2015 American College of Medical Genetics and Genomics (ACMG) and the Association for Molecular Pathology (AMP) guidelines for sequence variant interpretation.[14] In this framework, germline variants are classified using a five-tier system: benign (BEN), likely benign (LBEN), variant of uncertain significance (VUS), likely pathogenic (LPATH) and pathogenic (PATH). During sequence variant interpretation, laboratories systematically review the supporting criteria of a genomic variant, such as: minor allele frequencies (MAF), computational predictions, functional experiments and segregation with disease in order to determine the five-tier classification.[14-16]

Although the ACMG/AMP guidelines provide a comprehensive framework for sequence variant interpretation, the high rate of VUS and curation discrepancies continue to be an impediment to accurate clinical annotation and interpretation of genomic variants.[6,7] To encourage genomic and phenotypic data sharing, and engage experts in consensus-driven variant interpretation, the Clinical Genome Resource (ClinGen) convened Variant Curation Expert Panels (VCEP) to develop gene- and disease-specific modifications of the original guidelines and provide expert-reviewed variant classification for depositing into ClinVar (*Online Supplementary Figure S1*).[17] In 2018, the American Society of Hematology (ASH) sponsored a ClinGen Myeloid Malignancy Variant Curation Expert Panel (MM-VCEP), composed of 34 international members, who started working on gene- and disease-specific rules for *RUNX1* as the first of several genes conferring predisposition to myeloid malignancies (*Online Supplementary Figure S1A*). After designing, modifying and testing the preliminary *RUNX1* rules on 52 pilot variants, which improved classification in 33% VUS or variants with conflicting interpretations (CONF), MM-VCEP-specified ACMG/AMP rules were approved by the ClinGen oversight committee and efforts to curate variants to ClinVar using the Variant Curation Interface have commenced (*Online Supplementary Figure S1B*).[18] This pilot effort resulted in one variant being upgraded to PATH, two variants being upgraded to LPATH, and three variants being downgraded to LBEN. ClinGen's website contains the MM-VCEP variant classification recommendations and any subsequent modifications to these codes over time (*https://www.clinicalgenome.org/affiliation/10034/*).

Herein, we demonstrate the application of *RUNX1*-specific rules (Table 2) to classify nine representative *RUNX1* variants in six examples (Table 3) while reviewing phenotypic criteria for FPD/AML and summarizing molecular and functional roles of *RUNX1*.

Example 1. Early nonsense variants, (p.Arg204Ter) (PATH with PVS1, PM2, PS4_supporting, and PP1)

A 50-year old female with new pancytopenia was referred to a hematology service. A bone marrow biopsy showed hypocellularity with severe trilineage dysplasia and 12% blasts, diagnostic of MDS with excess blasts (MDS-EB-2). Further investigation showed pathogenic variants in *RUNX1* (NM_001754:c.610C>T, (p.Arg204Ter)), *BCOR* and *ASXL1* with a normal karyotype. The medical history was positive for thrombocytopenia (baseline 70-120x10^9/L) and a propensity to excessive bleeding after tooth extractions. The family history was positive for two sons with persistent thrombocytopenia (baseline 50-100x10^9/L) not otherwise explained and a granddaughter with thrombocytopenia and MDS with monosomy 7 (Figure 1). During the initial assessment, an increase in lactate dehydrogenase and the peripheral blast count were noted. A second marrow biopsy confirmed transformation into AML with 40% blasts. The patient underwent induction chemotherapy without achieving remission and clofarabine bridging for unrelated stem cell transplantation. During conditioning, the patient developed sepsis with Gram-negative bacteria and died shortly afterwards. Since she had a remarkable personal and family history pointing towards a germline predisposition syndrome, a skin biopsy was performed at the time of the diagnosis of MDS, and DNA testing from cultured skin

Table 1. Clinical phenotypes of RUNX1 familial platelet disorder and hereditary malignancies.

Clinical and laboratory features	Details	Life-time risk
Hematologic malignancy	Commonly AML or MDS; less frequently T-ALL; and rarely mixed MPN/MDS such as CMML, as well as B-ALL, and hairy cell leukemia	~44%
Thrombocytopenia	Mild to moderate thrombocytopenia with normal platelet size, in the absence of other causes	Most patients
Platelet functional and/or ultrastructural defects	Includes impaired platelet aggregation (particularly in response to collagen and epinephrine) and platelet alpha or dense granule secretion defects	Not known

Adapted from Table 2 from Luo and Feurstein, *et al.*[18] AML: acute myeloid leukemia; ALL: acute lymphoblastic leukemia; MPN: myeloproliferative neoplasms; MDS: myelodysplastic syndrome, CMML: chronic myelomonocytic leukemia.

Table 2. Clinical Genome Resource Myeloid Malignancy Variant Curation Expert Panel-approved rules for *RUNX1* variant interpretation.

ACMG/AMP CC	Original ACMG/AMP rule summary	Specification	Stand alone	Very strong	Strong	Moderate	Supporting	Comments
BA1	Allele frequency is >5% in ESP, 1000G, or ExAC.	Disease-specific	MAF ≥ 0.0015 (0.15%)	na	na	na	na	(1) The variant is present in any general continental population dataset with a minimum number of 2,000 alleles and variant present in ≥5 alleles.
BS1	Allele frequency is greater than expected for disorder.	Disease-specific	na	na	MAF between 0.00015 (0.015%) and 0.0015 (0.15%)	na	na	(1) The variant is present in any general continental population dataset with a minimum number of 2,000 alleles and variant present in ≥5 alleles. (2) Variant can be classified as likely benign based on BS1 alone if there is no contradictory evidence supporting pathogenicity.
BS2	Observed in a healthy adult individual for a recessive (homozygous), dominant (heterozygous), or X-linked (hemizygous) disorder, with full penetrance expected at an early age.	na						FPD/AML patients display incomplete penetrance and the average age of onset of hematologic malignancies is 33 years.
BS3	Well-established *in vitro* or *in vivo* functional studies show no damaging effect on protein function or splicing.	Gene-specific, strength	na	na	(1) Transactivation assays demonstrating normal transactivation (80-115% of wt) AND (2) data from a secondary assay demonstrating normal function.	na	Transactivation assays demonstrating normal transactivation (80-115% of wt).	See PS3 (1) and (2)
BS4	Lack of segregation in affected members of a family.	General rec	na	na	Applied when seen in ≥2 informative meioses.	na	na	This code should only be applied for genotype-positive, phenotype-negative (with sufficient laboratory evidence) family members.
BP1	Missense variant in a gene for which primarily truncating variants are known to cause disease.	na						FPD/AML is caused by both pathogenic missense and truncating variants.
BP2	Observed *in trans* with a pathogenic variant for a fully penetrant dominant gene/disorder or observed *in cis* with a pathogenic variant in any inheritance pattern.	General rec	na	na	na	na	Per original ACMG/AMP guidelines.	BP2 can also be applied if the variant is detected in a homozygous state.
BP3	In-frame deletions/insertions in a repetitive region without a known function.	na						*RUNX1* does not contain a repetitive region without known function.
BP4	Multiple lines of computational evidence suggest no impact on gene or gene product.	General rec	na	na	na	na	Per original ACMG/AMP guidelines.	BP4 should be applied for missense variants if all of the following apply: (1) REVEL score <0.15, (2) SSF and MES predict either an increase in the canonical splice

continued on the next page

continued from the previous page

ACMG/ AMP CC	Original ACMG/AMP rule summary	Specification	Stand alone	Very strong	Strong	Moderate	Supporting	Comments
								site score or a decrease of the canonical splice site score by no more than 10%, and (3) no putative cryptic splice sites are created. BP4 should also be applied for synonymous, intronic and non-coding variants for which SSF and MES predict either an increase in the canonical splice site score or a decrease of the canonical splice site score by no more than 10% and no putative cryptic splice sites are created.
BP5	Variant found in a case with an alternate molecular basis for disease.	na						In rare circumstances, a patient can carry two variants in genes predisposing to hematologic malignancies.
BP6	Reputable source recently reported variants as benign, but data are not available for laboratories to perform independent evaluations.	na						According to SVI recommendations.
BP7	A synonymous variant for which splicing prediction algorithms predict no impact to the splice consensus sequence nor the creation of a new splice site AND the nucleotide is not highly conserved.	General rec	na	na	na	na	Per original ACMG/AMP guidelines. BP7 cannot be applied in combination with PP3.	Also applicable to intronic/non-coding variants at or beyond positions +7/-21 for which (1) SSF and MES predict either an increase in the canonical splice site score or a decrease of the canonical splice site score by no more than 10% and no putative cryptic splice sites are created AND (2) evolutionary conservation prediction algorithms predict the site as not conserved (e.g. PhyloP score <0.1 or the variant is the reference nucleotide in one primate and/or three mammal species.).
PVS1	Null variant in a gene for which LOF is a known mechanism of disease.	Gene-specific, strength	na		Per modified *RUNX1* PVS1 decision tree for SNV, indels and CNV and table of splicing effects.		na	*RUNX1* LOF variants are a common mechanism of disease in FPD/AML. Three major isoforms (A, B, C) are expressed by use of two promotors and alternative splicing. C-terminal variants not predicted to undergo NMD are classified as PVS1_strong, deletions of exons 2 and 3, presumably only affecting RUNX1 isoform 1C, meet PVS1_moderate.
PS1	Same AA change as a previously established pathogenic variant regardless of nucleotide change.	Strength	na	na	Same AA change as a previously established pathogenic variant regardless of nucleotide change.	Same AA change as a previously established likely pathogenic variant regardless of nucleotide change.	na	(1) RNA data or agreement in splicing predictors show no splicing effects (SSF and MES predict either increase in canonical splice site score or decrease of canonical splice score by no more than 10% and no putative splice site are created). (2) The previously established PATH/LPATH variant must be asserted pathogenic/likely pathogenic based on MM-VCEP rules for *RUNX1* before this rule can be applied.
PS2	De novo (maternity and paternity confirmed) in a patient with the disease and no family history.	Disease-specific, strength	na	na	na	≥ 2 proven *de novo* occurrences (maternity	1 proven *de novo* occurrence (maternity	(1) No family history is defined as: absence of the variant and any of the *RUNX1*-phenotypic criteria in first- and/or second-degree relatives. (2) The proband must exhibit at least one phenotypic FPD/AML criterion. (3) The

continued on the next page

continued from the previous page

ACMG/AMP CC	Original ACMG/AMP rule summary	Specification	Stand alone	Very strong	Strong	Moderate	Supporting	Comments
						and paternity confirmed) in patients with the *RUNX1*-phenotype.	and paternity confirmed) in a patient with the *RUNX1*-phenotype.	maximum allowable strength by combining PS2 and PM6 criteria is to apply one moderate or two supporting rules.
PS3	Well-established *in vitro* or *in vivo* functional studies supportive of a damaging effect.	Gene-specific, strength	na	na	Transactivation assays demonstrating altered transactivation (<20% of wt, and/or reduced to levels similar to well-established pathogenic variants such as Arg201Gln or Arg166Gln) AND data from a secondary assay demonstrating altered function. PS3 cannot be applied if the variant meets PVS1. If the variant meets criteria for PVS1_strong and PS3, we recommend either applying PVS1_strong and PS3_moderate or upgrading PVS1_strong to PVS1 without applying PS3.	Transactivation assays demonstrating altered transactivation (<20% of wt, and/or reduced to levels similar to well-established pathogenic variants such as Arg201Gln or Arg166Gln) OR ≥2 secondary assays demonstrating altered function.	Transactivation assays demonstrating enhanced transactivation (>115% of wt).	(1) Transactivation assays should include wt and known pathogenic controls, as well as co-expression with *CBFβ*. Promoter sequences of *CSF1R* (M-CSF-R), *PF4*, *C-FMS* and *GZMB*, containing consensus *RUNX1* binding sites have been used for transactivation assays. (2) The following secondary assays have been performed: EMSA and yeast hybrid assays (decreased DNA-binding affinity), co-IP, FRET and affinity assays (diminished heterodimerization ability with CBFβ), IF and WB with cell fractionation (abnormal cellular localization), colony-forming assays (reduced colony-forming potential), xenotransplantation experiments (abnormal function of mutant RUNX1 *in vivo)*. (3) PS3 can also be applied for evidence of very low or abnormal mRNA/protein expression of the variant allele as a functional consequence of a null variant or incorrect mRNA/protein products.
PS4	The prevalence of the variant in affected individuals is significantly increased compared to the prevalence in controls.	Disease-specific, strength	na	na	≥ 4 probands meeting *RUNX1*-phenotypic criteria.	2-3 probands meeting *RUNX1*-phenotypic criteria.	1 proband meeting *RUNX1*-phenotypic criteria.	The affected individual has to fit at least one of the *RUNX*1-phenotypic criteria AND variant has to be either absent from gnomAD (overall population) or only present once.
PM1	Located in a mutational hot spot and/or critical and well-established functional domain without benign variation.	Gene-specific, strength	na	na	na	Variant affecting one of the following 13 hotspot residues: Arg107, Lys110, Ala134, Arg162, Arg166, Ser167, Arg169, Gly170, Lys194, Thr196, Asp198, Arg201,	Variant affecting one of the other AA residues 105-204 within the RHD.	The RHD (AA 77-204) has been established to be a highly conserved DNA-binding domain without any benign variation in ClinVar. No germline pathogenic variants have been reported in residues in the region (AA 77-104) to date. The AA range under PM1_supporting may be expanded in the future to other parts of the protein if more evidence emerges.

continued on the next page

continued from the previous page

ACMG/ AMP CC	Original ACMG/AMP rule summary	Specification	Stand alone	Very strong	Strong	Moderate	Supporting	Comments
						Arg204.		
PM2	Absent from controls.	General rec	na	na	na	Per original ACMG/AMP guidelines.	na	Variant must be completely absent from all population databases. The mean coverage of *RUNX1* in the population database used should be at least 20x.
PM3	For recessive disorders, detected *in trans* with a pathogenic variant.	na						FPD/AML is inherited in an autosomal dominant manner.
PM4	Protein length changes due to in-frame deletions/insertions in a non-repeat region or stop-loss variants.	Gene-specific, strength	na	na	na	In-frame deletion/insertion impacting at least one of the 13 hotspot residues Arg107, Lys110, Ala134, Arg162, Arg166, Ser167, Arg169, Gly170, Lys194, Thr196, Asp198, Arg201, Arg204	Other in-frame deletion/ insertion impacting residues 105-204 within the RHD.	see PM1
PM5	Missense change at AA residue where a different missense change determined to be pathogenic has been seen before.	Strength	na	na	Missense change at the same residue where ≥2 different missense changes have previously been determined to be pathogenic. PM5_strong cannot be applied together with PM1.	Missense change at the same residue where a different missense change has previously been determined to be pathogenic.	Missense change at the same residue where a different missense change has previously been determined to be likely pathogenic.	see PS1
PM6	Assumed *de novo* (but without confirmation of maternity and paternity) in a patient with the disease and no family history.	Disease-specific, strength	na	na	na	≥4 assumed *de novo* occurrences (without confirmation of maternity and paternity) in patients with the *RUNX1*-	2 or 3 assumed *de novo* occurrences (without confirmation of maternity and paternity) in patients with the *RUNX1*-	see PS2

continued on the next page

continued from the previous page

ACMG/AMP CC	Original ACMG/AMP rule summary	Specification	Stand alone	Very strong	Strong	Moderate	Supporting	Comments
						phenotype.	phenotype.	
PP1	Co-segregation with disease in multiple affected family members.	Disease-specific, strength	na	na	≥ 7 meioses observed within one or across multiple families.	5 or 6 meioses observed within one or across multiple families.	3 or 4 meioses observed within one or across multiple families.	(1) Affected individuals show at least one of the *RUNX1*-specific phenotypic criteria. (2) Only genotype and phenotype positive individuals and obligate carriers are counted. (3) Demonstration of co-segregation in multiple families is not required since many *RUNX1* variants are unique and only occur in one family.
PP2	Missense variant in a gene that has a low rate of benign missense variation and where missense variants are a common mechanism of disease.	na						Missense constraint z-score for *RUNX1* is <3.09.
PP3	Multiple lines of computational evidence support a deleterious effect on the gene or gene product.	General rec	na	na	na	na	Per original ACMG/AMP guidelines.	(1) PP3 should be applied for missense variants with a REVEL score of >0.75 (2) PP3 should be applied for missense or synonymous variants if the variant alters the last three bases of an exon preceding a donor splice site or the first three bases of an exon following a splice acceptor site and the predicted decrease in the score of the canonical splice site (measured by both MES and SSF) is at least 75% regardless of the predicted creation/presence of a putative cryptic splice site. (3) PP3 should also be applied for intronic variants (in introns 4-8) located in reference to exons at positions +3 to +5 for splice donor sites or -3 to -5 for splice acceptor sites for which the predicted decrease in the score is at least 75% (measured by both MES and SSF) regardless of the predicted creation/presence of a putative cryptic splice site. (4) PP3 cannot be applied for canonical splice site variants.
PP4	Patient's phenotype or family history is highly specific for a disease with a single genetic etiology.	na						FPD/AML does not exhibit a highly specific phenotype and there is substantial genetic heterogeneity.
PP5	Reputable source recently reports variant as pathogenic, but the evidence is not available to the laboratory to perform an independent analysis.	na						According to SVI recommendations.

Adapted from Table 1 of Luo and Feurstein *et al.*[18] ACMG: American College of Medical Genetics; AMP: Association for Molecular Pathology; CC: criteria code; , ESP: Exome Sequencing Project; 1000G: 1000 Genome project; ExAc: Exome Aggregation Consortium; MAF: minor allele frequency; na: not applicable; FPD/AML: familial platelet disorder with predisposition to acute myeloid leukemia; rec: recommendation; SSF: splice site finder; MES: MaxEntScan; SVI: ClinGen Sequence Variant Interpretation Working Group; LOF: loss-of-function; SNV: single-nucleotide variant; CNV: copy number variant; NMD: nonsense-mediated decay; AA: amino acid; MM-VCEP: Myeloid Malignancy Variant Curation Expert Panel; wt: wildtype; EMSA: electrophoretic mobility shift assay; IP: immunoprecipitation; FRET: fluorescence resonance energy transfer; IF: immunofluorescence; WB: western blot; gnomAD: Genome Aggregation Database; RHD: Runt homology domain.

fibroblasts later confirmed the germline, nonsense *RUNX1* variant. Her two sons and granddaughter also tested positive for the *RUNX1* variant (Figure 1).

Similar to this case, most patients with FPD/AML will have a characteristic phenotype (Table 1) including mild to moderate thrombocytopenia with normal platelet size, platelet α or dense granule secretion defects and impaired platelet aggregation, particularly in response to collagen and epinephrine as well as a predisposition to hematologic malignancies. Although there is variability in disease onset in FPD/AML,[3] development of a hematologic malignancy is common with a lifetime risk of ~44%: AML and MDS are common, other malignancies occur less frequently (Table 1).[19-23] FPD/AML has a high but incomplete

Table 3. Summary of *RUNX1* variant examples with application of the Myeloid Malignancy Variant Curation Expert Panel criteria.

Example No.	*RUNX1* variant NM_001754 (isoform C)	ClinVar Assertion	Criteria	MM-VCEP classification
1	c.610C>T (p.Arg204Ter)	PATH	PVS1, PM2, PS4_supporting, PP1	PATH
2	c.314A>C p.(His105Pro) c.315C>A p.(His105Gln)	VUS	PM2, PP3, PS4_supporting, PM1_supporting, PM5_supporting PS3, PM2, PP3, PM1_supporting	LPATH LPATH
3	c.253C>A p.(His85Asn)	CONF: OMIM: PATH Invitae: VUS	BS1, BS3, PP3	LBEN
4	c.508+3delA	PATH	PS3, PP1_strong, PM2, PP3, PS4_supporting	PATH
	c.444C>T p.(Thr148=)	Illumina: VUS Invitae: LBEN	BP4, BP7	LBEN
	c.1257G>A p.(Val419=)	VUS		VUS
5	Copy number variant, deletion of exon 2		PS4, PP1_strong, PM2, PVS1_moderate	PATH
6	c.1118C>A (p.Ser373Ter)		PVS1_strong, PM2, PS4_supporting	LPATH

The five-tier ClinVar classification: PATH (pathogenic), LPATH (likely pathogenic), VUS (variant of uncertain significance), LBEN (likely benign), BEN (benign); CONF (conflicting interpretations in ClinVar); criteria from Luo and Feurstein *et al.*[18]

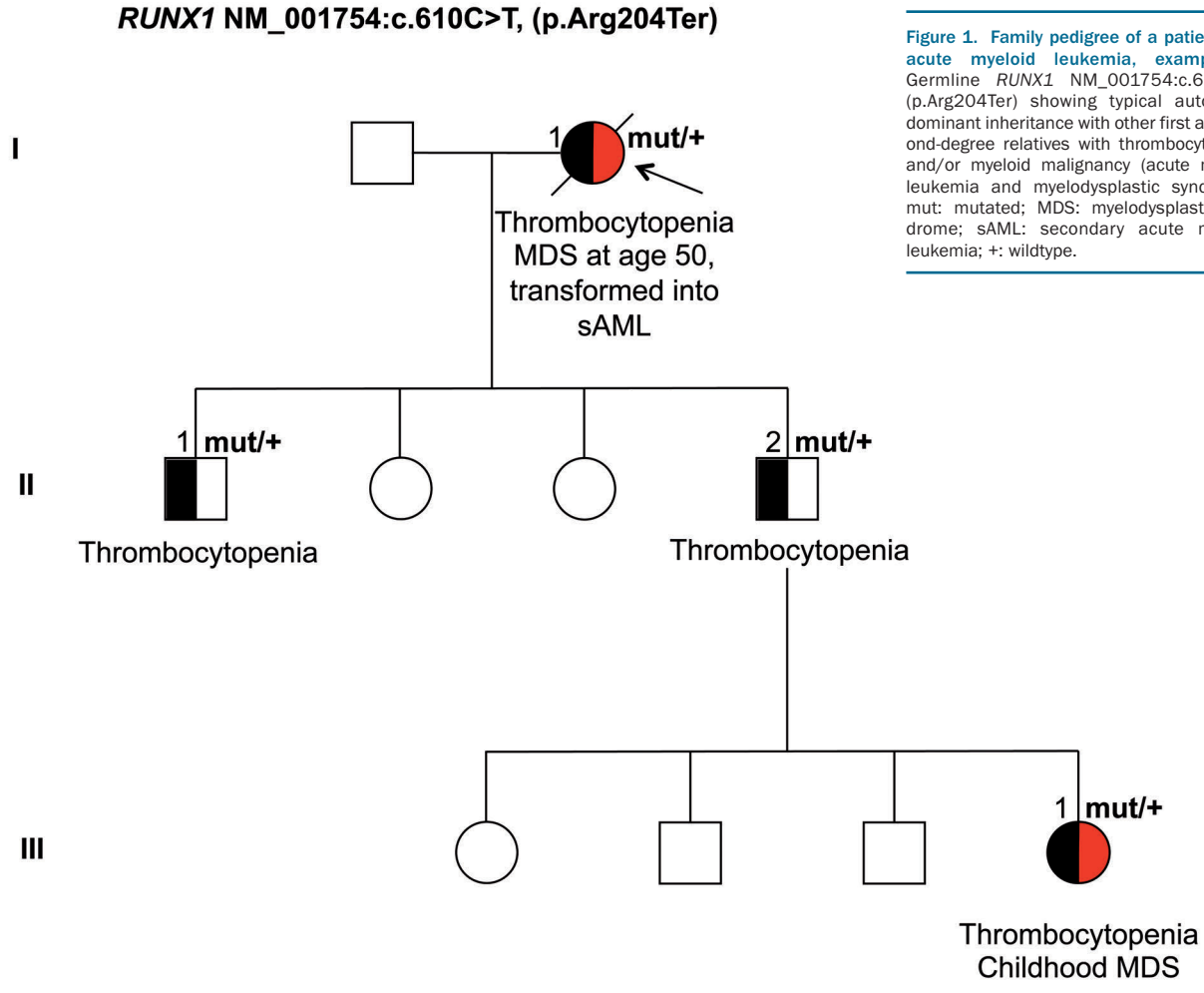

Figure 1. Family pedigree of a patient with acute myeloid leukemia, example 1. Germline *RUNX1* NM_001754:c.610C>T, (p.Arg204Ter) showing typical autosomal dominant inheritance with other first and second-degree relatives with thrombocytopenia and/or myeloid malignancy (acute myeloid leukemia and myelodysplastic syndrome). mut: mutated; MDS: myelodysplastic syndrome; sAML: secondary acute myeloid leukemia; +: wildtype.

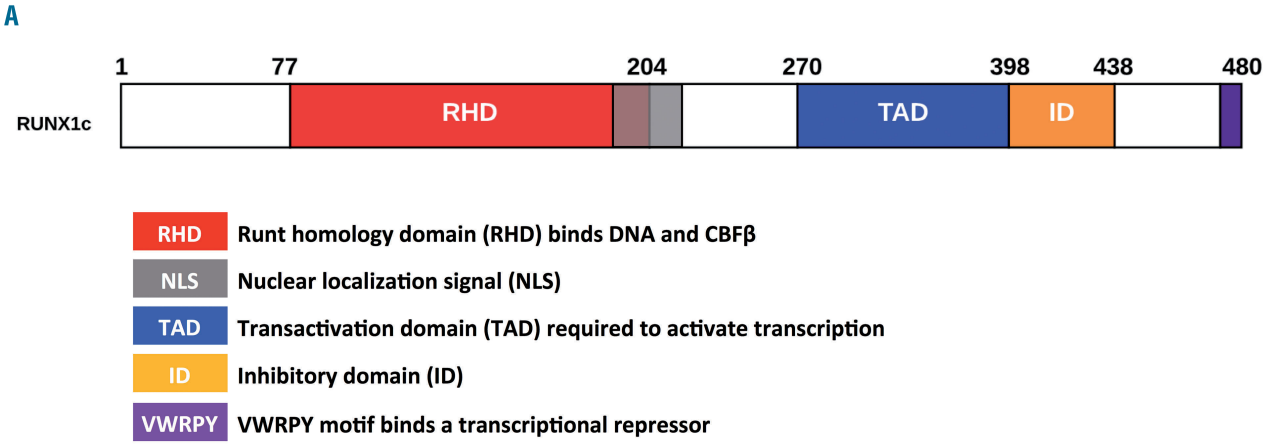

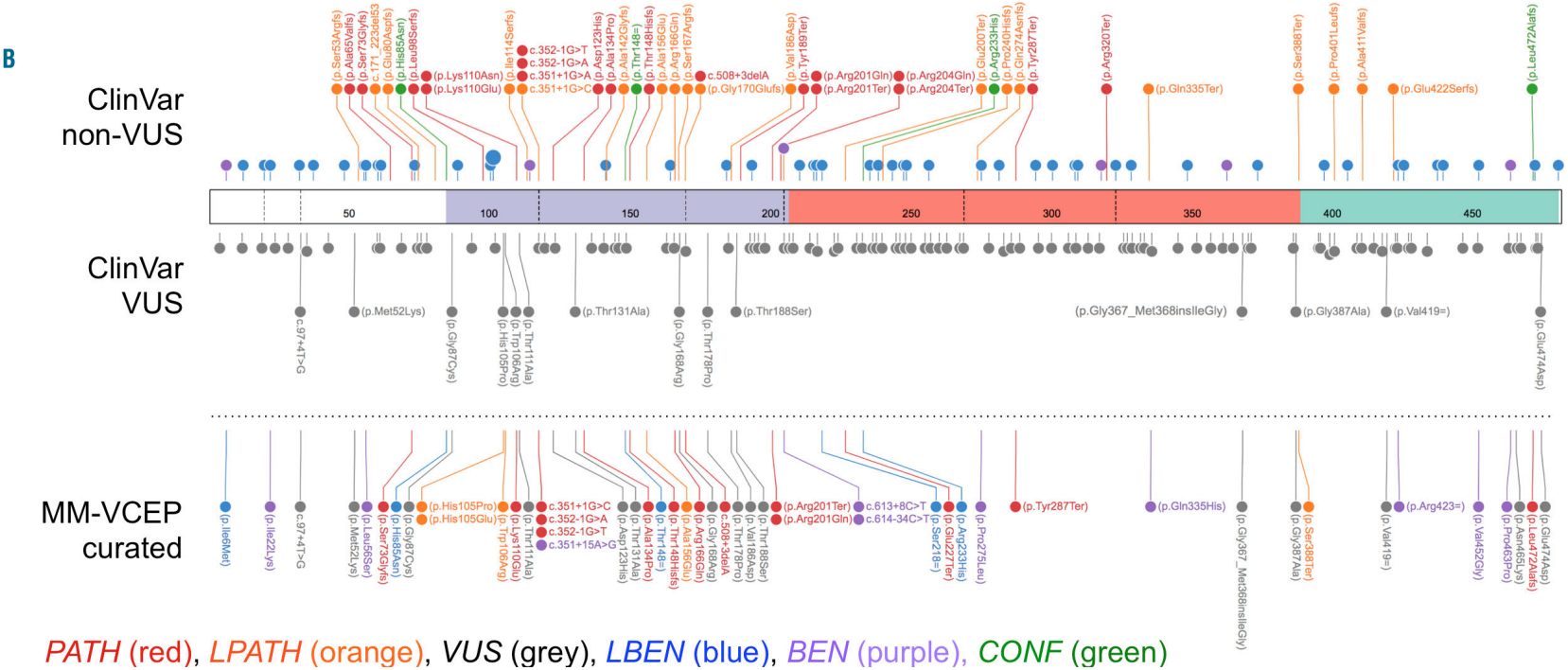

Figure 2. Overview of RUNX1 protein domains, ClinVar-deposited and MM-VCEP curated pilot and COSMIC variants. (A) Schematic of the RUNX1 protein showing its key domains, including the Runt homology domain (RHD); annotation according to MM-VCEP is based on *RUNX1* transcript isoform C (NM_001754). (B) Schematic of ClinVar-deposited *RUNX1* variants in a one-dimensional line plot showing the current ClinVar five-tier classification; data plotted using *proteinpaint* from St. Jude.org with data from ClinVar (accessed 6/2019); RHD (purple), and ID (green) are highlighted; numbers indicate amino acid; dotted lines indicate exon boundaries. Some ClinVar-deposited variants (in 5' and 3' untranslated regions and large deletions) are not shown. Lollipops representing the variants are colored as follows: PATH (red), LPATH (orange), VUS (grey), LBEN (blue), BEN (purple), CONF (green). MM-VCEP pilot variants[18] are shown in the third row. (*continued on next page*)

C

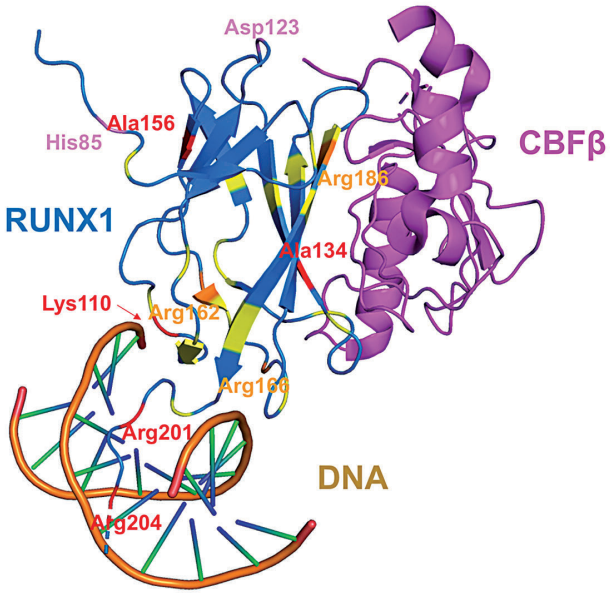

(*continued from previous page*) (C) Three-dimensional structure of the RHD of RUNX1 (blue) complexed to CBFβ (pink) and DNA (orange).[82] ClinVar *RUNX1* variants in this domain (codons 81 to 204 only) are shown using PyMOL, version 2.3.0, as follows: yellow = VUS (n=20), pink = CONF (n=2), orange = LPATH (n=3), red = PATH (n=5); BEN and LBEN variants (n=0). Non-missense variants are not shown. (D) One-dimensional line plot of somatic variants deposited with the Catalog of Somatic Mutations in Cancer (COSMIC: data release 3 Nov. 2018, version 87; *https://cancer.sanger.ac.uk/cosmic*). MM-VCEP: Myeloid Malignancy Variant Curation Expert Panel; PATH: pathogenic; LPATH: likely pathogenic; VUS: variant of uncertain significance; LBEN: likely benign; BEN: benign; CONF: conflicting interpretations in ClinVar.

D

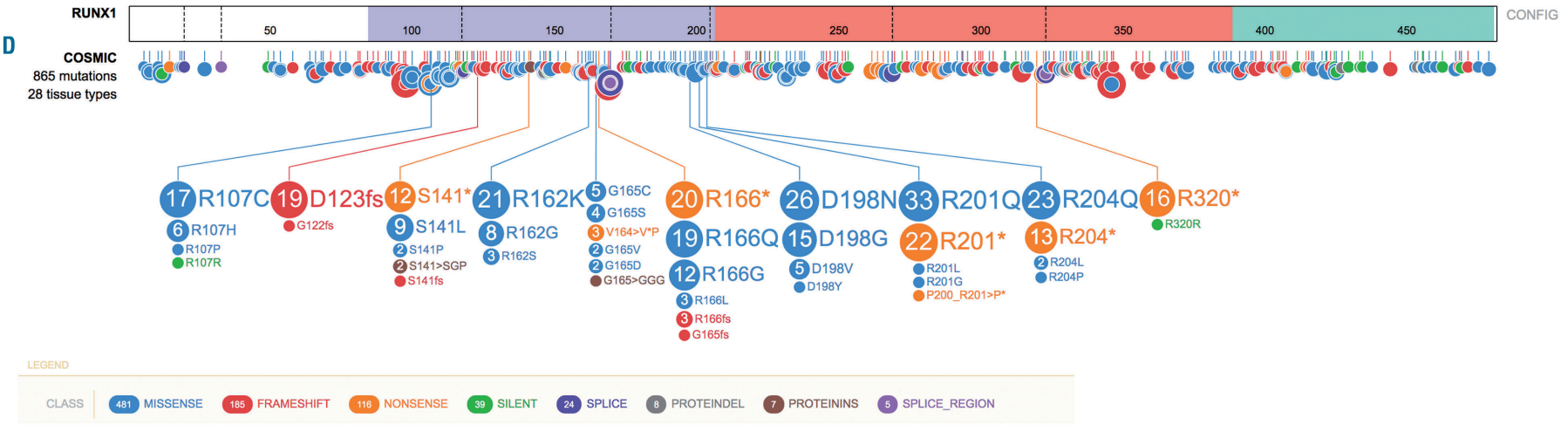

penetrance, with several affected individuals reported to have normal platelet counts or function.[19,24] The nonsense mutation in this patient (p.Arg204Ter) is predicted to lead to nonsense-mediated decay of the *RUNX1* mRNA transcript. *RUNX1* is located on the long arm of chromosome 21 and is translated into three major isoforms, designated RUNX1A, RUNX1B, and RUNX1C, by using two different promoters and alternative splicing. All transcripts are expressed during hematopoietic differentiation and/or maintenance of normal bone marrow function.[25-32] For variant annotation, the MM-VCEP utilizes the longest isoform, RUNX1C (NM_001754), as the default transcript, which includes all key domains such as the 128 amino acid (AA) long RUNT homology domain for DNA binding (RHD, AA 77-204), transactivation domain (TAD), inhibitory domain (ID) and the transcriptional repressor binding motif (VWRPY) and is most often used by clinical laboratories for *RUNX1* variant curation (Figure 2A). Germline variants have been reported throughout the gene in ClinVar with the majority currently classified as VUS (Figure 2B). The RUNX1 protein heterodimerizes through its RHD with CBFβ to form a master hematopoietic transcription factor (Figure 2C), which is essential for proliferation and differentiation of hematopoietic stem and progenitor cells, especially in the case of megakaryocytic differentiation.[33-35] Somatic mutations commonly occur in *RUNX1* (Figure 2D). According to *RUNX1*-specific criteria (Table 2),[18] the MM-VCEP applied the following codes (Table 3): PVS1 (nonsense variant predicted to undergo nonsense-mediated decay), PM2 (absence in all population databases), PS4_supporting (one proband meeting at least one of the *RUNX1* phenotype criteria), PP1 (co-segregation with disease in the family, three meioses) and arrived at a consensus classification of PATH.

Example 2. Missense variants, p.(His105Pro) (LPATH with PM2, PP3, PS4_supporting, PM1_supporting, and PM5_supporting) and p.(His105Gln) (LPATH with PS3, PM2, PP3, and PM1_supporting)

Missense mutations in *RUNX1* commonly occur in the RHD in somatic and germline contexts.[36-38] Of 325 *RUNX1* ClinVar variants 122 (37.5%) are missense, and currently in ClinVar, none in the RHD has been classified as BEN or LBEN (Figure 2C). When a novel missense variant is identified which has not been established as PATH or LPATH, it can be difficult to know whether the given change will affect protein function and explain the patient's phenotype. For example, two *RUNX1* missense variants in the RHD (NM_001754:c.314A>C, p.(His105Pro); and NM_001754:c.315C>A, p.(His105Gln)) were considered during the pilot variant analysis. The former was initially classified as a VUS in ClinVar (Figure 2B), but subsequently revised to LPATH upon MM-VCEP review (Figures 2B, 3A and 4). The conclusion of the LPATH assertion is based on the codes applied for this variant: PM2, PP3, PS4_supporting, PM1_supporting, and PM5_supporting (Table 3). Since the variant is completely absent from population databases, the MAF code PM2 is applied. For *in-silico* evaluation of missense variants, the MM-VCEP recommends using REVEL, a meta-predictor that combines 13 individual tools with high sensitivity and specificity, which has demonstrated the highest performance compared with individual tools or other ensemble methods.[39-41] The computational prediction code PP3 is applicable to the p.His105Pro variant due to a high REVEL score of 0.953 (MM-VCEP defined >0.75 as the cutoff). The ClinVar submitter (SCV000807773.1) provided us with the patient's clinical data from their laboratory and the proband met at least one of the *RUNX1* phenotype criteria (Table 1) which qualified for PS4_supporting. This example emphasizes the critical value of sharing internal laboratory data. There is only one meiosis in this family which is lower than the three required for the segregation code PP1. The MM-VCEP defined 13 residues in the RHD as the mutational hotspots for the PM1 code. In addition, variants in other parts of the RHD (AA 105-204) can have a reduced strength-level resulting in application of PM1_supporting. The last code PM5_supporting is applied on the p.(His105Pro) variant, because a different missense change p.(His105Gln) at the same residue has been classified as LPATH by the MM-VCEP (Table 3).

The codes PM2, PP3, PM1_supporting are also applicable to the p.(His105Gln) variant for the same reasons described. Furthermore, a strong pathogenic code PS3 is applied which contributes a significant weight to the final assertion. Transactivation assays of the p.(His105Gln) variant demonstrate altered transactivation (<20% of wildtype) and secondary assays also indicate altered DNA binding and functional consequences in a mouse model[42,43] manifested by disturbed myeloid differentiation and induction of a blast crisis or accelerated phase–like phenotype in mice.[42] These variants highlight the importance of evaluating similar variants and the critical benefit of functional studies showing that variants whose clinical significance were initially uncertain can be subsequently clarified to provide more definitive clinical classification and minimize reporting of VUS. Moreover, these variants demonstrate the value of leveraging the information on one variant to help classify another and data sharing between laboratories (Table 3).

Example 3. Missense variant, p.His85Asn (LBEN with BS1, BS3, and PP3)

RUNX1 NM_001754:c.253C>A, p.(His85Asn) is a missense mutation located within the RHD, but not within the mutational hotspot region (AA 105-204), with conflicting interpretations of pathogenicity in ClinVar (Figure 2B, C). Specifically, this variant had three submissions in ClinVar with two being PATH (submitted in 2002) and one being a VUS (submitted in 2018). The two 2002 submissions are from OMIM, which cited evidence from individual literature sources without a systematic curation process. Osato *et al.* reported an adult patient with AML carrying this variant.[44] However, the germline nature of the variant was not definitively determined. This variant has also been reported in an infant diagnosed with transient myeloproliferative disorder and Down syndrome whose phenotype does not meet any of the *RUNX1* phenotype criteria.[45] After analysis and curation by the MM-VCEP using the *RUNX1*-specific classification rules,[18] this variant was re-classified as LBEN, meeting codes BS1 and BS3, despite meeting PP3 (Table 3). According to the penetrance, prevalence and genetic and allelic heterogeneity of *RUNX*1, MM-VCEP refined the *RUNX1* specific MAF threshold for application of BS1 to 0.00015 (0.015%). The highest MAF of the p.His85Asn variant is 0.00043 (8 out of 18,768 alleles) from the East Asian subpopulation in the Genome Aggregation Database (gnomAD) which is higher than the *RUNX1*-

specific BS1 cutoff. Experimental studies have shown that this missense change displays normal transactivation activities (80-114% of wildtype) and does not affect DNA binding, heterodimerization with CBFβ or subcellular localization of the RUNX1 protein.[44,46] Therefore, the strong benign functional evidence code, BS3, is applied. Although this variant disrupts KMT2A binding, which impairs proper H3K4 histone methylation, this is not a qualified functional assay based on the MM-VCEP *RUNX1*-specific PS3/BS3 rule. Moreover, another well-established BEN variant p.(Leu56Ser) also impairs KMT2A binding.[46] Likely due to the location of the p.(His85Asn) variant within the RHD (Figure 2B), the REVEL score (0.852) of this variant is higher than the MM-VCEP defined 0.75 cutoff,[18] which results in the variant meeting a conflicting PP3 code. However, combining the BS1, BS3 and PP3 codes, a final assertion of LBEN is made based on a Bayesian classification framework.[15] Given that His85 is located away from binding interfaces in the three-dimensional structure (Figure 3B), it seems reasonable that variants at this position are LBEN.

This example highlights the value of functional studies in the context of the MM-VCEP variant curation and shows that substantive corrections of variant annotation may occur upon application of ClinGen MM-VCEP rules.[18] Implicit in this process is the expectation that as knowledge about FPD/AML improves with more functional or family data becoming available, the MM-VCEP rules are subject to revision so that annotation of clinical variants will become more accurate (Figure 4). ClinVar variant classifications such as VUS or those with conflicting interpretations may thus evolve to more diagnostic certainty.[47,48]

Example 4. Synonymous/intronic/non-coding variants, c.508+3delA (PATH with PS3, PP1_strong, PM2, PP3, PS4_supporting), p.Thr148= (LBEN with BP4, BP7) and p.Val419= (VUS with no codes)

RUNX1 variants affecting canonical splice positions ±1 or 2 at intron-exon boundaries are expected to disrupt

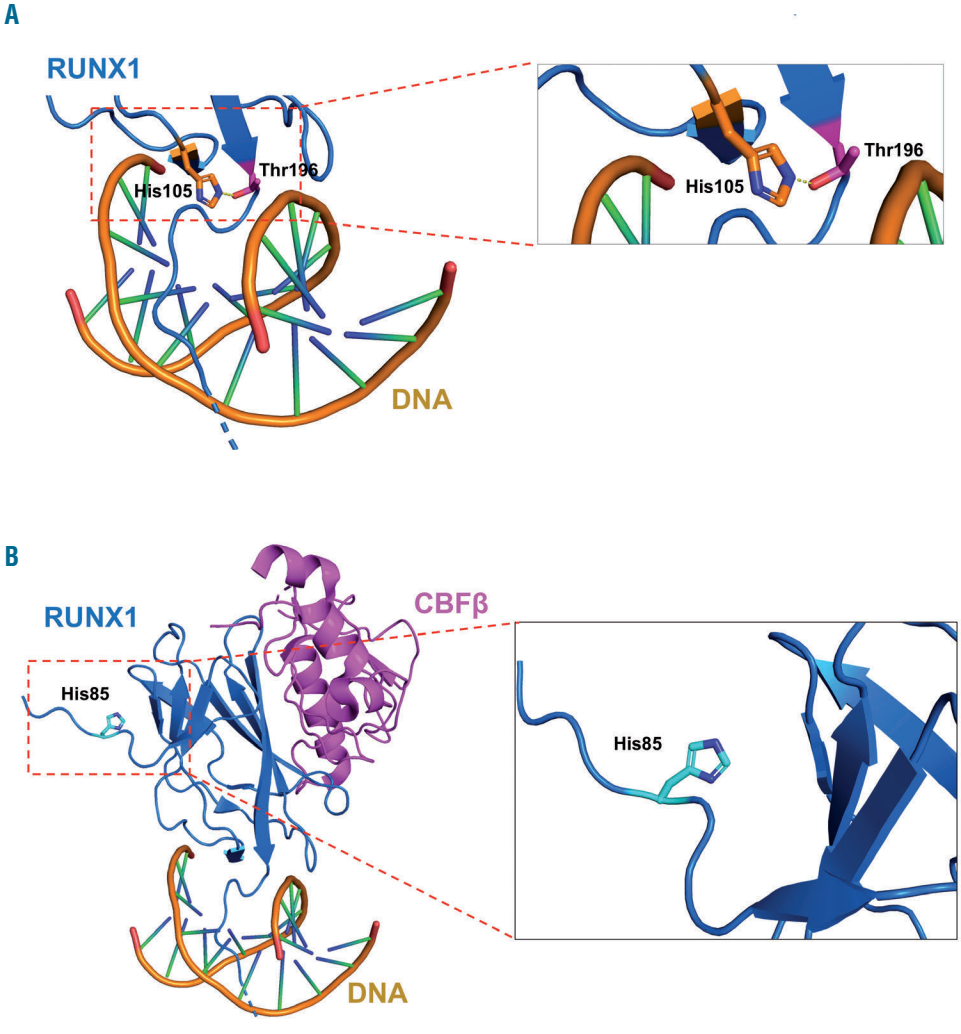

Figure 3. Three-dimensional structure of RUNX1 missense variants His105 and His85 considered as examples 2 and 3. (A) RUNX1 His105 is important functionally due to its location and thus involvement in DNA binding and close interaction with Thr196 by hydrogen bonding. Thr196 is a hotspot residue known to be critical. This structure-function relationship further supports classification of His105 variants as likely pathogenic (LPATH). (B) RUNX1 His85 is located close to the start of the Runt homology domain in a linker region, and is located far from the DNA binding surface. It is not involved in the core β-barrel structure and does not show any interactions, further supporting its classification as likely benign (LBEN). Structure of RUNX1 complexed to DNA and CBFβ (*https://www.rcsb.org/structure/1H9D*)[82] and plotted using PyMOL version 2.3.0.

splicing, leading to protein dysfunction (see *Online Supplementary Table S3* of reference by Luo and Feurstein[18]). All of the three canonical splicing site variants in the pilot set were classified as PATH or LPATH. More challenging, however, is the consideration of synonymous/intronic/non-coding variants which may result in cryptic splice site activation, and/or enhancement or repression of adjacent canonical splice sites. For example, the intronic NM_001754:c.508+3delA variant has been reported in a single family with disease segregation (8 meioses, PP1_strong). Several family members were diagnosed with thrombocytopenia, aspirin-like platelet aggregation defects, and dense granule abnormalities.[49] This variant is absent from population databases (PM2) and both splicing predictors (MaxEntScan and SpliceSiteFinder)[50,51] predict a significant decrease in the score of the canonical splice site (PP3). Moreover, experimental reverse transcriptase polymerase chain reaction studies (PS3), using RNA derived from two affected family members, were performed and indicate the creation of a novel cryptic splice site 23 nucleotides upstream of the normal splice site resulting in a frameshift p.(Arg162fs*177), and the transcript is predicted to undergo nonsense-mediated decay.[49] Combining all of these codes, a final assertion of PATH is given by the MM-VCEP (Table 3).

BP7 is a benign code specifically designed to evaluate synonymous/intronic/non-coding variants in the ACMG/AMP framework. BP7 can be applied if computational evidence suggests no impact on splicing, and the nucleotide is not conserved. The ClinVar variant with conflicting interpretations in ClinVar, NM_001754:c.444C>T, p.(Thr148=), has been classified as LBEN by the MM-VCEP using BP7 and the benign *in silico* prediction code, BP4 (Table 3). This nucleotide change is predicted to have no impact on splicing and it is also not conserved (phyloPscore: -4.3832, below the MM-VCEP-specified threshold of <0.1[18]). Clinical data from seven individuals with this variant were acquired from the original ClinVar submitter (SCV000761123.1) and revealed that none of the probands met any of the *RUNX1* phenotypic criteria.[18] Currently, only two *RUNX1* variants have been reported to display an abnormal splicing effect as demonstrated by RNA assays.[11,49] The potential effects of other splicing variants rely solely on *in silico* predictions. Although there is robust effort in consideration of algorithms to predict the effects of splicing variants, these algorithms require further evaluation. Indeed, we know of only limited experimental data within the *RUNX1* gene specifically to test these tools. Accordingly, the synonymous variant, NM_001754:c.1257G>A, p.(Val419=) is predicted to create alternative splice acceptor sites, but is not expected to abolish any existing consensus sites, as it is too far away from either end of the exon. Due to this *in silico* prediction result, none of the PP3/BP4 and BP7 codes can be assigned, and the classification of this variant remains a VUS. Further resolution of the significance of this variant could be obtained through parental testing, and/or RNA-sequencing data.

Example 5. Copy number variants, deletion of exon 2 (PATH with PVS1_moderate, PM2, PS4, and PP1_strong)

Not infrequently, patients with FPD/AML have been reported to have copy number variants resulting in intragenic deletions of *RUNX1*.[52] As part of our pilot cohort, we evaluated several probands with copy number variants which at a minimum include *RUNX1* exon 2 deletion; data from two cases are shown (Figure 5). The analysis of copy number variants by using next-generation sequencing and/or single nucleotide polymorphism microarrays is particularly challenging because the breakpoints are often not captured in the sequenced regions or the microarray resolution defines only a range for the chromosomal location of the breakpoint, respectively, and thus the nucleotide level breakpoint may remain unknown. It can, therefore, be difficult to know the effect of partial gene/exon deletions, such as if the deletion is in- or out-of-frame, the latter of which may also lead to the introduction of a premature stop codon. Nevertheless, partial or whole gene deletion of *RUNX1* is expected to result in haploinsufficiency of the RUNX1 protein. Although MM-VCEP rules did not include recommendations for the formal classification of copy number variants,[18] several points should be noted. First, evaluation of the reference *Database of Genomic Variants* (*http://dgv.tcag.ca/dgv/app/home*) shows that copy number variants affecting *RUNX1* do not appear to be frequent.[18] Second, annotation of the specific breakpoints of these intragenic deletions may not always be possible, given that whole genome sequencing is not typically performed. Since contiguous exon deletion is a common pathogenic disease mechanism, it is imperative that laboratories performing germline testing for *RUNX1* use concurrent microarray testing, develop appropriate next-generation sequencing bioinformatics pipelines, or use alternate molecular techniques, such as quantitative polymerase chain reaction and multiplex ligation-dependent probe amplification, to screen for and exclude copy loss,

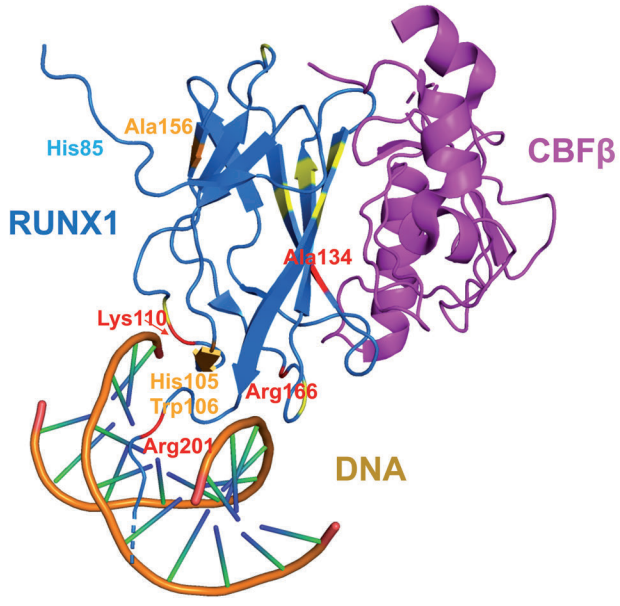

Figure 4. Three-dimensional structure of MM-VCEP-classified RUNX1 missense variants in the RHD. Variants in the RUNX1 RHD (blue) are shown highlighting the PATH, LPATH, and LBEN missense variants curated according to ClinGen MM-VCEP rules. PATH (red, n=4), LPATH (orange, n=4) and LBEN (cyan, n=1) variants are found proximate to key interaction domains of RUNX1 with DNA or its binding partner *CBFβ* (pink). VUS missense variants are shown in yellow (n=7). Non-missense variants and variants outside the RHD are not shown. (PyMOL version 2.3.0; structural data *https://www.rcsb.org/structure/1H9D*[82]). MM-VCEP: Myeloid Malignancy Variant Curation Expert Panel; RHD: Runt homology domain; PATH: pathogenic; LPATH: likely pathogenic; VUS: variant of uncertain significance; LBEN: likely benign; BEN: benign; CONF: conflicting interpretations in ClinVar.

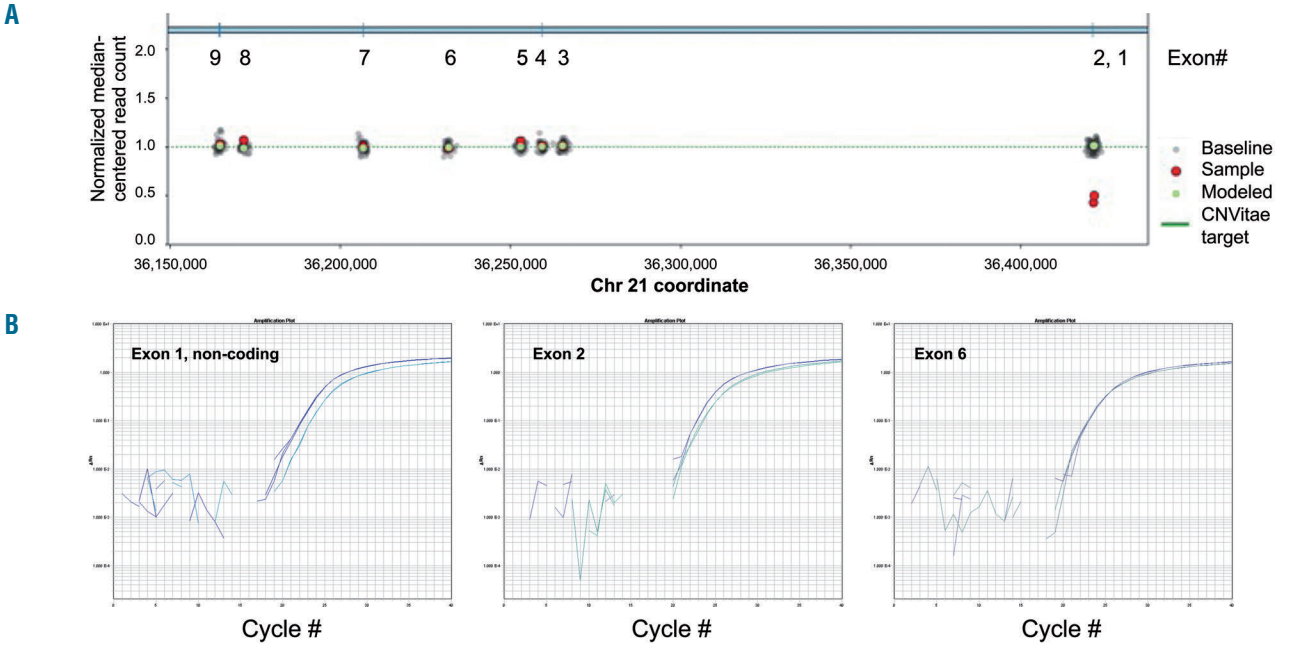

Figure 5. Copy number variant, deletion of exons of *RUNX1*. Testing for germline variants should include evaluation for copy number variants (CNV). (A; B) Clinical data from two different patients showing copy loss of *RUNX1* exons 1 and 2; one proband was identified by next-generation sequencing (A) and the other by single nucleotide polymorphism array analysis (data not shown), and confirmed by quantitative polymerase chain reaction (qPCR) (B). For the latter patient, qPCR confirmation showed heterozygous deletion of exons 1 and 2 with no loss in other exons (exon 6 only shown). CNV are difficult for annotation as breakpoints of the deletion may not be captured and thus, whether the deletion is in- or out-of-frame may not be known without whole genome sequencing. Testing of a germline sample (e.g. fibroblasts) is preferred to blood or bone marrow for CNV evaluation, as somatic copy loss may also occur in the tumor context.

Table 4. Variant details for example 6 from genome and exome sequencing, RNA-sequencing and karyotype analysis.

Structural	*KMT2A*, NM_005933, 11q23 (chr11:118347001-118353900) partial tandem duplication exons 4-8, predicted to be in-frame
SNVs and indels	*IDH1*, NM_005896:c.394C>T, p.(Arg132Cys), VAF ~50% *PHF6*, NM_001015877:c.860G>T, p.(Gly287Val), VAF ~ 95% *RUNX1*, NM_001754:c.1118C>A, (p.Ser373Ter), VAF ~50%
Copy number variants	*PALB2*, heterozygous exon 7 copy loss, NM_02467, chr16p12.2(23637272_23637800)x1 for hg19

Chr: chromosome; VAF: variant allele frequency.

as sequencing for single nucleotide variants and indels alone is insufficient for comprehensive germline evaluation. For the two cases herein (Figure 5), although we do not know the specific breakpoints for each, the common deletion of at least exon 2 allows us to apply the following codes: PVS1_moderate, PM2, PS4 (4 probands: 3 with chronic thrombocytopenia and 1 with AML), PP1_strong (7 meioses) to arrive at a PATH classification (Table 3).

Example 6. Late truncation variant, (p.Ser373Ter) (LPATH with PVS1_strong, PM2, and PS4_supporting)

A 14-year old male with a non-contributory family history presented with malaise, poor appetite, night sweats, and intermittent fever of about 1-month duration, thrombocytopenia ($27x10^9$/L), and subsequent bone marrow biopsy showed AML (PS4_supporting). After whole genome and exome sequencing on paired tumor and germline samples, along with RNA-sequencing (directed for recurrent fusion identification), his leukemia sample was shown to be *RUNX1*-mutated (NM_001754:c.1118C>A, (p.Ser373Ter)), hypodiploid with Y chromosome loss, without chromosomal fusions, and loss of heterozygosity, but had additional mutations including an intragenic heterozygous deletion of one copy of exon 7 of *PALB2* (Table 4).

Similar to Example 1, this *RUNX1* (p.Ser373Ter) variant is a nonsense mutation; however, it is not predicted to undergo nonsense-mediated decay, but rather is expected to generate a truncated protein without part of the TAD, ID and the VWRPY motif (Figure 2A). From a computational and predictive perspective, a PVS1_strong code is assigned following the PVS1 decision tree for null or truncating variants in *RUNX1*.[18] The variant is absent from the gnomAD and other population databases (with confirmed >20x sequencing coverage at this position in gnomAD). Given the variant's absence from population databases and adequate sequencing coverage of the region, a PM2 code is assigned. Although no additional evidence for the other categories (functional, segregation, *de novo* and allelic data) are available, this variant can be classified as LPATH (PVS1_strong, PM2, PS4_supporting). It is of interest to note that the somatic alterations reported in the diagnostic leukemia sample included partial tandem duplication of *KMT2A* and a single nucleotide varia-

tion in *PHF6*. Alterations in these two genes have been reported as cooperating events seen in leukemias from patients with germline *RUNX1* mutations.[37,53]

Importantly, if consideration is given to the mutations found in the leukemic cells in isolation, one cannot determine the germline or somatic origin of the variants reported. This is the case for most of the 'tumor-only' analyses being performed in many clinical laboratories. Without paired analysis of true germline tissue (e.g. cultured skin fibroblasts), such studies cannot definitively identify germline variants. In this case, the *KMT2A* partial tandem duplication and single nucleotide variation in *PHF6* and *RUNX1* could be tumor-drivers in the AML. However, given the sequencing data, including the variant allele frequency, both the *RUNX1* mutation and the *PALB2* exon 7 intragenic deletion could be germline variants. A detected variant allele frequency approaching 50% or 100% in the tumor may indicate potential germline origin[1] with either an intact wildtype allele or loss of heterozygosity, respectively. However, a high variant allele frequency cannot reliably serve as a proxy for testing of a true germline source. Therefore, if there is concern that a variant could be constitutional, testing of true germline material is critical.[1]

Discussion

Kindreds with FPD/AML were first reported by Luddy *et al.* in 1978[54] and phenotypically well-described as having a bleeding diathesis and myeloid neoplasia by Dowton *et al.* in 1985.[55,56] Subsequent linkage analysis identified *RUNX1* as the candidate gene at chromosome 21q22,[11] and mutations were detected in FPD/AML families in 1999.[11] Since these initial early reports, routine clinical testing for *RUNX1* gene mutations is now commonplace for the evaluation of somatic and germline disease in patients with myeloid neoplasms and thrombocytopenia.

In general, *RUNX1* variants include single nucleotide variations and indels, such as missense, nonsense, frameshift, and splice site variants, and copy number variations such as whole-gene and intragenic deletions. *RUNX1* is also frequently mutated somatically in AML and often the partner of various translocations resulting in gene fusions, such as t(8;21)(q22;q22) *RUNX1-RUNX1T1*.[57,58] To date, fusions of *RUNX1* have not been reported in the germline context, and most germline *RUNX1* variants are unique,[24] although some have been rarely seen in unrelated families. Given the limited data on rare variants, the clinical annotation of new variants remains challenging. The MM-VCEP was convened by ASH/ClinGen (*Online Supplementary Figure S1*) to develop rules for curating gene variant causing predisposition to myeloid neoplasia (Table 2). In this review, we describe the classification of six variant examples (Table 3) using the gene- and disease-specific rule modifications of the original ACMG/AMP 2015 framework.[14] Several points should be made.

First, it is critical to ensure that genomic testing intended to assess a germline predisposition is performed on a definitive germline sample because malignant hematologic diseases involve the peripheral blood and bone marrow, and somatic variants in these diseases can confound variant interpretation if an inappropriate sample is used. Here, in keeping with our MM-VCEP rules, cultured skin fibroblasts (gold standard, albeit invasive, costly, and time-consuming), cultured bone marrow mesenchymal stromal cells or DNA from hair roots are appropriate sources.[59,60] Alternatively, confirmation of the germline nature of a variant can be achieved by demonstrating its presence in two or more related individuals. The possibility of sample contamination by malignant cells is significant and consequently, peripheral blood, bone marrow, saliva, buccal swabs, DNA from paraffin blocks and even fingernails, which can contain monocytes, are inappropriate samples for germline testing. In some institutions, laboratories may accept T cells, enriched via flow cytometry sorting or column-based magnetic cell separation, as a germline sample for testing. It is important to recognize that some somatic alterations may occur early in hematopoietic stem and progenitor cells with multilineage potential to differentiate into T cells,[61] as recent single-cell studies have confirmed.[62-65] Thus, if T cells are used, the possibility that a detected variant may be somatic should still be considered. Once a variant is confirmed to be germline in a proband, however, additional testing for the known variant in related family members can be performed on any tissue source.

Second, we should keep an open mind about disease-causing alleles and the type of variants that may be seen and thus, we advocate for a broad testing approach. For example, in some laboratories, non-coding variants are automatically filtered as part of bioinformatic pipelines and may thus be omitted from subsequent review and interpretation. Recently, however, synonymous variants[66] in the *GATA2* gene, another gene predisposing to myeloid malignancy, were reported in addition to the known pathogenic deep intronic variants of an enhancer region of *GATA2*.[67] In *ANKRD26*, variants of the 5' untranslated region cause disease.[68,69] Furthermore, copy number alterations may not be assessed in somatic tumor testing panels. As diagnosticians, it is important to think broadly when analyzing genomic information for germline pathogenic variants. Given that these are rare diseases, we should not inadvertently exclude disease mechanisms and/or specific classes of mutations. For example, in case 4, some variants may remain as VUS until additional functional or familial segregation data become available for reclassification.[47,48]

Third, definitive annotation of variants by one institution will likely remain challenging. However, consistent application of MM-VCEP rules with ClinVar data deposition and thus inter-laboratory correspondence can significantly improve the accuracy and consistency of variant curation. In this regard, examples 2, 3, and 5 show how leveraging shared genomic and phenotypic data can be helpful to clarify VUS. We therefore advocate that clinical variant data be deposited into ClinVar. Specifically, laboratories offering germline testing should modify their test requisition forms to indicate that de-identified phenotype and variant data will be deposited into ClinVar as part of ongoing quality assurance and improvement efforts (*https://www.clinicalgenome.org/share-your-data/laboratories/*).[70,71] Additional details of the ClinVar deposition process are included in *Online Supplementary Figure S1*.

Fourth, *RUNX1* variant curation will improve as more is understood about the disease and gene through functional and family studies. Currently, variant annotation remains a challenging task, because of limited data for

determining the functional effect of a given variant change, despite methods of engineering variants for functional assessment.[72-74] Early studies in Speck's laboratory on *RUNX1* showed the significance of key residues in the RHD of RUNX1 by performing alanine scanning mutagenesis.[75,76] However, these early approaches are limited in that not every combination of nucleotide change was explored. By contrast, recent high-throughput functional genomic methods,[77] known as deep mutational scanning, utilize large-scale approaches to mutate every nucleotide of a gene, permitting one to test the functional consequence of all single nucleotide variations. This has, for example, been recently demonstrated for *BRCA1*.[78] Additionally, systematic mutagenesis of *PTEN* has provided a wealth of functional data to inform the classification of *PTEN* variants,[79] in conjunction with published rules developed by the PTEN-VCEP.[80] In the future, focused functional assays targeting specific VUS[16] and deep mutational scanning of genes should contribute to variant curation to resolve VUS.

Fifth, while functional testing of every given genomic variant is possible, it can be costly and difficult to do for every clinically significant gene. In this regard, family studies can aid in the classification of VUS. By systematically evaluating disease segregation in family members with paired genotyping for a known variant, accurate classification of a given variant can be achieved. For example, a recent study showed that this family-based method for variant classification can resolve a VUS classification more frequently than other traditional approaches can.[7,81] For rare diseases, such as FPD/AML, detailed pedigree and segregation analyses can be incredibly informative, and clinicians should be encouraged to test family members when possible, seeking help from local genetic counselors and/or geneticists as needed.[81] Hematologists and oncologists need to consistently take a detailed family and genetic history.

Summary

RUNX1 germline mutations associated with FPD/AML are key events in myeloid neoplasms, thrombocytopenia and leukemogenesis and represent a model of a germline gene disorder with pathogenic variants predisposing to myeloid and (to a lesser extent) lymphoid malignancies.[36] Providing an accurate clinical and pathologic variant interpretation for genomic variants detected in routine laboratory testing will remain critical for the provision of appropriate clinical care, including genetic counseling for the index patient and their at-risk relatives and donor-selection, in some cases benefiting from stem cell transplantation.

The ClinGen MM-VCEP variant interpretation process requires a detailed understanding of the biological and functional properties of *RUNX1* and disease phenotype. Here, we demonstrate the process for sequence variant interpretation of six variant examples. By introducing and thus standardizing genomic variant interpretation, we hope to improve patients' care, identify VUS that may benefit from directed research and encourage sharing of internal laboratory data to resolve uncertainty. In doing so, the MM-VCEP rules may ensure optimal insurance coverage for appropriate genomic testing and screening of family members, and ensure appropriate reimbursement for clinical laboratories. Overall, the ASH/ClinGen collaboration resulting in the first set of modified criteria for germline *RUNX1* variants should improve clinical care and recommendations for FPD/AML patients.

Acknowledgments

The Variant Curation Expert Panel (VCEP) thanks the Clinical Genome Resource (ClinGen) Sequence Variation Interpretation Working Group as well as the Executive Committee of the Hereditary Cancer Clinical Domain Working Group. The variant curation rules discussed in this publication were generated by the American Society of Hematology (ASH) in collaboration with Baylor College of Medicine and the University of North Carolina, National Institutes of Health (NIH)-funded ClinGen grant award recipients. The NIH supported this work through: U41HG009649 (to XL, and SEP) and U41HG009650 (to SM and JER), and the 2018 NIH/NCI Leukemia SPORE DRP award (P50CA100632-16, project 00007529) (C.D.D.).

The ASH-ClinGen Myeloid Malignancy MM-VCEP collaborative group includes co-authors (DW and LAG as co-chairs; XL, SF, SM, CK and DEP), and others, as follows:[18] Christopher Porter (Emory University, USA), Sarah Jackson (GeneDx, USA), Sioban Keel (University of Washington, USA), Michael Chicka (Prevention Genetics, USA), Anna Brown (Center for Cancer Biology, Australia), Anupriya Agarwal (Oregon Health & Science University, The Knight Cancer Institute, USA), Minjie Luo (Children's Hospital of Philadelphia, USA), Zejuan Li (Houston Methodist Institute for Academic Medicine, USA), Justyne E. Ross (University of North Carolina, USA), Panagiotis Baliakas (Uppsala University, Sweden), Courtney D. DiNardo (UT MD Anderson Cancer Center, USA), Alison Bertuch (Baylor College of Medicine, USA), Nikita Mehta (Mayo Clinic, USA), Thomas Vulliamy (Queen Mary University of London, UK), Ying Wang (BioReference, USA), Kim Nichols (St Jude Children's Research Hospital, USA), Luca Malcovati (University of Pavia & S. Matteo Hospital, Italy), Michael Walsh (Memorial Sloan Kettering Cancer Center, USA), Lesley Rawlings (Centre for Cancer Biology, Australia), Shannon McWeeney (Oregon Health & Science University, USA), Jean Soulier (Hopital Saint-Louis and University de Paris, France), Anna Raimbault (INSERM U1016, Institut Cochin, France), Mark Routbort (UT MD Anderson Cancer Center, USA), Liying Zhang (Memorial Sloan Kettering Cancer Center, USA), Gabriella Ryan (American Society of Hematology, USA), Nancy Speck (Abramson Family Cancer Research Institute, USA), and Sharon E. Plon (Baylor College of Medicine, USA).

References

1. Drazer MW, Kadri S, Sukhanova M, et al. Prognostic tumor sequencing panels frequently identify germ line variants associated with hereditary hematopoietic malignancies. Blood Adv. 2018;2(2):146-150.
2. Churpek JE, Pyrtel K, Kanchi KL, et al. Genomic analysis of germ line and somatic variants in familial myelodysplasia/acute myeloid leukemia. Blood. 2015;126(22):2484-2490.
3. Churpek JE, Bresnick EH. Transcription factor mutations as a cause of familial myeloid neoplasms. J Clin Invest. 2019;129(2):476-488.
4. Arber DA, Orazi A, Hasserjian R, et al. The 2016 revision to the World Health Organization classification of myeloid neoplasms and acute leukemia. Blood. 2016;127(20):2391-2405.
5. Swerdlow SH CE, Harris NL, Jaffe ES, Pileri SA, Stein H, Thiele J. WHO Classification of Tumours of Haematopoietic and Lymphoid Tissues, 2017.
6. Kohane IS, Masys DR, Altman RB. The incidentalome: a threat to genomic medicine. JAMA. 2006;296(2):212-215.
7. Shirts BH, Pritchard CC, Walsh T. Family-specific variants and the limits of human genetics. Trends Mol Med. 2016;22(11):925-934.
8. Beri-Dexheimer M, Latger-Cannard V, Philippe C, et al. Clinical phenotype of germline RUNX1 haploinsufficiency: from point mutations to large genomic deletions. Eur J Hum Genet. 2008;16(8):1014-1018.
9. Schlegelberger B, Heller PG. RUNX1 deficiency (familial platelet disorder with predisposition to myeloid leukemia, FPDMM). Semin Hematol. 2017;54(2):75-80.
10. Sood R, Kamikubo Y, P. L. Role of RUNX1 in hematological malignancies. Blood. 2017;129(15):2070-2082. Erratum in: Blood. 2018;131 (3):373.
11. Song WJ, Sullivan MG, Legare RD, et al. Haploinsufficiency of CBFA2 causes familial thrombocytopenia with propensity to develop acute myelogenous leukaemia. Nat Genet. 1999;23(2):166-175.
12. Landrum MJ, Lee JM, Riley GR, et al. ClinVar: public archive of relationships among sequence variation and human phenotype. Nucleic Acids Res. 2014;42(Database issue):D980-985.
13. Rehm HL, Berg JS, Brooks LD, et al. ClinGen--the Clinical Genome Resource. N Engl J Med. 2015;372(23):2235-2242.
14. Richards S, Aziz N, Bale S, et al. Standards and guidelines for the interpretation of sequence variants: a joint consensus recommendation of the American College of Medical Genetics and Genomics and the Association for Molecular Pathology. Genet Med. 2015;17(5):405-424.
15. Tavtigian SV, Greenblatt MS, Harrison SM, et al. Modeling the ACMG/AMP variant classification guidelines as a Bayesian classification framework. Genet Med. 2018;20(9):1054-1060.
16. Brnich SE, Rivera-Munoz EA, Berg JS. Quantifying the potential of functional evidence to reclassify variants of uncertain significance in the categorical and Bayesian interpretation frameworks. Hum Mutat. 2018;39(11):1531-1541.
17. Rivera-Munoz EA, Milko LV, Harrison SM, et al. ClinGen Variant Curation Expert Panel experiences and standardized processes for disease and gene-level specification of the ACMG/AMP guidelines for sequence variant interpretation. Hum Mutat. 2018;39(11):1614-1622.
18. Luo X, Feurstein S, Mohan S, et al. Gene-specific criteria for germline RUNX1 variant curation: recommendations from the ClinGen Myeloid Malignancy Variant Curation Expert Panel. Blood Adv. 2019;3(20):2962-2979.
19. Owen CJ, Toze CL, Koochin A, et al. Five new pedigrees with inherited RUNX1 mutations causing familial platelet disorder with propensity to myeloid malignancy. Blood. 2008;112(12):4639-4645.
20. Shiba N, Hasegawa D, Park MJ, et al. CBL mutation in chronic myelomonocytic leukemia secondary to familial platelet disorder with propensity to develop acute myeloid leukemia (FPD/AML). Blood. 2012;119(11):2612-2614.
21. Linden T, Schnittger S, Groll AH, Juergens H, Rossig C. Childhood B-cell precursor acute lymphoblastic leukaemia in a patient with familial thrombocytopenia and RUNX1 mutation. Br J Haematol. 2010;151(5):528-530.
22. Toya T, Yoshimi A, Morioka T, et al. Development of hairy cell leukemia in familial platelet disorder with predisposition to acute myeloid leukemia. Platelets. 2014;25(4):300-302.
23. Nickels EM, Soodalter J, Churpek JE, Godley LA. Recognizing familial myeloid leukemia in adults. Ther Adv Hematol. 2013;4(4):254-269.
24. Latger-Cannard V, Philippe C, Bouquet A, et al. Haematological spectrum and genotype-phenotype correlations in nine unrelated families with RUNX1 mutations from the French network on inherited platelet disorders. Orphanet J Rare Dis. 2016;11:49.
25. Challen GA, Goodell MA. Runx1 isoforms show differential expression patterns during hematopoietic development but have similar functional effects in adult hematopoietic stem cells. Exp Hematol. 2010;38(5):403-416.
26. Komeno Y, Yan M, Matsuura S, et al. Runx1 exon 6-related alternative splicing isoforms differentially regulate hematopoiesis in mice. Blood. 2014;123(24):3760-3769.
27. Brady G, Elgueta Karstegl C, Farrell PJ. Novel function of the unique N-terminal region of RUNX1c in B cell growth regulation. Nucleic Acids Res. 2013;41(3):1555-1568.
28. Lacaud G, Gore L, Kennedy M, et al. Runx1 is essential for hematopoietic commitment at the hemangioblast stage of development in vitro. Blood. 2002;100(2):458-466.
29. Navarro-Montero O, Ayllon V, Lamolda M, et al. RUNX1c regulates hematopoietic differentiation of human pluripotent stem cells possibly in cooperation with proinflammatory signaling. Stem Cells. 2017;35(11):2253-2266.
30. Lorsbach RB, Moore J, Ang SO, et al. Role of RUNX1 in adult hematopoiesis: analysis of RUNX1-IRES-GFP knock-in mice reveals differential lineage expression. Blood. 2004;103(7):2522-2529.
31. Tsuzuki S, Hong D, Gupta R, et al. Isoform-specific potentiation of stem and progenitor cell engraftment by AML1/RUNX1. PLoS Med. 2007;4(5):e172.
32. Tsuzuki S, Seto M. Expansion of functionally defined mouse hematopoietic stem and progenitor cells by a short isoform of RUNX1/AML1. Blood. 2012;119(3):727-735.
33. Elagib KE, Racke FK, Mogass M, et al. RUNX1 and GATA-1 coexpression and cooperation in megakaryocytic differentiation. Blood. 2003;101(11):4333-4341.
34. Kuvardina ON, Herglotz J, Kolodziej S, et al. RUNX1 represses the erythroid gene expression program during megakaryocytic differentiation. Blood. 2015;125(23):3570-3579.
35. Li Y, Jin C, Bai H, et al. Human NOTCH4 is a key target of RUNX1 in megakaryocytic differentiation. Blood. 2018;131(2):191-201.
36. Bellissimo DC, Speck NA. RUNX1 Mutations in inherited and sporadic leukemia. Front Cell Dev Biol. 2017;5:111.
37. Gaidzik VI, Bullinger L, Schlenk RF, et al. RUNX1 mutations in acute myeloid leukemia: results from a comprehensive genetic and clinical analysis from the AML study group. J Clin Oncol. 2011;29(10):1364-1372.
38. Tang JL, Hou HA, Chen CY, et al. AML1/RUNX1 mutations in 470 adult patients with de novo acute myeloid leukemia: prognostic implication and interaction with other gene alterations. Blood. 2009;114(26):5352-5361.
39. Bean LJH, Hegde MR. Clinical implications and considerations for evaluation of in silico algorithms for use with ACMG/AMP clinical variant interpretation guidelines. Genome Med. 2017;9(1):111.
40. Ghosh R, Oak N, Plon SE. Evaluation of in silico algorithms for use with ACMG/AMP clinical variant interpretation guidelines. Genome Biol. 2017;18(1):225.
41. Ioannidis NM, Rothstein JH, Pejaver V, et al. REVEL: an ensemble method for predicting the pathogenicity of rare missense variants. Am J Hum Genet. 2016;99(4):877-885.
42. Zhao LJ, Wang YY, Li G, et al. Functional features of RUNX1 mutants in acute transformation of chronic myeloid leukemia and their contribution to inducing murine full-blown leukemia. Blood. 2012;119(12):2873-2882.
43. Tsai SC, Shih LY, Liang ST, et al. Biological activities of RUNX1 mutants predict secondary acute leukemia transformation from chronic myelomonocytic leukemia and myelodysplastic syndromes. Clin Cancer Res. 2015;21(15):3541-3551.
44. Osato M, Asou N, Abdalla E, et al. Biallelic and heterozygous point mutations in the runt domain of the AML1/PEBP2alphaB gene associated with myeloblastic leukemias. Blood. 1999;93(6):1817-1824.
45. Taketani T, Taki T, Takita J, et al. Mutation of the AML1/RUNX1 gene in a transient myeloproliferative disorder patient with Down syndrome. Leukemia. 2002;16(9):1866-1867.
46. Koh CP, Wang CQ, Ng CE, et al. RUNX1 meets MLL: epigenetic regulation of hematopoiesis by two leukemia genes. Leukemia. 2013;27(9):1793-1802.
47. Mersch J, Brown N, Pirzadeh-Miller S, et al. Prevalence of variant reclassification following hereditary cancer genetic testing. JAMA. 2018;320(12):1266-1274.
48. Slavin TP, Manjarrez S, Pritchard CC, Gray S, Weitzel JN. The effects of genomic germline variant reclassification on clinical cancer care. Oncotarget. 2019;10(4):417-423.
49. Michaud J, Wu F, Osato M, et al. In vitro analyses of known and novel RUNX1/AML1 mutations in dominant familial platelet disorder with predisposition to acute myelogenous leukemia: implications for mechanisms of pathogenesis. Blood. 2002;99(4):1364-1372.
50. Yeo G, Burge CB. Maximum entropy modeling of short sequence motifs with applications to RNA splicing signals. J Comput Biol. 2004;11(2-3):377-394.
51. Desmet FO, Hamroun D, Lalande M, et al. Human Splicing Finder: an online bioinformatics tool to predict splicing signals. Nucleic Acids Res. 2009;37(9):e67.

52. Cavalcante de Andrade Silva M, Krepischi ACV, Kulikowski LD, et al. Deletion of RUNX1 exons 1 and 2 associated with familial platelet disorder with propensity to acute myeloid leukemia. Cancer Genet. 2018;222-223:32-37.
53. Papaemmanuil E, Gerstung M, Bullinger L, et al. Genomic classification and prognosis in acute myeloid leukemia. N Engl J Med. 2016;374(23):2209-2221.
54. Luddy RE, Champion LA, Schwartz AD. A fatal myeloproliferative syndrome in a family with thrombocytopenia and platelet dysfunction. Cancer. 1978;41(5):1959-1963.
55. Dowton SB, Beardsley D, Jamison D, Blattner S, Li FP. Studies of a familial platelet disorder. Blood. 1985;65(3):557-563.
56. Liew E, Owen C. Familial myelodysplastic syndromes: a review of the literature. Haematologica. 2011;96(10):1536-1542.
57. Miyoshi H, Shimizu K, Kozu T, et al. t(8;21) breakpoints on chromosome 21 in acute myeloid leukemia are clustered within a limited region of a single gene, AML1. Proc Natl Acad Sci U S A. 1991;88(23):10431-10434.
58. Erickson P, Gao J, Chang KS, et al. Identification of breakpoints in t(8;21) acute myelogenous leukemia and isolation of a fusion transcript, AML1/ETO, with similarity to Drosophila segmentation gene, runt. Blood. 1992;80(7):1825-1831.
59. Feurstein S, Drazer MW, Godley LA. Genetic predisposition to leukemia and other hematologic malignancies. Semin Oncol. 2016;43(5):598-608.
60. Churpek JE, LA G. How I diagnose and manage individuals at risk for inherited myeloid malignancies. Blood. 2016;128 (14):1800-1813.
61. Shlush LI, Zandi S, Mitchell A, et al. Identification of pre-leukaemic haematopoietic stem cells in acute leukaemia. Nature. 2014;506(7488):328-333.
62. Arends CM, Galan-Sousa J, Hoyer K, et al. Hematopoietic lineage distribution and evolutionary dynamics of clonal hematopoiesis. Leukemia. 2018;32(9):1908-1919.
63. Thol F, Klesse S, Kohler L, et al. Acute myeloid leukemia derived from lymphomyeloid clonal hematopoiesis. Leukemia. 2017;31(6):1286-1295.
64. Petti AA, Williams SR, Miller CA, et al. Mutation detection in thousand of acute myeloid leukemia cells using single cell RNA-sequencing. bioRxiv. 2018 October 17. [Epub ahead of Print]
65. Velten L, Story BA, Hernancez-Malmierca P, et al. MutaSeq reveals the transcriptomic consequences of clonal evolution in acute myeloid leukemia. bioRxiv. 2018 December 21 [Epub ahead of Print]
66. Wehr C, Grotius K, Casadei S, et al. A novel disease-causing synonymous exonic mutation in GATA2 affecting RNA splicing. Blood. 2018;132(11):1211-1215.
67. Hsu AP, Johnson KD, Falcone EL, et al. GATA2 haploinsufficiency caused by mutations in a conserved intronic element leads to MonoMAC syndrome. Blood. 2013;121(19):3830-38371.
68. Pippucci T, Savoia A, Perrotta S, et al. Mutations in the 5' UTR of ANKRD26, the ankirin repeat domain 26 gene, cause an autosomal-dominant form of inherited thrombocytopenia, THC2. Am J Hum Genet. 2011;88(1):115-120.
69. Noris P, Perrotta S, Seri M, et al. Mutations in ANKRD26 are responsible for a frequent form of inherited thrombocytopenia: analysis of 78 patients from 21 families. Blood. 2011;117(24):6673-6680.
70. Azzariti DR, Riggs ER, Niehaus A, et al. Points to consider for sharing variant-level information from clinical genetic testing with ClinVar. Cold Spring Harb Mol Case Stud. 2018;4(1).
71. Riggs ER, Azzariti DR, Niehaus A, et al. Development of a consent resource for genomic data sharing in the clinical setting. Genet Med. 2019;21(1):81-88.
72. Ma N, Zhang JZ, Itzhaki I, et al. Determining the pathogenicity of a genomic variant of uncertain significance using CRISPR/Cas9 and human-induced pluripotent stem cells. Circulation. 2018;138(23): 2666-2681.
73. Sander JD, Joung JK. CRISPR-Cas systems for editing, regulating and targeting genomes. Nat Biotechnol. 2014;32(4):347-355.
74. Tsai SQ, Joung JK. Defining and improving the genome-wide specificities of CRISPR-Cas9 nucleases. Nat Rev Genet. 2016;17(5):300-312.
75. Zhang L, Li Z, Yan J, et al. Mutagenesis of the Runt domain defines two energetic hot spots for heterodimerization with the core binding factor beta subunit. J Biol Chem. 2003;278(35):33097-33104.
76. Li Z, Yan J, Matheny CJ, et al. Energetic contribution of residues in the Runx1 Runt domain to DNA binding. J Biol Chem. 2003;278(35):33088-33096.
77. Findlay GM, Boyle EA, Hause RJ, Klein JC, Shendure J. Saturation editing of genomic regions by multiplex homology-directed repair. Nature. 2014;513(7516):120-123.
78. Findlay GM, Daza RM, Martin B, et al. Accurate classification of BRCA1 variants with saturation genome editing. Nature. 2018;562(7726):217-222.
79. Matreyek KA, Starita LM, Stephany JJ, et al. Multiplex assessment of protein variant abundance by massively parallel sequencing. Nat Genet. 2018;50(6):874-882.
80. Mester JL, Ghosh R, Pesaran T, et al. Gene-specific criteria for PTEN variant curation: recommendations from the ClinGen PTEN Expert Panel. Hum Mutat. 2018;39(11):1581-1592.
81. Garrett LT, Hickman N, Jacobson A, et al. Family studies for classification of variants of uncertain classification: current laboratory clinical practice and a new web-based educational tool. J Genet Couns. 2016;25(6): 1146-1156.
82. Bravo J, Li Z, Speck NA, Warren AJ. The leukemia-associated AML1 (Runx1)--CBF beta complex functions as a DNA-induced molecular clamp. Nat Struct Biol. 2001;8 (4):371-378.

REVIEW ARTICLE

Ferrata Storti Foundation

Glanzmann thrombasthenia: genetic basis and clinical correlates

Juliana Perez Botero,[1] Kristy Lee,[2] Brian R Branchford,[3] Paul F Bray,[4] Kathleen Freson,[5] Michele P. Lambert,[6] Minjie Luo,[7] Shruthi Mohan,[2] Justyne E. Ross,[2] Wolfgang Bergmeier[8] and Jorge Di Paola[9] on behalf of the ClinGen Platelet Disorder Variant Curation Expert Panel

[1]Versiti and Division of Hematology/Oncology, Medical College of Wisconsin, Milwaukee, WI, USA; [2]Department of Genetics, University of North Carolina at Chapel Hill, NC, USA; [3]University of Colorado School of Medicine, Department of Pediatrics, Division of Hematology/Oncology/Bone Marrow Transplant, Aurora, CO, USA; [4]Molecular Medicine Program, Division of Hematology and Hematologic Malignancies, Department of Medicine, University of Utah, Salt Lake City, UT, USA; [5]Center for Molecular and Vascular Biology, University of Leuven, Leuven, Belgium; [6]The Children's Hospital of Philadelphia and Department of Pediatrics, Perelman School of Medicine, Philadelphia, PA, USA; [7]Department of Pathology and Laboratory Medicine, The Children's Hospital of Philadelphia, Perelman School of Medicine, Philadelphia, PA, USA; [8]Department of Biochemistry and Biophysics and UNC Blood Research Center, University of North Carolina at Chapel Hill, NC, USA and [9]Division of Pediatric Hematology Oncology, Department of Pediatrics, Washington University School of Medicine in St. Louis, MO, USA

Haematologica 2020
Volume 105(4):888-894

Correspondence:

JORGE DI PAOLA
dipaolaj@wustl.edu

Received: December 18, 2019.

Accepted: February 7, 2020.

Pre-published: March 5, 2020.

doi:10.3324/haematol.2018.214239

Check the online version for the most updated information on this article, online supplements, and information on authorship & disclosures: www.haematologica.org/content/105/4/888

ABSTRACT

Glanzmann thrombasthenia (GT) is an autosomal recessive disorder of platelet aggregation caused by quantitative or qualitative defects in integrins αIIb and β3. These integrins are encoded by the *ITGA2B* and *ITGB3* genes and form platelet glycoprotein (GP)IIb/IIIa, which acts as the principal platelet receptor for fibrinogen. Although there is variability in the clinical phenotype, most patients present with severe mucocutaneous bleeding at an early age. A classic pattern of abnormal platelet aggregation, platelet glycoprotein expression and molecular studies confirm the diagnosis. Management of bleeding is based on a combination of hemostatic agents including recombinant activated factor VII with or without platelet transfusions and antifibrinolytic agents. Refractory bleeding and platelet alloimmunization are common complications. In addition, pregnant patients pose unique management challenges. This review highlights clinical and molecular aspects in the approach to patients with GT, with particular emphasis on the significance of multidisciplinary care.

Introduction

The Swiss pediatrician Eduard Glanzmann was the first to describe in 1918 a type of purpura that presented with normal platelet count and size in patients with absent/decreased clot retraction and prolonged bleeding time.[1] In 1962, Caen and Cousin described the lack of platelet aggregation with multiple agonists,[2] and a few years later correlated the platelet aggregation result with decreased platelet fibrinogen and a slight reduction in clot retraction in individuals with Glanzmann thrombasthenia (GT).[3] The lack of one of the three major platelet surface glycoproteins in GT was reported by Nurden and Caen in 1974;[4] several other scientists subsequently identified this as the glycoprotein (GP) IIb/IIIa complex. Additional studies with more advanced glycoprotein imaging techniques provided evidence for the definition of two disease groups: type I with absent IIb/IIIa expression (<5% of normal) and type II with reduced expression (5-20% of normal GP IIb/IIIa).[5] A third type (type III) has normal levels of integrin but the protein is non-functional.

Glanzmann thrombasthenia is considered a rare disease, defined in the United States as those affecting less than 200,000 individuals.[6] The exact incidence has been difficult to calculate, but is estimated at one in 1,000,000. With an autosomal recessive inheritance, males and females are affected equally. There is a world-

wide distribution; however, a large proportion of the cases have been described in selected populations such as the French Romani,[7] South Indian Hindus, Iraqi Jews, and Jordanian nomadic tribes,[8] in all of which consanguinity is common. Type I is the most common subtype and accounts for around 78% of patients with GT type II and type III (functional variant in receptor) constituting around 14% and 8% of cases, respectively.[9]

GPIIb/IIIa (integrin αIIbβ3) is a heterodimeric receptor present in large quantities in the plasma membrane of platelets. Activation of this integrin and binding of soluble ligands [primarily fibrinogen, but also von Willebrand factor (vWF) and fibronectin] are essential for platelet aggregation. In the resting state, the integrin has low affinity for ligands. During platelet activation, driven by exposure to soluble agonists or the subendothelial matrix, "inside out" cellular signaling generates a conformational change in GPIIb/IIIa that allows high affinity binding for fibrinogen, which serves as a "bridge" to other activated platelets, eventually forming the platelet plug. Protein kinase C (PKC), diaglycerol-regulated guanine nucleotide exchange factor I (CalDAG-GEFI or RASGRP2), and phosphoinositide 3-kinase (PI3K) participate in this signaling pathway. Subsequent "outside in" signaling triggers additional granule secretion, cytoskeletal interactions (that allow for platelet spreading), stabilization and clot retraction to consolidate the fibrin clot. Kindlins (including kindlin-3) and talins are key regulators of integrin activation.[10, 11]

Glanzmann thrombasthenia is usually caused by decreased or absent expression of αIIb or β3, abnormalities in protein folding, defective post-translational processing or transport of either integrin subunit causing decreased surface expression, or abnormalities affecting protein function. Other defects change integrin function by altering the ligand binding pocket (interface between αIIb and β3), which modifies the cytoplasmic domain and affects binding of regulators, or locks the integrin in the activated form.

Molecular basis of Glanzmann thrombasthenia

The *ITGA2B* and *ITGB3* genes are located on chromosomes 17q21.31 and 17q21.32, respectively, and are independently expressed. GT is caused by pathogenic variants in both alleles of either of the two genes; concomitant pathogenic variants in both genes, but affecting only one allele of each, is not known to cause GT. Due to the autosomal recessive inheritance, compound heterozygosity is frequent, except in selected ethnic groups where homozygosity is more likely due to consanguinity. A higher percentage of pathogenic variants occur in *ITGA2B*, likely because of the larger size of this gene with 30 exons encoding 1,039 amino acids, compared to *ITGB3* which is composed of 15 exons with 788 amino acids.[7] The clinical phenotypes associated with either gene are indistinguishable.[12]

Pathogenic nonsense, missense and splice site variants are common and large deletions and duplications, although rare, have also been described.[13] Pathogenic missense variants impair subunit biosynthesis in megakaryocytes or inhibit the transport of the pro-αIIbβ3 complexes from the endoplasmic reticulum (ER) to the Golgi apparatus or the export of the mature complexes to the cell surface. A large proportion of variants affect the β-propeller region of αIIb and the epithelial growth factor domains of β3.[14]

A different type of variant affecting specific regions of these genes has been more recently described to cause a mild autosomal dominant macrothrombocytopenia[15] by interfering with proplatelet formation.[16] These "gain of function" variants cause spontaneous activation of GPIIb/IIIa (αIIbβ3) by affecting the cytoplasmic domains or the membrane proximal residues in the extracellular domains. The majority of these are in *ITGB3* and affect the MIDAS (metal ion dependent adhesion site), ADMIDAS (adjacent to MIDAS) or SyMBS (synergistic metal ion binding site) regions. A small proportion have been reported in *ITGA2B* and affect the conserved intracellular GFFKR sequence.[17]

Clinical manifestations and diagnosis

Bleeding phenotype

With integrins αIIb and β3 participating in primary hemostasis, the bleeding manifestations are typically purpura, epistaxis (60-80%), gum bleeding (20-60%), and menorrhagia (60-90%). Gastrointestinal bleeding in the form of melena or hematochezia is present in 10-20%, and 1-2% develop intracranial hemorrhage.[9] Mucocutaneous bleeding can be spontaneous or occur after minimal trauma. Epistaxis is the most common cause of severe bleeding, especially in the pediatric population, and risk of severe nosebleeds decreases with age as the septal arterial plexus becomes less friable and children grow out of the habit of nose picking. Menorrhagia is highly prevalent in affected females and there is a higher risk of severe bleeding at the time of menarche due to the prolonged estrogen influence on the proliferative endometrium that occurs during anovulatory cycles. Bleeding complications during pregnancy are uncommon; however, the risk of obstetric hemorrhage at the time of delivery and postpartum is high. Hematuria and spontaneous hemarthrosis have been described in some cases but are not usually part of the bleeding phenotype.

Several bleeding scores have been developed with the goal of standardizing the assessment of bleeding and facilitating the diagnosis of patients with a suspected inherited bleeding disorder. These are useful tools that assist in communication of the bleeding phenotype in the clinical and research setting; however, they have not been widely validated for patients with inherited platelet function disorders. Therefore, specific cutoffs to define a positive bleeding score have not been established for this population.[18] This is of particular relevance in GT, because while the types of bleeding are consistent among individuals, the degree of bleeding is highly variable. Given the severity of this disorder, historically, most patients have been diagnosed in childhood (before 5 years of age), but there are some patients that reach adulthood without having severe bleeding.[9] In general, the severity of bleeding (except for menorrhagia and pregnancy-associated bleeding) decreases with age.

Laboratory phenotype

Complete blood count

There should be normal platelet count and size with normal granularity on evaluation of the peripheral blood smear by light microscopy. If bleeding is severe and/or

chronic, patients can have low hemoglobin, microcytosis and increased red cell distribution width from secondary iron deficiency. Other abnormalities of the complete blood count (CBC), suggest an alternative diagnosis.

Coagulation screening tests

Routine tests ordered in the workup of a patient with abnormal bleeding, such as prothrombin time (PT), activated thromboplastin time (aPTT) and fibrinogen, are usually normal, unless a patient is being evaluated in the setting of significant acute hemorrhage and has evidence of consumptive coagulopathy.

Platelet function screening tests

The platelet function analyzer (PFA)-100 provides a measure of platelet function under high shear. It is convenient as it uses low volume whole blood samples and is widely available to clinicians. Very prolonged closure times (>300 seconds) are compatible with GT but not specific, as other disorders, such as severe von Willebrand disease, Bernard Soulier syndrome and afibrinogenemia, can produce the same result. However, a normal PFA-100 has a very high negative predictive value for GT and virtually excludes this diagnosis.[19]

Platelet light transmission aggregometry

Despite its limited availability and the need for larger-volume samples and immediate processing, platelet light transmission aggregometry (LTA) remains the gold standard in the clinical diagnosis of GT. It is based on the decreased turbidity generated by platelet agglutinates or aggregates in platelet rich plasma after exposure to different agonists. Decreased/absent aggregation (<10%) with all physiologic agonists, together with a normal agglutination response to ristocetin (mediated by GPIb-IX-V), is the classic pattern observed in patients with GT.[20] Due to the large variability in platelet aggregation results and the significant effect of pre-analytical variables on this test, confirmation of the findings in a second sample is recommended.

Whole blood impedance aggregometry

This is available in several centers worldwide. While it can be performed in whole blood samples and using lower volumes, there is not enough evidence to support equivalent sensitivity and reproducibility when compared to LTA.[21] There is some clinical utility to this test in cases in which access to LTA is difficult; however, patients should preferably be referred for evaluation at a center that has LTA capacity at least once to confirm the diagnosis.

Platelet glycoprotein expression study by flow cytometry

This assesses quantitative platelet surface glycoprotein deficiencies using fluorescent-conjugated antibodies that are specific towards GP.[22] This test can be performed in low sample volumes shipped for analysis; however, it will not identify type III (functional) defects that are caused by qualitative but not quantitative defects in GPIIb/IIIa (Figure 1).

Differential diagnosis

Leukocyte adhesion deficiency type III

Leukocyte adhesion deficiency type III (LAD-III) is an autosomal recessive disorder caused by pathogenic variants in the kindlin 3 gene *FERMT3*[23] that also presents failure of the "inside-out" integrin activation in platelets, white cells and endothelial cells,[11] causing bleeding, infections and impaired wound healing. Due to the functional integrin defect affecting platelets, these patients have the same platelet aggregation pattern as those with GT and similar to type III (variant) GT, but have normal platelet glycoprotein expression by flow cytometry. The associated neutrophil dysfunction leading to frequent bacterial infections and impaired wound healing in patients with LAD-III may help clinicians distinguish these patients from those with GT.

RASGRP2 related platelet dysfunction

RASGRP2 encodes calcium and diacylglycerol-regulated guanine exchange factor I (CalDAG-GEFI), a protein that also participates in "inside out" signaling of integrins. Pathogenic variants in this gene lead to autosomal recessive non-syndromic platelet dysfunction characterized by moderate to severe bleeding and decreased platelet aggregation with ADP and epinephrine, and, in some cases, arachidonic acid, collagen and thrombin.[24]

Bernard Soulier syndrome

Bernard Soulier syndrome (BSS) is also an autosomal recessive disorder caused by pathogenic variants in *GP1BA*, *GP1BB* and *GP9*. The clinical presentation in terms of bleeding phenotype is very similar to GT; however, BSS is relatively easy to distinguish due to macrothrombocytopenia, platelet LTA with normal aggregation with all agonists except ristocetin, and protein assessment (e.g. flow cytometry) showing decreased/absent CD42a (GPIX) and CD42b (GPIb-alpha).

Acquired Glanzmann thrombasthenia

Acquired GT is typically caused by antibodies with specificity against GPIIb/IIIa (or nearby epitopes) that block the interaction of the receptor with fibrinogen and von Willebrand factor. It presents with late-onset, severe mucocutaneous bleeding in the setting of normal platelet counts[25] and is usually secondary to autoimmune, lymphoproliferative or plasma cell disorders. Medications, specifically anti-thrombotics that block GPIIb/IIIa such as abciximab, eptifibatide and tirofiban, have also been implicated.[26] The absence of lifelong bleeding and presence of concomitant systemic disorder should lead the clinician to suspect this diagnosis.

- Normal platelet count, size and granularity on light microscopy
- Platelet light transmission aggregometry with decreased/absent aggregation (<10%) with all agonists except ristocetin
- Platelet glycoprotein expression study by flow cytometry with decreased/absent (<20%) CD41 (GPIIb) and CD61 (GPIIIa)

Figure 1. Typical laboratory phenotype in Glanzmann thrombasthenia (GT).

Molecular confirmation

Genetic analysis is clinically useful for confirmation of the diagnosis, identification of at-risk carriers, reproductive risk counseling for a given couple/family, and for definitive prenatal or preimplantation genetic diagnosis. Genetic counseling plays an essential role in the genetic testing process, obtaining informed consent regarding the unique considerations, benefits, and limitations of genetic testing, and addressing the complexities of clinical application or molecular findings, unexpected results, variants of uncertain significance, and familial implications for medical risks or biological relationships. Genetic coun-

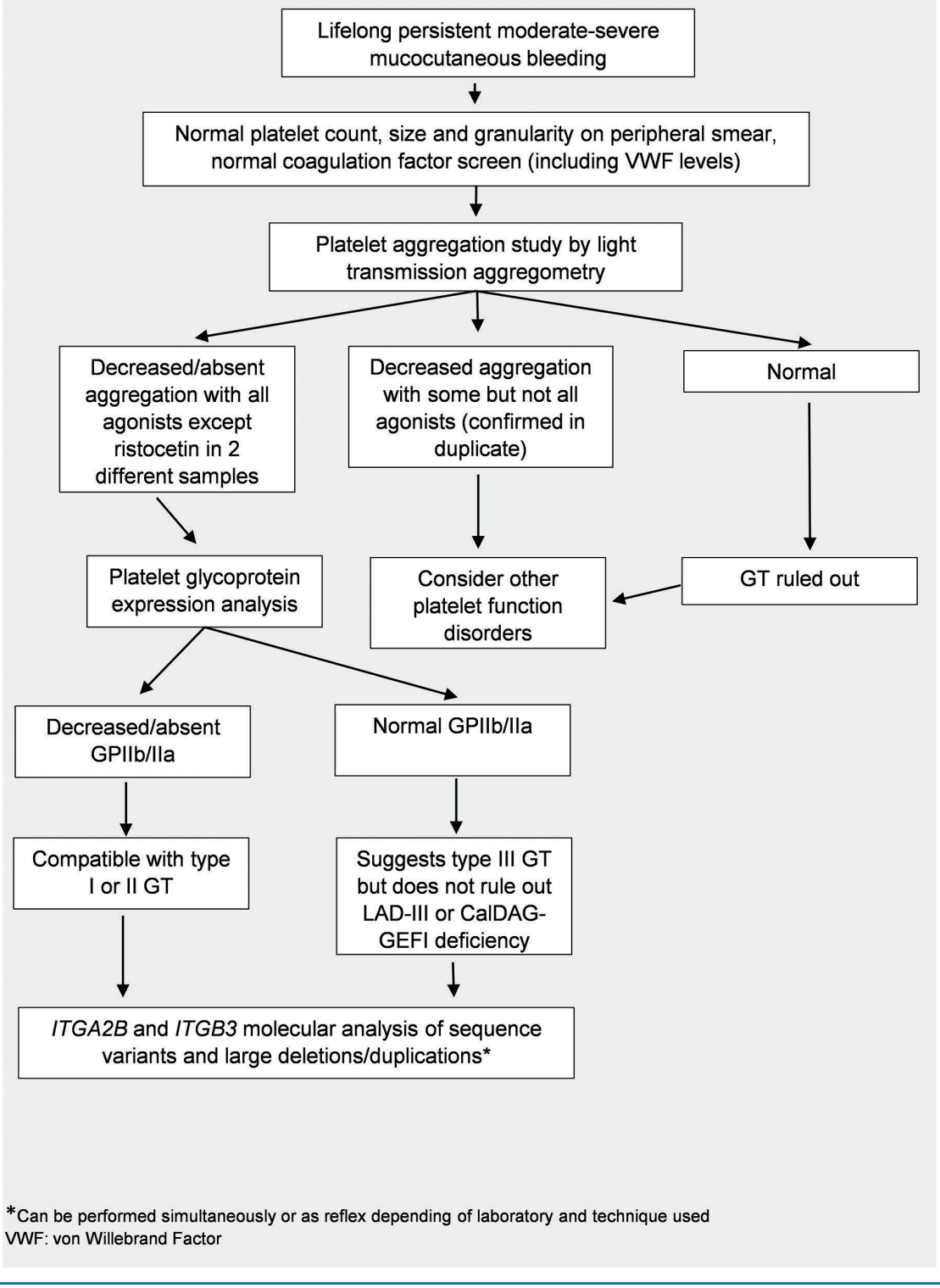

Figure 2. Diagnostic flow chart for the laboratory evaluation of a patient with suspected Glanzmann thrombasthenia (GT).

selors can support clinicians by providing pre- and post-test genetic counseling to patients and families in the clinical setting, and can also aid clinicians in test selection and ordering, and in navigating the process of obtaining insurance approval for payment. This is particularly relevant in healthcare systems with multiple payers and multiple testing options. As commercial laboratories offer different services, the clinician should be familiar with the testing methodology and any related limitations.

Given the highly specific phenotype of GT, after platelet aggregation studies and flow cytometry have been performed, genetic testing of *ITGA2B* and *ITGB3* only, as opposed to a panel approach that includes multiple other genes, is appropriate (Figure 2). Sequence analysis will detect the vast majority of pathogenic variants; when sequencing fails to identify both pathogenic variants in a patient with GT, specific deletion/duplication analysis should be considered.

Targeted variant analysis, which is expected to save time and money, can be performed in populations with a known pathogenic variant(s) and high rates of consanguinity; however, with this approach, a second GT variant in the same gene may go undetected.[27] Targeted variant analysis is best adopted when the pathogenic variant in each allele has been identified in an affected individual.

Variant curation and initiatives for standardization

In recent years, several initiatives have been taken to provide guidance for the analysis and reporting of molecular findings, specifically in terms of variant classification when attributing pathogenicity. In the United States, the American College of Medical Genetics and Genomics (ACMG) and Association for Molecular Pathology (AMP) published guidelines in 2015 for the interpretation of variants, providing a framework for clinical molecular laboratories.[14] While these guidelines have been extremely useful in the laboratory practice, they are not disease specific, and significant challenges remain when applied to particular disease states. In an effort to address this limitation, and to improve the quality, consistency and access to clinical genomic data, the National Institutes of Health (NIH) funded resource ClinGen is leading initiatives including the formation of Variant Curation Expert Panels (VCEP). Each VCEP consists of a cross-institutional team of experts from complementary specialties, the fields of hematology and genetics, from academia and industry, working collaboratively with the goal of adapting the ACMG criteria for specific genes or disorders.[28]

The Platelet Disorder Variant Curation Expert Panel (VCEP) created in 2018 and supported by the American Society of Hematology, is composed of 28 international scientists and clinicians with expertise in hematology and genetics, and has been working on the adaptation of the ACMG rules for the interpretation of variants in *ITGA2B* and *ITGB3*. The goals of this collaboration are to produce high quality variant curation data that are publicly available and create a framework for GT variant curation that allows others to systematically and comprehensively approach genetic data encountered in clinical and research settings.

The VCEP has used estimates of prevalence and population data to define criteria for allele frequency that ultimately serve as standalone, strong or supporting evidence to classify variants as benign, which is a difficult task in rare disorders for which the precise incidence data are not available. Clinical expertise was key in defining the phenotype from a clinical presentation (bleeding phenotype) and clinical laboratory standpoint (platelet aggregation and glycoprotein expression studies), which together are unique to GT. Knowledge of the molecular biology of the disorder allowed for elimination of codes that do not apply for this disease state and points for segregation analysis were modified taking into account the disease inheritance, low frequency and specific clinical phenotype. Special consideration was given to defining the type of assays that provide quality functional evidence in different *in vivo* and *in vitro* systems and models. The disease specified rules were tested in a subset of variants which will be uploaded to ClinVar with a 3-star rating. Variants assessed by approved ClinGen VCEP also receive a US Food and Drug Administration (FDA) approval label. A detailed description of the rule specifications for GT will soon be available to the public.

Management

Patients with GT benefit from being managed at a center with expertise in inherited bleeding disorders, with access to staff who are able to provide recommendations and

Table 1. Measures and medications available for the management of bleeding in Glanzmann thrombasthenia (GT).

Treatment	Clinical situation
Local measures • Compression • Gauze or sponge dipped in antifibrinolytic or topical thrombin • Nasal packing • Gel foam soaked in antifibrinolytic or topical thrombin	Mild bleeding at a visible/compressible site
Antifibrinolytics • Tranexamic acid • Aminocaproic acid	As monotherapy in mild bleeding As combination therapy in moderate and severe bleeding
rFVIIa	Moderate to severe bleeding Alone for minor surgical procedures or in combination with antifibrinolytics and/or platelet transfusions for major procedures and severe or life-threatening bleeding
Platelet transfusion*	In combination with rFVIIa and/or antifibrinolytics in severe bleeding and major surgical procedures

rFVIIa: recombinant activated coagulation factor VII. *Risk of lack of efficacy in the setting of alloimmunization.

treatment any time of day, and also benefit from being provided directly with medical alerts, and emergency medical contact and treatment information to present when seeking urgent care from clinicians who are not familiar with their case history. Education on avoidance of over-the-counter medications that increase bleeding risk such as non-steroidal anti-inflammatories and aspirin products should be provided. Prescription medications that can affect hemostasis should be carefully monitored.[29]

Hemostatic management

The treatment of bleeding in patients with GT includes management of acute or chronic bleeding and prevention of hemorrhagic complications around the time of procedures. The choice of treatment depends on the severity of bleeding (Table 1), availability of products, and prior responses to therapy, and is similar in some aspects to the management of patients with other severe bleeding disorders. Note that desmopressin (DDAVP), commonly used in von Willebrand Disease and other milder disorders of platelet function, is of limited clinical utility in the treatment of GT (Table 1).

Recombinant activated factor VII (rFVIIa) is approved by the European Medicines Agency (EMA) and the FDA for the treatment of patients with GT. The approval of this drug has changed the landscape of treatment of GT and has allowed for better hemostatic outcomes in all patients, especially those who do not respond to platelet transfusions. Optimal dosing and interval of doses vary by center and clinical situation. Typical doses for acute bleeding are 90 mcg/kg intravenous (IV) every 2-6 hours until hemostasis is achieved (at least 3 doses). Perioperative dosing is 90 mcg/kg immediately before surgery and every two hours during the procedure, with doses every 2-6 hours postoperatively to prevent post-surgical bleeding.[30] Effectiveness of this drug in the treatment of acute bleeding is high[31] when started early in the course of bleeding and used in combination with other hemostatic treatment. It is also useful for perioperative management.[32] Although cases of thromboembolism during rFVIIa therapy in GT patients have occurred, it remains a safe medication in this population, with low rates of adverse reactions.

Transfusion

Patients with GT have a high risk of development of isoantibodies, with up to 30% of patients developing anti-GPIIb/IIIa or anti-HLA antibodies after platelet transfusion.[33] Patients with pathogenic variants causing premature stop codons and leading to absent GPIIb/IIIa are at the highest risk of anti GPIIb/IIIa alloimmunization compared to those with other types of variants (81% *vs.* 25%).[34] Once these antibodies develop, the patient may no longer respond to platelet transfusion. For this reason, platelet transfusions should be reserved for only major surgeries, life-threatening bleeding, and significant bleeding that does not respond to the above measure. Transfusions in women of reproductive age should ideally be avoided as the antibodies can cross the placenta and affect the fetus.[35]

Bone marrow transplant

Allogeneic stem cell transplantation has been successfully performed in selected patients with severe recurrent bleeding using reduced intensity conditioning with good clinical outcomes.[36,37] The presence in the recipient of antiplatelet antibodies affecting the graft remains a challenge in this patient population.[38]

Pregnancy

Pregnant women with GT have a high rate of complications and are best managed in a specialized center with a multidisciplinary team. While most complications relate to bleeding and occur at the time of delivery, management of the pregnant GT patients should start in the prenatal period. Counseling of the pregnancy-associated risks and screening of the father in consanguineous families to identify at-risk fetuses is important. Identification of HLA or GPIIb/IIIa antibodies during pregnancy, which are present in up to 70% of patients, is key for planning delivery. In general, regional anesthesia is contraindicated and support with rFVIIa and antifibrinolytics is given for vaginal deliveries with the option of adding platelet transfusion for cesarian sections.[39] Primary post-partum hemorrhage is common, and a large proportion of women will require red cell transfusion. Clinicians should be aware that, given the phenotypic variability of this disorder, around half the women with GT who are pregnant may not be aware of the diagnosis.[35]

Future directions

Gene therapy is highly promising in providing a cure for patients with GT, with significant progress made using different techniques, vectors and model organisms.[40-42] However, further advances that allow safe transgene delivery and stable expression in human models are still required.[33]

Ongoing challenges

Despite advances in the understanding of the pathophysiology, the relative ease of access to clinical laboratory techniques, and recent improvements in treatment options (such as rFVIIa), many challenges remain in the care of patients with this rare disorder. Access to clinicians and laboratories with the required expertise and resources to diagnose and treat GT is difficult, especially in areas of the world with limited resources. Large-scale data analysis and clinical research are problematic given the limited numbers of patients available and the highly constrained funding for rare disorders. Initiatives through the World Federation of Hemophilia for clinical care and multinational collaborations including the Glanzmann Thrombasthenia Registry for analysis of clinical outcomes, and sharing of molecular data through creation of publicly accessible databases have taken important steps in bridging the gaps. However, more investment is needed to guarantee timely access to quality care, until a true cure for the disease is developed.

References

1. Commentary on and reprint of Glanzmann E, Hereditäre häemorrhagische thrombasthenie. Ein Beitrag zur Pathologie der Blutplättchen [Hereditary hemorrhagic thrombasthenia: A contribution on the pathology of blood platelets], in Jahrbuch für Kinderheilkunde (1918) 88:113–141. In: Lichtman MA, Spivak JL, Boxer LA, Shattil SJ, Henderson ES, eds. Hematology. San Diego: Academic Press, 2000:55-III.
2. Caen J, Cousin C. ["In vivo" disorder of platelet adhesiveness in Willebrand's disease and Glanzmann's thrombasthenias. Trial interpretation]. Nouv Rev Fr Hematol. 1962;2:685-694.
3. Caen JP, Castaldi PA, Leclerc JC, et al Congenital bleeding disorders with long bleeding time and normal platelet count: I. Glanzmann's thrombasthenia (report of fifteen patients). Am J Med. 1966;41(1):4-26.
4. Nurden AT, Caen JP. An abnormal platelet glycoprotein pattern in three cases of Glanzmann's thrombasthenia. Br J Haematol. 1974;28(2):253-260.
5. Phillips DR, Agin PP. Platelet membrane defects in Glanzmann's thrombasthenia. Evidence for decreased amounts of two major glycoproteins. J Clin Invest. 1977;60(3):535-545.
6. Disorders NOfR. NORD Resource Guide Orphan Disease Update [Newsletter] 2019 April 8, 2019 [cited 2019 April 22]; Available from: https://rarediseases.org
7. Nurden AT, Fiore M, Nurden P, Pillois X. Glanzmann thrombasthenia: a review of ITGA2B and ITGB3 defects with emphasis on variants, phenotypic variability, and mouse models. Blood. 2011;118(23):5996-6005.
8. Toogeh G, Sharifian R, Lak M, Safaee R, Artoni A, Peyvandi F. Presentation and pattern of symptoms in 382 patients with Glanzmann thrombasthenia in Iran. Am J Hematol. 2004;77(2):198-199.
9. George JN, Caen JP, Nurden AT. Glanzmann's thrombasthenia: the spectrum of clinical disease. Blood. 1990;75(7):1383-1395.
10. Marder VJ. Hemostasis and Thrombosis: Basic Principles and Clinical Practice: Wolters Kluwer Health, 2012.
11. Coller BS, Shattil SJ. The GPIIb/IIIa (integrin alphaIIbbeta3) odyssey: a technology-driven saga of a receptor with twists, turns, and even a bend. Blood. 2008;112(8):3011-3025.
12. Coller BS, Seligsohn U, Peretz H, Newman PJ. Glanzmann thrombasthenia: new insights from an historical perspective. Semin Hematol. 1994;31(4):301-311.
13. Nurden AT, Pillois X. ITGA2B and ITGB3 gene mutations associated with Glanzmann thrombasthenia. Platelets. 2018;29(1):98-101.
14. Richards S, Aziz N, Bale S, et al. Standards and guidelines for the interpretation of sequence variants: a joint consensus recommendation of the American College of Medical Genetics and Genomics and the Association for Molecular Pathology. Genet Med. 2015;17(5):405-424.
15. Kashiwagi H, Kunishima S, Kiyomizu K, et al. Demonstration of novel gain-of-function mutations of alphaIIbbeta3: association with macrothrombocytopenia and glanzmann thrombasthenia-like phenotype. Mol Genet Genomic Med. 2013;1(2):77-86.
16. Bury L, Malara A, Gresele P, Balduini A. Outside-in signalling generated by a constitutively activated integrin alphaIIbbeta3 impairs proplatelet formation in human megakaryocytes. PLoS One. 2012;7(4):e34449.
17. Nurden AT, Nurden P. Congenital platelet disorders and understanding of platelet function. Br J Haematol. 2014;165(2):165-178.
18. Lowe GC, Lordkipanidze M, Watson SP, UK GAPP study group. Utility of the ISTH bleeding assessment tool in predicting platelet defects in participants with suspected inherited platelet function disorders. J Thromb Haemost. 2013;11(9):1663-1668.
19. Harrison P. The role of PFA-100 testing in the investigation and management of haemostatic defects in children and adults. Br J Haematol. 2005;130(1):3-10.
20. Gresele P, Subcommittee on Platelet Physiology of the International Society on T, Hemostasis. Diagnosis of inherited platelet function disorders: guidance from the SSC of the ISTH. J Thromb Haemost. 2015;13(2):314-322.
21. Al Ghaithi R, Drake S, Watson SP, Morgan NV, Harrison P. Comparison of multiple electrode aggregometry with lumi-aggregometry for the diagnosis of patients with mild bleeding disorders. J Thromb Haemost. 2017;15(10):2045-2052.
22. Miller JL. Glycoprotein analysis for the diagnostic evaluation of platelet disorders. Semin Thromb Hemost. 2009;35(2):224-232.
23. Kuijpers TW, van de Vijver E, Weterman MA, et al. LAD-1/variant syndrome is caused by mutations in FERMT3. Blood. 2009;113(19):4740-4746.
24. Westbury SK, Canault M, Greene D, et al. Expanded repertoire of RASGRP2 variants responsible for platelet dysfunction and severe bleeding. Blood. 2017;130(8):1026-1030.
25. Tholouli E, Hay CR, O'Gorman P, Makris M. Acquired Glanzmann's thrombasthenia without thrombocytopenia: a severe acquired autoimmune bleeding disorder. Br J Haematol. 2004;127(2):209-213.
26. Nurden AT. Acquired Glanzmann thrombasthenia: From antibodies to anti-platelet drugs. Blood Rev. 2019;36:10-22.
27. Nurden AT. Glanzmann thrombasthenia. Orphanet J Rare Dis. 2006;1:10.
28. Resource CG. [cited 2019 May 2]; Available from: https://www.clinicalgenome.org/
29. Grainger JD, Thachil J, Will AM. How we treat the platelet glycoprotein defects; Glanzmann thrombasthenia and Bernard Soulier syndrome in children and adults. Br J Haematol. 2018;182(5):621-632.
30. Inc NN. NovoSeven RT [package insert]. Plainsboro, NJ; 2019.
31. Poon MC, D'Oiron R, Von Depka M, et al. Prophylactic and therapeutic recombinant factor VIIa administration to patients with Glanzmann's thrombasthenia: results of an international survey. J Thromb Haemost. 2004;2(7):1096-1103.
32. Poon MC, d'Oiron R, Zotz RB, et al. The international, prospective Glanzmann Thrombasthenia Registry: treatment and outcomes in surgical intervention. Haematologica. 2015;100(8):1038-1044.
33. Poon MC, Di Minno G, d'Oiron R, Zotz R. New Insights Into the Treatment of Glanzmann Thrombasthenia. Transfus Med Rev. 2016;30(2):92-99.
34. Fiore M, Firah N, Pillois X, Nurden P, Heilig R, Nurden AT. Natural history of platelet antibody formation against alphaIIbbeta3 in a French cohort of Glanzmann thrombasthenia patients. Haemophilia. 2012;18(3):e201-209.
35. Siddiq S, Clark A, Mumford A. A systematic review of the management and outcomes of pregnancy in Glanzmann thrombasthenia. Haemophilia. 2011;17(5):e858-869.
36. Bellucci S, Damaj G, Boval B, et al. Bone marrow transplantation in severe Glanzmann's thrombasthenia with antiplatelet alloimmunization. Bone Marrow Transplant. 2000;25(3):327-330.
37. Ramzi M, Dehghani M, Haghighat S, Nejad HH. Stem Cell Transplant in Severe Glanzmann Thrombasthenia in an Adult Patient. Exp Clin Transplant. 2016;14(6):688-690.
38. Nurden AT, Pillois X, Wilcox DA. Glanzmann thrombasthenia: state of the art and future directions. Semin Thromb Hemost. 2013;39(6):642-655.
39. Bolton-Maggs PH, Chalmers EA, Collins PW, et al. A review of inherited platelet disorders with guidelines for their management on behalf of the UKHCDO. Br J Haematol. 2006;135(5):603-633.
40. Wilcox DA, Olsen JC, Ishizawa L, et al. Megakaryocyte-targeted synthesis of the integrin beta(3)-subunit results in the phenotypic correction of Glanzmann thrombasthenia. Blood. 2000;95(12):3645-3651.
41. Fang J, Hodivala-Dilke K, Johnson BD, et al. Therapeutic expression of the platelet-specific integrin, alphaIIbbeta3, in a murine model for Glanzmann thrombasthenia. Blood. 2005;106(8):2671-2679.
42. Sullivan SK, Mills JA, Koukouritaki SB, et al. High-level transgene expression in induced pluripotent stem cell-derived megakaryocytes: correction of Glanzmann thrombasthenia. Blood. 2014;123(5):753-757.

ARTICLE

Megakaryocyte volume modulates bone marrow niche properties and cell migration dynamics

Maximilian G. Gorelashvili,[1*] Oğuzhan Angay,[2*] Katherina Hemmen,[2] Vanessa Klaus,[1] David Stegner[1,2] and Katrin G. Heinze[2]

[1]Institute of Experimental Biomedicine, University Hospital Würzburg and [2]Rudolf Virchow Center for Experimental Biomedicine, University of Würzburg, Würzburg, Germany

**MGG and OA contributed equally to this work*

Ferrata Storti Foundation

Haematologica 2020
Volume 105(4):895-904

ABSTRACT

All hematopoietic cells that develop in the bone marrow must cross the endothelial barrier to enter the blood circulation. Blood platelets, however, are released by bigger protrusions of huge progenitor cells, named megakaryocytes, and enter the blood stream as so-called proplatelets before fragmenting into mature platelets. Recently, a second function of megakaryocytes has been identified, as they modulate the quiescence of hematopoietic stem cells, mostly via different soluble factors. We know from light sheet fluorescence microscopy images that megakaryocytes are distributed throughout the bone marrow facing a dense vascular network. Here, we used such three-dimensional images to provide a realistic simulation template reflecting the *in vivo* cell-vessel distributions resulting in reliable whole-bone analysis *in silico*. Combining this approach with an automated image analysis pipeline, we found that megakaryocytes influence migration of neutrophils and hematopoietic stem cells, and thus act as biomechanical restrainers modulating cell mobility and extravasation. Indeed, as a consequence of increased megakaryocyte volumes in platelet-depleted mice neutrophil mobility was reduced in these animals.

Introduction

Hematopoiesis is the process of forming blood cells, which occurs predominantly in the bone marrow (BM). During this process, hematopoietic stem cells (HSC) undergo lineage restriction and differentiate into restricted hematopoietic progenitors, which then give rise to blood cells by proliferation and further differentiation.

During the last decade, the identification of new HSC markers, development of genetically modified mouse strains and microscopy techniques enabled the identification and intensive investigation of the perivascular niche as the major site of HSC localization and activity, where 80% of HSC were found to be associated with sinusoids, 10% with arterioles and a further 10% with transition zone vessels.[1-4] The perivascular niche has been determined to be a microenvironment containing different cell types and signaling molecules, together regulating HSC maintenance, quiescence, proliferation, differentiation and migration.[5-8]

Blood cells differentiated from HSC leave the BM by migrating towards the sinusoids to enter the circulation.[9] In general, many of these migratory processes are chemotactic, i.e. driven by chemoattractants.[9] One of the most prominent cell types of the BM are neutrophils, which are the most abundant subpopulation of leukocytes; neutrophils have a short lifespan (6-12 h) in the circulation, after which they quickly migrate to tissues where they perform their functions.[10] Neutrophil homeostasis is orchestrated through a balance of neutrophil production and release from BM into the blood and migration back into the BM for elimination.[11] The neutrophil reserve within the BM is estimated to be 6×10^{11} in humans and 12×10^{7} in mice.[10,12]

Megakaryocytes are derived from multipotent HSC and belong to the myeloid cell lineage.[13] Megakaryocytes mainly reside in the BM, mostly in close proximity

Correspondence:

KATRIN HEINZE
katrin.heinze@virchow.uni-wuerzburg.de

DAVID STEGNER
stegner@virchow.uni-wuerzburg.de

Received: July 15, 2018.

Accepted: June 25, 2019.

Pre-published: June 27, 2019.

doi:10.3324/haematol.2018.202010

Check the online version for the most updated information on this article, online supplements, and information on authorship & disclosures: www.haematologica.org/content/105/4/895

to the vasculature,[14,15] and have a diameter of up to 50 µm in mice and 50-100 µm in humans.[13] Mature megakaryocytes produce platelets and release them into the blood circulation in order to maintain constant platelet counts. In addition, they actively regulate HSC proliferation in both positive and negative manners.[16-19] Recent studies revealed that most HSC are in close proximity to sinusoidal blood vessels.[1,4,20] Likewise, more than 70% of megakaryocytes were found to be in contact with the BM vasculature.[15] Besides this indirect correlation, at least a subset of megakaryocytes was found to be in close proximity to HSC.[16,18,19] Moreover, megakaryocytes were shown to influence HSC quiescence via different cytokines, such as CXCL4,[16] transforming growth factor β1 (TGFβ1)[17] and thrombopoietin.[18,21] However, very recently it was shown that liver-derived, and not megakaryocyte-derived, thrombopoietin is required for HSC maintenance in the BM.[22]

Nevertheless, megakaryocyte activity in the intact medullary space and its interplay with other BM cells has gained great attention in the last decade; numerous *in vitro* investigations, based on two-dimensional (2D) cryosections, and *in vivo* (two-photon) imaging studies have been reported.[23] Intrinsic limitations of these methods such as loss of volume information, cutting artifacts or small field of view impair scientific models[15] and treatment of patients.[24] Recently, whole bone optical clearing and imaging have been established to overcome these limitations. Despite the significant advances in imaging technology, tools for correct quantitative analysis of the geometry and localization of megakaryocytes, HSC and other BM components are still in their infancy. As image segmentation is a complex and error-prone method, exact definition of the image-processing pipeline is of great importance. The recently developed machine learning toolkits[25,26] are powerful complements to the portfolio, and allow for more comprehensive data analysis, and access to previously masked information. Successful segmented objects derived from complex microscopy data can be used for *in silico* analysis of cell distributions within the BM architecture as recently demonstrated.[15,16,20]

Modular toolkits in particular have been proven to be powerful, not only for image analysis, but also for structure reconstruction as well as simulations of growth and organization.[27,28] Unfortunately, these tools are not yet universally applicable. Here, we developed and compared different image processing pipelines and simulation scenarios for precise identification of megakaryocytes in three-dimensional (3D) light sheet fluorescence microscopy (LSFM) image stacks of uncut murine bones. Megakaryocytes have been described to have an impact, based on biochemical processes, on cell migration in the BM. However, the impact of increases in their number and size is unclear. To date, the only available technique for investigating cell migration in the BM is intravital imaging, which is hampered by the limited time during which measurements can be made because of the need for anesthesia of the animals and accumulating phototoxicity,[29] limited penetration depth[30] and a relatively small field of view of typically 300-500 µm^2 that does not allow observation of the whole bone simultaneously. Here, computational simulations represent an important complementing and well-controllable tool for elucidating underlying cell mechanisms.[31-33] Typically, simulation studies use artificial meshes as templates due to the lack of experimental data or to minimize the computational effort. Unfortunately, such simplified artificial templates for megakaryocytes and the vasculature can bias simulations and lead to misinterpretations as we show in this study. Here, we demonstrate that using the segmented cell and vessel objects of true 3D images can overcome those limitations, providing a simulation framework that has the prerequisites to reflect the physiological situation optimally.

Methods

More methodological details are present in the *Online Supplementary Material*.

Mice

All animal experiments were approved by the district government of Lower Frankonia (Bezirksregierung Unterfranken). We used 8- to 12-week old C57BL/6JRj (Janvier Labs) or *Lyz2*^{GFP} mice.[34]

Thrombocytopenia was induced by intravenous injection of rat anti-GPIbα[35] (CD42b; 2.0 µg/g body weight Emfret Analytics, Eibelstadt, Germany;).

Two-photon intravital imaging

Lyz2^{GFP} mice[34] were anesthetized by intraperitoneal injection of medetomidine 0.5 mg/g, midazolam 5 mg/g and fentanyl 0.05 mg/g body weight. A 1-cm midline incision was made to expose the frontoparietal skull, while carefully avoiding damage to the bone tissue. The mouse was placed on a custom-designed metal stand equipped with a stereotactic holder to immobilize the head. BM vasculature was visualized by injection of bovine serum albumin-Alexa546 (8 µg/g body weight) and anti-CD105 Alexa546 (0.6 µg/g body weight). Neutrophils were visualized by the endogenously expressed green fluorescent protein. Stacks were acquired at a frame rate of 1/min on an upright two-photon fluorescence microscope (TCS SP8 MP, Leica Microsystems, Wetzlar, Germany) equipped with a 25x water objective with a numerical aperture of 1.0. A tunable broad-band Ti:Sa laser (Chameleon, Coherent, Dieburg, Germany) was used at 780 nm to capture green fluorescent protein and Alexa546 fluorescence. For each mouse, three time series of z-stacks were recorded (20 min each, 1 z-stack/min) with a voxel size of 0.87 x 0.87 x 1 µm^3. Details on image analysis are provided in the *Online Supplementary Material*.

Light sheet fluorescence microscopy image processing and segmentation

Image stacks were processed, visualized, and analyzed using FIJI,[36] Ilastik 1.2.[25] and Imaris® 8.4 (Bitplane AG, Zurich, Switzerland). The four different analysis pipelines (I-IV), shared the same image-preprocessing steps performed in FIJI and Imaris. In the first pipeline (I), the membrane algorithm was directly applied on megakaryocytes. The second, simple one-pass pipeline (II) utilized the Imaris cell soma algorithm with one seeding step, whereas the extended two-pass pipeline (III) employed two subsequent seeding steps for large and small megakaryocytes. Our customized pipeline (IV) corrected for fake invaginations by creating virtual cell somata before applying two-step seeding. Bone and BM were identified using the pixel classification algorithm of Ilastik software, with results transferred to Imaris 8.4 for segmentation and further analysis. Details are provided in the *Online Supplementary Material*.

Static and dynamic computational simulations

Simulations of megakaryocyte distribution (static) and cell migration (dynamic) in the BM were performed by custom-written algorithms (*Online Supplementary Figures S4* and *S6*) in Matlab

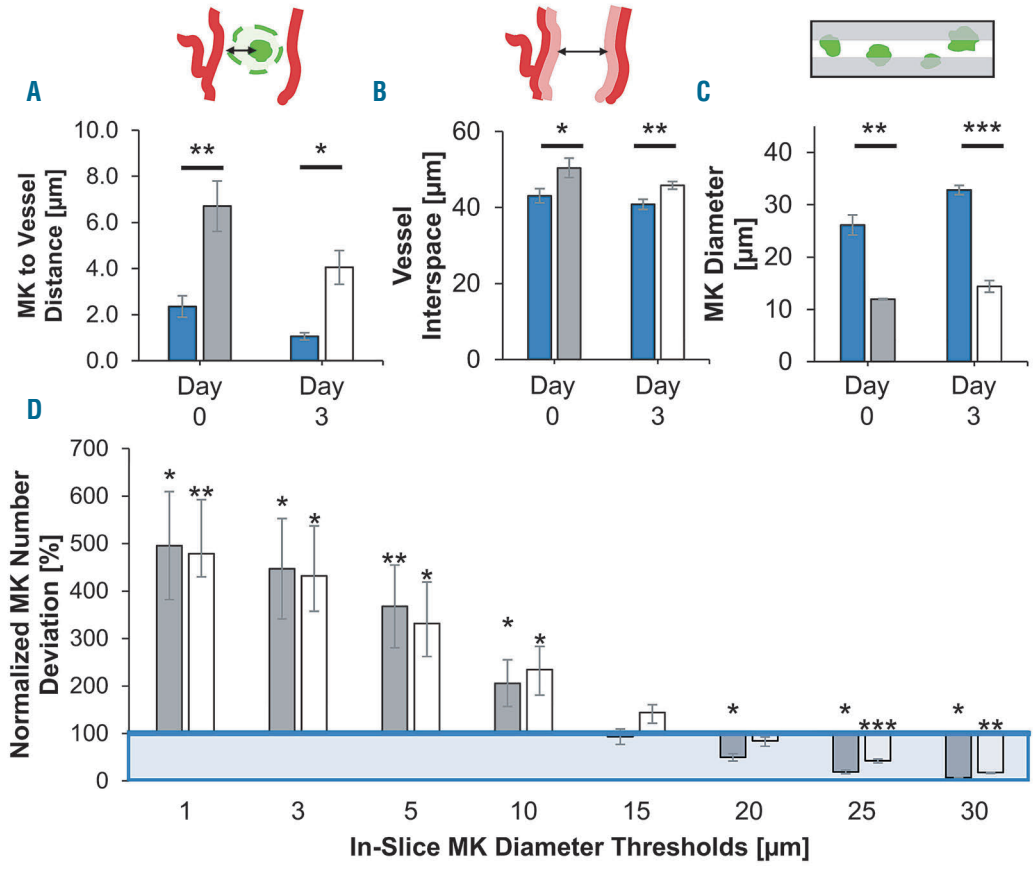

Figure 1. Comparison of data derived from full image stacks and virtual slices. Data displayed for two time points: before induced thrombopoiesis with generally smaller megakaryocytes (day 0, dark gray bars) and after with very large megakaryocytes (day 3, white bars) in comparison to three-dimensional stack ground truth (blue bars/box). Virtual slices extracted from full image stacks. Binary mask of stack megakaryocytes (=ground truth) was used for in-slice megakaryocyte segmentation (see inset 1C). Bar graphs represent the mean ± standard deviation (SD). Two-parameter t-test: stack vs. virtual slice data for day 0 and day 3, respectively. **P*<0.05; ***P*<0.01; ****P*<0.001. (A) Mean megakaryocyte-to-vessel distance is increased in slices compared to full stack analysis. (B) Measured vessel interspace is significantly greater in virtual slices than in full stacks. (C) Mean megakaryocytes diameter is massively underestimated in virtual slices. (D) Megakaryocyte numbers in slices deviate significantly from stack ground truth depending on diameter threshold of the megakaryocytes. Megakaryocyte numbers normalized to equal marrow volume; percentage relative to stack ground truth. Mk: megakaryocyte.

(Mathworks, Natick, MA, USA) which virtually reconstruct the BM space using 3D images at a voxel level and simulate cell distribution and/or migration depending on various adjustable parameters (cell type, BM crowdedness, cell velocity, chemotaxis and vessel stickiness) as indicated in the Results section. All migrating cells (HSC or neutrophils) are placed into the template (*Online Supplementary Figure S5*) so that spatial overlap with the vasculature or other cells is avoided. Megakaryocytes are preset in the template according to the vessel-biased distributions identified by Stegner *et al.*[15] Details are provided in the *Online Supplementary Material*.

Statistical analysis

Data exported from Imaris were processed with Microsoft Excel 2016 (Microsoft Corporation, Redmond, WA, USA) and statistics were analyzed using OriginPro 2016 (OriginLab Corporation, Northampton, MA, USA) or SigmaPlot (Systat Software, San Jose, CA, USA). We tested datasets for variance homogeneity (Levene test). The Mann-Whitney test, two-parameter *t*-test and one-way analysis of variance (with the Tukey post-hoc test) were applied where appropriate. *P*-values ≥0.05 were considered as not significant (ns), while *P*-values <0.05 were considered statistically significant (**P*< 0.05; ***P*<0.01; ****P*<0.001).

Results

A full three-dimensional dataset is crucial for unbiased quantification of megakaryocyte-vasculature characteristics and interplay

First, we assessed the potential benefits of whole stack imaging compared to sectioning. To do this, we virtually sliced existing image stacks (10 slices per stack each with a thickness of 10 µm), and compared exemplified slices (mimicking a typical experimental setting) to the complete 3D image. We compared key parameters such as megakaryocyte-to-vessel distance, vessel interspace, and mean megakaryocyte diameter. It should be noted that this is not an assessment of the bias of cutting artifacts, but purely the impact of the intrinsically 2D-limited information in exemplified slices. Due to the elaborate and complex sample preparation, including critical chemicals to acquire 3D BM images, it is not possible to subsequently process the same bones for 2D analysis, so virtual slices are used. For completeness, we evaluated datasets for steady-state conditions (day 0) and 3 days after complete platelet depletion (day 3) individually.

We first measured the mean megakaryocyte-to-vessel distance (edge-to-edge). Our data revealed fundamentally

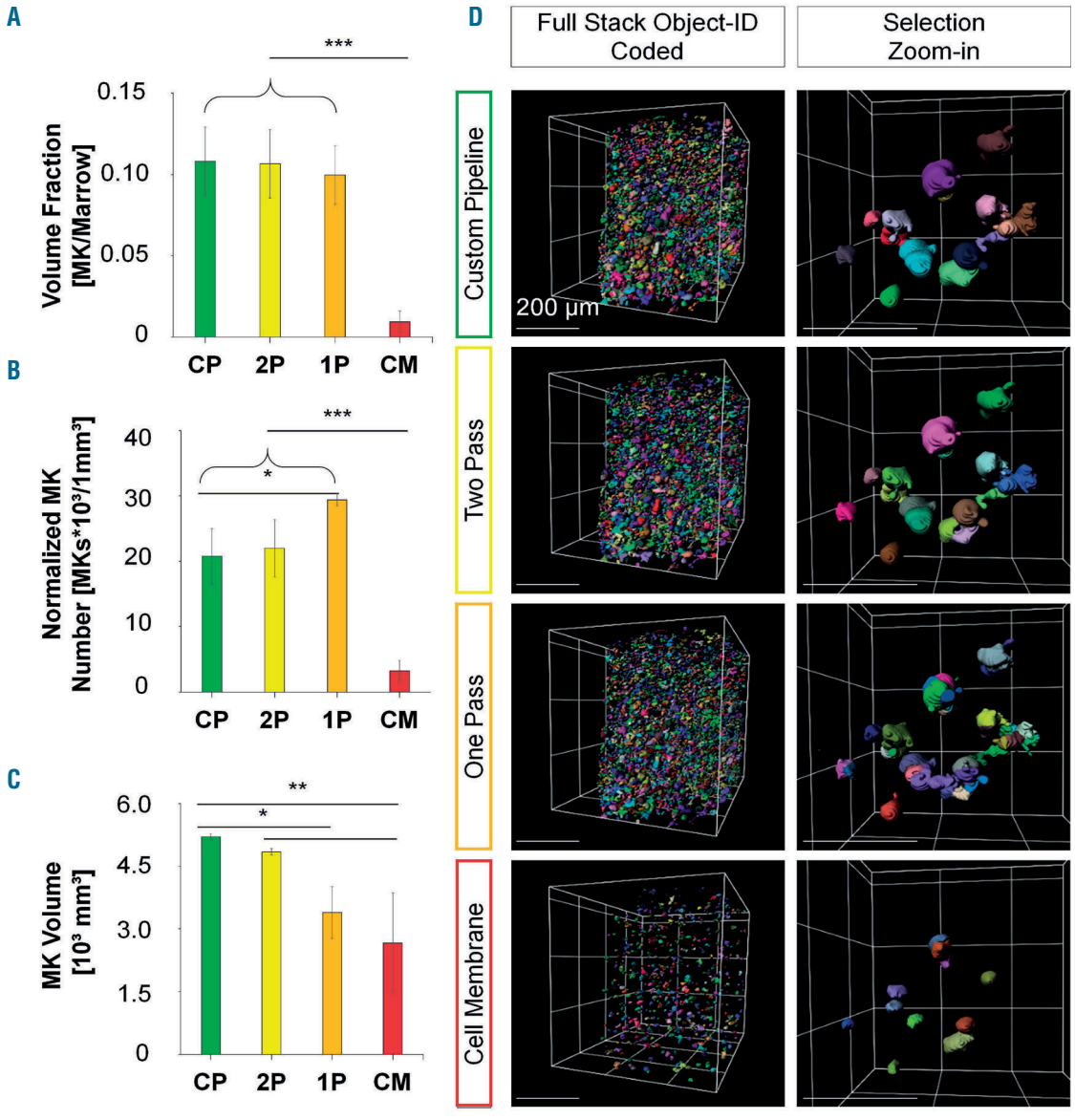

Figure 2. Segmentation performance of the customized pipeline compared with the one-/two-pass pipelines and the Imaris cell membrane algorithm on day 0. (A-C) Data depicted for the customized pipeline (CP; green bars), two-pass pipeline (2P; yellow bars), one-pass pipeline (1P; orange bars), and Imaris cell membrane algorithm (CM; red bars) before induced thrombopoiesis (day 0). (A) Megakaryocyte-to-marrow volume fraction is comparable between the customized and one-/two-pass pipelines with a massive decrease when the Imaris cell membrane algorithm is used. (B) Normalized mean megakaryocyte numbers are comparable with the customized and two-pass pipelines, whereas they are significantly increased with the one-pass pipeline and massively decreased with the Imaris cell membrane algorithm. (C) Customized and two-pass pipelines deliver comparable mean megakaryocyte volumes, whereas those yielded by the one-pass pipeline or the Imaris cell membrane algorithm are significantly decreased. Bar graphs represent the mean ± standard deviation. *P<0.05; **P<0.01; ***P<0.001 (one-way analysis of variance, Tukey post-hoc test). (D) Exemplified segmentation results. Left column: full stack with segmented megakaryocytes, object ID color-coded. Sparsely located megakaryocytes with cell membrane algorithm opposed to other pipelines. Right column: zoom-in to selection. Megakaryocyte fragmentation is higher in the one- and two-pass pipelines compared to the customized pipeline. Cell membrane algorithm with sparse and small megakaryocytes. Grid size and scale bar = 200 µm. Mk: megakaryocyte.

increased distances in virtual slices compared to the distances in full stacks. While megakaryocytes in stacks were generally located in closest proximity of vessels ≈ 1.1 - 2.4 µm, we observed a roughly 3- to 4-fold increase in virtual slices for both measurement time points. Day 3 megakaryocytes, usually larger than day 0 megakaryocytes, were generally situated closer to blood vessels than day 0 megakaryocytes in 3D stacks and virtual slices alike (Figure 1A, *Online Supplementary Table S1*). Second, we assessed the available interspace between vessels in BM. In stacks, the distances we measured were the same at both time points. In slices, distances were significantly increased at both time points compared to the respective ground truth values, being roughly 17% higher at day 0 and 12% at day 3 (Figure 1B, *Online Supplementary Table S1*). Third, we determined the mean megakaryocyte diameter. In stacks, megakaryocyte diameters on day 3 were about 26% larger than on day 0 ($Ø_{day0}$=26.1 ± 1.9 µm *vs.* $Ø_{day3}$=32.8 ± 0.9 µm). In contrast, the average diameters we measured in slices were almost half at both time points, being 46% and 44%

of the stack megakaryocyte diameters on day 0 and 3, respectively (Figure 1C, *Online Supplementary Table S1*).

As we measured clear bias by analysis of the sliced stack, we wondered whether there was a megakaryocyte number bias in slices. Here, we first determined the ground truth of intact stacks by counting megakaryocytes, and normalizing the number to a defined volume of BM: n_{MK_day0} = 20801 ± 4223 megakaryocytes/mm^3 and n_{MK_day3} = 15992 ± 1700 megakaryocytes/mm^3 in stacks and exemplified slices alike. We set a threshold megakaryocyte size to discard artifacts and cell fragments. In stacks, we defined 525 μm^3 (equivalent to 10 μm sphere diameter) as the minimum megakaryocyte volume. In slices we applied a range of increasing minimum diameter thresholds (1 μm to 30 μm), and compared the deviation to stack megakaryocyte numbers. Lower thresholds resulted in massive overestimation of megakaryocyte numbers, from roughly 500% with the 1 μm threshold to around 200% with the 10 μm threshold. We measured stack-comparable megakaryocyte numbers at 15 μm and 15/20 μm on day 0 and 3, respectively. Higher diameter thresholds led to significant underestimation of in-slice megakaryocyte numbers at both time points (Figure 1D).

An iterative multi-step image processing pipeline is essential for reliable segmentation of megakaryocytes

Megakaryocyte segmentation was challenging because of the considerable variability in cell shape and size, ranging over several orders of magnitude, hampering pre- and post-segmentation artifact removal. To optimize the analysis, we tested four different analysis pipelines, using both FIJI and Imaris for different tasks, and compared their segmentation performance: (i) Imaris cell membrane, (ii) one-pass, (iii) two-pass, and (iv) custom-designed. A manual side-by-side comparison of their relative performance (Figure 2, *Online Supplementary Figures S1* and *S2*, Table 1) revealed a severe amount of fake invaginations and false seeding points for (i)-(iii), although the effect was least severe for (iii). Thus, we successfully extended the two-pass pipeline into a (iv) customized pipeline by one additional step of correction (Figure 2D, *Online Supplementary Figure S2D*), achieving a superior performance and minimizing artifacts compared to the previous algorithms. The Imaris cell membrane tool showed the most severe underperformance: megakaryocyte-to-marrow volume fraction, normalized mean megakaryocyte numbers, and mean megakaryocyte volume were greatly underestimated. Overall, only a few megakaryocytes were recognized and only the unstained innermost lumen was segmented. The one-pass pipeline delivered megakaryocytes to the same marrow fractions as our customized pipeline. However, the strong increase of normalized mean megakaryocyte numbers and the decrease in mean megakaryocyte volumes indicated high over-segmentation of megakaryocytes. The two-pass pipeline, as the direct progenitor of our customized pipeline, performed better in the comparison of (i) and (iii). We found comparable values for total megakaryocyte volume fraction (normalized to marrow volume) and mean megakaryocyte numbers. However, for the much larger megakaryocytes on day 3 after platelet depletion, the mean megakaryocyte volume was underestimated by 16% while no deviation was observed for the smaller megakaryocytes on day 0.

The results suggest that the suitability and performance of pipelines (i)-(iii) depend on the volume of the megakaryocytes. To pinpoint this correlation, we sorted our data by megakaryocyte volume, and compared deviations of megakaryocyte numbers and volumes systematically to our optimized custom pipeline (*Online Supplementary Figure S1*): the greatest deviation was shown by (i) which underestimated megakaryocyte numbers throughout all volume classes. Large megakaryocytes were widely neglected, while the volume of small megakaryocytes was overrepresented due to over-fragmentation. The same tendency, albeit less pronounced, was observed for (ii) (*Online Supplementary Figure S1*). Pipeline (iii) performed more comparably to (iv). However, the numbers of very small megakaryocytes were still slightly overestimated on both day 0 and day 3, and we found significantly underestimated numbers of mid-to-larger megakaryocytes on day 3. Volumes of the largest megakaryocytes were significantly underestimated on both days (*Online Supplementary Figure S1*).

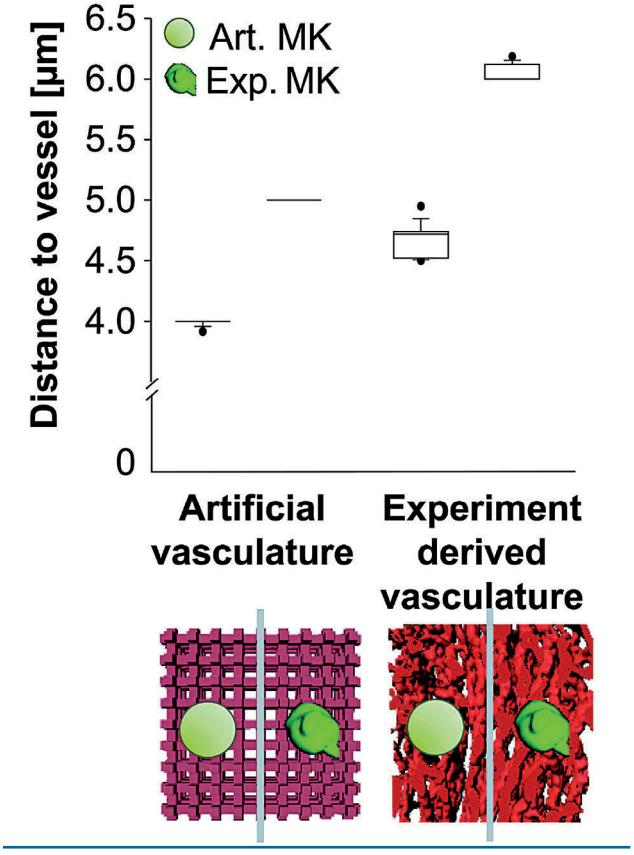

Figure 3. Vessel and megakaryocyte shape changes the outcome of simulated megakaryocyte distribution in the bone marrow. Megakaryocyte distribution in the bone marrow was simulated and the edge-to-edge distance between the cells and the vasculature was calculated. Simulations were performed either with a simplified artificial vessel lattice (light red) or with real bone marrow vasculature imaged by light sheet fluorescence microscopy (red). In both vessel templates, artificial (non-hatched) or real megakaryocytes (hatched) were placed randomly. For the artificial megakaryocyte simulations only one spherical megakaryocyte type was used, while real megakaryocyte simulations were performed with a pool of different megakaryocytes with a representative distribution of diameters. In total, ten simulations of each type were performed with 700 or 1100 megakaryocytes per simulation for artificial and real vasculature, respectively. Differences between all groups were significant at $P<0.001$ (one-way analysis of variance and pairwise comparison procedures with the Dunn method) Mk: megakaryocyte.

Experimental three-dimensional image stacks serve as templates for realistic simulation of cell distribution in the bone marrow

We recently showed that segmented 3D LSFM images can be used as templates for static simulation of megakaryocyte distribution in the BM.[15] Here, we systematically compared this approach to conventional simulation methods. To do this, we used experimentally derived structures of megakaryocytes (MK^{exp}) and vessels (V^{exp}) on the one hand, and simplified artificial structures (MK^{art}, V^{art}) on the other hand. To acknowledge the complexity of the *in vivo* system we employed a voxel-based simulation model using a Brownian walk with obstacles (*Online Supplementary Figure S4*). The artificial vasculature was constructed as a 3D lattice with correct intervascular distances and megakaryocytes were spherical objects of proper size (*Online Supplementary Figure S3*). We combined all four possible pairs ($MK^{art}V^{art}$, $MK^{exp}V^{exp}$, $MK^{art}V^{exp}$, $MK^{exp}V^{art}$) for *in silico* modeling (Figure 3).

For the simulation megakaryocytes were randomly placed in the intervascular space without overlaps with vessels or other megakaryocytes (*Online Supplementary*

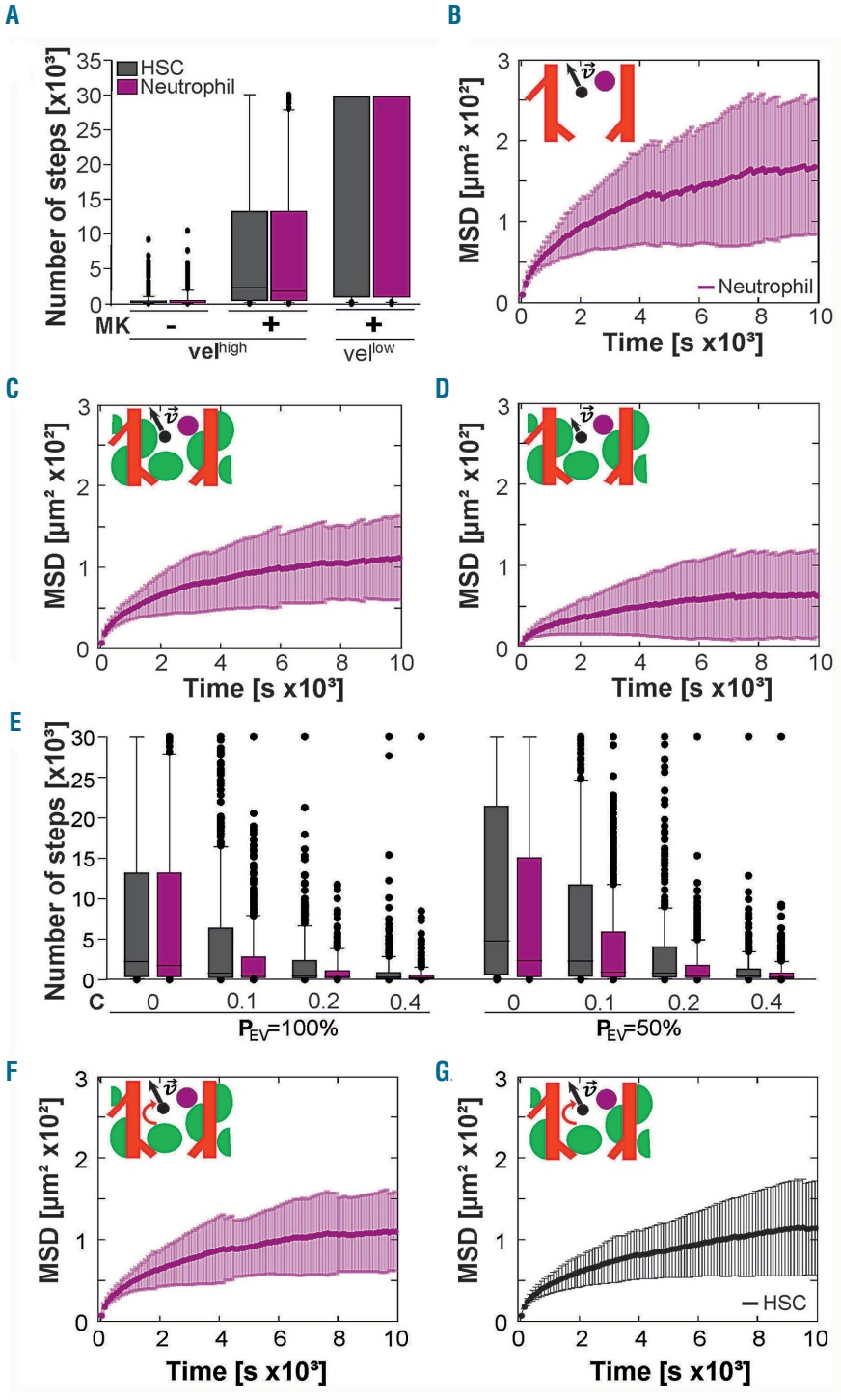

Figure 4. Adjustable biophysical parameters influence simulated cell migration in the bone marrow. Simulation of cell migration in bone marrow was performed with adjustable parameters: cell type, bone marrow crowdedness, cell velocity, chemotaxis and vessel stickiness. (A) Number of steps until entering the vessel lumen for artificial hematopoietic stem cells (HSC; black) and neutrophils (magenta) migrating in the bone marrow with or without increased crowdedness resulting from the presence of megakaryocytes at high and low instantaneous velocities of V_{high} = 3 ± 2 µm/step and V_{low} = 2 ± 1 µm/step, respectively. The probability of entering the vessel lumen after contact (P_{EV}) was set at P_{EV} = 100% and chemotaxis was absent (C = 0). (B-D) Mean squared displacement (MSD) and neutrophil trajectories for the megakaryocyte-free template at high velocities (B) and a megakaryocyte-containing simulation environment at high (C) and low (D) velocities. P_{EV} = 100% and C = 0. (E) Number of steps until entering the vessel lumen for P_{EV} = 100% and P_{EV} = 50% for increasing chemotaxis (C = 0; 0.1; 0.2; 0.4) in the presence of megakaryocytes. (F-G) MSD analysis of neutrophil and HSC migration data from (E) for P_{EV} = 50% and C = 0. Six hundred simulations were performed for each simulation type. Plots for HSC migration are shown in *Online Supplementary Figure S7*.

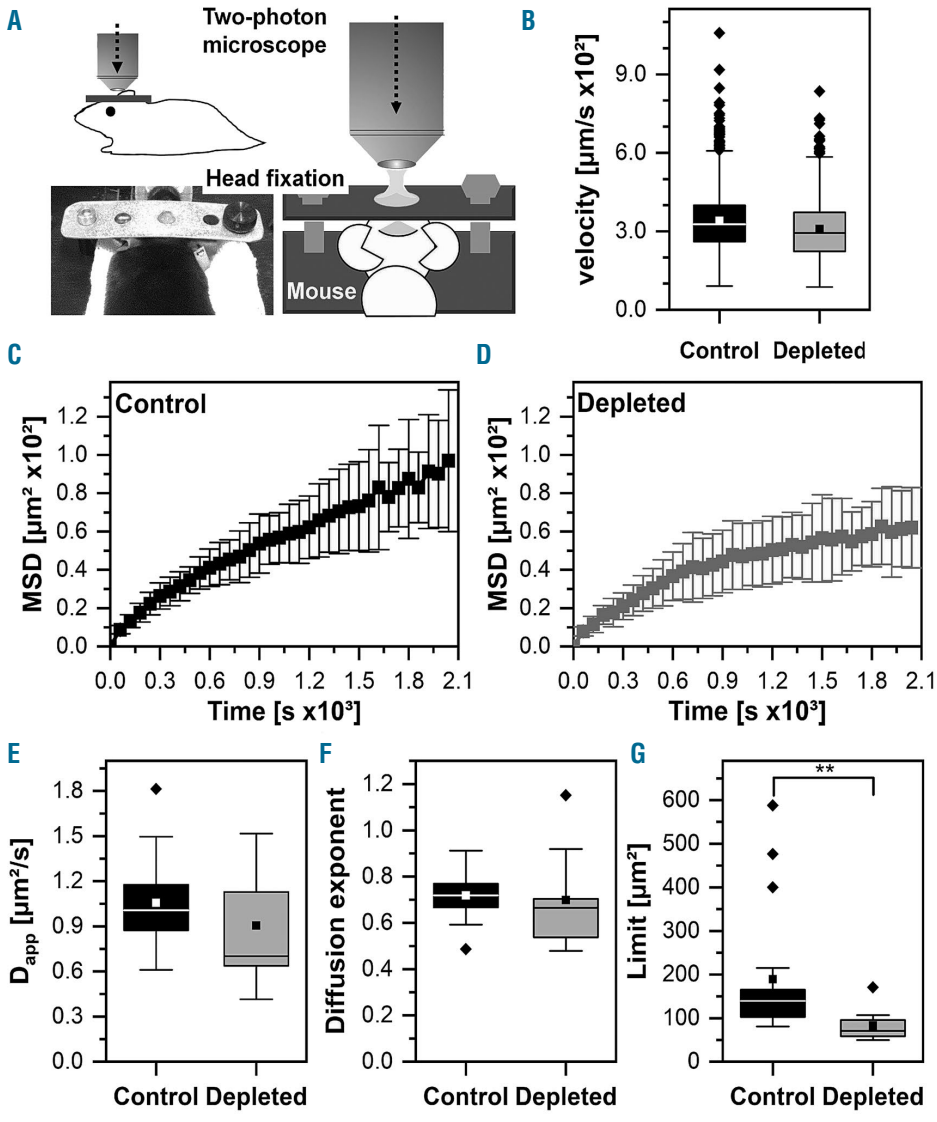

Figure 5. Intravital imaging reveals decreased mobility of neutrophils in platelet-depleted mice. (A) Scheme of two-photon microscopy of the bone marrow 72 h after the induction of platelet depletion (or mock injection) through a 1 cm open cranial window (thinned skull) using a head-fixation in a stereotactic holder as illustrated. (B) Instantaneous velocities of neutrophils (62-149 per mouse) tracked in mice depleted of platelets (n=3 mice, 0.034 ± 0.011 µm/s) and the control group (n=5, 0.031 ± 0.011 µm/s). (C, D) Mean and standard deviation of the time-dependent mean squared displacement of the control group and the megakaryocyte-depleted mice. (E-F) The apparent diffusion coefficient, D_{app}, and diffusion exponent, α, for the control group (D_{app}= 106 ± 32 µm², α = 0.72 ± 0.10) and megakaryocyte-depleted mice (D_{app} = 90.5 ± 38.4 µm², α = 0.70 ± 0.21) as obtained from equation 3. *P*=0.129 for D_{app} and *P*=0.092 for α (Mann-Whitney test). (E) Saturation limit, *L*, for the control group (*L* = 189 ± 150 µm²) and megakaryocyte-depleted mice (*L* = 82.7 ± 38.0 µm², *P*=0.0018) as obtained from equation 2. MSD: mean squared displacement.

Figure S4). It should be noted that we used randomly distributed objects of the same average diameter for all four possible megakaryocyte-vessel pairings, so that the resulting megakaryocyte-to-vessel distances would be comparable, if the approaches were comparable. However, for MK^{art} the cells were found to be closer to the vessels than for MK^{exp} no matter whether the vessels were artificial (3.99 ± 0.03 µm *vs*. 5.00 ± 0.00 µm) or had been experimentally derived (4.67 ± 0.14 µm *vs*. 6.04 ± 0.07 µm) (Figure 3). For all cases with V^{art}, the cell-vessel distance for both MK^{art} and MK^{exp} appeared to be decreased. Thus, the cell distribution in the BM looks significantly different when simplified artificial 3D objects are chosen.

Megakaryocytes hamper simulated cell migration in the bone marrow

Next, we used the 3D LSFM templates for simulations of cell migration (*Online Supplementary Figure S5*). Physiologically, HSC and neutrophils are recruited to the peripheral blood during stem cell mobilization or inflammatory processes, respectively. In this context, we aimed to learn more about the recruitment process and the role of megakaryocytes, cell velocity and cell size in HSC and neutrophil migration to BM vasculature *in silico*. To simulate migration of small HSC and bigger neutrophils in the BM, we designed artificial cells considering the real diameter and sphericity of these types of cells.[37,38] The HSC and neutrophils were set to migrate randomly in the intervas-

cular space with a predefined step size of 3 ± 2 μm (mean ± standard deviation). The time between two steps was set at 20 s. To analyze migration towards the vasculature, the number of steps until first contact with a BM vessel was assessed, assuming that the cell would subsequently migrate into the intraluminal space. To further characterize the migration, the mean squared displacement (MSD) of cell trajectories was determined for different time scales. Simulations were performed with and without megakaryocytes in the BM to assess the influence of BM crowdedness on cell migration (Figure 4A-C; *Online Supplementary Figure S7*). We found that megakaryocytes dramatically reduced the motility of HSC and neutrophils. The number of steps (n^{steps}) to reach the vasculature increased in the presence of megakaryocytes (HSC: from n_{steps} = 513 ± 1107 to n_{steps} = 8057 ± 10310, neutrophils: from n_{steps} = 628 ± 1270 to n_{steps} = 7869 ± 10175) (Figure 4A) and the trajectories exhibited lower MSD values (HSC: from MSD_{20s} = 9.52 ± 5.95 μm² to MSD_{20s} = 6.85 ± 1.27 μm², neutrophils: from $MSD20_s$ =10.57 ± 5.06 μm² to MSD_{20s} = 6.96 ± 1.26 μm²) (Figure 4B, C; *Online Supplementary Figure S7*). Fitting the first 25% of the MSD trajectories to determine the apparent diffusion coefficient (D_{app})[39] revealed reduced D_{app} in the presence of megakaryocytes (*Online Supplementary Table S3*). Likewise, saturation limits of the MSD curves were reduced in the presence of megakaryocytes (HSC: from 171 ± 1.3 μm² to 133 ± 0.8 μm²; neutrophils: from 182 ± 1.8 μm² to 116 ± 0.5 μm²) (*Online Supplementary Table S4*). Collectively, these data suggest that megakaryocytes represent passive obstacles, and significantly hamper cell migration in the BM. Lowering cell velocity (step size of 2 ± 1 μm) further suppressed migration for both HSC and neutrophils (HSC: n_{steps} = 8100 ± 13162 and MSD_{20s} = 3.73 ± 1.13 μm², neutrophil: n_{steps} = 19694 ± 13924 and MSD_{20s} = 3.91 ± 1.02 μm²) (Figure 4A, D). Interestingly, there were no significant differences between the investigated cell types, despite their different size and shape.

Chemotaxis and weak cell-to-vessel adhesion reveal the impact of cell size on migration *in silico*

Cell migration in the BM can be guided by chemotactic processes. Thus, we introduced chemotaxis into our cell migration algorithm, with the vessel walls being assumed to be the source of the chemoattractant (*Online Supplementary Figure S6*). Furthermore, we extended the algorithm with an adjustable probability for entering the vessel (P_{EV}) to reflect a highly physiological cell migration process. We found that the number of required steps to reach and enter the vessels decreased (*Online Supplementary Table S2*) as the chemotaxis increased with a stronger gradient guiding the cells towards nearby vessels (Figure 4E). At the same time the corresponding MSD values for both investigated P_{EV} of 100% and 50% significantly increased (*Online Supplementary Table S2* and *S3*, Figure 4F). Here, neutrophils appeared to enter the vasculature faster than HSC, which is in contrast to the simulations without chemotaxis. As expected, reducing P_{EV} from 100% to 50% increased the time until entering the vasculature (*Online Supplementary Table S2*, Figure 4E), but did not change the MSD values (*Online Supplementary Table S2*, Figure 4C, G). Interestingly, for probability P_{EV}=50% neutrophils reached the vasculature significantly faster than HSC even in the absence of chemoattractants. In other words, cell size matters for migration to the vasculature, and this size effect can even be augmented by biophysical parameters such as chemotaxis and cell-to-vessel adhesion probability.

Treatment known to deplete circulating platelets and increase megakaryocyte volume is associated with a reduction in neutrophil mobility in the bone marrow

Next, we assessed whether the data obtained from the computational simulations could be validated *in vivo* (Figure 5; *Online Movies 1* and *2*). A depletion of megakaryocytes would inevitably also remove the biochemical factors derived from megakaryocytes. Factors such as platelet factor-4 (PF4) and TGFβ1 have been shown to modulate HSC quiescence[16,17] so it would be impossible to discriminate between the biochemical and biomechanical effects of megakaryocyte depletion. As an alternative approach we treated platelets with anti-GPIbα antibodies, which do not deplete megakaryocytes, but result in increased megakaryocyte volume of vessel-associated megakaryocytes on day 3 after platelet depletion.[15] In our computational simulations the larger megakaryocytes had a greater impact than steady-state megakaryocytes on neutrophil mobility (*not shown*). Thus, we compared neutrophil mobility in naïve mice and mice on day 3 following platelet-depletion (Figure 5) with the parameters detailed in the *Online Supplementary Material* (*Online Supplementary Tables S3* and *S4*). As expected from our simulations neutrophil mobility was decreased in platelet-depleted mice (saturation limit from 120 ± 5.58 μm² to 66.7 μm² in platelet-depleted mice), supporting our hypothesis that megakaryocytes restrain the mobility of neutrophils.

Supporting information

We have uploaded two supporting videos - one exemplary dataset of naïve and megakaryocyte-depleted mice – as well as the MatLab scripts used in the simulation and the Ilastik training file used in bone and BM segmentation on Zenodo under DOI: 10.5281/zenodo.3144732.

Discussion

Here, we provide a profound 3D image reconstruction and segmentation pipeline for different BM components and use these data for computational simulations by complex tailored cell localization and migration algorithms. Realistic simulation templates were deployed for migration simulations of HSC and neutrophils. Our data clearly show that volumetric analysis of the number and localization of megakaryocytes provides additional information.

Furthermore, we performed computational 3D simulations of megakaryocyte distribution and BM cell migration using the 3D segmented LSFM data. These simulations suggest that megakaryocytes play an important role in cell migration even if not migrating themselves. Instead, they represent passive obstacles, and thus significantly influence migration of other cells, such as HSC and neutrophils, in the BM. We discovered this from realistic simulations using templates with high physiological relevance derived from segmented cell and vessel objects in 3D LSFM images.

The image analysis pipeline is clearly superior to commonly used strategies, and minimizes bias of crucial parameters such as cell number and volume. Our data

emphasize the need for (customized) multistage segmentation pipelines with active artifact removal when studying complex specimens. While both common pipelines failed significantly, the two-pass algorithm performed closest to our custom pipeline, albeit with some flaws. Besides the risk of over-segmentation, further manual assessment confirmed incomplete segmentation of larger megakaryocyte somata with weak and irregular staining as often found in typical samples. Unfortunately, this results in invaginations and consequently volume underestimation. During segmentation, seeding points were often not set properly. They were preferentially placed on high intensity membrane or cell-cell touching areas and often missed cell centers, which leads to inaccurate determination of cell volumes, but similar cell numbers (Figure 2D, *Online Supplementary Figure S2D*).

Previous studies often utilized Ilastik pixel classification for discrimination of distinct objects such as co-cultured cells.[40] In line with recent work,[25] we demonstrated successful segmentation of challenging tissue structures. Although the best results were achieved here with the full feature set for pixel classification, these sets could be reduced and optimized to smaller structure/pattern sizes that also suit memory-limited scenarios.

The segmented objects of the LSFM images are not only important for proper quantitative imaging, but are also very advantageous when it comes to realistic simulations of cellular distributions, dynamics and interactions of cells within the BM. Thus, we found that real sample templates were highly advantageous, in terms of accuracy, compared to simplified artificial 3D objects. Of course, the conventional method using periodic and other simple structures would minimize computational time, but could lead to biased results, masking important features of a given distribution.

Previous studies have shown that the deletion of megakaryocytes activates quiescent HSC and expands the HSC pool as well as increasing HSC mobilization and proliferation.[16-18] These effects could be partially reproduced by ablation of cytokines, such as TGFβ1[17] and CXCL4[16] in megakaryocytes and platelets. However, as megakaryocytes, despite their relatively low number (accounting for less than 0.1% of all BM cells), make up a significant volume within the BM and are distributed along the blood vessels, we hypothesized that megakaryocytes might serve as passive obstacles hindering the egress of other cells from the BM. As the biomechanical barrier function of megakaryocytes cannot be technically uncoupled from the potential chemical effects (e.g. cytokine release) of megakaryocytes, which are also abolished if these cells are depleted, *in vivo*, we took advantage of mathematical modeling approaches using LSFM-derived objects. These simulations based on 3D Brownian dynamics clearly demonstrate that megakaryocytes might act as a biomechanical restraint hindering BM egress of HSC or neutrophils (Figure 4). Importantly, this effect comes into play even under circumstances such as chemotactic cues or high cell velocities, indicating that it is an important factor modulating the egress of cells from the BM. Other cell features, such as deformability have also been shown to be important when it comes to extravasation and tumor growth[41] or immune responses.[42] Extravasation conditions and prerequisites have been modeled previously e.g. by Xiao and colleagues[43] with the interesting result that cell shape rather than elasticity may play an important role when squeezing through a narrow gap. This knowledge may guide more complex simulations in the future. However, to date it exceeds the computational power of common laboratories and facilities. In contrast, the simulations presented here can be run on a single workstation in a few hours, still being sufficient to describe a typical large-tissue scenario observed in animal experiments. One limitation of using platelet depletion is that this treatment might potentially affect other features of the BM environment that could influence the migration of BM cells. On the other hand, the use of anti-GPIbα antibodies to deplete platelets is the 'gold standard' in the field and has no obvious effects on immune cells.[35] Moreover, our first *in vivo* data on neutrophil mobility in naïve and platelet-depleted mice (Figure 5; *Online Supplementary Tables S3* and *S4*) support the hypotheses derived from our mathematical modeling approach, as the saturation limit of the neutrophil MSD trajectories in platelet depletion was significantly reduced compared to steady-state conditions (Figure 5G; *Online Supplementary Table S3*). Consequently, this study points to the importance of biomechanical properties of the BM environment in regulating cell motility, a factor which has so far not been appreciated sufficiently. Moreover, our study showcases how the combination of advanced imaging approaches in combination with computational simulations can refine hypotheses.

Funding

Funded by the Deutsche Forschungsgemeinschaft (DFG, German Research Foundation) – Projektnummer 374031971 – TRR 240, TP B06, and the Rudolf Virchow Center of the University of Würzburg, Germany.

Acknowledgments

The authors thank Hannah Heil (RVZ, University of Würzburg) for help with the graphics concerning Figure 4.

References

1. Kiel MJ, Yilmaz OH, Iwashita T, et al. SLAM family receptors distinguish hematopoietic stem and progenitor cells and reveal endothelial niches for stem cells. Cell. 2005;121(7):1109-1121.
2. Ding L, Saunders TL, Enikolopov G, Morrison SJ. Endothelial and perivascular cells maintain haematopoietic stem cells. Nature. 2012;481(7382):457-462.
3. Chen JY, Miyanishi M, Wang SK, et al. Hoxb5 marks long-term haematopoietic stem cells and reveals a homogenous perivascular niche. Nature. 2016;530(7589):223-227.
4. Acar M, Kocherlakota KS, Murphy MM, et al. Deep imaging of bone marrow shows non-dividing stem cells are mainly perisinusoidal. Nature. 2015;526(7571):126–130.
5. Asada N, Kunisaki Y, Pierce H, et al. Differential cytokine contributions of perivascular haematopoietic stem cell niches. Nat Cell Biol. 2017;19(3):214-223.
6. Morrison SJ, Scadden DT. The bone marrow niche for haematopoietic stem cells. Nature. 2014;505(7483):327-334.
7. Boulais PE, Frenette PS. Making sense of hematopoietic stem cell niches. Blood. 2015;125(17):2621-2629.
8. Crane GM, Jeffery E, Morrison SJ. Adult haematopoietic stem cell niches. Nat Rev Immunol. 2017;17(9):573-590.
9. Abarrategi A, Mian SA, Passaro D, et al. Modeling the human bone marrow niche in

mice: from host bone marrow engraftment to bioengineering approaches. J Exp Med. 2018;215(3):729-743.
10. Summers C, Rankin SM, Condliffe AM, et al. Neutrophil kinetics in health and disease. Trends Immunol. 2010;31(8):318-324.
11. Christopher MJ, Link DC. Regulation of neutrophil homeostasis. Curr Opin Hematol. 2007;14(1):3-8.
12. Furze RC, Rankin SM. Neutrophil mobilization and clearance in the bone marrow. Immunology. 2008;125(3):281-288.
13. Machlus KR, Italiano JE Jr. The incredible journey: from megakaryocyte development to platelet formation. J Cell Biol. 2013;201(6):785-796.
14. Lichtman MA, Chamberlain JK, Simon W, Santillo PA. Parasinusoidal location of megakaryocytes in marrow: a determinant of platelet release. Am J Hematol. 1978;4(4):303-312.
15. Stegner D, van Eeuwijk JMM, Angay O, et al. Thrombopoiesis is spatially regulated by the bone marrow vasculature. Nat Commun. 2017;8(1):127.
16. Bruns I, Lucas D, Pinho S, et al. Megakaryocytes regulate hematopoietic stem cell quiescence through CXCL4 secretion. Nat Med. 2014;20(11):1315-1320.
17. Zhao M, Perry JM, Marshall H, et al. Megakaryocytes maintain homeostatic quiescence and promote post-injury regeneration of hematopoietic stem cells. Nat Med. 2014;20(11):1321-1326.
18. Nakamura-Ishizu A, Takubo K, Fujioka M, Suda T. Megakaryocytes are essential for HSC quiescence through the production of thrombopoietin. Biochem Biophys Res Commun. 2014;454(2):353-357.
19. Heazlewood SY, Neaves RJ, Williams B, et al. Megakaryocytes co-localise with hemopoietic stem cells and release cytokines that up-regulate stem cell proliferation. Stem Cell Res. 2013;11(2):782-792.
20. Pinho S, Marchand T, Yang E, et al. Lineage-biased hematopoietic stem cells are regulated by distinct niches. Dev Cell. 2018;44(5):634-641.
21. Olson TS, Caselli A, Otsuru S, et al. Megakaryocytes promote murine osteoblastic HSC niche expansion and stem cell engraftment after radioablative conditioning. Blood. 2013;121(26):5238-5249.
22. Decker M, Leslie J, Liu Q, Ding L. Hepatic thrombopoietin is required for bone marrow hematopoietic stem cell maintenance. Science. 2018;360(6384):106-10.
23. Schulze H, Stegner D. Imaging platelet biogenesis in vivo. Res Pract Thromb Haemost. 2018;2(3):461-468.
24. Rastogi V, Puri N, Arora S, et al. Artefacts: a diagnostic dilemma - a review. J Clin Diagn Res. 2013;7(10):2408-2413.
25. Sommer C, Straehle C, Köthe U, Hamprecht FA. Ilastik: interactive learning and segmentation toolkit. IEEE International Symposium on Biomedical Imaging: From Nano to Macro. 2011;230-233.
26. Arganda-Carreras I, Kaynig V, Rueden C, et al. Trainable Weka Segmentation: a machine learning tool for microscopy pixel classification. Bioinformatics. 2017;33(15): 2424-2426.
27. Hoehme S, Drasdo D. A cell-based simulation software for multi-cellular systems. Bioinformatics. 2010;26(20):2641-2642.
28. Friebel A, Neitsch J, Johann T, et al. TiQuant: software for tissue analysis, quantification and surface reconstruction. Bioinformatics. 2015;31(19):3234-3236.
29. Icha J, Weber M, Waters JC, Norden C. Phototoxicity in live fluorescence microscopy, and how to avoid it. Bioessays. 2017;39(8).
30. Masedunskas A, Milberg O, Porat-Shliom N, et al. Intravital microscopy: a practical guide on imaging intracellular structures in live animals. Bioarchitecture. 2012;2(5): 143-157.
31. Medyukhina A, Timme S, Mokhtari Z, Figge MT. Image-based systems biology of infection. Cytometry A. 2015;87(6):462-470.
32. Yankeelov TE, Atuegwu N, Hormuth D, et al. Clinically relevant modeling of tumor growth and treatment response. Sci Transl Med. 2013;5(187):187ps9.
33. Vandenberghe F, Saigi-Morgui N, Delacretaz A, et al. Prediction of early weight gain during psychotropic treatment using a combinatorial model with clinical and genetic markers. Pharmacogenet Genomics. 2016;26(12):547-557.
34. Faust N, Varas F, Kelly L, Heck S, Graf T. Insertion of enhanced green fluorescent protein into the lysozyme gene creates mice with green fluorescent granulocytes and macrophages. Blood. 2000;96(2):719-726.
35. Elzey BD, Tian J, Jensen RJ, et al. Platelet-mediated modulation of adaptive immunity A communication link between innate and adaptive immune compartments. Immunity. 2003;19(1):9-19.
36. Schindelin J, Arganda-Carreras I, Frise E, et al. Fiji: an open-source platform for biological-image analysis. Nat Methods. 2012;9 (7):676-682.
37. Zuba-Surma EK, Kucia M, Abdel-Latif A, et al. Morphological characterization of very small embryonic-like stem cells (VSELs) by ImageStream system analysis. J Cell Mol Med. 2008;12(1):292-303.
38. Boxio R, Bossenmeyer-Pourié C, Steinckwich N, Dournon C, Nüße O. Mouse bone marrow contains large numbers of functionally competent neutrophils. J Leukoc Biol. 2004;75(4):604-611.
39. Qian H, Sheetz MP, Elson EL. Single particle tracking. Analysis of diffusion and flow in two-dimensional systems. Biophys J. 1991;60(4):910-921.
40. Logan DJ, Shan J, Bhatia SN, Carpenter AE. Quantifying co-cultured cell phenotypes in high-throughput using pixel-based classification. Methods. 2016;96:6-11.
41. Chen J, Zhou W, Jia Q, et al. Efficient extravasation of tumor-repopulating cells depends on cell deformability. Sci Rep. 2016;6:19304.
42. Schnoor M, Alcaide P, Voisin MB, van Buul JD. Crossing the vascular wall: common and unique mechanisms exploited by different leukocyte subsets during extravasation. Mediators Inflamm. 2015;2015: 946509.
43. Xiao LL, Liu Y, Chen S, Fu BM. Numerical simulation of a single cell passing through a narrow slit. Biomech Model Mechanobiol. 2016;15(6):1655-1667.

ARTICLE

RUNX3 levels in human hematopoietic progenitors are regulated by aging and dictate erythroid-myeloid balance

Peter Balogh,[1] Emmalee R. Adelman,[2] John V. Pluvinage,[3] Brian J. Capaldo,[4] Katie C. Freeman,[1] Sandeep Singh,[1] Kamaleldin E. Elagib,[1] Yukio Nakamura,[5] Ryo Kurita,[6] Goro Sashida,[7] Eli R. Zunder,[8] Hui Li,[1] Alejandro A. Gru,[1] Elizabeth A. Price,[9] Stanley L. Schrier,[9] Irving L. Weissman,[10] Maria E. Figueroa,[2] Wendy W. Pang,[11*] and Adam N. Goldfarb[1*]

[1]Department of Pathology, University of Virginia School of Medicine, Charlottesville, USA; [2]Sylvester Comprehensive Cancer Center, University of Miami Health System, Miami, Florida, USA; [3]Department of Medicine, Stanford University, Stanford, California, USA; [4]Flow Cytometry Core Facility, University of Virginia School of Medicine, Charlottesville, Virginia, USA; [5]Cell Engineering Division, RIKEN BioResource Center, Tsukuba, Ibaraki, Japan; [6]Research and Development Department, Central Blood Institute, Blood Service Headquarters, Japanese Red Cross Society, Tatsumi, Koto-ku, Tokyo, Japan; [7]Laboratory of Transcriptional Regulation in Leukemogenesis IRCMS, Kumamoto University, Chuo-ku, Kumamoto, Japan; [8]Department of Biomedical Engineering, University of Virginia, Charlottesville, Virginia, USA; [9]Department of Medicine, Division of Hematology, Stanford University, Stanford, California, USA; [10]Institute for Stem Cell Biology and Regenerative Medicine, Stanford University, Stanford, California, USA and [11]Department of Medicine, Division of Blood and Bone Marrow Transplantation, Stanford University, Stanford, California, USA

WWP and ANG contributed equally to this work

Ferrata Storti Foundation

Haematologica 2020
Volume 105(4):905-913

ABSTRACT

Healthy bone marrow progenitors yield a co-ordinated balance of hematopoietic lineages. This balance shifts with aging toward enhanced granulopoiesis with diminished erythropoiesis and lymphopoiesis, changes which likely contribute to the development of bone marrow disorders in the elderly. In this study, RUNX3 was identified as a hematopoietic stem and progenitor cell factor whose levels decline with aging in humans and mice. This decline is exaggerated in hematopoietic stem and progenitor cells from subjects diagnosed with unexplained anemia of the elderly. Hematopoietic stem cells from elderly unexplained anemia patients had diminished erythroid but unaffected granulocytic colony forming potential. Knockdown studies revealed human hematopoietic stem and progenitor cells to be strongly influenced by RUNX3 levels, with modest deficiencies abrogating erythroid differentiation at multiple steps while retaining capacity for granulopoiesis. Transcriptome profiling indicated control by RUNX3 of key erythroid transcription factors, including *KLF1* and *GATA1*. These findings thus implicate RUNX3 as a participant in hematopoietic stem and progenitor cell aging, and a key determinant of erythroid-myeloid lineage balance.

Introduction

Hematopoietic stem and progenitor cells (HSPC) execute tightly co-ordinated self-renewal and lineage commitment programs that generate a balanced output of peripheral blood cell types. With aging, these programs undergo perturbation resulting in increased numbers and decreased function within the stem cell compartment as well as a shift in the balance of cell types produced – namely, an increased proportion of granulocytes at the expense of erythroid and lymphoid lineages.[1-4] Thus normal aged mice have diminished peripheral red blood cells and lymphocytes, increased circulating neutrophils and monocytes, and increased sensitivity to granulocyte-colony stimulating factor (G-CSF)-induced leukocytosis and HSPC mobilization.[5,6] The transplantability of age-related HSPC changes highlights

Correspondence:

ADAM N. GOLDFARB
ang3x@virginia.edu

Received: October 19, 2018.

Accepted: June 5, 2019.

Pre-published: June 6, 2019.

doi:10.3324/haematol.2018.208918

Check the online version for the most updated information on this article, online supplements, and information on authorship & disclosures: www.haematologica.org/content/105/4/905

the importance of cell-intrinsic determinants, although micro-environmental factors also exert a critical influence.[7-9]

The transcription factor RUNX3 has been characterized as a participant in neural and lymphocyte development, TGFβ signaling, and solid tumor suppression.[10-14] Several studies have also demonstrated its repression in aged normal as well as tumor tissues, with the principal mechanism of inactivation being epigenetic alterations, particularly DNA methylation.[15-18] Emerging data suggest a role in hematopoiesis, with zebrafish and murine loss of function studies revealing progenitor perturbations, although the extent of its role has remained unclear due to redundancy with Runx1.[19-21] Most notably, induction of hematopoietic *Runx3* deletion in mice elicited marrow changes similar to those reported with normal aging: increased marrow colony forming units (CFU) and increased peripheral blood mobilization of CFU by G-CSF treatment.[5,22]

This study shows *RUNX3* to be expressed in murine and human HSPC, where it undergoes repression and epigenetic modification during normal aging. HSPC levels of RUNX3 were found to determine developmental potential, with deficiency restricting erythropoiesis at commitment and subsequent stages while fully permitting granulopoiesis. HSPC purified from patients with unexplained anemia of aging manifested RUNX3 deficiency and similar developmental alterations. Changes in HSPC transcriptome due to *RUNX3* deficiency suggest a role upstream of the erythroid master regulatory transcription factors KLF1 and GATA1.

Methods

Cell culture

Human CD34$^+$ expansion medium consisted of Iscove's modified Dulbecco's medium (IMDM) supplemented with bovine serum albumin, insulin and transferrin (BIT) 9500, and 100 ng/mL each of rhTPO, rhSCF, and rhFlt3-l, plus 10 ng/ml rhIL-3. Erythroid medium consisted of IMDM supplemented with BIT 9500, and 4.5 U/mL rhEPO and 25 ng/mL rhSCF. Megakaryocyte medium consisted of IMDM supplemented with BIT 9500, and 40 ng/mL rhTPO, 25 ng/mL rhSCF, and 20 ng/mL rhSDF1-alpha. Granulocyte medium consisted of IMDM supplemented with BIT 9500, and 25 ng/mL rhSCF, 10 ng/mL rhIL-3, and 20 ng/mL rhG-CSF. Colony formation assays were conducted using methylcellulose supplemented with 50 ng/mL rhSCF, 10 ng/mL rhIL-3, 20 ng/mL rhIL-6, 3 U/mL rhEPO, 20 ng/mL rhG-CSF, and 10 ng/mL rhGM-CSF.

Mass cytometry

Cells were stained for viability with 100 μM cisplatin, fixed with 1.6% paraformaldehyde, and stored at -80°C. Thawed samples were barcoded, pooled, and surface stained at room temperature for 30 minutes (min). Cells were then permeabilized with methanol and stained for intercellular antigens for 1 hour (h) at room temperature. Next, cells were incubated with Fluidigm CellID Ir-Intercalator, re-suspended in water with normalization beads, and analyzed on a Fluidigm CyTOF 2. Data were bead-normalized and underwent barcode deconvolution using the debarcoding tool MATLAB standalone executable.[23]

Data were inverse hyberbolic sine-transformed using a co-factor of 0.25. FlowSOM was used to construct a self-organizing map, and each cell was assigned a phenocode for every lineage marker using flowType. Each grid point was then immunophenotyped, and cell counts were tabulated to form a hierarchical count table. Differential abundance was tested for using edgeR with a quasi-likelihood framework as specified by the cydarTM package.

RNA-sequencing

RNA was extracted using the QIAgen RNeasy Plus Mini Kit, with added DNA digestion. Samples underwent ribosomal reduction, and sequencing with 100bp, paired-end, and 50 million read-depth parameters on an Illumina HiSeq 2500 machine. Data were processed online at usegalaxy.org. Trimmomatic was used to eliminate low quality sequences from the reads, followed by alignment to the hg19 reference genome using HISAT2, and RmDup to eliminate PCR duplicates. Differential gene expression was assessed with both DESeq2 and Cufflinks tools. The Synergizer tool was used to convert UCSC gene identifiers into hgnc gene symbols.

Unexplained anemia of the elderly studies

Mononuclear cells were sorted phenotypically: HSC, Lin$^-$ CD34$^+$CD38$^-$CD904$^+$ CD45RA$^-$; MEP, Lin$^-$CD34$^+$CD38$^+$CD123$^-$ CD45RA$^-$. Colony assays were performed using complete methylcellulose with 12-14 days incubation. For microarray, RNA samples were quantified, subjected to reverse transcription, underwent two rounds of linear amplification, and biotinylated. 15 μg of RNA per sample was assayed using Affymetrix HG U133 Plus 2.0 microarrays. Data were analyzed using the gene expression commons platform.

Ethics statement

This study was reviewed and approved by the institutional review boards of the respective institutions and was conducted in accordance with the principles of the Declaration of Helsinki.

Data and software availability

RNA-sequencing accession numbers: GSE119264, GSE104406. Microarray accession number: GSE123991.

Results

Hematopoietic stem cell *RUNX3* levels decline with aging

Prior reports have shown marrow-specific *Runx3* knockout to elicit aspects of the aging phenotype and to exaggerate the myeloid skewing associated with aging.[5,22] We therefore assessed *RUNX3* expression in rigorously purified human and murine hematopoietic stem cells. In humans, RNA-seq has been conducted on Lin$^-$CD34$^+$CD38$^-$ marrow cells from healthy young (18-30 years old) and aged (65-75) subjects (GSE104406). In mice, side population (SP) Lin$^-$Sca$^+$Kit$^+$CD150$^+$ marrow cells from young (4 months old) and aged (24 months) animals have undergone RNA-seq3 (GSE47819). Both datasets demonstrated HSC expression of RUNX3 with significant decreases associated with aging (Figure 1A and B). Human CD34$^+$CD38$^+$ later stage progenitors also showed diminished *RUNX3* expression with aging, indicating that the changes are not HSC-restricted (*Online Supplementary Figure S1A*). Evidence for an aging-associated decline in progenitor protein levels was seen in human marrow samples immunostained for *RUNX3* (*Online Supplementary Figure S1B*). Analysis of murine bone marrow single-cell RNA-seq datasets[24] (GSE89754) from animals with or without erythropoietin (EPO) treatment confirmed that

the signals for *Runx3* expression came from multipotent and early committed erythroid progenitors rather than contaminant lymphocytes. Discrimination of HSC *versus* MPP compartments is not possible by this approach (*Online Supplementary Figure S1C*).

Because epigenetic changes occur with HSC aging and participate in regulation of RUNX3,[25-27] we investigated the effect of aging on DNA and histone modifications within the murine and human loci. Analysis of comprehensive DNA methylation mapping by whole genome bisulfite sequencing[3] (GSE47819) revealed significant increases in P2 promoter methylation in aged murine HSC (Figure 1C

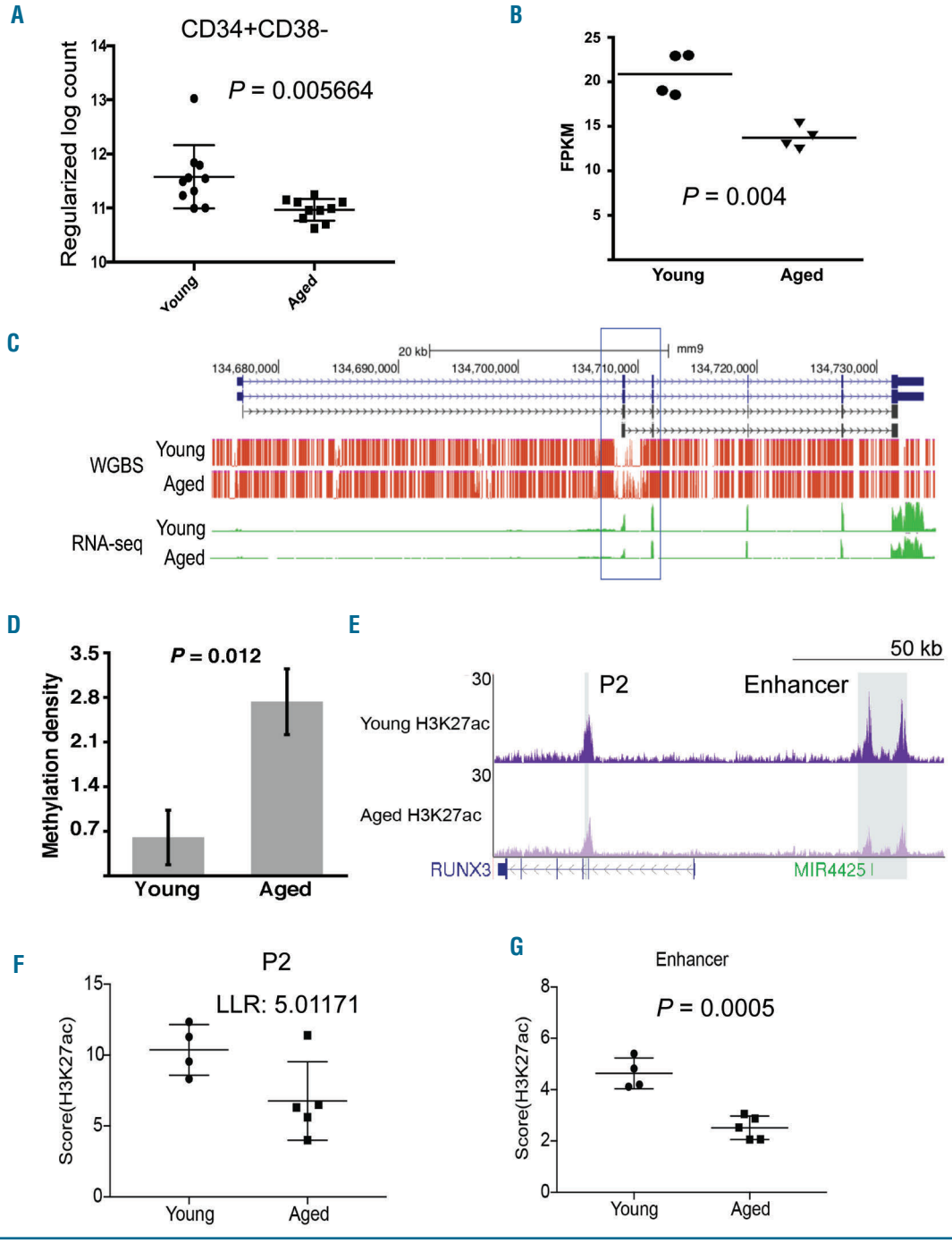

Figure 1. Hematopoietic stem and progenitor cells (HSPC) and SPC *RUNX3* levels decline with aging. (A) Human *RUNX3* mRNA levels in Lin$^-$CD34$^+$CD38$^-$ bone marrow (BM) HSPC obtained from healthy young and aged individuals. N=10 per group. (B) Mouse *Runx3* mRNA levels in side population, Lin$^-$Sca1$^+$Kit$^+$CD150$^+$ BM HSC obtained from healthy young and aged animals (GSE478193). N=4 per group. (C and D) Tracks for DNA methylation by whole genome bisulfite sequencing (WGBS, red) and RNA-seq read counts (green) within the mouse Runx3 locus in HSC from healthy young and aged animals (GSE47819[3]). The blue box highlights the DNA methylation trough associated with the P2 promoter. (D) Mean methylation density (% of CpG reads with methylation) within trough. N=5-6 per group. (E-G) Histone H3K27 acetylation by chromatin immunoprecipitation (ChIP)-sequencing within the human locus in HSPC from healthy young and aged individuals. Gray shading highlights peaks within the P2 promoter and upstream super-enhancer. (F) H3K27ac score for the P2 promoter peak, and (G) the sum of peak scores across the enhancer. N=4-5 per group. All statistics two-tailed Student *t*-test, except in F: log likelihood ratio (LLR). Error bars+standard error of mean. FPKM: fragments per kilobase of transcript per million.

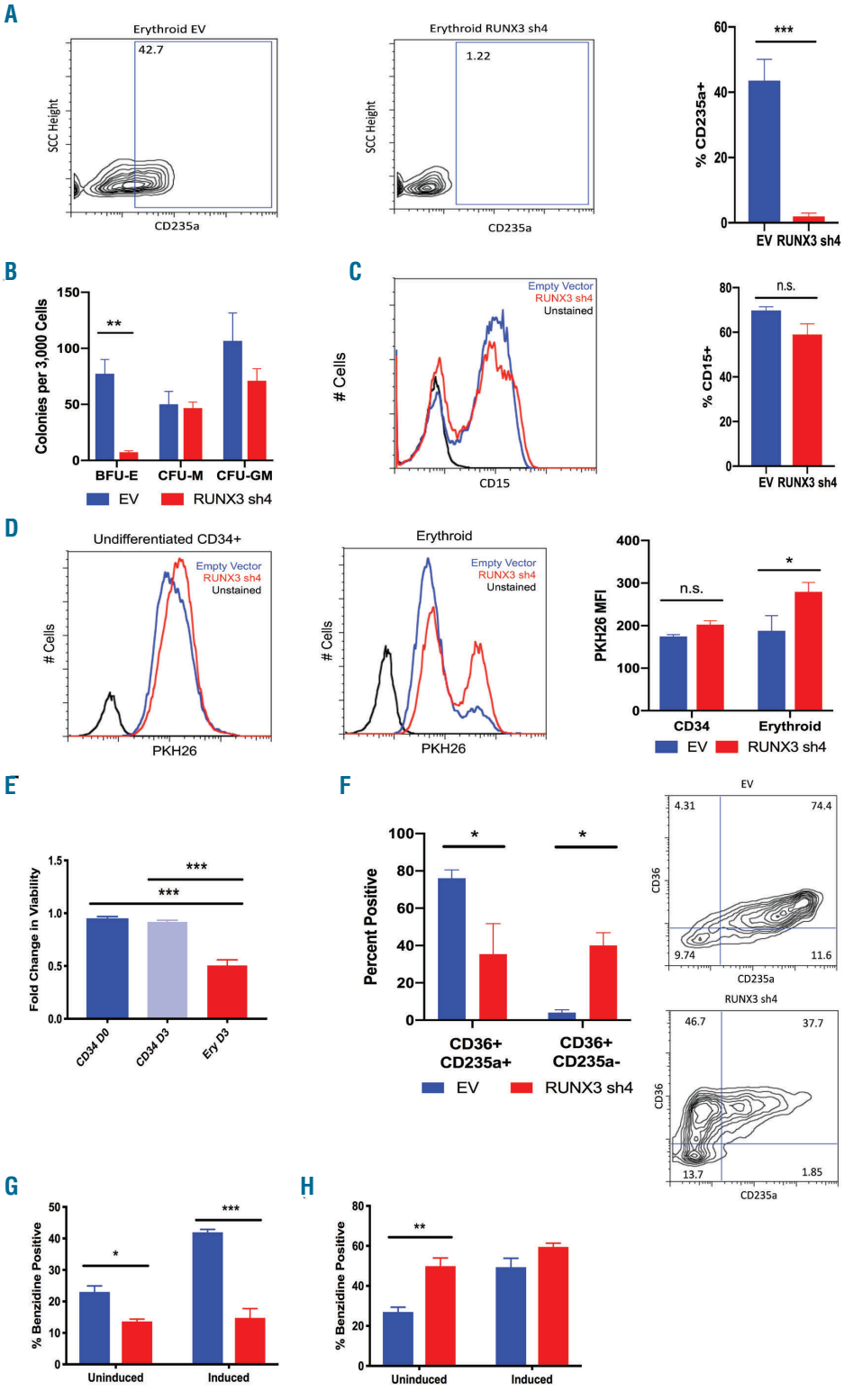

Figure 2. RUNX3 participates in erythroid but not granulocytic differentiation of human progenitors. (A) Flow cytometry plots for erythroid differentiation of CD34$^+$ cells transduced with empty vector (EV) or RUNX3-targeting (RUNX3 sh4) lentiviral shRNA constructs and subjected to unilineage erythroid culture for three days. Graph summarizes the quantitation of erythroid differentiation from three independent experiments. (B) Summary of colony formation assays on CD34$^+$ cells transduced as in (A). (C) Flow cytometry histogram overlays for granulocyte differentiation of CD34$^+$ cells transduced as in (A) and subjected to unilineage granulocytic culture for eight days. Representative results from three independent experiments. (D) Flow cytometry histogram overlays for cell proliferation by dye dilution. Transduced CD34$^+$ cells were stained with PKH26 followed by three days of culture in expansion medium (CD34) or erythroid medium. Graph summarizes mean fluorescence intensity due to dye retention from three independent experiments. (E) Summary of viability as assessed by flow cytometry on CD34$^+$ cells transduced as in (A) and cultured in expansion or erythroid medium for indicated days. (F) Flow cytometry plots for erythroid differentiation of CD36$^+$ CD235a$^-$ early committed erythroid progenitors transduced as in (A) and cultured in erythroid medium for three days. Graph summarizes quantitation of erythroid differentiation from three independent experiments. (G and H) Summary of hemoglobinization, i.e. percent cells positive for benzidine staining, in HUDEP-2 cells transduced with control vectors (EV), RUNX3-knockdown lentivirus (sh4), or RUNX3-overexpression retrovirus (OE). Cells were cultured 48 hours in HUDEP-2 expansion (Uninduced) or differentiation (Induced) medium. N=3. (A and C) Two-tailed Student *t*-test. (B, D, and F-H) Two-way ANOVA with Bonferroni's test. (E) One-way ANOVA with Tukey's test. *P<0.05; **P<0.01; ***P<0.005. Error bars+standard error of mean.

and D). Datasets for H3K27ac in young *versus* aged murine HSC are not currently available. The human RUNX3 locus showed aging-associated decreases in H3K27ac within the P2 promoter, as well as the super-enhancer region located approximately 97 kilobases upstream of the P2 promoter28 (GSE104406) (Figure 1E-G).

RUNX3 in human hematopoietic stem and progenitor cells participates in erythroid programming

The decline in HSC RUNX3 levels with aging illustrated in Figure 1A raised questions about potential roles in human hematopoietic differentiation. Human CD34$^+$ HSPC cultures were used to examine protein expression

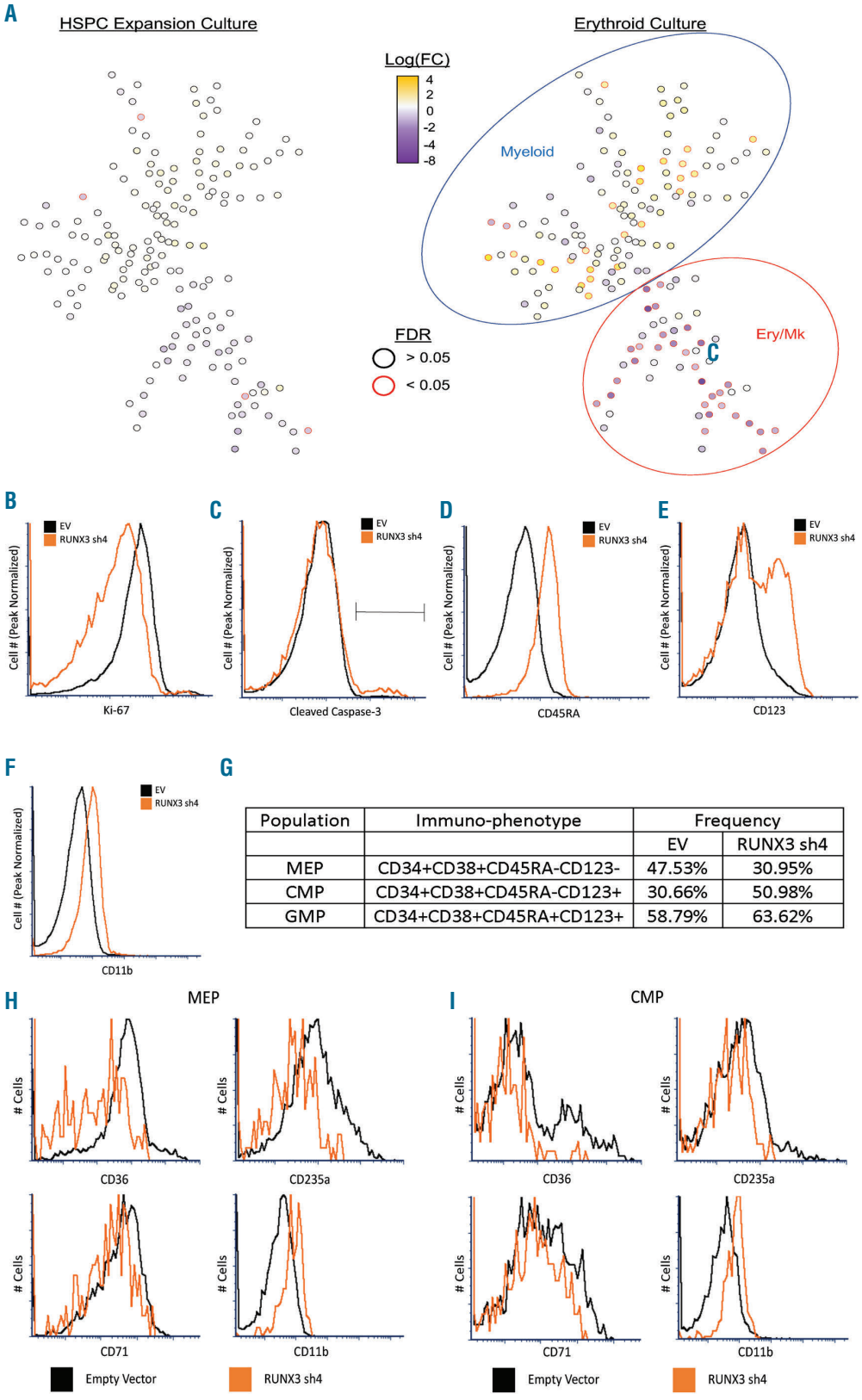

Population	Immuno-phenotype	Frequency	
		EV	RUNX3 sh4
MEP	CD34+CD38+CD45RA-CD123-	47.53%	30.95%
CMP	CD34+CD38+CD45RA-CD123+	30.66%	50.98%
GMP	CD34+CD38+CD45RA+CD123+	58.79%	63.62%

Figure 3. RUNX3 levels influence progenitor lineage output balance. (A) Minimum spanning tree plots depicting cell population-nodes identified by cytometry on a Fluidigm CyTOF 2 on indicated cultures of transduced CD34$^+$ progenitors. Heatmap coloration of nodes reflects log2(fold changes) in their frequency associated with RUNX3 knockdown. Erythroid-megakaryocytic (Ery/Mk) and myeloid compartments are indicated by red and blue ovals, respectively. (B and C) CyTOF histogram overlays from transduced progenitors cultured in erythroid medium, comparing expression of Ki-67 and cleaved caspase-3 between control (EV, black) and RUNX3-deficient (RUNX3 sh4, orange) populations in the Ery/Mk compartment. (D-F) CyTOF histogram overlays from transduced progenitors cultured in erythroid medium, comparing expression of CD123, CD45RA, and CD11b between control (EV, black) and RUNX3-deficient (RUNX3 sh4, orange) populations in the Ery/Mk compartment. (G) Frequencies of megakaryocyte-erythroid progenitors (MEP), common myeloid progenitors (CMP), and granulocyte-monocyte progenitor (GMP) populations calculated from all cells cultured in erythroid medium. (H and I) Histogram overlays comparing CD36, CD235a, CD71, and CD11b expression between control (EV, black) and RUNX3-deficient (RUNX3 sh4, orange) MEP and CMP.

and function. By immunoblot, the initial undifferentiated population displayed relatively high *RUNX3* levels, with a gradual decline occurring during erythroid differentiation (*Online Supplementary Figure S2A*). Immunofluorescent staining revealed predominantly cytoplasmic localization in the undifferentiated cells and enhanced nuclear localization associated with erythroid differentiation (*Online Supplementary Figure S3*). Transduction of HSPC with empty or *RUNX3*-targeting lentiviral shRNA vectors did not alter the localization of *RUNX3* in erythroid differentiated cells. Both nuclear and cytoplasmic patterns of *RUNX3* localization have been observed in prior studies, and may reflect SMAD or STAT activation status as previously described.[29-32]

Partial knockdown of RUNX3 with three independent lentiviral short RNA hairpins blocked erythroid differentiation of CD34$^+$ progenitors, preventing expression of glycophorin A (CD235a) (Figure 2A and *Online Supplementary Figure S2B*). Subsequent experiments employed short hairpin #4 due to robust knockdown (approx. 60% protein loss) with no significant cross-inhibition of other RUNX proteins (*Online Supplementary Figure S2C*). As additional controls, CD34$^+$ progenitors also underwent transduction with shRNA vectors targeting GFP, which had no effect on erythroid differentiation, and *RUNX1*, which slightly enhanced erythroid differentiation as described[33] (*Online Supplementary Figure S2D and E*). *RUNX3* deficiency in CD34$^+$ HSPC also blocked erythroid colony formation in semi-solid medium, with no significant impact on monocyte or mixed granulocyte-monocyte colonies (Figure 2B). As with the colony assays, *RUNX3* deficiency caused minimal changes in granulocyte differentiation (CD15) after eight days of suspension culture (Figure 2C). When maintained in uni-lineage, serum-free erythroid medium containing EPO and stem cell factor (SCF), *RUNX3*-deficient progenitors showed time-dependent declines in proliferation and viability (Figure 2D and E). By contrast, *RUNX3*-deficient progenitors cultured in expansion medium with SCF, IL-3, thrombopoietin (TPO), and Flt3-ligand retained normal proliferation and near-normal viability (Figure 2D and E). However, *RUNX3* knockdown did prevent HSPC upregulation of CD41 in megakaryocytic cultures, suggesting an influence at the level of erythro-megakaryocytic progenitors (*Online Supplementary Figure S2F*).

To determine contributions to post-commitment human erythropoiesis, we knocked down *RUNX3* in sorted CD36$^+$CD235a$^-$ early erythroid progenitors. *RUNX3* deficiency in these cells impaired their progression to the more mature CD36$^+$CD235a$^+$ stage, indicating involvement in post-commitment differentiation (Figure 2F). Knockdown of RUNX3 in the human HUDEP-2 pro-ery-

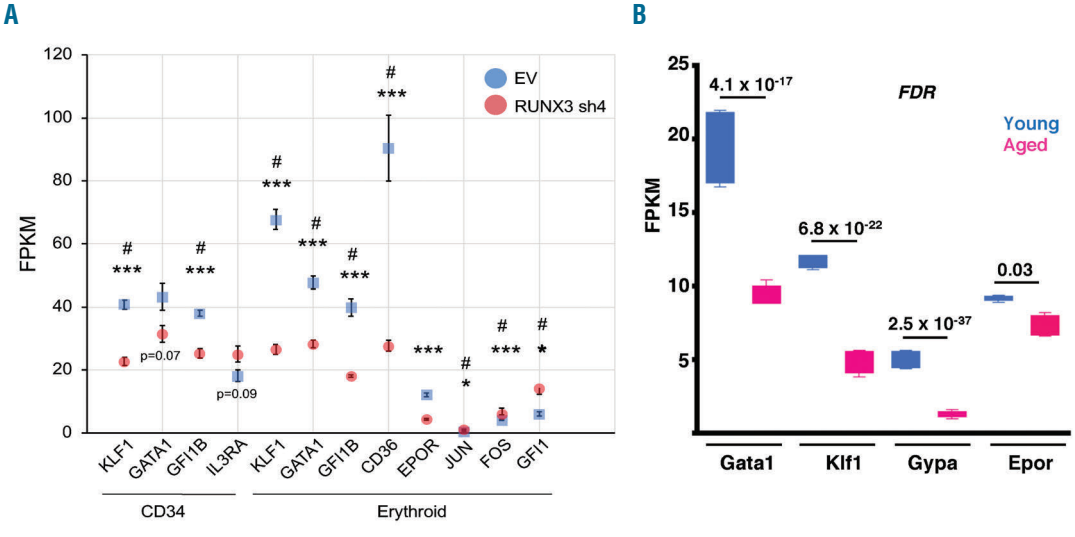

C

Gene Ontology: Biological Process	Fold Enrichment	FDR
Oxygen transport	27.98	2.38E-05
Establishment of protein localization to mitochondrial membrane	23.32	2.58E-03
Protein import into mitochondrial matrix	14.73	1.26E-02
Mitochondrial translational elongation	12.08	1.45E-10
Mitochondrial translational termination	11.81	1.65E-10
Mitochondrial respiratory chain complex assembly	5.54	6.63E-03
Platelet degranulation	5.25	2.27E-03
Platelet activation	4.7	5.37E-03

Figure 4. **RUNX3 deficiency causes perturbations in erythroid transcriptional program.** (A) Fragments per kilobase of transcript per million (FPKM) read counts of relevant genes in transduced progenitors cultured in expansion or erythroid medium. N=3. (B) FPKM read counts of key erythroid genes in young and aged murine hematopoietic stem cells (HSC) as in Figure 1B (GSE478193). (C) Gene Ontology classification by biological process of gene sets significantly down-regulated in association with RUNX3 deficiency in cells undergoing erythroid culture. N=3. All statistics False Discovery Rate (FDR), denoted by '#' in (A) (DESeq2), plus two-tailed Student *t*-test for FPKM values denoted by asterisks in (A). *P≤0.05; **P≤0.01; ***P≤0.005. Error bars±standard error of mean. EV: control vectors.

throblast line shifted the cells to a less mature phenotype, characterized by increased CD71 and diminished CD235a expression, and blocked induction of hemoglobinization (Figure 2G and *Online Supplementary Figure S2G-I*). Conversely, retroviral overexpression of RUNX3 in HUDEP-2 pro-erythroblasts enhanced their hemoglobinization (Figure 2H and *Online Supplementary Figure S2I*).

Progenitor deficiency of RUNX3 alters the balance of lineage output

To analyze in greater detail the effects of RUNX3 deficiency on progenitor fates, mass cytometry (CyTOF) was employed for comprehensive single cell profiling of cells in HSPC expansion culture, and cells in erythroid, megakaryocyte, or granulocyte culture conditions for 48 h. Cells from each culture condition were clustered into populations defined by surface marker staining, followed by construction of minimum spanning tree (MST) plots describing average fold changes in population abundance associated with RUNX3 knockdown (Figure 3A and *Online Supplementary Figure S4A and B*). These populations segregated into two main branches: a lower erythro-megakaryocytic compartment (Ery/Mk: red oval) defined by CD36 and/or CD41 positivity, and an upper compartment (Myeloid: blue oval) lacking both markers (*Online Supplementary Figure S4C and D*). As expected from results in Figure 2, RUNX3 knockdown selectively diminished cell populations within the Ery/Mk compartment in lineage culture conditions, but not in HSPC expansion conditions (Figure 3A and *Online Supplementary Figure S4A*). This contraction was associated with impaired proliferation, as reflected by decreased Ki-67 expression, but with no evidence of increased apoptosis (Figure 3B and C).

Notably, populations in the myeloid compartment (blue oval) were augmented in RUNX3-deficient progenitors grown in erythroid medium but not in other culture conditions. Analysis of these populations revealed a myeloid-skewed shift in HSPC distribution, similar to what has been described in aged bone marrow. These populations displayed a GMP (granulocyte-monocyte progenitor) phenotype, based on expression of CD34, CD38, CD123, and CD45RA in various combinations (*Online Supplementary Table S1*). Strikingly, RUNX3-deficient populations in the Ery/Mk compartment (red oval) exhibited aberrant retention of CD123, as well as global upregulation of the GMP marker CD45RA and the myeloid differentiation antigen CD11b (Figure 3D-F).

The CyTOF panel permitted assessment of the frequencies of cells with marker profiles of megakaryocyte-erythroid progenitors (MEP), common myeloid progenitors (CMP), and granulocyte monocyte progenitors (GMP).[34] This analysis showed RUNX3 deficiency to decrease MEP frequency and increase CMP and GMP frequencies (Figure 3G and *Online Supplementary Figure S4E*). Within the CMP and MEP compartments, knockdown of RUNX3 was associated with diminished expression of erythroid markers CD36 and CD235a, but enhanced expression of the myeloid marker CD11b (Figure 3H and I and *Online Supplementary Figure S4F*).

RUNX3 deficiency causes perturbations in erythroid transcriptional program

To identify the genes affected by RUNX3 knockdown, we performed mRNA sequencing on undifferentiated CD34$^+$ cells and cells in erythroid culture for 24 h, before cell viability was impacted by RUNX3 deficiency. In line with our other data, few changes were found between control and RUNX3-deficient undifferentiated cells (<70 genes with differential expression). However, among the down-regulated genes were key erythroid transcription factors including *KLF1, GATA1,* and *GFI1B* (Figure 4A). Several globin- and erythroid blood group antigen-encoding genes were decreased as well (*data not shown*). Notably, Klf1, Gata1, and downstream erythroid target genes Gypa and Epor also underwent downregulation in aged *versus* young murine HSC (Figure 4B). When comparing control and RUNX3-deficient progenitors in erythroid culture, approximately 1,100 genes showed differential expression. These included many of the same genes affected in the undifferentiated cells as well as additional erythroid genes such as CD36 and EPOR (Figure 4A). In addition, several granulocytic transcription factors were aberrantly up-regulated, including GFI1, JUN, and FOS (Figure 4A). Gene ontology (GO) analysis of genes differentially expressed in control *versus* RUNX3-deficient undifferentiated progenitors revealed only two significant functional categories, oxygen transport (i.e. erythroid; >100-fold enrichment; FDR 1.22E-6) and blood coagulation (i.e. megakaryocytic; 15.08-fold enrichment; FDR 1.91E-3), both of which showed downregulation. GO analysis of progenitors in erythroid culture yielded similar results but also included genes related to mitochondrial protein synthesis/transport and ribosomal biogenesis (Figure 4C).

Hematopoietic stem and progenitor cells RUNX3 deficiency occurs in human anemias associated with aging

Because RUNX3 expression levels strongly influence human erythroid differentiation, its downregulation could potentially contribute to anemias associated with aging. To address this possibility, we analyzed highly purified marrow progenitors from the following subjects: normal non-anemic young (20-35 years old), non-anemic aged (>65 years old), and aged (>65 years old) subjects with unexplained anemia of the elderly (UAE). The diagnosis of UAE was made by ruling out all other potential causes of anemia, as per the criteria of Goodnough and Schrier.[35] Gene expression profiling by microarray confirmed RUNX3 downregulation in UAE *versus* aged HSC4 (GSE32719) (Figure 5A). Functional studies revealed intrinsic differences in lineage output between UAE and non-anemic old progenitors. UAE HSC yielded fewer erythroid colonies (BFU-E) but similar numbers of myeloid colonies (CFU-GM) (Figure 5B). These findings resemble the effects of RUNX3 knockdown on colony formation by CD34$^+$ progenitors (Figure 2B). Furthermore, UAE MEP also showed poor TGFβ responsiveness in erythroid colony (CFU-E) enhancement (Figure 5C), a notable finding given the known influences of HSC aging and RUNX3 expression on this pathway.[3,36]

Discussion

Hematopoietic stem cell alterations with aging are complex; they result from cell-autonomous and micro-environmental mechanisms, and involve transcriptional changes in numerous genes. Interestingly, several of the

transcriptional programs affected have been previously linked to RUNX3 function, including quiescence, DNA-damage responsiveness, and TGFβ signaling.[12,20,26,36,37] Decreased *RUNX3* in aged tissues has been previously reported but was analyzed in heterogeneous mixtures of mature cell types.[15-18] Our results derive from purified, long-lived stem cells and reveal conservation between mice and humans. The repressive mechanism likely relates to the aging-associated epigenetic changes identified. Beerman *et al*. have shown that murine HSC aging and proliferative stress reconfigure the DNA methylation landscape, with key erythroid and lymphoid regions targeted for hyper-methylation and repression.[6] The increased *Runx3* P2 promoter methylation we identified in aged murine HSC has also been found in aging of other tissues and cancers.[16,27,38] The aging-associated decreases in H3K27ac that we identified at the human *RUNX3* promoter and upstream super-enhancer may contribute to its repression in human HSC.

A feature of HSC aging conserved from mice to humans consists of myeloid skewing characterized by augmented marrow production of neutrophils and monocytes at the expense of erythroid and lymphoid cells.[1-3] RUNX3 deficiency in aged mice likewise yields increased myelopoiesis; however, it presents as a myeloproliferative disorder, which appears to be distinct from age-associated myeloid skewing due to lack of B-cell and T-cell perturbations, and a relatively mild erythroid deficit that may be secondary to leukocytosis.[22] Despite these differences, our study indicates that loss of RUNX3 diminishes the expression of genes required for the erythroid program, and potentially de-represses myeloid genes. Epigenetic and transcriptomic analysis of aged HSC have also indicated that myeloid-skewing may manifest after similar changes.[6,7] Other aging-like phenotypes of RUNX3 deficiency include expansion of the LSK$^+$ HSPC compartment, and increased HSPC mobilization in response to G-CSF.[22] Thus, loss of RUNX3 contributes to age-associated HSPC phenotypes, although likely co-operates with other perturbations to generate *bona fide* myeloid-skewing.

Additional studies have implicated RUNX3 in non-lymphoid hematopoietic development. In human CD34$^+$ cell erythroid cultures, RUNX3 was predicted by Cytoscape MiMI analysis of gene expression profiles to be a "parent protein," i.e. a central node, in an erythroid transcription factor network.[39] In zebrafish, morpholino knockdown of *runx3* during embryogenesis resulted in severe anemia.[19] Our results define a novel role for RUNX3 in the erythropoietic program, governing the expression of lineage-specific transcription factors such as *KLF1, GATA1,* and *GFI1B*. Notably, Klf1 and Gata1 displayed downregulation in aged murine HSC. We further show that RUNX3 deficiency produces perturbations at multiple developmental stages including MEP and committed erythroid progenitors. The decreased proliferation seen in RUNX3-deficient progenitors may contribute to differentiation impairment. However, the retained capacity for myeloid differentiation

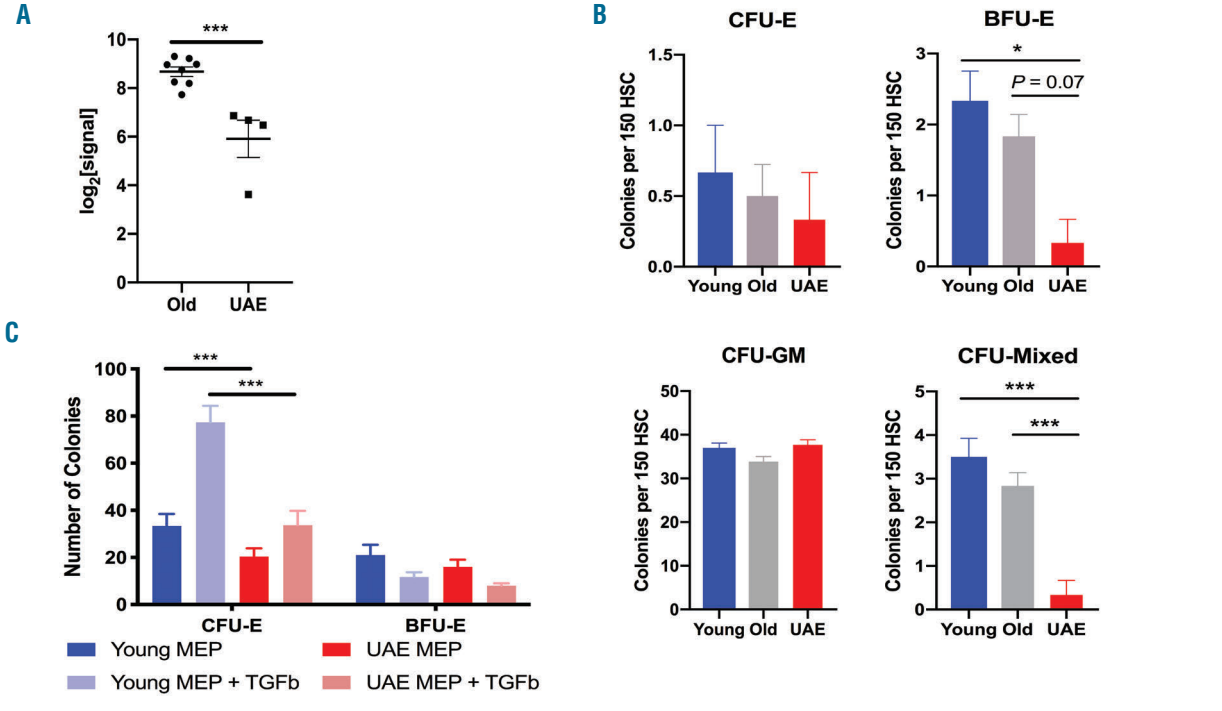

Figure 5. Decreased *RUNX3* expression and impaired erythropoiesis in unexplained anemia of the elderly. (A) Log_2[signal] derived from microarray analysis of *RUNX3* mRNA levels in purified human marrow hematopoietic stem cells (HSC) and common myeloid progenitors (CMP) from normal old and unexplained anemia of the elderly (UAE) subjects. N=4-8 per group. (B) Summary of colony formation assays on 150 HSC from normal young, normal old, and UAE subjects. N=3-6 per group. (C) Summary of erythroid colony formation assays ± TGFβ on 150 megakaryocyte-erythroid progenitors (MEP) from normal young *versus* UAE subjects. (A) Two-tailed Student *t*-test. (B) One-way ANOVA with Tukey's Test. (C) Two-way ANOVA with Bonferroni's test. *P≤0.05; **P≤0.01; ***P≤0.005. Error bars+standard error of mean. CFU-E: colony forming unit erythroid; BFU-E: burst forming unit erythroid; CFU-GM: granulocyte-macrophage progenitor.

and the aberrant retention of GMP markers such as CD123 and CD45RA on RUNX3 deficient cells suggests an additional role in lineage resolution. Taken together, the current findings implicate RUNX3 in the maintenance of bone marrow lineage balance and identify its decline in aged HSPC as a likely contributory factor in aging-associated anemias.

Acknowledgments

Thank you to Nicole Brimer for providing the packaging plasmids for production of retroviral particles. Thank you to Joanne Lannigan, Michael Solga, Claude Chew, Alexander Wendling, and Lesa Campbell for assistance with flow cytometry experiments at the University of Virginia Flow Core Facility. Thank you to Pat Pramoonjago and Rebecca Blackwell for assistance with immunohistochemistry experiments at the Biorepository and Tissue Research Facility. Thank you to Janet Cross, Michael McConnell, John Bushweller and Mazhar Adli for project guidance and discussion.

Funding

This work was funded by the following NIH grants: R01 HL130550, R01 DK079924, R01 DK101550. PB was supported in part by grant NIH T32 CA009109-39 (Cancer Research Training in Molecular Biology) awarded to the University of Virginia.

References

1. Choudry FA, Frontini M. Epigenetic Control of Haematopoietic Stem Cell Aging and Its Clinical Implications. Stem Cells Int. 2016;2016:5797521.
2. Akunuru S, Geiger H. Aging, Clonality and Rejuvination of Hematopoietic Stem Cells. Trends Mol Med. 2016;22(8):701-712.
3. Sun D, Luo M, Jeong M, et al. Epigenomic profiling of young and aged HSCs reveals concerted changes during aging that reinforce self-renewal. Cell Stem Cell. 2014; 14(5):673-688.
4. Pang WW, Price E a, Sahoo D, et al. Human bone marrow hematopoietic stem cells are increased in frequency and myeloid-biased with age. Proc Natl Acad Sci. 2011; 108(50):20012-20017.
5. Xing Z, Ryan MA, Daria D, et al. Increased hematopoietic stem cell mobilization in aged mice. Blood. 2012;108(7):2190-2197.
6. Beerman I, Bock C, Garrison BS, et al. Proliferation-dependent alterations of the DNA methylation landscape underlie hematopoietic stem cell aging. Cell Stem Cell. 2013;12(4):413-425.
7. Rossi DJ, Bryder D, Zahn JM, et al. Cell intrinsic alterations underlie hematopoietic stem cell aging. Proc Natl Acad Sci U S A. 2005;102(26):9194-9199.
8. Yamamoto R, Wilkinson AC, Ooehara J, et al. Large-Scale Clonal Analysis Resolves Aging of the Mouse Hematopoietic Stem Cell Compartment. Cell Stem Cell. 2018; 22(4):600-607.
9. Maryanovich M, Zahalka AH, Pierce H, et al. Adrenergic nerve degeneration in bone marrow drives aging of the hematopoietic stem cell niche. Nat Med. 2018;24(6):782-791.
10. Chi XZ, Lee JW, Lee YS, Park IY, Ito Y, Bae SC. Runx3 plays a critical role in restriction-point and defense against cellular transformation. Oncogene. 2017;36(50):6884-6894.
11. Krishnan V, Chong YL, Tan TZ, et al. TGF promotes genomic instability after loss of RUNX3. Cancer Res. 2018;78(1):88-102.
12. Fainaru O, Woolf E, Lotem J, et al. Runx3 regulates mouse TGF-♀♀-mediated dendritic cell function and its absence results in airway inflammation. EMBO J. 2004; 23(4):969-979.
13. Ebihara T, Song C, Ryu SH, et al. Runx3 specifies lineage commitment of innate lymphoid cells. Nat Immunol. 2015; 16(11):1124-1133.
14. Inoue KI, Shiga T, Ito Y. Runx transcription factors in neuronal development. Neural Dev. 2008;3(1):1-7.
15. Meng G, Zhong X, Mei H. A systematic investigation into Aging Related Genes in Brain and Their Relationship with Alzheimer's Disease. PLoS One. 2016;11(3):1-17.
16. So K, Tamura G, Honda T, et al. Multiple tumor suppressor genes are increasingly methylated with age in non-neoplastic gastric epithelia. Cancer Sci. 2006;97(11):1155-1158.
17. Tserel L, Kolde R, Limbach M, et al. Age-related profiling of DNA methylation in CD8+ T cells reveals changes in immune response and transcriptional regulator genes. Sci Rep. 2015;5:13107.
18. Wolff EM, Liang G, Cortez CC, et al. RUNX3 methylation reveals that bladder tumors are older in patients with a history of smoking. Cancer Res. 2008;68(15):6208-6214.
19. Kalev-Zylinska ML, Horsfield JA, Flores MVC, et al. Runx3 Is Required for Hematopoietic Development in Zebrafish. Dev Dyn. 2003;228(3):323-336.
20. Wang CQ, Krishnan V, Tay LS, et al. Disruption of Runx1 and Runx3 leads to bone marrow failure and leukemia predisposition due to transcriptional and DNA repair defects. Cell Rep. 2014;8(3):767-782.
21. Bruijn M De, Dzierzak E. Runx transcription factors in the development and function of the de fi nitive hematopoietic system. Blood. 2017;129(15):2061-2070.
22. Wang CQ, Motoda L, Satake M, et al. Runx3 deficiency results in myeloproliferative disorder in aged mice. Blood. 2013; 122(4):562-567.
23. Finck R, Zunder ER, Gonzalez VD, et al. Palladium-based mass tag cell barcoding with a doublet-filtering scheme and single-cell deconvolution algorithm. Nat Protoc. 2015;10(2):316-333.
24. Tusi BK, Wolock SL, Weinreb C, et al. Population snapshots predict early haematopoietic and erythroid hierarchies. Nature. 2018;555(7694):54-60.
25. Wahlestedt M, Norddahl GL, Sten G, et al. An epigenetic component of hematopoietic stem cell aging amenable to reprogramming into a young state. Blood. 2013; 121(21):4257-4264.
26. Ren R, Ocampo A, Liu GH, Izpisua Belmonte JC. Regulation of Stem Cell Aging by Metabolism and Epigenetics. Cell Metab. 2017;26(3):460-474.
27. Waki T, Tamura G, Sato M, Terashima M, Nishizuka S, Motoyama T. Promoter methylation status of DAP-kinase and RUNX3 genes in neoplastic and non-neoplastic gastric epithelia. Cancer Sci. 2003; 94(4):360-364.
28. Gunnell A, Webb HM, Wood CD, et al. RUNX super-enhancer control through the Notch pathway by Epstein-Barr virus transcription factors regulates B cell growth. Nucleic Acids Res. 2016;44(10):4636-4650.
29. Mabuchi M, Kataoka H, Miura Y, et al. Tumor suppressor, AT motif binding factor 1 (ATBF1), translocates to the nucleus with runt domain transcription factor 3 (RUNX3) in response to TGF- signal transduction. Biochem Biophys Res Commun. 2010;398(2):321-325.
30. Ogawa S, Satake M, Ikuta K. Physical and functional interactions between STAT5 and Runx transcription factors. J Biochem. 2008;143(5):695-709.
31. Torquati A, O'Rear L, Longobardi L, Spagnoli A, Richards WO, Daniel Beauchamp R. RUNX3 inhibits cell proliferation and induces apoptosis by reinstating transforming growth factor beta responsiveness in esophageal adenocarcinoma cells. Surgery. 2004;136(2):310-316.
32. Chen X, Deng Y, Shi Y, et al. Loss of expression rather than cytoplasmic mislocalization of RUNX3 predicts worse outcome in non-small cell lung cancer. Oncol Lett. 2018;15(4):5043-5055.
33. Kuvardina ON, Herglotz J, Kolodziej S, et al. RUNX1 represses the erythroid gene expression program during megakaryocytic differentiation. Blood. 2015;125(23):3570-3579.
34. Bagger FO, Kinalis S, Rapin N. BloodSpot: a database of healthy and malignant haematopoiesis updated with purified and single cell mRNA sequencing profiles. Nucleic Acids Res. 2019;47(D1):D881-D885.
35. Goodnough LT, Schrier SL. Evaluation and Management of Anemia in the Elderly. Am J Hematol. 2014;89(1):88-96.
36. Krishnan V, Ito Y. RUNX3 loss turns on the dark side of TGF-beta signaling. Oncoscience. 2017;4(11-12):156-157.
37. Mendelson A, Frenette PS. Hematopoietic stem cell niche maintenance during homeostasis and regeneration. Nat Med. 2014;20(8):833-846.
38. Waki T, Tamura G, Sato M, Motoyama T. Age-related methylation of tumor suppressor and tumor-related genes: An analysis of autopsy samples. Oncogene. 2003; 22(26):4128-4133.
39. Li B, Ding L, Yang C, et al. Characterization of transcription factor networks involved in umbilical cord blood CD34+ stem cells-derived erythropoiesis. PLoS One. 2014;9(9):e107133.

Ferrata Storti Foundation

Haematologica 2020
Volume 105(4):914-924

Ephrin/Eph receptor interaction facilitates macrophage recognition of differentiating human erythroblasts

Lea A. Hampton-O'Neil,[1,2,3] Charlotte E. Severn,[1,2,3] Stephen J. Cross,[1,4] Sonam Gurung,[1] Catherine D. Nobes[1] and Ashley M. Toye[1,2,3]

[1]School of Biochemistry, Biomedical Sciences Building, University of Bristol, University Walk, Bristol; [2]Bristol Institute for Transfusion Sciences, NHS Blood and Transplant, Filton, Bristol; [3]National Institute for Health Research (NIHR) Blood and Transplant Unit in Red Blood Cell Products, University of Bristol, Bristol and [4]Wolfson Bioimaging Facility, Biomedical Sciences Building, University of Bristol, University Walk, Bristol, UK

ABSTRACT

Erythropoiesis is one of the most efficient cellular processes in the human body producing approximately 2.5 million red blood cells every second. This process occurs in a bone marrow niche comprised of a central resident macrophage surrounded by differentiating erythroblasts, termed an erythroblastic island. It is not known what initially attracts the macrophage to erythroblasts to form these islands. The ephrin/Eph receptor family are known to regulate heterophilic cell-cell adhesion. We find that human VCAM1$^+$ and VCAM1$^-$ bone marrow macrophages and *in vitro* cultured macrophages are ephrin-B2 positive, whereas differentiating human erythroblasts express EPHB4, EPHB6 and EPHA4. Furthermore, we detect a rise in integrin activation on erythroblasts at the stage at which the cells bind which is independent of EPH receptor presence. Using a live cell imaging assay, we show that specific inhibitory peptides or shRNA depletion of EPHB4 cause a significant reduction in the ability of macrophages to interact with erythroblasts but do not affect integrin activation. This study demonstrates for the first time that EPHB4 expression is required on erythroblasts to facilitate the initial recognition and subsequent interaction with macrophages, alongside the presence of active integrins.

Correspondence:

ASHLEY TOYE
ash.m.toye@bristol.ac.uk

Received: December 20, 2018.

Accepted: June 7, 2019.

Pre-published: June 13, 2019.

doi:10.3324/haematol.2018.215160

Check the online version for the most updated information on this article, online supplements, and information on authorship & disclosures: www.haematologica.org/content/105/4/914

Introduction

Erythropoiesis is the process whereby hematopoietic stem cells (HSC) develop to mature red blood cells by undergoing multiple stages of cell division and differentiation before enucleating to form nascent reticulocytes. In humans, this process occurs in the bone marrow (BM). HSC undergo asymmetric division and lineage restriction to form pro-erythroblasts in the HSC niche, where they bind a macrophage to form a specialized niche called an erythroblastic island. This niche is formed by a central resident macrophage which is surrounded by differentiating erythroblasts.[1] The erythroblastic island is important for proliferation and terminal differentiation of erythroid cells, as macrophages are thought to supply nutrients to the surrounding erythroid cells, promote growth through survival signals, and phagocytose the pyrenocyte after enucleation.[2-4]

Multiple receptors are present on the surface of macrophages and erythroblasts which are involved in erythroblastic island interactions. These include intercellular adhesion molecule 4 (ICAM4), vascular cell adhesion molecule 1 (VCAM1), erythroblast-macrophage protein (Emp), Fms related tyrosine kinase 3 (Flt3), proto-oncogene tyrosine-protein kinase MER (Mer-TK), dystroglycan (DG) receptor, integrins, and EPH receptors.[4-10] It has already been established that ICAM4$^{-/-}$ mice formed significantly less erythroblastic islands than control mice[6] and the loss of erythroblast-macrophage protein (Emp) in mice leads to apoptosis of erythroid precursors and enucleation failure.[5,11] Finally, integrin β3 knockout mice have a higher amount of early erythroblast release from erythroblastic islands.[7] Overall, although we now know more about the importance of certain receptors for erythroblastic island integrity in mice, we do not know exactly which receptors are involved in

the formation and maintenance of human erythroblastic islands or how these two different cell types specifically recognize one another as binding partners.

The EPH receptor family is the largest tyrosine kinase receptor family.[12] It is separated into two protein branches which are largely distinct: the A family and the B family.[13] EPH receptors are very versatile as they can control adhesion, migration and proliferation;[12,14,15] leading to their important role in development, in particular, through their role in contact inhibition of locomotion (CIL). One current model for CIL suggests that depending on which EPH receptors and their ligands ephrins are present and their abundance at the surface will dictate the response of cells as they come into contact.[16] As both EPHB and EPHA receptors can be simultaneously expressed on the surface of cells, it is thought that the ratio of EPHA to EPHB receptor abundance at the surface of the cells determines the behavior of the two cells as they collide.[16,17] Hence, when EPHA receptors are in excess and engage the ligand, the cells will be repulsed, whereas if EPHB are in excess and activated, this can lead to attraction and possibly drive adhesion.

Recently, several reports have discussed the importance of EPH receptor function within the BM niche. In mice, one EPHB4 ligand, ephrin-B2 is expressed on HSC and is important for the release of the progenitor cells into the bloodstream.[14,18] EPHB4 is also reported to exert control over niche size, as transgenic mice that over-express EPHB4 produce more HSC cells and display a higher BM reconstitution capacity.[19,20] However, the role that EPH receptors play specifically in the erythroid lineage is based primarily upon the demonstration of EPHB4 expression on human BM CD34$^+$ cells and from the observed increase in CFU-E formation upon co-culture with stromal cells over-expressing ephrin-B2 or HSC overexpressing EPHB4.[21-23] More recently, Anselmo *et al.*[9] proposed a role for EPHB1 in the activation of integrins *via* an agrin-dependent pathway in mice and hypothesized that this facilitates erythroblast binding to macrophages. Whether this observation extends to a human macrophage island context is unknown.

We find that for humans, EPHB4, EPHB6 and EPHA4 are the only EPH receptors present on erythroblasts and that these proteins are differentially expressed on the surface during terminal differentiation. Specifically, we found high EPHB4 and EPHB6 expression in the early stages of erythropoiesis, and by the reticulocyte stage, only EPHA4 is detected. We also demonstrate that during the expansion phase where EPHB4 and EPHB6 are highly expressed, erythroblasts also have an increase in active integrin. Using live cell imaging we show that the inhibition of EPHB4 interaction with ephrin-B2 results in a decrease in the association between erythroblasts and macrophages despite the continued presence of active integrins. This work demonstrates for the first time that ephrin/EPH interactions, as well as the presence of integrins, drive the recognition between macrophages and erythroblasts during human erythroblastic island formation.

Methods

Bone marrow isolation

Bone marrow aspirate samples were provided by Dr Michael Whitehouse (University of Bristol) with informed consent for research use. The use of donated BM was approved by the Bristol Research Ethics Committee (REC no. 12/SW/0199). Cells were washed from a universal sample tube using HBSS (Sigma-Aldrich, Gillingham, UK) containing 0.6% acid citrate dextrose (ACD) to remove the heparin-coated beads (included to prevent coagulation). The red pulp was macerated onto a 70 μm filter. Cells were washed once more with HBSS and ACD, and centrifuged at 300g between washes. Red cells were lysed using red cell lysis buffer (155mM NH4Cl, 0.137mM EDTA, 1mM KHCO3, pH 7.5) for ten minutes on ice, cells were washed a further time in HBSS with ACD, counted and stored until required.

FACS

Mononuclear cells (MNC) were thawed and washed twice with PBS containing 1% BSA and 2% glucose (PBSAG). CD14$^+$ isolation was performed on thawed BM MNC according to the manufacturer's instructions (Miltenyi Biotech, Woking, UK). Cells were counted and resuspended in PBSAG and CD14-Pacific Blue, CD106-PE and CD169-APC antibodies were added for 30 minutes at 4°C in the dark. The cells were washed twice in PBSAG, and then the CD14$^+$CD106$^+$and CD14$^+$CD106$^-$ populations were sorted using a BD Influx Cell Sorter.

Live cell imaging

Macrophages were grown for seven days, as described above, in a 24-well plate (Corning, New York, USA). At day 7, cells were labeled with Cell Tracker Green CFMDA (ThermoFisher, Loughborough, UK) following the manufacturer's instructions. For BM macrophages, the labeling was conducted immediately after sorting. Erythroblasts on day 6 of expansion were added to the macrophages and left overnight in culture media [IMDM (Life Technologies, Paisley, UK), 3%v/v Human serum (Sigma-Aldrich), 10 U/mL erythropoietin (Roche, Basel, Switzerland) and 1mg/mL holotransferrin (Sanquin Blood Supply, Netherlands)]. The biotinylated TNYLFSPNGPIARAWGSGSK-Biotin (TNYL), EILDVPSTGSGSK-Biotin (EIL) and the control peptide DYPSMAMYSPSVGSGSK-Biotin (DYP) were synthesized by Cambridge Peptides UK (Birmingham, UK) and added where indicated. The media was changed the next day with phenol-red free imaging media with replenished peptides where indicated. The optimal final ratio of cells used was 2 erythroblasts to 1 macrophage to prevent overcrowding. The plate was imaged using the Incucyte (Essen BioScience, Welwyn Garden City, UK) every hour at 20x magnification. The spatial relationship between erythroblasts and macrophages was characterized using Fiji.[24,25] Initially, lateral drift in the phase-contrast and fluorescence images over time was corrected using the StackReg plugin.[26] A difference of Gaussian filter (approximating the equivalent Laplacian of Gaussian[27]) was then applied to the phase-contrast channel to enhance features with diameters matching those expected for erythroblasts. Erythroblasts were subsequently identified with the TrackMate plugin using the Laplacian of Gaussian feature detector.[28] Fluorescence channel images were processed with rolling-ball and Gaussian filters to remove inhomogeneity of illumination and high-frequency noise, respectively. The images were then thresholded using the Otsu method[29] with a user-defined fixed multiplier offset and passed through the ImageJ particle analyzer to identify macrophages. Macrophages were tracked between frames using the Apache HBase (v1.3.1; Apache Software Foundation, *https://hbase.apache.org*) implementation of the Munkres algorithm with costs assigned based on object centroid separation.[30] Instances where objects in the phase-contrast channel coincided with macrophages identified in the fluorescence channel were removed, as these likely corresponded to accidental detection of macrophages. Finally, spatial relationships between

erythroblasts and macrophages were determined based on the maximum separation of object perimeters. Multiple erythroblasts could be assigned to a single macrophage. This program can be found at: doi: 10.5281/zenodo.3237585 (Stephen Cross. (2018, March 14). SJCross/RelateCells v1.2.2 (Version v1.2.2). Zenodo.).

Antibodies, cell culture, lentiviral transduction, real-time quantitative polymerase chain reaction, western blotting, flow cytometry, cytospins and statistics

Details of all these methods can be found in the *Online Supplementary Methods*.

Results

Ephrin-B2 is expressed by M2-like macrophages and bone marrow macrophages

As reported previously by Heideveld *et al*. macrophages treated with dexamethasone (+Dex) phenotypically resemble the resident macrophages found in BM and fetal liver,[31] exhibiting a high level of CD163 and CD169, similar to BM macrophages (*Online Supplementary Figure S1*). Furthermore, these cultured macrophages are known to be able to help the erythroblasts expand,[32,33] form erythroblastic islands, and phagocytose nuclei.[31] However, whereas up to 70% of BM isolated $CD14^{+}CD16^{+}$ macrophages are $VCAM1^{+}$, +Dex macrophages are $VCAM1^{-}$. It is known that BM stromal cells, including macrophages, express ephrinB2.[23] Figure 1A and B confirms that all three macrophage types, +Dex *in vitro* cultured, $VCAM1^{+}$ and $VCAM1^{-}$ BM macrophages express ephrin-B2, the most potent receptor for EPHB4 and EPHB6 receptors (*see below*). There was no discernible difference between the expression levels of ephrin-B2 on sorted $VCAM1^{+}$ and $VCAM1^{-}$ macrophages, but the *in vitro* culture +Dex macrophages express higher levels (Figure 1C).

EPHB4, EPHB6 and EPHA4 are expressed in expanding and differentiating erythroblasts

To determine which EPH receptors are expressed in erythroblasts at different stages of development, real-time quantitative polymerase chain reaction (RT-PCR) was performed on three independent *in vitro* cultured differentiation courses. In these cultures, $CD34^{+}$ cells are isolated and expanded for eight days, called D0 to D7. During this time, the cells express CD34 and CD36, markers of the BFU-E and CFU-E. The cells are then differentiated for eight days: T0 to T168. These stages of differentiation can be separated by their morphology using cytospins (*Online Supplementary Figure S2A and B*). EPHB4, EPHB6 and EPHA4 mRNAs were expressed in expanding day 6 and differentiating T0, representing the proerythroblast/basophilic stage in our culture system. RNA for numerous EPH receptors (EPHA1, EPHA2, EPHA3, EPHA6, EPHA7, EPHA8, EPHB2 and EPHB3) was not detected during erythropoiesis (Figure 1D). Western blots confirmed EPHB4, EPHB6 and EPHA4 protein expression (Figure 1E). EPHA4 expression diminished but was still retained at the reticulocyte stage. Unlike in mice,[9] EPHB1 was not reproducibly detected at either the RNA or protein level (being detected by RT-PCR only once in 4 separate erythroid differentiation courses). Interestingly, the ligand ephrin-B2 is also present in the late stage of expansion in erythroblasts.

Erythroblast surface expression of EPH receptors is dynamic during terminal differentiation

To assess the timeframe in which the EPH receptors are expressed on the surface of erythroblasts during differentiation, a surface binding assay was performed. Ephrin-B2 was chosen as the ligand used in this experiment as it binds all EPHB receptors.[34] Ephrin-B2 was clustered with a fluorescently-conjugated IgG antibody and added to the live cells. Figure 1F demonstrates that the cells bind ephrin-B2-Fc during the final part of the expansion phase (D5 and D6) when cells are $CD34^{low}/CD36^{high}$ proerythroblasts (Figure 2A). As cells commence terminal differentiation (T0 hours), there is a steady reduction of ligand binding (no statistically significant binding after T0), and by T72 hours all binding is lost. At T72 hours, the majority of erythroblasts present in culture are beyond the basophilic stage (*Online Supplementary Figure S2A*), confirming that EPHB receptors are expressed during the early phases of terminal differentiation.

Integrins are crucial in cell-cell contact and adhesion with macrophages through the formation of focal adhesion points.[6,7,9,35] Therefore, we tested whether the appearance of integrins on the erythroblast surface coincided with EPHB4 receptor surface expression. To detect integrins, a surface binding experiment was conducted using VCAM1-Fc where the integrins were pre-activated with manganese to ensure VCAM1-Fc construct binding. Without pre-activation, no binding was found (*Online Supplementary Figure S3*), but when all the integrins were activated, VCAM1-Fc bound throughout erythroblast differentiation until approximately T144 hours when 50% of the cells were reticulocytes (Figure 1F). Manganese treatment was observed to increase cell death and clustering. Therefore flow cytometry analysis was performed only on live single cells during the surface assay by gating on unclustered propidium iodide negative cells.

Baseline activation of integrins occurs during the height of EPHB4 and EPHB6 expression

We next wanted to establish the level of integrin activation during the stages at which EPHB4/B6 become more pronounced at the surface of erythroblasts. To do this, we used an antibody that specifically recognizes the active form of integrin β1, which is present in both the VLA-4 (integrin α4β1) and VLA-5 (integrin α5β1) complexes. Manganese was used to activate integrins beforehand as a positive control. We detected a marked increase of integrin activation in a small percentage of the cells between days 4 and 5 on erythroblasts in the absence of any treatment, representing an increase in 10-30% of cells at day 5 and 90% at day 6 (Figure 2B). This increase represents 50% of the mean fluorescent intensity (MFI) observed with the manganese treatment, which activates all the integrins (Figure 2C). The $CD36^{high}/CD34^{low/-}$ populations displayed this rise in baseline integrin activation (Figure 2A).

To establish the effects of EPH receptor stimulation on integrin activation, the amount of active form of integrin β1 was monitored in the presence of clustered ephrin-B2. Surprisingly, EPH receptor engagement had no significant effect on the level of activation of integrin β1 (Figure 2B).

Peptide inhibition of EPHB4 activation impacts on macrophage-erythroblast interactions

The EPHB4 receptor inhibitor (TNYL-RAW peptide) competes selectively with ephrin-B2 binding to EPHB4

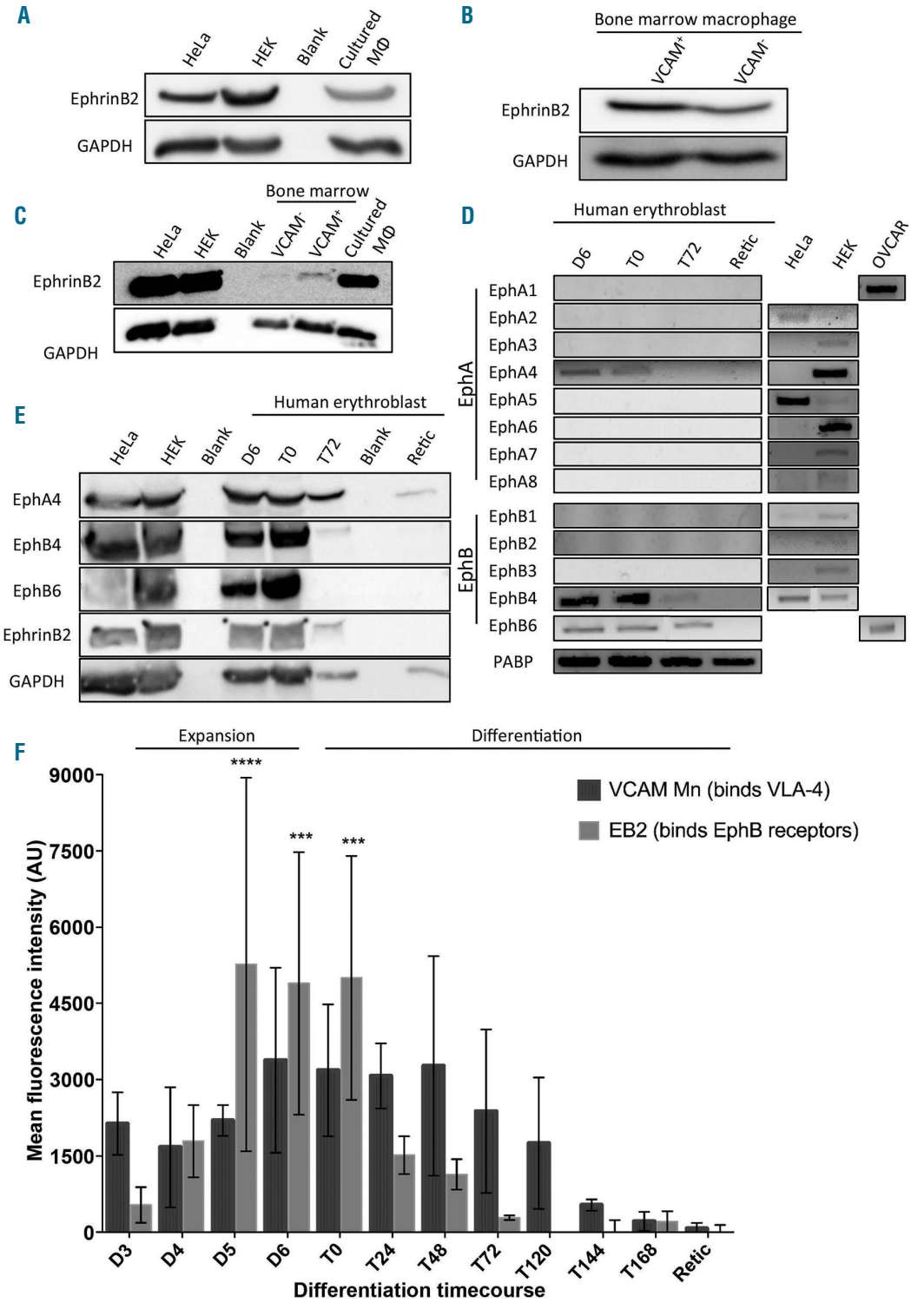

Figure 1. EPH receptor expression profile is specific to the cell type and its differentiation. (A) Lysates from cultured macrophages, HeLa and HEK cells were western blotted for ephrin-B2 and GAPDH. This is a representative blot (n=3). (B) Lysates from sorted VCAM$^+$ and VCAM- bone marrow (BM) CD14$^+$ cells were blotted for ephrin-B2 and GAPDH. This is a representative blot (n=2). (C) Lysates from HEK, HeLa, sorted BM and cultured macrophages with dexamethasone (+Dex) were probed for ephrinB2 and GAPDH. This is a representative blot (n=2). (D) Representative DNA gels showing the polymerase chain reaction products from an erythroblast differentiation course using primers against EPHA1-8 and EPHB1-6 (n=3). For each sample, a negative control was also performed to confirm the absence of genomic DNA contamination. HEK293, OVCAR 3 and HeLa cells were used as positive controls. (E) Lysates from HeLa, HEK cells and an erythroblast differentiation course were blotted for EPHB4, EPHB6, EPHA4, ephrin-B2 and GAPDH. This is a representative blot (n=3). (A, B, C and E) All lanes were loaded with 1x10^6 cells. (F) Graph showing the mean fluorescent intensity (MFI) obtained by flow cytometry of the ephrin-B2-Fc and VCAM-Fc constructs binding to erythroblasts throughout terminal differentiation. EB2 is ephrin-B2-Fc, and VCAM Mn is VCAM-Fc with manganese activation. The ephrin constructs were pre-clustered. All points are means for ephrin-Fc constructs (n=5) and VCAM (n=3). The error bars represent the standard error of the mean. Binding to the constructs was statistically compared to the IgG control using two-way ANOVA: ***P<0.001; ****P<0.0001. The control for VCAM binding without manganese is in *Online Supplementary Figure S3*. D: day; T: time course; AU: arbitrary units.

but does not activate the receptor.[36] In a competition assay, it was observed that addition of EPHB4 inhibitor caused a significant decrease in ephrin-B2 binding to the cells at day 5, with a marked decrease at day 4 as well, but this did not occur using the DYP control peptide (Figure 2D). This effect on ephrin-B2 binding did not have an effect on the increase in integrin β1 activation (Figure 2E).

Using a live cell imaging assay described recently in Heideveld *et al.*[31] and further developed (see *Online Supplementary Figure S4)*, the role of the EPH receptor in macrophage-erythroblast interaction was investigated in the presence or absence of inhibitory peptide (Figure 3A). The number of interactions an individual macrophage makes with erythroblasts in each image frame is referred

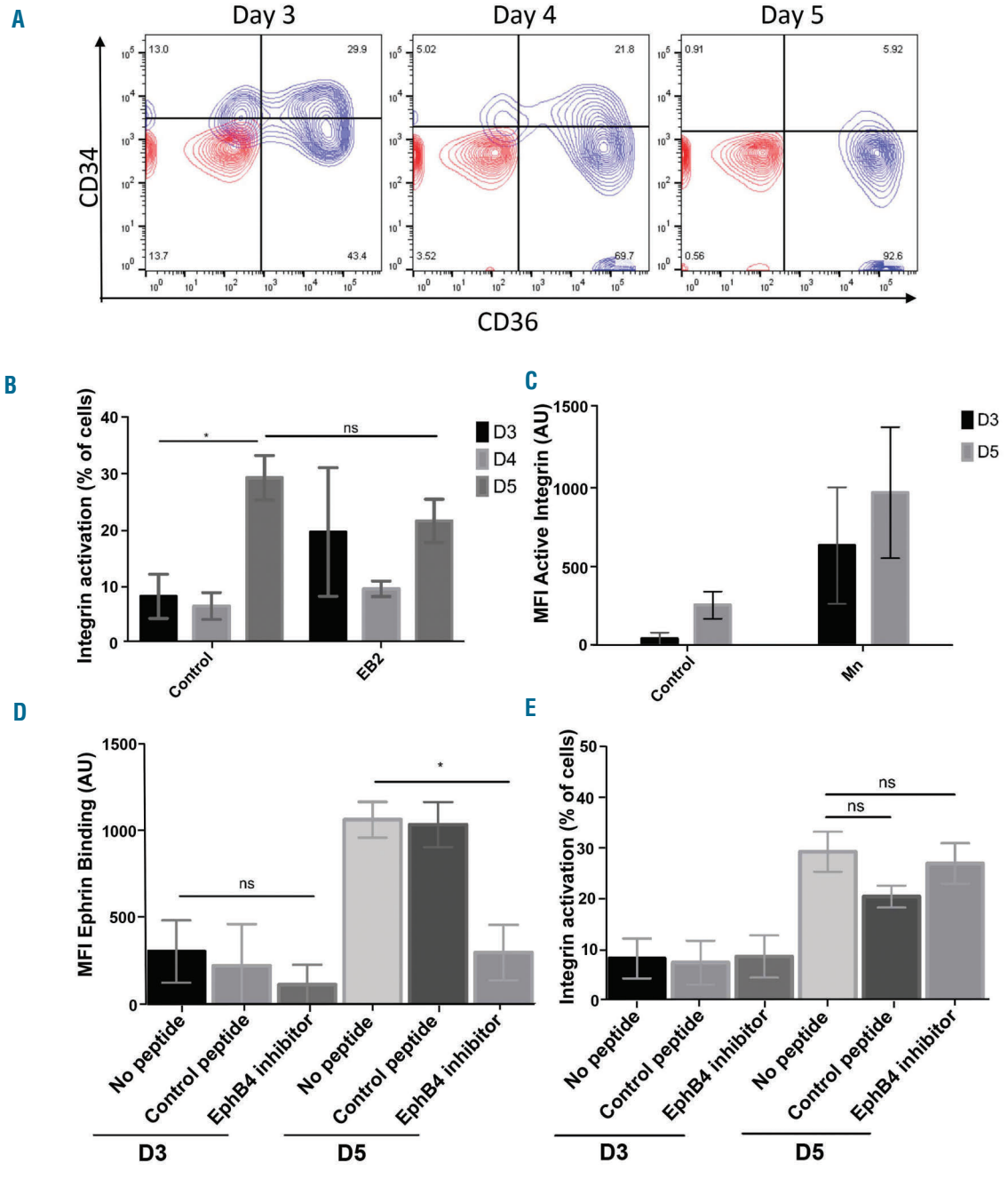

Figure 2. Activated Integrin β1 on proerythroblasts is not affected by EPHB4 inhibition. (A) Representative contour plot of the erythroblasts at different stages of expansion on days (D) 3, 4 and 5 of culture (n=5). IgG is in red, and antibodies are in blue. (B) Graph showing the percentage of cells with active integrin obtained by flow cytometry of these cells with the active form of integrin β1 (clone HUTS-21) through D3, D4 and D5 of erythroblast expansion (n=4). Mixed effects analysis was run on the samples. (C) Graph showing the mean fluorescence intensity (MFI) of active integrin β1 through D3 and D5 of expanding erythroblasts and after stimulation with manganese (Mn+; n=4). (D) Graph showing the MFI value obtained by flow cytometry of the ephrin-B2 construct binding on D3 and D5 of expansion of the erythroblasts with 15-minute treatments of either no peptide, a control peptide (DYP), or an EphB4 inhibitor (TNYL) (n=3). (E) Graph showing the percentage of cells obtained by flow cytometry expressing the active form of integrin β1 (clone HUTS-21) on D3 and D5 of erythroblast expansion with 15-minute treatments of either no peptide, a control peptide (DYP), or an EphB4 inhibitor (TNYL) (n=2). The error bars represent the standard error of the mean. Comparison between the samples was conducted using one-way ANOVA: ns: not significant; *$P \leq 0.05$. AU: arbitrary units.

to as links. Images were taken every hour to screen as many conditions as possible on the Incucyte and ensure comparability. The box plots in Figure 3B and C demonstrate that the addition of the EPHB4 inhibitor TNYL-RAW significantly reduced the average number of interactions (50% *vs.* 75% macrophage with more than 1 link on average; $P<0.0001$) but not the mean duration of these contacts. Importantly, the movement of the macrophages was not affected by the addition of inhibitors, as +Dex macrophages still exhibit a high degree of movement with

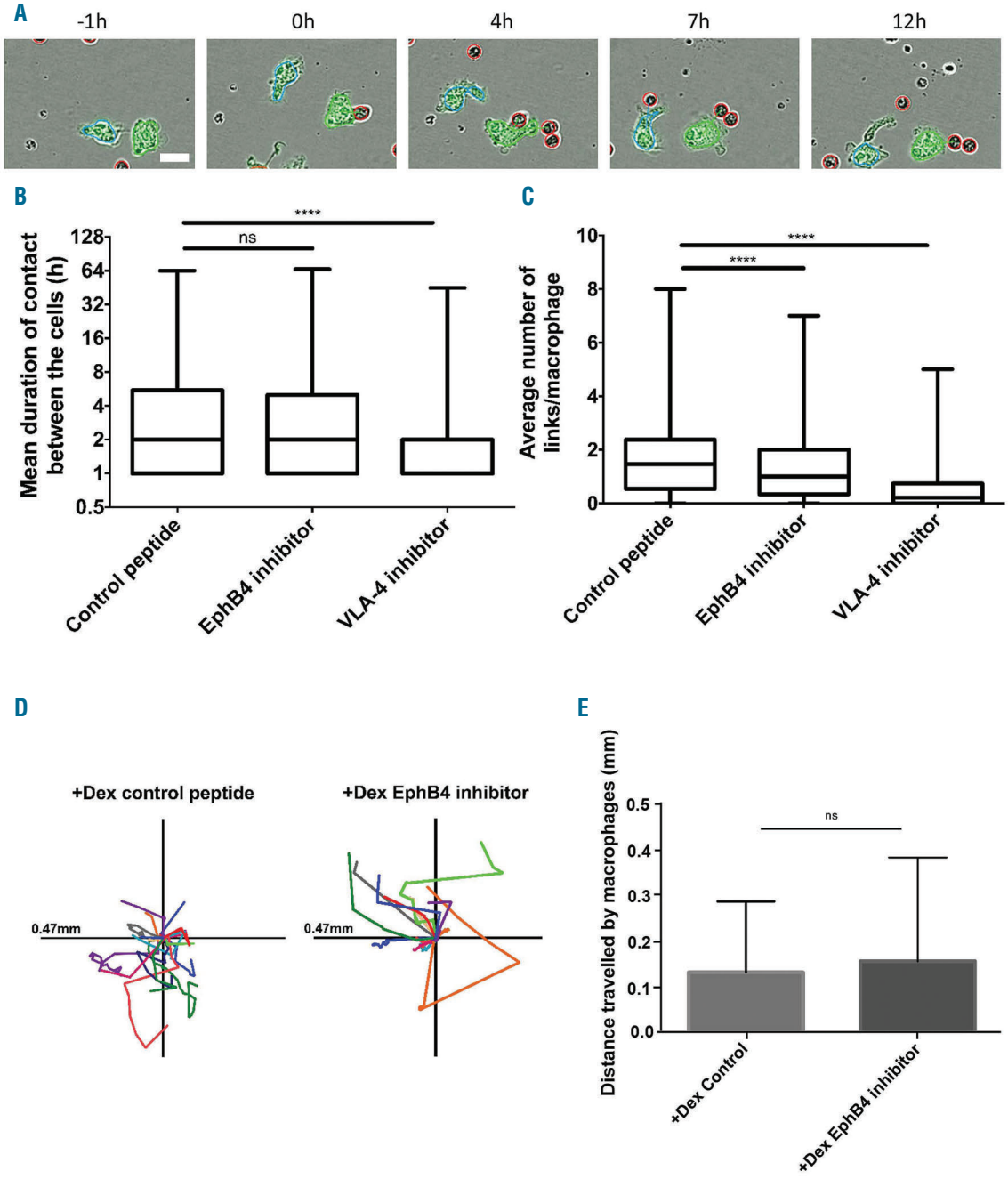

Figure 3. EPHB4 is required for contact inhibition of locomotion in erythroblastic island formation. (A) Example of analysis performed on an Incucyte experiment with the control peptide, DYP. Dexamethasone (+Dex) macrophages (labeled with Cell Tracker green) were grown from the peripheral blood mononuclear cells (PBMC) selected by adherence. The erythroblasts were added at a ratio of 10:1. The excess erythroblasts were gently removed by washing with media after 16 hours (h) incubation. The cells were imaged every hour. Macrophages are individually identified by the program due to their green color. The program then recognizes at each frame how many erythroblasts (red) are in contact (link) with the identified macrophage. Scale bar is 20 μm. (B) Min to max boxplot showing the mean duration of links between macrophages and erythroblasts. Kruskal-Wallis test was performed on 2,038 macrophages for +Dex EPHB4 inhibitor, 2,444 for +Dex Control peptide, and 1,841 for +Dex VLA-4 inhibitor (n=3). The y-axis is a log2 scale. (C) Min to max boxplot showing the average number of links between macrophages and erythroblasts. Kruskal-Wallis test was performed on 2,038 macrophages for +Dex EPHB4 inhibitor, 2,444 for +Dex Control peptide, and 1,841 for +Dex VLA-4 inhibitor (n=3). (D) Scaled cell-displacement vector diagrams of macrophage movement for 18 randomly selected macrophages from control peptide and 13 from the EPHB4 inhibitor condition. (E) Mean plot of total path length for 82 randomly selected macrophages from control peptide and 46 from EPHB4 inhibitor conditions. Two-tailed *t*-test was run on these samples. ns: not significant ($P\geq0.05$); **** $P\leq0.0001$.

each peptide treatment (Figure 3D and E). Although +Dex macrophages do not express VCAM1, we also tested whether other integrin interactions contribute to the macrophage-erythroblast relationship in addition to EPHB4. An inhibitory peptide designed against VLA-4, EIL peptide, was introduced in the formation assay.[37] This peptide was generated from a fragment of fibronectin which binds and locks the integrin β1 into the active form. The presence of the VLA-4 inhibitor in the formation assay led to a loss in mean duration (75% of cells have

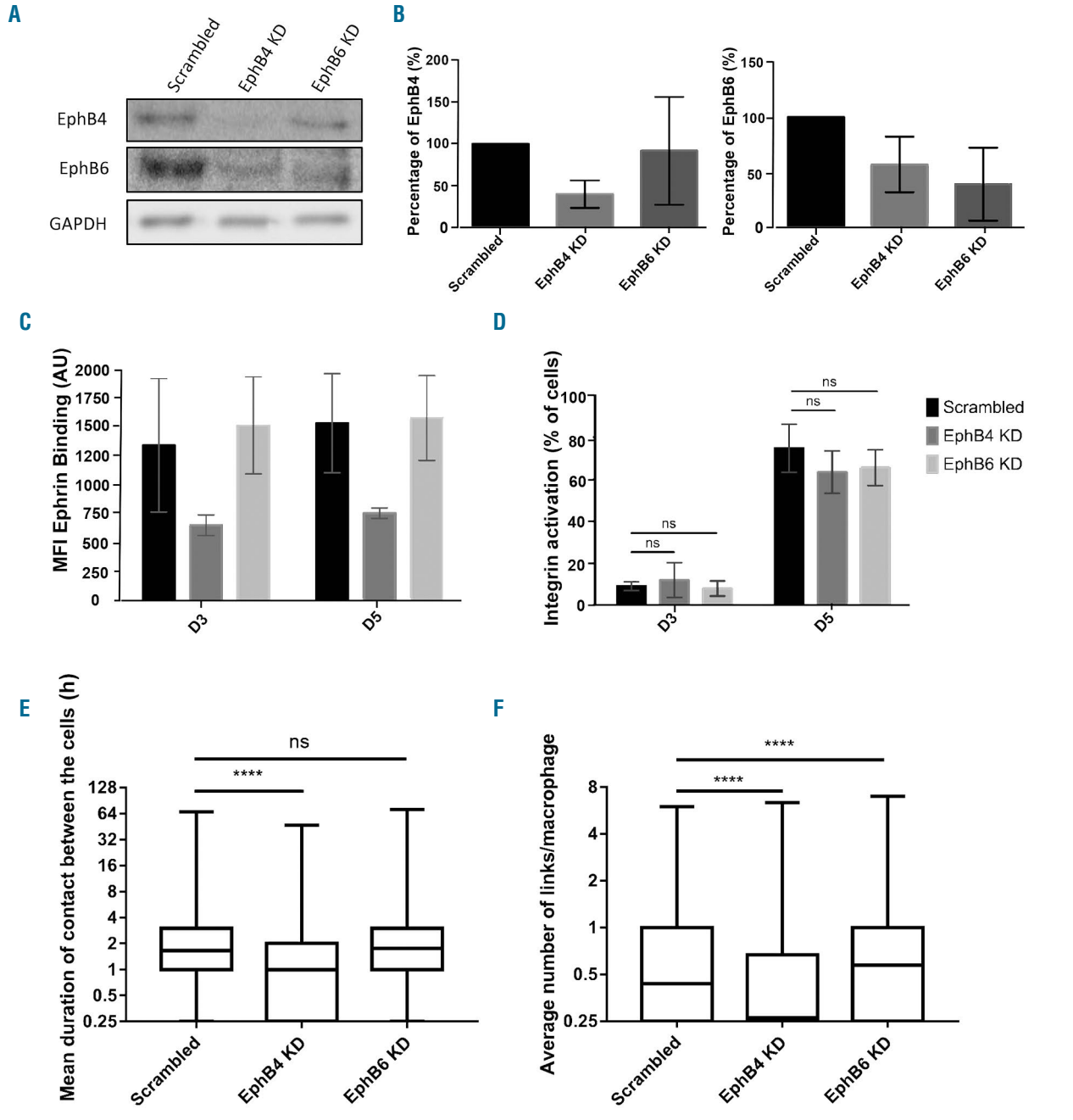

Figure 4. Loss of EPHB4, not EPHB6, in erythroblasts impacts macrophage-erythroblast interactions. (A) Lysates from day (D)4 expanding erythroblasts, treated with either scrambled control, EPHB4 or EPHB6 shRNA, and were blotted for EPHB4, EPHB6 and GAPDH. This is a representative plot (n=5). (B) Quantification of the blots in (A) and four other repeats (n=5), normalized to GAPDH. Comparison between the samples was made with a two-way ANOVA. (C) Graph showing the mean fluorescence intensity (MFI) obtained by flow cytometry of the ephrin-B2 construct binding through three days of erythroblast expansion. Erythroblasts were treated with either scrambled, EphB4 or EphB6 shRNA prior to the binding construct experiment (n=4). (D) Graph showing the percentage of cells obtained by flow cytometry expressing the active form of integrin β1 (clone HUTS-21) through three days of expansion of shRNA-treated erythroblasts (n=4). Comparison between the samples was made with a two-way ANOVA. (E) Min to max boxplot showing the mean duration of links between macrophages and erythroblasts on D3 and D5 of erythroblast culture. Erythroblasts were transduced with either scrambled, EphB4 or EphB6 shRNA before co-culturing with macrophages and assessment of link formation. Kruskal-Wallis test was performed on 5023 macrophages for scrambled, 6060 for EPHB4 KD, and 3467 for EPHB6 KD (n=3). The y-axis is a log2 scale. (F) Min to max boxplot showing the average number of links between macrophages and erythroblasts. Kruskal-Wallis test was performed on 5,023 macrophages for Scrambled, 6060 for EPHB4 KD, 3467 for EPHB6 KD (n=3). The y-axis is a log2 scale. The error bars represent the standard error of the mean: ns: not significant ($P \geq 0.05$); *$P \leq 0.05$; ****$P \leq 0.0001$. AU: arbitrary unit.

contacts which last less than 1h compared to 75% which last more) and an average number of links in +Dex cells (Figure 3B and C).

EPHB4 depletion using shRNA impacts macrophage-erythroblast interaction

To assess the specific importance of EPH receptor expression and rule out secondary binding of the inhibitory peptides, EPHB4 and EPHB6 were depleted individually using lentiviral shRNA transduction of early erythroblasts. When EPHB4 is silenced, we observed that there is a concomitant loss of EPHB6 (Figure 4A). This was not a reciprocal relationship, as EPHB6 depletion did not reduce the level of EPHB4 expression, as can be observed in Figure 4B. Heterodimerization of EPHB6 with EPHB4 may, therefore, be important for its stability on the erythroblast surface but not *vice versa*.[38] This occurred in the presence of two different shRNA for each protein (*data not shown*). Importantly, depletion of EPHB4 reduced ephrin-B2 binding in a surface binding assay but not when EPHB6 alone was knocked down, suggesting that EPHB4 is responsible for the majority of ephrin-B2 binding (Figure 4C). As was seen with the inhibitors, the depletion of the EPHB receptors did not lead to a reduction in integrin β1 activation

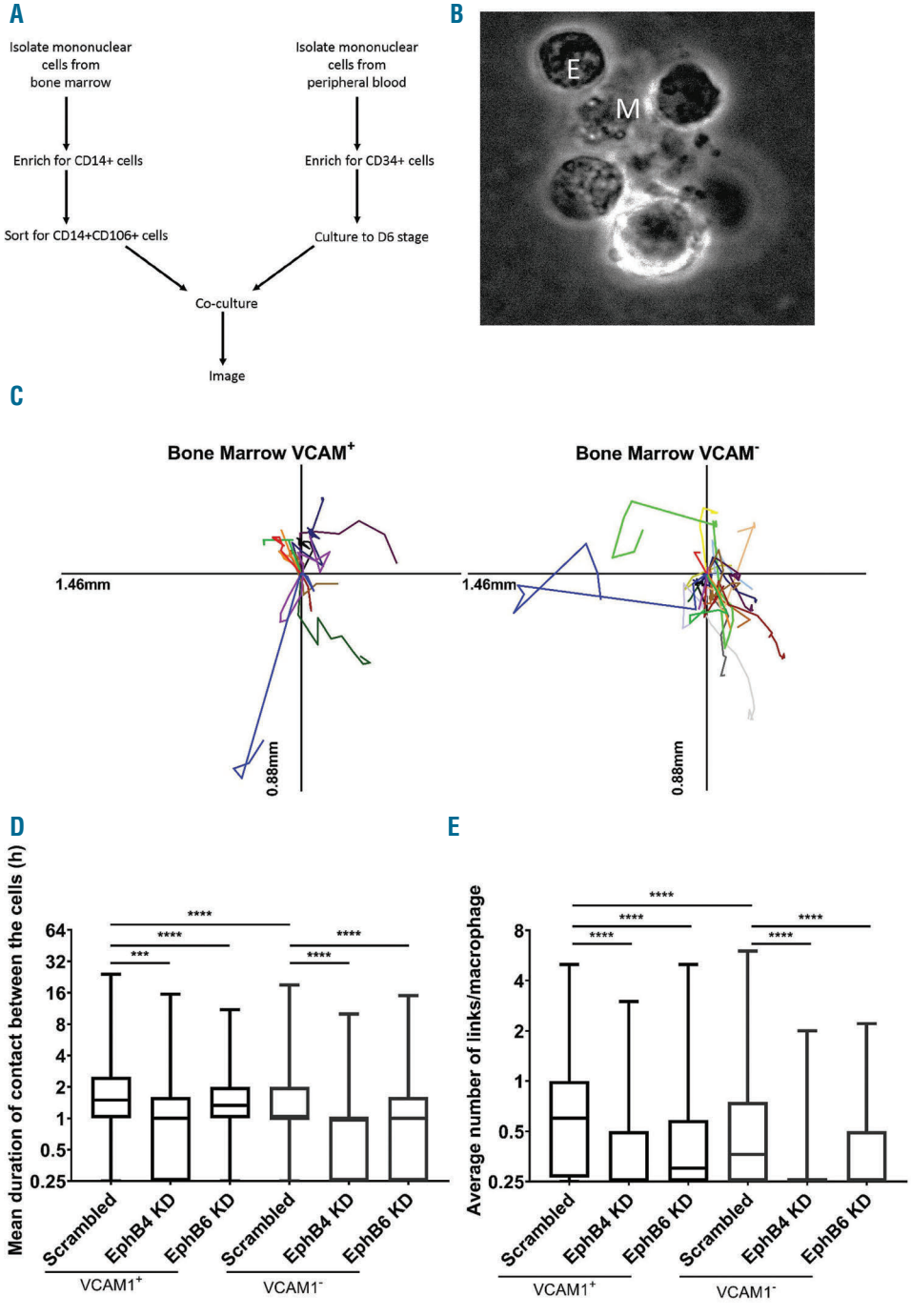

Figure 5. Bone marrow (BM) macrophage-erythroblast interaction is sensitive to EPHB4 and EPHB6 depletion. (A) Schematic representation of workflow for island reconstitution. (B) Widefield image of a cluster in a VCAM$^+$ sample. M: central macrophage; E: erythroblasts. (C) Scaled cell-displacement vector diagrams of macrophage movement for 11 randomly selected VCAM$^+$ macrophages and 20 VCAM$^-$. (D) Min to max boxplot showing the mean hours (h) duration of links between BM macrophages and erythroblasts. Kruskal-Wallis test was performed on 1,123 macrophages for scrambled VCAM$^+$ cells, 615 for EPHB4 KD VCAM$^+$ cells, 647 for EPHB6 KD VCAM$^+$ cells, 779 for scrambled VCAM$^-$ cells, 164 for EPHB4 KD VCAM$^-$ and 432 for EPHB6 KD VCAM$^-$ from two separate experiments from the same donor. The y-axis is a log2 scale. (E) Min to max boxplot showing the average number of links between BM macrophages and erythroblasts. Kruskal-Wallis test was performed on 1,332 macrophages for scrambled VCAM$^+$ cells, 875 for EPHB4 KD VCAM$^+$ cells, 854 for EPHB6 KD VCAM$^+$ cells, 963 for scrambled VCAM$^-$ cells, 164 for EPHB4 KD VCAM$^-$ and 714 for EPHB6 KD VCAM$^-$ from two separate experiments from the same donor. The y-axis is a log2 scale. ***$P \leq 0.001$; ****$P \leq 0.0001$. h: hours.

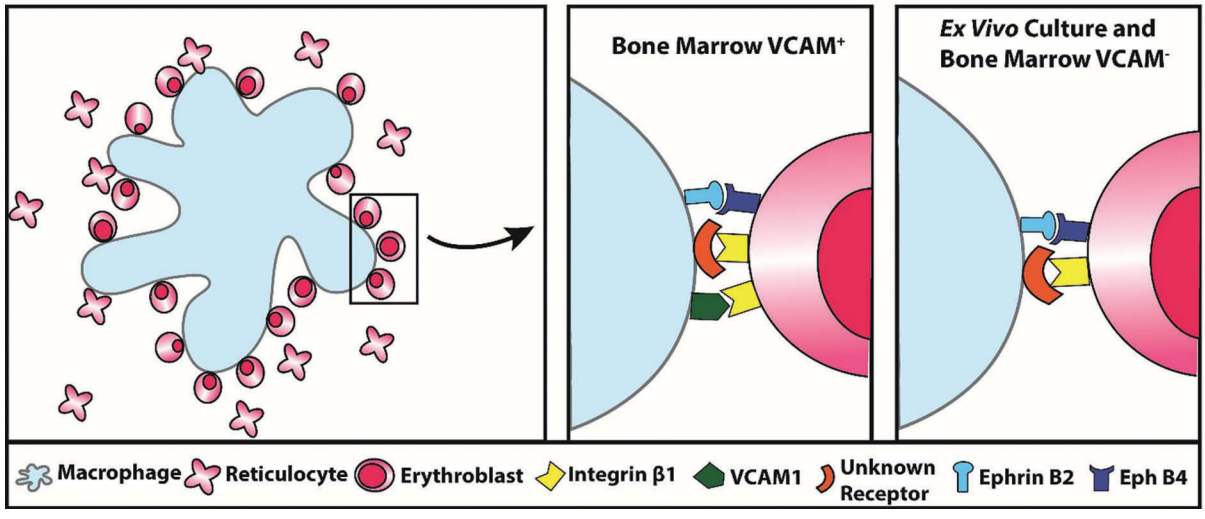

Figure 6. Schematic representation of the role of receptors in erythroblastic island development. Summary diagram of the receptors involved in macrophage-erythroblast binding in erythroblastic island development in the VCAM$^+$ cells of the bone marrow compared to *ex vivo* culture and VCAM$^-$ cells.

(Figure 4D). Therefore, integrin activation at the surface of proerythroblasts is not due to the presence or activation of EPHB4.

When EPHB knockdown erythroblasts were added to +Dex macrophages, only erythroblasts with EPHB4 depletion caused a loss of both average number of links (scrambled control median of 0.43 *vs.* EPHB4 KD median of 0.26) and the mean duration of these contacts between +Dex macrophages (75% last longer than 1 hour in scrambled control *vs.* 50% in EPHB4 KD on average). The loss of EPHB6 did not lead to any differences in mean duration to the scrambled control (Figure 4E and F); therefore, confirming the EPHB4 peptide inhibitor result. Interestingly, EPHB6 knockdown leads to a statistically higher number of contacts (median of 0.43 *vs.* 0.57; $P<0.0001$), indicating that the sole presence of EPHB4 is enough to have a higher number of long-lasting contacts with macrophages. It should be noted that knockdown experiments are less sensitive to the macrophage:erythroblast ratio than the peptide experiments, probably due to peptide saturation occurring.

Primary bone marrow macrophages also require EPHB4 expression on erythroblasts for interaction

To extend a role for ephrin interactions to *ex vivo* BM macrophages, erythroblastic islands were reconstituted using human BM aspirates. VCAM1$^+$ and VCAM1- macrophage populations were isolated in a two-stage process, first by isolating CD14$^+$ cells using magnetic beads and then sorting for CD14$^+$ VCAM1$^+$ cells (Figure 5A). Flow cytometry confirmed that VCAM1$^+$ cells were also CD169$^+$ as described previously[39] (*Online Supplementary Figure S1*). Erythroblasts cultured from CD34$^+$ cells were then introduced at the same stage as for the +Dex macrophages in earlier experiments. Clusters of cells composed of macrophages and erythroblasts were observed following this method of reconstitution (Figure 5B and *Online Supplementary Figure S5*). Furthermore, these macrophages are highly motile as witnessed for the +Dex macrophages (Figure 5C).[40] In Figure 5D and E, VCAM1$^+$ BM macrophages have long-lasting interactions with multiple erythroblasts. VCAM1- BM macrophages have 50% of contacts lasting more than 1h compared to 75% of VCAM1$^+$ cells. Furthermore, VCAM1- cells form statistically fewer links ($P<0.0001$). Therefore, as demonstrated with +Dex macrophages, a lack of VCAM1 does not stop interactions with erythroblasts, but its presence does indicate a macrophage with a subtly enhanced erythroblast binding ability.

Importantly, the results with VCAM1$^+$ and VCAM1$^-$ cells reproduced those observed using +Dex cultured macrophages with the loss of EPHB4 impacting on erythroblast association. However, unlike +Dex cultured macrophages, the loss of EPHB6 also significantly affected the initiation of associations between BM macrophages and erythroblasts. Therefore, EPHB6 appears to be as equally important as EPHB4 in erythroblastic island reconstitutions when BM macrophages are used (Figure 5D and E). These results confirm the importance of EPHB receptors' presence at the same time as active integrins for the recognition of erythroblasts as binding partners by macrophages.

Discussion

This work has used an imaging-based assay to interrogate the importance of EPH receptor interactions in the initial association between macrophages and erythroblasts. We have demonstrated that EPHB receptors are present at the surface of erythroblasts during terminal differentiation between the proerythroblast and orthochromatic stages, and that this temporal expression profile coincides with increased integrin activation (Figures 1 and 2). The depletion of EPHB4 causes macrophages and erythroblasts to have fewer long-duration contacts, and the removal of EPHB4 or its inhibition had no effect on integrin activation (Figures 4 and 5). Therefore, loss of EPHB4 alone is sufficient to reduce macrophage recognition of erythroblasts as binding partners. We, therefore, suggest ephrin-B2 binding alongside integrin activation reinforces recognition. We therefore propose a new model of interaction whereby EPHB receptors and integrin engagement

act in concert as a coincidence detector, to ensure that the macrophage associates and binds to the differentiating progenitor cell at the appropriate time (Figure 6).

Furthermore, contact inhibition of locomotion is thought to be controlled by a ratio of EPHB and EPHA receptors.[16] Interestingly, we observed that erythroblasts have a high level of EPHB and EPHA receptors during early stages of differentiation but lose EPHB receptors by the final stages of differentiation, while EPHA is retained (albeit at lower levels). We hypothesize that EPH receptors may contribute throughout the whole process of differentiation; in the early stages of differentiation, EPHB receptor is present in higher amounts than EPHA leading to recognition between the cells, supported by the EPHB4 inhibition disrupting this interaction. As the cells differentiate, the amount of EPHA receptor becomes dominant over EPHB, tantalisingly suggesting that, once the erythroblast has enucleated to form a reticulocyte, EPHA4 may be involved in the separation of the cells; a hypothesis that will need to be explored in future experiments.

It is notable that, in humans, EPH receptor activation did not affect integrin activation at day 5, which contradicts the findings of a recent report,[9] which showed that, in mice, EPHB1 receptor engagement caused a rise in CD29 and its activation at the surface of erythroblasts after agrin treatment. We cannot exclude the possibility that agrin still has a role in the integrin β1 activation observed in this study, separate from its additional role in activating the EPHB receptors at the surface. However, our results indicate that these two events are likely independent and that the difference between the previous study and ours is due to differences in species.

Our observation here that VCAM1$^-$ macrophages are capable of interacting with erythroblasts confirms work by Wei and Frenette[41] and Falchi *et al.*[33] All three types of macrophages tested in this study were capable of binding erythroblasts to some degree. This change in the level of binding could be related to the subtle changes which exist between these cells, be it the presence of VCAM1, different levels of ephrin-B2 at their surface or other unknown differences. Indeed, it is known that varying levels of ephrin-B2 can influence the function of EPHB6.[42] As the BM macrophages express lower amounts of ephrin-B2 expression than cultured macrophages, this may explain the former's interaction sensitivity to EPHB6 silencing. Taken together, the experiments have shown that EPH receptors are more important to the recognition between erythroblasts and macrophages than VCAM1. This mirrors the results found by Wei and Frenette who reported that EMP is more important than VCAM1 for the further stages of the interaction.[41] However, we do not fully understand the hierarchy between EPH receptors and the integrins. Our experiments do, however, demonstrate that both EPH and integrins together are essential for the interaction and recognition of the macrophages to the erythroblasts.

The evidence presented here also suggests a VCAM1$^-$ independent interaction for integrins in erythroblastic island formation, or perhaps associations are more promiscuous than anticipated. In addition, although a large number of mature macrophages in the human BM are VCAM1$^+$, indicating a preference for this phenotype in island formation, the ability for VCAM1$^-$ macrophages to form interactions with erythroblasts indicates a flexibility in terms of the type of macrophages which can participate in erythroblastic island formation, which may be important during stress erythropoiesis. The role of VCAM1 in helping erythroblasts expand[40] would explain this preference.

In addition to driving interactions, the EPH receptors may play additional supportive roles within the erythroblastic island. It was previously reported that overexpression of EPHB4 increases HSC numbers;[20] therefore, EPHB4 might have a proliferative role within the niche. Finally, the observation that erythroblasts express both ephrin-B2 and EPHB4, raises the potential for homophilic cell interaction that could lead to higher proliferation, and also explains the ability of erythroblasts to proliferate *in vitro* in the absence of macrophages.

In summary, it has previously been difficult to determine the specific contribution certain receptors play in human macrophage-erythroblast interactions during erythropoiesis. This study has successfully employed live imaging of human macrophages and erythroblasts to probe the role of a potential receptor interaction between the cells over time. This has shown, for the first time, a dependence on EPHB interactions for the macrophage and erythroblast interaction, and we believe this imaging assay can help further delineate the importance of other receptors in the interaction between erythroblasts and macrophages in future experiments.

Acknowledgments

We would like to thank Dr. Emile van den Akker for discussion on development of an antibody panel for macrophages; Dr. Andrew Herman and Lorena Sueiro for the Biomedical Sciences Flow Cytometry Facility for FACS sorting; the Wolfson Bioimaging facility for access to the Incucyte, widefield and all their help; Abi Gartner for his help with analysis. We thank the Elizabeth Blackwell Institute Wellcome Trust ISSF Award for providing funding for Stephen Cross.

Funding

This work was funded by NHS Blood and Transplant R&D grants (WP15-05); a Wellcome Trust PhD studentship (LHO-N; 105385/Z/14/Z). This work is also funded by the National Institute for Health Research (NIHR) Blood and Transfusion Research Unit (NIHR BTRU) in Red Cell Products (NIHR-BTRU-2015-10032). The views expressed are those of the authors and not necessarily those of NIHR or the Department of Health and Social Care.

References

1. Socolovsky M. Exploring the erythroblastic island. Nat Med. 2013;19(4):399-401.
2. Hanspal M, Hanspal JS. The association of erythroblasts with macrophages promotes erythroid proliferation and maturation: a 30-kD heparin-binding protein is involved in this contact. Blood. 1994;84(10):3494-3504.
3. Rhodes MM, Kopsombut P, Bondurant MC, Price JO, Koury MJ. Adherence to macrophages in erythroblastic islands enhances erythroblast proliferation and increases erythrocyte production by a different mechanism than erythropoietin. Blood. 2007;111(3):1700-1708.
4. Toda S, Segawa K, Nagata S. MerTK-mediated engulfment of pyrenocytes by central macrophages in erythroblastic islands. Blood. 2014;123(25):3963-3971.
5. Soni S, Bala S, Gwynn B, Sahr KE, Peters

LL, Hanspal M. Absence of Erythroblast Macrophage Protein (Emp) Leads to Failure of Erythroblast Nuclear Extrusion. J Biol Chem. 2006;281(29):20181-20189.
6. Lee G, Lo A, Short SA, et al. Targeted gene deletion demonstrates that the cell adhesion molecule ICAM-4 is critical for erythroblastic island formation. Blood 2006; 108(6):2064-2071.
7. Wang Z, Vogel O, Kuhn G, Gassmann M, Vogel J. Decreased stability of erythroblastic islands in integrin β3-deficient mice. Physiol Rep. 2013;1(2):e00018.
8. Fraser ST, Midwinter RG, Coupland LA, et al. Heme oxygenase-1 deficiency alters erythroblastic island formation, steady-state erythropoiesis and red blood cell lifespan in mice. Haematologica. 2015;100(5):601-610.
9. Anselmo A, Lauranzano E, Soldani C, et al. Identification of a novel agrin-dependent pathway in cell signaling and adhesion within the erythroid niche. Cell Death Differ. 2016;23(8):1322-1330.
10. Jacobsen RN, Nowlan B, Brunck ME, Barbier V, Winkler IG, Levesque J-P. Fms-like tyrosine kinase 3 (Flt3) ligand depletes erythroid island macrophages and blocks medullar erythropoiesis in the mouse. Exp Hematol. 2016;44(3):207-212
11. Soni S, Bala S, Hanspal M. Requirement for erythroblast-macrophage protein (Emp) in definitive erythropoiesis. Blood Cells Mol Dis. 2008;41(2):141-147.
12. Kullander K, Klein R. Mechanisms and functions of Eph and ephrin signalling. Nat Rev Mol Cell Biol. 2002;3(7):475-486.
13. Pasquale EB. Eph receptors and ephrins in cancer: bidirectional signalling and beyond. Nat Rev Cancer. 2010;10(3):165-180.
14. Okubo T, Yanai N, Obinata M. Stromal cells modulate ephrinB2 expression and transmigration of hematopoietic cells. Exp Hematol. 2006;34(3):330-338.
15. Rutkowski R, Mertens-Walker I, Lisle JE, Herington AC, Stephenson SA. Evidence for a dual function of EphB4 as tumor promoter and suppressor regulated by the absence or presence of the ephrin-B2 ligand. Int J Cancer. 2012;131(5):E614-E624.
16. Astin J, Batson J, Kadir S, et al. Competition amongst Eph receptors regulates contact inhibition of locomotion and invasiveness in prostate cancer cells. Nat Cell Biol. 2010;12(12):1194-1204.
17. Alfaro D, Mũoz JJ, García-Ceca J, Cejalvo T, Jiménez E, Zapata AG. The Eph/ephrinB signal balance determines the pattern of T-cell maturation in the thymus. Immunol Cell Biol. 2011;89(8):844-852.
18. Kwak H, Salvucci O, Weigert R, et al. Sinusoidal ephrin receptor EPHB4 controls hematopoietic progenitor cell mobilization from bone marrow. J Clin Invest. 2016; 126(12):4554-4568.
19. Tosato G. Ephrin ligands and Eph receptors contribution to hematopoiesis. Cell Mol Life Sci. 2017;74(18):3377-3394.
20. Nguyen TM, Arthur A, Panagopoulos R, et al. EphB4 expressing stromal cells exhibit an enhanced capacity for hematopoietic stem cell maintenance. Stem Cells. 2015; 33(9):2838-2849.
21. Suenobu S, Takakura N, Inada T, et al. A role of EphB4 receptor and its ligand, ephrin-B2, in erythropoiesis. Biochem Biophys Res Commun. 2002;293(3):1124-1131.
22. Inada T, Iwama A, Sakano S, Ohno M, Sawada K, Suda T. Selective expression of the receptor tyrosine kinase, HTK, on human erythroid progenitor cells. Blood. 1997;89(8):2757-2765.
23. Wang Z, Miura N, Bonelli A, et al. Receptor tyrosine kinase, EphB4 (HTK), accelerates differentiation of select human hematopoietic cells. Blood. 2002;99(8):2740-2747.
24. Schneider CA, Rasband WS, Eliceiri KW. NIH Image to ImageJ: 25 years of image analysis. Nat Methods. 2012;9(7):671-675.
25. Schindelin J, Arganda-Carreras I, Frise E, et al. Fiji: An open-source platform for biological-image analysis. Nat Methods. 2012; 9(7):676-682.
26. Thévenaz P, Ruttimann UE, Unser M. A pyramid approach to subpixel registration based on intensity. IEEE Trans Image Process. 1998;7(1):27-41.
27. Marr D, Hildreth E. Theory of Edge Detection. Proc R Soc B Biol Sci. 1980; 207(1167):187-217.
28. Tinevez JY, Perry N, Schindelin J, et al. TrackMate: An open and extensible platform for single-particle tracking. Methods. 2017;11580-11590.
29. Otsu N. A Threshold Selection Method from Gray-Level Histograms. IEEE Trans Syst Man Cybern. 1979;9(1):62–66.
30. Munkres J. Algorithms for the assignment and transportation problems. J Soc Ind Appl Math. 1957;5(1):32–38.
31. Heideveld E, Hampton-O'Neil LA, Cross SJ, et al. Glucocorticoids induce differentiation of monocytes towards macrophages that share functional and phenotypical aspects with erythroblastic island macrophages. Haematologica. 2018; 103(3):395-405.
32. Heideveld E, Masiello F, Marra M, et al. CD14+ cells from peripheral blood positively regulate hematopoietic stem and progenitor cell survival resulting in increased erythroid yield. Haematologica. 2015;100(11):1396-1406.
33. Falchi M, Varricchio L, Martelli F, et al. Dexamethasone targeted directly to macrophages induces macrophage niches that promote erythroid expansion. Haematologica. 2015;100(2):178-187.
34. Zhou R. The Eph Family Receptors and Ligands. Pharmacol Ther. 1998;77(3):151-181.
35. Eshghi S, Vogelezang MG, Hynes RO, Griffith LG, Lodish HF. Alpha4beta1 integrin and erythropoietin mediate temporally distinct steps in erythropoiesis: integrins in red cell development. J Cell Biol. 2007; 177(5):871-880.
36. Wang Y, Menendez A, Fong C, Elalieh HZ, Chang W, Bikle DD. Ephrin B2/EphB4 mediates the actions of IGF-I signaling in regulating endochondral bone formation. J Bone Miner Res. 2014;29(8):1900-1913.
37. Spring FA, Parsons SF, Ortlepp S, et al. Intercellular adhesion molecule-4 binds α4β1 and α v-family integrins through novel integrin-binding mechanisms. Blood. 2001;98(2):458-466.
38. Kaenel P, Mosimann M, Andres AC. The multifaceted roles of Eph-ephrin signaling in breast cancer. Cell Adh Migr. 2012; 6(2):138-147.
39. Chow A, Huggins M, Ahmed J, et al. CD169+ macrophages provide a niche promoting erythropoiesis under homeostasis and stress. Nat Med. 2013;19(March):429-436.
40. Belay E, Hayes BJ, Blau CA, Torok-Storb B. Human cord blood and bone marrow CD34+ cells generate macrophages that support erythroid islands. PLoS One. 2017;12(1):e0171096.
41. Wei Q, Frenette PS. Macrophage Erythroblast Attacher (MAEA), but Not VCAM1, Is Required for the Bone Marrow Erythroblastic Niche. Blood. 2015; 126(23):2128.
42. Matsuoka H, Obama H, Kelly ML, Matsui T, Nakamoto M. Biphasic functions of the kinase-defective Ephb6 receptor in cell adhesion and migration. J Biol Chem. 2005; 280(32):29355-29363.

ARTICLE

ARHGEF12 regulates erythropoiesis and is involved in erythroid regeneration after chemotherapy in acute lymphoblastic leukemia patients

Yangyang Xie,[1]* Li Gao,[2]* Chunhui Xu,[3] Liming Chu,[3,7] Lei Gao,[4] Ruichi Wu,[1] Yu Liu,[1] Ting Liu,[1] Xiao-jian Sun,[5] Ruibao Ren,[5] Jingyan Tang,[1] Yi Zheng,[6] Yong Zhou[7] and Shuhong Shen[1]

[1]Key Lab of Pediatrics Hematology/Oncology, Ministry of Health, Department of Hematology/Oncology, Shanghai Children's Medical Center, Shanghai Jiao Tong University, Shanghai, China; [2]Department of Hematology and Oncology, Children's Hospital of Soochow University, Suzhou, China; [3]Shanghai Institute of Nutrition and Health, University of Chinese Academy of Sciences, Chinese Academy of Sciences, Shanghai, China; [4]CAS Key Laboratory of Genome Sciences and Information, Beijing Institute of Genomics, Beijing, China; [5]State Key Laboratory for Medical Genomics, Shanghai Institute of Hematology, Ruijin Hospital, Shanghai, China; [6]Division of Experimental Hematology and Cancer Biology, Cincinnati Children's Hospital Research Foundation, Cincinnati, OH, USA and [7]CAS Key Laboratory of Tissue Microenvironment and Tumor, Shanghai Institute of Nutrition and Health, University of Chinese Academy of Sciences, Chinese Academy of Sciences, Shanghai, China

YX and LG contributed equally to this work.

Ferrata Storti Foundation

Haematologica 2020
Volume 105(4):925-936

ABSTRACT

Hematopoiesis is a finely regulated process in vertebrates under both homeostatic and stress conditions. By whole exome sequencing, we studied the genomics of acute lymphoblastic leukemia (ALL) patients who needed multiple red blood cell (RBC) transfusions after intensive chemotherapy treatment. *ARHGEF12*, encoding a RhoA guanine nucleotide exchange factor, was found to be associated with chemotherapy-induced anemia by genome-wide association study analyses. A single nucleotide polymorphism (SNP) of *ARHGEF12* located in an intron predicted to be a GATA1 binding site, rs10892563, is significantly associated with patients who need RBC transfusion (P=3.469E-03, odds ratio 5.864). A luciferase reporter assay revealed that this SNP impairs GATA1-mediated trans-regulation of *ARHGEF12*, and quantitative polymerase chain reaction studies confirmed that the homozygotes status is associated with an approximately 61% reduction in *ARHGEF12* expression (P=0.0088). Consequently, erythropoiesis was affected at the pro-erythroblast phases. The role of *ARHGEF12* and its homologs in erythroid differentiation was confirmed in human K562 cells, mouse 32D cells and primary murine bone marrow cells. We further demonstrated in zebrafish by morpholino-mediated knockdown and CRISPR/Cas9-mediated knockout of *arhgef12* that its reduction resulted in erythropoiesis defects. The p38 kinase pathway was affected by the ARHGEF12-RhoA signaling in K562 cells, and consistently, the Arhgef12-RhoA-p38 pathway was also shown to be important for erythroid differentiation in zebrafish as active RhoA or p38 readily rescued the impaired erythropoiesis caused by *arhgef12* knockdown. Finally, ARHGEF12-mediated p38 activity also appeared to be involved in phenotypes of patients of the rs10892563 homozygous genotype. Our findings present a novel SNP of *ARHGEF12* that may involve ARHGEF12-RhoA-p38 signaling in erythroid regeneration in ALL patients after chemotherapy.

Introduction

Chemotherapy for hematologic malignancies such as acute lymphoblastic leukemia (ALL) often causes anemia. To alleviate chemotherapy-induced anemia, red blood cell (RBC) transfusion has become standard care. The need for RBC

Correspondence:

YI ZHENG
Yi.Zheng@cchmc.org

YONG ZHOU
zhouyong@sibs.ac.cn

SHUHONG SHEN
shenshuhong@scmc.com.cn

Received: October 30, 2018.

Accepted: August 22, 2019.

Pre-published: August 29, 2019.

doi:10.3324/haematol.2018.210286

Check the online version for the most updated information on this article, online supplements, and information on authorship & disclosures: www.haematologica.org/content/105/4/925

transfusion varies significantly among patients who have undergone similar treatment protocols at similar intensities. Sensitivity of erythrocytes to the cytotoxicity of chemotherapy and the recovery rate of erythropoiesis are contributing factors related to the severity and duration of the anemia. Genetic diversity in genes regulating these response processes can be a cause for the variations between patients. Uncovering the genetic basis for the variable response is important for understanding the molecular mechanisms underlying erythropoiesis and its relationship to chemotherapy-induced anemia.

In this study, we performed genome-wide association study (GWAS) analyses of samples from individuals who had undergone multiple RBC transfusions (MRT) and from those who received no RBC transfusion (NRT) when a remission was achieved. By counting the cell line, primary bone marrow (BM) cells, and considering the results of animal model and human genetic studies, we suggest a novel molecular pathway involved in erythroid regeneration in ALL patients after chemotherapy.

Methods

Patients

From January 1st 2001 to December 31st 2014, a total of 452 patients diagnosed with childhood ALL were recruited in this study. The patients included were enrolled on Shanghai Children's Medical Center -Acute Lymphoblastic Leukemia-2005 (SCMC-ALL-2005) protocol. Standard induction and consolidation chemotherapy were used. Blood transfusion records were collected from the transfusion department of SCMC and clinical data were reviewed to exclude the events needed for additional transfusions of RBC, such as transplantation, gastrointestinal bleeding, surgery, etc. Patients who abandoned treatment or who died were not included in this study. Only total RBC transfusion units after achieving complete remission was included in the count and this number was normalized by body surface area (Unit/m^2) to exclude the influence of patient's age, mass, and the disease itself on blood transfusion units. Patients who received more than eight RBC units/m^2 were defined as MRT. This study has been approved by Shanghai Children's Medical Center Ethics Committee (n. SCMCIRB-K2018052).

Dual Luciferase reporter assays

A total of 933 bp DNA fragments surrounding rs10892563 CC and TT genotype were cloned into the firefly Luciferase vector pGl4.27 (Promega); 293T cells were transfected with 5 g PRL-TK vector and 300 ng PCDNA3-Flag expression GATA1 *via* lipofectemin. Luciferase activity was measured in a Varioskan Flash spectral scanning multimode reader (Thermo) using the Dual-Luciferase Reporter Assay system kit (Promega).

Targeted single nucleotide polymorphism genotyping by polymerase chain reaction

The candidate SNP rs10892563 on ARHGEF12 at position 119,729,754 bp was analyzed by polymerase chain reaction (PCR) on 381 ALL patients enrolled in the SCMC-ALL-2005 protocols for which genomic DNA samples were still available. The DNA segment containing the candidate mutation was amplified by PCR using the following primers:

5′-00ATAGGGATACCTGGCCCCTA-3′ and *5′-ndATAGGGATACCTGGCCCCTA-3′*

These PCR products were subsequently Sanger sequenced.

Table 1. Morpholino sequences and concentrations used in this study.

Target	Sequence	Concentration (mM)
arhgef12a MO	TGACTGTAGACCGTGTGTCGCTCAT	0.5
arhgef12a MIS	TGAgTcTAcACCGTcTcTCGCTCAT	0.5
arhgef12b MO	CACCAGTCTGAACACCAGCTCGCAT	0.5
arhgef12b MIS	CACgAcTCTcAACACgAcCTCGCAT	0.5

Whole-mount *in situ* hybridization

The antisense probes of *arhgef12a* and *arhgef12b* were obtained by PCR with the primers

(*arhgef12a* forward primer, 5'-GCGGAATTCCCACCTCAAGGAGATGGAAA-3';

reverse primer, 5'-GCGGGTACCCCAAAAGCATGCAAGAAACA-3';

arhgef12b forward primer, 5'-GCCGAATTCTCCAGCATGAGTGGTTGGTA-3';

reverse primer, 5'-ATTGGTACCCTCAACAGAAAGCCGAGACC-3'), and added with EcoR1/Kpn1 restriction enzyme sites for cloning into pCS2+ vector. Antisense digoxigenin (DIG)–labeled RNA probes were generated by *in vitro* transcription and whole-mount *in situ* hybridization (WISH) was performed as described previously.[1] The results were imaged using a stereomicroscope Nikon SMZ1500 with a 1 x HR Plan Apo objective and ACT-1 vision software.

Micro-injection

One-cell-stage embryos were injected with 2 nL of morpholino (MO) or mismatch morpholino (MIS) mixes (*arhgef12a* and *arhgef12b*) purchased from Gene-Tools. The MO sequences and concentrations are listed in Table 1.

CRISPR/Cas9 mutagenesis

The *arhgef12a* gRNA (5'-GGACGTGGGTCTCGAGTCAC-3') and *arhgef12b* gRNA (5'-GGAATCTGAGGCAGGCCCGG-3') were synthesized. The zebrafish optimized Cas9 mRNA was synthesized *in vitro* from the pCS2-nCas9n plasmid (addgene, #47929) as described.[2] The Cas9 mRNA was synthesized *in vitro* by SP6 mMessage mMachine Transcription Kit (Ambion). *arhgef12a* gRNA (50pg), *arhgef12b* gRNA (50pg), and Cas9 mRNA (150pg) were co-injected into one-cell stage embryos.

Statistical analysis

Results are expressed as mean±standard deviation considering the number of experiments. Statistical comparisons between groups were performed by two-tailed *t*-test or one-sided *t*-test using Graphpad Prism version 6.0.

Other methods

Whole exome sequencing, GWAS, cell sorting, quantitative real-time (qRT)-PCR, plasmid construction, *in vitro* RNA synthesis, micro-injection and anisomycin treatment were performed as described in the *Online Supplementary Appendix*.

Results

An *ARHGEF12* polymorphism in acute lymphoblastic leukemia patients is associated with susceptibility to chemotherapy-induced anemia

We performed whole exome sequencing in 31 individuals who had undergone at least eight RBC transfusions

(MRT) and 31 patients with no RBC transfusion (NRT), all from the SCMC-ALL-2005 cohort (Figure 1A). Considering the variations in patient age and body weight, the RBC transfusion amount was normalized by patient body surface area taking into account only post-remission transfusions in order to minimize the effect of ALL itself. By a GWAS analysis, 1,708 SNPs of 281 genes passed the criterion of the primary cut: a call rate of >95% and $P<0.01$. Of interest, most of the SNPs were located in introns adjacent to exons, suggesting that these polymorphisms are relevant to chemotherapy-induced anemia by regulating gene expression. These genes could be highly expressed in hematopoietic cells and involved in erythroid differentiation from hematopoietic stem/progenitor cells.

To address this possibility, we sorted the primary gene list with expression patterns in primitive CD34$^+$ cells before erythroid differentiation and in erythrocytes based on the Differentiation Map Portal (DMAP) database.[3] A total of 35 genes were enriched by this analysis. Among them, 12 genes were highly expressed in hematopoietic stem/progenitor cells (HSPC) and 23 genes were expressed in erythrocytes with over two times the average expressions. At the top of this enriched list were *GUCY1A3*,[4] *NUCB2, TFDP2*,[5] *CHPT1*,[6] *PLCB1*,[7] *LPIN2*,[8] *TNS1*,[9,10] *BSG*,[11,12] *COL5A1*,[13] *ANXA7*,[14] *EPB42,15*,[16] *RAP1GAP*,[17] *ARHGEF12*,[10,18] *ABCC4*[19] *and FARP1*[20] (Tables 2 and 3 and Figure 1B). Interestingly, most of these genes are well-known in association with erythropoiesis or cytotoxicity

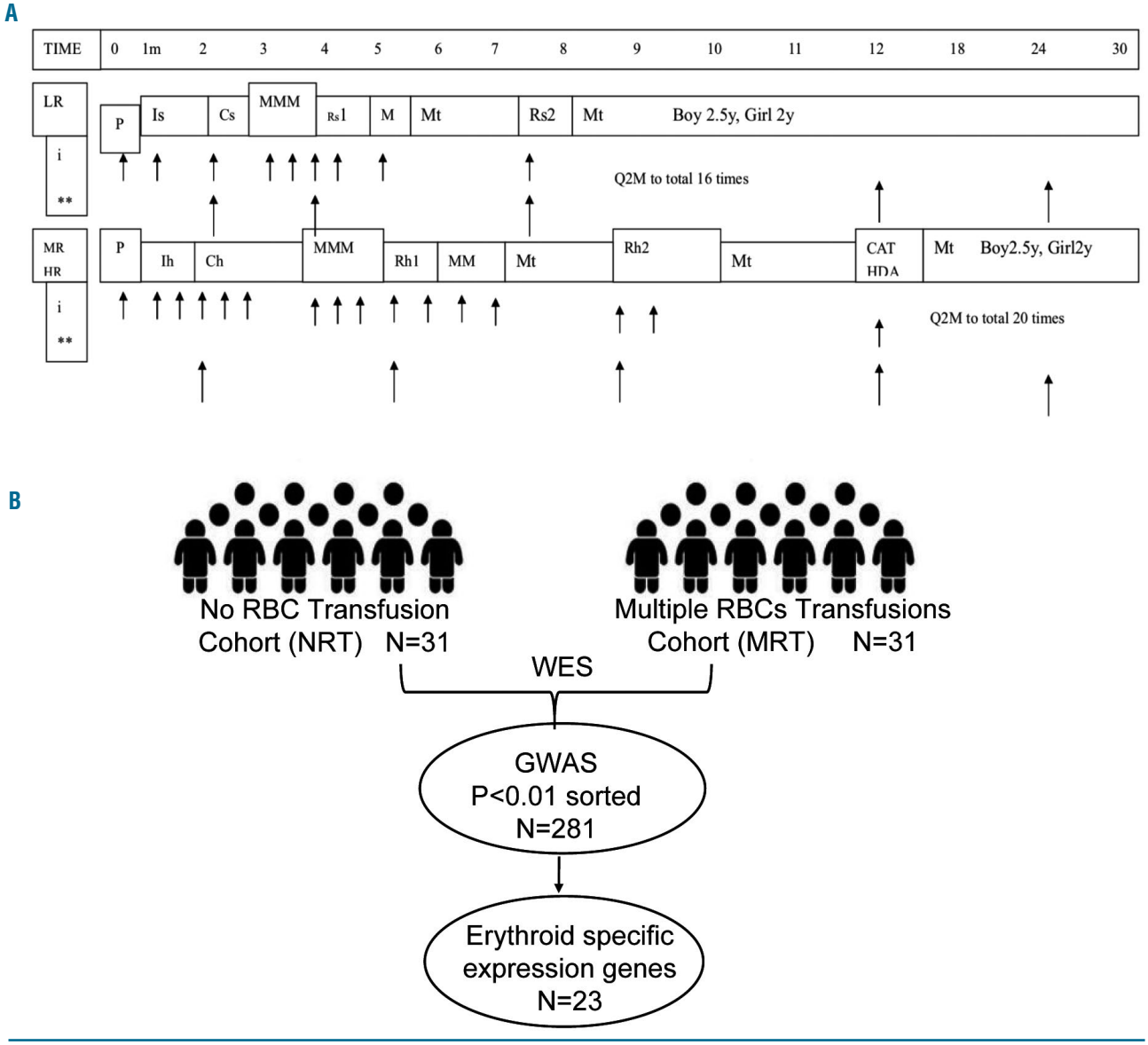

Figure 1. Genomic characterizations of chemotherapy-induced anemia in children with acute lymphoblastic leukemia (ALL). (A). The schematic treatment plan of SCMC-ALL 2005. LR: low-risk group; MR: medium-risk group; HR: high-risk group; P: prednisone window phase; Is: induction for standard-risk patients; Ih: induction for higher risk patients; Cs: consolidation for standard patients; Ch: consolidation for higher risk patients; M: high-dose methotrexate; Rs: re-induction for standard-risk patients; Rh: re-induction for higher risk patients; Mt: maintenance therapy; CAT HAD: chemotherapy course composed of cyclophosphamide, cytarabine, thiopurine and high-dose cytarabine. (B). An outline of the genomic characterizations. Genome-wide association study (GWAS) was performed based on whole exome sequencing data for 31 cases in each cohort of multiple red blood cell transfusion (MRT, >8 units/m^2) and no red blood cell transfusion (NRT). 23 genes highly expressed in erythoid committed and 12 genes highly expressed in pre-erythroid committed were on the list of genes with significance (call rate >95% and $P<0.01$).

susceptibility to chemotherapy.[21] Of note, four of these genes, i.e. *RAP1GAP, ARHGEF12, TNS1* and *FARP1,* are related to small GTPase regulation (Table 2 and 3). *ARHGEF12,* a RhoA-specific guanine-exchange factor (GEF), can specifically activate RhoA[18] which is essential for embryonic erythropoiesis.[10] *ARHGEF12* is thus possibly one of the associated genes involved in the regulatory mechanism of erythroid regeneration from anemia induced by chemotherapy. Among the SNP found in *ARHGEF12,* the most significant association Was rs76693355 (*P*=3.469E-03, odds ratio 5.864). All SNP were screened with linkage disequilibrium 0.2<r2<1 related to rs76693355 in the 5-kb flanking regions of ARHGEF12. We found that rs10892563 is located at a predicted binding site of the erythroid-specific transcription factor GATA1.[22] To test if such a variant could disrupt this GATA1 binding site function, we employed a dual luciferase assay in 293T cells with an expression vector containing this intron motif of rs10892563 in the promoter region. The expression assay showed that the minor allele change of rs10892563 was able to down-regulate *ARHGEF12* transcriptional regulation by GATA1 (Figure 2A and B). To examine if the rs10892563 SNP is actually associated with ALL patient RBC function, the CD71-positive erythroid cells from the ALL patient BM samples were isolated by flow cytometry[23] for sequencing and gene expression verifications. qRT-PCR analysis found that rs10892563 homozygosity in the patients is associated with an approximately 61% reduction in ARHGEF12 expression (*P*=0.0088) (Figure 2C and D).

Further verifying an involvement of rs10892563, additional targeted SNP genotyping of 452 ALL patients enrolled in the SCMC-ALL-2005 protocol showed that the genotype frequencies were CC in 7.52%, CT in 41.37%, and TT in 51.11% patients. The average normalized RBC transfusion was 4.533 units/m^2 in patients with CC genotype, 2.353 and 2.335 in patients with CT and TT genotypes, respectively (Figure 2E and *Online Supplementary Figure S1*). All patients who were homozygous needed RBC transfusion to maintain hemoglobin >65 g/L during the course of chemotherapy, whereas among those who were heterozygous or wild-type, the frequencies were 61.497% and 70.996%, respectively. Patients who were homozygous or heterozygous had a significantly higher probability of requiring MRT than patients carrying wild-type alleles (Figure 2F). Collectively, these results suggest that the *ARHGEF12* polymorphism rs10892563 is involved in the susceptibility to chemotherapy-induced anemia

ARHGEF12 reduction blocks erythroid differentiation of K562 cells

The findings that a polymorphism of *ARHGEF12* is associated with chemotherapy-induced anemia and that this gene is heavily transcribed in the human erythroid lineage (*Online Supplementary Figure S2A*) based on the analyses of several public databases[3] suggest that *ARHGEF12* is involved in erythropoiesis. As an initial test, we performed ARHGEF12 knockdown in the human erythroleukemia cell line K562 using lentiviral shRNA constructs (*Online Supplementary Figure S2B*). GPA expression and the benzidine cytochemical test showed that ery-

Table 2. Gene function of top 10 genes highly expressed in hematopoietic cells along erythroid differentiation from hematopoietic stem cells.

SNP	P value	OR	Func.ref Gene	Gene.refGene	Gene Function
rs11569201	0.00146	0.067	intronic	*TFDP2*	Can stimulate E2F-dependent transcription
rs3764973	0.0017	0.277	intronic	*CHPT1*	Lipid modification is associated with *CHPT1*
rs3745011	0.00227	3.241	intronic	*LPIN2*	Adipose tissue development and triglyceride metabolism
rs4672856	0.00262	0.208	intronic	*TNS1*	Positive regulator of RhoA
rs2283573	0.00312	0.228	intronic	*BSG*	Transmembrane glycoprotein that belongs to the immunoglobulin superfamily
rs3750575	0.00333	0	exonic	*ANXA7*	Member of the annexin family of calcium-dependent phospholipid binding proteins
rs494863	0.00336	0.291	intronic	*EPB42*	ATP-binding protein which may regulate the association of protein 3 with ankyrin
rs3767111	0.00346	0.28	intronic	*RAP1GAP*	Rap1 GTPase-activating protein, inactivation Rap1
rs76693355	0.00347	5.864	intronic	*ARHGEF12*	RhoA specific guanine exchange factor
rs3742106	0.00351	3.11	UTR3	*ABCC4*	Member of the superfamily of ATP-binding cassette (ABC) transporters

throid differentiation of the cells, under hemin induction, decreased significantly compared to the non-targeted (NT) cells (*Online Supplementary Figure S2C*).

ARHGEEF12 or its orthologs is involved in erythroid differentiation in murine progenitor cells and in a zebrafish model

To rule out potential effects by the neoplastic background of K562 cells, we knocked down *Arhgef12* expression in mouse hematopoietic cell line 32D cells and in primary mouse BM cells by lentiviral shRNA transduction. Erythropoietin-induced erythroid differentiation was significantly blocked by the interference of *Arhgef12* expression as by observed erythroid immunophenotyping by flow cytometry and in the burst forming units-erythroid and colony forming unit-erythroid colony forming assays (*Online Supplementary Figure S3*).

Zebrafish genome harbors two orthologs of *ARHGEF12*: *arhgef12a* on chromosome 15 and *arhgef12b* on chromosome 5. By comparing their sequences (*arhgef12a*, ENSDARG00000030532; *arhgef12b*, ENSDARG00000067634) with human ARHGEF12, we found that the similarities were 54% and 55%, respectively. Synteny analysis also showed the relatively conserved positions for both *arhgef12a* and *arhgef12b* (*Online Supplementary Figure S4A*). *Arhgef12a* is selectively enriched in early erythroid progenitors (*Online Supplementary Figure S4B*) whereas *arhgef12b* is expressed in early erythroid progenitors (*Online Supplementary Figure S4C*).

To study the role of *arhgef12* in erythropoiesis, we performed microinjections of *arhgef12a* and *arhgef12b* morpholino both in combination (*arhgef12* MO) and separately (*arhgef12a* MO and *arhgef12b* MO). Firstly, we performed WISH at 22 hours post fertilization (hpf) to analyze the primitive wave[24] of hematopoiesis. Expressions of the erythroid progenitor marker gata1, the mature erythrocyte marker *αe1-globin*, the hematopoietic lineage marker scl, and the myeloid markers *pu.1* and *lysozyme C* remained unchanged in *arhgef12* MO-injected embryos (*Online Supplementary Figure S5*). At 36 hpf, the definitive hematopoiesis stage of zebrafish, the expression of αe1-globin was dramatically decreased in *arhgef12a*- and arhgef12b-deficient embryos, whereas the hematopoietic stem cells (HSC) markers *runx1* and *c-myb* and the vascular morphology and marker *flk1* were unchanged (Figure 3A). At four days post-fertilization (dpf), the markers representing mature RBC including *αe1-globin*, *βe1-globin*, *βe2-globin*, *band3*, and *alas2* were severely reduced (Figure 3B). Of interest, *gata1* was associated with an obvious increase in caudal hematopoietic tissue (CHT) (Figure 3B), indicating that the erythroid defect may be caused by an impaired differentiation. Of interest, *gata1* was associated with an obvious CHT (Figure 3B), indicating that the erythroid defect may be caused by an impaired differentiation. Consistent with this possibility, o-Dianisidine stained hemoglobin showed that erythrocytes from *arhgef12* MO-injected embryos were more immature than those from the control group at 36 hpf and 4 dpf (Figure 3C). Subsequent examinations of *arhgef12a* and *arhgef12b* double knockout mutants by using the CRISPR/Cas9 method followed by o-Dianisidine staining found that mature erythrocytes were significantly decreased at 4 dpf in the mutant CHT and heart (Figure 3D and E). These results indicate that *arhgef12a* and arhgef12b are required for erythroid differentiation and maturation in zebrafish.

ARHGEF12 regulates erythroid differentiation through a RhoA-p38 pathway

RhoA is a well-defined substrate of ARHGEF12, which activates the exchange of RhoA bound GDP in the inactivated form for GTP to yield the active RhoA-GTP.[26] We hypothesized that RhoA is the key target of ARHGEF12 to mediate its function in erythrocyte maturation. Because zebrafish harbors 5 *rhoa* genes[27] and they all have an amino acid sequence which is quite similar (identity >90%) to human RhoA, we inferred that human RhoA mutant mRNA dominant-negative (DN) mutant RhoA T19N[28] and constitutively active mutant RhoA Q63[29] would also function in zebrafish. In fact, injection of dominant-negative RhoA mRNA led to anemia, which mimicked the arhgef12 deficiency phenotype (Figure 4A), but the anemia seemed to be less severe than with MO injec-

Table 3. Gene function related to erythropoiesis.

Gene.refGene	Gene Function related to Erythropoiesis
TFDP2	Coupling the erythroid cell cycle with terminal differentiation[5]
CHPT1	Lipid modification is associated with erythrocytes vulnerability[6]
LPIN2	Homozygous mutations in *LPIN2* are responsible for Majeed syndrome7
TNS1	RhoA is immportant to Erythropoiesis[8,9]
BSG	Unavailability of *BSG* leads to selective erythrocyte trapping in the spleen and promotes sensitivity to chemocherapy[10,11]
ANXA7	ANXA7 deficiency fosters suicidal death of erythrocytes or eryptosis[12]
EPB42	EPB42 is related to Hereditary Spherocytosis[13,14]
RAP1GAP	Rap1 is important to Erythropoiesis [15]
ARHGEF12	RhoA is important to Erythropoiesis [9,16]
ABCC4	ABCC4 has been associated with chemotherapy sensitivity[17]

tion, possibly due to mRNA instability. On the other hand, based on o-Dianisidine staining and WISH analysis of *αe1-globin*, a co-injection of constitutively active mutant RhoA Q63L mRNA was able to restore the erythropoiesis defect caused by *arhgef12* MO (Figure 4A). These results indicate that Arhgef12 activates RhoA to control erythroid differentiation.

To further understand the molecular events downstream of RhoA in erythropoiesis, the K562 cell line in which ARHGEF12 is important for its erythroid differentiation was examined. An antibody microarray screen found that phosphorylation of molecules in the p38 MAPK pathway was significantly decreased in the ARHGEF12 knockdown K562 cells (*Online Supplementary Figure S6A*). Western blotting confirmed this effect on p38 phosphorylation (*Online Supplementary Figure S6B*), suggesting that the p38 MAPK signaling pathway may contribute to the ARHGEF12-regulated erythropoiesis. Further confirmation using the p38 inhibitor SB202190 in zebrafish found that p38 inhibition resulted in a similar block of erythropoiesis as in the *arhgef12* morphants at 4 dpf (Figure 4B). Application of anisomycin, a p38 MAPK activator, was able to restore the erythrocyte maturation in the *arhgef12* morphants (Figure 4C). Thus, an ARHGEF12-RhoA-p38 pathway is likely to be involved in erythroid differentiation.

STAT1 expression can rescue the erythroid phenotype caused by arhgef12 knockdown in zebrafish

Human STAT1 produces two splicing variants that differ at their carboxy terminus. Zebrafish has two orthologous genes related to human *STAT1*: *stat1a* and *stat1b*. It has been shown that p38 MAPK-STAT1 pathways can regulate neutrophil development. Meanwhile, our antibody microarray screen showed that the phosphorylation of STAT1 at serine (S) 727 was decreased approximately 2-fold in ARHGEF12 knockdown K562 cells (*Online Supplementary Figure S6A*). We thus further examined whether STAT1 may be downstream of p38 MAPK in regulating erythropoiesis. We co-injected the *HA-stat1a* construct together with *arhgef12* MO in zebrafish, and observed that the phenotype of erythropenia was restored (Figure 5A a-c, a'-c') and *αe1-globin* expression recovered (Figure 5A e-g, e'-g'), compared with control embryos. A

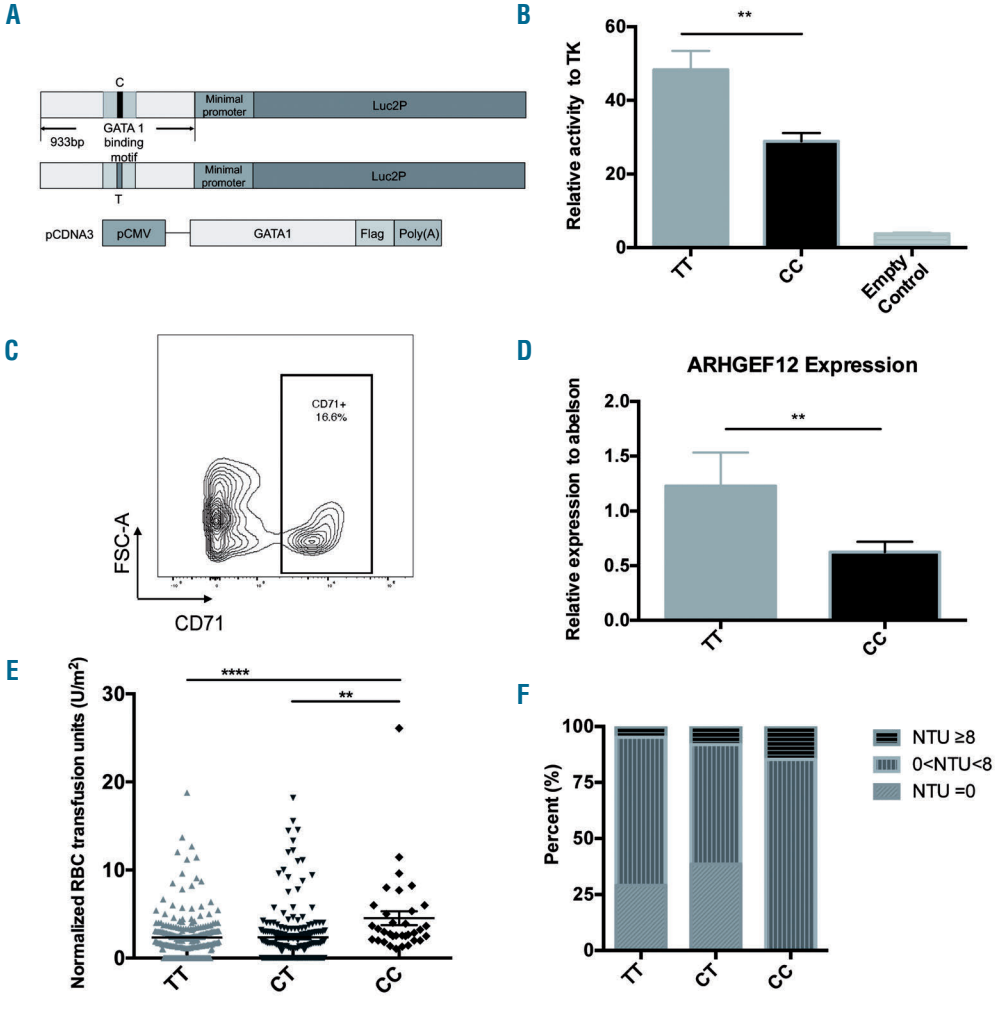

Figure 2. rs10892563 may disrupt a GATA1-binding cis element and is related to chemotherapy-induced anemia. (A and B) rs10892563 is located at a binding site of erythroid-specific transcription factor GATA1. Dual luciferase assay with the vector inserted with a stretch of sequence with the motif revealed that C allele of rs10892563 down-regulated GATA1 cis-transcriptional function compared to the major allele T in 293T cells; *P*=0.0038. (C and D) CD71-positive nucleated erythroid cells were sorted from banked bone marrow samples of acute lymphoblastic leukemia patients in remission state by fluorescence-activated cell sorting. The relative gene expression of ARHGEF12 was reduced in CC genotype at rs10892563 *versus* TT genotypes by quantitative real-time polymerase chain reaction assay; *P*=0.0088. (E) A total of 452 children with ALL enrolled in the Shanghai Children's Medical Center-Acute Lymphoblastic Leukemia-2005 (SCMC-ALL-2005) protocol were genotyped targeting rs10892563. The average normalized red blood cell (RBC) transfusion units was significantly higher in patients with CC genotype than the CT genotype (*P*=0.0011) and the TT genotype (*P*<0.0001); each point represents one patient's record. (F) Distribution of RBC transfusions across different rs10892563 genotypes. All patients with CC genotype (n=34) need RBC transfusions, whereas in patients with CT and TT genotype, proportions of RBC transfusions were 61.5% and 71%, respectively. Concerning multiple red blood cell transfusions (MRT), the proportion in CC, CT and TT were 14.705%, 8.021%, and 4.762%, respectively (*P*<0.001).

cytology assay by Wright-Giemsa staining showed that the co-injection of stat1a mRNA with *arhgef12* MO appeared to promote the immature erythrocyte differentiation (Figure 5B). In addition, *stat1* MO injection increased *gata1* expression (Figure 5C a, a', b, b') but reduced *αe1-globin* expression (Figure 5C c, c', d, d'), similar to that by *arhgef12* MO injection. It is thus likely that STAT1 is involved in the ARHGEF12-p38 MAPK signaling function in erythroid differentiation.

The ARHGEF12-p38 pathway is associated with erythroid regeneration in acute lymphoblastic leukemia patients after chemotherapy

To examine whether *ARHGEF12* polymorphism-associated anemia after chemotherapy in ALL patients may engage the p38 pathway, we measured p38 phosphorylation in erythroid cells in seven remission-related BM from ALL patients during maintenance therapy by phosphoflow.[30] All seven patient samples with the rs10892563 CC

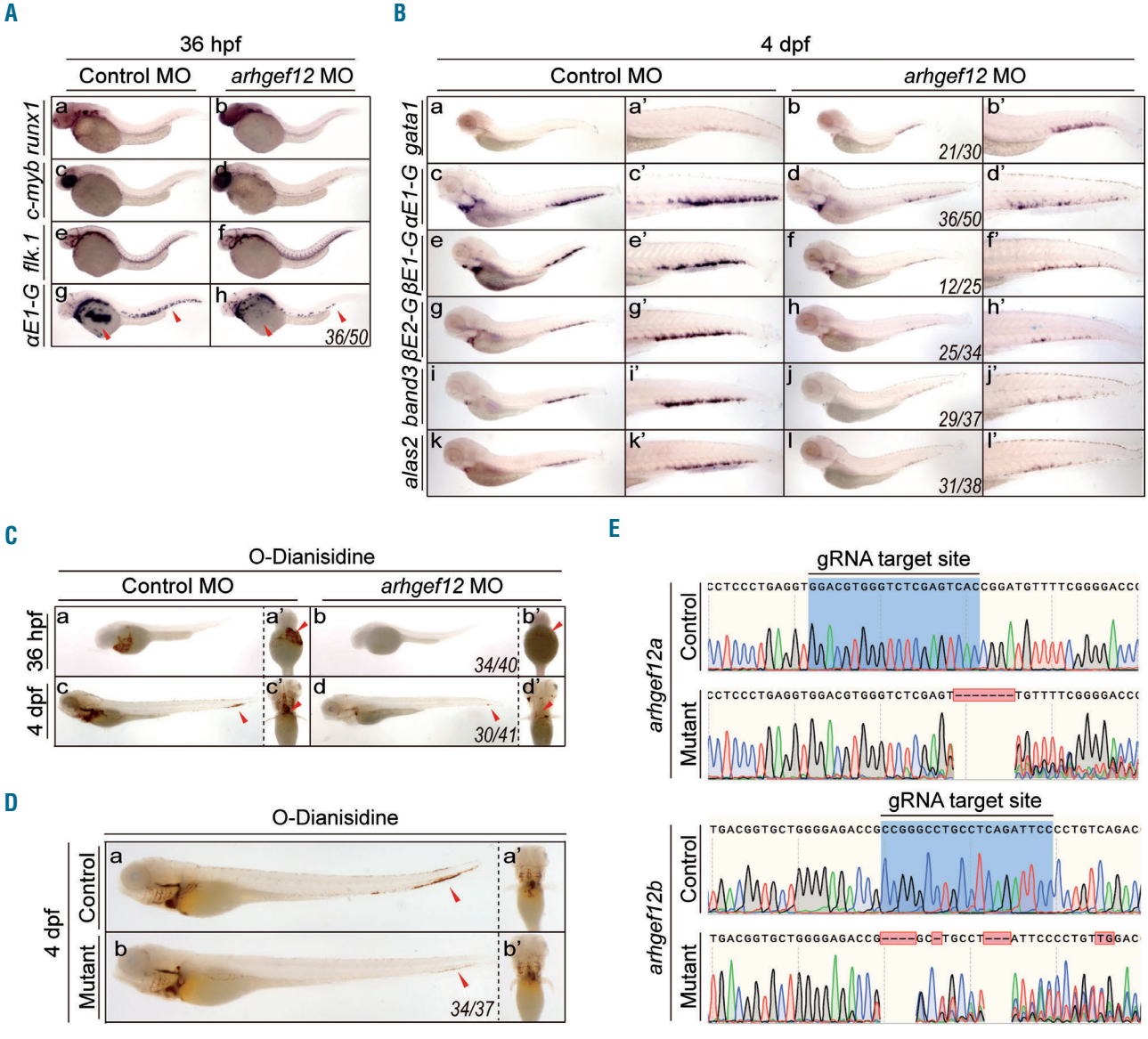

Figure 3. Knockdown by morpholino (MO) or knockout by CRISPR/Cas9 of *arhgef12* impairs erythroid differentiation in the zebrafish model. (A) Whole-mount *in situ* hybridization (WISH) results of hematopoietic and vascular markers in both control and *arhgef12a & arhgef12b* double MO injected embryos at 36 hours post fertilization (hpf). Definitive hematopoietic markers *runx1* (A-a, b) , c-myb (A-c, d) , and endothelial cell marker *flk.1* (A-e, f) indicated no obvious defect of definitive hematopoiesis and vasculogenesis in *arhgef12* morphants at 36 hpf. The erythrocyte marker *αE1-globin* (A-g, h) indicated obvious defect in erythroid differentiation in *arhgef12* morphants at 36 hpf. Red arrowheads indicate the yolk sac region and posterior blood island. (B) WISH results of erythrocyte markers in both control and *arhgef12a & arhgef12b* double MO injected embryos at 4 dpf. The increased progenitor erythrocyte marker gata1 (a, b), and decreased mature erythrocyte markers *αE1-globin* (c, d), *βE1-globin* (e, f), *βE2-globin* (g, h), *band3* (i, j) and *alas2* (k, l) indicated obvious block in erythroid differentiation in *arhgef12* morphants at 4 dpf. The corresponding magnifications are indicated as a'-l'. (C) The decreased O-Dianisidine staining of hemoglobin, which labeled mature erythrocytes, in both control and *arhgef12a & arhgef12b* double MO injected embryos at 36 hpf (a, a', b, b') and 4 dpf (c, c', d, d') suggested the defect in erythroid differentiation. Red arrowheads indicated the mature erythrocytes in yolk sac region (a', b'), caudal hematopoietic tissue (CHT) (c, d) and heart (c', d'). (D) The decreased O-Dianisidine staining of hemoglobin, in both control and *arhgef12a & arhgef12b* double knockout embryos at 4 dpf (a, b) suggested the defect in erythroid differentiation. Red arrowheads in a and b indicated the CHT, and the ventral view was shown in a' and b'. (E) Genotyping of *arhgef12a* and *arhgef12b* mutants constructed by CRISPR/Cas9. The gRNA target sites are as labeled.

genotype showed consistently reduced phosphorylated p38 in pro-erythroblasts (Figure 6C and D). Similar to the case of *arhgef12* MO, where the p38 activity is inhibited in the zebrafish, these rs10892563 CC genotype patients showed an erythroid differentiation block at the erythroblast stage (Figure 6A and B), suggesting a strong association with the ARHGEF12-p38 pathway.

Discussion

For leukemia patients, hematologic toxicity is the most common side effect of chemotherapy as the hematopoietic cells are among the tissues most vulnerable to therapy-related damage, in part due to their active cell cycle status. Anemia is one of the most frequently recorded manifestations of the hematopoietic toxic effects during the course of chemotherapy. Chemotherapy-induced anemia can be caused by cytotoxic inhibition of normal hematopoiesis similar to chemotherapy-induced neutropenia and thrombocytopenia. Chemotherapy agent-related autoimmune hemolysis[31,32] and chemotherapy-induced eryptosis can also cause anemia.[33] Our current GWAS studies have found that chemotherapy-induced anemia is associated with SNP in *CHPT1*,[6] *BSG*,[11,12] *ANAX7*,[14] *EPB42*,[15,16] and *ABCC417* that may be related to increased erythrocyte

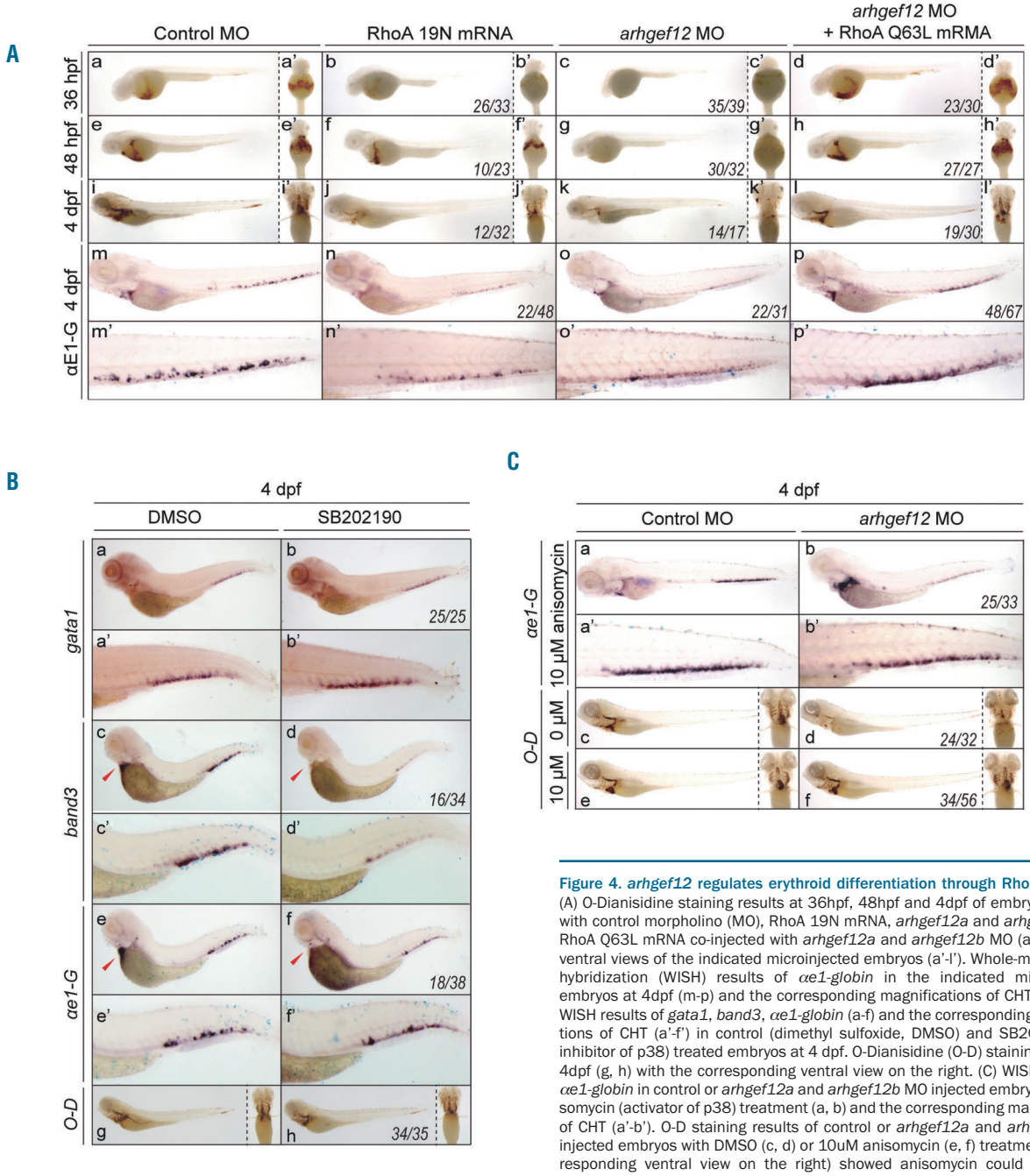

Figure 4. *arhgef12* regulates erythroid differentiation through RhoA and p38. (A) O-Dianisidine staining results at 36hpf, 48hpf and 4dpf of embryos injected with control morpholino (MO), RhoA 19N mRNA, *arhgef12a* and *arhgef12b* MO, RhoA Q63L mRNA co-injected with *arhgef12a* and *arhgef12b* MO (a-l). Yolk sac ventral views of the indicated microinjected embryos (a'-l'). Whole-mount *in situ* hybridization (WISH) results of *αe1-globin* in the indicated microinjected embryos at 4dpf (m-p) and the corresponding magnifications of CHT (m'-p'). (B) WISH results of *gata1*, *band3*, *αe1-globin* (a-f) and the corresponding magnifications of CHT (a'-f') in control (dimethyl sulfoxide, DMSO) and SB202190 (the inhibitor of p38) treated embryos at 4 dpf. O-Dianisidine (O-D) staining results at 4dpf (g, h) with the corresponding ventral view on the right. (C) WISH results of *αe1-globin* in control or *arhgef12a* and *arhgef12b* MO injected embryos with anisomycin (activator of p38) treatment (a, b) and the corresponding magnifications of CHT (a'-b'). O-D staining results of control or *arhgef12a* and *arhgef12b* MO injected embryos with DMSO (c, d) or 10uM anisomycin (e, f) treatment (the corresponding ventral view on the right) showed anisomycin could rescue the blocked erythroid differentiation in the morphants at 4dpf. The indicated embryos were treated by DMSO (labeled by 0uM) and anisomycin (labeled by 10uM) for 24 hours (from 3dpf to 4dpf).

loss. There is evidence to suggest that: (i) ANAX7 is related to erythrocyte death;[34] (ii) EPB42[15,16] is related to hereditary spherocytosis in which eryptosis is an important cause of anemia; (iii) CHPT1[6] and BSG[11,12] may be related to the vulnerability of RBC to chemotherapy; and (iv) ABCC4,[17] a membrane transporter, is related to accumulation of cytotoxic agents in cells and chemo-sensitivity of hematopoietic cells. Other direct or indirect evidence based on the known functions of the gene products suggests that the remaining genes in the top ten list of GWAS in our study, *TFDP2*, *LPIN2*, *TNS1*, *RAP1GAP*, *ARHGEF12*, could also be related to impaired hematopoiesis in response to chemotherapy.

Erythropoiesis is a tightly regulated process in which the hemoglobin level is maintained in a narrow window between 135g/L and 155g/L under normal conditions or in

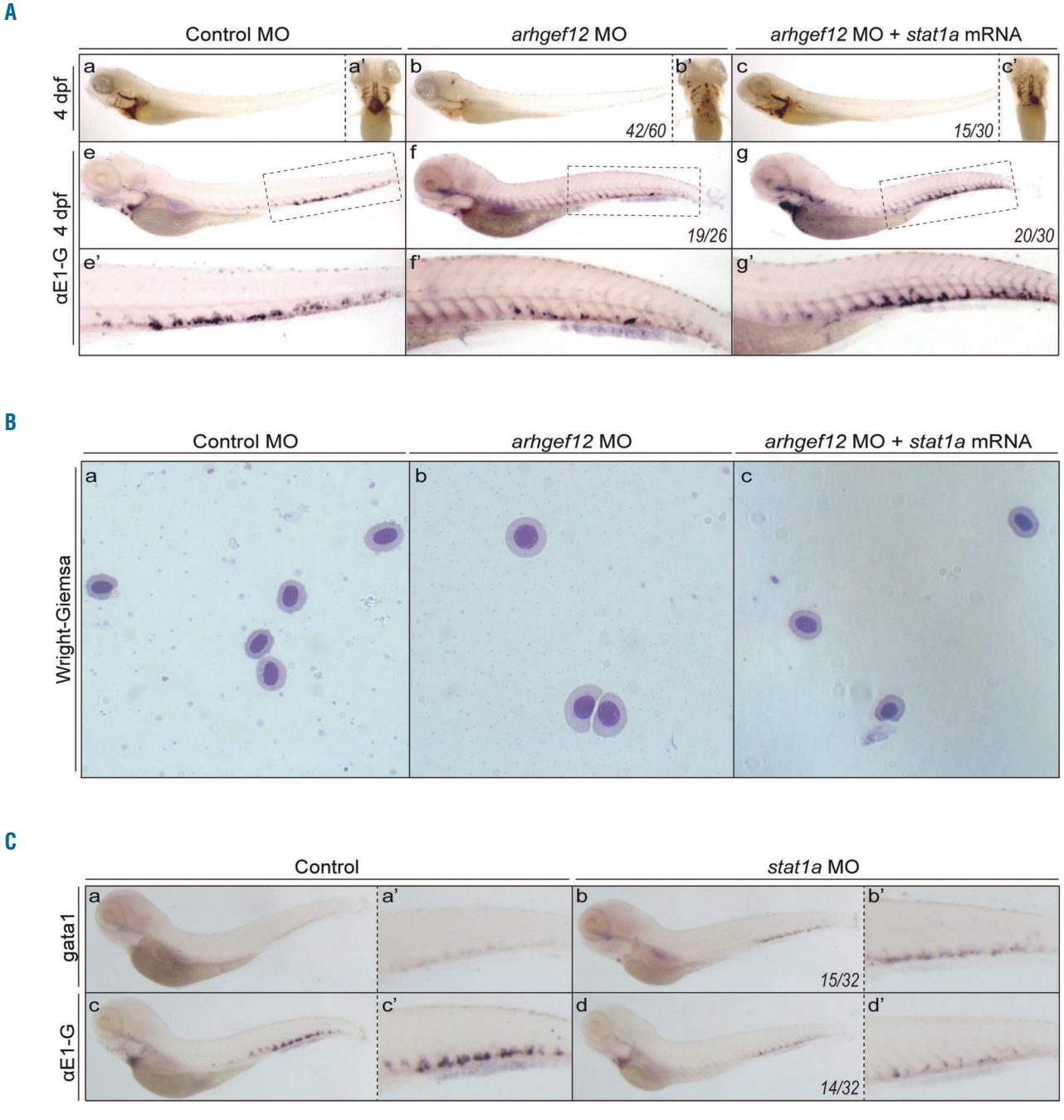

Figure 5. STAT1 expression rescues the erythroid differentiation phenotype by *arhgef12* knockdown in zebrafish. (A) O-Dianisidine staining results of embryos injected with control morpholino (MO) (a), *arhgef12a* & *arhgef12b* MO (b), and *arhgef12a* & *arhgef12b* MO with *stat1a* mRNA (c) at 4dpf. Yolk sac ventral views of the indicated microinjected embryos (a'-c'). Whole-mount *in situ* hybridization (WISH) results of αe1-globin in the embryos injected with control MO (e), *arhgef12a* & *arhgef12b* MO (f), and *arhgef12a* and *arhgef12b* MO with *stat1a* mRNA (g) at 4dpf and the corresponding magnifications of CHT (e'-g'). (B) Wright-Giemsa results of erythrocytes, which were isolated from control MO (a), *arhgef12a* and *arhgef12b* MO (b), and *arhgef12a* & *arhgef12b* MO with *stat1a* mRNA (c) injected embryos at 4 dpf. (C) WISH results of *gata1* in the embryos injected with control MO (a), *stat1a* MO (b) at 4dpf and the corresponding magnifications of CHT (a',b'). WISH results of αe1-globin in the embryos injected with control MO (c), *stat1a* MO (d) at 4dpf and the corresponding magnifications of CHT (c',d').

response to stress such as chemotherapy. A complex lineage-specific transcription factor network underlies the homeostatic hematopoiesis and erythropoiesis mechanisms. In such a transcription network, the GATA transcription factor family plays a central role in the proper differentiation of erythroid cells together with Friend of GATA (FOG-1). The GATA family is composed of six members in mammals that are highly conserved in expression patterns in vertebrates, and GATA-1, GATA-2 and GATA-3 are classified into the hematopoietic GATA subfamily based on their expression profiles and domain structures. GATA-1 is important in adult hematopoiesis especially for erythropoiesis and regulates multiple target genes during the development and differentiation of erythroid and megakaryocytic lineages by binding to the GATA motif (A/T)GATA(A/G). In this study, we identified a novel SNP of *ARHGEF12 gene*, rs10892563, located in a regulatory GATA motif and found that the erythroid expression of *AEHGEF12* is significantly down-regulated in rs10892563 homogeneous ALL patients who have undergone chemotherapy.

ARHGEF12 encodes a RhoA specific guanine nucleotide exchange factor which positively regulates the RhoA GDP/GTP exchange reaction. *ARHGEF12* plays crucial roles in the cyclic–stretch–induced cell and stress fiber reorientation responses,[35] mesenchymal stem cell fate,[36] and cell migration and invasion,[37] by regulating RhoA activity. *ARHGEF12* is important for platelet activation and thrombosis in mice,[38] but its role in erythropoiesis has not been defined. As a founding member of the Rho GTPase family, RhoA is involved in many important cellular functions, including gene transcription, survival, adhesion, and cytoskeleton reorganization. RhoA is important for hematopoiesis, regulating HSPC trafficking, interaction with the BM microenvironment, proliferation, survival, and self-renewal, and for fetal erythropoiesis in mitosis and cytokinesis.[10] Interestingly, among the top ten in our GWAS list, there are three genes related to small GTPase functions: TNS1, *RAP1GAP*, and *ARHGEF12*. We focused our attention on *ARHGEF12* because RhoA knockout in mice causes cytokinesis failure in erythroblasts through actomyosin and midbody dysregulation and p53 activation.[10]

To define the functional and mechanistic role of *arhgef12* in erythropoiesis, we have used a zebrafish model to knockdown or knockout *arhgef12* isoforms. We show a causal role of the ARHGEF12-RhoA signaling in this model in mediating the p38 MAPK and Stat1 pathway in erythropoiesis. In zebrafish, erythroid defects caused by *arhgef12* knockdown can be rescued by p38 MAPK activator and *stat1* expression. Conversely, a p38 inhibitor can induce erythropoiesis defects mimicking that of the *arhgef12* knockout or knockdown. This signaling effect seems to be conserved in mammals, as the ARHGEF12-RhoA-p38 function appears to also regulate the erythroid differentiation of erythroleukemia cell line K562. A num-

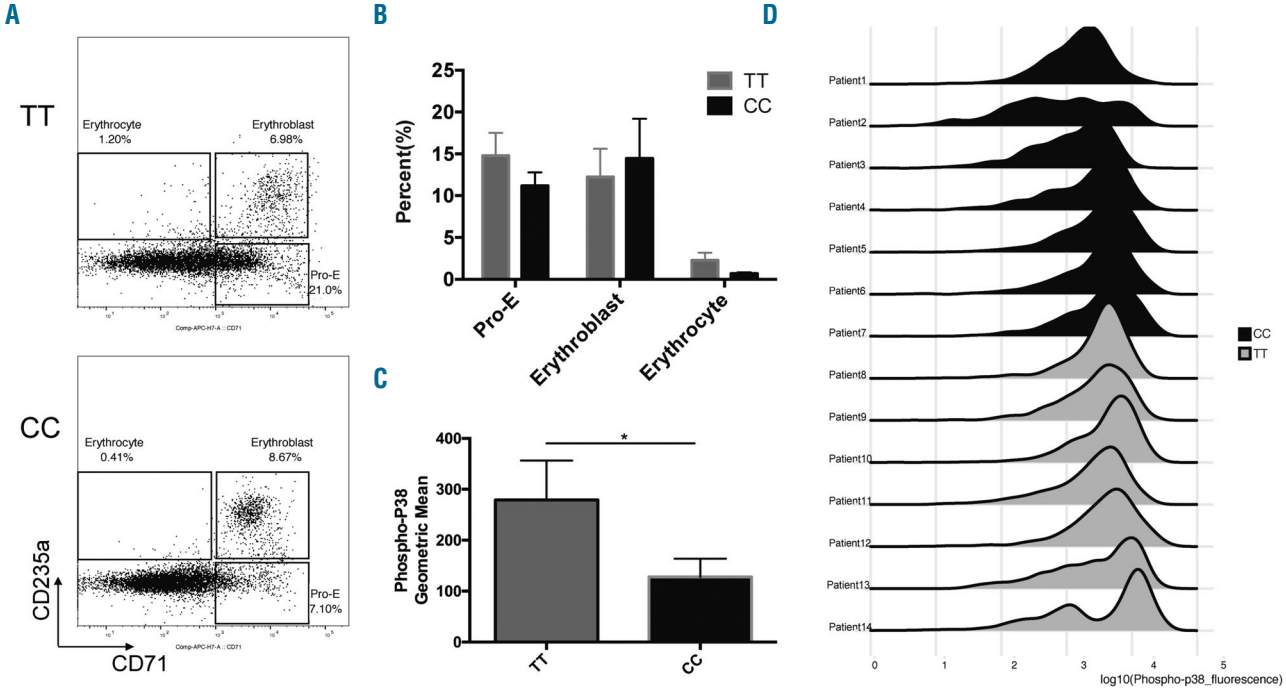

Figure 6. The ARHGEF12-RhoA-p38 pathway is associated with erythroid regeneration from chemotherapy-induced anemia in acute lymphoblastic leukemia (ALL) patients. (A) Erythroid differentiation evaluation by flow cytometry of cryopreserved bone marrow (BM) samples from patients in remission with different rs10892563 genotypes. Three populations of different development stages, i.e. CD71$^+$CD235a- pro-erythroblasts (Pro-E), CD71$^+$CD235a$^+$ erythroblasts and CD71$^-$CD235a$^+$ erythrocytes can be discriminated. Representative flow cytometry dot plots showing the percentage of erythroblasts in patients with CC genotype was higher than TT genotype, whereas the pro-erythroblasts (Pro-E) and erythrocytes were reduced in CC genotype. (B) The TT group and the CC group each had nine samples. Proportion statistics of each stage of erythroid differentiation are shown. (C) Statistics of mean fluorescence intensity of phospho-p38. We compared the base-2 log of phospho-p38 levels between the CC and TT genotypes, phospho-p38 levels are lower in the CC genotype patients (P=0.0471, one-tailed t-test). (D) Phospho-flow histograms of phospho-p38 on pro-erythroblasts with different rs10892563 genotypes. Phosphorylated p38 was stained with anti-pT180/pY182 antibody on cryopreserved BM samples from patients in remission with different rs10892563 genotypes as well as CD71 and CD235a monoclonal antibody. Histograms showing phospho-p38 peaks shifted left in CC genotype (black) comparing TT genotype (gray).

ber of studies have reported that p38 MAPK is involved in erythroid differentiation,[39-41] yet the role of p38 MAPK in stress erythropoiesis is still poorly understood. P38α regulates erythroblast enucleation in a cell-autonomous manner *in vivo* during fetal and anemic stress erythropoiesis.[42] Remarkably, loss of p38α leads to downregulation of p21Cip1, and decreased activation of the p21Cip1 inactivates Rb, both of which are critical regulators of erythroblast enucleation. Hu *et al.* suggested P38α could act as a molecular brake to limit over-active erythropoiesis in response to stress-relief of this molecular brake by inhibiting P38-enhanced stress erythropoiesis and accelerated recovery from anemia.[43] Our observed association of a down-regulated erythroid p38 phosphorylation in patients with the ARHGEF12 polymorphism who need multiple RBC transfusions to overcome chemotherapy-induced anemia also supports the involvement of such a pathway. Pharmacological activation of wild-type p53 is a logical therapeutic strategy for leukemia where the p53 pathway could be down-regulated by abnormalities in p53-regulatory proteins.[44] It has been reported that p38 kinase can positively regulate p53, and activation of p38 not only promotes erythropoiesis, but also potentially maintains a higher level of p53 in cancer cells, which can be a dual benefit for cancer patients who carry wild-type p53 alleles.

Several reported GWAS studies related to hematologic traits failed to find a correlation between *ARHGEF12* and erythroid phenotypes[45,46] in normal populations, which may suggest there are functional redundancies to the ARHGEF12-RhoA-p38 pathway in homeostatic erythropoiesis. Suboptimal level of guanine nucleotide exchange activity may be compensated by down-regulated RhoA negative regulator, GTPase-activating proteins, or by other guanine nucleotide exchange factors, such as ARHGEF3, which was shown to be important for erythropoiesis through RhoA in a zebrafish model.[47] Our GWAS results draw a clear association between *ARHGEF12* at rs10892563 with erythrocyte regeneration under chemotherapy stress, suggesting that this gene/SNP status may be considered a biomarker to predict severity of chemotherapy-induced anemia among the patients.

In addition to the erythropoiesis differentiation mechanism, genes expressed in HSPC can also be associated with chemotherapy-associated anemia. To this end, we analyzed the primary gene list with expression patterns in the $CD34^+$ cell population before erythroid differentiation with the same database as we did for the erythrocyte-specific genes. Among the genes highly expressed in HSPC, four of the top five have known functional connection with erythropoiesis (Figure 1C). While a correlation analysis between RBC transfusion and severity of neutropenia reveals that RBC transfusions had no significant correlation with neutropenia, there was a significance in correlation with thrombocytopenia (*Online Supplymentary Figure S7*). This suggests that it is possible that effects on HSPC such as megakaryocyte-erythroid progenitors could be a contributing factor to chemotherapy-induced anemia.

Combining our patient SNPs and phenotype observations, biochemical analyses of patient samples, and human and murine cells, together with the zebrafish genetic model characterizations, our studies unveil a novel SNP related to chemotherapy-induced anemia in *ARHGEF12* and the associated signaling pathway. These findings will be useful for future consideration of strategies to overcome the chemotherapy-induced anemia in some ALL patients.

Acknowledgments

The authors would like to thank the staff of Shanghai Institute of Hematology for their assistance with zebrafish husbandry, particularly Yi Chen. We thank Yongjuan Zhang for the SNP linkage disequilibrium analysis and Professor Xiaojian Sun for helpful discussions.

Funding

This research was supported by grants from the National Natural Science Foundation of China (n. 81270623), The National Key R&D Program of China, Stem Cell and Translation Research (n. 2016YFA0102000) and The fourth round of Three-Year Public Health Action Plan (2015-2017) (GWIV-25). This research was also supported by the National Natural Science Foundation of China (No. 81900114).

References

1. Sun XJ, Xu PF, Zhou T, et al. Genome-Wide Survey and Developmental Expression Mapping of Zebrafish SET Domain-Containing Genes. PLoS One. 2008;3(1): e1499.
2. Jao LE, Wente SR, Chen W. Efficient multiplex biallelic zebrafish genome editing using a CRISPR nuclease system. Proc Natl Acad Sci U S A. 2013;110(34):13904–13909.
3. Novershtern N, Subramanian A, Lawton LN, et al. Densely interconnected transcriptional circuits control cell states in human hematopoiesis. Cell. 2011;144(2):296–309.
4. Ikuta T, Sellak H, Odo N, Adekile AD, Gaensler KML. Nitric Oxide-cGMP Signaling Stimulates Erythropoiesis through Multiple Lineage- Specific Transcription Factors : Clinical Implications and a Novel Target for Erythropoiesis. Plos One. 2016;11(1):e0144561.
5. Chen C, Lodish HF. Global analysis of induced transcription factors and cofactors identifies Tfdp2 as an essential coregulator during terminal erythropoiesis. Exp Hematol. 2014;42(6):464–476.
6. Henneberry AL, Wistow G, Mcmaster CR. Cloning, genomic organization, and characterization of a human cholinephosphotransferase. J Biol Chem. 2000;8(4):29808–29815.
7. Cocco L, Manzoli L, Faenza I, et al. Advances in Biological Regulation Modulation of nuclear PI-PLCbeta1 during cell differentiation. Adv Biol Regul. 2016;60:1–5.
8. Ferguson PJ, Chen S, Tayeh MK, et al. Homozygous mutations in LPIN2 are responsible for the syndrome of chronic recurrent multifocal osteomyelitis and congenital dyserythropoietic anaemia (Majeed syndrome). J Med Genet. 2005;42(7):551–557.
9. Shih YP, Sun P, Wang A, Lo SH. Tensin1 positively regulates RhoA activity through its interaction with DLC1. Biochim Biophys Acta - Mol Cell Res. 2015;1853(12):3258–3265.
10. Konstantinidis DG, Giger KM, Risinger M, et al. Cytokinesis failure in RhoA-deficient mouse erythroblasts involves actomyosin and midbody dysregulation and triggers p53 activation. Blood. 2015;126(12):1473–1482.
11. Coste I, Gauchat JF, Wilson A, et al. Unavailability of CD147 leads to selective erythrocyte trapping in the spleen. Blood. 2001;97(12):3984–3988.
12. Ma C, Wang J, Fan L, Guo Y. Inhibition of CD147 expression promotes chemosensitivity in HNSCC cells by deactivating MAPK/ERK signaling pathway. Exp Mol Pathol. 2017;102(1):59–64.
13. Dorn I, Meyer G, Lindner U, Driller B, Schlenke P. The influence of extracellular matrix proteins and mesenchymal stem cells on erythropoietic cell maturation. Vox Sang. 2011;101(1):65–76.
14. Abed M, Balasaheb S, Towhid ST, Daniel C, Amann K, Lang F. Adhesion of Annexin 7 Deficient Erythrocytes to Endothelial Cells. PLoS One. 2013;8(2):1–10.
15. Hayette S, Dhermy D, dos Santos ME, et al. A deletional frameshift mutation in protein 4.2 gene (allele 4.2 Lisboa) associated with

hereditary hemolytic anemia. Blood. 1995; 85(1):250–256.
16. Yawata Y, Kanzaki A, Yawata A, Doerfler W, Ozcan R, Eber SW. Characteristic features of the genotype and phenotype of hereditary spherocytosis in the Japanese population. Int J Hematol. 2000;71(2):118-135.
17. Satyanarayana A, Gudmundsson KO, Chen X, et al. RapGEF2 is essential for embryonic hematopoiesis but dispensable for adult hematopoiesis. Blood. 2010;116(16):2921–2931.
18. Kourlas PJ, Strout MP, Becknell B, et al. Identification of a gene at 11q23 encoding a guanine nucleotide exchange factor: evidence for its fusion with MLL in acute myeloid leukemia. Proc Natl Acad Sci U S A. 2000;97(5):2145–2150.
19. Drenberg C, Hu S, Li L, et al. ABCC4 Is a Determinant of Cytarabine-Induced Cytotoxicity and Myelosuppression. Clin Transl Sci. 2016;9(1):51–59.
20. Yang L, Wang L, Kalfa TA, et al. Cdc42 critically regulates the balance between myelopoiesis and erythropoiesis. Blood. 2007;110(12):3853-3861.
21. Ghiaur G, Lee A, Bailey J, JA C, Zheng Y, DA W. Inhibition of RhoA GTPase activity enhances hematopoietic stem and progenitor cell proliferation and engraftment. Blood. 2006;108(6):2087–2094.
22. Sankaran VG, Ghazvinian R, Do R, et al. Exome sequencing identifies GATA1 mutations resulting in Diamond-Blackfan anemia. J Clin Invest. 2012;122(7):2439-2443.
23. van Lochem EG, van der Velden VHJ, Wind HK, te Marvelde JG, Westerdaal NAC, van Dongen JJM. Immunophenotypic differentiation patterns of normal hematopoiesis in human bone marrow: Reference patterns for age-related changes and disease-induced shifts. Cytometry. 2004;60B(1):1–13.
24. Orkin SH and Zon LI. Hematopoiesis: an evolving paradigm for stem cell biology. Cell. 2008;132(4):631–644.
25. Paffett-Lugassy NN, Zon LI. Analysis of hematopoietic development in the zebrafish. Methods Mol Med. 2005;105: 171–198.
26. Reuther GW, Lambert QT, Booden MA, et al. Leukemia-associated Rho Guanine Nucleotide Exchange Factor, a Dbl Family Protein Found Mutated in Leukemia, Causes Transformation by Activation of RhoA. J Biol Chem. 2001;276(29):27145–27151.
27. Salasvidal E, Meijer AH, Cheng X, Spaink HP. Genomic annotation and expression analysis of the zebrafish Rho small GTPase family during development and bacterial infection. Genomics. 2005;86(1):25–37.
28. Qiu RG, Chen J, Mccormick F, Symons M. A Role for Rho in Ras Transformation. Proc Natl Acad Sci U S A. 1995;92(25):11781–11785.
29. Dvorsky R, Ahmadian MR. Always look on the bright site of Rho: structural implications for a conserved intermolecular interface. EMBO Rep. 2004;5(12):1130–1136.
30. Perez OD, Mitchell D, Campos R, Gao GJ, Li L, Nolan GP. Multiparameter analysis of intracellular phosphoepitopes in immunophenotyped cell populations by flow cytometry. Curr Protoc Cytom. 2005;Chapter 6:Unit 6.20.
31. Ahlgren J, Patel N, Simmens S, et al. O-MAX chemotherapy: high activity in metastatic esophagogastric adenocarcinoma and possible relation to subclinical hemolysis. Oncology. 2014;87(6):371–380.
32. Betensky M, Witmer C, Fisher MJ, Nance S, Weiss MJ, Sesok-Pizzini DA. Immune hemolytic anemia with drug-induced antibodies to carboplatin and vincristine in a pediatric patient with an optic pathway glioma. Transfusion. 2015;54(11):2901–2905.
33. Lang E, Bissinger R, Qadri SM, Lang F. Suicidal death of erythrocytes in cancer and its chemotherapy: A potential target in the treatment of tumor-associated anemia. Int J Cancer. 2017;141(8):1522–1528.
34. Lang E, Lang PA, Shumilina E, et al. Enhanced eryptosis of erythrocytes from gene-targeted mice lacking annexin A7. Pflugers Arch. 2010;460(3):667–676.
35. Abiko H, Fujiwara S, Ohashi K, et al. Rho guanine nucleotide exchange factors involved in cyclic-stretch-induced reorientation of vascular endothelial cells. J Cell Sci. 2015;128(9):1683-1695.
36. Thompson WR, Yen SS, Uzer G, et al. LARG GEF and ARHGAP18 orchestrate RhoA activity to control mesenchymal stem cell lineage. Bone. 2018;107:172–180.
37. Shi GX, Yang WS, Jin L, Matter ML, Ramos JW. RSK2 drives cell motility by serine phosphorylation of LARG and activation of Rho GTPases. Proc Natl Acad Sci U S A. 2018;115(2):E190–E199.
38. Williams CM, Harper MT, Goggs R, Walsh TG, Offermanns S, Poole AW. Leukemia-associated Rho guanine-nucleotide exchange factor is not critical for RhoA regulation, yet is important for platelet activation and thrombosis in mice. J Thromb Haemost. 2015;13(11):2102–2107.
39. Hua WK, Chang YI, Yao CL, Hwang SM, Chang CY, Lin WJ. Protein Arginine Methyltransferase 1 Interacts with and Activates p38α to Facilitate Erythroid Differentiation. PLoS One. 2013;8(3): e56715.
40. Shahab U, Jeong AK, Jodie U, Dolores M, Amittha W. Differentiation stage-specific activation of p38 mitogen-activated protein kinase isoforms in primary human erythroid cells. Proc Natl Acad Sci U S A. 2004;101(1): 147–152.
41. Pace BS, Qian XH, Sangerman J, et al. p38 MAP kinase activation mediates γ-globin gene induction in erythroid progenitors. Exp Hematol. 2003;31(11):1089–1096.
42. Schultze SM, Mairhofer A, Li D, et al. p38α controls erythroblast enucleation and Rb signaling in stress erythropoiesis. Cell Res. 2012;22(3):539–550.
43. Hanenberg H, Filippi M-D, Ivan M, et al. P38α/JNK signaling restrains erythropoiesis by suppressing Ezh2-mediated epigenetic silencing of Bim. Nat Commun. 2018;9 (1):3518.
44. Bulavin DV, Saito S, Hollander MC, et al. Phosphorylation of human p53 by p38 kinase coordinates N-terminal phosphorylation and apoptosis in response to UV radiation. Embo J. 1999;18(23):6845–6854.
45. Kuhnel B, Aspelund T, Yang Q, et al. Multiple loci influence erythrocyte phenotypes in the CHARGE Consortium. Nat Genet. 2009;41(11):1191–1198.
46. Kamatani Y, Matsuda K, Okada Y, et al. Genome-wide association study of hematological and biochemical traits in a Japanese population. Nat Publ Gr. 2010;42(3):210–215.
47. Serbanovic-Canic J, Cvejic A, Soranzo N, Stemple DL, Ouwehand WH, Freson K. Silencing of RhoA nucleotide exchange factor , ARHGEF3, reveals its unexpected role in iron uptake. Blood. 2011;118(18):4967–4977.

ARTICLE

Glutathione peroxidase 4 and vitamin E control reticulocyte maturation, stress erythropoiesis and iron homeostasis

Sandro Altamura,[1,2,*] Naidu M. Vegi,[3*] Philipp S. Hoppe,[4] Timm Schroeder,[4] Michaela Aichler,[5] Axel Walch,[5] Katarzyna Okreglicka,[6] Lothar Hültner,[7] Manuela Schneider,[8] Camilla Ladinig,[7] Cornelia Kuklik-Roos,[7] Josef Mysliwietz,[9] Dirk Janik,[5] Frauke Neff,[5] Birgit Rathkolb,[10-12] Martin Hrabé de Angelis,[11-13] Christian Buske,[3] Ana Rita da Silva,[1,2] Katja Muedder,[1,2] Marcus Conrad,[14] Tomas Ganz,[15] Manfred Kopf,[6] Martina U. Muckenthaler[1,2] and Georg W. Bornkamm[7,#]

*These authors contributed equally to this work

[1]Department of Pediatric Hematology, Oncology and Immunology - University of Heidelberg, Heidelberg, Germany; [2]Molecular Medicine Partnership Unit, Heidelberg, Germany; [3]Institute of Experimental Cancer Research, Universitätsklinikum Ulm, Ulm, Germany; [4]Department of Biosystems Bioscience and Engineering, ETH Zürich, Basel, Switzerland; [5]Research Unit Analytical Pathology, Helmholtz Zentrum München, Deutsches Forschungszentrum für Gesundheit und Umwelt (GmbH), Neuherberg, Germany; [6]Institute of Molecular Health Sciences, ETH Zurich, Zürich, Switzerland; [7]Institute of Clinical Molecular Biology and Tumor Genetics, Helmholtz Zentrum München, Deutsches Forschungszentrum für Gesundheit und Umwelt (GmbH), München, Germany; [8]Institute for Stroke and Dementia Research (ISD), Klinikum der Universität München, München, Germany; [9]Institute of Molecular Immunology, Helmholtz Zentrum München, Deutsches Forschungszentrum für Gesundheit und Umwelt (GmbH), München, Germany; [10]Institute of Molecular Animal Breeding and Biotechnology, Ludwig-Maximilians-Universität München, Genzentum, München, Germany; [11]Institute of Experimental Genetics, Geman Mouse Clinic (GMC), Helmholtz Zentrum München, Deutsches Forschungszentrum für Gesundheit und Umwelt (GmbH), Neuherberg, Germany; [12]German Center for Diabetes Research (DZD), Neuherberg, Germany; [13]Chair of Experimental Genetics, School of Life Science Weihenstephan, Technische Universität München, Freising, Germany; [14]Institute of Developmental Genetics, Helmholtz Zentrum München, Deutsches Forschungszentrum für Gesundheit und Umwelt (GmbH), Neuherberg, Germany and [15]Departments of Medicine and Pathology, David Geffen School of Medicine, UCLA, Los Angeles, CA, USA

Ferrata Storti Foundation

Haematologica 2020
Volume 105(4):937-950

ABSTRACT

Glutathione peroxidase 4 (GPX4) is unique as it is the only enzyme that can prevent detrimental lipid peroxidation *in vivo* by reducing lipid peroxides to the respective alcohols thereby stabilizing oxidation products of unsaturated fatty acids. During reticulocyte maturation, lipid peroxidation mediated by 15-lipoxygenase in humans and rabbits and by 12/15-lipoxygenase (ALOX15) in mice was considered the initiating event for the elimination of mitochondria but is now known to occur through mitophagy. Yet, genetic ablation of the *Alox15* gene in mice failed to provide evidence for this hypothesis. We designed a different genetic approach to tackle this open conundrum. Since either other lipoxygenases or non-enzymatic autooxidative mechanisms may compensate for the loss of *Alox15*, we asked whether ablation of *Gpx4* in the hematopoietic system would result in the perturbation of reticulocyte maturation. Quantitative assessment of erythropoiesis indices in the blood, bone marrow (BM) and spleen of chimeric mice with *Gpx4* ablated in hematopoietic cells revealed anemia with an increase in the fraction of erythroid precursor cells and reticulocytes. Additional dietary vitamin E depletion strongly aggravated the anemic phenotype. Despite strong extramedullary erythropoiesis reticulocytes failed to mature and accumulated large autophagosomes with engulfed mitochondria. *Gpx4*-deficiency in hematopoietic cells led to systemic hepatic iron overload and simultaneous severe iron demand in the erythroid system. Despite extremely high erythropoietin and erythroferrone levels in the plasma, hepcidin expression remained unchanged. Conclusively, perturbed reticulocyte maturation in response to *Gpx4* loss in hematopoietic cells thus causes ineffective erythropoiesis, a phenotype partially masked by dietary vitamin E supplementation.

Correspondence:

GEORG W. BORNKAMM
georg.bornkamm@t-online.de

Received: November 24, 2018.

Accepted: June 20, 2019.

Pre-published: June 27, 2019.

doi:10.3324/haematol.2018.212977

Check the online version for the most updated information on this article, online supplements, and information on authorship & disclosures: www.haematologica.org/content/105/4/937

Introduction

Glutathione peroxidase 4 (GPX4) is unique in its ability to reduce lipid peroxidation products in biological membranes *in vivo*. Lipid peroxidation is brought about either enzymatically by lipoxygenases at specific sites or unselectively by non-enzymatic mechanisms, usually through Fe^{2+}-driven Fenton chemistry.[3] Lipoxygenases are dioxygenases that catalyze the incorporation of molecular oxygen into polyunsaturated fatty acids (PUFA) in a site- and stereospecific manner thus yielding the respective hydroxyperoxides. Lipoxygenases become activated by low concentrations of peroxides (the so called "peroxide tone") that oxidize Fe^{2+} to Fe^{3+} in the catalytic site.[4] The peroxide tone and the activity of lipoxygenases is under the control of GPX4. 12/15-Lipoxygenase and GPX4 act antagonistically as far as oxidation (lipoxygenases) and reduction (GPX4) of substrates, and induction of cell death and cell survival are concerned. 12/15-Lipoxygenase induces cell death in murine fibroblasts, whereas GPX4 rescues cells from lipoxygenase-induced cell death.[5] But in other settings, lipoxygenases and GPX4 biochemically cooperate: lipoxygenases generate highly reactive peroxidation products of unsaturated fatty acids (P-O-O-H) that are prone to further uncontrolled lipid membrane peroxidation. GPX4 reduces these peroxides to stable hydroxyl-derivatives (P-O-H).[6-9] Thereby, 15-lipoxygenase in humans or 12/15-lipoxygenase, its functional homolog in mice, and GPX4 constitute a pair of enzymes whose activities are tightly interconnected. In the interplay of lipoxygenases and GPX4 the role of vitamin E also has to be considered. Vitamin E intercalates into membranes, acts as a chain breaker of lipid peroxidation through its high affinity for unpaired electrons and thus antagonizes peroxide production.

GPX4 is 1 of 24 (25 in man) selenoproteins in mammals[10] and is positioned at the top of the hierarchy of selenoproteins, *i.e. Gpx4* expression is maintained even under severe selenium-deficiency when the synthesis of most other selenoproteins has ceased.[11] GPX4 has evolved to carry the 21st amino acid selenocysteine rather than its functional counterpart cysteine in the active site which renders the enzyme highly resistant to irreversible overoxidation through peroxides.[12] Dietary selenium is known to be required for stress erythropoiesis in mice and blockage of the synthesis of all selenoproteins in hematopoietic cells by selective deletion of the selenocysteine-specific t-RNA Trsp in the BM of chimeric mice severely impairs stress erythropoiesis.[13]

Mitochondria are removed from reticulocytes by a particular form of autophagy, called mitophagy, and oxidized lipids are considered to play a crucial role in triggering autophagy in various cell types. Furthermore, macrophages from *12/15-lipoxygenase* knockout (k.o.) mice exhibit abnormal mitochondria, cytoplasmic vacuoles and an altered phospholipidomics pattern indicative of impaired autophagy.[19] In addition, the 12/15-lipoxygenase oxidation product 12-hydroxyeicosatetraenoic acid-phosphatidylethanolamine (12-HETE-PE) was shown to be a better substrate for yeast Atg8 than native PE, whereas native as well as oxidized PE were both effective substrates for LC3 lipidation. With regard to reticulocyte maturation current data suggest that elimination of mitochondria through mitophagy may be stimulated by oxidation products of polyunsaturated membrane phospholipids.

15-lipoxygenase is highly expressed in reticulocytes and was reported to be involved in the elimination of mitochondria by Rapoport and his coworkers.[20-23] The initial work of the Rapoport group was confirmed and extended by van Leyen *et al*. who reported a similar 12/15-lipoxygenase-driven mechanism that degrades organelles in the eye lens.[24,25] Yet, the great interest in this early work decreased with the findings that erythrocyte and reticulocyte counts were normal in *12/15-lipoxygenase* ko mice.[26] Definitive genetic proof for a role of lipid oxidation during reticulocyte maturation is thus still lacking. Several reasons may account for the fact that *12/15-lipoxygenase* k.o. mice exhibit normal red blood and reticulocyte counts: (i) lipoxygenases other than *12/15-lipoxygenase* may compensate for the targeted loss of reticulocyte 12/15-lipoxygenase; (ii) lipoxygenases may become dispensable if non-enzymatic mechanisms of lipid oxidation prevail;[27-29] or (iii) lipid oxidation events are dispensable during reticulocyte maturation.

Our present work was conceived to definitively answer if lipid oxidation is indeed critically involved in mitophagy in reticulocytes using a well-defined genetic approach. Whereas many different enzymatic and non-enzymatic mechanisms may account for the initial lipid oxidation step, GPX4 stands out as the only enzyme that effectively prevents detrimental lipid peroxidation and allows lipid oxidation to proceed in a highly controlled manner. Thus, if lipid oxidation is an essential step in the elimination of mitochondria in reticulocytes, ablation of *Gpx4* should result in uncontrolled lipid peroxidation and perturbation of reticulocyte maturation. Since GPX4 is essential for early embryonic development and the survival of adult mice,[30,31] *Gpx4* had to be deleted specifically in hematopoietic cells. To this end, we took advantage of the Tamoxifen-inducible Cre/lox system,[32] which is of invaluable help when the side effects of Cre[33-37] and Cre activators[38] or inducers[39] are properly controlled. We show that GPX4 is required for stress erythropoiesis. Deletion of *Gpx4* in adult mice causes anemia and ineffective erythropoiesis due to impaired reticulocyte maturation, a phenotype dramatically aggravated by depleting vitamin E from the diet. As a consequence hepatic iron overload develops despite the continuous iron demand for red blood cell production.

Methods

Mice

Mice were bred under SPF conditions. *Gpx4$^{fl/fl}$;CreERT2* mice were backcrossed for at least ten generations onto C57BL/6J mice (Taconic Biosciences, Köln, Germany). All animal experiments were performed according to the institutional guidelines and were approved by the local ethic committees on animal experimentation and by the Government of Upper Bavaria and Kantonales Veterinäramt in Zürich, respectively.

Generation of chimeric mice with *Gpx4*-proficient and *Gpx4*-deficient hematopoietic cells and analysis of blood parameters

Female wild-type (wt) recipient mice of 10 to 12 weeks (Taconic Biosciences, Köln) were lethally irradiated with 850 cGy and reconstituted with 10^6 BM cells from *Gpx4$^{fl/fl}$;CreERT2* or *Gpx4$^{wt/wt}$;CreERT2* donor mice. BM cells had been collected by flushing the leg bones and crushing the pelvic bone.

Gpx4$^{fl/fl}$;*CreERT2* and *Gpx4*$^{wt/wt}$;*CreERT2* mice have been described.[5,31,32] 150 mg/kg 5-fluorouracil (FU) had been administered to donor mice by intraperitoneal (i.p.) injection 24 hours prior to collecting BM cells from donor mice. After hematopoietic reconstitution mice were allowed to recover for 25 weeks. Mice were fed a tamoxifen citrate containing diet for three weeks following the protocol of Kiermayer *et al.*[40] to delete *Gpx4*. Ethylenediamine tetraacetic acid (EDTA)-blood was collected from the tail vein before, at the last day of and at different time points after tamoxifen administration, and subjected to the analy-

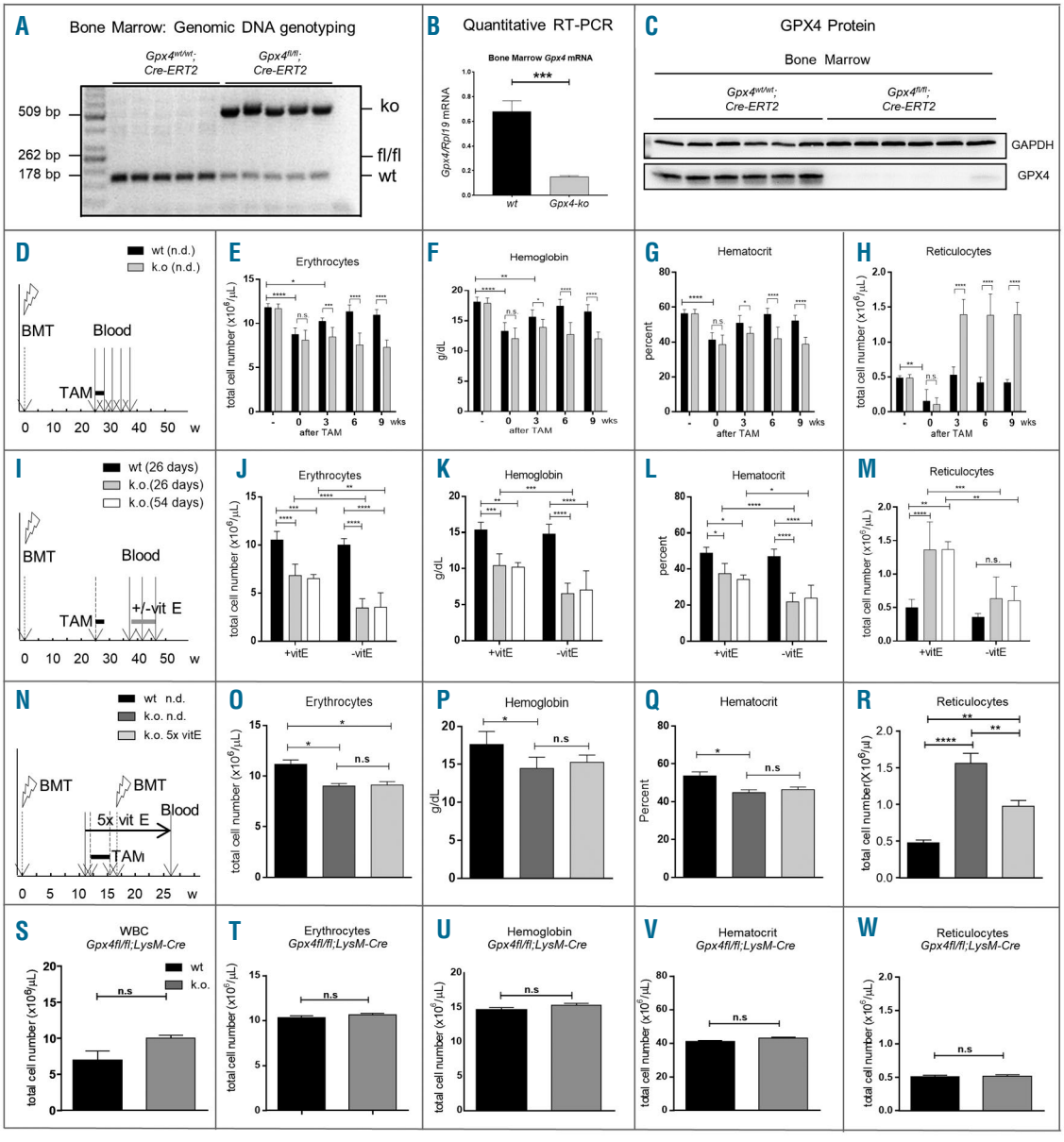

Figure 1. (A-H) *Gpx4* is required for stress erythropoiesis in the recovery phase of anemia. Deletion of *Gpx4* in the bone marrow (BM) was monitored by PCR using two primers pairs. One detects the deleted allele (509 bp), the other discriminates between the floxed and wild-type (wt) allele. Absence of the floxed allele indicates that deletion was complete. (A) Presence of the wt band indicates that BM cells contain a small proportion of cells of non-hematopoietic origin. (B) Quantification of *Gpx4* mRNA in the bone marrow by quantitative RT-PCR. (C) Detection of GPX4 protein by Western blot analysis. (D) Temporal scheme of bone marrow transplantation (BMT), tamoxifen treatment (TAM) and determination of red blood cell (RBC) parameters. Lethally irradiated mice were reconstituted with 10^6 BM cells of *Gpx4*$^{wt/wt}$*; Cre ERT2* (designated wt, black columns, n=10) and *Gpx4*$^{fl/fl}$*Cre ERT2* mice (designated k.o., grey columns, n=19). Mice were fed a tamoxifen citrate containing diet for three weeks. Blood was drawn before (left columns, - TAM), at the last day of (0), and 3, 6, and 9 weeks after tamoxifen administration (+TAM), and (E) erythrocyte counts, (F) hemoglobin, (G) hematocrit , and (H) reticulocyte counts were determined. (I-M) Vitamin E depletion in the diet severely aggravates the anemia caused by *Gpx4*-deficiency in hematopoietic cells. (I) Temporal scheme of BMT, tamoxifen administration, vitamin E depletion and determination of red blood parameters. Lethally irradiated mice were reconstituted with BM cells of *Gpx4*$^{wt/wt}$*;Cre-ERT2* (designated wt, black columns) and *Gpx4*$^{fl/fl}$*Cre ERT2* mice (designated k.o., grey and white columns). After tamoxifen administration for three weeks, mice were allowed to recover for 12 weeks before the vitamin E-depleted diet was started (- vitE, n=7 for wt, n=7 for k.o.) or the normal diet continued (+ vitE, n=3 for wt, n=7 for k.o.). Blood was drawn before vitamin E depletion (time point 9 weeks in Figure 1D-H), and 26 (black and grey columns) and 54 days [white columns], n=3) after starting the vitamin E-depleted diet for the determination of (J) erythrocyte counts, (K) hemoglobin, (L) hematocrit levels, and (M) reticulocyte counts. Red blood parameters of blood taken 54 days after starting the vitamin E-depleted diet were unaltered as compared to the earlier time point. N-R) Administration of a vitamin E-enriched diet. (N) Temporal scheme of feeding the mice a vitamin E-enriched diet. (R) A 5-fold increase of α-tocopherol in the diet reduced the degree of reticulocytosis but had not impact on (O) erythrocyte counts, (P) hemoglobin and (Q) hematocrit levels. S-W) White blood counts and red blood parameters and in *Gpx4*$^{fl/fl}$*;LysMCre* and control mice. There is no difference in (S) white blood cell (WBC) counts, (T) erythrocytes, (U) hemoglobin, (V) hematocrit, and (W) reticulocyte counts between *Gpx4*$^{fl/fl}$*LysMCre* and control mice.

sis of blood parameters using a Sysmex XT-2000iV apparatus as described.[41]

Vitamin E depletion and repletion

Mice were deprived from vitamin E by feeding a vitamin E-depleted diet (SSNIFF, Soest, Germany) containing 7ppm α-tocopherol as compared to 55ppm in the normal diet. In initial experiments the conditions for ruling out side effects of Cre activation[33] with and without vitamin E-depletion using *Gpx4*$^{wt/wt}$*;CreERT2* mice as controls were defined (*Online Supplementary Figure S1*). This allowed to apply a simplified protocol with C57BL/6J mice as controls and tamoxifen-treated, lethally irradiated wt mice reconstituted with BM cells of *Gpx4*$^{fl/fl}$*;CreERT2* mice receiving a normal or a vitamin E-depleted diet as experimental groups (Figure 2-5 and *Online Supplementary Figure S5*). The vitamin E-repleted diet (5x vitamin E) contained 275ppm α-tocopherol (SSNIFF, Soest, Germany).

Staining of erythroid precursor cells from BM and spleen

Spleens were smashed and washed and the four leg bones flushed with 5 mL PBS containing 1mM EDTA and 2% fetal calf

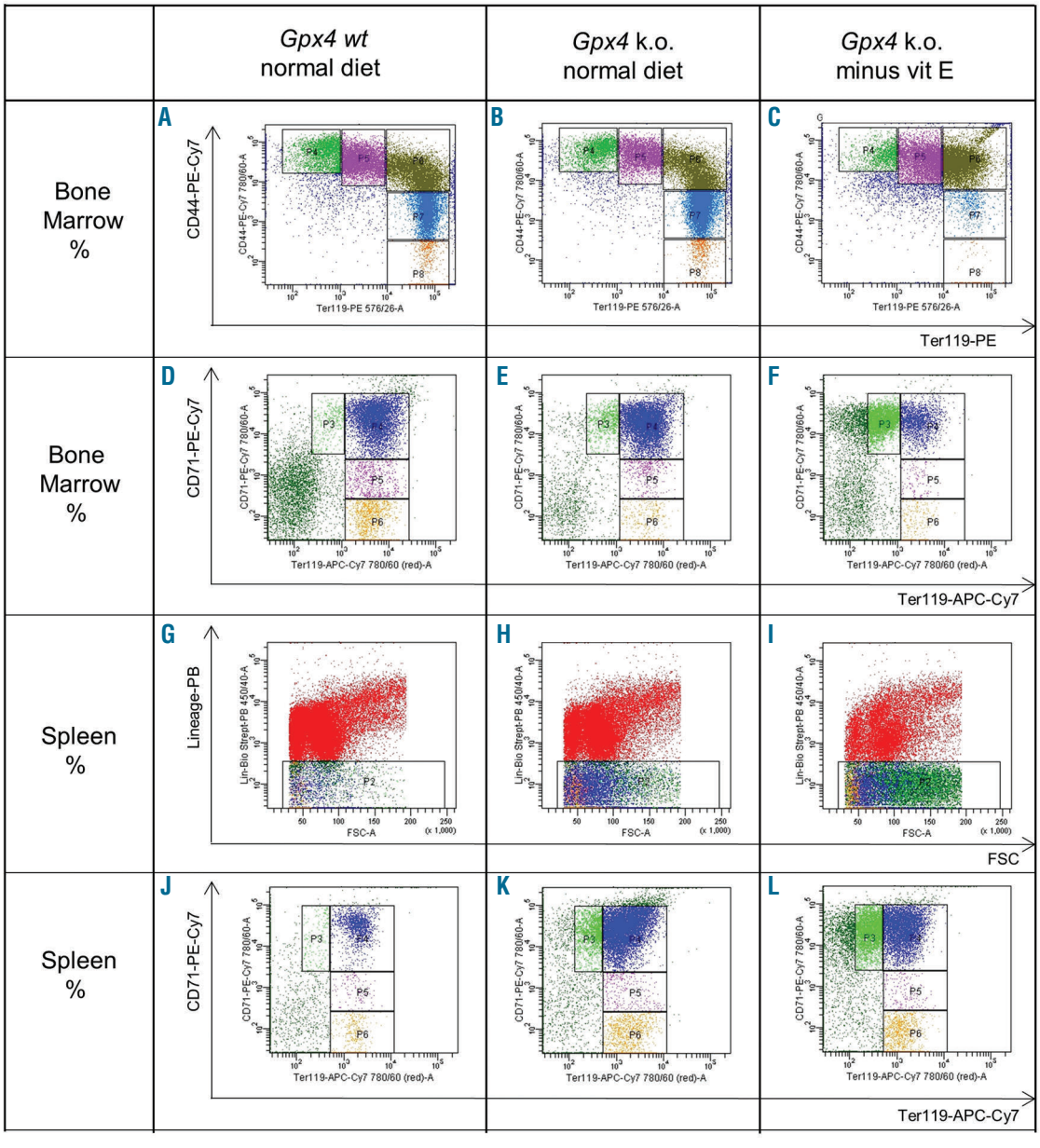

Figure 2. Relative increase in immature erythroid precursor cells in the bone marrow and spleen of mice with *Gpx4*-deficiency in the hematopoetic system. Representative fluorescence-activated cell sorting (FACS) staining of (A-F) BM and (G-L) spleen cells with CD44-PE-Cy7 and Ter119-PE (A-C) as well as with CD71-PE-Cy7 and Ter119-PE antibodies (D-F, J-L). The gate set by forward sideward scatter (FSC) and lineage marker-negative cells (G-I) illustrates the increase in extramedullary erythropoiesis in the spleen of mice with *Gpx4*-deficient hematopoietic cells kept on a (H) normal or (I) on a vitamin E-depleted diet as compared to (G) *Gpx4* wt mice kept on a normal diet. The shift towards immature erythroid precursor cells is strongly increased under combined *Gpx4*- and vitamin E-deficiency (C, F, L).

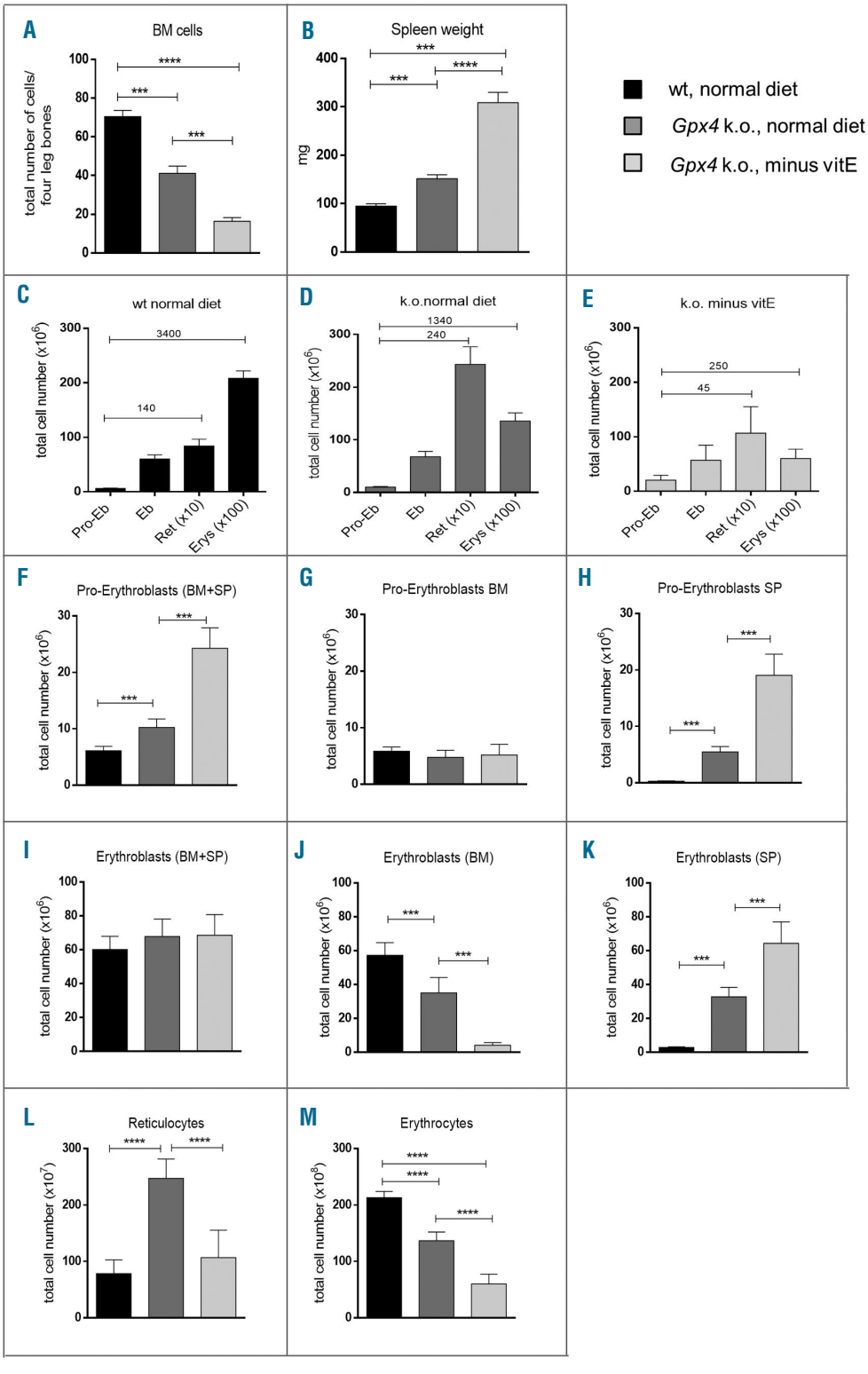

Figure 3. Ineffective erythropoiesis in mice with *Gpx4*-deficiency in the hematopoietic system and severe aggravation by dietary vitamin E deficiency. Total numbers of bone marrow (BM) cells collected from (A) two femura and two tibiae and (B) spleen weights of wild-type (wt) mice (n=8) and of mice with *Gpx4*-deficient hematopoiesis maintained either on a normal (n=8) or a vitamin E-depleted diet (n=9). The total numbers of proerythroblasts and erythroblasts in the BM and spleen, and of reticulocytes and erythrocytes in the blood were assessed as described in the *Online Supplementary Materials and Methods*. Comparative quantification of the total numbers of (F-H) proerythroblasts (n=8 for each condition), of (I-K) erythroblasts (n=8 for each condition), (L) reticulocytes and (M) erythrocytes (both n=42 wt; n=23 k.o., normal diet; n=16 k.o. minus vitE). Proerythroblasts in the BM and spleen were quantified separately in G and H, and erythroblasts in J and K, respectively. The significance was calculated by the Mann-Whitney test. The erythropenia caused by *Gpx4*-deficiency in hematopoietic cells is compensated to a large extent by increased extramedullary erythropoiesis and strongly elevated reticulocyte counts. Under combined *Gpx4*- and vitamin E-deficiency, the number or erythrocytes is strongly decreased, but the number of reticulocytes is not significantly higher than in wt mice. This points to a loss of erythroid progenitor cells at the proerythroblast and/or erythroblast stage in addition to the reticulocyte maturation defect under these conditions.

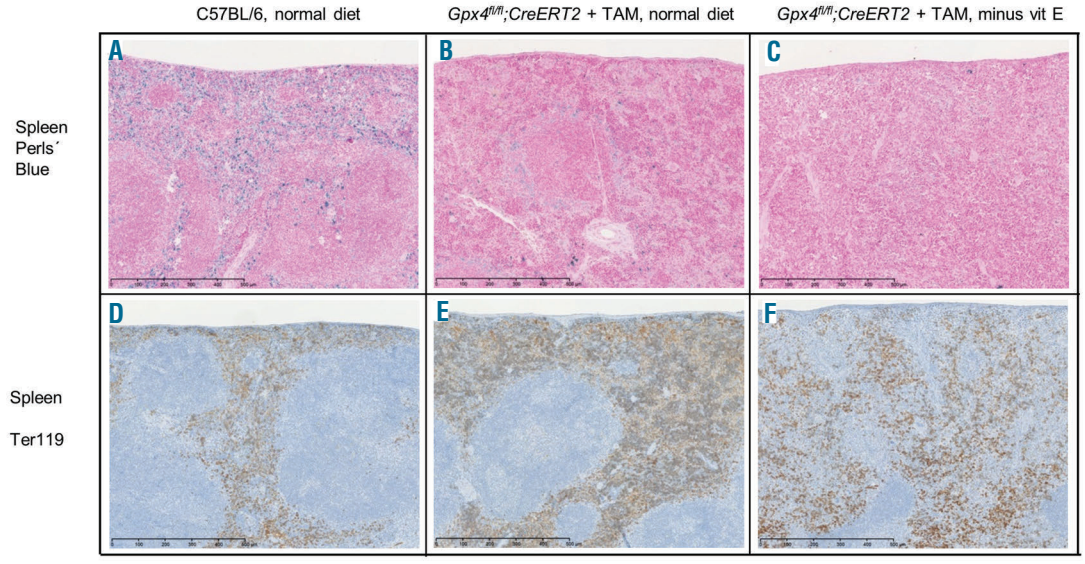

Figure 4. Extramedullary hematopoiesis in lethally irradiated wild-type (wt) mice reconstituted with *Gpx4*-deficient BM cells. (A-F) Histological sections of the spleen of (A,D) *Gpx4* wt mice kept on a normal diet and (B,E) of mice with *Gpx4*-deficient hematopoiesis maintained either on a (C) normal or on a (F) vitamin E-depleted diet, stained with Perls´ blue stain (A-C) or by immunohistochemistry with anti-Ter119 antibody (D-F). The splenic red pulp is increased in mice with *Gpx4*-deficient hematopoiesis (B,E) and the white pulp is almost completely dissipated when vitamin E is additionally depleted (C,F). (A) Iron deposits derived from erythrocyte turnover are clearly visible in the red pulp of wt mice kept on a normal diet, but (B,C) are only faintly visible in the periphery of follicles in the white pulp of mice with *Gpx4*-deficient hematopoiesis. Iron deposits are decreased rather than increased in the spleen of severely anemic mice arguing against increased hemolysis as the cause of anemia.

serum. Cells were individualized, filtered through a 40 μm cell strainer (BD Falcon) and incubated with 0.5 μg anti-CD16/32 antibody in 50 μL

PBS for 30min on ice. BM cells were stained with 0.3 μg CD44-PE-Cy7 (or CD71-PE-Cy7), 0.3 μg Ter119-PE or Ter119-APC-Cy7 antibodies. Spleen cells were stained with the following lineage mix: each 0.5 μg biotinylated CD3e (clone 145-2C11), CD11b (clone M1/70), CD19 (clone 1D3), B220 (clone RA3-6B2) and Gr-1 (clone RB6-8C5) antibodies. Cells were washed and stained with Streptavidin-Pacific Blue (Thermo Fisher) and 0.3 μg CD71-PE-Cy7 and 0.3 μg Ter119-PE (or Ter119-APC-Cy7) antibodies. Lineage-negative cells were gated and plotted as CD71-PE-Cy7-versus Ter119-APC-Cy7-positive cells. Cells were analysed on a FACSAriaI (Becton Dickinson).

Antibodies and primers

See *Online Supplementary Materials and Methods*.

Results

Gpx4-deficiency in hematopoietic cells impairs stress erythropoiesis

To study the role of GPX4 in hematopoiesis, chimeric mice were generated by reconstitution of lethally irradiated wt mice with *Gpx4*$^{fl/fl}$*;Cre ERT2* or *Gpx4*$^{wt/wt}$*;Cre-ERT2* BM cells. *Gpx4* deletion in the hematopoietic system was induced by feeding tamoxifen citrate for three weeks.40 At the last day of feeding tamoxifen red blood cell (RBC) parameters and white blood cell (WBC) counts were significantly decreased and platelet indices increased in the experimental as well as in the control group revealing apparent Cre-mediated side effects[33] (*Online Supplementary Figure S1*). Lymphocyte and monocyte counts were further decreased by simultaneous deletion of *Gpx4* (*Online supplementary Figure S1N-O*).

Thus, the inducible activation of Cre-ERT2 by tamoxifen caused an aplastic anemia with a moderate decrease in red blood cell RBC counts presumably through induction of a DNA damage response regardless of the presence or absence of *Gpx4* in hematopoietic cells. To separate a phenotype caused by *Gpx4*-deficiency from that of Cre side effects, tamoxifen-treated mice harboring *Gpx4*$^{fl/fl}$*;Cre ERT2* and *Gpx4*$^{wt/wt}$*;Cre ERT2* BM cells were allowed to recover and blood was drawn every three weeks (Figure 1). Mice with *Gpx4*-deficient BM cells remained anemic with strongly elevated reticulocyte counts, whereas mice harboring *Gpx4*$^{wt/wt}$*;Cre ERT2* BM normalized their RBC parameters within three to six weeks (Figure 1E-H, additional RBC parameters in the *Online Supplementary Figure S2B-F*). Since recovery from anemia involves stress erythropoiesis,[42] *Gpx4*-deficiency in the hematopoietic compartment thus impairs stress erythropoiesis. The erythropenic phenotype could be serially transplanted into lethally irradiated wt mice in two further rounds using *Gpx4*-deficient BM donor cells. *Gpx4*$^{fl/fl}$*;Cre-ERT2* mice served as controls except that tamoxifen feeding was omitted after the first transplantation (*Online Supplementary Figure S3*). WBC and platelet parameters remained normal except for single outliers that were not reproduced during serial transplantation. The stable transmission of the erythropenic phenotype by serial transplantation is consistent with a marked defect in stress erythropoiesis, as hematopoietic reconstitution after lethal irradiation is driven by stress hematopoiesis.[43]

Gpx4-deficient macrophages do not contribute to the development of erythropenia induced by deletion of *Gpx4* in the hematopoietic system

In our experimental strategy *Gpx4* was deleted in all hematopoietic cells including cells of the myeloid lineage. As macrophages are known to contribute to erythro-

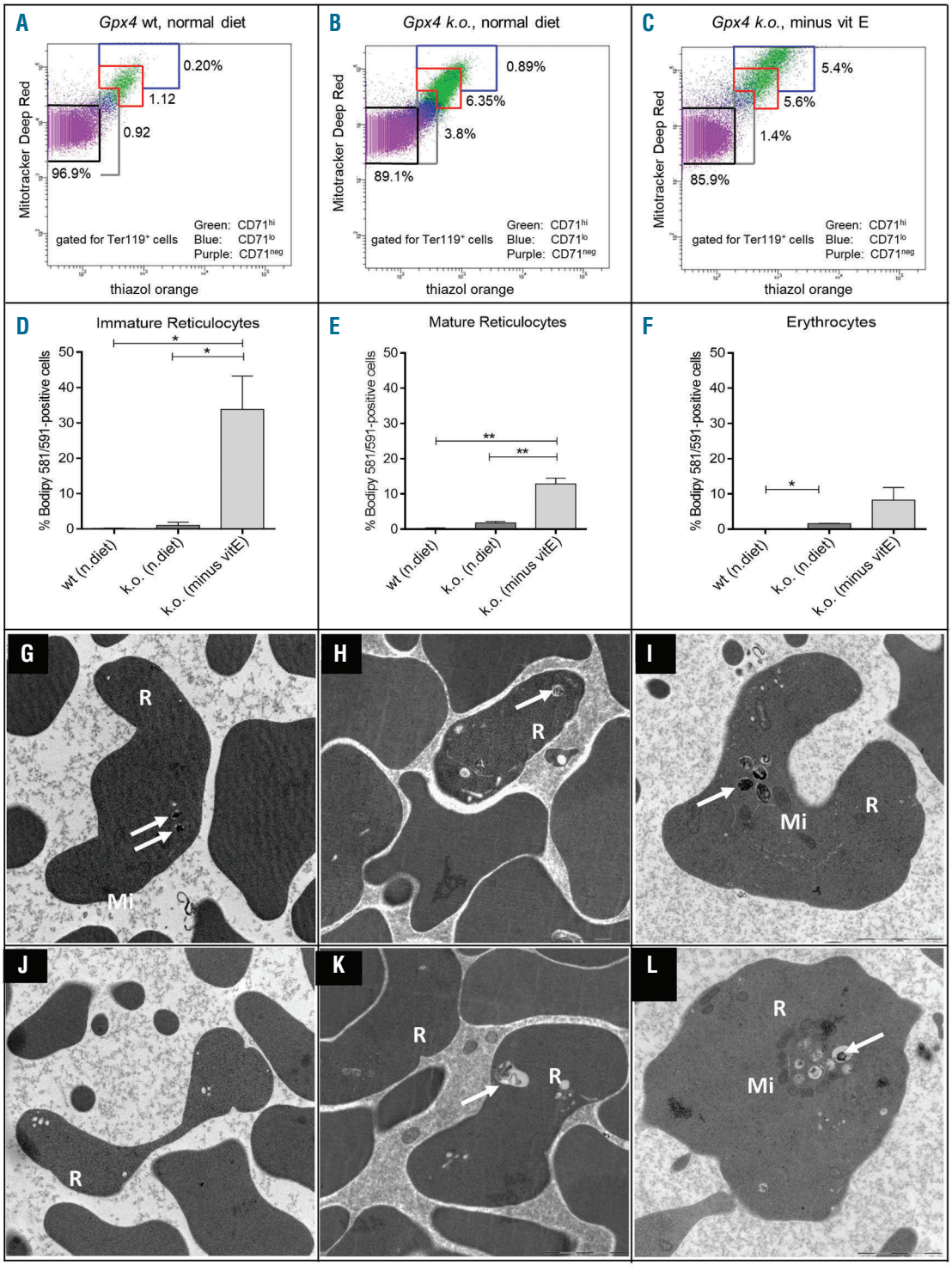

Figure 5. (A-C) *Gpx4*-deficiency in hematopoietic cells causes a reticulocyte maturation defect that is to a large extent compensated by vitamin E *in vivo*. Representative fluorescence-activated cell sorting (FACS) stainings of peripheral blood cells of (A) *Gpx4* wt mice kept on a normal diet and of mice with *Gpx4*-deficient hematopoiesis maintained either on (B) a normal or on (C) a vitamin E-depleted diet (C), stained with Mitotracker Deep Red (MTDR), thiazol orange (TO), and CD71-PE-Cy7 and Ter119-PE antibodies. The experiment is described and quantitatively evaluated in the *Online Supplementary Figure 5*. Ter119-positive cells were gated and plotted as shown in A-C. Immature reticulocytes ($CD71^{high}$) are shown in green, mature reticulocytes ($CD71^{low}$) in blue and erythrocytes ($CD71^{neg}/Ter119^{+}$) in purple. $CD71^{high}$ cells were subdivided into immature and highly immature reticulocytes based on MTDR and TO staining. (C) Under combined *Gpx4*- and vitamin E-deficiency the fraction of highly immature reticulocytes was strongly increased. D-F) Lipid peroxidation is increased in *Gpx4*-deficient reticulocytes and erythrocytes. Peripheral blood cells of the mice shown in A-C mice were stained with anti-CD71-PE-Cy7- and anti-Ter119-APC-Cy7-antibodies and with 2 μM C11-Bodipy(581/591). Ter119-positive cells were gated and the increase in % green fluorescence-positive cells was measured in $CD71^{high}$ cells (immature reticulocytes, D), in $CD71^{low}$ cells (mature reticulocytes, E) and in CD71neg cells (erythrocytes, F) upon excitation at 488 nm. Wild-type, normal diet, (n=2); k.o., normal diet (n=2); k.o., minus vitamin E (n=3). The significance was calculated using an unpaired T-Test. Note the high degree of lipid peroxidation in *Gpx4*-deficient immature reticulocytes upon feeding a vitamin E-depleted diet. G-L) Ultrastructural analysis of red blood cells from the mice shown in A-C. Remnants of mitochondria (Mi) are marked by white arrows. Under *Gpx4*-deficiency (H and K), and more so under combined *Gpx4*- and vitamin E-deficiency (I and L) large unphagocytosed vesicles containing mitochondria accumulated in reticulocytes (R). Blood pellets were processed for transmission electron microscopy as described in the *Online Supplementary Materials and Methods*.

poiesis by forming erythropoietic islands in the BM,[44] it was important to discriminate whether erythropenia is brought about by a cell-autonomous effect of GPX4 on the erythroid lineage or by a cell-non-autonomous effect of GPX4 on macrophages. Liao *et al.* recently described that loss of all selenoproteins in hematopoietic cells by deletion of selenocysteine-specific t-RNA impairs stress erythropoiesis and have attributed this to the loss of selenoprotein W in macrophages.[13] Despite the high position of GPX4 in the hierarchy of selenoproteins, a cell-autonomous contribution of GPX4 to stress erythropoiesis was not considered by the authors.

To address a potential contribution of GPX4 in macrophages on stress erythropoiesis, we used *Gpx4*$^{fl/fl}$*;LysM-Cre* mice that delete Gpx4 in macrophages and neutrophils[45] and analyzed BM erythroblastic island

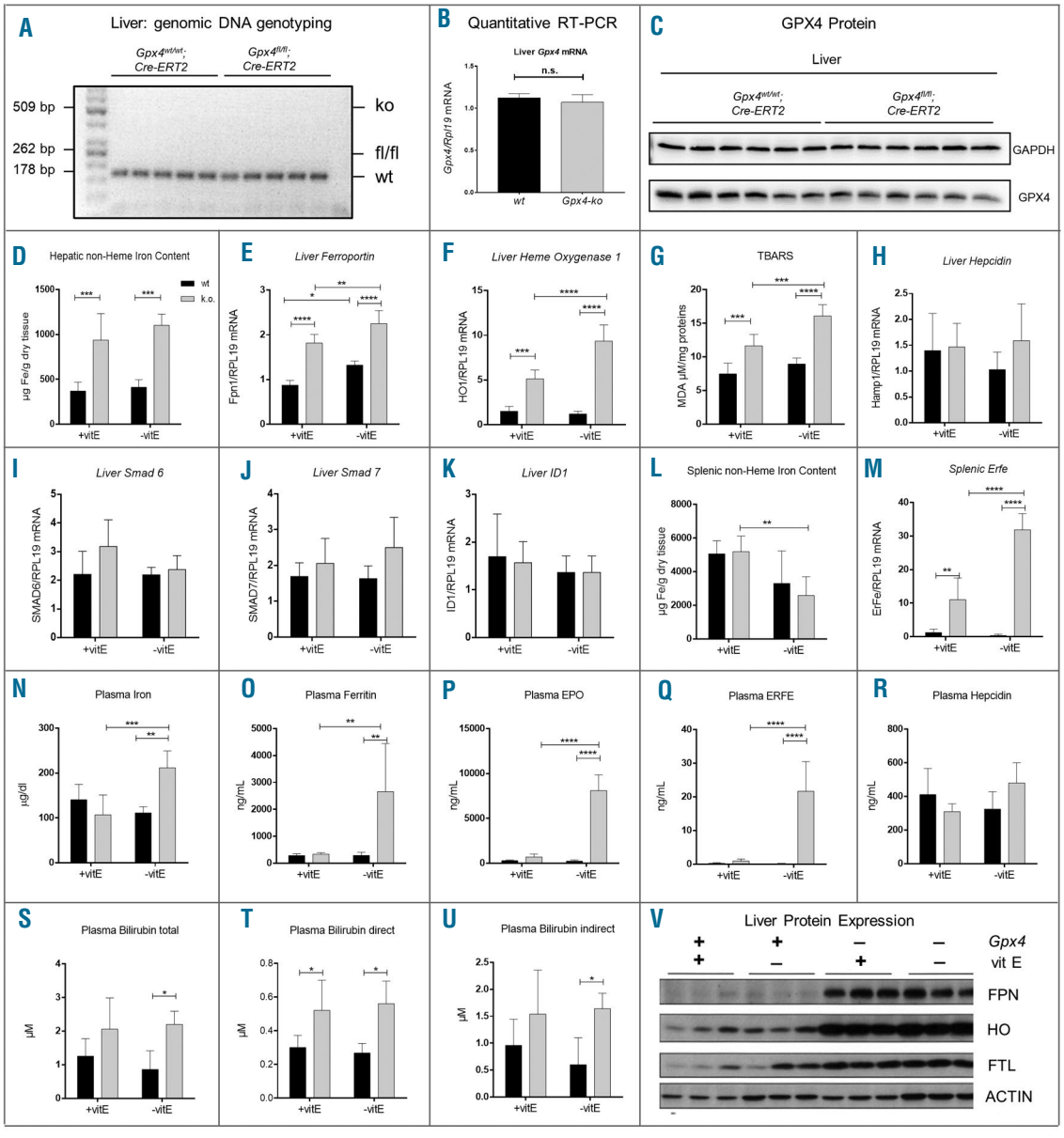

Figure 6. Iron overload in the liver and simultaneous iron demand for erythropoiesis in mice with a *Gpx4*-deficient hematopoietic system. In the liver of mice with *Gpx4*-proficient and *Gpx4*-deficient hematopoiesis only the wild-type (wt) allele of *Gpx4* is detected (A), and the same levels of *Gpx4* mRNA (B) and protein (C) are expressed. (D-K, V) Parameters of iron metabolism in the liver: Non-heme hepatic iron (D), *ferroportin* mRNA (E), *heme oxygenase-1* mRNA (F), thiobarbituric acid reactive substances (TBARS)(G), *hepcidin* mRNA (H), *Smad6* mRNA (I), *Smad7* mRNA (J), and *ID1* mRNA (K). The proteins ferroportin (FPN), heme oxygenase (HO-1), and ferritine light chain (FTL) are expressed at higher level in mice with a *Gpx4*-deficient hematopoietic system (V). Parameters of splenic and peripheral iron metabolism: non-heme splenic iron (L), *splenic Erfe* mRNA (M), plasma iron (N), plasma ferritine (O), plasma EPO (P), plasma ERFE (Q), plasma hepcidin (R), plasma bilirubin total (S), plasma bilirubin direct (T), plasma bilirubin indirect (U). Increased hepatic non-heme iron and TBARS as well as elevated ferroportin and heme oxygenase-1 expression point to hepatic iron overload, whereas highly increased EPO and ERFE levels in the plasma and elevated *Erfe* mRNA expression levels are strong indicators of severe iron demand in the erythropoietic system. Note that hepcidin expression is not down regulated despite the strong erythropoietic iron demand. For HO-1/actin ratio in the liver and duodenal ferroportin expression, see *Online Supplementary Figure S7A-B*.

macrophages (BMEIM) and spleen red pulp macrophages (RPM) by flow cytometry. The number of BMEIM was slightly reduced, while the number of RPM remained unaffected in the absence of *Gpx4* (*Online Supplementary Figure S4A-C*). Importantly, erythrocyte and reticulocyte counts were unaltered as well as hemoglobin and hematocrit values (Figure 1T-W) indicating that GPX4 in macrophages plays a minor if any role in the development of the erythropenia. This strongly argues for a cell-autonomous action of GPX4 in the erythroid system.

Vitamin E-deficiency severely aggravates erythropenia caused by *Gpx4*-deficiency

In cell culture and in certain tissues (endothelium, T cells, hepatocytes) the phenotype of *Gpx4*-deficiency can be partially or completely masked by vitamin E *in vivo*. Vitamin E thus acts as a full or partial backup system for GPX4 in some cell types *in vitro* and *in vivo*. To exclude unintended side effects of Cre and Cre inducers or activators with vitamin E deficiency, *Gpx4* was deleted prior to vitamin E deprivation. Feeding the vitamin E-depleted diet for three to four weeks to mice with *Gpx4*-deficiency severely aggravated erythropenia. Despite the strong decrease in RBC count as well as hemoglobin and hematocrit levels, reticulocyte counts were increased only to a small and non-significant extent (Figure 1I-M). This indicates that the anemia caused by *Gpx4*-deficiency could no longer be compensated by increased production of reticulocytes when the dietary vitamin E level was reduced. In wt control mice, dietary vitamin E deprivation had no impact on RBC parameters (*Online Supplementary Figure S5*). An increase of the vitamin E (i.e. α-tocopherol) concentration to the 5-fold level in the diet had no impact on erythrocyte counts, hemoglobin and hematocrit values but led to a significant decrease in reticulocyte counts (Figure 1N-R) corroborating the fact that reticulocyte counts respond more sensitively to external factors with impact on erythropoiesis than do other RBC parameters.

Ineffective erythropoiesis in mice with *Gpx4*-deficient hematopoietic cells

To get deeper insight into the dynamics of *Gpx4*-deficient erythropoiesis, we quantified the percentage of erythroid precursor cells in the BM and spleen by fluorescence-activated cell sorting (FACS) analysis (Figure 2) and calculated the total numbers of erythroid precursors in these organs (Figure 3A-B). Cell suspensions of BM and spleen were stained with antibodies for CD44 or CD71 and Ter119. Erythroid precursor cells were classified into proerythroblasts based on the expression level of CD44 or CD71 and Ter119. These analyses revealed a marked increase in extramedullary erythropoiesis in the spleen of mice with *Gpx4*-deficient hematopoiesis (Figure 2H,K), and a pronounced shift towards immature precursors cells in the BM and spleen when vitamin E was additionally depleted (Figure 2 F,L). The dynamic changes became more apparent when the total numbers of erythroid precursors were calculated under the different conditions. In mice with *Gpx4*-deficient hematopoietic cells the total number of proerythroblasts increased by a factor of 1.7-fold under a normal diet, and to about 4-fold when vitamin E was additionally depleted (Figure 3F). This increase was due to an increase of proerythroblasts in the spleen (Figure 3H). The number of erythroblasts in the spleen of these mice also increased significantly, and again to a much higher extent when vitamin E was depleted (Figure 3K). Under both conditions of *Gpx4*-deficiency (normal versus vitamin E-depleted diet) the number of erythroblasts in the spleen increased at the expense of erythroblasts in the BM leaving the total number of erythroblasts virtually unchanged (Figure 3 I-K).

The ratio of erythrocytes to proerythroblasts illustrates the efficacy of erythropoiesis. It decreased from about 3400 in wt mice to 1340 in mice with *Gpx4*-deficient hematopoiesis (Figure 3C-D). While the total number of reticulocytes increased by almost 3-fold and the ratio of reticulocytes to total proerythroblasts increased from 140 in wt mice to 240 in mice with *Gpx4*-deficient hematopoiesis, RBC counts decreased to 65% (Figure 3L-M) indicating that maturation of reticulocytes to erythrocytes is defective under *Gpx4*-deficiency.

Under combined *Gpx4*- and vitamin E-deficiency, the ratio of erythrocytes to proerythroblasts decreased to about 250 (Figure 3E). Erythrocyte counts dropped to less than 30% (compared to wt) (Figure 3M), while the number of reticulocyte counts increased only by about 1.3 fold (Figure 3L). The only moderate and non-significant increase in reticulocyte counts is in stark contrast to the severe anemia under these conditions. The ratio of reticulocytes to total proerythroblasts decreased from 240 in mice with *Gpx4*-deficient hematopoiesis to 45 in mice with combined *Gpx4*- and vitamin E-deficiency suggesting that erythroid progenitor cells were lost during differentiation from proerythroblasts to reticulocytes, in addition to the reticulocyte maturation defect observed under these conditions. Mice with *Gpx4*-deficiency in hematopoietic cells (on a normal diet) showed an increase in the size of the red pulp and the number of Ter119-positive cells (Figure 4B,E) corroborating data showing ineffective erythropoiesis. Yet, iron deposits in the red pulp stemming from physiological RBC turnover diminished (Figure 4B), arguing against hemolysis as the cause of anemia. Upon *Gpx4*-deficiency and vitamin E depletion, the white pulp dispersed to a large extent and was intermingled with Ter119-positive erythroid cells (Figure 4C,F).

Impaired reticulocyte maturation and increased lipid peroxidation in *Gpx4*-deficient erythroid cells and aggravation of the phenotype by vitamin E-depletion

Next, we attempted to define the maturation state of the reticulocytes in the anemic mice. To this end, peripheral blood cells were stained with CD71, Ter119, Mitotracker Deep Red, and thiazol orange. Representative examples of mice are depicted in Figure 5A-C (quantification of total numbers of mature, immature and highly immature reticulocytes in the *Online Supplementary Figure S6A-F*). Deletion of *Gpx4* increased not only the total number of reticulocytes, but also that of each fraction: 2.1-fold of mature, 3.5-fold of immature, and 4.2-fold of highly immature reticulocytes (*Online Supplementary Figure S6D-F*). The differentially higher increase in more immature reticulocytes led to a general shift towards more immature reticulocytes. Under combined *Gpx4* and vitamin E deficiency, the number of highly immature reticulocytes increased 7-fold, while the total number of mature reticulocytes decreased by 20%. The failure of reticulocytes to undergo maturation was associated with an increase in lipid peroxidation of reticulocytes and erythrocytes as revealed by Bodipy 581/591-C11-staining. Lipid peroxidation was particularly pronounced in immature

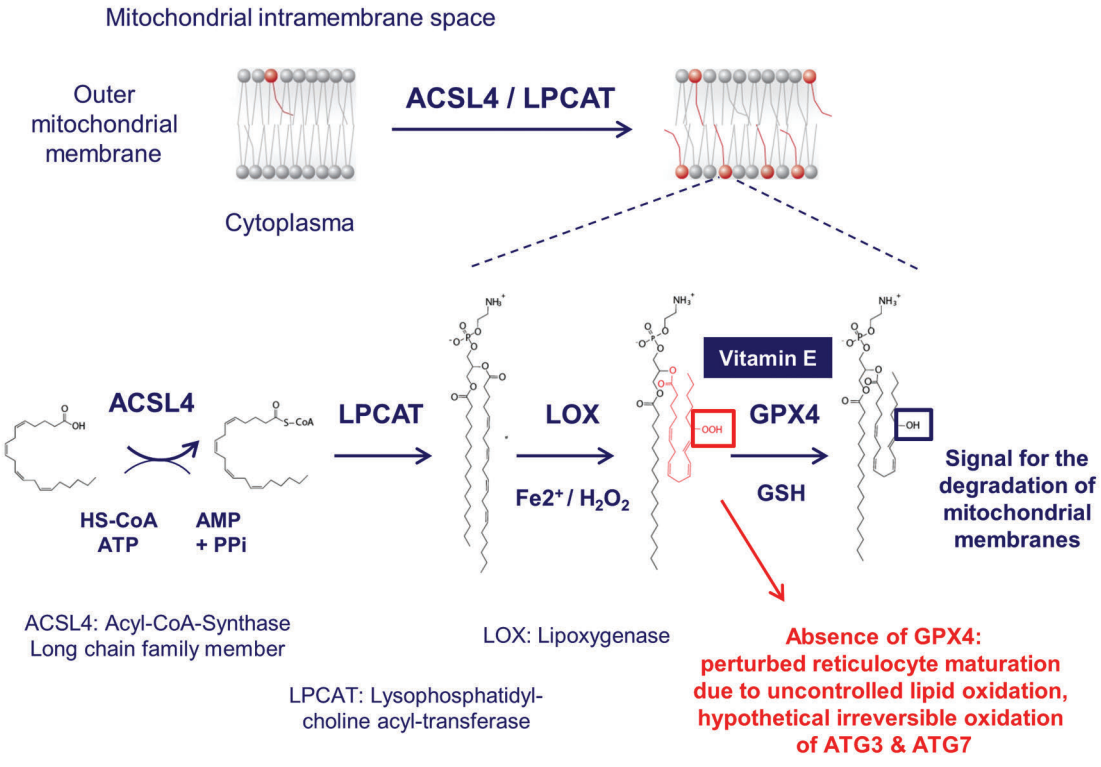

Figure 7. Proposed model for the role of 12/15-lipoxygenase, GPX4 and vitamin E during reticulocyte maturation.

reticulocytes when vitamin E was additionally depleted (Figure 5D).

To further study potential subcellular alterations in response to *Gpx4* loss, erythrocytes and reticulocytes of the peripheral blood were subjected to ultrastructural analysis by electron microscopy (Figure 5G-L). Reticulocytes in blood of wt mice and in blood of mice lacking *Gpx4* in hematopoietic cells were characterized by remnants of ribosomes (fine granular structure) and mitochondria. An accumulation of unphagocytosed mitochondria in large vacuoles was evident when vitamin E was depleted in mice with *Gpx4*-deficient hematopoiesis in vivo (white arrows in Figure 5G-L) indicating that GPX4 and vitamin E physiologically contribute to mitochondrial clearance during reticulocyte maturation.

Iron overload and oxidative stress in the liver of mice with *Gpx4*-deficient hematopoiesis

As shown above, *Gpx4*-deficiency in the hematopoietic system is characterized by ineffective erythropoiesis that is severely aggravated by additional vitamin E deprivation. Ineffective erythropoiesis is also a hallmark of β-thalassemia, and β-thalassemia is associated with iron overload that is known to sustain and to aggravate the anemia in mouse models of β-thalassemia.[51] To address whether similar mechanisms are operating in *Gpx4*-deficient erythropoiesis, iron-related parameters were analyzed in the liver, spleen, and plasma of mice with *Gpx4*-deficient hematopoiesis. Non-heme iron content in the liver was significantly increased upon deletion of *Gpx4* (Figure 6D). At the molecular level iron overload in the liver was confirmed by elevated levels of the iron storage protein Ferritin L (FTL) (Figure 6V). An excess of free iron triggers the formation of reactive oxygen species (ROS) and lipid peroxidation *via* the Fenton reaction.[3] Consistently, markers of oxidative stress such as increased lipid peroxidation products (as revealed by TBARS production) (Figure 6G) and elevated heme oxygenase-1 mRNA and protein levels (Figure 6F,V) were detected in the liver. Combined *Gpx4*- and vitamin E-deficiency further increased heme oxygenase-1 mRNA and protein levels as well as TBARS production in the liver.

Unaltered hepcidin levels despite higher erythropoietic iron demand

Systemic iron homeostasis is maintained by the hepcidin/ferroportin regulatory system. Hepcidin regulates the amount of iron exported into systemic circulation by modulating cell surface expression of the iron exporter ferroportin on iron exporting cells. Remarkably, despite increased liver non-heme iron levels in mice with *Gpx4*-deficient hematopoietic cells, hepatic hepcidin mRNA expression was not affected, regardless whether mice were kept on a normal or on a vitamin E-depleted diet (Figure 6H). Likewise, target genes of the iron-sensing BMP/SMAD signaling pathway in the liver (SMAD6, SMAD7, and ID1) were not significantly altered by *Gpx4*- and vitamin E-deficiency (Figure 6I-K). Hepatic ferroportin mRNA and protein levels were increased upon *Gpx4* ablation with or without vitamin E-deficiency (Figure 6E,V), a finding explained by the oxidative stress that occurs in the liver (Figure 6G). Ferroportin expression in the duodenum was unaltered (*Online Supplementary Figure S7*).

We next measured iron-related plasma parameters. Plasma iron levels were not increased upon *Gpx4* deletion, but were increased when *Gpx4* was deleted and vitamin E simultaneously depleted (Figure 6N). Despite this, hepcidin levels in the plasma were not altered (Figure 6R). Bilirubin levels appeared to increase with the ablation of *Gpx4* under both conditions (± vitamin E), but the standard deviation (SD) was high so that differences became barely significant (Figure 6S-U). Consistent with elevated liver iron levels, plasma ferritin was highly increased under combined *Gpx4*- and vitamin E-deficiency (Figure 6O).

In mouse models with β-thalassemia plasma erythropoietin (EPO) levels are increased. EPO stimulates the expression of the blood hormone erythroferrone (ERFE) in erythroid precursor cells, which then down regulates hepcidin levels. Similarly, EPO and ERFE levels appeared to be increased in mice with *Gpx4*-deficient hematopoiesis, but only EPO levels reached significance. Under combined *Gpx4*- and vitamin E-deficiency plasma EPO and ERFE levels increased to very high and highly significant levels (Figure 6P,Q), apparently mirroring the severity of erythropenia under combined *Gpx4*- and vitamin E-deficiency.[52] Taken together, the defect in reticulocyte maturation by loss of the *Gpx4* gene causes ineffective erythropoiesis with simultaneous iron overload in the liver and iron-deficiency in the hematopoietic system and this phenotype is to a large part masked by vitamin E in the normal diet.

Discussion

Based on biochemical studies Schewe *et al*. reported in 1975 that mitochondrial clearance during reticulocyte maturation is initiated by enzymatic lipid peroxidation.[20] These authors purified the enzyme 15-lipoxygenase from rabbit reticulocytes and showed that it oxidizes polyunsaturated fatty acids in mitochondrial membranes as an initiating event in the disposal of mitochondria. Even though the work has been confirmed and extended by others, these studies fell into oblivion due to the fact that erythropoiesis including erythrocyte and reticulocyte counts appeared to be normal in mice lacking *12/15-lipoxygenase*.[26]

However, for a few years the work of the Rapoport group has been regaining attention due to several important novel findings: (i) GPX4 was shown to be an antagonist of a novel 12/15-lipoxygenase-induced, non-apoptotic cell death pathway in murine fibroblasts,[5] (ii) this mode of cell death initiated by ablation of *Gpx4* has been shown to be driven by iron-induced lipid peroxidation and is now known as ferroptosis, (iii) distinct phospholipid hydroperoxide species have been identified that act as death signals and inducers of ferroptosis in various cell types,[54] (iv) vitamin E synergizes with GPX4 in antagonizing the action of lipid hydroxyperoxides *in vitro* and *in vivo*, (v) 12/15-lipoxygenase and its hydroxylated oxidation products are involved in the regulation of autophagy in murine macrophages,[19] (vi) autophagy is inhibited by oxidation of enzymes like ATG3 and ATG7 that catalyze ATG8/LC3 lipidation,[56] (vii) lipoxygenases are not necessarily the decisive source of lipid hydroperoxides, they may rather sensitize cells to iron-mediated non-enzymatic autoxidation.[29]

It was the aim of our study to identify a missing link between membrane lipid oxidation and reticulocyte maturation by genetic means. Based on the finding that GPX4 is unique in antagonizing lipid membrane hydroperoxides and stabilizing the hydroxylated oxidation products, we hypothesized that deletion of *Gpx4* in hematopoietic cells would perturb mitophagy and thus reticulocyte maturation.

The role of GPX4 in hematopoietic cells had already been studied by Canli *et al*. using *Gpx4*$^{fl/fl}$*;Mx1-Cre* mice.[55] These authors primarily focused, however, on the mode of cell death in hematopoietic precursor cells and not on a comprehensive view on *Gpx4*-deficient erythropoiesis at a quantitative level.

As an inducible k.o. model for *Gpx4* exclusively in hematopoietic cells, we have reconstituted lethally irradiated wt mice with *Gpx4*$^{fl/fl}$*;Cre-ERT2* or *Gpx4*$^{wt/wt}$*;CreERT2* BM cells. We now show that activation of Cre by feeding a tamoxifen-containing diet induces an aplastic anemia affecting RBC as well as WBC not only in mice reconstituted with *Gpx4*-deficient, but also in control mice with *Gpx4*$^{wt/wt}$*;CreERT2* BM cells thus confirming the acute toxic effect of Cre activation on the hematopoietic system described by Higashi *et al*.[33] There is, however, a clear difference between mice harboring or lacking the *Gpx4* gene in hematopoietic cells: mice reconstituted with *Gpx4*$^{wt/wt}$*;CreERT2* BM cells recovered within three to six weeks whereas mice reconstituted with cells lacking the *Gpx4* gene failed to fully recover and remained partially anemic. The erythropenic phenotype could be stably transmitted into lethally irradiated wt mice by two consecutive rounds of transplantation. It is noteworthy that Cre activation by tamoxifen and *Gpx4* ablation cause different types of anemia. Cre activation leads to an aplastic anemia with cessation of RBC (*Online Supplementary Figure S1F*) and WBC formation (*Online Supplementary Figure S1L-P*), whereas ablation of *Gpx4* in the hematopoietic system causes ineffective erythropoiesis with increased formation of reticulocytes (Figure 1H). As recovery from anemia as well as from hematopoietic reconstitution is driven by stress erythropoiesis,[43] stress erythropoiesis is perturbed by *Gpx4*-deficiency in hematopoietic cells. Depletion of vitamin E in the diet strongly aggravated the anemic phenotype. To exclude unintended side effects of vitamin E depletion with the well-known toxicity of Cre and Cre inducers and activators, the *Gpx4* gene was deleted prior to vitamin E depletion. The dynamics of erythropoiesis under the various conditions including the maturation state of reticulocytes was assessed by FACS staining of proerythroblasts and erythroblasts in the BM and spleen and of reticulocytes in the peripheral blood. A more comprehensive picture emerged (i) by calculating the total number of proerythroblasts and erythroblasts in the BM and spleen, (ii) by extrapolating to the total number of reticulocytes and erythrocytes per mouse, and (iii) by quantifying the fraction of mature, immature and highly immature reticulocytes.

In mice with *Gpx4*-deficient hematopoiesis the total number of proerythroblasts was increased, mainly due to an increase in extramedullary erythropoiesis. Total numbers of mature, immature as well as highly immature reticulocytes were also increased. The differentially higher increase in immature and highly immature reticulocytes led to a shift towards immature reticulocytes. This indicates that under hematopoietic *Gpx4*-deficiency the rate

of reticulocyte production exceeded the rate of reticulocyte maturation, a disequilibrium that resulted in ineffective erythropoiesis.

Under combined *Gpx4*- and vitamin E-deficiency the number of proerythroblasts in the spleen was further strongly increased. Within the reticulocyte fraction, there was a pronounced shift towards highly immature reticulocytes. Yet, production of reticulocytes did not keep up with the production of proerythroblasts as total reticulocyte counts were not significantly higher than in wt mice. This suggests that, in addition to the severe reticulocyte maturation defect, erythroid progenitor cells were lost during differentiation from the proerythroblast to the reticulocyte stage. Highest levels of lipid peroxidation, as assessed by C11-Bodipy(581/591)-staining, were observed in immature reticulocytes under combined *Gpx4*- and vitamin E-deficiency which correlates with the severity of the phenotype. Ultrastructural analysis revealed remnants of mitochondria and ribosomes in reticulocytes of wt mice and mice with *Gpx4*-deficient hematopoiesis, and a pronounced accumulation of large vacuoles containing unphagocytosed mitochondria, when dietary vitamin E was lowered. The data support the model that mitophagy is triggered by lipid oxidation that is kept in check by GPX4. Hence, loss of *Gpx4*, especially under vitamin E-restricted conditions, leads to uncontrolled lipid peroxidation and as a consequence, to severely perturbed mitophagy (Figure 7).

The anemia caused by hematopoietic *Gpx4*-deficiency shares a number of features with β-thalassemia, for which the term ineffective erythropoiesis has been coined: decreased RBC, elevated reticulocyte counts, overactive extramedullary erythropoiesis, elevated erythroid progenitors, absence of hemolysis, and systemic iron overload linked to severe iron demand for the erythroid system.[51] This prompted us to study iron metabolism in mice with *Gpx4*-deficient hematopoiesis. Hematopoietic *Gpx4*-deficiency caused liver iron overload and oxidative stress, elevated plasma ferritin and iron levels, parameters aggravated by vitamin E depletion. Despite signs of iron overload in the liver and plasma, there was continuous demand for iron in the erythroid system. As a consequence of the anemia, plasma EPO and ERFE levels were elevated. Likewise, *Erfe* splenic mRNA expression was increased, particularly when *Gpx4* deletion and vitamin E-deficiency were combined. Since ERFE mirrors the erythropoietic activity and there is virtually no background of extramedullary erythropoiesis in the spleen of wt mice under steady state conditions, spleen *Erfe* mRNA emerged as the most sensitive parameter of iron demand.

Despite the dramatic increase in ERFE production in mice with combined *Gpx4*- and vitamin E-deficiency, hepcidin expression in the liver plasma was unchanged. This is reminiscent to what has been observed in β-thalassemic $Th^{3/+}$ mice older than six weeks.[57] Suppression of hepcidin expression is only seen when the mice are young and still loading their livers with iron. Once enough iron has been loaded, hepcidin begins to rise, driven by hepatic iron stores, despite high erythroferrone, so that older mice have high liver iron but normal hepcidin which slows down further iron loading. Thus, hypoxia and elevated iron demand for erythropoiesis decrease hepcidin expression, whereas high plasma and hepatic iron levels counteract the response to ERFE in the liver. An alternative explanation is that a yet-unrecognized factor induced in response to oxidative stress or a direct oxidative modification of ERFE counteracts the action of ERFE on hepcidin expression.

The pronounced similarity between anemia caused by hematopoietic *Gpx4*-deficiency and β-thalassemia raises the question whether underlying pathogenic principles are shared between both conditions. A common denominator is by no doubt the involvement of oxygen radicals. In case of *Gpx4*-deficiency, they arise from increased lipid peroxidation, in case of β-thalassemia from inappropriate folding of globin chains and hemoglobin assembly. This liberates oxygen, heme and iron thus favoring the production of oxygen radicals through non-enzymatic autoxidation. There is ample evidence in the literature that increased lipid peroxidation in RBC and decreased lipid-soluble antioxidant levels in the plasma as well as in erythrocytes are consistent features of β-thalassemia.[59-63] Administration of vitamin E normalized the plasma oxidant/antioxidant balance and vitamin E content of erythrocytes, yet, the clinical benefit of vitamin E administration remained limited due to the persistence of iron-overload in affected patients.[62-65] Taken together, perturbed reticulocyte maturation through uncontrolled lipid peroxidation may be the underlying cause of ineffective erythropoiesis in both conditions.

It still remains unclear to which extent lipoxygenase-mediated enzymatic and/or non-enzymatic mechanisms contribute to lipid peroxidation in the anemia described here. Lipoxygenases lower the threshold for non-enzymatic autoxidation[29] and may be required for initiating lipid oxidation in mitochondrial membranes. In the absence of *12/15-lipoxygenase* other lipoxygenases may functionally compensate for the loss of the missing enzyme. A scenario of non-enzymatic lipid peroxidation is, however, also conceivable. Once lipid peroxidation is triggered, the process may be self-sustaining due to the high concentration of iron, heme compounds and oxygen rendering enzymatic lipid peroxidation dispensable.

Another critical determinant of physiological reticulocyte maturation is the cholesterol concentration in the reticulocyte membrane as well as in the plasma. Holm *et al*. have shown in an elegant study that mice lacking *apolipoprotein E* and *high-density lipid protein receptor I (SR-BI)* are unable to expel autophagocytosed organelles and accumulate autophagolysosomes in their reticulocytes.[66] These mice lack mature erythrocytes and their gas transport relies exclusively on reticulocytes. Remarkably, the block in terminal reticulocyte maturation is cell-non-autonomous in these mice and reversible: transfusion of these reticulocytes into wt mice or hematopoietic reconstitution of lethally irradiated wt mice with *apoliporotein E*- and *SR-BI*-deficient BM cells completely normalized reticulocyte maturation. The phenotype could also be reversed through sequestration of free cholesterol: administration of cyclodextrin led to immediate expulsion of stored autophagolysosomes in vivo and in vitro and normalized the phenotype. Contrary to the apolipoprotein E- and SR-BI-model of Holm *et al*., we are dealing in our model with a cell-autonomous effect of *Gpx4*-deficiency to which cell-nonautonomous factors like the plasma concentration of vitamin E also contribute to a significant extent. In both conditions, the precise molecular underpinnings underlying the defects in reticulocyte maturation await to be elucidated.

Funding

MUM acknowledges funding from the Deutsche Forschungsgemeinschaft (SFB1036, SFB1118); SA is supported by the European Hematology Association (Advanced Research fellowship). Support by the German Federal Ministry of Education and Research Infrafrontier grant 01KX1012 for German Mouse Clinic (GMC) infrastructure (to MHA). MK and KO were funded by a grant from SNF 310030_163443/1.

Acknowledgments

We thank Prof. Anton Berns, the Netherland Cancer Institute, Amsterdam, for providing Rosa26-CreERT2 mice. MC and GWB thank Matilde Maiorino and Fulvio Ursini for many helpful discussions. We are most grateful to Martina Mötscher, Jasmin Teutsch and Michael Hagemann for breeding the mice.

References

1. Ursini F, Maiorino M, Valente M, Ferri L, Gregolin C. Purification from pig liver of a protein which protects liposomes and biomembranes from peroxidative degradation and exhibits glutathione peroxidase activity on phosphatidylcholine hydroperoxides. Biochim Biophys Acta. 1982;710(2):197-211.
2. Maiorino M, Conrad M, Ursini F. GPx4, Lipid Peroxidation, and Cell Death: Discoveries, Rediscoveries, and Open Issues. Antioxid Redox Signal. 2018; 29(1):61-74.
3. Hentze MW, Muckenthaler MU, Andrews NC. Balancing acts: molecular control of mammalian iron metabolism. Cell. 2004; 117(3):285-297.
4. Bordet JC, Guichardant M, Lagarde M. Hydroperoxides produced by n-6 lipoxygenation of arachidonic and linoleic acids potentiate synthesis of prostacyclin related compounds. Biochim Biophys Acta. 1988; 958(3):460-468.
5. Seiler A, Schneider M, Forster H, et al. Glutathione peroxidase 4 senses and translates oxidative stress into 12/15-lipoxygenase dependent- and AIF-mediated cell death. Cell Metab. 2008;8(3):237-248.
6. Thomas JP, Maiorino M, Ursini F, Girotti AW. Protective action of phospholipid hydroperoxide glutathione peroxidase against membrane-damaging lipid peroxidation. In situ reduction of phospholipid and cholesterol hydroperoxides. J Biol Chem. 1990;265(1):454-461.
7. Weitzel F, Wendel A. Selenoenzymes regulate the activity of leukocyte 5-lipoxygenase via the peroxide tone. J Biol Chem. 1993;268(9):6288-6292.
8. Schnurr K, Belkner J, Ursini F, Schewe T, Kuhn H. The selenoenzyme phospholipid hydroperoxide glutathione peroxidase controls the activity of the 15-lipoxygenase with complex substrates and preserves the specificity of the oxygenation products. J Biol Chem. 1996;271(9):4653-4658.
9. Kuhn H, Borchert A. Regulation of enzymatic lipid peroxidation: the interplay of peroxidizing and peroxide reducing enzymes. Free Radic Biol Med. 2002; 33(2):154-172.
10. Kryukov GV, Castellano S, Novoselov SV, et al. Characterization of mammalian selenoproteomes. Science. 2003; 300(5624):1439-1443.
11. Burk RF, Hill KE. Regulation of selenium metabolism and transport. Annu Rev Nutr. 2015;35:109-134.
12. Ingold I, Berndt C, Schmitt S, et al. Selenium Utilization by GPX4 is required to orevent hydroperoxide-induced ferroptosis. Cell. 2018;172(3):409-422.
13. Liao C, Hardison RC, Kennett MJ, Carlson BA, Paulson RF, Prabhu KS. Selenoproteins regulate stress erythroid progenitors and spleen microenvironment during stress erythropoiesis. Blood. 2018;131(23):2568-2580.
14. Kaushal N, Hegde S, Lumadue J, Paulson RF, Prabhu KS. The regulation of erythropoiesis by selenium in mice. Antioxid Redox Signal. 2011;14(8):1403-1412.
15. Schweers RL, Zhang J, Randall MS, et al. NIX is required for programmed mitochondrial clearance during reticulocyte maturation. Proc Natl Acad Sci U S A. 2007; 104(49):19500-19505.
16. Sandoval H, Thiagarajan P, Dasgupta SK, et al. Essential role for Nix in autophagic maturation of erythroid cells. Nature. 2008; 454(7201):232-235.
17. Chu CT, Ji J, Dagda RK, et al. Cardiolipin externalization to the outer mitochondrial membrane acts as an elimination signal for mitophagy in neuronal cells. Nat Cell Biol. 2013;15(10):1197-1205.
18. Kagan VE, Tyurina YY, Tyurin VA, et al. Cardiolipin signaling mechanisms: collapse of asymmetry and oxidation. Antioxid Redox Signal. 2015;22(18):1667-1680.
19. Morgan AH, Hammond VJ, Sakoh-Nakatogawa M, et al. A novel role for 12/15-lipoxygenase in regulating autophagy. Redox Biol. 2015;4:40-47.
20. Schewe T, Halangk W, Hiebsch C, Rapoport SM. A lipoxygenase in rabbit reticulocytes which attacks phospholipids and intact mitochondria. FEBS Lett. 1975;60(1):149-152.
21. Rapoport SM, Schewe T, Wiesner R, et al. The lipoxygenase of reticulocytes. Purification, characterization and biological dynamics of the lipoxygenase; its identity with the respiratory inhibitors of the reticulocyte. Eur J Biochem. 1979;96(3):545-561.
22. Rapoport SM, Schewe T. The maturational breakdown of mitochondria in reticulocytes. Biochim Biophys Acta. 1986;864(3-4):471-495.
23. Kuhn H, Brash AR. Occurrence of lipoxygenase products in membranes of rabbit reticulocytes. Evidence for a role of the reticulocyte lipoxygenase in the maturation of red cells. J Biol Chem. 1990;265(3):1454-1458.
24. van Leyen K, Duvoisin RM, Engelhardt H, Wiedmann M. A function for lipoxygenase in programmed organelle degradation. Nature. 1998;395(6700):392-395.
25. Grullich C, Duvoisin RM, Wiedmann M, van Leyen K. Inhibition of 15-lipoxygenase leads to delayed organelle degradation in the reticulocyte. FEBS Lett. 2001;489(1):51-54.
26. Sun D, Funk CD. Disruption of 12/15-lipoxygenase expression in peritoneal macrophages. Enhanced utilization of the 5-lipoxygenase pathway and diminished oxidation of low density lipoprotein. J Biol Chem. 1996;271(39):24055-24062.
27. Szebeni J, Winterbourn CC, Carrell RW. Oxidative interactions between haemoglobin and membrane lipid. A liposome model. Biochem J. 1984;220(3):685-692.
28. NaveenKumar SK, SharathBabu BN, Hemshekhar M, Kemparaju K, Girish KS, Mugesh G. The role of reactive oxygen species and ferroptosis in heme-mediated activation of human platelets. ACS Chem Biol. 2018;13(8):1996-2002.
29. Shah R, Shchepinov MS, Pratt DA. Resolving the role of lipoxygenases in the initiation and execution of ferroptosis. ACS Cent Sci. 2018;4(3):387-396.
30. Yant LJ, Ran Q, Rao L, et al. The selenoprotein GPX4 is essential for mouse development and protects from radiation and oxidative damage insults. Free Radic Biol Med. 2003;34(4):496-502.
31. Friedmann Angeli JP, Schneider M, Proneth B, et al. Inactivation of the ferroptosis regulator Gpx4 triggers acute renal failure in mice. Nat Cell Biol. 2014;16(12):1180-1191.
32. Hameyer D, Loonstra A, Eshkind L, et al. Toxicity of ligand-dependent Cre recombinases and generation of a conditional Cre deleter mouse allowing mosaic recombination in peripheral tissues. Physiol Genomics. 2007;31(1):32-41.
33. Higashi AY, Ikawa T, Muramatsu M, et al. Direct hematological toxicity and illegitimate chromosomal recombination caused by the systemic activation of CreERT2. J Immunol. 2009;182(9):5633-5640.
34. Loonstra A, Vooijs M, Beverloo HB, et al. Growth inhibition and DNA damage induced by Cre recombinase in mammalian cells. Proc Natl Acad Sci U S A. 2001;98(16):9209-9214.
35. Zhu J, Nguyen MT, Nakamura E, Yang J, Mackem S. Cre-mediated recombination can induce apoptosis in vivo by activating the p53 DNA damage-induced pathway. Genesis. 2012;50(2):102-111.
36. Janbandhu VC, Moik D, Fassler R. Cre recombinase induces DNA damage and tetraploidy in the absence of loxP sites. Cell Cycle. 2014;13(3):462-470.
37. Pepin G, Ferrand J, Honing K, et al. Cre-dependent DNA recombination activates a STING-dependent innate immune response. Nucleic Acids Res. 2016;44(11): 5356-5364.
38. Huh WJ, Khurana SS, Geahlen JH, Kohli K, Waller RA, Mills JC. Tamoxifen induces rapid, reversible atrophy, and metaplasia in mouse stomach. Gastroenterology. 2012; 142(1):21-24.
39. Velasco-Hernandez T, Sawen P, Bryder D, Cammenga J. Potential pitfalls of the Mx1-Cre system: implications for experimental modeling of normal and malignant Hematopoiesis. Stem Cell Reports. 2016; 7(1):11-18.

40. Kiermayer C, Conrad M, Schneider M, Schmidt J, Brielmeier M. Optimization of spatiotemporal gene inactivation in mouse heart by oral application of tamoxifen citrate. Genesis. 2007;45(1):11-16.
41. Rathkolb B, Fuchs H, Gailus-Durner V, Aigner B, Wolf E, Hrabe de Angelis M. Blood collection from mice and hematological analyses on mouse blood. Curr Protoc Mouse Biol. 2013;3(2):101-119.
42. Lenox LE, Perry JM, Paulson RF. BMP4 and Madh5 regulate the erythroid response to acute anemia. Blood. 2005;105(7):2741-2748.
43. Harandi OF, Hedge S, Wu DC, McKeone D, Paulson RF. Murine erythroid short-term radioprotection requires a BMP4-dependent, self-renewing population of stress erythroid progenitors. J Clin Invest. 2010;120(12):4507-4519.
44. Chasis JA, Mohandas N. Erythroblastic islands: niches for erythropoiesis. Blood. 2008;112(3):470-478.
45. Clausen BE, Burkhardt C, Reith W, Renkawitz R, Forster I. Conditional gene targeting in macrophages and granulocytes using LysMcre mice. Transgenic Res. 1999;8(4):265-277.
46. Wortmann M, Schneider M, Pircher J, et al. Combined deficiency in glutathione peroxidase 4 and vitamin E causes multiorgan thrombus formation and early death in mice. Circ Res. 2013;113(4):408-417.
47. Matsushita M, Freigang S, Schneider C, Conrad M, Bornkamm GW, Kopf M. T cell lipid peroxidation induces ferroptosis and prevents immunity to infection. J Exp Med. 2015;212(4):555-568.
48. Carlson BA, Tobe R, Yefremova E, et al. Glutathione peroxidase 4 and vitamin E cooperatively prevent hepatocellular degeneration. Redox Biol. 2016;9:22-31.
49. Chen K, Liu J, Heck S, et al. Resolving the distinct stages in erythroid differentiation based on dynamic changes in membrane protein expression during erythropoiesis. Proc Natl Acad Sci U S A. 2009; 106(41):17413-17418.
50. Marsee DK, Pinkus GS, Yu H. CD71 (transferrin receptor): an effective marker for erythroid precursors in bone marrow biopsy specimens. Am J Clin Pathol. 2010; 134(3):429-435.
51. Rivella S. Ineffective erythropoiesis and thalassemias. Curr Opin Hematol. 2009; 16(3):187-194.
52. Kautz L, Jung G, Valore EV, Rivella S, Nemeth E, Ganz T. Identification of erythroferrone as an erythroid regulator of iron metabolism. Nat Genet. 2014; 46(7):678-684.
53. Yang WS, SriRamaratnam R, Welsch ME, et al. Regulation of ferroptotic cancer cell death by GPX4. Cell. 2014;156(1-2):317-331.
54. Kagan VE, Mao G, Qu F, et al. Oxidized arachidonic and adrenic PEs navigate cells to ferroptosis. Nat Chem Biol. 2017;13(1):81-90.
55. Canli O, Alankus YB, Grootjans S, et al. Glutathione peroxidase 4 prevents necroptosis in mouse erythroid precursors. Blood. 2016;127(1):139-148.
56. Frudd K, Burgoyne T, Burgoyne JR. Oxidation of Atg3 and Atg7 mediates inhibition of autophagy. Nat Commun. 2018;9(1):95.
57. Kautz L, Jung G, Du X, et al. Erythroferrone contributes to hepcidin suppression and iron overload in a mouse model of beta-thalassemia. Blood. 2015;126(17):2031-2037.
58. Tappel AL. Unsaturated lipide oxidation catalyzed by hematin compounds. J Biol Chem. 1955;217(2):721-733.
59. Rachmilewitz EA, Shohet SB, Lubin BH. Lipid membrane peroxidation in beta-thalassemia major. Blood. 1976;47(3):495-505.
60. Rachmilewitz EA, Shifter A, Kahane I. Vitamin E deficiency in beta-thalassemia major: changes in hematological and biochemical parameters after a therapeutic trial with alpha-tocopherol. Am J Clin Nutr. 1979;32(9):1850-1858.
61. Rachmilewitz EA, Kornberg A, Acker M. Vitamin E deficiency due to increased consumption in beta-thalassemia and in Gaucher's disease. Ann N Y Acad Sci. 1982; 393:336-347.
62. Fibach E, Rachmilewitz EA. The role of antioxidants and iron chelators in the treatment of oxidative stress in thalassemia. Ann N Y Acad Sci. 2010;1202:10-16.
63. Livrea MA, Tesoriere L, Pintaudi AM, et al. Oxidative stress and antioxidant status in beta-thalassemia major: iron overload and depletion of lipid-soluble antioxidants. Blood. 1996;88(9):3608-3614.
64. Giardini O, Cantani A, Donfrancesco A, et al. Biochemical and clinical effects of vitamin E administration in homozygous beta-thalassemia. Acta Vitaminol Enzymol. 1985;7(1-2):55-60.
65. Tesoriere L, D'Arpa D, Butera D, et al. Oral supplements of vitamin E improve measures of oxidative stress in plasma and reduce oxidative damage to LDL and erythrocytes in beta-thalassemia intermedia patients. Free Radic Res. 2001;34(5):529-540.
66. Holm TM, Braun A, Trigatti BL, et al. Failure of red blood cell maturation in mice with defects in the high-density lipoprotein receptor SR-BI. Blood. 2002;99(5):1817-1824.

ARTICLE

Genomic profiling of primary histiocytic sarcoma reveals two molecular subgroups

Caoimhe Egan,[1] Alina Nicolae,[1] Justin Lack,[2] Hye-Jung Chung,[1] Shannon Skarshaug,[1] Thu Anh Pham,[1] Winnifred Navarro,[1] Zied Abdullaev,[1] Nadine S. Aguilera,[3] Liqiang Xi,[1] Svetlana Pack,[1] Stefania Pittaluga,[1] Elaine S. Jaffe[1] and Mark Raffeld[1]

[1]Laboratory of Pathology, National Cancer Institute, National Institutes of Health, Bethesda, MD; [2]NIAID Collaborative Bioinformatics Resource (NCBR), National Institute of Allergy and Infectious Diseases, National Institutes of Health, Bethesda, MD and [3]University of Virginia Health System, Charlottesville, VA, USA

Ferrata Storti Foundation

Haematologica 2020
Volume 105(4):951-960

ABSTRACT

Histiocytic sarcoma is a rare malignant neoplasm that may occur *de novo* or in the context of a previous hematologic malignancy or mediastinal germ cell tumor. Here, we performed whole exome sequencing and RNA-sequencing (RNA-Seq) on 21 archival cases of primary histiocytic sarcoma. We identified a high number of genetic alterations within the RAS/RAF/MAPK pathway in 21 of 21 cases, with alterations in *NF1* (6 of 21), *MAP2K1* (5 of 21), *PTPN11* (4 of 21), *BRAF* (4 of 21), *KRAS* (4 of 21), *NRAS* (1 of 21), and *LZTR1* (1 of 21), including single cases with homozygous deletion of *NF1*, high-level amplification of *PTPN11*, and a novel *TTYH3-BRAF* fusion. Concurrent *NF1* and *PTPN11* mutations were present in 3 of 21 cases, and 5 of 7 cases with alterations in *NF1* and/or *PTPN11* had disease involving the gastrointestinal tract. Following unsupervised clustering of gene expression data, cases with *NF1* and/or *PTPN11* abnormalities formed a distinct tumor subgroup. A subset of *NF1/PTPN11* wild-type cases had frequent mutations in B-cell lymphoma associated genes and/or clonal IG gene rearrangements. Our findings expand the current understanding of the molecular pathogenesis of this rare tumor and suggest the existence of a distinct subtype of primary histiocytic sarcoma characterized by *NF1/PTPN11* alterations with predilection for the gastrointestinal tract.

Introduction

Histiocytic sarcoma (HS) is a rare and aggressive malignant neoplasm that has morphological and immunophenotypic features of mature tissue histiocytes.[1] It predominantly occurs in adulthood, although any age may be affected. Sites of involvement may be nodal or extranodal, and include the gastrointestinal (GI) tract, skin, and liver.[2] Histologically, the tumor cells are usually pleomorphic with cytologic atypia and can be multinucleated or have a spindled or xanthomatous morphology. The diagnosis of HS requires the demonstration of histiocytic markers (CD68, CD163, CD4 or lysozyme) and the exclusion of tumors of other lineages by negativity of immunohistochemical stains for Langerhans cells (CD1a, langerin), follicular dendritic cells (CD21, CD23, clusterin), B and T cells, cells of myeloid or epithelial lineage (MPO, CK), and melanocytic markers.[3,4]

Histiocytic sarcoma may arise as a primary neoplasm (pHS), but is also well described in the context of an existing or concurrently diagnosed hematologic malignancy, most frequently a follicular lymphoma, but also chronic lymphocytic leukemia (CLL) and B- or T-lymphoblastic leukemia (B-ALL/T-ALL).[5-9] Rare cases have also been associated with mediastinal germ cell tumor.[3] Cases arising in the context of a lymphoid neoplasm are often referred to as "secondary" HS (sHS), and frequently possess identical clonal antigen receptor gene rearrangements or occasionally identical structural events (e.g. identical IGH/*BCL2* rearrangements) as in the associated lymphoma. However, on histological and immunophenotypic

Correspondence:

MARK RAFFELD
mraff@mail.nih.gov

Received: June 25, 2019.

Accepted: August 21, 2019.

Pre-published: August 22, 2019.

doi:10.3324/haematol.2019.230375

Check the online version for the most updated information on this article, online supplements, and information on authorship & disclosures: www.haematologica.org/content/105/4/951

examination they have no other evidence of lymphoid origin.[5,6,10] Rather, these cases express markers of histiocytic/monocytic differentiation, but are nonetheless thought to be related to the associated B-cell neoplasm through a poorly understood process sometimes referred to as transdifferentiation[5] or origin from a common neoplastic progenitor.[11] Interestingly, the presence of clonal IG gene rearrangements or a *BCL2* translocation is not restricted to secondary cases associated with a B-cell malignancy, as both abnormalities have also been observed in sporadic or "primary" cases of HS.[12,13]

In contrast to the more comprehensive studies performed in other histiocytic tumors, especially Langerhans cell histiocytosis and Erdheim-Chester disease,[14-17] until recently, molecular analysis of HS has remained relatively underexplored.[18] *BRAF* p.V600E mutations have been reported in approximately 12% of 108 published cases with molecular or immunohistochemical data, and additional alterations in members of the RAS/MAPK and PI3K/AKT pathways, including other *BRAF* variants, *KRAS, HRAS, NRAS, MAP2K1, PIK3CA, PTPN11* and *PTEN* are also described (see *Online Supplementary Tables S1* and *S2* for a complete list of references). The distinction between pHS and sHS is often not clearly defined in these studies. To better understand the genetic landscape of alterations in a well-characterized series of pHS, we performed an integrated genomic analysis of 21 cases utilizing whole exome sequencing, whole transcriptome sequencing, and copy number analysis. Cases of sHS were intentionally excluded from this study.

Methods

Case selection, IGH/*BCL2* and clonality studies

Twenty-one cases of pHS were identified from the files of the Hematopathology Section of the National Cancer Institute under an Institutional Review Board approved protocol (*Online Supplementary Methods*). The histological and immunophenotypic features and clonality characteristics of the cases are detailed in Figure 1 and *Online Supplementary Table S3*. DNA and RNA were isolated from formalin-fixed paraffin embedded (FFPE) tissue. Immunoglobulin (IGH and IGK) and T-cell receptor (TRG) gene rearrangement studies were performed in 19 of 21 cases and IGH/*BCL2* (MBR) translocation analysis in 17 of 21 cases (*Online Supplementary Methods*).

Whole exome sequencing

Samples were sequenced in two groups: an initial cohort of 15 tumor samples with two matched normal samples on an Illumina HiSeq2500 with TruSeq V4 chemistry and a subsequent cohort of six tumor samples with one matched normal sample on an Illumina HiSeq3000 with TruSeq V2 chemistry (Illumina, San Diego, CA, USA). Alignment and variant calling were performed following the Center for Cancer Research Collaborative Bioinformatics Resource (CCBR) pipeline (*https://github.com/CCBR/Pipeliner*) as described in the *Online Supplementary Methods*.

Variant analysis

Germline variants were excluded in three cases with available matched normal samples. Exonic variants with a depth of coverage ≥ 20 and a read count ≥ 6 were retained. As matched germline samples were unavailable for most cases, we generated a targeted gene list to reduce the number of variants for review. Genes were compiled from the COSMIC Cancer Gene Census (*http://cancer.sanger.ac.uk*)[19] and literature review to select disease relevant genes with a potential oncogenic role. The list was supplemented with additional genes identified by filtering the exome sequencing data to include recurrently mutated genes (≥ 3 samples) after removing variants based on CADD phred-like scores[20] and population allele frequencies (*Online Supplementary Methods*). All variants involving genes in the targeted gene list were evaluated and categorized as significant based on set criteria (*Online Supplementary Methods* and *Online Supplementary Figure S1*). Variants not meeting the set criteria were excluded. Mutations were reviewed in the Integrative Genomics Viewer (IGV).[21]

RNA sequencing

Details of RNA library preparation, sequencing and fusion detection are described in the *Online Supplementary Methods*. RNA-Seq analysis was conducted using the CCBR RNA-Seq pipeline *(https://github.com/CCBR/Pipeliner*). Gene set enrichment analysis was performed using Ensemble of Gene Set Enrichment Analyses (EGSEA data version: 1.6.0)[22] and sorted by average rank.

Copy number analysis

Nine samples were successfully assessed using the OncoScan CNV FFPE Assay (Affymetrix, Santa Clara, CA, USA) according to the manufacturer's protocol. Copy number was estimated from the exome sequencing data in the remaining cases using default settings for CNVkit v0.8.5[23] and PureCN v1.8.1.[24] Calls from CNVkit were exported in nexus.ogt format for review and annotation in Nexus 9.0 Software (BioDiscovery, Hawthorne, CA, USA). Alterations called by both algorithms were further analyzed as described in the *Online Supplementary Methods*.

Data sharing

All genomic data from this study will be deposited in the dbGaP database (*www.ncbi.nlm.nih.gov/gap*) with the accession number phs001748.v1.p1.

Results

Primary histiocytic sarcoma is characterized by frequent alterations involving the RAS/MAPK pathway

Whole exome sequencing was performed on 21 cases of pHS as defined in the *Online Supplementary Methods*, and on three matched normal controls (His01, His08, His16), in two groups. The median coverage in the first 15 cases ranged from 106-165x, and in the second six cases from 205-305x. Sequencing depth for the three matched controls ranged from 72-143x. Variants were filtered as described in the *Online Supplementary Methods* using stringent criteria, and all candidates were individually reviewed in IGV.

Multiple and occasionally concurrent mutations involving genes of the RAS/MAPK pathway (Figure 2, *Online Supplementary Table S4* and *Online Supplementary Figure S2*) were identified in 19 of the 21 cases. The most frequently mutated RAS/MAPK pathway genes were *NF1* and *MAP2K1* (5 cases each). Interestingly, 4 of 5 cases with *NF1* mutations involved the GI tract, although one biopsy sequenced was a supraclavicular lymph node. Three of the cases had a single *NF1* mutation (p.Q1822* [His01]; p.V1182D [His02]; p.Q1086* [His16]), whereas the other two had two mutations each (p.R304* and p.Q1775* [His12]; p.L298* and p.K660fs [His17]). Six of the seven variants were nonsense mutations or frameshift deletions

and therefore predicted to be inactivating. The single missense mutation (p.V1182D) was predicted to be deleterious or probably damaging by functional impact algorithms SIFT[25] and PolyPhen-2.[26] In addition to *NF1* mutations, 3 of the 5 cases showed concurrent mutations in *PTPN11* (p.F71V [His01]; p.E76G [His02]; p.A72V [His12]). *PTPN11* mutations were present within the autoinhibitory N-SH2 domain at amino acid residues known to be associated with a gain-of-function consequence and described in Noonan syndrome and juvenile myelomonocytic leukemia (JMML).[27,28] One case without a *PTPN11* mutation [His17] had an additional mutation in *GNAI2* at p.R179H, a codon previously shown to be targeted by activating mutations[29] and 1 of the 5 *NF1* mutated cases also had a mutation in *JAK2* at p.V617F [His12]. A fourth *PTPN11* mutated case at p.E76K [His18] did not have another RAS pathway mutation; however, it had high level amplification of the mutated *PTPN11* allele (*see below*).

Additional mutations involving the RAS/MAPK pathway were detected in another 13 cases, none of which had

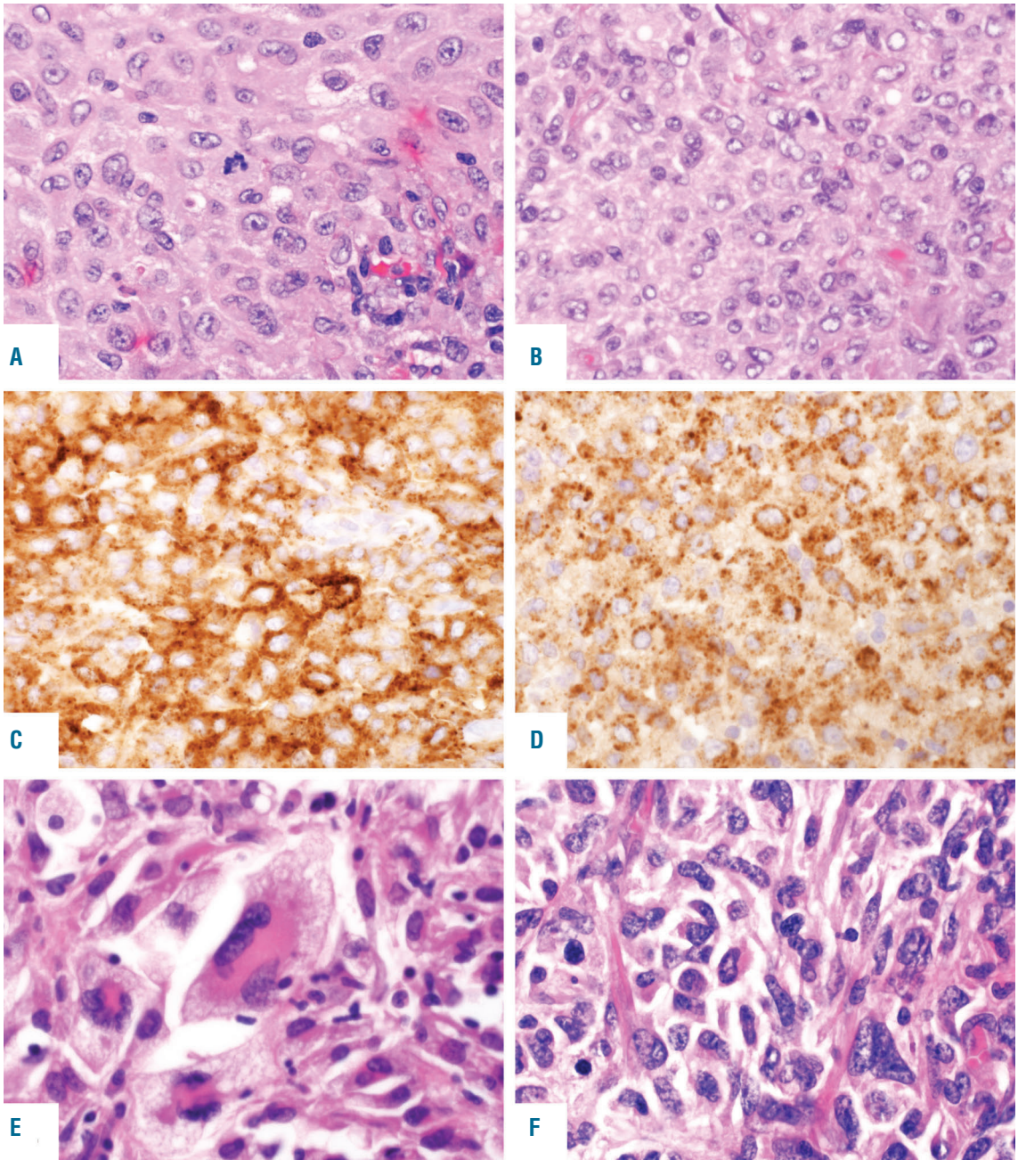

Figure 1. Histological features of primary histiocytic sarcoma (pHS). Cases involving lymph node (A) and tonsil (B) showing moderate nuclear atypia and abundant eosinophilic cytoplasm; Hematoxylin & Eosin (H&E) staining, original magnification x400. The cells express (C) CD163; original magnification x400 and (D) CD68; original magnification x400. (E and F) Two extranodal (gastrointestinal tract) cases showing marked nuclear pleomorphism, multinucleated cells and foam cells; H&E stain, original magnification x400.

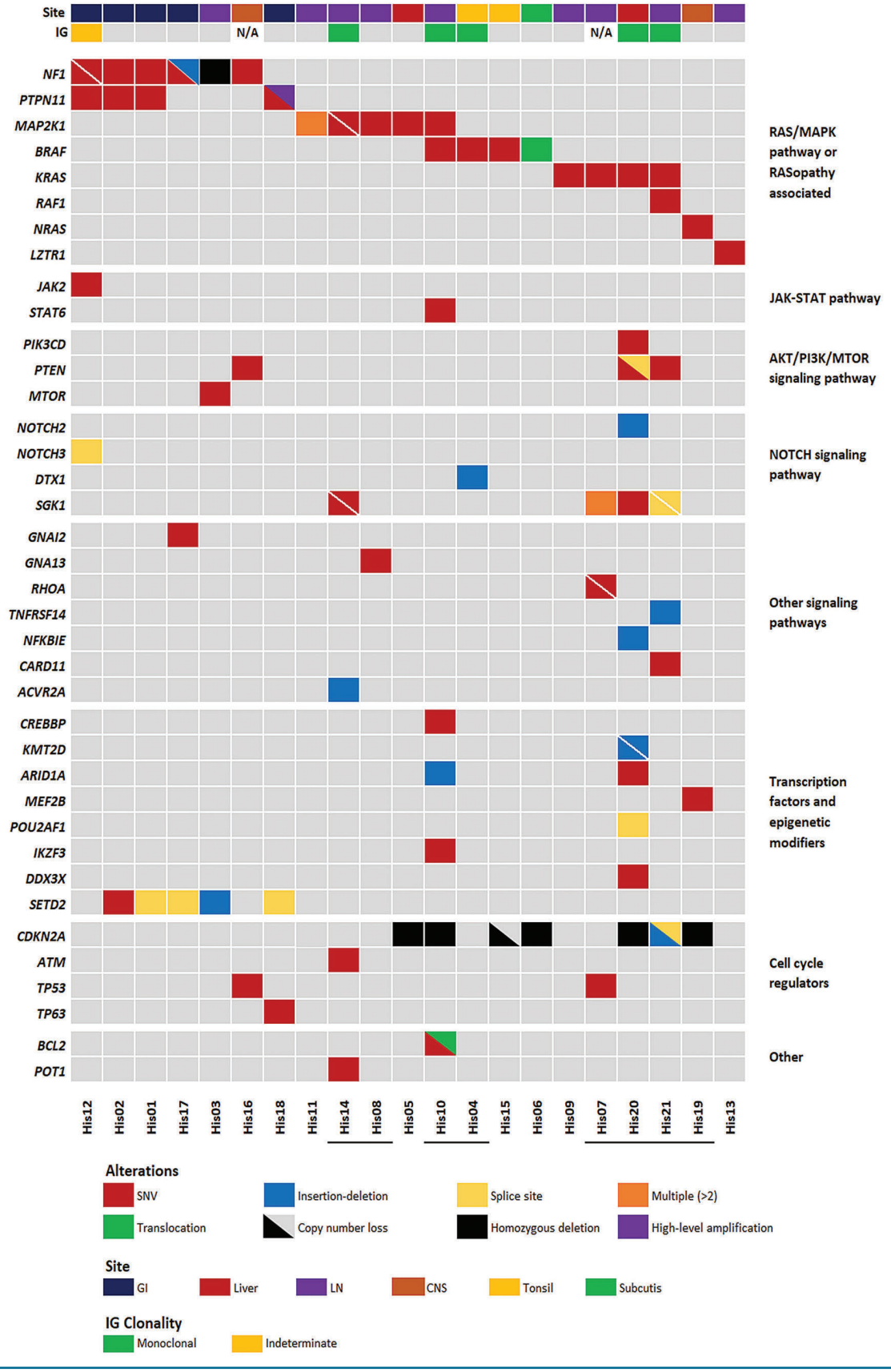

Figure 2. Selected molecular alterations in primary histiocytic sarcoma (pHS) cases. Genes are listed in the rows and organized by pathway or function. Samples are listed in columns. Site and IG gene rearrangement status are indicated in the top annotation bar. Underlined sample labels indicate a case with a B-cell lymphoma associated mutation or clonal IG gene rearrangement. Annotated focal copy number alterations and translocations were detected by OncoScan and/or verified by fluorescence *in situ* hybridization or polymerase chain reaction. GI: gastrointestinal tract; LN: lymph node; CNS: central nervous system.

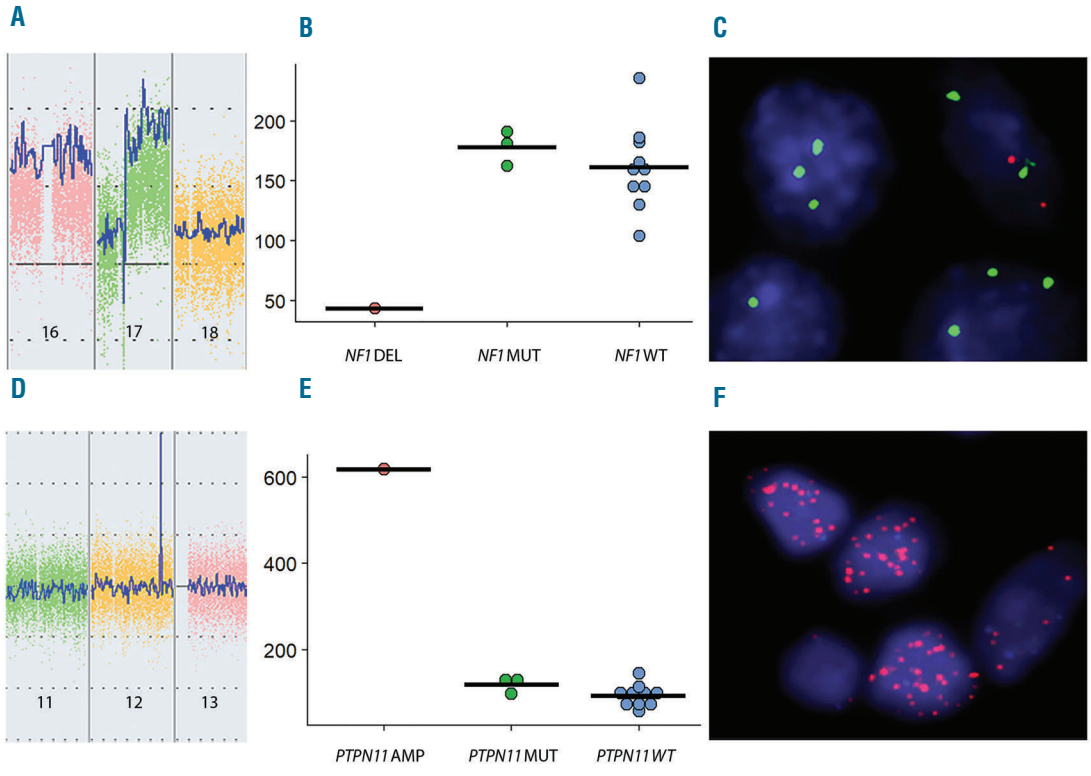

Figure 3. *NF1* homozygous deletion. (A) Inverted peak in chromosome 17 consistent with homozygous deletion of *NF1* (ChAS 3.3). (B) Reduction in *NF1* transcript in the case with homozygous deletion (DEL) compared with *NF1* mutated (MUT) and wild-type (WT) cases [normalized RNA-sequencing (RNA-Seq) count data]. (C) Fluorescence *in situ* hybridization (FISH) showing multiple copies of the CEP 17 probe (green) with loss of the *NF1* probe (orange) (D-F). *PTPN11* amplification. (D) Peak in chromosome 12 consistent with high-level amplification of *PTPN11* (ChAS 3.3). (E) Increased *PTPN11* transcript in the amplified (AMP) case compared with *PTPN11* mutated (MUT) and wild-type (WT) cases (normalized RNA-Seq count data). (F) FISH showing multiple copies of the *PTPN11* gene (orange) in a double minute pattern.

NF1 or *PTPN11* mutations. *MAP2K1* mutations were present in five cases and involved known hotspot regions in exons 2 and 3, the negative regulatory region (p.F53L [His10, His14]; p.K57E [His05]) and the catalytic core domain (p.I103N [His14]; p.C121S [His08, His11]).[30] As well as the mutation at p.C121S, case [His11] had two additional *MAP2K1* mutations at p.Y125C and p.R181K. The functional consequences of these mutations are not known; however, the p.Y125C substitution also involved the catalytic core domain in the same allele as the pathogenic p.C121S mutation. One case with a *MAP2K1* mutation had a co-occurring non-canonical *BRAF* mutation (p.G469V [His10]) and two additional cases had *BRAF* p.V600E [His04 and His15] mutations. Pathogenic *KRAS* mutations were detected in four cases (p.G12D [His21]; p.G12C [His09]; p.Q61H [His07] and p.A146V [His20]), one of which, [His21] also had a mutation in *RAF1* (p.D486G). A single case had an *NRAS* mutation at p.Q61R [His19]. Finally, a mutation in *LZTR1* (p.R118H) was identified in case [His13]. *LZTR1* encodes an adaptor for CUL3 ubiquitin ligase complexes[31] and is implicated in Noonan syndrome,[32,33] malignancy[31] and schwannomatosis.[34] Mutations in *LZTR1* have recently been shown to dysregulate RAS ubiquitination leading to increased RAS activity.[35] The p.R118H mutation affects a conserved residue in the Kelch domain and is reported once in the COSMIC database. Mutations in *LZTR1* are not typically associated with histiocytic tumors. This case met our inclusion criteria, but notably had some atypical features including aberrant expression of perforin and CD7 and a clonal TRG gene rearrangement.

Mutations involving the PI3K pathway were identified in four cases, including two with *KRAS* mutations and two with *NF1* alterations, with mutations identified in *PTEN* (p.Q171* [His16]; p.D24H and c.79+1G>C [His20] and p.L140* [His21]), *PIK3CD* (p.E1021K [His20]) and *MTOR* (p.I2501F [His03]). Additional mutations in genes previously reported to be mutated in B-cell lymphomas were detected in *SGK1* (p.R285K, p.I238T, p.H237Y, p.K213R and p.P147S [His07]; p.E162G and p.K136R [His14]; p.Q125H [His20]; c.437+1G>A and c.362-1G>A [His21]), *NOTCH2* (p.I2304fs [His20]), *DTX1* (p.W37* [His04]), *TNFRSF14* (p.T169fs [His21]), *CARD11* (p.R179Q [His21]), *NFKBIE* (p.L410fs [His20]), *GNA13* (p.F4V [His08]), *POT1* (p.R273W [His14]) and *BCL2* (p.E136D [His10]).[36-40]

In addition to mutations in the signaling pathways described above, mutations in epigenetic modifiers and/or transcription factors were detected in eight cases, including five with *SETD2* mutations (c.7432-2A>C [His01]; p.V1820E [His02]; p.P132fs [His03]; c.4715+1G>T [His17] and c.7432-1G>A [His18]), two with *ARID1A* mutations (p.L2011fs [His10] and p.G2087R [His20]) and single cases with *CREBBP* (p.Y1433C [His10]), *KMT2D* (p.E2225fs and p.K1752fs [His20]), *DDX3X* (p.V206M [His20]), *POU2AF1* (c.16+2T>G [His20]), *IKZF3* (p.L162R [His10]), *STAT6*

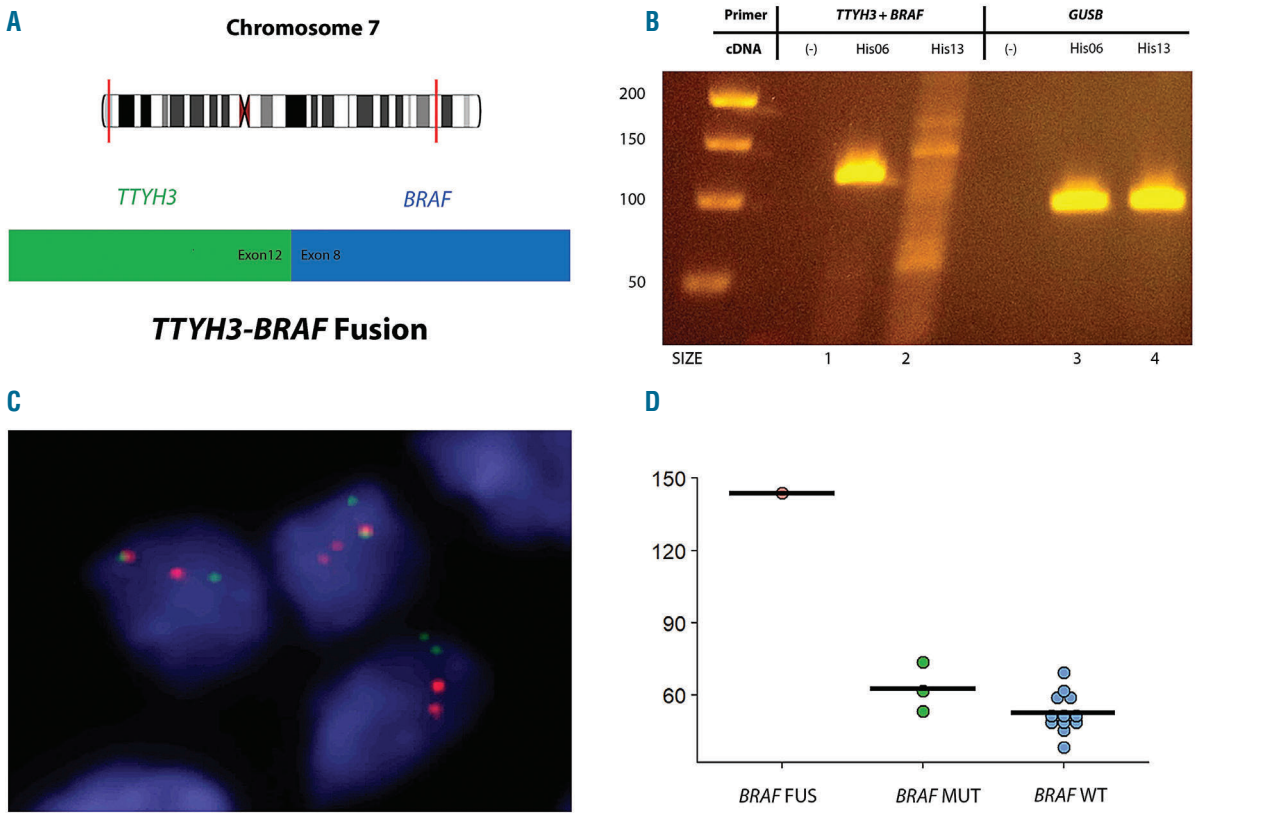

Figure 4. *TTYH3-BRAF* fusion. (A) Diagram of the intrachromosomal fusion on chromosome 7 of *TTYH3* (exon 12) to *BRAF* (exon 8). (B) Gel electrophoresis of the reverse transcription polymerase chain reaction confirming the presence of the *TTYH3-BRAF* fusion in Lane 1. (Lane 2 – Negative control; Lanes 3 and 4 – Positive controls). (C) Demonstration of split signals by fluorescence *in situ* hybridization, indicating a *BRAF* translocation (*BRAF* break apart probe, orange – 3'; green – 5'). (D) Increased *BRAF* transcript in the case with the fusion (FUS) compared with *BRAF* mutated (MUT) and wild-type (WT) cases (normalized RNA-Seq count data).

(p.D419G [His10]) and *MEF2B* (p.R64H [His19]) mutations. *SETD2* mutations were exclusive to the *NF1/PTPN11* mutated group, including one case found to have homozygous deletion of *NF1* and one case with *PTPN11* gene amplification (both described below), while the *ARID1A, CREBBP, KMT2D, DDX3X, IKZF3, STAT6* and *MEF2B* mutations were present in the *NF1/PTPN11* wild-type group. Known pathogenic mutations in *TP53* were identified in 2 of 21 cases (p.G245S [His07]; p.R175H [His16]).

Copy number analysis shows additional alterations in *NF1, PTPN11* and *CDKN2A*

A homozygous deletion in the *NF1* gene was identified in an additional case [His03] from a lymph node and confirmed using a fluorescence *in situ* hybridization (FISH) probe targeting the deleted area. RNA-Seq data showed markedly lower counts of *NF1* transcript in this case in comparison to the other samples, consistent with loss of *NF1* (Figure 3A-C). The three cases with a single *NF1* mutation [His01, His02 and His16] showed loss-of-heterozygosity (LOH) or copy number loss involving chromosome 17 including the *NF1* gene.

Interestingly, a focal high-level amplification in chromosome 12 targeting *PTPN11* was discovered in a further case [His18] involving the GI tract. This case harbored a known variant in the N-SH2 domain (p.E76K) of the amplified *PTPN11* allele. In contrast to the other *PTPN11* mutated cases, no mutation of *NF1* was detected by exome sequencing. This high-level amplification was confirmed by FISH which showed multiple copies of the *PTPN11* gene in the tumor cells in a double minute pattern. The amplified segment involved the entire *PTPN11* gene, with the breakpoints identified by OncoScan in an adjacent gene, *RPH3A*, and 5' to *PTPN11* involving *HECTD4* on the complementary strand. This event was associated with a dramatic increase in *PTPN11* transcripts in comparison to the other cases (Figure 3D-F).

Cases with *NF1/PTPN11* alterations had associated losses or LOH of chromosome 10 or 10q and chromosome 17 or 17p in 3 of 5 cases assessed by OncoScan [His01, His02, His12] and confirmed by FISH in two cases (*Online Supplementary Figure S3A-C*). Focal *CDKN2A* losses were present by OncoScan or confirmed by FISH in six cases that were *NF1/PTPN11* wild-type [His05, His06, His10, His15, His19, His20] and included five cases with homozygous deletion [His05, His06, His10, His19, His20]. All homozygous deletions were confirmed by FISH (*Online Supplementary Figure S3D and E*). Both *TP53* mutated cases had LOH involving the gene, with one *NF1* mutated case [His16, not assessed by OncoScan] showing a near-haploid genome with loss of chromosome 17 and the second case [His07] showing LOH at chromosome 17p.

Identification of a novel *TTYH3-BRAF* fusion

Fusion calling of RNA-Seq data identified a novel intrachromosomal fusion transcript between exon 12 of

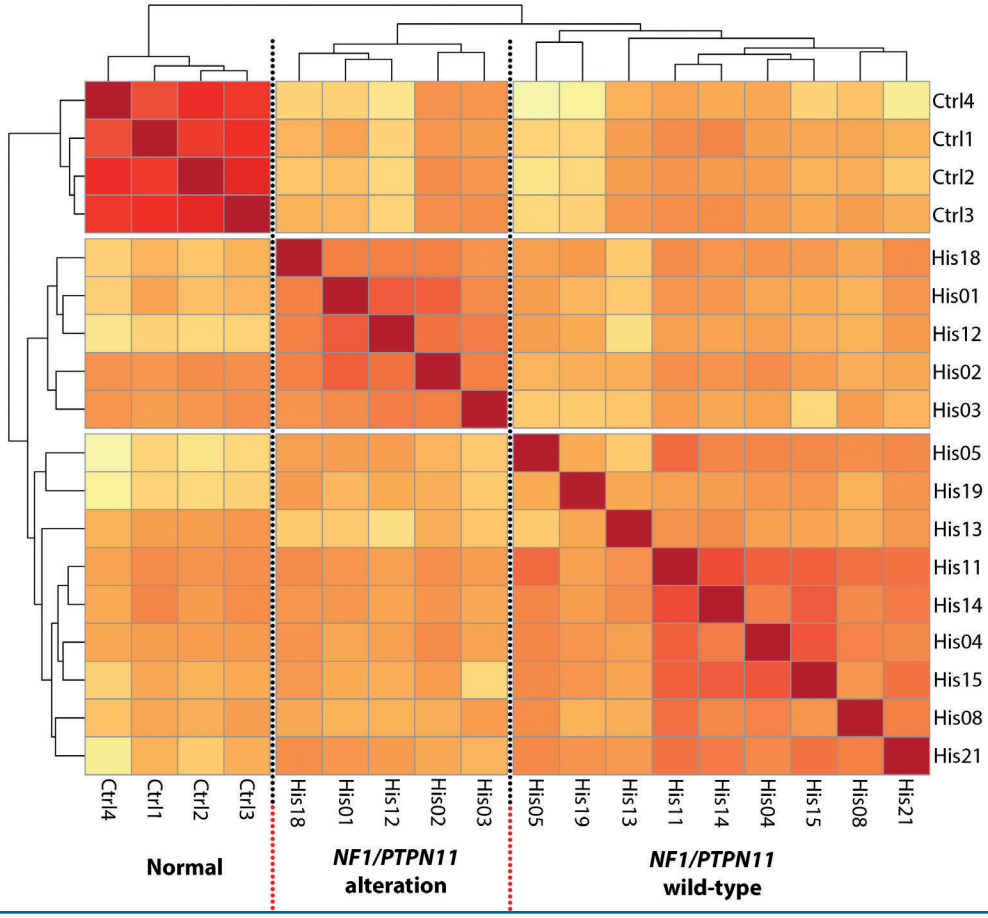

Figure 5. Exploratory analysis of RNA-sequencing (RNA-Seq) data. Unsupervised clustering based on transcriptome-wide gene expression and using Euclidean distance with complete linkage identifies three clusters corresponding to the normal samples, tumor samples with alterations in *NF1/PTPN11* and the remaining *NF1/PTPN11* wild-type tumor samples.

TTYH3 and exon 8 of *BRAF* on chromosome 7 in a case without any other known driver mutation [His06]. This novel *TTYH3-BRAF* fusion has a similar structure to other reported *BRAF* fusions,[41,42] with replacement of the RAS-binding domain of *BRAF* by a 5' fusion partner, in this case, a chloride ion channel gene, *TTYH3* (Figure 4A). The presence of the fusion transcript was confirmed by reverse transcription polymerase chain reaction (RT-PCR) using primers for exon 12 of *TTYH3* and exon 8 of *BRAF* (Figure 4B), as well as by FISH (Figure 4C). Interestingly, RNA-Seq data showed markedly higher levels of *BRAF* transcript as compared to all other samples, suggesting that the *TTYH3* gene partner contributed an active promoter to the fusion gene (Figure 4D). *TTYH3* was found to be highly expressed in all cases with RNA-Seq data (*data not shown*).

Identification of two primary histiocytic sarcoma subgroups by whole transcriptome sequencing: association with *NF1/PTPN11* mutational status

We examined the gene expression profile of pHS through whole transcriptome sequencing of 17 of the tumor samples using four cases of reactive nodal histiocytic infiltrates as controls. Three of the 17 tumor samples initially sequenced were excluded from the differential expression analysis as they failed quality control metrics and/or were outliers within the tumor group [His10] or within the data as a whole [His06, His09] (*Online Supplementary Figure S4*). Re-clustering segregated the remaining samples into three groups: normal controls (4 samples), cases with *NF1* or *PTPN11* abnormalities (5 samples), and a third heterogeneous group comprising *NF1/PTPN11* wild-type cases (9 samples) (Figure 5).

Gene set enrichment analysis shows enrichment of cell cycle processes in cases without *NF1/PTPN11* abnormalities

To better understand the potential biological significance of the two pHS subgroups, we performed gene set enrichment analysis using EGSEA. This analysis showed significant enrichment of cell cycle pathway and cell proliferation gene sets in the *NF1/PTPN11* wild-type tumor samples relative to samples with *NF1/PTPN11* alterations. Ki67 immunohistochemistry was performed on a subset of cases and confirmed the lower proliferation rate in the *NF1/PTPN11* subgroup (Figure 6 and *Online Supplementary Table S3*).

The two tumor subgroups were also evident in the differential expression analysis comparing the normal and tumor samples when the genes with significant differential expression (FDR < 0.05, absolute log fold change > 1) were visualized across samples (*Online Supplementary Table S5* and *Online Supplementary Figure S5*). We took advantage of this to explore the possibility that disease site might be influencing the clustering of the tumor sub-

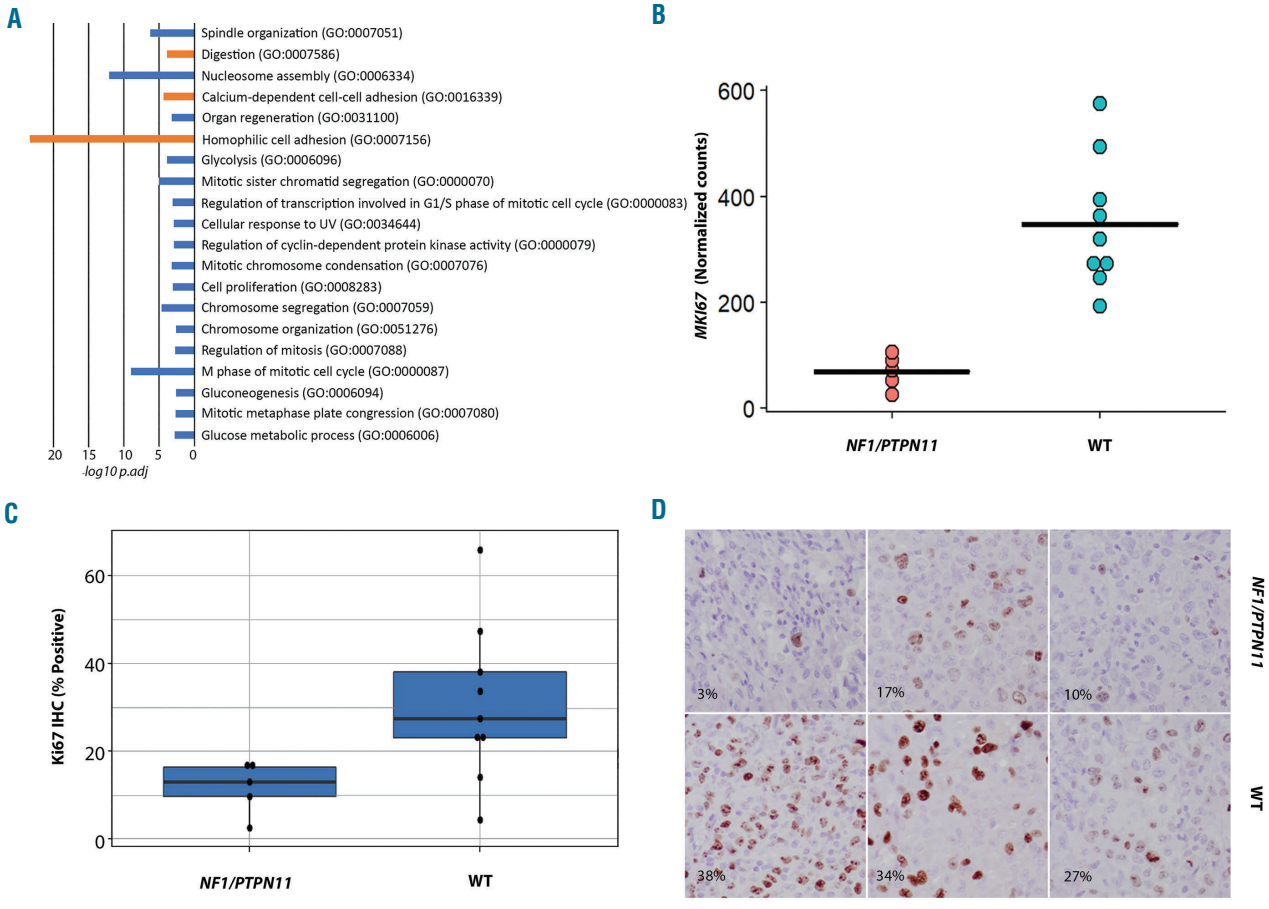

Figure 6. Cell cycle and proliferation. (A) The -log10 adjusted *P*-values of the top 20 GO Biological Processes (GeneSetDB Gene Ontology) by gene set enrichment analysis using EGSEA, sorted by average rank. There is enrichment for cell cycle and proliferation-related processes in the *NF1/PTPN11* wild-type (WT) cases (blue) relative to the cases with *NF1/PTPN11* alterations. (B) Normalized counts from RNA-sequencing data showing differences in *MKI67* transcript between the *NF1/PTPN11* altered and *NF1/PTPN11* WT groups. (C) Bar plot of the difference in proliferation index between the tumor subgroups by Ki67 immunohistochemistry. (D) Photomicrograph showing immunohistochemical expression of Ki67 in the tumor subgroups.

groups, as four of the five *NF1/PTPN11* samples subjected to unsupervised clustering were GI excisions. When we excluded genes associated with GI site from this tumor *versus* normal comparison, the two tumor subclusters were unaffected; however, a set of genes that were more clearly differentially expressed between the tumor subgroups were revealed that upon removal resulted in the elimination of the tumor subgroups. Functional enrichment of this set of genes using ToppFun (*https://toppgene.cchmc.org*) showed enrichment for cell cycle processes, supporting the EGSEA result and the interpretation that the observed clustering was related to the difference in cell cycle processes between tumor groups rather than the tumor site (*Online Supplementary Tables S6-S8* and *Online Supplementary Figures S6 and S7*).

Correlation of clonal IG rearrangement status and B-cell associated mutations with *NF1/PTPN11* wild-type status

Clonal analysis to detect rearrangements of IG and TRG genes was performed on 19 of 21 cases, including 6 of 7 *NF1/PTPN11* cases and 13 of 14 *NF1/PTPN11* wild-type cases. Five cases had clonal rearrangement of the IGH and/or the IGK locus [His04, His10, His14, His20, His21], while two cases (including one with IG rearrangement) showed rearrangements of the TRG locus [His13, His20]. One case was indeterminate for a significant clonal IG rearrangement [His12]. All five clonally rearranged cases for IG were *NF1/PTPN11* wild-type and all had additional mutations in transcriptional regulators and/or signaling pathway genes previously reported altered in B-cell lymphoma (see above). Three additional cases in the *NF1/PTPN11* wild-type group had at least one B-cell associated gene mutation [His07, His08 and His19]. IGH/*BCL2* (MBR) translocation analysis was positive in 1 of 17 cases [His10] (*Online Supplementary Table S3*). In total, 8 of the 14 cases in the *NF1/PTPN11* wild-type subgroup had clonal IG gene rearrangements or mutations in genes reported to be mutated in B-cell lymphomas (Figure 2).

Discussion

Our study furthers the current understanding of the genomic landscape of primary HS through integration of whole exome sequencing and gene expression analysis. It confirms the central role of the RAS/MAPK pathway in the pathogenesis of pHS, with RAS pathway abnormalities identified in all cases in this study. Moreover, it identifies

two molecular subgroups based on the presence or absence of *NF1/PTPN11* alterations and prevalence of *SETD2* mutations, and independently through unsupervised clustering of RNA-Seq data. In addition, our study identifies novel mechanisms of RAS/MAPK pathway activation, including a previously unreported intrachromosomal fusion between *TTYH3* and *BRAF* that preserves the BRAF kinase domain, and high-level *PTPN11* amplification. Perhaps the most surprising finding of our study was the discovery of the *NF1/PTPN11* subgroup with its distinct molecular characteristics and tissue site of involvement. In contrast to the *NF1/PTPN11* wild-type subgroup, none of these cases harbored abnormalities in genes associated with B-cell lymphomas beyond *SETD2* or had clonal IG rearrangements. GSEA revealed that this subgroup was characterized by a relative loss of gene sets related to cellular proliferation and the cell cycle compared to those harboring other RAS/MAPK alterations, a finding supported by Ki67 immunohistochemistry.

The majority of the *NF1/PTPN11* mutant cases had more than one MAPK pathway activating mutation. Three of the seven cases had co-occurring *NF1* and *PTPN11* mutations, while a fourth case had a co-occurring mutation in *GNAI2* involving a codon previously shown to activate the MAPK pathway.[29] Additionally, while the remaining *PTPN11* mutated case did not have a co-occurring *RAS* mutation, it did have high-level amplification of the mutated *PTPN11* allele. In *NF1* mutant melanoma, the frequent presence of a second gene mutation often involving *PTPN11* (or another RASopathy gene) has led to the suggestion that *NF1* inactivation is insufficient to cause full activation of the downstream MAPK pathway and tumorigenesis.[43] This hypothesis has been given further credence by recent data showing that *NF1* loss-of-function mutant cell lines are dependent on SHP2 (encoded by *PTPN11*) mediated signaling for oncogenic RAS/MAPK pathway activation,[44] raising the possibility that activating mutations of *PTPN11* may synergize with *NF1* loss-of-function mutations to further potentiate the oncogenic activity of the pathway.

In contrast to the *NF1/PTPN11* positive subgroup, the *NF1/PTPN11* wild-type cluster was comprised primarily of cases with prototypic RAS/MAPK pathway activating mutations involving *KRAS, NRAS, BRAF* and *MAP2K1*. Interestingly, eight of the 14 cases in this subgroup contained IG gene rearrangements and/or additional mutations in genes commonly associated with B-cell lymphoproliferative disorders. These included one or more mutations in epigenetic regulators, transcription factors or signaling pathway genes, including *CREBBP, KMT2D, DDX3X, ARID1A, MEF2B, SGK1, TNFRSF14, DTX1, GNA13, STAT6* and *CARD11*.[36-40] Clonal IG rearrangements were identified in five cases and a *BCL2* gene rearrangement was identified in one case, while neither were definitively detected in the *NF1/PTPN11* subgroup. In our series, it is worth noting that none of our cases had evidence of a concurrent or previous lymphoma, although we cannot exclude the possibility of an occult or unreported B-cell lymphoma being present. The finding of additional mutations associated with B-cell lymphomas and clonal IG gene rearrangements suggests that some cases of *NF1/PTPN11* wild-type pHS may be similar in origin to the sHS that are associated with B-cell malignancies, which often share IG gene rearrangements with the associated B-cell lymphoma.[5,6] This overlap has also been recently reported by Shanmugam *et al.*[18] In their series, they showed enrichment for a mutational signature resembling aberrant somatic hypermutation in cases that had a history of B-cell lymphoma or that had mutations in genes that are frequently mutated in B-cell lymphoma. Interestingly, they also found recurrent *CDKN2A* alterations that were more frequent in cases with a history of B-cell lymphoma or the aberrant somatic hypermutation signature. Similarly, our study identified a high frequency of focal *CDKN2A* losses/alterations in the *NF1/PTPN11* wild-type subgroup which, in our cohort, frequently had molecular alterations associated with B-cell lymphoma.

Concurrent mutations in RAS/MAPK pathway genes were less common in the *NF1/PTPN11* wild-type group, occurring in 4 of 14 cases with alterations. Two cases had concurrent mutations in *MAP2K1* [His11 and His14]. The other two had co-occurring *BRAF* (p.G469V) and *MAP2K1* (p.F53L) mutations [His10] or *KRAS* (p.G12D) and *RAF1* (p.D486G) mutations [His21]. These data are consistent with the limited published data in HS in which reported occurrences of multiple RAS/MAPK pathway mutations tend to manifest as co-occurring *MAP2K1* mutations[18] or involve atypical *BRAF* mutations, with co-occurring *BRAF* (p.G464V) and *KRAS* (p.Q61H),[45] *BRAF* (p.D594N) and *KRAS* (p.A146T),[18] *BRAF* (p.G469R) and *NF1* (p.W2229*)[18] and *BRAF* (p.F595L) and *HRAS* (p.Q61R) mutations[46] described. Interestingly, in the latter case the unusual *BRAF* mutation was shown to have weak oncogenic activity requiring the co-operation of the *HRAS* mutation for full activity.

Two of the analytical challenges in our study included the lack of available matched germline samples in all but three cases, and the possibility that over-representation of GI site in the *NF1/PTPN11* group could bias the RNA-Seq clustering. To exclude as many germline SNPs as possible we filtered all variants using stringent criteria for their representation in control populations (gnomAD)[47] and took CADD scores,[20] as well as presence in the Catalogue of Somatic Mutations in Cancer (COSMIC)[48] into consideration. In assessing potential site bias in gene expression clustering, we found that the separation of the tumor samples into the subgroups in the differential expression analysis was influenced by the removal of cell cycle-related genes but not by exclusion of GI site-associated genes. This, in addition to the similar mutational alterations in the cases, suggests that the clustering observed occurs independently of site.

In conclusion, our study provides further insight into the molecular pathogenesis of pHS. We show frequent mutations and alterations in genes of the RAS/MAPK pathway, suggesting that patients could potentially benefit from genomic evaluation and targeted therapy, and we report a distinct molecular subtype of pHS that correlates with the *NF1/PTPN11* status of the tumor and frequently involves the GI tract. Finally, we also identify a subset of *NF1/PTPN11* wild-type cases with mutations in B-cell lymphoma associated genes and/or clonal IG gene rearrangements. The identification of molecular subtypes of primary histiocytic sarcoma may prove to have clinical relevance in future studies.

Acknowledgments

The authors would like to thank Andrea O'Hara (BioDiscovery) and Karen Gustashaw (Thermo Fisher Scientific) for their assistance and software support in the interpretation of the OncoScan data; Arati Raziuddin, Xiaolin Wu, Jyoti Shetty, Bao Tran and Nina Bubunenko (Frederick National Laboratory for Cancer Research, Leidos Biomedical Research, Inc.) for per-

forming the library preparation, exome and RNA-Seq and OncoScan assay; Louis M. Staudt (Lymphoid Malignancies Branch, Center for Cancer Research, National Cancer Institute) for his critical reading of our manuscript.

Funding

This work was supported by the intramural research program of the Center for Cancer Research, National Cancer Institute, National Institutes of Health.

References

1. Swerdlow SH, Campo E, Harris NL, et al., eds. WHO Classification of Tumours of Haematopoietic and Lymphoid Tissues. Revised 4th Edition ed. Lyon, France: IARC, 2017.
2. Kommalapati A, Tella SH, Durkin M, Go RS, Goyal G. Histiocytic sarcoma: a population-based analysis of incidence, demographic disparities, and long-term outcomes. Blood. 2018;131(2):265-268.
3. Facchetti F, Pileri SA, Lorenzi L, et al. Histiocytic and dendritic cell neoplasms: what have we learnt by studying 67 cases. Virchows Arch. 2017;471(4):467-489.
4. Emile JF, Abla O, Fraitag S, et al. Revised classification of histiocytoses and neoplasms of the macrophage-dendritic cell lineages. Blood. 2016;127(22):2672-2681.
5. Feldman AL, Arber DA, Pittaluga S, et al. Clonally related follicular lymphomas and histiocytic/dendritic cell sarcomas: evidence for transdifferentiation of the follicular lymphoma clone. Blood. 2008;111(12):5433-5439.
6. Shao H, Xi L, Raffeld M, et al. Clonally related histiocytic/dendritic cell sarcoma and chronic lymphocytic leukemia/small lymphocytic lymphoma: a study of seven cases. Mod Pathol. 2011;24(11):1421-1432.
7. Feldman AL, Minniti C, Santi M, Downing JR, Raffeld M, Jaffe ES. Histiocytic sarcoma after acute lymphoblastic leukaemia: a common clonal origin. Lancet Oncol. 2004;5(4):248-250.
8. Soslow RA, Davis RE, Warnke RA, Cleary ML, Kamel OW. True histiocytic lymphoma following therapy for lymphoblastic neoplasms. Blood. 1996;87(12):5207-5212.
9. Alten J, Klapper W, Leuschner I, et al. Secondary histiocytic sarcoma may cause apparent persistence or recurrence of minimal residual disease in childhood acute lymphoblastic leukemia. Pediatr Blood Cancer. 2015;62(9):1656-1660.
10. Hure MC, Elco CP, Ward D, et al. Histiocytic sarcoma arising from clonally related mantle cell lymphoma. J Clin Oncol. 2012;30(5):e49-53.
11. Brunner P, Rufle A, Dirnhofer S, et al. Follicular lymphoma transformation into histiocytic sarcoma: indications for a common neoplastic progenitor. Leukemia. 2014;28(9):1937-1940.
12. Chen W, Lau SK, Fong D, et al. High frequency of clonal immunoglobulin receptor gene rearrangements in sporadic histiocytic/dendritic cell sarcomas. Am J Surg Pathol. 2009;33(6):863-873.
13. Hayase E, Kurosawa M, Yonezumi M, Suzuki S, Suzuki H. Aggressive sporadic histiocytic sarcoma with immunoglobulin heavy chain gene rearrangement and t(14;18). Int J Hematol. 2010;92(4):659-663.
14. Emile JF, Diamond EL, Helias-Rodzewicz Z, et al. Recurrent RAS and PIK3CA mutations in Erdheim-Chester disease. Blood. 2014;124(19):3016-3019.
15. Chakraborty R, Hampton OA, Shen X, et al. Mutually exclusive recurrent somatic mutations in MAP2K1 and BRAF support a central role for ERK activation in LCH pathogenesis. Blood. 2014;124(19):3007-3015.
16. Diamond EL, Durham BH, Haroche J, et al. Diverse and targetable kinase alterations drive histiocytic neoplasms. Cancer Discov. 2016;6(2):154-165.
17. Badalian-Very G, Vergilio JA, Degar BA, et al. Recurrent BRAF mutations in Langerhans cell histiocytosis. Blood. 2010; 116(11):1919-1923.
18. Shanmugam V, Griffin GK, Jacobsen ED, Fletcher CDM, Sholl LM, Hornick JL. Identification of diverse activating mutations of the RAS-MAPK pathway in histiocytic sarcoma. Mod Pathol. 2019;32(6):830-843.
19. Sondka Z, Bamford S, Cole CG, Ward SA, Dunham I, Forbes SA. The COSMIC Cancer Gene Census: describing genetic dysfunction across all human cancers. Nat Rev Cancer. 2018;18(11):696-705.
20. Rentzsch P, Witten D, Cooper GM, Shendure J, Kircher M. CADD: predicting the deleteriousness of variants throughout the human genome. Nucleic Acids Res. 2019;47(D1):D886-D894.
21. Robinson JT, Thorvaldsdottir H, Winckler W, et al. Integrative genomics viewer. Nat Biotechnol. 2011;29(1):24-26.
22. Alhamdoosh M, Ng M, Wilson NJ, et al. Combining multiple tools outperforms individual methods in gene set enrichment analyses. Bioinformatics. 2017;33(3):414-424.
23. Talevich E, Shain AH, Botton T, Bastian BC. CNVkit: genome-wide copy number detection and visualization from targeted DNA sequencing. PLoS Comput Biol. 2016; 12(4):e1004873.
24. Riester M, Singh AP, Brannon AR, et al. PureCN: copy number calling and SNV classification using targeted short read sequencing. Source Code Biol Med. 2016;11:13.
25. Kumar P, Henikoff S, Ng PC. Predicting the effects of coding non-synonymous variants on protein function using the SIFT algorithm. Nat Protoc. 2009;4(7):1073-1081.
26. Adzhubei IA, Schmidt S, Peshkin L, et al. A method and server for predicting damaging missense mutations. Nat Methods. 2010;7(4):248-249.
27. Kratz CP, Niemeyer CM, Castleberry RP, et al. The mutational spectrum of PTPN11 in juvenile myelomonocytic leukemia and Noonan syndrome/myeloproliferative disease. Blood. 2005;106(6):2183-2185.
28. Tajan M, de Rocca Serra A, Valet P, Edouard T, Yart A. SHP2 sails from physiology to pathology. Eur J Med Genet. 2015; 58(10):509-525.
29. Nairismagi ML, Tan J, Lim JQ, et al. JAK-STAT and G-protein-coupled receptor signaling pathways are frequently altered in epitheliotropic intestinal T-cell lymphoma. Leukemia. 2016;30(6):1311-1319.
30. Brown NA, Furtado LV, Betz BL, et al. High prevalence of somatic MAP2K1 mutations in BRAF V600E-negative Langerhans cell histiocytosis. Blood. 2014;124(10):1655-1658.
31. Frattini V, Trifonov V, Chan JM, et al. The integrated landscape of driver genomic alterations in glioblastoma. Nat Genet. 2013;45(10):1141-1149.
32. Johnston JJ, van der Smagt JJ, Rosenfeld JA, et al. Autosomal recessive Noonan syndrome associated with biallelic LZTR1 variants. Genet Med. 2018;20(10):1175-1185.
33. Tidyman WE, Rauen KA. Expansion of the RASopathies. Curr Genet Med Rep. 2016; 4(3):57-64.
34. Piotrowski A, Xie J, Liu YF, et al. Germline loss-of-function mutations in LZTR1 predispose to an inherited disorder of multiple schwannomas. Nat Genet. 2014;46(2):182-187.
35. Steklov M, Pandolfi S, Baietti MF, et al. Mutations in LZTR1 drive human disease by dysregulating RAS ubiquitination. Science. 2018;362(6419):1177-1182.
36. Karube K, Enjuanes A, Dlouhy I, et al. Integrating genomic alterations in diffuse large B-cell lymphoma identifies new relevant pathways and potential therapeutic targets. Leukemia. 2018;32(3):675-684.
37. Chapuy B, Stewart C, Dunford AJ, et al. Molecular subtypes of diffuse large B cell lymphoma are associated with distinct pathogenic mechanisms and outcomes. Nat Med. 2018;24(5):679-690.
38. Reddy A, Zhang J, Davis NS, et al. Genetic and Functional Drivers of Diffuse Large B Cell Lymphoma. Cell. 2017;171(2):481-494.e15.
39. Schmitz R, Wright GW, Huang DW, et al. Genetics and pathogenesis of diffuse large B-cell lymphoma. N Engl J Med. 2018; 378(15):1396-1407.
40. Landau DA, Sun C, Rosebrock D, et al. The evolutionary landscape of chronic lymphocytic leukemia treated with ibrutinib targeted therapy. Nat Commun. 2017; 8(1):2185.
41. Ross JS, Wang K, Chmielecki J, et al. The distribution of BRAF gene fusions in solid tumors and response to targeted therapy. Int J Cancer. 2016;138(4):881-890.
42. Ciampi R, Knauf JA, Kerler R, et al. Oncogenic AKAP9-BRAF fusion is a novel mechanism of MAPK pathway activation in thyroid cancer. J Clin Invest. 2005; 115(1):94-101.
43. Krauthammer M, Kong Y, Bacchiocchi A, et al. Exome sequencing identifies recurrent mutations in NF1 and RASopathy genes in sun-exposed melanomas. Nat Genet. 2015; 47(9):996-1002.
44. Nichols RJ, Haderk F, Stahlhut C, et al. RAS nucleotide cycling underlies the SHP2 phosphatase dependence of mutant BRAF-, NF1- and RAS-driven cancers. Nat Cell Biol. 2018;20(9):1064-1073.
45. Liu Q, Tomaszewicz K, Hutchinson L, Hornick JL, Woda B, Yu H. Somatic mutations in histiocytic sarcoma identified by next generation sequencing. Virchows Arch. 2016;469(2):233-241.
46. Kordes M, Roring M, Heining C, et al. Cooperation of BRAF(F595L) and mutant HRAS in histiocytic sarcoma provides new insights into oncogenic BRAF signaling. Leukemia. 2016;30(4):937-946.
47. Lek M, Karczewski KJ, Minikel EV, et al. Analysis of protein-coding genetic variation in 60,706 humans. Nature. 2016;536(7616):285-291.
48. Forbes SA, Beare D, Boutselakis H, et al. COSMIC: somatic cancer genetics at high-resolution. Nucleic Acids Res. 2017; 45(D1):D777-D783.

ARTICLE

Thrombomodulin-expressing monocytes are associated with low-risk features in myelodysplastic syndromes and dampen excessive immune activation

Nathalie van Leeuwen-Kerkhoff,[1] Theresia M. Westers,[1] Pino J. Poddighe,[2] Tanja D. de Gruijl,[3]* Shahram Kordasti[4]* and Arjan A. van de Loosdrecht[1]*

[1]Department of Hematology, Amsterdam UMC, Cancer Center Amsterdam, the Netherlands; [2]Department of Clinical Genetics, Amsterdam UMC, Amsterdam, the Netherlands; [3]Department of Medical Oncology, Amsterdam UMC, Cancer Center Amsterdam, the Netherlands and [4]Comprehensive Cancer Center, King's College London and Guy's Hospital, London, UK

**TDdG, SK and AAvdL contributed equally to this work.*

Ferrata Storti Foundation

Haematologica 2020
Volume 105(4):961-971

ABSTRACT

The bone marrow of patients with low-risk myelodysplastic syndromes (MDS) is often an inflammatory environment and associated with an active cellular immune response. An active immune response generally contributes to antitumor responses and may prevent disease progression. However, chronic immune stimulation can also induce cell stress, DNA damage and contribute to the pathogenesis of MDS. The protective mechanisms against excessive immune activation are therefore an important aspect of the pathophysiology of MDS and characterizing them may help us to better understand the fine balance between protective and destabilizing inflammation in lower-risk disease. In this study we investigated the role of thrombomodulin (CD141/BDCA-3) expression, a molecule with anti-inflammatory properties, on monocytes in the bone marrow and peripheral blood of MDS patients in different risk groups. Patient-derived classical monocytes showed high expression levels of thrombomodulin, whereas monocytes from healthy donors hardly expressed any thrombomodulin. The presence of thrombomodulin on monocytes from MDS patients correlated with lower-risk disease groups and better overall and leukemia-free survival. Using multidimensional mass cytometry, in an *in-vitro* setting, we showed that thrombomodulin-positive monocytes could polarize naïve T cells toward cell clusters which are closer to T helper type 2 and T regulatory cell phenotypes and less likely to contribute to effective immune surveillance. In conclusion, the expression of thrombomodulin on classical monocytes is a favorable and early prognostic marker in patients with low-risk MDS and may represent a new mechanism in the protection against disproportionate immune activation.

Introduction

The immune system plays an important role in the pathogenesis and disease course of myelodysplastic syndromes (MDS). The immune status can be markedly different between MDS prognostic risk groups. Low-risk disease is often characterized by an increased number and activation state of pro-inflammatory immune cells [i.e. T helper (Th)17, natural killer (NK) and $CD8^+$ cytotoxic T cells[1–6]] whereas in high-risk disease an immunosuppressive response is the dominant feature [i.e. expansion of T regulatory cells (Treg)[7–10] and myeloid-derived suppressor cells[11]] which could facilitate immune escape and eventually progression to acute myeloid leukemia. Although an "activated" immune system and associated tumor-specific immune responses are crucial for effective immune surveillance and elimination of the malignant clone, in the longer term chronic immune stimulation may enhance the risk of genomic instability and development of MDS/acute myeloid leukemia.[12] Smoldering inflammation as a result of aberrant activation of inflammatory path-

Correspondence:

ARJAN A. VAN DE LOOSDRECHT
a.vandeloosdrecht@vumc.nl

Received: February 12, 2019.

Accepted: July 2, 2019.

Pre-published: July 4, 2019.

doi:10.3324/haematol.2019.219303

Check the online version for the most updated information on this article, online supplements, and information on authorship & disclosures: www.haematologica.org/content/105/4/961

ways, e.g. Toll-like receptor (TLR) signaling, can induce malignant transformation and disease progression by causing genotoxic cell stress. Indeed, in low-risk MDS elevated levels of several stress-inducing molecules, such as the damage-associated molecular pattern molecules S100A8/A9, are actively secreted from mesenchymal niche cells in the bone marrow (BM) microenvironment, thereby causing niche-induced DNA damage in hematopoietic stem and progenitor cells.[13] High S100A9 levels in MDS BM also result in inflammasome assembly and subsequent initiation of pyroptosis, an immunogenic form of cell death, which could potentially explain the high rate of cell death in low-risk MDS BM.[14–16] These soluble inflammatory molecules are able to bind to TLR on the surface of hematopoietic stem and progenitor cells and immune cells. Constitutively activated TLR-signaling and downstream mitogen-activated protein kinase (MAPK) and nuclear factor kappa B (NF-κB) activation are evident and have been implicated in the pathogenesis of MDS.[17–24] Besides active secretion of stress-inducing molecules, passive release from cells undergoing immunogenic cell death has also been described in MDS. Levels of high mobility group box 1 (HMGB1), a mediator strongly involved in inflammatory processes and a ligand for TLR4, were found to be increased in the BM of MDS patients due to impaired clearance of apoptotic cells causing secondary necrosis and leakage of this molecule into the BM environment.[25]

As a result of this vicious circle of inflammation and cell death, immune-inhibitory mechanisms that interfere with this excessive inflammatory process kick in. While these immune-inhibitory pathways may control the inflammatory response to some extent, they also facilitate the expansion of immunosuppressive cells, such as Treg and myeloid-derived suppressor cells, which further suppress the already weakened immune surveillance against the malignant clone. A delicate balance between immune activation and inhibition is, therefore, required to maintain effective immunosurveillance. Thrombomodulin (TM) is known for its anticoagulant function by serving as a cofactor for thrombin. Notably, the lectin-like domain of the TM molecule has marked anti-inflammatory activities and interferes with the complement pathway.[26–28] Several studies have shown strong correlations between disease severity and TM levels in, for instance, autoimmune and infectious diseases as well as in cancer.[29–31] In the immune system, TM, also known as CD141 or BDCA-3, is mainly expressed on dendritic cells.[32–34] We have previously described elevated expression of TM/BDCA-3 on tumor-conditioned and immunosuppressive monocyte-derived dendritic cells that acquire a M2-like macrophage phenotype.[35,36] The anti-inflammatory potential of TM has also been assigned to the fact that TM is able to bind HMGB1, thereby inhibiting the strong pro-inflammatory effect of this molecule. Since high levels of this molecule were found in low-risk MDS BM, this interactive mechanism may be relevant in keeping excessive immune activation to a minimum. The aim of this study was to evaluate the possible role and prognostic value of TM in regulating the inflammatory immune response in MDS. The expression of TM was evaluated on different monocyte subsets (classical, intermediate and non-classical) in the peripheral blood (PB) and BM within different MDS risk groups. Multidimensional mass cytometry was used to investigate the putative impact of TM+ monocytes on the T-cell phenotype. The cell surface expression of TM was higher on classical monocytes in both the PB and BM of MDS patients than on healthy donor-derived monocytes. The expression of TM was related to a more favorable prognosis and functional skewing of the T-cell response toward a more tolerized state.

Methods

Patient and control samples

Twenty-nine PB and 154 BM samples from newly diagnosed MDS patients were collected in this study. Patients were assigned to different risk categories using the Revised International Prognostic Scoring System (IPSS-R) and the 2016 World Health Organization (WHO) classification (details are given in the *Online Supplementary Methods* file and Table 1). A set of 25 age-matched control BM samples was obtained after written informed consent from hematologically healthy patients who were undergoing cardiac surgery at Amsterdam University Medical Center (the Netherlands). For the PB analysis, 31 control samples were collected. The study was approved by the local ethical committee and was conducted in accordance with the declaration of Helsinki.

Flow cytometry and fluorescence *in situ* hybridization

PB and BM cells were analyzed on a flow cytometer (FACSCanto™, BD Biosciences, San Jose, CA, USA) after incubation with a panel of monoclonal antibodies (see *Online Supplementary Methods* for details). Data were analyzed using FlowJo software (Tree Star, Ashland, OR, USA). Monocyte subsets were identified based on the differential expression of CD14, CD16 and M-DC8 [anti-6-Sulfo LacNAc (Slan)], using recent recommendations (*Online Supplementary Figure S1*).[37,38] Classical monocytes were characterized by high CD14 expression, and CD16 and M-DC8 negativity. Intermediate and non-classical monocytes were both defined as $CD16^+$. However, only intermediate monocytes expressed CD14. We used M-DC8 as a marker to discriminate between intermediate and non-classical monocytes as suggested by Hofer *et al.* (Figure 1A).[38]

Three samples containing monocytes with high TM expression and a known cytogenetic aberrancy were used for the isolation of classical monocytes and subsequent interphase fluorescence *in situ* hybridization (FISH) analysis (details are given in the *Online Supplementary Methods*).

T-cell cultures and multidimensional mass cytometry

A multiparameter deep-phenotyping strategy, known as cytometry by time-of-flight (CyTOF), was used for T cells cultured in the presence of MDS-derived TM^- or TM^+ monocytes (culture details are provided in the *Online Supplementary Methods*). Data were analyzed using a combination of automated dimension reduction and clustering methods including t-distributed stochastic neighbor embedding (t-SNE)[39] to visually (viSNE) identify cell populations.[40] This was followed by spanning-tree progression analysis of density-normalized events (SPADE)[41] for the clustering of T cells as published before.[42,43] The deep immunophenotyping of T-cell clusters was performed using our in-house pipeline (publicly available here: *https://github.com/kordastilab/cytoClustR*) followed by marker enrichment modeling (MEM) to calculate MEM scores of the identified subpopulations.[44]

Statistical analysis

Significant differences for two-group comparisons were analyzed by applying a non-parametric Mann-Whitney U test, whereas for multi-group comparisons a Kruskal-Wallis test with

the Dunn multiple comparisons test was used. A Spearman correlation was computed for PB and BM comparisons. *P* values <0.05 were considered statistically significant. Graphpad Prism 6 software (San Diego, CA USA) was used for graphic display and statistical calculations. A multivariate Cox regression analysis for overall and leukemia-free survival was performed using IBM SPSS Statistics software version 22 (New York, NY, USA).

Results

Classical monocytes in patients with myelodysplastic syndromes express thrombomodulin

Monocyte subsets were identified by flow cytometric analysis based on the expression of CD14, CD16 and M-DC8 according to recently published recommendations.[38] Classical, intermediate and non-classical monocytes were characterized by using the above mentioned markers (Figure 1A). Subsequently, the expression of TM and HLA-DR, a major histocompatibility complex (MHC) molecule class II, was assessed on all monocyte subsets derived from normal bone marrow (NBM) and MDS BM samples. Monocyte subsets from MDS patients showed high levels of TM expression on their cell surface, whereas NBM-derived monocytes showed very low levels of TM. HLA-DR expression, too, was higher on all monocyte subsets in MDS BM than it was in NBM (Figure 1A). The levels of expression on different monocyte subsets were quantified in a larger cohort of patients (NMB samples, n=10 and MDS BM samples, n=24). Total percentages of monocyte subsets in MDS BM compared to NBM were not significantly different. However, the percentage of monocytes that expressed TM was significantly higher for MDS-derived classical monocytes compared to the same monocyte subset in NBM (37.3% *vs.* 9.9%; *P*<0.0001) (Figure 1B). The percentages of TM expression on intermediate and non-classical monocytes were equally distributed between MDS BM and NBM (Figure 1B). The median fluorescent intensity of TM and HLA-DR was evaluated on the three distinct monocyte subsets using the same set of samples. Classical monocytes from MDS BM showed higher levels of TM expression compared to classical monocytes fron NMB (3.7-fold higher; *P*<0.0001). HLA-DR expression levels were higher for all MDS-derived monocyte subsets (classical monocytes: 2.0-fold, *P*=0.0015; intermediate monocytes: 1.8-fold, *P*=0.0154; non-classical monocytes: 1.5-fold, *P*<0.0001) (Figure 1B). TM expression remained unchanged upon overnight stimulation with TLR ligands in a preliminary set of samples (*Online Supplementary Figure S2*).

Classical monocytes were then analyzed in a larger set of samples, since this subset forms the most prevalent subset in NBM as well as in MDS BM, and revealed the most prominent difference in TM expression. The PB compartment was also included in the analysis. The cohort was extended with 130 MDS BM-derived samples and 15 NBM samples. The PB and BM samples in the extended control and patient cohorts (normal PB, n=31; MDS PB, n=29; NBM, n=25 and MDS BM, n=154) were screened for the presence of TM on classical monocytes (Figure 1C). MDS-derived classical monocytes in both the PB and BM compartment showed higher expression of TM compared to the expression on classical monocytes from normal PB and NBM samples (PB: 33.6% *vs.* 17.8%, *P*=0.015; BM: 37.0% *vs.* 8.6%, *P*<0.0001). Furthermore, a strong positive correlation was found for the percentage of classical monocytes expressing TM in the two compartments in 25 paired MDS samples (r=0.83, *P*<0.0001) (Figure 1C). The same flow cytometric panel was used to study TM expression on other cell types present in the PB and BM,. We were able to identify granulocytes, eosinophils and B cells. TM was exclusively expressed on MDS-derived monocytes (*Online Supplementary Figure S3*) and none of the other cell types in PB and BM showed positivity for TM, including the non-B cell lymphocytic compartment consisting of T and NK cells (*data not shown*).

Table 1. Characteristics of the patients and controls.

Characteristics	Value	[min-max]
Total number		
HD	56	
MDS	183	
Peripheral blood samples		
Number	60	
HD	31	
MDS	29	
Age – mean, years		
HD	-	
MDS	69	[45-85]
Sex		
HD – male/female	-	
MDS – male/female	20/9	
Bone marrow samples		
Number	179	
HD	25	
MDS	154	
Age – mean,y		
HD	62	[20-86]
MDS	69	[36-94]
Sex		
HD – male/female	18/7	
MDS – male/female	110/44	
IPSS-R		
Very low risk		
Low	20	
Low risk	34	
Intermediate risk	22	
High risk	8	
Very high risk	8	
WHO classification		
MDS-SLD	5	
MDS-MLD	48	
MDS-RS-SLD	8	
MDS-RS-MLD	27	
MDS-EB1	22	
MDS-EB2	20	
Del5q	12	
% Blasts		
<5%	97	
≥5%	44	
Ring sideroblasts		
No	106	
Yes	40	

HD: healthy donor; MDS: myelodysplastic syndrome; IPSS-R: Revised International Prognostic Scoring System; WHO, World Health Organization; SLD, single lineage dysplasia; MLD, multilineage dysplasia; RS, ring sideroblasts; EB, excess blasts; Del5q: deletion 5q.

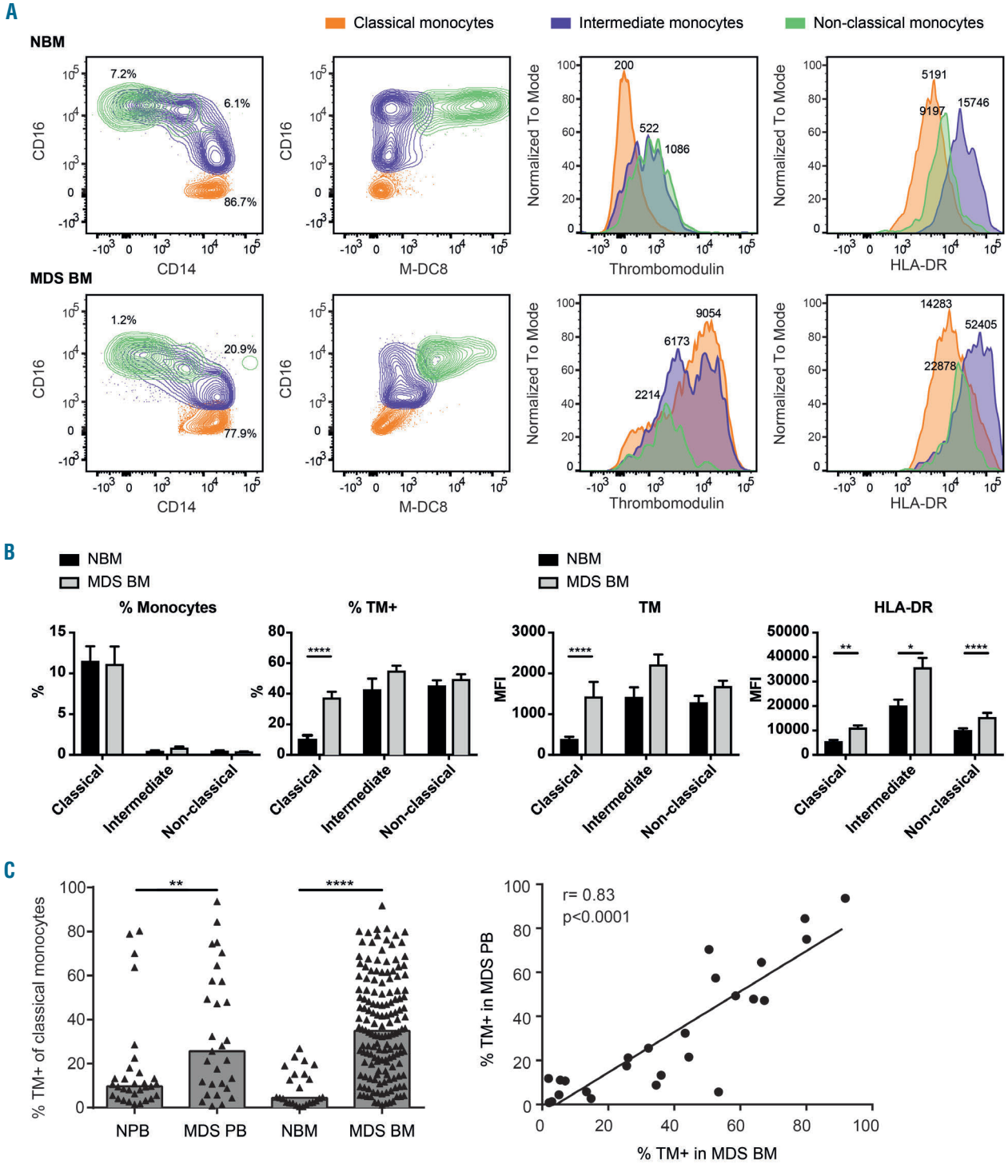

Figure 1. Thrombomodulin-expressing monocyte subsets in normal and myelodysplastic syndrome bone marrow and peripheral blood samples. (A) Identification of different monocyte subsets in normal bone marrow (NBM) and myelodysplastic syndrome (MDS) bone marrow (BM). Three markers, CD14, CD16 and M-DC8, were used to identify classical ($CD14^{++}CD16^{-}M\text{-}DC8^{-}$, in orange), intermediate ($CD14^{+}CD16^{+}M\text{-}DC8^{-}$, in purple) and non-classical monocytes ($CD14^{+/-}CD16^{+}M\text{-}DC8^{+}$, in green). The levels of expression of thrombomodulin (TM) and HLA-DR were assessed on all separate monocyte subsets. The median fluorescence intensity (MFI) value for each subset is shown for a representative sample. (B) Frequencies of monocyte subsets in the BM of ten healthy individuals and 24 MDS patients. Percentages were calculated from the total $CD45^{+}$ mononuclear cell fraction. Mean frequencies ± standard error of mean (SEM) are given (NBM *vs.* MDS BM: classical monocytes 11.47% ± 1.86 *vs.* 11.11% ± 2.20, intermediate monocytes 0.45% ± 0.12 *vs.* 0.85% ± 0.17, non-classical monocytes 0.46% ± 0.11 *vs.* 0.38% ± 0.05). Furthermore, the percentage of monocytes that express TM is displayed (NBM *vs.* MDS BM: classical monocytes 9.94% ± 2.82 *vs.* 37.27% ± 4.00, intermediate monocytes 42.60% ± 7.27 *vs.* 54.90% ± 3.48, non-classical monocytes 45.11% ± 3.72 *vs.* 49.46% ± 3.34). Expression levels of TM and HLA-DR on NBM and MDS BM monocyte subsets are also shown. Mean MFI values ± SEM are shown for ten NBM and 24 MDS BM samples (TM in NBM *vs.* MDS BM: classical monocytes 382 ± 65 *vs.* 1425 ± 367, intermediate monocytes 1414 ± 245 *vs.* 2208 ± 259, non-classical monocytes 1279 ± 169 *vs.* 1676 ± 144. HLA-DR in NBM *vs.* MDS BM: classical monocytes 5426 ± 715 *vs.* 11010 ± 1056, intermediate monocytes 20062 ± 2529 *vs.* 35639 ± 3989, non-classical monocytes 10117 ± 856 *vs.* 15255 ± 1915). (C) Percentages of TM-expressing classical monocytes in peripheral blood (PB) and BM. Bars indicate mean frequencies [normal PB (NPB, n=31) *vs.* MDS PB (n=29): 17.8% *vs.* 33.6%. normal BM (NBM, n=25) *vs.* MDS BM (n=154): 8.6% *vs.* 37.0%]. TM expression was correlated in PB- and BM-derived classical monocytes. In total, 25 paired MDS samples were included. **P*<0.05, ***P*<0.01, *****P*<0.0001.

Thrombomodulin-expressing monocytes are clonally involved and are associated with the features of low-risk myelodysplastic syndromes

In order to investigate the clonal involvement of TM+ monocytes in MDS, cells from three different patients were sorted and screened for the presence of a known cytogenetic aberration according to their karyotype. Almost all monocytes of these patients showed high expression of TM.

One patient had a deletion of chromosome 5q (del5q) in all cells (karyotype: 46,XY,del(5)(q22q33)[10]), one showed trisomy for chromosome 8 in 65% of the cells (karyotype: 47,XY,+8[13]/46,XY[7]) and one case had a monosomy 7 (karyotype: 45,XY,-7[10]). In all cases, TM+ monocytes were highly involved in the dysplastic clone and showed a high percentage of cells with the respective cytogenetic abnormality, suggesting that they did not come from healthy CD34+ cells. The isolated CD34+ progenitor cells showed a similar pattern, since the known cytogenetic aberration was present in most analyzed cells. As expected, B cells were not involved. Partial involvement was found in whole BM samples (Figure 2A).

To further correlate TM expression with different MDS subgroups, the patients' clinical data were collected and their IPSS-R scores, reflecting survival and the risk of disease progression, were calculated. Furthermore, patients were categorized using the 2016 WHO classification system which incorporates clinical characteristics, PB and BM findings and cytogenetic analysis. The percentage of monocytes displaying TM expression was higher for patients who had a very low- or low-risk score in the IPSS-R than for patients in higher-risk groups and healthy controls (very low/low 40.1% *vs*. intermediate 22.7% *vs*. high/very high 28.3% *vs*. NBM 11.3%) (Figure 2B). Additionally, TM expression was elevated in WHO categories related to lower-risk disease, such as MDS single and multiple lineage dysplasia with or without ring sideroblasts, compared to categories related to higher-risk MDS, i.e. MDS with excess blasts 1 and 2. The percentage of monocytes expressing TM was higher in all WHO subgroups than in NBM (single/multiple lineage dysplasia with/without ring sideroblasts, 40.9% *vs*. MDS with excess blasts 1 and 2, 24.2% *vs*. NBM, 11.3%) (Figure 2B). Using the percentage of BM blast cells as a reflection of disease stage, patients with blast percentages below 5% harbored higher numbers of TM+ monocytes than patients with 5% or more blast cells (41.3% *vs*. 25.7%, respectively; $P<0.0001$) (Figure 2C). Finally, a relation between the percentage of monocytes expressing TM and the presence of ring sideroblasts (erythroblasts with mitochondrial iron accumulation) was found (present 45.4% *vs*. absent 33.2%; $P=0.003$) (Figure 2C). As an "indirect" indication of the presence of a *SF3B1* mutation, the percentage of TM+ monocytes was compared between subtypes with ring sideroblasts and other MDS subtypes (*Online Supplementary Figure S4*). Significantly higher percentages of TM+ monocytes were found in cases with ring sideroblasts than in those with MDS with excess blasts 1 or 2. A trend to higher frequencies was observed for the comparisons with other subtypes.

Myelodysplastic syndrome-derived thrombomodulin-positive monocytes polarize CD4+ T cells to an immunosuppressive phenotype

The next research focus was to study the effect of TM+ monocytes on the phenotype of CD4+ T cells and to determine whether they could induce an anti-inflammatory T-cell phenotype. Healthy donor-derived CD4+ T cells were co-cultured with sorted TM- or TM+ monocytes from two MDS patients (*Online Supplementary Figure S5*). After 5 days, T cells were harvested and labeled with a comprehensive panel of metal-tagged antibodies (*Online Supplementary Table S1*) for mass cytometry (CyTOF). Using our data analysis pipeline, T-cell subsets were identified (*Online Supplementary Figure S6*) and compared between the conditions (i.e. day 0, control stimulated and cultures with TM- or TM+ monocytes) (Figure 3A). Compared to day 0, all conditions showed expansion of specific T-cell subsets. To further characterize these cell islands, T cells were clustered by SPADE on tSNE (see Methods). Using selected T-cell markers various subsets could be characterized (Figure 3B). Then frequencies of clusters between the conditions were compared (Figure 3C). Nodes highlighted with red circles refer to the most frequent T cell clusters in the TM- condition whereas black circles indicate a higher percentage in the TM+ condition. For both conditions the top five of highest frequencies were selected. The expression profiles of T cells in the identified clusters were evaluated next, using MEM (see Methods). T-cell clusters were divided into two groups for comparison: clusters with highest frequency in the TM+ condition (called "up") and clusters with highest frequency in the TM- condition (called "down"). MEM scores were calculated for each marker in each group for further comparison.[44] Interestingly, T cells that were predominantly present upon culturing with TM+ monocytes (group called "up") showed an anti-inflammatory profile (Figure 3C). They were polarized toward Th2, Treg and PD-1-expressing clusters of T cells, since they expressed high levels of FoxP3, GATA3 and CD279 (PD-1) and had elevated concentrations of intracellularly measured interleukin-4 and interleukin-10. In contrast, T cells cultured in the presence of TM- monocytes (group called "down") were mainly positive for interferon-γ and hardly for immunosuppressive cytokines.

The presence of thrombomodulin-positive monocytes is related to a better overall and leukemia-free survival

In order to determine the clinical significance of the presence of TM+ monocytes, overall survival and leukemia-free survival were calculated. As a cut-off for TM expression monocytes from the healthy donor cohort were used. The mean TM percentage plus two standard deviations was calculated resulting in a cut-off of 25.53%. In total, overall survival data for 122 MDS patients and leukemia-free survival data for 102 patients were available. Interestingly, the presence of TM on MDS monocytes was significantly associated with a better overall survival ($P=0.006$) as well as a better leukemia-free survival ($P=0.029$) (Figure 4A). The median overall survival for patients with TM+ monocytes was 58 months, whereas that of patients without TM+ monocytes was 30 months. For a subgroup of patients, data were available for further risk stratification into IPSS and IPSS-R risk groups. Following the hypothesis that TM is mainly present in an inflammatory environment, survival and leukemia-free survival data were also analyzed in low-risk MDS groups (i.e. IPSS low and intermediate groups or IPSS-R very low, low and intermediate groups). The presence of TM+ monocytes resulted in better overall survival in this sub-

A

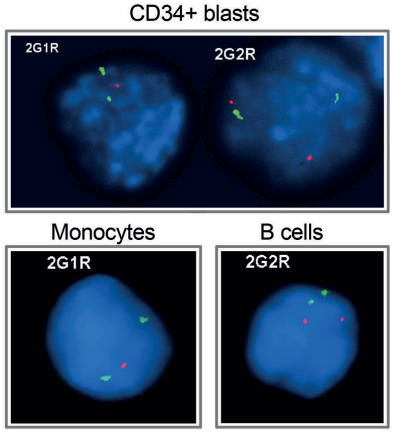

Cell type	FISH results: number of cells	
	Monosomy 7	**Two chromosome 7**
Whole bone marrow	57	43
Monocytes	99	1
B cells	0	100
CD34+ blasts	96	4
	Del 5q	**Normal chromosome 5**
Whole bone marrow	163	37
Monocytes	93	7
B cells	2	98
CD34+ blasts	96	4
	Trisomy 8	**Two chromosome 8**
Whole bone marrow	56	44
Monocytes	81	19
B cells	0	91
CD34+ blasts	77	23

B

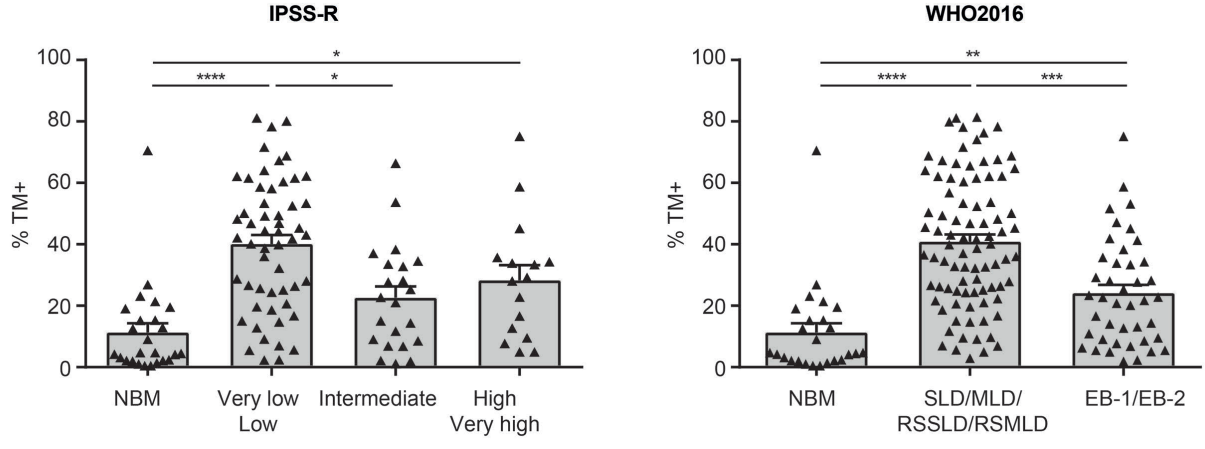

C

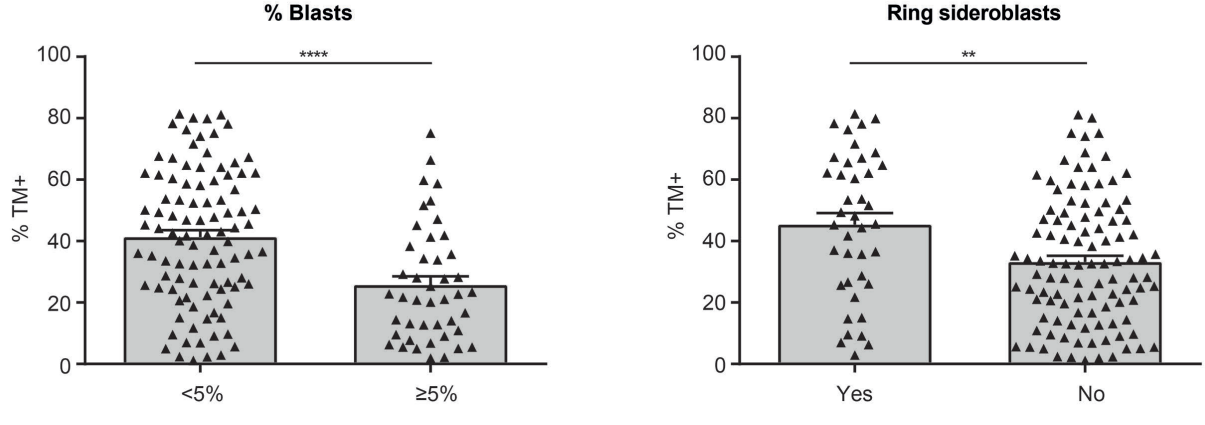

Figure 2. Classical monocytes are clonally involved and the presence of thrombomodulin correlates with disease states. (A) Sorted cells, including B cells and CD34$^+$ blast cells, from patients with a known cytogenetic aberrancy were subjected to fluorescence *in situ* hybridization (FISH) analysis. Furthermore, whole bone marrow (BM) samples were used for degree of cytogenetic load. Representative interphase cells hybridized with the chromosome 5q probe, showing loss of 5q in CD34$^+$ blasts and monocytes, and no loss of 5q in B cells. In three tested cases (monosomy 7, deletion 5q and trisomy 8), classical monocytes and CD34$^+$ blast cells were highly involved in the dysplastic clone, whereas B cells were not involved. Interphase FISH on whole BM samples showed both an aberrant and a normal cell line. (B) Thrombomodulin-positive (TM$^+$) classical monocytes in different myelodysplastic syndrome (MDS) risk groups defined according to the Revised International Prognostic Scoring System and the World Health Organization (WHO) 2016 classification. The percentage of classical monocytes that express TM was highest in the very low/low-risk groups: the percentage of TM expression was significantly reduced in higher-risk groups compared to the lower-risk group [mean ± standard error of mean (SEM): normal BM (n=25) 11.3% ± 3.0% *vs.* very low/low-risk MDS BM (n=54) 40.1% ± 2.9% *vs.* intermediate-risk MDS BM (n=22) 22.7% ± 3.7% *vs.* high/very high-risk MDS BM (n=16) 28.3% ± 4.9%). Patients with low-risk MDS according to the WHO 2016 classification (single/multiple lineage dysplasia with or without ring sideroblasts, n=87) had higher percentages of TM expression on monocytes (40.9% ± 2.3%) compared to patients in higher-risk groups (excess blasts-1 and -2, n=42) (24.2% ± 2.7%) and normal BM (n=25) (11.3% ± 3.0%). (C) Percentages of classical monocytes that are positive for TM in patients with low and higher blast counts. The percentage of monocytes expressing TM was significantly higher in the group of patients with blast counts below 5% (n=97) than in the group of patients with blast counts ≥5% (n=44) (blast count <5%, 41.3% ± 2.2% *vs.* blast count ≥5%, 25.7% ± 2.8%). Patients with ring sideroblasts (RS) (n=40) had higher percentages of TM$^+$ monocytes than patients who did not have RS (n=106) (RS yes, 45.4% ± 3.7% *vs.* RS no, 33.2% ± 2.0%). **P*<0.05, ***P*<0.01, ****P*<0.001, *****P*<0.0001. IPSS-R: Revised International Prognostic Scoring System; NBM: normal bone marrow; SLD: single lineage dysplasia; MLD: multilineage dysplasia;.RS: ring sideroblasts; EB, excess blasts.

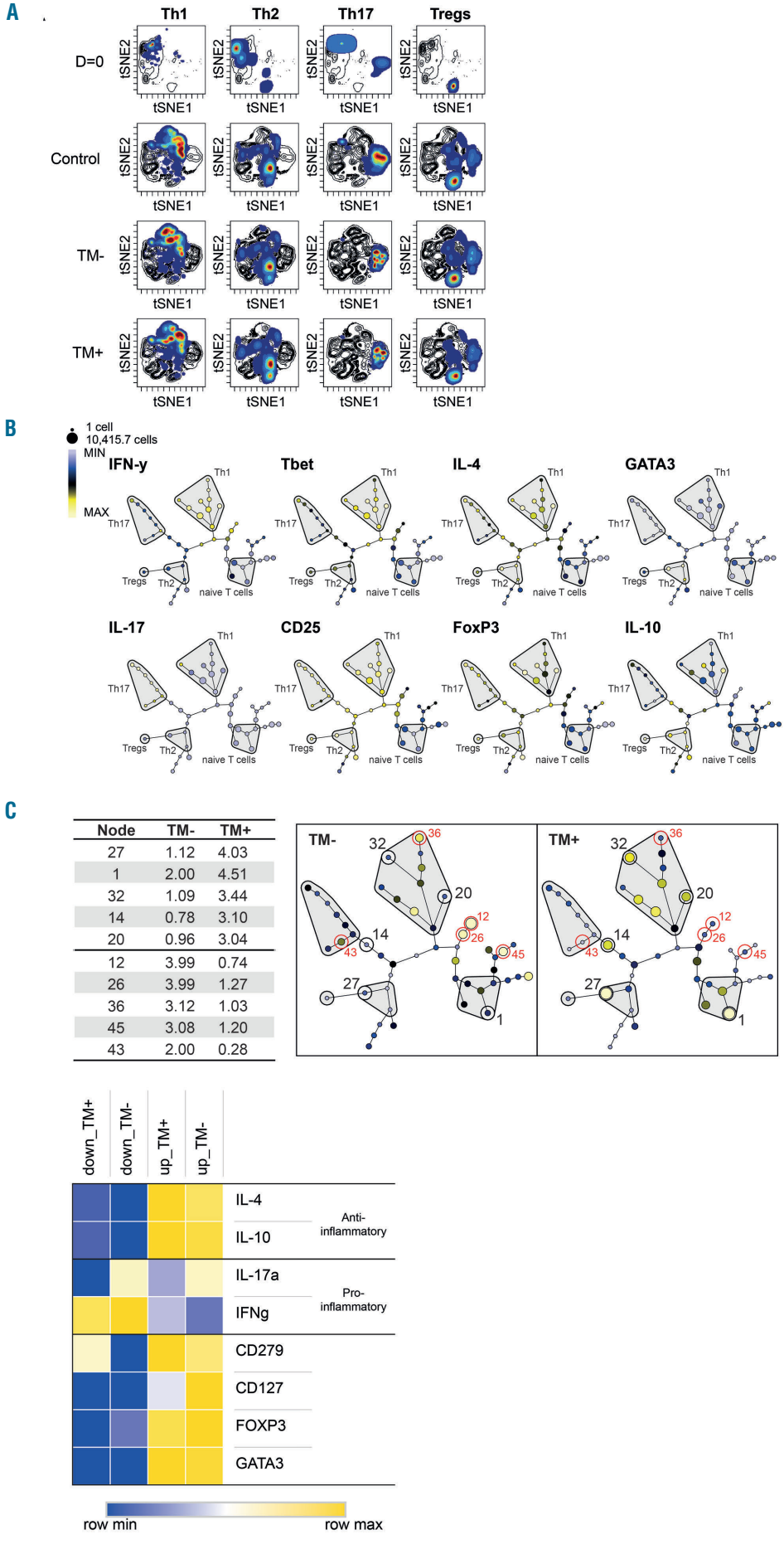

Node	TM-	TM+
27	1.12	4.03
1	2.00	4.51
32	1.09	3.44
14	0.78	3.10
20	0.96	3.04
12	3.99	0.74
26	3.99	1.27
36	3.12	1.03
45	3.08	1.20
43	2.00	0.28

Figure 3. Deep phenotyping of T cells after co-culture with thrombomodulin-negative or –positive monocytes from patients with myelodysplastic syndromes. Healthy donor-derived CD4+ T cells were co-cultured with thrombomodulin (TM)-negative or -positive monocytes from two patients with myelodysplastic syndromes (MDS), or in the stimulated control condition with plate-bound anti-CD3 antibody only. After culture for 5 days, T cells were stained with an extensive panel of surface and intracellular markers as well as stains for transcription factors and cytokines and analyzed using time of flight mass cytometry. (A) Viable T cells were identified and visualized using stochastic neighbor embedding (viSNE). Different T-cell subsets were identified based on interferon (IFN)-γ, GATA3, interleukin (IL)-17, IL-4, FoxP3 and CD127 (Th1 were considered to be IFN-γ+, IL-17 and GATA3-; Th2 were GATA3+IL-4+; Th17 were IL-17+; Treg were CD127- and FoxP3+CD25+ and IFN-γ) (*Online Supplementary Figure S6*). Overlays were created from condition-specific biaxial viSNE contour plots and each individual T-cell subset. T-cell populations at the start of the experiment (D=0) and after 5 days of culture with anti-CD3 only, TM- monocytes or TM+ monocytes are shown for a representative sample. (B) Cells were then further clustered with spanning-tree progression analysis of density-normalized events (SPADE) into 50 nodes using the clustering channels tSNE1 and tSNE2. Different clusters of nodes representing various T-cell subsets could be identified in the stimulated control condition by using selected markers. The color intensity in each node reflects the expression level of the indicated marker and the size of the node reveals the number of cells involved. (C) Frequencies of all clusters were compared between the TM- and TM+ conditions. T-cell clusters that were most prevalent in the TM- condition are highlighted in red. Black circles represent clusters that show higher percentages in the TM+ condition. The top five of highest frequencies for both conditions are shown. Using marker enrichment modeling (MEM), profiles of T-cell clusters with highest frequencies in TM- or TM+ cells were characterized. Two subgroups of clusters were generated: (i) five nodes with highest frequency in the TM+ condition (called "up") and (ii) five nodes with highest frequency in TM- condition (called "down"). Expression levels of given markers are shown for the TM+ as well as the TM- conditions, showing that global expression in the identified set of clusters for the different markers is nearly similar in both conditions. MEM scores were calculated for the markers and results are presented in a heat map. The group of nodes that are present in a higher percentage in cultures with TM+ monocytes compared to cultures with TM- monocytes reflect an anti-inflammatory profile. T cells in this group (all within "non-Treg nodes") express higher levels of FoxP3, GATA3, CD279 (PD-1), IL-4 and IL-10, a phenotype which suggests they are polarizing toward a Treg phenotype. tSNE, t-distributed stochastic neighbor embedding.

group of patients as well (Figure 4B). A difference in leukemia-free survival did not reach statistical significance, probably because of the small numbers of patients (Figure 4C). To test whether TM as a single marker has an independent prognostic value in overall and leukemia-free survival a multivariate Cox regression analysis with backward stepwise elimination was performed. Covariates that were included in this analysis were hemoglobin level, absolute neutrophil count, platelet count, bone marrow blast percentage, cytogenetic risk group and percentage of TM expression on monocytes. Information on all variables was available for 60 patients (not shown). Covariates with a *P* value >0.10 were removed. Both the cytogenetic risk group as well as the percentage of TM expression were predictive markers for overall survival (*P*=0.001 and *P*=0.064, respectively). For leukemia-free survival, the percentage of blasts and TM expression had predictive value (*P*=0.010 and *P*=0.077, respectively).

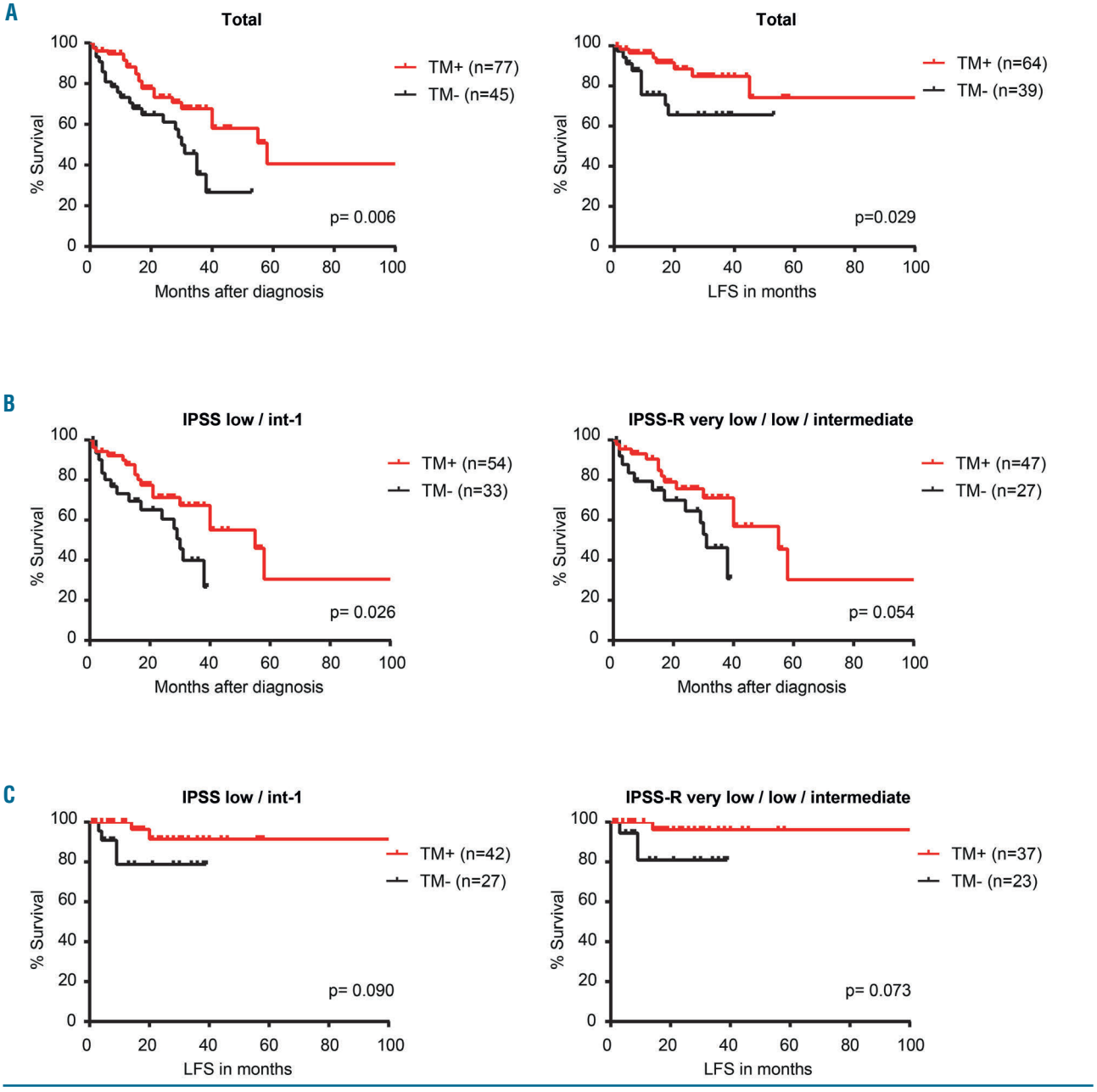

Figure 4. Overall and leukemia-free survival is related to the presence of thrombomodulin-positive monocytes. As a cut-off percentage for the presence of thrombomodulin (TM) on myelodysplastic syndrome (MDS) monocytes, the expression rate in the healthy donor cohort was used. The mean percentage + two standard deviations was calculated, resulting in a cut-off of 25.53%. Statistical differences were calculated using the log-rank test. (A) Overall survival data for 122 MDS patients and leukemia-free survival (LFS) data for 102 patients. A significant difference in overall survival was found between MDS patients with or without TM on BM monocytes (*P*=0.006). The median overall survival for patients with TM$^+$ monocytes was 58 months while that for patients without TM was 30 months. The time to development of leukemia was significantly longer for patients with TM expression than for patients without TM expression (*P*=0.029). (B) Patients were further selected based on their low-risk status. Survival curves are shown for low-risk patients (according to the International Prognostic Scoring System and its revision) with or without TM$^+$ monocytes. (C) LFS of low-risk patients in the TM$^+$ and TM$^-$ groups. IPSS: International Prognostic Scoring System; IPSS-R: Revised International Prognostic Scoring System.

Discussion

The BM microenvironment in MDS, and particularly in low-risk groups, is often characterized by the presence of pro-inflammatory cells and molecules. While increased inflammation and the subsequent cellular immune response are crucial to eliminate malignant cells, continuous immune stimulation could lead to genomic instability and inevitable malignant transformation.[12] Identifying the factors that could maintain a healthy overall immune response in MDS is important and clinically relevant. In mice, it has been shown that lack of the lectin-like domain of TM leads to reduced survival after exposure to endotoxins, whereas a recombinant form diminished NF-κB and MAPK activation.[45] In the current study, we therefore investigated the presence of TM on immune cells in MDS-derived BM and PB samples and its immune-modulatory role in MDS. TM was mainly expressed on monocyte subsets and not on granulocytes, lymphocytes or eosinophils. The difference in TM expression between monocytes from healthy donors and those from patients with MDS was most evident for classical monocytes. FISH analysis showed clonal involvement for these TM+ monocytes. This subset showed hardly any TM expression on cells derived from either healthy BM or healthy PB. In MDS patients there was marked variation in monocytes expressing TM. Some patients showed expression levels similar to those on healthy donor-derived monocytes, whereas for others nearly all monocytes expressed TM. We found that the percentage of TM expression was clearly higher in low-risk MDS groups than in higher-risk groups, suggesting that the presence of TM may be primarily observed in a pro-inflammatory environment (i.e. low-risk MDS). Interestingly, Talati *et al.* previously described a correlation between the presence of classical monocytosis in MDS and favorable prognostic factors such as increased white blood cell counts and absolute neutrophil counts.[46] Furthermore, an increased percentage of monocytes was associated with lower MDS risk groups and good-risk cytogenetics. SF3B1 was present at a higher frequency in this MDS group and overall survival of these patients tended to be better. In this perspective, it would be interesting to investigate the presence of TM in a same set of samples in future research.

Besides active secretion and passive release of inflammatory molecules in the MDS BM environment, certain T-cell subsets, particularly Th1 and Th17 type T cells, contribute to an immune-active state by the secretion of high amounts of interferon-γ and interleukin-17. In order to investigate the effect of monocytes on T-cell skewing, healthy T cells were cultured in the presence of TM+ or TM- MDS monocytes. Using mass cytometry, we were able to utilize a comprehensive panel of surface and intracellular markers for this purpose. Interestingly, T cells cultured in the presence of TM+ monocytes showed an anti-inflammatory skewed profile. Compared to T cells cultured with TM- monocytes, they showed less interferon-γ positivity and higher concentrations of interleukin-4 and interleukin-10 measured intracellularly. While the number of patients' samples was limited and data need to be interpreted with caution, our findings suggest that TM+ monocytes polarize T cells toward Th2 and/or Treg phenotypes.

Collectively, our data point to an interesting function for TM-expressing monocytes in the highly inflammatory environment of low-risk MDS patients. They could play an essential role in dampening disproportionate immune activation by inducing anti-inflammatory T-cell subsets. In keeping with this notion, overall and leukemia-free survival was better for patients in whom the BM contained TM+ monocytes than for patients lacking TM expression, supporting a clinically relevant mechanism. Nevertheless, in the longer term, this mechanism could lead to a profound immunosuppressive state which would prevent effective immune surveillance; a common condition in higher-risk MDS.

Acknowledgments

We thank M.G.H.P. Raaijmakers for a critical review of our manuscript. Furthermore, we acknowledge financial support from the Department of Health via the National Institute for Health Research (NIHR) Biomedical Research Centre awarded to Guy's & St Thomas' NHS Foundation Trust in Partnership with King's College London and King's College Hospital NHS Foundation Trust.

References

1. Kordasti SY, Afzali B, Lim Z, et al. IL-17-producing CD4(+) T cells, pro-inflammatory cytokines and apoptosis are increased in low risk myelodysplastic syndrome. Br J Haematol. 2009;145(1):64-72.
2. Epling-Burnette PK, Bai F, Painter JS, et al. Reduced natural killer (NK) function associated with high-risk myelodysplastic syndrome (MDS) and reduced expression of activating NK receptors. Blood. 2007;109(11):4816-4824.
3. Hejazi M, Manser R, Frobel J, et al. Impaired cytotoxicity associated with defective natural killer cell differentiation in myelodysplastic syndromes. Haematologica. 2015;100(5):643-652.
4. Fozza C, Contini S, Galleu A, et al. Patients with myelodysplastic syndromes display several T-cell expansions, which are mostly polyclonal in the CD4(+) subset and oligoclonal in the CD8(+) subset. Exp Hematol. 2009;37(8):947-955.
5. Fozza C, Longu F, Contini S, et al. Patients with early-stage myelodysplastic syndromes show increased frequency of CD4+CD25+CD127(low) regulatory T cells. Acta Haematol. 2012;128(3):178-182.
6. Bouchliou I, Miltiades P, Nakou E, et al. Th17 and Foxp3(+) T regulatory cell dynamics and distribution in myelodysplastic syndromes. Clin Immunol. 2011;139(3):350-359.
7. Kordasti SY, Ingram W, Hayden J, et al. CD4+CD25high Foxp3+ regulatory T cells in myelodysplastic syndrome (MDS). Blood. 2007;110(3):847-850.
8. Kotsianidis I, Bouchliou I, Nakou E, et al. Kinetics, function and bone marrow trafficking of CD4+CD25+FOXP3+ regulatory T cells in myelodysplastic syndromes (MDS). Leukemia. 2009;23(3):510-518.
9. Mailloux AW, Epling-Burnette PK. Effector memory regulatory T-cell expansion marks a pivotal point of immune escape in myelodysplastic syndromes. Oncoimmunology. 2013;2(2):e22654.
10. Kahn JD, Chamuleau MED, Westers TM, et al. Regulatory T cells and progenitor B cells are independent prognostic predictors in lower risk myelodysplastic syndromes. Haematologica. 2015;100(6):e220-222.
11. Kittang AO, Kordasti S, Sand KE, et al. Expansion of myeloid derived suppressor cells correlates with number of T regulatory cells and disease progression in myelodysplastic syndrome. Oncoimmunology. 2015;5(2):e1062208.
12. Kristinsson SY, Björkholm M, Hultcrantz M, Derolf ÅR, Landgren O, Goldin LR. Chronic immune stimulation might act as a trigger for the development of acute myeloid leukemia or myelodysplastic syndromes. J

Clin Oncol. 2011;29(21):2897-2903.
13. Zambetti NA, Ping Z, Chen S, et al. Mesenchymal inflammation drives genotoxic stress in hematopoietic stem cells and predicts disease evolution in human pre-leukemia. Cell Stem Cell. 2016;19(5):613-627.
14. Basiorka AA, McGraw KL, Eksioglu EA, et al. The NLRP3 inflammasome functions as a driver of the myelodysplastic syndrome phenotype. Blood. 2016;128(25):2960-2975.
15. Shetty V, Hussaini S, Alvi S, et al. Excessive apoptosis, increased phagocytosis, nuclear inclusion bodies and cylindrical confronting cisternae in bone marrow biopsies of myelodysplastic syndrome patients. Br J Haematol. 2002;116(4):817-825.
16. Zang DY, Goodwin RG, Loken MR, Bryant E, Deeg HJ. Expression of tumor necrosis factor-related apoptosis-inducing ligand, Apo2L, and its receptors in myelodysplastic syndrome: effects on in vitro hemopoiesis. Blood. 2001;98(10):3058-3065.
17. Dimicoli S, Wei Y, Bueso-Ramos C, et al. Overexpression of the toll-like receptor (TLR) signaling adaptor MYD88, but lack of genetic mutation, in myelodysplastic syndromes. PLoS One. 2013;8(8):e71120.
18. Gañán-Gómez I, Wei Y, Yang H, et al. Overexpression of miR-125a in myelodysplastic syndrome CD34+ cells modulates NF-κB activation and enhances erythroid differentiation Arrest. PLoS One. 2014;9(4):e93404.
19. Wei Y, Dimicoli S, Bueso-Ramos C, et al. Toll-like receptor alterations in myelodysplastic syndrome. Leukemia. 2013;27(9):1832-1840.
20. Maratheftis CI, Andreakos E, Moutsopoulos HM, Voulgarelis M. Toll-like receptor-4 is up-regulated in hematopoietic progenitor cells and contributes to increased apoptosis in myelodysplastic syndromes. Clin Cancer Res. 2007;13(4):1154-1160.
21. Gañán-Gómez I, Wei Y, Starczynowski DT, et al. Deregulation of innate immune and inflammatory signaling in myelodysplastic syndromes. Leukemia. 2015;29(7):1458-1469.
22. Kondo A, Yamashita T, Tamura H, et al. Interferon-γ and tumor necrosis factor-a induce an immunoinhibitory molecule, B7-H1, via nuclear factor-κB activation in blasts in myelodysplastic syndromes. Blood. 2010;116(7):1124-1131.
23. Navas TA, Mohindru M, Estes M, et al. Inhibition of overactivated p38 MAPK can restore hematopoiesis in myelodysplastic syndrome progenitors. Blood. 2006;108(13):4170-4177.
24. Navas TA, Zhou L, Estes M, et al. Inhibition of p38alpha MAPK disrupts the pathological loop of proinflammatory factor production in the myelodysplastic syndrome bone marrow microenvironment. Leuk Lymphoma. 2008;49(10):1963-1975.
25. Velegraki M, Papakonstanti E, Mavroudi I, et al. Impaired clearance of apoptotic cells leads to HMGB1 release in the bone marrow of patients with myelodysplastic syndromes and induces TLR4-mediated cytokine production. Haematologica. 2013;98(8):1206-1215.
26. Shi C-S, Shi G-Y, Hsiao H-M, et al. Lectin-like domain of thrombomodulin binds to its specific ligand Lewis Y antigen and neutralizes lipopolysaccharide-induced inflammatory response. Blood. 2008;112(9):3661-3670.
27. van de Wouwer M, Plaisance S, de Vriese A, et al. The lectin-like domain of thrombomodulin interferes with complement activation and protects against arthritis. J Thromb Haemost. 2006;4(8):1813-1824.
28. Wang H, Vinnikov I, Shahzad K, et al. The lectin-like domain of thrombomodulin ameliorates diabetic glomerulopathy via complement inhibition. Thromb Haemost. 2012;108(6):1141-1153.
29. Zhang Y, Weiler-Guettler H, Chen J, et al. Thrombomodulin modulates growth of tumor cells independent of its anticoagulant activity. J Clin Invest. 1998;101(7):1301-1309.
30. Horowitz N a, Blevins E a, Miller WM, et al. Thrombomodulin is a determinant of metastasis through a mechanism linked to the thrombin binding domain but not the lectin-like domain. Blood. 2011;118(10):2889-2895.
31. Hanly M, Redmond M, Winter DC, et al. Thrombomodulin expression in colorectal carcinoma is protective and correlates with survival. Br J Cancer. 2006;94(9):1320-1325.
32. Dzionek A, Fuchs A, Schmidt P, et al. BDCA-2, BDCA-3, and BDCA-4: three markers for distinct subsets of dendritic cells in human peripheral blood. J Immunol. 2000;165(11):6037-6046.
33. MacDonald KPA, Munster DJ, Clark GJ, Dzionek A, Schmitz J, Hart DNJ. Characterization of human blood dendritic cell subsets. Blood. 2002;100(13):4512-4520.
34. Jongbloed SL, Kassianos AJ, McDonald KJ, et al. Human CD141+ (BDCA-3)+ dendritic cells (DCs) represent a unique myeloid DC subset that cross-presents necrotic cell antigens. J Exp Med. 2010;207(6):1247-1260.
35. van de Ven R, Lindenberg JJ, Oosterhoff D, de Gruijl TD. Dendritic cell plasticity in tumor-conditioned skin: CD14+ cells at the cross-roads of immune activation and suppression. Front Immunol. 2013;(4):403.
36. Lindenberg JJ, van de Ven R, Lougheed SM, et al. Functional characterization of a STAT3-dependent dendritic cell-derived CD14+ cell population arising upon IL-10-driven maturation. Oncoimmunology. 2013;2(4):e23837.
37. Ziegler-Heitbrock L, Ancuta P, Crowe S, et al. Nomenclature of monocytes and dendritic cells in blood. Blood. 2010;116(16):e74-80.
38. Hofer TP, Zawada AM, Frankenberger M, et al. slan-defined subsets of CD16-positive monocytes: impact of granulomatous inflammation and M-CSF receptor mutation. Blood. 2015;126(24):2601-2611.
39. Van Der Maaten L, Hinton G. Visualizing data using t-SNE. J Mach Learn Res. 2008;9(nov):2579-2605.
40. Amir ED, Davis KL, Tadmor MD, et al. viSNE enables visualization of high dimensional single-cell data and reveals phenotypic heterogeneity of leukemia. Nat Biotechnol. 2013;31(6):545-552.
41. Qiu P, Simonds EF, Bendall SC, et al. Extracting a cellular hierarchy from high-dimensional cytometry data with SPADE. Nat Biotechnol. 2011;29(10):886-891.
42. Kordasti S, Costantini B, Seidl T, et al. Deep phenotyping of Tregs identifies an immune signature for idiopathic aplastic anemia and predicts response to treatment. Blood. 2016;128(9):1193-1205.
43. Kotecha N, Krutzik PO, Irish JM. Web-based analysis and publication of flow cytometry experiments. Curr Protoc Cytom. 2010;Chapter 10:Unit10.17.
44. Diggins KE, Greenplate AR, Leelatian N, Wogsland CE, Irish JM. Characterizing cell subsets using marker enrichment modeling. Nat Methods. 2017;14(3):275-278.
45. Conway EM, Van De Wouwer M, Pollefeyt S, et al. The lectin-like domain of thrombomodulin confers protection from neutrophil-mediated tissue damage by suppressing adhesion molecule expression via nuclear factor kappaB and mitogen-activated protein kinase pathways. J Exp Med. 2002;196(5):565-577.
46. Talati C, Zhang L, Shaheen G, et al. Monocyte subset analysis accurately distinguishes CMML from MDS and is associated with a favorable MDS prognosis. Blood. 2017;129(13):1881-1883.

ARTICLE

Leprosy drug clofazimine activates peroxisome proliferator-activated receptor-γ and synergizes with imatinib to inhibit chronic myeloid leukemia cells

Harish Kumar,[1] Sourav Chattopadhyay,[1,2] Nabanita Das,[1] Sonal Shree,[3] Dinesh Patel,[4] Jogeswar Mohapatra,[4] Anagha Gurjar,[1,2] Sapana Kushwaha,[1] Abhishek Kumar Singh,[1] Shikha Dubey,[3] Kiran Lata,[3] Rajesh Kushwaha,[5] Riyazuddin Mohammed,[6] Krishnarup Ghosh Dastidar,[4] Namrata Yadav,[4] Achchhe Lal Vishwakarma,[7] Jiaur Rahaman Gayen,[6,2] Sanghamitra Bandyopadhyay,[5] Abhijit Chatterjee,[4] Mukul Rameshchandra Jain,[4] Anil Kumar Tripathi,[8] Arun Kumar Trivedi,[1,2] Naibedya Chattopadhyay,[9,2] Ravishankar Ramachandran[2,3] and Sabyasachi Sanyal[1,2]

[1]Division of Biochemistry, CSIR-Central Drug Research Institute, Lucknow; [2]AcSIR, CSIR-Central Drug Research Institute Campus, Lucknow; [3]Division of Molecular and Structural Biology, CSIR-Central Drug Research Institute, Lucknow; [4]Zydus Research Center, Moraiya, Ahmedabad, Gujarat; [5]Developmental Toxicology Laboratory, Systems Toxicology and Health Risk Assessment Group, CSIR-Indian Institute of Toxicology Research, Lucknow; [6]Pharmacokinetics and Metabolism Division, CSIR-Central Drug Research Institute, Lucknow; [7]Sophisticated Analytical Instrument Facility, CSIR-Central Drug Research Institute, Lucknow; [8]Department of Clinical Hematology and Medical Oncology, King George's Medical University, Lucknow, Uttar Pradesh and [9]Division of Endocrinology, CSIR-Central Drug Research Institute, Lucknow, India

Ferrata Storti Foundation

Haematologica 2020
Volume 105(4):971-986

ABSTRACT

Leukemia stem cells contribute to drug-resistance and relapse in chronic myeloid leukemia (CML) and BCR-ABL1 inhibitor monotherapy fails to eliminate these cells, thereby necessitating alternate therapeutic strategies for patients CML. The peroxisome proliferator-activated receptor-γ (PPARγ) agonist pioglitazone downregulates signal transducer and activator of transcription 5 (STAT5) and in combination with imatinib induces complete molecular response in imatinib-refractory patients by eroding leukemia stem cells. Thiazolidinediones such as pioglitazone are, however, associated with severe side effects. To identify alternate therapeutic strategies for CML we screened Food and Drug Administration-approved drugs in K562 cells and identified the leprosy drug clofazimine as an inhibitor of viability of these cells. Here we show that clofazimine induced apoptosis of blood mononuclear cells derived from patients with CML, with a particularly robust effect in imatinib-resistant cells. Clofazimine also induced apoptosis of $CD34^{+}38^{-}$ progenitors and quiescent $CD34^{+}$ cells from CML patients but not of hematopoietic progenitor cells from healthy donors. Mechanistic evaluation revealed that clofazimine, via physical interaction with PPARγ, induced nuclear factor κB-p65 proteasomal degradation, which led to sequential myeloblastoma oncoprotein and peroxiredoxin 1 downregulation and concomitant induction of reactive oxygen species-mediated apoptosis. Clofazimine also suppressed STAT5 expression and consequently downregulated stem cell maintenance factors hypoxia-inducible factor-1α and -2α and Cbp/P300 interacting transactivator with Glu/Asp-rich carboxy-terminal domain 2 (CITED2). Combining imatinib with clofazimine caused a far superior synergy than that with pioglitazone, with clofazimine reducing the half maximal inhibitory concentration (IC_{50}) of imatinib by >4 logs and remarkably eroding quiescent $CD34^{+}$ cells. In a K562 xenograft study clofazimine and imatinib co-treatment showed more robust efficacy than the individual treatments. We propose clinical evaluation of clofazimine in imatinib-refractory CML.

Correspondence:

SABYASACHI SANYAL
sanyal@cdri.res.in

Received: April 11, 2019

Accepted: July 12, 2019.

Pre-published: August 1, 2019.

doi:10.3324/haematol.2018.194910

Check the online version for the most updated information on this article, online supplements, and information on authorship & disclosures: www.haematologica.org/content/105/4/971

Introduction

The therapy of chronic myeloid leukemia (CML) has seen tremendous advances following the discovery of imatinib and other BCR-ABL1 tyrosine kinase inhibitors. However, complete molecular response, defined as undetectable *BCR-ABL1* transcripts, is not achieved in the majority of patients.[1] Resistance to tyrosine kinase inhibitors may occur due to *BCR-ABL1* mutations; however, in approximately 50% of the cases BCR-ABL1-independent mechanisms, including tyrosine kinase inhibitor-refractory leukemia stem cells (LSC), contribute to resistance and recurrence.[1] Therefore therapeutic approaches capable of overcoming resistance to tyrosine kinase inhibitors are needed. Peroxisome proliferator-activated receptor-γ (PPARγ) agonists, pioglitazone in particular, were reported to erode quiescent LSC by targeting signal transducer and activator of transcription 5 (STAT5) expression.[1,2] Unfortunately, pioglitazone increases the risk of bladder cancer.[3] Although rosiglitazone has not been found to increase the incidence of bladder cancer, it is associated with severe cardiovascular risks.[4]

To identify new therapeutic strategies we screened 800 Food amd Drug Administration-approved drugs for their anti-CML efficacy in the K562 cell line and identified clofazimine as a potent inhibitor of viability. Clofazimine, a riminophenazine leprosy drug, is also effective against multidrug-resistant tuberculosis[5] and imparts its anti-bacterial actions by generating reactive oxygen species (ROS), particularly superoxides and hydrogen peroxide (H_2O_2).[6] Clofazimine also displays anti-inflammatory properties that are important for its suppression of leprosy-associated immune reactions.[6] Additionally, clofazimine was shown to be effective against various autoimmune diseases, including discoid lupus erythematosus, Crohn disease, ulcerative colitis, psoriasis, Meischer granuloma and graft-*versus*-host disease.[7] Clofazimine is reported to exert its immunomodulatory activities by blocking KV1.3 voltage-gated potassium channels[7] and thereby inhibiting chronic lymphocytic leukemia cells.[8,9]

Here we report the anti-CML efficacy of clofazimine in cells lacking KV1.3,[8,10] and show that clofazimine exerted its effects by binding to PPARγ. Clofazimine not only suppressed STAT5 expression by modulating PPARγ transcriptional activity but also regulated a novel signaling cascade by increasing PPARγ-mediated p65 nuclear factor kappa B (NFκB) degradation, which caused transcriptional downregulation of cellular myeloblastoma oncoprotein (MYB), leading to suppression of peroxiredoxin 1 (PRDX1) expression and consequent induction of ROS-mediated apoptosis and differentiation.

Methods

Cell lines and human primary cells

K562 (CCL-243), HL-60 (CCL-240), U937 (CRL-1593.2), and HEK-293 (CRL-1573) cells were from the American Type Culture Collection (ATCC; Manassas, VA, USA) and were maintained as per ATCC instructions. Peripheral blood samples were obtained from BCR-ABL1$^+$ CML patients (newly diagnosed, imatinib-resistant and imatinib responders), and healthy donors from King George's Medical University (Clinical Hematology and Medical Oncology Division, Lucknow, India) following ethical approval (approval n. 1638/R. Cell-12) as per institutional ethical guidelines after written consent (patients' details in *Online Supplementary Table S1*). Peripheral blood mononuclear cells were isolated on a Percoll (Sigma) density gradient by centrifugation. All analyses of peripheral blood mononuclear cells were conducted on gated mononuclear cells excluding lymphocytes.

Other methods

Chemicals, antibodies, plasmid information and experimental procedures are detailed in the *Online Supplementary Methods*.

Statistical analysis

Data are expressed as the mean ± standard error of mean of three independent experiments, unless otherwise indicated. Statistical analyses were performed using GraphPad Prism 5.0. An unpaired two-tailed Student *t*-test or Mann-Whitney U test was used to compare two groups. Equality of variances was assessed by the F-test. Statistical analyses involving more than two groups were performed by one- or two-way analysis of variance followed by the Bonferroni post-test, or Kruskal-Wallis test followed by the Dunn test. For intra-group variances, we used the Levene median test (equal sample size; using XLSTAT) or Bartlett test (unequal sample size). $P<0.05$ was accepted as statistically significant.

Results

Clofazimine induces apoptosis and differentiation in chronic myeloid leukemia cells

In a screening in K562 cells, we identified clofazimine as a potent inhibitor of viability. Clofazimine has been reported to induce cytotoxicity by targeting KV1.3.[7-9] Intriguingly, although K562 does not express KV1.3[8,10] (*Online Supplementary Figure S1A*), clofazimine reduced the viability of these cells with a pharmacologically relevant half maximal inhibitory concentration (IC_{50}) of 5.85 μM (Figure 1A). The human plasma C_{max} of clofazimine is 0.4-4 mg/L, equivalent to 0.84-8.4 μM.[6,11-13] The loss of viability was due to apoptosis, as demonstrated by annexin V staining (Figure 1B, *Online Supplementary Figure S1B*), poly (ADP-ribose) polymerase (PARP) cleavage (Figure 1C) and terminal deoxynucleotidyl transferase dUTP nick end labeling (TUNEL) (*Online Supplementary Figure S1C*). Clofazimine induced cytochrome C release and activated caspase -3 and -9 but not -8 (Figure 1D), suggesting mitochondria-mediated apoptosis, which was consistent with decreased B-cell lymphoma 2 (BCL-2) and increased BAX expression (Figure 1D). Clofazimine also induced apoptosis in peripheral blood mononuclear cells from patients with chronic phase CML (CP-CML cells; one newly diagnosed patient was in accelerated phase, one imatinib-responder was in blast crisis) with an efficacy similar to that of cells from patients with newly diagnosed CML and imatinib-responders but higher than that of imatinib and dasatinib in imatinib-resistant cells, while it did not affect healthy donor cells (Figure 1E, *Online Supplementary Figure S1D*). Among the 21 imatinib-resistant patients (Figure 1E), seven harbored the following *BCR-ABL1* mutations; M244V (n=1), Y253H (n=2), M351T (n=3) and F359V (n=1); clofazimine showed efficacy in all cases (Figure 1F; upper panel). A separate analysis of apoptosis in imatinib-resistant patients without *BCR-ABL1* mutations (from Figure 1E) also showed significant clofazimine-induced apoptosis (n=6: vehicle, imatinib, clofazimine; n=5; dasatinib. Figure 1F; lower panel), indicating that clofazimine-

induced apoptosis in imatinib-resistant cells is independent of *BCR-ABL1* mutations.

We next assessed whether clofazimine inhibited LSC. Increased aldehyde dehydrogenase activity is a hallmark of cancer stem cells[14] and clofazimine reduced it in imatinib-resistant CP-CML cells at par with the positive control salinomycin (Figure 1G, *Online Supplementary Figure S2A*). Clofazimine also reduced colony formation in CML CD34$^+$ cells (Figure 1H, *Online Supplementary Figure S2C*). To further confirm its anti-LSC efficacy we treated purified CML CD34$^+$ cells with clofazimine and analyzed them by CD34 or annexin V staining. Clofazimine reduced the CD34$^+$ population and induced apoptosis in these cells (Figure 1I, *Online Supplementary Figure S2B*). Treating CML CD34$^+$ cells with clofazimine and analyzing them by CD34, CD38 and annexin V co-staining revealed that clofazimine induced apoptosis in both committed CD34$^+$38$^+$ and primitive CD34$^+$38$^-$ progenitor cells (Figure 1J). Clofazimine however, caused <5% loss in viability and no apoptosis in hematopoietic progenitor cells from healthy donors (Figure 1K, L, *Online Supplementary Figure S2D*) indicating that it specifically targets LSC. Clofazimine's effects in CML CD34$^+$ cells were not routed through KV1.3 as KV1.3 transcript was undetectable in CD34$^+$-enriched CP-CML cells (n=7; *Online Supplementary Figure S3*).

We next investigated whether clofazimine induced differentiation at sub-lethal concentrations. In K562 cells that predominantly undergo erythroid or megakaryocytic differentiation upon various stimuli, clofazimine induced a megakaryocyte-like phenotype characterized by increased cellular size, nuclear to cytoplasmic ratio, vacuolation, and lobulated nuclei (*Online Supplementary Figure S4A*). Consistently, clofazimine increased megakaryocytic surface markers CD61 and CD41 in K562 (*Online Supplementary Figure S4B-D*) and CML (one newly diagnosed patient was in accelerated phase, one imatinib-resistant patient was in blast crisis) cells (Figure 1M, *Online Supplementary Figure S4E-F*). Clofazimine treatment in CML CD34$^+$ cells followed by May-Grünwald-Giemsa staining revealed increased monocyte-like morphology (Figure 1N, *Online Supplementary Figure S4G*). Concurrently, expression of the monocyte/macrophage differentiation marker CD11b was increased in clofazimine-treated CD34$^+$ cells (Figure 1O, *Online Supplementary Figure S4H*). Furthermore, clofazimine also induced CD61 in CD34$^+$ cells (Figure 1P, *Online Supplementary Figure S4H*).

Apoptosis- and differentiation-inducing effects of clofazimine are associated with enhanced reactive oxygen species and decreased PRDX1 expression

We next asked how clofazimine exerts its action and decided to address its differentiation-inducing activity first. Megakaryocytic differentiation in K562 cells is typically associated with prolonged extracellular signal-regu-

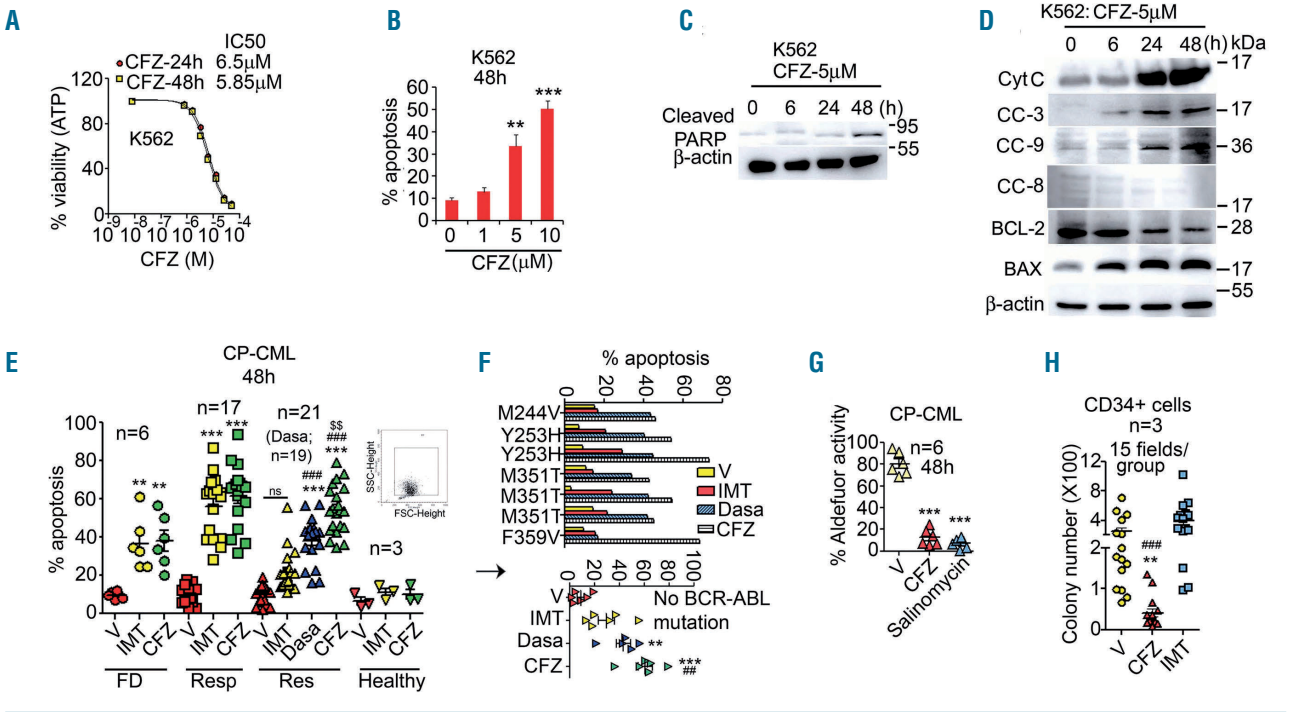

Figure 1. Clofazimine induces apoptosis and differentiation in K562 and chronic phase chronic myeloid leukemia cells and reduces leukemia stem cell load. (A, B) Clofazimine (CFZ) reduces K562 cell viability and induces apoptosis. (A) CFZ dose response, as determined by a CellTiter-Glo assay. (B) Apoptosis (n=3; representative dot plot in *Online Supplementary Figure S1B)*. (C) Poly (ADP-ribose) polymerase cleavage in K562 cells. (D) CFZ induces cytochrome C release, caspase cleavage, BAX expression and suppresses BCL-2 in K562 cells. (E, F) CFZ (all drugs 5 µM) induces apoptosis in chronic phase chronic myeloid leukemia (CP-CML) cells (annexin/propidium iodide (PI) staining; dot plots in *Online Supplementary Figure S1D*). (F) Percentage apoptosis in cells from imatinib-resistant patients in Figure 1E, harboring the indicated BCR-ABL1 mutations (upper panel) and CP-CML cells in which no BCR-ABL1 mutations were detected (lower panel). (G) CFZ (or salinomycin; both at a concentration of 5 µM) reduced aldehyde dehydrogenase activity, determined by percentage aldefluor activity in CP-CML cells (dot plots in *Online Supplementary Figure S2A*). (H) CFZ reduces the number of colony-forming cells in soft agar (images in *Online Supplementary Figure S2C*; imatinib 1 µM, CFZ 2.5 µM). *(continued on next page)*

lated kinase (ERK) activation.[15,16] Interestingly, mitogen-activated protein kinase (MAPK) kinase inhibitor U0126 failed to inhibit clofazimine but not phorbol myristate acetate (PMA)-induced CD41 expression (Figure 2A, *Online Supplementary Figure S5A*). Consistently, PMA but not clofazimine induced ERK phosphorylation in K562 cells (Figure 2B). Apart from ERK, ROS induces megakaryocytic differentiation[17-19] and determination of cellular ROS revealed that clofazimine significantly enhanced ROS production from 12 h onwards (Figure 2C, *Online Supplementary Figure S5B*). Clofazimine also enhanced mitochondrial superoxide (Figure 2D, E) and H_2O_2 (Figure 2F) and caused mitochondrial membrane depolarization (Figure 2G, *Online Supplementary Figure S5C*). Co-treatment with ROS scavengers and inhibitors revealed that α-tocopherol, which interacts with superoxides[20] and also blocks H_2O_2 and peroxynitrite-mediated toxicity,[21-23] completely abrogated clofazimine-induced cell death while the ROS scavenger N-acetyl-L-cysteine and H_2O_2 decomposer catalase had lesser but significant effects, and the mitochondrial complex inhibitors rotenone and antimycin and the NADPH oxidase inhibitor diphenyleneiodonium were ineffective (Figure 2H). α-tocopherol also inhibited clofazimine-induced CD41 and CD61 expression (Figure 2I, *Online Supplementary Figure S5D-F*). These results indicate that clofazimine induced ROS-dependent cell death and differentiation.

Cancer cells, including cancer stem cells, display high levels of ROS coupled with increased antioxidants that help them detoxify ROS.[24-27] We thus investigated whether

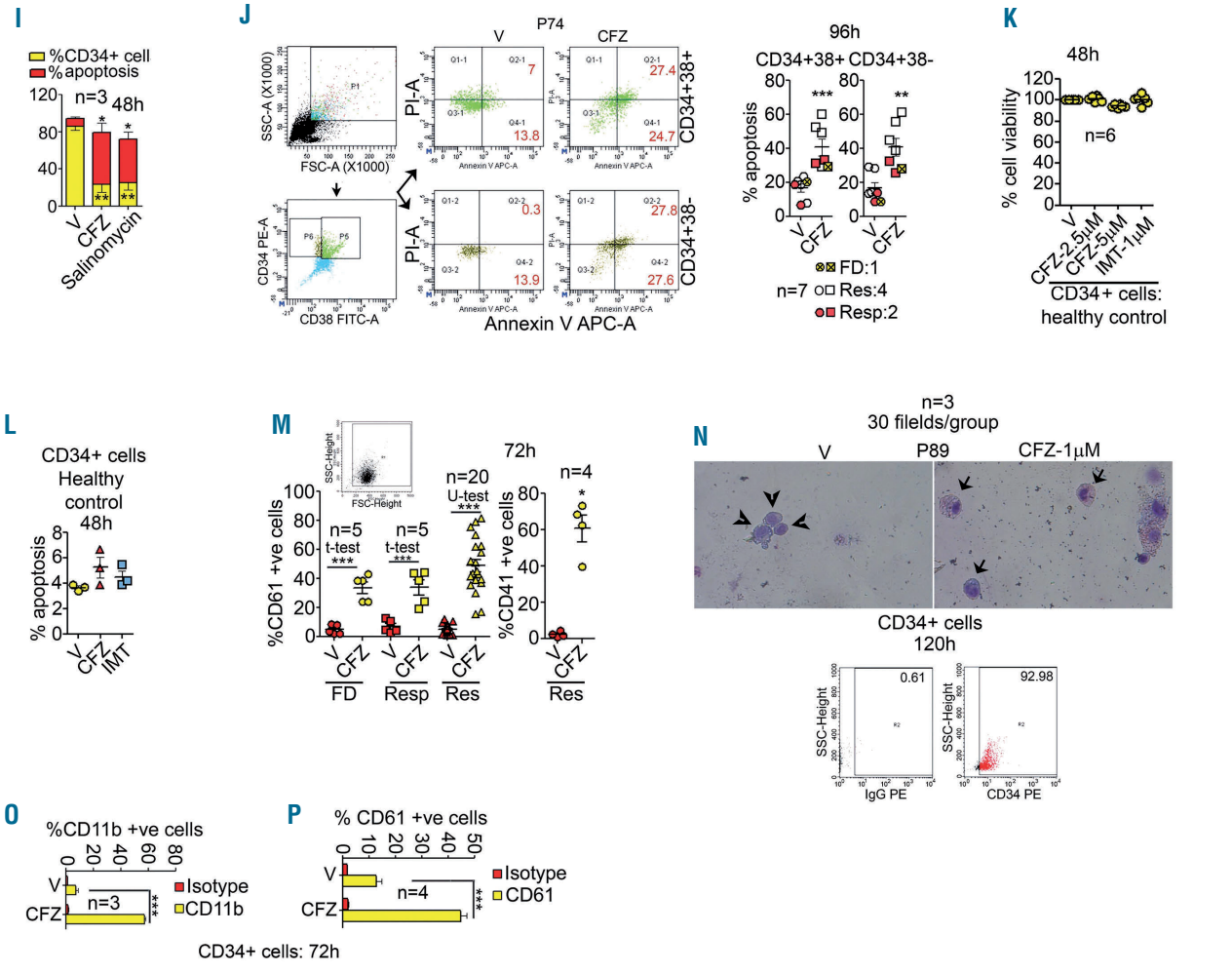

Figure 1. *(continued from previous page)* (I, J) CFZ induces apoptosis in CP-CML CD34⁺ cells. (I) CD34⁺ cells from imatinib-resistant patients were isolated using a CD34 microbead kit (Miltenyi Biotech) and were treated with 5 μM CFZ or salinomycin for 48 h. Cells were then divided into two groups. One group was assessed by immunostaining for CD34 and the other group was stained with annexin V/PI and the cells were then analyzed by flow cytometry (dot plots in Online Supplementary Figure S2B). (J) The CD34⁺ population from imatinib-resistant CP-CML cells was treated with CFZ (2.5 μM) for 96 h, stained with anti-CD34 and anti-CD38 antibodies and assessed for apoptosis. (K, L) CFZ does not affect viability of hematopoietic progenitors from healthy controls. (K) Cell viability, determined by a CellTiter-Glo assay. (L) Apoptosis by annexin V staining (dot plots in *Online Supplementary Figure S2D*). (M) CFZ (1 μM) induces CD61 and CD41 in CP-CML cells (dot plots in *Online Supplementary Figure S4E, F*). (N) CFZ induces monocyte-like morphology in CD34⁺ cells (cropped images shown; corresponding original images in *Online Supplementary Figure S4G*). (O, P) CFZ (1 μM) induces CD11b (O) and CD61 (P) in CD34⁺ CP-CML cells (histograms in Online Supplementary Figure S4H). Graphs illustrate the mean ± standard error mean. *P<0.05, **P<0.01, ***P<0.001; one-way analysis of variance followed by the Bonferroni post-test (except J, O, P; unpaired two-tailed t-test, H; Kruskal-Wallis test followed by the Dunn test, M; left panel, as indicated and right panel; Mann-Whitney U test). *Vehicle *vs.* treatment, #imatinib *vs.* other treatments, $dasatinib *vs.* CFZ. Microscopic images; n=3 (Leica DMI6000B, 30 fields/group). Blots are representative of three independent experiments (all full blots in *Online Supplementary Figure S14*). A letter P followed by a number (in N and subsequent figures) designates the patient's identity. PARP: poly (ADP-ribose) polymerase; Cyt C: cytochrome C; CC; cleaved caspase; V: vehicle; IMT; imatinib; Dasa; dasatinib; FD; freshly diagnosed, Resp; imatinib-responder, Res; imatinib-resistant.

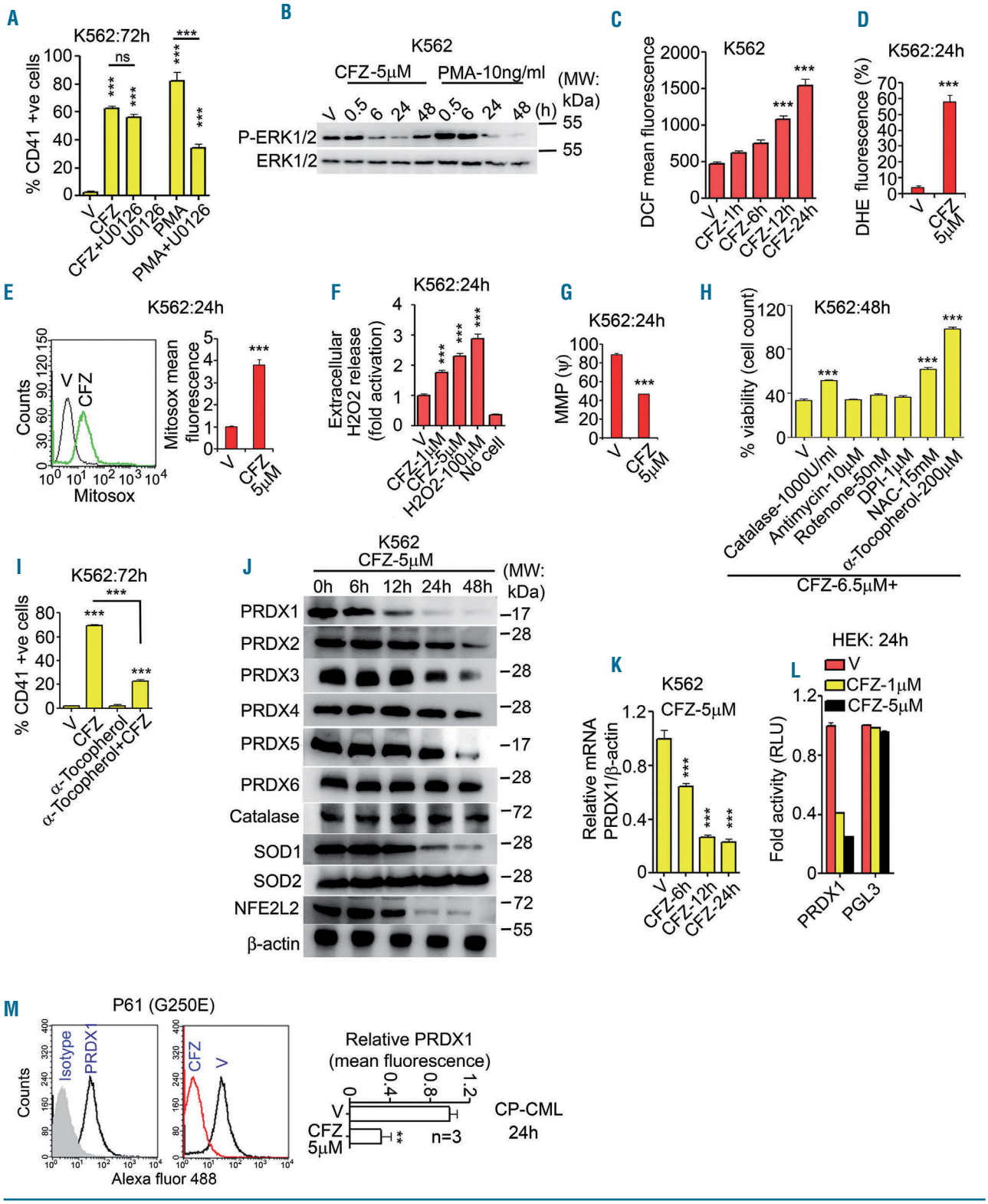

Figure 2. Clofazimine downregulates PRDX1 expression, which leads to reactive oxygen species-dependent differentiation and apoptosis. (A) Phorbol myristate acetate (10 ng/mL) but not clofazimine (CFZ) (2.5 μM)-induced CD41 expression in K562 cells is blocked by U0126 (10 μM; 30 min pre-treatment). Representative histograms are shown in *Online Supplementary Figure S5A*. (B) CFZ does not induce ERK phosphorylation. (C-F) CFZ induces the production of cellular reactive oxygen species (ROS). Total ROS (C; representative histograms in *Online Supplementary Figure S5B*), total superoxide (D), mitochondrial superoxide (E), and H_2O_2 (F). (G) CFZ induces mitochondrial membrane depolarization (dot plot in *Online Supplementary Figure S5C*). (H) α-tocopherol completely blocks CFZ-induced loss of K562 viability. (I) α-tocopherol (200 μM) blocks CFZ (2.5 μM)-induced CD41 expression in K562 cells (representative histograms in *Online Supplementary Figure S5D*). (J) CFZ reduces peroxiredoxin 1 (PRDX1) protein level within 12 h. (K) CFZ reduces *PRDX1* mRNA within 6 h in K562 cells. (L) CFZ reduces a PRDX1 (-1096-+83) promoter-driven luciferase reporter activity in HEK-293 cells. (M) CFZ reduces PRDX1 protein in cells from patients with imatinib-resistant chronic phase chronic myeloid leukemia. Immunoblots are representative of three independent experiments. Graphs illustrate the mean ± standard error of mean. ***P*<0.01, ****P*<0.001 (A,C,F,H,I,K; one-way analysis of variance followed by the Bonferroni post-test. D,E,G,M; unpaired two-tailed Student *t*-test). V: vehicle; PMA: phorbol myristate acetate, ERK: extracellular signal-regulated kinase; MW: molecular weight; DHE: dihydroethidium; MMP: matrix metalloproteinase; DPI: diphenyleneiodonium; NAC: N-acetyl-L-cysteine; SOD: superoxide dismutase; NFE2L2: Nuclear factor erythroid 2 like 2; CP-CML: chronic phase chronic myeloid leukemia.

clofazimine altered the expression of factors that modulate cellular ROS or impart protection against them. Evaluation of peroxiredoxin thioperoxidases, which catalyze reduction of peroxynitrite, H_2O_2 and organic hydroperoxides[24,28] revealed that clofazimine reduced PRDX1 expression at 12 h (Figure 2J) which coincided with clofazimine-induced ROS production (Figure 2C). Clofazimine also reduced PRDX3 (24 h), PRDX2 and PRDX5 (48 h) but not PRDX4 and PRDX6 (Figure 2J). Clofazimine suppressed cytosolic superoxide dismutase SOD1 (24 h onwards) but not mitochondrial SOD2 expression (Figure 2J). Nuclear factor erythroid 2 like 2 (NFE2L2), which regulates expression of various cytoprotective and multidrug resistant proteins,[29] was also downregulated by clofazimine (24 h onwards; Figure 2J). Clofazimine did not alter catalase expression (Figure 2J).

Since suppression of PRDX1 expression was the most proximal event observed (Figure 2J), we studied it in detail. Clofazimine suppressed *PRDX1* mRNA in K562 cells as early as 6 h (Figure 2K; quantitative real-time polymerase chain reaction primer sequences are listed in *Online Supplementary Table S2*) indicating that clofazimine may regulate the *PRDX1* promoter. We thus assessed clofazimine's effect in HEK-293 cells transfected with a *PRDX1* promoter-driven luciferase reporter (PRDX1-luc; -1065-+83) or an empty reporter and found that clofazimine specifically repressed the PRDX1-luc (Figure 2L), confirming that it modulates the *PRDX1* promoter. Figure 2L also indicates that factor(s) responsible for clofazimine-mediated downregulation of the *PRDX1* promoter is(are) endogenously expressed in HEK-293. Clofazimine also reduced PRDX1 protein in CML cells (Figure 2M).

Introduction of exogenous PRDX1 ameliorates clofazimine-induced generation of cellular reactive oxygen species, differentiation and apoptosis

We next asked whether clofazimine's actions were mediated by PRDX1 and thus conducted rescue experiments with exogenous PRDX1. PRDX1 overexpression in K562 cells abrogated clofazimine-induced ROS production (Figure 3A), caspase cleavage and BAX expression (Figure 3B). Clofazimine-induced K562 apoptosis and differentiation were also blocked in PRDX1-transfected cells (Figure 3C, D and *Online Supplementary Figure S6A,B*). Consistently, clofazimine failed to induce ROS and apoptosis in PRDX1-transfected CML $CD34^+$ cells (Figure 3E-H). Given its observed protective function we investigated whether *PRDX1* expression is elevated in CML cells and found that there was a trend to increased *PRDX1* mRNA (albeit statistically insignificant) in CP-CML cells compared to healthy donor cells (Figure 3I). We also compared *PRDX1* levels in LSC *versus* non-LSC. Both $CD34^+38^+$ and $CD34^+38^-$ cells expressed significantly higher levels of *PRDX1* transcript than did $CD34^-38^+$ cells (which were primarily gated monocytic cells), with the highest expression observed in the $CD34^+38^+$ population (Figure 3J, *Online Supplementary Figure S6C*). These results indicate that clofazimine-mediated transcriptional repression of *PRDX1* expression plays a key role in imparting clofazimine's actions.

Clofazimine-mediated suppression of PRDX1 expression is achieved through downregulation of MYB expression

Clofazimine decreased *PRDX1* mRNA at 6 h (Figure 2K) and suppressed a *PRDX1* promoter reporter (Figure 2L), indicating that it may regulate transcription factors that modulate the *PRDX1* promoter. A literature search revealed predicted binding sites for MYB, E2F transcription factor 1 (E2F1), glucocorticoid receptor (GR), CCAAT/enhancer binding protein alpha (CEBPα), cAMP response element binding protein (CREB), activating transcription factor 4 (ATF-4) and activator protein 1 (AP-1) on the *PRDX1* promoter.[30] In K562 cells, clofazimine treatment decreased MYB expression from 3 h and CREB from 12 h onwards but had only a modest or no effect on GR, E2F1, C-Jun, C-Fos and ATF-4 (Figure 4A, *Online Supplementary Figure S7*).

Since MYB downregulation was the most proximal event observed which preceded PRDX1 downregulation and that MYB is endogenously expressed in HEK-293 cells,[31] we studied it in detail. Clofazimine reduced *MYB* transcripts in K562 cells from 1 h onwards (Figure 4B). Consistently, clofazimine suppressed a canonical MYB response element-driven reporter (3X MRE), while transfection of exogenous MYB rescued it (Figure 4C). We next assessed whether MYB could regulate *PRDX1* promoter, and introduction of exogenous MYB did indeed activate PRDX1-luc (-1065-+83) (Figure 4D). Furthermore, clofazimine downregulated PRDX1-luc in vector-transfected cells, and introduction of exogenous MYB dampened it (Figure 4D). These results indicate that MYB regulated the *PRDX1* promoter probably by directly binding to it, and clofazimine suppressed PRDX1 expression by downregulating endogenous MYB expression. We thus attempted to identify the MYB-responsive element on the *PRDX1* promoter. *PRDX1* promoter deletion-mapping revealed that MYB activated the -11-+83 but not the +9-+83 construct (Figure 4E). Analysis of the -11-+9 region revealed a sequence resembling the consensus MYB binding site "PyAACG/TG"[32,33] in reverse and complementary orientation; "CCGTTC", at position -8--3. Mutation of this sequence in the -11-+83 promoter reporter to "CCGggC", led to complete loss of MYB-responsiveness (Figure 4F). To further confirm that this sequence is indeed the MYB-responsive region on the *PRDX1* promoter, we constructed a reporter containing three copies of the -11-+9 sequence (PRDX-MYB-RE) and co-transfected it with MYB or empty vector and found that MYB did indeed specifically activate PRDX-MYB-RE (Figure 4G). Chromatin immunoprecipitation confirmed that MYB was recruited on the *PRDX1* promoter and that clofazimine reduced its recruitment, and consequently reduced histone H3 acetylation (indicating reduced transcription) (Figure 4H). Consistently, clofazimine reduced MYB protein in CP-CML (Figure 4I-J), and *MYB* transcript in CML $CD34^+$ cells (Figure 4K).

We next assessed whether the introduction of exogenous MYB could compromise clofazimine's actions and found that MYB overexpression in K562 cells did indeed mitigate the clofazimine-mediated decrease in PRDX1 expression and increase in caspase-3 cleavage, apoptosis, differentiation and ROS (Figure 4L-O, *Online Supplementary Figure S8A,B*). *MYB* mRNA expression in both imatinib-resistant and -responsive CP-CML cells was significantly higher than in control cells (Figure 4P). These results indicate that MYB binds to the *PRDX1* promoter and regulates its expression and clofazimine-mediated cellular functions are achieved through downregulation of MYB.

Clofazimine reduces MYB expression by rapid degradation of p65 NFκB protein

Clofazimine reduced *MYB* mRNA expression from 1 h in K562 cells (Figure 4B); we therefore investigated whether it regulates any factor that regulates MYB expression itself. A literature search revealed that NFκB transcription factors regulate MYB expression by various mechanisms.[34-37] Consistent with a reported NFκB response element (NFκB-RE) in the *MYB* promoter situated at -278 to -256 bp upstream of the transcriptional start site,[37] tumor necrosis factor-α treatment, or p65/RELA transfection activated a *MYB* (-687-+204) promoter reporter[38] (Figure 5A). Given that clofazimine downregulated *PRDX1* promoter luc in HEK-293 cells (Figure 2L) and that p65 is endogenously expressed in HEK-293 cells,[39] we investigated whether clofazimine regulates p65 expression. Clofazimine reduced p65 protein in K562 cells within 15 min, without affecting other NFκB family members, p50, p105 and C-Rel (Figure 5B). Clofazimine did, however, fail to alter *p65* mRNA expression (Figure 5C) indicating that clofazimine-mediated p65 downregulation may happen at a post-transcriptional or -translational level.

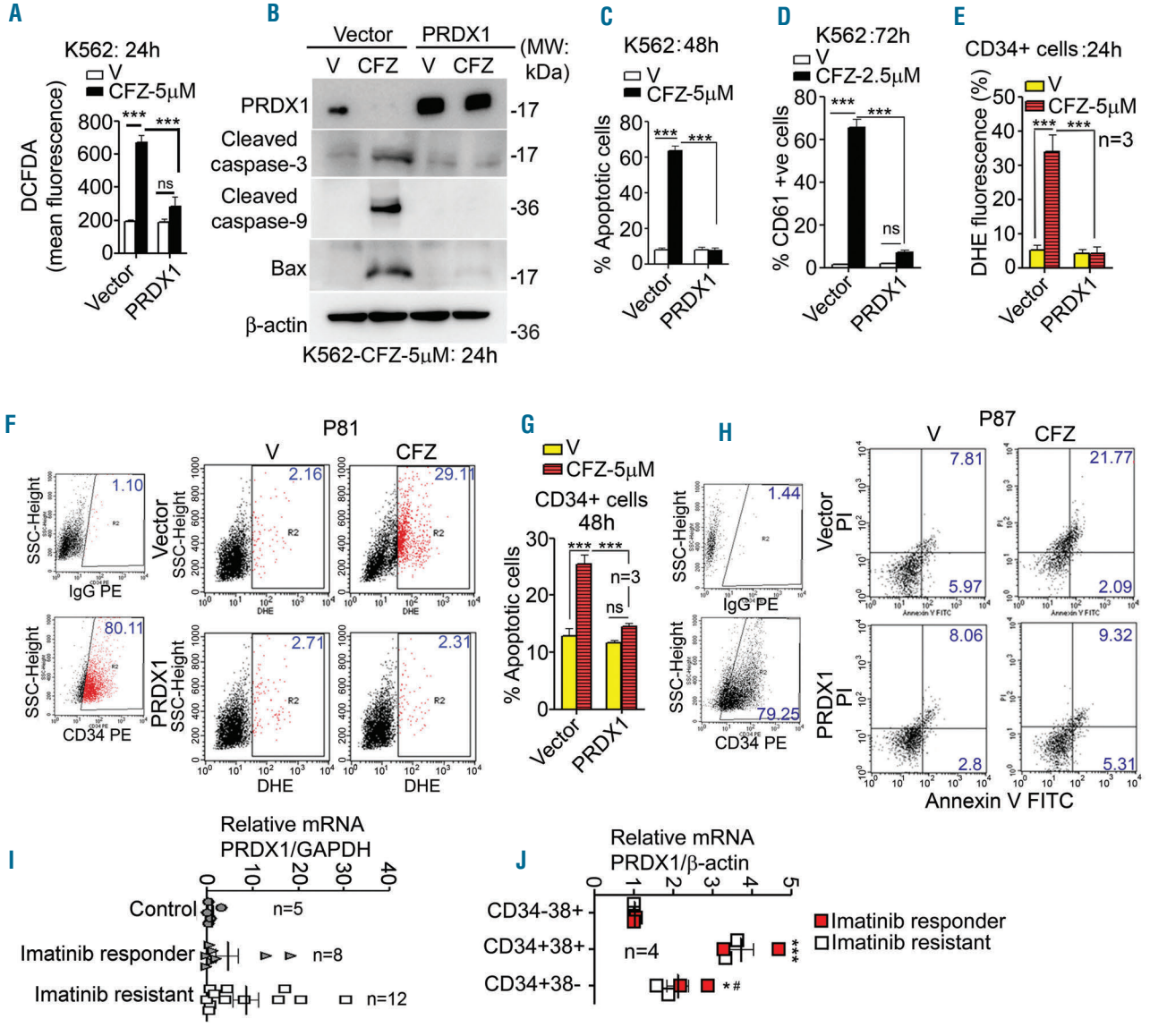

Figure 3. Introduction of exogenous PRDX1 in cells compromises clofazimine-induced reactive oxygen species generation, apoptosis and differentiation. (A-D) Overexpression of peroxiredoxin 1 (PRDX1) in K562 cells ameliorates clofazimine (CFZ)-induced reactive oxygen species generation (A), caspase cleavage and BAX expression (B), apoptosis (C; representative dot plots in *Online Supplementary Figure S6A)*, and CD61 expression (D; representative histograms in *Online Supplementary Figure S6B*). (E-H). $CD34^+$ chronic myeloid leukemia (CML) cells transfected with PRDX1 are protected from CFZ-induced ROS generation and apoptosis. (E, F) $CD34^+$ cells were isolated from chronic phase (CP)-CML cells as described above and were transfected with empty vector or a PRDX1 expression plasmid. Cells were then treated with CFZ (5 μM; 24 h) and dihydroethidium fluorescence was measured by flow cytometry (E; graphical representation, F; representative dot plots). (G, H) $CD34^+$ cells transfected with empty vector or PRDX1 were treated with CFZ (5 μM; 48 h) and apoptosis was assessed by annexin V staining followed by flow cytometry (G; graphical representation, H; representative dot plots). (I) *PRDX1* mRNA expression in CP-CML cells determined by quantitative real-time polymerase chain reaction (QRT-PCR). (J) PRDX1 mRNA expression in $CD34^-38^+$, $CD34^+38^+$ and $CD34^+38^-$ cells by QRT-PCR. Graphs (except I & J) are mean ± standard error of mean of three independent experiments. Immunoblots are representative of three independent experiments. $^{**}P<0.01$, $^{***}P<0.001$ (A,C,D-E,G; two-way analysis of variance followed by the Bonferroni post-test. I,J; Kruskal-Wallis test followed by the Dunn test). DCFDA: 2',7'-dichlorofluorescein diacetate; V: vehicle; SSC; side scatter; DHE: dihydroethidium; PE: phycoerythrin.

Furthermore, consequent to its downregulation of p65, clofazimine suppressed an NFκB-RE reporter (Figure 5D). We next investigated whether the clofazimine-mediated rapid decrease in p65 was due to proteasomal degradation, and found that clofazimine failed to reduce p65 in the presence of the proteasomal inhibitors MG132 and lactacystin (Figure 5E). p65 degradation was associated with its increased ubiquitination by clofazimine (Figure 5F). These results indicate that clofazimine causes p65 ubiquitination leading to its proteasomal degradation. Clofazimine also significantly decreased p65 protein in CP-CML cells (Figure 5G).

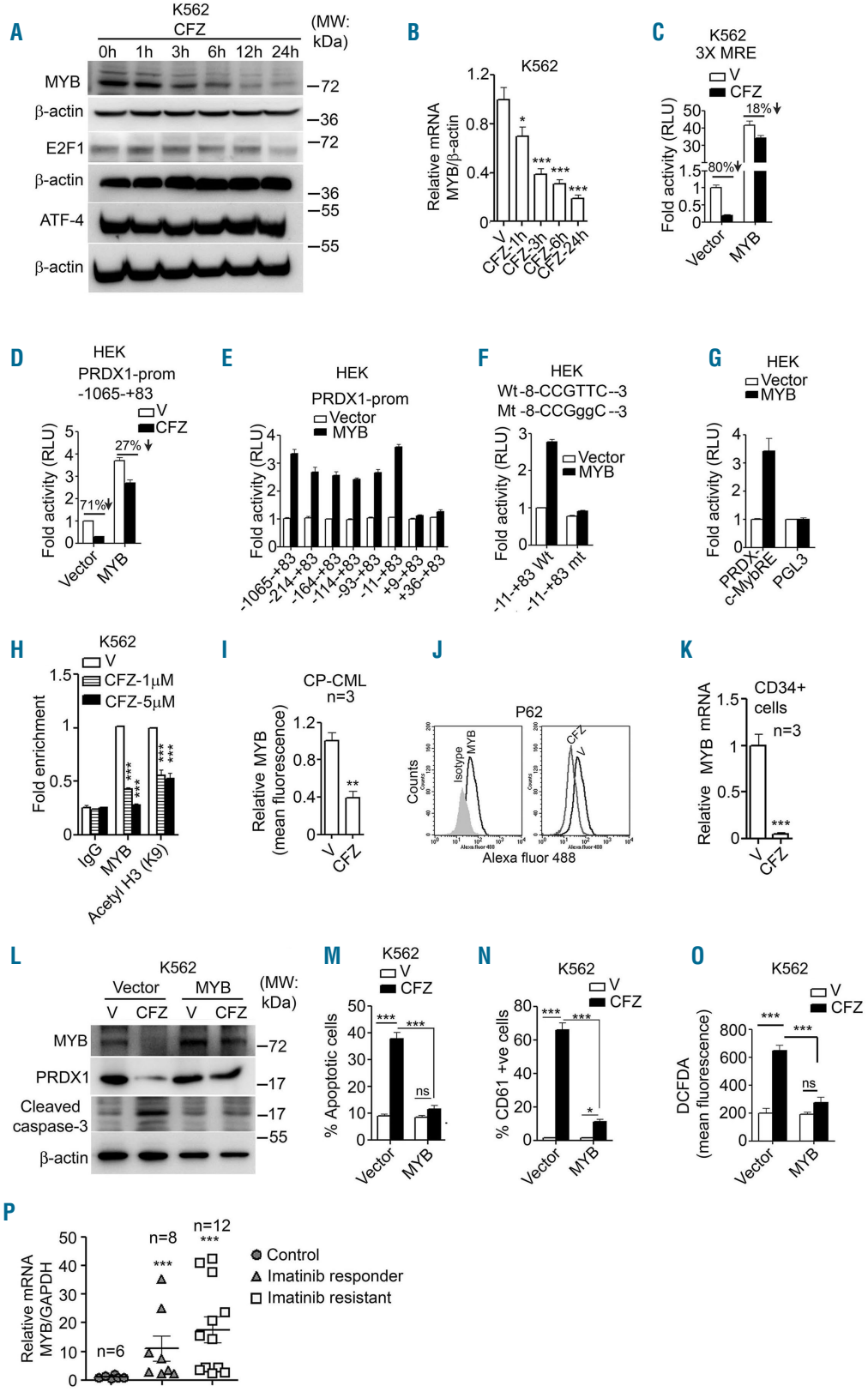

Figure 4. Clofazimine modulates PRXD1 expression via transcriptional regulation of MYB. (A, B) Clofazimine (CFZ) (5 μM) reduces myeloblastoma oncoprotein (MYB) protein (A), mRNA (B) expression in K562 cells. (C) CFZ (5 μM, 24 h) reduces a three copy MYB consensus response element-containing reporter activity in K562 cells and overexpression of MYB, mitigates this repression. (D) CFZ (5 μM, 24 h) represses the peroxiredoxin 1 (PRDX1) promoter-luc and overexpression of MYB activates this reporter and ameliorates its CFZ-mediated repression. (E) Deletion mapping of the ~1 kb PRDX1 promoter in HEK-293 cells reveals MYB response between the -11 to +9 region in the MYB promoter. (F) MYB activates a reporter containing -11 to +83 wildtype (Wt) but not mutated (mt; mutated bases in lower case letters) PRDX1 promoter sequence in HEK-293 cells. (G) MYB activates a reporter containing the -11 to +9 PRDX1 promoter sequence in three tandem repeats in HEK-293 cells. (H) MYB is recruited to the endogenous PRDX1 promoter in K562 cells and CFZ (24 h) reduces its recruitment and concomitantly reduces histone 3 (K9) acetylation. (I, J) CFZ (5 μM, 24 h) reduces MYB protein in imatinib-resistant chronic phase chronic myeloid leukemia (CP-CML) cells (I; graphical representation, J; representative histogram). (K). CFZ (5 μM, 24 h) suppresses MYB expression in CD34$^+$ cells. (L-O; treatment concentration and duration same as Figure 3A-D) Overexpression of MYB in K562 cells mitigates CFZ-mediated downregulation of PRDX1 protein level, and induction of caspase-3 cleavage (L), enhanced K562 apoptosis (M; dot plots in *Online Supplementary Figure S8A*), CD61 expression (N; histograms in *Online Supplementary Figure S8B*) and cellular reactive oxygen species (O). (P) MYB mRNA expression in CP-CML cells. Graphs, except (P), show the mean ± standard error of mean of three independent experiments. Immunoblots are one representative of three independent experiments. *P<0.05, **P<0.01, ***P<0.001. (B, H) one-way, (M-O) two-way ANOVA followed by the Bonferroni post-test. (I, K); unpaired two-tailed Student t-test. (P) Kruskal-Wallis test followed by the Dunn test. E2F1; E2F transcription factor ATF-4: activating transcription factor 4; RLU: relative light unit; 3X MRE: three copy MYB consensus response element; V; vehicle; DCFDA: 2',7'-dichlorofluorescein diacetate; GAPDH: glyceraldehyde 3-phosphate dehydrogenase.

We next evaluated whether the introduction of exogenous p65 could affect clofazimine's actions and found that p65 overexpression did indeed ameliorate the clofazimine-mediated decrease in MYB and PRDX1 expression, increased caspase-3 cleavage (Figure 5H), apoptosis, differentiation and ROS production in K562 cells (Figure 5I-K, *Online Supplementary Figure S9A, B*). There was a trend (albeit not statistically significant) to increased p65 mRNA in CP-CML cells compared to the level in cells from healthy donors (Figure 5L). Together, the results indicate

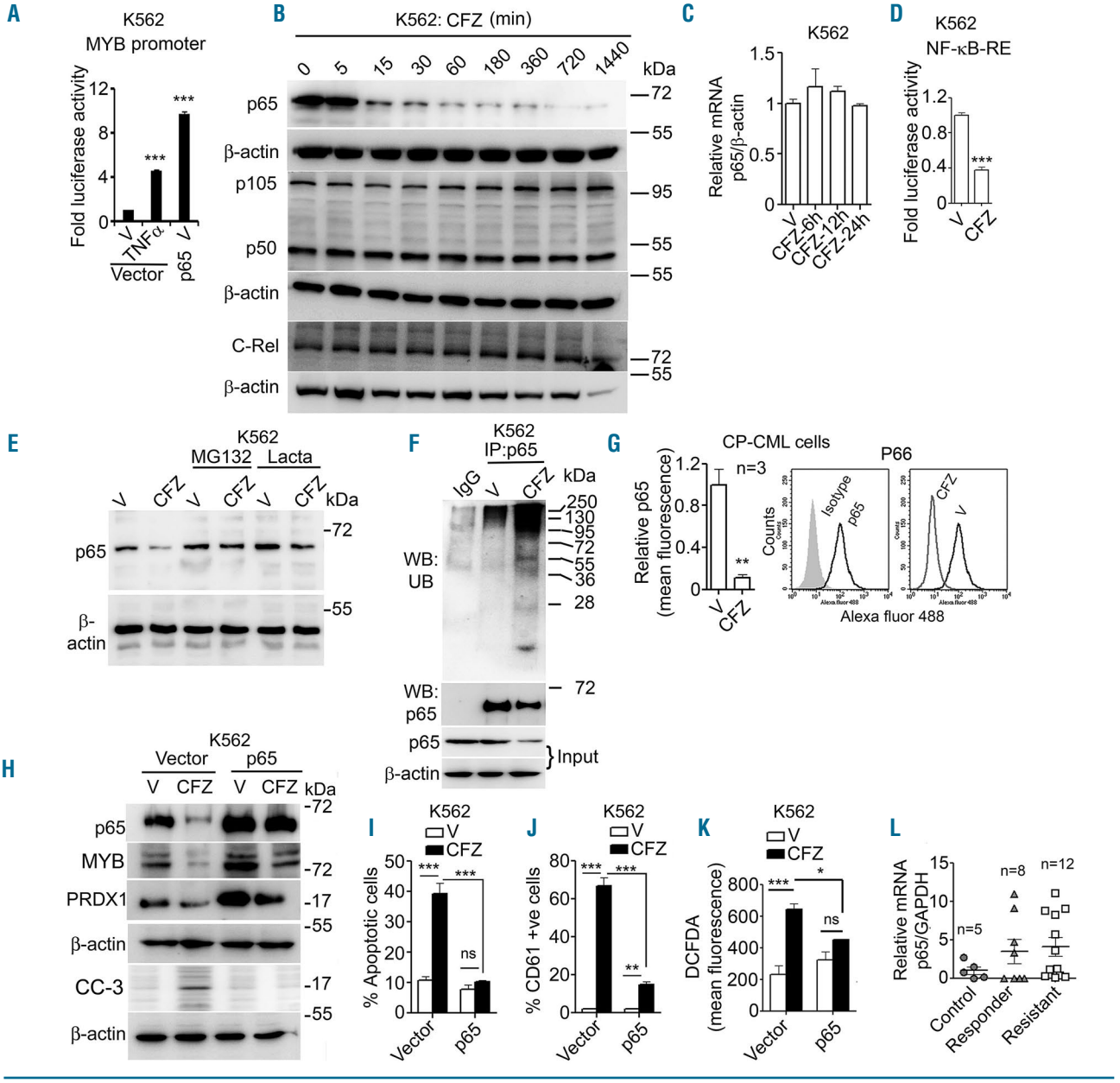

Figure 5. Clofazimine regulates myeloblastoma oncoprotein expression via rapid proteasomal degradation of p65 NFκB. (A) Transfected p65 or tumor necrosis factor-α (10 ng/mL) activates a myeloblastoma oncoprotein (MYB) promoter (-687-+204)-driven luciferase reporter in K562 cells. (B, C) Clofazimine (CFZ) (5 μM) rapidly reduces p65 protein level (B) but does not alter p65 mRNA (C) in K562 cells. (D) CFZ (5 μM, 24 h) reduces a nuclear factor kappa B response element-driven reporter in K562 cells. (E) MG132 or lactacystin (10 μM, 6 h pretreatment) prevents the CFZ (5 μM, 1 h)-mediated reduction in p65 protein level in K562 cells. (F) CFZ (5 μM, 1 h) induces ubiquitination of p65. Proteins were immunoprecipitated with a rabbit p65 antibody followed by western blotting with mouse ubiquitin or p65 antibodies. To avoid the possibility of detection of IgG heavy chain (~50 kDa), an IgG light chain-specific secondary antibody was used. (G) CFZ (5 μM, 24 h) reduces p65 protein in imatinib-resistant chronic phase chronic myeloid leukemia (CP-CML) cells. (H-K; treatment concentration and duration same as in Figure 3A-D) p65 overexpression in K562 cells mitigates CFZ-induced downregulation of MYB and peroxiredoxin 1 and upregulation of caspase 3 cleavage (H), CFZ-mediated apoptosis (I; dot plots in *Online Supplementary Figure S9A*), CD61 expression (J; dot plots in *Online Supplementary Figure S9B*) and generation of cellular reactive oxygen species (K). (L) p65 expression in CP-CML cells. Graphs (except L) illustrate the mean ± standard error of mean of three independent experiments. (B,E,H) are one representative of three independent experiments. (F) is one representative of two independent experiments. **P*<0.05, ***P*<0.01, ****P*<0.001. (A) One-way analysis of variance (ANOVA), (I-K) Two-way ANOVA followed by the Bonferroni post-test. (C, L); Kruskal-Wallis test followed by the Dunn test. (D, G) Unpaired two-tailed Student *t*-test. MYB: myeloblastoma oncoprotein; V: vehicle; NFκB: uclear factor kappa B; TNF-α: tumor necrosis factor-alpha; Lacta: lactacystin; IP: immunoprecipitation; WB: western blot; UB: ubiquitin; PRDX1: peroxiredoxin 1; CC; cleaved caspase; DCFDA: 2',7'-dichlorofluorescein diacetate; GAPDH: glyceraldehyde 3-phosphate dehydrogenase.

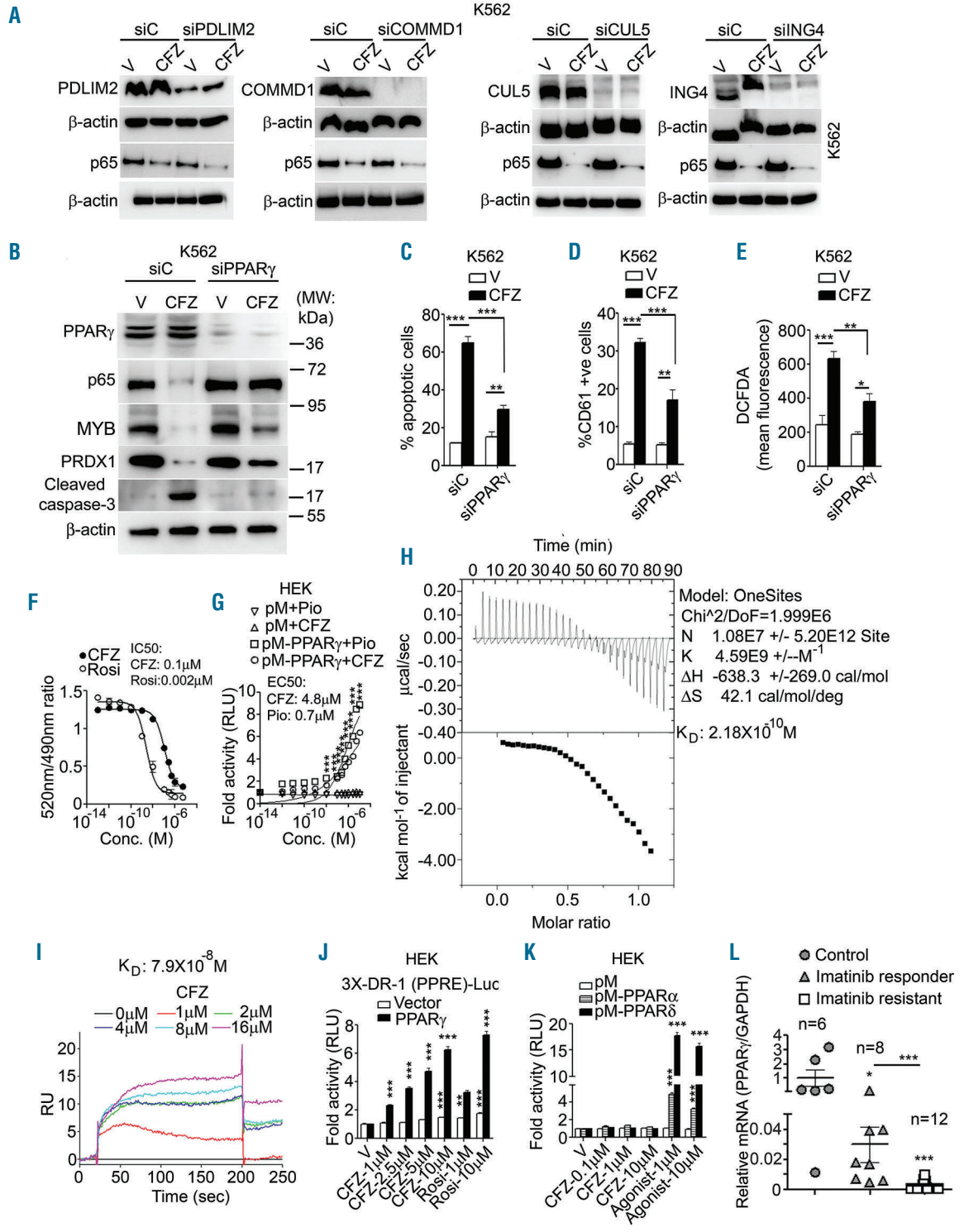

Figure 6. Clofazimine regulates p65 level, apoptosis and differentiation via a direct interaction with PPARγ. (A) Depletion of ubiquitin ligases PDLIM2, COMMD1, Cul5 and ING4 does not affect clofazimine (CFZ) (5 μM, 24 h)-mediated decrease in p65 protein (B-E). Treatment concentration and duration same as in Figure 3A-D). Peroxisome proliferator-activated receptor (PPAR)-γ depletion in K562 cells compromises CFZ-induced downregulation of p65, myeloblastoma oncoprotein (MYB), and peroxiredoxin 1 (PRDX1) and upregulation of cleaved caspase-3 (B), apoptosis (C; dot plots in *Online Supplementary Figure S10A*), CD61 expression (D; histograms in *Online Supplementary Figure S10B*) and generation of reactive oxygen species (E). (F-J) CFZ physically interacts with PPARγ and increases its transcriptional activity. (F) The PPARγ-CFZ interaction as determined by a cell-free time-resolved fluorescence resonance energy transfer lanthascreen assay. (G) CFZ increases transcriptional activity of a Gal4DBD-PPARγLBD fusion protein (pM-PPARγ) on a GAL4 response element-containing reporter (GAL4-UAS-Luc) in transfected HEK-293 cells (H) CFZ alters thermodynamic properties of purified PPARγLBD. Isothermal titration calorimetry to probe interaction of CFZ with PPARγLBD (protein purification and characterization in *Online Supplementary Figure S11A-D*); CFZ (250 μM) was titrated into PPARγLBD solution (50 μM). The titration curve shows a series of endothermic reactions followed by exothermic isotherms. (I) The interaction between PPARγ-LBD and CFZ was evaluated using a Biacore 3000 instrument. SPR sensogram curves showing the interactions between the indicated concentrations of CFZ and his-tagged PPARγLBD captured over an anti-his antibody immobilized CM5 chip. (J) CFZ increases three-copy DR-1 PPRE luc reporter activity in HEK-293 cells transfected with a PPARγ expression plasmid. (K) CFZ does not alter transcriptional activities of PPARα or PPARδ (agonists used; GW7647 for PPARα and GW0742 for PPARδ; all treatments 24 h). (L) PPARγ mRNA expression in CP-CML cells. Graphs (except L) are mean±SEM of three independent experiments. Blots are one representative of three independent experiments. (H-I) One representative of two independent experiments. **P*<0.05, ***P*<0.01, ****P*<0.001 (C-E, G). Two-wayanalysis of variance (ANOVA), (J-K) One-way ANOVA followed by the Bonferroni post-test. L; (K) Kruskal-Wallis test followed by the Dunn test.

that clofazimine causes *p65* proteasomal degradation by ubiquitinating it, which leads to sequential MYB and PRDX1 downregulation, ultimately resulting in the cellular effects imparted by clofazimine.

Clofazimine functions through a direct interaction with PPARγ.

Since clofazimine induced p65 ubiquitination (Figure 5F), we next investigated whether clofazimine modulated any of the E3 ubiquitin ligases that are reported to ubiquitinate p65. PDZ and LIM domain protein 2 (PDLIM2), inhibitor of growth family member 4 (ING4), cullin 5 (CUL5), copper metabolism domain containing 1 (COMMD1; also called MURR1) and PPARγ ubiquitinate p65 and cause its proteasomal degradation.[40,41] We thus assessed whether clofazimine acted through any of these factors. While RNAi-mediated depletion of PDLIM2, ING4, CUL5 and COMMD1 failed to affect clofazimine-induced p65 degradation (Figure 6A), PPARγ depletion mitigated clofazimine-mediated decrease in p65, MYB and PRDX1 and increase in caspase-3 cleavage, apoptosis, differentiation and ROS (Figure 6B-E, *Online Supplementary Figure S10A, B*) indicating that clofazimine may modulate PPARγ activity (it is important to note here that HEK-293 cells also express endogenous PPARγ[42,43]).

We therefore evaluated whether clofazimine interacts with PPARγ and assessed its interaction with purified PPARγ protein in a cell-free, time-resolved fluorescence resonance energy transfer assay. Clofazimine successfully competed with a fluorophore-labeled PPARγ agonist for binding to purified PPARγ-LBD with an IC_{50} of 0.1 μM (Figure 6F). Since PPARγ is also a transcription factor, we assessed whether clofazimine also modulated its transcriptional activity in a heterologous system, in which the cells were transfected with pM-PPARγ [Gal4-DNA-binding-domain (DBD) fused to PPARγ-ligand-binding domain] or an empty pM vector containing Gal4-DBD, and a Gal-UAS-luc reporter containing binding sites for GAL4-DBD. Clofazimine concentration-dependently increased the GAL-UAS reporter activity in the presence of pM-PPARγ but not pM alone (Figure 6G). To confirm clofazimine-mediated transcriptional activation of PPARγ we also studied it on a direct repeat-1 (DR-1; 3-copy) PPAR response element-driven reporter (PPRE-luc) using full-length PPARγ and, in this case too, clofazimine increased PPRE-Luc activity in the presence of transfected PPARγ (a modest response was also seen in vector-transfected cells; due to endogenous PPARγ) (Figure 6J). To further probe the interaction of clofazimine with PPARγ, we titrated clofazimine with PPARγ-LBD (the purification and characterization of PPARγ-LBD are illustrated in *Online Supplementary Figure S11A-D*) by isothermal titration calorimetry. The titration curve of clofazimine with PPARγ-LBD shows a series of endothermic reactions followed by exothermic isotherms (Figure 6H). Stoichiometry calculated by integrating isotherms was one: i.e., one molecule of clofazimine bound to one macromolecule of PPARγ-LBD. The equilibrium rate dissociation constant (K_D) value was 0.2178 nM (Figure 6H). PPARγ also interacted with clofazimine in a surface plasmon resonance experiment (Figure 6I; the K_D calculated by this method was 79 nM). Clofazimine did not alter the activities of pM-PPARα or pM-PPARδ, indicating its specificity for PPARγ (Figure 6K).

We next assessed whether there is any difference in PPARγ mRNA expression between healthy control and CP-CML cells. A remarkably lower level of PPARγ transcripts was observed in the CP-CML cells than in healthy donors' cells, with the difference being more pronounced in cells from imatinib-resistant patients (Figure 6L). Together, these results demonstrate that clofazimine binds to PPARγ and modulates its transcriptional as well as E3 ubiquitin ligase activity and via its increased ubiquitin ligase activity PPARγ induces proteasomal degradation of p65 which in turn results in sequential transcriptional downregulation of *MYB* and *PRDX1* leading to the cellular effects of clofazimine.

Clofazimine shows superior cytotoxic activity compared to thiazolidinediones, acts in synergy with imatinib and drastically reduces quiescent CD34$^+$ cells

The PPARγ agonist pioglitazone synergizes with imatinib in eroding LSC by transcriptional downregulation but not dephosphorylation of STAT5.[1] Since clofazimine modulated PPARγ transcriptional activity, we determined whether clofazimine also regulated STAT5 expression. As expected, clofazimine suppressed STAT5 protein (Figure 7A) and mRNA (Figure 7C) expression without altering its phosphorylation in K562 cells (Figure 7B). Consistent with the ability of PPARγ agonists to suppress BCL-2 expression in CML cells[44] clofazimine decreased *BCL-2* mRNA (Figure 7C) and protein (Figure 1D). Clofazimine did not alter CrkL or BCR-ABL1 phosphorylation (Figure 7D) indicating that it is not a BCR-ABL1 inhibitor *per se*. Furthermore, like pioglitazone,[1] clofazimine also reduced *STAT5B* and other LSC maintenance factors such as *HIF-1α, HIF-2α* and *CITED2* transcripts in CD34$^+$ cells from imatinib-resistant patients (Figure 7E).

We next compared the anti-CML efficacy of clofazimine with that of other PPARγ agonists. In a cell viability assay, clofazimine was found to be the most potent among all the PPARγ ligands tested. While the IC_{50} of clofazimine was 6.08 μM, those of rosiglitazone, troglitazone and pioglitazone were 32.28 μM, 50.01 μM, and 37.39 μM, respectively (Figure 7F).

Since pioglitazone and imatinib synergistically inhibit CML cells,[1] we assessed whether the same was true with clofazimine. In a K562 viability assay imatinib, dasatinib and clofazimine displayed IC_{50} values of 0.95 μM, 0.64 μM and 4.13 μM respectively. However, combining 1.56 μM clofazimine, which is close to the average human plasma level of clofazimine (0.7 mg/L) following daily oral administration of 100 mg clofazimine,[6] with imatinib reduced the IC_{50} of imatinib to 36.4 pM (Figure 7G). The combination index (CI) calculated using the Compusyn program revealed CI values <1 (*Online Supplementary Table S3*), indicating a synergistic effect. Compared to clofazimine, pioglitazone (48 h) showed a rather modest effect, which although synergistic (*Online Supplementary Table S4*), only reduced the IC_{50} of imatinib from 0.399 μM (alone) to 0.052 μM (with 5 μM pioglitazone) or 0.032 μM (with 10 μM pioglitazone) (Figure 7H). Clofazimine also displayed synergism with dasatinib, where the IC_{50} of dasatinib of 0.64 μM (alone) was reduced to 0.0124 μM in the presence of clofazimine (Figure 7G) and the calculated CI was <1 (*Online Supplementary Table S5*). We next assessed whether the combination of imatinib and clofazimine, like pioglitazone,[1] also eroded LSC. First, we performed a colony-forming assay in which clofazimine alone drastically reduced colony number compared to vehicle or imatinib,

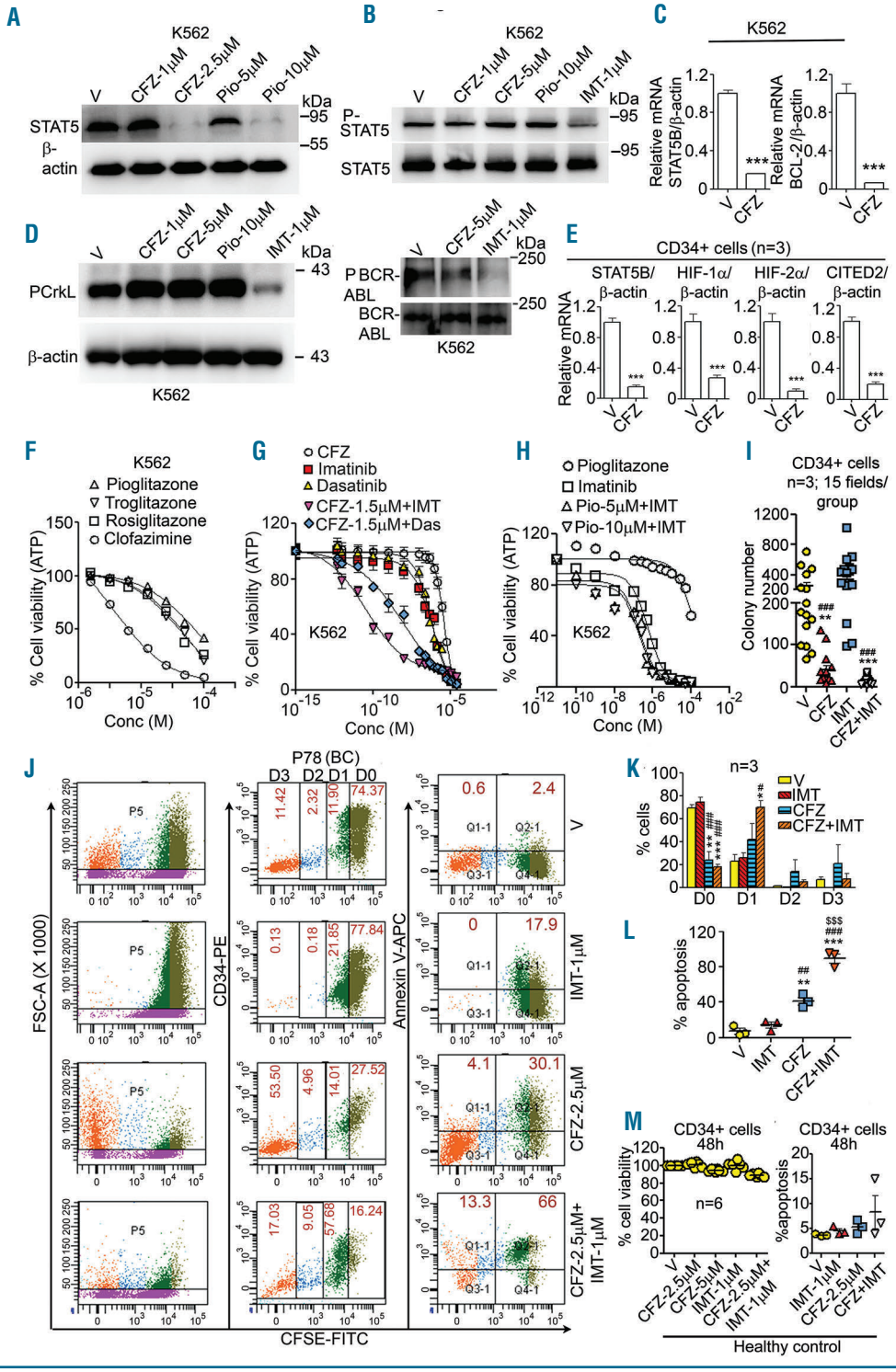

Figure 7. Clofazimine modulates PPARγ target gene expression and shows synergy with imatinib. (A) Clofazimine (CFZ) and pioglitazone (Pio) reduce signal transducer and activator of transcription 5 (STAT5) protein level in K562 cells (96 h). (B) Imatinib (IMT) but not CFZ or Pio (30 min) reduces STAT5-Y694 phosphorylation. (C) CFZ (5 μM, 24 h) reduces STAT5B and BCL-2 transcripts in K562 cells. (D) IMT, but not CFZ or Pio (30 min), reduces CrkL-Y207 and BCR-ABL1 (ABL1-Y245) phosphorylation. (E) CFZ (5 μM, 24 h) reduces STAT5B, hypoxia-inducible factor (HIF)-1α, HIF-2α and CITED2 transcripts in CD34$^+$ cells isolated from IMT-resistant chronic phase chronic myeloid leukemia (CP-CML) cells. (F) CFZ (72 h) shows superior cytotoxicity to thiazolidinediones in K562 cells. (G, H) CFZ (48 h) shows superior cytotoxic synergy with IMT in K562 cells (G) than Pio (H). (I) CFZ alone or in combination with IMT reduces colony-forming cells in soft agar assay (images in *Online Supplementary Figure S2C*, I; same set of data as Figure 1H, with the addition of the CFZ+IMT group). (J-L) CFZ alone or in combination with IMT erodes the quiescent CD34$^+$ population and induces apoptosis in these cells. The CD34$^+$ population from IMT-resistant CP-CML cells (n=3) were labeled with 2 μM carboxyfluorescein succidimidyl ester (CFSE) and treated as indicated (96 h). Cells were gated on the basis of CFSE intensity. The distribution (%) of CFSE/CD34$^+$cells in each cell division is shown by different colored dots (D0-D3 represent the cell division number). Apoptosis in these cells was determined by annexin V staining. (J) Representative dot plots corresponding to patient 78 (P78) who was in blast crisis. (K) Cell numbers (%) on D0-D3 from three patients (dot plots corresponding to other patients are presented in *Online Supplementary Figure S12*). (L) Percentage mean apoptosis from three patients whose data are plotted (see also *Online Supplementary Figure S12*). (M, N) CFZ alone or in combination with IMT does not alter viability (M) of CD34$^+$ cells from healthy controls or induce apoptosis in these cells (N; dot plots in *Online Supplementary Figure S2D*). (M, N) Same set of data as in Figure 1K, with the addition of the CFZ+IMT group. Immunoblots are one representative of three independent experiments. Graphs are mean ± standard error of mean of three independent experiments. *,#P<0.05, **, ##P<0.01, ***,###,$$$$P$<0.001. *V *vs.* treatment, #IMT *vs.* CFZ, $CFZ *vs.* IMT+CFZ. (C, E); Mann-Whitney U test. (I) Kruskal-Wallis test followed by the Dunn test. (K, L, N) One-way analysis of variance followed by the Bonferroni post test.

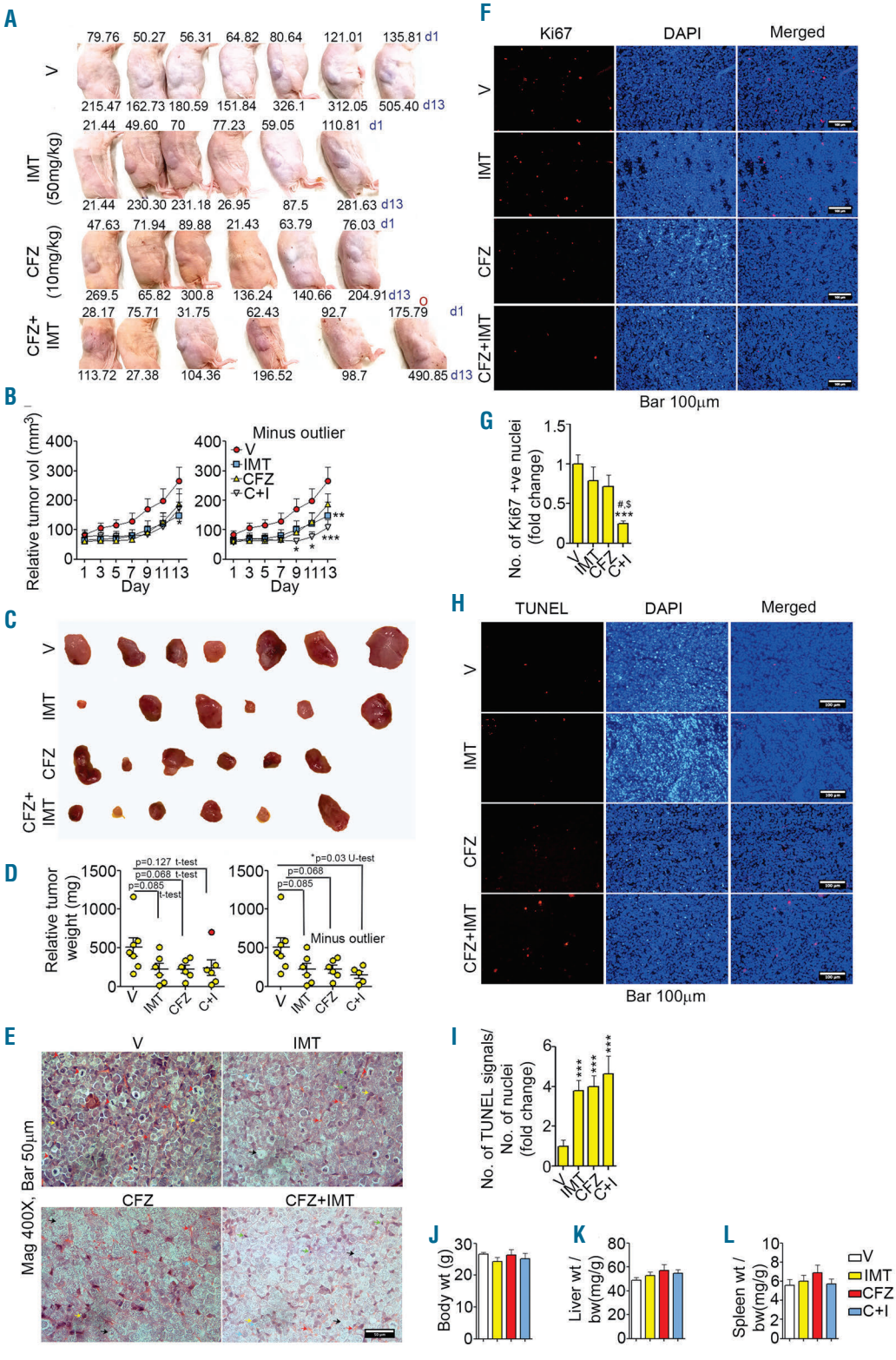

Figure 8. Effects of clofazimine and clofazamine + imatinib on K562 xenografts. (A) Photographs of mice with tumor, tumor volumes on day 1 (d1) and day 13 (d13) are given. The red 'O' represents an outlier based on d1 tumor volume (>150 mm^3). (B) Relative tumor volume (day wise), left panel; all data included, right panel; minus the outlier (as shown in A). (C) Photographs of tumors. (D) Tumor weight, left panel; all data included (outlier marked in red); right panel: minus outlier. (E) Hematoxylin & eosin staining of tumor sections (red arrowhead: mitotic cells; red arrow: vasculature; yellow arrow: myeloblasts; green arrow: pyknotic nuclei; cyan arrow; karyorrhexis; black arrow: degenerating cells). (F) Ki67 staining. (G) Number of Ki67-positive nuclei. (H) Terminal deoxynucleotidyl transferase dUTP nick end labeling (TUNEL) assay. (I) Number of TUNEL signals/ number of nuclei in a field. (E-I) Eighteen fields/group (6 animals/group). (J-L) Body weight (J), body weight normalized liver weight (K), and body weight normalized spleen weight. (J-L) Vehicle; n=7, all treatment groups, n=6 per group. Microscopy was performed with a Leica DMI6000B microscope (Leica) and the findings were quantified with Image J software. (F, H) For counting, intensity of all images was enhanced in Microsoft office picture manager at a mid-tone setting of 80. Cropped images with uniformly increased brightness are given here for clarity; corresponding full-size images are presented in *Online Supplementary Figure S13A, B*. *,#,$$P$<0.05, **$P$<0.01, ***$P$<0.001. (B) Two-way analysis of variance (ANOVA), (J-L) One-way ANOVA followed by the Bonferroni post-test, (D) As indicated. (G, I) Kruskal-Wallis test followed by the Dunn test.

and combining clofazimine with imatinib caused a further reduction (Figure 7I, *Online Supplementary Figure S2C*) (although the difference in effect of clofazimine *vs*. clofazimine + imatinib was not statistically insignificant, the *P* values for the differences in effect between vehicle *vs*. clofazimine and for vehicle *vs*. clofazimine + imatinib were $P<0.01$-0.001 and $P<0.001$, respectively).

We next evaluated whether clofazimine alone or in combination with imatinib could erode quiescent LSC. To that prupose, we labeled $CD34^+$ cells from imatinib-resistant patients (one patient in blast crisis) with carboxyfluorescein succidimidyl ester (CFSE) and treated them with the indicated drugs for 96 h. While imatinib failed to reduce $CFSE^{bright}$ (non-dividing) cells, clofazimine alone or in combination with imatinib drastically reduced their number and increased the $CFSE^{dim}$ (dividing cell) population (Figure 7J, K, *Online Supplementary Figure S12*). Evaluation of apoptosis in these cells revealed that clofazimine alone caused apoptosis in both $CFSE^{bright}$ and $CFSE^{dim}$ cells while combining clofazimine with imatinib caused their near obliteration (Figure 7L, *Online Supplementary Figure S12*). Clofazimine + imatinib did not affect normal $CD34^+$ hematopoietic progenitors from healthy donors as clofazimine alone or in combination with imatinib caused <14% loss of viability (Figure 7M) and did not induce apoptosis in them (Figure 7N, *Online Supplementary Figure S2D*).

Effect of clofazimine and the combination of clofazimine and imatinib in K562 xenografts

To assess the effect of clofazimine, imatinib or their combination *in vivo*, athymic nude (nu/nu) mice harboring K562 xenografts were orally administered vehicle (0.5% methyl cellulose), imatinib (50 mg/kg/day; roughly equivalent to a human dose of 200 mg), clofazimine (10 mg/kg/day, human equivalent dose of 50 mg) or a combination of clofazimine and imatinib (10 mg/kg/day and 50 mg/kg/day, respectively) for 12 days. Analysis of tumor volume revealed a decreasing trend in all treatment groups which although not statistically significant (except for the imatinib group in which the tumor volume was statistically significantly reduced on day 13), became so after removal of an outlier (starting tumor volume >150 mm^3, marked as red 'O', Figure 8A) in the clofazimine + imatinib group in which the reduction in tumor volume was statistically significant from day 9 onwards, while that in the imatinib group was statistically significant on day 13 only (Figure 8A, B). Analysis of tumor weight (tumor images in Figure 8C) showed a similar pattern, with a decreasing trend in all treatment groups. However, upon removal of the outlier (marked red in Figure 8D, left panel and corresponding to the tumor shown in Figure 8A) a statistically significant reduction was present only in the clofazimine + imatinib group (Figure 8D). Histological analysis of the tumors revealed well-defined vasculature and a substantial number of mitotic cells in the group treated with vehicle, which were reduced in treatment groups, especially in the clofazimine + imatinib group (Figure 8E). Furthermore, karyopyknosis, karyorrhexis and degenerating cells were visible in treatment groups, especially in the clofazimine + imatinib group (Figure 8E). Staining of tumor sections for the cellular proliferation marker Ki67 revealed a significant reduction in the clofazimine + imatinib group, compared to the groups treated with vehicle or the individual drugs (Figure 8F, G). Determination of apoptotic cells by TUNEL staining revealed a significant enhancement of signals in all treatment groups (Figure 8H, I). None of the animals in any of the treatment groups showed changes in body, liver or spleen weight (Figure 8J-L). Together, these results indicate that combining clofazimine and imatinib causes a more robust anti-tumor activity than any of the drugs alone.

Discussion

Here, we identified clofazimine as an anti-CML agent that was particularly effective in cells from imatinib-resistant patients and robustly downregulated LSC including quiescent LSC. Clofazimine exerted its effect through PPARγ. Recent evidence suggests that combining thiazolidinediones with tyrosine kinase inhibitors is an effective way to counter drug resistance in CML by eroding quiescent LSC that do not require BCR-ABL1 for survival.[1,45] Thiazolidinediones inhibit quiescent cells by transcriptional downregulation of *STAT5*, which is highly expressed in LSC, while imatinib regulates STAT5 phosphorylation.[1] Combining both drugs thus causes stronger downregulation of STAT5 targets HIF-1α, HIF-2α and CITED2, which are critical for LSC quiescence and maintenance.[1] Here, we show that in addition to STAT5, clofazimine also regulated a novel pathway by modulating PPARγ ubiquitin ligase activity, which resulted in ROS-dependent apoptosis via downregulation of *PRDX1*.

PRDX1, originally cloned from K562 cells,[46] was initially described as a tumor suppressor[47,48] but was later identified as an oncogene in various types of cancer in which its increased expression is associated with poor clinical outcome.[49] *PRDX1* mRNA was reported to be elevated in imatinib-resistant patients in whom no reduction in *BCR-ABL1* was co-related with higher *PRDX1* transcript.[50] We also observed a higher level of *PRDX1* transcripts in cells from CP-CML patients than in those from healthy donor, although the difference was not statistically significant. A significantly higher expression of *PRDX1* was also observed in both $CD34^+38^-$ and $CD34^+38^+$ LSC than in non-LSC, with the highest expression in $CD34^+38^+$ cells. Interestingly, PRDX1 is a secreted protein that enhances secretion of inflammatory cytokines by interacting with toll-like receptor 4.[52,53] Clofazimine suppression of *PRDX1* may thus explain its clinically observed anti-inflammatory functions[6] and the anti-LSC activities seen here. Although PRDX1 has been well-studied in solid tumors, its function in CML is not clear and our study suggests that a detailed exploration of its role in CML progression will be important.

A plethora of reports implicate *MYB* in leukemogenesis which regulates factors such as c-Kit,[54] CD34,[55] and FLT3,[56] which are highly expressed in early progenitor cells and whose aberrant expression or mutations are associated with leukemia and poor clinical outcome.[54-56] While MYB overexpression induces transformation in hematopoietic cells,[57,58] its depletion inhibits colony growth in cells from CML patients including those in blast crisis.[59,60] Here we found that clofazimine suppressed *PRDX1* transcription by downregulating MYB expression and, for the first time, identified a specific MYB target sequence on the *PRDX1* promoter.

NFκB is one of the important downstream signaling pathways of the BCR-ABL1 oncoprotein.[45,61] Abnormal

NFκB activation has been reported in CML[61] and LSC.[62] Furthermore, p65 inhibition was shown to inhibit CML cells including those harboring the multidrug-resistant T315I BCR-ABL1 mutation.[63,64] Our results show that clofazimine decreased p65 protein by increasing the ubiquitin ligase activity of PPARγ. While thiazolidinediones increase PPARγ ubiquitin ligase activity at a supratherapeutical concentration of ≥100 μM,[41] clofazimine was effective at a concentration of 5 μM. Clofazimine also displayed superior cytotoxic effects than thiazolidinediones. Furthermore, combining clofazimine with imatinib reduced the IC_{50} of imatinib by >4 logs whereas pioglitazone reduced it by 7- to 10-fold only. Combining imatinib with clofazimine in a K562 xenograft study caused greater reductions in tumor volume and weight than either drug alone, effects which were accompanied by substantially reduced proliferation and increased degenerative morphological changes in the group given combination therapy.

Pioglitazone is associated with cardiac and hepatic safety issues along with a significant risk of bladder cancer in users.[3] That rosiglitazone does not increase the risk of bladder cancer[3] indicates that this side effect is not associated with all PPARγ agonists. Being a phenazine derivative, clofazimine belongs to a different class of molecule. Given its superior efficacy over thiazolidinediones and that long-term assumption of clofazimine is not associated with major adverse effects; we propose clinical evaluation of clofazimine in combination with tyrosine kinase inhibitors in CML.

Acknowledgments

We dedicate this paper to the memory of Ranjan Kumar Bhagat. We thank Rune Toftgard, Odd Stokke Gabrielsen, Miguel Campanero, Chieko Kai, Giorgio Pochetti, David Mangelsdorf and Kimitoshi Kohno for kind gifts of plasmids. We thank Sharad Sharma and Madhav Nilkanth Mugale for help with histological analyses, and Dipak Datta and Jayanta Sarkar for useful discussions. SS acknowledges a mission-mode in-house project for cancer from CSIR, NC acknowledges funding from CSIR network project ASTHI (BSC 0201) and a grant-in-aid from the Department of Health Research-Indian Council of Medical Research (5/10/FR/5/2012-RHN/156), Government of India and AKT acknowledges funding from the CSIR network project INDEPTH. The authors acknowledge the sophisticated analytical instrument facility at CSIR-CDRI for FACS studies. HK, SoS, SC and RK were supported by fellowships from the University Grants Commission. AKS, SK, AG, SD, KL and RM were supported by fellowships from CSIR. ND acknowledges the DBT-RA Program in Biotechnology and Life Sciences for a Fellowship. CDRI communication number: 9805.

References

1. Prost S, Relouzat F, Spentchian M, et al. Erosion of the chronic myeloid leukaemia stem cell pool by PPARγ agonists. Nature. 2015;525(7569):380-383.
2. Glodkowska-Mrowka E, Manda-Handzlik A, Stelmaszczyk-Emmel A, et al. PPARγ ligands increase antileukemic activity of second- and third-generation tyrosine kinase inhibitors in chronic myeloid leukemia cells. Blood Cancer J. 2016;6:e377.
3. Tuccori M, Filion KB, Yin H, Yu OH, Platt RW, Azoulay L. Pioglitazone use and risk of bladder cancer: population based cohort study. BMJ. 2016;352(i)1541.
4. Nissen SE, Wolski K. Effect of rosiglitazone on the risk of myocardial infarction and death from cardiovascular causes. N Engl J Med. 2007;356(24):2457-2471.
5. Gopal M, Padayatchi N, Metcalfe JZ, O'Donnell MR. Systematic review of clofazimine for the treatment of drug-resistant tuberculosis. Int J Tuberc Lung Dis. 2013;17(8):1001-1007.
6. Cholo MC, Steel HC, Fourie PB, Germishuizen WA, Anderson R. Clofazimine: current status and future prospects. J Antimicrob Chemother. 2012;67(2):290-298.
7. Ren YR, Pan F, Parvez S, et al. Clofazimine inhibits human Kv1.3 potassium channel by perturbing calcium oscillation in T lymphocytes. PLoS One. 2008;3(12):e4009.
8. Leanza L, Henry B, Sassi N, et al. Inhibitors of mitochondrial Kv1.3 channels induce BAX/Bak-independent death of cancer cells. EMBO Mol Med. 2012;4(7):577-593.
9. Leanza L, Trentin L, Becker KA, et al. Clofazimine, Psora-4 and PAP-1, inhibitors of the potassium channel Kv1.3, as a new and selective therapeutic strategy in chronic lymphocytic leukemia. Leukemia. 2013;27(8):1782-1785.
10. Smith GA, Tsui HW, Newell EW, et al. Functional up-regulation of HERG K+ channels in neoplastic hematopoietic cells. J Biol Chem. 2002;277(21):18528-18534.
11. Schaad-Lanyi Z, Dieterle W, Dubois JP, Theobald W, Vischer W. Pharmacokinetics of clofazimine in healthy volunteers. Int J Lepr Other Mycobact Dis. 1987;55(1):9-15.
12. Yawalkar SJ, Vischer W. Lamprene (clofazimine) in leprosy. Basic information. Lepr Rev. 1979;50(2):135-144.
13. O'Connor R, O'Sullivan JF, O'Kennedy R. The pharmacology, metabolism, and chemistry of clofazimine. Drug Metab Rev. 1995;27(4):591-614.
14. Marcato P, Dean CA, Giacomantonio CA, Lee PW. Aldehyde dehydrogenase: its role as a cancer stem cell marker comes down to the specific isoform. Cell Cycle. 2011;10(9):1378-1384.
15. Melemed AS, Ryder JW, Vik TA. Activation of the mitogen-activated protein kinase pathway is involved in and sufficient for megakaryocytic differentiation of CMK cells. Blood. 1997;90(9):3462-3470.
16. Fichelson S, Freyssinier JM, Picard F, et al. Megakaryocyte growth and development factor-induced proliferation and differentiation are regulated by the mitogen-activated protein kinase pathway in primitive cord blood hematopoietic progenitors. Blood. 1999;94(5):1601-1613.
17. Sardina JL, Lopez-Ruano G, Sanchez-Abarca LI, et al. p22phox-dependent NADPH oxidase activity is required for megakaryocytic differentiation. Cell Death Differ. 2010;17(12):1842-1854.
18. Nurhayati RW, Ojima Y, Nomura N, Taya M. Promoted megakaryocytic differentiation of K562 cells through oxidative stress caused by near ultraviolet irradiation. Cell Mol Biol Lett. 2014;19(4):590-600.
19. Chen S, Su Y, Wang J. ROS-mediated platelet generation: a microenvironment-dependent manner for megakaryocyte proliferation, differentiation, and maturation. Cell Death Dis. 2013;4:e722.
20. Shibayama-Imazu T, Sonoda I, Sakairi S, et al. Production of superoxide and dissipation of mitochondrial transmembrane potential by vitamin K2 trigger apoptosis in human ovarian cancer TYK-nu cells. Apoptosis. 2006;11(9):1535-1543.
21. Dabrosin C, Ollinger K. Protection by alpha-tocopherol but not ascorbic acid from hydrogen peroxide induced cell death in normal human breast epithelial cells in culture. Free Radic Res. 1998;29(3):227-234.
22. Makpol S, Zainuddin A, Rahim NA, Yusof YA, Ngah WZ. Alpha-tocopherol modulates hydrogen peroxide-induced DNA damage and telomere shortening of human skin fibroblasts derived from differently aged individuals. Planta Med. 2010;76(9):869-875.
23. da Silveira Vargas F, Soares DG, Ribeiro AP, Hebling J, De Souza Costa CA. Protective effect of alpha-tocopherol isomer from vitamin E against the H2O2 induced toxicity on dental pulp cells. Biomed Res Int. 2014;2014:895049.
24. Liou GY, Storz P. Reactive oxygen species in cancer. Free Radic Res. 2010;44(5):479-496.
25. Trachootham D, Alexandre J, Huang P. Targeting cancer cells by ROS-mediated mechanisms: a radical therapeutic approach? Nat Rev Drug Discov. 2009;8(7):579-591.
26. Panieri E, Santoro MM. ROS homeostasis and metabolism: a dangerous liason in cancer cells. Cell Death Dis. 2016;7(6):e2253.
27. Shi X, Zhang Y, Zheng J, Pan J. Reactive oxygen species in cancer stem cells. Antioxid

Redox Signal. 2012;16(11):1215-1228.
28. Hofmann B, Hecht HJ, Flohe L. Peroxiredoxins. Biol Chem. 2002;383(3-4):347-364.
29. Ma Q. Role of nrf2 in oxidative stress and toxicity. Annu Rev Pharmacol Toxicol. 2013;53:401-426.
30. Kim JH, Bogner PN, Baek SH, et al. Up-regulation of peroxiredoxin 1 in lung cancer and its implication as a prognostic and therapeutic target. Clin Cancer Res. 2008;14(8):2326-2333.
31. Tanno B, Sesti F, Cesi V, et al. Expression of Slug is regulated by c-Myb and is required for invasion and bone marrow homing of cancer cells of different origin. J Biol Chem. 2010;285(38):29434-29445.
32. Wang QF, Lauring J, Schlissel MS. c-Myb binds to a sequence in the proximal region of the RAG-2 promoter and is essential for promoter activity in T-lineage cells. Mol Cell Biol. 2000;20(24):9203-9211.
33. Deng QL, Ishii S, Sarai A. Binding site analysis of c-Myb: screening of potential binding sites by using the mutation matrix derived from systematic binding affinity measurements. Nucleic Acids Res. 1996;24(4):766-774.
34. Suhasini M, Pilz RB. Transcriptional elongation of c-myb is regulated by NF-kappaB (p50/RelB). Oncogene. 1999;18(51):7360-7369.
35. Pereira LA, Hugo HJ, Malaterre J, et al. MYB elongation is regulated by the nucleic acid binding of NFκB p50 to the intronic stem-loop region. PLoS One. 2015;10(4):e0122919.
36. Toth CR, Hostutler RF, Baldwin AS, Jr., Bender TP. Members of the nuclear factor kappa B family transactivate the murine c-myb gene. J Biol Chem. 1995;270(13):7661-7671.
37. Lauder A, Castellanos A, Weston K. c-Myb transcription is activated by protein kinase B (PKB) following interleukin 2 stimulation of Tcells and is required for PKB-mediated protection from apoptosis. Mol Cell Biol. 2001;21(17):5797-5805.
38. Campanero MR, Armstrong M, Flemington E. Distinct cellular factors regulate the c-myb promoter through its E2F element. Mol Cell Biol. 1999;19(12):8442-8450.
39. Kim MY, Koh DI, Choi WI, et al. ZBTB2 increases PDK4 expression by transcriptional repression of RelA/p65. Nucleic Acids Res. 2015;43(3):1609-1625.
40. Xu H, You M, Shi H, Hou Y. Ubiquitin-mediated NFκB degradation pathway. Cell Mol Immunol. 2015;12(6):653-655.
41. Hou Y, Moreau F, Chadee K. PPARγ is an E3 ligase that induces the degradation of NFκB/p65. Nat Commun. 2012;3:1300.
42. Camacho IE, Serneels L, Spittaels K, Merchiers P, Dominguez D, De Strooper B. Peroxisome-proliferator-activated receptor gamma induces a clearance mechanism for the amyloid-beta peptide. J Neurosci. 2004;24(48):10908-10917.
43. Aprile M, Cataldi S, Ambrosio MR, et al. PPARγδ5, a naturally occurring dominant-negative splice isoform, impairs PPARγ function and adipocyte differentiation. Cell Rep. 2018;25(6):1577-1592 e1576.
44. Liu JJ, Huang RW, Lin DJ, et al. Expression of survivin and bax/bcl-2 in peroxisome proliferator activated receptor-gamma ligands induces apoptosis on human myeloid leukemia cells in vitro. Ann Oncol. 2005;16(3):455-459.
45. Bitencourt R, Zalcberg I, Louro ID. Imatinib resistance: a review of alternative inhibitors in chronic myeloid leukemia. Rev Bras Hematol Hemoter. 2011;33(6):470-475.
46. Sauri H, Ashjian PH, Kim AT, Shau H. Recombinant natural killer enhancing factor augments natural killer cytotoxicity. J Leukoc Biol. 1996;59(6):925-931.
47. Neumann CA, Krause DS, Carman CV, et al. Essential role for the peroxiredoxin Prdx1 in erythrocyte antioxidant defence and tumour suppression. Nature. 2003;424(6948):561-565.
48. Cao J, Schulte J, Knight A, et al. Prdx1 inhibits tumorigenesis via regulating PTEN/AKT activity. EMBO J. 2009;28(10):1505-1517.
49. Ding C, Fan X, Wu G. Peroxiredoxin 1 - an antioxidant enzyme in cancer. J Cell Mol Med. 2017;21(1):193-202.
50. Mascarenhas C, Woldmar L, Almeida MH, Andrade RV, Cunha AF, De Souza CA. Evaluation of peroxiredoxins (PRDX1, PRDX2 and PRDX6) expression in patients with chronic myeloid leukemia (CML) treated with imatinib in first line. Blood. 2014;124(21):5545-5545.
51. Nieborowska-Skorska M, Kopinski PK, Ray R, et al. Rac2-MRC-cIII-generated ROS cause genomic instability in chronic myeloid leukemia stem cells and primitive progenitors. Blood. 2012;119(18):4253-4263.
52. Riddell JR, Wang XY, Minderman H, Gollnick SO. Peroxiredoxin 1 stimulates secretion of proinflammatory cytokines by binding to TLR4. J Immunol. 2010;184(2):1022-1030.
53. Liu CH, Kuo SW, Hsu LM, et al. Peroxiredoxin 1 induces inflammatory cytokine response and predicts outcome of cardiogenic shock patients necessitating extracorporeal membrane oxygenation: an observational cohort study and translational approach. J Transl Med. 2016;14(1):114.
54. Ratajczak MZ, Perrotti D, Melotti P, et al. Myb and ets proteins are candidate regulators of c-kit expression in human hematopoietic cells. Blood. 1998;91(6):1934-1946.
55. Melotti P, Ku DH, Calabretta B. Regulation of the expression of the hematopoietic stem cell antigen CD34: role of c-myb. J Exp Med. 1994;179(3):1023-1028.
56. Volpe G, Walton DS, Del Pozzo W, et al. C/EBPα and MYB regulate FLT3 expression in AML. Leukemia. 2013;27(7):1487-1496.
57. Lutwyche JK, Keough RA, Hughes TP, Gonda TJ. Mutation screening of the c-MYB negative regulatory domain in acute and chronic myeloid leukaemia. Br J Haematol. 2001;114(3):632-634.
58. Bussolari R, Candini O, Colomer D, et al. Coding sequence and intron-exon junctions of the c-myb gene are intact in the chronic phase and blast crisis stages of chronic myeloid leukemia patients. Leuk Res. 2007;31(2):163-167.
59. Ratajczak MZ, Hijiya N, Catani L, et al. Acute- and chronic-phase chronic myelogenous leukemia colony-forming units are highly sensitive to the growth inhibitory effects of c-myb antisense oligodeoxynucleotides. Blood. 1992;79(8):1956-1961.
60. Calabretta B, Sims RB, Valtieri M, et al. Normal and leukemic hematopoietic cells manifest differential sensitivity to inhibitory effects of c-myb antisense oligodeoxynucleotides: an in vitro study relevant to bone marrow purging. Proc Natl Acad Sci U S A. 1991;88(6):2351-2355.
61. Kirchner D, Duyster J, Ottmann O, Schmid RM, Bergmann L, Munzert G. Mechanisms of BCR-ABL1-mediated NF-kappaB/Rel activation. Exp Hematol. 2003;31(6):504-511.
62. Guzman ML, Neering SJ, Upchurch D, et al. Nuclear factor-kappaB is constitutively activated in primitive human acute myelogenous leukemia cells. Blood. 2001;98(8):2301-2307.
63. Lounnas N, Frelin C, Gonthier N, et al. NF-kappaB inhibition triggers death of imatinib-sensitive and imatinib-resistant chronic myeloid leukemia cells including T315I BCR-ABL1 mutants. Int J Cancer. 2009;125(2):308-317.
64. Lu Z, Jin Y, Chen C, Li J, Cao Q, Pan J. Pristimerin induces apoptosis in imatinib-resistant chronic myelogenous leukemia cells harboring T315I mutation by blocking NF-kappaB signaling and depleting BCR-ABL1. Mol Cancer. 2010;9:112.

ARTICLE

Mesenchymal stromal cells confer chemoresistance to myeloid leukemia blasts through Side Population functionality and ABC transporter activation

Laetitia Boutin,[1,2] Pierre Arnautou,[3] Aurélie Trignol,[1] Amandine Ségot,[3] Thomas Farge,[4] Christophe Desterke,[5] Sabrina Soave,[2] Denis Clay,[5] Emmanuel Raffoux,[6] Jean-Emmanuel Sarry,[4] Jean-Valère Malfuson,[2,3] Jean-Jacques Lataillade,[1,2] Marie-Caroline Le Bousse-Kerdilès[2*] and Adrienne Anginot[2*]

*AA and MCLBK contributed equally to this work

[1]CTSA, IRBA, Clamart; [2]Inserm UMR-S-MD1197, Paul Brousse Hospital, Paris 11 University, Villejuif; [3]Hematology Department, HIA Percy, Clamart; [4]Inserm U1037, Cancer Research Center of Toulouse, University of Toulouse, Toulouse; [5]Inserm UMS33, Paul Brousse Hospital, Paris 11 University, Villejuif and [6]Adult Hematology Department, Saint Louis Hospital, Paris, France

Ferrata Storti Foundation

Haematologica 2020
Volume 105(4):987-998

ABSTRACT

Targeting chemoresistant malignant cells is one of the current major challenges in oncology. Therefore, it is mandatory to refine the characteristics of these cells to monitor their survival and develop adapted therapies. This is of particular interest in acute myeloid leukemia (AML), for which the 5-year survival rate only reaches 30%, regardless of the prognosis. The role of the microenvironment is increasingly reported to be a key regulator for blast survival. In this context, we demonstrate that contact with mesenchymal stromal cells promotes a better survival of blasts in culture in the presence of anthracycline through the activation of ABC transporters. Stroma-dependent ABC transporter activation leads to the induction of a Side Population (SP) phenotype in a subpopulation of primary leukemia blasts through alpha (α)4 engagement. The stroma-promoting effect is reversible and is observed with stromal cells isolated from either healthy donors or leukemia patients. Blasts expressing an SP phenotype are mostly quiescent and are chemoresistant *in vitro* and *in vivo* in patient-derived xenograft mouse models. At the transcriptomic level, blasts from the SP are specifically enriched in the drug metabolism program. This detoxification signature engaged in contact with mesenchymal stromal cells represents promising ways to target stroma-induced chemoresistance of AML cells.

Introduction

Acute myeloid leukemias (AML) represent a set of hemopathies characterized by a clonal expansion in bone marrow (BM) and blood of immature myeloid cells, called blasts, blocked at different stages of differentiation. AML can be classified according to the degree of immaturity [as according to the French-American-British (FAB) classification] or depending on the cytogenetic or molecular events observed in patients (according to the World Health Organization 2016 criteria).[1] AML are also subdivided into three groups that condition therapy: favorable AML, which may be cured without hematopoietic stem cell transplant, and intermediate and adverse AML which may require an allogenic graft. Despite the significant progress made in supportive care, there has been no radical change in the prognosis of AML; the 5-year survival rate is 30% for all groups of AML and 10% for adverse AML. The conventional chemotherapy based on the injection of a nucleoside analog combined with an anthracycline is used to kill AML cells. However, many patients relapse, mainly due to the persistence of rare chemore-

Correspondence:

ADRIENNE ANGINOT
adrienne.anginot@inserm.fr

Received: December 14, 2018.

Accepted: July 5, 2019.

Pre-published: July 9, 2019.

doi:10.3324/haematol.2018.214379

Check the online version for the most updated information on this article, online supplements, and information on authorship & disclosures: www.haematologica.org/content/105/4/987

sistant AML cells able to re-initiate the disease; these are likely to correspond to leukemia stem cells (LSC).

As a mirror of normal hematopoiesis, several studies reported a specific phenotype for LSC or leukemia-initiating cells. Although this generated heterogeneous results,[2] it was nevertheless reported that cells able to engraft *de novo* or after a secondary transplant were present in the $CD34^+CD38^-CD123^+$ hematopoietic population.[3-5] However, other studies showed that cells able to initiate leukemia concerned $CD34^-$, $CD33^+$ or $CD13^+$ cells.[6] Recently, Farge *et al*. demonstrated that chemoresistance was more related to a specific oxidative metabolism than to a level of progenitor/stem cell phenotype.[7] Moreover, the high oxidative phosphorylation status is associated with elevated fatty acid oxidation and high expression of CD36, a fatty acid translocase recently identified as a marker of an LSC subpopulation.[8]

Considering hematopoietic neoplasms, it is now mandatory to also include environmental factors in order to understand their development, resistance and dissemination. In adults, hematopoiesis develops in the BM where a dialogue between hematopoietic stem /progenitor cells (HSPC) and the microenvironment, including mesenchymal stromal cells (MSC), extracellular matrix components and soluble factors,[9,10] is critical for maintaining stem cell function and homeostasis. Such a protective microenvironment has been reported to be implicated in the stemness and chemoresistance of leukemia blasts at the origin of the process of Environment Mediated-Drug Resistance (EM-DR), and specifically of Cell Adhesion Mediated-Drug Resistance (CAM-DR).[8,11] Quiescence, as well as protection against environmental and drug aggressions, are major characteristics of stem cells also characterized by the Side Population (SP) phenotype.[12] We have previously shown that, whereas circulating HSPC from heathy donors (HD) do not exhibit a SP phenotype, this functionality can be induced after co-culture with MSC in a VLA4- and CD44-dependent manner.[13] Interestingly, this MSC-induced SP population is enriched in HSC, as shown by its engraftment in immunodeficient mice.[13]

In the present work, conducted on a cohort of 34 AML patients, we show that MSC activate ABC transporters in a subpopulation of primary blasts, resulting in the induction of an SP phenotype. SP blasts are mostly quiescent and exhibit a low reactive oxygen species (ROS) transcriptional pathway compared to non-SP [Main Population (MP)] blasts. Furthermore, they are capable of effluxing chemotherapy agents *in vitro* in cultures as well as *in vivo* in patient-derived xenograft models treated by cytarabine, validating a higher chemoresistance of SP cells compared to their MP counterparts. Altogether, our results demonstrate that the stroma-induced SP functionality is a new mechanism of CAM-DR for AML blasts.

Methods

Preparation of primary acute myeloid leukemia cells

Peripheral blood samples were collected at Percy (Clamart, France) and Saint Louis (Paris, France) hospitals after the informed consent of patients in accordance with the principles of the Declaration of Helsinki (IDRCB 2017-A02149-44, CPP 2017-juill.-14644 ND-1eravis, CNIL MR001). The patient cohort represents 34 patients with primary AML (*Online Supplementary Figure S1*). Patients were untreated at the time of blood uptake. Blood mononuclear cells were isolated on density gradient (1.077g/mL) before freezing.[13]

Co-culture of primary acute myeloid leukemia cells on mesenchymal stromal cells

Primary AML mononuclear cells were plated at $2x10^5/cm^2$ in SynH (Abcell-Bio) supplemented with L-Glutamine, non-essential amino acids and 10% fetal bovine serum for 3-4 days on confluent MSC isolated from the BM of either AML patients (n=9) or HD (n=5) (*Online Supplementary Appendix*). AML blasts were cultured without MSC feeders for controls. Transwell and neutralization experiments are described in the *Online Supplementary Appendix*.

In some experiments, mitoxantrone (50nM; Sigma Aldrich) was added to the co-culture for 24 hours (h) and cells were pre-treated or not with verapamil (50 μM) for 2 h before adding mitoxantrone and during mitoxantrone treatment.

At the end of co-cultures, non-adherent cells were flushed and stained with anti-CD45 antibody and annexin V (Invitrogen). Counting beads (CountBright, Life Technologies) were added to cell suspension to quantify cell populations by flow cytometry using Fortessa apparatus with Diva software (Becton Dickinson).

Side Population cell detection and characterization

Hoechst staining was performed as previously described[13,14] (*Online Supplementary Appendix*). After Hoechst incubation, cells were placed on ice and stained with anti-CD45 antibody and a viability dye. Flow cytometry analysis was carried out on BD Fortessa apparatus. CD45 staining was use to gate on AML blasts and to avoid stromal contamination for SP analysis.

Drug efflux - to analyze drug efflux concomitantly with SP cell detection, mitoxantrone (90nM) was added to the cell suspension during the last 30 minutes (min) of Hoechst staining.

ABC transporter functionality

Specific probes for ABCB1 ($DioC_2(3)$), ABCC1 (CMFDA), and ABCG2 (Purpurin 18) were incubated during 30 min at 37°C after co-culture or during Hoechst staining. Cells were then stained with CD45 antibodies and with a viability dye (*Online Supplementary Table S2*).

Transcriptomic analysis

See the *Online Supplementary Appendix*.

Patient-derived xenograft model

Patient-derived xenografts (PDX) were achieved as previously described[7,15] (*Online Supplementary Appendix*) under French Institutional Animal Care and Use (Committee of "Midi-Pyrénées" region-France) approval.

Statistical analysis

Raw data of each group were analyzed using R (3.3.3) and Rstudio (0.99.896) software. The packages used were stats, coin and multcomp for tests. Graphic representations of data were made for each group using Prism 6 or R (3.3.3) software (package ggplot2). Statistical comparisons between groups on a single quantitative variable were run as follows: resampling tests were used for group *versus* group comparisons, pairing on AML donor levels or on AML MSC donor level. When multiple comparisons were used inside a single experiment, *P*-values were corrected using the Benjamini/Hochberg method. $P=0.05$ was considered statistically significant; tests were bilateral unless stated. Data are expressed as median with 25-75% interquartile intervals.

Results

Leukemia blasts cultivated on mesenchymal stromal cells actively efflux chemotherapy drugs by activating ABC transporters

We first characterized MSC isolated from the BM of AML patients (AML MSC) at diagnosis and compared them to MSC isolated from BM of healthy donors (HD MSC). The number of cumulative population doubling was slower for AML MSC than for HD MSC (*Online Supplementary Figure S2A*). AML MSC clonogenicity was also weaker than that of HD MSC (*Online Supplementary Figure S2B*). Because AML MSC were morphologically different from HD MSC, we quantified senescent cells using the β-galactosidase activity test. We observed that AML MSC showed 5-10 times more senescent cells than HD MSC as soon as passage 4 (*Online Supplementary Figure S2C*). This result can explain the limited expansion capacity and clonogenicity of AML MSC. Despite these growth alterations, no differences were observed regarding their phenotype ($CD45^{-}CD90^{+}CD73^{+}CD105^{+}$) (*Online Supplementary Figure S3A*) or differentiation capacities, since they were able to differentiate into adipocytes, osteoblasts, and chondrocytes similarly to HD MSC (*Online Supplementary Appendix* and *Online Supplementary Figure S3B* and *C*). We further analyzed their functional roles on AML blast survival by co-culturing blasts on either AML or HD MSC. After a 3-day co-culture, cells were removed and blast viability was evaluated using Annexin V and 7AAD co-staining. Co-culture with HD or AML MSC significantly increases AML blast survival (n>12; *P*=0.0004) (Figure 1A, left). This difference was also observed when mitoxantrone, a chemotherapy drug, was added to co-cultures (n>12; *P*=0.0003) (Figure 1A, right).

To try to explain this increased survival, we evaluated the intracellular amount of mitoxantrone in the blast population co-cultivated with or without MSC isolated from HD or AML patients (Figure 1B). All blasts were positive

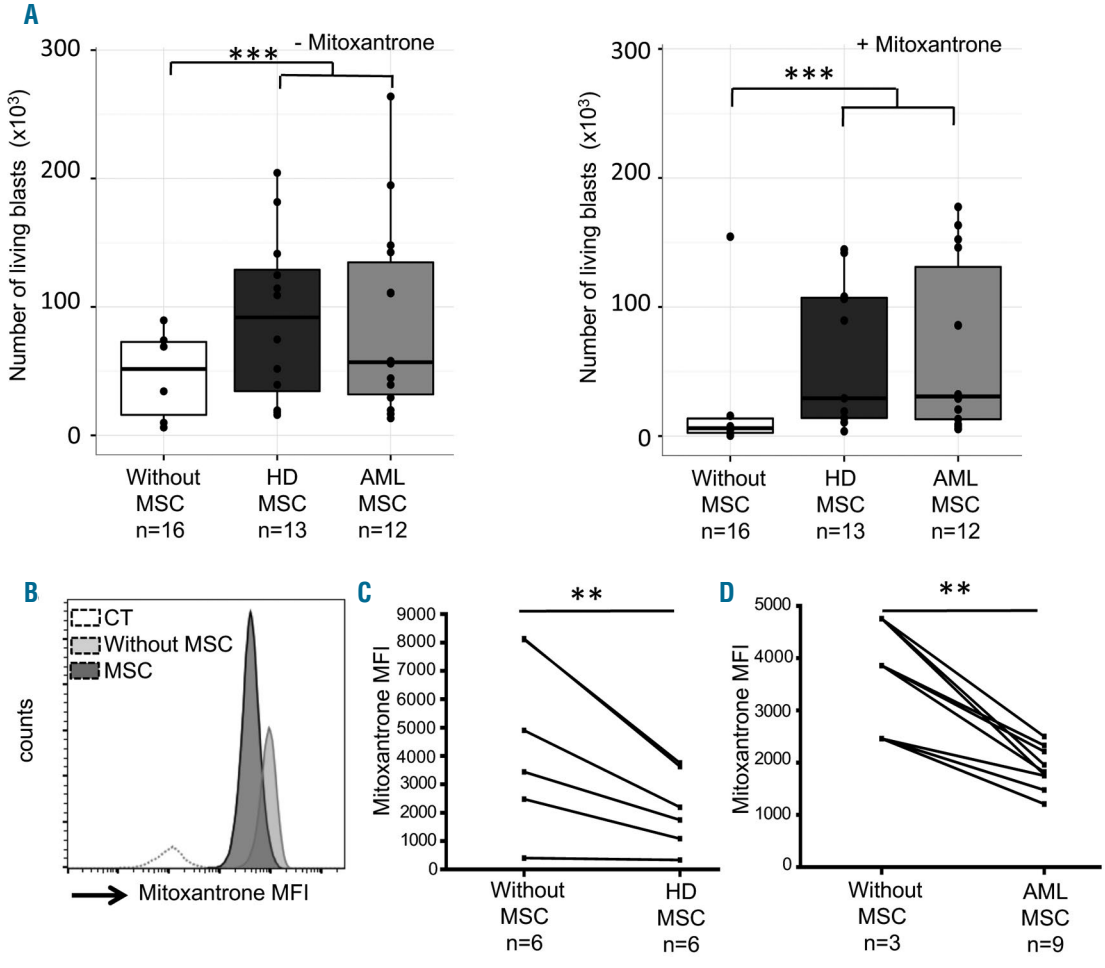

Figure 1. Mesenchymal stromal cells (MSC) from heathy donors (HD) or from acute myeloid leukemia (AML) patients confer a better survival to leukemia blasts, even in the presence of chemotherapy agents. (A, left) Histogram representing the number of living AML blasts after a 3-day culture without MSC [median 51,655 (56,830)] or with MSC from HD [median 91,815 (94,556)] or AML patients [median 56,896 (102,863)]. (Right) The same conditions but in the presence of 50nM of mitoxantrone. Culture conditions in the presence of the different types of MSC confer a significantly improved survival to AML blasts (left: ***P=0.0004; right: ***P=0.0003, n>10, represents the number of AML blasts/MSC donor combinations). (B) Histogram showing fluorescence intensity of AML blasts stained with mitoxantrone after a 3-day culture with or without MSC from HD (one representative experiment of the 6 performed). Control (CT) represents non-stained blasts. (C) Mitoxantrone mean fluorescence intensity (MFI) in AML blasts cultivated [median 2,191 (2,032)] or not [median 3,676 (3,546)] on HD MSC (**P=0.01, n=6, Wilcoxon test). (D) Mitoxantrone MFI in AML blasts cultivated [median 3,861 (1,147)] or not [median 1,821 (460)] on AML MSC (**P=0.01, n=3-9, Wilcoxon test). n: number. **P<0.01; ***P<0.001.

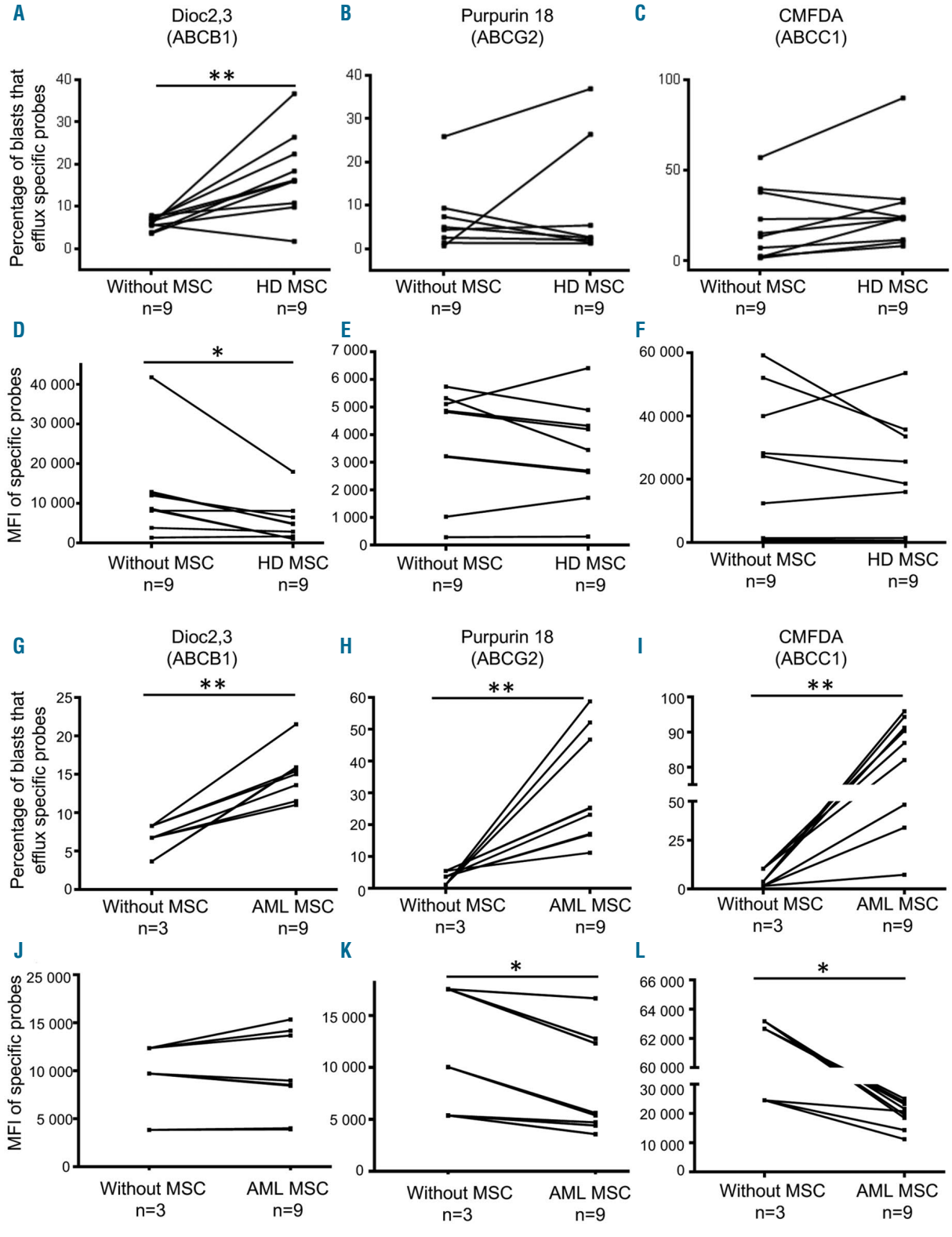

Figure 2. Co-culture between acute myeloid leukemia (AML) blasts and mesenchymal stromal cells (MSC) modulates the ABC transporter functionality on leukemia blasts in a patient-dependent manner. (A-C) Percentage of AML blasts that efflux specific probes (ABC transporter activity) after a 3-day co-culture on healthy donor (HD) MSC. ABC transporter activities were quantified using specific probes (Dioc2,3, Purpurin 18, CMFDA for ABCB1, ABCG2, ABCC1, respectively) as shown on the histograms. ABCB1 activity is significantly increased (P=0.0059, n=9, Wilcoxon test) by AML blasts after a 3-day co-culture on HD MSC. (D-F) Corresponding probe mean fluorescence intensity (MFI) in AML blasts; Dioc2,3 MFI is significantly decreased (P=0.02, n=9, Wilcoxon test) in blasts after co-culture with HD MSC. (G-I) Percentage of AML blasts that efflux specific probes after a 3-day co-culture on AML MSC. Activity of the ABCB1, ABCG2 and CMFDA transporters was significantly increased (P=0.01, P=0.02 and P=0.008, respectively; n=3 without MSC and n=9 with AML MSC, Wilcoxon test). (J-L) Corresponding MFI in AML blasts. Purpurin 18 and CMFDA MFI are significantly decreased (P=0.01 and P=0.01, respectively; n=3 without MSC and n=9 with AML MSC, Wilcoxon test) in co-culture conditions. *P<0.05; **P<0.01.

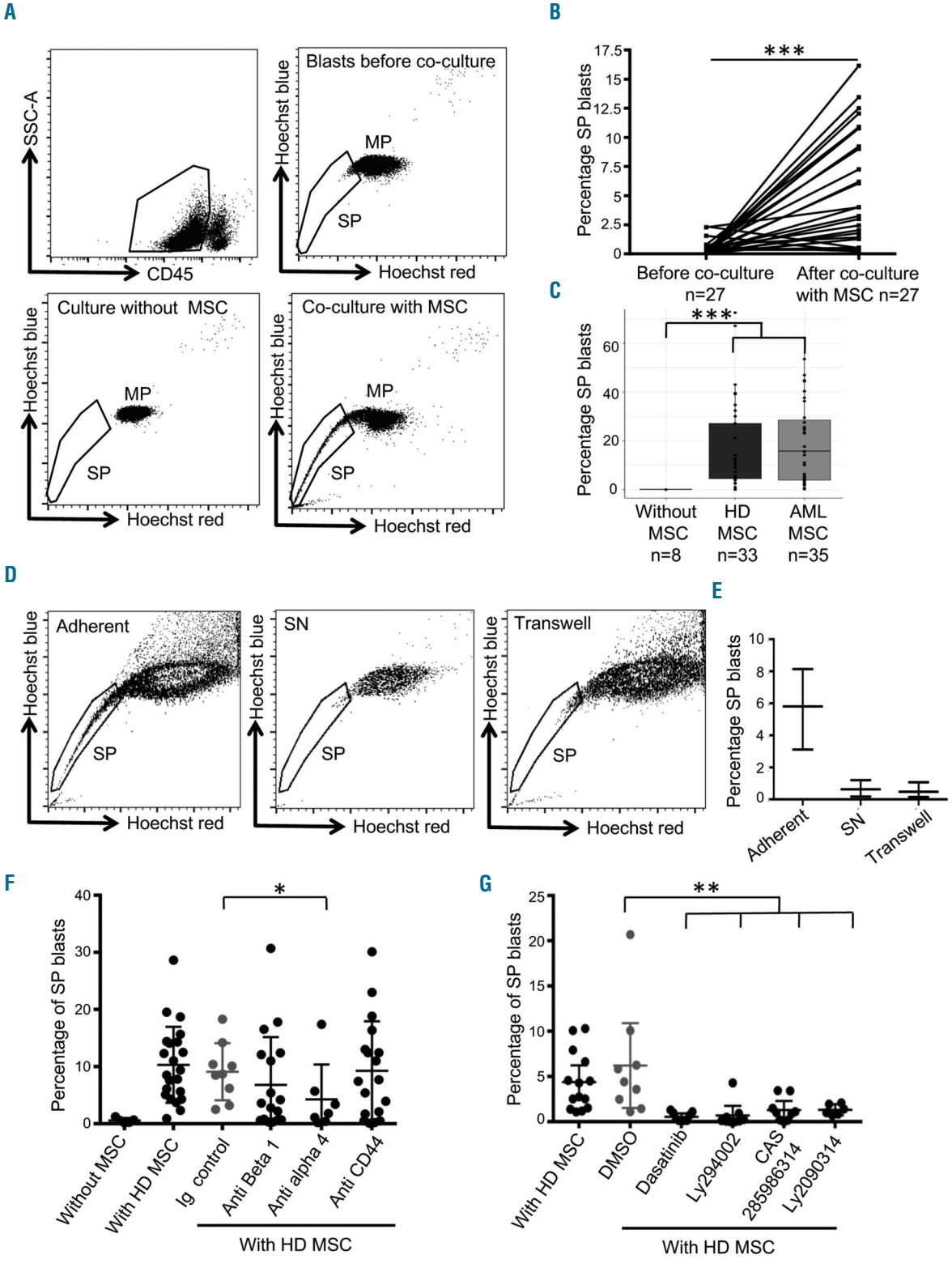

Figure 3. Circulating leukemia blasts acquire a Side Population (SP) phenotype in contact with mesenchymal stromal cells (MSC) from healthy donors (HD) or acute myeloid leukemia (AML) patients through α4 integrin interaction. (A) Cytograms illustrating the gating strategy of AML blasts for cytometry analysis (top left) and SP visualization before co-culture (top right) and after a 3-day culture without (bottom left) or with (bottom right) HD MSC. (B) Percentage of SP AML blasts before and after a 3-day co-culture on MSC (either from HD or AML patients) (P<0.001, n=27, Wilcoxon test). (C) Percentage of SP AML blasts after co-culture with HD MSC (P<10^{-4}, n=8-33) or AML patients (P<10^{-4}, n=8-35). (D) Cytograms showing SP phenotype observed on AML blasts from MSC adherent (left) or supernatant fractions (SN, middle) and in transwell experiments (right) after a 3-day co-culture with HD MSC. (E) Percentage of SP blasts in the three experimental conditions. (F and G) Percentage of SP AML blasts after co-culture or not with HD MSC and after inhibition of β1 (n=18) and α4 (n=7) integrins (P=0.04) or CD44 (n=18) (F) and their downstream signaling pathways (G) using dasatinib, LY294002, CAS2859863 and LY209031, inhibiting Src (P=0.002, n=9), AKT (P=0.003, n=9), STAT5 (P=0.009, n=9), and GSK3 pathways (P=0.01, n=6), respectively. *P<0.05; **P<0.01; ***P<0.001.

for mitoxantrone after a 3-day culture without MSC. However, when blasts were co-cultivated in the presence of MSC either from HD (Figure 1C) or AML patients (Figure 1D), the mitoxantrone mean fluorescence intensity (MFI) was lower than that of blasts cultured without MSC. This reduction was observed in most of the patients studied, regardless of the MSC origin (P=0.01, n=6 for HD MSC and n=9 for AML MSC).

Because blasts co-cultured on MSC exhibit a lower intracellular amount of mitoxantrone compared to cells cultivated without MSC, we studied by which mechanism the amount of intracellular mitoxantrone was reduced. It is now well known that ATP-binding cassette (ABC) transporters can efflux several molecules including chemotherapy drugs.[16] Therefore, we used specific probes such as $Dioc_2(3)$, CMFDA and purpurin[18] to evaluate the activity of three main pump families such as ABCB1 (MDR1), ABCC1 and ABCG2, respectively. There was a significant increase in the percentage of blasts that efflux the Dioc2(3) probe after a 3-day co-culture on HD MSC [median 16.1% (12.8%) with MSC *vs.* 6.18 (2%) without MSC; P=0.005, n=9] demonstrating the implication of the ABCB1 pump as part of this process (Figure 2A). The Dioc2,3 MFI was also significantly decreased in AML blasts (P=0.02, n=9) (Figure 2D). We also noticed an increase in ABCC1 and ABCG2 pump activities in a small number of AML patients (Figure 2B and C), but with no significant modulation of CMFDA and purpurin[18] MFI (Figure 2E and F). However, when activities of these three ABC transporters were analyzed individually, patient per patient, we observed that their activities were systematically modulated by MSC contact (except for one patient, AML 44) (*Online Supplementary Figure S4*) and that ABC transporters were differentially active from one patient to another. When blasts were co-cultured on MSC isolated from AML patients, we observed an activation of the three ABC transporters (P=0.01, 0.02 and 0.008, respectively; n=3-9) (*Online Supplementary Figure S2G-I*) associated with a decrease in specific probe MFI (P=0.01, n=3-9) (Figure 2J and L), except for Dioc2,3 MFI which remained high (Figure 2J).

Therefore, our results show that leukemia blasts demonstrate a specific pattern of ABC transporter activity that is modulated by contact with stromal cells in a patient-dependent manner. Moreover, the modulation of ABC transporter activities appears higher when blasts are co-cultivated with MSC isolated from AML patients.

Leukemia blasts adopt a Side Population phenotype after close contact with mesenchymal stromal cells through integrin interactions

ABC transporter activation is known to be involved in SP phenotype acquisition. We therefore analyzed the SP phenotype of blasts before and after co-culture with MSC. Circulating blasts were gated on their SSC $CD45^{low}$ profile in flow cytometry (Figure 3A). In contrast to circulating Lin^- HSPC freshly isolated from HD,[13] a small proportion of blasts (0.2%; interquartile 0.44%) isolated from approximately 50% of AML patients expressed a SP phenotype before any stromal co-culture (Figure 3B). However, after a 3-day co-culture on HD MSC, we observed for all AML patients that a SP population had emerged or was increased within blast cells with a median of around 4%, with an interquartile of 8.65% (P<0.001, n=27). We then analyzed whether co-culture with AML MSC also induced or increased the percentage of circulating leukemia blasts with an SP phenotype. Similarly to MSC isolated from HD, co-cultures of blasts with AML MSC systematically increased the percentage of SP blasts ($P=10^{-4}$, n= 8-35) (Figure 3C).

We further studied whether a close contact between blasts and MSC was required to promote the SP phenotype of blasts. We first addressed this question by analyzing the proportion of SP blasts in the adherent fraction of the co-cultures and compared it with that detected in the supernatants (SN). SP-expressing cells were mostly found in the adherent fraction (Figure 3D). We then confirmed the requirement of cell-cell interactions using transwell experiments in which the percentage of SP blasts was strongly reduced when blasts and stromal cells were separated by the transwell insert (n=3) (Figure 3D and E). Therefore, close contacts between leukemia and stromal cells appear to be essential to the promotion of the SP phenotype in blasts.

We had previously demonstrated that the SP phenotype induced on circulating Lin^- HSPC from HD by MSC co-culture was dependent on α4 and β1 integrins as well as CD44 engagement.[13] Using blocking antibodies, we tested whether the promotion of the SP phenotype on AML blasts was dependent on MSC interactions through these molecules. Blocking α4 integrin significantly reduced the percentage of SP blasts after MSC co-culture (P=0.04, n=7) while blocking β1 integrin and CD44 interactions had a slight but not significant effect on this proportion (Figure 3F). We then tested the effect of pharmacological inhibitors on the main signaling pathways directly or indirectly activated by integrins. To do this, we first assessed the 'efficient dose', corresponding to the highest dose that did not induce toxicity for dasatinib (pSrc inhibitor), LY294002 (pAKT inhibitor), CAS2859863 (pSTAT5 inhibitor) and LY209031 (pGSK3 inhibitor), CPD22 (pILK inhibitor), and simvastatine (HMG coA reductase inhibitor) (*data not shown*). We then added these inhibitors to co-cultures and quantified the proportion of blasts that have adopted an SP phenotype after a 3-day co-culture on HD MSC. Whereas addition of CPD22 or simvastatine did not affect the percentage of SP blasts (data not shown), a significant decrease in SP blasts was observed when Src (P=0.002, n=9), AKT (P=0.003, n=9), STAT5 (P=0.009, n=9), and GSK3 (P=0.01, n=6) pathways were inhibited (Figure 3G). These data confirm that the stroma-induced SP functionality on AML blasts was partly dependent on integrin interactions, and especially of α4 integrin activation.

Side Population acute myeloid leukemia blasts are quiescent and able to actively efflux chemotherapy through ABCB1 transporters

Side Population phenotype is reported to be linked to quiescence.[12–14] Therefore, we used flow cytometry to analyze the cell cycle phases of AML blasts expressing or not expressing the SP phenotype (SP *vs.* non-SP population/MP for Main Population) after a 3-day co-culture on HD MSC. As expected, SP blasts were in the majority in the G0 phase [median 76% (16.5%)] in contrast to MP blasts [median 33.45% (18.6%)], which were mainly in the G1-S-G2-M phases (Figure 4A). In agreement with this result, gene set enrichment analysis (GSEA) performed with the Kyoto Encyclopedia of Genes and Genomes (KEGG) database on data obtained from

transcriptomic experiments comparing sorted SP *vs.* MP blasts showed a repression of cell cycle and DNA replication gene expression in SP than MP cells (Figure 4B). When cultivated on MSC, circulating AML blasts acquire the capability to efflux mitoxantrone through ABC transporter activation (Figure 1B and C). We therefore analyzed whether the drug efflux was restricted to SP blasts. To do this, blasts which were co-cultivated on MSC during three days were incubated with mitoxantrone for the last 30 min of Hoechst incubation. We showed that SP blasts had a lower amount of mitoxantrone compared to MP blasts (Figure 4C). Quantification of mitoxantrone MFI (Figure 4D) in the SP population [median 1,584 (1,545)] showed a 2-fold decrease compared to the MP one [median 3,219 (1,706)] (P=0.0052; n=12) for most of the patients analyzed. We thus evaluated which ABC transporters were

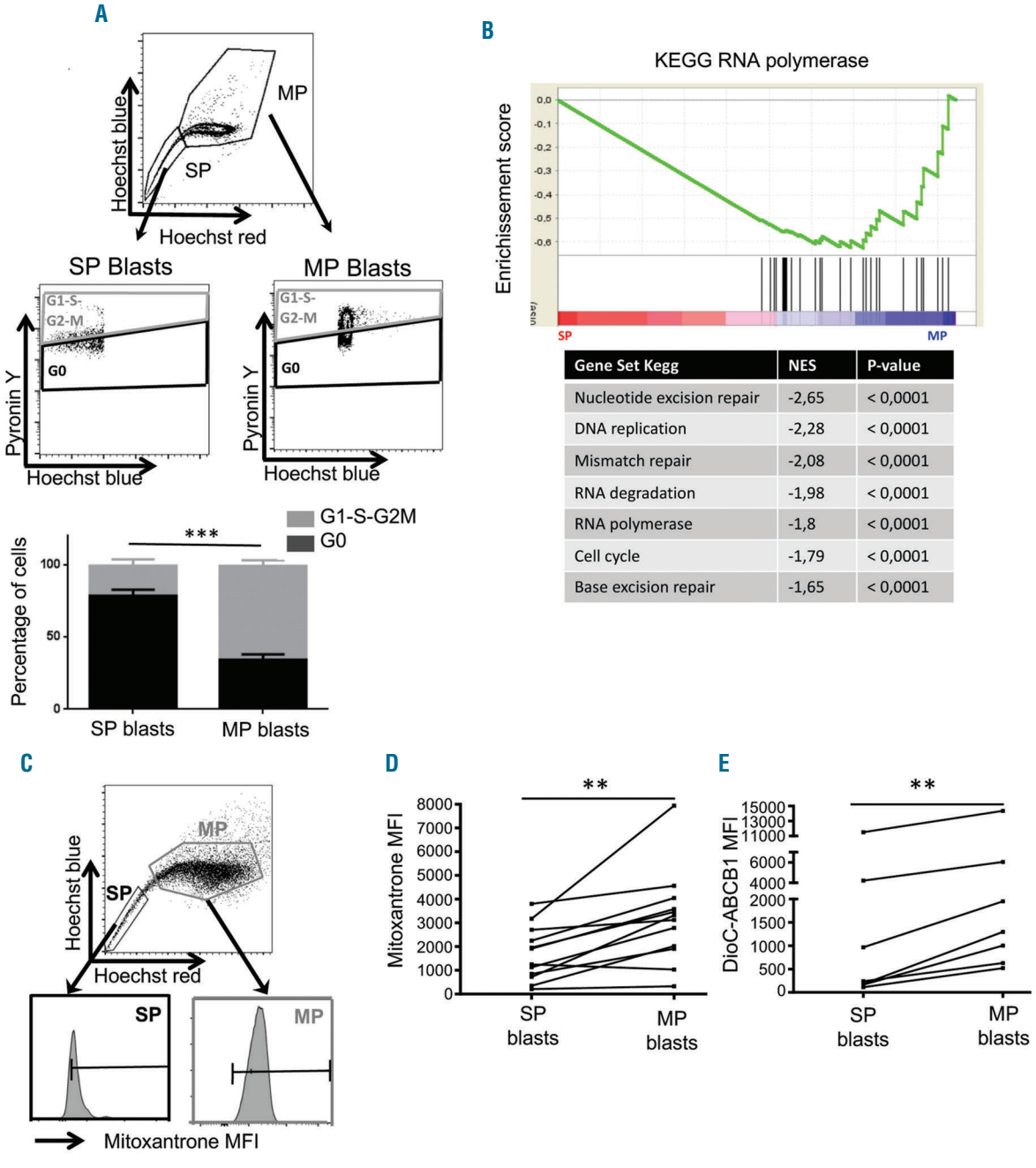

Gene Set Kegg	NES	P-value
Nucleotide excision repair	-2,65	< 0,0001
DNA replication	-2,28	< 0,0001
Mismatch repair	-2,08	< 0,0001
RNA degradation	-1,98	< 0,0001
RNA polymerase	-1,8	< 0,0001
Cell cycle	-1,79	< 0,0001
Base excision repair	-1,65	< 0,0001

Figure 4. The mesenchymal stromal cells (MSC)-induced Side Population (SP) functionality in leukemia blasts is associated with quiescence and chemotherapy efflux through ABC transporter activation. (A) Cytograms and histograms showing gating strategies and percentage of SP and MP blasts in G0 and in G1-S-G2-M after a 3-day co-culture on HD MSC. Cell cycle status of SP *versus* Main Population (MP) blasts was analyzed adding pyronin Y during Hoechst staining. SP blasts are mostly in G0 [median 76% (16.5%)] compared to MP [median 33.45% (18.6%)] blasts which are in G1-S-G2-M (P=0.0009, n=12, Wilcoxon test). (B) Transcriptomic analysis of SP blasts compared to MP blasts. (C) Cytograms showing gating strategy to evaluate mitoxantrone efflux in SP or MP blasts. Quantification of mitoxantrone MFI (D) in SP [median 1,584 (1,845)] and in MP [median 3219 (1,706)] blasts (P=0.0052, n=12, Wilcoxon test). (E) DioC2,3 MFI evaluating ABCB1 activity in SP [median 239 (4,056)] and MP [median 1,298 (5418)] cells (P=0.023, n=7, Wilcoxon test). **P<0.01; ***P<0.001.

activated in SP *versus* MP cells using specific probes. The ABCB1 transporter was significantly more active in SP [MFI Dioc2(3) 239 (2,422)] than in MP blasts [MFI Dioc2(3) 1,298 (3,182)] (P=0.023, n=7) (Figure 4E). In contrast, ABCG2 and ABCC1 did not appear to be involved in this process (*data not shown*).

Altogether, our results demonstrate that AML blasts adopting SP phenotype after contact with MSC are quiescent and able to actively efflux chemotherapy agents through ABC transporters and, in particular, through ABCB1.

Side Population blasts are more *in vitro* and *in vivo* chemoresistant than non-SP cells and this chemoresistance can be partially reversed by ABC transporter inhibition

We first tested whether the SP phenotype induced by contact with MSC conferred a better *in vitro* survival to

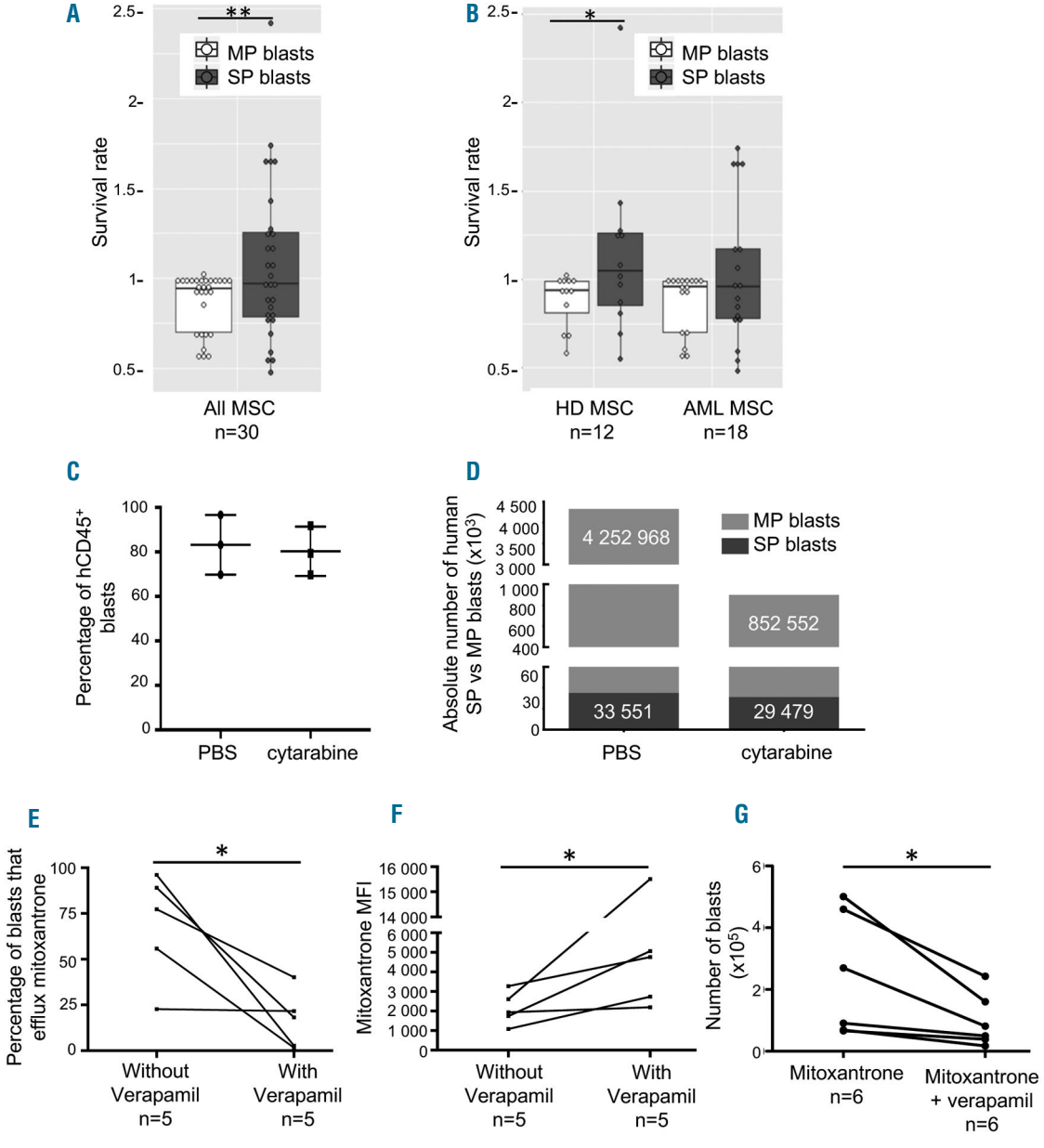

Figure 5. Side Population (SP) functionality of acute myeloid leukemia (AML) blasts induced by mesenchymal stromal cell (MSC) interactions is associated with chemoresistance. (A) Survival rate of SP [median 0.98 (0.46)] or Main Population (MP) [median 0.95 (0.24)] blasts after a 3-day co-culture with MSC in presence of mitoxantrone (P=0.041, n=30, Wilcoxon test). (B) Survival rate of SP or MP blasts after a 3-day co-culture with MSC from healthy donors (HD) or AML patients. (C) Percentage of hCD45$^+$ blasts within the total CD45$^+$ population. (D) Absolute number of human SP and MP blasts in the femur of patient-derived xenograft (PDX) mice after a 5-day treatment with either phosphate buffered saline or cytarabine (30 mg/kg) (n=3 mice per patient). (E) Percentage of blasts that efflux mitoxantrone with or without verapamil after a 3-day co-culture on AML MSC (P=0.05, n=5, Wilcoxon test) and (F) the corresponding mitoxantrone mean fluorescence intensity (MFI) in AML blasts (P=0.05, n=5, Wilcoxon test). (G) Number of living blasts co-cultivated on AML or HD MSC after 24 hours of mitoxantrone and treatment with or without verapamil (P=0.01, n=6, Wilcoxon test) *P<0.05; **P<0.01.

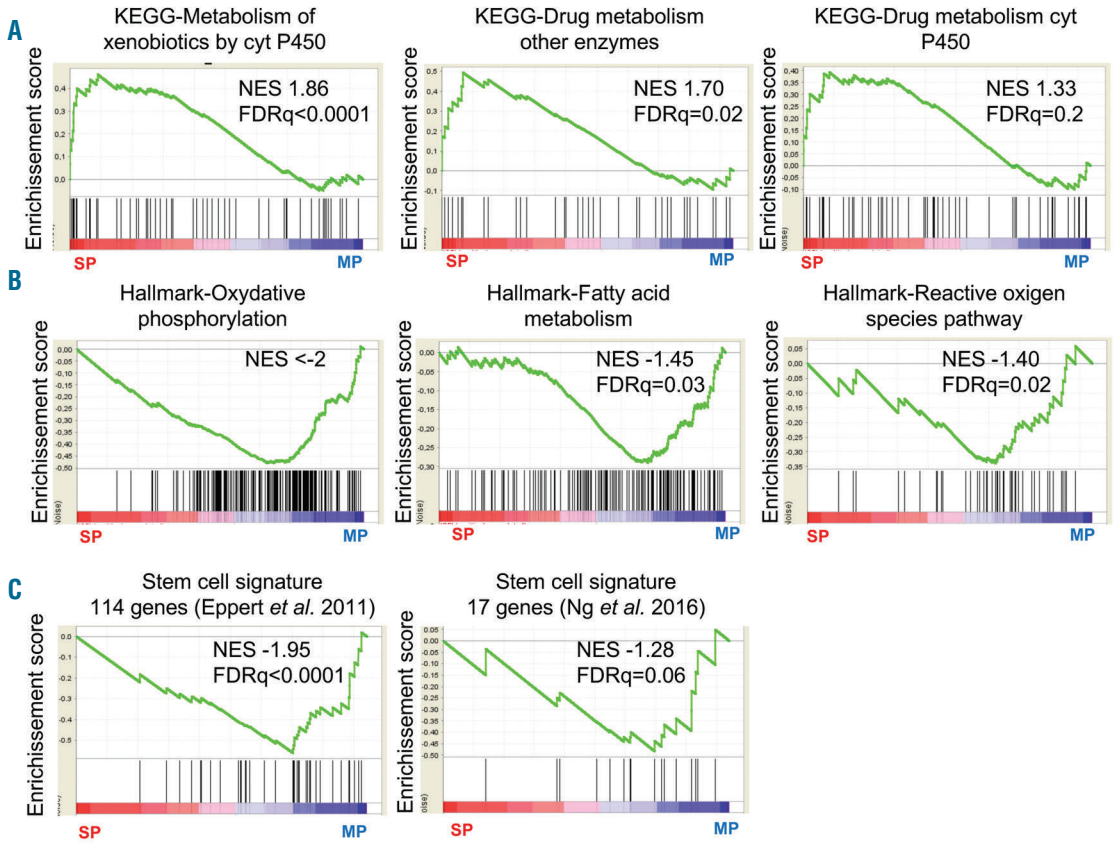

Figure 6. Side Population (SP) blasts exhibit a detoxification program signature. Gene set enrichment analysis with transcriptomics data of sorted SP and Main Population (MP) blasts after a 3-day co-culture on healthy donor (HD) mesenchymal stromal cells (MSC) shows an upregulation in SP cells of genes of xenobiotic metabolism and drug metabolism through the cytochrome P450 or other enzymes (A), an upregulation in MP blasts of genes of oxidative phosphorylation, fatty acid metabolism and reactive oxygen pathway (B), as well as of genes from the stem cell signatures reported by Eppert *et al.*[20] and Ng *et al.*[21] (C).

leukemia blasts in the presence of chemotherapy drugs. We thus co-cultured blasts and MSC isolated from HD or AML patients in the presence or not of mitoxantrone. After a 3-day co-culture, we quantified the absolute number of SP and MP blasts in both conditions and calculated the survival rate of SP and MP cells by dividing the absolute number of SP or MP cells in the treated cultures by their absolute numbers in the non-treated cultures. The survival rate of SP cells was significantly higher than that of MP cells (P=0.041; n=30) when leukemia blasts were co-cultivated on MSC independently of their origin (Figure 5A) or based on their origin (Figure 5B).

We further compared the *in vivo* chemoresistance of SP *versus* MP cells in NSG mice grafted with primary AML blasts (PDX model). Twelve weeks after engraftment, the presence of human CD45$^+$ leukemic cells in mice was controlled by blood analysis. Mice were then treated daily with cytarabine during five days to reduce the human blast population.[7] Three days after treatment arrest, mice were euthanized and their BM was harvested. We estimated the cell chimerism and showed that human CD45$^+$ cells represented 70-96% of the whole CD45$^+$ population (Figure 5C). We then quantified the absolute number of total human blasts and of SP *versus* MP human blasts present in the mouse BM. As expected, there was a large reduction in the global number of human blasts after the cytarabine treatment compared to phosphate buffer solution injection. However, and more interestingly, the absolute number of blasts expressing the SP functionality remained unchanged after cytarabine treatment in contrast to that of MP blasts that was reduced 5-fold (Figure 5D). These results show that cytarabine was active *in vivo* on MP blasts but less or not active on SP blasts.

Altogether, our results suggest that SP blasts are more resistant than MP cells to chemotherapy agents both *in vitro* and *in vivo*.

We then analyzed whether the chemosensitivity of AML blasts could be restored after blocking ABC transporters. We previously showed that ABC transporter activities (modulated on blasts after contact with MSC) were differentially active and were patient dependent (*Online Supplementary Figure S4*). Thus, we used verapamil, a broad spectrum ABC transporter inhibitor, to inhibit the SP phenotype.[12,13] Addition of verapamil into AML blast and MSC co-cultures significantly reduced the percentage of blasts that efflux mitoxantrone (P=0.05, n=5) (Figure 5E) as well as mitoxantrone MFI (P=0.05, n=5) (Figure 5F). Furthermore, when co-cultures were treated with a non-toxic dose of verapamil, we also observed a significant reduction in the number of living blasts compared to that observed with mitoxantrone alone (P=0.01, n=6) (Figure 5G), suggesting that blocking ABC transporters restores blast mitoxantrone chemosensitivity.

Acute myeloid leukemia Side Population blasts exhibit a detoxification transcriptional signature

As SP blasts were more chemoresistant *in vitro* and *in vivo* than their MP counterparts, we analyzed their transcriptomic profiles to highlight a specific signature of these cells. To do this, we sorted SP *versus* MP blasts from two AML patients after a 3-day co-culture on HD MSC. A global transcriptomic analysis of sorted SP *versus* MP AML blasts demonstrated an enrichment of genes implicated in a detoxification program in SP cells. Indeed, using the KEEG database, GSEA analysis showed that the expression of genes involved in xenobiotic and drug metabolism *via* cytochrome P450 or by other enzymes was up-regulated in SP blasts (Figure 6A). Surprisingly, the expression of ABC transporter transcripts was not homogeneously differentially modulated in SP *versus* MP cells (*Online Supplementary Figure S5*), suggesting that, in our experimental conditions, SP phenotype induction is not associated with an increase in ABC transporter mRNA level at steady state, as already suggested in other studies,[17] but mainly after drug exposure.[18,19] We also observed that, oxidative phosphorylation, fatty acid metabolism and ROS pathway signatures of the Hallmark database were enriched in MP blasts (Figure 6B). Surprisingly, while SP phenotype is a common feature of stem cells,[12] and the $CD34^+$ $CD38^-$ SP blast population is enriched in cells with a $CD123^+$ stem phenotype (*Online Supplementary Figure S6*) as compared to $CD34^+$ $CD38^-$ MP cells, the stem cell transcriptional signatures proposed by Eppert *et al.*[20] and Ng *et al.*[21] were preferentially observed in the AML MP population (Figure 6C).

Discussion

Chemoresistance of leukemia cells is one of the major challenges which hematologists have to face in order to cure AML. Therefore, a better understanding of this process constitutes the keystone of next generation therapies. It is now well known that the BM microenvironment is a key actor in leukemia development and resistance to treatment, but the underlying mechanisms are still unclear.

Our present study shows that MSC that play a central role in BM stromal niches sustain the survival and chemoresistance of AML blasts through the induction of an SP phenotype. This chemoresistance mechanism involves activation of ABC transporters, responsible for drug efflux, in a small proportion of leukemia cells after co-culture with MSC. Whereas these transporters were not active or were poorly active in circulating blasts, interactions with stromal cells constantly increased the proportion of SP cells in the blast population. Interestingly, the ABC transporter activation pattern appears to be patient dependent. While MSC-induced ABC transporter activation is common to all types of AML, we did not found any correlation between specific probe efflux and patient characteristics. However, because AML is an heterogeneous group of diseases, a larger patient study cohort is required in order to identify a potential correlation between ABC transporter activation patterns and AML types. Besides a limited expansion capacity and clonogenicity, the capacity of AML MSC to promote SP phenotype on blasts was similar and even better than that of HD MSC. This observation suggests that the BM stroma of patients may be adapted to promote blast protection/survival and supports the hypothesis of a specific crosstalk between pathological blasts and MSC.

Previous data from our group have demonstrated that BM MSC modulate the SP phenotype of HSC from HD.[13] In the present study, we show that they also control the induction of the SP functionality on AML blasts. Interestingly, SP leukemic blasts are mostly found in the MSC-adherent fraction, suggesting that close contacts between blasts and stromal cells are required for SP phenotype induction. As for HD samples, this process is partially dependent on α4 integrin. However, in contrast to HD, for half of the patients studied, this induction is not dependent, or is so at a lower level, on β1 integrin or CD44, two cell-surface glycoproteins known to be involved in BM niche HSC nesting. BM niches are reported to be crucial for HSC long-term maintenance[22–24] and SP cell quiescence.[25] In patients, we show that the proportion of quiescent blasts is higher in the stroma induced-SP cell population than in their MP counterparts. Quiescence is often related to chemoresistance, as only proliferating cells are sensitive to anthracyclines or nucleoside analogs. In the current study, we show that SP blasts are more chemoresistant than MP cells, either *in vitro* or *in vivo* in PDX models. This result is confirmed by our data showing that sorted SP blasts express a specific transcriptomic profile focused on genes involved in drug and environment stress detoxification,[16] known to participate in the chemoresistance process.[26] Therefore, SP cell detection could allow chemoresistant blasts to be monitored during the course of the disease and, targeting stroma-blast interactions would reinitiate cell cycling and, consequently, blast sensitization to chemotherapy. As VLA4 and CD44 play a role in the stroma-induced SP phenotype in HD HSC, but only partially in AML blasts, it would be interesting to identify specific interactions between MSC and blasts to specifically target leukemia cells. Deep analyses using transcriptomic and interactomic approaches[27] focused on MSC, SP and MP cells from AML patients and HD should highlight new pairs of exclusive interactors involved in stroma-blast interactions that would be promising drugable targets.

An important clinical concern is the quest for leukemia stem/initiating cells.[28] SP cells exhibit some features of stem cells since they are mostly in G0[12,14,25] and since their ROS level is lower than that of their MP counterparts.[29] In our study, the transcriptomic analysis of SP AML blasts does not correlate with the 114 and 17 gene stemness signatures reported by Eppert *et al.* and Ng *et al.*, respectively,[20,21] suggesting that SP AML cells are not enriched in such stem cells. Interestingly, Farge *et al.*[7] and Boyd *et al.*[30] demonstrated that chemotherapy-resistant human AML cells are not necessarily enriched in LSC, but exhibit increased fatty-acid oxidation, high oxidative phosphorylation (OXPHOS) gene signature, and up-regulated CD36 expression. By associating a reduction in transcripts for oxidative phosphorylation, fatty acid metabolism and ROS in SP as compared to MP blasts, our results are in line with those from Ye *et al.*, suggesting that chemoresistance is not necessarily restricted to the LSC compartment but rather could be associated to metabolic adaptations induced by their microenvironment.[8]

By promoting a better survival of blasts, the stroma-induced SP functionality we identified in blasts could represent a new mechanism of CAM-DR. Whereas BM MSC from HD or AML patients exhibit similar survival and SP-

promoting effects on blasts, preliminary results on four patients suggest that cultivating MSC and blasts in autologous conditions would bring a supplemental advantage on blast survival and chemoresistance (Boutin L *et al.*, 2018, unpublished data). This suggests that an intimate crosstalk has taken place *in vivo* between MSC and blasts and has been conserved *in vitro*. Recently, Moschoi *et al.*[31] proposed that mitochondrial transfers from BM stromal cells to AML blasts provided them with a protective effect following chemotherapy. Other communication modes such as exosome exchange, metabolite secretion, and nanotube formation could also be suggested to participate in this process and must be identified to disrupt the stroma-induced chemoresistance of AML blasts.

Induction of SP/chemoresistance phenotype on AML blasts is of major interest to clinicians as ABC transporters implicated in drug/chemotherapy agent efflux could be targeted.[32,33] In that context, we have shown that mitoxantrone efflux and blast survival are reversible *in vitro* by addition of verapamil. However, results from clinical trials using P-glycoprotein inhibitors in AML patients are discouraging.[34,35] Our data showing that the functionality of the main ABC transporters implicated in MDR[36] is promoted by blast-MSC interactions, and that this process is patient-dependent, suggest that it is time to revisit the role of ABC transporters in therapeutic failure in the context of personalized medicine.[37,38]

In conclusion, our results show the critical role of stroma interactions in blast chemoresistance through SP phenotype promotion and ABC transporter activation. Therefore, targeting these interactions in combination with the development of new improved inhibitors of ABC transporter function[39] could be an attractive therapeutic alternative.

Acknowledgments

We thank the molecular core facility of Cochin Institute for transcriptomic analysis. We are very grateful to the polyclinic of Blois and particularly to Dr Denis Burgot as well as all the orthopedic surgery staff for providing human bone marrow samples from hip replacement. We thank Dr Cedric Thépenier for the statistical analysis and sharpened advices. We also thank Pr Christophe Martinaud for blast analysis on blood smears.

Funding

This work was supported by grants from Association "Laurette Fugain" (ALF 2013/08) and Association "Vaincre le Cancer-Nouvelles Recherches Biomédicales".

References

1. Arber DA, Orazi A, Hasserjian R, et al. The 2016 revision to the World Health Organization classification of myeloid neoplasms and acute leukemia. Blood. 2016;127(20):2391–2405.
2. Taussig DC, Miraki-Moud F, Anjos-Afonso F, et al. Anti-CD38 antibody-mediated clearance of human repopulating cells masks the heterogeneity of leukemia-initiating cells. Blood. 2008;112(3):568–575.
3. van Rhenen A, Feller N, Kelder A, et al. High stem cell frequency in acute myeloid leukemia at diagnosis predicts high minimal residual disease and poor survival. Clin Cancer Res. 2005;11(18):6520–6527.
4. Vergez F, Green AS, Tamburini J, et al. High levels of CD34+CD38low/–CD123+ blasts are predictive of an adverse outcome in acute myeloid leukemia: a Groupe Ouest-Est des Leucémies Aiguës et Maladies du Sang (GOELAMS) study. Haematologica. 2011;96(12):1792–1798.
5. Jordan CT, Upchurch D, Szilvassy SJ, et al. The interleukin-3 receptor alpha chain is a unique marker for human acute myelogenous leukemia stem cells. Leukemia. 2000;14(10):1777–1784.
6. Sarry J-E, Murphy K, Perry R, et al. Human acute myelogenous leukemia stem cells are rare and heterogeneous when assayed in NOD/SCID/IL2Rγc-deficient mice. J Clin Invest. 2011;121(1):384–395.
7. Farge T, Saland E, de Toni F, et al. Chemotherapy-Resistant Human Acute Myeloid Leukemia Cells Are Not Enriched for Leukemic Stem Cells but Require Oxidative Metabolism. Cancer Discov. 2017;7(7):716–735.
8. Ye H, Adane B, Khan N, et al. Leukemic stem cells evade chemotherapy by metabolic adaptation to an adipose tissue niche. Cell Stem Cell. 2016;19(1):23–37.
9. Shafat MS, Gnaneswaran B, Bowles KM, Rushworth SA. The bone marrow microenvironment - Home of the leukemic blasts. Blood Rev. 2017;31(5):277–286.
10. Tabe Y, Konopleva M. Leukemia Stem Cells Microenvironment. Adv Exp Med Biol. 2017;1041:19–32.
11. Cukierman E, Bassi DE. The mesenchymal tumor microenvironment. Cell Adhes Migr. 2012;6(3):285–296.
12. Goodell MA, Brose K, Paradis g, Conner AS, Mulligan RC. Isolation and functional properties of murine hematopoietic stem cells that are replicating in vivo. J Exp Med. 1996;183(4):1797–1806.
13. Malfuson J-V, Boutin L, Clay D, et al. SP/drug efflux functionality of hematopoietic progenitors is controlled by mesenchymal niche through VLA-4/CD44 axis. Leukemia. 2014;28(4):853–864.
14. Pierre-Louis O, Clay D, Brunet de la Grange P, et al. Dual SP/ALDH functionalities refine the human hematopoietic Lin-CD34+CD38- stem/progenitor cell compartment. Stem Cells. 2009;27(10):2552–2562.
15. Saland E, Boutzen H, Castellano R, et al. A robust and rapid xenograft model to assess efficacy of chemotherapeutic agents for human acute myeloid leukemia. Blood Cancer J. 2015;5(3):e297.
16. Challen GA, Little MH. A side order of stem cells: the SP phenotype. Stem Cells. 2006;24(1):3–12.
17. Svirnovski AI, Shman TV, Serhiyenka TF, Savitski VP, Smolnikova VV, Fedasenka UU. ABCB1 and ABCG2 proteins, their functional activity and gene expression in concert with drug sensitivity of leukemia cells. Hematol Amst Neth. 2009;14(4):204–212.
18. Imrichova D, Messingerova L, Seres M, et al. Selection of resistant acute myeloid leukemia SKM-1 and MOLM-13 cells by vincristine-, mitoxantrone- and lenalidomide-induced upregulation of P-glycoprotein activity and downregulation of CD33 cell surface exposure. Eur J Pharm Sci. 2015;77:29–39.
19. Nieth C, Lage H. Induction of the ABC-transporters Mdr1/P-gp (Abcb1), mrpl (Abcc1), and bcrp (Abcg2) during establishment of multidrug resistance following exposure to mitoxantrone. J Chemother. 2005;17(2):215–223.
20. Eppert K, Takenaka K, Lechman ER, et al. Stem cell gene expression programs influence clinical outcome in human leukemia. Nat Med. 2011;17(9):1086–1093.
21. Ng SWK, Mitchell A, Kennedy JA, et al. A 17-gene stemness score for rapid determination of risk in acute leukaemia. Nature. 2016;540(7633):433–437.
22. Birbrair A, Frenette PS. Niche heterogeneity in the bone marrow. Ann N Y Acad Sci. 2016;1370(1):82–96.
23. Crane GM, Jeffery E, Morrison SJ. Adult haematopoietic stem cell niches. Nat Rev Immunol. 2017;17(9):573–590.
24. Wei Q, Frenette PS. Niches for Hematopoietic Stem Cells and Their Progeny. Immunity. 2018;48(4):632–648.
25. Arai F, Hirao A, Suda T. Regulation of hematopoietic stem cells by the niche. Trends Cardiovasc Med. 2005;15(2):75–79.
26. Gillet J-P, Gottesman MM. Overcoming multidrug resistance in cancer: 35 years after the discovery of ABCB1. Drug Resist Updat. 2012;15(1–2):2–4.
27. Balzano M, De Grandis M, Vu Manh T-P, et al. Nidogen-1 Contributes to the Interaction Network Involved in Pro-B Cell Retention in the Peri-sinusoidal Hematopoietic Stem Cell Niche. Cell Rep. 2019;26(12):3257-3271.e8.
28. De Grandis M, Mancini SJ, Aurrand-Lions M. In quest for leukemia initiating cells in AML. Oncoscience. 2018;5(1–2):9–10.
29. Hosokawa K, Arai F, Yoshihara H, et al. Function of oxidative stress in the regulation of hematopoietic stem cell-niche inter-

action. Biochem Biophys Res Commun. 2007;363(3):578–583.
30. Boyd AL, Aslostovar L, Reid J, et al. Identification of Chemotherapy-Induced Leukemic-Regenerating Cells Reveals a Transient Vulnerability of Human AML Recurrence. Cancer Cell. 2018;34(3):483-498.e5.
31. Moschoi R, Imbert V, Nebout M, et al. Protective mitochondrial transfer from bone marrow stromal cells to acute myeloid leukemic cells during chemotherapy. Blood. 2016;128(2):253–264.
32. Saygin C, Matei D, Majeti R, Reizes O, Lathia JD. Targeting Cancer Stemness in the Clinic: From Hype to Hope. Cell Stem Cell. 2019;24(1):25–40.
33. Varatharajan S, Abraham A, Karathedath S, et al. ATP-binding casette transporter expression in acute myeloid leukemia: association with in vitro cytotoxicity and prognostic markers. Pharmacogenomics. 2017;18(3):235–244.
34. Kolitz JE, George SL, Marcucci G, et al. P-glycoprotein inhibition using valspodar (PSC-833) does not improve outcomes for patients younger than age 60 years with newly diagnosed acute myeloid leukemia: Cancer and Leukemia Group B study 19808. Blood. 2010;116(9):1413–1421.
35. Cripe LD, Uno H, Paietta EM, et al. Zosuquidar, a novel modulator of P-glycoprotein, does not improve the outcome of older patients with newly diagnosed acute myeloid leukemia: a randomized, placebo-controlled trial of the Eastern Cooperative Oncology Group 3999. Blood. 2010;116(20):4077–4085.
36. Dean M, Hamon Y, Chimini G. The human ATP-binding cassette (ABC) transporter superfamily. J Lipid Res. 2001;42(7):1007–1017.
37. Sawicki E, Schellens JHM, Beijnen JH, Nuijen B. Pharmaceutical development of an amorphous solid dispersion formulation of elacridar hydrochloride for proof-of-concept clinical studies. Drug Dev Ind Pharm. 2017;43(4):584–594.
38. Robey RW, Pluchino KM, Hall MD, Fojo AT, Bates SE, Gottesman MM. Revisiting the role of ABC transporters in multidrug-resistant cancer. Nat Rev Cancer. 2018;18(7):452-464.
39. Wijaya J, Fukuda Y, Schuetz JD. Obstacles to Brain Tumor Therapy: Key ABC Transporters. Int J Mol Sci. 2017;18(12).

ARTICLE

Clinical and preclinical characterization of CD99 isoforms in acute myeloid leukemia

Vijaya Pooja Vaikari,[1] Yang Du,[1] Sharon Wu,[1] Tian Zhang,[2] Klaus Metzeler,[3] Aarif M.N. Batcha,[4,5] Tobias Herold,[3,6] Wolfgang Hiddemann,[3] Mojtaba Akhtari[7] and Houda Alachkar[1,7]

[1]Titus Family Department of Clinical Pharmacy, School of Pharmacy, University of Southern California, Los Angeles, CA, USA; [2]Medical Biology Program, Keck School of Medicine, University of Southern California, Los Angeles, CA, USA; [3]Laboratory for Leukemia Diagnostics, Department of Medicine III, University Hospital, LMU Munich, Munich, Germany; [4]Institute of Medical Data Processing, Biometrics and Epidemiology (IBE), Faculty of Medicine, LMU Munich, Munich, Germany; [5]Data Integration for Future Medicine (DiFuture, www.difuture.de), LMU Munich, Germany; [6]Research Unit Apoptosis in Hematopoietic Stem Cells, Helmholtz Zentrum München, German Center for Environmental Health (HMGU), Munich Germany and [7]USC Norris Comprehensive Cancer Center, University of Southern California, Los Angeles Southern California, Los Angeles, CA, USA

Ferrata Storti Foundation

Haematologica 2020
Volume 105(4):999-1012

ABSTRACT

In an effort to identify target genes in acute myeloid leukemia (AML), we compared gene expression profiles between normal and AML cells from various publicly available datasets. We identified *CD99*, a gene that is up-regulated in AML patients. In 186 patients from The Cancer Genome Atlas AML dataset, *CD99* was over-expressed in patients with *FLT3*-ITD and was down-regulated in patients with *TP53* mutations. CD99 is a transmembrane protein expressed on leukocytes and plays a role in cell adhesion, trans-endothelial migration, and T-cell differentiation. The *CD99* gene encodes two isoforms with distinct expression and functional profiles in both normal and malignant tissues. Here we report that, although the CD99 long isoform initially induces an increase in cell proliferation, it also induces higher levels of reactive oxygen species, DNA damage, apoptosis and a subsequent decrease in cell viability. In several leukemia murine models, the CD99 long isoform delayed disease progression and resulted in lower leukemia engraftment in the bone marrow. Furthermore, the CD99 monoclonal antibody reduced cell viability, colony formation, and cell migration, and induced cell differentiation and apoptosis in leukemia cell lines and primary blasts. Mechanistically, CD99 long isoform resulted in transient induction followed by a dramatic decrease in both ERK and SRC phosphorylation. Altogether, our study provides new insights into the role of CD99 isoforms in AML that could potentially be relevant for the preclinical development of CD99 targeted therapy.

Introduction

The outcome of patients with acute myeloid leukemia (AML) remains dismal due to the high relapse rate.[1] To identify target genes that were differentially over-expressed in AML compared with normal hematopoietic cells, we leveraged genomic and transcriptomic data and discovered *CD99*.

CD99, a membrane glycoprotein,[2] is normally expressed in cortical thymocytes, mature plasma cells, granulosa cells of the ovary, Sertoli cells of the testis, and pancreatic islet cells.[3] The *CD99* gene encodes two distinct proteins that are produced by alternative splicing of the *CD99* transcript. The alternative spliced short isoform results from a deletion in its intracytoplasmic fragment.[2] CD99 plays a role in cell migration,[4] adhesion, differentiation of thymocytes and T cells,[2] and regulation of diapedesis.[5] In cancer cells, CD99 is highly expressed on the cell surface of Ewing's sarcoma (EWS),[6] gliomas[7] and other mesenchymal,[8,9] hematopoietic,[10-12] and epithelial cancers.[13,14] In EWS, engagement with the anti-CD99 antibody enhanced apoptosis and sensitivity to chemotherapy.[15] High CD99 correlated with enhanced invasion of glioma cells.[7]

Correspondence:

HOUDA ALACHKAR
alachkar@usc.edu

Received: September 17, 2018.

Accepted: July 25, 2019.

Pre-published: August 1, 2019..

doi:10.3324/haematol.2018.207001

Check the online version for the most updated information on this article, online supplements, and information on authorship & disclosures: www.haematologica.org/content/105/4/999

CD99 immunoreactivity was found in AML but rarely in myeloproliferative disorders, myelodysplastic syndromes, remission, and normal marrow samples.[16] A recent study, however, showed that CD99 is a disease stem cell marker, and CD99 antibody proved beneficial in xenograft mice models of myeloid malignancies.[17] With growing evidence that CD99 plays a role in cancer, and particularly in AML, and that CD99 isoforms are differentially expressed and play different roles in different hematopoietic cells,[18] investigating the roles of the two isoforms is crucial for CD99 preclinical development as a therapeutic target. Here we characterize CD99 upregulation in patients with AML and its association with clinical and molecular characteristics, and determine the function of CD99 long (L) and short (S) isoforms in preclinical leukemia models.

Methods

Patients' samples

Diagnostic or relapse blood was obtained from AML patients treated at the Norris Comprehensive Cancer Center at the University of Southern California (USC) after obtaining written informed consent. The use of human materials was approved by the Institutional Review Boards of the USC in accordance with the Declaration of Helsinki.

Patient datasets and gene expression analysis

The Cancer Genome Atlas (TCGA) AML dataset was downloaded from oncomine.[19,20] Patients data from the GSE7186,[21] GSE13159,[22] GSE1159,[23] GSE15434,[24] GSE3077,[25] GSE425,[26] GSE12417,[27] and GSE17855[28] datasets were downloaded from the GEO database. Details of analysis methods are available in the *Online Supplementary Appendix.*

Cell lines and primary blasts

Acute myeloid leukemia cell lines were grown in Roswell Park Memorial Institute (RPMI) medium supplemented with 10% fetal bovine serum (FBS) and 100U/mL penicillin. Peripheral blood mononuclear cells (PBMC) from AML patients and from healthy donors were isolated by density gradient centrifugation using Ficoll-Paque. Primary cells were grown in RPMI plus 20% FBS and cytokine cocktails CC100 (Flt3L, SCF, IL-3 and IL-6).

In vivo studies

Animal protocols were approved by the Institution for Animal Care and Use Committee (IACUC) of the USC. For THP-1 and MOLM-13 xenograft experiments, $2.5x10^6$ cells were injected *via* tail-vein (IV) into 4-6 week-old NOD-*scid* /Il2rg$^{-/-}$ (NSG) mice (Jackson). For the primary blasts xenograft experiment, $1x10^6$ cells were IV engrafted into irradiated mice. Details of the methods used, including plasmids, primer sequences, antibodies and *in vivo* experiments are available in the *Online Supplementary Appendix*.

Results

CD99 is up-regulated in acute myeloid leukemia

In an effort to identify target genes that were differentially over-expressed in AML, we compared gene expression profiles between normal and AML cells from various available public datasets. We found that *CD99* was significantly up-regulated in AML compared with normal cells in five datasets with available measurements of *CD99* RNA levels in both leukemia and normal cells (oncomine median ranking among up-regulated measured genes 155, *P*=0.013; TCGA data did not have *CD99* levels in normal cells). *CD99* was significantly higher in 23 AML samples compared with six normal bone marrow (BM) samples (GSE7186: 3.5-fold, *P*<0.0001) (Figure 1A). Consistently, *CD99* was significantly over-expressed in blasts of 542 patients with AML compared with PBMC from 74 healthy donors (HD) (GSE13159: 2-fold, *P*<0.0001) (Figure 1B). Similarly, *CD99* expression was 1.8-fold higher in blasts from 285 patients with AML compared with HD cells (GSE1159: *P*=0.003) (*Online Supplementary Figure S1A*). There was a 2.3-fold increase in *CD99* expression (GSE13164: *P*<0.001) (*Online Supplementary Figure S1B*) in blasts of 257 AML patients compared with PBMC of 58 HD. In the GSE995 dataset, *CD99* expression was 3-fold higher in blasts from nine AML patients compared with that in cells from six HD (*P*=0.028) (*Online Supplementary Figure S1C*). We also analyzed the expression of CD99 protein coding transcripts in patients with AML (GSE106291; n=246). ENST00000381192.10 (CD99-L) and ENST00000611428.5 (CD99-S) were the top expressed transcripts (Figure 1C). The combined expression of ENST00000482405.7 and ENST00000611428.5 (both code for CD99-S) was significantly higher (*P*=0.0073) than the level of ENST00000381192.10 (CD99-L) (*Online Supplementary Figure S1D*). Transcript Ensembl IDs are described in *Online Supplementary Table S1*. The transcript expression of the two isoforms were positively correlated (*Online Supplementary Figure S1E* and *F*).

Several reports suggested that CD99 is up-regulated on leukemia stem cells.[29-31] To validate this, we assessed *CD99* expression in the GSE3077 dataset that has gene expression data of leukemia blasts obtained from 23 patients with AML sorted according to their CD34 and CD38 expression levels. We found that *CD99* expression was significantly higher (1.34-fold, *P*<0.001) (Figure 1D) in the $CD34^+CD38^+$ and $CD34^+CD38^-$ combined subpopulation compared with $CD34^-CD38^-$ and $CD34^-CD38^+$ combined.

CD99 overexpression is positively associated with *FLT3*-ITD and reversely with *TP53* mutations

We assessed the association between *CD99* upregulation and the presence of AML mutations. In the TCGA dataset, *CD99* expression was significantly higher (*P*=0.004) in patients with *FLT3*-ITD (n=37) compared with patients with *FLT3* point mutations (n=16) and *FLT3* wild-type (n=133) (1.3 fold, *P*=0.002) (Figure 1E). Similarly, there was a significant association between high *CD99* (above the median) and the presence of *FLT3*-ITD mutation (Fisher's exact test, *P*=0.04) (*Online Supplementary Table S2*). A similar association was found in the GSE17855 and GSE15434 datasets with childhood AML and patients with cytogenetically normal karyotype, respectively. *CD99* is significantly higher in patients with *FLT3*-ITD compared with patients with *FLT3* wild-type (*FLT3*-WT) (1.3-fold, *P*=0.03, *Online Supplementary Figure S1G*; 1.4-fold, *P*<0.001, *Online Supplementary Figure S1H*; respectively). We next examined the association of each *CD99* transcript with *FLT3*-ITD mutation. ENST00000381187.8 and ENST00000624481.4 were significantly higher in *FLT3*-ITD compared with *FLT3*-WT patients (*P*=0.001 and *P*=0.002) (*Online Supplementary Figure S1I-N*). ENST00000611428.5 (CD99-S) was not significantly associated with *FLT3*-ITD after adjusting for

multiple hypotheses testing (unadjusted *P*=0.049).

CD99 expression was significantly lower (1.9-fold, *P*<0.001) in patients with mutated *TP53* (n=15) compared with patients with *TP53*-WT (n=171) (*Online Supplementary Figure S1O*; Fisher's Exact test, *P*=0.0006, *Online Supplementary Table S1*). *CD99* expression was not associated with other mutations (*Online Supplementary Table S2* and *Online Supplementary Figure S2*).

CD99 expression levels according to patients' clinical characteristics

We dichotomized patients into high and low groups based on *CD99* median expression. Patients with *CD99*-low had a significantly lower percentage of bone marrow (BM) blasts (median, 66.2 *vs*. 72.5, *P*=0.024), peripheral blood (PB) blasts (median, 23.7 *vs*. 50.7, *P*<0.0001), and white blood cell (WBC) count (median, 27.7 *vs*. 45.8, *P*=0.019). The median age was 57.8 years in *CD99*-low and 52.1 years in *CD99*-high groups (*Online Supplementary Table S3*).

According to the National Comprehensive Cancer Network (*NCCN*), AML is classified into favorable, intermediate and poor-risk groups based on patients molecular and cytogenetic characteristics. *CD99* expression was significantly higher in the favorable-risk group than that in the intermediate-risk (1.2-fold, *P*<0.01) and poor-risk (2-fold, *P*<0.0001) groups (Figure 2A). According to the AML French-American-British (FAB) classification data, patients with M5-AML had lower *CD99* expression compared with M1, M2, M3 and M4 (*Online Supplementary Figure*

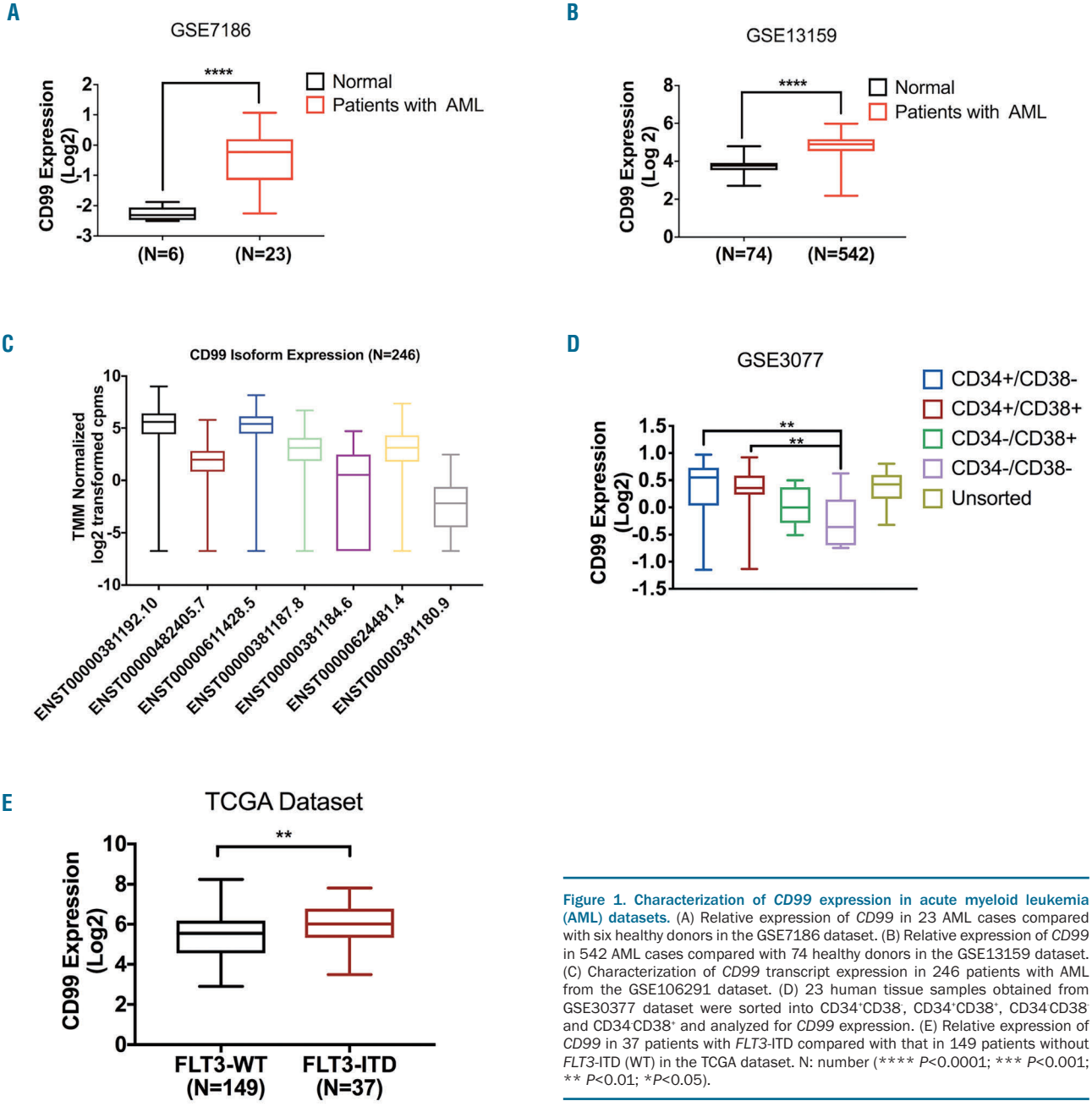

Figure 1. Characterization of *CD99* expression in acute myeloid leukemia (AML) datasets. (A) Relative expression of *CD99* in 23 AML cases compared with six healthy donors in the GSE7186 dataset. (B) Relative expression of *CD99* in 542 AML cases compared with 74 healthy donors in the GSE13159 dataset. (C) Characterization of *CD99* transcript expression in 246 patients with AML from the GSE106291 dataset. (D) 23 human tissue samples obtained from GSE30377 dataset were sorted into $CD34^+CD38^-$, $CD34^+CD38^+$, $CD34^-CD38^-$ and $CD34^-CD38^+$ and analyzed for *CD99* expression. (E) Relative expression of *CD99* in 37 patients with *FLT3*-ITD compared with that in 149 patients without *FLT3*-ITD (WT) in the TCGA dataset. N: number (**** *P*<0.0001; *** *P*<0.001; ** *P*<0.01; **P*<0.05).

S3A). Based on leukemia cytogenetics, no significant differences in *CD99* expression was found in patients with complex karyotype, Inv (16), t (15; 17), t (8,21), del (7q) / 7q- and trisomy 8, compared with normal karyotype (*Online Supplementary Figure S3B*).

CD99 overexpression is associated with better clinical outcome

The overall survival (OS) of *CD99*-high patients (based on median cut-off) was significantly longer than that of *CD99*-low patients (median: 27 *vs*. 11.2 months; *P*=0.0026) (Figure 2B). Patients with t(15;17) are treated with all-trans retinoic acid (ATRA) and have a better outcome, thus they were excluded from the survival analyses. When patients were stratified into cytogenetically normal (CN) and cytogenetically abnormal (CA), we found that in CA-AML, but not in CN-AML, *CD99*-high survived significantly longer than *CD99*-low patients (CA-AML: median OS: 32.3 *vs*. 11 months, *P*=0.02, Figure 2C; CN-AML: *P*=0.24, *Online Supplementary Figure S4A*). Yet, there was no significant difference in *CD99* levels between CN-AML and CA-AML (*P*=0.33) (*Online Supplementary Figure S4B*). There was no significant difference in event-free survival (EFS) between *CD99*-high and *CD99*-low patients (median: 15.6 *vs*. 13.3 months; *P*=0.13) (*Online Supplementary Figure S4C-E*).

In the GSE425 dataset of 71 patients with CA-AML, *CD99*-high patients survived significantly longer than *CD99*-low patients (*P*=0.04) (*Online Supplementary Figure S5B*). No significant difference in OS was found when we included CN-AML patients or analyzed them separately (*Online Supplementary Figure S5A* and *C*). In the GSE12417 dataset, which includes only CN-AML patients, no significant difference between *CD99*-high and *CD99*-low patients (n=163) was observed (*Online Supplementary Figure S5D*).

In a multivariable analysis, high *CD99* was not significantly associated with OS when adjusted by age, cytogenetic risk, transplant status, *DNMT3A* mutation status, and *TP53* mutation status (*P*=0.364) (*Online Supplementary Table S4*).

We also assessed the association of *CD99* transcript upregulation with OS in 246 patients with AML using median cut-off for each transcript. High ENST00000381192.10 (CD99-L) exhibited a trend of association with better OS (GSE106291: median OS: 908 *vs*. 445 days; *P*=0.06) (Figure 2D). No difference in survival between high and low expression was observed for the other transcripts (*Online Supplementary Figure S6A-G*).

Differential effect of *CD99* isoform expression on leukemia growth

In a panel of AML cell lines (KG-1, KG-1A, MOLM13, MV4-11, Kasumi-1, THP-1, NB4, U937, UOC-M1), CD99 surface levels are higher than that of healthy cord blood cells (Figure 3A). Western blots revealed 28 and 32kDa bands corresponding to CD99-L and -S in U937, KG-1A and Kasumi-1 cells, but only the lower band was recognized in THP-1, MOLM-13, $CD34^+$ cells and two HD PBMC lysates (Figure 3B and *Online Supplementary Figure*

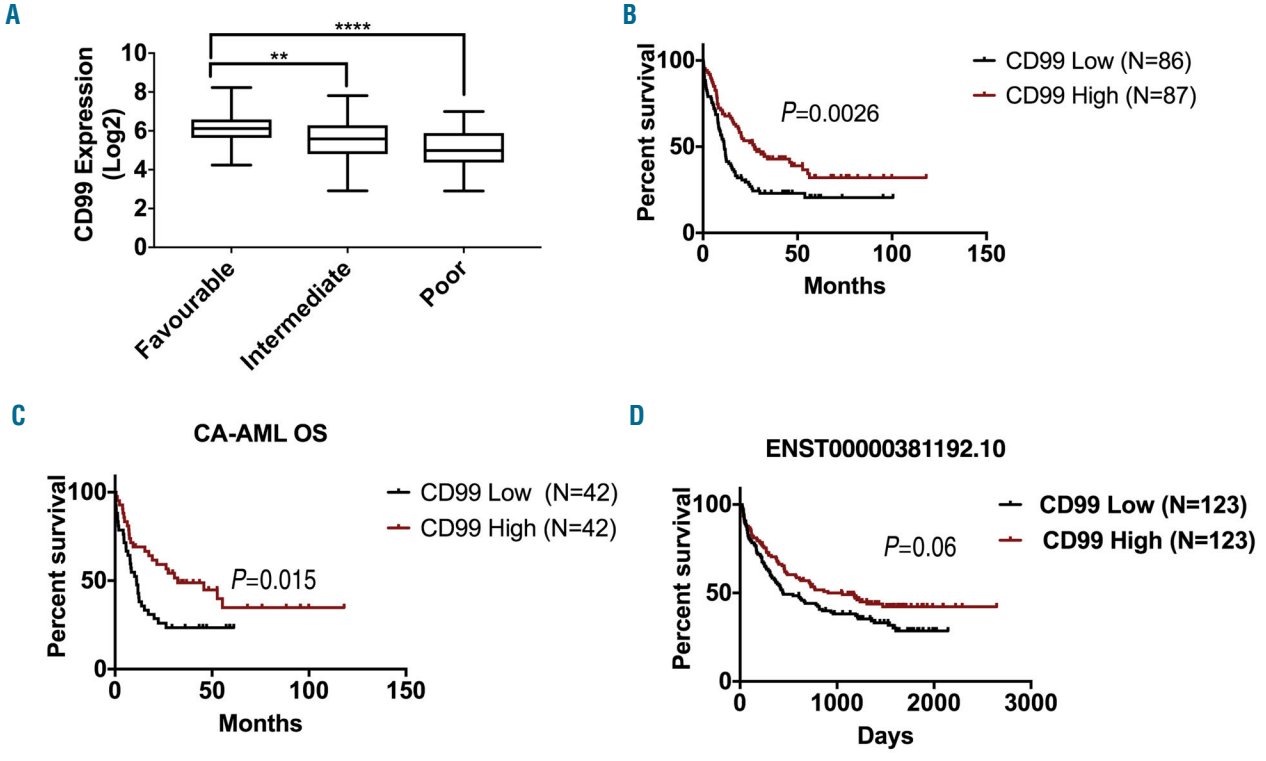

Figure 2. Association of *CD99* expression with patients' clinical characteristics in acute myeloid leukemia (AML) datasets. (A) Relative expression of *CD99* according to the National Comprehensive Cancer Network (NCCN) risk status classification in the The Cancer Genome Atlas (TCGA) dataset. (B) Overall survival (OS) of 173 patients grouped based on *CD99* median expression into *CD99* high (n=87) and *CD99* low (n=86) from the TCGA dataset. (C) OS of cytogenetically abnormal (CA-AML) cases grouped based on *CD99* median expression into *CD99* high (n=42) and *CD99* low (n=42). (D) OS of 146 patients grouped based on ENST00000381192.10 transcript isoform based on median expression into high (n=123) and low (n=123) from the GSE106291 dataset. (****P<0.0001; ** P<0.01).

S7A). Similarly, quantitative polymerase chain reaction (qPCR) analysis showed that *CD99* transcripts were up-regulated in AML blast samples (n=9) and AML cell lines (KG-1a, U937, THP-1, and MOLM-13) compared with HD PBMC (n=3) and CD34⁺ cells. Transcript ENST00000482405.7 is higher in CD34⁺ cells than in AML cell lines (*Online Supplementary Figure S7B*; for qPCR primers see *Online Supplementary Table S5*).

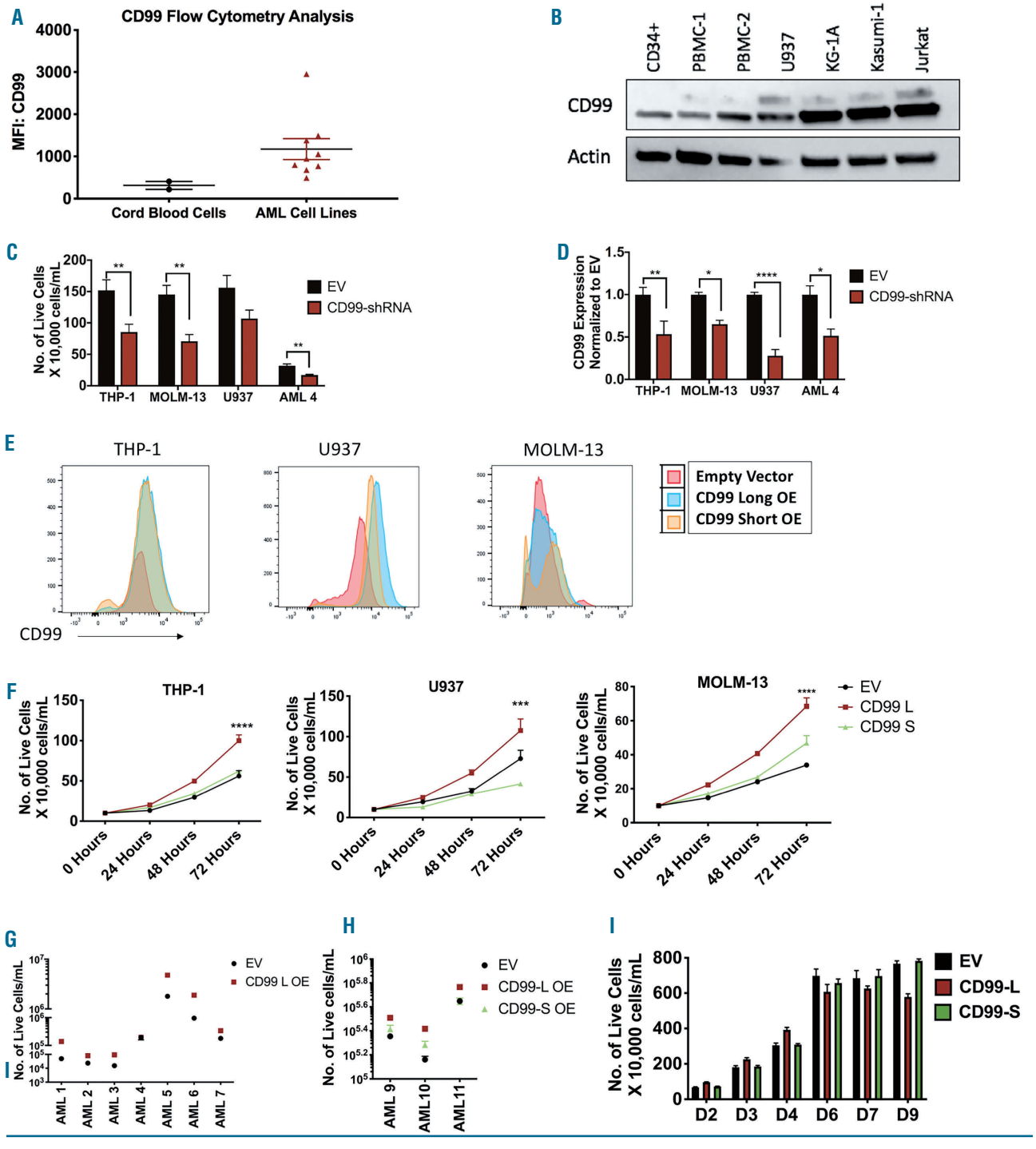

Figure 3. Effect of CD99 isoform expression on acute myeloid leukemia (AML) cell proliferation. (A) Relative CD99 expression in cord blood cells (n=2) and AML cell lines (n=9) measured by flow cytometry. (B) Western blot analysis of CD99 isoform expression in CD34⁺ cells, healthy donor peripheral blood mononuclear cells (PBMC) and AML cell lines. (C) Viability of *CD99*-shRNA knockdown in THP-1, MOLM-13, U937 and AML-4 cells measured 96 hours (h) after transfection using trypan-blue and alamar-blue. (D) Quantative polymerase chain reaction (qPCR) analysis using *CD99* TaqMan assay to confirm *CD99* knockdown in THP-1, MOLM-13, U937 and AML-4 cells transfected with CD99-shRNA plasmid (or EV) for 96 h. CD99 expression was normalized to EV cells. (E) *CD99* expression in EV, CD99-L OE and CD99-S OE cells measured by flow cytometry in THP-1, U937 and MOLM-13 cells.(F) Proliferation assay of EV, CD99-L and CD99-S measured at 24,48 and 72 h by trypan-blue (n=4) in THP-1, U937, and MOLM-13 cells. Data reported as number of live cells. (G) Viability of AML blasts over-expressing CD99-L or EV measured 96 h after lentiviral transduction using trypan-blue (n=7). Data reported as total number of live cells/mL. (H) Viability of AML blasts over-expressing CD99 L, CD99-S or EV measured 96 h after lentiviral transduction using trypan-blue (n=3). Data reported as the number of live cells/mL. (I) Long-term proliferation assay of EV, CD99-L and CD99-S cells measured at days 2, 3, 4, 6, 7 and 9 by trypan-blue assay. (*****P*<0.0001; ****P*<0.001; ***P*<0.01; **P*<0.05).

We then examined the effect of *CD99* knockdown on cell viability. Transducing cells with lentiviral-*CD99*-shRNA significantly reduced primary AML blast viability (n=4) (Figure 3C and *Online Supplementary Figure S7C*) and AML cell lines (THP-1, MOLM-13, and U937) (40-60%; $P<0.05$) (Figure 3C). Knockdown was confirmed by qPCR (Figure 3D) and western blot (*Online Supplementary Figure S7D*). THP-1 and MV4-11 cells had an approximately 35-50% decrease in cell viability when transiently transfected by elecroporation with *CD99*-siRNA compared with negative-control-siRNA ($P=0.001$ and $P=0.001$, respectively) (*Online Supplementary Figure S7E-G*).

We also established a gain-of-function approach to study *CD99*-L and *CD99*-S isoform functions. We performed lentiviral transduction to over-express *CD99*-L and *CD99*-S in THP-1, U937 and MOLM-13 cells expressing variable endogenous levels of CD99 isoforms (Figure 3E and *Online Supplementary Figure S7H* and *I*). *CD99*-L transduced cells had increased cell proliferation at 72 hours (h) compared with their respective empty vector (EV) controls and *CD99*-S transduced cells, respectively, counted by trypan-blue in THP-1 (1.78-fold, $P<0.001$; 1.61-fold, $P<0.01$), U937 (1.47-fold, $P<0.001$; 2.59-fold, $P<0.0001$), and MOLM-13 cells (2-fold, $P<0.0001$; 1.45-fold, $P<0.0001$) (Figure 3F). This was also confirmed by alamar-blue assay (*Online Supplementary Figure S8A*) and by BrdU staining (1.6-fold, $P=0.006$) (*Online Supplementary Figure S8B*) suggesting enhanced metabolic activity and DNA synthesis in these cells, respectively.

We also ectopically over-expressed *CD99*-L in AML blasts (n=7) (*Online Supplementary Table S6*) using lentiviral transduction. Overexpression of CD99-L was confirmed using western blot and fluorescence microscopy for green fluorescent protein (GFP) (*Online Supplementary Figure S8C* and *D*). Higher cell number was observed in lenti-*CD99* blasts compared with lenti-EV transduced blasts 96 h after viral transduction (2.8-fold, $P<0.0001$) (Figure 3G). We also observed a modest increase in the number of colonies on day 14 in 3 of 6 patient samples over-expressing CD99-L compared with their respective controls: AML-3 (6 *vs*. 15, $P=0.02$), AML-4 (6 *vs*. 14, $P=0.02$), and AML-5 (42 *vs*. 128, $P=0.001$) (*Online Supplementary Figure S8E*). Furthermore, we ectopically expressed CD99-L and CD99-S in three additional AML blast samples (*Online Supplementary Figure S8F*). Cell viability was measured 96 h after transduction using trypan-blue and alamar-blue. A higher number of live cells was observed in *CD99*-L transduced blasts compared with lenti-EV (1.5-fold, $P<0.0001$) and *CD99*-S transduced blasts (1.3-fold, $P<0.0001$) (Figure 3H). More colonies were observed in one sample over-expressing CD99-L compared with their respective controls; AML-10 (49.5 *vs.* 101.5, $P=0.04$) (*Online Supplementary Figure S8G*).

However, long-term culture of *CD99*-L transduced cells showed a subsequent drop in cell viability, and cells could not be maintained in culture for more than 4-6 weeks. To validate this, we performed a long-term culture assay for ten days starting approximately two weeks post viral transduction. Proliferation of CD99-L cells started to decline by day 5 of initial serum stimulation compared with EV and CD99-S cells, even when cell density and nutrients were accounted for (Figure 3I). In $CD34^+$ cells, we observed no significant change in the number of viable cells between cells transduced with CD99-L, -S isoform or EV (*Online Supplementary Figure S8H)* at 96 h post transduction. Transducing cells with lentiviral-*CD99*-shRNA resulted in a slight decrease in cell viability (*Online Supplementary Figure S8I*).

Ectopic expression of *CD99* long isoform enhances reactive oxygen species levels, DNA damage, and induces cell apoptosis

Because the initial enhanced proliferation of CD99-L cells was serum induced and reversed with further expansion *in vitro*, we speculated that the serum-induced cell growth would stimulate higher production of reactive oxygen species (ROS) in these cells. Indeed, THP-1 cells transduced with CD99-L exhibit a 2.5- and 1.6-fold increase in ROS levels compared with CD99-S and EV cells, respectively (Figure 4A and B). Because of their higher ROS levels, we asked whether DNA damage is increased in these cells. Western blot analysis showed that CD99-L cells exhibit a higher level of the DNA damage marker H2Axγ compared with CD99-S and EV cells (Figure 4C). Furthermore, apoptosis was also enhanced in CD99-L transduced cells measured by annexin-V staining in THP-1 (CD99-L *vs.* EV: 3.48-fold, $P=0.001$; CD99-L *vs.* CD99-S: 6.32-fold, $P=0.0027$), U937(CD99-L *vs*. EV: 3.26-fold, $P=0.07$; CD99-L *vs*. CD99-S: 3.67-fold, $P=0.10$), and MOLM-13 cells (CD99-L *vs*. EV: 4.88-fold, $P=0.0032$; CD99-L *vs*. CD99-S: 4.2-fold, $P=0.0042$) (Figure 4D and E). The enhanced apoptosis was also confirmed by the increase of cleaved caspase-3 (Figure 4F).

Ectopic expression of CD99-L isoform induces myeloid differentiation and reduces cell migration

Previous studies have demonstrated that CD99 homotypic interaction in CD99 expressing cells[32-34] plays a role in monocyte trans-endothelial migration.[4] Thus, we asked which isoform is responsible for cell homotypic interaction, and whether they affect cell migration and myeloid differentiation differently. Cells were seeded at $1x10^5$cells/mL per well in a 6-well-plate and images were taken 6 h later; CD99-L THP-1 cells displayed higher cell aggregation compared with EV and CD99-S cells (Figure 5A). CD99-L cells exhibit decreased migration towards SDF-1α in a transwell chamber compared with EV and CD99-S cells; THP-1 (70%, $P<0.0001$; 66%, $P<0.0001$), U937 (80%, $P<0.0001$; 83%, $P<0.0001$), and MOLM-13 (80%, $P<0.0001$; $P=0.0032$) (Figure 5B and C).

CD99-L expressing cells showed an increase in CD11b surface marker measured by flow cytometry 24 h after cells were seeded in THP-1 (CD99-L *vs*. EV: 2-fold, $P=0.0027$; CD99-L *vs*. CD99-S: 1.63-fold, $P=0.043$), U937 (CD99-L *vs*. EV: 1.56-fold, $P=0.01$; CD99-L *vs*. CD99-S: 1.29-fold, $P=0.11$), and MOLM-13 (CD99-L *vs*. EV: 1.89-fold, $P<0.0001$; CD99-L *vs*. CD99-S: 1.68-fold, $P<0.079$) (Figure 5D).

Ectopic expression of *CD99* long isoform delayed leukemia engraftment in acute myeloid leukemia murine models

Next, we investigated the effect of ectopic expression of CD99 isoforms in murine leukemia models. THP-1 cells stably over-expressing CD99-L (n=6), CD99-S (n=3), or EV (n=6) were injected into NSG mice. Mice were sacrificed on day 30-32 post implantation. Mice engrafted with CD99-L cells had smaller spleens compared with EV mice (0.04g *vs*. 0.07g, $P=0.010$) and CD99-S mice (0.04g *vs*. 0.06g, $P=0.0003$) (Figure 6A and B). hCD45 flow analysis revealed that CD99-L mice had significantly less BM engraftment

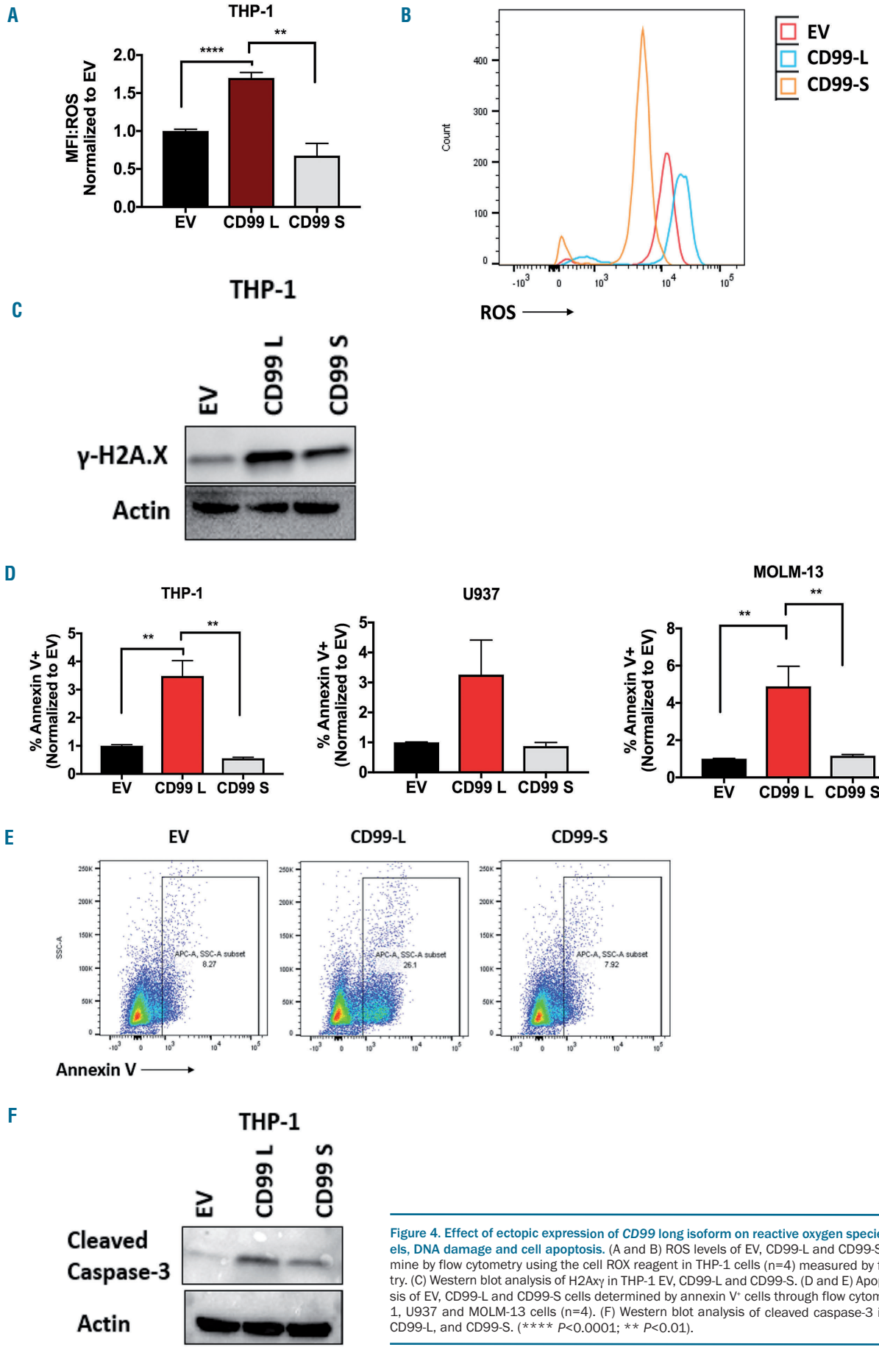

Figure 4. Effect of ectopic expression of *CD99* long isoform on reactive oxygen species (ROS) levels, DNA damage and cell apoptosis. (A and B) ROS levels of EV, CD99-L and CD99-S cells determine by flow cytometry using the cell ROX reagent in THP-1 cells (n=4) measured by flow cytometry. (C) Western blot analysis of H2Axγ in THP-1 EV, CD99-L and CD99-S. (D and E) Apoptosis analysis of EV, CD99-L and CD99-S cells determined by annexin V$^+$ cells through flow cytometry in THP-1, U937 and MOLM-13 cells (n=4). (F) Western blot analysis of cleaved caspase-3 in THP-1 EV, CD99-L, and CD99-S. (**** P<0.0001; ** P<0.01).

compared with EV (7.29% *vs.* 19.47%; *P*=0.02) and CD99-S mice (7.29% *vs.* 18.9%; *P*=0.04) (Figure 6C). CD99-L mice had significantly less PB engraftment compared with EV (14.73% *vs.* 84.52 %; *P*=0.0002) and CD99-S mice (14.73% *vs.* 83.3 %; *P*=0.006) (Figure 6D and *Online Supplementary Figure S9*). No difference in engraftment was seen in the liver (*Online Supplementary Figure S10A*) or spleen (*Online Supplementary Figure S10B*) between groups.

In the MOLM-13 murine model, mice were engrafted with CD99-L, CD99-S and EV mice (n=6 for EV and CD99-L, and n=3 for CD99-S) and were sacrificed on day 19 post transplantation. Mice engrafted with CD99-L cells had smaller spleens than EV mice (0.048g *vs.* 0.11g, *P*=0.004) and CD99-S mice (0.048g *vs.* 0.10g, *P*=0.026). (Figure 6E and F). CD99-L mice had significantly less engraftment than the EV mice in the BM (25.38% *vs.* 59.57%, *P*=0.003) (Figure 6G), PB (15.03% *vs.* 50.5%, *P*=0.0051) (Figure 6H), and liver (21.6% *vs.* 44.03%, *P*=0.011) (*Online Supplementary Figures S10C* and *S11*). No difference in engraftment was seen in spleen (*Online Supplementary Figure S10D*). Additionally, to determine whether mice engrafted with CD99-L cells developed deadly leukemia, two CD99-L engrafted mice were sacrificed only when mice appeared sick (days 29 and 44). We observed PB engraftment in both mice and in the BM of one mouse (*Online Supplementary Figure S10*). Hematoxylin & Eosin staining of the liver, spleen and sternum showed that EV and CD99-S tissues presented a higher percentage of infiltrated blasts compared with the CD99-L mice tissues (*Online Supplementary Figure S10*). We also found higher CD45 immunostaining (CD99-L *vs.* EV, *P*=0.004; CD99-L *vs.* CD99-S, *P*=0.13) and Ki67 staining (CD99-L *vs.* EV, *P*=0.0002; CD99-L *vs.* CD99-S, *P*=0.17) in

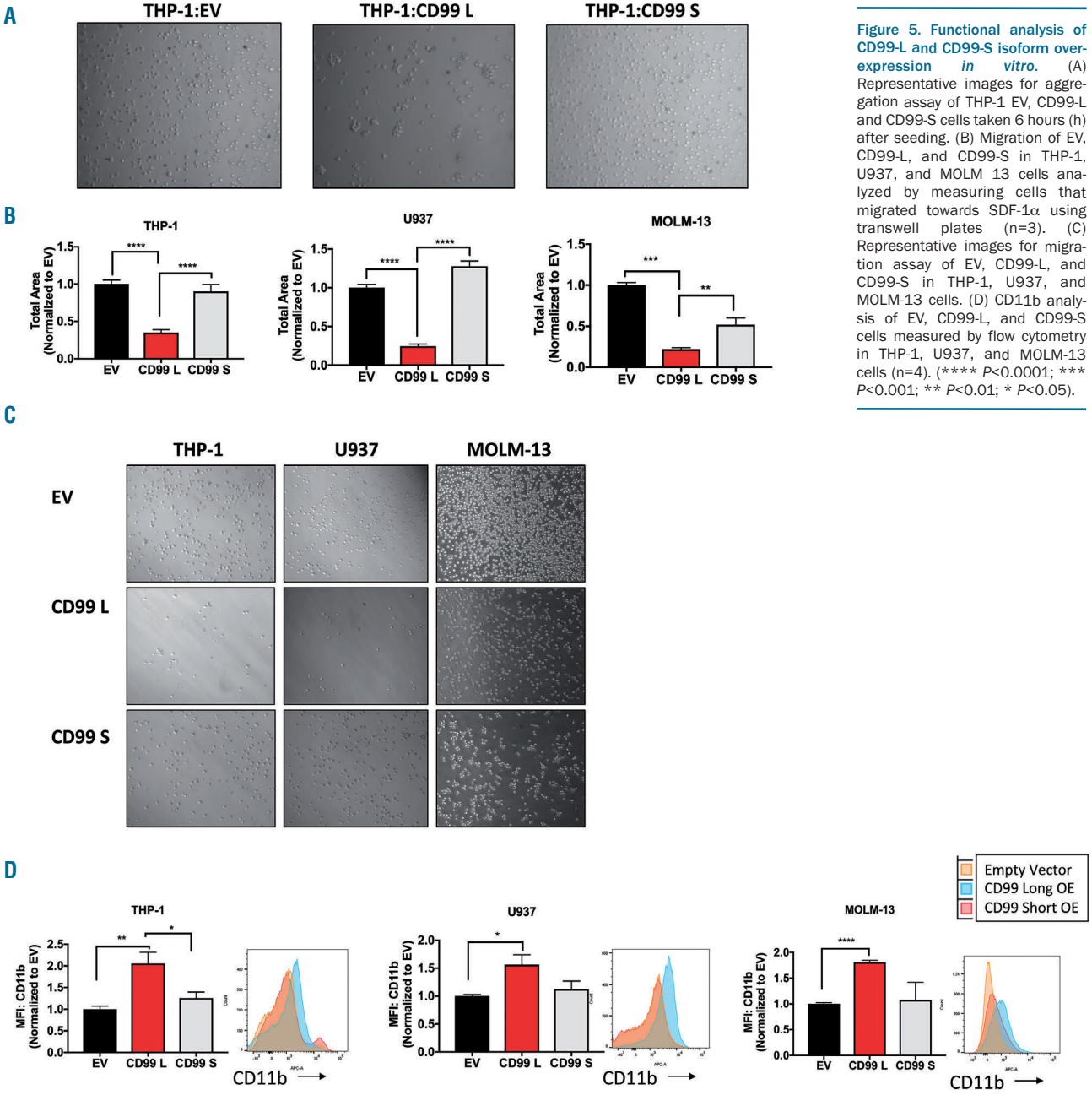

Figure 5. Functional analysis of CD99-L and CD99-S isoform overexpression *in vitro*. (A) Representative images for aggregation assay of THP-1 EV, CD99-L and CD99-S cells taken 6 hours (h) after seeding. (B) Migration of EV, CD99-L, and CD99-S in THP-1, U937, and MOLM 13 cells analyzed by measuring cells that migrated towards SDF-1α using transwell plates (n=3). (C) Representative images for migration assay of EV, CD99-L, and CD99-S in THP-1, U937, and MOLM-13 cells. (D) CD11b analysis of EV, CD99-L, and CD99-S cells measured by flow cytometry in THP-1, U937, and MOLM-13 cells (n=4). (**** *P*<0.0001; *** *P*<0.001; ** *P*<0.01; * *P*<0.05).

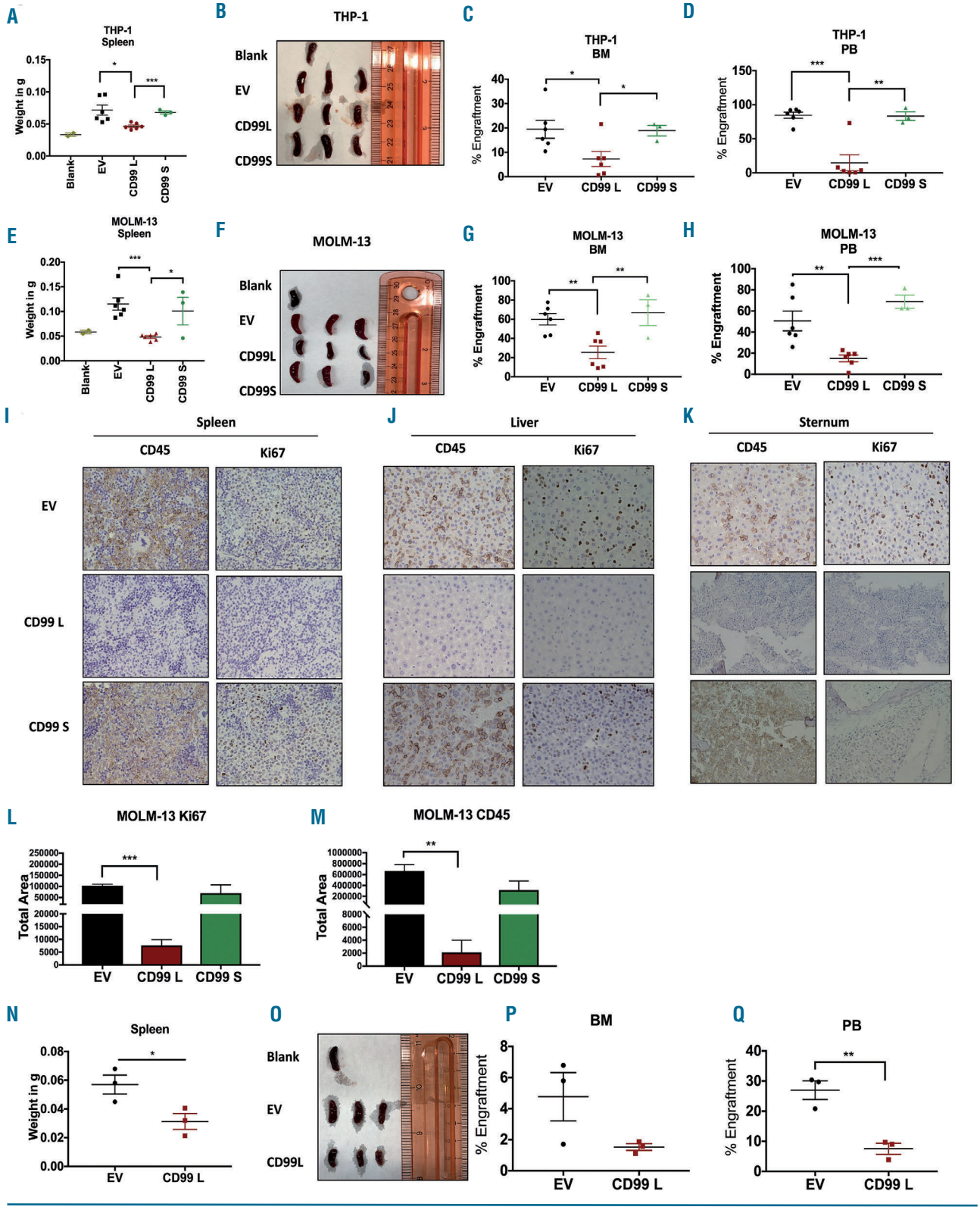

Figure 6. Effect of CD99-L and CD99-S isoform overexpression in acute myeloid leukemia (AML) murine models. 2.5x10^6 THP-1 EV (n=6), CD99-L (n=6), or CD99-S (n=3) cells were implanted in mice and sacrificed when sick (days 30-32 post implantation). (A and B) Spleen weight and images of blank, EV, CD99-L, and CD99-S mice at time of sacrifice. (C and D) Bone marrow (BM) and peripheral blood (PB) engraftment of THP-1 cells in EV, CD99-L and CD99-S mice determined by quantitative analysis of CD45$^+$ cells through flow cytometry. 2.5x10^6 MOLM-13 EV (n=6), CD99-L (n=6), or CD99-S (n=3) cells were implanted in mice and sacrificed when mice were sick. (E and F) Spleen weight and images of blank, EV, CD99-L, and CD99-S mice at time of sacrifice. (G and H) BM and PB engraftment of MOLM-13 cells in EV, CD99-L, and CD99-S mice determined by quantitative analysis of CD45$^+$ cells through flow cytometry. (I-K) Representative images of immunostaining for CD45 and Ki67 on collected tissues of (I) spleen, (J) liver, and (K) sternum. (L and M) Quantitative analysis of Ki67 and CD45 cells in the liver tissues of mice engrafted with MOLM-13 EV, CD99-L, and CD99-S cells quantified using ImageJ. 1x10^6 primary AML cells over-expressing EV (n=3) or CD99-L (n=3) cells were engrafted in mice and sacrificed when mice were sick (day 19 post-cell transplantation). (N and O) Spleen weight and images of EV and CD99-L mice at the time of sacrifice (4-months post transplantation). (P and Q) BM and PB engraftment of primary AML cells in EV and CD99-L mice determined by quantitative analysis of CD45$^+$ cells by flow cytometry. (****P<0.0001; ***P<0.001; **P<0.01; *P<0.05).

EV and CD99-S tissues compared with CD99-L tissues, confirming a decrease in leukemia engraftment in mice with CD99-L cells (Figure 6I-M).

In a primary blast murine model, we engrafted primary AML samples (AML-4) transduced with CD99-L (n=3) or EV (n=3) in sub-lethally irradiated mice. Mice were sacrificed four months post engraftment (Figure 6N-O). CD99-L mice had less BM engraftment, though this was not significant compared with the EV mice (1.52 *vs.* 4.76%, *P*=0.1) (Figure 6P), and a significant decrease in hCD45^{+} cells in PB (7.5% *vs.* 26.9 %, *P*=0.005) (Figure 6Q and *Online Supplementary Figures S10* and *S12)*.

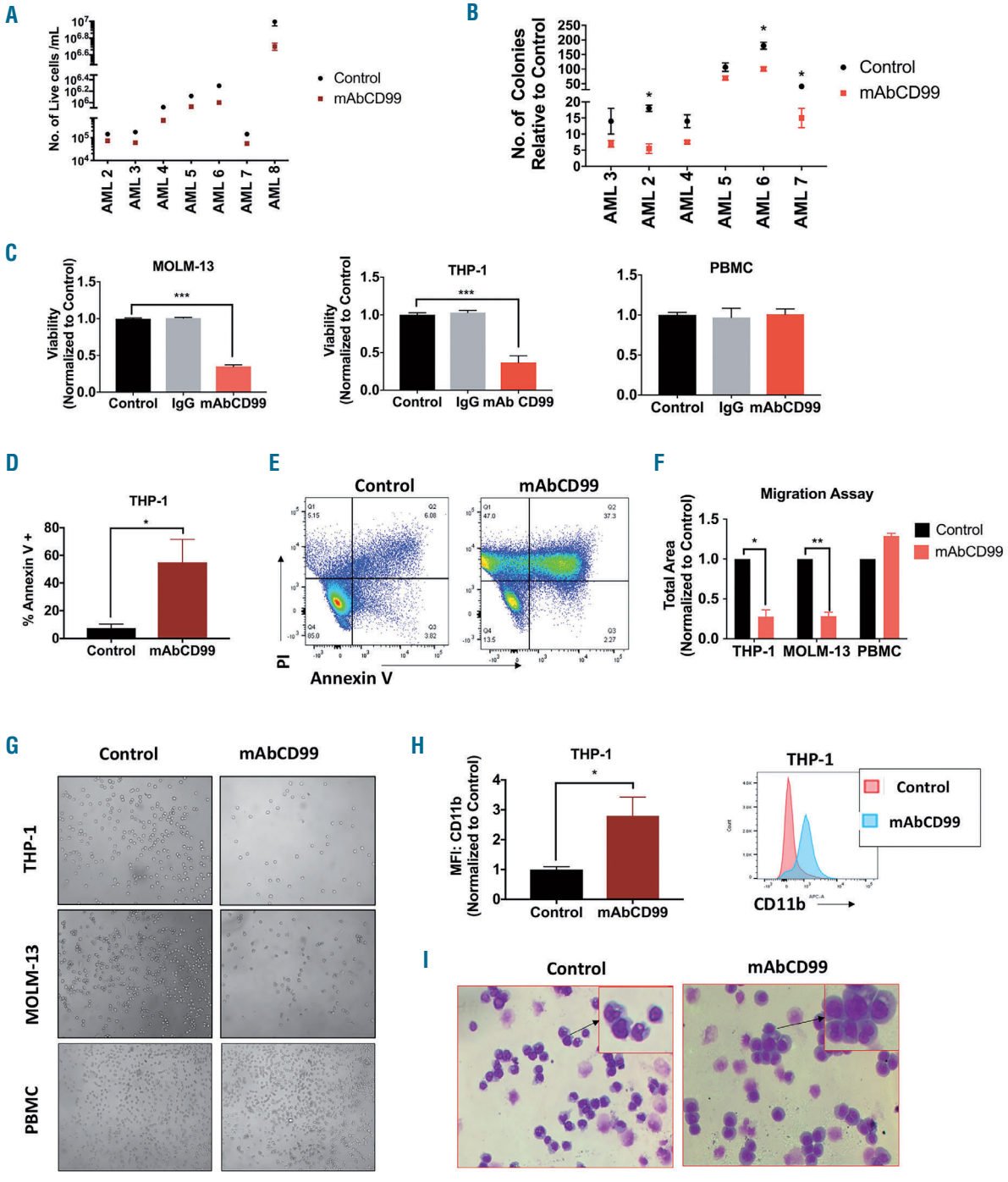

Figure 7. Effect of CD99 mAB on acute myeloid leukemia (AML) cells. (A) Cell viability of AML blasts treated with 20µg/mL of mAbCD99 for 48 hours (h) and measured using trypan-blue (n=7). (B) Total number of colonies comparison between AML blasts treated with mAb CD99 and control blasts (n=6). (C) Viability of THP-1, MOLM-13 and healthy donor peripheral blood mononuclear cells (PBMC) treated with 5µg/mL of mAbCD99 for 48 h and measured using alamar blue. (D and E) Apoptosis measured in THP-1 and MOLM-13 cells treated with mAbCD99 for 72 h and stained with Annexin V for flow cytometry analysis. (F and G) Quantitative analysis and representative images of migration of THP-1, MOLM-13 and PBMC treated with mAB CD99 towards SDF-1α performed in a transwell plate. (H) CD11b measured by flow cytometry in THP-1 cells 72 h post treatment with 2.5 µg/mL of mAB CD99. (I) Representative images for Wright-Giemsa staining of THP-1 cells treated with 2.5 µg/mL of mAb CD99 for 72 h. (***P<0.001; **P<0.01; *P<0.05).

CD99 monoclonal antibody treatment exhibits antileukemia activity in acute myeloid leukemia cells

Acute myeloid leukemia patient blasts (n=7) incubated with monoclonal CD99 antibody (mAbCD99: 20 μg/mL) showed a significant decrease in cell viability (48 h: 0.5±0.02-fold, P<0.0001) (Figure 7A). Treatment with mAbCD99 caused a decrease in colony formation in 3 of 6 patient samples: AML-2 (0.5-fold, P=0.02), AML-6 (0.65-

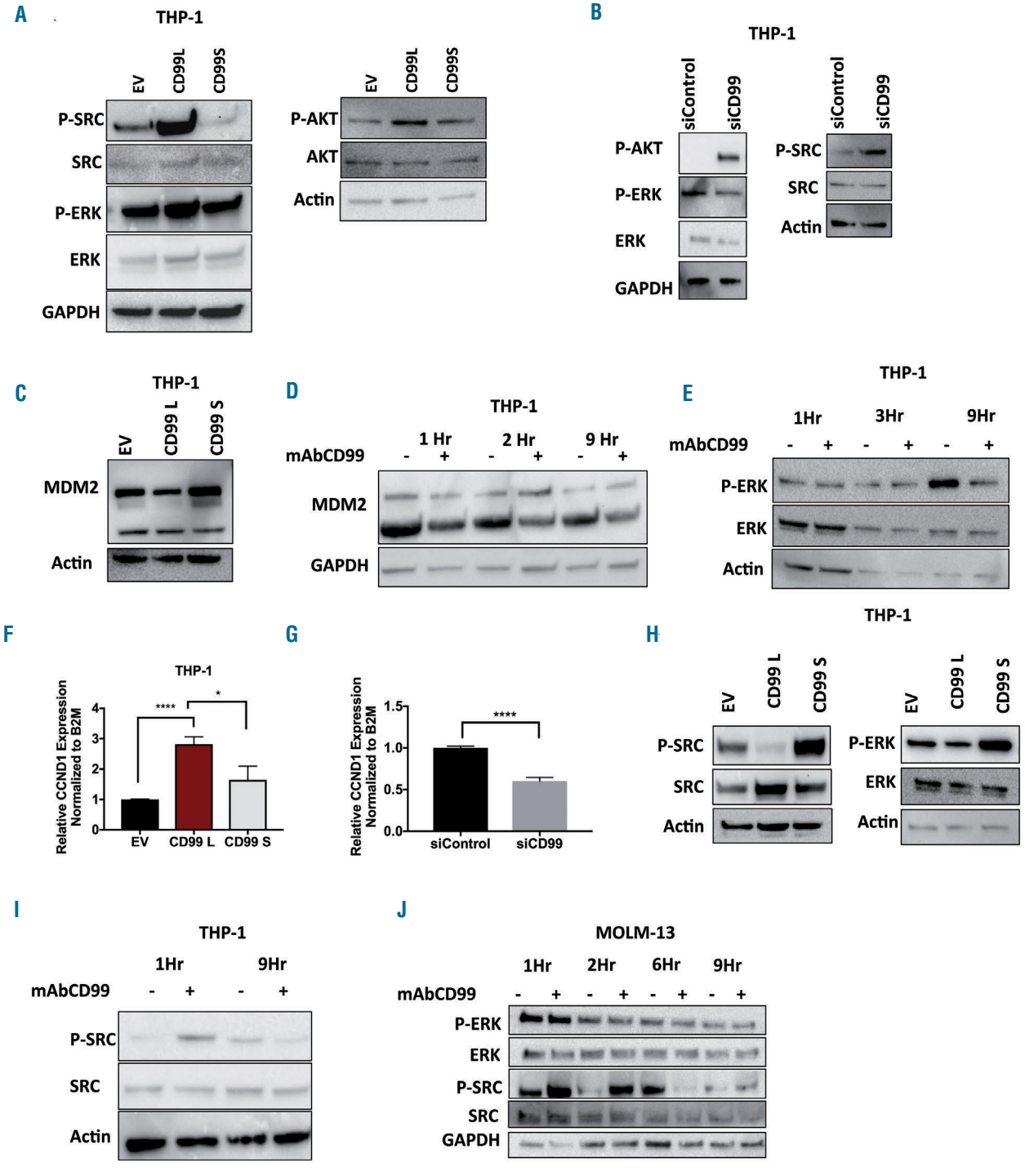

Figure 8. Effect of CD99 on ERK and SRC signaling pathways in acute myeloid leukemia (AML) cells. (A) Western blot analysis of SRC and ERK signaling pathways in THP-1 cells transduced with EV, *CD99*-L, and *CD99*-S lenti-virus for 72 hours (h). (B) Western blot analysis of SRC and ERK signaling pathways in THP-1 cells transfected with si*CD99* for 48 h. (C) MDM2 western blot analysis in THP-1 cells transduced with EV, *CD99*-L, and *CD99*-S lentivirus. (D) MDM2 analysis performed by western blot in THP-1 cells treated with mAbCD99 for 1, 2, and 9 h. (E) ERK signaling pathway analyzed in THP-1 cells treated with mAbCD99 for 1, 3, and 9 h. (F) Cyclin D1 mRNA expression measured by taqman assay in THP-1 cells transduced with EV, *CD99*-L and <*CD99*-S lentivirus. (G) CCND1 mRNA expression measured by taqman assay in THP-1 cells transfected with si*CD99*. (H) Western blot analysis of SRC and ERK signaling pathways in THP-1 stable cells transduced with EV, *CD99*-L and *CD99*-S lentivirus. (I) SRC signaling pathway analyzed in THP-1 cells treated with mAbCD99 for 1 and 9 h. (J) ERK and SRC signaling pathway analyzed in MOLM-13 cells treated with mAbCD99 for 1, 2, 6, and 9 h. (****P<0.0001; *P<0.05).

fold, *P*=0.03), and AML-7 (0.36-fold, *P*=0.01) (Figure 7B). Treatment with mAbCD99 (5 μg/mL) caused a 50% decrease in cell viability at 48 h in THP-1 and MOLM-13 cells but not in healthy donor PBMC (*P*<0.0001 and *P*<0.001, respectively) (Figure 7C). The decrease in viability was accompanied by an increase in Annexin-V apoptosis stain in THP-1 (7.35-fold, *P*=0.04) (Figure 7D and E). Four hours after treatment with mAbCD99 (5 μg/mL) we found an approximately 70% decrease in cell migration in both THP-1 and MOLM-13 cells (*P*=0.01 and *P*=0.004, respectively) (Figure 7F and G). Treatment of THP-1 cells with mAbCD99 triggered an increase in $CD11b^+$ population, indicative of myeloid differentiation (2.79-fold, *P*=0.04) (Figure 7H). Consistently, Wright-Giemsa stain revealed that mAbCD99 (2.5 μg/mL) induced differentiation with morphology resembling more mature cell fates (Figure 7I).

CD99 modulates ERK and SRC signaling pathways in acute myeloid leukemia cells

Because the initial enhanced proliferation of CD99-L expressing cells was serum stimulated and transient, we speculated that growth factor-induced signaling pathways are affected by CD99. In EWS and osteosarcoma, CD99 was found to modulate ERK pathways.[35,36] Thus, we examined the effect of ectopic expression of CD99 isoforms on AKT and ERK kinase activity. We also assessed changes in SRC signaling, previously shown to be affected by CD99.[17,37] CD99-L induces transient upregulation of P-ERK, P-AKT and P-SRC compared with CD99-S and EV expressing cells (Figure 8A and *Online Supplementary Figure S13*) measured 72 h post viral transduction. CD99 knockdown (against both S and L) decreased P-ERK but increased P-AKT and P-SRC (THP-1 cells express mainly CD99-S isoform) (Figure 8B). In EWS, treatment with CD99-antibody induced cell death *via* rapid decrease of MDM2 and activation of IGF-1R and ERK signaling.[35,36] Thus, we asked whether MDM2 is affected by CD99 expression. CD99-L cells exhibit lower MDM2 protein levels compared with CD99-S and EV cells (Figure 8C). In addition, MDM2 is reduced in cells treated with CD99mAb 2-9 h post treatment (Figure 8D), yet P-ERK was not changed (Figure 8E and J). Because MDM2 is known to ubiquitinate IGF-1R, we speculated that CD99-induced reduction in MDM2 may up-regulate IGF-1R downstream target genes such as Cyclin D1.[38] *CCND1* mRNA levels in CD99-L cells were higher than that in CD99-S (1.75-fold, *P*=0.02) or EV (2.8-fold, *P*<0.0001) (Figure 8F). CD99 knockdown also decreased *CCND1* mRNA (*P*<0.0001) (Figure 8G). We also examined P-ERK and P-SRC in stable cells maintained in culture for >2 weeks (Figure 8H). Contrary to the early effect, we found a dramatic decrease in P-SRC in CD99-L cells. Similarly, cells treated with anti-CD99mAb showed a rapid increase in P-SRC observed within 1-2 h followed by a decrease in P-SRC observed 3-9 h post treatment (Figure 8I and J).

Discussion

CD99 upregulation has been implicated in several malignancies and is mostly known for its role in EWS.[6,39] Chung *et al.* have recently shown that $CD99^+$ cells expressed an antigenic profile that enriches leukemia stem cells in the majority of human AML. They also demonstrated anti-leukemia activity of the CD99-antibody both in cellular and murine models.[17] Because AML is a heterogeneous disease, it is essential to identify patients with high *CD99* expression that may benefit from treatments aimed to target this gene. Our analysis revealed an association between *CD99* overexpression and the presence of *FLT3*-ITD. A previous study has shown that CD123/CD99/$CD25^{(+)}$ cells in a $CD34^+$ cell fraction predict *FLT3*-ITD mutations.[40] Patients with *FLT3*-ITD have a dismal clinical outcome. Whether targeting CD99 in this patient population provides a therapeutic advantage remains to be investigated. Despite its upregulation in AML, high *CD99* was associated with better outcome. Yet this association was only observed in CA-AML and was not significant in multivariate survival analysis. The inverse correlation between high *CD99* and *P53* mutations is likely driving its association with better clinical outcome as *P53* mutations are most common in complex karyotype patients and associated with inferior outcome.[41]

CD99 is expressed as short and long isoforms with tissue-specific differential expression. However, the different roles of CD99 isoforms in normal and malignant tissues is only supported by limited research. Considering the increased interest in CD99 as a therapeutic target in AML, investigating the roles of its isoforms in preclinical studies is essential.[18] RNA sequencing data of patients' samples revealed that transcripts coding for CD99-S and L isoforms are both expressed in AML. We further observed varying levels of CD99 isoform protein expression in HD PBMC and AML cell lines. However, the ability of western blot to compare isoform levels is limited by the antibodies that are generated against different epitopes. Furthermore, CD99 is highly glycosylated, which also affects the size of the protein band. Due to the limited number of cells in our experiments, we were unable to distinguish CD99 isoform protein expression in primary AML blasts.

The two isoforms have distinct, and maybe opposite, functions in malignancies. Studies of the ectopic expression of CD99-L isoform supported an oncosuppressor function in osteosarcoma.[42] Overexpression of CD99-S isoform, however, resulted in decreased cell aggregation and increased cell migration in osteosarcoma and prostate cancer cells.[42] In EWS, CD99-S inhibited cell differentiation and contributed to the maintenance of stemness.[43] Downregulation of CD99-L transformed B lymphocytes to Hodgkin and Reed-Sternberg phenotype.[44] Our data suggest that CD99-L cells are more responsive to serum stimuli with increased DNA synthesis and cell growth; however, over time, these cells accumulate higher ROS and DNA damage, resulting in apoptosis. We speculate that CD99 homotypic interaction is likely driving the later reduction of cell viability in CD99-L cells. While this phenomenon resembles oncogene-induced senescence,[45] only a slight increase in P16 was observed in CD99-L cells (*data not shown*).

CD99-L consistently delayed disease progression in AML murine models. Whether CD99 interaction with the murine microenvironment inhibits cell homing to the BM is unclear. Yet we observed no change in CXCR4 and CD49d (VLA-4a) on the surface of CD99-L cells (*data not shown*). Mechanistically, CD99-L induced P-SRC and P-ERK is likely driving the initial increase in cell growth. A CD99-derived agonist peptide that specifically interacts with conserved motifs in the CD99 extracellular domain was previously found to inhibit fibronectin-mediated β1

integrin activation through the SHP2/ERK/PTPN12/FAK signaling pathway;[37] they also found that ERK is essential for CD99 homotypic aggregation.[46] CD99 homotypic interactions driving a negative feedback loop or *via* its subsequent binding with caveolin may explain the later inhibition of ERK and SRC.[42] CD99 was found to drive terminal differentiation of osteosarcoma cells *via* activation of membrane-bound/cytoplasmic ERK rather than affecting its nuclear localization.[47] Yet, in EWS, CD99 knockdown led to prolonged nuclear phosphorylation of ERK1/2 and neural differentiation.[48] In addition, CD99mAb was shown to act as an agonist, and reported similar phenotypes to those observed in our study.[46,49] Both CD99-L ectopic expression and CD99mAb induced similar cellular effects, and, likewise, modulated P-SRC. However, further biochemical studies are required to establish whether CD99mAb acts as an agonist for CD99 long isoform.

In summary, our results present unique insights into the clinical, functional, and mechanistic roles of CD99 isoforms in AML. The mechanisms by which *CD99* is upregulated and those that govern its function in leukemia initiation remain to be investigated.

Acknowledgments

We would like to thank the Bioinformatics core at the Norris Medical Library, University of Southern California and TCGA. This work was supported by grant UL1TR001855 from the National Center for Advancing Translational Science (NCATS) of the US National Institutes of Health, the Southern California Clinical, Translational Science Institute KL-2 funding (KL2TR001854) and the Ming Hsieh Institute Funding. AMNB is funded by the BMBF grant 01ZZ1804B (DIFUTURE). KM is supported by the German Research Foundation (DFG SFB 1243). TH is supported by the Wilhelm Sander Foundation (2013.086.2) and by the Physician Scientists Grant (G-509200-004) from the Helmholtz Zentrum München.

References

1. Lowenberg B. Acute myeloid leukemia: the challenge of capturing disease variety. Hematology Am Soc Hematol Educ Program. 2008:1-11.
2. Gelin C, Aubrit F, Phalipon A, et al. The E2 antigen, a 32 kd glycoprotein involved in T-cell adhesion processes, is the MIC2 gene product. Embo J. 1989;8(11):3253-3259.
3. Dworzak MN, Fritsch G, Buchinger P, et al. Flow cytometric assessment of human MIC2 expression in bone marrow, thymus, and peripheral blood. Blood. 1994;83(2):415-425.
4. Schenkel AR, Mamdouh Z, Chen X, et al. CD99 plays a major role in the migration of monocytes through endothelial junctions. Nat Immunol. 2002;3(2):143-150.
5. Sullivan DP, Watson RL, Muller WA. 4D intravital microscopy uncovers critical strain differences for the roles of PECAM and CD99 in leukocyte diapedesis. Am J Physiol Heart Circ Physiol. 2016;311(3):H621- H632.
6. Ambros IM, Ambros PF, Strehl S, et al. MIC2 is a specific marker for Ewing's sarcoma and peripheral primitive neuroectodermal tumors. Evidence for a common histogenesis of Ewing's sarcoma and peripheral primitive neuroectodermal tumors from MIC2 expression and specific chromosome aberration. Cancer. 1991;67(7):1886-1893.
7. Seol HJ, Chang JH, Yamamoto J, et al. Overexpression of CD99 Increases the Migration and Invasiveness of Human Malignant Glioma Cells. Genes Cancer. 2012;3(9-10):535-549.
8. Pelmus M, Guillou L, Hostein I, et al. Monophasic fibrous and poorly differentiated synovial sarcoma: immunohistochemical reassessment of 60 t(X;18)(SYT-SSX)-positive cases. Am J Surg Pathol. 2002;26(11): 1434-1440.
9. Hartel PH, Jackson J, Ducatman BS, Zhang P. CD99 immunoreactivity in atypical fibroxanthoma and pleomorphic malignant fibrous histiocytoma: a useful diagnostic marker. J Cutan Pathol. 2006;33 Suppl 2:24-28.
10. Dworzak MN, Fritsch G, Fleischer C, et al. CD99 (MIC2) expression in paediatric B-lineage leukaemia/lymphoma reflects maturation-associated patterns of normal B-lymphopoiesis. Br J Haematol. 1999;105(3):690-695.
11. Sung CO, Ko YH, Park S, Kim K, Kim W. Immunoreactivity of CD99 in non-Hodgkin's lymphoma: unexpected frequent expression in ALK-positive anaplastic large cell lymphoma. J Korean Med Sci. 2005;20(6):952-956.
12. Buxton D, Bacchi CE, Gualco G, et al. Frequent expression of CD99 in anaplastic large cell lymphoma: a clinicopathologic and immunohistochemical study of 160 cases. Am J Clin Pathol. 2009;131(4):574-579.
13. Jung KC, Park WS, Bae YM, et al. Immunoreactivity of CD99 in stomach cancer. J Korean Med Sci, 2002:483-489.
14. Yoo SH, Han J, Kim TJ, Chung DH. Expression of CD99 in Pleomorphic Carcinomas of the Lung. J Korean Med Sci. 2005;20(1):50-55.
15. Ventura S, Aryee DNT, Felicetti F, et al. CD99 regulates neural differentiation of Ewing sarcoma cells through miR-34a-Notch-mediated control of NF-l[kappa]lB signaling. Oncogene. 2015;35(30):3944-3954.
16. Zhang PJ, Barcos M, Stewart CC, et al. Immunoreactivity of MIC2 (CD99) in acute myelogenous leukemia and related diseases. Mod Pathol. 2000(4):452-458.
17. Chung SS, Eng WS, Hu W, et al. CD99 is a therapeutic target on disease stem cells in myeloid malignancies. Sci Transl Med. 2017;9(374).
18. Pasello M, Manara MC, Scotlandi K. CD99 at the crossroads of physiology and pathology. J Cell Commun Signal. 2018;12(1):55-68.
19. Gao J, Aksoy BA, Dogrusoz U, et al. Integrative analysis of complex cancer genomics and clinical profiles using the cBioPortal. Sci Signal. 2013;6(269):pl1.
20. Ley TJ, Miller C, Ding L, et al. Genomic and epigenomic landscapes of adult de novo acute myeloid leukemia. N Engl J Med. 2013;368(22):2059-2074.
21. Andersson A, Ritz C, Lindgren D, et al. Microarray-based classification of a consecutive series of 121 childhood acute leukemias: prediction of leukemic and genetic subtype as well as of minimal residual disease status. Leukemia. 2007;21 (6):1198-1203.
22. Haferlach T, Kohlmann A, Wieczorek L, et al. Clinical utility of microarray-based gene expression profiling in the diagnosis and subclassification of leukemia: report from the International Microarray Innovations in Leukemia Study Group. J Clin Oncol. 2010;28(15):2529-2537.
23. Valk PJ, Verhaak RG, Beijen MA, et al. Prognostically useful gene-expression profiles in acute myeloid leukemia. N Engl J Med. 2004;350(16):1617-1628.
24. Klein HU, Ruckert C, Kohlmann A, et al. Quantitative comparison of microarray experiments with published leukemia related gene expression signatures. BMC Bioinformatics. 2009;10:422
25. Barnes M, Freudenberg J, Thompson S, Aronow B, Pavlidis P. Experimental comparison and cross-validation of the Affymetrix and Illumina gene expression analysis platforms. Nucleic Acids Res. 2005;33(18):5914-5923.
26. Bullinger L, Dohner K, Bair E, et al. Use of gene-expression profiling to identify prognostic subclasses in adult acute myeloid leukemia. N Engl J Med. 2004;350(16):1605-1616.
27. Metzeler KH, Hummel M, Bloomfield CD, et al. An 86-probe-set gene-expression signature predicts survival in cytogenetically normal acute myeloid leukemia. Blood. 2008;112(10):4193-4201.
28. Balgobind BV, Van den Heuvel-Eibrink MM, De Menezes RX, et al. Evaluation of gene expression signatures predictive of cytogenetic and molecular subtypes of pediatric acute myeloid leukemia. Haematologica. 2011;96(2):221-230.
29. Han L, Qiu P, Zeng Z, et al. Single-cell mass cytometry reveals intracellular survival/proliferative signaling in FLT3-ITD-mutated AML stem/progenitor cells. Cytometry A. 2015;87(4):346-356.
30. Bonardi F, Fusetti F, Deelen P, van Gosliga D, Vellenga E, Schuringa JJ. A proteomics and transcriptomics approach to identify leukemic stem cell (LSC) markers. Mol Cell Proteomics. 2013;12(3):626-637.
31. Kikushige Y, Shima T, Takayanagi S, et al. TIM-3 is a promising target to selectively kill

acute myeloid leukemia stem cells. Cell Stem Cell. 2010;7(6):708-717.
32. Bernard G, Zoccola D, Deckert M, et al. The E2 molecule (CD99) specifically triggers homotypic aggregation of CD4+ CD8+ thymocytes. J Immunol. 1995;154(1):26-32.
33. Cerisano V, Aalto Y, Perdichizzi S, et al. Molecular mechanisms of CD99-induced caspase-independent cell death and cell-cell adhesion in Ewing's sarcoma cells: actin and zyxin as key intracellular mediators. Oncogene. 2004;23(33):5664-5674.
34. Byun HJ, Hong IK, Kim E, et al. A splice variant of CD99 increases motility and MMP-9 expression of human breast cancer cells through the AKT-, ERK-, and JNK-dependent AP-1 activation signaling pathways. J Biol Chem. 2006;281(46):34833-34847.
35. Manara MC, Terracciano M, Mancarella C, et al. CD99 triggering induces methuosis of Ewing sarcoma cells through IGF-1R/RAS/Rac1 signaling. Oncotarget. 2016;7 (48):79925-79942.
36. Guerzoni C, Fiori V, Terracciano M, et al. CD99 triggering in Ewing sarcoma delivers a lethal signal through p53 pathway reactivation and cooperates with doxorubicin. Clin Cancer Res. 2015;21(1):146-156.
37. Lee KJ, Kim Y, Yoo YH, et al. CD99-Derived Agonist Ligands Inhibit Fibronectin-Induced Activation of beta1 Integrin through the Protein Kinase A/SHP2/Extracellular Signal-Regulated Kinase/PTPN12/Focal Adhesion Kinase Signaling Pathway. Mol Cell Biol. 2017;37(14).
38. Warsito D, Sjostrom S, Andersson S, Larsson O, Sehat B. Nuclear IGF1R is a transcriptional co-activator of LEF1/TCF. EMBO Rep. 2012;13(3):244-250.
39. Kavalar R, Pohar Marinsek Z, Jereb B, Cagran B, Golouh R. Prognostic value of immunohistochemistry in the Ewing's sarcoma family of tumors. Med Sci Monit. 2009;15(8):CR442-452.
40. Angelini DF, Ottone T, Guerrera G, et al. A Leukemia-Associated CD34/CD123/CD25/CD99+ Immunophenotype Identifies FLT3-Mutated Clones in Acute Myeloid Leukemia. Clin Cancer Res. 2015;21(17): 3977-3985.
41. Kadia TM, Jain P, Ravandi F, et al. TP53 mutations in newly diagnosed Acute Myeloid Leukemia –Clinico-molecular characteristics, response to therapy, and outcomes. Cancer. 2016;122(22):3484-3491.
42. Scotlandi K, Zuntini M, Manara MC, et al. CD99 isoforms dictate opposite functions in tumour malignancy and metastases by activating or repressing c-Src kinase activity. Oncogene. 2007;26(46):6604-6618.
43. Lee EJ, Lee HG, Park SH, Choi EY. CD99 type II is a determining factor for the differentiation of primitive neuroectodermal cells. Exp Mol Med. 2003;35(5):438-447.
44. Kim SH, Shin YK, Lee IS, et al. Viral latent membrane protein 1 (LMP-1)-induced CD99 down-regulation in B cells leads to the generation of cells with Hodgkin's and Reed-Sternberg phenotype. Blood. 2000;95(1): 294-300.
45. Michaloglou C, Vredeveld LC, Soengas MS, et al. BRAFE600-associated senescence-like cell cycle arrest of human naevi. Nature. 2005;436(7051):720-724.
46. Hahn MJ, Yoon SS, Sohn HW, et al. Differential activation of MAP kinase family members triggered by CD99 engagement. FEBS Lett. 2000;470(3):350-354
47. Sciandra M, Marino MT, Manara MC, et al. CD99 drives terminal differentiation of osteosarcoma cells by acting as a spatial regulator of ERK 1/2. J Bone Miner Res. 2014;29(5):1295-1309.
48. Rocchi A, Manara MC, Sciandra M, et al. CD99 inhibits neural differentiation of human Ewing sarcoma cells and thereby contributes to oncogenesis. J Clin Invest. 2010;120(3):668-680.
49. Lee HJ, Kim E, Jee B, et al. Functional involvement of src and focal adhesion kinase in a CD99 splice variant-induced motility of human breast cancer cells. Exp Mol Med. 2002;34(3):177-183.

ARTICLE

Methotrexate-associated toxicity in children with Down syndrome and acute lymphoblastic leukemia during consolidation therapy with high dose methotrexate according to ALL-BFM treatment regimen

Mirko Kroll,[1] Kirsten Kaupat-Bleckmann,[1] Anja Mörickel,[1] Julia Altenl,[1] Denis M. Schewel,[1] Martin Stanullal,[2] Martin Zimmermann,[2] Martin Schrappe[1] and Gunnar Cario[1]

[1]Department of Pediatrics I, University Hospital Schleswig-Holstein, Kiel and [2]Department of Pediatric Hematology and Oncology, Hannover Medical School, Hannover, Germany

Ferrata Storti Foundation

Haematologica 2020
Volume 105(4):1013-1020

ABSTRACT

Children with Down syndrome (DS) and acute lymphoblastic leukemia (ALL) often suffer from severe toxicities during treatment, especially with high-dose methotrexate (HD-MTX). Systematic data on methotrexate (MTX) toxicity in these patients are rare. We analyzed seven MTX-associated toxicities during consolidation therapy in 103 DS- and 1,109 non-DS-patients (NDS) with ALL (NDS-ALL) enrolled in ALL-Berlin–Frankfurt–Münster (ALL-BFM) trials between 1995–2016 and 1995–2007, respectively. Patients received four courses MTX (5 g/m^2 each) plus intrathecal MTX and 6-mercaptopurine (6-MP). From 2004 onwards, a dose of 0.5 g/m^2 in the first MTX course has been recommended for DS-patients. DS-patients showed higher rates of grade 3/4 toxicities after the first course with 5 g/m^2 MTX compared to NDS-patients (grade 3/4 toxicities 62 in 45 DS-patients *vs.* 516 in 1,089 NDS-patients, P<0.001). The dose reduction (0.5 g/m^2) in DS-patients has reduced toxicity (39 in 51 patients, P<0.001) without increasing the relapse risk (reduced dose, 5-year cumulative relapse incidence = 0.09±0.04 *vs.* high dose, 0.10±0.05, P=0.51). MTX dose escalation to 1.0 g/m^2 for DS-patients who tolerated 0.5 g/m^2 (n= 28 of 51 patients) did not result in an increased rate of grade 3/4 toxicities after the second course (P=0.285). Differences in MTX plasma levels at 42 and 48 hours after the start of the first methotrexate infusion did not explain higher toxicity rates in DS-patients treated with 0.5 g/m^2 compared to NDS-patients treated with 5 g/m^2. Within the DS cohort a higher MTX plasma level was associated with increased toxicity. In conclusion, dose reduction in the first MTX course reduced severe toxicities without increasing the risk of relapse. (*ClinicalTrials.gov identifier: NTC00430118, NCT01117441*).

Introduction

Children and adolescents with Down syndrome (DS) DS have an approximately 10-fold higher risk of acquiring acute lymphoblastic leukemia (ALL)[1] and have shown an inferior outcome compared to children with NDS-ALL.[2-5] The worse outcome for DS-ALL has been attributed to a higher risk of relapse as well as higher levels of chemotherapy-associated toxicities and treatment-related mortality.[2,6-8] Severe toxicities may eventually lead to chemotherapy dose reduction which in turn might increase the risk of relapse.[2,5,6]

Methotrexate (MTX is a folate antagonist that interferes with the *de novo* synthesis of nucleotides in proliferating cells and plays a crucial role in the treatment of pediatric ALL in which MTX is administered in high doses (HD-MTX, ≥ 0.5 g/m^2 per intravenous [*i.v.*] application).[9] Many patients with DS-ALL suffer from severe side effects after receiving HD-MTX. Common MTX-associated side effects in DS-ALL are severe mucositis and stomatitis, infections, bone marrow suppression, hepato-, nephro- and neurotoxicity.[2,6-8]

In order to extend our knowledge on MTX-associated toxicities in DS-ALL, we

Correspondence:

GUNNAR CARIO
gunnar.cario@uksh.de

Received: April 15, 2019.

Accepted: July 24, 2019.

Pre-published: August 1, 2019.

doi:10.3324/haematol.2019.224774

Check the online version for the most updated information on this article, online supplements, and information on authorship & disclosures: www.haematologica.org/content/105/4/1013

analyzed clinical data from DS-ALL and NDS-ALL patients who were treated according to ALL-BFM protocols in Germany and Switzerland (ALL-BFM 1995, ALL-BFM 2000 and AIEOP-BFM ALL 2009). We focused on toxicities occurring after HD-MTX administrations during the consolidation element Protocol M in which patients receive four courses of *i.v.* HD-MTX (5 g/m^2 each, 24-hour infusion).

Additionally, we investigated the influence of the rs1051266 80G>A polymorphism of the chromosome 21-encoded folate carrier *SLC19A1 (RFC1)* on MTX toxicity in DS-ALL. *SLC19A1* functions as the main transporter for MTX into cells. Therefore rs1051266 may alter the transportation rate of MTX into cells and thus may affect the severity of toxicities.[10-12]

Methods

Patients

A total of 1,212 patients were selected from three consecutive multicenter ALL-BFM trials (ALL-BFM 95, ALL-BFM 2000 and AIEOP-BFM ALL 2009; diagnosed between January 13, 1996 and September 6, 2016 for DS-ALL and between April 11, 1995 and May 4, 2007 for NDS-ALL patients) according to the following inclusion criteria: age at diagnosis between ≥ 1 year and ≤ 18 years, no initial high risk (HR) features, consolidation treatment with HD-MTX (Protocol M) and availability of treatment and toxicity data. Detailed information on the different recruitment periods and treatment stratification is given in the *Online Supplementary Materials and Methods*. Informed consent from the patients and/or guardians was obtained and the studies were approved by the responsible ethical committees.

Consolidation Protocol M is an 8-week therapy element given to non-HR patients only. Patients receive four courses of *i.v.* HD-MTX (5 g/m^2 each, 24-hour infusion) every second week in addition to an age-adapted intrathecal MTX and daily oral 6-MP (25 mg/m^2 /day). MTX plasma levels were measured at various time points after the start of each MTX infusion and each HD-MTX course was followed by an *i.v.* leucovorine (LCV) rescue (15 mg/m^2) at 42, 48 and 54 hours after the start of the MTX infusion (for details on Protocol M see the *Online Supplementary Material and Methods*).[13] Patients who qualified for the HR group only after the start of Protocol M and who were therefore allocated to the HR treatment arm of the respective study were included in the toxicity analysis for the HD-MTX courses they had received (usually only the first course) but not for outcome analysis.

As of 2004, the study group recommended to administer the first HD-MTX course with a reduced dose of 0.5 g/m^2 in order to reduce severe toxicities in DS-ALL patients. A subsequent increase of MTX dosages could be performed if no severe toxicity had occurred. After each HD-MTX course, toxicity grading was performed for leukopenia, thrombocytopenia, infections, stomatitis, hepatotoxicity, nephrotoxicity and bilirubinemia according to the Common Terminology Criteria for Adverse Events (CTCAE) version 2.0 (for details see the *Online Supplementary Materials and Methods and Online Supplementary Table S1*). In some patients reporting was incomplete covering only some of the seven toxicities.

Statistical analysis

Statistical analysis included χ^2-, Fisher's exact, Mann-Whitney-U and McNemar tests as indicated in the figure legends and tables. The 5-year-cumulative incidence risk of relapse was calculated according to Kalbfleisch and Prentice and compared using the Gray's test. Analyses were done using IBM SPSS 22 and SAS 9.4. A *P*-value ≤ 0.05 was considered to be statistically significant.

DNA and allelic discrimination assay

Information on patient DNA preparation and SLC19A1 rs1051266 80G>A genotyping can be found in the *Online Supplementary Materials and Methods*.

Results

Patients, treatment discontinuation and MTX dosages

1,212 patients were included in this study, 103 DS-ALL and 1,109 NDS-ALL. The comparison of both groups showed no significant differences in the median age at diagnosis, sex distribution, and white blood cell counts at diagnosis (Table 1). None of the DS patients had T-cell ALL in contrast to 12.4% of the NDS-ALL group (*P*=0.006) and a hyperdiploid karyotype was less frequent in DS-ALL compared to NDS-ALL patients (*P*=0.002). Furthermore, NDS-ALL had more *ETV6-RUNX1* rearrangements compared to DS-ALL patients (*P*<0.001) (Table 1).

Of the 103 DS-ALL patients who started HD-MTX consolidation 95 patients (92.2%) completed the protocol. Seven DS-ALL patients discontinued consolidation treatment at various time points due to a switch to HR treatment (n= 4) or severe infections (n= 2). Analysis could not be performed in one patient with DS-ALL for the fourth HD-MTX course due to incomplete toxicity data. One DS-ALL patient died after the second course from septic shock in neutropenia after receiving 5 g/m^2 MTX doses in the first and second course. In contrast, 1,083 of 1,109 NDS-ALL patients (97.7%) completed consolidation. Consolidation discontinuation in 26 NDS-ALL patients was due to a switch to HR treatment (n=24) or severe toxicities (neurotoxicity, n=1 and severe infection, n=1). Three additional patients could not be analyzed due to incomplete data. None of the NDS-ALL patients died during HD-MTX consolidation (Figure 1).

As of 2004, the ALL-BFM study group recommended for DS-ALL patients to administer a reduced MTX dose of 0.5 g/m^2 in the first HD-MTX course and to subsequently increase the dose if no severe side effects occur. Therefore, 51 of 103 (49.5%) DS-ALL patients received the first HD-MTX course with a dose of 0.5 g/m^2 (±10%) and 45 of 103 (43.7%) received 5 g/m^2 (±10%) in the first course (Table 1). Of note, in some DS-ALL patients a MTX dose of 0.5 g/m^2 was given already before 2004 and some DS-ALL patients still received 5 g/m^2 doses after the 2004 recommendation, (DS-ALL with 0.5 g/m^2 MTX in the first course before 2004, n= 6 of 42 [14.3%] and 5.0 g/m^2 in first course since 2004, n=11 of 61 [18.0%]).

In contrast, 1,089 of 1,109 (98.2%) non-DS-ALL patients received 5 g/m^2 MTX. As expected, the MTX dosages in the course of the consolidation treatment were more heterogeneous in DS-ALL as compared to NDS-ALL (Table 1).

Toxicities after HD-MTX

Initially we focused on toxicities after the first HD-MTX course because latter courses might be more biased by toxicities and MTX dosages from previous HD-MTX courses, especially in those patients for whom the dose has been adopted after the recommendation in 2004. After receiving a MTX dose of 5 g/m^2 patients with DS-ALL showed significantly higher rates of grade 3/4 leukopenia, thrombocytopenia, infections and stomatitis compared to

Table 1. Patient characteristics, methotrexate dosages in the first high-dose methotrexate course and total methotrexate dosage trend during consolidation for Down syndrome and non-Down syndrome acute lymphoblastic leukemia patients.

		DS-ALL (n=103)	NDS-ALL (n=1,109)	*P*
Age at diagnosis	Median	4.8 years	5.9 years	0.564[a]
Range		1.2 – 17.7 years	1.0 – 18.0 years	
Sex	Male	64/103 (62.1%)	599/1,109 (54.0%)	0.113[b]
Female		39/103 (37.9%)	510/1,109 (46.0%)	
WBC at diagnosis	Median	9,850 /μL	10,700 /μL	0.411[a]
Range		870 – 205,000	100 – 686,000	
< 10,000/μL		55/102 (53.9%)	544/1,109 (49.1%)	
10,000 – 49,999/μL		37/102 (36.3%)	364/1,109 (32.8%)	
> 50,000/μL		10/102 (9.8%)	201/1,109 (18.1%)	
B-/T-cell lineage	B-ALL	101/101 (100%)	937/1,070 (87.6%)	<0.001[b]
T-ALL		0/101 (0%)	133/1,070 (12.4%)	
Karyotype	Normal karyotype	28/55 (50.9%)	61/215 (28.4%)	0.002[b]
	Hyperploidy (> 50 chr.)	5/55 (9.1%)	62/215 (28.8%)	0.002[b]
Genetic features	*ETV6-RUNX1*	7/92 (7.6%)	205/810 (25.3%)	<0.001[b]
	BCR-ABL	0/92 (0%)	0/810 (0%)	
MTX dose 1st course	5 g/m² ± 10% (full dose)	45/103 (43.7%)	1,089/1,109 (98.2%)	
	0.551 – 4.499 g/m²	7/103 (6.8%)	20/1,109 (1.8%)	
	0.5 g/m² ± 10% (reduced dose, low dose)	51/103 (49.5%)	0/1,109 (0%)	
MTX dosage trend[c]	started with full dose, full dose continued	25/103 (24.3%)	1,049/1,109 (94.6%)	
	started with full dose, then reduced	14/103 (13.6%)	12/1,109 (1.1%)	
	started with low dose, then escalated	31/103 (30.1%)	0/1,109 (0%)	
	started with low dose, low dose continued	19/103 (18.4%)	0/1,109 (0%)	
	discontinuation due to death	1/103 (1.0%)	0/1,109 (0%)	
	discontinuation due to severe toxicity	2/103 (1.9%)	2/1,109 (0.2%)	
	intermediate dose in all four courses[d,e]	6/103 (5.8%)	19/1,109 (1.7%)	
	switch to high risk treatment[e,f]	4/103 (3.9%)	24/1,109 (2.2%)	
	incomplete data[e,d]	1/103 (1.0%)	3/1,109 (0.3%)	

ALL: acute lymphoblastic leukemia; DS-ALL: Down syndrome ALL; NDS-ALL: non-Down syndrome ALL; chr: chromosomes; y: years; MTX: methotrexate; HD: high dose; n.a.: not applicable; WBC: white blood cell count; [a]Mann-Whitney U test; [b]χ^2 test; [c]overall changes in MTX dosage in the course of consolidation therapy; [d]one DS-ALL patient received three courses with intermediate MTX doses but no information about the last course were available; [e]one NDS-ALL patient was allocated to high risk treatment after receiving three courses of intermediate MTX doses during consolidation; [f]patients that started HD-MTX consolidation but qualified for high risk treatment during Protocol M.

NDS-ALL who received the same dose (leukopenia, DS-ALL n=19 of 44 [43.2%] *vs.* NDS-ALL n=255 of 961 [26.5%], *P*=0.023; thrombocytopenia, 14 of 43 [32.6%] *vs.* 84 of 957 [8.8%], *P*<0.001; infections, 4 of 43 [9.3%] *vs.* 15 of 939 [1.6%], *P*=0.008; stomatitis, 18 of 43 [41.9%] *vs.* 56 of 951 [5.9%], *P*<0.001) (Figure 2A). An initial MTX dose of 0.5 g/m² led to a significantly reduced rate of grade 3/4 leukopenia, thrombocytopenia and stomatitis in DS-ALL compared to DS-ALL who received 5 g/m² (leukopenia, 0.5 g/m² n=11 of 50 [22.0%] *vs.* 5 g/m² n= 19 of 44 [43.2%], *P*=0.045; thrombocytopenia, 7 of 50 [14.0%] *vs.* 14 of 43 [32.6%], *P*=0.046; stomatitis, 9 of 49 [18.4%] *vs.* 18 of 43 [41.9%], *P*=0.021). However, DS-ALL patients treated with a reduced MTX dose still suffered from significantly higher rates of grade 3/4 infections, stomatitis and hepatotoxicity compared to NDS-ALL who received 5 g/m² MTX (infections, DS-ALL n= 3 of 48 [6.3%] *vs.* NDS-ALL n= 15 of 939 [1.6%], *P*=0.05; stomatitis, 9 of 49 [18.4%] *vs.* 56 of 951 [5.9%], *P*=0.003; hepatotoxicity, 9 of 49 [18.4%] *vs.* 59 of 945 [6.2%], *P*=0.004). An increase of MTX after the first dose to a median dose of 1.0 g/m² (range 0.94–2.06 g/m²) in the second course was feasible in 28 of 51 (54.9%) DS-ALL patients who initially received 0.5 g/m² (Figure 2B). Dose escalation did not result in an increased rate of toxicities (11 grade 3/4 toxicities in 28 patients after the first course with 0.5 g/m² MTX *vs.* 16 of 28 patients after the second course with 1.0 g/m² MTX, *P*=0.285).

Further dose escalation in subsequent HD-MTX courses occurred in 15 of these 28 dose escalated patients: 12 patients (23.5% of the initial 51 DS-ALL patients with 0.5 g/m² MTX in the first course) received 5 g/m² from the third course on and three additional patients in the fourth course. In the remaining 13 of the 28 patients, an intermediate MTX dose was either continued throughout the remaining consolidation (n= 10), or was reduced to a low dose in the fourth course (n= 1), or was decreased to an intermediate dose in the fourth course after being increased to 5 g/m² in the third course (n= 1) or the therapy was switched to HR treatment after the second course (n=1). In 4 of 51 patients who were initially treated with 0.5 g/m² MTX in the first course, MTX dose escalation

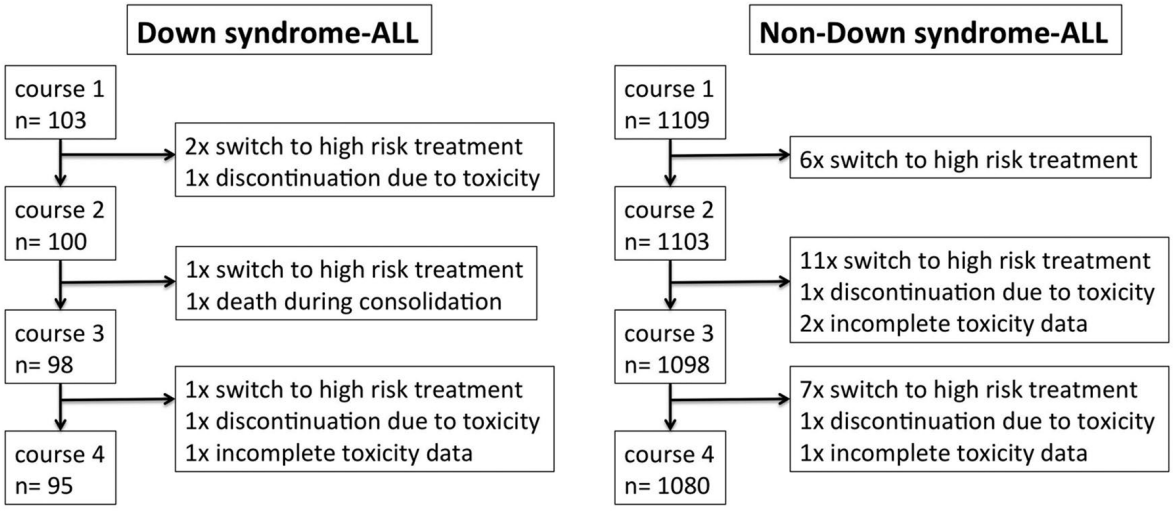

Figure 1. Flow chart showing patient numbers in individual high-dose methotrexate courses including drop outs during high dose methotrexate consolidation.

was performed later in the course of consolidation, i.e. in the third (n=3) or the fourth course (n=1). The remaining 19 of the 51 patients were treated with a 0.5 g/m^2 MTX dose throughout the whole consolidation phase.

Next we analyzed toxicities after the first and the forth HD-MTX course of all the DS-ALL patients who completed consolidation (n=95) (Figure 2C-D). DS-ALL patients showed a significant decrease in the rate of grade 3/4 stomatitis after the last course as compared to the initial course (stomatitis, in the first course n=27 of 93 [29.0%], in the fourth course n=9 of 91 [9.9%], *P*=0.002). In contrast, the number of patients with grade 3/4 leukopenia significantly increased (30 of 94 [31.9%] *vs.* 45 of 89 [50.6%], *P*=0.01). Similarly, NDS-ALL patients showed a decrease in grade 3/4 stomatitis and an increase in grade 3/4 leukopenia during the course of consolidation therapy (stomatitis, 53 of 942 [5.6%] *vs.* 9 of 923 [1.0%], *P*<0.001; leukopenia, 250 of 952 [26.3%] *vs.* 477 of 935 [51.0%], *P*<0.001).

Impact of MTX dose reduction on cumulative incidence of relapses

The 5-year-cumulative incidence risk of relapse (5y-CIR) was compared between DS-ALL patients who received a dose of 0.5 g/m^2 in the first HD-MTX course with those who received 5 g/m^2 (Figure 3A). No significant differences in 5y-CIR were observed (0.5 g/m^2 subgroup n=5 of 50, 5y-CIR±SE=0.09±0.04 *vs.* 5 g/m^2 subgroup n=7 of 41, 5y-CIR=0.10±0.05, *P*=0.51). Next we compared the 5y-CIR of DS-ALL patients who received a 0.5 g/m^2 MTX dose in the first course and increased dosages in subsequent courses with those of patients who were treated with a MTX dose of 0.5 g/m^2 throughout the whole consolidation phase. No significant CIR difference between both groups was observed (0.5 g/m^2 and escalated, 5y-CIR= 0.14±0.07 *vs.* 0.5 g/m^2 and continued, 5y-CIR=0.00±0.00, *P*=0.42) (Figure 3B).

Association of MTX plasma levels and toxicity

To investigate whether differences in MTX plasma levels might explain the high rates of severe toxicities observed in DS-ALL we analyzed MTX plasma levels of all patients at 42 and 48 hours after the start of the initial MTX infusion (Figure 4A-B). At 42 hours median MTX plasma levels in DS-ALL were 0.21 μmol/L (range 0.05–3.40 μmol/L) for 0.5 g/m^2 MTX and 0.90 μmol/L (0.17–4.60) for 5 g/m^2 MTX (*P*<0.001). At 48 hours DS-ALL median plasma levels were 0.16 μmol/L (0.01–1.80) and 0.43 μmol/L (0.22–3.60), respectively (*P*<0.001). For NDS-ALL patients who received a 5 g/m^2 MTX dose median MTX plasma levels were 0.50 μmol/L (0.04–21.60) at 42 hours and 0.31 μmol/L (0.00–10.99) at 48 hours after the start of the first MTX infusion. Thus, at both time points DS-ALL patients showed significantly higher MTX plasma levels after 5 g/m^2 MTX compared to NDS-ALL who received the same dose. DS-ALL patients treated with 0.5 g/m^2 MTX had significantly lower MTX plasma levels compared to DS-ALL treated with 5 g/m^2 MTX and NDS-ALL treated with 5 g/m^2 at both time points (*P*<0.001 for each comparison). To further analyze whether MTX plasma levels may have an impact on toxicity within the DS-ALL cohort we analyzed the occurrence of grade 3/4 toxicities according to MTX plasma level quartiles at 42 and 48 hours (Figure 4C-D). At 42 hours DS-ALL patients with MTX plasma levels within the highest quartile (≥0.905 μmol/L, n=23) suffered from grade 3/4 leukopenia, thrombocytopenia and stomatitis significantly more often compared to patients within the lowest quartile (≤0.200 μmol/L, n=24) (leukopenia, highest quartile n=7 of 22 [31.8%] *vs.* lowest quartile n=1 of 22 [4.6%], *P*=0.046; thrombocytopenia, 7 of 22 [31.8%] *vs.* 0 of 22 [0%], *P*=0.009; stomatitis, 9 of 21 [42.9%] *vs.* 0 of 22 [0%], *P*=0.001). DS-ALL patients with MTX levels within the highest quartile at 48 hours (≥0.470 μmol/L, n=22) showed significantly higher rates of grade 3/4 thrombocytopenia and stomatitis compared to the lowest quartile (≤0.160 μmol/L, n=25) (thrombocytopenia, 9 of 21 [42.9%] *vs.* 1 of 25 [4.0%], *P*=0.003; stomatitis, 10 of 20 [50.0%] *vs.* 2 of 25 [8.0%], *P*=0.002).

SLC19A1 polymorphism rs1051266

The chromosome 21-encoded and ubiquitously

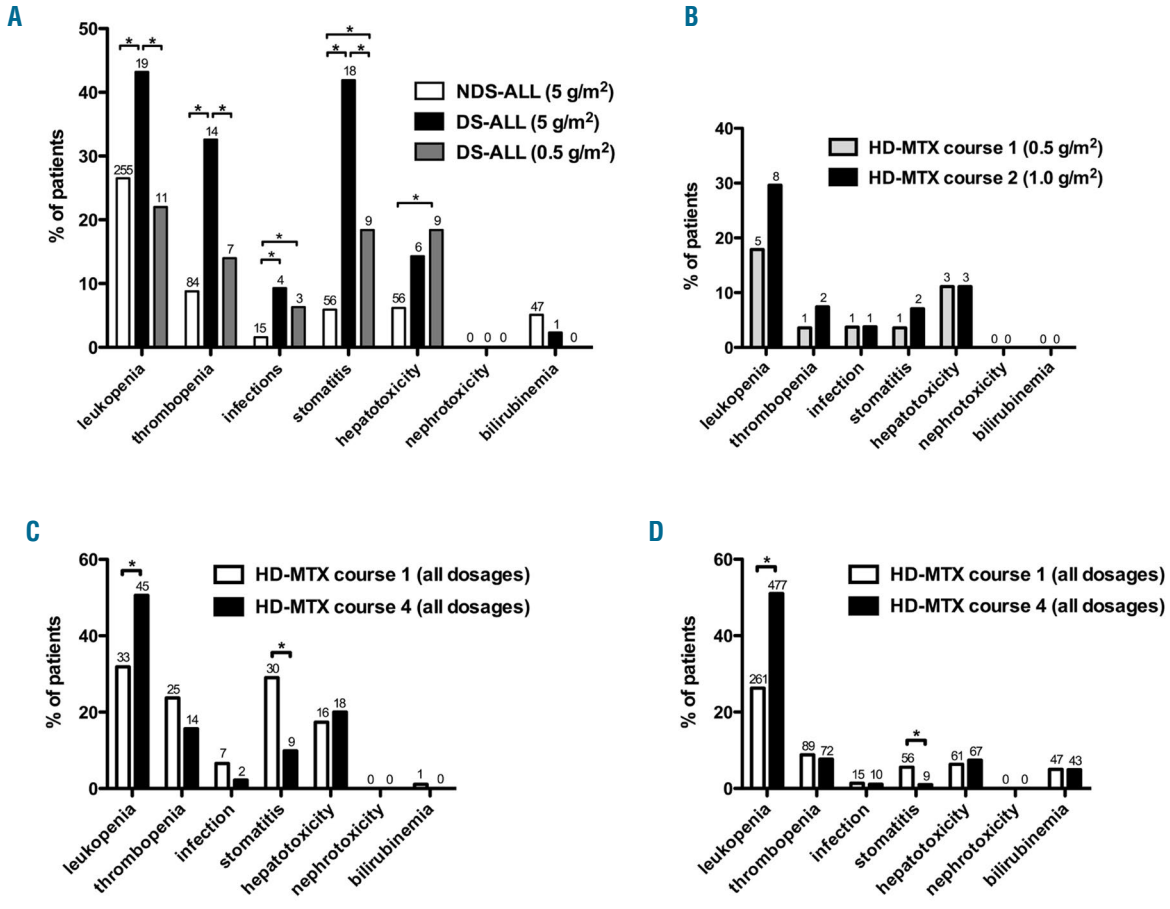

Figure 2. Comparison of toxicities after first high-dose methotrexate (HD-MTX) course in Down syndrome acute lymphoblastic leukemia (DS-ALL) *versus* non-Down syndrome acute lymphoblastic leukemia (NDS-ALL) and comparison of toxicities in DS-ALL after the initial and later HD-MTX courses. (A) Comparison of grade 3/4 toxicities after application of the first HD-MTX course in DS-ALL patients who received 5 g/m² (n=45 of 103) or 0.5 g/m² methotrexate (MTX) (n=51 of 103) and NDS-ALL patients who received 5 g/m² MTX (n=1,089/1,109). **P*≤0.05, Fisher's exact test. (B) Comparison of grade 3/4 toxicities after the first and second HD-MTX course in DS-ALL patients who initially received 0.5 g/m² MTX and were escalated to a median MTX dose of 1.0 g/m² in the second course (n=28 of 51). No significant differences according to McNemar test. (C) and (D) Comparison of grade 3/4 toxicities after the first and last HD-MTX course in all DS-ALL (C) and NDS-ALL patients (D), including patients with intermediate MTX doses. **P*≤0.05 according to McNemar-test. The number on top of each bar represents the number of patients.

expressed folate carrier *SLC19A1 (RFC1)* functions as the main MTX transporter into cells.[10] The single nucleotide polymorphism (SNP) rs1051266 80G>A has been described to affect the transportation rate of the SLC19A1 carrier.[11] To gain further insight into MTX-associated toxicities in DS-ALL patients, we investigated whether rs1051266 allele combinations were associated with higher rates of toxicity in DS-ALL patients. Therefore, we genotyped rs1051266 80G>A in n=95 of 103 DS-ALL patients and compared grade 3/4 toxicities after the initial HD-MTX course between the homozygous allele carriers (i.e. GGG and AAA) (*Online Supplementary Table S2*). After subgrouping according to the administered MTX dose, no statistically significant association between the occurrence of grade 3/4 toxicities and the allele status was observed, except for a significant higher rate of grade 3/4 leukopenia after the first HD-MTX course in GGG allele carriers who received 5 g/m² MTX compared to AAA carriers that received the same dose (GGG n= 8 of 9 [88.9%] *vs.* AAA n= 0 of 5 [0%], *P*=0.003). However, this finding could not be reproduced for subsequent courses. Moreover, no significant correlation between other allele combinations and toxicities as well as allele carrier status and median MTX plasma levels at 42 and 48 h after the start of the initial MTX infusion were observed.

Discussion

In order to increase our knowledge of MTX-associated toxicities in DS-ALL patients after HD-MTX administration, we analyzed treatment and toxicity data of a large DS-ALL cohort uniformly treated according to ALL-BFM protocols. DS-ALL patient characteristics differed slightly from those in published studies,[2,6,14] most likely because only patients who underwent HD-MTX consolidation treatment in the non-HR arm were included.

MTX dosages in DS-ALL were heterogeneous, especially since the release of the 2004 study group recommendations of a MTX starting dose of 0.5 g/m² for the first course which can eventually be increased in the following courses in the absence of severe toxicity. MTX dose heterogeneity and higher levels of MTX-associated toxicities have already been described by us and others.[2,5,8,15,16]

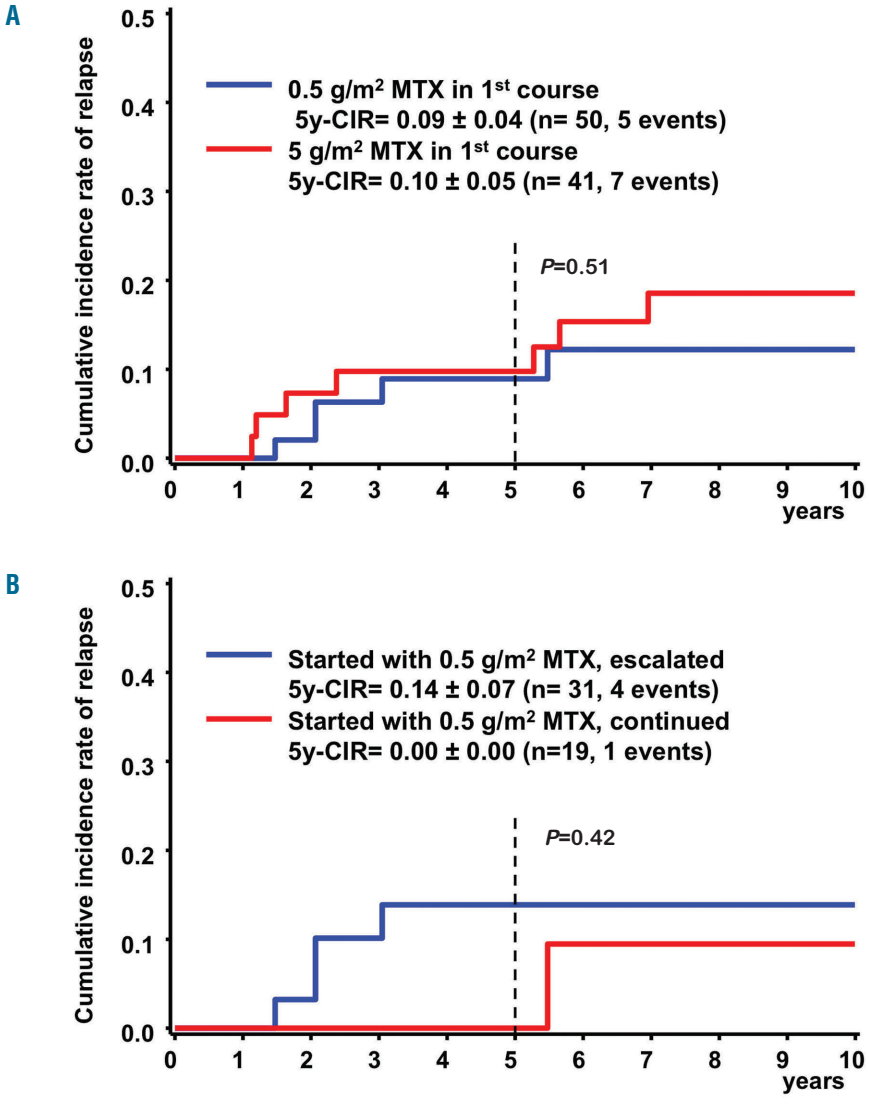

Figure 3. Five-year-cumulative incidence risk of relapse in Down syndrome acute lymphoblastic leukemia. (A) Comparison of the 5-year-cumulative incidence risk (5y-CIR) of Down syndrome acute lymphoblastic leukemia (DS-ALL) patients who received a first high dose methotrexate (HD-MTX) course of 0.5 g/m² (blue) or 5 g/m² MTX (red). No significant differences according to Gray's test. (B) Comparison of the 5y-CIR of DS-ALL who initially received 0.5 g/m² MTX in the first course and were eventually dose escalated in the course of consolidation with DS-ALL who received 0.5 g/m² MTX throughout the whole consolidation therapy. No significant differences were found according to Gray's test.

Together, these findings point to an increased awareness of the higher susceptibility of DS-ALL patients to MTX-related toxicity and the need of MTX dose modifications in recent years.

In DS-ALL patients who received a MTX dose of 5 g/m² in the first course we observed significantly higher rates of grade 3/4 leukopenia, thrombocytopenia, infection and stomatitis compared to NDS-ALL. Similar results in smaller cohorts of heterogeneously treated DS-ALL patients have also been observed by other groups.[5,8,15,16] However, here we showed for the first time that the administration of a low MTX dose of 0.5 g/m² to patients with DS-ALL leads to a significant reduction of grade 3/4 toxicity. Furthermore, the MTX dose could subsequently be escalated to 1.0 g/m² in more than half of the patients without resulting in higher rates of grade 3/4 toxicities after the second course compared to the initial course. These data support the study group's recommendation to increase the MTX dose if no severe toxicity occurrs in the previous course. However, since reduced doses still bear a risk of severe side effects in individual DS-ALL patients, consolidation treatment should be administered cautiously and under close clinical control.

Dose reduction of chemotherapeutic drugs during cancer treatment may raise the concern of impairing long-term outcomes in the affected patients. Here, we did not find any differences in the 5y-CIR in DS-ALL patients who started consolidation with 5 g/m² MTX compared to patients who received 0.5 g/m² MTX. These findings raise the question whether DS-ALL patients require a high MTX dose in consolidation or whether a low dose between 0.5-1.0 g/m² might be sufficient to optimize their outcome by balancing treatment-related complications with relapse rates. While others found impaired outcome of DS-ALL patients who were treated with reduced drug doses,[2,5] two studies described no differences in event free and overall survival between patients with or without dose reductions.[15,16] The authors speculate that modern, more effective ALL therapy and supportive treatment may contribute to an improved outcome in DS patients treated with a reduced dose. Other groups also described a trend towards a better outcome for DS-ALL in recent times.[6,14]

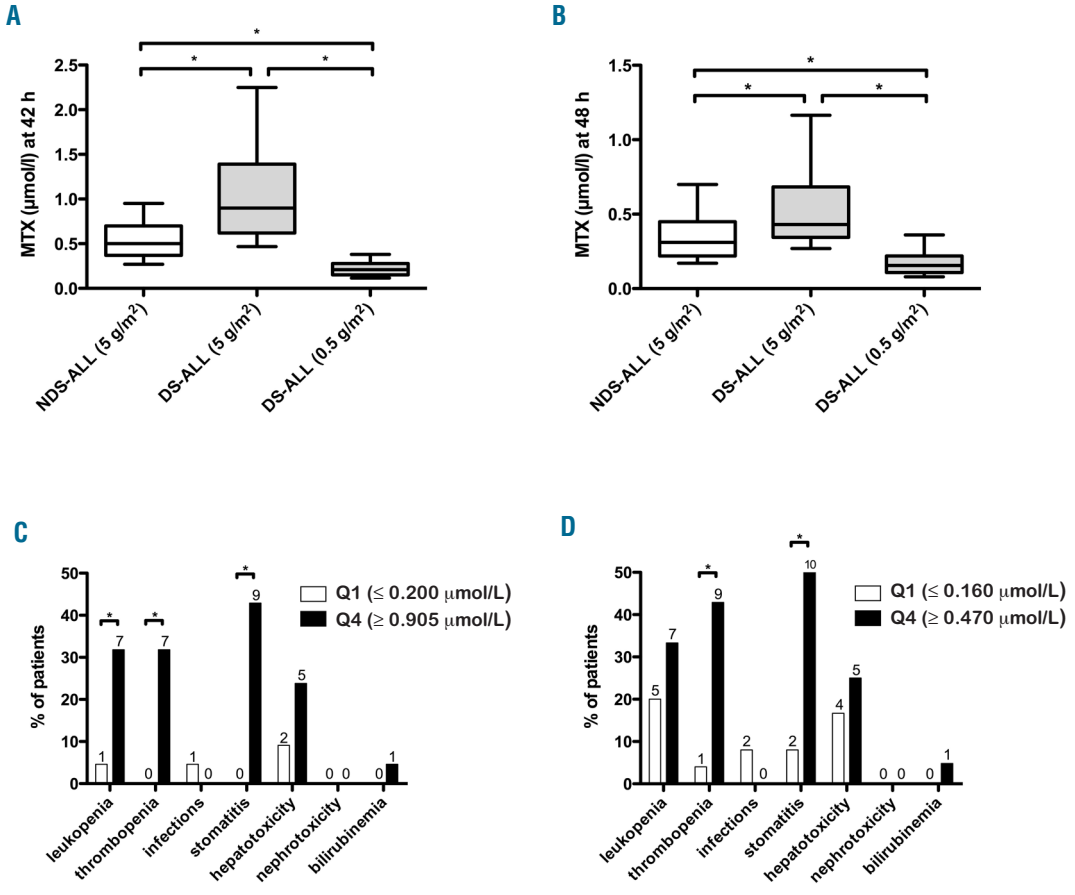

Figure 4. Methotrexate (MTX) plasma levels at 42 and 48 hours after the start of the first high dose MTX course and grade 3/4 toxicities in Down syndrome acute lymphoblastic leukemia according to MTX plasma levels. (A) and B) MTX plasma levels at 42 h (A) and 48 h (B) after start of the first HD-MTX administration. MTX dosage subgroups are indicated. *P≤0.05, Mann-Whitney U test. (C and D) Comparison of grade 3/4 toxicities in DS-ALL according to MTX plasma level quartiles at 42 hours (C) and 48 hours (D) after the start of the first high dose MTX (HD-MTX) administration. Q1: first/lowest quartile; Q4: fourth/highest quartile; respective MTX plasma concentration is given in µmol/L. *P≤0.05, Fisher's exact test. The number on top of each bar represents the number of patients.

Goto *et al*. proposed a lower MTX dose (< 3.0 g/m^2) for DS-ALL patients and possible treatment modifications with novel therapeutics considering the biology of DS-ALL, *e.g.* JAK2 inhibitors in those cases with JAK/STAT pathway activation.[5] In addition, the use of the bispecific antibody blinatumomab might be beneficial to patients with DS-ALL.[17]

Of note, in contrast to published data recently summarized[18] none of the patients included in our study suffered from grade 3/4 nephrotoxicity after the first HD-MTX course. There is no obvious explanation for this difference and we can only speculate that vigorous hydration and alkalization in our patients as described in detail in the protocol was sufficient to prevent MTX crystal precipitation in the kidneys and subsequent impairment of renal function.[19,20] Moreover, cut-offs to define nephrotoxicity might differ between the studies.

Among the DS-ALL cohort we found a MTX plasma level-toxicity correlation as patients with high plasma levels at 42 and 48 hours after the start of the first MTX infusion showed higher rates of grade 3/4 toxicities compared to patients within the lowest MTX plasma level quartile. This observation is consistent with another report showing higher rates of grade 3/4 mucositis in pediatric patients with osteosarcoma that had higher median MTX plasma levels at 48 hours. In addition, MTX plasma levels were higher in DS-ALL compared to NDS-ALL when the same doses were given, which could partially explain the higher toxicity in DS-ALL. In contrast, Buitenkamp *et al*. observed neither higher MTX levels in DS-ALL compared to NDS-ALL nor any association between MTX area under the curve (AUC) and toxicity.[8] The authors applied a case-control study approach and the number of DS-ALL patients was lower than this study. Moreover in this study, MTX AUC and not plasma levels were considered when looking at toxicity, and therefore the results are not directly comparable with ours. However, we agree with the conclusion made by Buitenkamp *et al*. that differences in pharmacodynamics could also significantly contribute to the higher MTX toxicity in DS-ALL patients.[8] This hypothesis is supported by our observation that DS-ALL patients who showed lower MTX plasma levels after 0.5 g/m^2 MTX than NDS-ALL with 5 g/m^2 still experienced higher rates of toxicity after the first HD-MTX course.

Based on our data one might speculate that lower cut offs for forced diuresis and LCV rescue may reduce toxicities in DS-ALL patients. Furthermore, since DS-ALL had higher MTX plasma levels after receiving 5 g/m^2 MTX

compared to NDS-ALL one could further argue that DS-ALL patients do not require MTX doses as high as 5 g/m^2 to get the same plasma levels and subsequent effect with respect to relapse prevention.

In an attempt to shed further light on MTX susceptibility in DS-ALL patients we genotyped the rs1051266 80G>A SNP of the folate and MTX transporter *SLC19A1* on chromosome.[21] The allele frequencies in our DS-ALL cohort are consistent with previous published frequencies in a healthy DS cohort.[22] Since Baslund *et al*. found the A-variant of the transporter to be more effective in taking up fluorescence labeled MTX into lymphocytes of healthy euploide blood donors,[11] we speculated that more MTX might be taken up into cells of DS-ALL patients that are homozygous for the presumably higher active A-variant (AAA) and that this may lead to higher rates of severe MTX-related toxicities compared to patients with the GGG allele combination. Thus, we hypothesized that genotyping of rs1051266 might be a diagnostic tool to predict the severity of toxicities in DS-ALL patients, but we were unable to confirm this hypothesis. However, pharmacokinetics of a single drug or the impact of a single SNP of a transporter in complex chemotherapy regimens may have limited power to explain the differences in effects and side effects. Other SNP in *SLC19A1* and SNP in other genes of transporters or enzymes in the folate/MTX metabolism may also play a role. Therefore, further research including haplotype analysis, investigations of the effect of trisomy 21 on MTX metabolism by using transcriptomics or microarrays and the evaluation of *SLC19A1* expression profile on mRNA and protein level as well as its transportation activity are needed. Moreover, 6-MP co-medication during consolidation should be considered as differences in DS patients with regards to 6-MP metabolism have been described.[23] This might be important in HD-MTX consolidation but also in maintenance therapy, in which both MTX and 6-MP are administered since up to 40% of treatment-related deaths in DS-ALL occur during maintenance therapy.[6,24]

In conclusion, dose reduction in the first HD-MTX course of consolidation therapy led to a decrease of severe MTX-associated toxicities without increasing the risk of relapse for DS-ALL patients.

Funding

The authors would like to thank Deutsche Krebshilfe, Deutsche José Carreras Leukämie-Stiftung (DJCLS), Gesellschaft für Pädiatrische Onkologie und Hämatologie (GPOH), José Carreras-GPOH Promotionsstipendium 03 PSG/2017 for financial support.

References

1. Hasle H, Friedman JM, Olsen JH, Rasmussen SA. Low risk of solid tumors in persons with Down syndrome. Genet Med. 2016;18(11): 1151-1157.
2. Dordelmann M, Schrappe M, Reiter A, et al. Down's syndrome in childhood acute lymphoblastic leukemia: clinical characteristics and treatment outcome in four consecutive BFM trials. Berlin-Frankfurt-Münster Group. Leukemia. 1998;12(5): 645-651.
3. Whitlock JA. Down syndrome and acute lymphoblastic leukaemia. Br J Haematol. 2006;135(5):595-602.
4. Arico M, Ziino O, Valsecchi MG, et al. Acute lymphoblastic leukemia and Down syndrome. Cancer. 2008;113(3):515-521.
5. Goto H, Inukai T, Inoue H, et al. Acute lymphoblastic leukemia and Down syndrome: the collaborative study of the Tokyo Children"s Cancer Study Group and the Kyushu Yamaguchi Children"s Cancer Study Group. Int J Hematol. 2011; 93(2):192-198.
6. Buitenkamp TD, Izraeli S, Zimmermann M, et al. Acute lymphoblastic leukemia in children with Down syndrome: a retrospective analysis from the Ponte di Legno study group. Blood. 2014;123(1):70-77.
7. Taub JW, Ge Y. Down syndrome, drug metabolism and chromosome 21. Pediatr Blood Cancer. 2004;44(1):33-39.
8. Buitenkamp TD, Mathot RAA, de Haas V, Pieters R, Zwaan CM. Methotrexate-induced side effects are not due to differences in pharmacokinetics in children with Down syndrome and acute lymphoblastic leukemia. Haematologica. 2010;95(7): 1106-1113.
9. Schmiegelow K. Advances in individual prediction of methotrexate toxicity: a review. Br J Haematol. 2009;146(5):489-503.
10. Matherly LH, Wilson MR, Hou Z. The major facilitative folate transporters solute carrier 19A1 and solute carrier 46A1: biology and role in antifolate chemotherapy of cancer. Drug Metabolism and Disposition. 2014;42(4):632-649.
11. Baslund B, Gregers J, Nielsen CH. Reduced folate carrier polymorphism determines methotrexate uptake by B cells and CD4+ T cells. Rheumatology. 2007;47(4):451-453.
12. Whetstine JR, Gifford AJ, Witt T, et al. Single nucleotide polymorphisms in the human reduced folate carrier: characterization of a high-frequency G/A variant at position 80 and transport properties of the His(27) and Arg(27) carriers. Clin Cancer Res. 2001;7(11):3416-3422.
13. Radtke S, Zolk O, Renner B, et al. Germline genetic variations in methotrexate candidate genes are associated with pharmacokinetics, toxicity, and outcome in childhood acute lymphoblastic leukemia. Blood. 2013; 121(26):5145-5153.
14. Whitlock JA, Sather HN, Gaynon P, et al. Clinical characteristics and outcome of children with Down syndrome and acute lymphoblastic leukemia: a Children's Cancer Group study. Blood. 2005;106(13):4043-4049.
15. Shah N, Al-Ahmari A, Al-Yamani A, Dupuis L, Stephens D, Hitzler J. Outcome and toxicity of chemotherapy for acute lymphoblastic leukemia in children with down syndrome. Pediatr Blood Cancer. 2009;52(1):14-19.
16. Derouet A, Petit A, Baruchel A, et al. Impact of therapy in a cohort of unselected children with Down Syndrome-associated Acute Lymphoblastic Leukaemia. Br J Haematol. 2016;174(6):983-985.
17. Wadhwa A, Kutny MA, Xavier AC. Blinatumomab activity in a patient with Down syndrome B-precursor acute lymphoblastic leukemia. Pediatr Blood Cancer. 2017;65(2):e26824.
18. Schmiegelow K, Müller K, Mogensen SS, et al. Non-infectious chemotherapy-associated acute toxicities during childhood acute lymphoblastic leukemia therapy. F1000Res. 2017;6:444.
19. Sand TE, Jacobsen S. Effect of urine pH and flow on renal clearance of methotrexate. Eur J Clin Pharmacol. 1981;19(6):453–456.
20. Garneau AP, Riopel J, Isenring P. Acute methotrexate-induced crystal nephropathy. N Engl J Med. 2015; 373(27):2691–2693.
21. Park JA, Shin HY. Influence of genetic polymorphisms in the folate pathway on toxicity after high-dose methotrexate treatment in pediatric osteosarcoma. Blood Res. 2016; 51(1):50-57.
22. Chango A, Willequet F, Fillon-Emery N, Nicolas JP, Bléhaut H. The single nucleotide polymorphism (80G-->A) of reduced folate carrier gene in trisomy 21. Am J Clin Nutr. 2004;80(6):1667-1669.
23. Palle J, Frost BM, Britt-Marie F, et al. Thioguanine pharmacokinetics in induction therapy of children with acute myeloid leukemia. Anti-Cancer Drugs. 2009;20(1):7-14.
24. O'Connor D, Bate J, Wade R, et al. Infection-related mortality in children with acute lymphoblastic leukemia: an analysis of infectious deaths on UKALL2003. Blood. 2014;124(7): 1056-1061.

ARTICLE

EZH2 inhibitors abrogate upregulation of trimethylation of H3K27 by CDK9 inhibitors and potentiate its activity against diffuse large B-cell lymphoma

Shao Xie,[1,2,#] Fan Wei,[1,3,#] Yi-ming Sun,[1] Ying-lei Gao,[1] Lu-lu Pan,[3,4] Min-jia Tan,[4] Shu-dong Wang,[5] Jian Ding[1] and Yi Chen[1]

[1]Division of Anti-Tumor Pharmacology, State Key Laboratory of Drug Research and Institute of Materia Medica, Chinese Academy of Sciences, Shanghai, China; [2]Key Laboratory of Breast Cancer, and Fudan University Shanghai Cancer Center, Fudan University, Shanghai, China; [3]University of Chinese Academy of Sciences, Beijing, China; [4]Chemical Proteomics Center, State Key Laboratory of Drug Research, Shanghai Institute of Materia Medica and Chinese Academy of Sciences, Shanghai, China and [5]Centre for Drug Discovery and Development, School of Pharmacy and Medical Sciences, University of South Australia Cancer Research Institute, Adelaide, Australia

[#]SX and FW are co-first authors.

Ferrata Storti Foundation

Haematologica 2020
Volume 105(4):1021-1031

ABSTRACT

Aberrant expression of CDK9/cyclin T1 has been found in diffuse large B-cell lymphoma (DLBCL), and suggests that CDK9 is a potential therapeutic target for DLBCL. Here, we firstly demonstrated that CDKI-73, a novel cyclin-dependent kinases (CDK) inhibitor, potently blocks CDK9, triggered apoptosis and dramatically repressed DLBCL cell growth owing to CDK9 inhibition. CDK9 inhibitors specifically elevated the trimethylation of H3K27, which we speculate was due to reduced expression of JMJD3/UTX. Considering the important role of the trimethylation of H3K27 in tumor progression, the synergistic effect of the combination therapy of CDK9 inhibitors with EZH2 inhibitors was investigated. EZH2 inhibitors reversed the upregulation of trimethylation of H3K27, and synergistically inhibited DLBCL and other solid tumors growth *in vitro* and *in vivo*. These findings provide a rational basis for the application of CDK9 inhibitors in combination with EZH2 inhibitors in clinical trials.

Introduction

Diffuselarge B-cell lymphoma (DLBCL) is the most common aggressive lymphoma, accounting for 30-40% of all Non-Hodgkin lymphoma incidences.[1] Despite the fact that the median survival time of DLBCL patients is over 8 years, more than 25-30% of the patients relapse,[1] making it necessary to develop more effective therapeutics.

CDK9, together with cyclin T/K, is responsible for the transcription elongation of most protein-coding genes through phosphorylating the RNA polymerase II (RNA Pol II) at the ser2 residual.[2,3] Similar to other lymphoma sub-types, DLBCL has a deregulated cell cycle. These alterations suggest that inhibitors of cyclin-dependent kinases (CDK) might be beneficial for patients affected by DLBCL.[4] Research indicates that CDK9/cyclin T1 is involved in lymphocyte differentiation and activation, and shows an aberrant expression in DLBCL.[5] In addition, MCL1 expression, which can be downregulated by CDK9 inhibition,[6] was found to be overexpressed in a significant fraction of DLBCL,[6,7] contributing to therapy resistance.[8] All these suggest that CDK9 inhibition seems to be a potential therapeutic strategy for the treatment of DLBCL.

Methylation of lysine 27 on histone H3 (H3K27me), a modification associated with gene repression, plays a critical role in regulating the expression of genes that determine the balance between cell differentiation and proliferation.[9] This modifi-

Correspondence:

YI CHEN
ychen@simm.ac.cn

JIAN DING
jding@simm.ac.cn

Received: March 26, 2019.

Accepted: July 5, 2019.

Pre-published: July 9, 2019.

doi:10.3324/haematol.2019.222935

Check the online version for the most updated information on this article, online supplements, and information on authorship & disclosures: www.haematologica.org/content/105/4/1021

cation is generated by the polycomb repressive complex 2 (PRC2), composed of the SET domain-containing histone methyltransferase EZH2, and accessory proteins EED, SUZ12.[10] However, the methylation of H3K27 can be removed by the histone demethylases UTX/KMD6A and JMJD3/KDM6B.[11] Given the critical role of the H3K27me in gene expression, it is not surprising that this chromatin modification plays a role in malignancies, such as lymphoma, breast and esophageal cancer.[12] Accumulating studies imply that H3K27me3 is closely engaged in the development of DLBCL, especially in the germinal center B-cell subtype,[13] reducing H3K27me3 level exhibits significant anti-proliferation activity against DLBCL.[14] Further, highly selective EZH2 inhibitors (EZH2i), such as GSK126, EPZ6438, and CPI-1205 are currently undergoing clinical evaluation against DLBCL, and show clinical efficiency by reducing the level of H3K27me3. However, clinical benefits of EZH2i remain unsatisfactory against other solid tumors.

CDKI-73 (also named LS-007, QHRD107), a novel phase I clinical stage CDK inhibitor in China, mainly targets CDK9 with sub-nanomolar biochemical potency and represses expression of MCL1 in multiple models of cancer, such as chronic lymphocytic leukemia (CLL), ovarian cancer, and acute leukemia.[15-17] CDKI-73 is highly cytotoxic to primary leukemia cells from CLL patients and showed >500-fold selectivity for primary leukemia cells over normal B-lymphocytes,[15] making it an attractive candidate for clinical development. In this study, firstly, we assessed the *in vitro* and *in vivo* activity of CDKI-73 against DLBCL. However, during the research, we found that CDKI-73 significantly elevated H3K27me3 level owing to CDK9 inhibition, accompanied with more pronounced transcriptional down-regulation of H3K27me3-targeted genes. Therefore, we hypothesized that the combined treatment of CDK9 inhibitors (CDK9i) and EZH2i would show greater antitumor activity than treatment with either inhibitor alone. We found a particularly potent synergy of this combination against both DLBCL and other solid tumors *in vitro* and *in vivo*, revealing that this potential therapeutic combination could be evaluated in patients.

Methods

Cell culture

All cells were purchased from ATCC (Manassas, VA, USA) or DSMZ (Brunswick, Germany) and maintained following the suppliers' instructions.

Cell proliferation, apoptosis, colony formation assay, comet assay, quantitative Real-Time PCR analysis, chemicals and antibodies were described in the *Online Supplementary Methods*.

Mass Spectrometry (MS) of histone modifications

Histones of SU-DHL-4 cells from SILAC (stable isotope labeling by amino acids) were manipulated as previously described.[18] Then the peptides were separated by EASY–nLC 1000 HPLC system and analyzed using Orbitrap Fusion mass spectrometer (Thermo Fisher Scientific). MS data were analyzed by Mascot software against an in-house human histone sequence database (83 sequences; 13,870 residues) generated from the UniProt database (updated on 01/27/2015). Peptides containing modifications were manually quantified using the Qual Browser (Thermo Fisher Scientific).

ChIP-Seq

H3K27me3 ChIP-seq data with spike-in was generated by Active Motif's Epigenetic Services team (Active Motif, CA, USA). Karpas-422 cells were harvested as previously described.[19] Cell pellets were snap-frozen in liquid nitrogen for 10 min, stored at -80°C and then shipped to Active Motif on dry ice for the H3K27me3 ChIP-seq assay.

Animal experiments

All experiments were performed according to the institutional ethical guidelines on animal care and approved by the Institute of Animal Care and Use Committee at the Shanghai Institute of Materia Medica (No. 2016-04-DJ-21). Pfeiffer, SU-DHL-6 were subcutaneously injected into the right flank of SCID mice and SW620 were subcutaneously injected into the right flank of nude mice at 5×10^6 cells/mouse (six mice per group). Tumor bearing mice were randomized into groups and started dosing when average tumor volume reached 100–200 mm^3. CDKI-73 (0.5% HPMC+ddH_2O) and EPZ6438 (0.5% CMCNa+1% Tween80+ddH_2O) were given orally daily. For combination treatment, drugs were given concurrently. Tumors and body weight were measured twice a week, and the relative tumor volume (RTV) was calculated with the formula: RTV =(½×length×width^2 of day n)/(½×length×width^2 of day 0). The therapeutic effect of the compounds was expressed as the volume ratio of treatment to control: T/C (%)=100 %×(mean $RTV_{treated}$)/(mean $RTV_{vehicle}$).

Statistical analysis

Combination index (CI) values were calculated using CalcuSyn software or using the IC_{50} ratio obtained with CDK9i plus EZH2i compared to that obtained with CDK9i alone as previously described.[20] Student's *t*-test was applied for statistical comparison using GraphPad Prism. Unless otherwise indicated, the results are expressed as the mean ± standard deviation (SD) from at least three independent experiments. Differences were considered to be statistically significant at $P<0.05$.

Results

CDKI-73 inhibits the growth of DLBCL cells *in vitro* and *in vivo*

The activity of CDKI-73 against human DLBCL was evaluated using a panel of established DLBCL cell lines. CDKI-73 remarkably restrained the proliferation of all tested DLBCL cell lines with the mean IC_{50} values of 87±40 nM, which was slightly lower than that of Flavopiridol, a reported potent CDK9 inhibitor (125±40 nM) (Figure 1A).

Considering that CDKI-73 has been reported to be a potent CDK9 inhibitor,[15-17] we investigated its influence on CDK9 activity in DLBCL cell lines. As expected, significant suppression of phosphorylation of RNA Pol II (ser2) was also found in SU-DHL-4, Pfeiffer and WSU-DLCL-2 cells treated with CDKI-73 in a dose-dependent manner (Figure 1B). As CDK9 plays a vital role in regulating the transcription of numerous anti-apoptotic proteins, its inhibition-induced cell death has been confirmed to be through apoptosis.[7] Therefore, we examined the effect of CDKI-73 on apoptosis. As expected, CDKI-73 led to apoptosis in three DLBCL cell lines, WSU-DLCL2, SU-DHL-4, and Pfeiffer, in a concentration- and time-dependent manner (Figure 1C). Simultaneously, PARP cleavage increased consistently with the occurrence of apoptosis

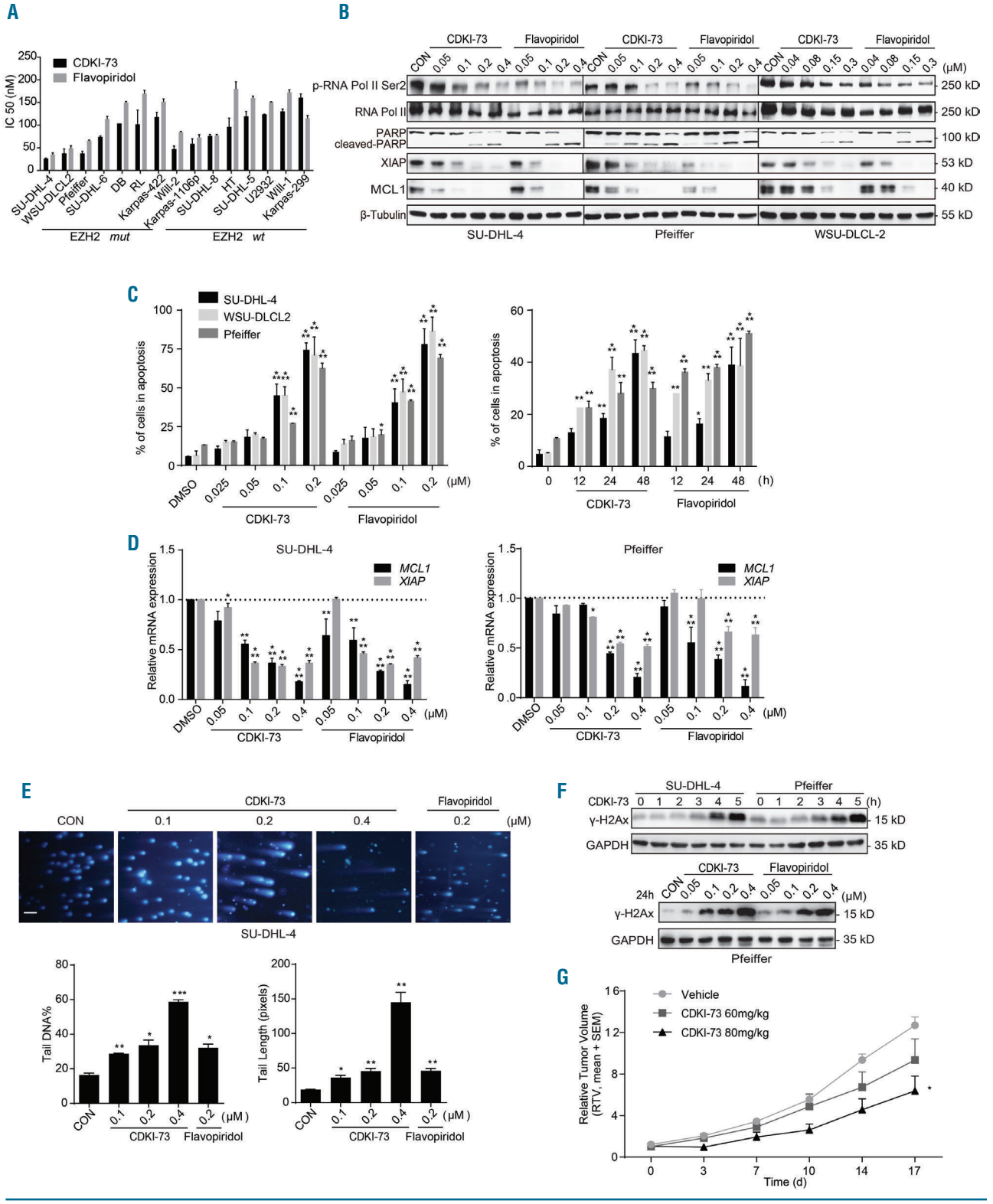

Figure 1. Efficiency of CDKI-73 on diffuse large B-cell lymphoma cells. (A) The IC_{50} values of diffuse large B-cell lymphoma (DLBCL) cell lines after exposure to CDKI-73/Flavopiridol for 72 hours (h). (B) Cellular CDK9 inhibition [2 h for detection of RNA polymerase II (RNA Pol II) (ser2)] and the level of apoptosis-related proteins (24 h) influenced by CDKI-73/Flavopiridol. (C) Apoptosis caused by CDKI-73/Flavopiridol. (D) The relative mRNA expression of *MCL1* and *XIAP* after treated with CDKI-73/Flavopiridol for 6 h. (E) Comet assay. Cells were treated with CDKI-73/Flavopiridol for 24 h (scale bar, 25 μm). Quantified results of the average DNA contents and the length of the comet tails using CometScor software. (F) γ-H2AX level in Pfeiffer and SU-DHL-4 cells treated with indicated time or dose of CDKI-73/Flavopiridol. (G) Tumor growth curve graphs RTV over time in each treatment group in Pfeiffer xenografts. Data are expressed as the mean + standard error of the mean (SEM). All data are representative of at least three independent experiments. ***P<0.001, **P<0.01, *P<0.05 compared with the control group. Mut: mutant; wt: wild-type.

(Figure 1B). Further, we assessed the impact of CDKI-73 on the expression of anti-apoptotic proteins MCL1 and XIAP, which were proved to be down-regulated by CDK9 inhibition.[7] Both SU-DHL-4 and Pfeiffer cells exposed to increasing doses of CDKI-73 exhibited decreased levels of MCL1 and XIAP at both protein (Figure 1B) and mRNA levels (Figure 1D), indicating transcriptional inhibition. The pattern is similar to that of Flavopiridol. These results indicated that CDKI-73 inhibits CDK9 activity efficiently in DLBCL cell lines.

In addition to its predominant participation in transcription, CDK9 also acts as a DNA damage response-related protein.[21] CDK9/cyclin K is directly involved in maintaining the genomic integrity.[21] Hence, we assessed the ability of CDKI-73 in inducing DNA damage in DLBCL cells. Both comet assay and γ-H2AX analysis indicated that CDKI-73 could induce DNA double strand breaks (DSB) in a dose- and time-dependent manner, as evidenced by the elevation of γ-H2AX expression, the frequent appearance and expanding volume of comet tails, as well as the shrinkage of comet heads (Figure 1E-F).

The results listed above show that CDKI-73 can potently inhibit the *in vitro* proliferation of DLBCL. Subsequently, the *in vivo* effect of CDKI-73 against DLBCL was assessed in Pfeiffer xenografts. The activity was weaker than expected. Orally-administered 60 mg/kg of CDKI-73 only slightly restrained the growth of subcutaneously Pfeiffer xenografts. Treatment with 80 mg/kg of CDKI-73 resulted in T/C [(mean $RTV_{treated}$)/(mean $RTV_{vehicle}$)×100] of 59.36 % at day 17 (Figure 1G).

CDKI-73 increases H3K27me3 through CDK9 inhibition

Considering the pivotal role of histone modifications in the development and/or progression of DLBCL, we next explored whether CDKI-73 affected the epigenetic modification of histones. We used mass spectrometry (MS) to detect the influence of CDKI-73 on 36 different epigenetic modifications of histone in DLBCL cell line. Notably, we found that treatment with 50 nM CDKI-73 for 24 hours could trigger upregulation of H3K18me1 (1.36-fold) and H3K27me3 (1.29-fold), while the modifications at other sites increased less than 1.20-fold (Figure 2A). In addition, the modification of some sites were suppressed, such as H3K27ac, which was downregulated 0.42-fold, ranked first in all downregulated sites (Figure 2A and *Online Supplementary Table S1*). In accordance with the MS profiling data, Flavopiridol and CDKI-73 all dramatically elevated the level of H3K27me3 accompanied by the upregulation of both H3K27me1 and H3K27me2 levels at the same site in DLBCL cells in Western blot analysis (Figure 2B and *Online Supplementary Figure S1A*). Meanwhile, CDKI-73 treatment did not remarkably alter other well-studied methylation sites on histone H3, including H3K36, H3K79 and H3K9 (Figure 2B and *Online Supplementary Figure S1A* and *Table S1*). To further dissect if CDKI-73 can influence H3K27me3 binding and how CDKI-73 alters the chromatin landscape of DLBCL cells, ChIP-seq was used to analyse the profile distribution of H3K27me3. As expected, we found a global up-regulation of H3K27me3 following CDKI-73 treatment for 24 hours (Figure 2C). Consistently, the transcription of the genes repressed by H3K27me3, *GATA4*,[22] *CDKN2A*,[23,24] *HOXC8*[8,25] and *TNFRSF21*,[14] was dramatically decreased (Figure 2D). All of these results indicated that CDKI-73 indeed elevated H3K27me3 in DLBCL.

Next, we attempted to determine the detailed mechanism underlying CDKI-73-induced H3K27me3 upregulation. We observed the upregulation of H3K27me3 along with the decline of MCL1 by other CDK9-specific inhibitors SNS-032, AT-7519, and Dinaciclib (Figure 2E). Furthermore the specific CDK4/6 inhibitor PD0332991 did not influence the level of H3K27me3 (Figure 2F). Then, we hypothesized that the upregulation of H3K27me3 is due to CDK9 inhibition. The lack of selectivity against other CDK of these small molecules led us to further confirm the mechanism by using specific RNA interference. As expected, only CDK9 depletion by RNA interference notably increased H3K27me3 in DLBCL cells, associated with the decline of MCL1 (Figure 2G). No change of H3K27me3 was displayed after CDK1, CDK2, CDK4 and CDK7 depletion (Figure 2H). Further, the transcription of the H3K27me3-targeted genes was also decreased in CDK9 silencing cells (Figure 2I). As the MS assay showed a down-regulation of H3K27ac (Figure 2A), we then investigated whether the decrease of H3K27ac is in response to CDK9 inhibition since the loss of H2K27ac may link to the increase in H3K27me3.[26] To our surprise, the level of H3K27ac, which declined after treatment with CDKI-73, remained unchanged in CDK9 knock-down cells (*Online Supplementary Figure S1C-D*). The detail mechanism of H3K27ac downregulation needs to be further studied and may be due to other CDK inhibition other than CDK9. These data strongly suggested that CDK9 inhibition indeed increased the level of H3K27 trimethylation in DLBCL cells.

H3K27 methylation has been shown to be catalyzed by EZH2,[10] while the demethylation is catalyzed by UTX and JMJD3.[11] We therefore tried to identify the protein regulated by CDK9 to adjust H3K27 methylation. As mentioned before, CDK9 has been shown to partcipiate in transcriptional processes, therefore reducing protein expression by CDK9 inhibition is the most important proposed mechanism. As expected, the mRNA and protein levels of demethylases (UTX and JMJD3) decreased after the treatment with CDK9i in a dose- and time-dependent manner (Figure 3A-B). UTX and JMJD3 almost were completely depleted when the cells were exposed for 24 hours to 0.05 μM and 0.1 μM CDKI-73/Flavopiridol, respectively (Figure 3B and *Online Supplementary Figure S2A*). To our surprise, the expression of methyltransferases, EZH2, EED, and SUZ12 was also lowered. However, these two CDK9i resulted in the decline of protein and mRNA levels of UTX and JMJD3, especially JMJD3, at lower doses and at early time points of treatment. Methyltransferases were almost completely depleted after treatment with 0.4 μM CDKI-73/Flavopiridol for 24 hours. As expected, the silencing of CDK9 and other three CDK9i (SNS-032, AT-7519, and Dinaciclib) also diminished JMJD3, UTX, and PRC2, but the effect on JMJD3 and UTX was more significant (Figure 3A-C). These data demonstrated that H3K27me3 stimulated by CDKI-73 was dependent on CDK9 inhibition.

Previous studies have indicated that CDK1- and CDK2-dependent phosphorylation of EZH2 can influence the methylation of H3K27.[27,28] However, we found no obvious change of EZH2 phosphorylation after treatment with the indicated dose of CDKI-73 (*Online Supplementary Figure S2B*).

EZH2i reversed the upregulation of H3K27me3 evoked by CDKI-73 and causes a synergistic effect in DLBCL

It has been reported that down-regulation of H3K27me3 expression by EZH2i has marked anti-tumor potency in EZH2 mutant (mut) DLBCL preclinical models.[14] Therefore, CDKI-73 improved H3K27me3 expression, which may attenuate its anti-tumor activity against DLBCL . This inspired us to explore whether EZH2i could

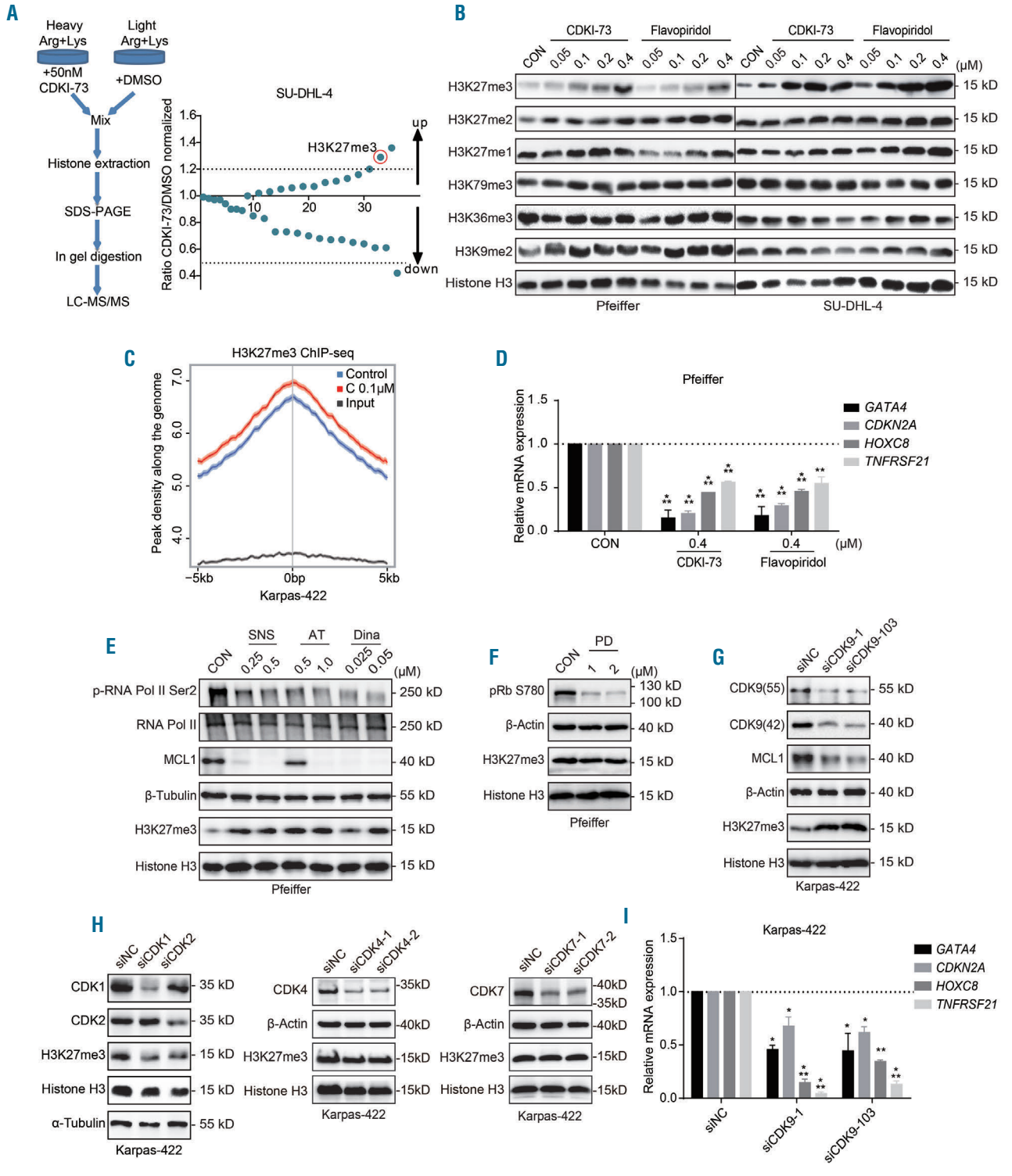

Figure 2. CDKI-73 induces H3K27me3 via CDK9 inhibition. (A) Mass Spectrometry assay (MS). Graphical illustration of MS process (left) and normalized CDKI-73/DMSO ration of 36 loci (right). H3K27me3 is labeled in the red circle. (B) Methylation level of histone in Pfeiffer and SU-DHL-4 cells after treated with CDKI-73/Flavopiridol for 24 hours (h). (C) Summary of ChIP-seq H3K27me3 peaks in the CDKI-73 (red) and control (blue) samples. "0bp" in X-axis indicates the H3K27me3 peak center. (D) The relative mRNA levels of H3K27me3 target genes *GATA4, CDKN2A, HOXC8*, and *TNFRSF21* in Pfeiffer when cells were treated with CDKI-73/Flavopiridol for 6 h. The influence of CDK9i (E) CDK4/6 inhibitor (F) and CDK9 (G) CDK1, CDK2, CDK4, CDK7 knock-down (H) on the protein level of H3K27me3. (I) The relative mRNA levels of *GATA4, CDKN2A, HOXC8*, and *TNFRSF21* in CDK9 depletion Karpas-422 cells. C: CDKI-73; SNS: SNS-032; AT: AT-7519; Dina: Dinaciclib; PD: PD0332991. All data are representative of at least three independent experiments. ***P<0.001, **P<0.01, *P<0.05 compared with the control group.

reverse the upregulation of H3K27me3, and then synergize the antitumor effect of CDKI-73. As expected, specific EZH2i, EPZ6438 or GSK126 exactly reversed the augmented H3K27me3 evoked by CDKI-73 (Figure 4A). Furthermore the transcription of all these four examined target genes of H3K27me3 was reactivated in co-treated cells compared with cells treated with CDKI-73 alone (Figure 4B). Next, we investigated whether EZH2i could potentiate the anticancer activity induced by CDKI-73. For this, DLBCL cell lines (Will-1, U2932, Karpas-422, SU-DHL-4, Pfeiffer, and SU-DHL-6) were treated with CDKI-73 alone, or in combination with EPZ6438/GSK126 for 72 hours. The combination effect was evaluated using the CI value according to the CalcuSyn software.[20] The effect is usually considered as synergistic when the CI value is less than 0.8, additive when the CI value is between 0.8-1.2, and antagonistic when the CI value is above 1.2.[20] In EZH2 mut cell lines, Pfeiffer (A677G), SU-DHL-4 (Y641S), Karpas-422 (Y641F), and SU-DHL-6 (Y641N), the average CI values were all below 0.8 (Figure 4C), indicating a synergistic interaction between CDKI-73 and EZH2i in EZH2 mut DLBCL cells. We also found that the IC_{50} for EZH2i was lower in CDK9 knock-down cells compared with parent Pfeiffer cells (*Online Supplementary Figure S3A*). However, in Will-1 and U2932 cells, which harbor wild-type (*wt*) EZH2, the combination with EZH2i didn't signif-

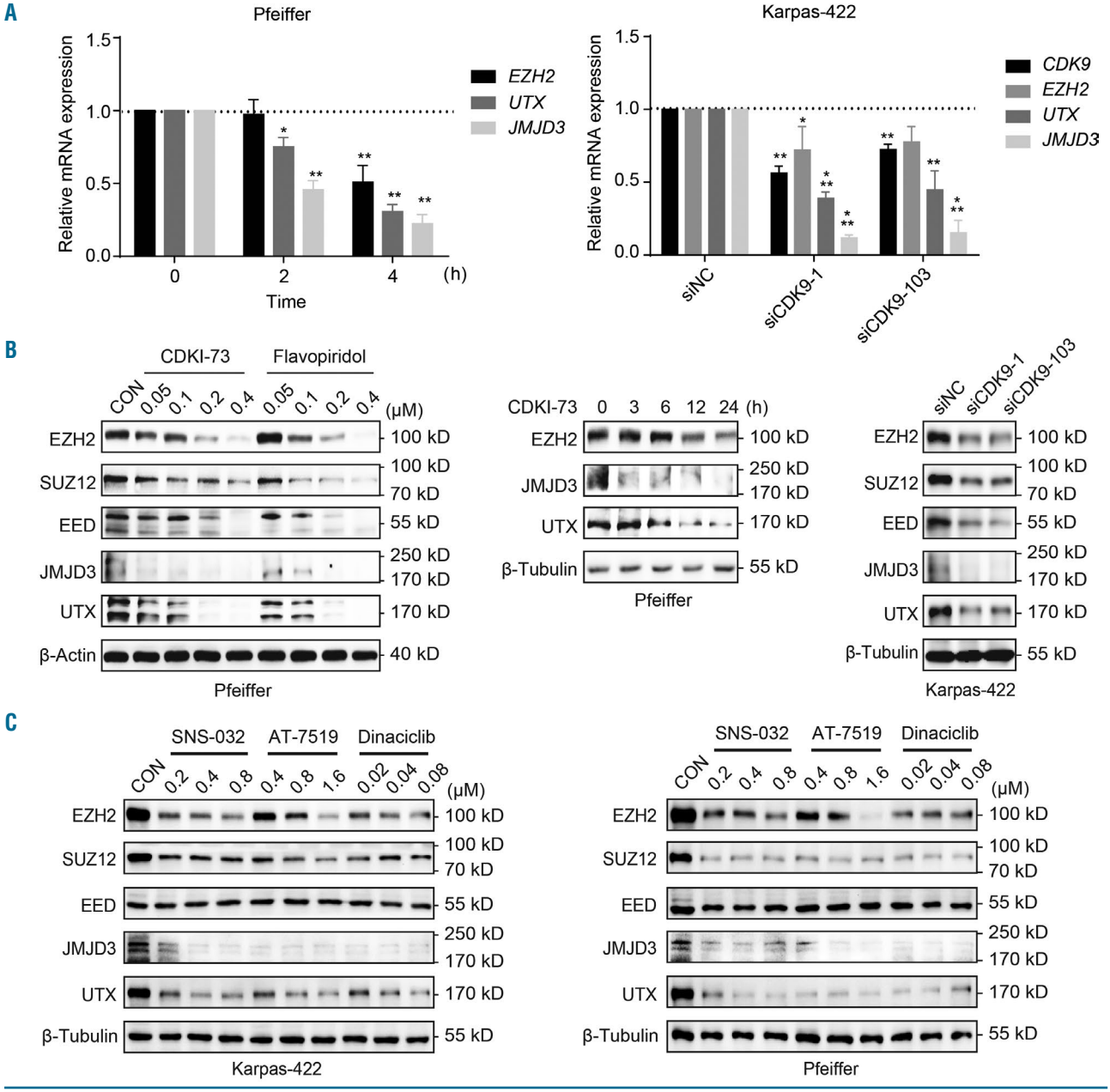

Figure 3. Transcriptional repression contributed to H3K27me3 elevation via CDK9 inhibition. (A) The relative mRNA levels of H3K27-related methyltransferases and demethylases after exposure to 0.1 μM CDKI-73 for 2 and 4 hours (h) or siCDK9. (B-C) The protein levels of H3K27-related methyltransferases and demethylases after exposure to CDKI-73/Flavopiridol, other cyclin-dependent kinases (CDK) inhibitors or siCDK9. All data are representative of at least three independent experiments. ***P<0.001, **P<0.01, *P<0.05 compared with the control group.

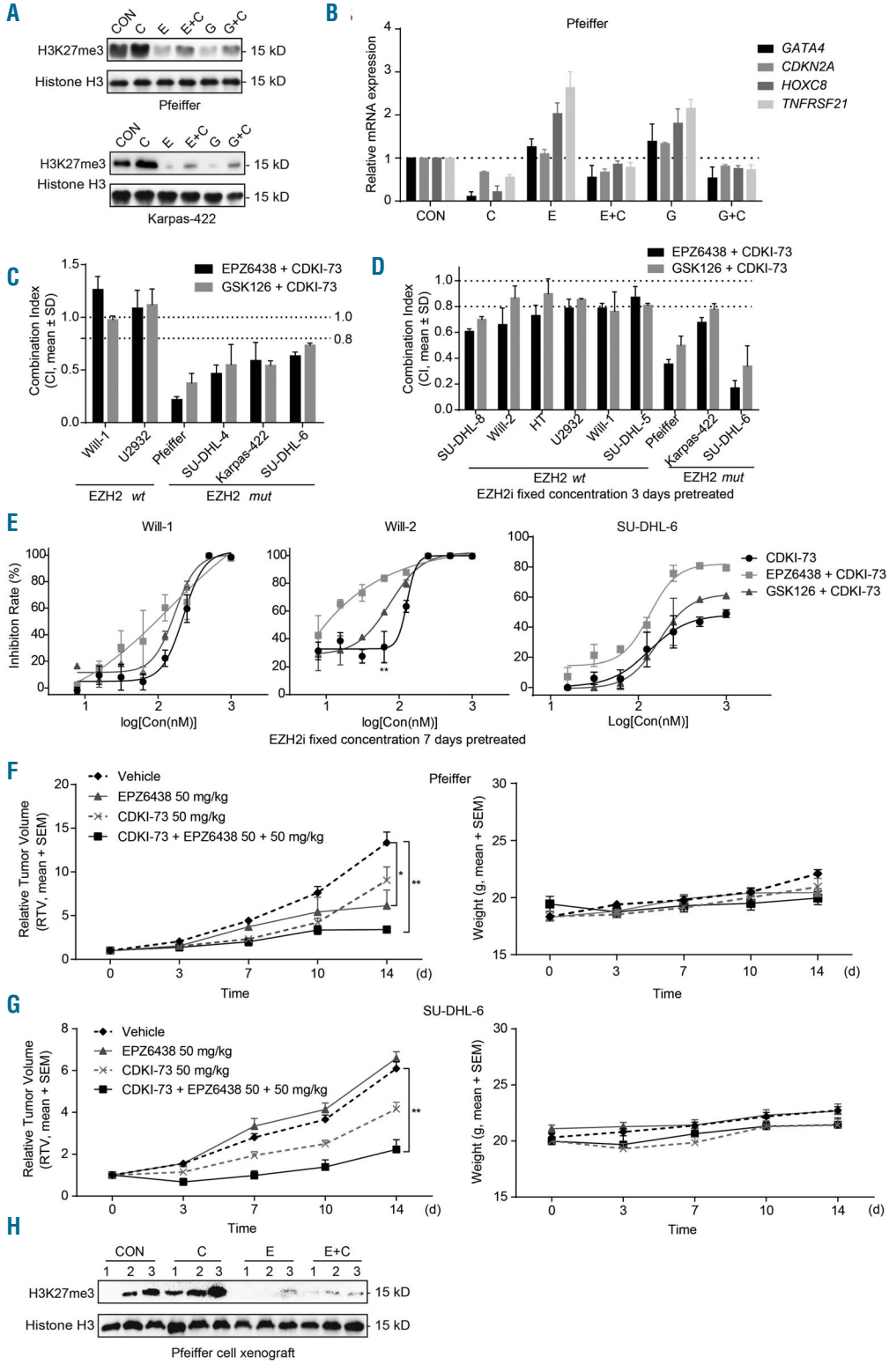

Figure 4. Combined anti-tumor effect of CDKI-73 and EPZ6438/GSK126 *in vitro* and *in vivo*. (A) The level of H3K27me3 in Pfeiffer and Karpass-422 cells after treated with CDKI-73, and EPZ6438/GSK126 alone or in combination. Cells were pretreated with 0.5 μM EPZ6438/GSK126 alone for 24 hours (h), and then treated in combination with 0.1 μM CDKI-73 for an additional 24 h. (B) The relative mRNA levels of *GATA4, CDKN2A, HOXC8,* and *TNFRSF21* in Pfeiffer cells when pretreated with 0.5 μM EPZ6438/GSK126 alone for 24 h, then treated in combination with 0.1 μM CDKI-73 for additional 6 h. (C) Average combination index (CI) values. Diffuse large B-cell lymphoma (DLBCL) cells were treated with different doses of CDKI-73 and EPZ6438/GSK126 alone or in combination for 72 h. (D) The CI values of nine different DLBCL cell lines. The combination groups were pretreated with a fixed dose of EPZ6438 or GSK126 for 72 h and then both CDKI-73 and combination groups were treated with increasing doses of CDKI-73 for additional 72 h. (E) The dose-response curves of Will-1, Will-2, and SU-DHL-6 cell lines. The combination groups were pretreated with a fixed dose of EPZ6438 or GSK126 for seven days and then both CDKI-73 and combination groups were treated with increasing doses of CDKI-73 for additional 72 h. (F-G) Relative tumor volume (RTV) and average body weight of nude mice treated with 50 mg/kg CDKI-73 and 50 mg/kg EPZ66438 alone or together with inoculated Pfeiffer and SU-DHL-6 cells. Data are expressed as the mean + standard error of the mean (SEM). (H) The level of H3K27me3 detected in Pfeiffer xenografts at the end of the in vivo experiment. C: CDKI-73; E: EPZ6438; G: GSK126. All data are representative of at least three independent experiments. ***P<0.001, **P<0.01, *P<0.05. Mut: mutant; wt: wild-type.

icantly improve the anti-proliferative activity of CDKI-73 in this scheme, with CI values higher than 0.8.

As EZH2i takes longer to exhibit weak proliferation inhibition in EZH2 wt cells in the *in vitro* assay,[14] we tried another combination scheme in a panel of DLBCL cell lines. The combination groups were pretreated with a fixed dose of EPZ6438/GSK126 for 72 hours, which was adequate to inhibit H3K27me3, and had no obvious proliferation inhibition (the inhibitory rate was controlled below 20%). The mean CI values of treatment with CDKI-73 and EZH2i were calculated as reported[29] and were also observed to be less than 0.8 in EZH2 mut DLBCL cells (Figure 4D). Even more gratifying was the observation that at least an additional effect was exhibited in SU-DHL-8, Will-1, Will-2, HT, SU-DHL-5, and U2932 cell lines which harbor wt EZH2 (Figure 4D), indicating that EZH2i can promote the anti-proliferative potency of CDKI-73 against DLBCL cell lines with the combination schedule regardless of the EZH2 phenotype. When the pretreatment time with EZH2i was extended to seven days (the inhibitory rate of EZH2i was still controlled below 20 %), the dose-response curves of all the co-treatment groups were apparently shifted to the left compared with the curves treated with CDKI-73 alone in EZH2 wt DLBCL cells, also indicating a synergistic effect (Figure 4E).

Thereafter, we evaluated whether EZH2i could enhance the anti-tumor ability of CDKI-73 *in vivo*. In Pfeiffer xenografts, CDKI-73 and EPZ6438 alone suppressed tumor growth compared to the vehicle, yielding a T/C rate of 67.69 % and 46.07 %, respectively. Combinatorial CDKI-73 and EPZ6438 therapy more potently inhibited tumor growth compared to treatment with CDKI-73, EPZ6438, and vehicle alone, yielding a T/C rate of 25.69 %, indicating 74.31 % inhibition of tumor growth (Figure 4F). Moreover, there was no obvious weight loss under the combined regimen as compared to the single treatments (Figure 4F). Similar results were observed in another model, SU-DHL-6 (Figure 4G). The superior in vivo anti-tumor activity of the combination therapy was also associated with a greater decline in H3K27me3, which was upregulated by CDKI-73 alone (Figure 4H).

Combination therapy synergistically induces apoptosis and DNA damage

As mentioned above, CDKI-73 alone induced apoptosis and DNA DSB in DLBCL, we next determined the combined effects on apoptosis and DNA damage. As expected, combination treatment remarkably increased the rate of apoptosis compared to each agent alone (Figure 5A). This was associated with a synergistic increase in the PARP cleavage, and a decline of anti-apoptotic proteins including MCL1, XIAP, and BCL-XL (Figure 5B). Similar results were obtained in the in vivo assay (Figure 5C). In addition, accumulating data suggest that EZH2 also participates in modulating the DNA damage response.[30] Therefore, we hypothesized that co-induction of DNA damage may be another mechanism contributing to the synergistic anti-tumor effect of the combination. As expected, both comet assay and γ-H2AX analysis indicated that CDKI-73 or EPZ6438/GSK126 alone could induce DNA damage both in Pfeiffer and SU-DHL-4 cells. However, the combined therapy resulted in a dramatic increase in γH2AX accumulation, and the frequent appearance and expanding volume of comet tails (Figure 5D-E).

CDK9 and EZH2 inhibition also exhibited synergistic antitumor activity in multiple solid tumors

We further studied whether the combination therapy was also effective against solid tumors. At first, we found that CDKI-73/Flavopiridol elevated H3K27me3 in various kinds of cancer cells, including MCF-7 (breast cancer), MDA-MB-453 (breast cancer), SGC-7901 (gastric cancer), and SW620 (colorectal cancer) (*Online Supplementary Figure S1A*). This finding might partially explain the observation that the inhibition of CDK9 is insufficient to inhibit tumor growth in clinical trials.[31] And as expected, EZH2i downregulated the augmented H3K27me3 levels induced by CDK9 inhibition and synergized with CDK9i in these solid tumor models *in vitro* and *in vivo* (Figure 6 and *Online Supplementary Figure S3B*). We also found that depletion of both CDK9 and EZH2 in MCF-7 cells delayed cells proliferation, as compared with siCDK9 alone (*Online Supplementary Figure S3C*). And the deletion of CDK9 also diminished PRC2, JMJD3, and UTX, leading to the observed increase of H3K27me3 in these cells (Figure 6E). All these data strongly suggested that CDK9 and EZH2 inhibition also exhibit synergistic interaction in multiple solid tumors.

Discussion

The frequent observance of resistance and relapse to first line therapy by DLBCL underscores the need for novel approaches to treat this disease. CDKI-73, as an example of a highly efficacious CDK9 inhibitor, has displayed potent anti-tumor activity *in vitro* and *in vivo*.[15-17] Previous studies also have shown that this agent had little toxicity on normal T and B cells while exhibiting potent efficiency against CLL,[15] suggesting it to be a far superior therapeutic agent for clinics. Here, we demonstrated that it retains efficacy in DLBCL *in vitro* and *in vivo*. CDKI-73 exhibited a broad ability to trigger apoptosis and dramatically repress the proliferation of 15 DLBCL cell lines, associated with lost MCL1 and XIAP proteins, owing to CDK9 inhibition. All these data provide a basis for moving forward with the clinical evaluation of CDKI-73 in DLBCL.

Deregulation of CDK has been used to develop antitumor target for more than 20 years. Although CDK inhibitors have always shown tremendous preclinical activity, their clinical application was limited by modest efficacy along with various side effects.[31] Here, in our study, we provided a view of 'CDK9-histone modification crosstalk', which expands the function of CDK9. We found that CDK9 inhibition specifically elevated the trimethylation of H3K27, which may restrain the antitumor potency against DLBCL and other solid tumor types. H3K27me3 is a transcription-repressing epigenetic modification that has been causally associated with the initiation and development of multiple tumor types, especially DLBCL. Recently, oncogenic heterozygous mutations were identified in the SET domain of EZH2 in DLBCL patients, which could elevate H3K27me3, and drive cell proliferation.[14] Moreover, selective EZH2i show preclinical and clinical efficiency against DLBCL by reducing the level of H3K27me3. Positive interim efficacy data from an ongoing phase II clinical trial of EPZ6438, as a single-agent treatment for patients with relapsed or refractory DLBCL, were released at the International Conference on Malignant Lymphoma (Lugano, Switzerland). An objec-

tive response rate of 17 % further provides a strong rationale for the inhibition of H3K27me3 to be a useful therapeutic strategy in DLBCL. Therefore, we used EZH2i for investigating their synergistic effect with CDK9i. As expected, EPZ6438/GSK126 reversed the elevated H3K27me3 triggered by CDK9i and reactivated the transcription of target genes, which was suppressed by H3K27me3. Also, apoptosis induced by the co-treatment was remarkable without reaching the dosages that induce obvious apoptosis by CDKI-73 or EZH2i alone, indicating strong efficacy with less toxicity at the same time. In addition, combination therapy also improved DNA damage compared to the single treatments alone and synergistically restrained DLBCL growth. More importantly, other CDK9 inhibitors in combination with EZH2i also resulted in a strong synergistic effect in all cases. By expanding our studies with this combination therapy to other solid tumors, in which EZH2i alone do not show any effect, we also demonstrated an impressive synergistic effect. Both preclinical and clinical evidences suggest that only very

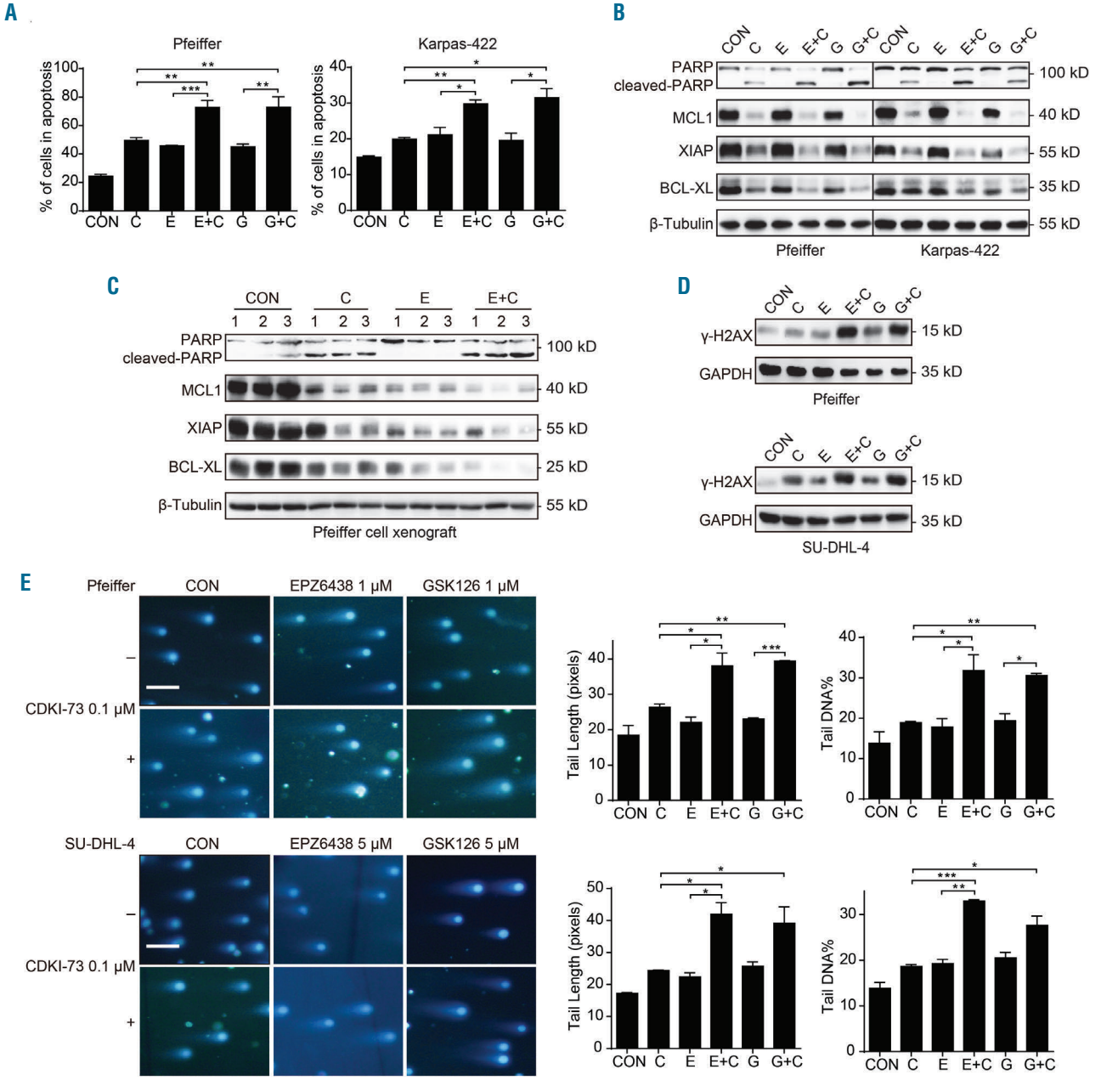

Figure 5. The combined effect of CDKI-73 and EPZ6438/GSK126 on apoptosis and DNA damage. (A-B) Quantitative assessment of apoptosis and the expression of apoptosis-related proteins in Pfeiffer and Karpas-422 cells pretreated with EPZ6438/GSK126 alone for 48 hours (h) and then together with CDKI-73 for another 24 h. (C) The level of apoptosis-related proteins detected in Pfeiffer xenografts at the end of the *in vivo* experiment. (D) γ-H2AX detection in Pfeiffer and SU-DHL-4 cells pretreated as mentioned in Figure 4A. (E) Comet assay. Cells were pretreated with EPZ6438/GSK126 alone for 24 h and then in combination with CDKI-73 for additional 24 h (scale bar, 25 μm). C: CDKI-73; E: EPZ6438; G: GSK126. All data are representative of at least three independent experiments. ***P<0.001, **P<0.01, *P<0.05.

small sets of cancers indeed benefited from EZH2-targeted therapies. Therefore, this study may also open opportunities for EZH2i in solid tumor.

Keeping in mind the important role of the methylation of H3K27 in tumor progression, we also tried to explore the detailed mechanism stimulating H3K27me3 by CDKI-73. In some studies CDK has been linked to H3K27 methylation. CDK1 and CDK2 have been reported to phosphorylate EZH2 at Thr350 and it is considered to be essential for the maintenance of H3K27me3 marks through cell division.[27] Additionally, Thr487 is another residue of EZH2 that can be phosphorylated through activation of CDK1, disrupting EZH2 binding with other PRC2 components, thereby resulting in a decline of

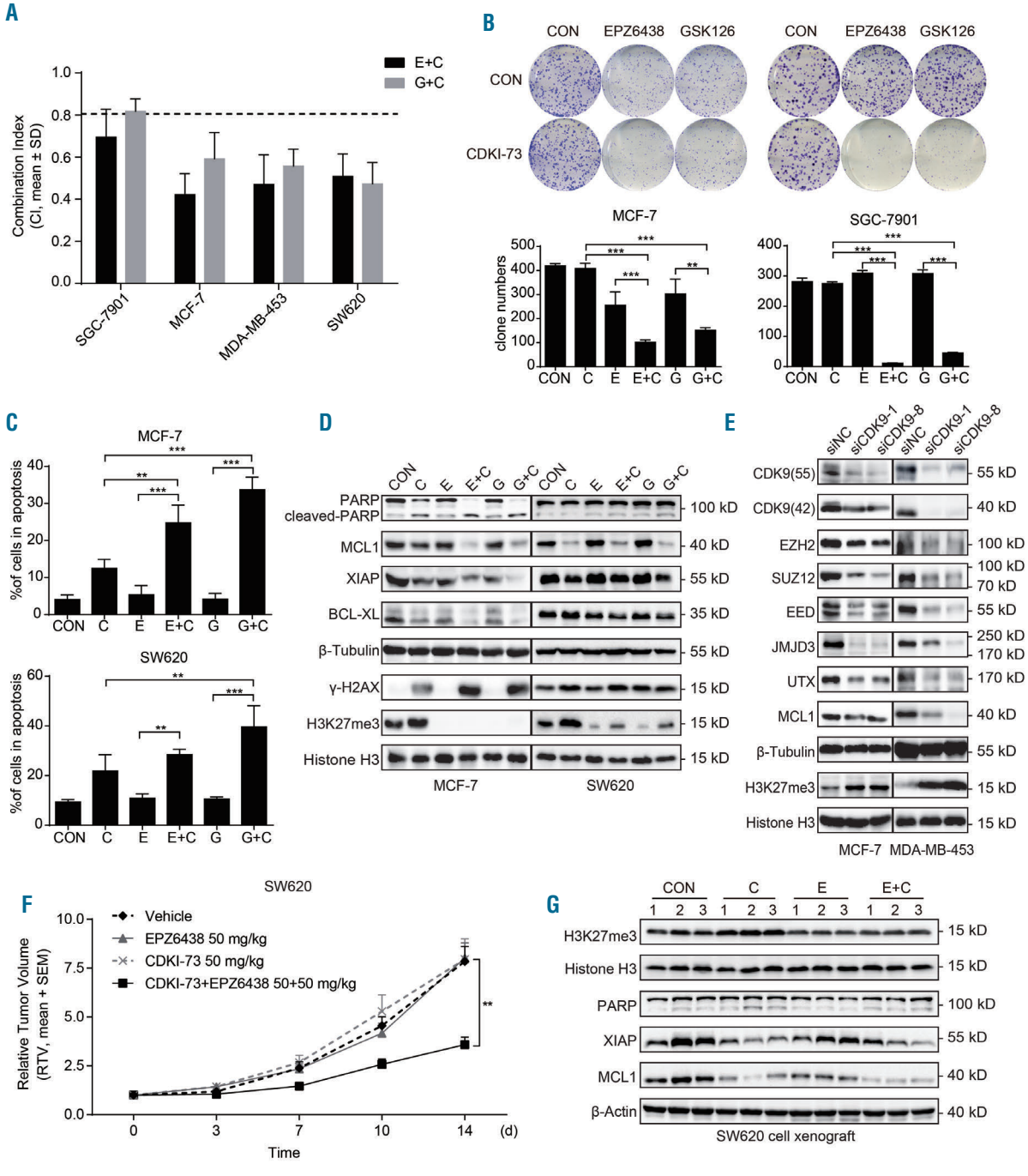

Figure 6. The combined effect of CDK9 and EZH2i in multiple solid tumors. (A) The average combination index (CI) values. SGC-7901, MCF-7, MDA-MB-453 and SW620 cells were treated as mentioned in Figure 4D. (B) The combination of CDKI-73 and EZH2i inhibited MCF-7 and SGC-7901 colony formation. (C-D) Quantitative assessment of apoptosis and the expression of apoptosis-related proteins, H3K27me3 and γ-H2AX in MCF-7 and SW620 cells pretreated with EPZ6438/GSK126 for 48 hours (h) and then in combination with CDKI-73 for additional 24 h. (E) H3K27me3, and its related methyltransferases and demethylases level in MCF-7 and MDA-MB-453 cells after siCDK9. (F) Relative tumor volume (RTV) and average body weight of nude mice treated with 50 mg/kg CDKI-73 and 50 mg/kg EPZ66438 alone or together with inoculated SW620 cells. Data are expressed as the mean + standard error of the mean (SEM). (G) H3K27me3 and apoptosis-related proteins level in SW620 xenografts at the end of the in vivo experiment. C: CDKI-73; E: EPZ6438; G: GSK126. All data are representative of at least three independent experiments. ***P<0.001, **P<0.01, *P<0.05.

H3K27me3.[28] In our case, CDKI-73 did not change the EZH2 phosphorylation status. The elevated H3K27me3 is related to multiple factors, such as the amplification of EZH2 or another subunit of PRC2 and so on, in numerous tumor types.[12] In addition, inactivation of UTX or JMJD3, resulting in the enrichment of H3K27me3, also has been detected in many kinds of cancers.[32,33] In the present study, surprisingly, the expression of H3K27me3 increased while EZH2 decreased after treatment with CDKI-73/Flavopiridol. Therefore, we paid more attention to the demethylases. Both the protein and mRNA levels of UTX and JMJD3 decreased earlier and more dramatically than EZH2, EED, and SUZ12 when exposed to CDK9i. Moreover, as expected, knock-down of CDK9 also elevated H3K27me3 and decreased the level of JMJD3/UTX more evidently than that of EZH2. Thus, we speculate that CDK9 inhibition reduced the expression of JMJD3/UTX more powerfully than that of EZH2, leading to H3K27me3 elevation. However, the detailed mechanism of upregulation of H3K27me3 by the loss of CDK9 still needs to be further explored.

In conclusion, we identified that the novel CDK9 inhibitor CDKI-73 exerts a potent anti-tumor activity against DLBCL both *in vitro* and *in vivo*, and represents an attractive therapeutic agent for DLBCL therapy. More importantly, EZH2i in combination with CDK9i results in a strong synergistic effect in DLBCL and other solid tumors by suppressing CDK9 inhibition-stimulated H3K27me3. These data provide a rational basis for the testing of CDK9i in combination with EZH2i in clinical trials.

References

1. Raut LS, Chakrabarti PP. Management of relapsed-refractory diffuse large B cell lymphoma. South Asian J Cancer. 2014;3(1):66-70.
2. Krystof V, Baumli S, Furst R. Perspective of cyclin-dependent kinase 9 (CDK9) as a drug target. Curr Pharm Des. 2012;18(20):2883-2890.
3. Wang S, Fischer PM. Cyclin-dependent kinase 9: a key transcriptional regulator and potential drug target in oncology, virology and cardiology. Trends Pharmacol Sci. 2008;29(6):302-313.
4. Sanchez-Beato M, Sanchez-Aguilera A, Piris MA. Cell cycle deregulation in B-cell lymphomas. Blood. 2003;101(4):1220-1235.
5. Bellan C, De Falco G, Lazzi S, et al. CDK9/CYCLIN T1 expression during normal lymphoid differentiation and malignant transformation. J Pathol. 2004;203(4):946-952.
6. Wenzel SS, Grau M, Mavis C, et al. MCL1 is deregulated in subgroups of diffuse large B-cell lymphoma. Leukemia. 2012;27(6):1381-1390.
7. Gregory GP, Hogg SJ, Kats LM, et al. CDK9 inhibition by dinaciclib potently suppresses Mcl-1 to induce durable apoptotic responses in aggressive MYC-driven B-cell lymphoma in vivo. Leukemia. 2014;29(6):1437-1441.
8. Yecies D, Carlson NE, Deng J, Letai A. Acquired resistance to ABT-737 in lymphoma cells that up-regulate MCL-1 and BFL-1. Blood. 2010;115(16):3304-3313.
9. Pan G, Tian S, Nie J, et al. Whole-genome analysis of histone H3 lysine 4 and lysine 27 methylation in human embryonic stem cells. Cell Stem Cell. 2007;1(3):299-312.
10. Kuzmichev A, Nishioka K, Erdjument-Bromage H, Tempst P, Reinberg D. Histone methyltransferase activity associated with a human multiprotein complex containing the Enhancer of Zeste protein. Genes Dev. 2002;16(22):2893-2905.
11. Hong S, Cho YW, Yu LR, Yu H, Veenstra TD, Ge K. Identification of JmjC domain-containing UTX and JMJD3 as histone H3 lysine 27 demethylases. Proc Natl Acad Sci U S A. 2007;104(47):18439-18444.
12. McCabe MT, Creasy CL. EZH2 as a potential target in cancer therapy. Epigenomics. 2014;6(3):341-351.
13. Morin RD, Johnson NA, Severson TM, et al. Somatic mutations altering EZH2 (Tyr641) in follicular and diffuse large B-cell lymphomas of germinal-center origin. Nat Genet. 2010;42(2):181-185.
14. McCabe MT, Ott HM, Ganji G, et al. EZH2 inhibition as a therapeutic strategy for lymphoma with EZH2-activating mutations. Nature. 2012;492(7427):108-112.
15. Walsby E, Pratt G, Shao H, et al. A novel Cdk9 inhibitor preferentially targets tumor cells and synergizes with fludarabine. Oncotarget. 2014;5(2):375-385.
16. Lam F, Abbas AY, Shao H, et al. Targeting RNA transcription and translation in ovarian cancer cells with pharmacological inhibitor CDKI-73. Oncotarget. 2014;5(17):7691-7704.
17. Xie S, Jiang H, Zhai XW, et al. Antitumor action of CDK inhibitor LS-007 as a single agent and in combination with ABT-199 against human acute leukemia cells. Acta Pharmacol Sin. 2016;37(11):1481-1489.
18. Shechter D, Dormann HL, Allis CD, Hake SB. Extraction, purification and analysis of histones. Nat Protoc. 2007;2(6):1445-1457.
19. Huang X, Yan J, Zhang M, et al. Targeting Epigenetic Crosstalk as a Therapeutic Strategy for EZH2-Aberrant Solid Tumors. Cell. 2018;175(1):186-199 e119.
20. Bijnsdorp IV, Giovannetti E, Peters GJ. Analysis of drug interactions. Methods Mol Biol. 2011;731(421-434.
21. Yu DS, Cortez D. A role for cdk9-cyclin k in maintaining genome integrity. Cell Cycle. 2014;10(1):28-32.
22. He A, Shen X, Ma Q, et al. PRC2 directly methylates GATA4 and represses its transcriptional activity. Genes Dev. 2012;26(1):37-42.
23. Tanaka S, Miyagi S, Sashida G, et al. Ezh2 augments leukemogenicity by reinforcing differentiation blockage in acute myeloid leukemia. Blood. 2012;120(5):1107-1117.
24. Shi J, Wang E, Zuber J, et al. The Polycomb complex PRC2 supports aberrant self-renewal in a mouse model of MLL-AF9;Nras(G12D) acute myeloid leukemia. Oncogene. 2013;32(7):930-938.
25. Kim SY, Paylor SW, Magnuson T, Schumacher A. Juxtaposed Polycomb complexes co-regulate vertebral identity. Development. 2006;133(24):4957-4968.
26. Pasini D, Malatesta M, Jung HR, et al. Characterization of an antagonistic switch between histone H3 lysine 27 methylation and acetylation in the transcriptional regulation of Polycomb group target genes. Nucleic Acids Res. 2010;38(15):4958-4969.
27. Chen S, Bohrer LR, Rai AN, et al. Cyclin-dependent kinases regulate epigenetic gene silencing through phosphorylation of EZH2. Nat Cell Biol. 2010;12(11):1108-1114.
28. Wei Y, Chen YH, Li LY, et al. CDK1-dependent phosphorylation of EZH2 suppresses methylation of H3K27 and promotes osteogenic differentiation of human mesenchymal stem cells. Nat Cell Biol. 2011;13(1):87-94.
29. Li X, Tong LJ, Ding J, Meng LH. Systematic combination screening reveals synergism between rapamycin and sunitinib against human lung cancer. Cancer Lett. 2014;342(1):159-166.
30. Campbell S, Ismail IH, Young LC, Poirier GG, Hendzel MJ. Polycomb repressive complex 2 contributes to DNA double-strand break repair. Cell Cycle. 2014;12(16):2675-2683.
31. Asghar U, Witkiewicz AK, Turner NC, Knudsen ES. The history and future of targeting cyclin-dependent kinases in cancer therapy. Nat Rev Drug Discov. 2015;14(2):130-146.
32. Ezponda T, Licht JD. Molecular pathways: deregulation of histone h3 lysine 27 methylation in cancer-different paths, same destination. Clin Cancer Res. 2014;20(19):5001-5008.
33. van Haaften G, Dalgliesh GL, Davies H, et al. Somatic mutations of the histone H3K27 demethylase gene UTX in human cancer. Nat Genet. 2009;41(5):521-523.

Ferrata Storti Foundation

Haematologica 2020
Volume 105(4):1032-1041

Daratumumab displays *in vitro* and *in vivo* anti-tumor activity in models of B-cell non-Hodgkin lymphoma and improves responses to standard chemo-immunotherapy regimens

Anna Vidal-Crespo,[1*] Alba Matas-Céspedes,[1,2*,a] Vanina Rodriguez,[1] Cédric Rossi,[3] Juan G. Valero,[1,2] Neus Serrat,[1,2] Alejandra Sanjuan-Pla,[4] Pablo Menéndez,[2,4,5] Gaël Roué,[6] Armando López-Guillermo,[2,7] Eva Giné,[2,7] Elías Campo,[2,8,9] Dolors Colomer,[2,8] Christine Bezombes,[10] Jeroen Lammerts van Bueren,[11,b] Christopher Chiu,[12] Parul Doshi[12,c] and Patricia Pérez-Galán[1,2]

[a]Current affiliation: Grifols, Barcelona, Spain; [b]Current affiliation: Merus, Utrecht, The Netherlands; [c]Current affiliation: Bristol Myers Squibb, Lawrenceville, NJ, USA

[1]Department of Hematology-Oncology, Institut d'Investigacions Biomèdiques August Pi i Sunyer (IDIBAPS), Barcelona, Spain; [2]Centro de Investigación Biomédica en Red-Oncología (CIBERONC), Barcelona, Spain; [3]Department of Hematology, Dijon University Hospital, Dijon, France; [4]Josep Carreras Leukemia Research Institute, Department of Biomedicine, School of Medicine, University of Barcelona, Barcelona, Spain; [5]Institució Catalana de Recerca i Estudis Avançats (ICREA), Barcelona, Spain; [6]Laboratory of Experimental Hematology, Department of Hematology, Vall d'Hebron Institute of Oncology, Vall d'Hebron University Hospital, Barcelona, Spain; [7]Department of Hematology, Hospital Clínic-IDIBAPS, Barcelona, Spain; [8]Hematopathology Unit, Department of Pathology, Hospital Clínic-IDIBAPS, Barcelona, Spain; [9]Faculty of Medicine, University of Barcelona, Barcelona Spain; [10]Centre de Recherches en Cancérologie de Toulouse (CRCT), UMR1037 INSERM, Université Toulouse III: Paul-Sabatier, ERL5294 CNRS, Université de Toulouse, Toulouse, France; [11]Genmab, Utrecht, the Netherlands and [12]Janssen R&D, Spring House, PA, USA

[*]AV-C and AM-C contributed equally to this work.

Correspondence:

PATRICIA PÉREZ-GALÁN
pperez@clinic.cat

Received: November 13, 2018.

Accepted: July 9, 2019.

Pre-published: July 11, 2019.

doi:10.3324/haematol.2018.211904

Check the online version for the most updated information on this article, online supplements, and information on authorship & disclosures: www.haematologica.org/content/105/4/1032

ABSTRACT

CD38 is expressed in several types of non-Hodgkin lymphoma (NHL) and constitutes a promising target for antibody-based therapy. Daratumumab (Darzalex) is a first-in-class anti-CD38 antibody approved for the treatment of relapsed/refractory (R/R) multiple myeloma (MM). It has also demonstrated clinical activity in Waldenström macroglobulinaemia and amyloidosis. Here, we have evaluated the activity and mechanism of action of daratumumab in preclinical *in vitro* and *in vivo* models of mantle cell lymphoma (MCL), follicular lymphoma (FL) and diffuse large B-cell lymphoma (DLBCL), as monotherapy or in combination with standard chemo-immunotherapy. *In vitro*, daratumumab engages Fc-mediated cytotoxicity by antibody-dependent cell cytotoxicity and antibody-dependent cell phagocytosis in all lymphoma subtypes. In the presence of human serum, complement-dependent cell cytotoxicity was marginally engaged. We demonstrated by Selective Plane Illumination Microscopy that daratumumab fully penetrated a three-dimensional (3D) lymphoma organoid and decreased organoid volume. *In vivo*, daratumumab completely prevents tumor outgrowth in models of MCL and FL, and shows comparable activity to rituximab in a disseminated *in vivo* model of blastic MCL. Moreover, daratumumab improves overall survival (OS) in a mouse model of transformed $CD20^{dim}$ FL, where rituximab showed limited activity. Daratumumab potentiates the antitumor activity of CHOP and R-CHOP in MCL and FL xenografts. Furthermore, in a patient-derived DLBCL xenograft model, daratumumab anti-tumor activity was comparable to R-CHOP and the addition of daratumumab to either CHOP or R-CHOP led to full tumor regression. In summary, daratumumab constitutes a novel therapeutic opportunity in certain scenarios and these results warrant further clinical development.

Introduction

B-cell non-Hodgkin's lymphoma (B-NHL) constitutes 4-5% of all hematologic neoplasia with increasing incidence in western countries.[1] DLBCL and FL represent the most frequent aggressive and indolent NHL, accounting for approximately 35% and 20% of all lymphomas, respectively.[2,3] Moreover, roughly one third of FL patients develop a histologic transformation (tFL) to DLBCL leading to a dismal prognosis.[4] Both entities are currently treated with chemo-immunotherapy including a rituximab backbone.[5,6] FL responses are usually high, although recurrence occurs in the majority of the cases.[7] In DLBCL, currently classified into germinal center type (GCB) or activated B-cell type (ABC),[8] treatment is not guided by subtype, and responses to chemo-immunotherapy are normally higher in the GCB subtype. Nevertheless, a portion of DLBCL (20%) do not respond to this regimen.[9] Several second-generation anti-CD20 antibodies, such as the Food and Drug Administration-approved obinutuzumab have been clinically tested to overcome these limitations.[10,11] However, an alternative evolving therapeutic approach is to target a different antigen. In this regard, both FL and DLBCL originate in the germinal center (GC) and consequently express high levels of CD38, making this molecule an attractive therapeutic target.[12]

MCL is a rare NHL (6% of all NHL) with an aggressive evolution and clinically challenging.[13,14] Its frontline therapy, although heterogeneous, typically consists of rituximab-based chemo-immunotherapy followed by autologous-stem cell transplantation and/or rituximab maintenance. Even with intensive therapy, MCL patients ultimately relapse.[15] Novel targeted therapies currently approved for R/R MCL include[14] the mTOR inhibitor temsirolimus, the immunomodulatory agent lenalidomide, the proteasome inhibitor bortezomib,[16] also approved in front-line, and the BTK inhibitor ibrutinib that achieves the highest response rates.[17] However, MCL patients failing ibrutinib treatment have very limited therapeutic options.[18] In this situation, where virtually all MCL cases express some level of CD38, this antigen represents a potential alternative target to be explored. Moreover, CD38 is associated with nodal disease and poorer survival[19,20] and high CD38 expression correlates with poor *in vivo* response to bortezomib.[21] Thus, targeting CD38 could hold promise as a strategy for MCL, also in bortezomib resistant tumors.

CD38 is present at high levels in bone marrow (BM) precursor cells and it is downregulated in resting normal B cells. The molecule is re-expressed at high density once naïve B lymphocytes are activated, and peaks when B cells enter the GC. Terminally differentiated plasma cells and their pathological counterparts express the highest surface density among human cells, while it is completely absent in memory B cells.[22] CD38 behaves simultaneously as an enzyme and as a receptor. The extracellular domain of CD38 contains an enzymatic site that can generate cyclic ADP ribose (cADPR) and ADPR from nicotine adenine dinucleotide (NAD^+). This control of adenosine synthesis by CD38 may be important in the context of the characteristic immunosuppressive tumor microenvironment.

Daratumumab (Darzalex) is a first-in-class, human IgG1κ monoclonal antibody (mAB) that targets the CD38 epitope. It was approved by the Food and Drug Administration in 2015 as a monotherapy for patients with MM, who have received at least three prior therapies.[23] Currently, daratumumab has been approved in combination with dexamethasone plus either lenalidomide or bortezomib, or pomalidomide for the treatment of relapsed MM patients.[24] Daratumumab has a broad-spectrum killing activity in MM engaging complement-dependent cytotoxicity (CDC), antibody-dependent cellular cytotoxicity (ADCC),[25] antibody-dependent cellular phagocytosis (ADCP),[26] and apoptosis.[27] Moreover, daratumumab modulates the enzymatic activity of CD38[28] and induces an immunomodulatory role in MM by depleting $CD38^+$ immune suppressive cells[29] contributing to its antitumor activity. In chronic lymphocytic leukemia (CLL), we have demonstrated that daratumumab induces cytotoxic activity *in vitro via* ADCC and ADCP in primary CLL cells and cell lines. *In vivo*, daratumumab significantly prolongs OS of animals in systemic CLL murine models. Daratumumab also affects tumor-microenvironment interactions by blocking CLL homing and dissemination to secondary lymphoid organs *in vitro* and *in vivo*.[30]

In the present study, we aimed to investigate *in vitro* and *in vivo* activity of daratumumab on MCL, FL and DLBCL cells as monotherapy and in combination with standard therapies.

Methods

Therapeutic drugs

Daratumumab (Darzalex, anti-CD38mAb, IgG1) and the isotype control mAb (CNTO 3930, IgG1) were provided by Janssen. Rituximab (Mabthera, anti-CD20 mAb, IgG1) and the chemotherapy regimen CHOP (cyclophosphamide, doxorubicin, vincristine, and prednisone) were obtained from the department of pharmacy of the Hospital Clínic of Barcelona.

Subcutaneous pre-emptive mouse models

SCID mice (Janvier Laboratories) were subcutaneously (sc) injected with $10x10^6$ RL-luc cells in the FL model or $10x10^6$ REC-1 cells in the MCL model, respectively, following a protocol approved by the Animal Testing Ethic committee of the University of Barcelona and Generalitat de Catalunya (Protocol # 9971). Mice were randomly assigned into cohorts of six mice per group and received one intraperitoneal (ip) injection of 10 mg/kg of daratumumab or isotype control every other week, starting the day of cell inoculation.

Patient-derived DLBCL xenograft model

ST1361 is a DLBCL patient-derived xenograft model developed using a DLBCL tumor originated in a metastatic site from a 58-year-old chemotherapy-naïve Hispanic male. ST1361 was GCB subtype transformed from an Epstein-Barr virus negative FL tumor.

The DLBCL tumor was homogeneously chopped into fragments of similar size and injected sc into SCID mice. Treatment was initiated when mean tumor volume was approximately 150-250 mm^3. Daratumumab 20 mg/kg was administered weekly for three weeks alone or in combination with CHOP (20 mg/kg cyclophosphamide, 1.25 mg/kg doxorubicin, 0.2 mg/kg vincristine [intravenously on Day 0], and 0.15 mg/kg prednisone [Days 0-4]; once a day (QD) for five days) or R-CHOP (10 mg/kg rituximab [intraperitoneally on Day 0]+ CHOP as before).

Statistical analysis

Unpaired and paired *t*-tests were used to assess statistical differences between two groups using GraphPad Prism software 4.0. For Kaplan-Meier survival curves, SPSS19 software was used.

Table 1. B-cell non-Hodgkin's lymphoma cell lines characterization and daratumumab activity.

Cell line	NHL subtype[1]	CD38 sABC[2]	%CD38[1]	MFIR CD38[3]	%CD20[1]	MFIR CD20[3]	%CD46[1]	%CD55[1]	%CD59[1]	%ADCC[4]	%ADCP[4]	%CDC[4]
Jeko	MCL	16253	84	22	100	46	92	98	61	58	41	7
REC-1	MCL	106234	100	155	100	77	99	99	88	60	46	18
HBL2	MCL	25317	100	92	100	99	98	96	98	28	21	0
Mino	MCL	127458	100	51	100	42	97	100	96	32	35	0
UPN1	MCL	54089	99	97	97	8	98	99	63	36	73	0
Z138	MCL	186239	100	120	100	28	100	75	69	53	89	0
DOHH2	FL	22369	87	20	99	31	100	76	98	25	38	0
SC-1	FL	71726	100	40	32	4	95	96	83	41	81	1
RL	FL	132684	96	76	93	49	100	94	97	52	45	6
WSU-FSCCL	FL	89707	97	354	8	2	82	81	94	67	92	7
Toledo	DLBCL	123539	99	186	89	13	94	99	97	34	50	14
WSU-DLCL2	DLBCL	14926	94	46	99	137	95	95	98	45	15	1
SU-DHL-6	DLBCL	174033	92	383	98	172	97	44	31	64	56	5
SU-DHL-4	DLBCL	96623	96	108	100	45	93	45	95	61	34	8
Daudi	BL	415667	100	276	99	30	88	17	9	63	79	96

[1]Percentage of positive cells for CD38, CD20, CD46, CD55 and CD59 determined by flow cytometry, referred to isotype control; [2]sABC: number of surface antibodies bound per cell evaluated by QuantiBRITETM CD38-PE; [3]MFIR: mean fluorescence ratio referred to isotype control; [4]Percentage of antibody-dependent cellular cytotoxicity (ADCC) and antibody-dependent cellular phagocytosis (ADCP) induction at 1 μg/mL daratumumab. Percentage of CDC induction at 10 μg/mL daratumumab. MCL: mantle cell lymphoma, FL: follicular lymphoma; DLBCL: diffuse large B-cell lymphoma; NHL: non-Hodgkin lymphoma; BL: Burkitt lymphoma.

Additional methodologic details are described in the *Online Supplementary Materials and Methods*.

Results

Daratumumab induces cell killing in the presence of external effectors in B-NHL

We first assessed by calcein-AM release assay, the ability of daratumumab to induce ADCC, ADCP and CDC in MCL, FL and DLBCL cell lines. Using peripheral blood mononuclear cells (PBMC) from healthy donors as external effectors we demonstrated that daratumumab engages ADCC in a panel of B-NHL cell lines (Table 1). Daratumumab induced a significant dose-dependent cell lysis reaching its maximum antitumor activity at 1 μg/mL on MCL cell lines (mean ± standard deviation [SD]=45±14%) (Figure 1A), at 0.1 μg/mL on FL cell lines (mean ± SD=48±18%) (Figure 1B), and at 0.1 μg/mL on DLBCL cell lines (mean ± SD=49±11%) (Figure 1C). The degree of ADCC induction did not correlate with the number of CD38 molecules per NHL cell specific antibody binding capacity (sABC) (r^2=0.1988; *Online Supplementary Figure S1A* and *Table 1*). A phagocytosis assay using mouse macrophages as effector cells was set up to determine daratumumab-mediated ADCP. Daratumumab induced significant ADCP at 1 μg/mL in MCL cell lines (mean ± SD=54±24; Figure 1D), FL cell lines (mean ± SD=64±26%; Figure 1E) and in DLBCL cell lines (mean ± SD=39±18%; Figure 1F). The degree of ADCP induction did not correlate with the number of CD38 sABC on NHL cell lines (r^2=0.2270; *Online Supplementary Figure S1B* and *Table 1*).

Interestingly, the daratumumab-opsonized cells that were exposed to macrophages and not phagocytosed, suffered a lost in CD38 surface expression, irrespective of the degree of ADCP induction (*Online Supplementary Figure S2*), in a process that may resemble trogocytosis as previously described in MM studies.[31,32]

We next evaluated the CDC activity and observed that, similar to that reported for CLL cells,[30] daratumumab induced low to marginal cell death in the presence of normal human serum (NHS 10%) (Table 1). Very similar results were obtained in these CDC experiments when 50% NHS was applied. The high expression of the complement regulatory proteins (CRP) CD46, CD55 and CD59, and an insufficient number of CD38 molecules per cell on NHL cells may explain the low CDC activity (Table 1).

Collectively, daratumumab effectively kills $CD38^+$ NHL cells through engagement of ADCC and ADCP but not CDC, independently of the expression levels of CD38.

Daratumumab enters and distributes homogeneously within a 3D lymphoma model

To model the compact aggregates of lymphoma cells growing in the patients' lymph nodes, 3D spheroids were generated by the hanging drop method,[33] using RL-GFP cells previously reported as an useful tool for antibody therapy studies.[34] We first sought to determine the degree to which daratumumab can penetrate these lymphoma aggregates depending on dose (1 and 10 μg/mL mAb) and time of exposure (4, 24 and 48 hours). First, we measured the percentage of mAb diffusion in the spheroid, representing the total amount of the mAb in the spheroid. The 3D reconstruction images obtained by SPIM (Figure 2A) revealed a maximum diffusion of daratumumab at 1 μg/mL after 48 hours of treatment (Figure 2B). Next, maximum depth of daratumumab in the spheroids was determined under the same conditions and represented as percentage of mAb penetration in the spheroid. As observed for the diffusion, a maximum penetration of daratumumab at 1 μg/mL after 48 hours of treatment was achieved

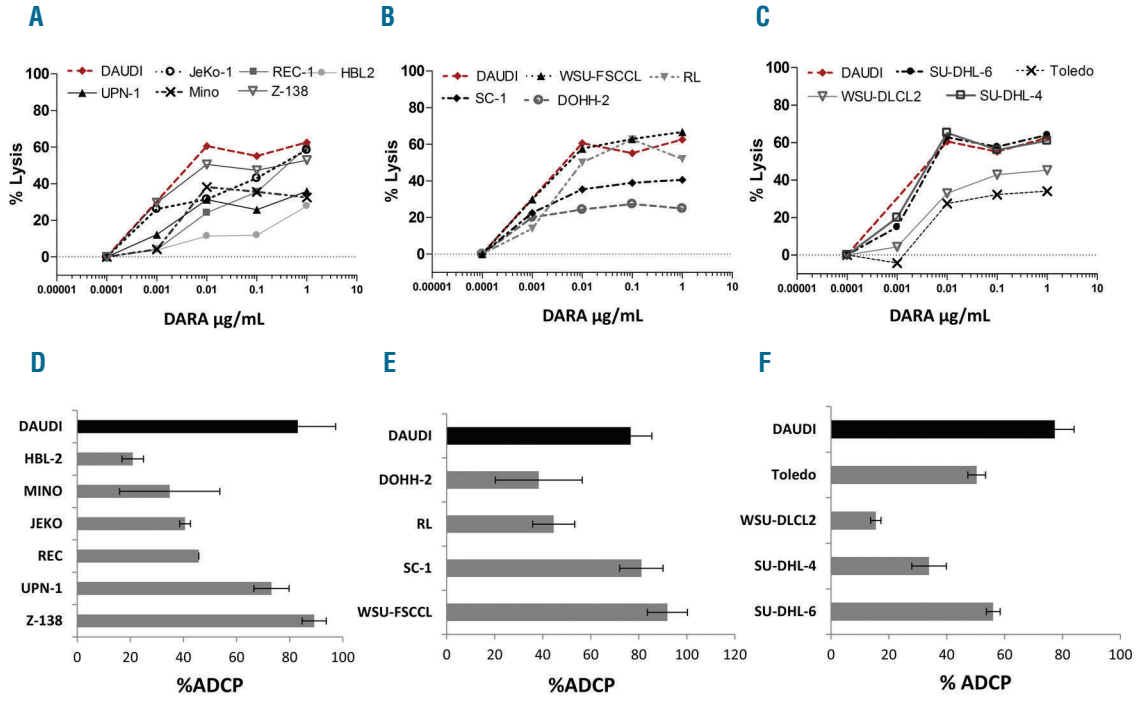

Figure 1. Daratumumab induces antibody-dependent cellular cytotoxicity and antibody-dependent cellular phagocytosis in the presence of external effectors in non-Hodgkin lymphoma. (A) Mantle cell lymphoma (MCL), (B) follicular lymphoma (FL), and (C) diffuse large B-cell lymphoma (DLBCL) cell lines were treated with increasing daratumumab doses (0.0001-1 µg/mL) in the presence of peripheral blood mononuclear cell (PBMC) from healthy donors at a E:T ratio of 50:1 for four hours. Viability was then evaluated by calcein release assay. The Burkitt lymphoma (BL) cell line, Daudi, was included as positive control. (D) MCL, (E) FL, and (F) DLBCL cell lines were labeled with calcein and incubated for 4 hours with the mΦ at an E:T ratio of 1:1 in the presence of a fixed daratumumab concentration of 1 µg/mL, followed by flow cytometry analysis in triplicates. Antibody-dependent cellular phagocytosis (ADCP) was calculated as the percentage of $CD19^+$ $calcein^+F4/80^-$ cells after daratumumab treatment referred to isotype-treated cells. Daudi cells were included as positive control. ADCC: antibody-dependent cellular cytotoxicity

(Figure 2C). Moreover, a significant dose-dependent reduction of the spheroid volume was observed after daratumumab treatment compared to isotype control (mean ± SD=15±6%, 20±7%, respectively at 1 and 10 µg/mL) (Figure 2D) showing a direct effect of daratumumab on tumor growth in 3D. This observation was validated in additional lymphoma cell lines. Daratumumab moderately but significantly (P<0.0001) reduced the spheroid volume in all the cell lines analyzed, albeit in a different degree (*Online Supplementary Figure S3A-B*), that was accompanied in most of cases by a concomitant decrease in the cell number. However, this observation did not apply to HBL-2 and *WSU-DLCL2* cell lines, where daratumumab may just generate a tighter spheroid (*Online Supplementary Figure S3C*).

These data demonstrate that daratumumab efficiently penetrates a lymphoma 3D structure and moderately reduces the growth of spheroids in the absence of external effectors.

Daratumumab prevents tumor outgrowth in MCL and FL xenografts

As a first test of daratumumab activity *in vivo* in NHL models, we inoculated SCID mice sc with two cell lines that we had previously set up: RL cells to model tFL,[35] and REC-1 cells to model MCL.[36] SCID mice have active natural killer (NK) cells and macrophages that can act as effector cells to engage daratumumab activity, as we have shown using *in vitro* models. Mice were treated with daratumumab or an isotype control (20 mg/kg) starting on the day of tumor injection. Subsequently, animals received antibody injections every other week (10 mg/kg) for a total of three doses and were sacrificed at day 30 (REC-1) (Figure 3A) or day 34 (RL) (Figure 3B). Daratumumab prevented tumor formation in all mice injected with REC-1, and in 5 of 6 mice injected with RL cells. In this latter model, a 20 mm^3 RL tumor was found in one daratumumab-treated mouse at the endpoint (day 34). As the RL cells inoculated expressed the luciferase gene, bioluminescence analysis at different time points further supported these results (Figure 3B). All animals receiving isotype control antibody formed tumors of at least 100 mm^3 within a mean of 18 days (REC-1) and 21 days (RL) and were bigger than 1,000 mm^3 at the end of the experiment.

Daratumumab prolongs OS and reduces tumor infiltration in systemic xenograft models of MCL and FL

Next, we generated a model for blastic MCL by inoculating Z-138 cells intravenously into SCID mice, and one week later mice were treated weekly with either daratumumab (D), rituximab (R) or isotype (I) control (20/10/10/10 mg/kg). Seven of ten isotype-treated mice had to be sacrificed between days 57 - 89 due to systemic signs of disease (Figure 4). Daratumumab significantly improved OS (I *vs.* D: ***P<0.001), with 90% of the mice treated with daratumumab surviving for over 107 days, (Figure 4A) compared to just 10 % alive in the controls. OS for the daratumumab group was slightly superior but did not reach statistical significance (D *vs.* R: ns, P=0.2907), compared to that observed in the rituximab-treated mice

(I *vs.* R: ***P*<0.01), where 70% of the mice were alive at day 107 (Figure 4). Mean survival was 73 days for the control group, 97 for rituximab and 103 for daratumumab groups. On autopsy, the disease had spread to the brain, BM, spleen and lungs (*Online Supplementary Figure S4A*). Daratumumab treatment reduced the disease burden in the brain, BM, and spleen by 93%, 63%, and 48%, respectively (*Online Supplementary Figure S4B*). Rituximab-treated mice showed a similar reduction in tumor load to that achieved by daratumumab in the brain (73%) and BM (69%) compared to that observed with the isotype control, while no effect was observed in spleen infiltration. Finally, daratumumab did not diminish lung infiltration, while a moderate reduction was seen in rituximab-treated mice (18%) compared to isotype control mice (*Online Supplementary Figure S4B*), suggesting an organ-dependent differential immunotherapeutic response.

In the FL systemic model, $CD20^{low}$ WSU-FSCCL cells (Table 1) were intravenously inoculated in SCID mice and one week later mice were treated weekly with daratumumab, rituximab or isotype control (20/10/10/10 mg/kg). All control-treated and rituximab-treated mice rapidly succumbed to the disease and died or had to be euthanized due to severe disease signs by day 40 (control group) and day 62 (rituximab group), respectively (Figure 4). In contrast, in the daratumumab-treated group, OS was significantly prolonged (I *vs.* D: ****P*<0.001; I *vs.* R: ***P*<0.01; D *vs.* R **P*< 0.05). Mean survival was 35 days for the control group, 41 for rituximab and 60 for daratumumab. By the end of the experiment (day 90), 30% of mice treated with daratumumab were cured (Figure 4). On autopsy, WSU-FSCCL cells showed systemic dissemination of disease in the brain, BM and spleen (identified as $huCD45^{+}/CD19^{+}CD10^{+}$; *Online Supplementary Figure S4C*). Daratumumab robustly decreased dissemination to the brain (90%, *P*< 0.01) compared to the control group, while rituximab was not effective (*Online Supplementary Figure S4D*). Homing of WSU-FSCCL cells to the spleen and BM was less prominent. There were no significant differences in the reduction of dissemination to the spleen and BM by daratumumab compared to the rituximab-treated group (*Online Supplementary Figure S4C*).

Altogether, these data confirm that daratumumab shows comparable to superior activity with respect to rituximab in systemic models of MCL and FL.

Daratumumab synergizes with R-CHOP to reduce tumor burden in pre-clinical models of MCL and FL

The synergy between daratumumab and rituximab and/or chemotherapy regimens was evaluated in MCL (REC-1) and tFL (RL) xenograft heterotopic models. SCID mice were inoculated subcutaneously with NHL cells and when tumors became palpable, mice were randomly assigned into the following groups: i) Isotype ii) daratumumab iii) CHOP iv) D-CHOP v) R-CHOP and vi) R-D-CHOP. Tumor volume was assessed twice a week and tumor weights at sacrifice. In the MCL model (Figure 5A), daratumumab induced significant anti-tumor activity

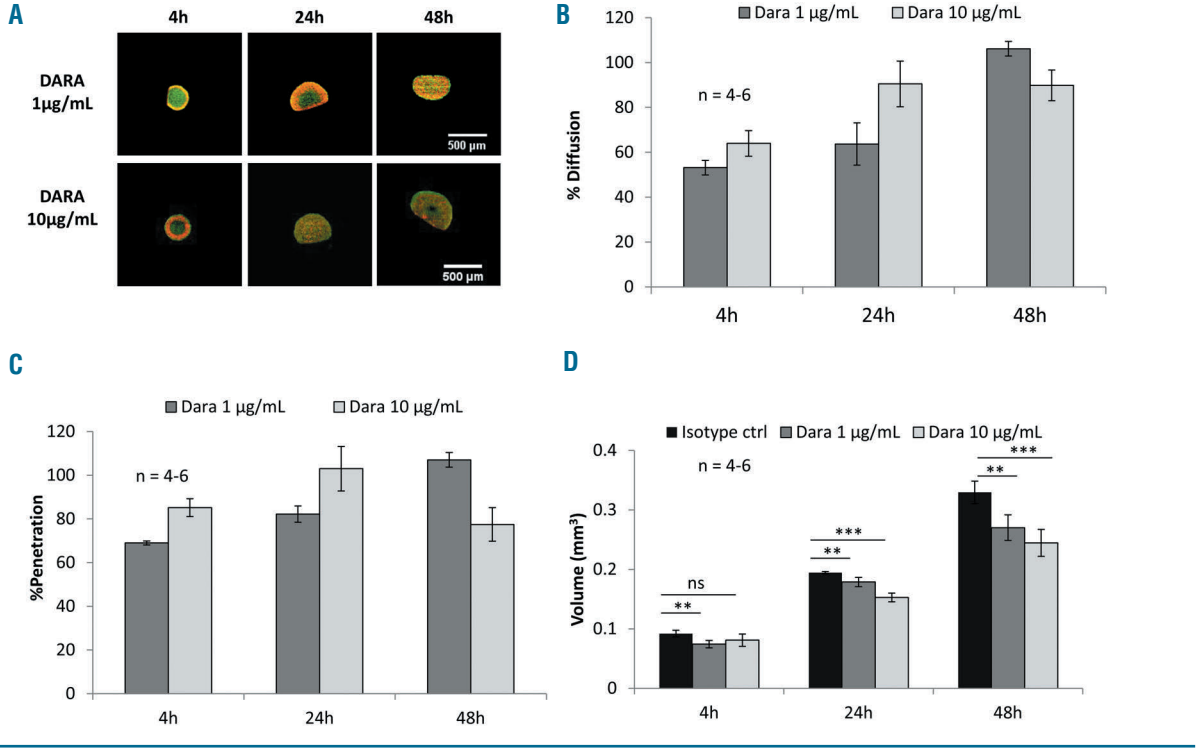

Figure 2. Daratumumab effect in a three-dimensional model of follicular lymphoma. Three-dimesional (3D) spheroids of RL-GFP cells were obtained after three days of culture in hanging drop plates or 96-well ultra-low attachment plates, and then treated with 10 µg/mL of Isotype control (IgG1), or 1 or 10 µg/mL of daratumumab at different times. (A) 3D reconstruction images produced by SPIM; fluorescence was measured at a λ_{ex} of 488nm (GFP) and 561nm (monoclonal antibody [mAb] labeling). (B) Percentage of mAb diffusion, representing quantity of the mAb in the spheroid. (C) Percentage of mAb penetration, representing maximum depth of the mAb in the spheroid. (D) Spheroid volume (mm^3) time course (n=number of spheroids per treatment). Statistical differences between groups were assessed by unpaired *t*-test (***P*<0.01; ****P*<0.001).

compared to the isotype control (42%, $P< 0.01$). CHOP alone marginally reduced tumor growth ($P=0.182$) and no difference was observed between daratumumab and D-CHOP groups ($P=0.451$). Importantly, adding rituximab to D-CHOP treatment (R-D-CHOP) induced a significant reduction in tumor volume compared to the isotype control (86%, $P<0.001$) and also compared to R-CHOP (73%, $P<0.001$) and D-CHOP (51%, $P< 0.05$) alone. Similarly, in the tFL model (Figure 5C-D), daratumumab treatment inhibited tumor growth compared to isotype control (36%, $P<0.001$). On the other hand, the combination D-CHOP inhibited tumor growth significantly better than daratumumab as a single agent (57%, $P<0.001$), resembling that achieved by R-CHOP (67%, $P<0.001$). In addition, the combination regimen of R-D-CHOP had a remarkable effect in impeding tumor growth (84% inhibition, $P<0.001$), which was superior than that achieved by each combination regimen separately ($P<0.001$). The results of the RL-luc model were further validated by bioluminescence and quantification of the signal captured at the endpoint (*Online Supplementary Figure S5A-B*). Moreover, tissue sections of selected mice of each group were analyzed by immunohistochemistry for the proliferation marker pH3 and the angiogenesis marker CD31, further confirming these results (*Online Supplementary Figure S5C*).

In conclusion, these data demonstrate the value of the combination R-D-CHOP as a new therapeutic strategy in MCL and tFL superior to the standard-of-care (R-CHOP).

Daratumumab induces tumor growth inhibition and prolongs survival in a patient-derived DLBCL xenograft model in combination with R-CHOP

To further evaluate the activity of daratumumab alone or in combination with the standard-of-care therapy we used a clinically more relevant patient-derived DLBCL xenograft model (ST1361) with detectable CD38 expression by immunohistochemistry (*Online Supplementary Figure S6*). Identical to the MCL and tFL models, all individual treatments were capable of reducing tumor volume over time ($P<0.001$, Figure 6A); however, daratumumab alone was strikingly efficient with an anti-tumor activity

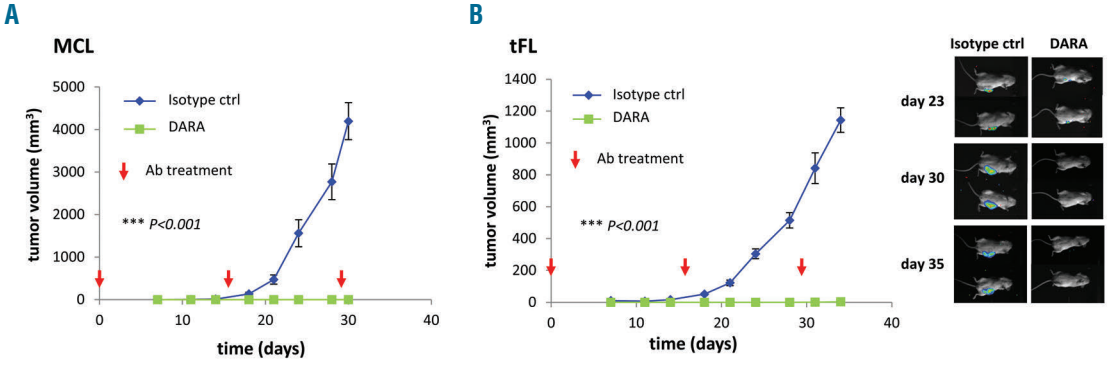

Figure 3. Daratumumab efficacy in pre-emptive models of mantle cell lymphoma and transfomed follicular lymphoma. 10x10^6 REC-1 cells (A) or RL-luc cells (B) were mixed with matrigel (1:1) and subcutaneously injected in SCID mice (n=6 per group). Animals received one dose every other week (10 mg/kg of isotype control [IgG1] or dartumumab) starting the day of cell inoculation. Tumor growth curves over time clearly show total regression was achieved in both models. As RL cell line expressed the luciferase gene, sequential bioluminescence images were captured at different time points (B). Statistical differences between groups were assessed by unpaired *t*-test (***P<0.001). MCL: mantle cell lymphoma; tFL: transfomed follicular lymphoma.

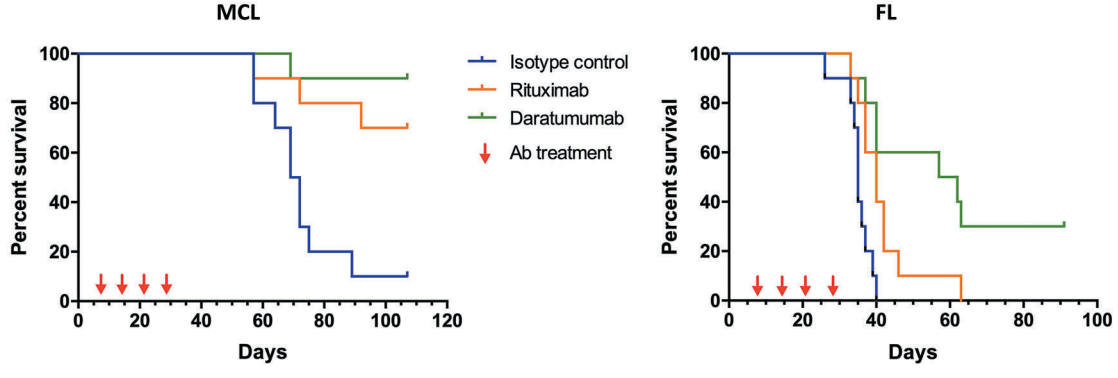

Figure 4. Daratumumab monotherapy in a systemic model of mantle cell lymphoma and follicular lymphoma compared to rituximab. 10x10^6 Z-138 mantle celle lymphoma (MCL) and WSU-FSCCL follicular lymphoma (FL) cells were intravenously injected in SCID mice (n=10 per group). Treatment (isotype control [IgG1]/ daratumumab/ rituximab) started one week after inoculation and went on weekly for four weeks (20/10/10/10 mg/kg), as indicated by the red arrows. Mice were monitored twice weekly for any sign of disease and were euthanized when body weight decreased 15-20%. Survival curves are represented. Statistical differences between groups were assessed by log-rank test. Z-138: Overall significance***P<0.001; Isotype; control *vs.* daratumumab ***P<0.01; daratumumab *vs.* rituximab not signficant (ns) P=0.2907. WSU-FSCCL: Overall significance ***P<0.001; isotype control *vs.* daratumumab ***$P\leq$0.001; daratumumab vs rituximab *P=0.045.

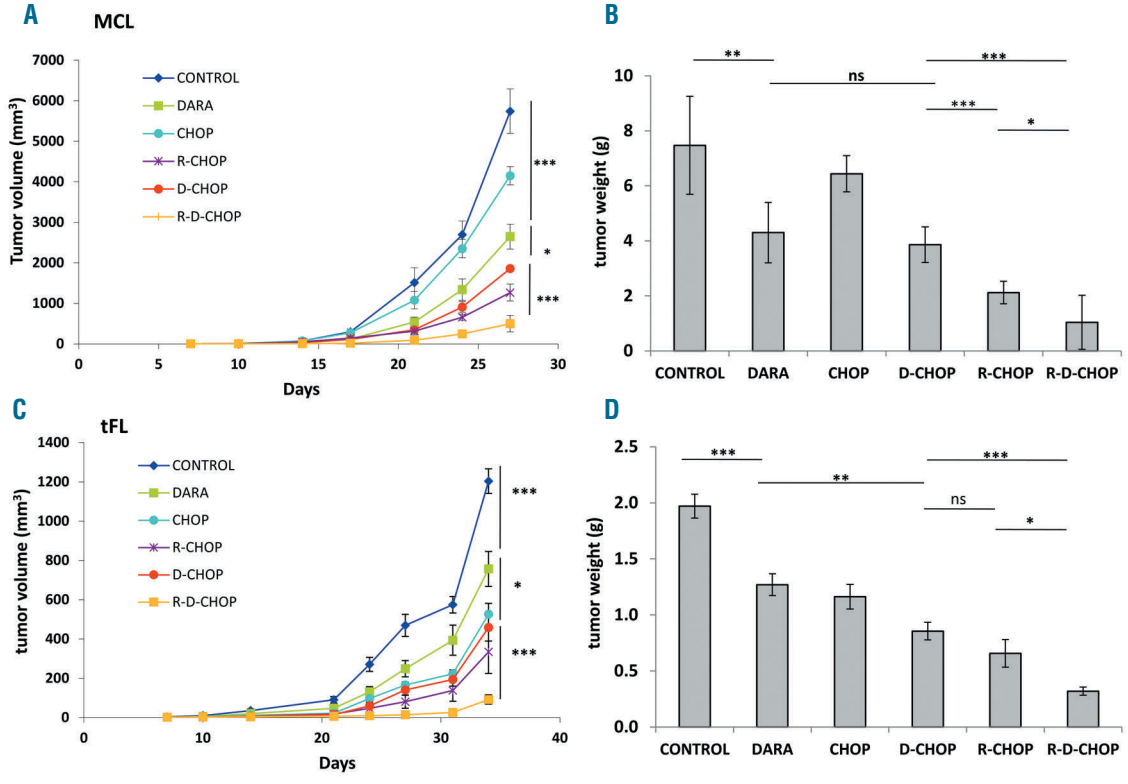

Figure 5. Daratumumab combined with R-CHOP in mantle cell lymphoma and transformed follicular lymphoma. 10x10⁶ REC-1 (A-B) and RL-luc (C-D) cells were mixed with matrigel (1:1) and subcutaneously injected in SCID mice (REC-1: n=5-7 per group; RL: n=7-10 per group). Treatment as monotherapy (isotype control [IgG1]/ daratumumab/ rituximab/ CHOP) or the combination regimen DARA ± RITUX ± CHOP started one week after inoculation and went on weekly for three weeks for the monoclonal antbodies (mAb) (20/10/10 mg/kg) in the REC model, and four weeks (20/10/10/10 mg/kg) for the RL model. CHOP was given as an initial unique dose the first day of treatment in both models. Tumor growth curves over time are represented for each cohort (A and C). Tumor weight for each treatment was averaged and represented at endpoint for REC-1 (B) and RL models (D). Statistical differences between groups were assessed by unpaired *t*-test (***P*<0.01; ****P*<0.001).

comparable to R-CHOP (*P*<0.001, Figure 6A). Furthermore, the addition of daratumumab to either CHOP or R-CHOP led to full tumor regression (*P*<0.001, Figure 6A). Importantly, tumor volume negatively correlated very well with the OS of xenograft-bearing mice, regardless the treatment group (Figure 6B). Thus, mice treated with either daratumumab alone or R-CHOP displayed identical OS and, in line with the full tumor regression achieved, daratumumab combined with either CHOP or R-CHOP resulted in 100% survival at the end of the experiment (*P*<0.05 after Bonferroni multiplicity correction, Figure 6A). Remarkably, full tumor regression and 100% survival at day 60 were observed even when daratumumab treatment was ceased as early as 14 days (total of three doses) after tumor cell inoculation. Collectively, these results indicate that tumor cells were completely eliminated within a short time and that no tumor escape occurred in this DLBCL patient-derived model.

Discussion

In this study we have demonstrated that daratumumab engages Fc-mediated cell killing of NHL cells by ADCC and ADCP. Variation in the extent of ADCC and ADCP could not be explained by the differences in CD38 expression levels. Similar observations were also reported for daratumumab-induced ADCC and ADCP in CLL cells.[30] The capacity of daratumumab to induce ADCC and phagocytosis may to some extent be related to other factors, such as the expression of different types of FcγR, KIRs and Natural Cytotoxic Receptors (NCR) on NK cells.[37] Moreover, the expression of the so-called 'don't eat me' signals, such as CD47, on tumor cells plays an important role in regulating phagocytosis. In fact, CD47 expression has been found to be increased on MCL, FL and DLBCL cells compared to normal cells, conferring a worse clinical prognosis.[38] Moreover, in agreement with previous results in MM,[32] the daratumumab-opsonized cells that were exposed to macrophages and not phagocytosed, suffered a loss in CD38 surface expression. This event may reduce the ability of daratumumab to kill lymphoma cells via CDC and ADCC, compromising the therapeutic efficacy of daratumumab. However, MM studies demonstrated that this phenomenon occurs early in the treatment irrespective of their clinical responses.[32] Therefore, CD38 reduction *via* trogocytosis should not necessarily be considered as an escape mechanism from daratumumab treatment. On the contrary, trogocytosis may be beneficial and represent a novel mechanism of action of daratumumab, as there is also a transfer of tumor cell membrane fragments containing important signaling molecules such as CD56 CD49d and CD138 in this process. The decreased expression of these adhesion molecules in tumor cells may

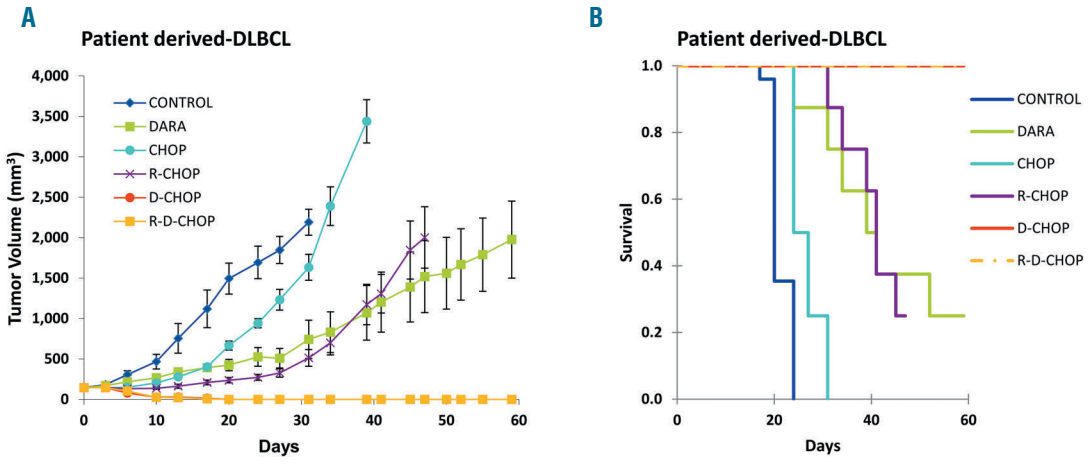

Figure 6. Daratumumab combined with R-CHOP in a patient-derived diffuse large B-cell lymphoma xenograft model. Fragments from a patient-derived diffuse large B-cell lymphoma (DLBCL) were injected subcutaneously into SCID mice (n=8-10) and staged to approximately 150-250 mm^3 mean tumor volume to measure (A) tumor growth and (B) overall survival (OS). 20 mg/kg daratumumab was administered weekly alone or in combination with CHOP (20 mg/kg cyclophosphamide, 1.25 mg/kg doxorubicin, 0.2 mg/kg vincristine, and 0.15 mg/kg prednisone) or R-CHOP (10 mg/kg rituximab+ CHOP) for a total of three weeks.

compromise their interaction with the tumor microenvironment as we reported in a previous work.[30]

Daratumumab did not induce CDC in FL, or DLBCL or MCL cell lines. Flow cytometry analysis demonstrated that MCL and FL cells show medium to high expression of CD38 while DLBCL cells tend to express higher levels of CD38. However, the number of molecules per cell in these NHL cell lines was lower than that found on the CDC-sensitive Daudi Burkitt lymphoma cell line, suggesting a threshold for CD38-targeted CDC lysis. In addition, this low induction of CDC was also associated with high expression of the CRP CD55 and CD59 that were lower in Daudi cells. These observations are in line with our previous data obtained for CLL cell lines and primary cells.[30] Overall, the baseline expression of CD38/CD55/CD59 appears to be associated with the response to daratumumab-induced CDC *in vitro* in FL, DLBCL and MCL cells. These results mirrored those obtain with the anti-CD20 rituximab in CLL cells.[39]

We have shown for the first time that daratumumab, at clinically achievable doses, effectively penetrates a lymphoma organoid in vitro model. A moderate but significant reduction of the sphere volume was observed with daratumumab in 3D lymphoma models, even though no significant effect was observed in a 2D model (data not shown). These results agree with daratumumab efficacy against subcutaneous tumors *in vivo* (Figure 5 and Figure 6).

In vivo results support the ability of daratumumab to prevent the outgrowth of MCL and FL cells, when administered in a prophylactic setting, prior to tumor development. These results open a window of opportunity for daratumumab as an alternative to rituximab maintenance therapy in these models, in the context of a complete response after the induction therapy.[40,41] Moreover, we have demonstrated that daratumumab shows single agent activity both in systemic and subcutaneous models of NHL, when administered after disease onset. More importantly, the data from the FL model using WSU-FSCCL cells point to a possible role for daratumumab as a therapeutic alternative to rituximab in NHL with reduced CD20 expression. Previous studies have shown a substantial and rapid reduction of CD20 in lymphoma patients treated with rituximab, which has been linked to the development of acquired resistance.[42,43] Thus, daratumumab treatment may be considered in these scenarios where anti-CD20 resistance has developed due to antigen shaving.[44] In addition, our results indicate that daratumumab significantly improves long-term survival when used as a single agent, indicating that it may be also an alternative to rituximab in NHL $CD20^{high}$, evidenced by the comparable activity of both antibodies in the blastic MCL model using Z-138 cells. We have also observed a remarkable effect of daratumumab in the tumor cell dissemination to the brain in FL and MCL systemic models. This may be related to the capacity of daratumumab to cross the hemato-encephalic barrier. In fact, daratumumab has shown efficacy in CNS plasmocytoma[45] and extramedullary myeloma.[46]

Finally, we have examined the combination of daratumumab with the standard-of-care therapy R-CHOP. Our data suggest that daratumumab significantly potentiates R-CHOP activity, inducing higher rates of tumor regression in MCL and FL. Moreover, we analyzed the efficacy of daratumumab in a DLBCL patient derived mouse xenograft, generated from a transformed FL, and usually less responsive to chemotherapy, as shown in our results where indeed the CHOP regimen displayed limited activity. In this model, daratumumab in combination only with CHOP, in the absence of rituximab leads to a complete abrogation of tumor growth. This strong synergy may be explained by the induction of stress-related cytokines by chemotherapeutic agents that can effectively target cancer cells for removal by the innate immune system through macrophage infiltration and phagocytic activity,[47] potentially augmenting the described ability of daratumumab to engage ADCP.[26]

In the phase II clinical trial CARINA, LYM2001 in R/R NHL, daratumumab monotherapy did not yield the expected results in heavily pretreated FL and DLBCL patients, while no results could be concluded in MCL because of insufficient patient recruitment. However, we have identified certain NHL scenarios were daratumumab shows comparable antitumor activity as rituximab (blastic

MCL) and other where exhibits superiority (transformed CD20dim FL). Moreover, daratumumab potentiates the antitumor activity of CHOP and R-CHOP in all three models.

In addition, as demonstrated in MM, it is likely that daratumumab may modulate the activity and frequency of CD38 expressing immune suppressive cell populations present in NHL, an effect not exerted by rituximab, and therefore may offer a superior overall antitumor effect.[29] These may be of special relevance in FL and DLBCL where infiltration of diverse T and myeloid subpopulations is specially prominent.[48] The immune-compromised mouse models used in this study preclude the analysis of this immune-modulating activity of daratumumab.

In conclusion, our findings warrant further clinical development of daratumumab in NHL providing a strong rationale for examining its clinical efficacy in different scenarios, including maintenance therapy after induction therapy, cases with anti-CD20 resistance, FL histologic transformation, and as frontline in combination with the standard of care (CHOP/ R-CHOP).

Acknowledgments

We thank Dr. Adrian Wiestner for his support with this study and his critical revision of the manuscript. Jocabed Roldan, Laura Jiménez, Sandra Cabezas and Ariadna Giro for their technical assistance. The authors would like to thank Dr J Rouquette and Ms L Teyssedre (Imaging facility, ITAV, Toulouse) for performing Daratumumab imaging within the 3D lymphoma cultures by SPIM, and Dr JJ Fournié (CRCT, Toulouse) for article comments.

Funding

This work was carried out at the Esther Koplowitz Center, Barcelona. Genmab and Janssen pharmaceuticals funded this research. Additional grants that contributed to this work included: Spanish Ministry of Economy and Competitiveness & European Regional Development Fund (ERDF) "Una manera de hacer Europa" for SAF2011/29326 and SAF2014/57708R to PP-G, SAF2015/31242R and SAF2015-31242-R to DC, CIBERONC (CB16/12/00334 and CB16/12/00225), the Integrated Excellence Grant from the Instituto de Salud Carlos III (ISCIII) PIE1313/00033 to EC and PP-G, and finally Generalitat de Catalunya support for AGAUR 2017SGR1009 to DC.

References

1. Chihara D, Nastoupil LJ, Williams JN, Lee P, Koff JL and Fowers CR. New insights into the epidemiology of non-Hodgkin lymphoma and implications for therapy. Expert Rev Anticancer Ther. 2015; 15(5):531-544.
2. Swerdlow SH, Campo E, Harris NL, et al. WHO Classification of tumours of haematopoietic and lymphoid tissues. 2008.
3. Swerdlow SH, Campo E, Pileri SA, et al. The 2016 revision of the World Health Organization (WHO) classification of lymphoid neoplasms. Blood. 2016; 127(20):2375-2390.
4. Lossos IS, Gascoyne RD. Transformation of follicular lymphoma. Best Pr Res Clin Haematol. 2011;24(2):147-163.
5. Hiddemann W, Kneba M, Dreyling M, et al. Frontline therapy with rituximab added to the combination of cyclophosphamide, doxorubicin, vincristine, and prednisone (CHOP) significantly improves the outcome for patients with advanced-stage follicular lymphoma compared with therapy with CHOP alone. Blood. 2005; 106(12):3725-3732.
6. Federico M, Luminari S, Dondi A, et al. R-CVP versus R-CHOP versus R-FM for the initial treatment of patients with advanced-stage follicular lymphoma: Results of the FOLL05 trial conducted by the Fondazione Italiana Linfomi. J Clin Oncol. 2013; 31(12):1506-1513.
7. Kridel R, Sehn LH, Gascoyne RD. Pathogenesis of follicular lymphoma. J Clin Invest. 2012;122(10):3424-3431.
8. Alizadeh AA, Eisen MB, Davis RE, et al. Distinct types of diffuse large B-cell lymphoma identified by gene expression profiling. Nature. 2000;403(6769):503-511.
9. Tilly H, Dreyling M. Diffuse large B-cell non-Hodgkin's lymphoma: ESMO Clinical Recommendations for diagnosis, treatment and follow-up. Ann Oncol. 2009;20 Suppl 4:110-112.
10. Lim SH, Vaughan AT, Ashton-Key M, et al. Fc gamma receptor IIb on target B cells promotes rituximab internalization and reduces clinical efficacy. Blood. 2011; 118(9):2530-2540.
11. Edelmann J, Gribben JG. Obinutuzumab for the treatment of indolent lymphoma. Futur Med. 2016;12(15):1769-1781.
12. Mantei K, Wood BL. Flow cytometric evaluation of CD38 expression assists in distinguishing follicular hyperplasia from follicular lymphoma. Cytom Part B Clin Cytom. 2009;76(5):315-320.
13. Pérez-Galán P, Dreyling M, Wiestner A. Mantle cell lymphoma: biology, pathogenesis, and the molecular basis of treatment in the genomic era. Blood. 2011;117(1):26-38.
14. Campo E and Rule S. Mantle cell lymphoma: evolving management strategies. Blood. 2015;125(1):48-55.
15. Dreyling M, Campo E, Hermine O, et al. Newly diagnosed and relapsed mantle cell lymphoma: ESMO Clinical Practice Guidelines for diagnosis, treatment and follow-up. Ann Oncol. 2017;28(suppl-4):iv62-iv71.
16. Cavalli F. Bortezomib-based therapy for mantle-cell lymphoma. N Engl J Med. 2015;372(23):2271.
17. Wang ML, Rule S, Martin P, et al. Targeting BTK with ibrutinib in relapsed or refractory mantle-cell lymphoma. N Engl J Med. 2013;369(6):507-516.
18. Martin P, Maddocks K, Leonard JP, et al. Postibrutinib outcomes in patients with mantle cell lymphoma. Blood. 2016; 127(12):1559-1663.
19. Orchard J, Garand R, Davis Z, et al. A subset of t(11; 14) lymphoma with mantle cell features displays mutated IgV H genes and includes patients with good prognosis, nonnodal disease. Blood. 2003; 101(12):4975-4981.
20. Camacho FI, Algara P, Rodríguez A, et al. Molecular heterogeneity in MCL defined by the use of specific V H genes and the frequency of somatic mutations. Blood. 2003; 101(10):4042-4046.
21. Pérez-Galán P, Mora-Jensen H, Weniger MA, et al. Bortezomib resistance in mantle cell lymphoma is associated with plasmacytic differentiation. Blood. 2011; 117(2):542-553.
22. Deaglio S, Vaisitti T, Aydin S, Ferrero E, Malavasi F. In-tandem insight from basic science combined with clinical research: CD38 as both marker and key component of the pathogenetic network underlying chronic lymphocytic leukemia. Blood. 2006;108(4):1135-1144.
23. McKeage K. Daratumumab: First Global Approval. Drugs. 2016;76(2):275-281.
24. https://www.accessdata.fda.gov/drugsatfda_docs/label/2017/761036s005lbl.pdf. Janssen Biotech Inc. DarzalexTM (daratumumab): prescribing information 2017;1-29.
25. de Weers M, Tai Y-T, van der Veer MS, et al. Daratumumab, a novel therapeutic human CD38 monoclonal antibody, induces killing of multiple myeloma and other hematological tumors. J Immunol. 2011;186(3):1840-1848.
26. Overdijk MB, Verploegen S, Bögels M, et al. Antibody-mediated phagocytosis contributes to the anti-tumor activity of the therapeutic antibody daratumumab in lymphoma and multiple myeloma. MAbs. 2015;7(2):311-320.
27. Overdijk MB, Jansen JHM, Nederend M, et al. The therapeutic CD38 monoclonal antibody daratumumab induces programmed cell death via Fc Receptor-mediated cross-linking. J Immunol. 2016;197(3):807-813.
28. Lammerts van Bueren J, Jakobs D, Kaldenhoven N, et al. Direct in vitro comparison of daratumumab with Surrogate analogs of CD38 antibodies MOR03087, SAR650984 and Ab79 [abstract]. Blood. 2014;124(21):Abstract 3474.
29. Krejcik J, Casneuf T, Nijhof IS, et al. Daratumumab depletes CD38+ immune-regulatory cells, promotes T-cell expansion, and skews T-cell repertoire in multiple myeloma. Blood. 2016;128(3):384-394.
30. Matas-Céspedes A, Vidal-Crespo A, Rodriguez V, et al. The human CD38 mon-

oclonal antibody daratumumab shows antitumor activity and hampers leukemia-microenvironment interactions in chronic lymphocytic leukemia. Clin Cancer Res. 2017;23(6):1493-505.
31. Krejcik J, van de Donk NWCJ. Trogocytosis represents a novel mechanism of action of daratumumab in multiple myeloma. Oncotarget. 2018;9(72):33621-33622.
32. Krejcik J, Frerichs KA, Nijhof IS, et al. Monocytes and granulocytes reduce CD38 expression levels on meloma cells in patients treated with daratumumab. Clin Cancer Res. 2017;23(24):7498-7511.
33. Eder T, Eder IE. 3D Hanging drop culture to establish prostate cancer organoids. In: Koledova Z, editor. 3D Cell Culture: Methods and Protocols. New York, NY: Springer New York; p. 167-175.
34. Decaup E, Jean C, Laurent C, et al. Anti-tumor activity of obinutuzumab and rituximab in a follicular lymphoma 3D model. Blood Cancer J. 2013;9(3):131.
35. Matas-Céspedes A, Rodriguez V, Kalko SG, et al. Disruption of follicular dendritic cells-follicular lymphoma cross-talk by the pan-PI3K inhibitor BKM120 (Buparlisib). Clin Cancer Res. 2014;20(13):3458-3471.
36. Moros A, Rodríguez V, Saborit-Villarroya I, et al. Synergistic antitumor activity of lenalidomide with the BET bromodomain inhibitor CPI203 in bortezomib-resistant mantle cell lymphoma. Leukemia. 2014; 28(10):2049-2059.
37. Campbell KS, Hasegawa J. Natural killer cell biology: an update and future directions. J Allergy Clin Immunol. 2013; 132(3):536-544.
38. Chao MP, Alizadeh AA, Tang C, et al. Anti-CD47 Antibody Synergizes with Rituximab to Promote Phagocytosis and Eradicate Non-Hodgkin Lymphoma. Cell. 2010;142(5):699-713.
39. Golay J, Lazzari M, Facchinetti V, et al. CD20 levels determine the in vitro susceptibility to rituximab and complement of B-cell chronic lymphocytic leukemia: further regulation by CD55 and CD59. Blood. 2001;98(12):3383-3389.
40. Vidal L, Gafter-Gvili A, Dreyling MH, et al. Maintenance therapy for Patients with mantle cell Lymphoma (MCL) - a systematic review and meta-analysis of randomized controlled trials (RCTs). Blood. 2016; 128(22):1802.
41. Vidal L, Gafter-Gvili A, Salles G, et al. Rituximab maintenance improves overall survival of patients with follicular lymphoma-Individual patient data meta-analysis. Eur J Cancer. 2017;76216-76225.
42. Foran JM, Norton AJ, Micallef IN, et al. Loss of CD20 expression following treatment with rituximab (chimaeric monoclonal anti-CD20): A retrospective cohort analysis. Br J Haematol. 2001;114(4):881-883.
43. Beers SA, French RR, Chan HT, et al. Antigenic modulation limits the efficacy of anti-CD20 antibodies: Implications for antibody selection. Blood. 2010; 115(25):5191-5201.
44. Beum PV, Peek EM, Lindorfer MA, et al. Loss of CD20 and bound CD20 antibody from opsonized B cells occurs more rapidly because of trogocytosis mediated by Fc receptor-expressing effector cells than direct internalization by the B cells. J Immunol. 2011;187(6):3438-3447.
45. Elhassadi E, Murphy M, Hacking D, Farrell M. Durable treatment response of relapsing CNS plasmacytoma using intrathecal chemotherapy, radiotherapy, and Daratumumab. Clin Case Rep. 2018; 6(4):723-728.
46. Touzeau C, Moreau P. How I treat extramedullary myeloma. Blood. 2016; 127(8):971-976.
47. Pallasch CP, Leskov I, Braun CJ, et al. Sensitizing protective tumor microenvironments to antibody-mediated therapy. Cell. 2014;156(3):590-602.
48. Tosolini M, Algans C, Pont F, Ycart B Fournié JJ. Large-scale microarray profiling reveals four stages of immune escape in non-Hodgkin lymphomas. Oncoimmunology. 2016;5(7):e1188246.

Ferrata Storti Foundation

Haematologica 2020
Volume 105(4):1042-1054

HIF-1α is over-expressed in leukemic cells from *TP53*-disrupted patients and is a promising therapeutic target in chronic lymphocytic leukemia

Valentina Griggio,[1,2*] Candida Vitale,[1,2*] Maria Todaro,[1,2] Chiara Riganti,[3] Joanna Kopecka,[3] Chiara Salvetti,[1,2] Riccardo Bomben,[4] Michele Dal Bo,[4] Daniela Magliulo,[5] Davide Rossi,[6] Gabriele Pozzato,[7] Lisa Bonello,[2] Monia Marchetti,[8] Paola Omedè,[1] Ahad Ahmed Kodipad,[9] Luca Laurenti,[10] Giovanni Del Poeta,[11] Francesca Romana Mauro,[12] Rosa Bernardi,[5] Thorsten Zenz,[13] Valter Gattei,[4] Gianluca Gaidano,[9] Robin Foà,[12] Massimo Massaia,[14] Mario Boccadoro[1,2] and Marta Coscia[1,2]

[1]Division of Hematology, A.O.U. Città della Salute e della Scienza di Torino, Turin, Italy; [2]Department of Molecular Biotechnology and Health Sciences, University of Turin, Turin, Italy; [3]Department of Oncology, University of Turin, Turin, Italy; [4]Clinical and Experimental Onco-Hematology Unit, CRO Aviano National Cancer Institute, Aviano, Italy; [5]Division of Experimental Oncology, IRCCS San Raffaele Scientific Institute, Milan, Italy; [6]Department of Hematology, Oncology Institute of Southern Switzerland and Institute of Oncology Research, Bellinzona, Switzerland; [7]Department of Internal Medicine and Hematology, Maggiore General Hospital, University of Trieste, Trieste, Italy; [8]Hematology Day Service, Oncology SOC, Hospital Cardinal Massaia, Asti, Italy; [9]Division of Hematology, Department of Translational Medicine, University of Eastern Piedmont, Novara, Italy; [10]Fondazione Policlinico Universitario Agostino Gemelli, Rome, Italy; [11]Division of Hematology, S. Eugenio Hospital and University of Tor Vergata, Rome, Italy; [12]Hematology, Department of Translational and Precision Medicine, Sapienza University, Policlinico Umberto I, Rome, Italy; [13]Department of Medical Oncology and Hematology, University Hospital and University of Zurich, Zurich, Switzerland and [14]Hematology Unit, ASO Santa Croce e Carle, Cuneo, Italy

**VG and CV contributed equally to this study.*

Correspondence:

MARTA COSCIA
marta.coscia@unito.it

Received: February 1, 2019.

Accepted: July 4, 2019.

Pre-published: July 9, 2019.

doi:10.3324/haematol.2019.217430

Check the online version for the most updated information on this article, online supplements, and information on authorship & disclosures: www.haematologica.org/content/105/4/1042

ABSTRACT

In chronic lymphocytic leukemia (CLL), the hypoxia-inducible factor 1 (HIF-1) regulates the response of tumor cells to hypoxia and their protective interactions with the leukemic microenvironment. In this study, we demonstrate that CLL cells from *TP53*-disrupted (*TP53*^{dis}) patients have constitutively higher expression levels of the α-subunit of HIF-1 (HIF-1α) and increased HIF-1 transcriptional activity compared to the wild-type counterpart. In the *TP53*^{dis} subset, HIF-1α upregulation is due to reduced expression of the HIF-1α ubiquitin ligase von Hippel-Lindau protein (pVHL). Hypoxia and stromal cells further enhance HIF-1α accumulation, independently of *TP53* status. Hypoxia acts through the downmodulation of pVHL and the activation of the PI3K/AKT and RAS/ERK1-2 pathways, whereas stromal cells induce an increased activity of the RAS/ERK1-2, RHOA/RHOA kinase and PI3K/AKT pathways, without affecting pVHL expression. Interestingly, we observed that higher levels of *HIF-1A* mRNA correlate with a lower susceptibility of leukemic cells to spontaneous apoptosis, and associate with the fludarabine resistance that mainly characterizes *TP53*^{dis} tumor cells. The HIF-1α inhibitor BAY87-2243 exerts cytotoxic effects toward leukemic cells, regardless of the *TP53* status, and has anti-tumor activity in Eμ-TCL1 mice. BAY87-2243 also overcomes the constitutive fludarabine resistance of *TP53*^{dis} leukemic cells and elicits a strongly synergistic cytotoxic effect in combination with ibrutinib, thus providing preclinical evidence to stimulate further investigation into use as a potential new drug in CLL.

Introduction

Chronic lymphocytic leukemia (CLL) patients with high-risk genomic features such as disruption of the *TP53* gene [i.e. del(17p) and *TP53* mutations] respond poorly to chemoimmunotherapy and frequently relapse.[1-9] Significant advances have been made in the treatment of CLL following the introduction of Bruton tyrosine kinase (BTK) inhibitors.[10] Ibrutinib, which is currently approved for the front-line treatment of CLL, induces long-lasting responses in the majority of patients, improving outcome with relatively limited toxicities.[10] However, patients with disruption of the *TP53* gene ($TP53^{dis}$) treated with ibrutinib are still characterized by a poorer outcome.[11]

Hypoxia inducible factor 1 (HIF-1) is an essential regulator of cell adaptation to hypoxia and is often up-regulated in tumors due to intratumoral hypoxia or activation of oncogenic pathways.[12,13] In tumors, HIF-1 fosters different tumor-promoting mechanisms, including metabolic adaptation, neoangiogenesis, cell survival and invasion.[14]

HIF-1 is a heterodimer, which consists of a constitutively expressed HIF-1β subunit and an inducible HIF-1α subunit. Besides its traditional regulation *via* proteasomal degradation, other signaling pathways, such as PI3K/AKT and RAS/ERK1-2, contribute to HIF-1α accumulation, *via* stability regulation or synthesis induction.[12,15]

HIF-1α is constitutively expressed in CLL cells compared to normal B cells due to microRNA-mediated down-regulation of the von Hippel-Lindau protein (pVHL),[16] a ubiquitin ligase responsible for HIF-1α degradation.[12] In addition, in CLL cells, HIF-1α is up-regulated by interactions with stromal cells (SC) and by exposure to hypoxic microenvironments, thus promoting the survival and propagation of leukemic cells, and their metabolic adaptation to the protective conditions of the tumor niche.[17-20] We have already reported that HIF-1α is involved in drug resistance mechanisms in patients with unmutated (UM) immunoglobulin heavy chain variable region genes (IGHV).[20] The *TP53* gene encodes one of the best-studied tumor suppressor proteins, which is often mutated in cancer, thus promoting cell survival, proliferation and drug resistance.[21] p53 may also play a pivotal role in the regulation of HIF-1α, since in conditions of prolonged hypoxia/anoxia, the protein accumulates and promotes HIF-1α destruction.[22] In solid tumors, loss of *TP53* function associates with constitutive elevated levels of HIF-1α.[12,22,23]

In this study, we found that HIF-1α is over-expressed in CLL cells from patients carrying *TP53* aberrations, also elucidating the molecular mechanisms implicated in the constitutive (*TP53*-related) and inducible (hypoxia- and SC-induced) HIF-1α upregulation. In addition, we observed that the HIF-1α inhibitor BAY87-2243 exerts potent anti-tumor functions, overcoming the constitutive fludarabine resistance of *TP53*-disrupted CLL cells, and eliciting a strong synergistic cytotoxic effect in combination with ibrutinib.

Methods

Patients' samples

A total of 102 patients with CLL, diagnosed according to the International Workshop on CLL-National Cancer Institute guidelines,[24] were included in the study [40 $TP53^{dis}$ and 62 *TP53*-wild type ($TP53^{wt}$) cases] (*Online Supplementary Table S1*). Healthy donors' (HD, n=2) samples were provided by the local blood bank. Patients were untreated or off-therapy for at least 12 months before sampling of peripheral blood (PB) for the experiments. Samples were collected after patients' informed consent in accordance with the Declaration of Helsinki and after approval by the local Institutional Review Board. PB mononuclear cells (PBMC) were isolated and characterized as detailed in the *Online Supplementary Appendix*.

Cell lines

The Burkitt's lymphoma cell line, Séraphine, and the mantle cell lymphoma cell line, Granta-519, were kindly provided by T. Zenz. The $TP53^{wt}$ and the CRISPR/Cas9-mediated *TP53* knockout version ($TP53^{ko}$) of Granta-519 and Séraphine cell lines were used in the study. The M2-10B4 murine SC line (ATCC #CRL-1972) was also used. Cell lines were maintained as reported in the *Online Supplementary Appendix*.

Animals

C57BL/6 Eμ-TCL1 mice were maintained in specific pathogen-free animal facilities and treated in accordance with European Union and Institutional Animal Care and Use Committee (number 716) guidelines. Splenic cells ($5x10^6$) were injected intraperitoneally into syngeneic C57BL/6 mice, and experiments were performed with groups of 4-6 mice. Leukemic mice were treated when tumor cells reached 10% in PB. BAY87-2243 was administered at 4 mg/kg in ethanol/solutol/water solution once daily by oral gavage. Mice were sacrificed at the end of treatment.

Cell culture

In selected experiments, CLL cells were cultured in the presence or absence of M2-10B4 SC, and exposed to PD98059 (Sigma Aldrich, Milan), Y27632 (Sigma Aldrich) or LY249002 (Sellekchem, Houston, TX, USA) for 48 hours (h). CLL cells were exposed for 48 h to BAY87-2243 (Sellekchem); 2-Fluoroadenine-9-β-D-arabinofuranoside (F-ara-A, Sigma Aldrich); ibrutinib (Sellekchem) used alone or in combination, at the indicated concentrations. Culture conditions were normoxia or mild hypoxia (1% O_2), 5% CO_2 at 37°C.

Western blot

Full details can be found in the *Online Supplementary Appendix* together with the list of antibodies used for western blot (WB) analyses.

Quantitative real-time polymerase chain reaction

Full details of quantitative real-time polymerase chain reaction (qRT-PCR) experiments can be found in the *Online Supplementary Appendix* together with the list of primer sequences.

Gene set enrichment analysis

Gene set enrichment analysis (GSEA, *http://www.broad.mit.edu/gsea/index.jsp*) was performed as previously described.[25,26] Gene sets were assessed as significantly enriched in one of the phenotypes if the nominal *P*-value and the false discovery rate (FDR)-q value were <0.05.

RHOA and RAS, ERK1-2, AKT and RHOA kinase activity

The isoprenylated membrane-associated RAS or RHOA proteins and the non-isoprenylated cytosolic forms were detected as previously described.[20] Details of measurement of ERK1-2, AKT and RHOA kinase activity are reported in the *Online Supplementary Appendix*.

Cell viability assay

Cell viability was evaluated by flow cytometry using Annexin-V/Propidium Iodide (Ann-V/PI) staining with the MEBCYTO-Apoptosis Kit (MBL Medical and Biological Laboratories, Naka-ku Nagoya).

Statistical analysis

GraphPad Prism (version 6.01, San Diego, CA, USA) was used to perform paired and unpaired *t*-test, and to calculate Pearson correlation coefficient. Results are expressed as mean±standard error of mean (SEM), unless otherwise specified. Statistical significance was defined as a $P<0.05$. Combination analysis was performed using Compusyn software; combinations were considered synergistic when the combination index (CI) was <1.

Results

HIF-1α is over-expressed in chronic lymphocytic leukemia cells from *TP53*^{dis} patients and in *TP53* knockout lymphoma cell lines

Expression levels of HIF-1α protein were comparatively evaluated in HD CD19$^+$ cells, and in CLL cells isolated from *TP53*^{dis} and *TP53*^{wt} samples. As expected, HD CD19$^+$ B cells did not express HIF-1α at the baseline normoxic conditions (*data not shown*). In contrast, leukemic cells from CLL patients exhibited detectable cytosolic and nuclear HIF-1α protein (Figure 1A). Interestingly, CLL cells from patients carrying *TP53* abnormalities (*TP53*^{dis} CLL cells) had significantly higher amounts of the cytosolic and nuclear fractions of HIF-1α subunit, as well as higher *HIF-1A* mRNA levels compared to CLL cells isolated from *TP53*^{wt} cases (*TP53*^{wt} CLL cells) (Figure 1A and B). We evaluated an enlarged cohort of cases and observed that the association between the expression of HIF-1α and the *TP53* status was not influenced by the IGHV mutational status (*Online Supplementary Figure S1*). The transcriptional activity of HIF-1α was evaluated through the expression of selected target genes.[13,15,27] We found a higher expression of *GLUT1* and *ENO1* in *TP53*^{dis} CLL cells, compared to *TP53*^{wt} samples (Figure 1C and D). To corroborate the finding of an association between HIF-1α expression and *TP53* status we exploited cell line models. Interestingly, the expression of HIF-1α protein and mRNA was higher in *TP53*^{ko} Granta-519 and Séraphine lymphoma cell lines, compared to the *p53*^{wt} (Figure 1E and F). In line with this finding, expression of *VEGF, GLUT1* and *ENO1* was also significantly higher in *TP53*^{ko} than in *TP53*^{wt} Granta-519 and Séraphine cell lines (Figure 1G).

To further investigate the link between TP53 and HIF-1α, we performed GSEA on previously published microarray data from tumor cells isolated from seven *TP53*^{dis} and 13 *TP53*^{wt} cases (geocode GSE18971).[28] Data of GSEA cases revealed that the *TP53* abnormalities were associated with an upregulation of a number of genes belonging to the "*GROSS_HYPOXIA_VIA_ELK3_AND_HIF1A_UP*" gene set (Figure 2A). The protein ELK3 participates in the transcriptional response to hypoxia and controls the expression of several regulators of HIF-1α stability.[29] Consistently, the baseline expression of ELK3 was higher in *TP53*^{dis} compared to *TP53*^{wt} CLL cells (Figure 2B).

Given its role in HIF-1α regulation,[12,30] we also compared pVHL expression in *TP53*^{dis} and *TP53*^{wt} samples. Notably, CLL cells from *TP53*^{dis} patients had reduced amounts of pVHL compared to *TP53*^{wt} patients, most likely being responsible for better stabilization of the HIF-1α protein and a repression of its proteasomal degradation in *TP53*^{dis} cells (Figure 2C). As for HIF-1α expression, there were no differences between pVHL levels according to IGHV mutational status (*Online Supplementary Figure S2*). These data suggest that *TP53* abnormalities lead to a reduced expression of pVHL and subsequently to an accumulation of HIF-1α protein.

Hypoxia and stromal cells further increase HIF-1α expression in chronic lymphocytic leukemia cells from *TP53*^{dis} and *TP53*^{wt} patients

We next investigated whether microenvironmental signals, such as oxygen deprivation[12] and the interactions with SC,[20] had differential effects on HIF-1α according to the *TP53* status of the leukemic cells, also in an attempt to better define the underlying molecular mechanisms. To this end, CLL cells were cultured for 48 h in condition of hypoxia or in the presence of SC. Of note, *ex vivo* culture partially abrogated the *TP53*-related differential expression of HIF-1α observed at the baseline in freshly isolated CLL cells. In hypoxia, we observed a marked upregulation of the cytosolic and nuclear fractions of HIF-1α protein, which was independent of *TP53* status (Figure 3A), and was associated to a reduced expression of pVHL (Figure 3B), and to an activation of the PI3K/AKT and RAS/ERK1-2 pathways (Figure 3C-F). Consistently, we observed that blocking concentration of pharmacologic agents inhibiting ERK1-2 (PD98059) and PI3K (LY294002) effectively counteracted the hypoxia-induced HIF-1α upregulation, independently of *TP53* status (Figure 3G).

In line with previous data,[20] we observed a marked upregulation of the cytosolic and nuclear amounts of the HIF-1α when CLL cells were co-cultured with SC (Figure 4A). SC-induced HIF-1α elevation was not associated to a reduced pVHL expression in leukemic cells (Figure 4B), whereas we observed an increased activation of RHOA/RHOA kinase (Figure 4C and D), PI3K/AKT (Figure 4E), and RAS/ERK1-2 (Figure 4F) signaling pathways. As confirmation, we found that targeted inhibition of ERK1-2, PI3K and RHOA kinase by blocking concentrations of pharmacologic agents (i.e. PD98059, LY294002 and Y27632, respectively) effectively counteracted SC-induced HIF-1α upregulation (Figure 4G).

The role of these pathways in modulating HIF-1α overexpression was corroborated by titration experiments showing that exposure of *TP53*^{dis} and *TP53*^{wt} CLL cells to increasing concentrations of PD98059, LY294002 and Y27632 induced a progressive reduction of the activity of the targeted kinases, which was associated to a dose-dependent decrease in HIF-1α levels (*Online Supplementary Figure S3*).

The selective HIF-1α inhibitor BAY87-2243 has anti-tumor activities in chronic lymphocytic leukemia

In line with the role of HIF-1α as a promoting factor for cell survival,[12] we found a positive correlation between the baseline levels of HIF-1A mRNA and the 48-h viability of CLL cells during *in vitro* culture (Figure 5A). Consistently, the viability of leukemic cells isolated from samples characterized by baseline *HIF-1A* mRNA levels above the median value of the entire cohort (*HIF-1A*^{high}) was significantly higher than the viability of CLL cells displaying lower *HIF-1A* values (*HIF-1A*^{low}) (Figure 5B and *Online*

Supplementary Figure S4). Based on these observations, and on previous data reporting HIF-1α as a potential therapeutic target in CLL,[17] we evaluated the anti-tumor effect of BAY87-2243, a selective inhibitor of HIF-1α. First, we observed that BAY87-2243 effectively inhibited HIF-1α protein expression at the cytosolic and nuclear level, both in *TP53*^{dis} and *TP53*^{wt} CLL cells (Figure 5C), also counteracting the HIF-1α upregulation exerted by hypoxia and SC (Figure 5D and E). After 48 h, BAY87-2243 determined a strong cytotoxic effect toward leukemic cells isolated from both patient subsets (Figure 5F and *Online Supplementary Figure S5*). Of note, the downregulation of HIF-1α was also evident at 24-h exposure, when cell viability was still well preserved, thus confirming that it was determined by a targeted inhibitory effect rather than by a consequence of cell death (*data not shown*). BAY87-2243 exerted a cyto-

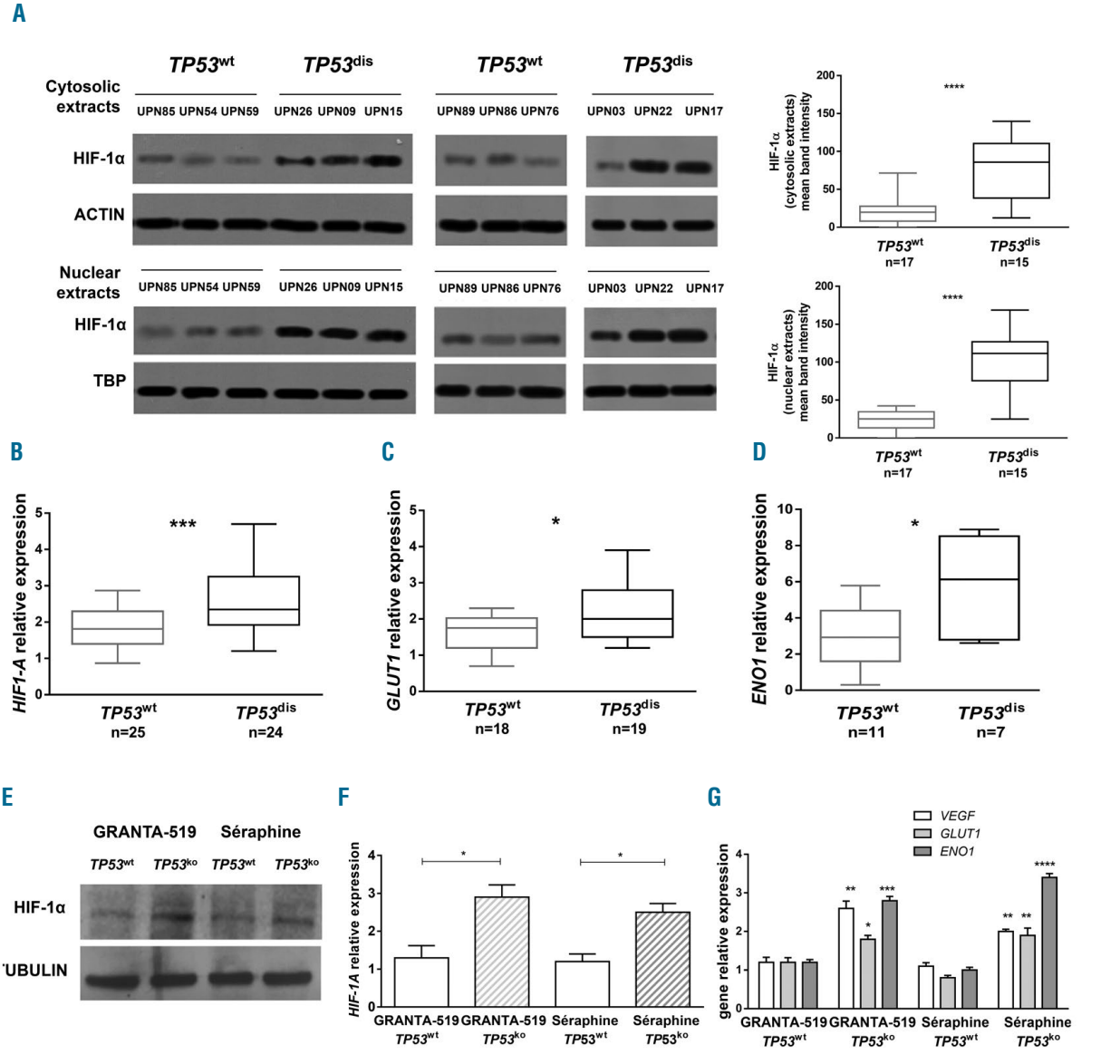

Figure 1. HIF-1α is over-expressed and more active in primary cells isolated from patients with chronic lymphocytic leukemia (CLL) and in lymphoma cell lines carrying a *TP53* disruption. The expression of HIF-1α and HIF-1α target genes was measured in *TP53*^{dis} and *TP53*^{wt} CLL cells and in lymphoma *TP53*^{wt} and *TP53*^{ko} cell lines. (A) Western blot (WB) analysis for HIF-1α protein expression in freshly isolated *TP53*^{dis} and *TP53*^{wt} CLL cells. A representative blot is shown with relative Unique Patient Numbers (UPN) and cumulative band intensity data obtained from the analysis of 17 *TP53*^{wt} and 15 *TP53*^{dis} CLL patients. Box plots represent median value and 25-75% percentiles, whiskers represent minimum and maximum values of band intensity for each group. (B-D) Real-time-polymerase chain reaction (RT-PCR) analysis of *HIF-1A*, and its target genes *GLUT1* and *ENO1* expression levels in *TP53*^{dis} and *TP53*^{wt} CLL cells. (E) WB analysis for HIF-1α protein expression in the *TP53*^{wt} and *TP53*^{ko} Granta-519 and Séraphine cell lines. Representative blot of three independent experiments is shown. (F) RT-PCR analysis of HIF-1A in the *TP53*^{wt} and *TP53*^{ko} Granta-519 and Séraphine cell lines. (G) RT-PCR analysis of *VEGF, GLUT1* and *ENO1* in the *TP53*^{wt} and *TP53*^{ko} Granta-519 and Séraphine cell lines showed a significantly higher expression level of all analyzed genes in *TP53*^{ko} samples.(B, C and D) Box and whiskers plots represent median values and 25-75% percentiles; whiskers represent minimum and maximum values for each group. (F and G) Bar graphs represent mean results obtained from three experiments together with standard error of mean. **P*<0.05; ***P*<0.01; ****P*<0.001; *****P*<0.0001.

toxic effect also when *TP53*^{dis} and *TP53*^{wt} CLL cells were cultured for 48 h in the presence of extrinsic signals inducing a further upregulation of baseline levels of HIF-1α, such as hypoxia (Figure 5G and *Online Supplementary Figure S6*) and co-culture with SC (Figure 5H and *Online Supplementary Figure S7*).

To further corroborate these data and the ability of BAY87-2243 to exert effective anti-tumor functions in CLL, we used a murine model derived from the transfer of Eμ-TCL1 leukemic cells into syngeneic mice.[17] In line with the results reported by Valsecchi *et al.*,[17] showing that HIF-1α regulates the interaction of CLL cells with the bone marrow (BM) microenvironment, we observed that BAY87-2243 significantly reduced BM infiltration by leukemic cells, also inducing cytotoxicity in a consistent proportion of CLL cells (Figure 5I-K). The anti-tumor effect observed with BAY87-2243 in the BM was not evident in the PB and spleen compartments (*data not shown*), suggesting that, in a murine model of aggressive and rapidly growing CLL, HIF-1α may serve as a pro-survival factor, especially for the leukemia reservoir residing in the BM.

In conclusion, our data indicate that HIF-1α is a pro-survival factor in CLL, which can be effectively targeted by the pharmacologic agent BAY87-2243, a specific inhibitor with potent anti-tumor effects both *in vitro* and *in vivo*.

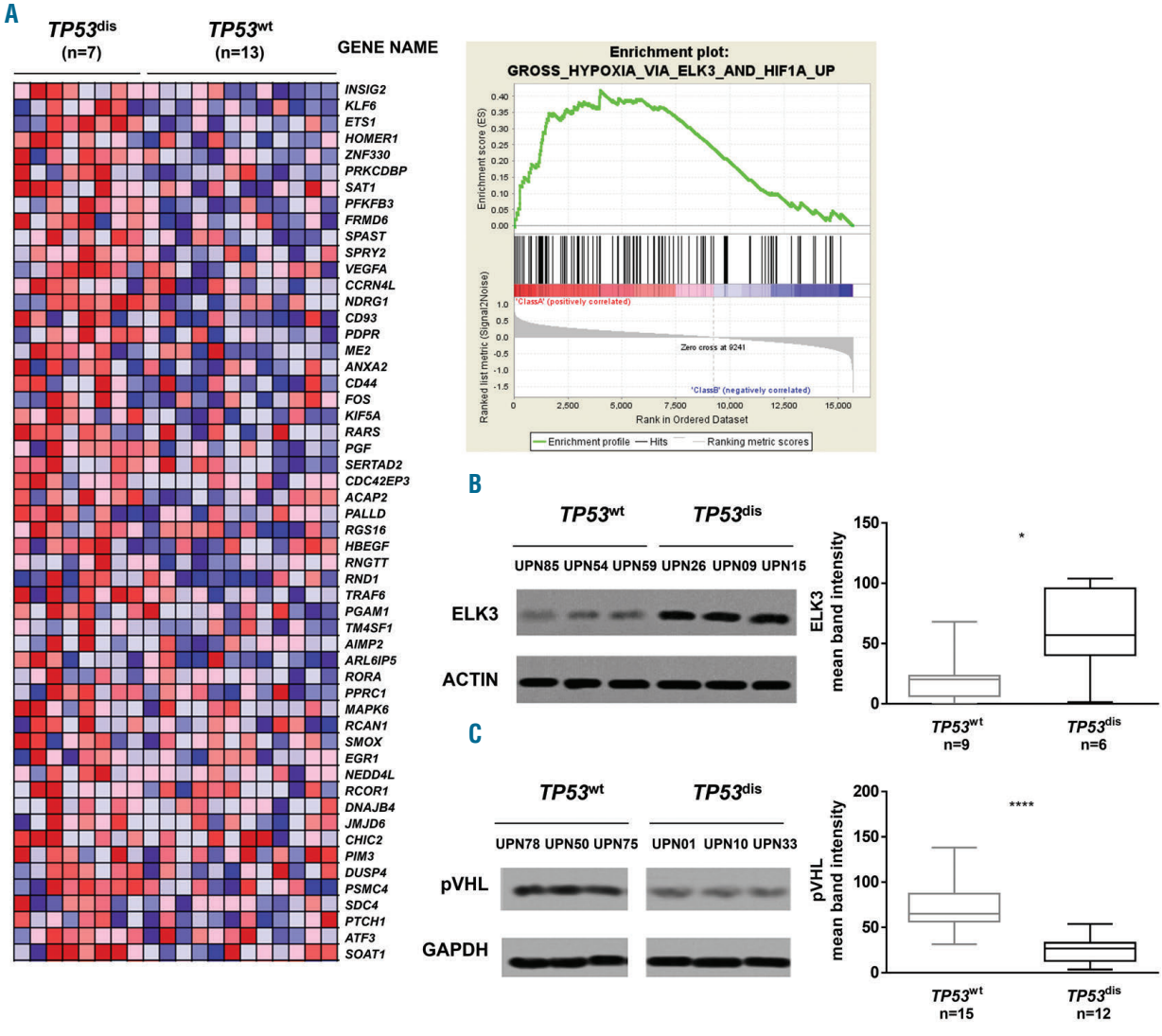

Figure 2. *TP53*^{dis} chronic lymphocytic leukemia (CLL) cells show an upregulation of several genes involved in response to hypoxia and express reduced levels of von Hippel-Lindau protein (pVHL). (A) Gene set enrichment analysis (GSEA) on CLL cells from *TP53*^{dis} and *TP53*^{wt} patients. The plot of the Enrichment Score (ES) *versus* the gene list index and a portion of the corresponding heatmap highlighting the relative expression of gene members belonging to the "*GROSS_HYPOXIA_VIA_ELK3_AND_HIF1A_UP*" gene set are depicted. 54 out of 126 genes from the gene set were significantly up-regulated in the *TP53*^{dis} cohort of patients compared to the *TP53*^{wt} cohort. (B) Western blot (WB) for *ELK3* baseline expression in *TP53*^{dis} and *TP53*^{wt} CLL cells. A representative blot is shown with relative Unique Patient Numbers (UPN) and cumulative band intensity data obtained from the analysis of 9 *TP53*^{wt} and 6 *TP53*^{dis} CLL patients. (C) WB for pVHL baseline expression in *TP53*^{dis} and *TP53*^{wt} CLL cells. A representative blot is shown with relative UPN and cumulative band intensity data obtained from the analysis of 15 *TP53*^{wt} and 12 *TP53*^{dis} CLL patients. Box plots represent median value and 25-75% percentiles; whiskers represent minimum and maximum values of band intensity for each group. *P<0.05; ****P<0.0001.

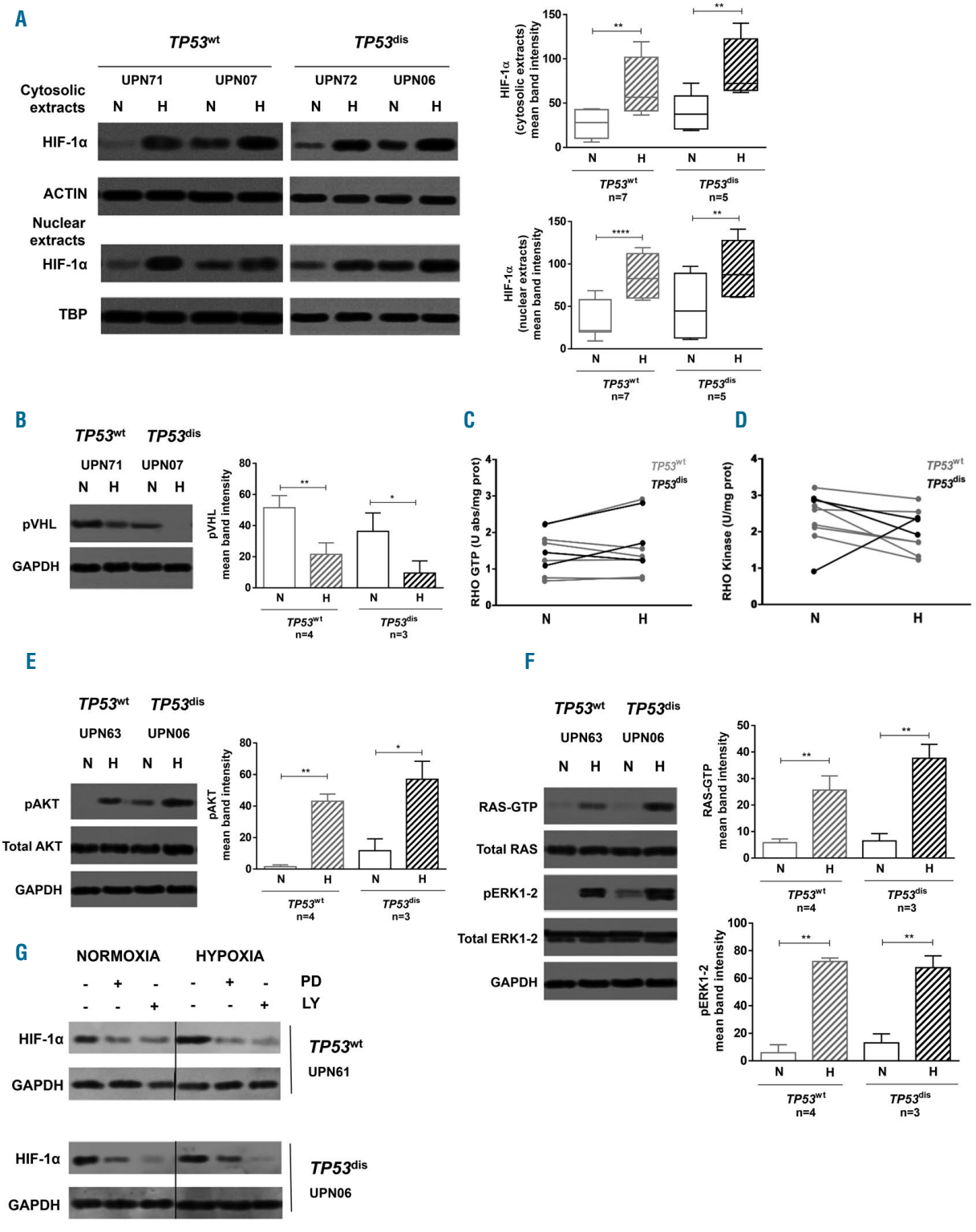

Figure 3. Hypoxia further increases HIF-1α expression in *TP53*^{dis} and *TP53*^{wt} chronic lymphocytic leukemia (CLL) cells *via* the PI3K/AKT and RAS/ERK1-2 signaling pathways. Primary CLL cells were cultured for 48 hours under normoxic and hypoxic conditions. (A and B) Western blot (WB) analyses detected a higher amount of cytosolic and nuclear HIF-1α and lower amount of von Hippel-Lindau protein (pVHL) in *TP53*^{dis} and *TP53*^{wt} CLL cells cultured in hypoxia (H) compared to normoxia (N). (C and D) Immuno-enzymatic measurement showed that RHOA-GTP and RHOA kinase activities were unaffected by hypoxia. (E and F) WB analyses for AKT, RAS and ERK1-2. *TP53*^{dis} and *TP53*^{wt} CLL cells had higher expression of the active form of AKT [p(Ser 473)AKT], RAS (RAS-GTP) and ERK1-2 [p(Thr202/Tyr204, Thr185/Tyr187]ERK1-2) in hypoxia compared to normoxia. (G) WB analyses for HIF-1α. The targeting of ERK1-2 with 10 μM PD98059 (PD) and of PI3K with 10 μM LY294002 (LY) reduced HIF-1α expression in CLL cells, both in hypoxia and normoxia, and independently from the *TP53* status. (A) Results from two representative cases of seven *TP53*^{wt} patients and two representative cases of five *TP53*^{dis} patients. Representative blots are shown with relative Unique Patient Numbers (UPN) and cumulative band intensity data. Box plots represent median values and 25-75% percentiles; whiskers represent minimum and maximum values of band intensity for each group. (B, E and F) Results from one representative experiment in four *TP53*^{wt} patients and one representative experiment in three *TP53*^{dis} patients. Bar graphs represent mean values together with standard error of mean. (C and D) Multiple line graphs represent individual data values for the same sample in each condition. (G) Results from one representative experiment in three *TP53*^{wt} patients and one representative experiment in three *TP53*^{dis} patients. Vertical lines have been inserted to indicate repositioned gel lanes. *P<0.05; **P<0.01; ****P<0.0001.

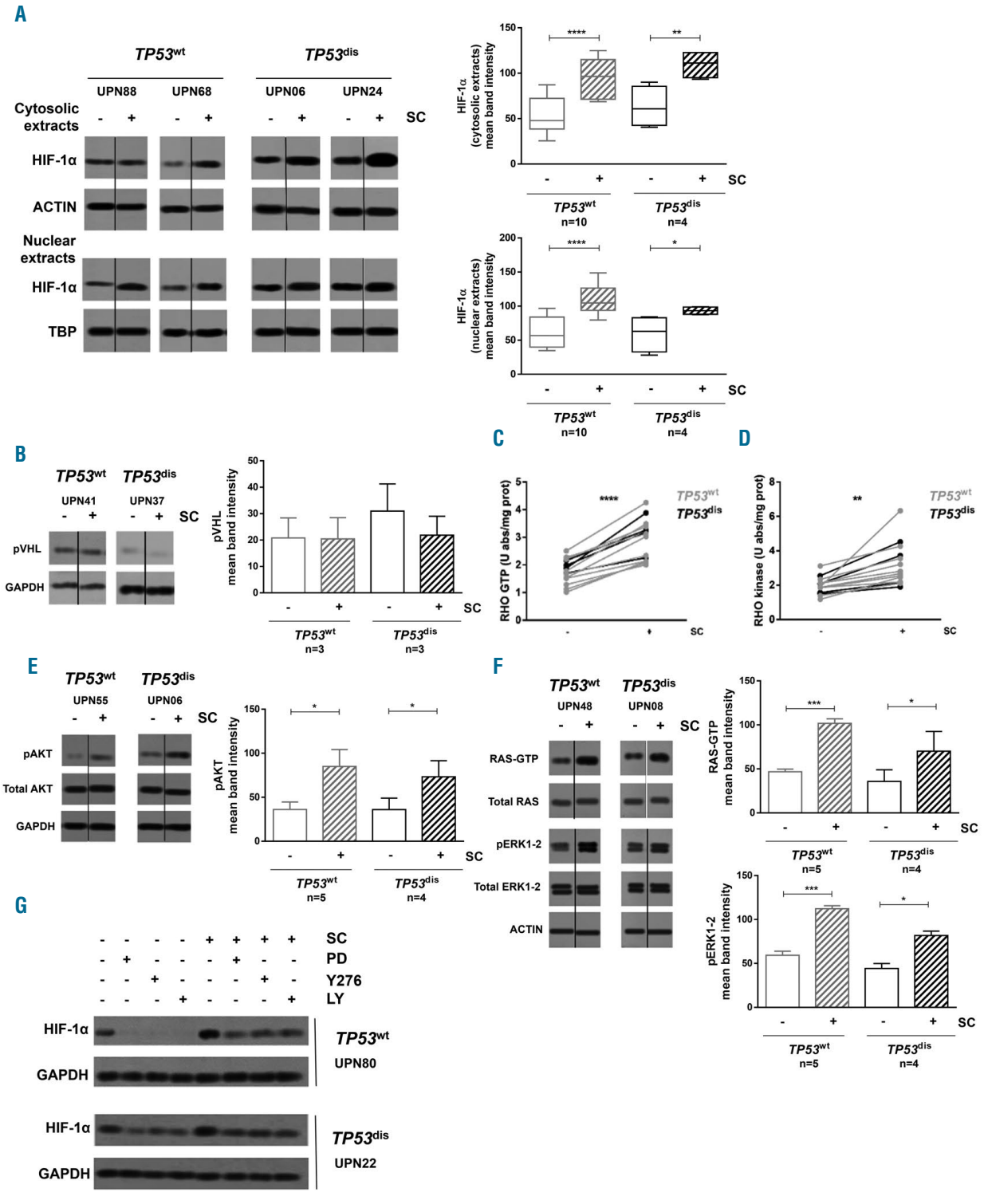

Figure 4. Stromal cells (SC) increase HIF-1α expression in *TP53*^{dis} and *TP53*^{wt} chronic lymphocytic leukemia (CLL) cells *via* PI3K/AKT, RAS/ERK1-2 and RHOA/RHOA kinase signaling pathways. Primary CLL cells were cultured for 48 hours in the presence and in the absence of M2-10B4 SC. (A and B) Western blot (WB) analyses for HIF-1α and von Hippel-Lindau protein (pVHL). SC up-regulated the cytosolic and nuclear expression of HIF-1α but did not affect pVHL expression in *TP53*^{dis} and *TP53*^{wt} CLL cells. (C and D) Immuno-enzymatic measurement showed that the co-culture with SC increased RHOA-GTP and RHOA kinase activities in *TP53*^{dis} and *TP53*^{wt} CLL cells. (E and F) WB analyses for AKT, RAS and ERK1-2. Higher amount of the active form of AKT [p(Ser 473)AKT], RAS (RAS-GTP) and ERK1-2 [p(Thr202/Tyr204, Thr185/Tyr187)ERK1-2] were detectable in both *TP53*^{wt} and *TP53*^{dis} CLL cells cultured with SC. (G) WB analyses for HIF-1α. The targeting of ERK1-2 with 10 μM PD98059 (PD), of RHOA kinase with 10 μM Y27632 (Y276), and of PI3K with 10 μM LY294002 (LY) reduced HIF-1α expression in CLL cells, both in the presence and in the absence of SC, regardless of the *TP53* status. (A) Results from two representative cases of ten *TP53*^{wt} patients and two representative cases of four *TP53*^{dis} patients. Representative blots are shown, together with Unique Patient Numbers (UPN) and cumulative band intensity data. Box plots represent median values and 25-75% percentiles; whiskers represent minimum and maximum values of band intensity for each group. (B and G) Results are from one representative experiment in three *TP53*^{wt} patients and one representative experiment in three *TP53*^{dis} patients. (C and D) Multiple line graphs represent individual data values for the same sample in each condition. (E and F) Results are from one representative experiment in five *TP53*^{wt} patients and one representative experiment in four *TP53*^{dis} patients. Bar graphs represent mean values together with standard error of mean. Vertical lines have been inserted to indicate repositioned gel lanes. **P*<0.05; ***P*<0.01; ****P*<0.001; *****P*<0.0001.

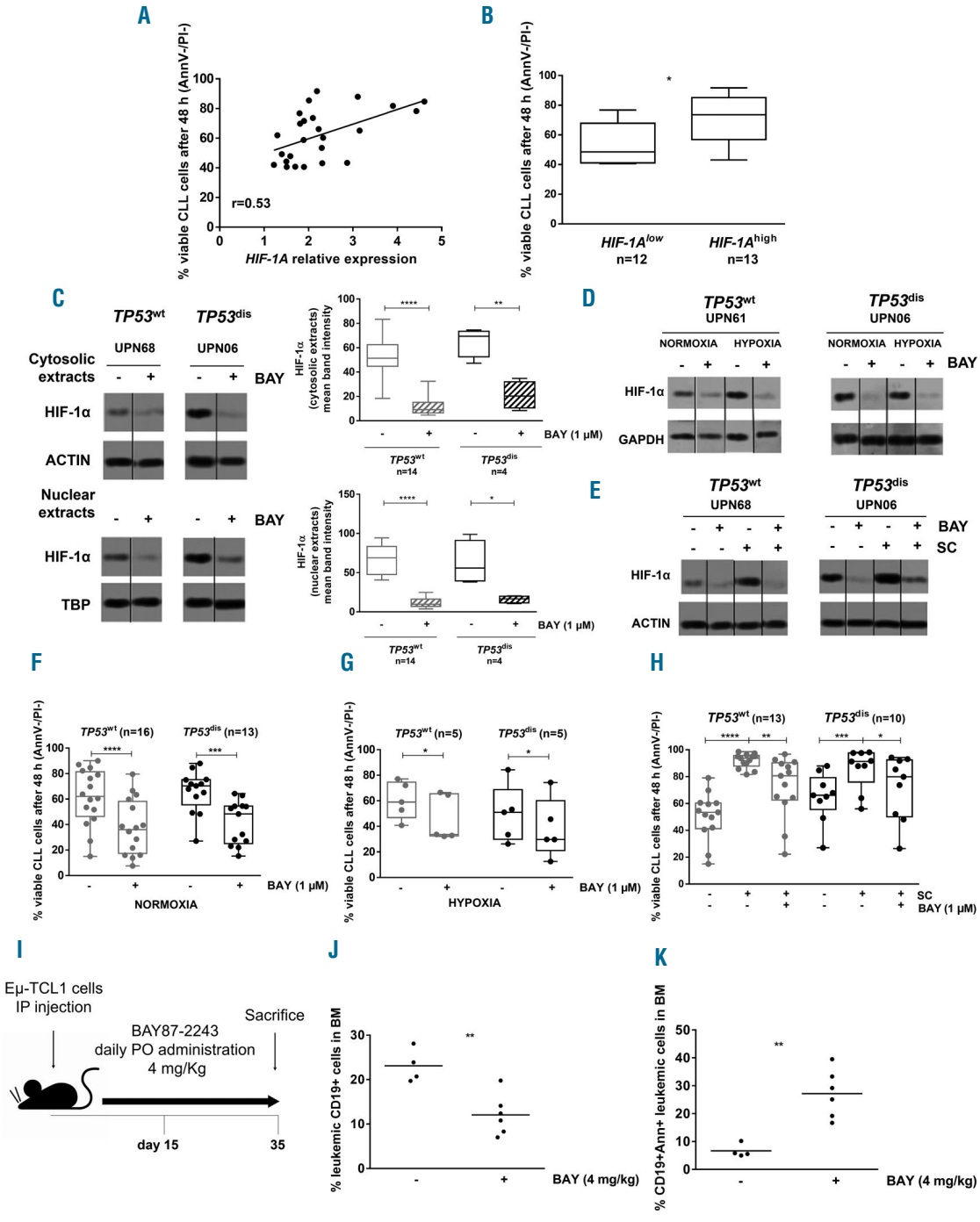

Figure 5. HIF-1α promotes chronic lymphocytic leukemia (CLL) cell survival and its inhibition exerts a direct cytotoxicity, also in the presence of HIF-1α inducing microenvironmental stimuli. (A) Correlation of *HIF-1A* gene expression and 48-hour (h) cell viability of CLL cells as determined by Annexin V/propidium iodide assay. (B) The median value of *HIF-1A* mRNA expression of a cohort of 25 CLL samples was selected as the cut-off to identify *HIF-1A*^{high} and *HIF-1A*^{low} CLL cells. *HIF-1A*^{high} showed significantly higher 48-h cell viability compared to *HIF-1A*^{low} CLL cells. (C) Western blot (WB) analyses for HIF-1α. The exposure to 1 μM BAY87-2243 (BAY) for 48 h reduced the cytosolic and nuclear amount of HIF-1α in CLL cells isolated from both *TP53*^{wt} and *TP53*^{dis} patient subsets. A representative blot is shown, together with Unique Patient Numbers (UPN) and cumulative band intensity data obtained from the analysis of 14 *TP53*^{wt} and 4 *TP53*^{dis} CLL patients. Box plots represent median value and 25-75% percentiles; whiskers represent minimum and maximum values of band intensity for each group. (D and E) Primary CLL cells were exposed to 1 μM BAY for 48 h under normoxic and hypoxic conditions, in the absence and in the presence of M2-10B4 stromal cells (SC), and evaluated for HIF-1α expression by WB. BAY87-2243 was able to lower HIF-1α expression in CLL cultured in normoxic and hypoxic conditions, and in the absence or in the presence of SC, independently of *TP53* status. (F-H) Cell viability of *TP53*^{dis} and *TP53*^{wt} CLL cells exposed for 48 h to 1 μM BAY87-2243, under normoxia and hypoxia, or in co-culture with SC. The treatment with BAY87-2243 determined a significant decrease in the viability of *TP53*^{wt} and *TP53*^{dis} CLL cells, compared to untreated controls, both in normoxia and hypoxia. After exposure to SC, BAY87-2243 significantly reduced the viability of *TP53*^{dis} and *TP53*^{wt} CLL cells, not completely overcoming the SC protective effect. In blot representations, vertical lines have been inserted to indicate repositioned gel lanes. (I) Scheme of the *in vivo* experiment with mice transplanted with the EμTCL1-derived leukemia. (J) Percentage of leukemic cells (CD19$^+$) in the bone marrow (BM) of mice transplanted with the Eμ-TCL1-derived leukemia, treated with BAY87-2243, and euthanized as in (I). (K) Percentage of AnnV$^+$ leukemic cells (CD19$^+$) in the BM of mice transplanted with Eμ-TCL1-derived leukemia, treated with BAY87-4432, and euthanized as in (I). (A) Data are represented by a scatter plot. (J and K) Data are represented as bee-swarm plots. (B) Box and whiskers plots represent median values and 25-75% percentiles; whiskers represent minimum and maximum values for each group. (D) Results are from one representative experiment in three *TP53*^{wt} patients and one representative experiment in three *TP53*^{dis} patients. (E) Results are from one representative experiment in seven *TP53*^{wt} patients and one representative experiment in four *TP53*^{dis} patients. (F, G and H) Box and whiskers plots represent median values and 25-75% percentiles; whiskers represent minimum and maximum values for each group, together with all points. *P<0.05; **P<0.01; ***P<0.001; ****P<0.0001.

BAY87-2243 restores fludarabine sensitivity of *TP53*^{dis} chronic lymphocytic leukemia cells and counteracts the protective effect of stromal cells

We next examined whether BAY87-2243 was also effective in overcoming the intrinsic resistance to fludarabine of CLL cells from *TP53*^{dis} patients.[9,31-33] As expected, in our cohort, the normalized cell viability after 48-h F-ara-A treatment was significantly higher in *TP53*^{dis} compared to *TP53*^{wt} CLL cells (Figure 6A). Consistently, we observed that CLL cells with a normalized cell viability ≥0.5, arbitrarily considered as fludarabine-resistant, were mostly *TP53*^{dis} and had a significantly higher baseline expression of *HIF-1A* mRNA compared to fludarabine-sensitive cells (i.e. normalized cell viability <0.5) (Figure 6B). Interestingly, BAY87-2243 enhanced the cytotoxicity of fludarabine on *TP53*^{dis} CLL cells, as shown by the significant impairment of cell viability observed after combined treatment with BAY87-2243 + fludarabine compared to each compound used as a single agent (Figure 6C). The cytotoxic effect exerted by the combination was strongly

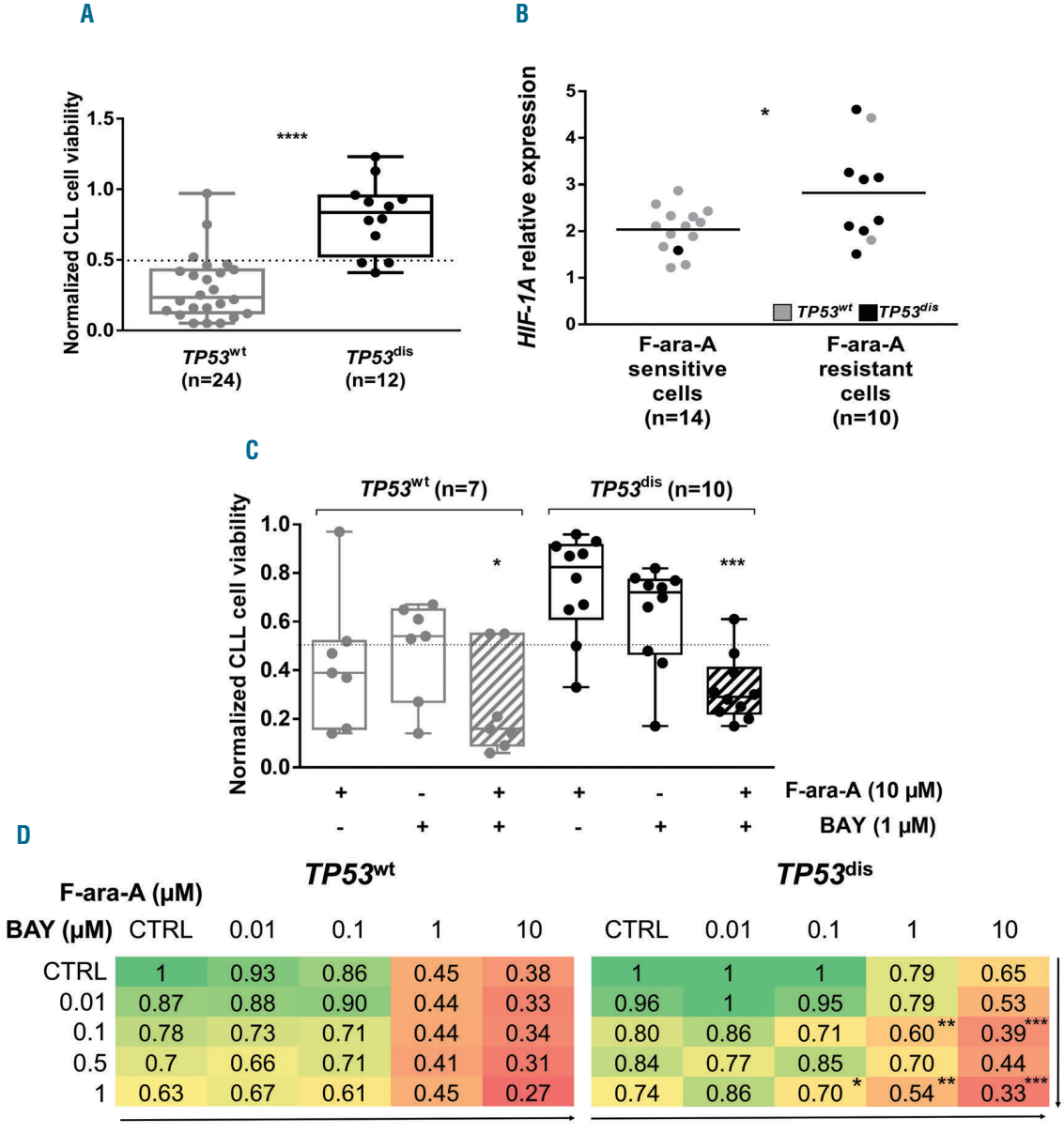

Figure 6. *HIF-1A* mRNA is over-expressed in fludarabine-resistant chronic lymphocytic leukemia (CLL) cells and HIF-1α inhibition is capable of restoring fludarabine sensitivity. (A) Normalized cell viability (i.e. the ratio between the percentage of AnnV/PI negative CLL cells cultured in the presence of F-ara-A and the percentage of AnnV/PI negative CLL cells left untreated) of *TP53*^{dis} and *TP53*^{wt} CLL cells exposed for 48 hours (h) to 10 μM F-ara-A. (B) A normalized cell viability of 0.5 was selected as the cut-off value to identify fludarabine-resistant (i.e. normalized cell viability ≥0.5) and fludarabine-sensitive (i.e. normalized cell viability <0.5) CLL cells. Fludarabine-resistant CLL cells showed significantly higher baseline levels of *HIF-1A* mRNA compared to fludarabine-sensitive. Eight of 10 (80%) fludarabine-resistant samples derived from *TP53*^{dis} patients, and 13 of 14 (93%) fludarabine-sensitive samples derived from *TP53*^{wt} patients. (C) Normalized cell viability of *TP53*^{dis} and *TP53*^{wt} CLL cells exposed for 48 h to 1 μM BAY87-2243 (BAY) and/or 10 μM F-ara-A. The combination BAY87-2243 + F-ara-A (striped pattern) determined a significant decrease in the viability of *TP53*^{wt} and *TP53*^{dis} CLL cells, compared to each compound used as single agent and to untreated controls. (D) Heatmaps showing normalized viability after 48-h treatment with BAY87-2243 + fludarabine as single agents or in combination, used at different concentrations. Asterisks indicate the combinations which determined a significant reduction in cell viability compared to each single agent, at the corresponding concentration. (A and C) Box plots represent median values and 25-75% percentiles; whiskers represent minimum and maximum values for each group, together with all points. (B) Data are represented as bee-swarm plot. *P<0.05; **P<0.01; ***P<0.001; ****P<0.0001.

synergistic (CI=0.17) on *TP53*^{dis} CLL cells and was also evident, although less remarkable, on *TP53*^{wt} CLL cells (Figure 6C and *Online Supplementary Figure S8*). Interestingly, we observed that combinations consisting of lower concentrations of BAY87-2243 + fludarabine were capable of inducing significant reductions in cell viability compared to each drug used as a single agent, and this effect was particularly evident in the *TP53*^{dis} CLL subset (Figure 6D). The cytotoxic activity of the combinations was also strongly synergistic, as shown by data on CI (*Online Supplementary Figure S9*). Notably, the significantly higher cytotoxicity of the combination BAY87-2243 + fludarabine was maintained even when both *TP53*^{dis} and *TP53*^{wt} CLL cells were cultured under hypoxia (*Online Supplementary Figure S10A and B*) or in the presence of SC (*Online Supplementary Figure S10C and D*).

These results indicate that BAY87-2243 and fludarabine synergistically eliminate primary CLL cells, and that their effect is maintained even in the presence of HIF-1α inducing factors that recapitulate the BM niche microenvironment.

The combination of BAY87-2243 and ibrutinib exerts a synergistic cytotoxic effect on chronic lymphocytic leukemia cells

Previously reported data indicate that *TP53*-mutated CLL cells have a lower sensitivity to ibrutinib cytotoxicity *in vitro*[34] and that ibrutinib-induced apoptosis is significantly reduced in conditions of hypoxia.[19] Therefore, we hypothesized that the combination of an HIF-1α inhibitor and ibrutinib may represent a potentially attractive next step for patients carrying *TP53* abnormalities, who are characterized by constitutively higher levels of HIF-1α. Our results show that the combination of BAY87-2243 + ibrutinib determined a significant impairment in the viability of *TP53*^{dis} and *TP53*^{wt} CLL cells compared to each compound used as a single agent, and was very strongly synergistic (Figure 7A and *Online Supplementary Figure S11*). Interestingly, similar effects were observed also with lower concentrations of both agents (Figure 7B and *Online Supplementary Figure S12*). Notably, the combination BAY87-2243 + ibrutinib exerted a significantly higher cytotoxic effect compared to each single compound even when CLL cells from both *TP53*^{dis} and *TP53*^{wt} samples were cultured in the presence of SC (Figure 7C).

Overall, these data demonstrate that BAY87-2243 exerts a compelling synergistic effect with ibrutinib, thus providing the rationale for future clinical translation.

Discussion

In this study, we investigated the expression and regulation of HIF-1α in *TP53*^{dis} CLL cells and its potential role as a therapeutic target. We found that CLL cells carrying *TP53* abnormalities express significantly higher baseline levels of HIF-1α and have increased HIF-1α transcriptional activity compared to *TP53*^{wt} cells. Regardless of *TP53* status, the resting levels of HIF-1α are susceptible to further upregulation by microenvironmental stimuli, such as hypoxia and SC. Our data show that HIF-1α is a suitable therapeutic target, the inhibition of which induces a strong cytotoxic effect, capable also of reversing the *in vitro* fludarabine resistance of *TP53*^{dis} CLL cells and of exerting synergistic effects with ibrutinib.

Hypoxia has a detrimental role in the pathobiology of several solid and hematologic tumors.[35,36] The identification of new potential targets in CLL is certainly important for high-risk patients, for whom there is still no effective cure, and, in addition, the development of new therapies might be effective in a broader setting of B-cell lymphoproliferative disorders.

It has been previously reported that HIF-1α levels vary considerably among CLL patients and that its overexpression is a predictor of a poor survival.[17,37] In line with observations made in solid tumors, where p53 promotes the ubiquitination and proteasomal degradation of the HIF-1α subunit in hypoxia,[12,22] we postulated that abnormalities of the *TP53* gene might have an influence on the regulation of HIF-1α in CLL cells. To the best of our knowledge, this is the first study examining the differential expression and transcriptional activity of HIF-1α in patients with *TP53*-deficient CLL, also uncovering new mechanisms for HIF-1α modulation in leukemic cells. Our data show that the high-resting levels of HIF-1α detected in *TP53*^{dis} samples associate both to an increased transcription, as shown by the higher *HIF-1A* mRNA levels, and to a decreased degradation, as shown by the higher baseline expression of ELK3 and by the lower pVHL amounts.

We next investigated the cellular pathways implicated in HIF-1α regulation mediated by extrinsic factors. Hypoxia-induced HIF-1α upregulation is not only due to a reduced pVHL-mediated protein degradation, which is a well-known mechanism in condition of oxygen deprivation, but also to an increased activation of RAS/ERK1-2 and PI3K/AKT signaling pathways. In contrast, pVHL expression in leukemic cells is not affected by SC, which instead activate the RAS/ERK1-2, RHOA/RHOA kinase and PI3K/AKT intracellular pathways, thus leading to HIF-1α overexpression. These results endorse recent data that implicate a number of paracrine factors in the transcriptional and translational regulation of HIF-1α in different tumor models.[38]

Previous data have suggested that HIF-1α targeting is a promising therapeutic strategy in CLL, potentially capable of synergizing with chemotherapeutic agents. The only HIF-1α inhibitor that has been preclinically tested in CLL is EZN-2208, a topoisomerase I inhibitor that has also been shown to down-modulate HIF-1α.[17] We therefore tested BAY87-2243, a more selective HIF-1α inhibitor that has already shown *in vivo* anti-tumor efficacy in a lung tumor model, without any signs of toxicity.[39] Interestingly, BAY87-2243 demonstrated a direct cytotoxicity towards leukemic cells isolated from CLL patients, and this effect was independent of *TP53* status. As far as we know, this is the first evidence of the anti-tumor activity of BAY87-2243 in hematologic tumors, and particularly in CLL.

Patients with CLL and *TP53* abnormalities are intrinsically resistant to fludarabine-based chemotherapy regimens.[9,31-33,40,41] Our data demonstrate: i) higher baseline levels of HIF-1α in fludarabine-resistant CLL cells; and ii) a further upregulation of HIF-1α after exposure to hypoxia and SC. Given this, we investigated the ability of BAY87-2243 to overcome both intrinsic (i.e. *TP53*-related) and inducible (i.e. SC-induced) resistance to fludarabine. Our data show that BAY87-2243 potently synergizes with fludarabine *in vitro*, and that their combined cytotoxic effect was especially evident in *TP53*^{dis} samples. Interestingly, HIF-1α inhibition was also effective in overcoming the *TP53*-independent fludarabine-resistance induced by

extrinsic factors recapitulating the BM microenvironment.

Since HIF-1α critically regulates the interactions of CLL cells with the BM stroma,[17] the cytotoxic effects exerted by BAY87-2243 in culture systems mimicking the tumor niche could, in part, be the result of a perturbation of molecular circuits triggered by microenvironmental stimuli that are implicated in cell survival and drug resistance. Data showing that hypoxia and SC induce HIF-1α overexpression support the hypothesis that, within the tumor niche, leukemic cells become highly dependent on its pro-survival effect. In line with this assumption, we found that treatment with BAY87-2243 induced a marked reduction in leukemic infiltration and a parallel increase in the proportion of apoptotic leukemic cells in the BM of a CLL transplantable model derived from the Eμ-TCL1 transgenic mice. Of note, the inhibition of HIF-1α may have beneficial effects also on the non-leukemic milieu. Recent data have shown that infiltration by CLL cells into BM could result in tissue-site hypoxia, causing: i) increased expression of HIF-1α in hematopoietic progenitors, which

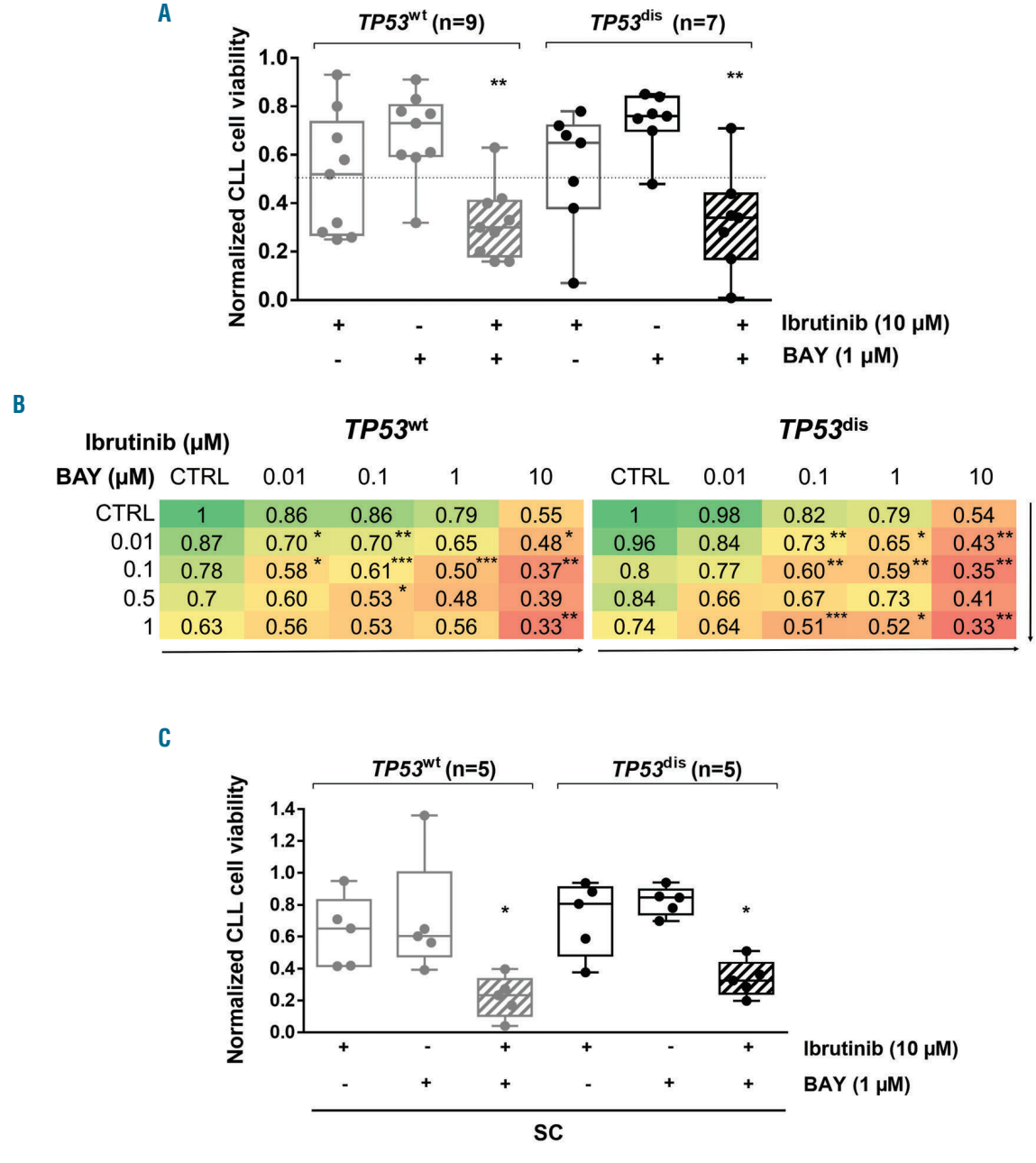

Figure 7. BAY87-2243 plus ibrutinib combinations exerts synergistic cytotoxic effects and is effective in impairing chronic lymphocytic leukemia (CLL) cell viability in the presence of stromal cells (SC). (A) Normalized 48-hour (h) viability of *TP53*^{dis} and *TP53*^{wt} CLL cells exposed to 1 μM BAY87-2243 (BAY) and 10 μM ibrutinib, used as single agents or in combination (striped pattern). Box plots represent median value and 25-75% percentiles; whiskers represent minimum and maximum values for each group, together with all points. (B) Heatmaps showing normalized viability after 48-h treatment with BAY87-2243 + ibrutinib as single agents or in combination, used at different concentrations. Asterisks indicate the combinations which determined a significant reduction in cell viability compared to each single agent, at the corresponding concentration. (C) Normalized 48-h viability of *TP53*^{dis} and *TP53*^{wt} CLL cells exposed to 1 μM BAY87-2243 and 10 μM ibrutinib, used as single agents or in combination (striped pattern), in co-culture with M2-10B4 SC. Box plots represent median value and 25-75% percentiles; whiskers represent minimum and maximum values for each group, together with all points. *P<0.05; **P<0.01; ***P<0.001.

leads to an impaired hematopoiesis and a reduced output of innate immune cells into the blood; and ii) impaired functions of different immune cell subsets.[19,42] Overall, this evidence endorses the concept of HIF-1α inhibition as a very promising therapeutic strategy in CLL.

In the era of new targeted treatments, ibrutinib has determined a dramatic change in the therapeutic landscape and has become the standard of care for the majority of CLL patients.[43-45] However: i) ibrutinib is not suitable for all CLL patients and may have limited availability in several countries; ii) complete responses are infrequent, and indefinite drug administration is usually needed to maintain a clinical response; and iii) the development of ibrutinib resistance in CLL cells has been demonstrated.[46,47] Even more importantly, *TP53*^{dis} CLL patients show a suboptimal long-term response to ibrutinib,[48] and *TP53*-mutated CLL cells have a lower sensitivity to ibrutinib cytotoxicity *in vitro*.[34] Since our data show that *TP53*^{dis} samples are characterized by higher levels and function of HIF-1α (which is a crucial target to overcome the constitutive and inducible drug resistance of CLL cells), we hypothesized that the combination of BAY87-2243 and ibrutinib might be an attractive approach for *in vitro* testing. We found that dual targeting of HIF-1α alongside BTK function produces a synergistic cytotoxic activity towards primary CLL cells, also in the presence of *TP53* abnormalities; thus suggesting the possibility of improving ibrutinib efficacy through this novel therapeutic association.

Overall, our data indicate that HIF-1α is over-expressed in CLL cells, especially in the presence of *TP53* aberrations, and that it is susceptible to further upregulation through microenvironmental stimuli. From the translational standpoint, the pharmacologic compound BAY87-2243, a selective inhibitor of HIF-1α, displays potent anti-tumor properties and warrants further pre-clinical evaluation in this disease setting, also in combination with other therapies. Indeed, on one hand, the synergism of BAY87-2243 and fludarabine may provide the rationale for future clinical application in countries with limited access to ibrutinib, particularly for the treatment of high-risk patients carrying *TP53* abnormalities. On the other hand, BAY87-2243 coupled with ibrutinib may offer a rational combination to increase the proportion of minimal residual disease negative remissions, thus reducing the development of CLL clones with resistant mutations.

Funding

The authors would like to thank: Italian Association for Cancer Research (AIRC IG15232 and AIRC IG21408) (CR), (AIRC IG13119, AIRC IG16985, AIRC IG2174) (MM), (AIRC IG17622) (VGa), (AIRC 5x1000 project 21198, Metastatic disease: the key unmet need in oncology) (GG), (AIRC 5x1000 Special Programs MCO-10007 and 21198) (RF); Fondazione Neoplasie Sangue (Fo.Ne.Sa), Torino, Italy; University of Torino (local funds ex-60%) (MC); Ministero della Salute, Rome, Italy (Progetto Giovani Ricercatori GR-2011-02347441 [RB], GR-2009-1475467 [R.Bomben], and GR-2011-02351370 [MDB]). Fondazione Cassa di Risparmio di Torino (CRT) (VGr was recipient of a fellowship), Fondazione "Angela Bossolasco" Torino, Italy (VGr was recipient of the "Giorgio Bissolotti e Teresina Bosio" fellowship), the Italian Association for Cancer Research (AIRC, Ref 16343 VGr was recipient of the "Anna Nappa" fellowship and MT is currently the recipient of a fellowship from AIRC Ref 19653). Associazione Italiana contro le Leucemie, Linfomi e Mieloma (AIL) (CV was recipient of a fellowship). Pezcoller Foundation in collaboration with SIC (Società Italiana Cancerologia) (CV was a recipient of a "Fondazione Pezcoller - Ferruccio ed Elena Bernardi" fellowship).

References

1. Hallek M, Fischer K, Fingerle-Rowson G, et al. Addition of rituximab to fludarabine and cyclophosphamide in patients with chronic lymphocytic leukaemia: a randomised, open-label, phase 3 trial. Lancet Lond Engl. 2010;376(9747):1164-1174.
2. Zenz T, Vollmer D, Trbusek M, et al. TP53 mutation profile in chronic lymphocytic leukemia: evidence for a disease specific profile from a comprehensive analysis of 268 mutations. Leukemia. 2010; 24(12): 2072-2079.
3. Parikh SA. Chronic lymphocytic leukemia treatment algorithm 2018. Blood Cancer J. 2018;8(10):93.
4. Sutton L-A, Rosenquist R. Deciphering the molecular landscape in chronic lymphocytic leukemia: time frame of disease evolution. Haematologica. 2015;100(1):7-16.
5. Zenz T, Eichhorst B, Busch R, et al. TP53 mutation and survival in chronic lymphocytic leukemia. J Clin Oncol. 2010;28(29): 4473-4479.
6. Gonzalez D, Martinez P, Wade R, et al. Mutational status of the TP53 gene as a predictor of response and survival in patients with chronic lymphocytic leukemia: results from the LRF CLL4 trial. J Clin Oncol. 2011;29(16):2223-2229.
7. Campo E, Cymbalista F, Ghia P, et al. TP53 aberrations in chronic lymphocytic leukemia: an overview of the clinical implications of improved diagnostics. Haematologica. 2018;103(12):1956-1968.
8. Seiffert M, Dietrich S, Jethwa A, Glimm H, Lichter P, Zenz T. Exploiting biological diversity and genomic aberrations in chronic lymphocytic leukemia. Leuk Lymphoma. 2012; 53(6):1023-1031.
9. Gaidano G, Rossi D. The mutational landscape of chronic lymphocytic leukemia and its impact on prognosis and treatment. Hematol Am Soc Hematol Educ Program. 2017;2017(1):329-337.
10. Thompson PA, Burger JA. Bruton's tyrosine kinase inhibitors: first and second generation agents for patients with Chronic Lymphocytic Leukemia (CLL). Expert Opin Investig Drugs. 2018;27(1):31-42.
11. O'Brien S, Furman RR, Coutre S, et al. Single-agent ibrutinib in treatment-naïve and relapsed/refractory chronic lymphocytic leukemia: a 5-year experience. Blood. 2018; 131(17):1910-1919.
12. Masoud GN, Li W. HIF-1α pathway: role, regulation and intervention for cancer therapy. Acta Pharm Sin B. 2015;5(5):378-389.
13. Semenza GL. Targeting HIF-1 for cancer therapy. Nat Rev Cancer. 2003;3(10):721.
14. Singh D, Arora R, Kaur P, Singh B, Mannan R, Arora S. Overexpression of hypoxia-inducible factor and metabolic pathways: possible targets of cancer. Cell Biosci. 2017;762.
15. Semenza G. Signal transduction to hypoxia-inducible factor 1. Biochem Pharmacol. 2002; 64(5-6):993-998.
16. Ghosh AK, Shanafelt TD, Cimmino A, et al. Aberrant regulation of pVHL levels by microRNA promotes the HIF/VEGF axis in CLL B cells. Blood. 2009;113(22):5568–5574.
17. Valsecchi R, Coltella N, Belloni D, et al. HIF-1α regulates the interaction of chronic lymphocytic leukemia cells with the tumor microenvironment. Blood. 2016; 127(16): 1987-1997.
18. Koczula KM, Ludwig C, Hayden R, et al. Metabolic plasticity in CLL: adaptation to the hypoxic niche. Leukemia. 2016;30(1):65-73.
19. Serra S, Vaisitti T, Audrito V, et al. Adenosine signaling mediates hypoxic responses in the chronic lymphocytic leukemia microenvironment. Blood Adv. 2016;1(1):47.
20. Rigoni M, Riganti C, Vitale C, et al. Simvastatin and downstream inhibitors circumvent constitutive and stromal cell-induced resistance to doxorubicin in IGHV unmutated CLL cells. Oncotarget. 2015;6(30):29833-29846.
21. Hientz K, Mohr A, Bhakta-Guha D, Efferth T. The role of p53 in cancer drug resistance and targeted chemotherapy. Oncotarget.

2016;8(5):8921-8946.
22. Amelio I, Melino G. The p53 family and the hypoxia-inducible factors (HIFs): determinants of cancer progression. Trends Biochem Sci. 2015;40(8):425-434.
23. Salnikow K, Costa M, Figg WD, Blagosklonny MV. Hyperinducibility of hypoxia-responsive genes without p53/p21-dependent checkpoint in aggressive prostate cancer. Cancer Res. 2000;60(20):5630-5634.
24. Hallek M, Cheson BD, Catovsky D, et al. Guidelines for the diagnosis and treatment of chronic lymphocytic leukemia: a report from the International Workshop on Chronic Lymphocytic Leukemia updating the National Cancer Institute-Working Group 1996 guidelines. Blood. 2008; 111(12):5446-5456.
25. Bomben R, Dal-Bo M, Benedetti D, et al. Expression of mutated IGHV3-23 genes in chronic lymphocytic leukemia identifies a disease subset with peculiar clinical and biological features. Clin Cancer Res. 2010; 16(2):620-628.
26. Subramanian A, Tamayo P, Mootha VK, et al. Gene set enrichment analysis: a knowledge-based approach for interpreting genome-wide expression profiles. Proc Natl Acad Sci U S A. 2005;102(43):15545-15550.
27. Semenza GL, Jiang BH, Leung SW, et al. Hypoxia response elements in the aldolase A, enolase 1, and lactate dehydrogenase A gene promoters contain essential binding sites for hypoxia-inducible factor 1. J Biol Chem. 1996;271(51):32529-32537.
28. Dal Bo M, Pozzo F, Bomben R, et al. ARHGDIA, a mutant TP53-associated Rho GDP dissociation inhibitor, is over-expressed in gene expression profiles of TP53 disrupted chronic lymphocytic leukaemia cells. Br J Haematol. 2013;161(4):596-599.
29. Gross C, Dubois-Pot H, Wasylyk B. The ternary complex factor Net/Elk-3 participates in the transcriptional response to hypoxia and regulates HIF-1 alpha. Oncogene. 2008; 27(9):1333-1341.
30. Liu W, Xin H, Eckert DT, Brown JA, Gnarra JR. Hypoxia and cell cycle regulation of the von Hippel-Lindau tumor suppressor. Oncogene. 2011;30(1):21-31.
31. Turgut B, Vural O, Pala FS, et al. 17p Deletion is associated with resistance of B-cell chronic lymphocytic leukemia cells to in vitro fludarabine-induced apoptosis. Leuk Lymphoma. 2007;48(2):311-320.
32. Dietrich S, Oleś M, Lu J, et al. Drug-perturbation-based stratification of blood cancer. J Clin Invest. 2018;128(1):427-445.
33. Nadeu F, Delgado J, Royo C, et al. Clinical impact of clonal and subclonal TP53, SF3B1, BIRC3, NOTCH1, and ATM mutations in chronic lymphocytic leukemia. Blood. 2016; 127(17):2122-2130.
34. Guarini A, Peragine N, Messina M, et al. Unravelling the suboptimal response of TP53-mutated chronic lymphocytic leukaemia to ibrutinib. Br J Haematol. 2019;184(3):392-396.
35. Kim J-Y, Lee J-Y. Targeting Tumor Adaption to Chronic Hypoxia: Implications for Drug Resistance, and How It Can Be Overcome. Int J Mol Sci. 2017;18(9):1854.
36. Muz B, de la Puente P, Azab F, Luderer M, Azab AK. The role of hypoxia and exploitation of the hypoxic environment in hematologic malignancies. Mol Cancer Res. 2014;12(10):1347-1354.
37. Kontos CK, Papageorgiou SG, Diamantopoulos MA, et al. mRNA overexpression of the hypoxia inducible factor 1 alpha subunit gene (HIF1A): An independent predictor of poor overall survival in chronic lymphocytic leukemia. Leuk Res. 2017; 53:65-73.
38. Kuschel A, Simon P, Tug S. Functional regulation of HIF-1α under normoxia--is there more than post-translational regulation? J Cell Physiol. 2012;227(2):514-524.
39. Ellinghaus P, Heisler I, Unterschemmann K, et al. BAY 87-2243, a highly potent and selective inhibitor of hypoxia-induced gene activation has antitumor activities by inhibition of mitochondrial complex I. Cancer Med. 2013;2(5):611-624.
40. Döhner H, Fischer K, Bentz M, et al. p53 gene deletion predicts for poor survival and non-response to therapy with purine analogs in chronic B-cell leukemias. Blood. 1995;85(6):1580-1589.
41. Zenz T, Häbe S, Denzel T, et al. Detailed analysis of p53 pathway defects in fludarabine-refractory chronic lymphocytic leukemia (CLL): dissecting the contribution of 17p deletion, TP53 mutation, p53-p21 dysfunction, and miR34a in a prospective clinical trial. Blood. 2009;114(13):2589-2597.
42. Manso BA, Zhang H, Mikkelson MG, et al. Bone marrow hematopoietic dysfunction in untreated chronic lymphocytic leukemia patients. Leukemia. 2019;33(3):638-652.
43. Eichhorst B, Robak T, Montserrat E, et al. appendix 6: Chronic lymphocytic leukaemia: eUpdate published online September 2016 (http://www.esmo.org/Guidelines/Haematological-Malignancies). Ann Oncol. 2016; 27(suppl 5):v143-v144.
44. Eichhorst B, Robak T, Montserrat E, et al. Chronic lymphocytic leukaemia: ESMO Clinical Practice Guidelines for diagnosis, treatment and follow-up. Ann Oncol. 2015; 26 Suppl 5:v78-84.
45. NCCN Guidelines Insights: chronic lymphocytic leukemia/small lymphocytic leukemia, version 1.2017. http://www.jnccn.org/content/15/3/293.long (accessed February 11, 2018).
46. Woyach JA, Ruppert AS, Guinn D, et al. BTKC481S-mediated resistance to Ibrutinib in chronic lymphocytic leukemia. J Clin Oncol. 2017;35(13):1437-1443.
47. Jones D, Woyach JA, Zhao W, et al. PLCG2 C2 domain mutations co-occur with BTK and PLCG2 resistance mutations in chronic lymphocytic leukemia undergoing ibrutinib treatment. Leukemia. 2017;31(7):1645-1647.
48. Byrd JC, Furman RR, Coutre SE, et al. Three-year follow-up of treatment-naïve and previously treated patients with CLL and SLL receiving single-agent ibrutinib. Blood. 2015; 125(16):2497-2506.

ARTICLE

Microhomology-mediated end joining drives complex rearrangements and overexpression of *MYC* and *PVT1* in multiple myeloma

Aneta Mikulasova,[1,2] Cody Ashby,[1] Ruslana G. Tytarenko,[1] Pingping Qu,[3] Adam Rosenthal,[3] Judith A. Dent,[1] Katie R. Ryan,[1] Michael A. Bauer,[1] Christopher P. Wardell,[1] Antje Hoering,[3] Konstantinos Mavrommatis,[4] Matthew Trotter,[5] Shayu Deshpande,[1] Shmuel Yaccoby,[1] Erming Tian,[1] Jonathan Keats,[6] Daniel Auclair,[7] Graham H. Jackson,[8] Faith E. Davies,[1] Anjan Thakurta,[4] Gareth J. Morgan[1] and Brian A. Walker[1,9]

[1]Myeloma Center, University of Arkansas for Medical Sciences, Little Rock, AR, USA; [2]Institute of Cellular Medicine, Newcastle University, Newcastle upon Tyne, UK; [3]Cancer Research and Biostatistics, Seattle, WA, USA; [4]Celgene Corporation, Summit, NJ, USA; [5]Celgene Institute for Translational Research Europe, Seville, Spain; [6]Translational Genomics Research Institute, Phoenix, AZ, USA; [7]Multiple Myeloma Research Foundation, Norwalk, CT, USA; [8]Northern Institute for Cancer Research, Newcastle University, Newcastle upon Tyne, UK and [9]Division of Hematology Oncology, Indiana Univeristy, Indianapolis, IN, USA

Ferrata Storti Foundation

Haematologica 2020
Volume 105(4):1055-1066

ABSTRACT

MYC is a widely acting transcription factor and its deregulation is a crucial event in many human cancers. *MYC* is important biologically and clinically in multiple myeloma, but the mechanisms underlying its dysregulation are poorly understood. We show that *MYC* rearrangements are present in 36.0% of newly diagnosed myeloma patients, as detected in the largest set of next generation sequencing data to date (n=1,267). Rearrangements were complex and associated with increased expression of *MYC* and *PVT1*, but not other genes at 8q24. The highest effect on gene expression was detected in cases where the *MYC* locus is juxtaposed next to super-enhancers associated with genes such as *IGH, IGK, IGL, TXNDC5/BMP6, FAM46C* and *FOXO3*. We identified three hotspots of recombination at 8q24, one of which is enriched for *IGH-MYC* translocations. Breakpoint analysis indicates primary myeloma rearrangements involving the *IGH* locus occur through non-homologous end joining, whereas secondary *MYC* rearrangements occur through microhomology-mediated end joining. This mechanism is different to lymphomas, where non-homologous end joining generates *MYC* rearrangements. Rearrangements resulted in overexpression of key genes and chromatin immunoprecipitation-sequencing identified that *HK2*, a member of the glucose metabolism pathway, is directly over-expressed through binding of *MYC* at its promoter.

Correspondence:

BRIAN A. WALKER
bw75@iu.edu

Received: January 29, 2019.

Accepted: June 13, 2019.

Pre-published: June 20, 2019.

doi:10.3324/haematol.2019.217927

Check the online version for the most updated information on this article, online supplements, and information on authorship & disclosures: www.haematologica.org/content/105/4/1055

Introduction

The genome of multiple myeloma (MM) is characterized by primary translocations in approximately 40% of newly diagnosed patients that are considered initiating events and involve rearrangements of the immunoglobulin heavy chain (*IGH*) locus on 14q32.[1] The partners of these rearrangements include 11q (*CCND1*, 15%), 4p (*FGFR3* and *MMSET*, 10%), 16q (*MAF*, 2-3%), 20q (*MAFB*, 1%), and 6q (CCND3, 1%). These rearrangements result in placement of the *IGH* super-enhancers next to a partner oncogene, resulting in its overexpression.[2] The rearrangements predominantly occur in the switch regions 5' of the constant regions in the *IGH* locus, where a high concentration of activation-induced cytidine deaminase (AID) binding motifs are found. Normally, AID binds to the switch regions leading to class switch recombination, resulting in antibody isotype

switching.[3] However, abnormal breaks in the switch regions, resulting from AID activity, result in *IGH* translocations.[4]

Secondary translocations involving *MYC*, located on 8q24.21, also occur in MM and are associated with disease progression and increased expression of *MYC*.[5-8] *MYC* encodes a transcriptional regulator and has been shown to be involved in proliferation, differentiation, protein synthesis, apoptosis, adhesion, DNA repair, chromosomal instability, angiogenesis, and metastasis.[9-13] Translocations and high expression of *MYC* are associated with poor outcome, especially in MM where it is a marker of aggressive disease.[5,14] *MYC* can be deregulated by a range of different mechanisms including chromosomal rearrangement,[5,6] copy-number gain/amplification,[15,16] protein stabilization,[17] *via* secondary messengers involved in *MYC* transcription[18] or miRNA such as *PVT1*.[19,20]

The frequency of *MYC* rearrangements seen in newly diagnosed MM (NDMM) varies from 15% to 50%, and is dependent on the method used to identify it.[5,6,21,22] The data are consistent with *MYC* rearrangements being rare in the asymptomatic stages, such as monoclonal gammopathy of uncertain significance and smoldering myeloma,[21] and increases as the disease progresses, with a high incidence (>80%) in myeloma cell lines.[22-24]

MYC rearrangements are not only seen in MM, but are also frequent in lymphomas, where they have been extensively studied.[25,26] In Burkitt's lymphoma and diffuse large B-cell lymphoma t(8;14), rearrangements between *IGH* and *MYC* have also been shown to result from abnormal class switch recombination.[27] The relevance of AID in these rearrangements is supported by data from IL-6 transgenic mice which also develop *MYC/IGH* rearrangements in B cells. Rearrangements, however, do not occur if the mice are also deficient in AID, indicating that class switch recombination *via* AID is key in generating these rearrangements.[4,28] In MM, while karyotypic abnormalities similar to those observed in Burkitt's lymphoma are seen, variant structures can also be detected, suggesting that the mechanism of rearrangement in MM may not be identical to that in lymphoma.[29] Indeed, *MYC* rearrangements are not considered to be predominantly primary translocations in MM, as they often develop at later stages of the disease;[22] whereas in lymphoma they are considered to be primary events.[27]

We and others have previously shown that *MYC* translocations result in the juxtaposition of immunoglobulin loci super-enhancers to *MYC* resulting in its overexpression.[6,30] However, the details of breakpoint locations, the presence of copy-number abnormalities, and the chromatin landscape of the rearrangement have not been well-characterized. In the present study, we analyzed a large dataset of 1,267 NDMM patients to determine the genomic architecture of *MYC* rearrangements and their effect on the expression of this proto-oncogene.

Methods

Patients' samples and next generation sequencing

A total of 1,267 NDMM patients were included in this study after giving informed consent and the study was approved by the Institutional Review Board at the University of Arkansas for Medical Sciences. Plasma cells were isolated from bone marrow aspirates by magnetic-activated cell sorting using CD138$^+$ marker, AutoMACS Pro (Miltenyi Biotec GmbH, Bergisch Gladbach, Germany) or Robosep (STEMCELL Technologies, Vancouver, BC, Canada). DNA from peripheral blood was used as a control sample for each patient to exclude germline variants. Three paired-end read sequencing platforms were combined without overlapping patients: targeted sequencing, whole exome sequencing, and low depth, long insert whole genome sequencing (*Online Supplementary Methods*). Additional expression data were available through either gene expression microarrays (Affymetrix, Santa Clara, CA, USA) or RNA-sequencing. An overall summary of methods, number of patients and external datasets are shown in *Online Supplementary Figure S1*. Patients' characteristics are summarized in *Online Supplementary Table S1* and *MYC* region capture is illustrated in *Online Supplementary Figure S2*.

Patient-derived xenografts

Patient-derived xenografts were generated by passaging primary patient CD138$^+$ selected cells through the previously described SCID-rab myeloma mouse model.[31] Tumors were dissected from the mouse, and pieces dispersed into a single cell population using a Kontes disposable tissue grinder. Cells were filtered through a 70 μm sterile filter, washed twice in PBS, treated with red cell lysis buffer, washed twice more, and treated immediately with Annexin V-coated magnetic beads (Miltenyi Biotec), resulting in a population of cells with a viability >95%, as checked by flow cytometry. Passaged cells underwent CD138$^+$ selection before being processed for 10x Genomics whole genome sequencing, RNA-sequencing, and chromatin immunoprecipitation-sequencing (ChIP-seq).

Chromatin immunoprecipitation-sequencing

Chromatin immunoprecipitation-sequencing was performed on the myeloma cell lines KMS11 and MM.1S as well as a PDX sample with an *MYC* rearrangement identified by whole genome sequencing. 1x10^7 cells per mark were fixed in a 1% formaldehyde solution, followed by the addition of glycine to a final concentration of 0.125 M. Cells were washed and resuspended in PBS containing 0.5% Igepal with 1% PMSF, before being pelleted and frozen at -80oC. ChIP-seq for the histone marks H3K4me1, H3K4me3, H3K9me3, H3K27me3, H3K27Ac, and H3K36me3 (Active Motif, Carlsbad, CA, USA), as well as the super-enhancer proteins BRD4 and MED1 (Bethyl, Montgomer, TX, USA), and the transcription factor MYC (Santa Cruz Biotechnology, Dallas, TX, USA) were performed by Active Motif. Controls without antibody input were performed to ensure data quality.

Data analysis

Data analysis was performed as described previously, with minor differences between sequencing modalities.[32] For details see *Online Supplementary Methods.*

Statistical analysis

Basic statistical analysis was performed using GraphPad Prism 7.01 (GraphPad Software, San Diego, CA, USA), R 3.4.4 and/or RStudio 1.1.442. Fisher's exact test, the Mann-Whitney U test, Spearman's rank correlation and Log-Rank test with Benjamini-Hochberg adjustment were used for data analysis. $P \leq 0.05$ was considered statistically significant.

Data access

Sequencing data have been deposited in the European Genomic Archive under the accession numbers EGAS00001001147, EGAS00001002859, or at dbGAP under Accession phs000748.v5.p4.

Results

MYC rearrangements are usually present as inter-chromosomal translocations, co-occur with secondary genetic events, and are associated with shorter survival in non-hyperdiploid cases

We examined a set of 1,267 NDMM patient samples that had undergone either whole genome sequencing, exome sequencing, or targeted sequencing, of which the latter two methods involved capture of 2.3 Mb and 4.5 Mb, respectively, surrounding the *MYC* locus. Structural abnormalities involving the region surrounding *MYC*, including translocations, inversions, tandem-duplications and deletions, were detected in 36.0% (456 of 1,267) of NDMM samples. Of these 456, 56.6% (258 of 456) had only a translocation, and 30.0% (137 of 456) had only an intra-chromosomal rearrangement. In 13.4% (61 of 456), both translocation and intra-locus rearrangement were present. Non-synonymous *MYC* mutations were rarely detected (0.7%, 9 of 1,264) (*Online Supplementary Table S2*).

The frequency of 8q24 abnormalities was significantly increased across International Scoring System (ISS) stages (I: 28.6%, II: 37.5%, III: 41.6%; $P<0.001$), and were higher in the International Myeloma Working Group (IMWG) high-risk (34.6%) and standard-risk (28.1%) groups than in the low-risk group (23.6%; $P<0.05$). The association of 8q24 abnormalities with these negative prognostic factors may suggest a worse outcome of patients with 8q24 abnormalities; however, analysis of this did not confirm the assumption in this dataset (*Online Supplementary Figure S4A*). In addition, 8q24 abnormalities were associated with lower, rather than higher, NF-κB pathway activation (*Online Supplementary Figure S3*). Additional analysis, however, showed a significant effect of 8q24 abnormalities within the non-hyperdiploid sub-group (Figure 1A).

Translocations were found in 25.2% (319 of 1,267) of

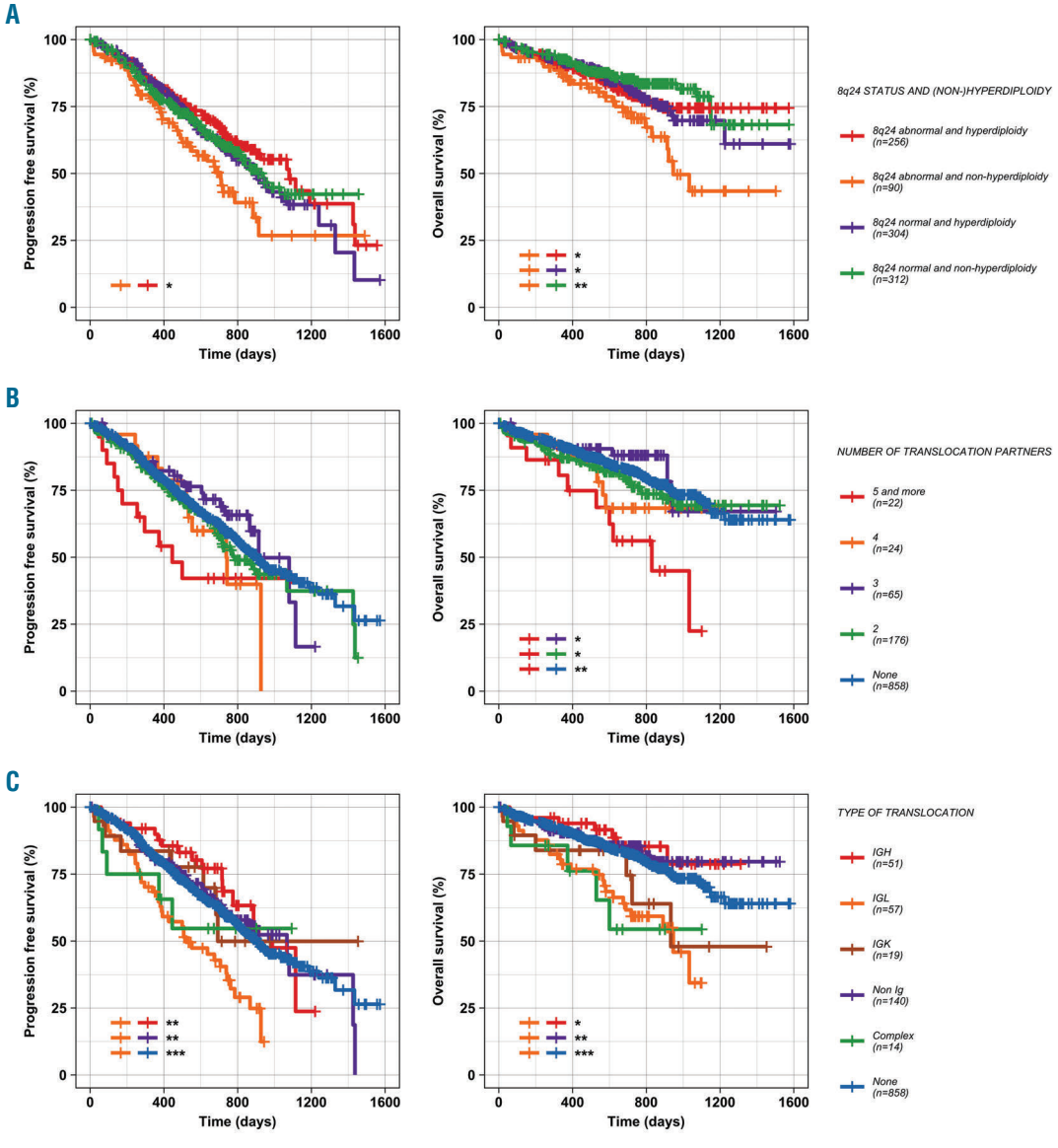

Figure 1. Effect of 8q24 abnormalities on patients' outcome. (A) 8q24 abnormalities and hyperdiploidy. (B) Translocation complexity. (C) Translocations involving specific types of immunoglobulin locus. *$P<0.05$; **$P<0.01$; ***$P<0.001$. n: number.

samples and occurred most frequently as inter-chromosomal translocations involving 2-5 chromosomes (90.3%, 288 of 319); but 4.4% (14 of 319) were highly complex and involved more than five chromosomal loci (Figure 2). Of the remaining cases, 5.3% (17 of 319) involved a large inversion of chromosome 8, >10 Mb in size. The proportion of *MYC* translocations involving 2, 3, 4, and 5 loci was 62.1% (198 of 319), 22.9% (73 of 319), 8.2% (26 of 319), and 2.5% (8 of 319), respectively. However, the number of chromosomes detected as being affected by rearrangements involving *MYC* was dependent on the sequencing capture method used, as rearrangements involving five or more chromosomes were detected only by whole genome sequencing (*Online Supplementary Tables S3 and S4*). These data demonstrate that *MYC* is affected through chromoplexy, where three or more loci are involved in rearrangements in 9.6% (121 of 1,267) of NDMM or 26.5% (121 of 456) of samples with *MYC* abnormalities.

IGH-MYC translocation breakpoints have a distinct distribution compared to primary translocations and involve recurrent partners with known super-enhancers

A total of 149 chromosomal loci were found to be involved in *MYC* translocations (Figure 2A and *Online Supplementary Tables S5 and S6*). Six translocation partners were found in at least ten cases and were the immunoglobulin loci, *IGH* (63 of 1,253, 5.0%), *IGL* (63 of 1,253, 5.0%), *IGK* (26 of 1,253, 2.1%), and also *TXNDC5/BMP6* on chromosome 6 (34 of 1,253, 2.7%), *FAM46C* on chromosome 1 (20 of 1,253, 1.6%), and *FOXO3* on chromosome 6 (14 of 1,253, 1.1%) (*Online Supplementary Table S5*). Each of these non-Ig loci was confirmed to contain highly-expressed genes in MM using

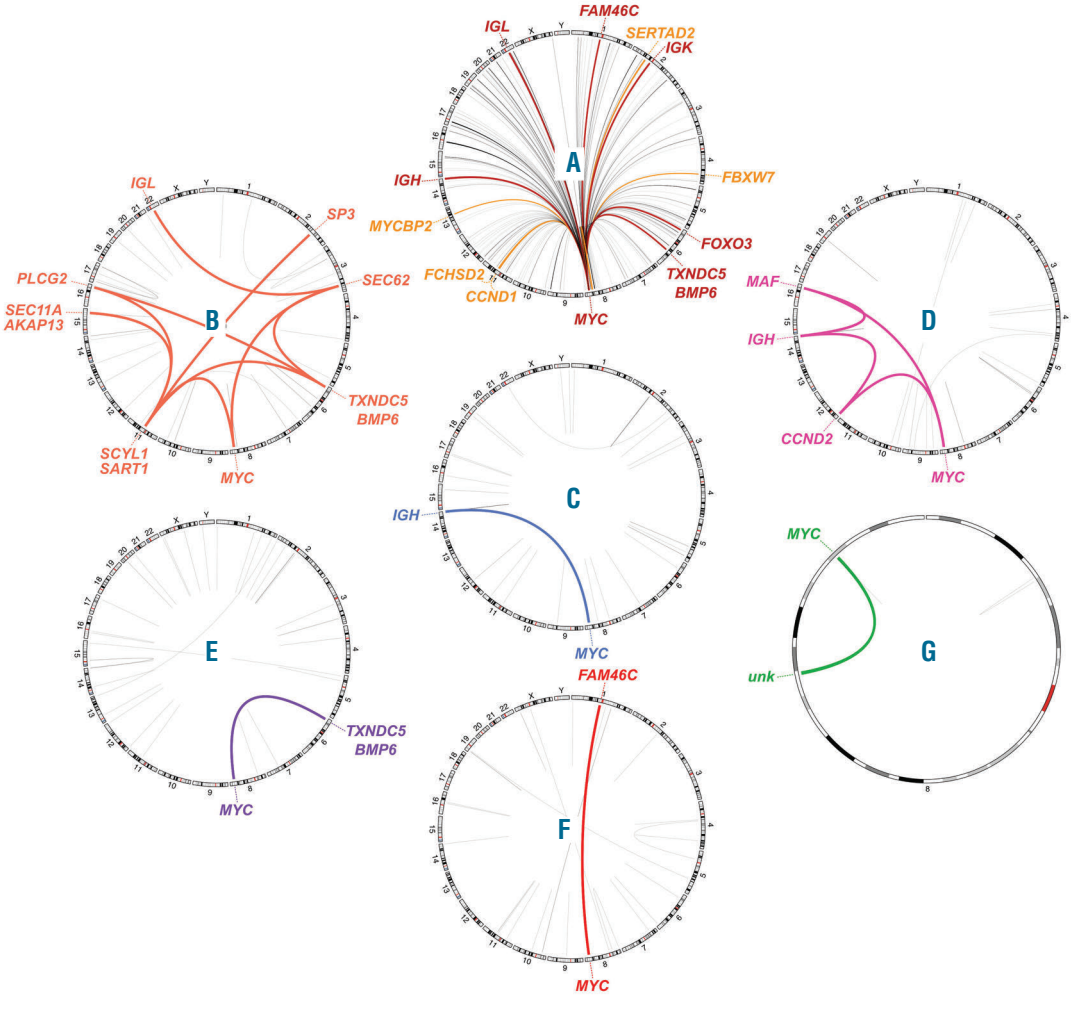

Figure 2. Circos plots of multiple myeloma samples showing various *MYC* rearrangements. (A) *MYC* translocations partners in the dataset of the 1,253 non-complex cases; loci present in 5-9 cases (orange lines) and ≥10 cases (red lines) are highlighted. (B) Complex chromoplexy involving seven chromosomes, including the *MYC* locus. (C) Simple *IGH-MYC* t(8;14). (D) t(14;16) with a secondary translocation to MYC. (E) Non-Ig *MYC* translocation involving *TXNDC5/BMP6* on chromosome 6. (F) Non-Ig *MYC* translocation involving FAM46C on chromosome 1. (G) Inversion on chromosome 8. Annotated genes in uncertain loci were chosen as the closest highly-expressed gene(s) (within 1 Mb maximum distance) defined as being present in >95% of patients with $\log_2$ normalized counts >10 in the dataset of 571 cases tested by RNA-sequencing.

RNA-sequencing data, being present in >95% of patients with $\log_2$ normalized counts >10. All of the loci except for *IGK* had super-enhancers previously identified in the MM.1S cell line; 67.2% (205 of 305) of cases with non-complex translocation (5 or less loci involved) had at least one of these super-enhancers involved in the translocation. Another five partners were present in 5-10 cases, three of which overlapped with the highly-expressed genes *FCHSD2, FBXW7* and *SERTAD2*, which are associated with known super-enhancers.[30]

Interestingly, 13 samples had complex *MYC* translocations with more than one of these super-enhancers. In addition, eight samples had rearrangements involving *IGH, MYC* and *CCND1*, and four samples had rearrangements with *IGH, MYC* and *MAF*, indicating that they may occur as primary events early in the disease process. All oncogenes involved in these translocations show high expression (*Online Supplementary Figure S5*). This targeting of multiple oncogenes may explain worse survival in patients with complex *MYC* translocations (Figure 1B). Ig loci were involved in 47.9% (146 of 305) of cases with an *MYC* translocation and were not associated with significantly higher *MYC* expression (Figure 3B and *Online Supplementary Figure S6B*) or patients' survival (*Online Supplementary Figure S4D*) compared to samples involving other super-enhancer-associated genes. In six cases, an *IGH* translocation occurred together with one of the light-chain immunoglobulin loci, but no sample involved both light chain loci. Within the Ig translocation groups, patients with *IGL* partners showed significantly worse outcome in comparison to *IGH* (P<0.05), other non-Ig translocations (P<0.01), and cases without *MYC* translocations (P<0.001) (Figure 1C).

Analysis of the breakpoints at the *IGH* locus indicated a different pattern of *MYC* rearrangements to that of the primary Ig translocations. The primary translocations involving t(4;14), t(6;14), t(11;14), t(14;16), and t(14;20) have breakpoints clustered around the constant switch regions where AID motifs are concentrated. However, the *MYC* translocations do not share this pattern and are dispersed across the constant region, showing no association with AID motif clusters. This indicates that the *MYC* translocations are likely to be independent of AID and occur in a manner that is distinct from that of the primary translocations (Figure 4A and B).

MYC breakpoints show evidence of recombination through microhomology

It is known that class switch recombination breakpoints in B cells occur through AID and non-homologous end joining (NHEJ), resulting in blunt ended DNA being ligated together.[33] As the *MYC* breakpoints identified here do not align to switch regions, and are presumably not mediated by AID, we examined the aligned breakpoints to determine if they were constructed through blunt ended joining or other mechanisms. In comparison to re-aligned t(4;14), t(6;14), t(11;14), t(14;16), and t(14;20) breakpoints, which are mediated by AID and NHEJ, the *MYC* breakpoints had significantly fewer blunt ended rearrangements (54.1% *vs.* 27.7%; P<0.001) and significantly more rearrangements

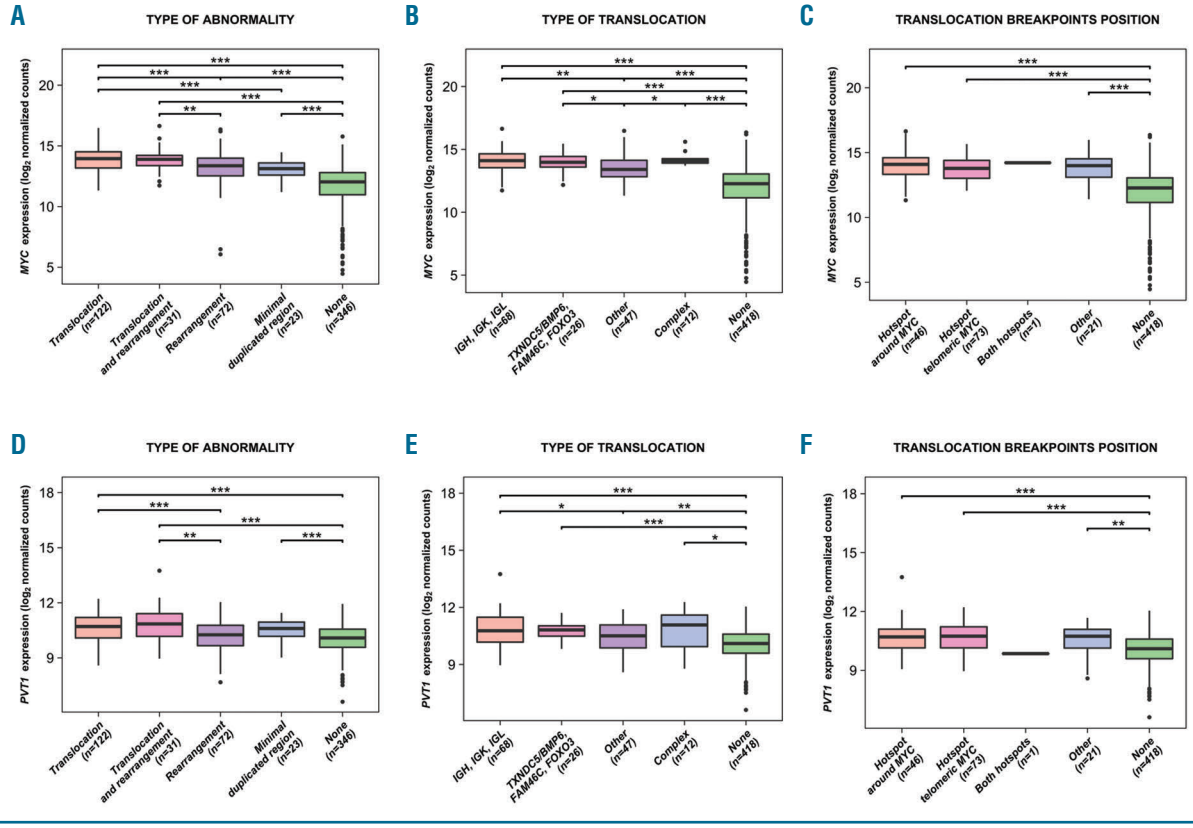

Figure 3. RNA-sequencing expression analysis of *MYC* and *PVT1* in relation to chromosomal abnormalities at 8q24. Effect of abnormality type (A and D), translocation category (B and E), and translocation breakpoint position (C and F) are shown for MYC and PVT1, respectively. *P<0.05; **P<0.01; ***P<0.001. n: number.

with at least two nucleotides of homology (25.4% *vs.* 45.8%) between the chromosomes (Figure 4C). Homologous sequences between chromosomes of up to 12 nts were found. Representative alignments of rearrangements are shown in the *Online Supplementary Appendix*. These homologous sequences are representative of microhomology-mediated end joining (MMEJ), which is a mechanism more common to all secondary translocation events (Figure 4C).

8q24 breakpoints occur in three hotspots and are associated with open chromatin markers

Breakpoints were determined in a region covering up to 2.5 Mb from *MYC* and were categorized by the type of rearrangement. Three clusters of chromosomal breakpoints related to translocations, inversions, deletions and tandem-duplications were identified in the region chr8:126.0-131.0 Mb (Figure 5).

Translocation breakpoint hotspots were located in two 310 kb regions: one around *MYC* (chr8:128.6-129.0 Mb) and one telomeric of *MYC* (chr8:129.1-129.4 Mb). When examining all translocations, 28.2% were centered around the first hotspot and 46.6% around the second hotspot. However, there was an enrichment of Ig partner breakpoints at the second hotspot (55.3%) compared to first hotspot (18.9%), which was not so pronounced with non-Ig partners (41.2% *vs.* 34.0%). There was no evidence of an AID motif cluster at the second hotspot, which could have explained the enrichment for Ig partners and there was no effect of the breakpoint position on patient outcome (*Online Supplementary Figure S4E*).

Tandem-duplication breakpoints were enriched at the second hotspot (69.0% of breakpoints) (Figure 5 and *Online Supplementary Figures S7 and S8*) as have previously been noted in MM cell lines.[34] Conversely, deletion breakpoints were enriched at the first hotspot (30.5%) and at an additional hotspot centromeric of *MYC* (chr8:126.3-126.4 Mb). Inversion breakpoints were equally spread across all three hotspots.

By examining histone marks from the U266 cell line and four myeloma samples, for which we generated ChIP-seq histone mark data, there was also a link with accessible chromatin marks (H3K4me1, H3K4me3, H3K27ac and H3K36me3), DNaseI hypersensitivity sites, and all three breakpoint hotspots, indicating that rearrangements may be more likely to happen in highly accessible, transcribed regions (Figure 5).

Figure 4. Primary *IGH* rearrangements and *MYC* rearrangements occur through different mechanisms. (A) The locations of classical *IGH* (green dots) and *IGH-MYC* (red dots) translocation breakpoints on 14q32.33. Yellow bars show super enhancers identified in MM.1S cell line. Purple bars show activation-induced cytidine deaminase motif clusters (>200 RGYW motifs per 2.5 kb) indicating switch (S-) regions. IGH constant regions are indicated as red blocks. (B) IGH-MYC breakpoints on 8q24.21 (red dots). Blue bars show the two breakpoint hotspots identified in Figure 5. The location of *MYC* (red) and other genes (gray) are indicated. (C) Primary *IGH* translocations, *MYC* translocations and other translocations were compared for microhomology between chromosomes surrounding the breakpoints. Primary translocations have significantly more blunt-ended rearrangements compared to *MYC* rearrangements ($P<0.001$), consistent with microhomology-mediated end joining.

Disruption of topologically associated domains by *MYC* rearrangements.

Topologically associated domains (TAD) have been shown to contain DNA elements that are more likely to interact with one another. Disruption of these TAD may bring super-enhancer elements into the same TAD as *MYC*, resulting in its increased expression. We examined the super-enhancers from the MM.1S cell line, and TAD from RPMI-8226 and U266 cell lines and integrated MYC breakpoints.

On the six frequent *MYC* translocation partner loci, breakpoints were clustered near to the super-enhancer and within the same TAD as the super-enhancer (Figure 6). At 8q24, the translocation breakpoints, at the two hotspots, were clustered within the TAD containing *MYC* and *PVT1*. The resulting rearrangements would bring the super-enhancer from the partner loci adjacent to MYC, resulting in the formation of a Neo-TAD (Figure 7B) and overexpression of *MYC*.

We identified a patient-derived xenograft sample with a t(4;8) that resulted in insertion of three regions of chromosome 4 next to *MYC* (Figure 7A). This resulted in the super-enhancer from *PCDH10*, defined by the presence of H3K27Ac and MED1 marks, being placed next to *MYC*, resulting in overexpression. This shows for the first time in a patient sample a rearrangement that confirms the importance of the placing of a super-enhancer next to *MYC*.

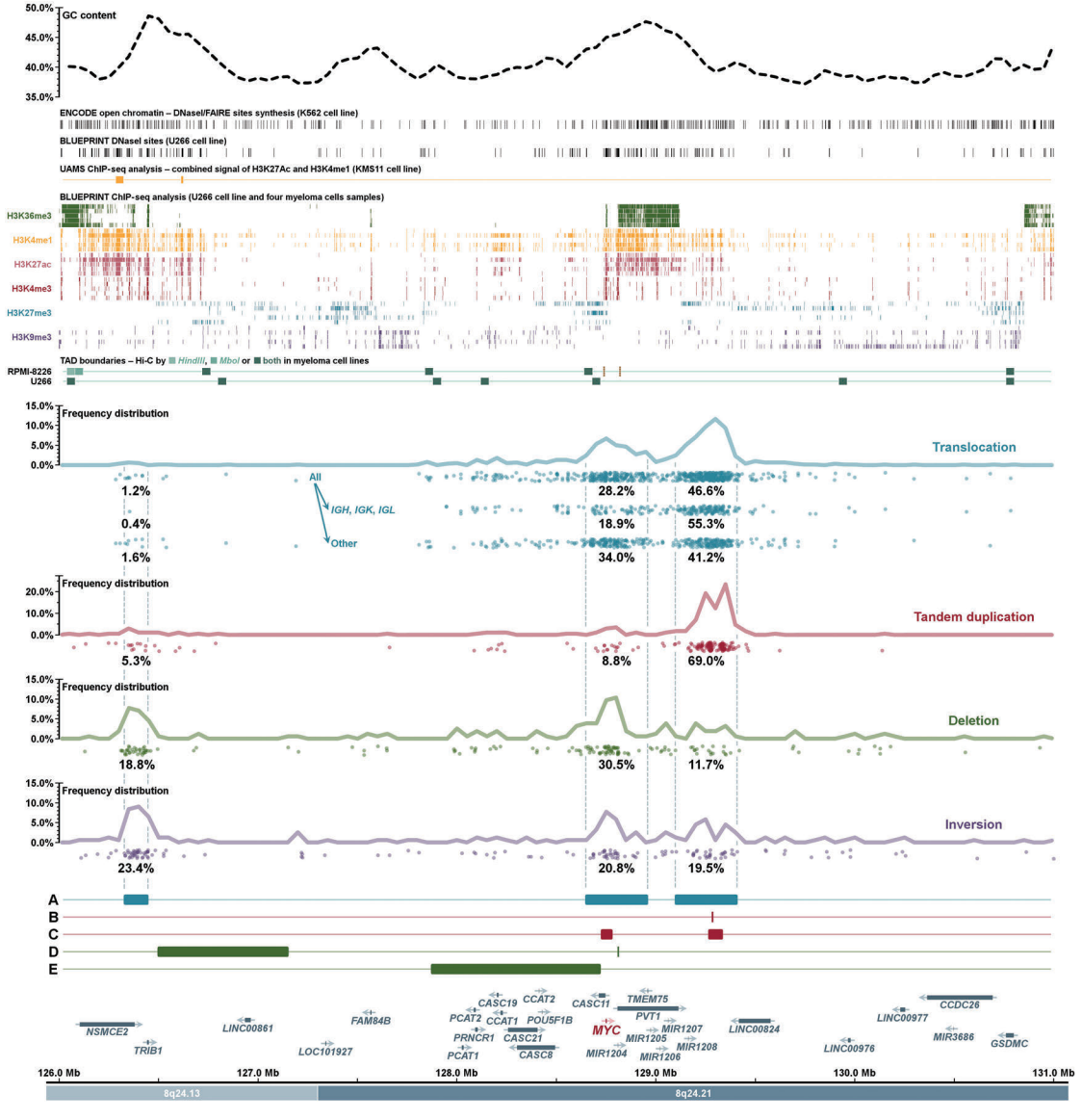

Figure 5. Distribution of chromosomal breakpoints and minimally altered regions detected at the *MYC* region. Percent values show proportion of breakpoints in the defined hotspot for a specific category of abnormalities. (A) Three breakpoints hotspots. (B) Minimal tandem-duplicated region. (C) Two minimal copy number gained regions (excluding tandem-duplications). (D) Two minimally deleted regions. (E) Minimal copy-number lost region (excluding deletions). Details of copy-number abnormalities analysis are given in *Online Supplementary Figures* S2 and S3. Upper dotted line shows germinal center (GC) content, ENCODE open chromatin markers identified by a combination of DNase-seq and FAIRE-seq in cell line K562, BLUEPRINT DNase-seq analysis of U266 cell line and BLUEPRINT chromatin immunoprecipitation (ChIP)-sequencing analysis in U266 cell line and four myeloma patients' samples.

Lastly, deletions at 8q24 centromeric of *MYC* are present in 2.9% (36 of 1,249) of samples (Figure 5 and *Online Supplementary Figures S7 and S8*), and most frequently result in contraction of the region bringing *NSMCE2* into close proximity of *MYC* (Figure 7C). This interstitial deletion results in TAD disruption, bringing the super-enhancer at *NSMCE2*, present in the cell lines KMS11 and MM.1S, into the same TAD as *MYC*, resulting in a fused TAD and overexpression of *MYC*.

8q24 translocations result in increased expression of *MYC* and *PVT1*

The biological consequence of rearrangements at 8q24 is thought to be increased expression of *MYC*, so we examined the available CoMMpass study RNA-sequencing data (Figure 3) and a set of microarray data (*Online Supplementary Figure S6*), and categorized samples by type and location of breakpoints. In addition to *MYC*, we examined the expression of other genes in the regions, but only found significant increases in *MYC* and the non-coding *RNA, PVT1* (Figure 3A-F), which were associated with particular types of rearrangements. Expression level of these two genes showed a significant but weak correlation (r=0.4, *P*<0.001).

The six *MYC* partner loci present in >10 samples (*IGH, IGK, IGL, TXNDC5/BMP6, FOXO3* and *FAM46C*) had significantly higher expression of *MYC* (*P*<0.001) and *PVT1* (*P*<0.001) compared to those without rearrangements or less frequent partners (Figure 3B and E). Complex rearrangements involving more than five loci also resulted in higher expression of *MYC* (*P*<0.001) and *PVT1* (*P*=0.02) compared to those without rearrangements, at levels equivalent to the frequent translocation partners indicating a selection pressure on these six loci for increased *MYC* expression. There was no difference in expression between samples with breakpoints at the hotspot around *MYC* or telomeric of *MYC* (Figure 3C and F). There was no difference in expression trends between hyperdiploid (*Online Supplementary Figure S9*) and non-hyperdiploid (*Online Supplementary Figure S10*) subgroups, but a comparison between specific *MYC* abnormality groups shows that *MYC* and *PVT1* expression is higher in the hyperdiploidy group (*Online Supplementary Figure S11*).

Integration of *MYC* binding sites with over-expressed genes identifies proliferation markers as key targets

We went on to determine if there is a gene expression signature associated with *MYC* abnormalities. We compared samples with and without any structural change at 8q24 and adjusted for hyperdiploidy status, as *MYC* abnormalities were present twice as often in samples with hyperdiploidy (46.0%, 290 of 630) as compared to non-hyperdiploid samples (22.7%, 102 of 449; *P*<0.001). A total of 121 genes (113 protein-coding and 8 non-coding *RNA* genes) were significantly de-regulated with a fold-change threshold of 1.8, of which 31.4% (38 of 121) were up-regulated and 68.6% (83 of 121) were down-regulated (Figure 8A). No significant pathway enrichment was detected by Gene Ontology Consortium[35] using both PANTHER[36,37] and Reactome[38] pathway analysis. (For details of each gene see *Online Supplementary Table S7*).

We performed ChIP-seq against c-Myc and determined

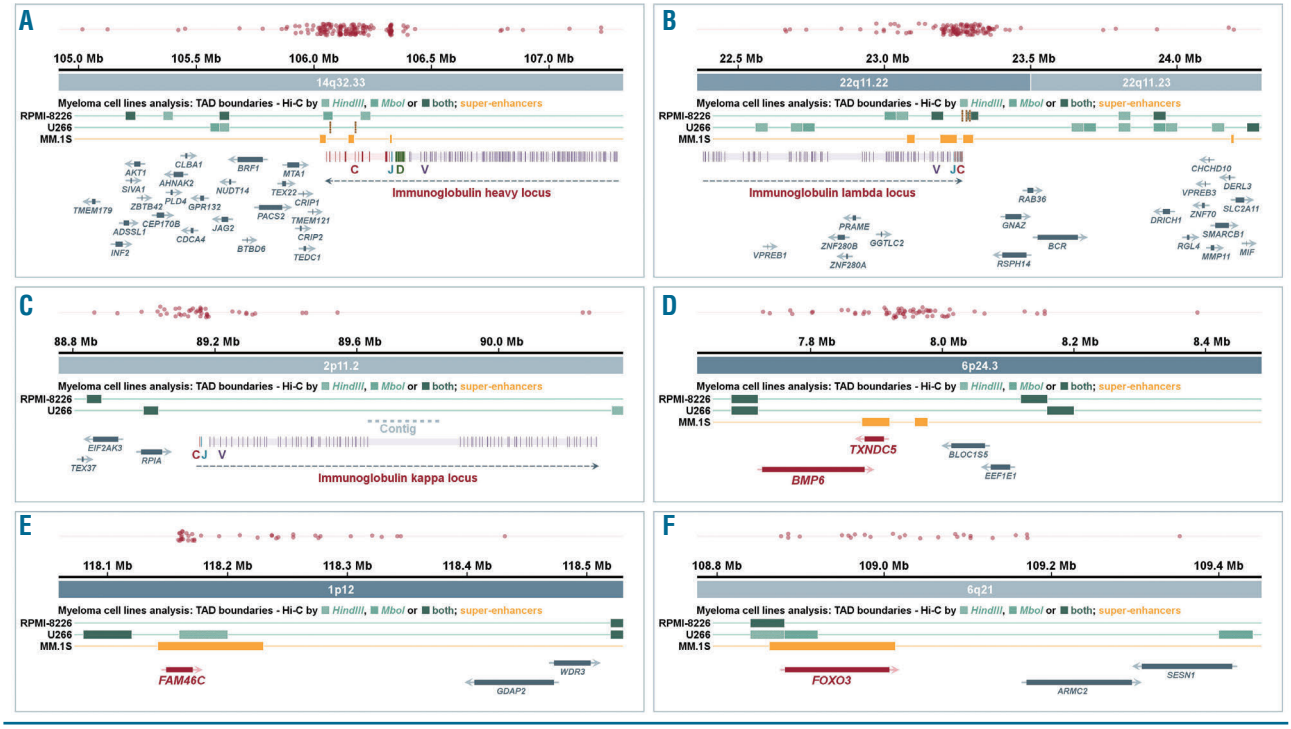

Figure 6. Chromosomal breakpoints in *MYC* translocation partners' regions. (A) *IGH* locus at 14q32.33. (B) *IGL* locus on 22q11.22-22q11.23. (C) *IGK* locus on 2p11.2. (D) *TXNDC5/BMP6* locus on 6p24.3. (E) *FAM46C* locus on 1p12. (F) *FOXO3* locus on 6q21. Yellow bars show super-enhancers identified in the MM.1S cell line; green bars show topologically associated domain (TAD) boundaries identified in RMPI-8226 and U266 cell lines. Ig genes are separated into constant (C, red), joining (J, blue), diversity (D, green) and variable (V, purple) regions; non-Ig highly-expressed genes (present in >95% of patients with $\log_2$ normalized counts >10 in the dataset of 571 cases tested by RNA sequencing) are in red and other genes in gray.

binding sites in two MM cell lines, MM.1S and KMS11, both of which have an *MYC* rearrangement. The peaks with a significance $P<10^{-100}$ using *MACS2* in either cell line were considered significant and accounted for 4.7% of peaks (1,266 of 27,006) (Figure 8B). The peaks were compared to the 121 genes that were significantly changed in expression (Figure 8A). Six genes were in the intersection between over-expressed and significant peaks: *HK2, MTHFD1L, SLC19A1, MFNG, SNHG4, GAS5,* (Figure 8C). Using less stringent ≥1.3 fold-change cut-off that provided 1,801 genes, of which 40.8% (735 of 1,801) were over-expressed, the intersection of over-expressed genes and those with a significant *MYC* binding peak was 25.3% (186 of 735). At the top of the list of 186 genes ordered by ChIP-seq -log10 P, we detected upregulation of the genes with known or potential oncogenic activity such as genes promoting cell proliferation, tumor growth and/or inhibition of apoptosis (*SNHG15, PPAN, MAT2A, METAP1D, MTHFD2, SNHG17*), translation factors (*EIF3B, EIF4A1, EEF1B2*), and genes involved in ribosome biosynthesis (*RPL10A, RPL35, RPL23A, RPSA, RPL13, WDR43*).

Importantly, we identified *HK2* and *PVT1* as direct targets of MYC. *HK2* is one of the most significant genes detected by ChIP-seq in both cell lines (-log10 *P*>200) (Figure 8C), as well as having the highest fold-change using RNA-sequencing analysis (*Online Supplementary Table S7*). This gene is an interesting direct target of MYC as it is part of the glucose metabolism pathway and would lead to increased energy metabolism and proliferation. *PVT1* showed a smaller fold-change by RNA-sequencing analysis (approx. 1.4) but had a significant c-Myc protein binding site identified by ChIP-seq, meaning that overexpression of *PVT1* is likely to be a downstream effect of *MYC* overexpression. This leads to a positive feedback loop and even higher *MYC* expression, as *PVT1* positively regulates *MYC* expression.[39]

Discussion

We show that *MYC* breakpoints in myeloma are clustered in three main hotspots on chromosome 8, one of which is associated with Ig translocations and tandem-

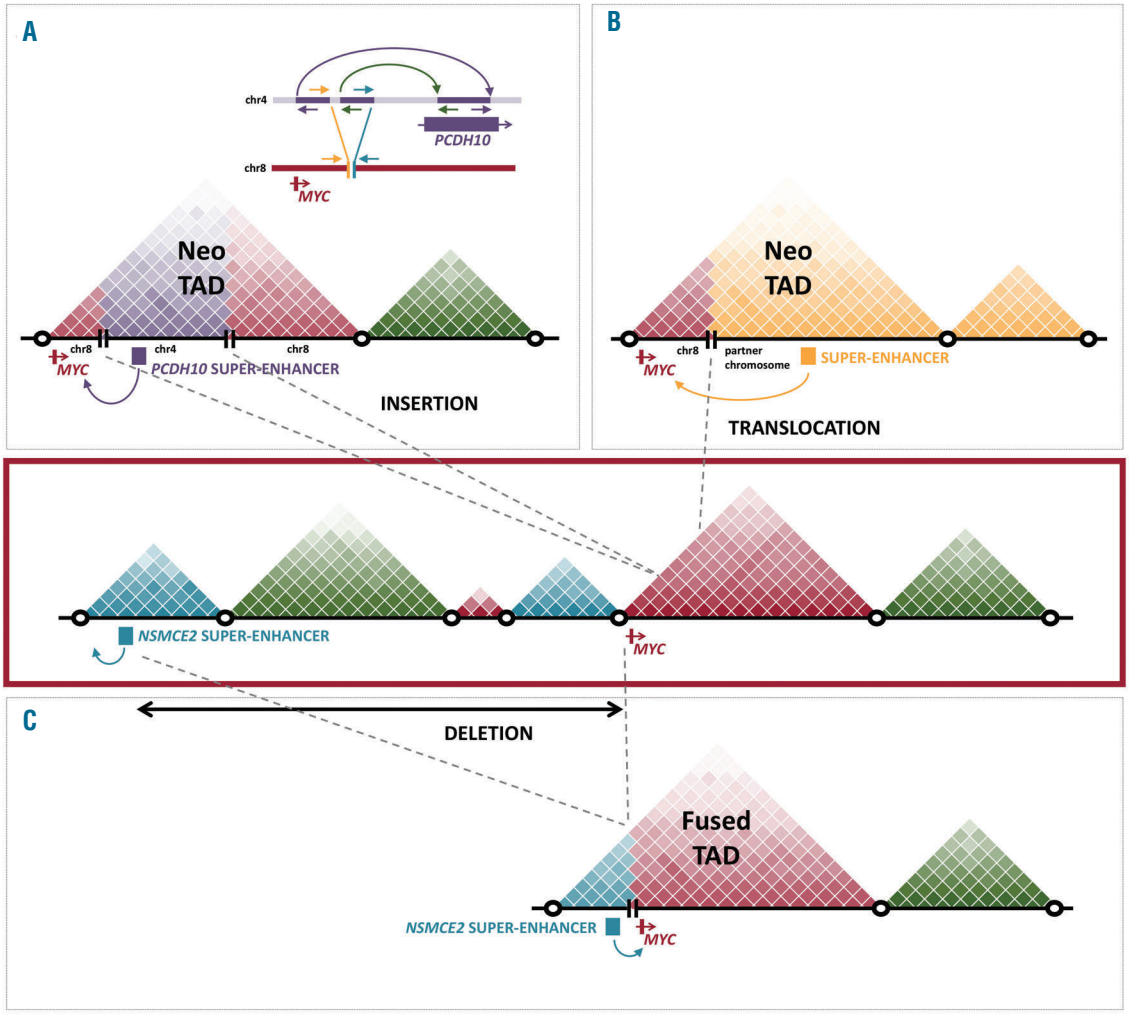

Figure 7. TAD reorganization through rearrangements places a super-enhancer next to *MYC*. The TAD architecture (colored triangles) surrounding *MYC* is indicated in the central panel (red box) as defined in U266 cells. (A) A patient sample with a t(4;8) involves the insertion of a super-enhancer from *PCDH10* (chr4) into chr8, creating a neo-TAD containing *MYC* and the super-enhancer. (B) A translocation from a key MYC partner introduces a super-enhancer into the *MYC* TAD. (C) Deletions centromeric of *MYC* result in fusion of TAD containing *MYC* and the super-enhancer next to *NSMCE2*.

duplications, another with non-Ig translocations and deletions, and the third with deletions and inversions. All breakpoints surrounding *MYC* result in increased expression of the oncogene, but inter-chromosomal translocations result in the largest increase in expression.

In this dataset, we have used 1,267 NDMM patient samples (of which 36.0% had *MYC* abnormalities) using next generation sequencing consisting of whole genome, exome and targeted panel data. The frequency of *MYC* abnormalities reported here is higher than previously seen using other techniques, such as karyotyping or fluorescence *in situ* hybridization (FISH). This is likely due to the increased resolution of sequencing technologies that can identify small insertions or deletions as well as translocations involving infrequent partner chromosomes. In addition, the complexity of breakpoints at 8q24 makes the placement of FISH probes difficult if all abnormalities are to be detected. The scale of this analysis has allowed us to define the molecular breakpoints surrounding *MYC* with unparalleled accuracy and without technical bias. One of the two rearrangement hotspots involved in inter-chromosomal translocations in MM is also seen in other B-cell malignancies. In Burkitt's lymphoma, two breakpoint clusters within exon 1 and intron 1 of *MYC* were defined, which corresponds in location to the non-Ig rearrangement hotspot in MM.[26] The same cluster is seen in diffuse large B-cell lymphoma, where other random breakpoints are also seen scattered both centromeric and telomeric of *MYC*.[25] Both of these studies looked at relatively small numbers of samples (78 and 17, respectively) and used older techniques, such as long distance PCR and FISH, to detect the breakpoints. It may be that there are also other breakpoint hotspots similar to MM in other B-cell malignancies.

The main chromosomal partner to *MYC* through inter-chromosomal rearrangements is chromosome 14, specifically the *IGH* locus. In Burkitt's lymphoma, the *IGH-MYC* breakpoints on this chromosome lie almost exclusively within the switch regions (87%), upstream of the *IGH* constant regions.[26] The remaining 13% are within the joining region of the locus. These breakpoints are consistent with the *IGH-MYC* rearrangement, being a primary event in Burkitt's lymphoma, occurring in 70-80% of patients.[40] In contrast, in MM, we clearly see that *IGH-MYC* breakpoints within the *IGH* locus are not in the switch or joining regions; instead, they are spread out across the constant regions of the locus. This spread is distinct from the five common primary translocation breakpoints in MM [t(4;14), t(11;14), etc.] which are restricted to the switch and joining regions. Even those with *MYC* breakpoints within switch regions (6.9% of *IGH-MYC* rearrangements) also have primary rearrangements or are hyperdiploid. This indicates that the *IGH-MYC* rearrangements are secondary events in MM and probably occur through a different molecular mechanism to the primary translocation events. It is known that the primary translo-

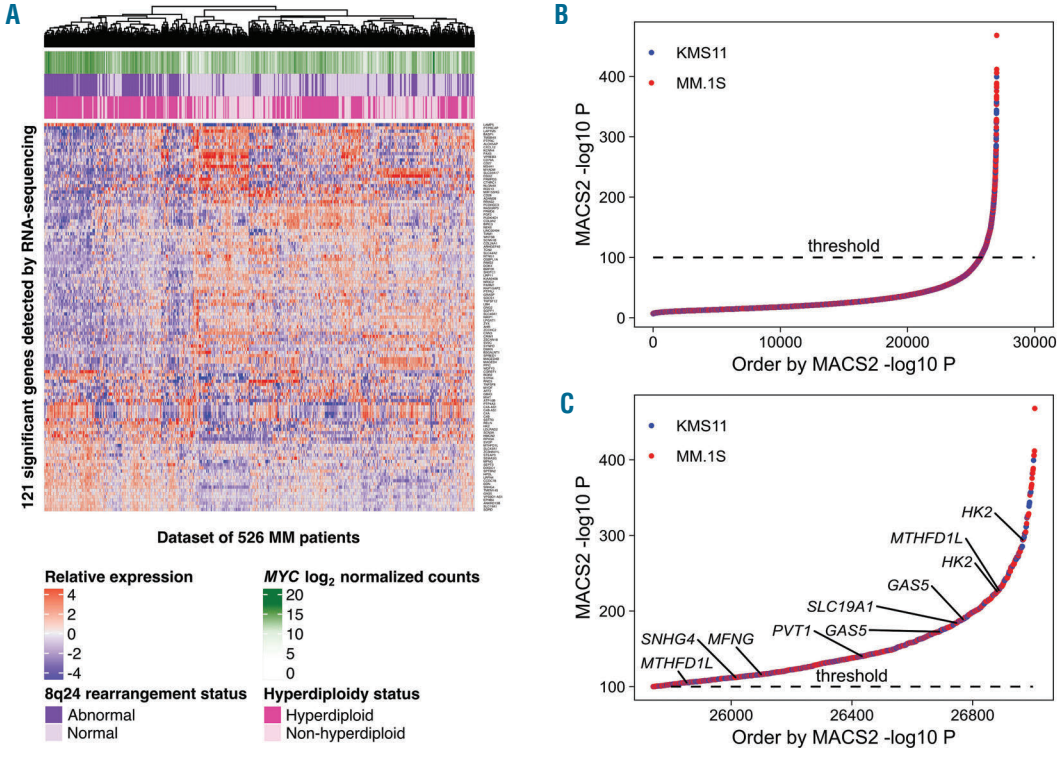

Figure 8. Integration of ChIP-seq for c-Myc and gene expression data identifies direct targets of *MYC* rearrangements. (A) 121 genes that were significantly changed in expression between samples with or without an *MYC* abnormality (FDR<0.05, fold-change ≥1.8) in the dataset of 526 multiple myeloma (MM) patients with RNA-sequencing. (B) All c-Myc ChIP-seq peaks detected in MM.1S and KMS11 cell lines and ordered by -log10 *P*-value. (C) Significant c-Myc ChIP-seq peaks (-log10 P-value >100) with highlighted *PVT1* gene and genes that overlap with 121 genes (A).

cations in MM, and the *IGH-MYC* primary events in Burkitt's lymphoma, are mediated by AID and class switch recombination.[2,4,41] Therefore, the *IGH-MYC* rearrangements may occur through an as yet unknown AID-independent mechanism.

The mechanism driving *MYC* rearrangements is likely not to involve NHEJ, which would result in blunt ended rearrangements.[33] We have shown that *MYC* rearrangements are more likely to have short homologous sequences in common to both partner chromosomes, which is not seen as frequently in the primary *IGH* translocations. Short homologous sequences are indicative of MMEJ,[42] rather than NHEJ, and result from fork stalling and template switching during DNA replication or through microhomology-mediated break induced repair.[43,44] The proteins involved in MMEJ include PARP1, Rad50, and Ercc1, whereas MMEJ is inhibited by functional ATM, H2AX, 53BP1, and BRCA1.[42] We have previously shown that mutation of *ATM, BRCA1* and other genes involved in DNA homologous recombination are associated with increased levels of loss of heterozygosity in MM patients.[45] It is likely that disruption of this pathway is key to genomic instability and progression of disease.

The non-Ig chromosomal partners of *MYC* are not random and are known to contain super-enhancer elements.[5,6] From our analysis of the breakpoints at the most frequent non-Ig locations [6p24.3 (*TXNDC5/BMP6*), 1p12 (*FAM46C*), 6q21 (*FOXO3*)], we show that the breakpoints at these genes are also clustered. The breakpoints are, in general, contained within TAD which are more likely to interact with one another.[46,47] Each TAD at the partner chromosome contains a super-enhancer and breakpoints rarely fall outside of the TAD. The rearrangements are predicted to result in a changed TAD structure that places *MYC* in the same domain as the super-enhancer from the partner locus. If breakpoints were to occur outside of the TAD with the super-enhancer, there would be a lower likelihood of it interacting with *MYC* and expression would not be enhanced.

We identified 149 partner loci for *MYC* rearrangements, but 67.2% of the samples with translocations involve one of the six main partners. The Ig partners have strong super-enhancers in MM, but there are many other active super-enhancers and so it is likely that these six main partners are constrained by chromatin structure. The breakpoints at 8q24 surround an epigenetically active region, defined by the active chromatin marks H3K27Ac, H3K36me3 and H3K4me1, as well as DNaseI hypersensitivity sites. It may be that epigenetically active, and therefore accessible, loci are preferred translocation partners,[48,49] and the nuclear localization of chromosomes may play a part, too.[50]

Each of these different rearrangements results in overexpression of *MYC*. *MYC* is not the only gene at 8q24, and, indeed, *PVT1* is significantly over-expressed in our dataset. *PVT1* is a long non-coding RNA and is associated with inhibition of apoptosis and increased proliferation.[51] It has also been shown that *PVT1* interacts with MYC, resulting in a stable protein, and that ablation of *PVT1* results in diminished tumorigenicity.[52] It may be that the gene complex encompassing *MYC* and *PVT1* is required for oncogenesis and merits further study.

Besides *PVT1*, we also identified other genes that are direct targets of c-Myc and are over-expressed in 8q24-rearranged samples. These included *HK2*, a key enzyme involved in glucose metabolism. It has previously been shown that silencing of *HK2* sensitizes cancer cells to other drugs, and so overexpression of *HK2* in *MYC*-rearranged myeloma may be a key drug resistance mechanism.[53] Additional genes involved in important cellular functions that increase the oncogenic potential of myeloma cells were also identified, such as ribosome biosynthesis and translation initiation; these are likely to contribute to the poor prognosis seen in *MYC*-rearranged myeloma.[5,14] Targeting MYC could, therefore, be an effective way to disrupt many essential tumor features in one hit.

This study provides evidence of complex chromosomal rearrangements at 8q24 as a key cause of *MYC* oncogenic upregulation. Although we found that several *MYC* abnormalities are associated with prognosis in this dataset, including *MYC-IGL* and complex translocations, we have previously shown that the association is not independent of other genomic and clinical markers.[54] However, it may be possible that, with longer follow up, *MYC* abnormalities may be independently associated with overall survival and be a marker of poor outcome. We also show a specific pattern of chromosomal breakpoints suggesting the role of the chromatin landscape in tumorigenesis. The mechanism of DNA breaks clearly differs between *MYC* rearrangements, resulting from MMEJ rather than NHEJ, and differs in myeloma compared to primary *MYC* translocations in lymphoma.

Funding

Funding support for the CoMMpass dataset was provided by the Myeloma Genome Project. The CoMMpass dataset was generated by the Multiple Myeloma Research Foundation in collaboration with the Multiple Myeloma Research Consortium.

References

1. Morgan GJ, Walker BA, Davies FE. The genetic architecture of multiple myeloma. Nat Rev Cancer. 2012;12(5):335-348.
2. Bergsagel PL, Chesi M, Nardini E, Brents LA, Kirby SL, Kuehl WM. Promiscuous translocations into immunoglobulin heavy chain switch regions in multiple myeloma. Proc Natl Acad Sci U S A. 1996;93(24):13931-13936.
3. Stavnezer J, Guikema JE, Schrader CE. Mechanism and regulation of class switch recombination. Annu Rev Immunol. 2008;26(261-292.
4. Ramiro AR, Jankovic M, Eisenreich T, et al. AID is required for c-myc/IgH chromosome translocations in vivo. Cell. 2004;118(4):431-438.
5. Walker BA, Wardell CP, Brioli A, et al. Translocations at 8q24 juxtapose MYC with genes that harbor superenhancers resulting in overexpression and poor prognosis in myeloma patients. Blood Cancer J. 2014;4:e191.
6. Affer M, Chesi M, Chen WG, et al. Promiscuous MYC locus rearrangements hijack enhancers but mostly super-enhancers to dysregulate MYC expression in multiple myeloma. Leukemia. 2014; 28(8):1725-1735.
7. Chng WJ, Huang GF, Chung TH, et al. Clinical and biological implications of MYC activation: a common difference between MGUS and newly diagnosed multiple myeloma. Leukemia. 2011;25(6):1026-1035.
8. Kuehl WM, Brents LA, Chesi M, Huppi K, Bergsagel PL. Dysregulation of c-myc in multiple myeloma. Curr Top MicrobiolImmunol. 1997;224:277-282.
9. Yu Q, Ciemerych MA, Sicinski P. Ras and Myc can drive oncogenic cell proliferation through individual D-cyclins. Oncogene. 2005;24(47):7114-7119.

10. Nesbit CE, Tersak JM, Grove LE, Drzal A, Choi H, Prochownik EV. Genetic dissection of c-myc apoptotic pathways. Oncogene. 2000;19(28):3200-3212.
11. Baudino TA, McKay C, Pendeville-Samain H, et al. c-Myc is essential for vasculogenesis and angiogenesis during development and tumor progression. Genes Dev. 2002;16(19):2530-2543.
12. Karlsson A, Deb-Basu D, Cherry A, Turner S, Ford J, Felsher DW. Defective double-strand DNA break repair and chromosomal translocations by MYC overexpression. Proc Natl Acad Sci U S A. 2003; 100(17):9974-9979.
13. Yin XY, Grove L, Datta NS, Long MW, Prochownik EV. C-myc overexpression and p53 loss cooperate to promote genomic instability. Oncogene. 1999;18(5):1177-1184.
14. Walker BA, Wardell CP, Murison A, et al. APOBEC family mutational signatures are associated with poor prognosis translocations in multiple myeloma. Nat Commun. 2015;6:6997.
15. Carrasco DR, Tonon G, Huang Y, et al. High-resolution genomic profiles define distinct clinico-pathogenetic subgroups of multiple myeloma patients. Cancer Cell. 2006;9(4):313-325.
16. Avet-Loiseau H, Li C, Magrangeas F, et al. Prognostic significance of copy-number alterations in multiple myeloma. J Clin Oncol. 2009;27(27):4585-4590.
17. Sears R, Nuckolls F, Haura E, Taya Y, Tamai K, Nevins JR. Multiple Ras-dependent phosphorylation pathways regulate Myc protein stability. Genes Dev. 2000;14 (19):2501-2514.
18. Shaffer AL, Emre NC, Lamy L, et al. IRF4 addiction in multiple myeloma. Nature. 2008;454(7201):226-231.
19. Manier S, Powers JT, Sacco A, et al. The LIN28B/let-7 axis is a novel therapeutic pathway in multiple myeloma. Leukemia. 2017;31(4):853-860.
20. Segalla S, Pivetti S, Todoerti K, et al. The ribonuclease DIS3 promotes let-7 miRNA maturation by degrading the pluripotency factor LIN28B mRNA. Nucleic Acids Res. 2015;43(10):5182-5193.
21. Avet-Loiseau H, Gerson F, Magrangeas F, et al. Rearrangements of the c-myc oncogene are present in 15% of primary human multiple myeloma tumors. Blood. 2001; 98(10):3082-3086.
22. Gabrea A, Martelli ML, Qi Y, et al. Secondary genomic rearrangements involving immunoglobulin or MYC loci show similar prevalences in hyperdiploid and nonhyperdiploid myeloma tumors. Genes Chromosomes Cancer. 2008;47(7):573-590.
23. Shou Y, Martelli ML, Gabrea A, et al. Diverse karyotypic abnormalities of the c-myc locus associated with c-myc dysregulation and tumor progression in multiple myeloma. Proc Natl Acad Sci U S A. 2000; 97(1):228-233.
24. Dib A, Gabrea A, Glebov OK, Bergsagel PL, Kuehl WM. Characterization of MYC translocations in multiple myeloma cell lines. J Natl Cancer Inst Monogr. 2008; (39):25-31.
25. Bertrand P, Bastard C, Maingonnat C, et al. Mapping of MYC breakpoints in 8q24 rearrangements involving non-immunoglobulin partners in B-cell lymphomas. Leukemia. 2007;21(3):515-523.
26. Busch K, Keller T, Fuchs U, et al. Identification of two distinct MYC breakpoint clusters and their association with various IGH breakpoint regions in the t(8;14) translocations in sporadic Burkitt-lymphoma. Leukemia. 2007;21(8):1739-1751.
27. Kuppers R, Dalla-Favera R. Mechanisms of chromosomal translocations in B cell lymphomas. Oncogene. 2001;20(40):5580-5594.
28. Robbiani DF, Nussenzweig MC. Chromosome translocation, B cell lymphoma, and activation-induced cytidine deaminase. Annu Rev Pathol. 2013;8:79-103.
29. Gabrea A, Leif Bergsagel P, Michael Kuehl W. Distinguishing primary and secondary translocations in multiple myeloma. DNA Repair (Amst). 2006;5(9-10):1225-1233.
30. Loven J, Hoke HA, Lin CY, et al. Selective inhibition of tumor oncogenes by disruption of super-enhancers. Cell. 2013; 153(2):320-334.
31. Yata K, Yaccoby S. The SCID-rab model: a novel in vivo system for primary human myeloma demonstrating growth of CD138-expressing malignant cells. Leukemia. 2004;18(11):1891-1897.
32. Walker BA, Mavrommatis K, Wardell CP, et al. Identification of novel mutational drivers reveals oncogene dependencies in multiple myeloma. Blood. 2018;132(13):1461.
33. Yan CT, Boboila C, Souza EK, et al. IgH class switching and translocations use a robust non-classical end-joining pathway. Nature. 2007;449(7161):478-482.
34. Demchenko Y, Roschke A, Chen WD, Asmann Y, Bergsagel PL, Kuehl WM. Frequent occurrence of large duplications at reciprocal genomic rearrangement breakpoints in multiple myeloma and other tumors. Nucleic Acids Res. 2016; 44(17):8189-8198.
35. Gene Ontology C. Gene Ontology Consortium: going forward. Nucleic Acids Res. 2015;43(Database issue):D1049-1056.
36. Mi H, Huang X, Muruganujan A, et al. PANTHER version 11: expanded annotation data from Gene Ontology and Reactome pathways, and data analysis tool enhancements. Nucleic Acids Res. 2017; 45(D1):D183-D189.
37. Mi H, Thomas P. PANTHER pathway: an ontology-based pathway database coupled with data analysis tools. Methods Mol Biol. 2009;563:123-140.
38. Fabregat A, Sidiropoulos K, Garapati P, et al. The Reactome pathway Knowledgebase. Nucleic Acids Res. 2016; 44(D1):D481-487.
39. Carramusa L, Contino F, Ferro A, et al. The PVT-1 oncogene is a Myc protein target that is overexpressed in transformed cells. J Cell Physiol. 2007;213(2):511-518.
40. Molyneux EM, Rochford R, Griffin B, et al. Burkitt's lymphoma. Lancet. 2012; 379(9822):1234-1244.
41. Kuehl WM, Bergsagel PL. Multiple myeloma: evolving genetic events and host interactions. NatRevCancer. 2002;2(3):175-187.
42. Ottaviani D, LeCain M, Sheer D. The role of microhomology in genomic structural variation. Trends Genet. 2014;30(3):85-94.
43. Lee JA, Carvalho CM, Lupski JR. A DNA replication mechanism for generating nonrecurrent rearrangements associated with genomic disorders. Cell. 2007;131(7):1235-1247.
44. Hastings PJ, Ira G, Lupski JR. A microhomology-mediated break-induced replication model for the origin of human copy number variation. PLoS Genet. 2009; 5(1):e1000327.
45. Pawlyn C, Loehr A, Ashby C, et al. Loss of heterozygosity as a marker of homologous repair deficiency in multiple myeloma: a role for PARP inhibition? Leukemia. 2018; 32(7):1561-1566.
46. Spielmann M, Lupianez DG, Mundlos S. Structural variation in the 3D genome. Nat Rev Genet. 2018;19(7):453-467.
47. Dixon JR, Selvaraj S, Yue F, et al. Topological domains in mammalian genomes identified by analysis of chromatin interactions. Nature. 2012;485 (7398):376-380.
48. Daniel JA, Nussenzweig A. The AID-induced DNA damage response in chromatin. Mol Cell. 2013;50(3):309-321.
49. Lu Z, Lieber MR, Tsai AG, et al. Human lymphoid translocation fragile zones are hypomethylated and have accessible chromatin. Mol Cell Biol. 2015;35(7):1209-1222.
50. Martin LD, Harizanova J, Righolt CH, et al. Differential nuclear organization of translocation-prone genes in nonmalignant B cells from patients with t(14;16) as compared with t(4;14) or t(11;14) myeloma. Genes Chromosomes Cancer. 2013;52(6): 523-537.
51. Guan Y, Kuo WL, Stilwell JL, et al. Amplification of PVT1 contributes to the pathophysiology of ovarian and breast cancer. Clin Cancer Res. 2007;13(19):5745-5755.
52. Tseng YY, Moriarity BS, Gong W, et al. PVT1 dependence in cancer with MYC copy-number increase. Nature. 2014; 512(7512):82-86.
53. Peng Q, Zhou J, Zhou Q, Pan F, Zhong D, Liang H. Silencing hexokinase II gene sensitizes human colon cancer cells to 5-fluorouracil. Hepatogastroenterology. 2009; 56(90):355-360.
54. Walker BA, Mavrommatis K, Wardell CP, et al. A high-risk, Double-Hit, group of newly diagnosed myeloma identified by genomic analysis. Leukemia. 2019;33(1):159-170.

ARTICLE

Fractures and survival in multiple myeloma: results from a population-based study

Sigrun Thorsteinsdottir,[1,2] Gauti Gislason,[2] Thor Aspelund,[3] Ingigerdur Sverrisdottir,[1,2] Ola Landgren,[4] Ingemar Turesson,[5] Magnus Björkholm[6] and Sigurður Y. Kristinsson[1,2]

[1]Department of Internal Medicine, Landspitali - The National University Hospital of Iceland, Reykjavik, Iceland; [2]Faculty of Medicine, University of Iceland, Reykjavik, Iceland; [3]Centre of Public Health Sciences, Faculty of Medicine, University of Iceland, Reykjavik, Iceland; [4]Myeloma Service, Division of Hematologic Oncology, Memorial Sloan-Kettering Cancer Center, New York, NY, USA; [5]Department of Hematology and Coagulation Disorders, Skane University Hospital, Malmo, Sweden and [6]Department of Medicine, Division of Hematology, Karolinska University Hospital and Karolinska Institutet, Stockholm, Sweden

Ferrata Storti Foundation

Haematologica 2020
Volume 105(4):1067-1073

ABSTRACT

Multiple myeloma causes lytic bone lesions and fractures. The impact of fractures on multiple myeloma (MM) survival is unclear. The aim of this study was to evaluate the effect of fractures on survival in MM using data from MM patients diagnosed in Sweden in the years 1990-2013, identified from the Swedish Cancer Registry. Information on date of birth, MM diagnosis, fractures, and death was collected from central registries. A Cox regression model was used to compare survival in patients with and without a fracture at MM diagnosis and another Cox model was used with fracture as a time-dependent variable to assess the effect of fracture on survival after MM diagnosis. Results were adjusted for age, sex, year of diagnosis, and previous fractures. A total of 14,013 patients were diagnosed with MM during the study, of whom 1,213 (8.7%) were diagnosed with a fracture at MM diagnosis, and 3,235 (23.1%) after diagnosis. Patients with a fracture at diagnosis were at a significantly increased risk of death (hazard ratio=1.28; 95% confidence interval: 1.19-1.37). The risk of death was significantly increased in patients with a fracture after MM diagnosis (2.00; 1.90-2.10). The impact of fractures on survival did not change significantly between the two calendar periods 1990-1999 and 2000-2013 (0.98; 0.89-1.08). Our large study shows that MM patients with fractures are at a significantly increased risk of dying compared to those without fractures, which stresses the importance of preventing bone disease in MM.

Introduction

Multiple myeloma (MM) is a malignant neoplasm of plasma cells in the bone marrow.[1,2] Skeletal abnormalities are found in the majority of MM patients at the time of diagnosis, and manifestations of bone disease in MM include osteolytic lesions, osteopenia/osteoporosis, and fractures.[3-5] Bone disease can be painful and reduces quality of life in MM patients.[6,7] In MM bone disease, the interaction between malignant plasma cells and the bone microenvironment leads to osteoclastic bone destruction, reduced osteoblast function, and blocking of bone repair.[8,9] This imbalance, along with decreased bone mineral density and treatment-related factors such as treatment with glucocorticoids, can lead to fractures in MM.[5,10,11] In a population-based retrospective study, MM patients were found to have a 9-fold increase in risk of fractures after MM diagnosis, as compared to expected fracture rates in the population.[5] To prevent skeletal-related events, treatment with bisphosphonates is recommended for most patients with MM, and treatment with zoledronic acid has been reported to improve overall survival in MM patients.[12,13]

Previous studies have shown that skeletal-related events (radiation to the bone, a pathologic or osteoporotic fracture, hypercalcemia, spinal cord compression, or surgery to the bone) are associated with reduced survival in both breast cancer and

Correspondence:

SIGRUN THORSTEINSDOTTIR
sth314@hi.is

Received: June 18, 2019.

Accepted: November 28, 2019.

Pre-published: December 2, 2019.

doi:10.3324/haematol.2019.230011

Check the online version for the most updated information on this article, online supplements, and information on authorship & disclosures: www.haematologica.org/content/105/4/1067

prostate cancer.[14-16] To our knowledge, only three studies have assessed the effect of fractures on survival in MM. In the largest study so far, a total of 513 MM patients diagnosed from 1998 to 2000 and enrolled in a clinical trial were included retrospectively; all patients had Durie-Salmon stage III, bone lesions, and a median age of 62 years. No significant difference in survival was observed between MM patients who developed a fracture during follow up as compared to patients that did not develop a fracture.[16] The second study was a small case-control study in which overall survival was found to be inferior in MM patients with pathologic fractures (n=24) compared to patients with no pathologic fractures (n=25).[17] However, in a large study from the UK including patients admitted with plasma cell dyscrasias (MM, plasmacytoma, and plasma cell leukemia), both previous and subsequent fractures were found to be a risk factor for worse survival after first admission for plasma cell dyscrasia.[18]

The aim of our study was to evaluate the impact of fractures and certain subtypes of fractures on survival after MM diagnosis in a whole population using real-world data on all MM patients diagnosed during a 23-year period in Sweden. We also aimed to compare the effect of fractures on survival in MM before and after the introduction of novel treatment agents that have greatly improved survival in the MM patient population.[19-21]

Methods

The Swedish Cancer Registry is a centralized, nationwide registry containing information on patients who have been diagnosed with a malignant disorder in Sweden since January 1st, 1958. Every physician and pathologist is obliged by law to report each case of cancer to the registry. The Swedish Cancer Registry contains information on sex, date of birth, date of diagnosis, and histopathologic diagnosis. In a validation study from 2007, the completeness and diagnostic accuracy of the Swedish Cancer Registry was found to be over 93% for MM patients.[22] Patients diagnosed with MM in the period from January 1990 to December 2013 were identified from the Swedish Cancer Registry. Information on date of birth, diagnosis, and death were collected. Information on clinical stage and laboratory results were not available for the patients. Each person in Sweden receives a unique personal identification number that is used to index all major health registers, making it possible to link information in the registries. Information on fractures, using ICD-10 and ICD-9 diagnostic codes (see *Online Supplementary Appendix*) was obtained from the Swedish Patient Registry, that contains inpatient data from 1987 as well as information on outpatient visits from 2000. Fractures from ten years before MM diagnosis and then afterwards were included (to adjust for previous fractures before MM diagnosis). Information on date of death was gathered from the Swedish Cause of Death Registry. End of follow up was December 31st, 2013. The study period was divided into two calendar periods: 1990-1999 and 2000-2013, respectively before and after the introduction of novel treatment options for MM in Sweden that have been shown to improve survival.[19,20] A total of 333 patients were excluded from analysis because of unknown age; 68 of these were patients with a fracture.

A Cox regression model was used to estimate the effect of a fracture at diagnosis (defined as 30 days before or after MM diagnosis) on survival after the time of MM diagnosis. All results were adjusted for age, sex, previous fracture and year of MM diagnosis. Results were presented as hazard ratios (HR) with 95% confidence intervals (CI). $P<0.05$ was considered significant and all statistical analysis was performed in R version 3.5.2.[23]

A landmark analysis was performed by selecting a subset of MM patients alive at six months after MM diagnosis and stratifying patients according to whether they had developed a fracture from the day of MM diagnosis (day 0) until six months after diagnosis or not. Fractures before the day of MM diagnosis were not included in the landmark analysis to avoid any immortal time bias.[24] A Cox regression model was used to assess the association of fracture status at six months and survival, and a Kaplan-Meier graph was generated to visualize the difference in survival between the two groups.

A Cox regression model was used with fracture as a time-dependent variable to assess the association of fracture and survival after MM diagnosis (from the day of MM diagnosis). The effect of fracture was assessed for any fracture or a specific subtype of fracture. Specifically, we assessed pathologic (all fractures registered as pathologic fractures), vertebral (both pathologic and others), hip, femoral, humerus, forearm, rib, pelvis, and ankle fractures. Either first fracture or the first subtype of fracture was used in the analysis. The effect of fracture was analyzed for males and females separately for two age groups (<70 years and ≥70 years old) and for the two calendar periods. Results were adjusted for age, sex, time of diagnosis, and previous fractures. To compare the difference in the association of fracture and survival between the two calendar periods, the two age groups, and sexes, the interaction effect of the variable and fracture was assessed in a Cox regression model. Because outpatient visits were included from year 2000, we performed an additional analysis with only inpatient diagnoses of fractures when comparing the calendar periods. Furthermore, we assessed the association of fractures and death after MM diagnosis for two calendar periods after year 2000: 2000-2006 and 2007-2013.

As an additional analysis, four controls, matched by gender, year of birth, and county of residence, were chosen randomly from the Swedish Register of Total Population. All controls were alive and free of MM at the time of MM diagnosis for the corresponding patient. Cox regression model was used with fracture as a time-dependent variable from MM diagnosis in the corresponding case to assess the association of fracture and survival in the matched controls. The effect of fracture was assessed for any fracture or a specific subtype of fracture (vertebral, femoral, humerus, rib, or ankle fracture).

Results

A total of 14,013 patients were diagnosed with MM in the period from 1st of January 1990 to 31st of December 2013. The median age was 72 years (range 20-99 years) and 54.9% were males (Table 1). A total of 4,146 (29.6%) patients developed a fracture including fractures that occurred a year before MM diagnosis and thereafter, with a sharp rise in fracture diagnoses around the time of MM diagnosis (Figure 1). Overall, 3,235 (23.1%) patients were diagnosed with a fracture at the same day or after MM diagnosis (Figure 1). A similar proportion of MM patients developed a fracture in the two calendar periods 1990-1999 and 2000-2013 (22.2 and 23.7%, respectively) (Table 1). During the period of follow up, 10,731 (76.6%) MM patients died, of whom 2,520 (77.9%) were patients with fractures. Median follow-up time from diagnosis to death or end of follow up was 2.4 years (range 1 day-23.8 years). Median overall survival for all MM patients was 3.0 years for the whole study period and improved from 2.6 years

Table 1. Characteristics of patients with multiple myeloma with and without fractures after multiple myeloma diagnosis.

Variable	All	Fracture at the same day or after MM diagnosis	No fractures at the same day or after MM diagnosis
Number of patients	14,013	3,235 (23.1%)	10,778 (76.9%)
Male/female %	54.9/45.1	45.7/54.3	57.6/42.4
Age mean	70.8	70.4	70.9
Age median	72	72	72
Age range	20-99	29-97	20-99
Year at MM diagnosis			
1990-1999	5,462	1,211 (22.2%)	4,251 (77.8%)
2000-2013	8,551	2,024 (23.7%)	6,527 (76.3%)

MM: multiple myeloma.

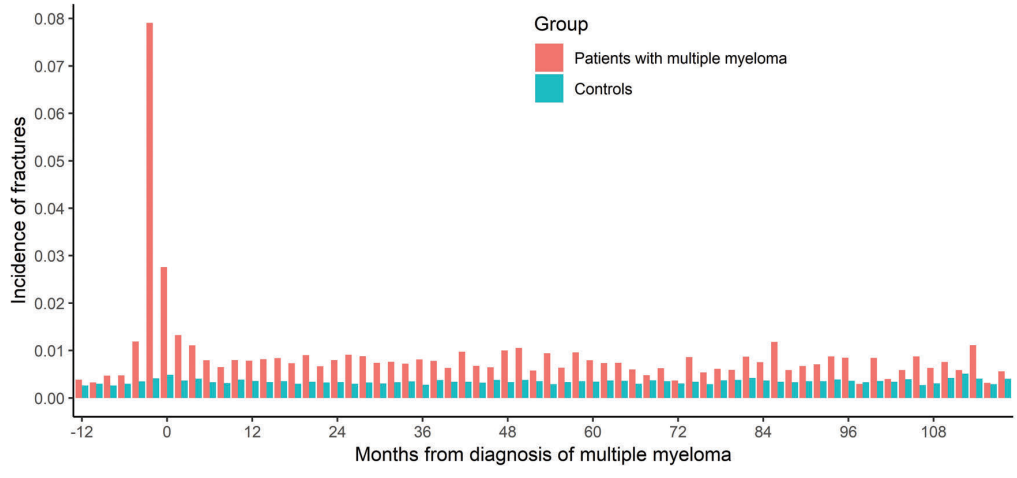

Figure 1. Incidence of fractures from 12 months before until ten years after multiple myeloma (MM) diagnosis in MM patients (n=14,013) and matched controls (n=53,154). For each individual, only a single fracture that occurs closest in time from MM diagnosis for the patient or the corresponding case is shown.

in 1990-1999 to 3.3 years in 2000-2013. Median time to first fracture was 1.5 years for MM patients with a fracture and 10.4 years for all MM patients (Figure 2).

Effect of fractures at diagnosis on survival and landmark analysis

A total of 1,213 (8.7%) of all MM patients were diagnosed with a fracture at MM diagnosis (within 30 days before or after MM diagnosis). The patients with a fracture at diagnosis were at a significantly increased risk of death compared to those without a fracture (HR=1.28; 95%CI: 1.19-1.37). A total of 11,541 patients were alive six months after MM diagnosis and were included in the landmark analysis. Of these, 876 (7.6%) patients developed a fracture during the first six months after MM diagnosis (from the day of MM diagnosis). Patients with a fracture during the first six months after MM diagnosis were at a significantly higher risk of death compared to those with no fractures in the first six months (HR=1.31; 95%CI: 1.20-1.42) (Figure 3).

Effect of fractures on survival after multiple myeloma diagnosis, by subtype, gender, age, and calendar period

The risk of death was significantly increased for patients who developed a fracture after the time of MM diagnosis (HR=2.00; 95%CI: 1.90-2.10) for all fractures combined. The risk of death was significantly increased in patients who developed all subtypes of fractures after MM diagnosis; pathologic fracture (HR=2.17; 95%CI: 2.03-2.32), vertebral fracture (1.74; 95%CI: 1.61-1.87), hip fracture (1.99; 95%CI: 1.82-2.18), femoral fracture (2.62; 95%CI: 2.32-2.98), humerus fracture (2.57; 95%CI: 2.31-2.85), forearm fracture (1.24; 95%CI: 1.05-1.46), rib fracture (1.52; 95%CI: 1.31-1.77), pelvis fracture (1.99; 95%CI: 1.74-2.29), except ankle fracture (1.07; 95%CI: 0.79-1.44) (Figure 4). The risk of death was similar for males and females with a fracture as compared to males/females without a fracture (HR=2.01; 95%CI: 1.88-2.16 and 1.99; 95%CI: 1.86-2.13, respectively). The risk of death for MM patients over 70 years old at diagnosis with a fracture compared to those without a fracture was significantly increased (HR=1.88; 95%CI: 1.77-2.00). However, in patients under 70 years old at MM diagnosis, the risk of death in patients with a fracture compared with those without a fracture was more pronounced (HR=2.28; 95%CI: 2.11-2.47). The interaction effect of fracture and age group was significant, signifying that the HR for MM patients under 70 years old at diagnosis was significantly higher than for patients ≥70 years old at diagnosis (HR=1.22; 95%CI: 1.11-1.34; $P<0.01$).

The risk of death for MM patients with a fracture after MM diagnosis was lower in patients diagnosed during 2000-2013 (HR=1.79; 95%CI: 1.67-1.91) compared to 1990-1999 (2.26; 95%CI: 2.10-2.42). This difference was

significant as the interaction effect of a fracture and calendar period was significant for 2000-2013 compared to 1990-1999 (HR=0.85; 95%CI: 0.77-0.93; *P*<0.01). When outpatient diagnoses of fractures were excluded, HR for 2000-2013 was 2.08 (95%CI: 1.94-2.23), HR for 1990-1999 was 2.29 (95%CI: 2.13-2.46), and the difference between the calendar periods was no longer significant (0.99; 95%CI: 0.90-1.09; *P*=0.91). When the association of fractures and death after MM diagnosis was assessed for the two calendar periods after year 2000, HR for 2000-2006 was 1.72 (95%CI: 1.59-1.87), and HR for 2007-2013 was 1.97 (95%CI: 1.77-2.20).

Effect of fracture on survival in matched controls

A total of 53,154 matched controls were included in the study, and 9,897 (18.6%) developed a fracture during the follow up. The median follow up for all controls was 6.8 years. The risk of death was increased for controls who developed a fracture after the time of MM diagnosis in the corresponding MM case as compared to controls without a fracture (HR=2.02; 95%CI: 1.95-2.08) for all fractures combined. The risk of death was increased for controls who developed a vertebral (HR=2.01; 95%CI: 1.88-2.15), femoral (2.17; 1.92-2.45), humerus (1.66; 95%CI: 1.54-1.79), and rib (1.62; 95%CI: 1.48-1.78) fracture.

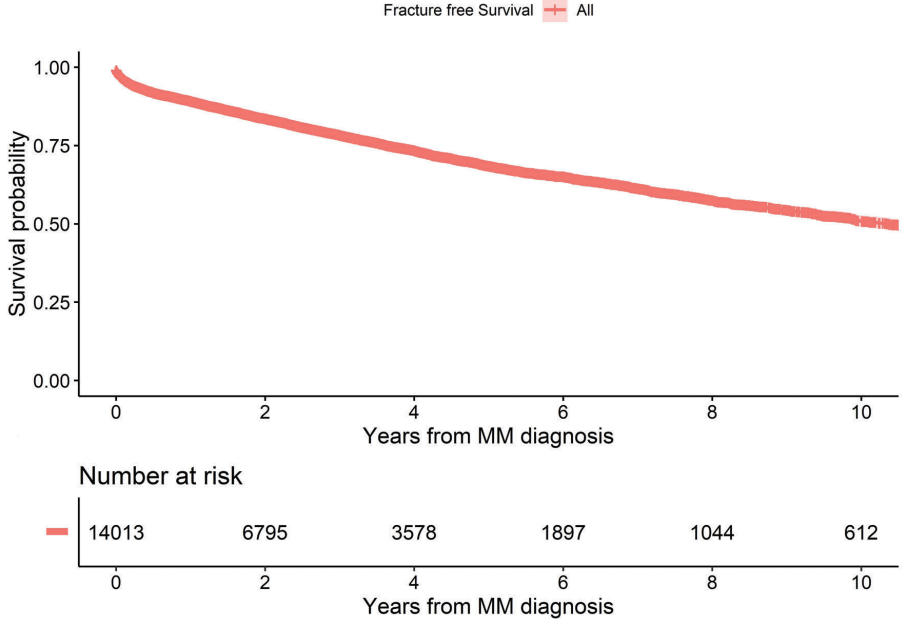

Figure 2. Fracture-free survival in multiple myeloma (MM) patients after MM diagnosis.

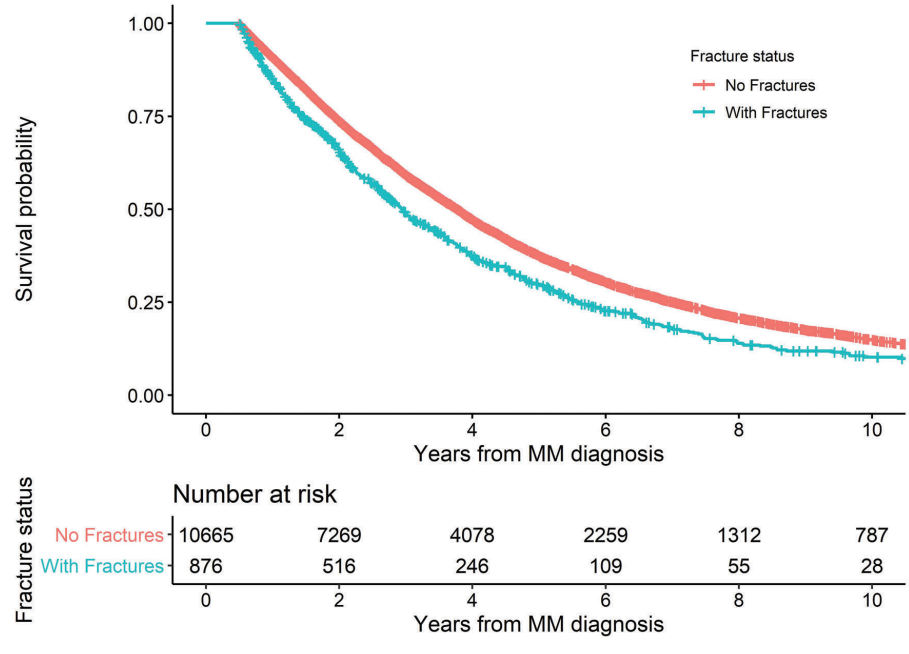

Figure 3. Landmark analysis showing survival probability in patients with and without a fracture during the first six months after multiple myeloma (MM) diagnosis.

Discussion

Our population-based study, including over 14,000 MM patients diagnosed in Sweden from 1990 to 2013, shows that MM patients with a fracture at MM diagnosis are at 28% higher risk of dying than those without a fracture at diagnosis. Furthermore, after MM diagnosis, patients who develop a fracture are at a 2-fold increased risk of dying, compared to MM patients who do not develop a fracture. These observations underline the clinical importance of fractures in MM patients in a real-world setting, from diagnosis and throughout the course of the disease.

We found that MM patients with a fracture at diagnosis had an inferior survival compared to MM patients without a fracture at diagnosis which indicates that fractures are a proxy for a more established and/or active disease at diagnosis. We previously showed in a population-based study that individuals with monoclonal gammopathy of undetermined significance (MGUS), a precursor condition preceding MM, had a 74% increased risk of fractures at five years compared to controls.[25] Furthermore, our group and others have shown that a prior diagnosis of MGUS or smoldering MM is associated with improved survival in MM, suggesting that early treatment leads to improved survival.[26,27] Possibly, a prior diagnosis of a precursor state could reduce the risk of fractures and/or the impact of fractures on survival after MM diagnosis. Our findings underline the importance of thorough evaluation of bone disease in precursor states as well as in active MM.

Our findings of a 2-fold higher risk of dying for MM patients with a fracture compared to patients without fractures demonstrates the significant impact of fractures on patients with MM, and is a higher risk than previously reported in clinical cohorts.[16] This is, to the best of our knowledge, the first real-world data analysis on the association of fractures and survival in MM. These results were further confirmed in our landmark analysis, where MM patients with fractures during the first months of the disease had a poorer survival than those without fractures. Our findings are partially in accordance with what has been observed in the general population, where fractures, especially osteoporotic fractures, have been associated with an increased risk of death, although not to the same extent as in MM patients.[28-30] In patients with metastatic or progressed solid tumors, skeletal-related events have been associated with increased mortality, even when adjusted for stage and/or treatment.[14,16] Fractures occurring after MM diagnosis may be an indication of aggressive relapse, although we cannot evaluate to what extent fractures are an independent prognostic factor because we do not have clinical data on these patients.

Our analyses on different subgroups of fractures in MM patients and controls indicate that the impact on survival in MM reflects both the effect of the fractures themselves as well as the progression of MM. Femoral fractures are well known to increase mortality in the elderly, especially in the first months after the fracture,[29] and were associated with the highest risk of dying in both MM and the controls in our study. The impact of humerus fractures on survival in MM, on the other hand, seems to reflect the effect of the progression of the disease, since MM patients who developed a humerus fracture after diagnosis had a 2.6-fold risk of dying compared to an only 1.7-fold risk in the controls with a humerus fracture. In addition to this, we found that ankle fractures were not associated with survival in MM, highlighting the fact that our findings are specific to MM-related or osteoporotic fractures and not all fractures in general. Our results, therefore, indicate that the effect of fractures on survival in MM is both due to the direct impact of fractures as well as through progression of MM, suggesting that patients with extensive MM bone disease have a more aggressive disease.

We did not find any significant change between the two calendar periods in the risk of death after first fracture in MM. More effective treatment agents were introduced in

	No.	HR	95% CI
All fractures	3,235	2.00	1.90-2.10
Males	1,479	2.01	1.88-2.16
Females	1,756	1.99	1.86-2.13
Age at diagnosis			
<70 years	1,359	2.28	2.11-2.47
>70 years	1,808	1.88	1.77-2.00
Calendar period*			
1990-1999	1,136	2.29	2.13-2.46
2000-2013	1,597	2.08	1.94-2.23
Fracture subtype			
Pathologic**	1,393	2.17	2.03-2.32
Vertebral***	1,083	1.74	1.61-1.87
Hip	594	1.99	1.82-2.18
Femoral	298	2.62	2.32-2.98
Humerus	476	2.57	2.31-2.85
Forearm	202	1.24	1.05-1.46
Rib	235	1.52	1.31-1.77
Pelvis	261	1.99	1.74-2.29
Ankle	75	1.07	0.79-1.44

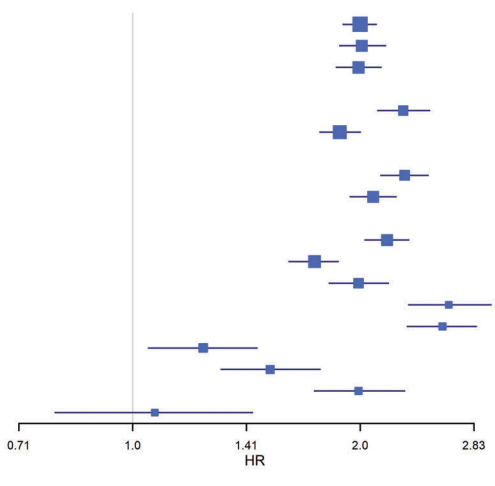

Figure 4. Risk of death in multiple myeloma (MM) patients who developed a fracture after MM diagnosis compared to patients who did not develop a fracture. Fractures as time dependent co-variates, adjusted for age, sex, year of diagnosis and previous fractures. *First inpatient fracture. **All fractures registered as pathologic. ***All vertebral fractures, both pathologic and others. CI: confidence interval; HR: hazard ratio; No: number.

MM after 2000.[19-21] These included the immunomodulators thalidomide and lenalidomide, and the proteasome inhibitor bortezomib, that were increasingly used during the later calendar period, and were used in over 80% of all MM patients in Sweden in 2013.[31] Previous studies have shown that bortezomib can both inhibit growth of osteoclasts and stimulate osteoblasts, thereby leading to bone healing in MM.[32,33] Furthermore, the immunomodulators also seem to prompt the bone microenvironment towards bone formation.[34,35] In addition to this, bisphosphonates, that are a well-established part of the treatment of MM patients, are known to reduce pathologic vertebral fractures, skeletal-related events, and pain.[36] Moreover, zoledronic acid, that was approved for MM in the later calendar period of the study, has shown a positive effect on overall survival.[13] In 2010, Swedish national guidelines recommended treatment with bisphosphonates from the time of MM diagnosis for all MM patients, irrespective of the presence of bone disease, and in the years 2008 to 2015, over 70% of MM patients received bisphosphonates as part of their disease management.[31] In our study, even in 2000-2013, when we had information on outpatient visits for fractures for the whole period, we found no change over time in the association of fracture after MM diagnosis and survival. Thus, despite the increasing use of more effective treatment agents and more widespread use of bisphosphonates, fractures are still an important predictor of overall survival.

The strengths of our study include the large population-based study design, including almost all patients diagnosed with MM in Sweden during a more than 20-year period.[22] Using these real-world data, all MM patients are included, and the results therefore reflect the actual patient population. Because of the unique identification numbers assigned to every individual in Sweden, we have extensive and accurate follow up for the majority of this large group of patients. Furthermore, the high number of MM patients and fractures yields the study high statistical power to analyze the effect of different subgroups of fractures.

The limitations of our study include the fact that we do not have information on clinical stage, other prognostic factors, or on what treatment the MM patients received. Therefore, it is not possible to determine from our data whether fracture is an independent risk factor for death in MM. Because the fractures occurred after the MM diagnosis, there is a risk of immortal time bias in our survival analysis. To address this, we used both the method of time dependent co-variatesand landmark analysis to accurately analyze the difference in survival between the fractured and unfractured groups.[24,37] In addition, we do not have access to radiographic images or individual patient records; therefore fractures, especially asymptomatic fractures, might be relatively underreported. In our study, a smaller proportion of patients were diagnosed with a fracture after MM diagnosis than had been previously reported.[5] The difference between these results might be explained by the study designs, the fact that ours is a large database study using ICD-codes, and that, in the older study, all patient records were searched retrospectively for the occurrence of a fracture. Finally, a limitation of our study is that our follow up ended in 2013; although it would have been interesting to perform our analyses on more recent data, we did not have access to a more up-dated database at the time of the study.

In conclusion, our population-based study shows that MM patients with a fracture at MM diagnosis have an inferior survival than patients without a fracture at diagnosis. Furthermore, we found that MM patients who develop a fracture after the time of MM diagnosis are at a 2-fold risk of dying compared to patients who do not develop a fracture, and that this risk did not decrease significantly after the introduction of more effective treatment agents in MM. Our results stress the importance of preventing bone disease in MM, not only to prevent the morbidity of fractures, but possibly to influence survival.

References

1. Swerdlow S, Campo E, Harris N, et al. WHO Classification of Tumours of Haematopoietic and Lymphoid Tissues. Vol 2. Revised 4th Edition ed. Lyon, France. IARC; 2016.
2. Rajkumar SV, Dimopoulos MA, Palumbo A, et al. International Myeloma Working Group updated criteria for the diagnosis of multiple myeloma. Lancet Oncol. 2014;15(12):e538-548.
3. Kyle RA, Gertz MA, Witzig TE, et al. Review of 1027 patients with newly diagnosed multiple myeloma. Mayo Clin Proc. 2003;78(1):21-33.
4. Kristinsson SY, Minter AR, Korde N, Tan E, Landgren O. Bone disease in multiple myeloma and precursor disease: novel diagnostic approaches and implications on clinical management. Expert Rev Mol Diagn. 2011;11(6):593-603.
5. Melton LJ, 3rd, Kyle RA, Achenbach SJ, Oberg AL, Rajkumar SV. Fracture risk with multiple myeloma: a population-based study. J Bone Miner Res. 2005;20(3):487-493.
6. Kiely F, Cran A, Finnerty D, O'Brien T. Self-reported quality of life and symptom burden in ambulatory patients with multiple myeloma on disease-modifying treatment. Am J Hosp Palliat Care. 2017;34(7):671-676.
7. Ramsenthaler C, Osborne TR, Gao W, et al. The impact of disease-related symptoms and palliative care concerns on health-related quality of life in multiple myeloma: a multi-centre study. BMC Cancer. 2016; 16:427.
8. Terpos E, Ntanasis-Stathopoulos I, Gavriatopoulou M, Dimopoulos MA. Pathogenesis of bone disease in multiple myeloma: from bench to bedside. Blood Cancer J. 2018;8(1):7.
9. Yaccoby S. Osteoblastogenesis and tumor growth in myeloma. Leuk Lymphoma. 2010;51(2):213-220.
10. Abildgaard N, Brixen K, Kristensen JE, Vejlgaard T, Charles P, Nielsen JL. Assessment of bone involvement in patients with multiple myeloma using bone densitometry. Eur J Haematol. 1996;57(5):370-376.
11. Dhodapkar MV, Weinstein R, Tricot G, et al. Biologic and therapeutic determinants of bone mineral density in multiple myeloma. Leuk Lymphoma. 1998;32(1-2):121-127.
12. Terpos E, Morgan G, Dimopoulos MA, et al. International Myeloma Working Group recommendations for the treatment of multiple myeloma-related bone disease. J Clin Oncol. 2013;31(18):2347-2357.
13. Morgan GJ, Davies FE, Gregory WM, et al. First-line treatment with zoledronic acid as compared with clodronic acid in multiple myeloma (MRC Myeloma IX): a randomised controlled trial. Lancet. 2010;376(9757):1989-1999.
14. Yong M, Jensen AO, Jacobsen JB, Norgaard M, Fryzek JP, Sorensen HT. Survival in breast cancer patients with bone metastases and skeletal-related events: a population-based cohort study in Denmark (1999-2007). Breast Cancer Res Treat. 2011;129(2):495-503.
15. Sathiakumar N, Delzell E, Morrisey MA, et al. Mortality following bone metastasis and skeletal-related events among men with prostate cancer: a population-based analysis of US Medicare beneficiaries, 1999-2006. Prostate Cancer Prostatic Dis. 2011;14(2):177-183.

16. Saad F, Lipton A, Cook R, Chen YM, Smith M, Coleman R. Pathologic fractures correlate with reduced survival in patients with malignant bone disease. Cancer. 2007;110 (8):1860-1867.
17. Sonmez M, Akagun T, Topbas M, et al. Effect of pathologic fractures on survival in multiple myeloma patients: a case control study. J Exp Clin Cancer Res. 2008;27:11.
18. McIlroy G, Mytton J, Evison F, et al. Increased fracture risk in plasma cell dyscrasias is associated with poorer overall survival. Br J Haematol. 2017;179(1):61-65.
19. Thorsteinsdottir S, Dickman PW, Landgren O, et al. Dramatically improved survival in multiple myeloma patients in the recent decade: results from a Swedish population-based study. Haematologica. 2018;103(9): e412-e415.
20. Kumar SK, Dispenzieri A, Lacy MQ, et al. Continued improvement in survival in multiple myeloma: changes in early mortality and outcomes in older patients. Leukemia. 2014;28(5):1122-1128.
21. Turesson I, Bjorkholm M, Blimark CH, Kristinsson S, Velez R, Landgren O. Rapidly changing myeloma epidemiology in the general population: Increased incidence, older patients, and longer survival. Eur J Haematol. 2018 Apr 20. [Epub ahead of print]
22. Turesson I, Linet MS, Bjorkholm M, et al. Ascertainment and diagnostic accuracy for hematopoietic lymphoproliferative malignancies in Sweden 1964-2003. Int J Cancer. 2007;121(10):2260-2266.
23. R: A language and environment for statistical computing. [computer program]. Vienna, Austria: R Foundation for Statistical Computing; 2018.
24. Gleiss A, Oberbauer R, Heinze G. An unjustified benefit: immortal time bias in the analysis of time-dependent events. Transpl Int. 2018;31(2):125-130.
25. Kristinsson SY, Tang M, Pfeiffer RM, et al. Monoclonal gammopathy of undetermined significance and risk of skeletal fractures: a population-based study. Blood. 2010;116 (15):2651-2655.
26. Goyal G, Rajkumar SV, Lacy MQ, et al. Impact of prior diagnosis of monoclonal gammopathy on outcomes in newly diagnosed multiple myeloma. Leukemia. 2019;33(5):1273-1277.
27. Sigurdardottir EE, Turesson I, Lund SH, et al. The Role of Diagnosis and Clinical Follow-up of Monoclonal Gammopathy of Undetermined Significance on Survival in Multiple Myeloma. JAMA Oncol. 2015;1 (2):168-174.
28. Cooper C, Atkinson EJ, Jacobsen SJ, O'Fallon WM, Melton LJ, 3rd. Population-based study of survival after osteoporotic fractures. Am J Epidemiol. 1993;137(9): 1001-1005.
29. Katsoulis M, Benetou V, Karapetyan T, et al. Excess mortality after hip fracture in elderly persons from Europe and the USA: the CHANCES project. J Intern Med. 2017;281 (3):300-310.
30. Ray R, Clement ND, Aitken SA, McQueen MM, Court-Brown CM, Ralston SH. High mortality in younger patients with major osteoporotic fractures. Osteoporos Int. 2017;28(3):1047-1052.
31. Blimark CH, Turesson I, Genell A, et al. Outcome and survival of myeloma patients diagnosed 2008-2015. Real-world data on 4904 patients from the Swedish Myeloma Registry. Haematologica. 2018;103(3):506-513.
32. von Metzler I, Krebbel H, Hecht M, et al. Bortezomib inhibits human osteoclastogenesis. Leukemia. 2007;21(9):2025-2034.
33. Lund T, Soe K, Abildgaard N, et al. First-line treatment with bortezomib rapidly stimulates both osteoblast activity and bone matrix deposition in patients with multiple myeloma, and stimulates osteoblast proliferation and differentiation in vitro. Eur J Haematol. 2010;85(4):290-299.
34. Breitkreutz I, Raab MS, Vallet S, et al. Lenalidomide inhibits osteoclastogenesis, survival factors and bone-remodeling markers in multiple myeloma. Leukemia. 2008;22(10):1925-1932.
35. Bolzoni M, Storti P, Bonomini S, et al. Immunomodulatory drugs lenalidomide and pomalidomide inhibit multiple myeloma-induced osteoclast formation and the RANKL/OPG ratio in the myeloma microenvironment targeting the expression of adhesion molecules. Exp Hematol. 2013;41(4):387-397.
36. Mhaskar R, Kumar A, Miladinovic B, Djulbegovic B. Bisphosphonates in multiple myeloma: an updated network meta-analysis. Cochrane Database Syst Rev. 2017;12:CD003188.
37. Therneau T, Crowson C, Atkinson E. Using time dependent covariates and time dependent coefficients in the cox model. 2019; http://cran.r-project.org/web/packages/survival/vignettes/timedep.pdf. Accessed March 29.

Ferrata Storti Foundation

Haematologica 2020
Volume 105(4):1074-1080

First-line therapy with either bortezomib-melphalan-prednisone or lenalidomide-dexamethasone followed by lenalidomide for transplant-ineligible multiple myeloma patients: a pooled analysis of two randomized trials

Alessandra Larocca,[1] Roberto Mina,[1] Massimo Offidani,[2] Anna Marina Liberati,[3] Antonio Ledda,[4] Francesca Patriarca,[5] Andrea Evangelista,[6] Stefano Spada,[1] Giulia Benevolo,[7] Daniela Oddolo,[1] Vanessa Innao,[8] Clotilde Cangiolosi,[9] Annalisa Bernardini,[1] Pellegrino Musto,[10] Valeria Amico,[11] Vincenzo Fraticelli,[12] Laura Paris,[13] Nicola Giuliani,[14] Antonietta Pia Falcone,[15] Renato Zambello,[16] Lorenzo De Paoli,[17] Alessandra Romano,[18] Antonio Palumbo,[1*] Vittorio Montefusco,[19] Roman Hájek,[20,21] Mario Boccadoro[1] and Sara Bringhen[1]

[1]Myeloma Unit, Division of Hematology, University of Torino, Azienda-Ospedaliero Universitaria (AOU) Città della Salute e della Scienza di Torino, Torino, Italy; [2]Clinica di Ematologia, AOU Ospedali Riuniti di Ancona, Ancona, Italy; [3]Università degli Studi di Perugia, Azienda Ospedaliera (AO) Santa Maria, Terni, Italy; [4]Ematologia/CTMO Ospedale "A. Businco", Cagliari, Italy; [5]Udine University Hospital, DAME, University of Udine, Udine, Italy; [6]Unit of Clinical Epidemiology, AOU Città della Salute e della Scienza di Torino e CPO, Piemonte, Torino, Italy; [7]Hematology, Città della Salute e della Scienza, Torino, Italy; [8]U.O.C. Ematologia AOU G. Martino, Messina, Italy; [9]AO Villa Sofia-Cervello, Divisione Ematologia I UTMO, Palermo, Italy; [10]Unit of Haematology and Stem Cell Transplantation, IRCCS-CROB, Referral Cancer Center of Basilicata, Rionero in Vulture, Italy; [11]DH-Ematologico AO "S.Pio", Benevento, Italy; [12]Fondazione "Giovanni Paolo II", Unità Operativa Complessa di Oncoematologia, Campobasso, Italy; [13]Hematology and Bone Marrow Transplant Unit, Azienda Socio Sanitaria Territoriale Papa Giovanni XXIII, Bergamo, Italy; [14]Department of Medicine and Surgery, University of Parma, Parma, Italy; [15]Ematologia, IRCCS "Casa Sollievo della Sofferenza" Hospita, San Giovanni Rotondo, Italy; [16]Padova University School of Medicine, Hematology and Clinical Immunology, Padova, Italy; [17]Università del Piemonte Orientale A. Avogadro, Novara, Italy; [18]Division of Hematology, AOU Policlinico, Department of Surgery and Medical Specialties, University of Catania, Italy; [19]Hematology, Fondazione IRCCS Istituto Nazionale Tumori, Milan, Italy; [20]Department of Hematooncology University Hospital Ostrava, Ostrava, Czech Republic and [21]Faculty of Medicine, University of Ostrava, Ostrava, Czech Republic

**Currently a GlaxoSmithKline AG employee.*

Correspondence:

ALESSANDRA LAROCCA
alelarocca@hotmail.com

Received: February 27, 2019.

Accepted: June 25, 2019.

Pre-published: June 27, 2019.

doi:10.3324/haematol.2019.220657

Check the online version for the most updated information on this article, online supplements, and information on authorship & disclosures: www.haematologica.org/content/105/4/1074

ABSTRACT

Bortezomib-melphalan-prednisone (VMP) and continuous lenalidomide-dexamethasone (Rd) represent the standard treatment of transplant-ineligible patients with newly diagnosed multiple myeloma (MM). To date, no randomized trial has compared VMP to Rd, and there is no evidence of the optimal treatment for newly diagnosed MM, particularly in patients with high-risk cytogenetics [del(17p), t(4;14) or t(14;16)]. We pooled together data from patients with newly diagnosed MM treated with VMP or Rd induction followed by lenalidomide maintenance 10 mg (Rd-R) enrolled in the GIMEMA-MM-03-05 and EMN01 trials, to evaluate the efficacy of these treatments in different subgroups of patients, focusing on those with standard- and high-risk cytogenetics. Overall, 474 patients were analyzed (VMP: 257 patients; Rd-R: 217 patients). No differences in progression-free survival (hazard ratio=0.96) and overall survival (hazard ratio=1.08) were observed between standard-risk patients treated with VMP or Rd-R, whereas among the high-risk patients, the probabilities of progression (hazard ratio=0.54) and death (hazard ratio=0.73) were lower in the patients treated with VMP than in those treated with Rd-R. In particular, standard-risk patients >75 years benefited less from VMP than from Rd-R

(hazard ratio for progression-free survival=0.96; hazard ratio for overall survival=1.81). In this non-randomized analysis, VMP and Rd-R were equally effective in younger (≤75 years), standard-risk patients, while older ones (>75 years) benefited more from Rd-R. In high-risk patients, VMP improved progression-free survival and overall survival irrespective of age. The source trials are registered at ClinicalTrials.gov (NCT01063179 and NCT01093196).

Introduction

Multiple myeloma (MM) is a disease that occurs predominantly in the elderly: the median age at diagnosis is 71 years and two-thirds of patients are over 65 years of age.[1,2] Elderly patients, defined as those older than 65-70 years of age, are usually considered ineligible for high-dose chemotherapy and autologous stem-cell transplantation (ASCT).[3] In Europe, standard initial therapy of older patients consists of either a triplet regimen including bortezomib-melphalan-prednisone (VMP) administered in a fixed-duration schedule, or a doublet combination of lenalidomide (25 mg) and dexamethasone (Rd), administered continuously until progression or intolerance.[3] The VISTA trial demonstrated that VMP was superior to melphalan-prednisone both in terms of progression-free survival [PFS: 21.7 *vs*. 15.2 months, hazard ratio (HR)=0.56; *P*<0.001] and overall survival (OS: 56.4 *vs*. 43.1 months, HR=0.69; *P*<0.001).[4,5] The FIRST trial showed that continuous Rd significantly prolonged the median PFS (26 *vs*. 21.9 months, HR=0.69; *P*<0.001) and OS (59.1 *vs*. 49.1 months, HR=0.78; *P*=0.0023) compared to the median PFS and OS achieved with melphalan-prednisone-thalidomide (MPT).[6,7] Based on the results of these two phase III studies, both VMP and continuous Rd were approved by the European Medicine Agency as standard treatments for patients with newly diagnosed MM ineligible for ASCT.

The most important prognostic factors in MM are age and frailty, disease stage defined by the International Staging System (ISS),[8] and chromosomal abnormalities, detected by fluorescent *in situ* hybridization (FISH). Patients harboring chromosomal abnormalities, including del(17p), t(4,14) and t(14,16), have a poor prognosis, with a higher risk of disease progression and death.[9] Approximately 15-20% of patients with newly diagnosed MM present with at least one cytogenetic abnormality and constitute the so-called "high-risk" population.

Despite recent therapeutic advances in MM, the results obtained with novel agent-based regimens in patients with high-risk chromosomal abnormalities are unsatisfactory and the prognosis of these patients remains poor. Moreover, limited data are available on high-risk, transplant-ineligible MM patients treated with bortezomib or lenalidomide in first-line therapy. In the VISTA trial, patients with high- or standard-risk cytogenetics who received VMP had similar times to progression (median 19.8 *vs*. 23.1 months, HR=1.29; *P*=0.55) and OS (HR=1.00; *P*=0.99).[4,5] In a subanalysis of the FIRST trial, which compared continuous Rd treatment until progression, Rd treatment for 72 weeks (Rd18) and MPT treatment, continuous Rd treatment resulted in PFS and OS benefits in comparison with MPT; however, these benefits were largely due to the improvements in PFS and OS in patients without high-risk cytogenetics (median PFS 31.1 *vs*. 21.2 *vs*. 24.9 months for continuous Rd *vs*. Rd18 *vs*. MPT). Indeed, in the high-risk group, the longest PFS was observed with Rd18 treatment (median 8.4 *vs*. 17.5 *vs*. 14.6 months for continuous Rd *vs*. Rd18 *vs*. MPT) while OS was similar across treatment arms.[10]

Unfortunately, VMP and Rd have never been formally compared in a randomized trial. Based on the different safety profiles of bortezomib and lenalidomide, bortezomib is usually preferred in patients with advanced renal failure, while lenalidomide can be the drug of choice for patients with pre-existing neuropathy, or when oral therapy is preferable.[11] Besides these considerations, VMP and Rd are equally recommended. Because a head-to-head comparison of VMP *vs*. Rd is lacking, the choice of first-line treatment of elderly MM patients is based mainly on the physician's and patient's preferences.

We previously published the results of two randomized, phase III studies investigating both VMP (GIMEMA-MM-03-05)[12–14] and Rd induction followed by lenalidomide maintenance (Rd-R) (EMN01)[15] as upfront therapies for elderly, transplant-ineligible MM patients. In order to provide clinicians with useful, and currently lacking, evidence that may help to tailor anti-myeloma treatment better in this population, we conducted a pooled, retrospective analysis comparing the efficacy of VMP and Rd-R in different subgroups of elderly, transplant-ineligible MM patients, focusing on cytogenetic profile.

Methods

Study design and participants

We pooled the single data from two phase III studies, the GIMEMA-MM-03-05 (NCT01063179) and the EMN01 (NCT01093196) trials. Both trials enrolled patients with newly diagnosed MM who were older than 65 years of age or younger but ineligible for ASCT. Inclusion and exclusion criteria, as well as treatment details of the source studies, have been published previously.[12–15] Further details on study treatments and procedures are reported in the *Online Supplementary Appendix*. For this retrospective, not pre-planned analysis, we selected only patients randomized to VMP or Rd-R. The source studies were approved by the institutional review boards at each of the participating centers. All patients gave written informed consent before entering the source studies, which were performed in accordance with the Declaration of Helsinki.

Statistical analysis

The primary objective of this analysis was to compare PFS and OS (see *Online Supplementary Appendix*) in patients treated with VMP or Rd-R, adjusting for patient and disease characteristics at baseline.

Single data from the two studies were pooled together and analyzed. Comparisons between different groups of patients were conducted using standard statistical tests. Time-to-event data were analyzed using the Kaplan–Meier method; survival curves were compared with the log-rank test. Results are presented as hazard ratios (HR), 95% confidence intervals (95% CI), and two-

sided *P*-values adjusted for age, ISS stage, cytogenetic risk as determined by FISH, Karnofsky Performance Status (PS) and extramedullary disease (yes *vs*. no) (main model). Subgroup analyses were performed to determine the consistency of treatment effects of VMP vs. Rd-R in the main model in the different subgroups using interaction terms between treatment and cytogenetics [also with single deletion and translocation, del(17p), t(4;14) and t(14;16)], ISS stage (I *vs*. II/III), age (≤75 *vs*. >75 years), Karnofsky PS (90-100 *vs*. 70-80 *vs*. 60) and extramedullary disease. The null hypothesis examined with the interaction test was that the HR of the comparison VMP *vs*. Rd-R would be the same in each subgroup. The models were adjusted for age as a continuous variable. Multivariate Cox models with a three-way interaction between treatment (VMP *vs*. Rd-R), cytogenetics (high-risk *vs*. standard-risk, missing *vs*. standard-risk) and age (≤75 *vs*. >75 years) were performed to evaluate the effect of treatment in different cytogenetic and age subgroups. The models were adjusted for other factors included in previous analyses. The different effect of VMP *vs*. Rd-R in cytogenetic subgroups was confirmed by a sensitivity analysis using the multiple imputation method for missing cytogenetic and ISS values. In detail, missing data were handled using the "jomo" package[16] to perform Cox model-compatible multiple imputation[17,18] with 50 imputations, 1,000 burn-in iterations and 1,000 iterations between two successive imputations.

In both trials, FISH was assessed centrally with a 10% cutoff for numerical aberrations and a 15% one for IgH translocations. High-risk cytogenetics was defined as the presence of at least one of the following chromosomal abnormalities: del(17p), t(4;14) or t(14;16). Patients not carrying any of these abnormalities were defined as standard-risk patients. Data were censored on June 18, 2014 for the GIMEMA-MM-03-05 study and on October 20, 2017 for the EMN01 study. Data were analyzed using R software (version 3.5.1).

Table 1. Baseline patients' characteristics in the intention-to-treat population.

	All patients (n=474)	VMP (n=257)	Rd-R (n=217)	*P*-value
Age – median (IQR)	72 (69-76)	71 (68-75)	73 (70-77)	<0.001
>75 years – n (%)	131 (28)	57 (22)	74 (34)	
Karnofsky PS – n (%)				
90-100	232 (49)	121 (47)	111 (51)	0.11
70-80	200 (42)	118 (46)	82 (38)	
60	42 (9)	18 (7)	24 (11)	
Creatinine – mg/dL (IQR)	1 (0.8-1.22)	1.01 (0.84-1.3)	0.94 (0.8-1.19)	0.002
LDH – UI/L (IQR)	286 (202-377)	293 (203-368)	284 (200-381)	0.753
missing – n (%)	80 (17)	36 (14)	44 (20)	
Extramedullary disease – n (%)	58 (12)	37 (14)	21 (10)	0.124
ISS – n (%)				0.96
I	117 (25)	56 (22)	61 (28)	
II	184 (39)	88 (34)	97 (45)	
III	117 (25)	57 (22)	59 (27)	
Missing	56 (12)	56 (22)		
Cytogenetics – n (%)				1
standard-risk	273 (58)	136 (53)	137 (63)	
high-risk*	95 (20)	48 (19)	47 (22)	
missing	106 (22)	73 (28)	33 (15)	
Del(17p) – n (%)				1
no	321 (68)	161 (63)	160 (74)	
yes	47 (10)	23 (9)	24 (11)	
missing	106 (22)	73 (28)	33 (15)	
t(4;14) – n (%)				0.88
no	318 (67)	158 (61)	160 (74)	
yes	50 (11)	26 (10)	24 (11)	
missing	106 (22)	73 (28)	33 (15)	
t(14;16) – n (%)				0.785
no	352 (74)	178 (69)	174 (80)	
yes	13 (3)	6 (2)	7 (3)	
missing	109 (23)	73 (28)	36 (17)	
t(11;14) – n (%)				0.038
no	308 (65)	164 (64)	144 (66)	
yes	54 (11)	20 (8)	34 (16)	
missing	112 (24)	73 (28)	39 (18)	

VMP: bortezomib-melphalan-prednisone; Rd-R: lenalidomide-dexamethasone followed by lenalidomide maintenance; IQR: interquartile range; PS: Performance Status; LDH: lactate dehydrogenase; ISS: International Staging System. *High-risk defined by the presence of any of del(17p), t(4;14), or t(14;16), detected by fluorescence *in situ* hybridization.

Results

Patients

A total of 474 patients were analyzed, 257 in the VMP group and 217 in the Rd-R group. Patients' demographic and baseline characteristics were well balanced between the two groups (Table 1). The median age of the overall population was 72 years [interquartile range (IQR) 69-76), with patients in the Rd-R group being slightly older (median, 73 years; IQR 70-77) than patients in the VMP group (median, 71 years; IQR 68-75; *P*<0.001). Similar proportions of patients in the VMP and Rd-R groups had ISS stage III disease (23% *vs*. 27%; *P*=0.74) and high-risk cytogenetics as determined by FISH (19% *vs*. 22%; *P*=1).

All patients started the assigned treatment. Overall, 61% and 64% of patients in the VMP and Rd-R groups, respectively, received a second-line treatment, which consisted of an immunomodulatory drug (IMiD)-based regimen in 63% of patients treated with VMP and of a proteasome inhibitor (PI)-based regimen in 84% of patients treated with Rd-R (Table 2).

The median follow-up for the entire study population was 70.2 months (IQR 54.7-80.6), without a significant difference between the VMP and Rd-R groups (72.6 *vs*. 64.4 months, respectively; *P*=0.16).

Survival outcomes

The median PFS in the overall population was 21.5 months (95% CI: 19.8-24.9) and was not significantly different between patients treated with VMP (25.1 months,

Table 2. Second-line treatment.

	All patients (n=474)	VMP (n=257)	Rd-R (n=217)	*P*-value
Second-line treatment – n (%)				0.70
Yes	296 (62)	158 (61)	138 (64)	
No	178 (38)	99 (39)	79 (36)	
Type of treatment – n (%)				
Proteasome inhibitor				
bortezomib	144 (49)	28 (18)	116 (84)	
carfilzomib	2 (0)	1 (0)	1 (0)	
Immunomodulatory drug				
lenalidomide	68 (23)	68 (43)	0 (0)	
thalidomide	34 (11)	32 (20)	2 (1)	
Other	48 (16)	29 (18)	19 (14)	

VMP: bortezomib-melphalan-prednisone; Rd-R: lenalidomide-dexamethasone followed by lenalidomide maintenance.

95% CI: 20.9-28.6) or Rd-R (18.6 months, 95% CI: 16-22.4) (HR=0.81, *P*=0.07). At 5 years, 15% and 18% of patients were alive and free from progression in the VMP and Rd-R groups, respectively. In the subgroup analyses (Figure 1), no clear differences in PFS were noted between the VMP and Rd-R groups according to age (in patients ≤75 years, HR=0.80; in patients >75 years, HR=0.84, interaction *P*=0.85), Karnofsky PS (score 90-100, HR=0.73; score 70-80, HR= 0.86, interaction *P*=0.43), ISS stage (stage I, HR=0.73; stage II/III, HR=0.85, interaction *P*=0.55) and the presence of extramedullary disease (yes, HR=0.75; no, HR=0.82, interaction *P*=0.78). As far as concerns FISH-determined cytogenetic risk, no difference in PFS was observed among standard-risk patients between the VMP and Rd-R groups (HR=0.96, 95% CI: 0.73-1.28), whereas in high-risk patients, a significant benefit was observed with VMP in comparison with Rd-R (HR=0.54, 95% CI: 0.34-0.84; interaction *P*=0.03). The advantage of VMP over Rd-R in high-risk patients was confirmed in the subgroups of single high-risk cytogenetic abnormalities, including del(17p) (HR=0.59, 95% CI: 0.32-1.09), t(4;14) (HR=0.50, 95% CI: 0.27-0.93) and t(14;16) (HR=0.35, 95% CI: 0.09-1.42) (*Online Supplementary Figure S1*).

The median OS in the overall population was 66.4 months (95% CI: 57.3-79.7); the median OS was not significantly different between patients treated with VMP (71 months; 95% CI: 58.2-not reached) or Rd-R (62 months, 95% CI: 48.2-83.3) (HR=0.85; *P*=0.28), with an equivalent proportion of patients alive at 5 years (55% *vs.* 51%, respectively). In the subgroup analysis (Figure 2), patients ≤75 years old benefited more from VMP than Rd-R (HR=0.71, 95% CI: 0.51-1.00), whereas patients >75 years old benefited more from Rd-R (HR=1.29, 95% CI: 0.79-2.13; interaction *P*=0.04). Similarly to PFS, no significant difference in OS was noted among standard-risk patients between those treated with VMP or Rd-R (HR=1.08, 95% CI: 0.74-1.58), but among patients with high-risk cytogenetics, an OS advantage was reported for VMP-treated patients over those treated with Rd-R (HR=0.73, 95% CI: 0.42-1.26) and those with missing data. The advantage for VMP over Rd-R in high-risk patients was confirmed in the subgroups of single high-risk cytogenetic abnormalities, including del(17p) (HR=0.81, 95% CI: 0.38-1.71), t(4;14) (HR=0.74, 95% CI: 0.35-1.56), and t(14;16) (HR=0.73, 95% CI: 0.13-4.05) (*Online Supplementary Figure S2*).

Multivariate Cox models with three-way interaction were performed to better evaluate the relationship between treatment regimen (VMP *vs.* Rd-R), age (≤75 *vs.* >75 years) and cytogenetic risk (standard vs. high). This analysis confirmed the absence of difference in PFS between VMP and Rd-R according to age in the standard-risk group, while confirmed the PFS benefit from VMP over Rd-R in high-risk patients (interaction *P*=0.03). With regards to OS, older (>75 years), standard-risk patients seemed to benefit more from Rd-R than from VMP (HR=1.81), while the OS advantage from VMP was confirmed in younger (≤75 years), standard-risk patients (HR=0.83). In high-risk patients, the OS benefit was confirmed irrespective of age (≤75 years, HR=0.75; >75 years, HR=0.65) (Table 3).

To better investigate the comparison between VMP and Rd-R and the effect of cytogenetics and age we performed a multiple imputation analysis for missing cytogenetics

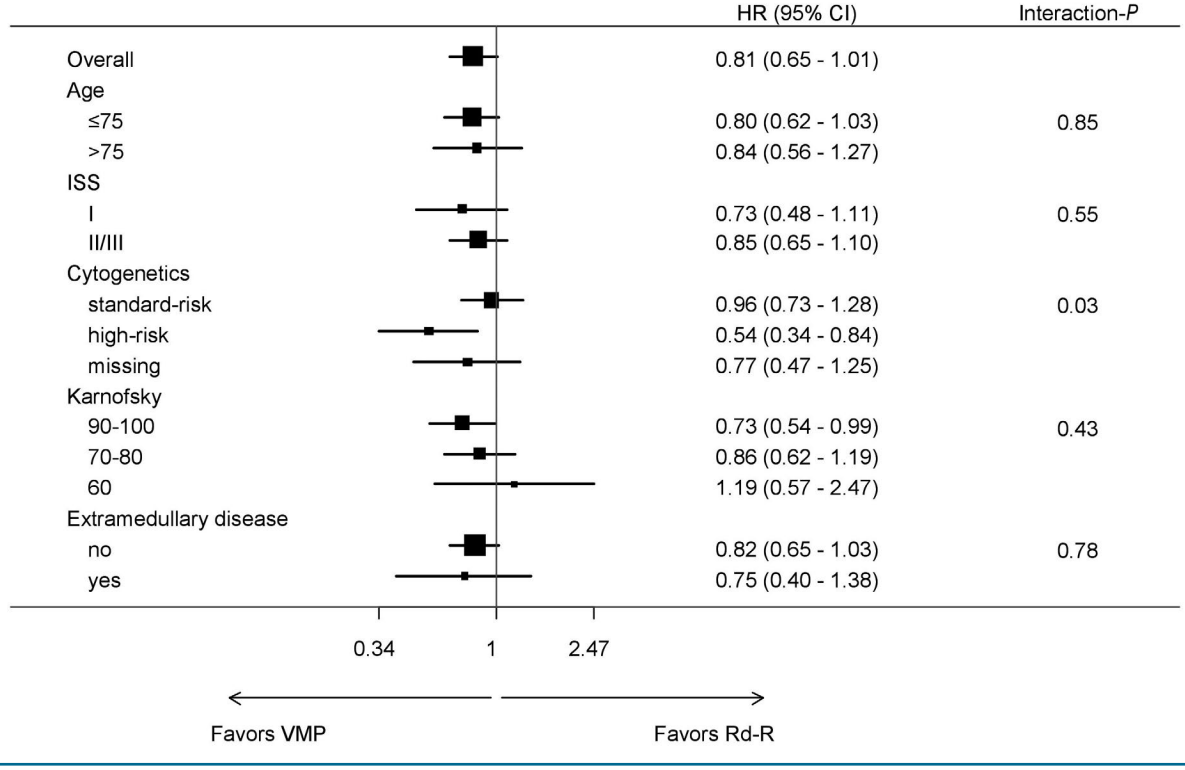

Figure 1. Subgroup analysis of progression-free survival in the intention-to-treat population for patients treated with VMP or Rd-R. VMP: bortezomib-melphalan-prednisone; Rd-R: lenalidomide-dexamethasone followed by lenalidomide maintenance; HR: hazard ratio; 95% CI: 95% confidence interval; ISS: International Staging System.

and ISS stage data. No difference in PFS was observed between the groups treated with VMP or Rd-R (HR=0.85, 95% CI: 0.69-1.04); subgroup analysis confirmed the previous results for cytogenetics, with no difference for standard-risk patients (HR=1.01, 95% CI: 0.78-1.30); while, in high-risk patients, there was a significant benefit from VMP treatment in comparison with Rd-R treatment (HR=0.53, 95% CI: 0.34-0.82; interaction *P*=0.02) (*Online Supplementary Figure S3*). No difference in OS was observed between the groups treated with VMP or Rd-R (HR=0.86, 95% CI: 0.66-1.13); subgroup analysis revealed that VMP was more beneficial than Rd-R for patients ≤75 years (HR=0.72, 95% CI: 0.52-0.99), whereas patients >75 years benefited more from Rd-R (HR=1.29, 95% CI: 0. 79-2.08; interaction *P*=0.05) (*Online Supplementary Figure S4*).

Multivariate Cox models with the three-way interaction confirmed the results for PFS and OS (*Online Supplementary Table S1*).

Discussion

In this pooled analysis of 474 transplant-ineligible patients with newly diagnosed MM, we evaluated the impact on survival outcomes of initial treatment, consisting of either a bortezomib-based regimen (VMP) or a lenalidomide-based one (Rd-R), in different subgroups of patients, focusing on groups with different cytogenetic risk profiles, as determined by FISH. We found no difference between VMP and Rd-R among standard-risk patients, whereas, among high-risk patients, VMP improved PFS (HR=0.54) and OS (HR=0.73) as compared to Rd-R.

Risk assessment and stratification have long been performed in MM, taking into consideration both the aggressiveness of the disease at presentation, based on ISS stage, and its cytogenetic features, determined by either FISH or gene expression profile. Many prognostic factors have been identified in myeloma, the most important ones being chronological and biological age, defined by frailty status in elderly patients, and the presence of chromosomal abnormalities identified by FISH.[11]

Although risk assessment had limited impact on therapeutic choices in the past, with the expanding armamentarium of treatments for MM and the growing evidence of effect modification, it is likely to become a fundamental factor in selecting and tailoring treatment. The International Myeloma Working Group (IMWG) guidelines recommend that all newly diagnosed (ND)MM patients be screened by FISH for chromosomal abnormalities, including del(17p), t(4;14) and t(14;16), and that all older patients undergo a geriatric assessment for the evaluation of frailty.[19] Despite these recommendations, to date no trial has prospectively evaluated the efficacy of standard therapies according to patients' risk status, either based on chromosomal abnormalities identified by FISH or on frailty status. Hence, very limited data are available about the efficacy of current standards of care, such as VMP and Rd, for NDMM patients with high-risk cytogenetics. The VISTA trial did not find any difference between high-risk and standard-risk patients treated with VMP.[4,5] In the FIRST trial, there was no evidence that lenalidomide improved outcome of patients with high-risk cytogenetics.[7] However, the small number of high-risk patients in both trials makes it difficult to draw definitive conclusions.

In our study, we defined high-risk patients as those carrying at least one cytogenetic abnormality, including

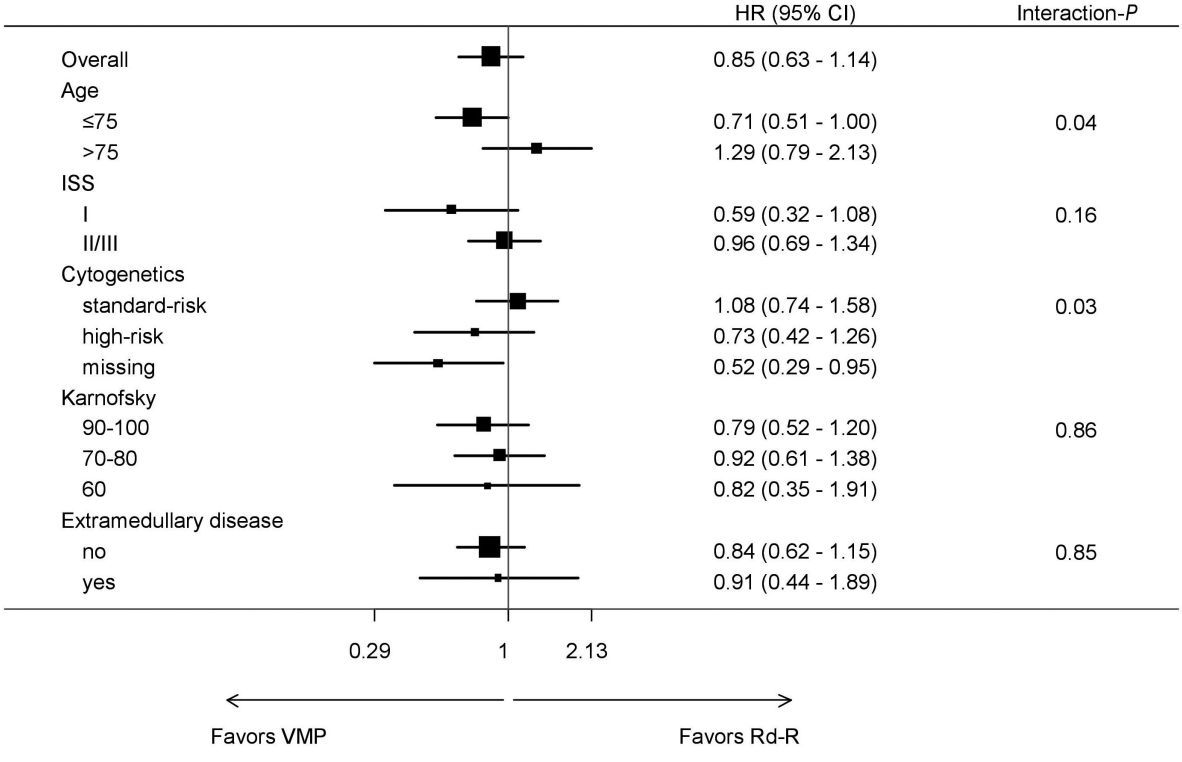

Figure 2. Subgroup analysis of overall survival in the intention-to-treat population for patients treated with VMP or Rd-R. VMP: bortezomib-melphalan-prednisone; Rd-R: lenalidomide-dexamethasone followed by lenalidomide maintenance; HR: hazard ratio; 95% CI: 95% confidence interval; ISS: International Staging System.

del(17p), t(4;14) and t(14;16), consistently with the IMWG recommendations. Major advantages of this study are the number of patients with available cytogenetic data and the fact that all FISH analyses were performed at one centralized facility only.

In our analysis, VMP resulted in a 45% reduction in the risk of death or progression, as compared to that achieved with Rd-R (HR=0.54), in the high-risk group, with the PFS benefit being confirmed across the single cytogenetic abnormalities, whereas no significant difference in PFS was found in the standard-risk group (HR=0.96, interaction *P*=0.03). Furthermore, high-risk patients treated with VMP had a reduced risk of death (HR: 0.73), confirmed across all cytogenetic subgroups, in comparison with patients treated with Rd-R, while no difference was noted between patients treated with VMP or Rd-R within the standard-risk group (HR=1.08). However, we could not distinguish the role of melphalan from that of bortezomib in improving the outcome of high-risk patients.

The PFS benefit for VMP over Rd-R in high-risk patients was seen in both younger (≤75 years; HR=0.75) and older patients (>75 years; HR=0.19), while in older, standard-risk patients VMP and Rd-R had similar effects on outcomes (HR=0.96). Similarly, while the OS benefit among high-risk patients was independent of age (patients ≤75 years, HR=0.75; patients >75 years, HR=0.65), older patients with standard-risk cytogenetics benefited less from VMP (patients >75 years, HR=1.81) than they did from Rd-R.

No data about the patients' frailty at diagnosis were available in the GIMEMA-MM-03-05 trial, and chronological age was the only parameter that could be evaluated in the two trials included in this analysis.

In order to better assess the efficacy of approved upfront regimens according to cytogenetic risk, we restricted our analysis to patients randomized to the VMP arm of the GIMEMA-MM-03-05 trial and the Rd-R arm of the EMN01 trial, since both VMP and Rd are approved combinations for patients with newly diagnosed MM who are ineligible for transplantation. Of note, in the EMN01-trial patients in the Rd-R arm received nine cycles of Rd followed by lenalidomide maintenance or lenalidomide-prednisone maintenance until progression (lenalidomide 10 mg/day), whereas in the standard approved regimen, Rd is administered continuously until progression.[15] This could in part explain the inferior PFS in the EMN01 trial (21 months) as compared to that in the FIRST trial (26 months).[7,15] On the other hand, we recently presented, at an American Society of Hematology meeting, preliminary results of a randomized phase III study comparing standard Rd to Rd-R in older, intermediate fit patients, defined by the IMWG frailty score,[19] showing no difference between continuous Rd and Rd-R in terms of PFS (HR=0.93, 95% CI: 0.64-1.34; *P*=0.681) and OS (HR=0.73, 95% CI: 0.40-1.33; *P*=0.306).[20]

In the VISTA trial, bortezomib was given twice weekly during cycles 1 to 4 and once weekly thereafter, while in the GIMEMA-MM-03-05-trial half of the patients in the VMP arm (n=191, 51%) received once-weekly bortezomib. However, we had previously shown that the once weekly schedule was equally effective as the twice weekly one in a subgroup analysis of the GIMEMA-MM-03-05 study, potentially due to a more tolerable safety profile of once weekly bortezomib.[13,14] This might explain a somewhat more favorable median PFS with VMP in the GIMEMA-MM-03-05 study (median, 24.8 months) as compared to the PFS reported in the VISTA trial (median, 21.7 months).[4]

The major limitation of this unplanned cross-trial comparison is the absence of randomization between the two treatments, so the results should be interpreted with particular caution. Despite similar eligibility criteria and a comparable follow-up of more than 5 years, there were some significant differences between the two populations. In fact, patients treated with Rd-R were significantly older and patients treated with VMP had a significantly higher creatinine level. Another limitation is that patients enrolled in the two source trials had to meet strict inclusion and exclusion criteria.

Despite these caveats, a head-to-head comparison between VMP and Rd is currently lacking, as is a prospective evaluation of the different treatments in high-risk and standard-risk MM patients. To the best of our knowledge, this is the first study that has pooled together and analyzed a large series of transplant-ineligible patients with NDMM treated with either a bortezomib- or lenalidomide-based combination, with the aim of providing an answer to the burning question of the optimal upfront treatment for NDMM patients according to their cytogenetic risk.

Our results suggest that the doublet regimen Rd may be a suboptimal option for patients with high-risk cytogenetics, further supporting the 2016 IMWG recommendations that a triplet regimen containing an IMiD and a PI should be used in this setting.[9] In this light, a major step forward has been made with the results of the Southwest Oncology Group (SWOG) S0777, which showed superior response rate, PFS and OS with the triplet regimen bortezomib-lenalidomide-dexamethasone (VRD) than with Rd in NDMM without intention to immediate transplantation.[21] Of note, the longest PFS in high-risk patients was obtained with VRD (38 months). Nevertheless, the analysis was based on only 44 high-risk patients.

The selection of treatment in elderly patients should also consider the risk of toxicity and the capability to tolerate treatment, since advanced age and the occurrence of severe adverse events may negatively affect survival.[22] In our analysis, this was particularly evident in standard-risk patients, in whom no difference was found between VMP and Rd-R and the benefit of Rd-R was more evident in patients over 75 years. In this context, the presence of specific comorbidities (such as peripheral neuropathy or renal insufficiency), older age (>75 years) or the presence of

Table 3. Multivariate Cox models with three-way interaction between treatment type, age and cytogenetics, adjusted for International Staging System stage, Karnofsky Performance Status, extramedullary disease and age as a continuous variable.

Main analysis	PFS HR* (95% CI)	OS HR* (95% CI)
Standard-risk cytogenetics - age ≤75	0.92 (0.67 - 1.27)	0.83 (0.53 - 1.29)
Standard-risk cytogenetics - age >75	0.96 (0.56 - 1.66)	1.81 (0.94 - 3.49)
High-risk cytogenetics - age ≤75	0.75 (0.45 - 1.26)	0.75 (0.39 - 1.43)
High-risk cytogenetics - age >75	0.19 (0.07 - 0.52)	0.65 (0.21 - 2.04)
3-way interaction-*P*	0.03	0.23
2-way cytogenetics interaction-*P*	0.03	0.23
2-way age interaction-*P*	0.85	0.04

PFS: progression-free survival; OS: overall survival; HR: hazard ratio; 95% CI: 95% confidence interval.

frailty, as well as the patient's compliance and treatment preference should be considered when choosing treatment.

Our results highlight the importance of performing FISH analysis in all cases of NDMM for risk stratification. Treatment decisions in elderly patients ineligible for transplant are extremely complex, since they should take into consideration not only the biology and the stage of the disease, but also the characteristics of patients (frailty status, comorbidities, hospitalization, concomitant medications, social support, compliance) and goals of care (depth of response or disease control). Therefore, both VMP and Rd are valid options for transplant-ineligible NDMM. Nevertheless, VMP could be preferred in patients with high-risk cytogenetics and severe renal insufficiency, whereas continuous Rd could be the treatment of choice in standard-risk patients, particularly those over 75 years, or if oral administration and avoidance of peripheral neuropathy are major considerations.

The results of this analysis are based on a selected population, including patients enrolled in clinical trials. Nevertheless, an ongoing trial will prospectively compare these two standard treatments, VMP and continuous Rd, and the impact of cytogenetics on outcomes in an unselected population of patients ≥65 years with MM in every day clinical practice (Real MM trial, ClinicalTrials.gov Identifier: NCT03829371).

Better treatment options and newer combinations are needed for high-risk disease. Recent trials incorporating the first-in-class monoclonal antibody anti-CD38 daratumumab combined with VMP (Dara-VMP)[23] or Rd (Dara-Rd)[24] showed that these regimes significantly reduced the risk of progression or death by 50% and 44%, respectively, as compared to standard VMP (Dara-VMP *vs*. VMP: median PFS not reached *vs*. 18.1 months, HR=0.50, 95% CI: 0.38-0.65) and Rd (Dara_Rd *vs*. Rd: median PFS not reached *vs*. 31.9 months, HR=0.56, 95% CI: 0.43-0.73). The benefit of Dara-VMP and Dara-Rd was evident in most of the subgroups analyzed; however the addition of daratumumab did not seem not to overcome the poor prognosis of high-risk patients.

Ongoing trials testing multi-drug combinations including IMiD, second-generation PI, such as carfilzomib and ixazomib, and monoclonal antibodies in the frontline setting will evaluate and, potentially, improve the outcome of high-risk patients.

Acknowledgments

The authors are grateful to the investigators of all participating sites and the patients who took part in the source studies. The authors also thank the data managers Debora Caldarazzo and Angela Jiang, and the nurses Rosalia Capobianco and Giacomo Castorina from the Torino site.

References

1. Palumbo A, Anderson K. Multiple myeloma. N Engl J Med 2011;364(11):1046-1060.
2. Howlader N, Noone A, Krapcho M, et al. SEER Cancer Statistics Review, 1975-2014. Bethesda, US-MD.
3. Moreau P, San Miguel J, Sonneveld P, et al. Multiple myeloma: ESMO clinical practice guidelines for diagnosis, treatment and follow-up. Ann Oncol Off J Eur Soc Med Oncol. 2017;28(Suppl_4):iv52-iv61.
4. San-Miguel JF, Schlag R, Khuageva NK, et al. Bortezomib plus melphalan and prednisone for initial treatment of multiple myeloma. N Engl J Med. 2008;359(9):906-917.
5. San-Miguel JF, Schlag R, Khuageva NK, et al. Persistent overall survival benefit and no increased risk of second malignancies with bortezomib-melphalan-prednisone versus melphalan-prednisone in patients with previously untreated multiple myeloma. J Clin Oncol. 2013;31(4):448-455.
6. Benboubker L, Dimopoulos MA, Dispenzieri A, et al. Lenalidomide and dexamethasone in transplant-ineligible patients with myeloma. N Engl J Med. 2014;371(10):906-917.
7. Facon T, Dimopoulos MA, Dispenzieri A, et al. Final analysis of survival outcomes in the phase 3 FIRST trial of up-front treatment for multiple myeloma. Blood. 2018;131(3):301-310.
8. Greipp PR, San Miguel J, Durie BGM, et al. International staging system for multiple myeloma. J Clin Oncol. 2005;23(15):3412-3420.
9. Sonneveld P, Avet-Loiseau H, Lonial S, et al. Treatment of multiple myeloma with high-risk cytogenetics: a consensus of the International Myeloma Working Group. Blood. 2016;127(24):2955-2962.
10. Avet-Loiseau H, Hulin C, Benboubker L, et al. Impact of cytogenetics on outcomes of transplant-ineligible patients with newly diagnosed multiple myeloma treated with continuous lenalidomide plus low-dose dexamethasone in the first (MM-020) Trial. Blood. 2015;126(23): 730.
11. Larocca A, Dold SM, Zweegman S, et al. Patient-centered practice in elderly myeloma patients: an overview and consensus from the European Myeloma Network (EMN). Leukemia. 2018;32(8):1697-1712.
12. Palumbo A, Bringhen S, Rossi D, et al. Bortezomib-melphalan-prednisone-thalidomide followed by maintenance with bortezomib-thalidomide compared with bortezomib-melphalan-prednisone for initial treatment of multiple myeloma: a randomized controlled trial. J Clin Oncol. 2010;28(34):5101-5109.
13. Palumbo A, Bringhen S, Larocca A, et al. Bortezomib-melphalan-prednisone-thalidomide followed by maintenance with bortezomib-thalidomide compared with bortezomib-melphalan-prednisone for initial treatment of multiple myeloma: updated follow-up and improved survival. J Clin Oncol. 2014;32(7):634-640.
14. Bringhen S, Larocca A, Rossi D, et al. Efficacy and safety of once-weekly bortezomib in multiple myeloma patients. Blood. 2010;116(23):4745-4753.
15. Magarotto V, Bringhen S, Offidani M, et al. Triplet vs doublet lenalidomide-containing regimens for the treatment of elderly patients with newly diagnosed multiple myeloma. Blood. 2016;127(9):1102-1108.
16. Carpenter JR, Kenward MG. Multiple Imputation and its Application. Chichester, UK: John Wiley & Sons, Ltd. 2015.
17. Bartlett JW, Seaman SR, White IR, Carpenter JR. Multiple imputation of covariates by fully conditional specification: accommodating the substantive model. Stat Methods Med Res. 2015;24(4):462-487.
18. Quartagno M, Carpenter JR. Multilevel multiple imputation in presence of interactions, non-linearities and random slopes. 49th Scientific Meeting of the Italian Statistical Society.
19. Palumbo A, Bringhen S, Mateos M-V, et al. Geriatric assessment predicts survival and toxicities in elderly myeloma patients: an International Myeloma Working Group report. Blood. 2015;125(13):2068-2074.
20. Larocca A, Salvini M, De Paoli L, et al. Efficacy and feasibility of dose/schedule-adjusted Rd-R vs. continuous Rd in elderly and intermediate-fit newly diagnosed multiple myeloma (NDMM) patients: RV-MM-PI-0752 phase III randomized study. 2018;132(Suppl 1):305.
21. Durie BGM, Hoering A, Abidi MH, et al. Bortezomib with lenalidomide and dexamethasone versus lenalidomide and dexamethasone alone in patients with newly diagnosed myeloma without intent for immediate autologous stem-cell transplant (SWOG S0777): a randomised, open-label, phase 3 trial. Lancet. 2017;389(10068):519-527.
22. Bringhen S, Mateos MV, Zweegman S, et al. Age and organ damage correlate with poor survival in myeloma patients: meta-analysis of 1435 individual patient data from 4 randomized trials. Haematologica. 2013;98(6):980-987.
23. Mateos M-V, Dimopoulos MA, Cavo M, et al. Daratumumab plus bortezomib, melphalan, and prednisone for untreated myeloma. N Engl J Med 2018;378(6):518-528.
24. Facon T, Kumar SK, Plesner T, et al. Phase 3 randomized study of daratumumab plus lenalidomide and dexamethasone (D-Rd) versus lenalidomide and dexamethasone (Rd) in patients with newly diagnosed multiple myeloma (NDMM) ineligible for transplant (MAIA). Blood. 2018;132(Suppl 1):LBA-2.

ARTICLE

The role of neuraminidase 1 and 2 in glycoprotein Ibα-mediated integrin αIIbβ3 activation

Dianne E. van der Wal,[1] April M. Davis,[1] Melanie Mach,[1] Denese C. Marks[1,2]

[1]Australian Red Cross Lifeblood (formerly known as Blood Service) and [2]Sydney Medical School, Uinversity of Sydney, Sydney, NSW, Australia

Ferrata Storti Foundation

Haematologica 2019
Volume 105(4):1081-1094

ABSTRACT

Upon vascular injury, platelets adhere to von Willebrand Factor (VWF) *via* glycoprotein Ibα (GPIbα). GPIbα contains many glycans, capped by sialic acid. Sialic acid cleavage (desialylation) triggers clearance of platelets. Neuraminidases (NEU) are responsible for desialylation and so far, NEU1-4 have been identified. However, the role of NEU in healthy platelets is currently unknown. Aim of the study was to study the role of NEU1 and NEU2 in platelet signalling. Membrane association of platelet attached glycans, NEU1 and NEU2 was measured following activation with agonists using flow cytometry. Adhesion on fibrinogen, aggregation and fibrinogen-binding were assessed with/without the NEU-inhibitor, 2-deoxy-2-3-dide-hydro-*N*-acetylneuraminic acid. Cellular localisation of NEU1 and NEU2 was examined by fluorescence microscopy. Desialylation occurred following GPIbα-clustering by VWF. Basal levels of membrane NEU1 were low; glycoprotein Ibα-clustering induced a four-fold increase (n=3, $P<0.05$). Inhibition of $\alpha_{IIb}\beta_3$-integrin prevented the increase in NEU1 membrane-association by ~60%. Membrane associated NEU2 increased two-fold (n=3, $P<0.05$) upon VWF-binding, while inhibition/removal of GPIbα reduced the majority of membrane associated NEU1 and NEU2 (n=3, $P<0.05$). High shear and addition of fibrinogen increased membrane NEU1 and NEU2. NEU-inhibitior prevented VWF-induced αIIbβ3-integrin activation by 50% (n=3, $P<0.05$), however, promoted VWF-mediated agglutination, indicating a negative feedback mechanism for NEU activity. NEU1 or NEU2 were partially co-localised with mitochondria and α-granules respectively. Neither NEU1 nor NEU2 co-localised with lysosomal-associated membrane protein 1. These findings demonstrate a previously unrecognised role for NEU1 and NEU2 in GPIbα–mediated and $\alpha_{IIb}\beta_3$-integrin signalling.

Introduction

Glyocoprotein Ibα (GPIbα), part of the GPIb-V-IX-complex, binds to von Willebrand Factor (VWF), initiating platelet adhesion to the endothelium following vascular injury. GPIbα is heavily glycosylated,[1] with both O-[2] and *N*-linked glycans.[3] When fully assembled, *N*-linked glycans are complex, branched carbohydrates, capped by sialic acid.[3] The majority of O-linked structures on GPIbα are core 2 and also capped by sialic acid.[4]

Sialic acid can be cleaved from platelet glycoproteins under various conditions, known as desialylation. Desialylation is important for the clearance of senescent platelets.[5] Desialylation also occurs following cold-storage of platelets, which also triggers GPIbα-clustering, resulting in rapid platelet clearance by liver phagocytes.[6]Additionally, desialylation is linked to platelet activation[7] and intrinsic apoptosis.[8,9] In the bleeding disorder immune thrombocytopenia (ITP), platelets are also desialylated and hyper-activated, resulting in clearance by the liver.[10,11]

Desialylation is mediated by neuraminidases (NEU), of which four have been described in mammalian cells,[12] NEU1, NEU2, NEU3 and NEU4. NEU desialylate their substrates at the α2,6 and/or the α2,3 glycan-linkages.[13] NEU differ in their intracellular location as well as their substrate specificity. NEU1 is typically located

Correspondence:

DIANNE E. VAN DER WAL
divanderwal@redcrossblood.org.au

Received: January 1, 2019.

Accepted: July 3, 2019.

Pre-published: July 4, 2019.

doi:10.3324/haematol.2019.215830

Check the online version for the most updated information on this article, online supplements, and information on authorship & disclosures: www.haematologica.org/content/105/4/1081

within lysosomes and cleaves oligosaccharides and glycopeptides. NEU2 and NEU3 are specific for gangliosides and located in the cytosol and on the plasma membrane respectively,[14,15] whereas NEU4 is located within mitochondria[16] and cleaves all aforementioned substrates. Sialic acid is also present in mitochondria.[17]

Within secretory lysosomes NEU1 is complexed with other degradation enzymes including sulphate 6-sulphatase, β-galactosidase and cathepsin A.[13] NEU are involved in many cell signalling processes: NEU1 binds Toll-like receptors,[18] negatively regulates lysosomal exocytosis[19] and suppresses cell adhesion by interfering with integrin phosphorylation, ERK1/2 and matrix metalloproteinase-7 signalling.[20] NEU3 also interacts with $\alpha_6\beta_4$-integrin, inducing ERK signalling.[21]

Earlier studies have shown upregulation of membrane-associated NEU1 in platelets following cold-storage,[22] and in ITP-patients where anti-GPIbα antibodies were present.[10] An association between sialic acid and platelet activation has been previously observed,[23] whereby surface sialic acid increases following stimulation of platelets by ADP, thrombin and collagen. Additionally, sialic acid is cleaved off the platelet membrane following GPIbα-clustering after binding its ligand VWF.[24] Addition of a NEU inhibitor, 2-deoxy-2-3-didehydro-N-acetylneuraminic acid (DANA), prevents clustering, indicating a potential role for desialylation in GPIbα-mediated platelet activation. While low levels of NEU activity have been demonstrated in platelets,[25] the role of NEU1-4 in the haemostatic function of platelets has not been studied. The aim of this study was therefore to investigate the role of both NEU1 and NEU2 in general platelet function under physiological conditions.

Methods

Ethics

Ethics approval was obtained from Australian Red Cross Blood Service Ethics Committee prior to conducting this study.

Platelet incubations

See the *Online Supplementary Material and Methods* (reagent sources, concentrations and further experimental details). Platelet rich plasma (PRP)/platelets were isolated[10] from whole blood, collected in sodium citrate, diluted ($200x10^9$/L with non-autologous apheresis-derived plasma/HEPES-Tyrode's buffer [Tyrode's] respectively), stimulated with agonists ± inhibitors (Table 1).[7]

Glycan binding lectins

Washed platelets/PRP/apheresis platelets were incubated with fluorescein-conjugated lectins (5 μg/mL), *Ricinus Communis* Agglutinin-1 (RCA-1, 1/500) and Wheat Germ Agglutinin (WGA, 1/1000) to assess galactose/sialic acid exposure respectively by flow cytometry (20 min, 21°C, BD FACSCAnto II, FACS Diva software, San Diego, CA, USA.).

Membrane NEU expression

PRP/washed platelets (± agonists/inhibitors) were diluted 1/2, stained with anti-NEU1, anti-NEU2 or anti-NEU4 (1/60, 30 min at 21°C) followed by anti-goat A488 or anti-rabbit A647 (1/60, 30 min, 21°C) antibodies respectively. Platelets were fixed (1% paraformaldehyde [PFA] prior to flow cytometry. Single platelets were gated; doublets and small aggregates were excluded.

Platelet activation markers

To assess $\alpha_{IIb}\beta_3$-integrin activation, PAC-1-FITC (neat, $2x10^6$ platelets), anti-fibrinogen-FITC was added (1/50) to 50 μL of $2x10^6$/L platelets (15 min, 21°C). Washed platelets were stimulated (VWF+ristocetin; VWF/risto), stained with anti-lysosomal-associated membrane protein 1 (LAMP-1, 1/50, 45 min, 21°C) and anti-mouse A488 or P-selectin-PE (45 min, 21°C).

Aggregation of washed platelets

Aggregation or agglutination (VWF/risto) was performed with indicated agonists using an AggRAM aggregometer (Helena Laboratories, Beaumont, TX, USA), stirring at 600 rpm.

NEU-activity

Activity of NEU in apheresis plasma (1/8 and 1/32 diluted in MQ H_20) was measured using an (adapted) protocol provided by C.A. Foote (Dalton Cardiovascular Research Center and[26], *Online Supplementary Materials and Methods*). Activity of recombinant NEU was measured by Amplex Red Sialidase kit (recNEU, 2.5-40 mU/mL, diluted in reaction buffer) ± fibrinogen, collagen and D-dimer (500 μg/mL). Fluorescence was measured after 30 min, (excitation λ_{ex}=530nm, emission λ_{em}=590nm).

Adhesion of platelets to fibrinogen

Glass coverslips were coated (100 μg/mL fibrinogen 2 hours [h], 21°C) and pre-blocked (1% BSA/PBS, 1 h, 21°C). PRP±DANA (1 mM, 15 min, 37°C), prior to adhesion ($30x10^9$/L; 30 min, 37°C). Platelets were fixed (2% PFA, 20 min, 21°C), permeabilised (0.5% Triton X-100) and blocked (5% BSA) prior to phalloidin-CF594 (1/42; 20 min, 21°C) staining. Fields of view (FOV) were analysed (ImagePro Premier v9.2, Media Cybernetics, Rockville, MD, USA).

Intracellular localisation of NEU1 and NEU2

Washed platelets (±VWF/risto, 5 min, 37°C) were fixed (1% PFA, 15 min, 21°C), unreacted aldehyde was neutralised (20 mM NH_4Cl-Tris) and adhered ($200x10^9$/L) to pre-coated microchannel slides (25 μg/mL laminin, 1 h, 37°C). Platelets were permeabilised (0.1% Triton X-100, 10 min, 21°C), blocked (1% BSA, 1 h, 21°C) prior to antibody staining (*Online Supplementary Materials and Methods*). Secondary anti-mouse A488 (1/2000), anti-rabbit A647 (1/800, 1 h, 21°C) and non-fading mounting media were added. Images (FITC and Texas Red filters) were captured with 60X water objective, additional 1.6X optical zoom (10X ocular; 960X total magnification) on Olympus IX71 (Olympus Corporation, Tokyo, Japan) inverted microscope (DP71 CCD camera). All images were taken with the same exposure time across treatments, with exception of NEU2 (1/2 exposure time), due to high fluorescence post-stimulation.

Statistics

Data were analysed using one-way ANOVA or paired *t*-tests using (GraphPad Software, Inc version 7.05.). A *P*-value of <0.05 was considered to be significant.

Results

Desialylation in platelets in presence of plasma

Platelets were stimulated with different agonists to investigate desialylation and cleavage of other glycans, using glycan-binding lectins and flow cytometry. Activation of GPIbα only by VWF (risto), but not ADP, increased desialylation by more than two-fold compared to unstimulated controls, as deduced from RCA-1-bind-

ing (to underlying galactose-residues), (Figure 1A). WGA-binding (to sialic acid and GlcNAc-residues), was decreased by 25% following ristocetin addition, also indicating some desialylation (Figure 1B). Similarly, the proportion of platelets binding RCA-1 increased significantly upon ristocetin stimulation (Figure 1, Table 1).

Additionally, binding to other lectins MAL-1 and ECL (bind to exposed β-galactosidase residues),[27] PNA (binds only to underlying GalNAc-residues on the T-antigen of VWF) and SNA (binds sialic acid) was examined in washed platelets (Figure 1C). MAL-1 and ECL-binding were increased following VWF/risto (Figure 1C), which was consistent with RCA-1 binding, although the increase was smaller (1.5-fold) when compared to over a two-fold increase on platelets in PRP (Figure 1A).

NEU1 and NEU2 are expressed on the platelet membrane

In order for desialylation to occur, it was hypothesised that the enzymes responsible, NEU1 and/or NEU2 were most likely associated with the plasma membrane. Since clustering of GPIbα specifically induced platelet desialylation, we investigated membrane association of both enzymes following addition of ristocetin. Following ristocetin-stimulation, there was a significant increase in membrane associated NEU1 and NEU2 (Figure 2A-B), demon-

Table 1. Concentrations of platelet agonists and inhibitors.

Platelet rich plasma Compound	Abbreviation	Function	Final concentration
Ristocetin	Risto	facilitates/potentiates vWF binding to GPIbα	3 mg/mL
Adenosine diphosphate	ADP	platelet agonist through binding to P2Y1 and P2Y12	200 μM
Arachidonic acid	AA	platelet agonist through formation of TXA_2	800 μM
O-sialoglycoprotein endopeptidase	OSGE	cleaves all O-linked glycans & GPIbα VWF-binding domain	80 μg/mL
Arg-Gly-Asp-Ser peptide	RGDS	inhibits fibrinogen binding to GPIIb/IIIa integrin	200 μM
N-acetylglucosamine	GlcNAc	inhibits GPIbα clustering	100 mM
Fibrinogen	Fg	binds GPIIb/IIIa integrin	500 μg/mL
2-deoxy-2-3-didehydro-N-acetylneuraminic acid	DANA	neuraminidase inhibitor	1 mM
Calcium chloride	$CaCl_2$	recalcification	1 mM
Collagen	coll	platelet agonist through binding to GPVI	10 μg/mL

Washed platelets Compound	Abbreviation	Function	Final concentration
Ristocetin + von Wilebrand factor	Risto + VWF	Platelet stimulation through activation of GPIbα	1.2 mg/mL + 10 μg/mL
Adenosine diphosphate	ADP	Platelet agonist through binding to P2Y1 and P2Y12	20 μM
Arachidonic acid	AA	Platelet agonist through formation of TXA_2	50 μM
O-sialoglycoprotein endopeptidase	OSGE	Cleaves all O-linked glycans & GPIbα VWF-binding domain	80 μg/mL
Peptide:N-glycosidase F	PNGAse F	Cleaves all N-linked glycans	10,000 U/mL + 1/10 reaction buffer
2-deoxy-2-3-didehydro-N-acetylneuraminic acid	DANA	Neuraminidase-inhibitor	1 mM
Collagen	coll	Platelet agonist through binding to GPVI	10 μg/mL
(Z)-7-[(1S,4R,5R,6S)-5-[(E,3S)-3-hydroxyoct-1-enyl]-3-oxabicyclo[2.2.1]heptan-6-yl]hept-5-enoic acid	U46619	TxA_2 mimetic	1 μM
α-thrombin	thr	Platelet stimulation through activation of GPIbα (low-dose only)	0.1 U/mL
1,2-Bis(2-aminophenoxy)ethane-N,N,N′,N′-tetraacetic acid tetrakis (acetoxymethyl ester)	BAPTA-AM	Calcium chelator	10 μM
Indomethacin	indo	Blocks TXA_2 formation;	
Cyclo-oxygenase-1 inhibitor	30 μM		
Apyrase		ADP inhibitor: hydrolyses ADP	0.1 U/mL
Calcium chloride	$CaCl_2$	recalcification	1 mM
Fibrinogen	Fg	binds GPIIb/IIIa integrin	500 μg/mL
Monosialodihexosylganglioside	GM3	ganglioside; NEU2 substrate and involved in GPIbα clustering	10 μM
Recombinant neuraminidase (Clostridium)	recNEU	desialylation enzyme	0.2 U/mL

All agonists and metabolic inhibitors used for stimulation or inhibition of platelet rich plasma (PRP) or washed platelets respectively were used at final concentrations as indicated. More details and abbreviations are described in the *Online Supplementary Materials and Methods*.

strating that in platelets from healthy individuals, a proportion of NEU1 and NEU2 is membrane expressed. Secondary antibody-only controls showed little non-specific fluorescence (Figure 2A-B). Blockade of GPIbα-clustering with GlcNAc[28] prevented the increase in NEU1 and NEU2 membrane association.

In addition, removal of the 45 kDa *N*-terminal domain of GPIbα (VWF-binding domain) with OSGE, to mimic GPIbα-deficient platelets,[29,30] prevented the ristocetin-induced increase in NEU1 (Figure 2A-B), suggesting that NEU1 expression is highly dependent on VWF-binding to GPIbα. Furthermore, when fibrinogen binding to $\alpha_{IIb}\beta_3$-integrin was blocked using RGDS peptide, the increase in membrane NEU1 was also significantly reduced by 50% (Figure 2A), and there was also a trend towards decreased NEU2 expression (Figure 2B). Similarly, the proportion of platelets that were positive for NEU1 and NEU2 increased in PRP stimulated with ristocetin, but these changes were not significantly different when compared to unstimulated platelets or those treated with inhibitors (Figure 2C).

Desialylation in washed platelets

Washed platelets were used to prevent interference by plasma proteins such as fibrinogen. Cleavage of the extracellular domain of GPIbα by OSGE to mimic GPIbα-deficient platelets,[31] reduced binding of all lectins by over 50% and below unstimulated control (*Online Supplementary Figure S1A*), demonstrating the importance of the VWF-binding domain in NEU mediated desialylation. When only *N*-linked glycans were cleaved by PNGase F, binding to most lectins was also reduced, albeit to a lesser degree, indicating desialylation of N-linked glycans (*Online Supplementary Figure S1A*).

Recombinant NEU (recNEU), which desialylates sialic acid at α2,3, α2,6, or α2,8-linkages was used as a positive control to achieve complete desialylation. RecNeu alone significantly increased binding of MAL-1, ECL and PNA (not shown). RecNEU treatment further increased RCA-1 binding (*Online Supplementary Figure S1B*), when compared to VWF/risto alone (Figure 4D), albeit to a lesser extent than ECL-binding. PNA-binding was significantly increased (*Online Supplementary Figure S1B*), demonstrating potential desialylation of VWF itself. SNA-binding however was insensitive to VWF/risto+recNEU, indicating different and more extensive desialylation by recNEU (*Online Supplementary Figure S1A*). As a negative control, washed platelets incubated with ristocetin only, which showed no increase in membrane NEU1 and NEU2 (*Online Supplementary Figure S1C*).

To further confirm the role of GPIbα-clustering in translocation of NEU to the membrane, washed platelets were activated with various agonists (VWF/risto, collagen, thrombin, AA, ADP and U46619). Only clustering of GPIbα by VWF/risto, and to a lesser extent, arachidonic

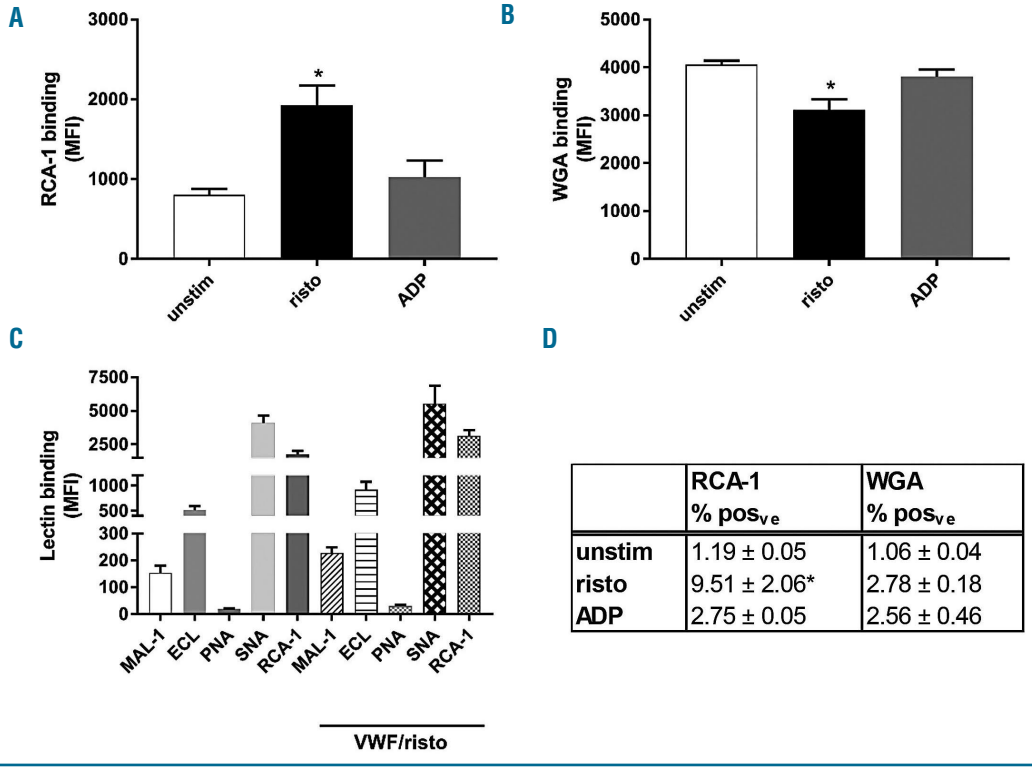

	RCA-1 % pos_{ve}	WGA % pos_{ve}
unstim	1.19 ± 0.05	1.06 ± 0.04
risto	9.51 ± 2.06*	2.78 ± 0.18
ADP	2.75 ± 0.05	2.56 ± 0.46

Figure 1. Platelet desialylation is induced by von Willebrand factor-mediated glycoprotein Ibα clustering. Platelets in platelet rich plasma (PRP) (200 x 10^6/mL) were stimulated with ristocetin (3 mg/mL) and ADP (200 μM), then stained with fluorescein-conjugated lectins (A) RCA-1 or (B) WGA; 10,000 single platelets (doublets and small aggregates were excluded from analysis) were measured by flow cytometry (n=3). Washed platelets were stimulated (VWF/risto: 10 μg/mL VWF/ 1.2 mg/mL ristocetin), and (C) binding to fluorescein-conjugated MAL-1, ECL, PNA, SNA and RCA-1 lectins was measured by flow cytometry (n=3). Mean fluorescent intensities (MFI) ± standard error of mean (SEM). *P<0.05 significant when compared to unstimulated controls (unstim) using a one-way ANOVA. (D) Lectin binding in unstimulated platelets was set at ~1% positive and samples were analysed following risto or ADP-addition. Data ± SEM. *P<0.05 significant when compared to unstimulated controls (t-test). VWF: von Willebrand factor; GPIbα: glycoprotein Ibα.

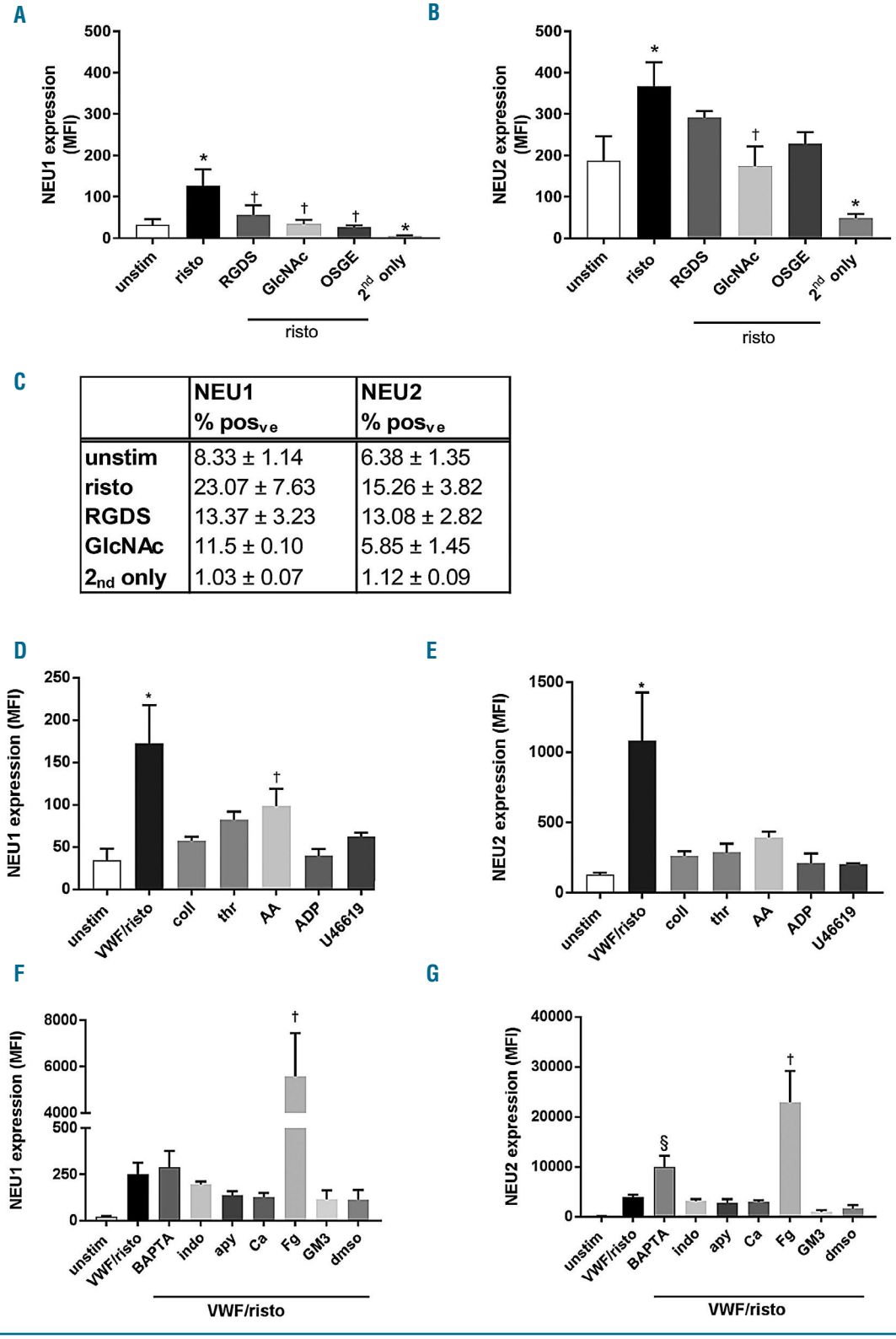

	NEU1 % pos_{ve}	NEU2 % pos_{ve}
unstim	8.33 ± 1.14	6.38 ± 1.35
risto	23.07 ± 7.63	15.26 ± 3.82
RGDS	13.37 ± 3.23	13.08 ± 2.82
GlcNAc	11.5 ± 0.10	5.85 ± 1.45
2_{nd} only	1.03 ± 0.07	1.12 ± 0.09

Figure 2. NEU1 and NEU2 membrane expression is mediated by von Willebrand factor-binding to glycoprotein Ibα. Platelets in platelet rich plasma (PRP) (200 x 10^6/mL) were pre-incubated with RGDS peptide (Arg-Gly-Asp-Ser, 200 μM), *N*-acetyl-*D*-glucosamine (GlcNAc, 100 mM) and *O*-sialo-glycoprotein endopeptidase (OSGE, 80 μg/mL) *prior* to ristocetin stimulation (3 mg/mL) and membrane association of (A) NEU1 and (B) NEU2 were measured by flow cytometry using NEU1 or NEU2 antibodies followed by fluorescently conjugated secondary antibodies. **P*<0.05 was considered significant when compared to unstimimulated (unstim)*, †: significant against risto (one-way ANOVA, n=3). (C) Secondary antibody-only controls (unstim platelets) were used to set a gate (~1%) and everything above this was considered positive (% pos_{ve}). Washed platelets were stimulated with VWF/risto (10 μg/mL VWF+ 1.2 mg/mL risto), collagen (10 μg/mL), thrombin (0.1 U/mL), AA (50 μM), ADP (20 μM), and U46619 (1 μM) *prior* to measurement of (D) NEU1 (n=4) or (E) NEU2 (n=4) membrane association by flow cytometry. *Prior* to VWF/risto stimulation, platelets were treated with the indicated inhibitors (n=4) for calcium (BAPTA-AM, 10 μM), TXA_2 (indomethacin, indo, 30 μM) and ADP (apyrase, 0.1 U/mL). As indicated calcium (1 mM), fibrinogen (500 μg/mL), GM3 (10 μM) were also used. (F) NEU1 or (G) NEU2 membrane association was measured. Results are shown as mean fluorescent intensities (MFI) ± standard error of mean (SEM). **P*<0.05 significant against unstimulated (unstim); †: significant against VWF/risto, §: significant against vehicle (dmso, one-way ANOVA); VWF: von Willebrand factor; GPIbα: glycoprotein Ibα.

acid, increased membrane association of NEU1 (Figure 2D) and was even more pronounced for NEU2 (Figure 2E). Although collagen binds to VWF upon vascular injury, it did not induce NEU membrane translocation. AA also significantly increased NEU1, which is in line with earlier findings that AA induced clustering of GPIbα, which may lead to subsequent desialylation (Figure 2D).[32] The VWF-induced increase in membrane NEU was less pronounced in PRP (Figure 2A-B) when compared to washed platelets (Figure 2D-E), suggesting a potential inhibitory effect of plasma proteins on NEU activation. Risto-only controls (without VWF-addition) did not induce NEU membrane expression (*Online Supplementary Figure S1C*). GPIbα is also clustered by low concentrations of thrombin,[33] however thrombin-stimulated washed platelets were not desialylated (*Online Supplementary Figure S1D*). Binding of all lectins was similar to unstimulated controls; demonstrating desialylation is specific for the VWF-GPIbα interaction. This data demonstrate that desialylation occurs upon specific clustering of GPIbα through binding to its ligand VWF, which in turn triggers membrane association of NEU1 and NEU2.

Signalling pathways involved in NEU expression

To further investigate the signalling pathways involved in NEU membrane association, platelets were incubated with metabolic inhibitors prior to VWF/risto-stimulation (Figure 2F-G). A negative feedback role of calcium was demonstrated as calcium-chelation by BAPTA-AM significantly increased NEU2 membrane-association (Figure 2G), while addition of calcium slightly decreased NEU2 (Figure 2G). GPIbα-clustering is known to trigger AA-release, leading to thromboxane (TX) A_2-formation.[34] Inhibition of TXA_2-formation with indomethacin reduced NEU2 membrane association slightly, as did apyrase, which hydrolyses ADP (Figure 2G). In contrast, addition of fibrinogen significantly increased membrane association of both NEU1 and NEU2 (Figure 2F-G) following VWF/risto-stimulation, demonstrating an important role for fibrinogen. Gangliosides (GM) (GM3: sialic acid-α2,3Galβ1,4Glcβ1,1Cer, a known substrate for NEU2) are able to inhibit platelet adhesion and aggregation[35] and bind to GPIbα following its clustering. Incubation of platelets with GM3 reduced membrane association of NEU2, and to a lesser extent, NEU1 (Figure 2F-G).

As the GPIbα-VWF interaction is highly dependent on shear stress, apheresis platelets were stimulated with ristocetin in combination with shear. NEU1 and NEU2 membrane association were both significantly higher when risto-stimulated platelets were subjected to high shear of 10,000s^{-1} (Figure 3A-B), confirming the link between GPIbα-signalling and NEU-translocation. At this stage, we started to look into NEU4, as this might also have a role in platelets as it cleaves gangliosides.[16] NEU4 was also membrane-associated following VWF/risto and increased further by shear, but not significantly (Figure 3C). Shear alone did increase NEU1 slightly, but did not affect NEU2 or NEU4 membrane-association (Figure 3A-C).

The data so far demonstrates that NEU1, NEU2 and even NEU4, may be released from their intracellular stores upon GPIbα-clustering, as granule/lysosome content may also be released.[36] In general, VWF/risto-stimulation without shear does not induce secretion in washed platelets.[27] However, since the indirect NEU staining protocol used for flow cytometry involved an incubation time of 90 min, which might potentiate α-/δ-granule/lysosome-release, these were examined following VWF/risto-stimulation. Both P-selectin and LAMP-1 surface expression following VWF/risto-stimulation were increased as a consequence of the longer incubation times (*Online Supplementary Figure*

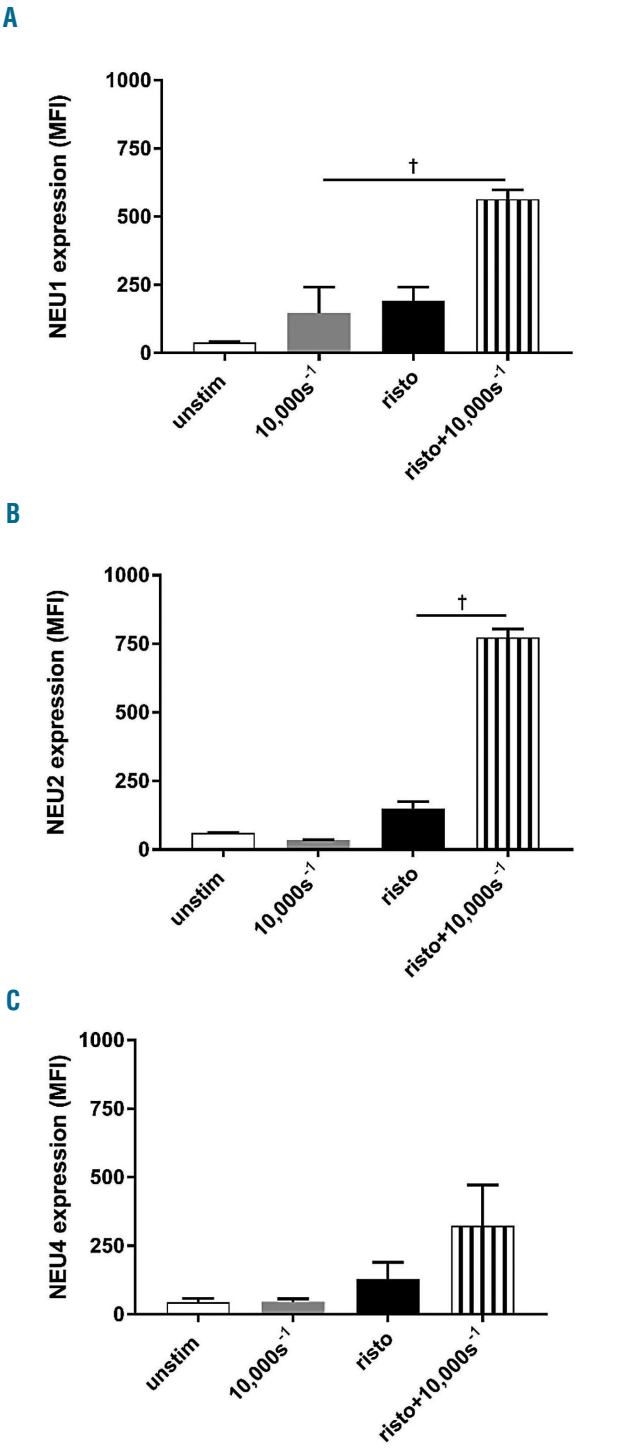

Figure 3. NEU1, NEU2 and NEU4 are membrane expressed following high shear. Apheresis platelets were treated with risto, high shear (10,000s^{-1}) or both and membrane expression of (A) NEU1 and (B) NEU2 were measured by flow cytometry. †Significant against shear or risto-only. **P*<0.05 significant against unstimulated (unstim), one-way ANOVA. (C) NEU4 was measured by flow cytometry. Results are shown as mean fluorescent intensities (MFI) ± standard error of mean (SEM).

S2A-B). RecNEU significantly enhanced LAMP-1 surface expression, P-selectin and PAC-1 binding relative to unstimulated platelets (*Online Supplementary Figure S2A-C*). Fibrinogen also potentiated LAMP-1 (*Online Supplementary Figure S2A*) when compared to VWF/risto-stimulation alone, while PAC-1 binding (*Online Supplementary Figure S2C*) was slightly decreased, as expected. As anticipated, addition of calcium increased PAC-1 and P-selectin (*Online Supplementary Figure S2B-C*), whereas OSGE abolished the VWF-induced increase in LAMP-1 and PAC-1-binding (*Online Supplementary Figure S2A, C*) indicating that dense granule/lysosome secretion and fibrinogen-binding do not occur when GPIbα is removed.

In summary, these findings demonstrate that NEU translocate to the plasma membrane following clustering of GPIbα by VWF, and NEU2 membrane expression is negatively controlled by high calcium concentrations. More importantly, fibrinogen-binding following platelet activation by VWF potentiated the NEU-translocation.

The role of NEU-activity in αIIbβ3-integrin activation

The data presented thus far demonstrate that NEU1 and NEU2 are specifically translocated to the membrane following VWF-mediated GPIbα-clustering, and is downstream of secondary signalling, leading to desialylation. To further investigate a potential role for NEU activity in platelet activation, a NEU-inhibitor DANA[10,22] was used. DANA inhibited desialylation, as RCA-1-binding was significantly decreased (approximately two-fold decrease), but not completely inhibited, following recNEU-treatment (*Online Supplementary Figure S3*).

Since our findings indicated that fibrinogen binding potentiated the membrane association of NEU1 in particular, the role of NEU activity in $\alpha_{IIb}\beta_3$-integrin activation was further studied using PAC-1 and fibrinogen antibodies. Incubation of PRP with DANA prior to addition of ristocetin significantly reduced fibrinogen binding (Figure 4A), suggesting NEU activity plays a role in fibrinogen binding. Furthermore, the partial inhibition of fibrinogen binding by RGDS was not observed in the presence of

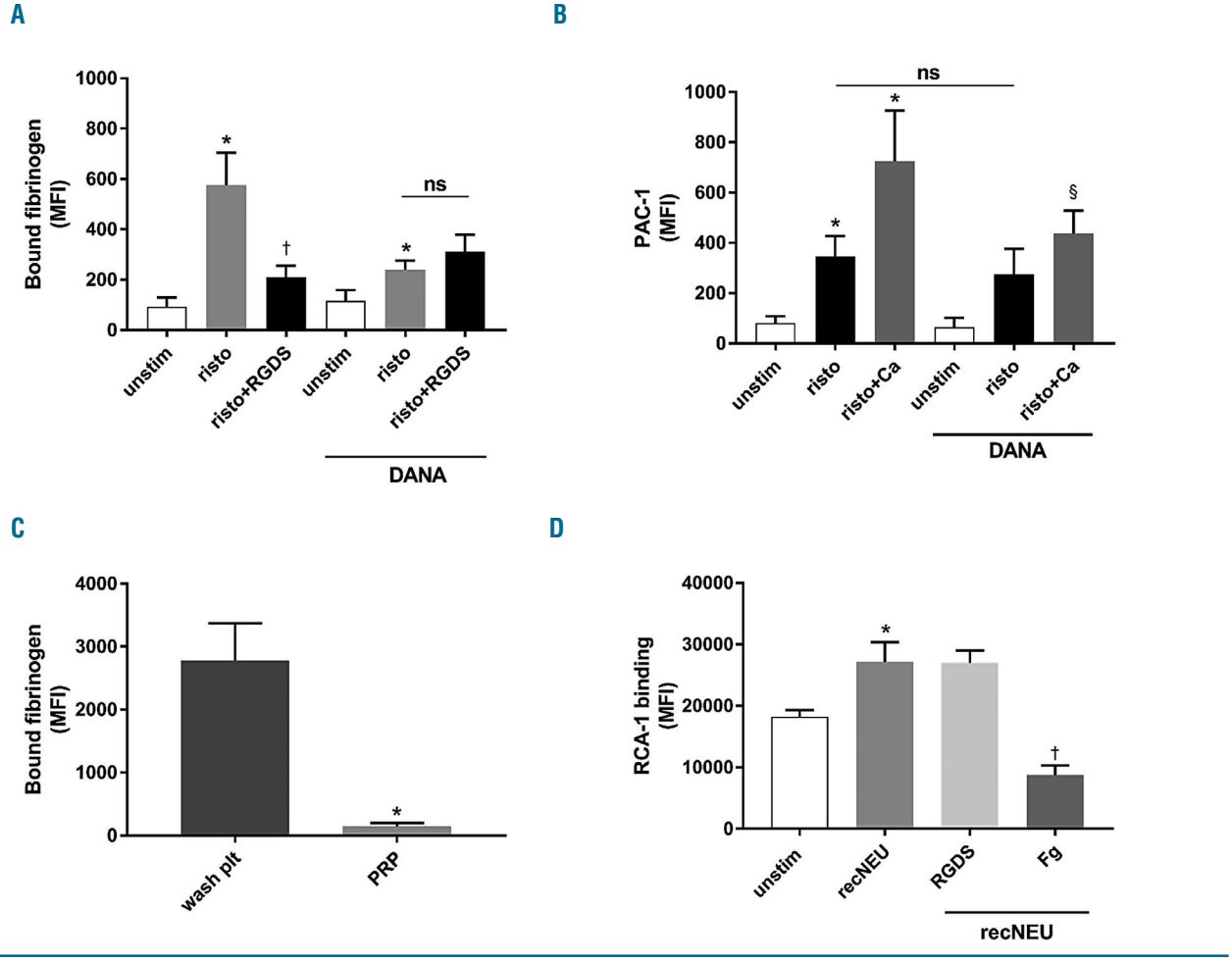

Figure 4. Neuramidase-inhibition reduces fibrinogen binding. Platelets in platelet rich plasma (PRP) were pre-incubated with neuramidase (NEU) inhibitor 2-deoxy-2-3-didehydro-N-acetylneuraminic acid (DANA) and/or +/- $\alpha_{IIb}\beta_3$ integrin inhibitor RGDS prior to stimulation with ristocetin (3 mg/mL) and then stained with (A) fibrinogen-FITC or (B) FITC-conjugated PAC-1 antibodies respectively. 10,000 single platelets were measured by flow cytometry. Data represents the mean fluorescent intensities (MFI) ± standard error of mean (SEM), n=3. *P<0.05, *: significant against unstimulated (unstim), §: significant against risto + calcium (Ca) (one-way ANOVA). (C) Unstimulated washed platelets (wash plt) or PRP were stained with fibrinogen-FITC antibody. (D) PRP was treated with RGDS, or fibrinogen, prior to recNEU-treatment (Table 1), then stained with fluorescein-conjugated RCA-1 (n=5). Data represents mean ± standard error of mean (SEM). *P<0.05 significant against unstimulated (unstim), †: significant against risto using a one-way ANOVA.

DANA, suggesting potential competition for the same binding site by NEU and RGDS, further linking $\alpha_{IIb}\beta_3$ activation and NEU activity. Cations are essential for complete fibrinogen-binding to $\alpha_{IIb}\beta_3$.[37] Ristocetin induced PAC-1 binding and was only sensitive to DANA-inhibition upon addition of calcium (Figure 4B). Similarly, PAC-1 binding was also further increased by calcium addition, confirming the importance of calcium in NEU activity (Figure 4B). In contrast, ADP-induced PAC-1 binding was unaffected by DANA treatment, demonstrating again that NEU activity is GPIbα-VWF specific (data not shown). Basal levels of fibrinogen binding in washed platelets were much greater than in PRP (Figure 4C), indicating some activation had occurred that may have led to higher basal NEU1 and NEU2 membrane association. Remarkably, the recNEU induced RCA-1 binding was significantly reduced by additional fibrinogen, due to saturation of $\alpha_{IIb}\beta_3$-integrin's fibrinogen binding site (Figure 4D); however fibrinogen-binding kinetics will be different during aggregation/adhesion.

These findings emphasise the importance of calcium in modulating surface bound NEU expression following GPIbα-clustering. This facilitates $\alpha_{IIb}\beta_3$ activation, which in turn potentiates NEU activity and is downregulated again by fibrinogen-binding.

NEU-activity and platelet aggregation

To further examine GPIbα-mediated signalling without plasma in a buffered system, washed platelets were stimulated by VWF/risto and agglutination was measured. DANA treatment increased agglutination, which was further increased by addition of fibrinogen (Figure 5A). When binding of fibrinogen to platelets was blocked with RGDS, agglutination was only slightly reduced. These data indicate an inhibitory role of NEU activity in VWF-mediated agglutination. Additionally, DANA treatment increased fibrinogen-binding to $\alpha_{IIb}\beta_3$ (Figure 5B). To investigate the role of NEU in other activation pathways, washed platelets were pre-incubated with DANA prior to addition of collagen and AA. DANA had no effect on platelet aggregation in response to these agonists (Figure 5C). Static adhesion and spreading of platelets to a fibrinogen coated surface was also unaffected by DANA (Figure 5D). It is important to note that additional platelet adhesion receptors and mechanisms are involved in platelet adhesion when compared to platelets in suspension. As fibrinogen binding appeared to be linked with NEU-activity, recNEU was incubated with fibrinogen and in line with the previous results; fibrinogen enhanced the activity of recNEU (Figure 5E). In contrast, when using control proteins of similar molecular weights, NEU-activity was completely abolished by collagen, while D-dimer showed inhibition by ~50% (Figure 5E). NEU activity in plasma (n=4) was 187.47±22.81 mU/mL (1/32 dilution), while only 84.28±11.26 mU/mL was found when a dilution of 1/8 was used, indicating an inhibitory effect by plasma factors. The maximum platelet activity of 80 mU/mL was reached following platelet permeabilisation by Triton X-100: using $400x10^6$/mL platelets. When NEU activity was measured without Triton X-100 (Amplex Red assay), only 35.45±3.51 mU/mL (1/8 dilution), which was ~40%.

Intracellular NEU localisation

It was hypothesised that in order for NEU to cleave their substrates, the enzymes would need to be localised on or within the platelet membrane. Previous findings in cold-stored[22] or platelets from ITP-patients[10] showed that intracellular stores of NEU1 appear to be localised in 'granule'-like organelles; however the actual location was not shown. Therefore, the intracellular origin of NEU was investigated. In permeabilised unstimulated platelets, NEU1 stained in a punctate pattern within the cytoplasm and on the cellular periphery, while NEU2 staining was mostly cytoplasmic and punctate (Figure 6A-B). NEU1 did not co-localise with the lysosomal/δ-granule markers LAMP-1 and β-galactosidase as initially anticipated, nor with an α-granule markers coagulation factor V (FV) (Figure 6A) and P-selectin (Figure 6C). Upon further investigation, NEU1 did however appeared to co-localise with mitochondria to a limited extent (Figure 6A) in approximately 20% of permeabilised platelets. Within these, 10-100% of NEU1 co-localised with mitochondria, whereas the remaining NEU1 was sequestered in other locations. Mitochondria did not stain in unstimulated and stimulated non-permeabilised platelets (*Online Supplementary Figure S4*), while granule and lysosome contents were released following VWF/risto incubation (*Online Supplementary Figure S2A*), in line with the flow cytometry data. Although mitochondria are potentially releasing NEU1, the mitochondrial protein was not retained on the platelet membrane (Figure 6A). NEU2 staining was mostly cytoplasmic and punctate (Figure 6B). Following GPIbα activation (stimulated), NEU2 surface localisation was significantly enhanced. Difficulties were encountered visualising this localisation and due to the large increase in fluorescence (Fig. 6B), the exposure time had to be halved. As with NEU1, NEU2 failed to co-stain with LAMP-1 (data not shown). In contrast to NEU1, NEU2 co-localised with P-selectin (Figure 6C), which is in line with results using DANA, whereby DANA partially reduced expression of P-selectin following ristocetin-stimulation (Figure 6D).

When using a general membrane dye (Figure 6E), some co-localisation was observed, although not 100%. As a control for non-specific staining, platelets were incubated with a secondary antibody only, and no fluorescence was observed (*not shown*). The overall findings from this study and a proposed model of NEU activity are presented in Figure 7.

Discussion

In this study, we have demonstrated a novel role for NEU1 and NEU2 in platelets, which is highly dependent on VWF-GPIbα and consequent $\alpha_{IIb}\beta_3$-integrin activation. Specifically, we have demonstrated that NEU1, NEU2 and NEU4 are present on the plasma membrane of unstimulated platelets. Specific clustering of GPIbα by VWF triggers increased membrane association of NEU1 and NEU2, partially from their respective intracellular stores mitochondria and α-granules, which is even more pronounced under high shear conditions. Membrane association of NEU is highly regulated by mechanisms different for NEU1 and NEU2.

GPIbα is heavily glycosylated, containing *N*- and *O*-linked glycans, capped by sialic acid. Desialylation has been studied before in cold-stored platelets and ITP.[6,10,38] The glycan changes in platelets under these conditions are similar to those observed following activation by VWF,[8,9,27,32,39] as clustered GPIbα leads to various degrees of glycan cleavage (*e.g.* sialic acid and/or galactose). To date,

the enzymes responsible for these changes, mammalian NEU (NEU1-4), have not been investigated in healthy platelets.

In this study, we did not discriminate between *N*- and O-linked glycans. Recent work has shown the importance of *N*-linked glycans in VWF-binding and its clearance.[40,41] Additionally, *O*-linked glycans have been implicated in both VWF-clearance[42] and binding.[43]

On platelets, *N*- and *O*-linked glycans are covalently bound *via* asparagine residues and capped by sialic acid.[2-4] The T-antigen (O-linked (sialic acid(α2-3)Gal-(β1-3)-[sialic acid(α2-6)]GalNAc) is present on VWF.[44] *O*-linked glycans

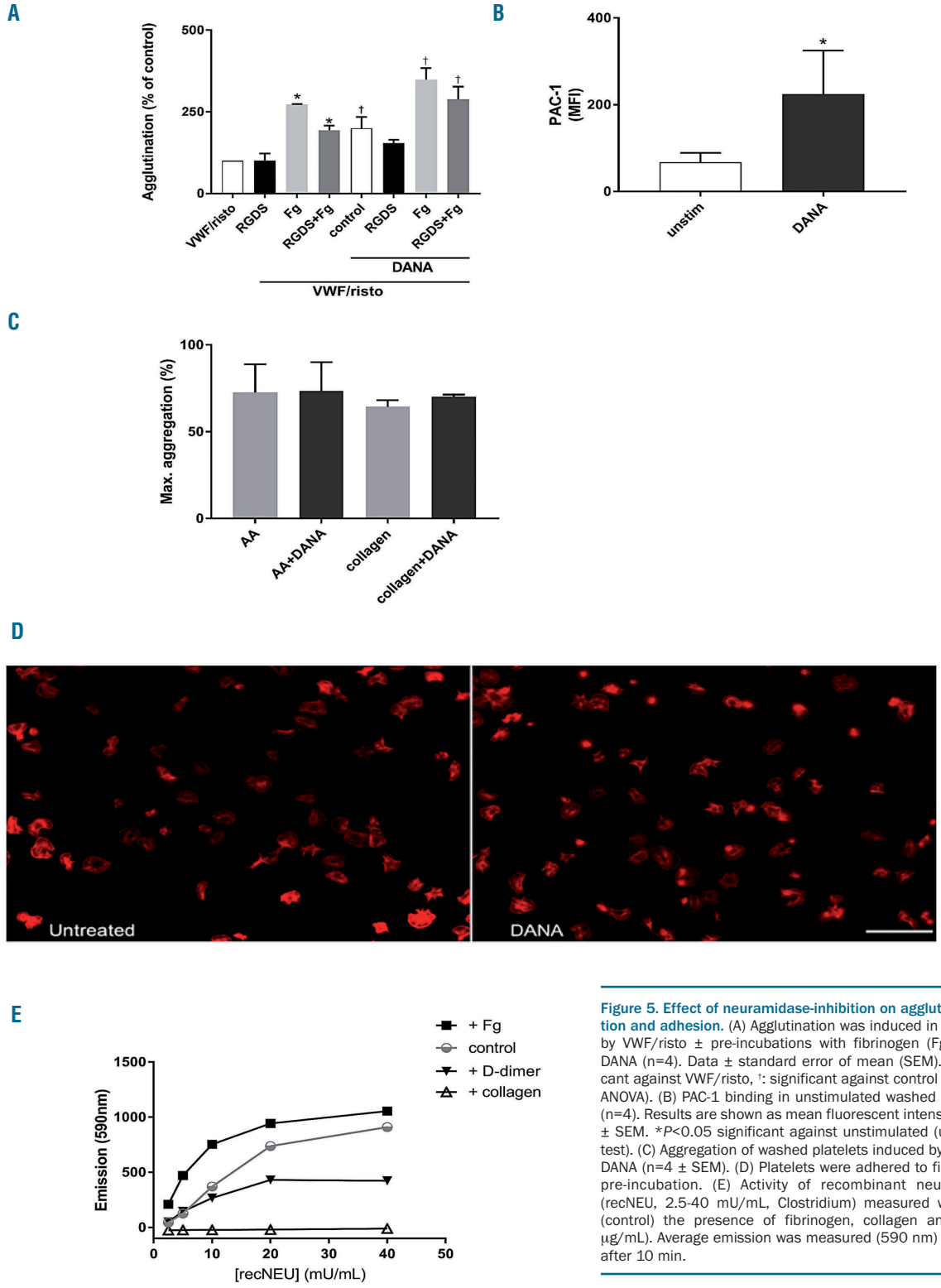

Figure 5. Effect of neuramidase-inhibition on agglutination, aggregation and adhesion. (A) Agglutination was induced in washed platelets by VWF/risto ± pre-incubations with fibrinogen (Fg), RGDS and/or DANA (n=4). Data ± standard error of mean (SEM). **P*<0.05 significant against VWF/risto, †: significant against control + DANA (one-way ANOVA). (B) PAC-1 binding in unstimulated washed platelets ± DANA (n=4). Results are shown as mean fluorescent intensities (MFI) values ± SEM. **P*<0.05 significant against unstimulated (unstim) (paired *t*-test). (C) Aggregation of washed platelets induced by AA or collagen ± DANA (n=4 ± SEM). (D) Platelets were adhered to fibrinogen ± DANA pre-incubation. (E) Activity of recombinant neuramidase (NEU) (recNEU, 2.5-40 mU/mL, Clostridium) measured with and without (control) the presence of fibrinogen, collagen and D-dimer (500 µg/mL). Average emission was measured (590 nm) at each [recNEU] after 10 min.

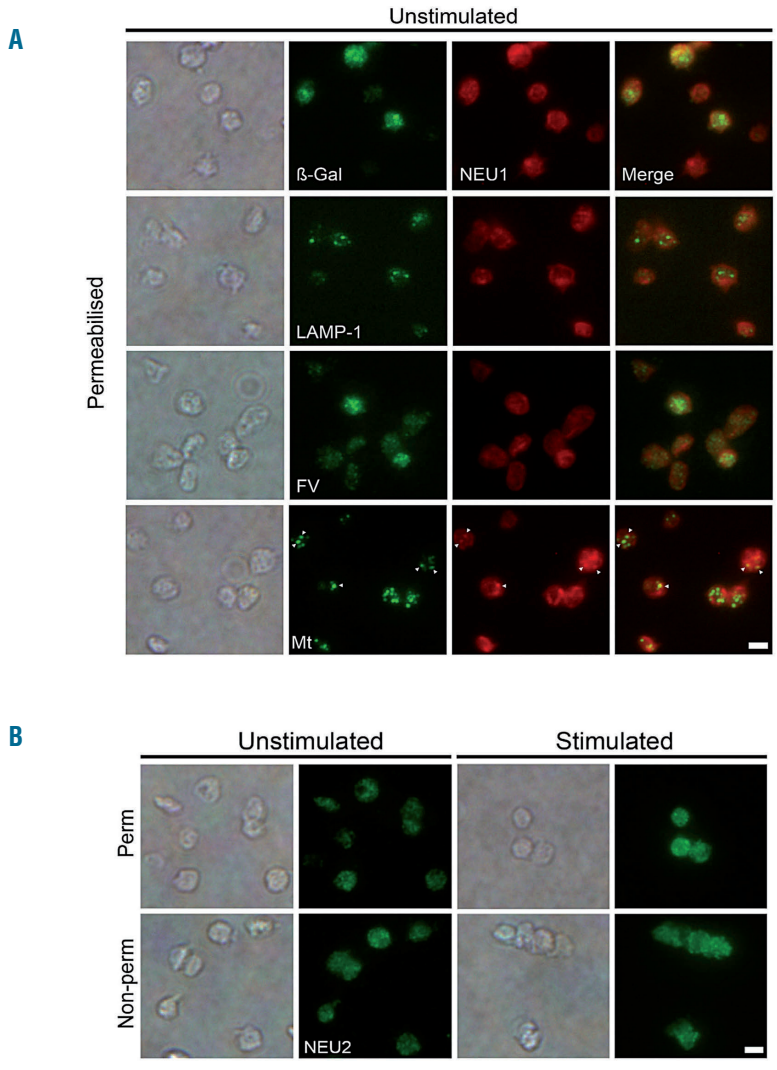

Figure 6. Membrane association and intracellular location of NEU1 and NEU2. NEU1 (red) and intracellular protein staining (green) for β-Galactosidase (β-Gal), LAMP-1, factor V (FV), mitochondria (Mt) were visualised by fluorescence microscopy and merged in (A) unstimulated + permeabilised washed platelets. (B) Unstimulated and stimulated (VWF + risto) washed platelets ± permeabilisation, were stained with NEU2 (green). Due to high fluorescence in stimulated platelets, ½ exposure time was used. (C) Unstimulated (non-) permeabilised washed platelets were stained for NEU1 (red), NEU2 (green) and P-selectin (P-Sel). (D) P-selectin expression was measured in unstimulated PRP *versus* risto ± DANA (n=4). Results are shown as mean fluorescent intensities (MFI) values ± standard error of mean (SEM). (E) unstimulated platelets and following VWF/risto (stimulated) were stained with NEU2 (green) and membrane dye CellBrite 640 (red). Exposure time 1/3.0 sec for unstimulated samples, and 1/6.0 sec exposure for stimulated samples due to high fluorescence. A total 960X magnification was used. Scale bar is 10 μm. VWF: von Willebrand factor.

in the A1 domain of VWF are critical for binding to GPIbα.[43] When sialic acid is cleaved from *O*-linked glycan structures, galactose-residues originally bound to GalNAc and GlcNac-residues become exposed, in contrast to N-linked glycans, where sialic acid is attached only to galactose residues. Additionally, the β_3-domain of $\alpha_{IIb}\beta_3$-integrin also contains *N*-linked glycans[45] and the majority of these structures are rich in mannose. It is currently unclear whether other platelet glycoproteins or plasma proteins (*e.g.* alpha2 macroglobulin) are affected by NEU. However platelet stimulation with other agonists did not lead to an increase in membrane-associated NEU.

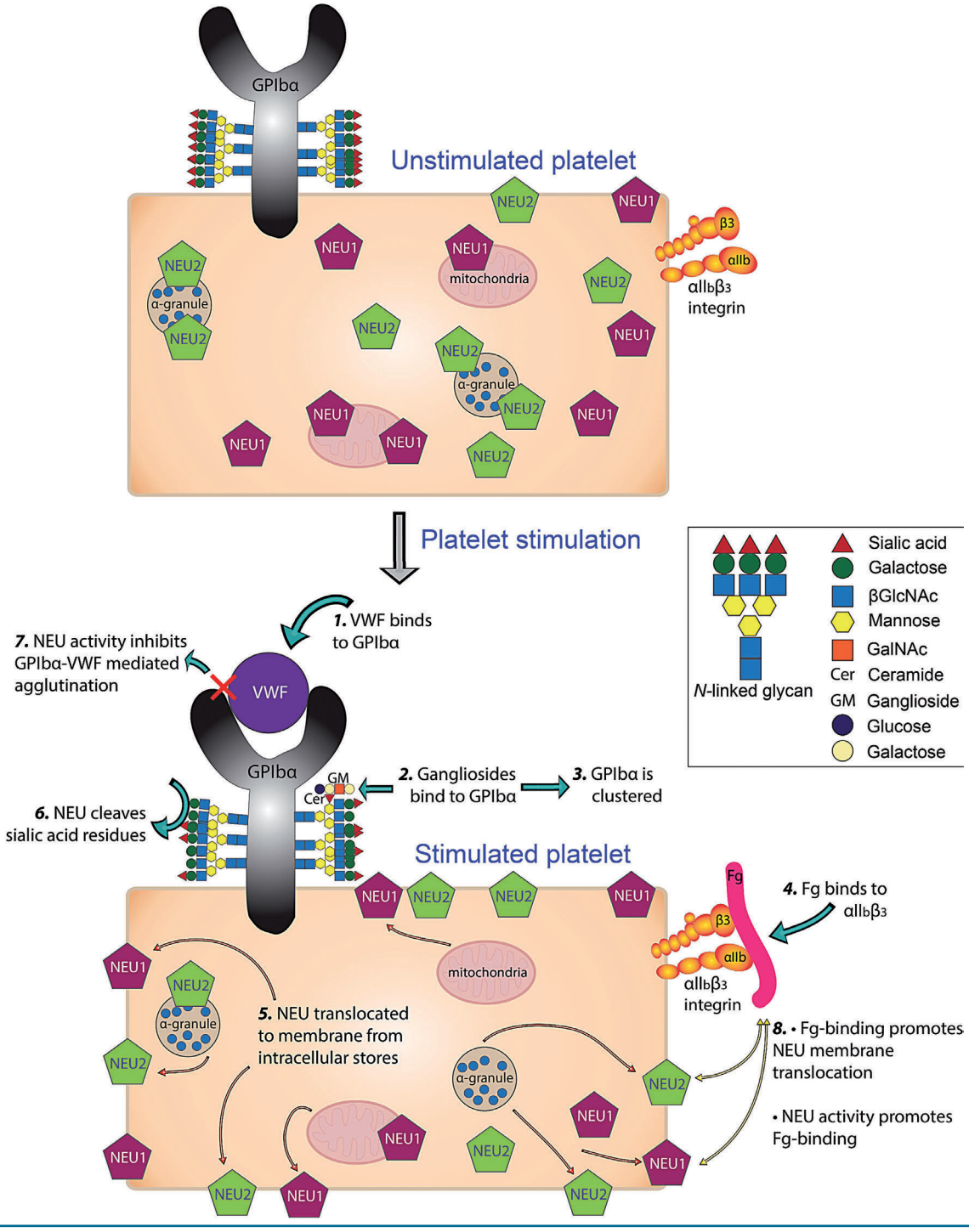

Figure 7: Model of neuramidase membrane-association, activity and feedback to fibrinogen binding. Based on the findings of this study, the following model is proposed: 1) Binding of von Willebrand factor (VWF) to glycoprotein Ibα (GPIbα) potentially leads to 2) gangliosides (GM) binding, 3) GPIbα clusters, leading to 4) fibrinogen binding to $\alpha_{IIb}\beta_3$-integrin, 5) NEU1 and NEU2 translocated to the plasma membrane from mitochondria or α-granules respectively, 6) neuramidase (NEU) cleaves sialic acid, 7) NEU activity inhibits VWF-mediated agglutination and 8) fibrinogen promotes further NEU membrane association in a feedback loop.

PNGase digestion did not affect SNA-binding, demonstrating that some sialic acid was still present on remaining *O*-linked glycans, potentially those on VWF, as shown by the small increase in PNA-binding to the VWF T-antigen. However, as SNA-binding was unchanged following VWF/risto-stimulation, these α2,3-linked glycans are not NEU1 and NEU2 substrates. In this study, we did not investigate whether VWF or GPIbα originated from a formerly internalised pool and was re-expressed on the membrane.

NEU membrane association is highly dependent on VWF-binding to GPIbα, as GPIbα removal by OSGE or inhibition by GlcNAc prevented membrane association. α2,3-linked sialic acid has been earlier described to be insensitive to OSGE-cleavage, indicating these structures might be attached to VWF or other platelet glycoproteins.[42] Control experiments with recNEU, which cleaves α2,3, α2,6 and α2,8-linked sialic acid, showed more binding to MAL-1, ECL and RCA-1 when compared to VWF/risto alone, demonstrating that more pronounced desialylation had occurred.

In general, platelet granule contents are not released following stimulation of GPIbα by VWF/risto without shear. However, this study showed that VWF-stimulation triggers P-selectin release as well as increased LAMP-1 membrane association, indicating release of α, δ-granule and lysosome content. This is consistent with the co-localisation of NEU2 with P-selectin. However, this can also be partly attributed to some degree of pre-activation due to the long incubation times required for NEU staining, as LAMP-1 membrane-association is dependent on platelet activation.[36]

This study demonstrates that a negative feedback loop exists between the activity of NEU and platelet agglutination, as inhibition of NEU activity by DANA potentiates platelet VWF-mediated agglutination. Following desialylation, the underlying glycans on GPIbα, including βGlcNAc-residues, are more prone to further cleavage, which was previously found to reduce VWF-binding to platelets.[3] NEU inhibition is described to block both desialylation and consequent degalactosylation by β-galactosidase, which was described as the first step in GPIbα-clustering.[32] Interestingly, NEU1 activity was inversely correlated with integrin-mediated adhesion to laminin.[20] Recent findings showed that pneumococcal NEUA induced platelet hyperactivity through desialylation, which was dependent on ADP-secretion.[46]

GM are glycosphingolipid-containing glycans involved in cell-cell recognition, adhesion and signal transduction, and may be another substrate for NEU1. GM3 blocks GPIbα-clustering by preventing linking with lipid rafts[24] and GM blocks the second wave of aggregation by ADP.[35] Our results demonstrate that GM might be important for NEU2 membrane association, and are potentially involved in the negative feedback loop between NEU activity and VWF-induced agglutination.

The results presented here also indicate that calcium inhibits NEU2 membrane association but promotes its activity, as treatment with DANA prevented the calcium-potentiated increase in PAC-1-binding. NEU activity is also important for integrin activation, as there was no further inhibition of fibrinogen binding by DANA in the presence of RGDS. Previous studies have shown that chelation of cations by EDTA generally inhibited the enzyme important for sialic acid metabolism, sialyl-transferase, as does ADP, and similar mechanisms might be important for NEU activity.[25] Also, full activity of NEU (*Vibrio cholera*) was induced by calcium (1 mM[47]), which is in line with our findings, whereby DANA only inhibited PAC-1 in the presence of calcium. DANA was able to inhibit fibrinogen-binding and consequent activation of $\alpha_{IIb}\beta_3$, although this inhibition was only partial. This could be due to DANA being more specific for NEU1 and less effective in NEU2 inhibition, as another NEU inhibitor, Zanamivir, is more specific for NEU2.[48] However, it is not known which NEU-inhibitor is most effective in blocking NEU activity in platelets. Also, NEU3 and NEU4 might also play a role in healthy platelets, further contributing to desialylation.

Following GPIbα-clustering, fibrinogen binds to $\alpha_{IIb}\beta_3$-integrin, a crucial step for platelet-platelet interactions and aggregation. Interestingly, in the presence of plasma, at least 50% of membrane expressed NEU1 was dependent on fibrinogen binding, as demonstrated by the RGDS blockade, while NEU2 was unaffected. Both NEU become highly membrane-bound when high concentrations of fibrinogen are present. Of interest, the amino acid sequence of NEU2 contains a RGD-motif, which could potentially interfere with fibrinogen-binding. Additionally, calcium signalling plays an important role as its chelation by BAPTA-AM enhanced membrane association of NEU2. The need for a fibrinogen binding conformation of $\alpha_{IIb}\beta_3$ has also been demonstrated, as PAC-1-binding following VWF/risto-stimulation is low in the absence of calcium.[27] Following VWF/risto-stimulation in the presence of saturating levels of fibrinogen, NEU1 and NEU2 became highly associated with the plasma membrane as shown by flow cytometry, potentially through their trans-membrane domain(s).[49] Similar results were found by microscopy for NEU2, which was more highly expressed on the platelet surface following VWF/risto-stimulation, even without additional fibrinogen.

Notably, washed platelets had a significantly higher MFI for RCA-1 binding in comparison to platelets from PRP, both pre- and post-stimulation with VWF/risto, correlating with higher fibrinogen binding due to washing and longer incubation times. Fibrinogen also increased recNEU activity. Earlier findings showed that two-thirds of asialo-VWF binds to GPIbα, while the remainder binds to $\alpha_{IIb}\beta_3$ in the presence of fibrinogen. Without fibrinogen, asialo-VWF binds exclusively to $\alpha_{IIb}\beta_3$.[50] When NEU becomes membrane-bound, it could potentially cleave platelet-bound VWF, thus enhancing its binding to GPIbα. In addition to cleavage of GPIbα itself, desialylation of glycosylated VWF and/or fibrinogen cannot be excluded, as desialylation also affects their platelet binding properties. Further to this, desialylated fibrinogen has a higher affinity for $\alpha_{IIb}\beta_3$[51,52] and platelet aggregation in response to asialo-VWF is approximately 60% lower than native VWF.[53] However, other studies have demonstrated spontaneous binding of asialo-VWF to GPIbα, in which was able to potentiate aggregation in the presence of fibrinogen.[54] These studies have established that the presence of plasma proteins including fibrinogen affect platelet desialylation and thereby also the VWF-binding potential. Whether NEU membrane expression is important for VWF clearance is currently unknown, however a recent study demonstrated a link between VWF-desialylation (terminal α(2-6)-linked sialic acid) and its clearance in low-VWF patients,[55] however no significant changes in SNA were observed.

This study shows for the first time that NEU1 co-localises with some but not all mitochondria within platelets, while it does not co-localise with LAMP as previously demonstrated.[56] In line with our NEU1 findings, NEU4 is located within mitochondria in other nucleated cells[16] and NEU4 also translocates to the platelet membrane following VWF addition under shear. Moreover, in our hands, NEU1 did not co-localise with β-galactosidase in unstimulated healthy or stimulated platelets, despite previous findings indicating these are both present in lysosomes, and not in platelet α and δ-granules.[36] This is in contrast with stored platelets, wherein some diffuse co-localisation of NEU1, with β-galactosidase was observed,[22] although this localisation was partial and mostly cytoplasmic. NEU2 however, was co-localised with the α-granule protein P-selectin, which is not surprising as P-selectin is sialylated[57] and DANA showed a trend towards inhibition of P-selectin expression post-ristocetin treatment.

The findings presented here demonstrate novel roles for NEU1 and NEU2 in healthy platelets, which are well regulated down-stream of GPIbα following VWF-binding, negatively by calcium (NEU2 only) and increased in presence of fibrinogen. Fibrinogen-binding is required for NEU1 and NEU2 membrane association, enhancing their activity. However when platelet $\alpha_{IIb}\beta_3$ is fully occupied with fibrinogen, NEU activity is inhibited.

Acknowledgements

We would like to thank Mikki Diep, Fiona Gardner, Jeannene Moore and Jenny Fisher for assistance with phlebotomy as well as all volunteers for donating blood. We would like to thank Dr. Anja Gerrits for fruitful discussions.

Funding

Australian governments fund the Australian Red Cross Blood Service to provide blood, blood products and services to the Australian community. The Australian & New Zealand society for Blood Transfusion (ANZSBT) provided funding for part of this project.

References

1. Jamieson GA, Okumura T, Hasitz M. Structure and function of platelet glycocalicin. Thromb haemost. 1980;42(5):1673-1678.
2. Tsuji T, Tsunehisa S, Watanabe Y, Yamamoto K, Tohyama H, Osawa T. The carbohydrate moiety of human platelet glycocalicin. J Biol Chem. 1983;258(10):6335-6339.
3. Korrel SA, Clemetson KJ, van HH, Kamerling JP, Sixma JJ, Vliegenthart JF. Identification of a tetrasialylated monofucosylated tetraantennary N-linked carbohydrate chain in human platelet glycocalicin. FEBS Lett. 1988;228(2):321-326.
4. King SL, Joshi HJ, Schjoldager KT, et al. Characterizing the O-glycosylation landscape of human plasma, platelets, and endothelial cells. Blood Aadv. 2017;1(7):429-442.
5. Grozovsky R, Hoffmeister KM, Falet H. Novel clearance mechanisms of platelets. Curr Opin Hematol. 2010;17(6):585-589.
6. Hoffmeister KM, Felbinger TW, Falet H, et al. The clearance mechanism of chilled blood platelets. Cell. 2003;112(1):87-97.
7. van der Wal DE, Verhoef S, Schutgens RE, Peters M, Wu Y, Akkerman JW. Role of glycoprotein Ibalpha mobility in platelet function. Thromb Haemost. 2010;103(5):1033-1043.
8. van der Wal DE, Du VX, Lo KS, Rasmussen JT, Verhoef S, Akkerman JW. Platelet apoptosis by cold-induced glycoprotein Ibalpha clustering. J Thromb Haemost. 2010;8(11):2554-2562.
9. Chen W, Druzak SA, Wang Y, et al. Refrigeration-induced binding of von Willebrand factor facilitates fast clearance of refrigerated platelets. Arterioscl Thromb Vasc Biol. 2017;37(12):2271-2279.
10. Li J, van der Wal DE, Zhu G, et al. Desialylation is a mechanism of Fc-independent platelet clearance and a therapeutic target in immune thrombocytopenia. Nat Comm. 2015;6:7737.
11. Urbanus RT, van der Wal DE, Koekman CA, et al. Patient autoantibodies induce platelet destruction signals via raft-associated glycoprotein Ibα and Fc RIIa in immune thrombocytopenia. Haematologica. 2013;98(7):e70-e72.
12. Monti E, Bonten E, D'Azzo A, et al. Sialidases in vertebrates: a family of enzymes tailored for several cell functions. Adv Carbohydr Chem Biochem. 2010;64:403-479.
13. Bonten E, van der Spoel A, Fornerod M, Grosveld G, d'Azzo A. Characterization of human lysosomal neuraminidase defines the molecular basis of the metabolic storage disorder sialidosis. Genes Devel. 1996;10(24):3156-3169.
14. Mozzi A, Mazzacuva P, Zampella G, Forcella ME, Fusi PA, Monti E. Molecular insight into substrate recognition by human cytosolic sialidase NEU2. Proteins. 2012;80(4):1123-1132.
15. Ha KT, Lee YC, Cho SH, Kim JK, Kim CH. Molecular characterization of membrane type and ganglioside-specific sialidase (Neu3) expressed in E. coli. Molec Cells. 2004;17(2):267-273.
16. Seyrantepe V, Landry K, Trudel S, Hassan JA, Morales CR, Pshezhetsky AV. Neu4, a novel human lysosomal lumen sialidase, confers normal phenotype to sialidosis and galactosialidosis cells. J Biol Chem. 2004;279(35):37021-37029.
17. Bosmann HB, Myers MW, Dehond D, Ball R, Case KR. Mitochondrial autonomy. Sialic acid residues on the surface of isolated rat cerebral cortex and liver mitochondria. J Cell Biol. 1972;55(1):147-160.
18. Abdulkhalek S, Amith SR, Franchuk SL, et al. Neu1 sialidase and matrix metalloproteinase-9 cross-talk is essential for TOLL-like receptor activation and cellular signaling. J Biol Chem. 2011;286(42):36532-36549.
19. Yogalingam G, Bonten EJ, van de Vlekkert D, et al. Neuraminidase 1 is a negative regulator of lysosomal exocytosis. Devel Cell. 2008;15(1):74-86.
20. Uemura T, Shiozaki K, Yamaguchi K, et al. Contribution of sialidase NEU1 to suppression of metastasis of human colon cancer cells through desialylation of integrin beta4. Oncogene. 2009;28(9):1218-1229.
21. Kato K, Shiga K, Yamaguchi K, et al. Plasma-membrane-associated sialidase (NEU3) differentially regulates integrin-mediated cell proliferation through laminin- and fibronectin-derived signalling. Biochem J. 2006;394(Pt 3):647-656.
22. Jansen AJ, Josefsson EC, Rumjantseva V, et al. Desialylation accelerates platelet clearance after refrigeration and initiates GPIbalpha metalloproteinase-mediated cleavage in mice. Blood. 2012;119(5):1263-1273.
23. Wu KK, Ku CS. Effect of platelet activation on the platelet surface sialic acid. Thromb Res. 1979;14(4-5):697-704.
24. Gitz E, Koekman CA, van den Heuvel DJ, et al. Improved platelet survival after cold storage by prevention of Glycoprotein Ibalpha clustering in lipid rafts. Haematologica. 2012;97(12):1873-1881.
25. Bosmann HB. Platelet adhesiveness and aggregation. II. Surface sialic acid, glycoprotein: N-acetylneuraminic acid transferase, and neuraminidase of human blood platelets. Biochim Biophys Acta. 1972;279(3):456-474.
26. Potier M, Mameli L, Belisle M, Dallaire L, Melancon SB. Fluorometric assay of neuraminidase with a sodium (4-methylumbelliferyl-alpha-D-N-acetylneuraminate) substrate. Anal Biochem. 1979;94(2):287-296.
27. Deng W, Xu Y, Chen W, et al. Platelet clearance via shear-induced unfolding of a membrane mechanoreceptor. Nat Commun. 2016;7:12863.
28. van der Wal DE, Gitz E, Du VX, et al. Arachidonic acid depletion extends survival of cold stored platelets by interfering with [Glycoprotein Ibalpha - 14-3-3zeta] association. Haematologica. 2012;97(10):1514-1522.
29. Ravanat C, Strassel C, Hechler B, et al. A central role of GPIb-IX in the procoagulant function of platelets that is independent of the 45-kDa GPIbalpha N-terminal extracellular domain. Blood. 2010;116(7):1157-1164.
30. Bergmeier W, Bouvard D, Eble JA, et al. Rhodocytin (aggretin) activates platelets lacking alpha(2)beta(1) integrin, glycoprotein VI, and the ligand-binding domain of glycoprotein Ibalpha. J Biol Chem. 2001;276(27):25121-25126.
31. Kinlough-Rathbone RL, Perry DW, Rand ML, Packham MA. Responses to aggregating agents after cleavage of GPIb of human

platelets by the O-sialoglycoprotein endoprotease from Pasteurella haemolytica-potential surrogates for Bernard-Soulier platelets? Thromb Res. 2000;99(2):165-172.
32. Gitz E, Koopman CD, Giannas A, et al. Platelet interaction with von Willebrand factor is enhanced by shear-induced clustering of glycoprotein Ibα.Haematologica. 2013;98(11):1810-1818.
33. Celikel R, McClintock RA, Roberts JR, et al. Modulation of alpha-thrombin function by distinct interactions with platelet glycoprotein Ibalpha. Science. 2003;301(5630):218-221.
34. Liu J, Pestina TI, Berndt MC, Jackson CW, Gartner TK. Botrocetin/VWF-induced signaling through GPIb-IX-V produces TxA2 in an alphaIIbbeta3- and aggregation-independent manner. Blood. 2005;106(8):2750-2756.
35. Guglielmone HA, Daniele JJ, Bianco ID, Fernandez EJ, Fidelio GD. Inhibition of human platelet aggregation by gangliosides. Thromb Res. 2000;98(1):51-57.
36. Febbraio M, Silverstein RL. Identification and characterization of LAMP-1 as an activation-dependent platelet surface glycoprotein. J Biol Chem. 1990;265(30):18531-18537.
37. Shattil SJ, Brass LF. The interaction of extracellular calcium with the platelet membrane glycoprotein IIb-IIIa complex. Nouv Rev Franc d'hematol. 1985;27(4):211-217.
38. Hoffmeister KM, Josefsson EC, Isaac NA, Clausen H, Hartwig JH, Stossel TP. Glycosylation restores survival of chilled blood platelets. Science. 2003;301(5639):1531-1534.
39. Li S, Wang Z, Liao Y, et al. The glycoprotein Ibalpha-von Willebrand factor interaction induces platelet apoptosis. J Thromb Haemost. 2009;8(2):341-350.
40. O'Sullivan JM, Aguila S, McRae E, et al. N-linked glycan truncation causes enhanced clearance of plasma-derived von Willebrand factor. J Thromb Haemost 2016;14(12):2446-2457.
41. Chion A, O'Sullivan JM, Drakeford C, et al. N-linked glycans within the A2 domain of von Willebrand factor modulate macrophage-mediated clearance. Blood. 2016;128(15):1959-1968.
42. Li Y, Fu J, Ling Y, et al. Sialylation on O-glycans protects platelets from clearance by liver Kupffer cells. Proc Natl Acad Sci U S A. 2017;114(31):8360-8365.
43. Nowak AA, Canis K, Riddell A, Laffan MA, McKinnon TA. O-linked glycosylation of von Willebrand factor modulates the interaction with platelet receptor glycoprotein Ib under static and shear stress conditions. Blood. 2012;120(1):214-222.
44. Wang Y, Jobe SM, Ding X, et al. Platelet biogenesis and functions require correct protein O-glycosylation. Proc Natl Acad Sci U S A. 2012;109(40):16143-16148.
45. Calvete JJ, Muniz-Diaz E. Localization of an O-glycosylation site in the alpha-subunit of the human platelet integrin GPIIb/IIIa involved in Baka (HPA-3a) alloantigen expression. FEBS Lett. 1993;328(1-2):30-34.
46. Kullaya V, de Jonge MI, Langereis JD, et al. Desialylation of platelets by pneumococcal neuraminidase A induces ADP-dependent platelet hyperreactivity. Infect Imm. 2018;86(10).
47. Holmquist L. Activation of Vibrio cholerae neuraminidase by divalent cations. FEBS Lett. 1975;50(2):269-271.
48. Hata K, Koseki K, Yamaguchi K, et al. Limited inhibitory effects of oseltamivir and zanamivir on human sialidases. Antimicrob Agents Chemother. 2008;52(10):3484-3491.
49. Maurice P, Baud S, Bocharova OV, et al. New insights into molecular organization of human neuraminidase-1: Transmembrane topology and dimerization ability. Sci Rep. 2016;6:38363.
50. Grainick HR, Williams SB, Coller BS. Asialo von Willebrand factor interactions with platelets. Interdependence of glycoproteins Ib and IIb/IIIa for binding and aggregation. J Clin Invest. 1985;75(1):19-25.
51. Diaz-Maurino T, Castro C, Albert A. Desialylation of fibrinogen with neuraminidase. Kinetic and clotting studies. Thromb Res. 1982;27(4):397-403.
52. Vermylen J, De Gaetano G, Donati MB, Verstraete M. Platelet-aggregating activity in neuraminidase-treated human cryoprecipitates: its correlation with factor-VIII-related antigen. Br J Haematol. 1974;26(4):645-650.
53. Sodetz JM, Paulson JC, Pizzo SV, McKee PA. Carbohydrate on human factor VIII/von Willebrand factor. Impairment of function by removal of specific galactose residues. J Biol Chem. 1978;253(20):7202-7206.
54. Gralnick HR. Factor VIII/von Willebrand factor protein. Galactose a cryptic determinant of von Willebrand factor activity. J Clin Invest. 1978;62(2):496-499.
55. Aguila S, Lavin M, Dalton N, et al. Increased galactose expression and enhanced clearance in patients with low von Willebrand factor. Blood. 2019;133(14):1585-1596.
56. Liang F, Seyrantepe V, Landry K, et al. Monocyte differentiation up-regulates the expression of the lysosomal sialidase, Neu1, and triggers its targeting to the plasma membrane via major histocompatibility complex class II-positive compartments. J Biol Chem. 2006;281(37):27526-27538.
57. Matsui NM, Borsig L, Rosen SD, Yaghmai M, Varki A, Embury SH. P-selectin mediates the adhesion of sickle erythrocytes to the endothelium. Blood. 2001;98(6):1955-1962.

ARTICLE

Mechanisms of increased mitochondria-dependent necrosis in Wiskott-Aldrich syndrome platelets

Sergey I. Obydennyi,[1,2] Elena O. Artemenko,[1,2] Anastasia N. Sveshnikova,[1,2,3,4] Anastasia A. Ignatova,[1,2] Tatiana V. Varlamova,[1] Stepan Gambaryan,[5] Galina Y. Lomakina,[6,7] Natalia N. Ugarova,[6] Igor I. Kireev,[8] Fazoil I. Ataullakhanov,[1,2,3,9] Galina A. Novichkova,[1] Aleksey A. Maschan,[1] Anna Shcherbina[1] and Mikhail Panteleev[1,2,3,9]

[1]National Scientific and Practical Center of Pediatric Hematology, Oncology and Immunology named after Dmitry Rogachev, Moscow; [2]Center for Theoretical Problems of Physicochemical Pharmacology, Moscow; [3]Faculty of Physics, Lomonosov Moscow State University, Moscow; [4]I.M. Sechenov First Moscow State Medical University, Moscow; [5]Sechenov Institute of Evolutionary Physiology and Biochemistry, Russian Academy of Sciences, St Petersburg, [6]Department of Chemistry, Lomonosov Moscow State University, Moscow; [7]Bauman Moscow State Technical University, Moscow; [8]Belozersky Institute of Physico-Chemical Biology, Lomonosov Moscow State University, Moscow and [9]Faculty of Biological and Medical Physics, Moscow Institute of Physics and Technology, Dolgoprudny, Russia

Ferrata Storti Foundation

Haematologica 2020
Volume 105(4):1095-1106

ABSTRACT

Wiskott-Aldrich syndrome (WAS) is associated with thrombocytopenia of unclear origin. We investigated real-time cytosolic calcium dynamics, mitochondrial membrane potential and phosphatidylserine (PS) exposure in single fibrinogen-bound platelets using confocal microscopy. The WAS platelets had higher resting calcium levels, more frequent spikes, and their mitochondria more frequently lost membrane potential followed by PS exposure (in 22.9% of platelets *vs.* 3.9% in controls; $P<0.001$) after the collapse of the last mitochondria. This phenomenon was inhibited by the mitochondrial permeability transition pore inhibitor cyclosporine A, as well by xestospongin C and lack of extracellular calcium. Thapsigargin by itself caused accelerated cell death in the WAS platelets. The number of mitochondria was predictive of PS exposure: 33% of platelets from WAS patients with fewer than five mitochondria exposed PS, while only 12% did among those that had five or more mitochondria. Interestingly, healthy donor platelets with fewer mitochondria also more readily became procoagulant upon PAR1/PAR4 stimulation. Collapse of single mitochondria led to greater cytosolic calcium increase in WAS platelets if they had one to three mitochondria compared with platelets containing higher numbers. A computer systems biology model of platelet calcium homeostasis showed that smaller platelets with fewer mitochondria could have impaired calcium homeostasis because of higher surface-to-volume ratio and greater metabolic load, respectively. There was a correlation ($C=0.81$, $P<0.02$) between the mean platelet size and platelet count in the WAS patients. We conclude that WAS platelets readily expose PS via a mitochondria-dependent necrotic mechanism caused by their smaller size, which could contribute to the development of thrombocytopenia.

Introduction

Wiskott-Aldrich syndrome (WAS) is an X-linked disorder classically characterized by thrombocytopenia, immunodeficiency and eczema.[1] Its pathophysiological mechanisms relate to defective actin polymerization and abnormal signal-mediated cytoskeleton rearrangements in hematopoietic cells as a result of deficient or dysregulated activity of the WAS protein that belongs to a distinct family of proteins involved in the transduction of signals from the cell surface to the actin cytoskele-

Correspondence:

MIKHAIL A. PANTELEEV
mapanteleev@yandex.ru

Received: December 18, 2018.

Accepted: July 4, 2019.

Pre-published: July 5, 2019.

doi:10.3324/haematol.2018.214460

Check the online version for the most updated information on this article, online supplements, and information on authorship & disclosures: www.haematologica.org/content/105/4/1095

ton.[2] The severity of immunodeficiency varies between WAS patients, whereas the platelet defect (reduced number and size) is the universal feature of the disease, and thrombocytopenia-related bleeding contributes greatly to mortality in untransplanted patients.[3] Although major platelet functions are retained in WAS platelets, there is evidence of defects in these platelets that could potentially contribute additionally to bleeding.[4]

The specific mechanisms of thrombocytopenia in WAS remain elusive. Studies of megakaryocytes from patients produced evidence both in favor of defects in platelet production[5] and against them.[6] On the other hand, platelets from WAS patients and murine WAS protein knockouts had shortened lifespan and were subject to increased phagocytosis.[7-9] In particular, it was shown previously that WAS platelets have increased phosphatidylserine (PS) exposure upon storage and activation,[10,11] which could be one of the mechanisms involved in their accelerated clearance by splenic macrophages and possibly contribute to thrombocytopenia. Indeed, recent evidence from diverse eukaryotic systems suggests that the actin cytoskeleton has a role in regulating apoptosis via interactions with mitochondria.[12] Changes to the dynamics of the actin cytoskeleton were implicated in the release of reactive oxygen species (ROS) from mitochondria and subsequent cell death.[13] Interestingly, recent studies discovered that platelets from patients with deficiency of actin filament branching regulator Arp2/3 have major phenotype features similar to those observed in WAS:[14,15] microthrombocytopenia, deficiency of dense granules and spreading.

Here we investigated the mechanism underlying cell death in platelet samples from a cohort of 35 WAS patients. The main conclusion is that the platelets are prone to PS exposure upon minor stimulation, which occurs as a result of mitochondrial permeability transition pore opening. We provide evidence for the two major mechanisms responsible for this: (i) an increased surface-to-volume ratio of these micro-platelets leading to dysregulation of calcium homeostasis; (ii) a decreased number of mitochondria per platelet, which results in a dramatic increase of cytosolic calcium upon opening of the mitochondrial permeability transition pores in a single mitochondrion. Platelet size correlated with platelet count in the untreated WAS patients.

Methods

A full description of the methods and reagents is available in the *Online Supplementary Material*.

Patients and healthy donors

A total of 35 patients with WAS were included in the study (Table 1). The diagnosis was made according to the diagnostic criteria of the European Society for Immunodeficiencies and genetically confirmed by identification of WAS mutations. Romiplostim was administered off-label at a dose of 9 μg/kg weekly, according to an institutional protocol. Twelve of 35 patients had a Zhu score of 1 or 2. Control samples included blood from children and healthy adults, as indicated in the experimental descriptions.

Blood collection and platelet isolation

Investigations were performed in accordance with the Declaration of Helsinki under approval of the Children's Center for Hematology Ethical Committee, and written informed consent was obtained from all patients (or their parents) and donors. Washed platelets were prepared essentially as described previously.[17]

Confocal microscopy experiments: general design

Glass coverslips were cleaned and coated with 1 mg/mL fibrinogen or monafram in phosphate-buffered saline. Washed platelets were attached to the protein-coated surface by incubating them at

Table 1. Characteristics of the patients with Wiskott-Aldrich syndrome.

Patient #	Age (years)	WAS gene mutation	Disease severity score*	Romiplostim treatment	Platelet count 10^9/L
1	12	c.777+1G>A	5	After	114
2	13	c .1453G>A, p.D485N		Before	52
			4	After	337
3	0.9	c.929_931+9del (c.929_931+ 9delAGGgtgagaccc)	5	Before After	30 24
4	2	c.223G>A, p.V75M	3	Before After	38 82
5	11	c.1201_1205dupCCACC, p.P403HfsTer44	5	After	34
6	0.8	c.777+1G>A	3	After	27
7	4	c.4A>T, p.S2C	1	Before After	38 145
8	12	c.560-1G>A	5	After	53
9	0.6	c.631C>T, p.R211Ter	4	After	12
10	10	c.116T>C, p.L39P	2	Before	7
11	17	c.223G>A, .V75M	2	After	34
12	12	c.134C> , p.T45M	2	Before	20
13	14	c.4A>T, p.S2C	2	Before	31
14	10	c.4A>T, p.S2C	2	Before	32
15	0.5	c.4A>T, p.S2C	2	Before	77
16	1	c.961 >T, p.R321Ter	3	After	170
17	0.6	c.107_108delTT, p.F36Ter	5	After	42
18	5	c.413G>A, p.R138Q	1	Before	54
19	0.9	c.37C>T, p.R13Ter	3	Before	19
20	7	c.961C>T, p.R321Ter	3	Before	11
21	2	c.559+5G>A	5	Before	55
22	1	c.631C>T, p.R211Ter	5	After	192
23	1	c.273+2T>C	5	Before	20
24	2	c.281G>C, p.R94P	1	After	81
25	2	c.777+2del4(GAGT)	5	After	73
26	2	c.2T>C, p.M1R	4	Before After	16 60
27	7	c.961 C T, p.R321Ter	3	After	20
28	11	c.559+5G>A	4	Before	17
29	7	c.107_108delTT, p. F36Ter	5	After	16
30	0.5	c.314T>C, p.L105P	1	Before	36
31	9	c.143 > , p.47I>T	3	After	72
32	8	c.223 G>A, .V75M	3	After	37
33	3	c.1430G>A, p.R477K	2	After	147
34	17	c.559+5G>A	5	Splenectomy	170
35	2	c.267 G>A, .R86H	2	After	30

* Scoring as suggested by Ochs *et al.*[40]

$1.3x10^5$/μL (or the maximal concentration attainable for WAS under conditions of thrombocytopenia) for 20 min and rinsing with buffer A with 1.5 mM $CaCl_2$. The PS^+ fraction was counted after incubation for a further 30 min.

Cytosolic calcium signaling and mitochondrial membrane potential change

The methodology for these investigations was essentially as described elsewhere.[18] Calibration for ratiometric measurements was performed separately for healthy and WAS platelets. Calcium concentrations were calculated using an equation for ratiometric indicators.[19] Tetramethylrhodamine methyl ester (TMRM) was used to detect mitochondrial potential dynamics.

Characterization of platelet response to TRAP-6 in platelet-rich plasma

Samples of platelet-rich plasma were diluted with platelet-poor plasma to a final concentration of 20,000/μL and buffered with HEPES at pH 7.4 (100 mM final concentration). The irreversible thrombin inhibitor Phe-Pro-Arg chloromethyl ketone (PPACK) was added to the final concentration of 100 μM in order to block spontaneous thrombin generation upon recalcification. Platelets were recalcified by addition of calcium chloride (final concentration 20 mM, which corresponds to 2 mM of free calcium[20]) and activated by 25 μM TRAP-6 (thrombin receptor agonist peptide-6) for 5 min at room temperature.

ATP measurement in platelets

In brief, platelets of the samples were lyzed (by addition of 90 μL dimethylsulfoxide to 10 μL platelet suspension) and analyzed by luciferase-luciferin assay as described previously[21,22] while the other part was stained with CD61-FITC and annexin V-Alexa Fluor 647 and analyzed by flow cytometry.

Flow cytometry characterization of platelet functional activity

The experiments were performed essentially as described previously[23,24] with minor modifications.

Transmission electron microscopy

The protocol was essentially as described elsewhere.[25]

Statistics

Data are presented as means ± standard deviations. The statistical significance of the differences between groups was determined with the non-parametric Mann–Whitney U-test (*P*) or Wilcoxon signed-rank test (*P**) for paired samples. Differences were considered to be statistically significant when the *P*-value was <0.05.

Computational modeling of platelet calcium homeostasis

A systems biology model of platelet calcium signaling was based on one developed previously.[18] In contrast to its predecessor pure calcium signaling/homeostasis models,[26,27] it had several mitochondrial compartments and included equations describing dependence of ATP production and calcium pump activity on mitochondrial inner membrane potential.

Results

Phosphatidylserine exposure by fibrinogen-immobilized Wiskott-Aldrich syndrome platelets

In order to gain insight into the mechanisms of increased/accelerated PS exposure of WAS platelets, we investigated dynamics of status change by the single fibrinogen-bound cells (Figure 1A). Unexpectedly, this relatively mild method of platelet immobilization produced massive spontaneous PS exposure in the WAS platelets during 30 min without any additional stimulation compared with PS exposure on platelets from either healthy adults (n=18) or children without WAS (n=6, aged 0-7 years, median 2.5 years) (Figure 1B). The smaller number of adherent platelets in some of the WAS patients could lead to some underestimation of their PS^+ platelets, so that the effect could be even greater. Taking into account that some of the patients received romiplostim, previously shown to potentially affect platelet function.[28,29] it was reasonable to evaluate its effect on platelets separately.[30,31] However, there was no statistically significant difference between PS externalization by platelets from untreated WAS patients and from those on romiplostim (Figure 1C): in both groups, approximately 20% of platelets, on average, exposed PS. The phenomenon was not fibrinogen-specific, as platelets attached to the $\alpha_{IIb}\beta_3$ antagonist monafram produced the same results (Figure 1D).

Functional activity of the Wiskott-Aldrich syndrome platelets

To thoroughly characterize the status of the WAS platelets involved in the study, we analyzed them by diluted whole blood flow cytometry using a comprehensive set of functional markers (Figure 2 and *Online Supplementary Figure S1*). Platelets were either left in the resting state or subjected to potent dual stimulation with TRAP-6 and collagen-related peptide (CRP). As a control, we used a group of 20 healthy children (9 boys and 11 girls, aged 0-13 years, median 5 years). The WAS platelets had significantly decreased forward scatter and levels of major surface glycoproteins (Figure 2A-C) reflecting their decreased size. There were two interesting exceptions: patients 5 and 18 had normal forward scatter. Patient 5 was splenectomized, which could be a plausible explanation of his larger platelets, while patient 18 had an exceptionally mild WAS phenotype. The size-independent parameter of shape change evaluated as the light scattering ratios for the resting/stimulated platelets (*Online Supplementary Figure S1A, B*) was significantly decreased in WAS. In order to take into account the difference in platelet size and surface area, we evaluated integrin $\alpha_{IIb}\beta_3$ activation and α-granule release by either the percentage of $PAC1^+$ (Figure 2D) or $CD62P^+$ (Figure 2E) platelets, or by normalizing the data on CD61 fluorescence intensity, as described elsewhere[31] (*Online Supplementary Figure S1*). In both cases, the response to activation was somewhat decreased in WAS platelets compared with healthy platelets. However, there was a relative increase in baseline platelet activation in the WAS patients compared with the controls, as judged by integrin (*Online Supplementary Figure S1D*) and P-selectin (*Online Supplementary Figure S1F*) surface expression of resting platelets. Dense granule release in WAS was essentially lower than in healthy children (Figure 2F). Interestingly, the completely size-independent response of procoagulant platelet formation evaluated as a percentage of annexin V^+ cells was also clearly decreased (Figure 2G). Neither of these phenomena changed in the romiplostim-treated patients compared with untreated ones. Analysis with TRAP stimulation in diluted platelet-rich plasma revealed a minor increase in

PS+ platelets under resting conditions and normal PS expression upon stimulation (*Online Supplementary Figure S2*). In summary, WAS platelets were small and demonstrated some decreased preactivation features in the resting state but they did not appear to have any drastic functional differences from normal platelets in an activated state.

Signaling events in single fibrinogen-attached Wiskott-Aldrich syndrome platelets

To identify the mechanisms of the PS externalization of the WAS platelets, we simultaneously examined dynamics of calcium in the cytosol, mitochondrial membrane potential and PS exposure in WAS and control platelets (Figure 3). The mean intracellular cytosolic calcium level in the WAS platelets was 4-fold greater than that in the control platelets at the beginning, and the average difference increased with time (Figure 3A). While healthy unstimulated platelets, in line with previous reports,[18,32] had only occasional calcium spikes when bound to fibrinogen (Figure 3B), unstimulated platelets from WAS patients had frequent oscillations with longer spike duration (Figure 3C, D). The mitochondria in the WAS platelets lost their membrane potential one after another and, if all of them became TMRM-negative, the cell began to bind annexin V within 10 s (Figure 3D), exactly as reported before for the PS+ platelet formation induced in healthy donors with TRAP-6 or thrombin.[18,27] This is in agreement with the scenario of mitochondrial calcium-overloading-induced necrosis of procoagulant platelet formation.[18,33,34]

Importantly, time lapse imaging revealed that mitochondrial collapse in WAS platelets with few mitochondria in turn led to a rapid cytosolic calcium increase

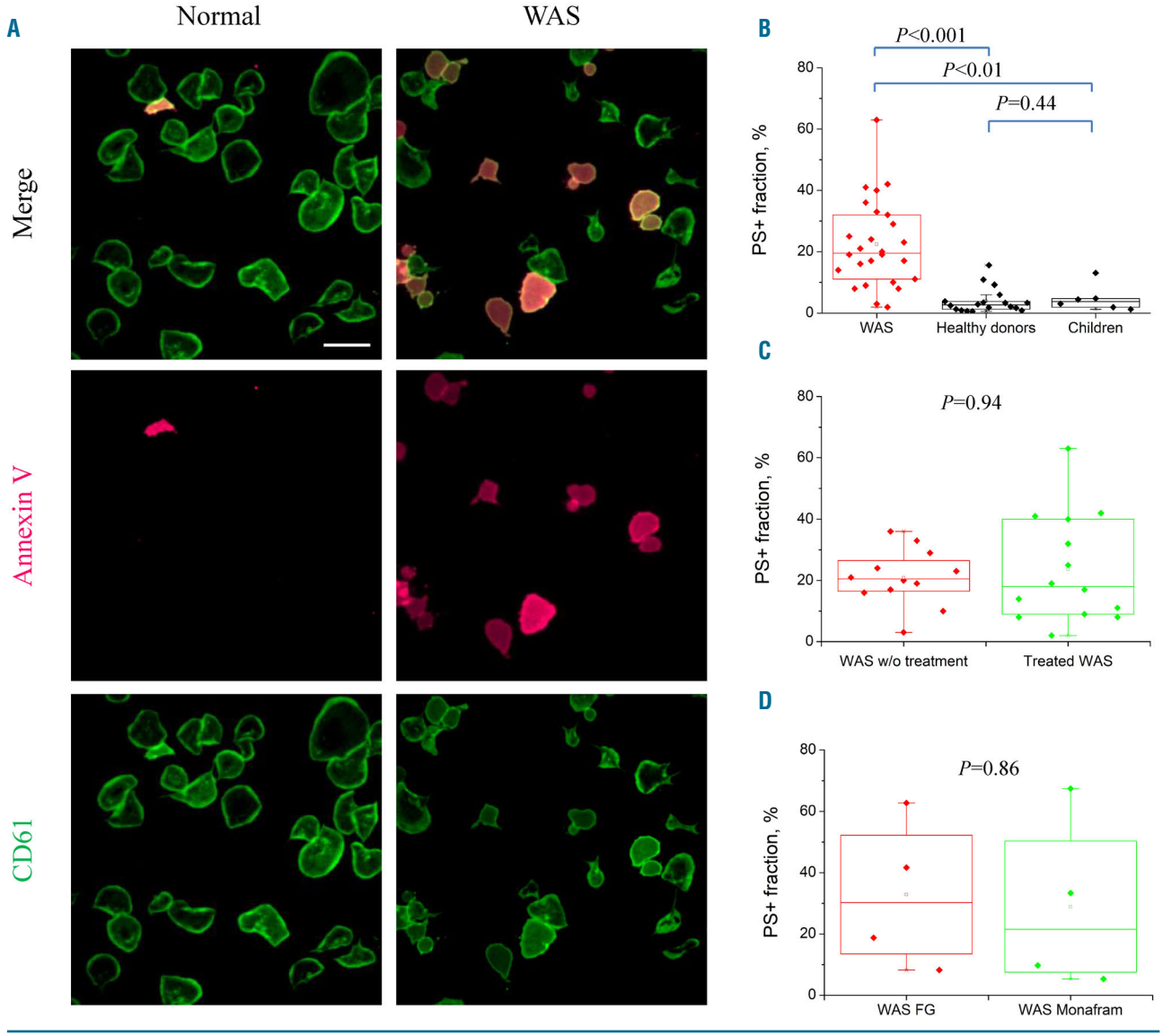

Figure 1. Exposure of phosphatidylserine by Wiskott-Aldrich syndrome platelets upon fibrinogen binding. (A) Confocal microscopy images of healthy (left) and Wiskott-Aldrich syndrome (WAS) (right) platelets after spreading for 30 min on a fibrinogen surface in the presence of 1.5 mM Ca^{2+}. The platelets are labeled with CD61 (green) and annexin V (red); scale bar: 10 μm. (B) Phosphatidylserine-positive (PS^+) fraction of platelets from the WAS patients (27 patients, >7,500 cells), adult healthy (18 donors, >6,500 cells) and 0- to 7-year old children without WAS (6 children, age: 0, 0, 2, 3, 4, 7 years, 2,300 platelets) on a fibrinogen surface. (C) PS^+ fraction of WAS platelets on the fibrinogen surface, showing a comparison of romiplostim-treated and untreated WAS patients, *P*=0.94. (D) Monafram-coated coverslips did not change the PS^+ fraction, *P*=0.86, n=4, 2,500 platelets. w/o: without; FG: fibrinogen.

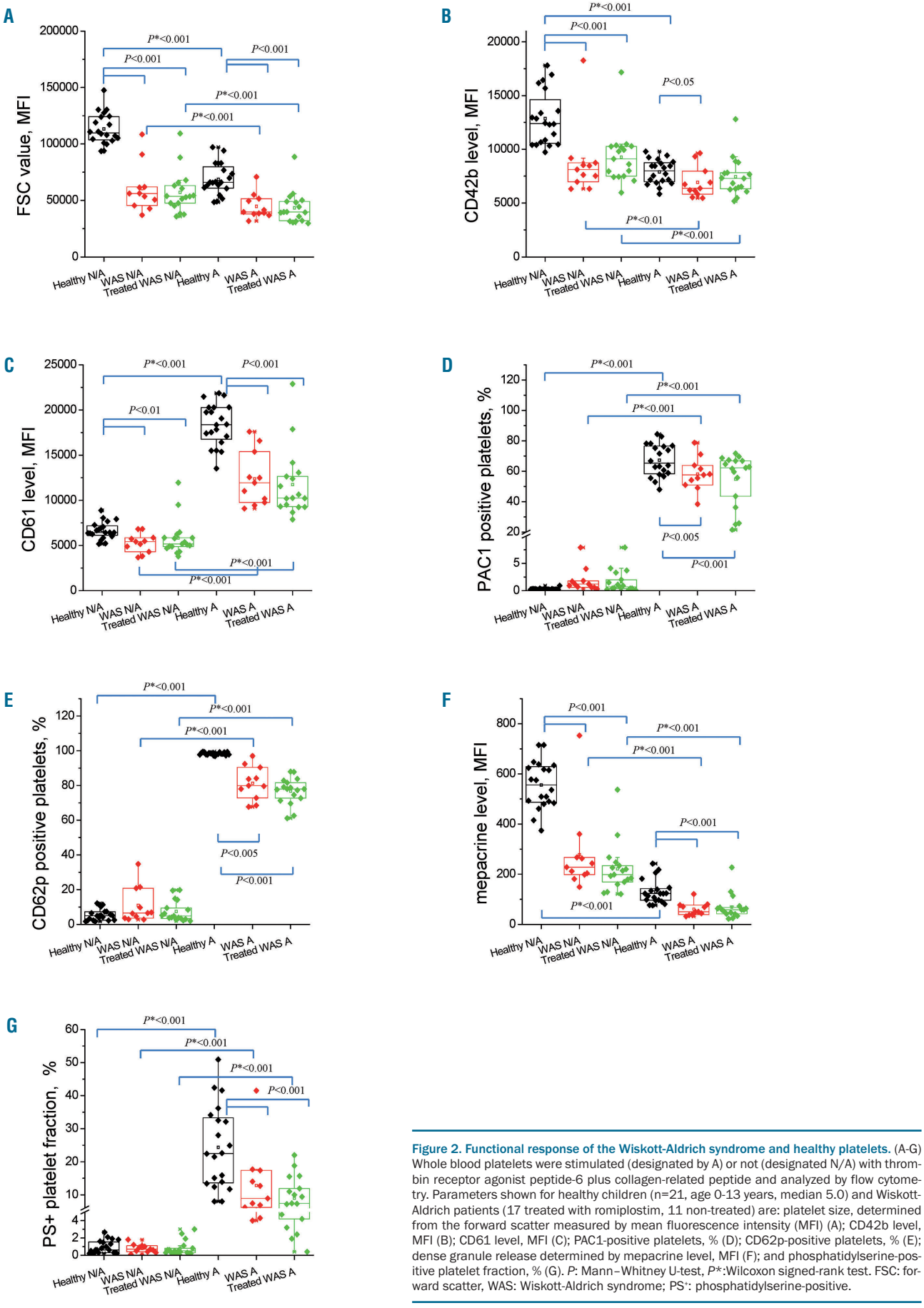

Figure 2. Functional response of the Wiskott-Aldrich syndrome and healthy platelets. (A-G) Whole blood platelets were stimulated (designated by A) or not (designated N/A) with thrombin receptor agonist peptide-6 plus collagen-related peptide and analyzed by flow cytometry. Parameters shown for healthy children (n=21, age 0-13 years, median 5.0) and Wiskott-Aldrich patients (17 treated with romiplostim, 11 non-treated) are: platelet size, determined from the forward scatter measured by mean fluorescence intensity (MFI) (A); CD42b level, MFI (B); CD61 level, MFI (C); PAC1-positive platelets, % (D); CD62p-positive platelets, % (E); dense granule release determined by mepacrine level, MFI (F); and phosphatidylserine-positive platelet fraction, % (G). *P*: Mann–Whitney U-test, *P**:Wilcoxon signed-rank test. FSC: forward scatter, WAS: Wiskott-Aldrich syndrome; PS⁺: phosphatidylserine-positive.

(*Online Supplementary Figure S3A*, time point 116 s). If it was reversed, calcium concentration also decreased (*Online Supplementary Figure S3A*, time point 146 s). This is drastically different from healthy donors' activated platelets, in which calcium was not so sensitive to the collapse of a single mitochondrion.[18] Interestingly, WAS platelets with large numbers of mitochondria had increased background cytosolic calcium and frequent oscillations, but were not sensitive to the collapse of single mitochondria either (*Online Supplementary Figure S3B*).

Phosphatidylserine exposure on Wiskott-Aldrich syndrome platelets is mediated by mitochondrial permeability transition pore opening

The critical element of mitochondrially driven necrosis is mitochondrial permeability transition pore opening. To check this, we added several inhibitors of different cell death-regulating signaling pathways during platelet incubation on fibrinogen (cyclosporine A, necrostatin-1, Z-VAD-FMK) or spreading (calpeptin). The mitochondrial permeability transition pore inhibitor cyclosporine A (5

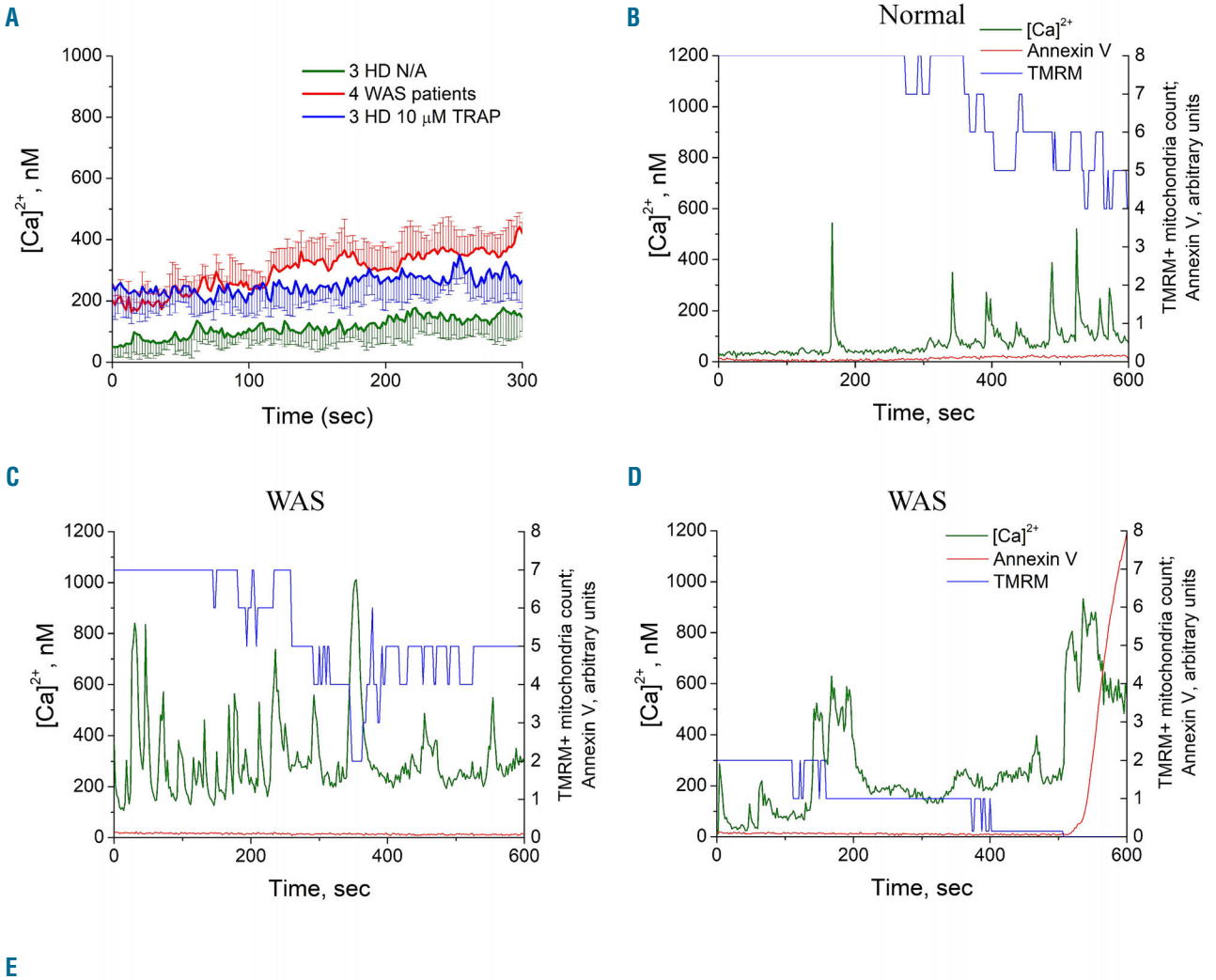

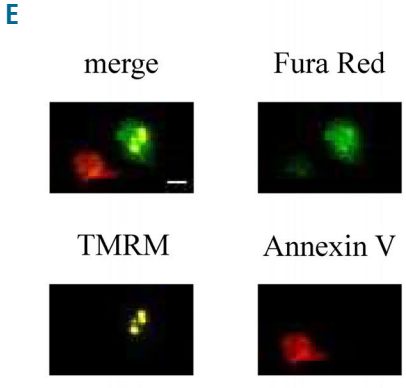

Figure 3. Dynamics of cytoplasmic calcium, mitochondrial potentials and phosphatidylserine exposure of single platelets. Plots show dynamics of intracellular calcium concentration and annexin V binding to single platelets during incubation on fibrinogen in the presence of 1.5 mM of extracellular calcium. (A) Averaged calcium dynamics (± standard deviation) for non-activated (N/A) platelets from patients with Wiskott-Aldrich syndrome (WAS) (4 patients, 34 platelets) and for platelets from healthy donors (HD) which were either activated with 10 μM TRAP (3 HD, 30 platelets) or not activated (3 HD, 26 platelets). (B) Dynamics for a single healthy phosphatidylserine-negative (PS^-) platelet; (C) the same for a WAS PS^- platelet; (D) the same for a WAS PS^+ platelet. The TMRM signal is represented as a number of TMRM-positive mitochondria in the platelet (B-D). Intracellular events leading to PS exposure induced with mitochondria collapse with following cytoplasmic calcium increase and PS exposure. All three processes were almost simultaneous, lasting decades of seconds. Both WAS (E) and normal (not shown) PS^+ platelets lost their mitochondrial potentials. Scale bar: 1 μm for all microscopic images. TRAP: thrombin receptor agonist peptide; TMRM: tetramethylrhodamine methyl ester.

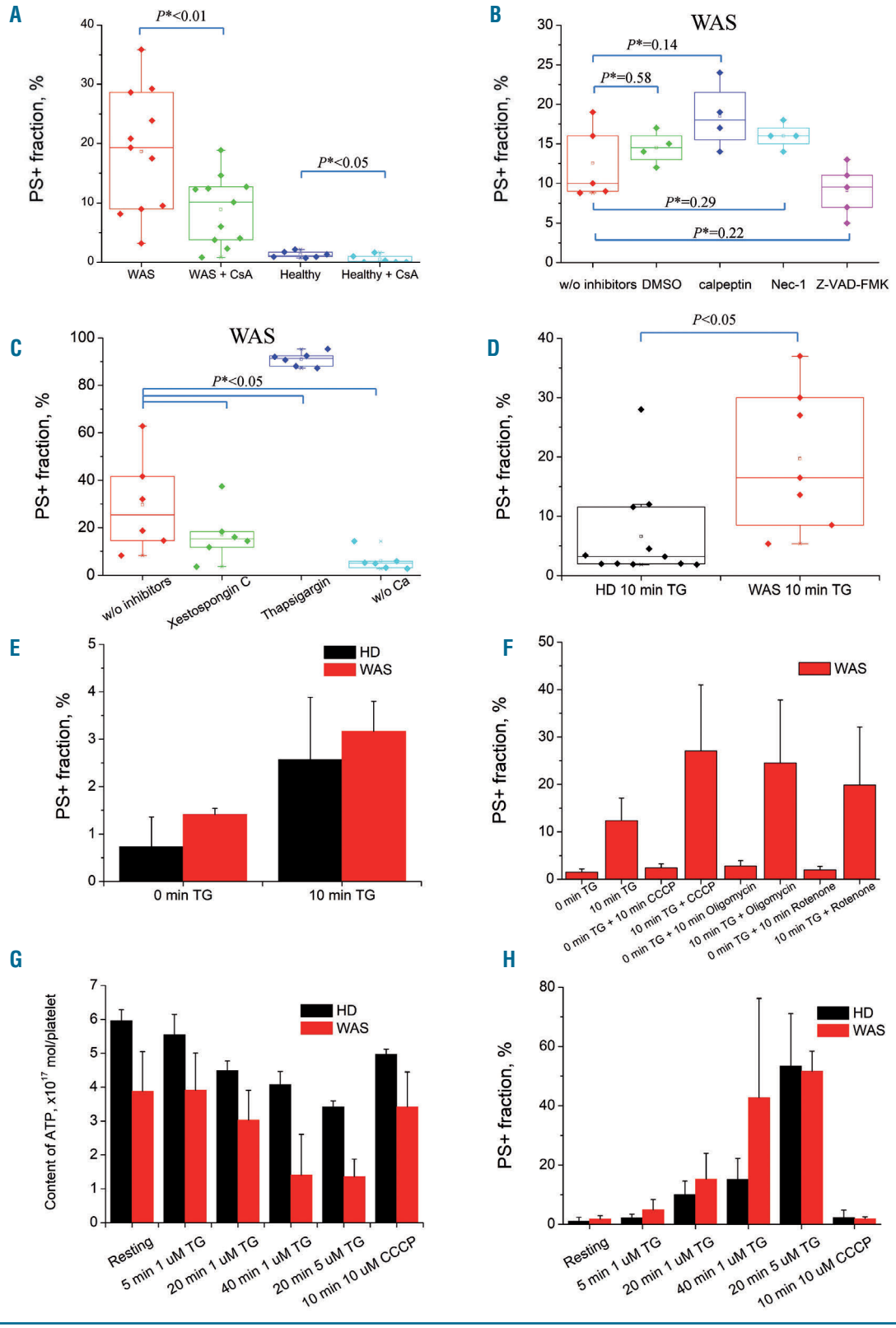

Figure 4. Prevention of mitochondrial permeability transition pore opening affects spontaneous phosphatidylserine exposure of Wiskott-Aldrich syndrome platelets. (A) Phosphatidylserine (PS) exposure of fibrinogen-spread platelets incubated in the absence or presence of 5 μM cyclosporine A (3,900 platelets from 11 patients and 4,000 platelets from 6 healthy donors). (B) PS exposure of platelets incubated with DMSO or programmed cell death inhibitors calpeptin (200 μM, 20 min incubation), Nec-1 (50 μM, 50 min incubation) and Z-VAD-FMK (50 μM, 50 min incubation) (100-300 platelets were observed for each dot). (C) Modulation of intracellular calcium signaling in spread platelets by xestospongin C (3 μM, 50 min); thapsigargin (TG, 1 μM, 30 min); with lactadherin and without addition of 1.5 mM $CaCl_2$ (n=5, 6,800 platelets). (D) Flow cytometry analysis of Wiskott-Aldrich syndrome (WAS) platelet PS exposure. Incubation of platelets in suspension with 1 μM TG in the presence of 1.5 mM $CaCl_2$ for 10 min induced a PS^+ platelet fraction comparable to that with fibrinogen-spreading for both WAS patients (n=7, mean ± standard deviation: 19.7%±11.8%) and healthy donors (n=11, 6.6%±8.0%). (E) Flow cytometry analysis of WAS platelet PS exposure in suspension without addition of $CaCl_2$ (n=3); (F) Analysis of the mitochondrial inhibitors in suspension at TG treatment (n=3); (G, H) ATP levels (G) *versus* the number of PS^+ platelets (H): in healthy donors and WAS patients at TG and CCCP treatment (n=3). CsA: cyclosporine A, DMSO: dimethylsulfoxide; HD: healthy donor.

μM) significantly diminished the PS^+ fraction formed by the WAS platelets on fibrinogen (Figure 4A). Other inhibitors, including necroptosis inhibitor necrostatin-1, calpain inhibitor calpeptin and pan-caspase inhibitor Z-VAD-FMK, had no significant effect on PS exposure (Figure 4B). These data strongly suggest that it is indeed the necrotic mechanism of mitochondrial permeability transition pore opening that is responsible for increased PS exposure in WAS platelets.

Role of calcium homeostasis, cellular energetics, and reactive oxygen species in phosphatidylserine exposure by Wiskott-Aldrich syndrome platelets

In order to get further insight into the necrosis of the surface-attached WAS platelets, they were treated with xestospongin C (an inositol trisphosphate receptor blocker), or thapsigargin (a sarco-endoplasmic reticulum Ca^{2+} ATPase inhibitor), or in buffer A without addition of calcium chloride (Figure 4C). Xestospongin C inhibited PS exposure suggesting involvement of inositol trisphosphate signaling, while thapsigargin potently boosted platelet necrosis. In contrast, the effects were drastically decreased in the absence of extracellular calcium.

Importantly, thapsigargin caused accelerated cell death in the WAS platelets compared with platelets from healthy controls in suspension as well without any surface attachment (Figure 4D), which suggests that the WAS platelets' propensity to necrosis is caused by dysregulation of their calcium homeostasis. The same experiment with lactadherin and without addition of extracellular calcium did not show an increased PS^+ fraction of WAS platelets (Figure 4E). For an additional check of the effect of outside-in signaling on thapsigargin-induced PS exposure in this design, we pre-treated platelets with the integrin $\alpha_{IIb}\beta_3$ antagonist monafram which did not affect the thapsigargin-induced PS exposure (*Online Supplementary Figure S4*). Pre-incubation of the WAS platelets with the mitochondrial ATPase inhibitor oligomycin or with the mitochondrial uncoupler CCCP increased the formation of PS^+ platelets at thapsigargin treatment in the case of WAS platelets, while the mitochondrial respiratory chain complex I inhibitor rotenone had less effect on the thapsigargin-induced PS exposure (Figure 4F); none of these three drugs caused platelet necrosis by themselves. These data indicate that an energy deficiency could be a factor contributing to platelet necrosis but not the defining one. In line with this, although the levels of ATP in cells were decreased in parallel with the increase of the PS^+ platelets upon thapsigargin treatment, the same decrease of ATP was caused by CCCP without PS exposure indicating that the observed phenomenon is not purely caused by an energy collapse (Figure 4G, H). ROS production in the WAS platelets was not essentially different from that in healthy donor platelets, and was only mildly increased upon stimulation with CRP (*Online Supplementary Figure S5*). The morphology of the mitochondria in WAS platelets was not apparently different from that of normal ones, as judged by transmission electron microscopy (*Online Supplementary Figure S6*).

Platelet necrosis correlates directly with the number of mitochondria

During examination of the images, it became apparent that the WAS platelets undergoing PS exposure and mitochondrial membrane potential loss rarely had more than two mitochondria per cell. We, therefore, performed experiments to count the number of mitochondria in each platelet and correlated this with the outcome (i.e. PS exposure) (Figure 5). For both WAS patients and healthy donors, the number of mitochondria was significantly lower in the platelets that became PS^+ (Figure 5A). This number affected the fate of platelets in a dose-dependent manner: about 33% of the WAS platelets exposed PS if they had one to four mitochondria per platelet, and only about 11% if they had more than five mitochondria (Figure 5B). A similar dependence was observed for platelets from healthy donors (Figure 5B), although they exposed PS more rarely. The histogram in Figure 5C shows the distributions of mitochondria number for platelets from WAS patients and healthy donors side by side. Importantly, although the mean number of mitochondria in WAS platelets was not much lower than that in the control platelets, there was significant skewing to the left of the curve: a total of 27±12% of WAS platelets had fewer than three mitochondria, compared to only 8.7±4.4% of healthy platelets. In order to check if the number of mitochondria has a wider significance in platelet necrosis, we performed experiments with fibrinogen-attached healthy platelets stimulated with TRAP-6 or thrombin, revealing the same pattern (Figure 5D, E).

Systems biology simulations reveal critical roles of mitochondrial number and surface-to-volume ratio in programmed cell death in Wiskott-Aldrich syndrome

In order to dissect the mechanisms of mitochondria-dependent necrosis in WAS, we developed a computational systems biology model of calcium signaling (Figure 6). In the model, which incorporated all compartments and major calcium signaling mechanisms, we investigated dependence of the platelet calcium response on two major variables that differ for the WAS platelets, the number of mitochondria and platelet size.

The model demonstrated that a decrease in the number of mitochondria should make platelets more sensitive to mitochondrial collapse and result in a higher increase in calcium because the remaining mitochondria could not bear the ATP production load (Figure 6A, B), which agrees well with the experimental observations. We also simulated platelets of different sizes; when scaling them, the ratio between surface and volume molecules was naturally changed (Figure 6), as volume is proportional to the size to the third degree, while surface is proportional to the size to the second degree. Upon stimulation, the virtual platelets with a smaller size had comparable active phospholipase C per volume (Figure 6C), but more inositol trisphosphate and ultimately much more calcium (Figure 6E) because they had more inositol trisphosphate receptors per volume (as these were assumed to be proportional to the surface). This is again in line with the experimental data presented above that showed increased calcium levels in WAS even prior to mitochondrial permeability transition pore opening, and with the sensitivity of the phenomenon to xestospongin C.

The model, therefore, predicted that the size of platelets from untreated WAS patients would negatively affect the platelets' ability to expose PS spontaneously and (if this is the mechanism underlying thrombocytopenia) positively affect the patients' platelet count. Interestingly, there was a significant positive correlation between platelet size and platelet count among the untreated WAS patients (*Online Supplementary Figure S7A*). Although we did not observe significant correlations with PS exposure, probably as a

result of the limited number of samples (*Online Supplementary Figure S7B, C*), it is interesting that patient #18 (indicated with a red arrow), who had normal-sized platelets and a mild phenotype, also had the least PS exposure upon immobilization and incidentally the highest platelet count.

Discussion

In this study, we show that the death of WAS platelets upon minor stimulation, such as fibrinogen attachment or low-dose thapsigargin treatment, follows the pathway of mitochondrial necrosis. It is a rapid process associated with opening of mitochondrial permeability transition pores, which actually precedes PS exposure at the single platelet level, extracellular calcium-dependent, and it is downregulated by cyclophilin D and inositol trispohosphate receptor antagonists, but not by apoptosis or necroptosis inhibitors. It is associated with decreased platelet ATP levels, and downregulation of the energy metabolism with CCCP, rotenone and oligomycin-promoted necrosis, but did not cause it by itself. This cell death phenomenon predominantly occurred in the

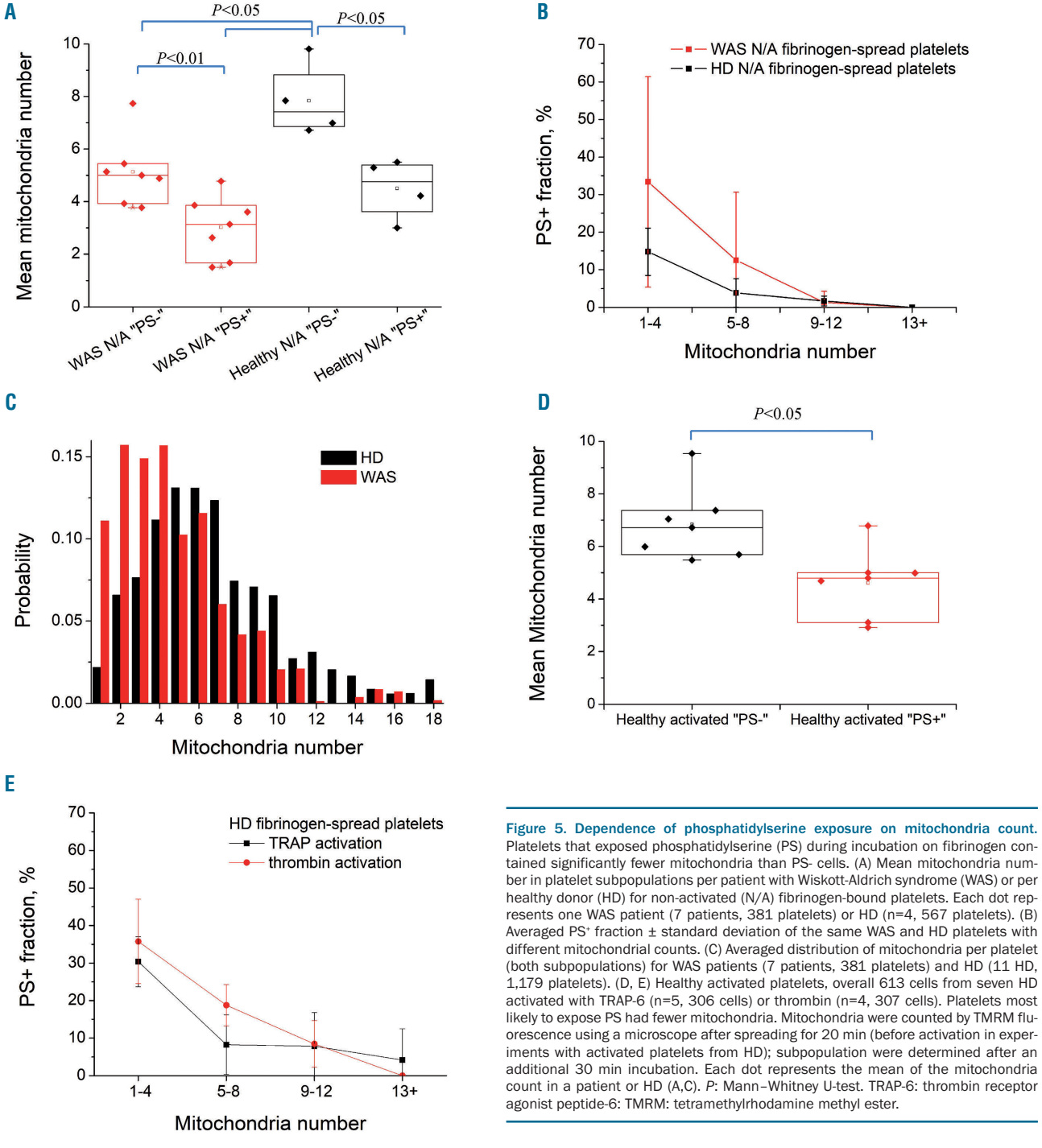

Figure 5. Dependence of phosphatidylserine exposure on mitochondria count. Platelets that exposed phosphatidylserine (PS) during incubation on fibrinogen contained significantly fewer mitochondria than PS- cells. (A) Mean mitochondria number in platelet subpopulations per patient with Wiskott-Aldrich syndrome (WAS) or per healthy donor (HD) for non-activated (N/A) fibrinogen-bound platelets. Each dot represents one WAS patient (7 patients, 381 platelets) or HD (n=4, 567 platelets). (B) Averaged PS^+ fraction ± standard deviation of the same WAS and HD platelets with different mitochondrial counts. (C) Averaged distribution of mitochondria per platelet (both subpopulations) for WAS patients (7 patients, 381 platelets) and HD (11 HD, 1,179 platelets). (D, E) Healthy activated platelets, overall 613 cells from seven HD activated with TRAP-6 (n=5, 306 cells) or thrombin (n=4, 307 cells). Platelets most likely to expose PS had fewer mitochondria. Mitochondria were counted by TMRM fluorescence using a microscope after spreading for 20 min (before activation in experiments with activated platelets from HD); subpopulation were determined after an additional 30 min incubation. Each dot represents the mean of the mitochondria count in a patient or HD (A,C). *P*: Mann–Whitney U-test. TRAP-6: thrombin receptor agonist peptide-6: TMRM: tetramethylrhodamine methyl ester.

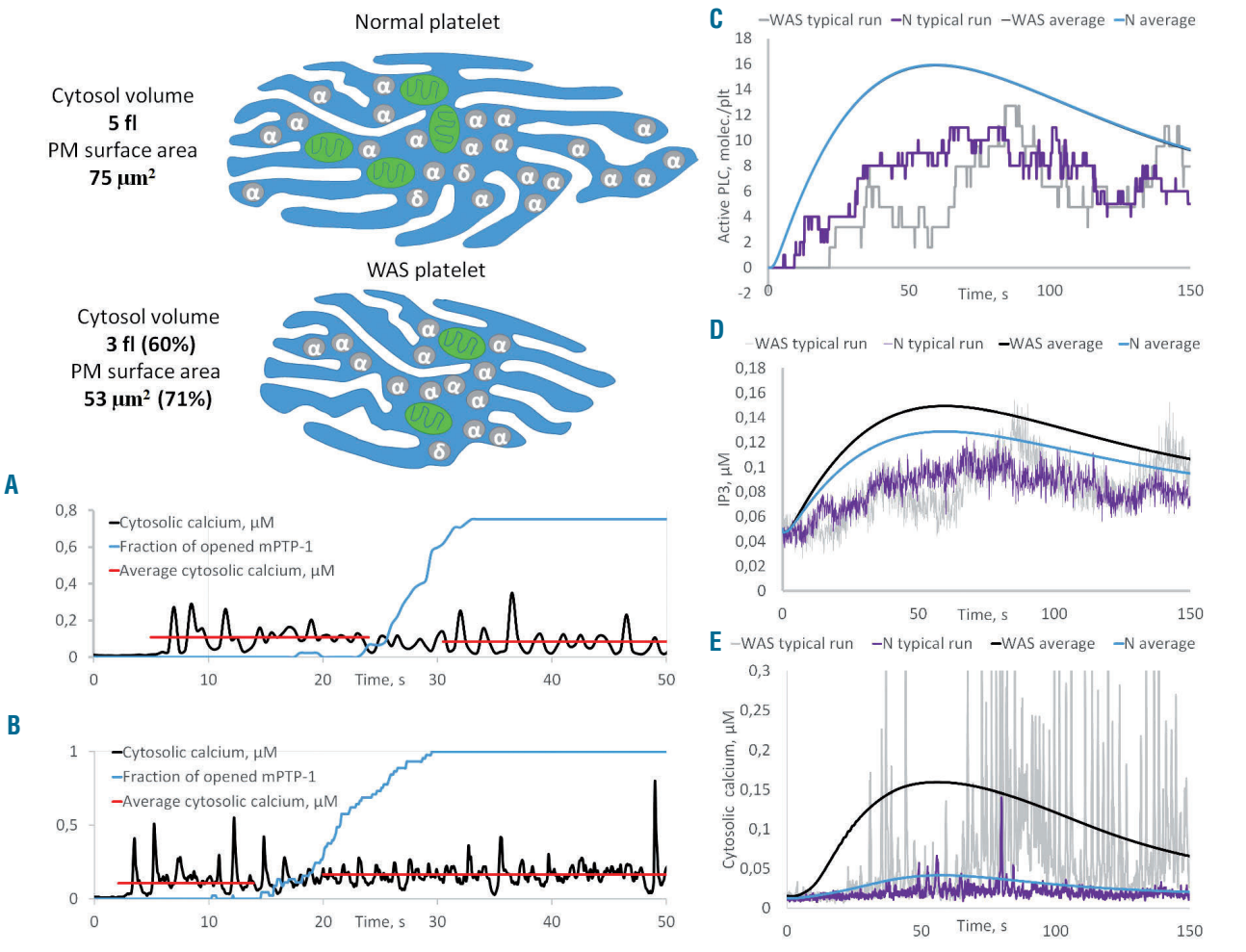

Figure 6. Increased cytosolic calcium as a result of downsizing: computer systems biology simulation of calcium signaling in normal and Wiskott-Aldrich syndrome platelets. Wiskott-Aldrich syndrome (WAS) platelets were assumed to have the same content of signaling proteins, scaled to the respective volume of compartments. (A, B) Stochastic simulation of the activation of normal platelets containing two (A) or four (B) mitochondria with 10 nM thrombin. With the collapse of one mitochondrion the average cytosolic calcium increases 1.5-fold (A) in the case of two mitochondria or does not change (B) in the case of four mitochondria. (C-E) Stochastic and deterministic simulations of normal and WAS platelets stimulated with 1 nM thrombin.

platelet fraction with fewer than four mitochondria per platelet. Importantly, although beyond the scope of this WAS study, the low number of mitochondria turned out to be predictive of the agonist-induced formation of procoagulant platelets by healthy donors. The immediate causes of this necrosis are: (i) increased calcium concentration and spiking frequency of WAS platelets upon spreading; and (ii) increased sensitivity of calcium homeostasis to collapse of single mitochondria in platelets with fewer mitochondria. Computational systems biology analysis confirmed that both increased surface-to-volume ratio (leading to impaired calcium homeostasis) and a lower number of mitochondria (resulting in increased sensitivity of calcium to mitochondrial collapse) contribute to the tendency of the WAS platelets to undergo necrosis upon minor stimulation. Although the clinical consequences of this phenomenon are beyond the scope of this paper, this mechanism is supported by the observation of a correlation between platelet size and platelet count in WAS. In contrast to the observations for immune thrombocytopenia,[29,35] there were no statistically significant changes in WAS platelet functionality upon romiplostim treatment.

The phenomena investigated in the present study agree well with previous observations by Shcherbina *et al.*[10,11] who reported increased, accelerated or spontaneous PS exposure by the platelets of WAS patients or WAS knockout mice associated with increased calcium levels at rest, and provide a molecular basis for the previous reports. The mechanism of this massive PS exposure in WAS platelets appears to be essentially similar to that determining agonist-induced procoagulant platelet formation in physiological potent platelet activation:[18,26,33,34,36,37] an increase of cytosolic calcium followed by mitochondrial calcium overload and collapse, ultimately leading to necrotic cell death. The difference was that PS exposure in WAS was triggered by weak stimuli, such as fibrinogen attachment, which, although recognized as being an activating stimulus,[38] produced negligible PS exposure in healthy donor platelets by itself. A high percentage of PS^+ platelets seems to be a universal feature of the disease, irrespective of its severity and absence\presence of other WAS features.

The similarity between these phenomena (PS exposure by normal platelets via thrombin and/or collagen recep-

tors and PS exposure by WAS platelets induced by fibrinogen attachment) goes so far that the phenomenon of predominant necrosis by platelets with fewer mitochondria was observed here for TRAP-6- or thrombin-stimulated healthy platelet activation as well. This is interesting in itself and might have implications beyond the scope of the present study: although several previous studies attempted to identify properties of platelets that predispose them to procoagulant formation such as age or resting calcium concentration,[18,33,39] the effects were much less than those of the number of mitochondria, and it has been generally assumed in the field that it is unclear which platelets become necrotic and which do not.

Although the data of the present study clearly characterize the immediate molecular cause and sequence of events leading to spontaneous PS exposure in WAS platelets, they are more limited with regard to linking this phenomenon to the genetic cause of the disease or clinical consequences. While a decreased number of mitochondria in the WAS platelets (natural because of their decreased size) is likely to contribute to their tendency to undergo necrosis, this difference by itself is not great enough to have such drastic consequences. Non-stimulated WAS platelets undergo necrosis more efficiently than non-stimulated healthy platelets having the same number of mitochondria (Figure 5), so there should be additional mechanisms. The most promising one is disruption of cytosolic calcium balance (even without regard to mitochondria) simply because of the greater surface-to-volume ratio in WAS platelets: computer systems biology simulations indicated that this mechanism alone would be sufficient to explain the platelets' necrosis. This hypothesis is supported by the sensitivity of the PS^+ fraction to xestospongin C and a decrease in extracellular calcium, as well as by the ability of the calcium pump inhibitor thapsigargin to promote WAS platelet necrosis much more rapidly than that of healthy donor platelets. The inability of mitochondrial function antagonists to cause necrosis by itself is also in line with the proposed picture of events. However, we did not show a causal relationship between size and calcium in direct experiments, and cannot exclude participation of other contributing factors. Furthermore, although it is tempting to speculate that increased PS exposure may promote platelet clearance by macrophages,[10,11] the statistics of the present study are not sufficient to confirm or disprove a relationship between clinical severity and the tendency of platelets to expose PS, despite showing a relationship between platelet count and platelet size. Involvement of impaired actin cytoskeleton dynamics due to WAS protein mutations in the programmed cell death of WAS platelets cannot be excluded either, and requires additional research.

Acknowledgments

We thank Prof. A.V. Mazurov and Prof. R.W. Farndale for their kind gifts of monafram and CRP. The project was supported by a grant from the endowment foundation "Doctors, Innovations, Science for Children", and by the Russian Foundation for Basic Research grants 17-00-00141 (17-00-00138/17-00-00139/17-00-00140), 17-04-01309 and 18-34-20026. Electron microscopy was supported by the Russian Science Foundation grant 17-15-01290. Computer modeling was supported by Russian Science Foundation grant 17-74-20045.

References

1. Candotti F. Clinical manifestations and pathophysiological mechanisms of the Wiskott-Aldrich syndrome. J Clin Immunol. 2018;38(1):13-27.
2. Rivers E, Thrasher AJ. Wiskott-Aldrich syndrome protein: emerging mechanisms in immunity. Eur J Immunol. 2017;47(11):1857-1866.
3. Sereni L, Castiello MC, Villa A. Platelets in Wiskott-Aldrich syndrome: victims or executioners? J Leukoc Biol. 2018;103(3):577-590.
4. Poulter NS, Pollitt AY, Davies A, et al. Platelet actin nodules are podosome-like structures dependent on Wiskott-Aldrich syndrome protein and ARP2/3 complex. Nat Commun. 2015;6:7254.
5. Kajiwara M, Nonoyama S, Eguchi M, et al. WASP is involved in proliferation and differentiation of human haemopoietic progenitors in vitro. Br J Haematol. 1999;107(2):254-262.
6. Haddad E, Cramer E, Riviere C, et al. The thrombocytopenia of Wiskott Aldrich syndrome is not related to a defect in proplatelet formation. Blood. 1999;94(2):509-518.
7. Prislovsky A, Zeng X, Sokolic RA, et al. Platelets from WAS patients show an increased susceptibility to ex vivo phagocytosis. Platelets. 2013;24(4):288-296.
8. Prislovsky A, Marathe B, Hosni A, et al. Rapid platelet turnover in WASP(-) mice correlates with increased ex vivo phagocytosis of opsonized WASP(-) platelets. Exp Hematol. 2008;36(5):609-623.
9. Sereni L, Castiello MC, Marangoni F, et al. Autonomous role of Wiskott-Aldrich syndrome platelet deficiency in inducing autoimmunity and inflammation. J Allergy Clin Immunol. 2018;142(4):1272-1284.
10. Shcherbina A, Rosen FS, Remold-O'Donnell E. Pathological events in platelets of Wiskott-Aldrich syndrome patients. Br J Haematol. 1999;106(4):875-883.
11. Shcherbina A, Cooley J, Lutskiy MI, Benarafa C, Gilbert GE, Remold-O'Donnell E. WASP plays a novel role in regulating platelet responses dependent on alphaIIbbeta3 integrin outside-in signalling. Br J Haematol. 2010;148(3):416-427.
12. Takano K, Sato K, Negishi Y, Aramaki Y. Involvement of actin cytoskeleton in macrophage apoptosis induced by cationic liposomes. Arch Biochem Biophys. 2012;518(1):89-94.
13. Mack TG, Kreis P, Eickholt BJ. Defective actin dynamics in dendritic spines: cause or consequence of age-induced cognitive decline? Biol Chem. 2016;397(3):223-229.
14. Kahr WH, Pluthero FG, Elkadri A, et al. Loss of the Arp2/3 complex component ARPC1B causes platelet abnormalities and predisposes to inflammatory disease. Nat Commun. 2017;8:14816.
15. Paul DS, Casari C, Wu C, et al. Deletion of the Arp2/3 complex in megakaryocytes leads to microthrombocytopenia in mice. Blood Adv. 2017;1(18):1398-1408.
16. Mazurov AV, Pevzner DV, Antonova OA, et al. Safety, inhibition of platelet aggregation and pharmacokinetics of Fab'2 fragments of the anti-glycoprotein IIb-IIIa monoclonal antibody FRaMon in high-risk coronary angioplasty. Platelets. 2002;13(8):465-477.
17. Topalov NN, Yakimenko AO, Canault M, et al. Two types of procoagulant platelets are formed upon physiological activation and are controlled by integrin alpha(IIb)beta(3). Arterioscler Thromb Vasc Biol. 2012;32(10):2475-2483.
18. Obydennyy SI, Sveshnikova AN, Ataullakhanov FI, Panteleev MA. Dynamics of calcium spiking, mitochondrial collapse and phosphatidylserine exposure in platelet subpopulations during activation. J Thromb Haemost. 2016;14(9):1867-1881.
19. Takahashi A, Camacho P, Lechleiter JD, Herman B. Measurement of intracellular calcium. Physiol Rev. 1999;79(4):1089-1125.
20. Dashkevich NM, Vuimo TA, Ovsepyan RA, et al. Effect of pre-analytical conditions on the thrombodynamics assay. Thromb Res. 2014;133(3):472-476.
21. Ugarova NN, Lomakina GY, Modestova Y, et al. A simplified ATP method for the rapid control of cell viability in a freeze-dried BCG vaccine. J Microbiol Methods. 2016;130:48-53.
22. Lomakina GY, Modestova YA, Ugarova NN. Bioluminescence assay for cell viability. Biochemistry (Mosc). 2015;80(6):701-713.
23. Ignatova AA, Karpova OV, Trakhtman PE, Rumiantsev SA, Panteleev MA. Functional characteristics and clinical effectiveness of platelet concentrates treated with riboflavin and ultraviolet light in plasma and in platelet additive solution. Vox Sang. 2016;110(3):244-252.
24. Poletaev AV, Koltsova EM, Ignatova AA, et

al. Alterations in the parameters of classic, global, and innovative assays of hemostasis caused by sample transportation via pneumatic tube system. Thromb Res. 2018;170: 156-164.
25. Podoplelova NA, Sveshnikova AN, Kotova YN, et al. Coagulation factors bound to procoagulant platelets concentrate in cap structures to promote clotting. Blood. 2016;128 (13):1745-1755.
26. Shakhidzhanov SS, Shaturny VI, Panteleev MA, Sveshnikova AN. Modulation and preamplification of PAR1 signaling by ADP acting via the P2Y12 receptor during platelet subpopulation formation. Biochim Biophys Acta. 2015;1850(12):2518-2529.
27. Sveshnikova AN, Balatskiy AV, Demianova AS, et al. Systems biology insights into the meaning of the platelet's dual-receptor thrombin signaling. J Thromb Haemost. 2016;14(10):2045-2057.
28. Suntsova EV, Demina IM, Ignatova AA, et al. Bleeding tendency and platelet function during treatment with romiplostim in children with severe immune thrombocytopenic purpura. Int J Hematol. 2017;105 (6):841-848.
29. Ignatova AA, Ponomarenko EA, Polokhov DM, et al. Flow cytometry for pediatric platelets. Platelets. 2019;30(4):428-437.
30. Rodeghiero F, Pecci A, Balduini CL. Thrombopoietin receptor agonists in hereditary thrombocytopenias. J Thromb Haemost. 2018;16(9):1700-1710.
31. Gerrits AJ, Leven EA, Frelinger AL, 3rd, et al. Effects of eltrombopag on platelet count and platelet activation in Wiskott-Aldrich syndrome/X-linked thrombocytopenia. Blood. 2015;126(11):1367-1378.
32. Heemskerk JW, Hoyland J, Mason WT, Sage SO. Spiking in cytosolic calcium concentration in single fibrinogen-bound fura-2-loaded human platelets. Biochem J. 1992;283 (Pt 2):379-383.
33. Sveshnikova AN, Ataullakhanov FI, Panteleev MA. Compartmentalized calcium signaling triggers subpopulation formation upon platelet activation through PAR1. Mol Biosyst. 2015;11(4):1052-1060.
34. Kholmukhamedov A, Janecke R, Choo HJ, Jobe SM. The mitochondrial calcium uniporter regulates procoagulant platelet formation. J Thromb Haemost. 2018;16(11):2315-2321.
35. Ignatova A, Suntsova E, Zharkov P, et al. Evolution of platelet function and bleeding in children and adults with chronic immune trombocytopenia on romiplostim treatment. Blood. 2017;130(Suppl 1):3636.
36. Jobe SM, Wilson KM, Leo L, et al. Critical role for the mitochondrial permeability transition pore and cyclophilin D in platelet activation and thrombosis. Blood. 2008;111(3): 1257-1265.
37. Alberio L, Ravanat C, Hechler B, Mangin PH, Lanza F, Gachet C. Delayed-onset of procoagulant signalling revealed by kinetic analysis of COAT platelet formation. Thromb Haemost. 2017;117(6):1101-1114.
38. Mangin PH, Onselaer MB, Receveur N, et al. Immobilized fibrinogen activates human platelets through glycoprotein VI. Haematologica. 2018;103(5):898-907.
39. Alberio L, Safa O, Clemetson KJ, Esmon CT, Dale GL. Surface expression and functional characterization of alpha-granule factor V in human platelets: effects of ionophore A23187, thrombin, collagen, and convulxin. Blood. 2000;95(5):1694-1702.
40. Ochs HD, Filipovich AH, Veys P, Cowan MJ, Kapoor N. Wiskott-Aldrich syndrome: diagnosis, clinical and laboratory manifestations, and treatment. Biol Blood Marrow Transplant. 2009;15(1 Suppl):84-90.

ARTICLE

Histone-induced thrombotic thrombocytopenic purpura in *adamts13*$^{-/-}$ zebrafish depends on von Willebrand factor

Liang Zheng,[1] Mohammad S. Abdelgawwad,[1] Di Zhang,[1] Leimeng Xu,[1] Shi Wei,[2] Wenjing Cao[1] and X. Long Zheng[1]

Divisions of [1]Laboratory Medicine and [2]Anatomic Pathology, Department of Pathology, The University of Alabama at Birmingham, Birmingham, AL, USA

Ferrata Storti Foundation

Haematologica 2020
Volume 105(4):1107-1119

ABSTRACT

Thrombotic thrombocytopenic purpura (TTP) is caused by severe deficiency of ADAMTS13 (A13), a plasma metalloprotease that cleaves endothelium-derived von Willebrand factor (VWF). However, severe A13 deficiency alone is often not sufficient to cause an acute TTP; additional factors may be required to trigger the disease. Using CRISPR/Cas9, we created and characterized several novel zebrafish lines carrying a null mutation in *a13*$^{-/-}$, *vwf*, and both. We further used these zebrafish lines to test the hypothesis that inflammation that results in neutrophil activation and release of histone/DNA complexes may trigger TTP. As shown, *a13*$^{-/-}$ zebrafish exhibit increased levels of plasma VWF antigen, multimer size, and ability of thrombocytes to adhere to a fibrillar collagen-coated surface under flow. The *a13*$^{-/-}$ zebrafish also show an increased rate of occlusive thrombus formation in the caudal venules after $FeCl_3$ injury. More interestingly, *a13*$^{-/-}$ zebrafish exhibit ~30% reduction in the number of total, immature, and mature thrombocytes with increased fragmentation of erythrocytes. Administration of a lysine-rich histone results in more severe and persistent thrombocytopenia and a significantly increased mortality rate in *a13*$^{-/-}$ zebrafish than in wildtype (*wt*) ones. However, both spontaneous and histone-induced TTP in *a13*$^{-/-}$ zebrafish are rescued by the deletion of *vwf*. These results demonstrate a potentially mechanistic link between inflammation and the onset of TTP in light of severe A13 deficiency; the novel zebrafish models of TTP may help accelerate our understanding of pathogenic mechanisms and the discoveries of novel therapeutics for TTP and perhaps other arterial thrombotic disorders.

Introduction

Thrombotic thrombocytopenic purpura (TTP), resulting from severe deficiency of the plasma metalloprotease ADAMTS13 (A13), is characterized by thrombocytopenia and microangiopathic hemolytic anemia with various degrees of organ dysfunction.[1,2] Most patients have immune-mediated TTP, caused by an immunoglobulin G (IgG) autoantibody that inhibits plasma A13 activity;[3-7] rarely, TTP may be caused by a hereditary mutation or mutations in *A13*,[8,9] resulting in defective secretion of A13 protein, known as congenital TTP.

A13 is primarily produced in hepatic stellate cells[10,11] and released into the blood stream where it cleaves endothelium-derived ultra-large (UL) von Willebrand factor (VWF).[12] The proteolysis of ULVWF by A13 is crucial for hemostasis[1,13] and inflammation.[14,15] When the ability to cleave ULVWF is compromised, due to deficiency of plasma A13 activity, ULVWF multimers accumulate on the surface of endothelium or at the site of vascular injury, recruit platelets from circulation, and promote formation of occlusive thrombi in small arterioles and capillaries – a pathognomonic feature of TTP.[12,16] A13 and VWF are highly conserved from zebrafish to mammals,[17,18] suggesting the importance of the A13/VWF axis in biology.

In the past two decades, studies have shown that patients with severe deficiency of plasma A13 activity often do not develop an acute TTP episode until a stressful

Correspondence:

X. LONG ZHENG
xzheng@uabmc.edu or
longzheng01@gmail.com

Received: September 11, 2019.

Accepted: November 21, 2019.

Pre-published: November 21, 2019.

doi:10.3324/haematol.2019.237396

Check the online version for the most updated information on this article, online supplements, and information on authorship & disclosures: www.haematologica.org/content/105/4/1107

event.[19,20] *A13*$^{-/-}$ mice rarely develop spontaneous TTP unless they are challenged by a bacterial shigatoxin[21,22] or a large dose of recombinant VWF.[23,24] Baboons with acquired A13 deficiency develop features of TTP, but not a fatal condition.[25] These findings indicate that additional environmental or genetic factors may be necessary for triggering severe TTP on top of A13 deficiency.

The potential triggers may be infection, inflammation, and pregnancy, etc.[26] Infections or inflammation, including systemic lupus erythematosus, may cause activation of neutrophils, resulting in cell death – a process termed NETosis.[27] This may lead to release of neutrophil granular contents including human neutrophil peptides (HNP),[28] myeloperoxidase,[29] and histone-DNA complexes.[27] The plasma levels of HNP1-3,[30,31] histone-DNA complexes,[29] and other inflammatory mediators are significantly increased in patients with acute immune-mediated TTP. HNP1-3 may be prothrombotic[31,32] or anti-thrombotic,[33] depending on the context and their redox status. Increased plasma levels of histone-DNA complexes correlate with low platelet counts and disease severity.[29] However, no direct evidence is available to date to support a causative role for any of these inflammatory mediators in the pathogenesis of TTP.

To test a hypothesis that inflammatory mediators, such as histones, may play a crucial role in triggering TTP when there is a severe deficiency of A13, we generated several novel zebrafish lines with a null mutation in *a13*, *vwf*, and both using CRISPR/Cas9. These novel models were then used to assess the role of a lysine-histone, which is known to activate endothelial exocytosis, in triggering acute TTP. Zebrafish have been extensively used for modeling human diseases,[34] including thrombosis and hemostasis.[35-37] Zebrafish provide advantages over other animal models in terms of speed, cost, and high-throughput capability, enabling rapid assessment of the role of various environmental and genetic factors in triggering TTP and identification of novel therapeutics for TTP and perhaps other arterial thrombotic or inflammatory disorders.

Methods

Zebrafish

Zebrafish (*Danio rerio*) were used according to the protocol approved by Institutional the Animal Care and Use Committee. The guide RNA (gRNA) was designed using the CRISPR design tool (*http://crispr.mit.edu/*). A 69-nt oligonucleotide, consisting of a T7 promoter, a target sequence, and a gRNA scaffold, was synthesized (ThermoFisher, Waltham, MA, USA). The gRNA was then generated using a Guide-it sgRNA transcription kit (Takara-Clontech, Mountain View, CA, USA). The Cas9 mRNA was synthesized from pT3TS-nCas9n using the mMESSAGE mMACHINE T3 kit (Life Technologies, Carlsbad, CA, USA). The final products (2 nL with 12.5 pg/nL gRNA and 300 pg/nL Cas9 mRNA) were co-injected into one-cell stage embryos of a double transgenic zebrafish (*gata1*-dsRed and *fli1*-eGFP).[38,39]

Western blotting

A capillary-based western blotting system (ProteinSimple, San Jose, CA, USA) was used to determine the presence of a13 protein in plasma and embryo lysate of zebrafish. The antibody was generated commercially (ABmart, Shanghai, China) by immunization of mice with nine synthetic peptides of zebrafish a13 protein (*Online Supplementary Table S2*).

Agarose gel electrophoresis

Plasma VWF multimers were determined by western blotting with anti-vwf IgG raised against zebrafish vwf peptides (ABclonal, Woburn, MA, USA) (*Online Supplementary Figure S2*) after electrophoresis on a 1.5% sodium dodecylsulfate-agarose gel.[31]

Microfluidic assay

Microchannels (Fluxion Bioscience, San Francisco, CA, USA) were coated with a fibrillar collagen (100 μg/mL). The surface was blocked with 0.5% bovine serum albumin. Pooled whole blood collected from ten adult zebrafish and anticoagulated with PPACK (100 μM) was diluted with 50 μL of phosphate-buffered saline (PBS) and perfused under 15 dyne/cm^2 over the collagen surface. The digital images were collected every 3 seconds for 120 seconds.

Administration of a lysine-rich histone

PBS or lysine-rich histone (H5505) (Sigma-Aldrich) (200 mg/kg body weight) was injected intraperitoneally into adult zebrafish.

Blood cell counts

Zebrafish whole blood was diluted (1:51) with PBS (containing 4 mM EDTA). The total cell counts (per μL of blood) were determined using a Hemavet 950FS Hematology Analyzer (Drew Scientific, Miami Lakes, FL, USA). Additionally, flow cytometry (BD Biosciences, San Jose, CA, USA) was performed to differentiate erythrocytes, immature thrombocytes, and mature thrombocytes. The percentages of erythrocytes and thrombocytes were determined in 50,000 cells per sample. The number of thrombocytes per liter of whole blood was calculated using the formula: Thrombocyte count=Total cell counts per liter x Thrombocyte percentage x Dilution factor.

Histological assessments

Zebrafish were fixed in 4% paraformaldehyde in PBS and embedded in paraffin for hematoxylin and eosin staining. Immunohistochemistry was then performed on the fixed tissue sections with a costumer-made rabbit anti-zebrafish vwf IgG (ABclonal, Woburn, MA, USA), followed by a horseradish peroxidase-conjugated anti-rabbit IgG and color reaction.

Statistical analysis

All data are presented as the mean ± standard errors (SEM) or the median in a box-whisker plot unless specified in the figure legends. Kaplan-Meier survival analysis was performed with a log-rank test. The Mann-Whitney test was used to determine the difference between two groups, while Krüskal-Wallis analysis was used to test the significance for more than three groups. All statistical analyses were carried out using Prism 7 software.

Results

Generation and characterization of *a13*$^{-/-}$ zebrafish

To generate a stable *a13*$^{-/-}$ zebrafish line, an *in vitro* transcript consisting of gRNA and *Cas9* mRNA that targets a signal peptide of zebrafish a13 protein (Figure 1A) was injected into one-cell embryos of a double transgenic zebrafish *(gata-1*/dsRed and *fli-1*/eGFP) which expresses a red fluorescent protein under the *gata-1* promoter in erythrocytes and immature thrombocytes and a green fluorescent protein under the *fli-1* promoter in the entire vasculature and thrombocytes. Of 22 F0 founders randomly selected, 19 demonstrated the formation of heteroduplexes consistent with a heterozygous allele of *a13* (*Online Supplementary Figure 1A*). The F0 founders were then out-

bred with a *wt* zebrafish on the double transgenic background to generate F1, F2, and F3 progenies. Sanger sequencing confirmed the presence of various mutations, deletions, and insertions in the region encoding the signal peptide of a13 (*Online Supplementary Figure S1B*). The CRISPR design tool provided the sgRNA sequence that specifically targets the *a13* gene. Any additional off-target was nearly eliminated after multiple generations of outbreeding with the *wt* zebrafish (*Online Supplementary Figure S1C*).

The resulting heterozygous siblings with an 8-bp deletion in a13 (Figure 1B) were selected for generating *a13*$^{-/-}$ zebrafish for our subsequent studies. To facilitate rapid genotyping, we developed a PCR-melting curve strategy. The difference in the melting temperature of amplicons for the area of interest was dramatic between zebrafish with *wt* and those with a mutated gene (*Online Supplementary Figure S2*). This strategy provided rapid but reliable genotyping. The 8-nt deletion was predicted to introduce a premature stop within the signal peptide of a13, resulting in no expression of a13 protein, as demonstrated by an automated western blotting system (WES) in the embryo lysates (5 days post-fertilization) and plasma of all adult zebrafish tested (Figure 1C). Additionally,

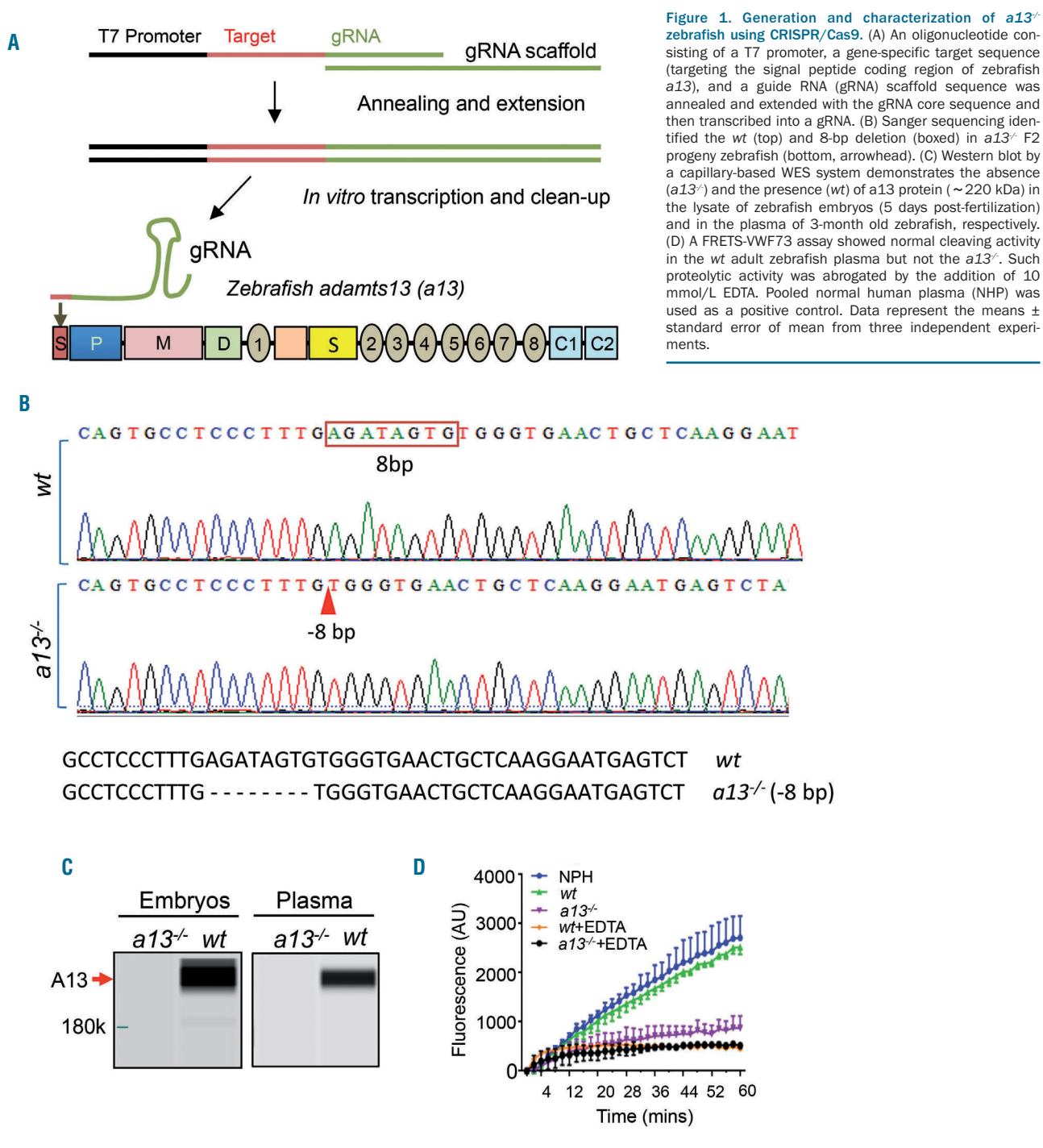

Figure 1. Generation and characterization of *a13*$^{-/-}$ zebrafish using CRISPR/Cas9. (A) An oligonucleotide consisting of a T7 promoter, a gene-specific target sequence (targeting the signal peptide coding region of zebrafish *a13*), and a guide RNA (gRNA) scaffold sequence was annealed and extended with the gRNA core sequence and then transcribed into a gRNA. (B) Sanger sequencing identified the *wt* (top) and 8-bp deletion (boxed) in *a13*$^{-/-}$ F2 progeny zebrafish (bottom, arrowhead). (C) Western blot by a capillary-based WES system demonstrates the absence (*a13*$^{-/-}$) and the presence (*wt*) of a13 protein (~220 kDa) in the lysate of zebrafish embryos (5 days post-fertilization) and in the plasma of 3-month old zebrafish, respectively. (D) A FRETS-VWF73 assay showed normal cleaving activity in the *wt* adult zebrafish plasma but not the *a13*$^{-/-}$. Such proteolytic activity was abrogated by the addition of 10 mmol/L EDTA. Pooled normal human plasma (NHP) was used as a positive control. Data represent the means ± standard error of mean from three independent experiments.

we demonstrated that there was no detectable a13 activity towards a FRETS-VWF73 substrate in zebrafish plasma (Figure 1D). Together, our results demonstrate that the *a13* gene in zebrafish is successfully deleted.

a13$^{-/-}$ zebrafish are in a prothrombotic state

Under unprovoked conditions, plasma levels of VWF antigen and multimer size were increased in *a13*$^{-/-}$ zebrafish compared with those in the *wt* controls (Figure 2A-C). When a caudal vein of a zebrafish larva (*gata-1*/dsRed and *fli-1*/eGFP) was exposed to 0.3% $FeCl_3$ (Figure 2D), an oxidative injury to vascular endothelium (the loss of green fluorescence) and an accumulation of erythrocytes (red fluorescence) were observed in *a13*$^{-/-}$ zebrafish (Figure 2E). The time to complete occlusion of the injured venule in *a13*$^{-/-}$ zebrafish was significantly shorter (mean ± SEM, 2.1±0.3 min) than that in the *wt* controls (13.6±1.8 min) (Figure 2F) (P<0.001).

To confirm the incorporation of thrombocytes into the growing thrombus, we performed a similar experiment in a different transgenic zebrafish line, in which *gata-1*/dsRed and *cd41*/eGFP were expressed to label erythrocytes (red) and thrombocytes (green), respectively. Confocal image analysis demonstrated the incorporation of thrombocytes and erythrocytes into the occlusive thrombus in the caudal vein of zebrafish larva after the oxidative injury (Figure 2G). Additionally, when anticoagulated whole blood was perfused over a fibrillar collagen-coated surface under arterial shear (15 dyne/cm^2), the surface coverage of *a13*$^{-/-}$ thrombocytes was dramatically increased compared with that of *wt* thrombocytes (Figure 2H) despite the similar initial rates of thrombocyte accumulation (Figure 2I). Supporting this, the length of thrombocyte-decorated VWF strings (mean±SEM) following perfusion of whole blood of *a13*$^{-/-}$ zebrafish (87.0±1.1 μm) was significantly longer than that following perfusion of whole blood of *wt* zebrafish (49.5±1.2 μm) (P<0.01) (Figure 2J). Together, these results demonstrate functional conservation of the a13/vwf axis in zebrafish hemostasis; and that the deletion of *a13* in zebrafish results in a prothrombotic phenotype.

a13$^{-/-}$ zebrafish develop a spontaneous but mild feature of thrombotic thrombocytopenic purpura

Using total cell counts coupled with flow cytometry, we were able to quantify total, immature, and mature thrombocytes in whole blood accurately. Under fluorescent microscope, rare mature (green) and immature (orange) thrombocytes on the background of a large number of erythrocytes could be identified (Figure 3A), as previously described.[39] The mean blood cell counts in *wt* and *a13*$^{-/-}$ adult zebrafish were 3.2 x10^{12}/L and 3.0 x10^{12}/L, respectively (P>0.05). Total thrombocytes (mean ± SEM) in *wt* zebrafish account for ~1% of total blood cells (i.e., 33.9±1.2 x10^9/L) while total thrombocytes in *a13*$^{-/-}$ zebrafish account for ~0.7% of total blood cells (i.e. 22.4±0.8 x10^9/L) (P<0.0001) (Figure 3B). There was a similar degree of reduction (~30%) in both immature (mean ± SEM, 16.5±0.6 x10^9/L) (Figure 3C) and mature (5.9±1.7 x10^9/L) (Figure 3D) thrombocytes in the *a13*$^{-/-}$ group compared with those in the *wt* controls (24.3±1.1 x10^9/L and 8.5±0.4 x10^9/L, respectively) (P<0.0001). The ratio of immature to mature thrombocytes (~74:26) was similar in both the *a13*$^{-/-}$ and *wt* groups, suggesting no thrombocyte maturation defect in *a13*$^{-/-}$ zebrafish. There was no difference in the number of total, immature, and mature thrombocytes observed between *wt* and *a13*$^{+/-}$ zebrafish (*data not shown*). The percentages of thrombocytes were also similar in different transgenic zebrafish lines *(gata1*-dsRed/*fli-1*-eGFP *vs. cd41*-mCherry) (*Online Supplementary Figure S3*), which further confirmed the accuracy of thrombocyte counts based on eGFP/dsRed expression under the *fli-1/gata-1* promotor.

Microscopic examination of the peripheral blood smears revealed the presence of fragmented erythrocytes in *a13*$^{-/-}$ (Figure 3E, right), but not in *wt* (Figure 3E, left) and *a13*$^{+/-}$ zebrafish (not shown). Quantitative analysis of more than ten blood smears from each group demonstrated a significant increase in the number of fragmented erythrocytes per high power field in *a13*$^{-/-}$ zebrafish (mean ± SEM, 3.9±2.3) compared to *wt* controls (0.4±0.5) (P<0.005) (Figure 3F). Together, our results demonstrate for the first time that *a13*$^{-/-}$ zebrafish could develop a spontaneous but mild phenotype of TTP.

Lysine-rich histone induces a more severe and persistent thrombotic thrombocytopenic purpura phenotype in *a13*$^{-/-}$ zebrafish than in *wt* ones

The plasma levels of histone/DNA complexes are significantly elevated in patients with acute thrombotic microangiopathy, including immune-mediated TTP.[29,40] When zebrafish were challenged with a single dose of lysine-rich histone, a significant drop in the number of total, immature, and mature thrombocytes within 24 to 48 h was observed in both *wt* and *a13*$^{-/-}$ zebrafish. As shown, in *wt* zebrafish the number of total (Figure 4A) and immature thrombocytes (Figure 4B) recovered within 48 h, while mature thrombocyte counts recovered 72 h after the histone challenge (Figure 4C). In *a13*$^{-/-}$ zebrafish, however, thrombocytopenia persisted after the histone challenge for the entire duration of observation (14 days) (Figure 4D). This was not the result of a decrease in immature thrombocytes (Figure 4E) but rather a reduction in mature thrombocytes (Figure 4F). At the end of 14 days after histone challenge, there were statistically significant differences in total (Figure 4G), immature (Figure 4H), and mature (Figure 4I) thrombocyte counts between *wt* and *a13*$^{-/-}$ zebrafish. Histone challenge also resulted in a marked reduction of erythrocyte counts in *a13*$^{-/-}$ zebrafish but not *wt* ones (*Online Supplementary Figure S4*). Together, these results indicate that an inflammatory mediator such as histone may trigger acute TTP in individuals with severe A13 deficiency.

Kaplan-Meier survival analysis demonstrated a higher mortality rate (~30%) in *a13*$^{-/-}$ zebrafish than in *wt* zebrafish (~10%) following the histone challenge (P=0.0002) (Figure 5A). No spontaneous death occurred in either *wt* or *a13*$^{-/-}$ zebrafish over a 6-month period of observation without additional stress. To determine whether neutrophil activation and death or other tissue injuries occurred in zebrafish that were challenged with histones, we determined plasma levels of histone/DNA complexes in zebrafish prior to (D0) and 7 days (D7) after histone challenge which allowed for the exogenous histone to be cleared. We showed that while there was no statistically significant difference in the plasma levels of histone/DNA complexes between *wt* and *a13*$^{-/-}$ zebrafish prior to histone challenge, there were significantly higher levels of these complexes in *a13*$^{-/-}$ than *wt* zebrafish 7 days after histone challenge when thrombocytopenia persisted

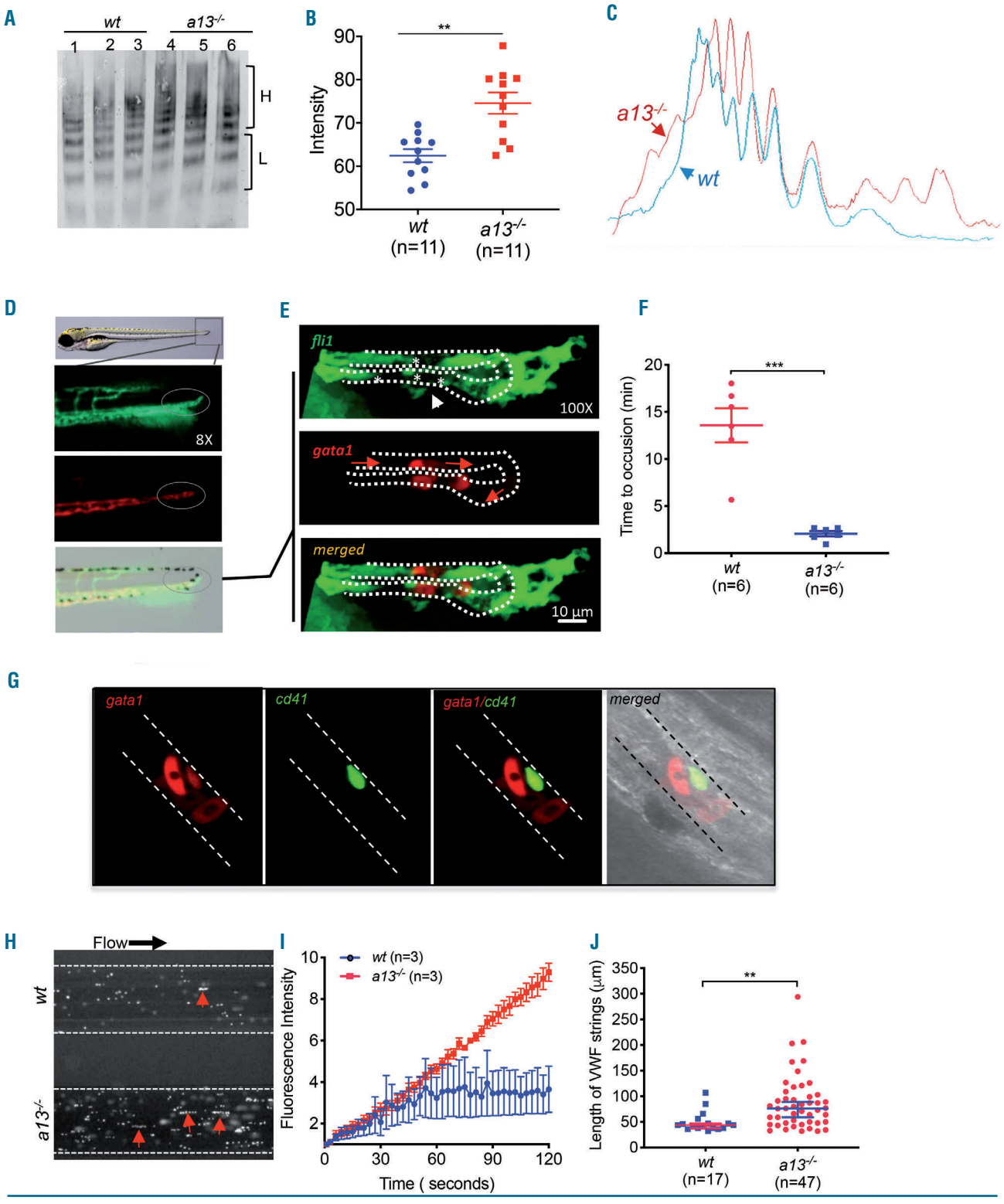

Figure 2. von Willebrand factor multimer and thrombus formation in *wt* and *a13*$^{-/-}$ zebrafish. (A) Plasma von Willebrand factor (VWF) multimers in *wt* (lanes 1-3) and *a13*$^{-/-}$ (lanes 4-6) zebrafish aged 3-4 months. Here, H and L on the right margin indicate high and low molecular weight VWF multimers, respectively. (B) Quantification of plasma VWF antigen levels by densitometry (all multimers in each sample were scanned together) in *wt* and *a13*$^{-/-}$ zebrafish. **P<0.01, Mann-Whitney test. (C) Representative densitometric scanning profiles of plasma vwf multimers in *a13*$^{-/-}$ (red) and *wt* (blue) zebrafish. (D) The caudal areas of zebrafish endogenously expressing *fli-1*/eGFP and *gata-1*/sRed: the square or ovals show where a drop of 0.3% ferric chloride was placed topically. (E) Confocal images demonstrated the presence of thrombocytes (red) and loss of endothelial integrity (green) in the caudal vessels (outlined with dotted lines). The red arrows indicate the direction of blood flow from artery to vein. (F) Quantitative data showing the time to complete occlusion in the caudal vessel in *wt* and *a13*$^{-/-}$ zebrafish after injury induced by 0.3% ferric chloride. ***P<0.005, Mann-Whitney test. (G) Confocal image demonstrated the incorporation of both erythrocytes (red) and thrombocytes (green) into the occlusive thrombus in the caudal vein of *wt* zebrafish endogenously expressing *gata-1*/dsRed (red blood cells) and *cd41*/eGFP (thrombocytes) after being exposed to 0.3% ferric chloride. (H) The surface coverage of fluorescent thrombocytes on a fibrillar collagen-coated surface in the microfluidic channel after perfusion of diluted whole blood (1:20), obtained from *wt* (top) and *a13*$^{-/-}$ (bottom) zebrafish, under arterial shear (15 dyne/cm^2). Red arrows indicate the thrombocyte-decorated strings formed on a vwf/collagen fiber. (I, J) The rate of fluorescence accumulation (means ± SEM, n=3) (I) and the lengths of thrombocyte-decorated strings (means ± SEM) (J), following perfusion of a diluted whole blood from *wt* and *a13*$^{-/-}$ zebrafish. **P<0.01, Mann-Whitney test.

(Figure 5B). These results suggest that histone and/or histone/DNA complexes may not only be biomarkers for acute TTP, but also potential triggers for such a potentially fatal syndrome.

Histology of tissue sections revealed the presence of multiple large microvascular thrombi primarily in the liver (Figure 5C-i) and mesenteric vessels (*not shown*) in *a13*$^{-/-}$ zebrafish after histone challenge, but rare, small thrombi in *wt* zebrafish following the same treatment (Figure 5C-ii). Under unprovoked conditions, there were occasional small microvascular thrombi in *a13*$^{-/-}$ zebrafish (Figure 5C-iii), but not in *wt* zebrafish (Figure 5C-iv). Quantitation of microvascular thrombi in multiple stained tissue sections of various organs demonstrated that a single dose of histone resulted in the formation of significantly more microvascular thrombi in the *a13*$^{-/-}$ than in the *wt* zebrafish (P<0.0001) (Figure 5D. Immunohistochemical analysis showed the presence of VWF-rich thrombi in the liver parenchyma in *a13*$^{-/-}$ zebrafish following histone challenge (Figure 5E, top). An omission of the primary antibody resulted in the complete absence of staining (Figure 5E, bottom). Agarose gel electrophoresis plus western blotting demonstrated the increased levels of plasma VWF antigen and multimer size 24 h (D1) after histone challenge in *a13*$^{-/-}$, but not in *wt* zebrafish after the same histone challenge (Figure 5F). Also, consumption of ULVWF in zebrafish with acute TTP was observed between days 3-7 (Figure 5F), consistent with findings in patients.[41] Together, these

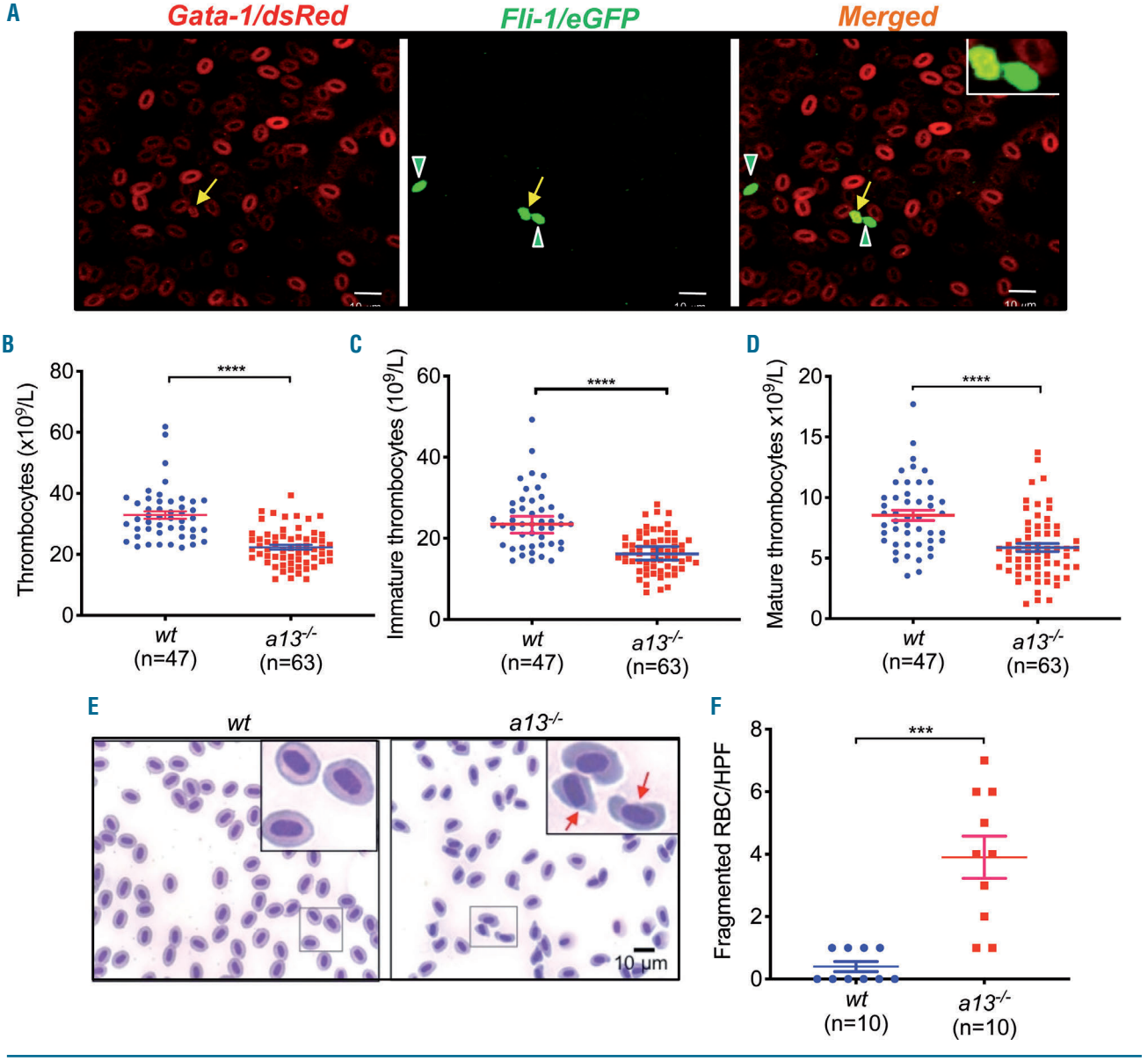

Figure 3. Microscopic and flow cytometric analyses of erythrocytes and/or thrombocytes in *wt* and *a13*$^{-/-}$ zebrafish. (A) The fluorescent microscopic images of erythrocytes (left, red) on the background, rare mature thrombocytes (middle, green with open arrowheads) and immature thrombocytes (right, yellow with an arrow). (B-D) The numbers of total (B), immature (C), and mature (D) thrombocytes in *wt* and *a13*$^{-/-}$ zebrafish at the age of 3 months. Bars within the dots indicate the means ± standard error of mean (SEM). ****P<0.0001, Mann-Whitney test. (E) Microscopic images of normal and fragmented nucleated erythrocytes (inset, arrows) in Geimsa-stained peripheral blood smears from *wt* and *a13*$^{-/-}$ zebrafish as indicated. (F) The number of fragmented erythrocytes per high power field (HPF) in the peripheral blood smear of *wt* and *a13*$^{-/-}$ zebrafish (100x). The lines within the individual dots represent the mean ± SEM (n=10). ***P<0.005, Mann-Whitney test.

results demonstrate that a lysine-rich histone may trigger an acute episode of TTP in *a13*$^{-/-}$ zebrafish.

Generation and characterization of *vwf*$^{-/-}$ and *a13*$^{-/-}$*vwf*$^{-/-}$ zebrafish

Lysine-rich histone is known to trigger the release of VWF from endothelial cells and enhance thrombus formation after vascular injury.[42] To assess the contribution of VWF in this model, we first treated cultured endothelial cells with a lysine-histone, at the concentration used in zebrafish experiments, for various times. We found that lysine-histone induced rapid release of VWF from the cultured endothelial cells, which bound fluorescein-labeled platelets in whole blood from *a13*$^{-/-}$ mice under arterial flow (*Online Supplementary Figure S5*). We then deleted *vwf* from zebrafish to see if *vwf*$^{-/-}$ zebrafish were protected from the development of TTP, either spontaneously or triggered by histone. To this end, we generated a *vwf*$^{-/-}$ zebrafish line by targeting the *vwf* gene encoding the propeptide region using the CRISPR-cas9 (Figure 6A). A 7-bp insertion mutant of *vwf* was identified by Sanger sequencing (Figure 6B), which was predicted to form a

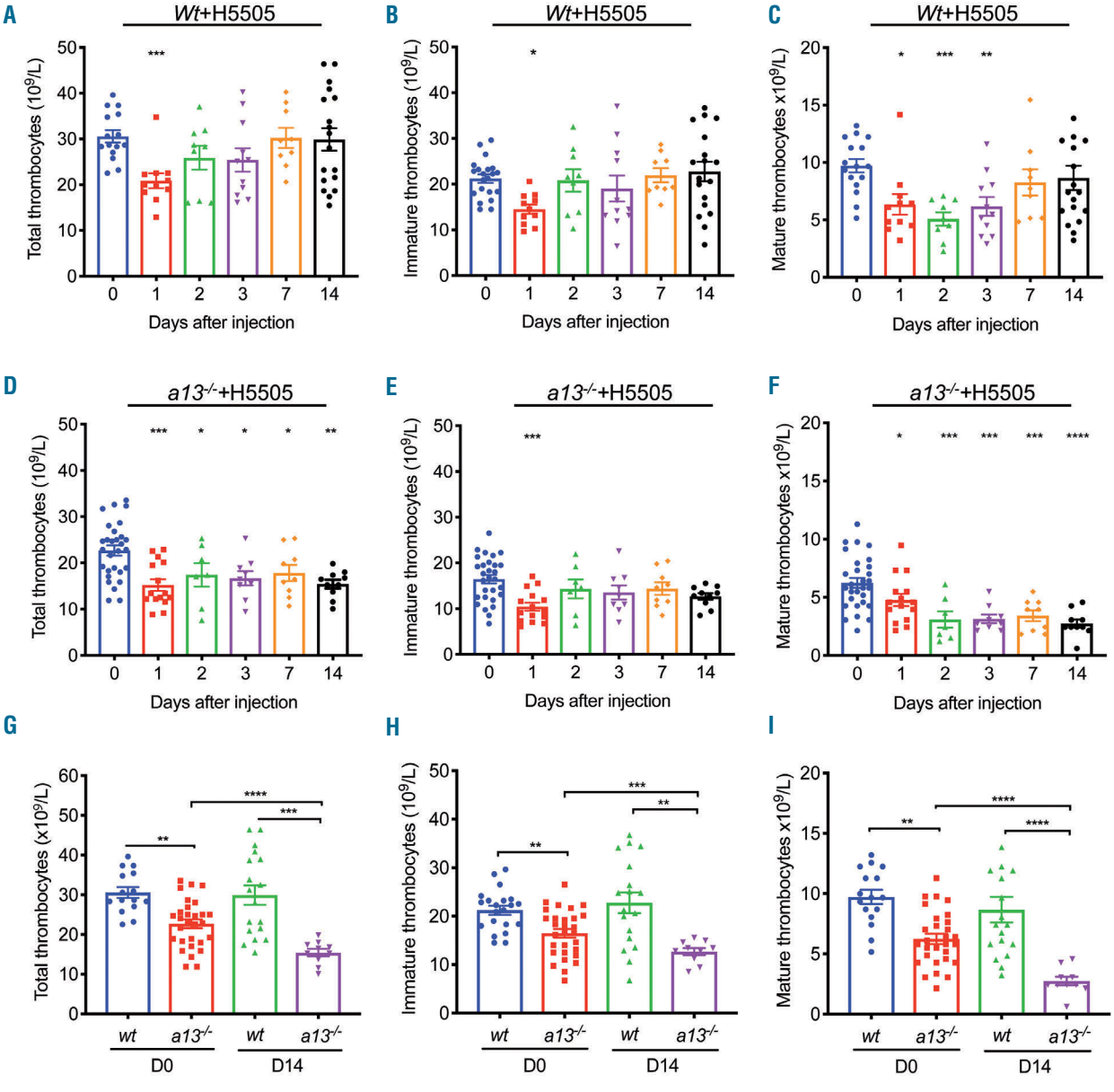

Figure 4. Lysine-rich histone induced more severe and persistent thrombocytopenia in *a13*$^{-/-}$ than in *wt* zebrafish. (A-C) The numbers of total (A), immature (B), and mature (C) thrombocytes per liter in wt zebrafish over 14 days after being challenged with 200 mg/kg body weight of a lysine-rich histone (H5505). (D-F) The numbers of total (D), immature (E), and mature (F) thrombocytes per liter in *a13*$^{-/-}$ zebrafish over 14 days following the same dose of lysine-histone (H5505) challenge. (G-I) Direct comparisons of total (G), immature (H), and mature (I) thrombocytes per liter between wt and *a13*-/- zebrafish prior to (D0) and 14 days (D14) following the histone (H5505) challenge. Kruskal-Wallis analysis was used to determine the difference among three or more groups (A-F), while the Mann-Whitney test was used to determine the difference between each two groups (G-I). All data are presented as dots, means, and ± standard error of mean. *P<0.05, **P<0.01, ***P<0.005, and ****P<0.0001.

premature stop within the propeptide, resulting in a *vwf*-null phenotype. Western blotting demonstrated the presence of vwf multimers in plasma of *wt*, but not *vwf*$^{-/-}$ (Figure 6C) or *a13*$^{-/-}$*vwf*$^{-/-}$ (*not shown*) zebrafish. These results demonstrate the successful deletion of the *vwf* gene in zebrafish.

To further assess zebrafish *vwf* function, we performed a microfluidic assay using whole blood from *wt* and *vwf*$^{-/-}$ zebrafish. When perfused through a fibrillar collagen-coated surface under arterial shear, the final surface coverage of fluorescein-labeled thrombocytes (Figure 6E) and the rate of thrombocyte adhesion and aggregation (Figure 6F) onto the collagen surface were dramatically reduced in *vwf*$^{-/-}$ and *a13*$^{-/-}$*vwf*$^{-/-}$ zebrafish compared with the *wt* controls (P<0.0001). Moreover, the time to form an occlusive thrombus, determined by intravital microscopy, in the caudal vein in *vwf*$^{-/-}$ or *a13*$^{-/-}$*vwf*$^{-/-}$ zebrafish after $FeCl_3$ injury was significantly prolonged when compared to that in the *wt* controls (Figure 6D). All *wt* zebrafish formed occlusive thrombi within 20 min after $FeCl_3$ injury, but nearly 50% of *vwf*$^{-/-}$ or *a13*$^{-/-}$*vwf*$^{-/-}$ zebrafish failed to form occlusive thrombi. These results demonstrate the relatively deficient hemostatic functions in *vwf*$^{-/-}$ and *a13*$^{-/-}$*vwf*$^{-/-}$ zebrafish.

vwf$^{-/-}$ and *a13*$^{-/-}$*vwf*$^{-/-}$ zebrafish are protected from developing spontaneous and histone-induced thrombocytopenia

Under unprovoked conditions, *vwf*$^{-/-}$ zebrafish with or without circulating plasma a13 exhibited normal counts of total (Figure 7A), immature (Figure 7B), and mature (Figure 7C) thrombocytes. Moreover, when challenged with a lysine-rich histone (H5505), *vwf*$^{-/-}$ or *a13*$^{-/-}$*vwf*$^{-/-}$ zebrafish exhibited no significant reduction in the numbers of total (Figure 7D, G), immature (Figure 7E, H), and mature (Figure 7F, I) thrombocytes over a 7-day period. However, 7 days after the histone challenge, there were significantly lower numbers of total (Figure 7J), immature (Figure 7K), and mature (Figure 7L) thrombocytes in *a13*$^{-/-}$ than in *a13*$^{-/-}$*vwf*$^{-/-}$ zebrafish. Together, these results demonstrate that *vwf*$^{-/-}$ zebrafish with or without circulating A13 are protected from developing spontaneous or histone-induced TTP.

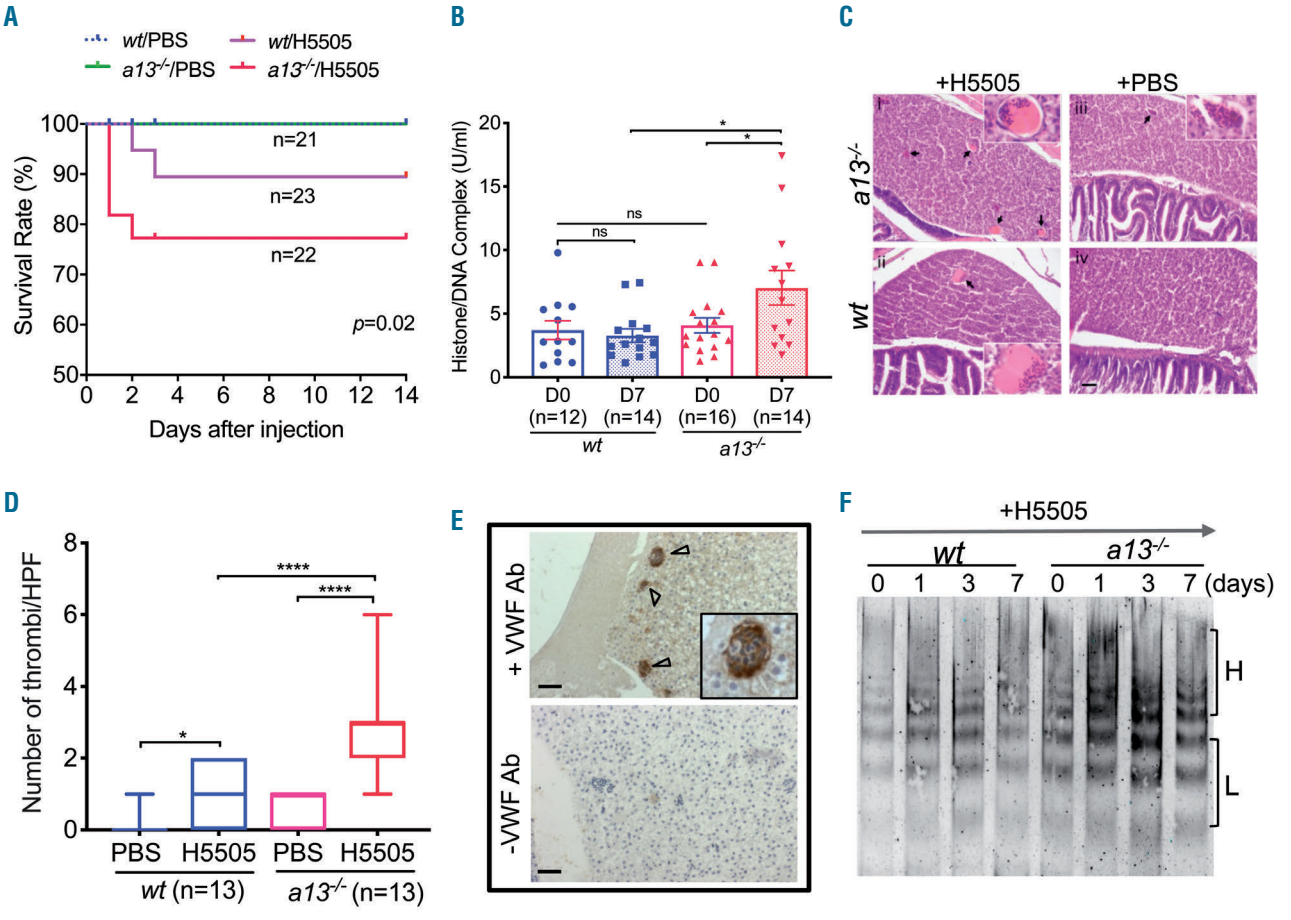

Figure 5. Kaplan-Meier survival analysis, plasma histone/DNA complexes, histology and von Willebrand factor multimers in *wt* and *a13*$^{-/-}$ zebrafish after histone challenge. (A) Survival rate (%) over a 2-week period in *wt* and *a13*$^{-/-}$ zebrafish after being challenged with phosphate-buffered saline (PBS) or lysine-rich histone (H5505) (200 mg/kg body weight). (B) Plasma levels of histone-DNA complexes in *wt* and *a13*$^{-/-}$ zebrafish prior to (D0) and day 7 (D7) following the histone (H5505) challenge. (C) Histological images of occlusive microvascular thrombi (arrowheads) in the liver tissue from *a13*$^{-/-}$ (top) and *wt* (bottom) zebrafish following lysine-histone (H5505) (left) or PBS challenge (right). (D) The numbers of microvascular thrombi per tissue section (box-and-whisker plot, with minimum to maximum) in *wt* and *a13*$^{-/-}$ zebrafish following the histone (H5505) or PBS challenge. A Mann-Whitney test was performed to test differences between two groups. *P<0.05, **P<0.01, ***P<0.005, and ****P<0.001. (E) Immunohistochemical staining showing von Willebrand factor (VWF)-rich microvascular thrombi (top, arrowheads). Scale bar represents 200 μm in length. (F) Plasma vwf multimer distribution in *wt* and *a13*$^{-/-}$ zebrafish prior to (D0), 1, 3, and 7 days after the histone (H5505) challenge. Here, H and L on the right margin indicate high and low molecular weight VWF multimers, respectively.

Discussion

The present study represents the first establishment and characterization of zebrafish models of TTP and the illustration of a potential trigger for the disorder on top of A13 deficiency. The *a13*$^{-/-}$ zebrafish exhibit a prothrombotic phenotype with increased levels of plasma VWF antigen and multimer size. This results in an enhanced ability of thrombocytes to adhere and aggregate on a fibrillar collagen surface under arterial flow. Additionally, *a13*$^{-/-}$ zebrafish show an accelerated rate of thrombus formation following oxidative injury. Such a prothrombotic phenotype in *a13*$^{-/-}$ zebrafish is completely rescued when *vwf* is genetically deleted, suggesting that the prothrombotic phenotype in *a13*$^{-/-}$ zebrafish can be attributed to the enhanced VWF function *in vivo*.

More interestingly, *a13*$^{-/-}$ zebrafish develop a spontaneous but mild TTP phenotype, which is characterized by low thrombocyte and erythrocyte counts with an increased number of fragmented red blood cells, as well as the formation of small occlusive thrombi in organ tissues. Such a TTP phenotype in the *a13*$^{-/-}$ zebrafish is significantly worsened and sometimes fatal following challenge with a lysine-rich histone, which has previously been shown to trigger endothelial exocytosis and release of ULVWF multimers from Weibel-Palade bodies of activated endothelium.[42] An intravenous administration of histones induces transient thrombocytopenia in mice,[43] although the mechanism underlying this transient effect is not known. We show here that both the spontaneous and histone-induced

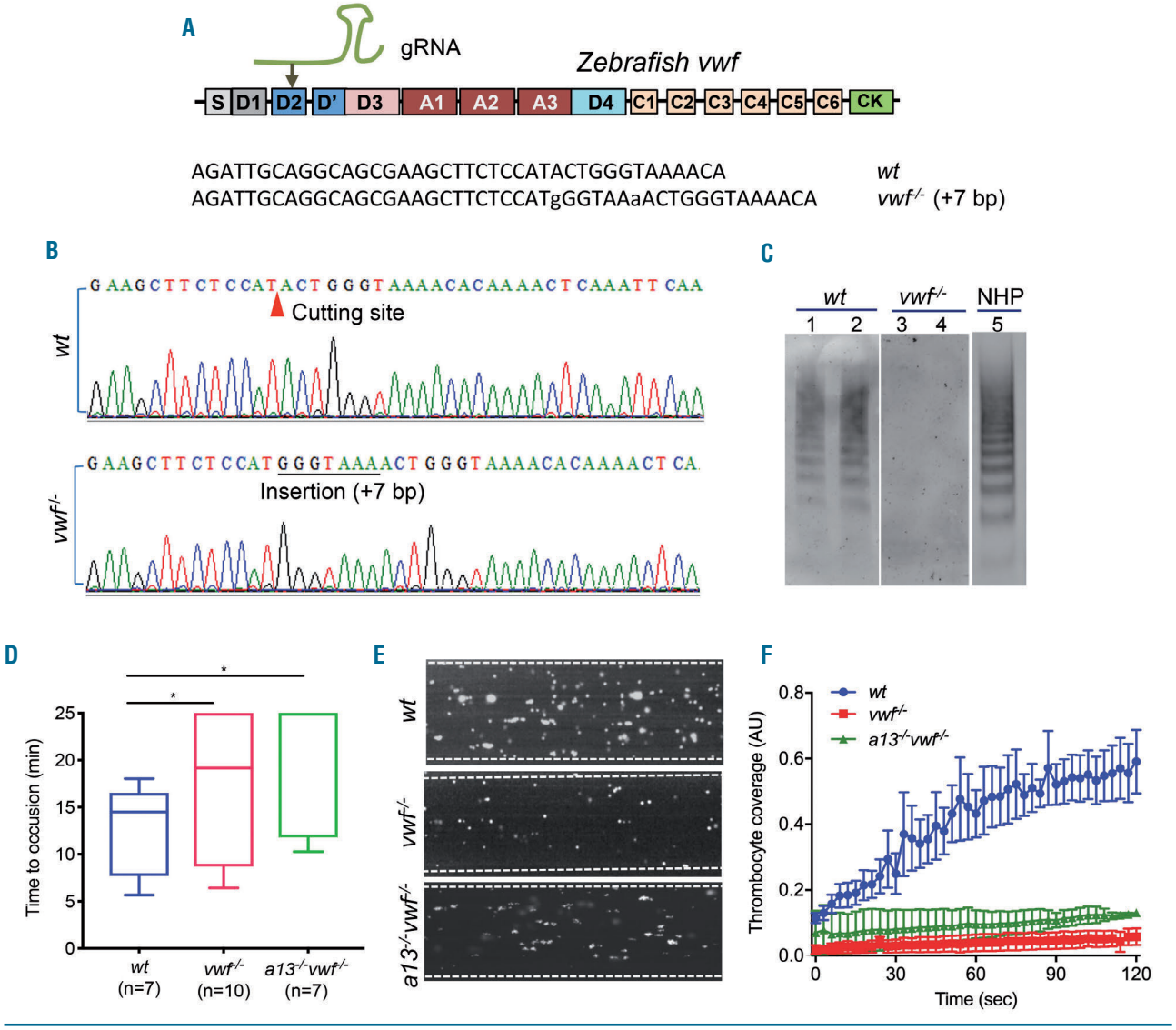

Figure 6. Generation and characterization of *vwf*$^{-/-}$ and *a13*$^{-/-}$*vwf*$^{-/-}$ zebrafish using CRISPR/Cas9. (A) A guide RNA (gRNA) oligonucleotide was used to target the propeptide D2 domain-coding region of zebrafish vwf. (B) Sanger sequencing confirming the wildtype (*wt*) sequence and the 7-bp insertion in the targeted region, as indicated, which results in vwf null by causing a frameshift and introduction of a premature stop. (C) Agarose gel electrophoresis and western blotting with a specific antibody raised against zebrafish VWF, demonstrating the presence of VWF multimers in *wt* plasma (2 and 4 μL in lane 1 and 2, respectively), but not in *vwf*$^{-/-}$ plasma (2 and 4 μL in lanes 3 and 4) at the age of 3 months. Normal human plasma (NHP) (0.5 μL) was used as a positive control (lane 5), run in a separate gel and blotted with an anti-human VWF IgG. (D) The time to form occlusive thrombi in *wt*, *vwf*$^{-/-}$, and *a13*$^{-/-}$*wf*$^{-/-}$ zebrafish after $FeCl_3$ injury at the caudal venule (box-and-whisker plots, with minimum to maximum). (E, F) The representative surface coverage and rate of accumulation of fluorescent thrombocytes (mean ± standard error of mean, n=3), respectively, on a fibrillar collagen surface following perfusion of a diluted whole blood from *wt*, *vwf*$^{-/-}$, and *a13*$^{-/-}$*vwf*$^{-/-}$ zebrafish under arterial shear (15 dyne/cm^2), as indicated.

TTP phenotype in *a13*$^{-/-}$ zebrafish is essentially eliminated when *vwf* is genetically deleted. Consistent with this result, the deletion of *vwf* also confers a*13*$^{-/-}$ zebrafish embryos resistance to histone challenge. Together, these findings indicate that VWF contributes to the pathophysiology of spontaneous and histone-induced thrombocytopenia or TTP in *a13*$^{-/-}$ zebrafish.

The structure and function of VWF are conserved from zebrafish to mammals with an overall similarity at the protein level of ~45%.[17] Plasma VWF multimers in zebrafish, visualized for the first time in this study, and recombinantly expressed VWF multimers reported previously,[17] are quite similar in pattern. Furthermore, zebrafish VWF is shown to interact with thrombocytes during

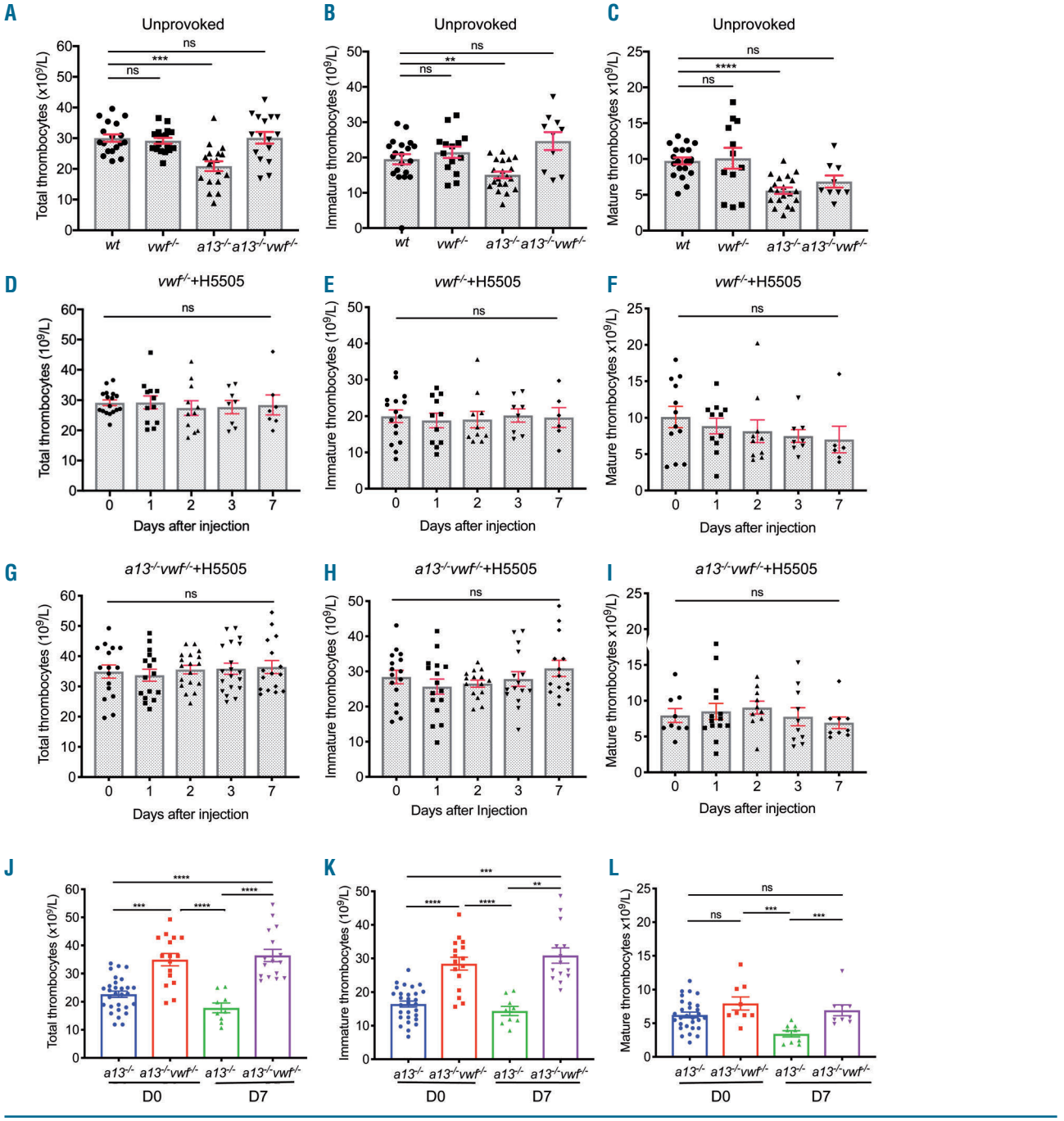

Figure 7. Deletion of *vwf* rescued histone-induced thrombotic thrombocytopenic purpura in *a13*$^{-/-}$ zebrafish. (A-C) The number of total (A), immature (B), and mature (C) thrombocytes per liter in *wt*, *vwf*$^{-/-}$, *a13*$^{-/-}$, and *vwf*$^{-/-}$*a13*$^{-/-}$ zebrafish at age of 3 months without any challenge. Kruskal-Wallis analysis was performed. (D-F) The number of total (D), immature (E), and mature (F) thrombocytes per liter in *vwf*$^{-/-}$ zebrafish prior to (D0), 1, 2, 3, and 7 days following histone (H5505) challenge. (G-I) The number of total (G), immature (H), and mature (I) thrombocytes per liter in *a13*$^{-/-}$*vwf*$^{-/-}$ zebrafish prior to (D0), 1, 2, 3, and 7 days following histone (H5505) challenge. (J-L) Direct comparisons of total (J), immature (K), and mature (L) thrombocytes per liter between *a13*$^{-/-}$ and *a13*$^{-/-}$*vwf*$^{-/-}$ zebrafish prior to (D0) and 7 days (D7) after histone (H5505) challenge. All data are expressed as individual values (dots) and the means ± standard error of mean. Kruskal-Wallis analysis and the Mann-Whitney test were used to determine the statistical significances among three or more groups and between two groups, respectively. ns: no statistically significant difference; **P*<0.05, ***P*<0.01, ****P*<0.005, and *****P*<0.001, respectively.

thrombus formation in our study. In the absence of circulating VWF, thrombocytes fail to adhere to the fibrillar collagen surface under flow and thrombus formation is significantly impaired in the small vessels after injury. During the revision of this manuscript, similar hemostatic defects were reported to occur when *vwf* is independently knocked out.[44] These findings support the crucial physiological function of zebrafish VWF in mediating thrombocyte adhesion/aggregation and thrombus formation.

The A13 protein in zebrafish is also conserved with a similar domain structure to that in mammals except for a longer signal peptide and propeptide. There is ~52% sequence similarity at the A13 protein level between zebrafish and humans (or mice). Surprisingly, zebrafish plasma A13 is able to cleave the human FRETS-rVWF73[45] at the similar rate as human plasma A13 does. This activity is abrogated by EDTA, which chelates divalent metal ions, suggesting that zebrafish A13 is also a metalloprotease. Additional evidence to support this notion is that plasma VWF multimers and thrombocyte-decorated VWF strings on the fibrillar collagen surface under flow are significantly increased in *a13*$^{-/-}$ zebrafish when compared with those in *wt* controls. The rate of thrombus formation in the caudal venules after oxidative injury is also dramatically accelerated in *a13*$^{-/-}$ zebrafish. More interestingly, *a13*$^{-/-}$ zebrafish develop a spontaneous but non-fatal TTP phenotype, similar to that in some patients with congenital TTP[20,46] and in a baboon model of acquired TTP induced by passive immunization.[25] Together, these results suggest that mild TTP may be compatible with life, but the affected individuals may have a significantly increased risk of developing catastrophic or potentially fatal TTP when an additional environmental trigger, such as infection or pregnancy, is present.

Infection or systemic inflammation often precedes the onset of TTP, which is thought to activate neutrophils, resulting in the release of their intracellular contents, including antimicrobial HNP1-3, proteolytic enzymes, nucleic acids, and histone-DNA complexes.[29,42] Plasma levels of histone-DNA complexes are markedly elevated in patients with acute TTP.[40] Although the causes of elevated levels of plasma histone-DNA are not fully understood. Histone-DNA has been shown to have deleterious effects with prothrombotic properties. Histones may activate platelets, enhance thrombin generation,[47] induce exocytosis of endothelial Weibel-Palade bodies, and trigger the release of ULVWF from endothelium.[42] Histones may also activate complement, resulting in the formation of a membrane attack complex that injures endothelium.[48] Based on our results and those published in the literature, we hypothesize that histones, likely derived from NETosis and other cell death after injury, are potent triggers for TTP. When plasma A13 activity is present, the released ULVWF multimers are rapidly cleaved into smaller forms.

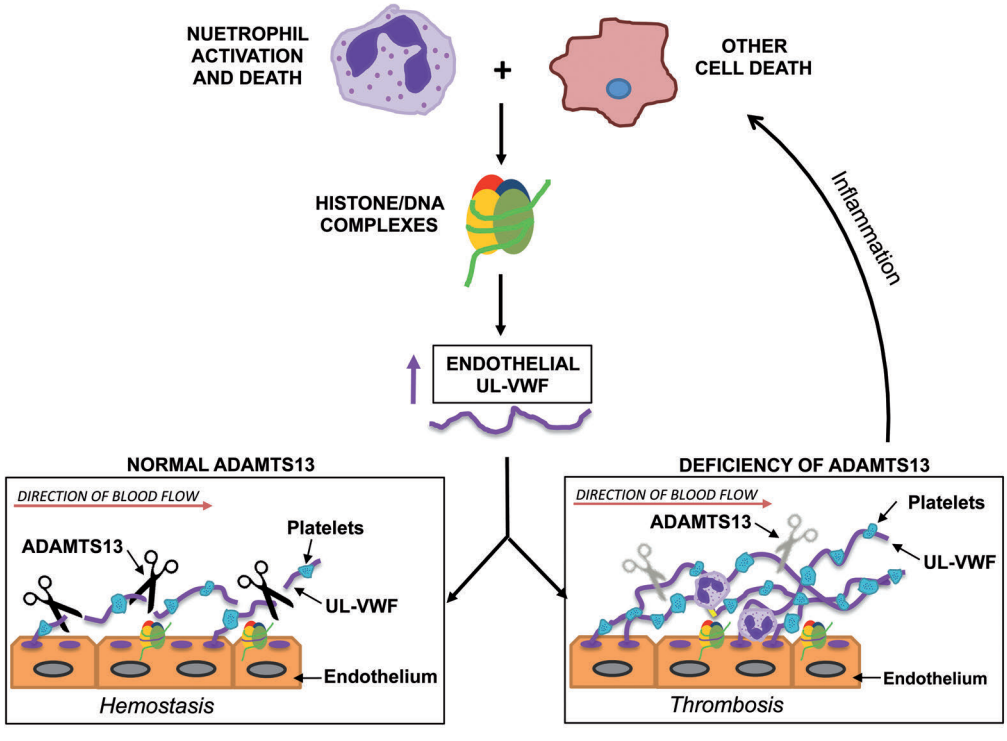

Figure 8. A proposed working model depicts how neutrophil activation and the release of histones induce microvascular thrombosis in *a13*$^{-/-}$ zebrafish. Infection and/or systemic inflammation may activate neutrophils and result in neutrophil death and tissue injury, leading to the release of their cellular contents including histone/DNA complexes or free histone. Histone/DNA complexes or free histone may then bind to endothelial receptors, which triggers exocytosis of Weibel-Palade bodies and the release of ultralarge multimers of von Willebrand factor (UL-VWF) from activated endothelium. These hyperactive UL-VWF multimers are rapidly removed by plasma ADAMTS13, so that normal hemostasis is maintained. However, when plasma ADAMTS13 is absent, as in cases of hereditary or acquired thrombotic thrombocytopenic purpura (TTP), the UL-VWF strings are not removed from the endothelial surface, resulting in an accumulation of platelets/thrombocytes and neutrophils, leading to thrombus formation and acute inflammation at sites of vascular injury. In the end, activation of the coagulation cascade, complement, and neutrophils may occur, resulting in further tissue damage and microvascular thrombosis, the characteristic pathological feature of TTP.

This prevents excessive thrombus formation at the sites of vascular injury; when plasma A13 activity is absent, the released ULVWF remain anchored on the endothelial surface, which can capture flowing platelets in circulation, resulting in occlusive thrombi and acute inflammation at the sites of vascular injury. This creates a positive feedback, resulting in more inflammation and cell death, which leads to the formation of a vicious cycle (Figure 8).

In conclusion, we report the generation and characterization of several novel zebrafish lines (*a13*$^{-/-}$, *vwf*$^{-/-}$, and *a13*$^{-/-}$*vwf*$^{-/-}$) and zebrafish models of TTP. With these new tools, we are able to demonstrate potentially mechanistic links between infection, innate immunity (such as neutrophil activation and the release of histone/DNA complexes), and the onset and progression of TTP in the setting of severe deficiency of plasma A13 activity. These novel zebrafish models with a robust high-throughput screening capability could help accelerate the discovery of potentially novel therapeutics for TTP and many other arterial thrombotic disorders, in which treatment options are quite limited.

Acknowledgments

This study was supported in part by a grant from the National Institutes of Health (HL126724) to XLZ and a postdoctoral fellowship (18POST33960098) to LZ from the American Heart Association. The authors also thank Drs. Daniel Gorelick and Shannon Romano from the Department of Pharmacology and Toxicology at UAB for providing a double transgenic zebrafish line expressing fli-1eGFP and gata-1dsRed, Dr. Susan Farmer at the Zebrafish Research Facility for providing wildtype zebrafish, and Drs. Robert I. Handin and Dongdong Ma, at Harvard Medical School, Boston, MA for helping us with the cd41-mCherry transgenic zebrafish line. The authors thank Nicole Kocher at UAB for her assistance and critical reading of this paper prior to its submission.

References

1. Zheng XL. ADAMTS13 and von Willebrand factor in thrombotic thrombocytopenic purpura Annu Rev Med. 2015;66:211-225.
2. Rock GA, Shumak KH, Buskard NA, et al. Comparison of plasma exchange with plasma infusion in the treatment of thrombotic thrombocytopenic purpura. Canadian Apheresis Study Group. N Engl J Med. 1991;325(6):393-397.
3. Tsai HM, Lian EC. Antibodies to von Willebrand factor-cleaving protease in acute thrombotic thrombocytopenic purpura. N Eng J Med. 1998;339(22):1585-1594.
4. Zheng XL, Wu HM, Shang D, et al. Multiple domains of ADAMTS13 are targeted by autoantibodies against ADAMTS13 in patients with acquired idiopathic thrombotic thrombocytopenic purpura. Haematologica. 2010;95(9):1555-1562.
5. Ostertag EM, Bdeir K, Kacir S, et al. ADAMTS13 autoantibodies cloned from patients with acquired thrombotic thrombocytopenic purpura: 2. Pathogenicity in an animal model. Transfusion. 2016;56(7):1775-1785.
6. Casina VC, Hu W, Mao JH, et al. High-resolution epitope mapping by HX MS reveals the pathogenic mechanism and a possible therapy for autoimmune TTP syndrome. Proc Natl Acad Sci U S A. 2015;112(31):9620-9625.
7. Thomas MR, de Groot R, Scully MA, Crawley JT. Pathogenicity of anti-ADAMTS13 autoantibodies in acquired thrombotic thrombocytopenic purpura. EBioMedicine. 2015;2(8):942-952.
8. Levy GG, Nichols WC, Lian EC, et al. Mutations in a member of the ADAMTS gene family cause thrombotic thrombocytopenic purpura. Nature. 2001;413(6855):488-494.
9. Zheng XL, Sadler JE. Pathogenesis of thrombotic microangiopathies. Annu Rev Pathol. 2008;3:249-277.
10. Uemura M, Tatsumi K, Matsumoto M, et al. Localization of ADAMTS13 to the stellate cells of human liver. Blood. 2005;106(3):922-924.
11. Zhou W, Inada M, Lee TP, et al. ADAMTS13 is expressed in hepatic stellate cells. Lab Invest. 2005;85(6):780-788.
12. Dong JF, Moake JL, Nolasco L, et al. ADAMTS-13 rapidly cleaves newly secreted ultralarge von Willebrand factor multimers on the endothelial surface under flowing conditions. Blood. 2002;100(12):4033-4039.
13. Sadler JE. von Willebrand factor: two sides of a coin. J Thromb Haemost. 2005;3(8):1702-1709.
14. Chauhan AK, Kisucka J, Brill A, et al. ADAMTS13: a new link between thrombosis and inflammation. J Exp Med. 2008;205(9):2065-2074.
15. De Meyer SF, Savchenko AS, Haas MS, et al. Protective anti-inflammatory effect of ADAMTS13 on myocardial ischemia/reperfusion injury in mice. Blood. 2012;120(26):5217-5223.
16. Arya M, Anvari B, Romo GM, et al. Ultralarge multimers of von Willebrand factor form spontaneous high-strength bonds with the platelet glycoprotein Ib-IX complex: studies using optical tweezers. Blood. 2002;99(11):3971-3977.
17. Ghosh A, Vo A, Twiss BK, et al. Characterization of zebrafish von Willebrand factor reveals conservation of domain structure, multimerization, and intracellular storage. Adv Hematol. 2012;2012:214209.
18. Jin SY, Skipwith CG, Zheng XL. Amino acid residues Arg(659), Arg(660), and Tyr(661) in the spacer domain of ADAMTS13 are critical for cleavage of von Willebrand factor. Blood. 2010;115(11):2300-2310.
19. Fujimura Y, Kokame K, Yagi H, et al. Hereditary deficiency of ADAMTS13 activity: Upshaw-Schulman syndrome. In: Rodgers GM, ed. ADAMTS13 Biology and Disease. Cham, Heidlberg, New York, Dordrecht, London: Springer. 2015:73-90.
20. Fujimura Y, Matsumoto M, Isonishi A, et al. Natural history of Upshaw-Schulman syndrome based on ADAMTS13 gene analysis in Japan. J Thromb Haemost. 2011;9 Suppl 1:283-301.
21. Motto DG, Chauhan AK, Zhu G, et al. Shigatoxin triggers thrombotic thrombocytopenic purpura in genetically susceptible ADAMTS13-deficient mice. J Clin Invest. 2005;115(10):2752-2761.
22. Jin SY, Xiao J, Bao J, et al. AAV-mediated expression of an ADAMTS13 variant prevents shigatoxin-induced thrombotic thrombocytopenic purpura. Blood. 2013;121(19):3825-3829.
23. Schiviz A, Wuersch K, Piskernik C, et al. A new mouse model mimicking thrombotic thrombocytopenic purpura: correction of symptoms by recombinant human ADAMTS13. Blood. 2012;119(25):6128-6135.
24. Pickens B, Mao Y, Li D, et al. Platelet-delivered ADAMTS13 inhibits arterial thrombosis and prevents thrombotic thrombocytopenic purpura in murine models. Blood. 2015;125(21):3326-3334.
25. Feys HB, Roodt J, Vandeputte N, et al. Thrombotic thrombocytopenic purpura directly linked with ADAMTS13 inhibition in the baboon (Papio ursinus). Blood. 2010;116(12):2005-2010.
26. Furlan M, Lammle B. Aetiology and pathogenesis of thrombotic thrombocytopenic purpura and haemolytic uraemic syndrome: the role of von Willebrand factor-cleaving protease. Best Pract Res Clin Haematol. 2001;14(2):437-454.
27. Martinod K, Wagner DD. Thrombosis: tangled up in NETs. Blood. 2014;123(18):2768-2776.
28. Ganz T, Selsted ME, Szklarek D, et al. Defensins. Natural peptide antibiotics of human neutrophils. J Clin Invest. 1985;76(4):1427-1435.
29. Fuchs TA, Kremer Hovinga JA, Schatzberg D, Wagner DD, Lammle B. Circulating DNA and myeloperoxidase indicate disease activity in patients with thrombotic microangiopathies. Blood. 2012;120(6):1157-1164.
30. Cao W, Pham HP, Williams LA, et al. Human neutrophil peptides and complement factor Bb in pathogenesis of acquired thrombotic thrombocytopenic purpura. Haematologica. 2016;101(11):1319-1326. .
31. Pillai VG, Bao J, Zander CB, et al. Human neutrophil peptides inhibit cleavage of von Willebrand factor by ADAMTS13: a poten-

tial link of inflammation to TTP. Blood. 2016;128(1):110-119.
32. Higazi AA, Ganz T, Kariko K, Cines DB. Defensin modulates tissue-type plasminogen activator and plasminogen binding to fibrin and endothelial cells. J Biol Chem. 1996;271(30):17650-17655.
33. McDaniel JK, Abdelgawwad MS, Hargett A, et al. Human neutrophil peptide-1 inhibits thrombus formation under arterial flow via its terminal free cysteine thiols. J Thromb Haemost. 2019;17(4):596-606.
34. Dooley K, Zon LI. Zebrafish: a model system for the study of human disease. Curr Opin Genet Dev. 2000;10(3):252-256.
35. Jagadeeswaran P, Cooley BC, Gross PL, Mackman N. Animal models of thrombosis from zebrafish to nonhuman primates: use in the elucidation of new pathologic pathways and the development of antithrombotic drugs. Circ Res. 2016;118 (9):1363-1379.
36. Jagadeeswaran P. Zebrafish: a tool to study hemostasis and thrombosis. Curr Opin Hematol. 2005;12(2):149-152.
37. Weyand AC, Shavit JA. Zebrafish as a model system for the study of hemostasis and thrombosis. Curr Opin Hematol. 2014;21 (5):418-422.
38. Delov V, Muth-Kohne E, Schafers C, Fenske M. Transgenic fluorescent zebrafish Tg(fli1:EGFP)y(1) for the identification of vasotoxicity within the zFET. Aquat Toxicol. 2014;150:189-200.
39. Jagadeeswaran P, Lin S, Weinstein B, Hutson A, Kim S. Loss of GATA1 and gain of FLI1 expression during thrombocyte maturation. Blood Cells Mol Dis. 2010;44(3):175-180.
40. Staley EM, Cao W, Pham HP, et al. Clinical factors and biomarkers predict outcome in patients with immune-mediated thrombotic thrombocytopenic purpura. Haematologica. 2019;104(1):166-175.
41. Moake JL, Rudy CK, Troll JH, et al. Unusually large plasma factor VIII:von Willebrand factor multimers in chronic relapsing thrombotic thrombocytopenic purpura. N Engl J Med. 1982;307(23):1432-1435.
42. Michels A, Albanez S, Mewburn J, et al. Histones link inflammation and thrombosis through the induction of Weibel-Palade body exocytosis. J Thromb Haemost. 2016;14(11):2274-2286.
43. Fuchs TA, Bhandari AA, Wagner DD. Histones induce rapid and profound thrombocytopenia in mice. Blood. 2011;118 (13):3708-3714.
44. Iyer N, Tcheuyap VT, Schneider S, Marshall V, Jagadeeswaran P. Knockout of von Willebrand factor in zebrafish by CRISPR/Cas9 mutagenesis. Br J Haematol. 2019;186(4):e76-e80.
45. Zhang L, Lawson HL, Harish VC, et al. Creation of a recombinant peptide substrate for fluorescence resonance energy transfer-based protease assays. Anal Biochem. 2006;358(2):298-300.
46. van Dorland HA, Mansouri Taleghani M, Sakai K, et al. The International Hereditary Thrombotic Thrombocytopenic Purpura Registry: key findings at enrolment until 2017. Haematologica. 2019;104(10):2107-2115.
47. Semeraro F, Ammollo CT, Morrissey JH, et al. Extracellular histones promote thrombin generation through platelet-dependent mechanisms: involvement of platelet TLR2 and TLR4. Blood. 2011;118(7):1952-1961.
48. Mizuno T, Yoshioka K, Mizuno M, et al. Complement component 5 promotes lethal thrombosis. Sci Rep. 2017;7:42714.

Ferrata Storti Foundation

Haematologica 2020
Volume 105(4):1120-1128

Cryptic non-canonical splice site activation is part of the mechanism that abolishes multimer organization in the c.2269_2270del von Willebrand factor

Viviana Daidone,[1] Eva Galletta,[1] Luigi De Marco[2] and Alessandra Casonato[1]

[1]University of Padua Medical School, Department of Medicine, First Chair of Internal Medicine, Padua and [2]IRCCS, C.R.O. Aviano, Department of Translational Research, Stem Cells Unit, Aviano, Italy

ABSTRACT

We report a new pathogenic mechanism in von Willebrand disease involving the use of a non-canonical splicing site. The proband, carrying the homozygous c.2269_2270del mutation previously classified as a type 3 mutation, showed severely reduced plasma and platelet von Willebrand factor antigen levels and functions, and no factor VIII binding capacity. A particular von Willebrand factor multimer pattern emerged in plasma, characterized by the presence of only two oligomers: the dimer and an unusually large band, with no intermediate components. There were von Willebrand factor multimers in platelets, but each band ran more slowly than the normal counterpart. No anti-von Willebrand factor antibodies were detectable. The proband was classified as having severe type 1 von Willebrand disease. Seeking the relationship between phenotype and genotype, we found the c.2269_2270del mutation associated with three different RNA: r.2269_2270del (RNAI), giving a truncated von Willebrand factor protein; r.[2269_2270del;2282_2288del] (RNAII), resulting from activation of a cryptic "AG" splicing site; and r.[2269_2270del;2281_2282insAG] (RNAIII), where the wild-type "AG" acceptor of exon 18 was retained due to the non-canonical 2279-2280 "CG" acceptor splicing site being used. The aberrant RNAII and RNAIII caused the alteration of the furin cleavage and binding sites, respectively, both resulting in a von Willebrand factor protein characterized by the persistence of von Willebrand factor propeptide, as confirmed by western blot analysis of the recombinant mutated von Willebrand factor molecules produced *in vitro*. Taken together, these findings explain the residual von Willebrand factor synthesis, slower-running multimers, and absent factor VIII binding capacity. The apparently pure gene null mutation c.2269_2270del profoundly alters von Willebrand factor gene splicing, inducing a complex RNA expression pattern.

Correspondence:

ALESSANDRA CASONATO
sandra.casonato@unipd.it

Received: April 2, 2019.

Accepted: July 10, 2019.

Pre-published: July 18, 2019.

doi:10.3324/haematol.2019.222679

Check the online version for the most updated information on this article, online supplements, and information on authorship & disclosures: www.haematologica.org/content/105/4/1120

Introduction

Von Willebrand factor (vWF) is a multimeric glycoprotein involved in the early stages of the hemostatic process. Synthesized by endothelial cells and megakaryocytes, vWF has two main functions: (i) it guarantees platelet recruitment and aggregation at the site of vascular injury; and (ii) it transports factor VIII (FVIII) in the blood circulation.[1-3] vWF function depends on its proper multimeric organization, comprising a set of discrete oligomers ranging from 500,000 to more than 20 million Daltons in size, the larger forms having the greater hemostatic capacity.[4] vWF is synthesized as a monomer of 2,813 amino acids, including a signal peptide of 22 amino acids, a propeptide of 741 amino acids, and a mature molecule of 2,050 amino acids. After dimerization in the endoplasmic reticulum (ER), vWF is multimerized in the Golgi apparatus by an inter-chain disulfide bond forming between cysteine residues 1099 and 1142 of two vWF dimers, thanks to the contribution of vWF propeptide (vWFpp). The propeptide is then cleaved by furin, and the mature vWF molecule is either

stored (in α-granules in platelets, or in Weibel-Palade bodies in endothelial cells) or secreted immediately in the circulation.[5-7] After its secretion, vWF is recognized by the proteolytic enzyme ADAMTS13 (a disintegrin and metalloproteinase with a thrombospondin type 1 motif, member 13), which promptly cuts the multimeric molecule, giving rise to the oligomer pattern characteristic of vWF.[8-10] Reduced levels of vWF, or abnormalities in vWF, are associated with von Willebrand disease (vWD), the most common inherited hemorrhagic disorder. vWD is classified as type 1 (a partial quantitative vWF defect, with a normal or almost normal multimer organization and function), type 3 (total absence of vWF), or type 2 (which includes various structural/functional vWF abnormalities and is further classified as types 2A, 2B, 2M or 2N, depending on which vWF domain is impaired).[11] VWD is caused by mutations in the vWF gene,[12] but many other genetic and environmental factors have a role in modulating circulating vWF levels, including ABO blood group, age, infections, stress, and hormone therapy.[13-15] The increasing use of genetic analysis (vWF gene sequencing) for diagnostic purposes is improving our ability to characterize vWD, especially in cases of type 1 vWD, which is the most difficult to diagnose correctly. Numerous mutations have emerged as causes of vWD, along with frequent cases of multiple vWF defects, and even more complex genetic pictures in which both quantitative and qualitative *vWF* abnormalities co-exist.[12,16] *vWF* cDNA sequencing showed that apparently silent mutations can activate cryptic splice sites or alter regulatory splicing elements, inducing exon skipping or RNA sequence deletions that often result in the formation of premature termination codons (PTC).[17,18] These aberrant vWF mRNA can undergo nonsense-mediated mRNA decay (NMD), a mechanism that triggers the degradation of mutated transcripts bearing PTC to avoid the synthesis of truncated proteins potentially deleterious to the cell.[19,20]

The above-described processes all contribute to making vWD a very complex and heterogeneous disorder, and new cases often pose a real diagnostic challenge. Here we describe a very particular vWD phenotype that is due to an equally particular genetic condition. The causative c.2269_2270del mutation was found to abolish vWF production, acting through a complex mechanism that also includes the recognition of a cryptic non-canonical splicing site in the *vWF* gene. To our knowledge, this is the first work to study the involvement of this rare, and still poorly understood, mechanism in the pathogenesis of vWD.

Methods

Patients

The patient investigated (proband) is a 50-year-old male with a lifelong history of severe bleeding. His 70-year-old mother and 76-year-old father, and his offspring (an 18-year-old daughter and a 15-year-old son) were also investigated. The subjects' bleeding scores (BS) were calculated with the International Society on Thrombosis and Haemostasis (ISTH) Bleeding Assessment Tool (BAT).[21] All subjects gave written informed consent in accordance with the Declaration of Helsinki.

Hemostatic analysis

Basic hemostatic tests were performed as explained elsewhere.[22-24] For more details, see also the *Online Supplementary Methods*. The proband's samples were diluted less than the control plasma to adjust for his markedly reduced vWF levels. vWF multimers were analyzed according to previously reported procedures.[25] Desmopressin (DDAVP) was administered subcutaneously at a dose of 0.3 μg/kg [26] Anti-vWF antibody detection was performed by ELISA.[27] ADAMTS13 activity was ascertained using FRETS-vWF73 (Peptide International, Lexington, KY, USA) as a substrate. A negative test was defined as a titer ≤16 IU/mL.

Genetic analysis

The patients' genomic DNA was obtained from whole blood; total RNA was extracted from platelets (see the *Online Supplementary Methods* for more details). Sequencing reactions were performed in an ABI3130 XL Genetic Analyzer.

Digital droplet polymerase chain reaction

The digital droplet polymerase chain reaction (ddPCR) assays were performed with the QX200 ddPCR system (Bio-Rad, Hercules, CA, USA) using the ddPCR™ Supermix for Probes (Bio-Rad), with different primer pairs and probes specifically designed for aberrant mRNA sequences (*Online Supplementary Methods*). The assay was run in multiplex, starting from 25 ng of the proband's cDNA, at T=56°C and adding 2% DMSO to the PCR mix. cDNA was obtained by retrotranscribing RNA extracted from the proband's platelets, as explained above.

In vitro expression experiments

The pRc/CMV-vWF vector containing the wild-type (WT) human full-length vWF cDNA was mutated by site-directed mutagenesis using the QUIKCHANGE II XL kit (Stratagene, La Jolla, CA, USA). The primer sequences used for mutagenesis are listed in the *Online Supplementary Methods*. The vectors were used to transiently transfect Human Embryonic Kidney 293T (HEK293T) cells. Transfections were performed in T25 flasks using the Lipofectamine 2000 transfection reagent (Life Biotechnology, Carlsbad, CA, USA) and 4 μg of vector/T25. After 48 hours of transfection, the media containing the recombinant vWF (rvWF) were collected, and the rvWF was quantified with ELISA. The rvWF intracellular content was also measured after lysing cells with a 2% Triton-X-100 solution, as previously reported.[17] The results of each transfection experiment were calculated as the mean of three replicates.

SDS-PAGE and western blot

rvWF samples were run in reducing conditions using the XCell SureLock Mini electrophoresis system (Invitrogen, CA, USA) on a Novex Tris-Glycine 3-8% precast gel (Invitrogen). After blotting, the membrane was incubated with a polyclonal rabbit anti-vWF (DAKO, Glostrup, Denmark), and then with a polyclonal anti-rabbit-HRP antibody (for further details see the *Online Supplementary Methods*).

Results

Characterization of a complex von Willebrand disease phenotype

The proband's main symptoms included epistaxis, oral cavity bleeding, frequent hematomas, and bleeding from minor wounds. He also reported episodes of hemarthrosis and severe hemorrhagic complications after tooth extractions. His BS was 30 (vs. 0-3 in normal males). His mother and father (who were consanguineous) were almost asymptomatic, and so were his offspring. Hemostatic tests on the proband revealed a severely impaired hemostatic picture, with a very prolonged activated partial thrombo-

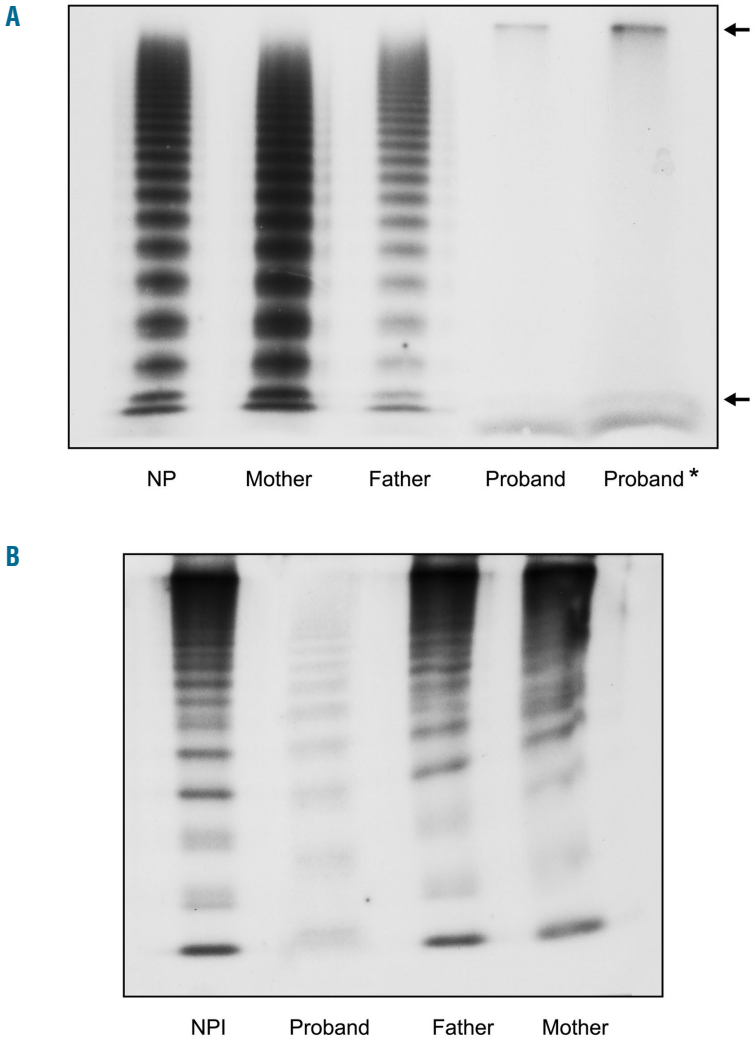

Figure 1. Plasma (A) and platelet (B) von Willebrand factor (vWF) multimer patterns in the proband and his parents, compared with normal plasma (NP) and platelets (NPI). Proband multimer pattern was obtained by plasma diluted 1:5 (left) and 1:2.5 (right*), as compared to the 1:20 dilution of the other samples. Large vWF multimers are at the top, smaller ones at the bottom. All vWF oligomers were absent except for the protomer and an ultra-large band in the patient's plasma, while both low-molecular-weight and intermediate oligomers are present (albeit significantly reduced) in his platelets. The patient's extra band below the first band of the other samples represents the non-specific binding of the anti-vWF polyclonal antibody to proteins other than vWF. This is more evident in the proband because of the less pronounced dilution of the samples. The slower running of each platelet vWF oligomer with respect to the normal counterpart provides evidence of the vWFpp persistence.

plastin time (aPTT), no PFA100 occlusion, and very low FVIII:C and plasma vWF:Ag levels (3.4 U/dL and 1.2 U/dL, respectively). Platelet vWF content was also severely reduced (1.7 U/dL), and plasma vWF was functionally impaired (vWF:RCo 3.8 U/dL and vWF:CB 1.9 U/dL). vWF:FVIIIB was undetectable (Table 1), suggesting a defective FVIII carrier function. All hemostatic parameters were normal, or slightly reduced, in both the proband's parents and offspring (Table 1). Analyzing the proband's vWF multimer pattern revealed no circulating oligomers, apart from two bands: a lower one corresponding to the vWF dimer, and an unusually large band significantly higher than the highest vWF band seen in normal plasma (Figure 1A). On the other hand, the proband's platelet vWF contained low and intermediate oligomers, albeit in significantly reduced quantities, but no large vWF multimers. In addition, each oligomer was found to run less than the corresponding band in normal platelets, a finding resembling the picture seen when there is a persistence of vWFpp[28] (Figure 1B). DDAVP challenge prompted an approximately 8-fold maximum increase in plasma vWF:Ag (120 minutes after injection), associated with a stronger representation of the two previously-identified circulating vWF oligomers (the dimer and the ultralarge band), but no other low or intermediate vWF oligomers appeared (Figure 2). No anti-vWF antibodies were detected in the plasma. The proband's ADAMTS13 activity level was normal at 116% (normal range 65-130%), and no anti-ADAMTS13 antibodies were detected.

Patients' genetic characterization

vWF gene sequencing revealed that the proband was homozygous for the c.2269_2270del mutation in exon 17, and the same mutation was found in both his parents and offspring at heterozygous level. This genetic condition has been described in the literature as a gene null mutation predicted to generate a truncated vWF protein.[29] It has been associated with type 3 VWD, but such a diagnosis is incompatible with our patient's phenotype. He had severely reduced but still detectable vWF levels, there were vWF oligomers in his platelets, and he also responded to DDAVP: this picture more closely resembles severe type 1 than type 3 VWD. The proband's total RNA was extracted and retrotranscribed, and his *vWF* cDNA was analyzed to clarify this apparent genotype-phenotype contradiction, and the cause of his residual vWF synthesis.

The finding of a noncanonical splicing site being used in the vWF gene - Sequencing of the proband's vWF cDNA confirmed the homozygous c.2269_2270del mutation, and revealed a second, unexpected sequence anomaly. Starting

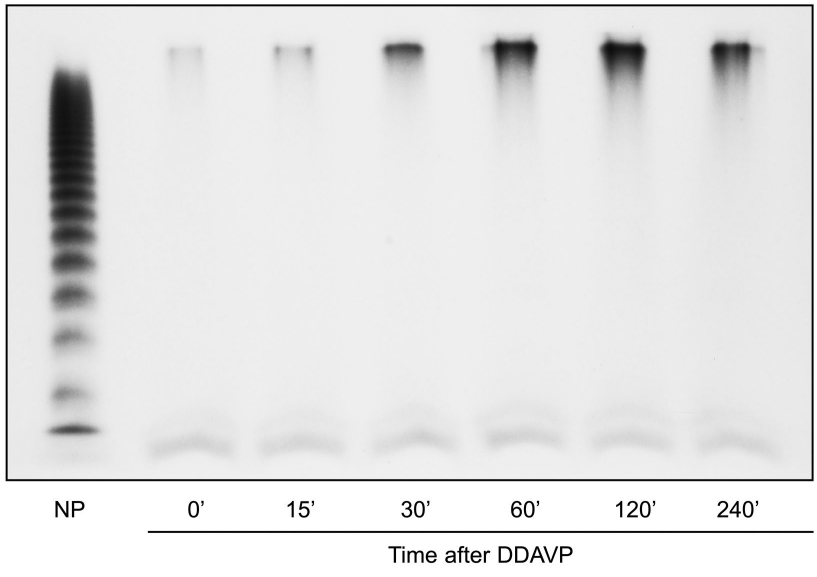

Figure 2. The proband's vWF multimer pattern before (0') and at various times after desmopressin (DDAVP) administration. The proband's multimer pattern was obtained from plasma diluted 1:2.5, instead of the 1:20 dilution used for the normal plasma (NP). Throughout the test, there was no sign of any discontinuous oligomers or additional discrete bands other than the protomer and the ultralarge band, while the two bands already seen before administering DDAVP appeared significantly increased. On the other hand, there was no evidence of any increase in the aspecific band below the dimer.

from position c.2281, at the beginning of exon 18, the chromatogram became triple, a condition not found in the patient's genomic DNA, suggesting the co-existence of more than one mRNA species. To separate and characterize these sequences, the PCR-amplified cDNA fragment spanning exons 15-18 was cloned into a TA-vector, then sequenced again. Three vWF mRNA species were thus identified: (i) the r.2269_2270del (RNAI), lacking the CT dinucleotide at position 2269-2270; (ii) the r.[2269_2270del;2282_2288del] (RNAII), in which the first seven nucleotides of exon 18 were also deleted (position c.2282-2288); and (iii) the r.[2269_2270del;2281_2282insAG] (RNAIII), where an AG insertion was found 11 nucleotides downstream from the CT deletion (Figure 3). The fact that neither the c.2282_2288del nor the c.2281_2282insAG mutations had been found in the patient's genomic DNA indicates that they were the result of an altered splicing of exon 18. The deletion of 7 nucleotides in RNAII could be explained by the use of the AG nucleotides at position c.2287-2288 as the acceptor site, instead of the WT one. This hypothesis was confirmed by an *in silico* analysis with the Human Splicing Finder 3.1 software, which predicted the c.2287-2288 AG dinucleotide as a potential cryptic acceptor site, with a consensus of 72.4 (in a range from 1 to 100, where 100 is the score corresponding to the normal splicing sites). On the other hand, the use of a non-canonical acceptor splicing site (the CG nucleotide pair at position c.2282-4_2282-3) might explain the retention of the c.2281-2282 AG dinucleotide in RNAIII, a pathogenic mechanism hitherto never described in vWD. The AG retention was confirmed by repeating the total RNA extraction and retrotranscription process twice, using different enzymes.

Genotype-phenotype correlation - Three different vWF mRNA were thus found associated with the c.2269_2270del genomic mutation. The RNAI form resulted in a truncated vWF (p.Leu757Valfs*22, indicated as P1 from now on), due to the generation of a premature translation stop codon as a consequence of the c.2269-2270 CT deletion. In RNAII, deriving from the usage of a cryptic AG splicing site, the further 7 nucleotide deletion (c.2282-2288) restored the altered reading frame, producing a mature vWF slightly shorter than normal, and lacking the Arg763-Ser764 furin cleavage site (p.L757_R763delinsVSSQ, named P2 from now on). In RNAIII, the c.2281-2282 AG retention resulting from the use of a non-canonical CG acceptor splicing site restored the reading frame lost due to the upstream CT dinucleotide deletion, producing an in-frame, full-length *vWF*, but with an altered 757-761 amino acid sequence (p.L757_761delinsVSSQG, named P3), corresponding to the consensus binding site of furin.[30] Assuming no contribution of RNAI to vWF production (the P1 *vWF* cannot dimerize), the patient's phenotype should be due to the co-existence of two mutated vWF species (P2 and P3 vWF), both resistant to the enzymatic action of furin. In our patient, the residual synthesis of mutated *vWF*, characterized by the persistence of its propeptide, confirms the presence of these P2 and P3 vWF forms.

Different expression of RNAI, RNAII and RNAIII - A multiplex ddPCR assay was performed on the proband's cDNA, to examine the levels of expression of the three mRNA. RNAI was found to be the dominant species (6.3 copies/ng, 83% of the total vWF mRNA), followed by RNAII (0.96 copies/ng, 12% of the total vWF mRNA), and RNAIII (0.37copies/ng, 5% of the total vWF mRNA). That the RNAI species encoding for the truncated p.Leu757Valfs*22 *vWF* accounts for more than 80% of the patient's *vWF* mRNA is consistent with his severe quantitative *vWF* defect.

In vitro expression experiments - To establish the effect of the single and combined aberrant mRNA on vWF synthesis and release, we ran *in vitro* experiments using HEK293T cells and vectors pRc/CMV-vWF, pRc/CMV-vWF-RNAI, pRc/CMV-vWF-RNAII and pRc/CMV-vWF-RNAIII, encoding for WT, P1, P2 and P3 vWF, respectively.

RNAI - No rvWF was found in the conditioned medium of HEK293T cells transfected with the pRc/CMV-vWF-RNAI, while co-transfection of both the WT and the mutated vector (mimicking a heterozygous condition) induced a drop in rvWF production of about 30% (Figure

4A). Analyzing the intracellular content of the transfected cells revealed a similar picture, with rvWF totally absent in the homozygous condition, and 30% lower than normal vWF in the heterozygous condition (Figure 4B). The vWF:CB/vWF:Ag and vWF:FVIIIB/vWF:Ag ratios (respectively indicative of the multimer organization of vWF and its capacity for binding FVIII) did not change when RNAI was co-expressed with the WT, which means that no functional alterations are associated with P1 vWF (Figure 4A). These results demonstrate that the P1 mutation behaves like a gene null mutation, inducing a pure quantitative vWF defect.

RNAII and RNAIII - Transfection of HEK293T cells with pRc/CMV-vWF-RNAII caused a reduction in rvWF secretion of about 40% or 60%, respectively, if the vector was expressed with or without the WT counterpart (Figure 4A). Conversely, there was an increase in rvWF intracellular content in the transfected cells that was more pronounced in the homozygous condition (Figure 4B), a finding suggestive of a partial retention of the P2 rvWF. A similar picture was seen for pRc/CMV-vWF-RNAIII: its expression was associated with a drop in rvWF secretion in the conditioned medium (of about 40% and 65% for the heterozygous and homozygous conditions, respectively), and a corresponding increase in the intracellular rvWF content (Figure 4B). The vWF:CB ratios were higher than normal, for both P2 and P3 rvWF (Figure 4A); in the homozygous condition, the ratios were 158.1% and 197.3%, respectively, of the WT (taken to be 100%), suggesting the presence of larger than normal vWF multimers. On the other hand, the vWF:FVIIIB ratios were lower when P2 and P3 were expressed at heterozygous level (i.e. 57.3% and 52.0% of the WT, respectively), and vWF:FVIIIB was completely undetectable when each mutation was expressed at homozygous level. The P2 and P3 vWF mutations therefore both cause a partial quantitative defect associated with a defective FVIII binding capacity of the mutated vWF.

Multimer analysis on the rvWF in the conditioned media confirmed the above results: oligomers of unusually high molecular weight were apparent for both P2 and P3 rvWF, with an accumulation of vWF oligomers on the boundary between the stacking and running gel and a relative representation of vWF multimers shifted towards the high-molecular-weight forms (Figure 5). All mutated rvWF oligomers also showed a delayed migration pattern, compared with WT (Figure 5), like the one seen in the patient's platelet multimers. This picture points to the persistence of vWFpp, a condition associated with vWF having an impaired FVIII carrier capacity.[28]

Co-transfection with RNAI, RNAII and RNAIII - Co-transfecting HEK293T cells with equal amounts of all vectors resulted in a 60% reduction in secreted rvWF, with a corresponding approximately 25% increase in intracellular rvWF content. In the conditioned medium, the rvWF:CB ratio was higher than normal, while vWF:FVIIIB levels

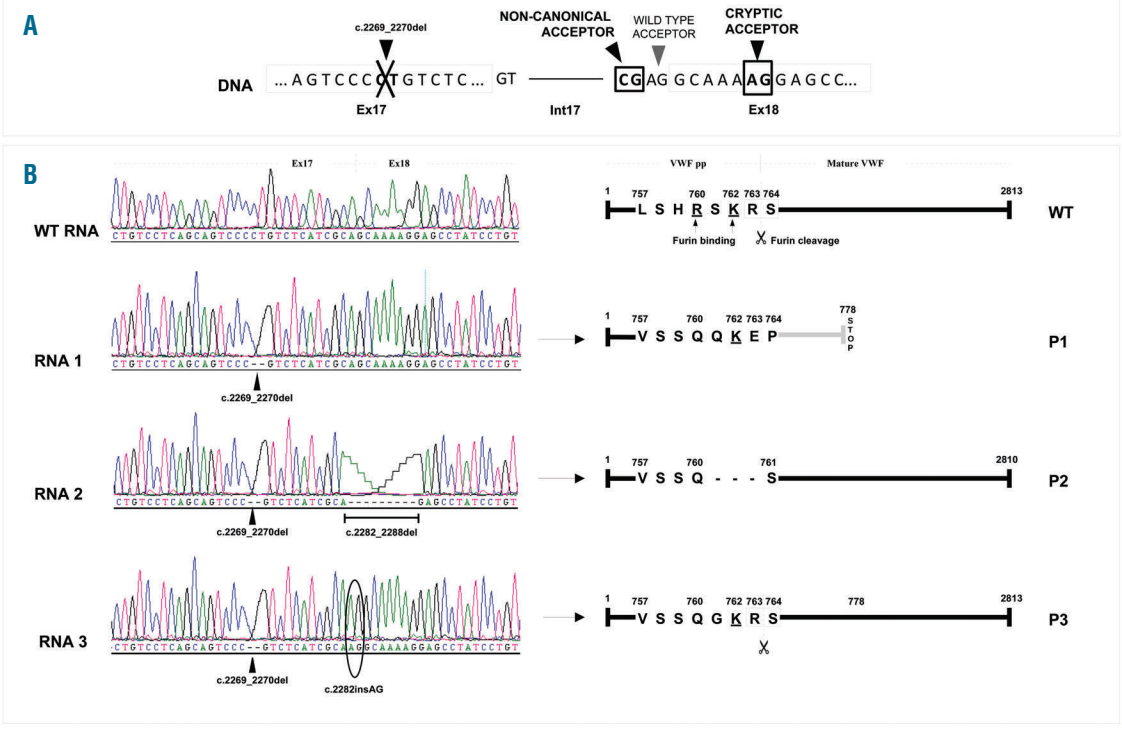

Figure 3. Schematic representation of the three mRNA associated with the c.2269_2270del *von Willebrand factor (vWF)* gene deletion, and the resulting mutated vWF proteins. RNAI deriving from the use of the wild-type (WT) donor and acceptor splicing sites encodes for a truncated vWF protein (P1, 778 amino acids long). RNAII resulting from the activation of a cryptic AG acceptor site within exon 18 encodes a protein with a 3 amino acids deletion, in which the furin cleavage site is lost (P2). Finally, RNAIII originates from the usage of a non-canonical CG acceptor site in intron 17, and results in a full-length vWF protein carrying a partially-altered furin recognition site (P3). vWFpp persistence is predicted for both P2 and P3 vWF, while no vWF secretion is expected for P1. The gray area identifies amino acids other than WT in P1, P2 and P3 vWF. Chromatograms were aligned with the SeqMan Pro software (DNASTAR, Madison, WI, USA). P1: p.Leu757Valfs*22; P2: p.L757_R763delinsVSSQ; P3: p.L757_761delinsVSSQG.

were undetectable. rvWF multimer analysis revealed larger than normal oligomers, and a delayed oligomer migration (Figure 5).

SDS-PAGE and western blot analysis - Analyzing samples with SDS-PAGE and western blotting in reducing conditions revealed a protein band with a molecular weight corresponding to the unprocessed vWF-pp (about 340KDa) in both P2 and P3 rvWF, while a band corresponding to the mature cleaved vWF (250KDa) was seen in the WT. These data confirmed the persistence of vWFpp in the P2 and P3 vWF (Figure 6).

Discussion

We report on a complex splicing alteration associated with the *vWF* c.2269_2270del mutation that involves the use of a non-canonical splicing site in a case of severe type 1 vWD characterized by a lack of multimer organization in the circulating vWF. The c.2269_2270del mutation was described in 2003 as a pure gene null mutation.[29] Here, we demonstrate that it alters *vWF* splicing, and induces the generation of three different aberrant mRNA species. The predominant specie, RNAI, encodes for the already-known truncated p.Leu757Valfs*22 vWF (P1 in the text), associated with a pure quantitative vWF defect.[29] The other two species found, RNAII and RNAIII, account for less than 20% of the total *vWF* mRNA expression, and are produced by the activation of two cryptic acceptor splicing sites (a canonical "AG" and an unusual "CG") in exon 18 and intron 17 of the vWF gene, respectively. RNAII encodes for a mature vWF characterized by loss of the furin cleavage site (p.L757_R763delinsVSSQ, P2), while RNAIII has an altered furin recognition site that impairs its

Table 1. Main hemostatic and genetic findings in the proband and his parents.

Patients	aPTT sec	PFA100 sec	RIPA %	FVIII:C U/dL	VWF:Ag U/dL	VWF:CB U/dL	VWF:CB ratio	VWF:FVIIIB U/dL	VWF:FVIIIB ratio	Platelet VWF U/dL	BS
Proband	54.6	>300	0 (5.6)*	3.4	1.2	1.9	1.58	0	NC	1.7	30
Mother	22.8	160	72.9	209.6	114.3	104.9	0.91	118.0	1.03	97.6	1
Father	31.0	198	74.2	89.1	39.3	40.4	1.03	38.2	0.97	103.0	0
Son	97.9	150	65.4	119.6	66.0	61.4	0.93	61.1	0.97	74.4	1
Daughter	93.2	145	72.3	108.2	56.3	63.6	1.13	55.0	0.97	83.9	1
Normal range	24-36	94-193	72±12	60-160	60-160	65-150	≥0.75	65-150	≥0.74	70-140	0-3/0-5 (M/F)

aPTT: activated partial thromboplastin time; RIPA: ristocetin induced platelet aggregation at 1.2 mg/mL ristocetin concentration; *RIPA value at 1.5 mg/mL ristocetin concentration; BS: Bleeding Score, calculated by the ISTH Bleeding Assessment tool (BAT); M/F: male/female; NC: not calculable.

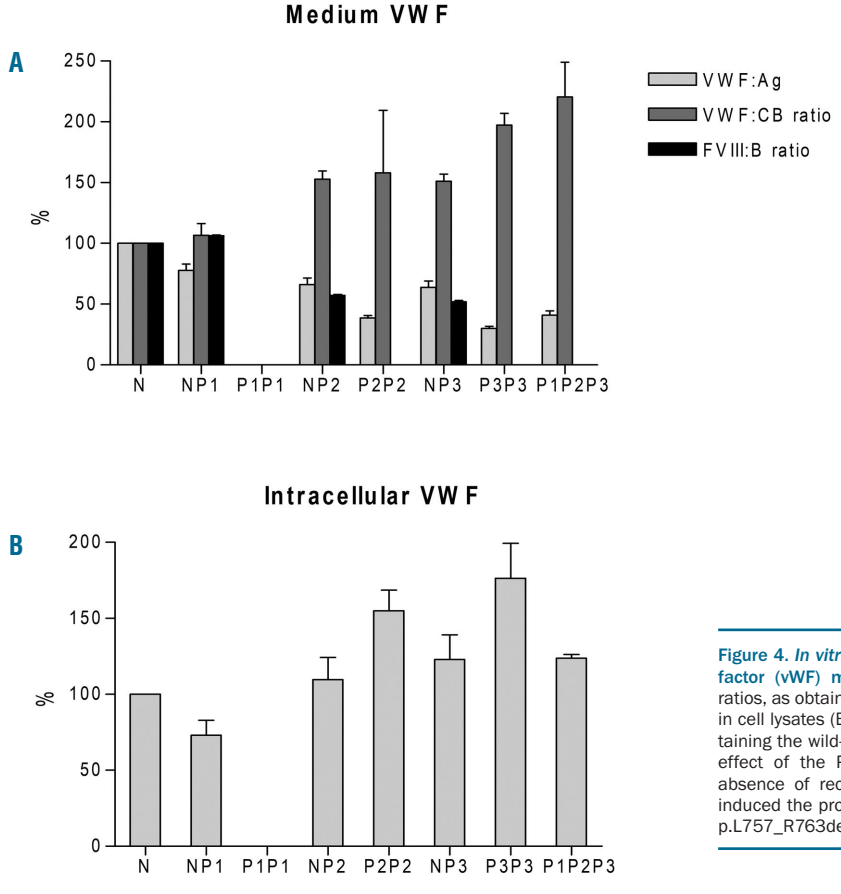

Figure 4. ***In vitro*** **expression of the P1, P2, and P3 von Willebrand factor (vWF) mutations.** Mean vWF:Ag, vWF:CB and vWF:FVIIIB ratios, as obtained in the conditioned culture media (A), and vWF:Ag in cell lysates (B) from HEK293T cells transfected with vectors containing the wild-type (WT) or the P1, P2, and P3 vWF. The gene null effect of the P1 mutation was demonstrated by the complete absence of recombinant vWF (rvWF), whereas both P2 and P3 induced the production of vWF protein. P1: p.Leu757Valfs*22; P2: p.L757_R763delinsVSSQ; P3: p.L757_761delinsVSSQG.

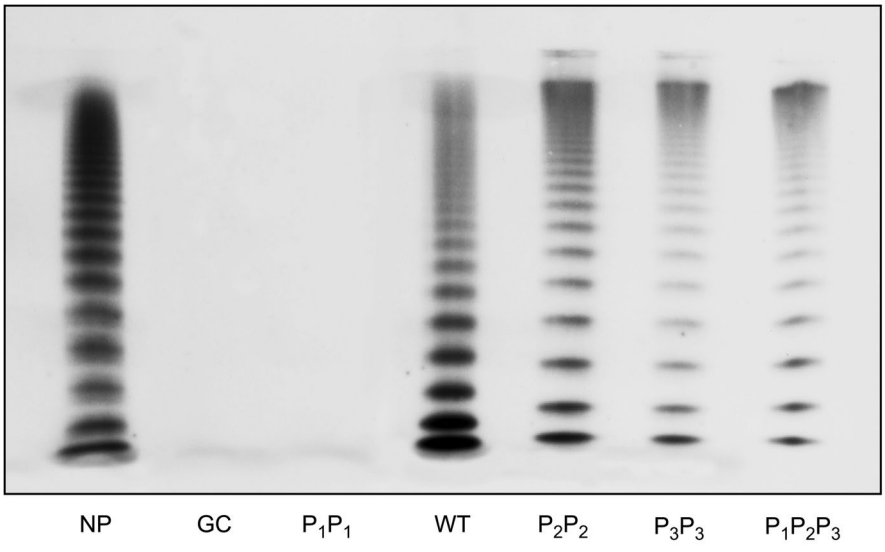

Figure 5. Multimer analysis of recombinant von Willebrand factor (rvWF). No rvWF was found in the conditioned medium from cells expressing the P1 vWF mutation. Both P2 and P3 rvWF were produced instead, and showed: (i) unusually large vWF multimers associated with the accumulation of multimers on the boundary of the running and stacking gel; (ii) an oligomer pattern that had shifted towards the high-molecular-weight forms; and (iii) oligomers with a slower migration pattern. P1: p.Leu757Valfs*22; P2: p.L757_R763delinsVSSQ; P3: p.L757_761delinsVSSQG.

enzymatic activity (p.L757_761delinsVSSQG, P3).[30] Despite bearing a PTC, RNAI seems to escape the NMD control mechanism, as it accounts for more than 80% of total mRNA expression.[19,31]

The proband was homozygous for the c.2269_2270del mutation, and carried no other mutations in his *vWF* gene. He had a very complex and severe phenotype characterized by both quantitative and qualitative vWF alterations. Both plasma and platelet vWF levels were significantly decreased, leading to a diagnosis of severe type 1 vWD. The multimer organization of his circulating *vWF* revealed a peculiar pattern involving the absence of any oligomers except for the vWF dimer, and an unusually ultra large band, without any intermediate components. This pattern did not change after DDAVP infusion, which increased the pre-DDAVP oligomers, without any other intermediate components being observed. On the other hand, the patient's platelet *vWF* showed a multimer organization (albeit lacking in the large components), with each oligomer characterized by a delayed migration, a picture suggestive of a persistence of vWFpp.[28] A similar vWF multimer pattern had previously been reported in a patient with systemic lupus erythematosus, who had the two above-described circulating vWF oligomers, but a normal platelet vWF content and multimer pattern in the presence of an anti-vWF antibody.[26] In contrast, no anti-vWF antibodies were detectable in our patient.

The delayed migration of the proband's platelet vWF oligomers was attributable to the presence of the P2 and P3 vWF forms, both resistant to the action of furin, and consequently characterized by the persistence of the vWFpp. This was confirmed by our patient's undetectable vWF:FVIIIB values, as well as by the P2 and P3 rvWF forms, which point to his vWF having an impaired capacity to carry FVIII.[32] The persistence of vWFpp is known to disrupt the capacity of vWF to bind FVIII because of a steric hindrance that makes the FVIII binding site in the D3 domain of vWF inaccessible.[28]

The DDAVP-induced release of vWF stored in the Weibel-Palade bodies, or a drop in ADAMTS13 concentration in the bloodstream are usually associated with the appearance of ultra large vWF multimers in the circulation. In both cases, all vWF oligomers are still present, however, whereas this was not so in our patient. There are also vWF mutations that interfere with the factor's recognition and/or binding by ADAMTS13, giving rise to the presence of unusually large vWF bands[33,34] that are not normally organized, a picture not seen in our patient either. Indeed, the multimer pattern of the proband's circulating vWF appeared to be more similar to that of vWF inside normal endothelial cells.[35] We know that the cysteine-linked vWF dimers grow in a concatemer *via* the formation of disulfide bonds at the N-terminal of the vWF molecule, with the contribution of vWFpp. After its secretion from endothelial cells, vWF remains anchored to the vessel wall and is then uncoiled by the action of the blood flow. This makes the Tyr1605-Met1606 bond accessible to ADAMTS13 for cleavage. The persistence of vWFpp could interfere with the unraveling of vWF during its release from endothelial cells;[36-39] alternatively, the P2 and P3 vWF forms might be unable to remain anchored to the vessel wall during their release. Intriguingly, p-selectin protein (which is known to anchor vWF to the endothelial vessel wall under normal conditions) binds vWF in the D'D3 region, very near where our P2 and P3 mutations occur.[40] While circulating vWF needs dynamic flow conditions for it to be cleaved by ADAMTS13 after its release, this might not be the case for vWF inside alpha-granules, and this would explain the different multimer organization in the two biological districts. A different contribution of aberrant vWF mRNA in endothelial cells and platelets is less plausible, but mRNA in endothelial cells would need to be explored to be able to verify this.

In vitro expression experiments confirmed that the c.2269_2270del mutation, hitherto considered a type 3 vWF defect,[29,41] is actually associated with a residual syn-

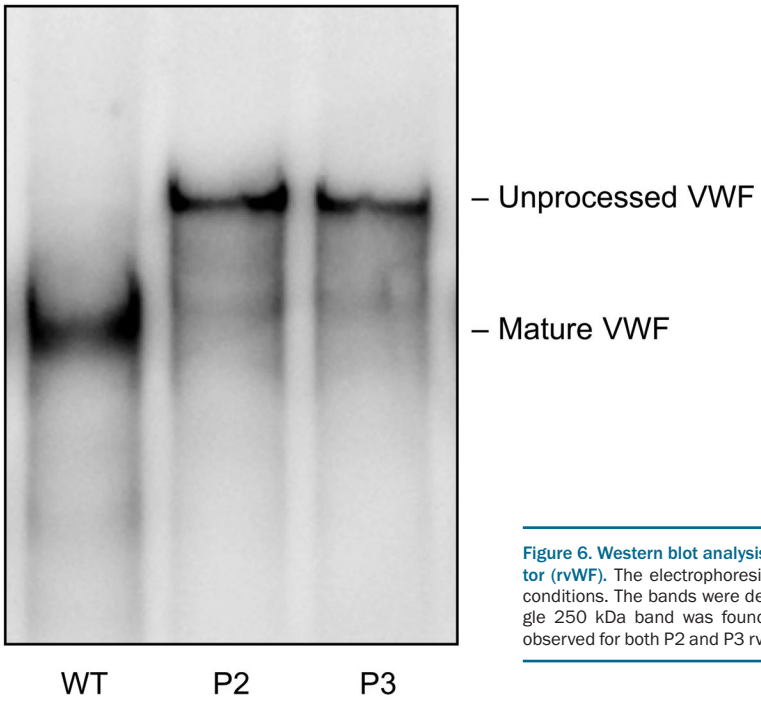

Figure 6. Western blot analysis on wild-type (WT), P2 and P3 recombinant von Willebrand factor (rvWF). The electrophoresis run was performed in a 3-8% Tris-Glycine gel under reducing conditions. The bands were detected using the Euroclone LiteAblot Turbo ECL substrate. A single 250 kDa band was found for the WT rvWF, in contrast with the about 340 kDa band observed for both P2 and P3 rvWF. P2: p.L757_R763delinsVSSQ; P3: p.L757_761delinsVSSQG.

thesis of vWF due to the presence of RNAII and RNAIII forms. While RNAI (the prevalent *vWF* mRNA form) produced no rvWF, both RNAII and RNAIII produced a rvWF molecule characterized by the persistence of vWFpp, as shown by the slower migration of each oligomer, and the weaker FVIII binding capacity. This finding was confirmed by western blot analysis, showing that both P2 and P3 rvWF were characterized by the presence of only the unprocessed vWF protein band. The presence of larger than normal vWF oligomers in the rvWF multimers, and their being in larger proportions than the low and intermediate forms, also confirm that the c.2269_2270del mutation induces ADAMTS13 resistance *in vitro*, and that vWF proteolysis can occur under static conditions (as seen also in the proband's platelets), thus explaining the proband's discrepant plasma and platelet vWF multimer patterns *in vivo*.

Interestingly, the c.2269_2270del mutation generates RNAII and RNAIII through the activation of two cryptic splicing sites in exon 18 and intron 17 of the *vWF* gene, respectively. The recognition of a cryptic splicing site is a known, not particularly rare, mechanism in vWD, which can be responsible for vWF lacking altogether,[42] or its levels only being reduced.[43] In our patient, the two new acceptor sites activated due to the mutation are one a canonical "AG", and the other an unusual "CG" acceptor splicing site, respectively generating RNAII and RNAIII. A non-canonical splicing site has very rarely been identified in human genes (the sequences of 5' donor and 3' acceptor splicing sites almost always obey the GT-AG rule)[44,45] and this is the first time it has been described in vWD. The new pathogenic mechanism behind vWD characterized in this work could have a significant impact on vWD diagnosis and management in future, bearing in mind the large proportion of vWD cases that, even nowadays, remain genetically unexplained.

To conclude, our investigation revealed the use of a non-canonical splicing site as a novel pathogenic mechanism behind vWD. This was associated with the previously reported, but only partially categorized, vWF c.2269_2270del mutation, and it resulted in a severe type 1 vWD featuring an extremely particular vWF multimer organization, and lacking the ADAMTS13-induced oligomer pattern.

Funding

This work was supported by a grant from the MURST (ex 60%, 2016).

References

1. Sadler JE. Biochemistry and genetics of von Willebrand factor. Annu Rev Biochem. 1998;67:395-424.
2. Ruggeri ZM. Structure of von Willebrand factor and its function in platelet adhesion and thrombus formation. Best Pract Res Clin Haematol. 2001;14(2):257-279.
3. Fay PJ, Cumans JV, Walker FJ. von Willebrand factor mediates protection of FVIII from activated protein C-catalyzed inactivation. J Biol Chem. 1991;266(4): 2172-2177.
4. Gralnick HR, Williams SB, Morisato DK. Effect of multimeric structure of the factor VIII/von Willebrand factor protein on binding to platelets. Blood. 1981;58(2):387-392.
5. Wagner DD, Marder VJ. Biosynthesis of von Willebrand protein by human endothelial cells: processing steps and their intracellular localization. J Biol Chem. 1984; 99(6):2123-2130.
6. Wagner DD, Lawrence SO, Ohlsson-Wilhelm BM, Fay PJ, MarderVJ. Topology and order of formation of interchain disulfide bonds in von Willebrand factor. Blood. 1987;69(1):27-32.
7. Wagner DD, Fay PJ, Sporn LA, Sinha S, Lawrence SO, Marder VJ. Divergent fates of von Willebrand factor and its propolypeptide (von Willebrand antigen II) after secretion from endothelial cells. Proc Natl Acad Scie USA. 1987;84(7):1955-1959.
8. Sadler JE. von Willebrand factor assembly and secretion. Thromb Haemost. 2009;7

Suppl 1:24-27.
9. Zheng X, Chung D, Takayama TK. Structure of von Willebrand factor-cleaving protease (ADAMTS13), a metalloprotease involved in thrombotic thrombocytopenic purpura. J Biol Chem. 2001;276(44):41059-41063.
10. Dent JA, Berkowitz SD, Ware J, Kasper CK, Ruggeri ZM. Identification of a cleavage site directing the immunochemical detection of molecular abnormalities in type IIA von Willebrand factor. Proc Natl Acad Sci USA. 1990;87(16):6306-6310.
11. Sadler JE, Budde U, Eikenboom JC, et al. Working Party on von Willebrand Disease Classification. Update on the pathophysiology and classification of von Willebrand disease: a report of the Subcommittee on von Willebrand factor. J Thromb Haemost. 2006;4(10):2103-2114.
12. Goodeve A. The genetic basis of von Willebrand disease. Blood Rev. 2010; 24(3):123-134.
13. Stakiw J, Bowman M, Hegadorn C, et al. The effect of exercise on von Willebrand factor and ADAMTS-13 in individuals with type 1 and type 2B von Willebrand disease. J Thromb Haemost. 2008;6(1):90-96.
14. Pottinger BE, Read RC, Paleolog EM, et al. Von Willebrand factor is an acute phase reactant in man. Thromb Res. 1989;53(4):387–394.
15. Stirling Y, Woolf L, North WR, et al. Hemostasis in normal pregnancy. Thromb Haemost. 1984;52(2):176–182.
16. Daidone V, Galletta E, Casonato A. Type 1 von Willebrand disease due to a vicinal cysteine loss (p.C524Y) disclosed after a thrombotic episode. Thromb Res. 2018;161:91-93.
17. Daidone V, Gallinaro L, Cattini MG, et al. An apparently silent nucleotide substitution (c.7056C>T) in the von Willebrand factor gene is responsible for type 1 von Willebrand disease. Haematologica. 2011;96(6):881-887.
18. Pagliari MT, Baronciani L, Garcìa Oya I, et al. A synonymous (c.3390C>T) or a splice-site (c.3380-2A>G) mutation causes exon 26 skipping in four patients with von Willebrand disease (2A/IIE). J Thromb Haemost. 2013;11(7):1251-1259.
19. Corrales I, Ramírez L, Altisent C, Parra R, Vidal F. The study of the effect of splicing mutations in von Willebrand factor using RNA isolated from patients' platelets and leukocytes. J Thromb Haemost. 2011;9(4):679-688.
20. Borràs N, Orriols G, Batlle J, et al. Unraveling the effect of silent, intronic and missense mutations on VWF splicing: contribution of next generation sequencing in the study of mRNA. Haematologica. 2019;104(3):587-598.
21. Rodeghiero F, Tosetto A, Abshire T, et al. on behalf of the ISTH/SSC Joint VWF and Perinatal/Pediatric Hemostasis Subcommittees Working Group. ISTH/SSC Bleeding Assessment Tool: a standardized questionnaire and a proposal for a new bleeding score for inherited bleeding disorders. J Thromb Haemost. 2010;8(9):2063–2065.
22. Casonato A, Pontara E, Sartorello F, et al. Reduced von Willebrand factor survival in type Vicenza von Willebrand disease. Blood. 2002;99(1):180-184.
23. Casonato A, Pontara E, Sartorello F, et al. Identifying carriers of type 2N von Willebrand disease: procedures and significance. Clin Appl Thromb Hemost. 2007;13(2):194-200.
24. Casonato A, Pontara E, Sartorello F, et al. Identifying type Vicenza von Willebrand disease. J Lab Clin Med. 2006;147(2):96-102.
25. Casonato A, Pontara E, Boscaro M, et al. Abnormalities of von Willebrand factor are also part of the prothrombotic state of Cushing's syndrome. Blood Coagul Fibrinolysis. 1999;10(3):145-151.
26. Gallinaro L, Cattini MG, Sztukowska M, et al. A shorter von Willebrand factor survival in O blood group subjects explains how ABO determinants influence plasma von Willebrand factor. Blood. 2008; 111(7):3540-3545.
27. Casonato A, Pontara E, Doria A, et al. Lack of multimer organization of von Willebrand factor in an acquired von Willebrand syndrome. Br J Haematol. 2002; 116(4):899-904.
28. Casonato A, Pontara E, Doria A, et al. An Arg760Cys mutation in the consensus sequence of the von Willebrand factor propeptide cleavage site is responsible for a new von Willebrand disease variant. Blood. 2003;101(1):151-156.
29. Baronciani L, Cozzi G, Canciani MT, et al. Molecular defects in type 3 von Willebrand disease: updated results from 40 multiethnic patients. Blood Cells Mol Dis. 2003; 30(3):264-270.
30. Rehemtulla A, Kaufman RJ. Preferred sequence requirements for cleavage of pro-von Willebrand factor by propeptide-processing enzymes. Blood. 1992;79(9):2349-2355.
31. Platè M, Duga S, Baronciani L, et al. Premature termination codon mutations in the von Willebrand factor gene are associated with allele-specific and position-dependent mRNA decay. Haematologica. 2010; 95(1):172–174.
32. Casonato A, Galletta E, Sarolo L, Daidone V. Type 2N von Willebrand disease: Characterization and diagnostic difficulties. Haemophilia. 2018;24(1):134-140.
33. Casonato A, Pontara E, Battiston M, et al. C2362F mutation gives rise to an ADAMTS13-resistant von Willebrand factor. Thromb Haemost. 2013;109(6):999-1006.
34. Daidone V, Saga G, Barbon G, et al. The p.R1819_C1948delinsS mutation makes von Willebrand factor ADAMTS13-resistant and reduces its collagen-binding capacity. Br J Haematol. 2015;170(4):564-573.
35. Tsai HM, Nagel RL, Hatcher VB, Sussman II. Multimeric composition of endothelial cell-derived von Willebrand factor. Blood. 1989;73(8):2074-2076.
36. Dong JF, Moake JL, Nolasco L, et al. ADAMTS-13 rapidly cleaves newly secreted ultralarge von Willebrand factor multimers on the endothelial surface under flowing conditions. Blood. 2002;100(12):4033-4039.
37. De Ceunynck K, De Meyer SF, Vanhoorelbeke K. Unwinding the von Willebrand factor strings puzzle. Blood. 2013;121(2):270-277.
38. Crawley JT, de Groot R, Xiang Y, Luken BM, Lane DA. Unraveling the scissile bond: how ADAMTS13 recognizes and cleaves von Willebrand factor. Blood. 2011; 118(12):3212-3221.
39. Turner NA, Nolasco L, Ruggeri ZM, Moake JL. Endothelial cell ADAMTS-13 and VWF: production, release, and VWF string cleavage. Blood. 2009;114(24):5102-5111.
40. Michaux G, Pullen TJ, Haberichter SL, Cutler DF. P-selectin binds to the D'-D3 domains of von Willebrand factor in Weibel-Palade bodies. Blood. 2006; 107(10):3922-3924.
41. Solimando M, Baronciani L, La Marca S, et al. Molecular characterization, recombinant protein expression, and mRNA analysis of type 3 von Willebrand disease: Studies of an Italian cohort of 10 patients. Am J Hematol. 2012;87(9):870-874.
42. Galletta E, Daidone V, Zanon E, Casonato S. Type 3 von Willebrand disease mistaken for moderate haemophilia A: a lesson still to be learned. Haemophilia. 2018; 24(3):154-157.
43. Casonato A, Cattini MG, Barbon G, Daidone V, Pontara E. Severe, recessive type 1 is a discrete form of von Willebrand disease: the lesson learned from the c.1534-3C>A von Willebrand factor mutation. Thromb Res. 2015;136(3):682-686.
44. Burset M, Seledtsov IA, Solovyev VV. Analysis of canonical and non-canonical splice sites in mammalian genomes. Nucleic Acids Res. 2000;28(21):4364-4375.
45. Sibley CR, Blazquez L, Ule J. Lessons from non-canonical splicing. Nat Rev Genet. 2016;17(7):407-421.

ARTICLE

Correction of bleeding in experimental severe hemophilia A by systemic delivery of factor VIII-encoding mRNA

Jules Russick,[1] Sandrine Delignat,[1] Peter Milanov,[2] Olivier Christophe,[3] Gábor Boros,[4] Cécile V. Denis,[3] Peter J. Lenting,[3] Srinivas V. Kaveri[1] and Sébastien Lacroix-Demazes[1]

[1]Centre de Recherche des Cordeliers, INSERM, Sorbonne Université, Université de Paris, Paris, France; [2]DRK-Blutspendedienst, Institut für Transfusionsmedizin und Immunhämatologie, Frankfurt am Main, Germany; [3]HITh, UMR_S1176, INSERM, Université Paris-Saclay, Le Kremlin-Bicêtre, France and [4]BioNTech RNA Pharmaceuticals, Mainz, Germany

Ferrata Storti Foundation

Haematologica 2020
Volume 105(4):1129-1137

ABSTRACT

The treatment or prevention of bleeding in patients with hemophilia A relies on replacement therapy with different factor VIII (FVIII)-containing products or on the use of by-passing agents, i.e., activated prothrombin complex concentrates or recombinant activated factor VII. Emerging approaches include the use of bispecific anti-factor IXa/factor X antibodies, anti-tissue factor pathway inhibitor antibodies, interfering RNA to antithrombin, and activated protein C-specific serpins or gene therapy. The latter strategies are, however, hampered by the short clinical experience and potential adverse effects including the absence of tight temporal and spatial control of coagulation and the risk of uncontrolled insertional mutagenesis. Systemic delivery of mRNA allows endogenous production of the corresponding encoded protein. Thus, injection of erythropoietin-encoding mRNA in a lipid nanoparticle formulation resulted in increased erythropoiesis in mice and macaques. Here, we demonstrate that a single injection of *in vitro* transcribed B domain-deleted FVIII-encoding mRNA to FVIII-deficient mice enables endogenous production of pro-coagulant FVIII. Circulating FVIII:C levels above 5% of normal levels were maintained for up to 72 h, with an estimated half-life of FVIII production of 17.9 h, and corrected the bleeding phenotype in a tail clipping assay. The endogenously produced FVIII did however exhibit low specific activity and induced a potent neutralizing IgG response upon repeated administration of the mRNA. Our results suggest that the administration of mRNA is a plausible strategy for the endogenous production of proteins characterized by poor translational efficacy. The use of alternative mRNA delivery systems and improved FVIII-encoding mRNA should foster the production of functional molecules and reduce their immunogenicity.

Introduction

Hemophilia A is a rare X-linked hemorrhagic disorder that results from insufficient plasma levels of pro-coagulant factor VIII (FVIII).[1] Replacement therapy using exogenous FVIII is to date the most efficient strategy to treat or prevent bleeds. It is however extremely expensive because of the elevated production costs, the short half-life of therapeutic FVIII and the need for life-long treatment. Several alternative strategies to correct bleeding include the use of FVIII by-passing agents, such as activated prothrombin complex concentrates, recombinant factor VIIa or monoclonal FVIII-mimicking bispecific antibodies,[2] the injection of anti-tissue factor pathway inhibitor,[3] of interfering RNA to antithrombin (AT)[4] or of activated protein C-specific serpins,[5] and gene therapy.[6] Each of these promising therapies does, however, have intrinsic challenges that may limit broad application.

In vivo production of proteins following the administration of mRNA was demonstrated in the early 1990s in the case of luciferase and β-galactosidase,[7] leading to the first clinical trial with mRNA a decade later.[8] Concomitantly, both double- and sin-

Correspondence:

SÉBASTIEN LACROIX-DESMAZES
sebastien.lacroix-desmazes@crc.jussieu.fr

Received: October 30, 2018.

Accepted: July 5, 2019.

Pre-published: July 9, 2019.

doi:10.3324/haematol.2018.210583

Check the online version for the most updated information on this article, online supplements, and information on authorship & disclosures: www.haematologica.org/content/105/4/1129

gle-stranded RNA were found to trigger innate immunity upon ligation of TLR3, 7 and 8, and RIG-1.[9-12] The replacement of uridines by 1-methylpseudouridines and the removal of double-stranded RNA by high performance liquid chromatography was demonstrated to abrogate the activation of innate immune cells,[13,14] and allowed the *in vivo* production of different proteins, including erythropoietin, factor IX and anti-human immunodeficiency virus antibodies without the induction of overt neutralizing immune responses.[15-19] Conversely, the administration of synthetic mRNA was also used in vaccination strategies either by direct injection[20] or upon adoptive transfer of *ex vivo*-transfected dendritic cells.[21,22]

Because of its monogenic nature and the requirements for low amounts of FVIII to correct the bleeding phenotype of affected patients, hemophilia A is a particularly suitable disease for treatment with mRNA. Furthermore, transfection with mRNA is by essence not integrative, and thus avoids risks of uncontrolled insertional mutagenesis that may occur with DNA-based gene therapy approaches. In addition, mRNA is translated only transiently and is degraded by physiological pathways, thus ensuring its safety and facilitating the control of the bioavailability of the encoded protein. Here, we investigated whether the intravenous administration of FVIII-encoding mRNA enables the production of therapeutic levels of pro-coagulant FVIII in FVIII-deficient mice.

Methods

Cloning of factor VIII

The cDNA encoding human B domain-deleted (BDD) FVIII (FVIII^{HSQ}), containing the 14-amino acid segment SFSQNPPVLKRHQR in place of the B domain, cloned in the ReNeo mammalian expression plasmid with geneticin resistance, has been described previously.[23] Codon optimization of the DNA sequence encoding human BDD-FVIII was adapted to the bias of *Homo sapiens* using in-house proprietary software (GeneOptimizer) from GeneArt (Thermo Fisher, Darmstadt, Germany). The GeneOptimizer software also calculates removal of *cis*-acting sequence motifs, including internal TATA-boxes, chi-sites and ribosomal entry sites, AT- or GC-rich sequence stretches, AU-rich elements, inhibitory and *cis*-acting repressor sequence elements, repeat sequences, RNA secondary structures, and all cryptic splice sites. The codon-optimized BDD-FVIII-encoding cDNA was also cloned in the ReNeo vector.

In vitro transcription of mRNA

mRNA were transcribed as previously described[15] using the linearized plasmids encoding BDD-FVIII (FVIII^{HSQ}), the codon-optimized BDD-FVIII (CoFVIII^{HSQ}) and firefly luciferase (Luciferase). The Megascript T7 RNA polymerase kit (Thermo Fisher) was used for transcription, and UTP was replaced with 1-methylpseudouridine triphosphate (m1ΨTP; TriLink, San Diego, CA, USA) to generate m1Ψ-containing mRNA. All mRNA were transcribed to contain 100-nucleotide long poly(A) tails. To obtain cap1, RNA was incubated with guanylyltransferase and 2´-*O*-methyltransferase (Vaccinia capping system; New England Biolabs, Frankfurt, Germany). All mRNA were purified and stored at -20°C.

In vitro transfection

For transient *in vitro* production of FVIII, baby hamster kidney (BHK) cells (0.5x10^6 cells in 48-well plates) were transfected with FVIII^{HSQ} or CoFVIII^{HSQ} cloned in the ReNeo vector (0.1 μg) using lipofectamine (Invitrogen, Carlsbad, CA, USA). For *in vitro* transfection using mRNA, mRNA (0.4 μg) was mixed with TransIT®-mRNA reagent (0.45 μL, Mirus Bio, Madison, WI, USA) and Boost reagent (0.29 μL) in a final volume of 50 μL of Dulbecco modified Eagle medium (DMEM) for 2 min at room temperature. HEK293 cells (50,000 cells/130 μL) were incubated with the formulated mRNA overnight in DMEM-F12 (Thermo Fisher). FVIII was measured in the supernatant after 24 h. Supernatant was kept frozen at -80°C until use.

Treatment of mice

Mice were 8- to 12-week old *F8* exon 16 knockout C57BL/6 mice (a kind gift from Prof H.H. Kazazian, Department of Genetics, University of Pennsylvania School of Medicine, Philadelphia, PA, USA). Mice were injected intravenously with recombinant BDD-FVIII (rFVIII, Refacto®, Pfizer, 150 IU/kg), or with mRNA (1 to 5 μg) formulated in TransIT® (100 to 350 μL final volume). Blood was collected from the retro-orbital sinus 6, 24, 48, 72 or 120 h following the injection of mRNA. Plasma was kept frozen at -80°C until use. Animals were handled in agreement with local ethical authorities (approval by Charles Darwin ethics committee, authorization #3335 2015121718044892). FVIII:Ag, FVIII:C, anti-FVIII IgG and FVIII inhibitors were measured as described in the *Online Supplementary Methods*.

Results

Codon-optimization of cDNA encoding factor VIII^{HSQ} improves *in vitro* factor VIII production

We first investigated whether codon-optimization of FVIII^{HSQ} improves the production of FVIII by BHK transfected cells. To this end, CoFVIII^{HSQ} was synthesized and inserted in the Reneo vector. BHK cells were transiently transfected with 0.1 μg FVIII^{HSQ} or CoFVIII^{HSQ}-encoding cDNA (Figure 1A). FVIII:Ag and FVIII:C were measured in the supernatant 24 h later by enzyme-linked immunosorbent assay (ELISA) and chromogenic assay. Transfection with CoFVIII^{HSQ}-encoding cDNA produced 4.2-fold more FVIII:Ag (mean ± standard error of mean: 0.11±0.01 IU/mL *vs*. 0.03±0.00 IU/mL, respectively; P<0.01) and 4.8-fold more FVIII:C (0.14±0.02 IU/mL *vs*. 0.03±0.01 IU/mL, respectively; P<0.01), than transfection with the non-optimized FVIII^{HSQ}-encoding cDNA. Our data confirm previous findings obtained upon gene therapy in preclinical models of hemophilia A,[24,25] on the capacity of codon optimization to increase the yields of FVIII production.

Transfection with factor VIII-encoding mRNA leads to factor VIII production *in vitro*

We then validated the capacity of mRNA transcribed *in vitro*, using the FVIII^{HSQ} and CoFVIII^{HSQ}-encoding cDNA as templates, to promote FVIII production. As the codon-optimization is for *Homo sapiens*, mRNA encoding FVIII^{HSQ} or CoFVIII^{HSQ} formulated in TransIT® was used to transfect human HEK293 cells (Figure 1B). As a negative control, HEK293 cells were transfected with luciferase-encoding mRNA. Transfection with the two FVIII-encoding mRNA led to the *in vitro* production of similar amounts of FVIII (FVIII:Ag: 0.28±0.03 IU/mL *vs*. 0.36±0.04 IU/mL for FVIII^{HSQ} and CoFVIII^{HSQ}, respectively) and similar activities (FVIII:C: 0.20±0.01 IU/mL *vs*. 0.24±0.02 IU/mL, respectively). Accordingly, the specific activity of FVIII produced using both mRNA did not dif-

fer (0.72±0.06 and 0.68±0.08, respectively), suggesting that codon optimization has no beneficial effect on the production of FVIII when cells are transfected with mRNA, in our experimental system.

Systemic delivery of factor VIII-encoding mRNA to factor VIII-deficient mice leads to the endogenous production of factor VIII

FVIII-deficient mice were injected intravenously with 1 μg FVIII^{HSQ}- or CoFVIII^{HSQ}-encoding mRNA formulated in TransIT® (Figure 2A). Plasma levels of FVIII:Ag and FVIII:C, measured after 24 h, were 1.00±0.15 IU/mL and 0.34±0.07 IU/mL in the case of FVIII^{HSQ}-encoding mRNA, and 1.30±0.19 IU/mL and 0.36±0.06 IU/mL in the case of CoFVIII^{HSQ}-encoding mRNA. Likewise, the specific activities of FVIII^{HSQ} and CoFVIII^{HSQ} (defined as the ratios of FVIII:C over FVIII:Ag) did not differ significantly: 0.31±0.06 and 0.25±0.02, respectively, but were more than 2-fold lower than specific activities measured *in vitro* (Figure 1B). To investigate for the presence of non-functional FVIII molecules, we measured plasma levels of FVIII light chain using a dedicated ELISA. Levels of FVIII:Ag and light chain were perfectly correlated (slope=1.15±0.10; P<0.0001) (Figure 2B). However, 14 of the 20 tested samples showed >10% more FVIII light chain than total FVIII, indicating that some FVIII in the plasma samples lacked its A2 domain (A2 domain dissociation is a feature of FVIII inactivation[26]).

The endogenous production of FVIII was then followed over 72 h after the injection of 1, 3 or 5 μg of CoFVIII^{HSQ}-encoding mRNA. At 24 h, the levels of FVIII:C reached in the circulation ranged from 0.27±0.11 to 0.42±0.14 IU/mL (Figure 3A, left panel). The effect of the dose of injected mRNA on the level of endogenously produced FVIII was statistically significant at 72 h (Figure 3A, right panel). Interestingly, the mean residual FVIII activity 72 h after the injection of 3 and 5 μg of mRNA, was above 5% of the theoretical FVIII:C in normal plasma (0.06±0.02 IU/mL and 0.11±0.03 IU/mL, respectively). We then estimated the total amount of FVIII:C produced over 72 h following injection of FVIII-encoding mRNA. To this end, mice were injected intravenously with either 3 IU of human rFVIII or 3 μg of CoFVIII^{HSQ}-encoding mRNA formulated in TransIT® (Figure 3B). The areas under the curves depicting the changes in FVIII:C plasma levels over time were 2.9 and 17.8 IU/mL x h, respectively, showing that the injection of 3 μg of mRNA allows the endogenous production over a period of 72 h of amounts of FVIII:C 6-fold greater than the amount of rFVIII injected at once. The half-life of rFVIII in the circulation was fitted using a two-phase decay equation: short and long half-lives of 0.9 and 4.7 h were calculated. An apparent half-life for the production of FVIII of 17.9 h was calculated by fitting the FVIII:C levels measured at 24, 48 and 72 h with a one-phase decay equation.

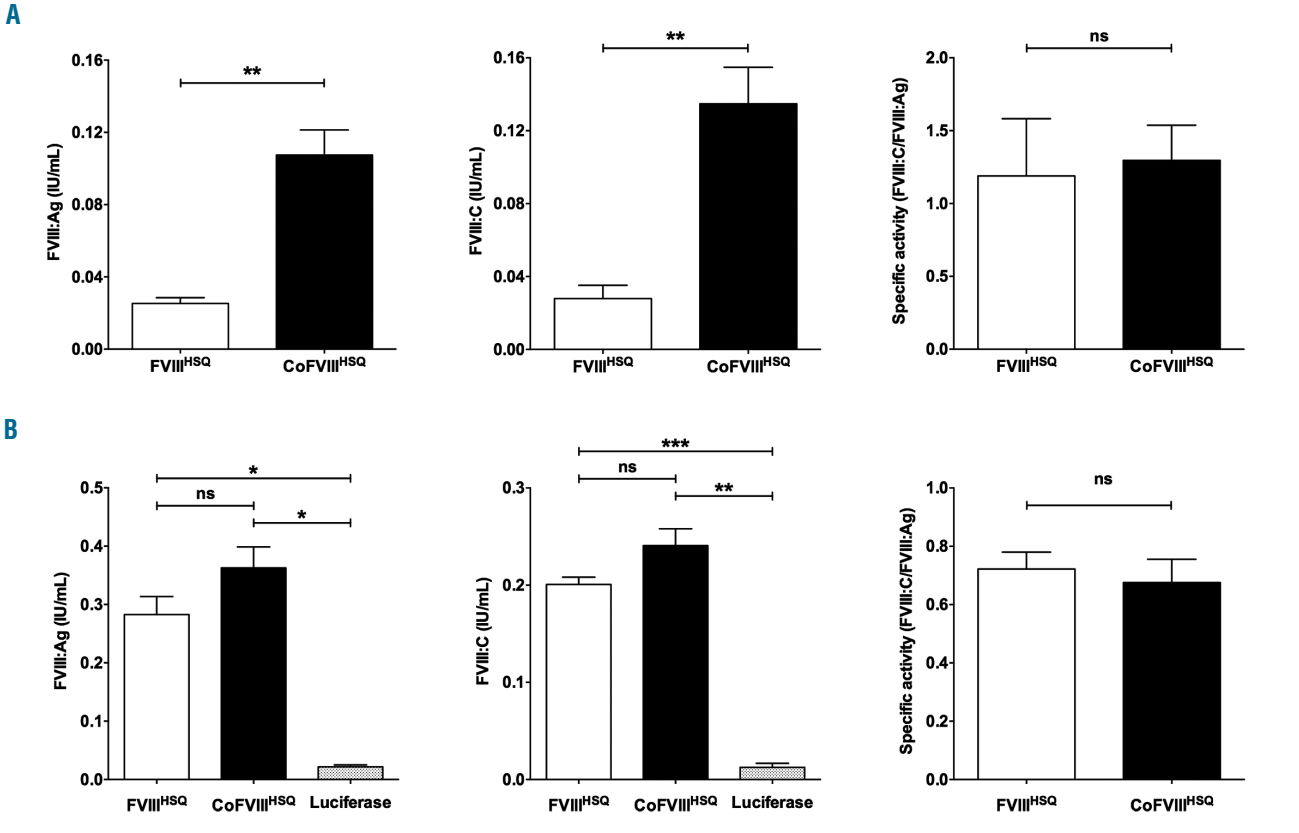

Figure 1. *In vitro* production of wildtype and codon-optimized factor VIII. (A, B) DNA in lipofectamine (0.1 μg) (A) or mRNA formulated in TransIT® (0.4 μg) (B) encoding B domain-deleted (BDD) factor VIII (FVIII^{HSQ}) and codon-optimized BDD-FVIII (CoFVIII^{HSQ}) were used to transfect BHK (A) or HEK293 (B) cells. mRNA encoding luciferase was used as a control (B). FVIII:Ag (left panels) and FVIII:C (middle panels) were measured in cell supernatant 24 h after transfection. The right panels show the specific activities as calculated by dividing the FVIII:C values by the FVIII:Ag values. Statistical differences were assessed using a two-tailed *t* test (ns: non-significant, *P<0.05, **P<0.01, ***P<0.001). Results are presented as the mean ± standard error of mean of three independent experiments.

Correction of the bleeding phenotype of factor VIII-deficient mice by the endogenously produced factor VIII

We then investigated the effect of a single injection of FVIII-encoding mRNA on the bleeding phenotype of FVIII-deficient mice. FVIII-deficient mice were injected with phosphate-buffered saline (PBS), with FVIII-encoding mRNA or with 1.2 or 3 IU rFVIII (Figure 4). The tip of the mouse tail was clipped after 30 min in the case of rFVIII or after 24 h in the case of PBS or mRNA, which correspond to the activity peak of each individual treatment. Blood loss was followed over 20 min. While the PBS-injected mice lost 274.3±53.4 μL of blood, injection of rFVIII protected the mice from major bleeding with blood loss of 86.0±44.9 μL and 12.2±0.9 μL for 1.2 IU (P<0.05) and 3 IU (P<0.001) rFVIII, respectively. Interestingly, mice injected with FVIII-encoding mRNA lost 45.8±24.6 μL of blood (P<0.001 as compared to PBS-treated mice), showing correction of the bleeding phenotype.

Multiple injections of factor VIII-encoding mRNA trigger an anti-factor VIII immune response

The repeated administration of rFVIII is known to trigger the production of inhibitory anti-FVIII IgG in mice after 3-5 injections.[27] We thus assessed the effect of multiple injections of FVIII-encoding mRNA on the onset of an anti-FVIII immune response. We treated FVIII-deficient mice with 1 μg FVIII-encoding mRNA once a week for 7 weeks. As a control, FVIII-deficient mice were injected once a week with 5 IU rFVIII. First, we measured residual plasma FVIII levels 24 h after rFVIII or mRNA injection (Figure 5A, B). Consistent with the short half-life of FVIII in mice, very low FVIII:Ag and FVIII:C were measured in plasma 24 h following injection of rFVIII during the first 3 weeks of treatment. In the case of mRNA-treated mice, a sharp decrease in both FVIII:Ag and FVIII:C was observed between the first (1.13±0.23 IU/mL and 0.37±0.11 IU/mL, respectively) and second (0.26±0.06 IU/mL and 0.05±0.05 IU/mL, respectively) injections. From the third week of treatment onwards, FVIII:C levels were below the level of detection.

We then investigated the presence of inhibitory anti-FVIII IgG 5 days after each administration of mRNA or rFVIII to the mice (Figure 5C, D). As described previously, the intravenous administration of rFVIII induced a progressive increase in levels of anti-FVIII IgG which reached a plateau after five injections (10168±4501 AU after 7 injections) (Figure 5C). This was mirrored by a gradual increase in levels of FVIII inhibitors, which crossed 10 BU/mL 5 days after the fourth injection to plateau at 111±79 BU/mL (Figure 5D). In the case of FVIII-encoding mRNA, levels of anti-FVIII IgG as high as those obtained after five injections of rFVIII were detected as early as 5 days following the second treatment. The plateau after 7 weeks of treatment (98060±8251 AU) was 10-fold higher in the case of mRNA than in the case of rFVIII. Likewise, while no FVIII inhibitory activity was detected 5 days after the first injection of mRNA, levels of 383±196 BU/mL were generated 5 days after the second injection, and gradually increased to reach a plateau at 2258±669 BU/mL after 7 weeks of treatment. The plateau of FVIII inhibitors was thus 20-fold higher in mice treated with

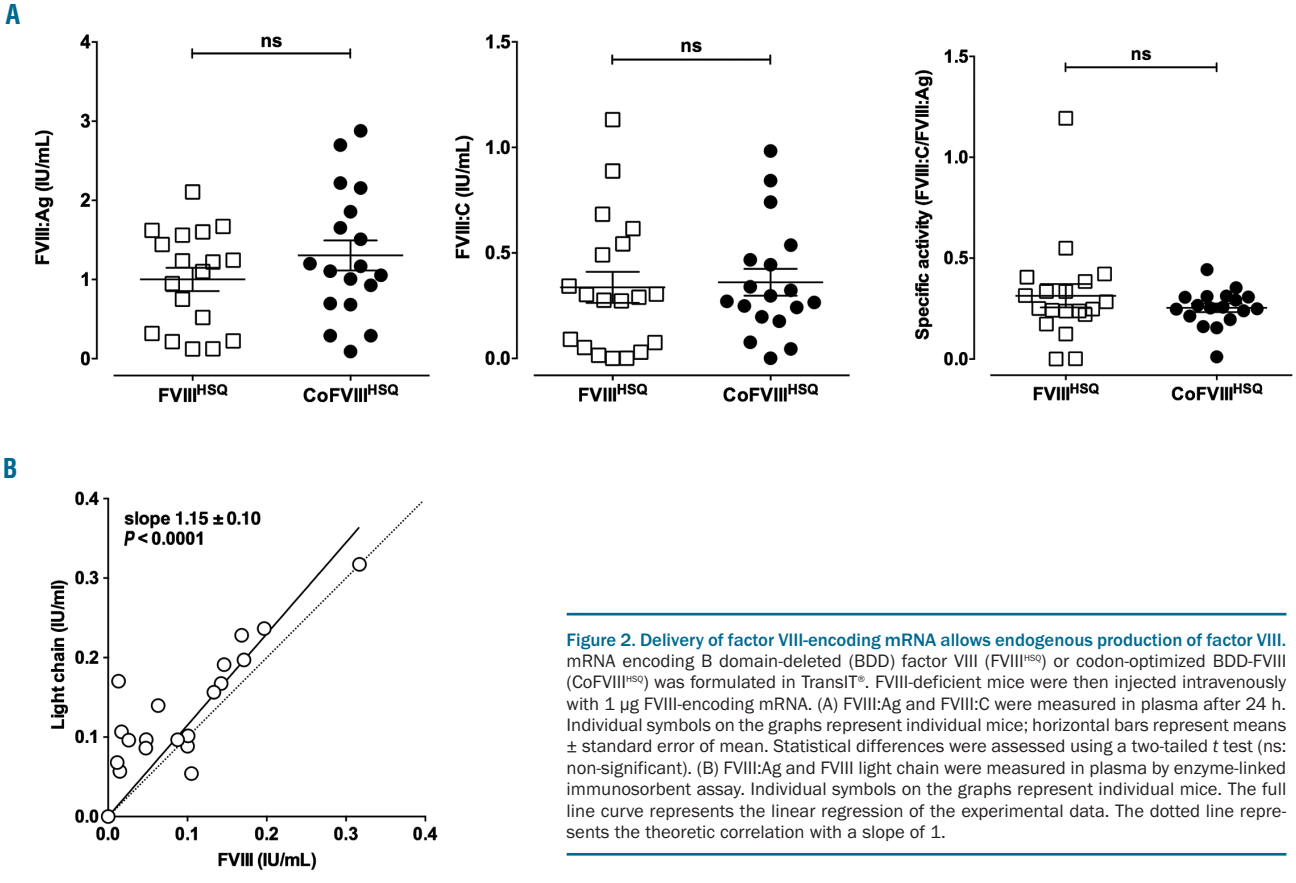

Figure 2. Delivery of factor VIII-encoding mRNA allows endogenous production of factor VIII. mRNA encoding B domain-deleted (BDD) factor VIII (FVIII^{HSQ}) or codon-optimized BDD-FVIII (CoFVIII^{HSQ}) was formulated in TransIT®. FVIII-deficient mice were then injected intravenously with 1 μg FVIII-encoding mRNA. (A) FVIII:Ag and FVIII:C were measured in plasma after 24 h. Individual symbols on the graphs represent individual mice; horizontal bars represent means ± standard error of mean. Statistical differences were assessed using a two-tailed t test (ns: non-significant). (B) FVIII:Ag and FVIII light chain were measured in plasma by enzyme-linked immunosorbent assay. Individual symbols on the graphs represent individual mice. The full line curve represents the linear regression of the experimental data. The dotted line represents the theoretic correlation with a slope of 1.

mRNA than in mice treated with rFVIII. Of note, the incubation of FVIII-encoding mRNA, TransIT® or TransIT®-formulated mRNA with immature human monocyte-derived dendritic cells failed to induce the production of tumor necrosis factor-α and interleukin-6 (Figure 5E, F), indicating that mRNA and TransIT® do not activate innate immune cells and are not responsible for triggering the anti-FVIII immune response. In additional experiments, we investigated the site of production of mRNA-encoded proteins following formulation in TransIT®. To this end, Balb/c mice were injected with luciferase-encoding mRNA formulated in TransIT®. The luminescence measured 24 h later was at least 2-fold greater in the spleen than in the liver (*Online Supplementary Figure S1*), suggesting that the liver and hepatocytes are not the main target for TransIT®-formulated mRNA. Attempts to detect FVIII in FVIII-encoding mRNA-treated FVIII-deficient mice led to occasional FVIII signals in the marginal zone of the spleen and constant absence of FVIII detection in the liver (*data not shown*).

Discussion

The present work documents the sustained endogenous production of pro-coagulant FVIII following the injection of FVIII-encoding mRNA into FVIII-deficient mice, and is of potential relevance for the improvement of treatment for patients with hemophilia A. FVIII levels achieved 24 h after the injection of mRNA were about 40% of the levels in normal plasma. The levels of FVIII expression are notoriously low because of poor transcriptional and translation efficacies[27-29] as well as retention of the protein in the endoplasmic reticulum.[30,31] Attempts to improve the levels of expression of FVIII include partial removal of the B domain with conservation of essential N-glycosylation sites,[24,31] mutation of an immunoglobulin binding-protein (BiP) binding site[32] to ensure improved transfer from the endoplasmic reticulum to the Golgi apparatus,[33] and codon optimization. Here, mRNA was generated using wild-type[23] or codon-optimized cDNA encoding human BDD-FVIII. While codon optimization improved FVIII production following transfection of eukaryotic cells with plasmid DNA *in vitro*, it did not increase the levels of FVIII:C or FVIII:Ag following *in vitro* mRNA transfection of cells or *in vivo* transfection of FVIII-deficient mice. Codon optimization aims at improving translation rates by using codons for which the cognate tRNA levels are not limiting. Thus, codon optimization of FVIII-encoding cDNA cloned in lentiviral vectors or adenoviral-associated vectors led to more than 10-fold increased FVIII levels after *in vitro* transfection of cell lines and after injection into wild-type or FVIII-deficient mice.[24,25] The lack of improvement in protein production associated with the administration of codon-optimized mRNA encoding FVIII suggests that codon optimization of FVIII preferentially targets transcriptional rather than translational events, as previously shown.[34,35] Alternatively, levels of mRNA introduced into each cell upon *in vivo* transfection with TransIT® may be much lower than that transcribed endogenously following transfection using DNA, and insufficient to exhaust non-abundant tRNA. Increasing the amount of mRNA injected *in vivo* did not, however, have drastic effects on the FVIII levels reached in the circulation.

Frequent spontaneous joint and muscle bleeds in patients with severe hemophilia A eventually lead to the development of arthropathy and functional joint impairment. An association between joint bleeds and baseline FVIII activity levels was demonstrated,[36] with FVIII levels above 5% of the normal values drastically reducing the occurrence of joint bleeds. Because the half-life of human FVIII in patients with hemophilia A is between 12 and 18

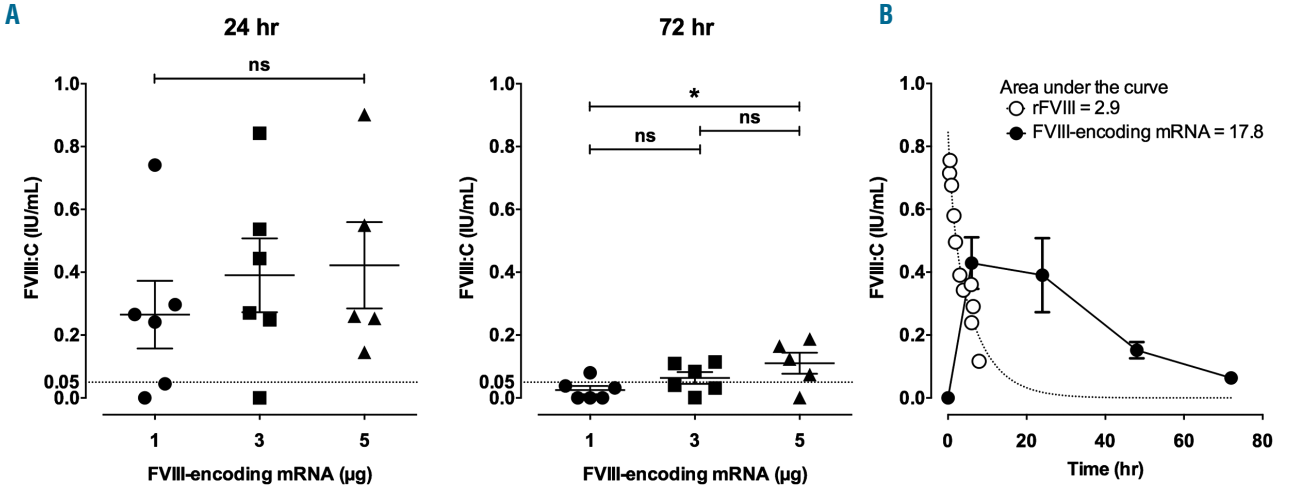

Figure 3. Time-dependent production of endogenous factor VIII after a single injection of factor VIII-encoding mRNA. mRNA encoding codon-optimized B domain-deleted (BDD) factor VIII (CoFVIII^{HSQ}) was formulated in TransIT®. (A) FVIII-deficient mice were then injected intravenously with 1, 3 or 5 µg FVIII-encoding mRNA. FVIII:C was measured in plasma after 24 and 72 h. Individual symbols on the graphs represent individual mice; horizontal bars represent means ± standard error of mean. The dotted line indicates the critical FVIII level (i.e., 5%) required to drastically reduce joint bleeds. Statistical differences were assessed using a two-tailed t test (ns: non-significant, *P<0.05). (B) Mice were injected with 3 µg CoFVIII^{HSQ}-encoding mRNA formulated in TransIT®, or with 100 µL of 10 nM recombinant BDD-FVIII (3 IU rFVIII). FVIII:C in plasma was measured after 30, 60, 90, 120, 180, 240, 360, 390 and 480 min in the case of rFVIII, in the case of mRNA. The dotted line depicts the non-linear fit (two-phase exponential decay: $y=0.62*e^{-0.15x}+0.2211*e^{-0.80x}$) of the experimental data obtained with rFVIII. The full circles and full line curve represent means ± standard error of mean of six mice treated with mRNA (representative of two independent experiments; fitted with a one-phase exponential decay for the values obtained at 24, 48 and 72 h: $y=0.99*e^{-0.03874x}$). Areas under the curves were calculated using Prism GraphPad (version 6).

h, prophylactic replacement therapy is the gold standard to maintain healthy joint function.[37] In FVIII-deficient mice, the half-life of human FVIII is between 4 and 6 h. Interestingly, delivery of FVIII-encoding mRNA yielded FVIII levels that corrected acute bleeding in a tail clipping assay, and were maintained above 5% for up to 72 h. The longer residence time of FVIII produced after mRNA delivery as compared to that of rFVIII results from the cumulative lifespans of the transfected mRNA in the cells and of the FVIII released in the circulation. mRNA-based therapy can be improved by engineering the encoded protein to extend its half-life.[38] For instance, a FVIII molecule with an increased half-life has been developed by fusion of FVIII to the Fc fragment of human IgG1.[48] We anticipate that the use of mRNA encoding long-lasting FVIII glycoproteins will allow a further increase in the duration of FVIII detection *in vivo*. Because peak expression levels of FVIII were reached in the mice between 6 and 24 h after the administration of mRNA, mRNA-based therapy may represent a surrogate for prophylactic treatment rather than for the on-demand treatment of sudden acute hemorrhagic events.

The specific activity of the rFVIII produced by eukaryotic cells *in vitro* was about 1.2 following transfection using cDNA and about 0.7 following transfection with mRNA. In contrast, the specific activity of the FVIII produced endogenously following injection of mRNA to the mice was about 0.3, suggesting the absence of pro-coagulant activity for a substantial proportion of the endogenously produced FVIII molecules. In parallel, we compared the levels of intact FVIII measured using a standard ELISA, wherein FVIII is captured with an anti-light chain antibody and detected with anti-heavy chain antibody, with that of FVIII light chain measured using a sandwich light chain-specific ELISA. A perfect correlation was obtained although with an overall tendency for 2-fold more light chains than intact molecules. Importantly, the levels of light chain may be under-estimated because of the short *in vivo* half-life of the light chain alone. Future experiments will indicate whether the use of mRNA encoding FVIII lacking the furin cleavage site[39,40] between the heavy and light chains, or FVIII mutants with increased FVIII A2 subunit stability[41] yields FVIII with improved specific activity. An alternative and non-exclusive explanation for the poor specific activity of the endogenously produced FVIII is the fact that the TransIT® used to formulate the mRNA does not target particular cell types. In fact, we show here that luciferase is produced by the spleen, rather than by the liver, following injection of mice with luciferase-encoding mRNA formulated with TransIT®. Accordingly, immunofluorescence experiments on mice treated with FVIII-encoding mRNA occasionally detected faint amounts of FVIII in the marginal zone of the spleen but never in the liver (not shown). Hence, TransIT® delivers FVIII mRNA to cells that are not dedicated to the production of FVIII,[42,43] thus potentially generating FVIII molecules that are improperly folded or have undergone incorrect post-translational modifications.

In patients with severe hemophilia A, inhibitory anti-FVIII IgG (FVIII inhibitors) generally develop within the first 20 cumulated days of exposure to therapeutic FVIII.[44] In the present work, and in agreement with previous studies in FVIII-deficient mice,[45] FVIII-binding IgG and FVIII inhibitors were detected after two and three intravenous injections of rFVIII, respectively. The levels of anti-FVIII IgG increased to reach a plateau at 10- to 100-fold higher levels after two to three additional injections of rFVIII. In the case of mRNA administration, however, close to maximal levels of FVIII-binding IgG and inhibitory antibodies were reached after only two injections of FVIII-encoding mRNA. Accordingly, endogenous FVIII:C was undetectable as early as after the second administration of mRNA. Different explanations for such a brisk and intense immune response to the endogenously produced FVIII may be envisaged. Because the mRNA used in our study was engineered to contain 1-methylpseudouridines and was purified by high performance liquid chromatography to remove double-stranded RNA, thus abrogating mRNA recognition by TLR3, TLR7, TLR8 and RIG-I,[9-12] it is not probable that the very mRNA plays an adjuvant role in the onset of the anti-FVIII immune response. Indeed, FVIII-encoding mRNA, alone or formulated in TransIT®, failed to activate human immature monocyte-derived dendritic cells *in vitro*. Interestingly, previous work on *in vivo* mRNA transfection without apparent induction of neutralizing immune responses used TransIT®[15] or other types of nanoparticles.[16,18] Most studies were however performed in immunocompromised animals[46] or in animals expressing the corresponding endogenous protein (e.g., the absence of induction of an anti-erythropoietin immune response in animals receiving erythropoietin-encoding mRNA[15,17] probably relates to the presence of the endogenous erythropoieitin molecule and associated ongoing active immune tolerance).

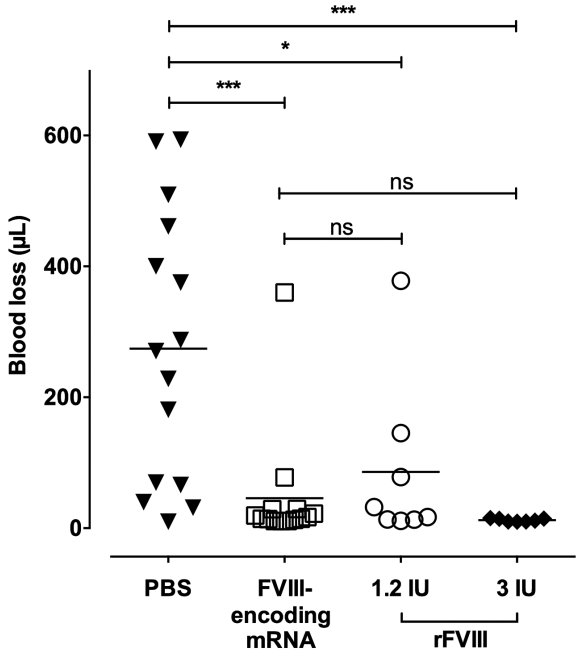

Figure 4. Injection of factor VIII-encoding mRNA corrects acute bleeding in factor VIII-deficient mice. Factor VIII (FVIII)-deficient mice were injected intravenously with 3 µg of FVIII-encoding mRNA (empty squares) formulated in TransIT®, with 1.2 IU (empty circles) or 3 IU (full diamonds) recombinant B domain-deleted-FVIII (rFVIII) or with phosphate-buffered saline (PBS) (full triangles). Mice tails were clipped 3 mm from the tip, 24 h after mRNA and PBS injection, or 30 min after rFVIII injection. Bleeding intensity was measured as the volume of blood lost during 20 min. Horizontal bars represent means and individual dots represent individual mice. Statistical differences were assessed using the double-sided Mann-Whitney test (ns: non-significant; *P<0.05; ***P<0.001).

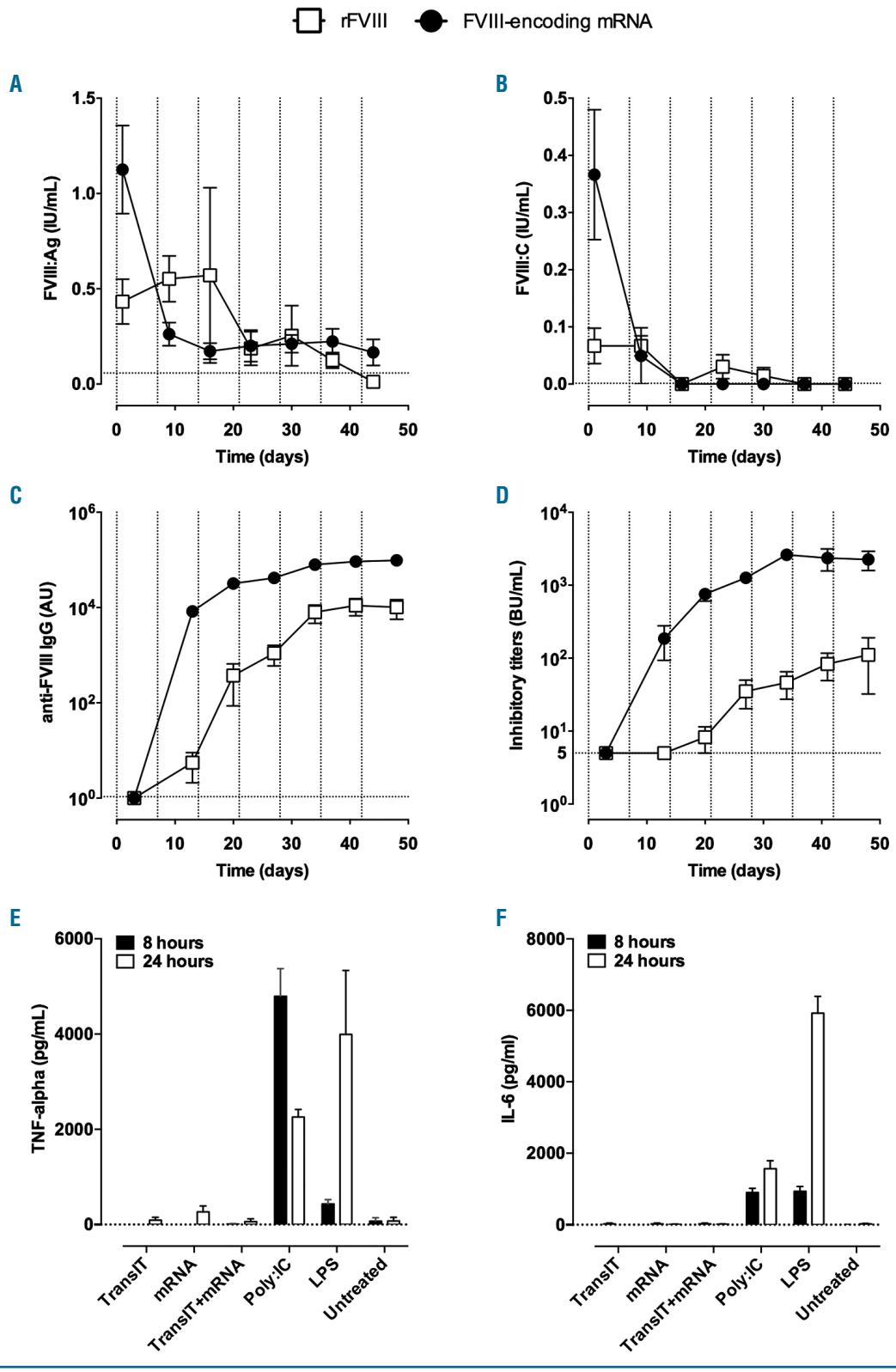

Figure 5. Induction of an anti-factor VIII immune response after repeated injections of factor VIII-encoding mRNA. (A-D) Factor VIII (FVIII)-deficient mice were injected intravenously with 1 μg of coFVIII^{HSQ}-encoding mRNA formulated in TransIT® (full circles), or with 5 IU recombinant BDD-FVIII (empty squares), once a week for 7 weeks. FVIII:Ag (A) and FVIII:C (B) were measured in plasma 24 h after each injection. Anti-FVIII IgG (C) and inhibitory titers (D) were measured in plasma 72 h after each injection. Results are depicted as the mean ± standard error of mean (SEM) for four to seven mice per group. The vertical dotted lines represent the days of FVIII/mRNA administration. The horizontal dotted lines represent the background levels (calculated as "mean + 1 x standard deviation") measured in six or seven FVIII-deficient mice (A: 0.045+0.013 IU/mL; B: 0.001±0.000 IU/mL; C: 0.84±0.23 μg/mL); or the threshold for detection (D: 5 BU/mL). (E and F) Five-day old immature monocyte-derived dendritic cells were incubated alone (Untreated) or in the presence of Poly:IC, lipopolysaccharide (LPS), TransIT® alone, 1 μg FVIII-encoding mRNA (mRNA) alone or 1 μg FVIII-encoding mRNA formulated in TransIT®. The panels show the levels of tumor necrosis factor-α (E) and interleukin-6 (F) measured in the culture supernatant 8 h (full bars) and 24 h (empty bars) later. Data are presented as the mean ± standard error of mean from two independent experiments. Differences between TransIT, mRNA, TransIT+mRNA and Untreated were not statistically significant (two-sided Mann-Whitney test).

In fact, the very formulation of mRNA in TransIT® may be a reason for induction of a strong anti-FVIII immune response. TransIT® was initially conceived for *in vitro* and not *in vivo* gene transfection. As explained above, protein production following injection of TransIT®-formulated mRNA is not targeted to the liver or endothelial cells, which produce FVIII under physiological conditions. This is reminiscent of the early works on gene therapy for hemophilia wherein the use of promoters with poor specificity for hepatocytes was associated with the induction of neutralizing anti-FVIII or anti-factor IX antibodies.[47]

Several lines of evidence suggest that the FVIII produced may itself be responsible for the sharp anti-FVIII immune response. As explained above, FVIII is a particularly immunogenic glycoprotein: e.g., a fusion protein between the light chain of FVIII and the first domain of hemagglutinin 1 (HA1) demonstrated greater anti-HA1 immunogenicity upon intravenous injection to FVIII-deficient mice than the HA1 molecule alone.[48] In contrast, the production of factor IX was induced in mice following administration of mRNA without report of a neutralizing immune response.[18] Of note, a relationship between the dose of FVIII injected and the kinetics of detection of the anti-FVIII IgG response was reported in mice[45] and in patients.[49] This is particularly relevant in view of the fact that the amount of active FVIII produced over 72 h after one injection of FVIII-encoding mRNA was equivalent to 6-fold the amount of rFVIII administered in a single injection. Furthermore, based on the poor specific activity of the endogenously produced FVIII, the total amount of FVIII molecules (active and inactive) probably exceeds 18-fold that of injected rFVIII. Further work will indicate whether targeting mRNA delivery to hepatocytes or to endothelial cells using improved lipid nanoparticle-based formulating agents,[50] using mRNA encoding single chain or A2 variant stable FVIII[39,40,41] and including miRNA target sequences to prevent off-target expression in hematopoietic cells[51] are plausible strategies to improve the specific activity and reduce the immunogenicity of the endogenously produced molecule.

Acknowledgment

We thank Dr Katalin Karikó (BioNTech RNA Pharmaceuticals, Mainz, Germany) for her constant support regarding this project and for providing the IVT mRNA. This study was supported by Institut National de la Santé et de la Recherche Médicale (INSERM), Centre National de la Recherche Scientifique (CNRS), Sorbonne Université, and by grants from CSL-Behring (Paris, France), ANR (Exfiltrin project: ANR-18-CE17-0010-02) and CEFIPRA (IFC/7126/ Hemophilia/1353). JR was the recipient of a fellowship from Ministère de l'Enseignement Supérieur et de la Recherche. We also thank the staff from the Center of Histology, Cell Imaging and Flow Cytometry (CHIC) and Centre d'Expérimentation Fonctionnelle for assistance (Centre de Recherche des Cordeliers, Paris).

References

1. Mannucci PM, Tuddenham EG. The hemophilias--from royal genes to gene therapy. N Engl J Med. 2001;344(23):1773-1779.
2. Oldenburg J, Mahlangu JN, Kim B, et al. Emicizumab prophylaxis in hemophilia A with inhibitors. N Engl J Med. 2017;377(9):809-818.
3. Chowdary P, Lethagen S, Friedrich U, et al. Safety and pharmacokinetics of anti-TFPI antibody (concizumab) in healthy volunteers and patients with hemophilia: a randomized first human dose trial. J Thromb Haemost. 2015;13(5):743-754.
4. Pasi KJ, Rangarajan S, Georgiev P, et al. Targeting of antithrombin in hemophilia A or B with RNAi therapy. N Engl J Med. 2017;377(9):819-828.
5. Polderdijk SG, Adams TE, Ivanciu L, et al. Design and characterization of an APC-specific serpin for the treatment of hemophilia. Blood. 2017;129(1):105-113.
6. Nathwani AC, Davidoff AM, Tuddenham EGD. Advances in gene therapy for hemophilia. Hum Gene Ther. 2017;28(11): 1004-1012.
7. Wolff JA, Malone RW, Williams P, et al. Direct gene transfer into mouse muscle in vivo. Science. 1990;247(4949 Pt 1):1465-1468.
8. Heiser A, Coleman D, Dannull J, et al. Autologous dendritic cells transfected with prostate-specific antigen RNA stimulate CTL responses against metastatic prostate tumors. J Clin Invest. 2002;109(3):409-417.
9. Alexopoulou L, Holt AC, Medzhitov R, Flavell RA. Recognition of double-stranded RNA and activation of NF-kappaB by Toll-like receptor 3. Nature. 2001;413(6857):732-738.
10. Heil F, Hemmi H, Hochrein H, et al. Species-specific recognition of single-stranded RNA via toll-like receptor 7 and 8. Science. 2004;303(5663):1526-1529.
11. Hornung V, Ellegast J, Kim S, et al. 5'-Triphosphate RNA is the ligand for RIG-I. Science. 2006;314(5801):994-997.
12. Schlee M, Roth A, Hornung V, et al. Recognition of 5' triphosphate by RIG-I helicase requires short blunt double-stranded RNA as contained in panhandle of negative-strand virus. Immunity. 2009;31(1):25-34.
13. Kariko K, Buckstein M, Ni H, Weissman D. Suppression of RNA recognition by Toll-like receptors: the impact of nucleoside modification and the evolutionary origin of RNA. Immunity. 2005;23(2):165-175.
14. Kariko K, Muramatsu H, Ludwig J, Weissman D. Generating the optimal mRNA for therapy: HPLC purification eliminates immune activation and improves translation of nucleoside-modified, protein-encoding mRNA. Nucleic Acids Res. 2011;39(21):e142.
15. Kariko K, Muramatsu H, Keller JM, Weissman D. Increased erythropoiesis in mice injected with submicrogram quantities of pseudouridine-containing mRNA encoding erythropoietin. Mol Ther. 2012;20(5): 948-953.
16. Li B, Luo X, Deng B, et al. An orthogonal array optimization of lipid-like nanoparticles for mRNA delivery in vivo. Nano Lett. 2015;15(12):8099-8107.
17. Thess A, Grund S, Mui BL, et al. Sequence-engineered mRNA without chemical nucleoside modifications enables an effective protein therapy in large animals. Mol Ther. 2015;23(9):1456-1464.
18. Ramaswamy S, Tonnu N, Tachikawa K, et al. Systemic delivery of factor IX messenger RNA for protein replacement therapy. Proc Natl Acad Sci U S A. 2017;114(10):E1941-E1950.
19. Pardi N, Hogan MJ, Pelc RS, et al. Zika virus protection by a single low-dose nucleoside-modified mRNA vaccination. Nature. 2017;543(7644):248-251.
20. Richner JM, Himansu S, Dowd KA, et al. Modified mRNA vaccines protect against zika virus infection. Cell. 2017;168(6):1114-1125 e1110.
21. Su Z, Dannull J, Heiser A, et al. Immunological and clinical responses in metastatic renal cancer patients vaccinated with tumor RNA-transfected dendritic cells. Cancer Res. 2003;63(9):2127-2133.
22. Kyte JA, Kvalheim G, Lislerud K, et al. T cell responses in melanoma patients after vaccination with tumor-mRNA transfected dendritic cells. Cancer Immunol Immunother. 2007;56(5):659-675.
23. Healey JF, Barrow RT, Tamim HM, et al. Residues Glu2181-Val2243 contain a major determinant of the inhibitory epitope in the C2 domain of human factor VIII. Blood. 1998;92(10):3701-3709.
24. McIntosh J, Lenting PJ, Rosales C, et al. Therapeutic levels of FVIII following a single peripheral vein administration of rAAV vector encoding a novel human factor VIII variant. Blood. 2013;121(17):3335-3344.
25. Ward NJ, Buckley SM, Waddington SN, et al. Codon optimization of human factor VIII cDNAs leads to high-level expression.

Blood. 2011;117(3):798-807.
26. Pipe SW, Eickhorst AN, McKinley SH, Saenko EL, Kaufman RJ. Mild hemophilia A caused by increased rate of factor VIII A2 subunit dissociation: evidence for nonproteolytic inactivation of factor VIIIa in vivo. Blood. 1999;93(1):176-183.
27. Kaufman RJ, Wasley LC, Davies MV, et al. Effect of von Willebrand factor coexpression on the synthesis and secretion of factor VIII in Chinese hamster ovary cells. Mol Cell Biol. 1989;9(3):1233-1242.
28. Lynch CM, Israel DI, Kaufman RJ, Miller AD. Sequences in the coding region of clotting factor VIII act as dominant inhibitors of RNA accumulation and protein production. Hum Gene Ther. 1993;4(3):259-272.
29. Hoeben RC, Fallaux FJ, Cramer SJ, et al. Expression of the blood-clotting factor-VIII cDNA is repressed by a transcriptional silencer located in its coding region. Blood. 1995;85(9):2447-2454.
30. Dorner AJ, Bole DG, Kaufman RJ. The relationship of N-linked glycosylation and heavy chain-binding protein association with the secretion of glycoproteins. J Cell Biol. 1987;105(6 Pt 1):2665-2674.
31. Miao HZ, Sirachainan N, Palmer L, et al. Bioengineering of coagulation factor VIII for improved secretion. Blood. 2004;103(9):3412-3419.
32. Swaroop M, Moussalli M, Pipe S, Kaufman R. Mutagenesis of a potential immunoglobulin-binding protein-binding site enhances secretion of coagulation factor VIII. J Biol Chem. 1997;272:24121-24124.
33. Zhang B, McGee B, Yamaoka JS, et al. Combined deficiency of factor V and factor VIII is due to mutations in either LMAN1 or MCFD2. Blood. 2006;107(5):1903-1907.
34. Zhou Z, Dang Y, Zhou M, et al. Codon usage is an important determinant of gene expression levels largely through its effects on transcription. Proc Natl Acad Sci U S A. 2016;113(41):E6117-E6125.
35. Kudla G, Lipinski L, Caffin F, Helwak A, Zylicz M. High guanine and cytosine content increases mRNA levels in mammalian cells. PLoS Biol. 2006;4(6):e180.
36. den Uijl IE, Fischer K, Van Der Bom JG, et al. Analysis of low frequency bleeding data: the association of joint bleeds according to baseline FVIII activity levels. Haemophilia. 2011;17(1):41-44.
37. Oldenburg J. Optimal treatment strategies for hemophilia: achievements and limitations of current prophylactic regimens. Blood. 2015;125(13):2038-2044.
38. Farelli JD, Asrani KH, Isaacs C, et al. Leveraging rational protein engineering to improve mRNA therapeutics. Nucleic Acid Ther. 2018;28(2):74-85.
39. Siner JI, Samelson-Jones BJ, Crudele JM, et al. Circumventing furin enhances factor VIII biological activity and ameliorates bleeding phenotypes in hemophilia models. JCI Insight. 2016;1(16):e89371.
40. Nguyen GN, George LA, Siner JI, et al. Novel factor VIII variants with a modified furin cleavage site improve the efficacy of gene therapy for hemophilia A. J Thromb Haemost. 2017;15(1):110-121.
41. Monaghan M, Wakabayashi H, Griffiths A, Wintermute J, Fay PJ. Enhanced factor VIIIa stability of A2 domain interface variants results from an increased apparent affinity for the A2 subunit. Results from an increased apparent affinity for the A2 subunit. Thromb Haemost. 2014;112(3):495-502.
42. Shahani T, Lavend'homme R, Luttun A, et al. Activation of human endothelial cells from specific vascular beds induces the release of a FVIII storage pool. Blood. 2010;115(23):4902-4909.
43. Pan J, Dinh TT, Rajaraman A, et al. Patterns of expression of factor VIII and von Willebrand factor by endothelial cell subsets in vivo. Blood. 2016;128(1):104-109.
44. Gouw SC, van den Berg HM, Fischer K, et al. Intensity of factor VIII treatment and inhibitor development in children with severe hemophilia A: the RODIN study. Blood. 2013;121(20):4046-4055.
45. Reipert BM, Ahmad RU, Turecek PL, et al. Characterization of antibodies induced by human factor VIII in a murine knockout model of hemophilia A. Thromb Haemost. 2000;84(5):826-832.
46. Pardi N, Secreto AJ, Shan X, et al. Administration of nucleoside-modified mRNA encoding broadly neutralizing antibody protects humanized mice from HIV-1 challenge. Nat Commun. 2017;8:14630.
47. VandenDriessche T, Collen D, Chuah MK. Gene therapy for the hemophilias. J Thromb Haemost. 2003;1(7):1550-1558.
48. Ing M, Gupta N, Teyssandier M, et al. Immunogenicity of long-lasting recombinant factor VIII products. Cell Immunol. 2016;301:40-48.
49. Gouw SC, van den Berg HM, le Cessie S, van der Bom JG. Treatment characteristics and the risk of inhibitor development: a multicenter cohort study among previously untreated patients with severe hemophilia A. J Thromb Haemost. 2007;5(7):1383-1390.
50. Dahlman JE, Barnes C, Khan O, et al. In vivo endothelial siRNA delivery using polymeric nanoparticles with low molecular weight. Nat Nanotechnol. 2014;9(8):648-655.
51. Matsui H, Hegadorn C, Ozelo M, et al. A microRNA-regulated and GP64-pseudotyped lentiviral vector mediates stable expression of FVIII in a murine model of hemophilia A. Mol Ther. 2011;19(4):723-730.

Ferrata Storti Foundation

Haematologica 2020
Volume 105(4):1138-1146

Allogeneic peripheral blood stem cell transplantation with anti-thymocyte globulin *versus* allogeneic bone marrow transplantation without anti-thymocyte globulin

Frédéric Baron,[1] Jacques-Emmanuel Galimard,[2-5] Myriam Labopin,[2-5] Ibrahim Yakoub-Agha,[6] Riitta Niittyvuopio,[7] Nicolaus Kröger,[8] Laimonas Griskevicius,[9] Depei Wu,[10] Edouard Forcade,[11] Carlos Richard,[12] Mahmoud Aljurf,[13] Grzegorz Helbig,[14] Hélène Labussière-Wallet,[15] Mohamad Mohty[2-5] and Arnon Nagler[2,16]

[1]Laboratory of Hematology, GIGA-I3, University of Liège and CHU of Liège, Liege, Belgium; [2]EBMT Paris study office/CEREST-TC, Paris, France; [3]Department of Haematology, Saint Antoine Hospital, Paris, France; [4]Sorbonne University, Centre De Recherche Saint Antoine, INSERM UMR938, Paris, France; [5]Sorbonne University, Paris, France; [6]University of Lille, INSERM, and CHU of Lille, INFINITE U1286, Lille, France; [7]HUCH Comprehensive Cancer Center, Stem Cell Transplantation Unit, Helsinki, Finland; [8]University Hospital Eppendorf, Bone Marrow Transplantation Center, Hamburg, Germany; [9]Institute of Clinical Medicine, Vilnius University and Vilnius University Hospital Santaros Klinikos, Vilnius, Lithuania; [10]First Affiliated Hospital of Soochow University, Department of Hematology, Suzhou, China; [11]CHU Bordeaux Hôpital Haut-Leveque, Pessac, France; [12]Hospital U. Marqués de Valdecilla, Servicio de Hematología-IDIVAL, Santander, Spain; [13]King Faisal Specialist Hospital & Research Centre Oncology, Riyadh, Saudi Arabia; [14]Silesian Medical Academy, University Department of Haematology and Bone Marrow Transplantation, Katowice, Poland; [15]Centre Hospitalier Lyon Sud, Service Hematologie, Lyon, France and [16]Division of Hematology and Bone Marrow Transplantation, The Chaim Sheba Medical Center, Tel-Hashomer, Ramat-Gan, Israel

ABSTRACT

We compared severe graft-*versus*-host-disease (GvHD) free and relapse-free survival and other transplantation outcomes of acute myeloid leukemia (AML) patients given bone marrow (BM) without anti-thymocyte globulin (ATG) *versus* peripheral blood stem cells (PBSC) with ATG after myeloablative conditioning. In the cohort of patients receiving grafts from a human leukocyte antigen (HLA)-matched sibling donor, patients given PBSC with ATG (n=1,021) and those given BM without ATG (n=1,633) presented comparable severe GvHD-free relapse-free survival (GRSF)(hazard ratio [HR]=0.9, 95% confidence interval [CI]: 0.8-1.1, *P*=0.5) and overall survival (HR=1.0, 95% CI: 0.8-1.2, *P*=0.8). They had however, a lower incidence of chronic GvHD (cGvHD) (HR=0.7, 95% CI: 0.6-0.9, *P*=0.01). In the cohort of patients receiving grafts from HLA-matched unrelated donor , patients given PBSC with ATG (n=2,318) had better severe GvHD-free and relapse-free survival (GRFS) than those given BM without ATG (n=303) (HR=0.8, 95% CI: 0.6-0.9, *P*=0.001). They also had a lower incidence of cGvHD (HR=0.6, 95% CI: 0.5-0.8, *P*=0.0006) and better overall survival (HR=0.8, 95% CI: 0.6-1.0, *P*=0.04). In summary, these data suggest that PBSC with ATG results in comparable (in the case of sibling donor) or significantly better (in the case of unrelated donor) severe GRFS than BM without ATG in patients with AML in complete remission receiving grafts after myeloablative conditioning.

Introduction

A number of phase III trials have compared peripheral blood stem cells (PBSC) with bone marrow (BM) as the stem cell source for allogeneic hematopoietic cell transplantation in patients given grafts after myeloablative regimens.[1,2] A meta-analysis of trials performed in patients given grafts from human leukocyte antigen (HLA)-matched sibling donors (MSD) revealed that the use PBSC of instead of BM was associated with a higher incidence of grade III-IV acute graft-*versus*-host dis-

Correspondence:

FRÉDÉRIC BARON
f.baron@ulg.ac.be

Received: May 28, 2019.

Accepted: August 13, 2019.

Pre-published: August 14, 2019.

doi:10.3324/haematol.2019.227603

Check the online version for the most updated information on this article, online supplements, and information on authorship & disclosures: www.haematologica.org/content/105/4/1138

ease (aGvHD) and (extensive) cGvHD, as well as a lower incidence of relapse (IR) and better overall survival (OS) in the subgroup of patients with late-stage disease.[3] Further, the only phase III trial performed in patients given grafts from HLA-matched unrelated donors (MUD) showed that patients randomized to the BM group had a lower inci-

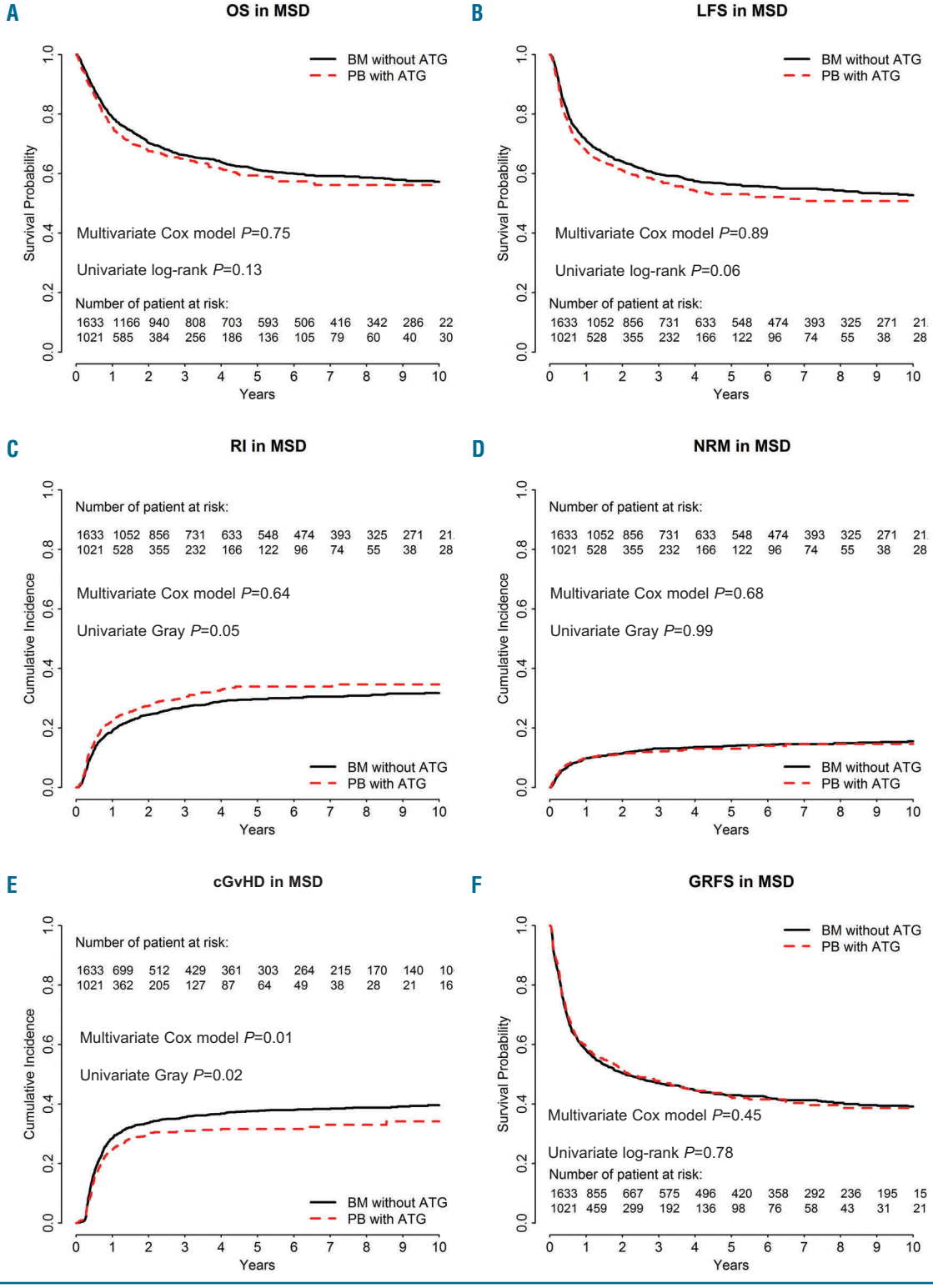

Figure 1. Comparison of outcomes in bone marrow (BM) patients without anti-thymocyte globulin (ATG) and in those given peripheral blood (PB) stem cells with ATG (the dotted line shows the PBSC with ATG curve adjusted for relevant covariates) in the cohort of patients receiving grafts from HLA-identical sibling donor (MSD). (A) Overall survival (OS), *P*=0.13. (B) Leukemia-free survival (LFS), *P*=0.065. (C) Incidence of relapse (RI), *P*=0.0496. (D) Non-relapse mortality (NRM), *P*=0.989. (E) chronic graft-*versus*-host disease (cGvHD), *P*=0.0186. (F) GvHD-free and relapse-free survival (GRFS), *P*=0.782.

dence of cGvHD, similar OS, and better patient-reported outcomes at 5 years after transplantation than those randomized to the PBSC arm.[4,5] This might suggest that, at least in the MUD setting, BM may be preferred over PBSC as a stem cell source in patients receiving grafts after myeloablative regimens. In concordance with these findings, a recent European Group for Blood and Marrow Transplantation (EBMT) study observed a better GvHD-free relapse-free survival (GRFS) with BM than with peripheral blood (PB) as the stem cell source.[6]

In the last two decades, five phase III trials have assessed the impact of anti-thymocyte globulins (ATG) on transplantation outcomes in patients given grafts (mainly PBSC) from MSD (n=1)[7] or MUD (n=4).[8-11] These five trials demonstrated a lower incidence of cGvHD with ATG.[12] Two of three trials assessing the impact of ATG on GRFS[13] observed better GRFS in patients randomized to ATG,[7,10] while the study by Soiffer *et al*. failed to demonstrate this effect.[11] ATG was also found to improve GRFS in a registry study including data from patients given grafts from HLA-identical siblings after myeloablative fludarabine + busulfan regimens.[13]

These findings prompted us to compare transplantation outcomes in AML patients following BMT without ATG *versus* PBSC transplantation with ATG in the first or second complete remission (CR).

Methods

Ethics

The scientific board of the Acute Leukaemia Working Party (ALWP) of the European Society for Blood and Marrow Transplantation (EBMT) approved this research project. The study was conducted according to the Declaration of Helsinki and Good Clinical Practice guidelines.

Inclusion/exclusion criteria and study endpoints

Inclusion criteria included adult patients, *de novo* or secondary AML, myeloablative conditioning, MSD or 10/10 HLA-matched unrelated donors (MUD), first or second CR, first allo-transplantation from 2000 to 2017 at an EBMT-affiliated center, and either BM without ATG, or PBSC with ATG. Exclusion criteria consisted of *in vitro* T-cell depletion of the graft, and prior administration of alemtuzumab. The primary endpoint was GRFS. Secondary endpoints included grade II-IV GvHD, RI, non-relapse mortality (NRM), leukemia-free survival (LFS) and OS.

Statistical analyses

Myeloablative conditioning was defined as use of ≥ 6 Gy TBI, busulfan > 8 mg/kg, or melphalan > 140 mg/m^2 as previously reported.[14] The cytogenetic AML risk was determined as previously reported.[15,16]

NRM was defined as death without prior or current disease recurrence. Events in the composite endpoint GRFS included grade III-IV aGvHD, extensive cGvHD, relapse or death as previously reported.[17]

OS, LFS and GRFS were estimated using the Kaplan-Meier estimates. Cumulative incidence functions (CIF) were used for RI and NRM in a competing risk setting, since death and relapse are competing together. In estimating the cumulative incidence of aGvHD and cGvHD, we considered relapse and death to be competing events. Univariate analyses were done using Gray's test for CIF and the log-rank test for GRFS, OS and LFS. Since there were some imbalances between the groups we performed multivariate Cox models to further determine the impact of the graft type on transplantation outcome. These Cox models were adjusted for disease status at transplantation, female donor to male recipient or not, CMV serostatus, use or not of total body irradiation (TBI), year of transplantation, age at transplantation, primary *versus* secondary AML, and cytogenetic risk. In order to take into account the center effect, we introduced a frailty for each center into the model, as previously reported.[18,19] Specifically, we introduced a random effect (also named frailty effect) in the Cox multivariate models. Then, the same random effect was shared by all patients within the same center. In order to assess whether there was a statistical interaction between the year of transplantation and the association between BMT without ATG *versus* PBSC with ATG and the incidence of relapse, we introduced the interaction term between cell source and year as a binary variable (with the median year by group as the cut-off) in the Cox multivariate model for relapse. Results are presented as hazard ratios (HR) and 95% confidence intervals (95% CI). The HR for year of transplantation corresponded to a 5-year increase and to a 10-year increase for the age at transplantation. As planned in the synopsis, the analyses were done separately for MSD and MUD. The interaction between graft type (i.e. BM without ATG or PBSC with ATG) and donor type (MSD *versus* MUD) was confirmed for several outcomes (*data not shown*).

Results

BM without ATG *versus* PBSC with ATG in MSD recipients

Patients

A total of 2,654 MSD recipients met the inclusion/exclusion criteria, comprising 1,633 BM without ATG patients and 1,021 PBSC with ATG patients (Table 1). In comparison to BM without ATG recipients, PBSC with ATG patients were older (median 48 years *vs.* 40 years old), were transplanted more recently (median year of transplantation 2014 *vs.* 2008), less likely to have a good cytogenetic risk (10% *vs.* 16%), more likely to have secondary AML (11% *vs.* 6%), less frequently received TBI in the conditioning regimen (12% *vs.* 32%), and were more frequently male patients receiving grafts from female donors (25% *vs.* 22%).

GvHD

The 100-day incidence of grade 2-4 aGvHD was 27% (95% CI: 25-29%) in BM without ATG recipients *versus* 18% (95% CI: 16-20%) in PBSC with ATG patients (P<0.001). For grades III-IV, the figures were 9% (95% CI: 8-11%) and 6% (95% CI: 4-7%), respectively (P=0.002). In multivariate analyses, the difference for grade II-IV aGvHD between PBSC with ATG *versus* BM without ATG was no longer statistically significant (HR=0.8, 95% CI: 0.7-1.1, P=0.12) (Table 2) while the use of TBI in the conditioning was associated with a higher incidence of grade II-IV aGvHD (HR=1.4, 95% C1: 1.1-1.8, P=0.004). In contrast, a more recent transplantation year was associated with a lower incidence of grade II-IV aGvHD (HR=0.8, 95% CI: 0.7-0.9, P=0.0004).

At 2 years the CI of cGvHD was 34% (95% CI: 31-36%) in BM without ATG recipients *versus* 30% (95% CI: 27-33%) in PBSC with ATG patients (P=0.02) (Figure 1E). This association remained statistically significant on multivariate analysis with a lower risk of cGvHD among PBSC with ATG recipients (HR=0.7, 95% CI: 0.6-0.9,

P=0.01). In contrast, female donor to male recipient (HR=1.5, 95% C1: 1.3-1.7, *P*<0.001), and older age at transplantation (HR=1.07, 95% C1: 1.0-1.14, *P*=0.049) were associated with a higher incidence of cGvHD.

Relapse and non-relapse mortality

The 2-year CI of relapse was 25% (95% CI: 22-27%) in BM without ATG recipients *versus* 28% (95% CI: 25-31%) in PBSC with ATG patients (*P*=0.0496) (Figure 1C). After

Table 1. Patient characteristics among human leucocyte antigen-identical sibling donor (MSD) recipients

Variable	BM without ATG (n=1633)	PBSC with ATG (n=1021)	*P*
Follow up, median (95% CI)	6.1 (5.9-6.5)	2.3 (2.1-2.5)	
Age of patient at HSCT (years), Median (IQR)	40 (30-48)	48 (38-56)	<0.0001
Sex, n (%)			0.04
Male	794 (49)	535 (53)	
Female	838 (51)	480 (47)	
Missing	1	6	
Karnofsky, n (%)			
<80	30 (2)	29 (3)	0.33
≥80	1270 (98)	950 (97)	
Missing	333	42	
Status at transplant, n (%)			
CR1	1407 (86)	893 (87)	0.34
CR2	226 (14)	128 (13)	
Cytogenetic risk			<0.0001
Good[1]	190 (16)	62 (10)	
Intermediate[2]	804 (70)	428 (68)	
Poor[3]	158 (14)	136 (22)	
Missing	481	395	
AML type			<0.0001
Primary	1537 (94)	908 (89)	
Secondary	96 (6)	113 (11)	
Year of transplant, Median (IQR)	2008 (2004-2012)	2014 (2011-2016)	<0.0001
Sex mismatch, n (%)			0.03
Female to male	355 (22)	257 (25)	
CMV donor/patient, n (%)			0.004
-/-	356 (24)	187 (19)	
+/-	137 (9)	103 (10)	
-/+	247 (17)	140 (14)	
+/+	753 (50)	555 (56)	
Missing	140	36	
Conditioning, n (%)			<0.0001
Chemotherapy-based MAC[4]	1118 (68)	896 (88)	
TBI-based MAC	515 (32)	125 (12)	
Post-grafting immunosuppression, n (%)			
CNI + MTX	1472 (90)	523 (51)	
CNI + MMF	58 (4)	193 (19)	
CNI alone	46 (3)	218 (21)	
Other/missing	57 (3)	87 (9)	
ATG, n (%)			
Thymoglobuline	–	249 (30)	
Median (IQR) dose, mg/kg		5.0 (5.0-5.6)	
ATG-Fresenius	–	569 (70)	
Median (IQR) dose, mg/kg		30 (30-35)	
Missing	–	203	

HLA: human leucocyte antigen; MSD: HLA-identical sibling donor; BM: bone marrow; PBSC: peripheral blood stem cells; CI: confidence interval; ATG: anti-thymocyte globulin; AML: acute myeloid leukemia; HSCT: hematopoietic stem cell transplantation; IQR: interquartile ranges; CR: complete remission; CMV: cytomegalovirus; MAC: myeloablative conditioning; TBI: total body irradiation; CNI: calcineurin inhibitor; MTX: methotrexate; MMF: mycophenolate mofetil; [1]defined as t(8;21), t(15;17), inv or del (16), or acute promyelocytic leukemia, these abnormalities only or combined with others; [2]defined as all cytogenetics not belonging to the good or high risk (including trisomies); [3]defined as 11q23 abnormalities, complex karyotype, abnormalities of chromosomes 5 and 7; [4]defined as use of ≥ 6 Gy TBI, busulfan > 8 mg/kg, or melphalan > 140 mg/m^2.

adjusting for potential confounding factors by multivariate analyses there was no significant impact of the graft type on relapse (HR=1.0, 95% CI: 0.8-1.2, *P*=0.6). In contrast, a more recent year of transplantation (HR=1.1, 95% C1: 1.0-1.2, *P*=0.02) was associated with a higher risk of relapse. There was no interaction between the association of graft type and the risk of relapse and year of transplantation (interaction test *P*=0.38). Unadjusted comparison of relapse incidence between the two groups *per* 6-year periods is shown in the *Online Supplementary Table S2*. We fur-

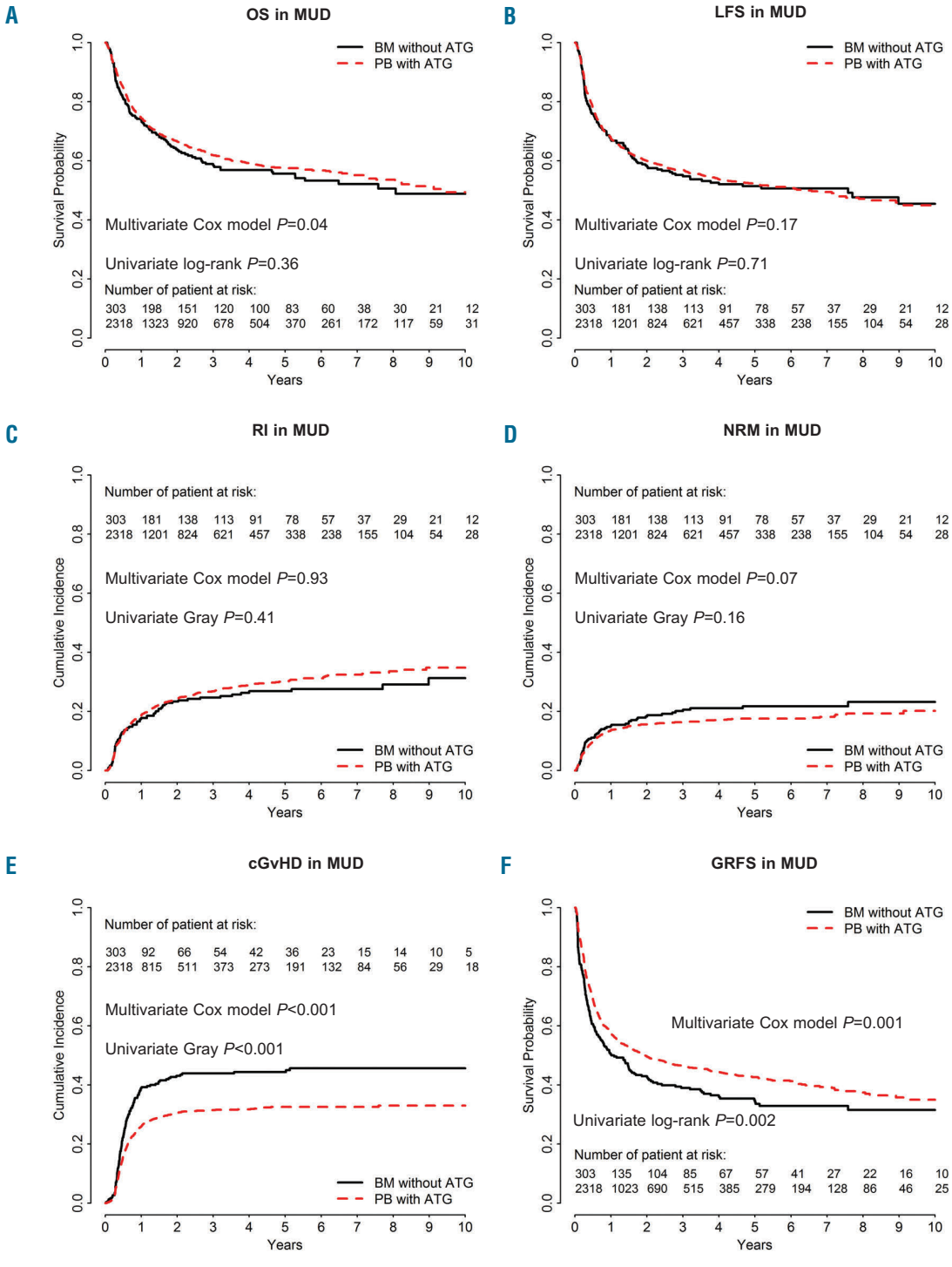

Figure 2. Comparison of outcomes in bone marrow (BM) patients without anti-thymocyte globulin (ATG)and in those given peripheral blood (PB) stem cells with ATG (the dotted line shows the PBSC with ATG curve adjusted for relevant covariates) in the cohort of patients receiving grafts from 10/10 HLA-matched unrelated donors (MUD). (A) Overall survival (OS), *P*=0.36. (B) Leukemia-free survival (LFS), P=0.71. (C) Incidence of relapse (RI), *P*=0.41.(D) Non-relapse mortality (NRM), *P*=0.16. (E) Chronic graft-*versus*-host disease (cGvHD), *P*<0.001. (F) GvHD-free and relapse-free survival (GRFS), *P*=0.002.

ther investigated whether there was a statistical interaction between the use of TBI in the conditioning regimen and the impact of graft type on relapse risk. Among patients given graft from MSD, there was no such interaction (*P*-value for the interaction test = 0.97).

The 2-year CI of NRM was 11.5% in both groups (Figure 1D). In multivariate analyses, PBSC with ATG was associated with a similar risk of NRM to BM (HR=1.1, 95% CI: 0.8-1.4, P=0.7). In contrast, older age at transplantation (HR=1.5, 95% CI: 1.4-1.7, *P*<0.001) and secondary *versus de novo* AML (HR=1.5, 95% CI: 1.0-2.1, *P*=0.03) were associated with a higher NRM while a more recent year of transplantation was associated with a lower NRM (HR=0.7, 95% C1: 0.6-0.8, *P*<0.001).

OS and LFS

The 2-year OS and LFS were 70% (95% CI: 68-73%) and 64% (95% CI: 62-66%) in BMT without ATG patients *versus* 68% (95% CI: 64-71%, P=0.1) and 61% (95% CI: 58-64%, *P*=0.06) in PBSC with ATG patients, respectively (Figure 1A-B). After adjusting for potential confounding factors by multivariate analyses, the use of PBSC with ATG was no different to BM with respect to OS (HR=1.0, 95% CI: 0.8-1.2, *P*=0.8) and LFS (HR=1.0, 95% CI: 0.8-1.2, *P*=0.9). In contrast, second CR at transplantation (HR=1.3, 95% CI: 1.0-1.5, *P*=0.03), and older patient age (HR=1.2, 95% CI: 1.1-1.3, *P*<0.001) were associated with worse OS. The same factors were also significantly associated with worse LFS: second CR at transplantation (HR=1.2, 95% CI: 1.0-1.5; *P*=0.04), and older patient age (HR=1.2, 95% CI: 1.1-1.2, *P*<0.001).

GRFS

At 2 years, GRFS was 50% (95% CI: 48-53%) in BMT without ATG patients *versus* 52% (95% CI: 48-55%) in the PBSC with ATG group (*P*=0.8) (Figure 1F). This was confirmed on multivariate analysis including data from all patients (HR=0.9, 95% CI: 0.8-1.1, *P*=0.5) as well as in further sensitivity analysis restricted to patients given a combination of a calcineurin inhibitor and methotrexate as GvHD prophylaxis (HR=1.0, 95% CI: 0.8-1.2, *P*=0.9). In contrast, female donor to male recipient (HR=1.2, 95% CI: 1.0-1.3, *P*=0.01), and older patient age (HR=1.1, 95% CI: 1.1-1.1, *P*<0.001) were associated with a worse GRFS.

BM without ATG *versus* PBSC with ATG in MUD recipients

Patients

A total of 2,621 recipients met the inclusion/exclusion criteria. Comprising 303 patients in the BM group and 2,318 in the PBSC with ATG group (Table 3). In comparison to BM recipients, PBSC with ATG patients were older (median 48 years *vs.* 42 years old), were transplanted more recently (median year of transplantation 2013 *versus* 2012) and were more frequently transplanted in the first CR (79% *vs.* 71%).

GvHD

The 100-day incidence of grade II-IV aGvHD was 44% in BMT without ATG recipients *vs.* 24% in PBSC with ATG recipients (*P*<0.0001). For grade 3-4, the figures were 17% (95% CI: 13-21%) and 7% (95% CI: 6-8%), respectively (*P*<0.001). In multivariate analysis, PBSC with ATG patients had a significantly lower incidence of grade II-IV aGvHD than BM recipients (HR=0.5, 95% CI: 0.4-0.7; *P*<0.001). No other factor was significantly associated with grade II-IV aGvHD in multivariate analysis (*Online Supplementary Table S4*).

The 2-year CI of cGvHD was 43% (95% CI: 37-49%) in BM without ATG recipients *versus* 30% (95% CI: 28-32%) in PBSC with ATG patients (*P*<0.0001) (Figure 2E). On multivariate analysis, PBSC with ATG, in comparison to BM without ATG, was associated with a lower incidence of cGvHD (HR=0.6, 95% CI: 0.5-0.8, *P*=0.0006) (Table 2), but no other factor was significantly associated with cGvHD.

Relapse and non-relapse mortality

The 2-year CI of relapse was 23% (95% CI: 19-29%) in BMT without ATG recipients *versus* 24% (95% CI: 23-26%) in PBSC with ATG patients (*P*=0.4) (Figure 2C). On multivariate analysis, as observed in the MSD cohort, there was no significant impact of the graft type on relapse (HR=1.0, 95% CI: 0.8-1.3, *P*=0.9), but a more recent transplantation was significantly associated with a higher risk of relapse (HR=1.2, 95% CI: 1.0-1.4, *P*=0.03) (*Online Supplementary Table S1*). There was no interaction between the association of graft type and the risk of relapse and year of transplantation (interaction test *P*=0.13). Unadjusted comparison of relapse incidence between the two groups per 6-year periods is shown in the *Online Supplementalry Table S2*. We further investigated whether there was a statistical interaction between the use of TBI in the conditioning regimen and the impact of the graft type on the relapse risk. Among patients given graft from MUD, there was such an interaction (*P*-value for the interaction test=0.05). Specifically, in the subgroup of patients given TBI-based

Table 2. Outcomes (multivariate Cox models).

Outcomes	HR (95% CI) PBSC with ATG vs BMT without ATG	*P* value[1]
MSD		
Grade II-IV acute GvHD	0.82 (0.64-1.05)	0.12
Chronic GvHD	0.74 (0.59-0.93)	0.01
Relapse incidence	0.96 (0.79-1.16)	0.64
Non relapse mortality	1.07 (0.79-1.44)	0.68
Leukemia-free survival	0.99 (0.84-1.16)	0.89
Overall survival	0.97 (0.81-1.16)	0.75
GvHD-free and relapse-free survival	0.94 (0.81-1.1)	0.45
MUD		
Grade 2-4 acute GvHD	0.54 (0.41-0.71)	<0.001
Chronic GvHD	0.62 (0.47-0.81)	<0.001
Relapse incidence	0.99 (0.77-1.27)	0.93
Non relapse mortality	0.72 (0.50-1.02)	0.07
Leukemia-free survival	0.87 (0.72-1.06)	0.17
Overall survival	0.80 (0.65-0.99)	0.04
GvHD-free and relapse-free survival[2]	0.76 (0.64-0.90)	0.001

HLA: human leucocyte antigen; MSD: HLA-identical sibling donor; MUD: 10/10 HLA-matched unrelated donors; HR: hazard ratio; CI: confidence interval; BM: bone marrow; BMT: bone marrow transplant; PBSC: peripheral blood stem cells; ATG: anti-thymocyte globulin; GvHD: graft-*versus*-host disease.[1]Factors included in the models are: disease status at transplantation, female donor to male recipient or not, cytomegalovirus (CMV) serostatus, use or not of total body irradiation (TBI), year of transplantation, age at transplantation, primary *versus* secondary acute myeloid leukemia (AML), cytogenetic risk and frailty center effect; [2]defined as no death, no relapse, no grade III-IV acute GvHD and no extensive chronic GvHD.

conditioning we observed a lower risk of relapse in PBSC with ATG patients than in BMT without ATG patients (HR=0.56, 95% CI: 0.39-0.81, *P*=0.002) while this was not the case in patients given chemotherapy-based conditioning (HR=0.94, 95% CI: 0.70-1.26, *P*=0.68).

The 2-year CI of non-relapse mortality was 18% in BMT without ATG patients *versus* 16% in PBSC with ATG patients (*P*=0.16) (Figure 2D). On multivariate analysis, there was a non-significant trend for lower NRM in PBSC with ATG patients (HR=0.7, 95% CI: 0.7-

Table 3. Patient characteristics among 10/10 human leucocyte antigen-matched unrelated donor recipients.

Variable	BM without ATG (n=303)	PBSC with ATG (n=2318)	*P*
Follow up, median (95% CI)	5.0 (4.0-5.4)	2.7 (2.5-3.0)	
Age of patient at HSCT (years), Median (IQR)	42 (31-50)	48 (37-56)	<0.001
Sex, n (%)			0.50
Male	152 (50)	1210 (52)	
Female	151 (50)	1108 (48)	
Missing	0	0	
Karnofsky, n (%)			0,99
<80	6 (2)	46 (2)	
≥80	283 (98)	2156 (98)	
Missing	14	116	
Status at transplant, n (%)			
CR1	215 (71)	1836 (79)	0.001
CR2	88 (29)	482 (21)	
Cytogenetic risk			0.94
Good[1]	30 (14)	176 (14)	
Intermediate[2]	137 (65)	793 (64)	
Poor[3]	43 (21)	266 (22)	
Missing	93	1083	
AML type			0.014
Primary	277 (91)	2002 (86)	
Secondary	26 (9)	316 (14)	
Year of transplant, Median (IQR)	2012 (2009-2014)	2013 (2011-2015)	<0.001
Sex mismatch, n (%)			
Female to male	28 (9)	279 (12)	0.15
CMV donor/patient, n (%)			0.09
-/-	99 (34)	608 (27)	
+/-	27 (9)	179 (8)	
-/+	84 (28)	703 (32)	
+/+	85 (29)	741 (33)	
Missing	8	87	
Conditioning, n (%)			<0.001
Chemotherapy -based MAC[4]	189 (62)	1873 (81)	
TBI-based MAC	114 (38)	445 (19)	
Post-grafting immunosuppression, n (%)			
CNI + MTX	262 (86)	1468 (63)	
CNI + MMF	17 (6)	556 (24)	
CNI alone	8 (3)	134 (6)	
Other/missing	16 (5)	160 (7)	
ATG, n (%)			
Thymoglobuline	–	736 (42)	
Median (IQR) dose, mg/kg		5.5 (5.0-6.0)	
ATG-Fresenius	–	1013 (58)	
Median (IQR) dose, mg/kg		40 (30-60)	
Missing	–	569	

HLA: human leucocyte antigen; MUD: 10/10 HLA-matched unrelated donors; CI: confidence interval; BM: bone marrow; PBSC: peripheral blood stem cells; AML: acute myeloid leukemia; ATG: anti-thymocyte globulin; HSCT: hematopoietic stem cell transplantation; IQR: interquartile range; CR: complete remission; CMV: cytomegalovirus; MAC: myeloablative conditioning; TBI: total body irradiation; CNI: calcineurin inhibitor; MTX: methotrexate; MMF: mycophenolate mofetil; [1]defined as t(8;21), t(15;17), inv or del (16), or acute promyelocyticleukemia, these abnormalities only or combined with others; [2]defined as all cytogenetics not belonging to the good or high risk (including trisomies); [3]defined as 11q23 abnormalities, complex karyotype, abnormalities of chromosomes 5 and 7, as well as 3q26 and 17p abnormalities, as defined previously16; [4]defined as use of ≥ 6 Gy TBI, busulfan > 8 mg/kg, or melphalan > 140 mg/m^2.

1.0, *P*=0.07). Factors associated with NRM on multivariate analysis included older age at transplantation (HR=1.4, 95% CI: 1.3-1.5, *P*<0.001) and secondary AML (HR=1.4, 95% CI: 1.1-1.9, *P*=0.01) while a more recent transplant year was associated with lower NRM (HR=0.8, 95% CI: 0.7-1.0, *P*=0.03).

OS and LFS

The 2-year OS and LFS were 64% (95% CI: 58-70%) and 58% (95% CI: 53-64%) in BMT without ATG patients *versus* 67% (95% CI: 64-69%, *P*=0.3) and 60% (95% CI: 58-62%, *P*=0.7) in PBSC with ATG patients, respectively (Figure 2A-B). After adjusting for potential confounding factors, the use of PBSC with ATG was associated with a better OS (HR=0.8, 95% CI: 0.6-1.0, *P*=0.04) than with BM, but there was no significant difference in LFS between the groups (HR=0.9, 95% CI: 0.7-1.1, *P*=0.2). As well as being in the BMT group, older age was significantly associated with a poorer OS (HR=1.2, 95% CI: 1.1-1.3, *P*<0.0001) and a worse LFS (HR=1.1, 95% CI: 1.1-1.2, *P*<0.0001).

Causes of death were comparable in both groups expect for a higher frequency of infectious-related death in the PBSC with ATG group (23% *vs.* 11%) (*Online Supplementary Table S3*).

GRFS

The 2-year GRFS was 43% (95% CI: 37-49%) *versus* 50% (95% CI: 47-52%) in BMT without ATG and PBSC with ATG recipients, respectively (*P*=0.002) (Figure 2F). This was confirmed in multivariate analysis including data from all patients (HR=0.8, 95% CI: 0.6-0.9, *P*=0.001) as well as in further sensitivity analysis restricted to patients given a combination of a calcineurin inhibitor and methotrexate as GvHD prophylaxis (HR=0.8, 95% CI: 0.6-0.9, *P*=0.01). Finally, older patient age was also associated with worse GRFS (HR=1.1, 95% CI: 1.0-1.1, *P*=0.004) in the whole cohort of patients.

Discussion

Several studies have now established that the use of PBSC (without ATG) instead of BM is associated with a high incidence of (severe) cGvHD affecting the long-term well-being of the patients.[2,5] In contrast, several phase III trials have demonstrated a beneficial impact of ATG on cGvHD.[12] Here, we compare the outcomes of AML patients given BMT without ATG *versus* PBSC with ATG, in the setting of AML in first or second CR. We elected to restrict the analyses of patients given grafts after myeloablative conditioning since it was a inclusion criteria in most phase III ATG studies, although many AML patients are nowadays transplanted following reduced-toxicity regimens.[20,21] Several observations can be made.

First, the use of PBSC with ATG was associated with a lower incidence of cGvHD both in the MSD and MUD datasets. This clearly demonstrates that ATG administration is able to counterbalance the high risk of cGvHD associated with the use of PBSC (instead of BMT without ATG).

Importantly, the incidence of relapse was not significantly different in BMT without ATG and in PBSC with ATG patients in both datasets. This may appear surprising given the tight association between cGvHD and graft-*versus*-leukemia effects, and is consistent with most phase III ATG trials showing,[22-24] a reduction of cGvHD without an increase in the relapse risk.[12] Similar findings were observed in the RIC setting in a large registry study.[25]

Given the data of the Soiffer *et al*. phase III study showing detrimental effects of ATG in patients given TBI-based conditioning regimen,[11] we investigated whether, in our study, there was a statistical interaction between graft type and the risk of relapse and the use of TBI in the conditioning regimen. Interestingly, we observed a lower risk of relapse only in the subgroup of patients given TBI-based conditioning suggesting no adverse effects of ATG in patients given TBI-based conditioning. These data are in concordance with recent observations reported by our group.[26]

The main endpoint of our retrospective study was GRFS, a relatively new composite endpoint which aims at capturing the rate of cure without ongoing transplant-related morbidity.[27] We observed a non-significant difference in GRFS with the two strategies in the cohort of patients given grafts from MSD, and a significantly better GRFS with PBSC with ATG in the cohort of patients given grafts from MUD. We thus advocate that our data might support the use of PBSC with ATG rather than BMT without ATG, in AML patients in CR at transplantation.

An interesting finding of our study was an increasing relapse incidence (but decreasing non relapse mortality incidence) with more recent transplantations. This might be due to a higher proportion at high risk of relapse (as example more patient with persistent minimal residual disease at transplantation) in more recent years of transplantation. Unfortunately, we do not have data on the MRD status at transplantation for many patients included in this survey.

There are some limitations of the study such as its design (it is however unlikely that a prospective randomized phase III trial will address this question in the near future), the lack of data on mutational AML landscape and minimal residual disease, a high proportion of missing cytogenetic data, the lack of ATG dose data for several patients, and some imbalances between the groups. However these imbalances were adjusted for in the multivariate Cox models. The strengths of the study are the number of patients in each group and their relative uniformity (one single disease, all patients in first or second CR at transplantation, no HLA-mismatches, only myeloablative conditioning regimen).

In conclusion, our data suggest that PBSC transplantation with ATG results in comparable (in case of MSD) or significantly better (in case of MUD) GRFS than BMT without ATG in patients with AML in CR receiving grafts after myeloablative conditioning. These data might support the use of PBSC with ATG compared to BMT without ATG in patients receiving grafts from MSD or MUD after myeloablative conditioning as treatment for AML in CR.

References

1. Blaise D, Kuentz M, Fortanier C, et al. Randomized trial of bone marrow versus lenograstim-primed blood cell allogeneic transplantation in patients with early-stage leukemia: a report from the SociÇtÇ Franáaise de Greffe de Moelle. J Clin Oncol. 2000;18(3):537-571.
2. Flowers MED, Parker PM, Johnston LJ, et al. Comparison of chronic graft-versus-host disease after transplantation of peripheral blood stem cells versus bone marrow in allogeneic recipients: long-term follow-up of a randomized trial. Blood. 2002; 100(2):415-419.
3. Stem Cell Trialists' Collaborative G. Allogeneic peripheral blood stem-cell compared with bone marrow transplantation in the management of hematologic malignancies: an individual patient data meta-analysis of nine randomized trials. J Clin Oncol. 2005;23(22):5074-5087.
4. Anasetti C, Logan BR, Lee SJ, et al. Peripheral-blood stem cells versus bone marrow from unrelated donors. N Engl J Med. 2012;367(16):1487-1496.
5. Lee SJ, Logan B, Westervelt P, et al. Comparison of patient-reported outcomes in 5-Year survivors who received bone marrow vs peripheral blood unrelated donor transplantation: long-term follow-up of a randomized clinical trial. JAMA Oncol. 2016;2(12):1583-1589.
6. Battipaglia G, Ruggeri A, Labopin M, et al. Refined graft-versus-host disease/relapse-free survival in transplant from HLA-identical related or unrelated donors in acute myeloid leukemia. Bone Marrow Transplant. 2018;53(10):1295-1303.
7. Kroger N, Solano C, Wolschke C, et al. Antilymphocyte globulin for prevention of chronic graft-versus-host disease. N Engl J Med. 2016;374(1):43-53.
8. Bacigalupo A, Lamparelli T, Barisione G, et al. Thymoglobulin prevents chronic graft-versus-host disease, chronic lung dysfunction, and late transplant-related mortality: long-term follow-up of a randomized trial in patients undergoing unrelated donor transplantation. Biol Blood Marrow Transplant. 2006;12(5):560-565.
9. Walker I, Schultz KR, Toze CL, et al. Thymoglobulin decreases the need for immunosuppression at 12 months after myeloablative and nonmyeloablative unrelated donor transplantation: CBMTG 0801, a randomized, controlled trial. Blood. 2014; 124(21):38.
10. Finke J, Schmoor C, Bethge WA, et al. Long-term outcomes after standard graft-versus-host disease prophylaxis with or without anti-human-T-lymphocyte immunoglobulin in haemopoietic cell transplantation from matched unrelated donors: final results of a randomised controlled trial. Lancet Haematol. 2017; 4(6):e293-e301.
11. Soiffer RJ, Kim HT, McGuirk J, et al. Prospective, randomized, double-blind, Phase III clinical trial of anti-T-lymphocyte globulin to assess impact on chronic graft-versus-host disease-free survival in patients undergoing HLA-matched unrelated myeloablative hematopoietic cell transplantation. J Clin Oncol. 2017;35(36):4003-4011.
12. Baron F, Mohty M, Blaise D, et al. Anti-thymocyte globulin as graft-versus-host disease prevention in the setting of allogeneic peripheral blood stem cell transplantation: a review from the Acute Leukemia Working Party of the European Society for Blood and Marrow Transplantation. Haematologica. 2017;102(2):224-234.
13. Rubio MT, D'Aveni-Piney M, Labopin M, et al. Impact of in vivo T cell depletion in HLA-identical allogeneic stem cell transplantation for acute myeloid leukemia in first complete remission conditioned with a fludarabine iv-busulfan myeloablative regimen: a report from the EBMT Acute Leukemia Working Party. J Hematol Oncol. 2017;10(1):31.
14. Baron F, Ruggeri A, Beohou E, et al. Occurrence of graft-versus-host disease increases mortality after umbilical cord blood transplantation for acute myeloid leukemia: a report from Eurocord and the ALWP of the EBMT. J Intern Med. 2018; 283(2):178-189.
15. Grimwade D, Hills RK, Moorman AV, et al. Refinement of cytogenetic classification in acute myeloid leukemia: determination of prognostic significance of rare recurring chromosomal abnormalities among 5876 younger adult patients treated in the United Kingdom Medical Research Council trials. Blood. 2010;116(3):354-365.
16. Baron F, Ruggeri A, Beohou E, et al. RIC versus MAC UCBT in adults with AML: A report from Eurocord, the ALWP and the CTIWP of the EBMT. Oncotarget. 2016; 7(28):43027-43038.
17. Ruggeri A, Labopin M, Ciceri F, Mohty M, Nagler A. Definition of GvHD-free, relapse-free survival for registry-based studies: an ALWP-EBMT analysis on patients with AML in remission. Bone Marrow Transplant. 2016;51(4):610-611.
18. Andersen PK, Klein JP, Zhang MJ. Testing for centre effects in multi-centre survival studies: a Monte Carlo comparison of fixed and random effects tests. Stat Med. 1999; 18(12):1489-1500.
19. Baron F, Labopin M, Ruggeri A, et al. Impact of donor type in patients with AML given allogeneic hematopoietic cell transplantation after low-dose TBI-based regimen. Clin Cancer Res. 2018; 24(12):2794-2803.
20. Potdar RR, Gupta S, Giebel S, et al. Current status and Perspectives of irradiation-based conditioning regimens for patients with acute leukemia undergoing hematopoietic stem cell transplantation. Clin Hematol International. 2019;1(1):19-27.
21. Baron F, Labopin M, Peniket A, et al. Reduced-intensity conditioning with fludarabine and busulfan versus fludarabine and melphalan for patients with acute myeloid leukemia: A report from the Acute Leukemia Working Party of the European Group for Blood and Marrow Transplantation. Cancer. 2015;121(7):1048-1055.
22. Weiden PL, Sullivan KM, Flournoy N, Storb R, Thomas ED, and the Seattle Marrow Transplant T. Antileukemic effect of chronic graft-versus-host disease. Contribution to improved survival after allogeneic marrow transplantation. N Engl J Med. 1981; 304(25):1529-1533.
23. Baron F, Maris MB, Sandmaier BM, et al. Graft-versus-tumor effects after allogeneic hematopoietic cell transplantation with nonmyeloablative conditioning. J Clin Oncol. 2005;23(9):1993-2003.
24. Baron F, Labopin M, Niederwieser D, et al. Impact of graft-versus-host disease after reduced-intensity conditioning allogeneic stem cell transplantation for acute myeloid leukemia: a report from the Acute Leukemia Working Party of the European group for blood and marrow transplantation. Leukemia. 2012;26(12):2462-2468.
25. Baron F, Labopin M, Blaise D, et al. Impact of in vivo T-cell depletion on outcome of AML patients in first CR given peripheral blood stem cells and reduced-intensity conditioning allo-SCT from a HLA-identical sibling donor: a report from the Acute Leukemia Working Party of the European Group for Blood and Marrow Transplantation. Bone Marrow Transplant. 2014;49(3):389-396.
26. Nagler A, Labopin M, Dholaria B, et al. Impact of antithymocyte globulin on outcomes of allogeneic hematopoietic cell transplantation with TBI. Blood Adv. 2019; 3(13):1950-1960.
27. Holtan SG, DeFor TE, Lazaryan A, et al. Composite end point of graft-versus-host disease-free, relapse-free survival after allogeneic hematopoietic cell transplantation. Blood. 2015;125(8):1333-1338.

ARTICLE

Effective hematopoietic stem cell-based gene therapy in a murine model of hereditary pulmonary alveolar proteinosis

Miriam Hetzel,[1] Elena Lopez-Rodriguez,[2] Adele Mucci,[1] Ariane Hai Ha Nguyen,[1] Takuji Suzuki,[3,4] Kenjiro Shima,[3] Theresa Buchegger,[1] Sabine Dettmer,[5] Thomas Rodt,[5] Jens P. Bankstahl,[6] Punam Malik,[7] Lars Knudsen,[2] Axel Schambach,[1,8] Gesine Hansen,[9] Bruce C. Trapnell,[3,10] Nico Lachmann[1*] and Thomas Moritz[1*]

[1]Institute of Experimental Hematology, Hannover Medical School, Hannover, Germany; [2]Institute of Functional and Applied Anatomy, Hannover Medical School, Hannover, Germany; [3]Translational Pulmonary Science Center, Division of Pulmonary Biology, Cincinnati Children's Hospital Medical Center, Cincinnati, OH, USA; [4]Division of Pulmonary Medicine, Jichi Medical University, Shimotsukeshi, Tochigi, Japan; [5]Department of Radiology, Hannover Medical School, Hannover, Germany; [6]Department of Nuclear Medicine, Hannover Medical School, Hannover, Germany; [7]Division of Experimental Hematology and Cancer Biology, Cancer and Blood Disease Institute (CBDI), Cincinnati Children's Hospital Medical Center, Cincinnati, OH, USA; [8]Division of Hematology/Oncology, Boston Children's Hospital, Harvard Medical School, Boston, MA, USA; [9]Department of Pediatrics, Allergology, and Neonatology, Hannover Medical School, Hannover, Germany and [10]Division of Pulmonary Medicine, Children's Hospital Medical Center, Cincinnati, OH, USA

NL and TM contributed equally to this work.

Ferrata Storti Foundation

Haematologica 2020
Volume 105(4):1147-1157

ABSTRACT

Hereditary pulmonary alveolar proteinosis due to GM-CSF receptor deficiency (herPAP) constitutes a life-threatening lung disease characterized by alveolar deposition of surfactant protein secondary to defective alveolar macrophage function. As current therapeutic options are primarily symptomatic, we have explored the potential of hematopoietic stem cell-based gene therapy. Using *Csf2rb*$^{-/-}$ mice, a model closely reflecting the human herPAP disease phenotype, we here demonstrate robust pulmonary engraftment of an alveolar macrophage population following intravenous transplantation of lentivirally corrected hematopoietic stem and progenitor cells. Engraftment was associated with marked improvement of critical herPAP disease parameters, including bronchoalveolar fluid protein, cholesterol and cytokine levels, pulmonary density on computed tomography scans, pulmonary deposition of Periodic Acid-Schiff^{+} material as well as respiratory mechanics. These effects were stable for at least nine months. With respect to engraftment and alveolar macrophage differentiation kinetics, we demonstrate the rapid development of CD11c^{+}/SiglecF^{+} cells in the lungs from a CD11c^{-}/SiglecF^{+} progenitor population within four weeks after transplantation. Based on these data, we suggest hematopoietic stem cell-based gene therapy as an effective and cause-directed treatment approach for herPAP.

Introduction

Hereditary pulmonary alveolar proteinosis (herPAP) represents an extremely rare life-threatening genetic disorder associated with malfunction of alveolar macrophages (AM).[1] HerPAP is caused by mutations in genes encoding the granulocyte/macrophage-colony-stimulating factor receptor (GM-CSFR), a high-affinity receptor complex composed of a cytokine-specific α (GM-CSFRα, *CSF2RA*) and a signal-transducing common β (GM-CSFRβ, *CSF2RB*) chain shared with the IL-3

Correspondence:

THOMAS MORITZ
moritz.thomas@mh-hannover.de

Received: December 17, 2018.

Accepted: July 5, 2019.

Pre-published: July 9, 2019.

doi:10.3324/haematol.2018.214866

Check the online version for the most updated information on this article, online supplements, and information on authorship & disclosures: www.haematologica.org/content/105/4/1147

and IL-5 receptor. Although the GM-CSFR is expressed on a wide variety of hematopoietic cells, mutations in either *CSF2RA*[2,3] or *CSF2RB*[4,5] almost exclusively affect the maturation and functionality of AM, leading to disturbed intracellular surfactant degradation, intrapulmonary deposition of phospholipids and lipoproteins, and, in turn, severe respiratory insufficiency. Current treatment options are symptomatic only and consist of vigorous treatment of pulmonary infections and whole lung lavage, a highly invasive procedure performed under general anesthesia, which may need to be repeated every 4-8 weeks. As for other hereditary diseases affecting the lymphohematopoietic system, allogeneic hematopoietic stem cell transplantation (alloHSCT) or hematopoietic stem cell-based gene therapy (HSC-GT) using retroviral vectors[6,7] potentially offer a permanent cure for herPAP patients and proof of concept for these concepts has been established in murine models.[8,9] However, in the clinical setting, both procedures are problematic due to the required chemo/radiotherapeutic preconditioning and the poor pulmonary status of herPAP patients.[3] On the other hand, over the last decade, substantial progress has been made in the fields of alloHSCT as well as HSC-GT, and in this context, successful alloHSCT has recently been reported in two patients suffering from secondary PAP[10] as well as in a herPAP patient.[11]

In addition, novel treatment strategies for herPAP are evolving. Thus, the direct intrapulmonary application of macrophages (pulmonary macrophage transplantation; PMT) has demonstrated profound and long-lasting therapeutic efficacy in two murine models of herPAP in the absence of any preconditioning.[12-16] While it is not clear yet whether in the human setting these pulmonary administered macrophages will permanently persist in the lungs and provide a long-term cure for herPAP patients, PMT might still improve the patients' general condition to allow for a more permanent approach such as alloHSCT or HSC-GT.

On this background, we here employed a state-of-the-art, 3rd generation self-inactivating (SIN) lentiviral vector and transduced lineage-negative hematopoietic stem and progenitor cells (lin$^-$ HSPC) derived from the bone marrow (BM) of *Csf2rb*$^{-/-}$ mice[17] to evaluate the feasibility and efficacy of an HSC-GT strategy for herPAP *in vivo*. In this study, we demonstrated robust and long-term pulmonary engraftment of AM which was associated with significant improvements of critical disease-related parameters such as elevated protein, cholesterol, or cytokine levels in the alveolar spaces. In addition, our study offers novel insights into the early reconstitution phase of a functional AM compartment following HSCT.

Methods

Mice

B6.SJL-Ptprca-Pep3b/BoyJZtm (Ly5.1; CD45.1) mice were used as wild-type (WT) controls, and B6;129P2-Csf2rb2^{tm1Mur} (*Csf2rb*$^{-/-}$) harboring a knockout in the *Csf2rb* gene served as a disease model of PAP. Mice were housed in the central animal facility of Hannover Medical School under specific-pathogen-free conditions in individually ventilated cages (IVC). Mice had access to food and water *ad libitum*. All animal experiments were approved by the Lower Saxony State animal welfare committee and were conducted according to the law governing animal welfare.

Isolation, cultivation, and transduction of lineage negative cells

Lineage negative cells were isolated from total bone marrow using lineage cell depletion kit (Miltenyi) following the manufacturer's instructions. Pre-stimulation of lineage negative cells was performed for 24 hours in STIF medium (StemSpan medium supplemented with 1mM Penicillin/Streptomycin, 2mM L-glutamine, 100 ng/mL mSCF, 20 ng/mL TPO, 20 ng/mL IGF-2 and 100 ng/mL FGF2). Following this, transduction of lineage negative cells was performed on RetroNectin® (Takara) coated plates using STIF medium and MOI between 10 and 20, as previously described.[18] For *in vitro* assays, cells were sorted for GFP expression using a FACSAria IIu.

Hematopoietic stem cell transplantation

Age-matched (12-16 week old) *Csf2rb*$^{-/-}$ recipient mice of both sexes were irradiated with a single dose of 9 Gy. Lin$^-$ BM cells of wild-type (WT) donor mice were isolated as described above and injected intravenously into the tail vein of recipient mice 24 hours post irradiation. Alternatively, lineage negative cells of *Csf2rb*$^{-/-}$ donor mice were isolated and transduced with SIN lentiviral gene therapy or GFP control vectors and transplanted by the same protocol. In secondary transplantation, BM of primary recipients was isolated, red blood cell lysis performed and subsequently, cells were injected by the same protocol as described above. For all experiments, non-sex- and non-age-matched (age ≤9 months), non-irradiated *Csf2rb*$^{-/-}$ and WT mice served as reference controls.

Bronchoalveolar lavage

After closing the left lung, the right lung was flushed three times with PBS (once with 0.6 mL and 2 times with 0.5 mL) to obtain bronchoalveolar lavage fluid (BALF). The turbidity of the fluid was measured by analyzing the OD600 value on a BioPhotometer (Eppendorf). The protein concentration of total BALF was analyzed using the Pierce™ BCA Protein Assay Kit (Thermo Fisher Scientific) according to the manufacturer's instructions. BALF samples were pelleted for 10 minutes at 400xg. Supernatants were used to determine the concentration of GM-CSF, M-CSF, and MCP-1 by ELISA (Mouse Quantikine Kits, R&D Systems), as described.[2] Cholesterol levels were measured by the amplex red cholesterol assay (Life Technologies) according to the manufacturer's protocol, as described.[19] Pelleted cells were stained and analyzed by flow cytometry using BD LSR II.

Statistical analysis

Statistical analysis was performed using the Prism 7 software (GraphPad) applying ANOVA and recommended *post hoc* testing. Unless otherwise stated, bars and average numbers in the text represent mean±standard error of mean (SEM).

Results

Lentiviral transduction restores GM-CSFRβ expression and GM-CSF-dependent functionality in *Csf2rb*$^{-/-}$ hematopoietic stem and progenitor cells and macrophages *in vitro*

A 3rd generation SIN lentiviral vector constitutively expressing murine *Csf2rb* cDNA from an elongation factor 1 α (EF1 α) promoter (Lv.Csf2rb) was employed, and for better visualization upon flow cytometry, an enhanced GFP (eGFP) reporter coupled to the transgene via an inter-

nal ribosomal entry site (IRES) was added (*Online Supplementary Figure S1A*). The construct was used to transduce lin⁻ HSPC from B6;129P2-Csf2rb2tm1Mur (*Csf2rb*$^{-/-}$) mice. These mice harbor a knock out in the *Csf2rb* gene and closely reflect the clinical herPAP disease phenotype.[17] Following HSPC transduction, robust GFP reporter expression (Figure 1A), as well as surface expression of the GM-CSFRβ chain (CD131) (Figure 1B), was observed. Of note, *Csf2rb*$^{-/-}$ lin⁻ cells contained a small population of CD131⁺ cells, most likely due to the additional and highly similar IL-3 specific β-chain present in mice[20] that is intact in *Csf2rb*$^{-/-}$ mice as well. When subjecting Lv.Csf2rb-transduced HSPC that were previously sorted for GFP⁺ cells to a colony assay with GM-CSF added as the only cytokine, significant restoration of GM-CSF-dependent colony formation was observed (WT 24±4, Lv.Csf2rb 17±6, *Csf2rb*$^{-/-}$ 0±0, mean±SEM) (Figure 1C) with colonies displaying similar morphologies as those derived from WT cells (*Online Supplementary Figure S1B* and *C*). No significant difference in colony numbers (WT 72±20, Lv.Csf2rb 38±8, *Csf2rb*$^{-/-}$ 71±11, mean±SEM) or morphology between Lv.Csf2rb-transduced and non-transduced

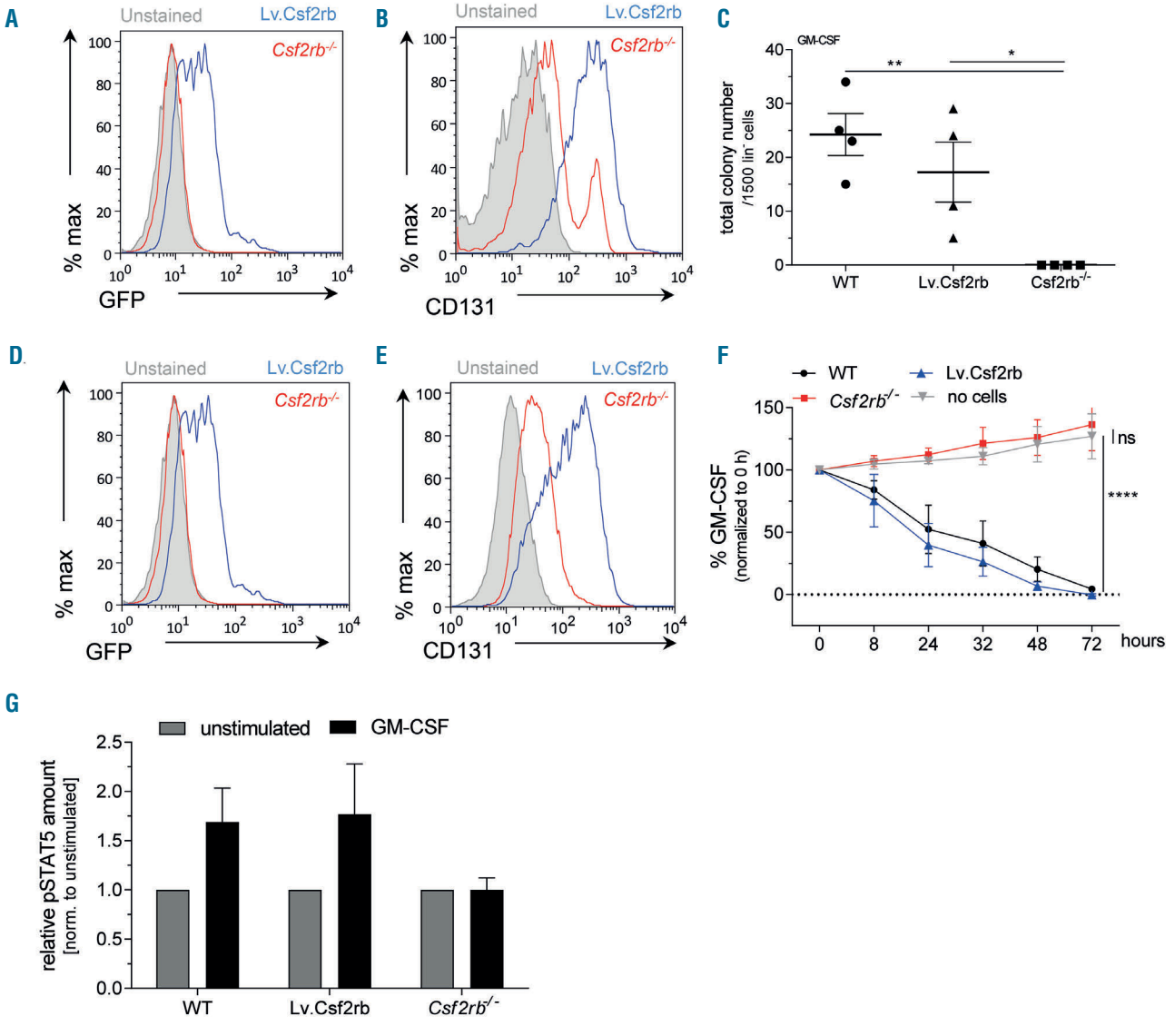

Figure 1. Lv.Csf2rb-transduction of *Csf2rb*$^{-/-}$ cells restores granulocyte/macrophage-colony-stimulating factor (GM-CSF)-dependent functionality of hematopoietic stem and progenitor cells (HSPC) and HSPC-derived macrophages. (A and B) Representative histograms depicting GFP (A) and CD131 (B) expression in hematopoietic stem and progenitor cells (HSPC). (C) Methylcellulose-based clonogenic colony growth in response to GM-CSF. Total colony number per 1,500 lineage negative (lin⁻) HSPC is given. N=2 in technical duplicates; bars indicate mean±standard error of mean (SEM); statistical calculation was done by one-way ANOVA with Dunnett's multiple comparisons test. (D and E) Representative histogram depicting GFP (D) and CD131 (E) expression in macrophages. (F) Clearance of GM-CSF from cell culture supernatant by macrophages. N=3. Data points indicate mean±SEM. Values are normalized to the 0 h time point. Statistical calculation was done by two-way ANOVA with Dunnett's multiple comparisons test. The significance is given for the 72h time point. (G) Increase of phosphorylated STAT5 (pSTAT5) after GM-CSF stimulation. Macrophages were stimulated with GM-CSF for 15 minutes or left without stimulation. Mean fluorescence intensity (MFI) was measured by flow cytometry, and MFI values for stimulated samples were normalized to the corresponding unstimulated sample. N=3. No statistically significant difference. Ns: not significant; **P*<0.05; ***P*<0.01; *****P*<0.0001. WT: wild-type.

cells were observed when a cocktail of IL-3, IL-6, SCF, and EPO was applied (*Online Supplementary Figure S1D and E*) demonstrating the GM-CSF specificity of Lv.Csf2rb-mediated effects.

Given that primarily macrophages (MΦ) are affected in herPAP, as a next step, lin$^-$ cells were differentiated towards MΦ *in vitro* by applying M-CSF and assessed for morphology, transgene expression, and GM-CSF-dependent functionality. Typical MΦ morphology similar to WT and *Csf2rb*$^{-/-}$ MΦ was observed for Lv.Csf2rb-transduced MΦ (*Online Supplementary Figure S1F*) and sustained GFP as well as CD131 expression was detected for these cells (Figure 1D and E). Moreover, Lv.Csf2rb-transduced MΦ, in clear contrast to non-transduced *Csf2rb*$^{-/-}$ MΦ, were able to bind and internalize GM-CSF with comparable efficiency as WT MΦ (Figure 1F). In addition, when we analyzed phosphorylation of the signal transducer and activator of transcription 5 (STAT5), a major component in the GM-CSFR signaling cascade, non-transduced *Csf2rb*$^{-/-}$ MΦ failed to phosphorylate STAT5 in response to GM-CSF, whereas STAT5 phosphorylation was restored following Lv.Csf2rb-transduction (Figure 1G).

These data demonstrate that the Lv.Csf2rb vector efficiently directs Csf2rb expression and restores GM-CSF-dependent functionality in *Csf2rb*$^{-/-}$ HSPC as well as thereof derived MΦ, whereas GM-CSF independent properties such as colony formation potential or differentiation properties in response to other cytokines were not affected. Thus, this vector appeared suitable for further evaluation *in vivo*.

Lv.Csf2rb-transduced lin$^-$ hematopoietic stem and progenitor cells engraft in *Csf2rb*$^{-/-}$ mice and reconstitute the hematopoietic system

For *in vivo* evaluation of our construct, we performed HSC-GT employing lethally irradiated *Csf2rb*$^{-/-}$ mice and either the Lv.Csf2rb construct or a control construct harboring GFP only (Lv.GFP) (Figure 2A). A cohort receiving healthy CD45.1$^+$ donor cells served as a positive control. To monitor engraftment and hematopoietic reconstitution, blood samples were taken four, eight, and twelve weeks after HSC-GT, the latter representing the time point of final analysis. Two independent rounds of transplantation were performed with a total of six mice receiving Lv.Csf2rb-

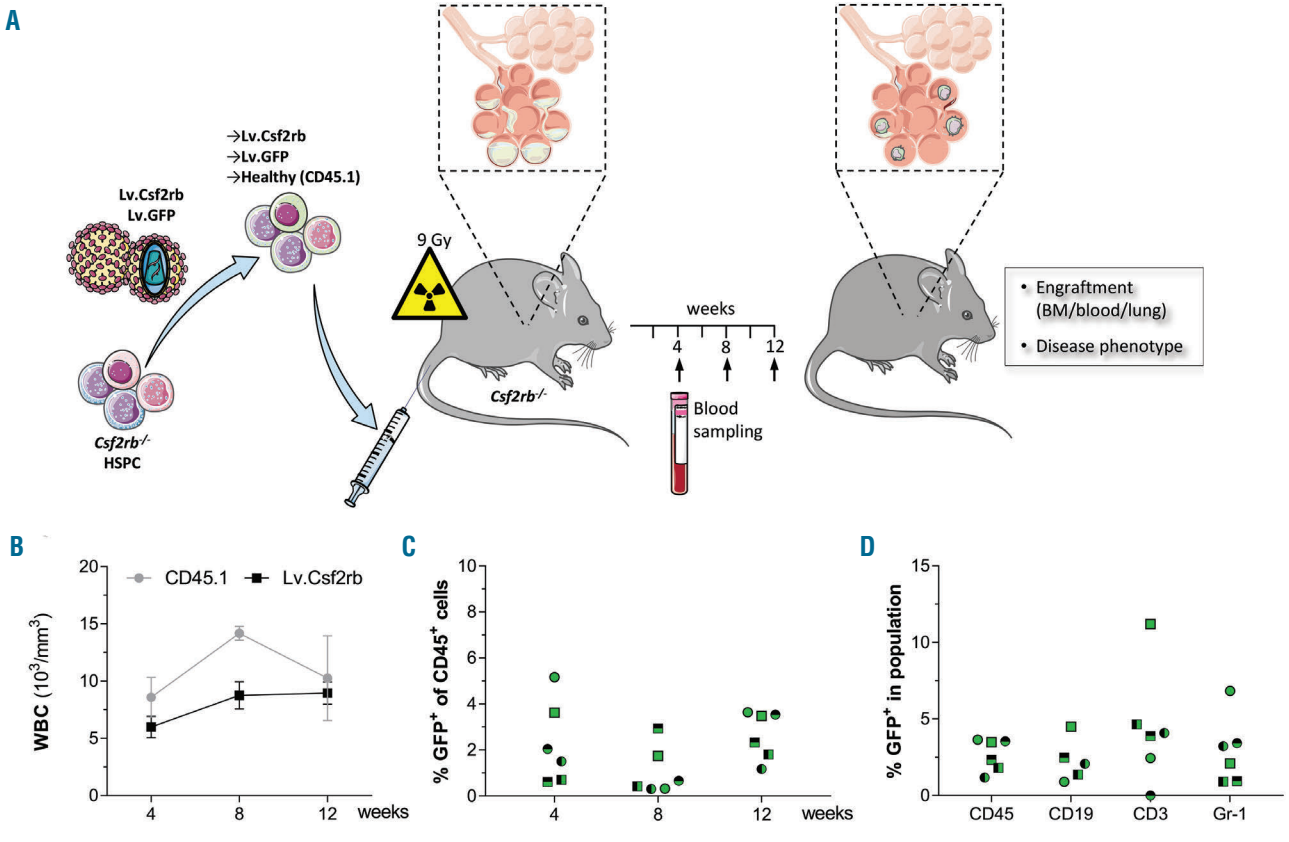

Figure 2. Hematopoietic reconstitution after Lv.Csf2rb hematopoietic stem cell-based gene therapy (HSC-GT). (A) Schematic representation of HSC-GT procedure. *Csf2rb*$^{-/-}$ hematopoietic stem and progenitor cells (HSPC) were isolated from donor mice and transduced with the gene therapy vector (Lv.Csf2rb) or a GFP control vector (Lv.GFP). Lv.Csf2rb-, Lv.GFP-transduced or healthy CD45.1 control HSPC were injected into *Csf2rb*$^{-/-}$ recipients previously lethally irradiated with a single dose of 9 Gy. Blood samples were drawn four, eight and 12 weeks after HSC-GT. The final analysis was performed 12 weeks after HSC-GT to evaluate engraftment of donor cells in bone marrow (BM), blood and lungs as well as to evaluate the reduction of lipoproteinaceous material in the lungs. All images in this illustration were adapted from Servier Medical Art (*https://smart.servier.com*) and are distributed under the CC-BY 3.0 license. (B) Blood count analysis showing total number of white blood cells (WBC) per mm^3 of peripheral blood four, eight and 12 weeks after HSC-GT in mice receiving Lv.Csf2rb-transduced *Csf2rb*$^{-/-}$ cells (black) or healthy CD45.1$^+$ cells (gray); n=6 in two independent experiments. Dots indicate mean±standard error of mean. (C) Percentage of GFP$^+$ cells in peripheral blood CD45$^+$ cells four, eight and 12 weeks after injection of Lv.Csf2rb-transduced cells; n=6 in two independent experiments. Circles belong to the first experiment, squares to the second experiment; equal symbols in (C) and (D) represent the same mice. (D) Percentage of GFP$^+$ cells in peripheral blood CD45$^+$, CD19$^+$, CD3$^+$ and Gr-1$^+$ subsets of mice transplanted with Lv.Csf2rb-transduced cells; n=6 in two independent experiments.

transduced cells, three mice receiving Lv.GFP-transduced cells, and four mice receiving healthy CD45.1$^+$ cells. Hematopoietic reconstitution in mice receiving Lv.Csf2rb-transduced cells was detected already at four weeks ($6.0\pm0.9x10^3/mm^3$ total white blood cells; WBC; mean±SEM), and WBC maintained stably thereafter until week 12 comparable to control mice transplanted with healthy CD45.1$^+$ HSPC (Figure 2B). A clear, though low-level, contribution of Lv.Csf2rb-transduced GFP$^+$ cells was observed during this period (Figure 2C) with a comparable contribution to T, B, and myeloid compartments when analyzed at the week 12 time point (Figure 2D).

Thus, all mice transplanted with Lv.Csf2rb-transduced cells presented effective reconstitution of the hematopoietic system, although at low levels of transduced cells.

Lv.Csf2rb-transduced cells migrate to the lungs and restore the alveolar macrophage pool

In a next step, we evaluated the engraftment of gene-modified cells in the alveolar spaces of *Csf2rb*$^{-/-}$ recipients following HSC-GT. While at the end of the experiment both *Csf2rb*$^{-/-}$ mice and control mice transplanted with Lv.GFP-transduced cells lacked endogenous AM, mice transplanted with Lv.Csf2rb-transduced cells similar to WT mice and controls transplanted with healthy CD45.1$^+$ cells presented a distinct population of Siglec-F$^+$ cells in their lungs, which resided in the alveolar spaces close to the alveolar septa (*Online Supplementary Figure S2A*). To analyze these cells in more detail, homogenized lung tissue was analyzed by flow cytometry (Figure 3A). Cells displaying a CD45$^+$F4/80$^+$Siglec-F$^+$CD11c^{high} phenotype characteristic of mature AM were detected in all mice transplanted with Lv.Csf2rb-transduced cells, similar to control animals receiving healthy CD45.1$^+$ cells or WT mice, while these cells were absent in *Csf2rb*$^{-/-}$ controls or mice transplanted with Lv.GFP-transduced cells (Figure 3B and *Online Supplementary Figure S2B*).

Corresponding results were obtained when the lungs were flushed, and the resulting bronchoalveolar lavage fluid (BALF) was analyzed by flow cytometry. As expected, AM were detected in mice transplanted with Lv.Csf2rb-transduced or healthy CD45.1$^+$ HSPC and in WT mice (Figure 3C and D and *Online Supplementary Figure S2C*). The majority of hematopoietic cells in the BALF of mice transplanted with Lv.Csf2rb-transduced cells was GFP$^+$ and showed robust CD131 expression comparable to mice transplanted with healthy CD45.1$^+$ cells. In contrast, GFP$^+$ cells were almost absent in mice receiving Lv.GFP-transduced cells (Figure 3E and *Online Supplementary Figure S2D*). Vector copy number (VCN) analysis of BALF cells confirmed the presence of genetically modified cells in the lungs of mice receiving Lv.Csf2rb- or Lv.GFP-transduced cells. However, mice receiving Lv.GFP-transduced cells exhibited similar VCN in BM, peripheral blood (PB), or BALF cells (*Online Supplementary Figure S2E*), whereas mice of the Lv.Csf2rb group showed substantially increased VCN in BALF as compared to BM or PB cells (Figure 3F). Enrichment of VCN in BALF *versus* BM cells was up to 16-fold, documenting the enhanced recruitment of corrected cells to the alveolar spaces in the Lv.Csf2rb-transduced cohort.

Taken together, these data demonstrate that, following HSC-GT, in the Lv.Csf2rb group a population of transduced cells migrates to the alveolar spaces and restores the deficient AM pool of *Csf2rb*$^{-/-}$ recipients.

Lv.Csf2rb hematopoietic stem cell-based gene therapy reverses the hereditary pulmonary alveolar proteinosis disease phenotype

A major hallmark of herPAP is the accumulation of surfactant proteins and lipids in the alveolar spaces giving rise to a turbid, milky appearance of the BALF. Following the transplantation of Lv.Csf2rb-transduced HSPC, however, the BALF acquires a clear appearance comparable to WT mice or mice transplanted with healthy CD45.1$^+$ cells (Figure 4A). This initial observation was confirmed by BALF turbidity (OD600 absorbance) and total protein analysis (Figure 4B and C). As the material accumulated in the alveolar spaces is characterized by a high contribution of cholesterol,[19] we also analyzed the cholesterol levels in BALF and detected significant improvements in mice transplanted with Lv.Csf2rb-transduced cells (Figure 4D). Moreover, in *Csf2rb*$^{-/-}$ mice, like in herPAP patients, BALF levels of GM-CSF, M-CSF and MCP-1 are markedly increased due to auto-regulatory mechanisms directed to stabilize the AM population.[1-5,21] While none of these parameters was improved by transplantation of Lv.GFP-transduced cells, twelve weeks after injection of Lv.Csf2rb-transduced cells, all parameters normalized mimicking the situation in WT or CD45.1 transplanted control animals (Figure 4E-G), highlighting the considerable potential of HSC-GT in herPAP.

As a next step, we evaluated lung sections for the deposition of Periodic-Acid Schiff (PAS) positive material. While lungs of untreated *Csf2rb*$^{-/-}$ mice and animals transplanted with Lv.GFP-transduced cells nicely showed the pathognomonic foci of accumulated PAS$^+$ surfactant material, these foci were virtually absent in mice transplanted with Lv.Csf2rb-transduced cells similar to animals of the CD45.1 and WT cohort (*Online Supplementary Figure S3A*). Morphometric quantification confirmed the pronounced reduction of PAS$^+$ areas following transplantation of Lv.Csf2rb-transduced cells (Figure 4H).

Given the characteristic ground-glass opacities in the lungs of herPAP patients on computed tomography (CT) scans, we also performed CT scans in our mice twelve weeks after HSC-GT and quantified lung densities during the inspiratory and expiratory phases (Figure 4I-K). In line with expectations and our data from BALF analysis, CT scans confirmed significant improvements in inspiration and expiration lung densities following Lv.Csf2rb HSC-GT when compared to non-treated *Csf2rb*$^{-/-}$ mice or the Lv.GFP cohort. These radiographic data were corroborated by mechanical data of the lung demonstrating improved static compliance and inspiratory capacity in *Csf2rb*$^{-/-}$mice upon transplantation of Lv.Csf2rb-transduced cells (*Online Supplementary Figure S3B and C*).

In summary, these data demonstrate that HSC-GT employing the Lv.Csf2rb vector significantly improves and (concerning some of these parameters) even completely normalizes the herPAP disease phenotype.

Lv.Csf2rb hematopoietic stem cell-based gene therapy provides long-term cure for hereditary pulmonary alveolar proteinosis disease phenotype

To better assess the long-term potential of our HSC-GT approach, we performed serial transplantation to secondary recipients. Indeed, in half of the secondary recipients, robust pulmonary engraftment of AM associated with pronounced clinical benefit similar to primary recipients was observed indicated by decreased turbidity and

improved total protein, cholesterol, GM-CSF, M-CSF and MCP-1 levels in the BALF twelve weeks after secondary HSC-GT (Figure 5A-G). These data, in combination with the low transgene levels and VCN observed in the PB and BM of the primary recipients (Figure 3F), suggested that only some of the secondary recipients engrafted with long-term reconstituting HSC. This was supported by VCN analysis in secondary recipients, which revealed that those mice not benefitting from the transplantation had no or barely detectable VCN in their BM (VCN 0 and 0.03), in contrast to the mice presenting with an improved PAP phenotype (VCN 0.46 and 1.93) (Figure 5H). These data clearly indicate that the disease phenotype can be ameliorated in secondary recipients, in which engraftment of gene-corrected cells can be achieved.

In addition to secondary transplantation, we also performed long-term studies in primary recipients. Here, 5 of 7 mice presented AM in the range of 8 to 64% of all

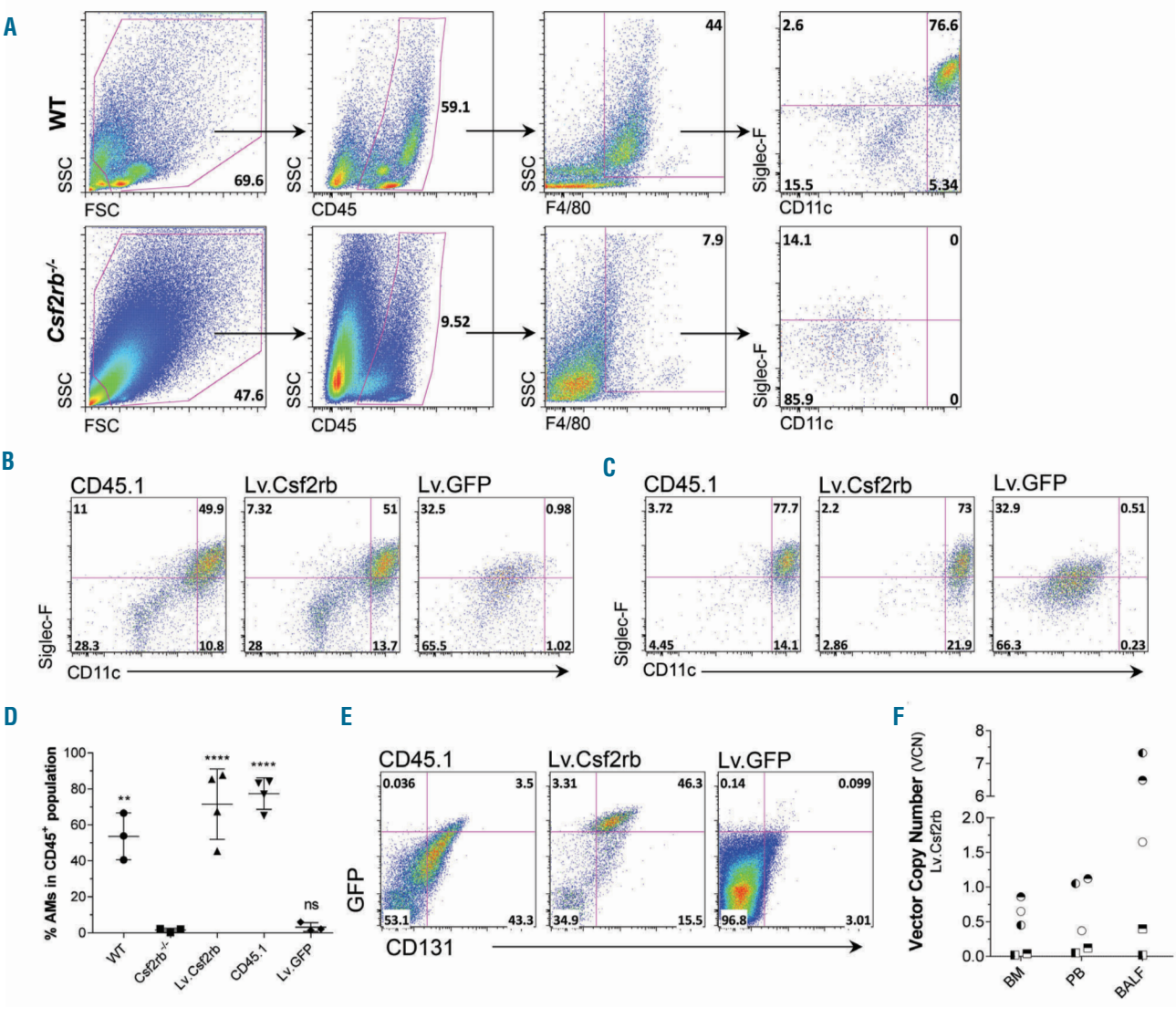

Figure 3. Lv.Csf2rb-transduced cells migrate to the lungs and reconstitute the alveolar macrophages (AM) pool upon hematopoietic stem cell-based gene therapy (HSC-GT). (A) Gating strategy for AM analysis. The first row is depicting a wild-type (WT) mouse, the second row depicts a *Csf2rb*$^{-/-}$ mouse with characteristic accumulation of events due to lipoproteinaceous material. Lung and bronchoalveolar lavage fluid (BALF) samples were pre-gated according to FSC/SSC to exclude debris (first plot). Within this population, CD45^{+} cells were gated (second plot). Out of the CD45^{+} population, all F4/80^{+} cells were gated to obtain the macrophage populations (third plot). Within the CD45^{+}F4/80^{+} population, CD11c^{high}Siglec-F^{+} represent the alveolar macrophages (fourth plot). (B) Representative pseudocolor plots of homogenized lung tissue pre-gated on CD45^{+}F4/80^{+} cells depicting the CD11c^{high}Siglec-F^{+} alveolar macrophage population in *Csf2rb*$^{-/-}$ mice transplanted with healthy CD45.1 or Lv.Csf2rb-transduced cells that is absent in mice transplanted with Lv.GFP-transduced cells. (C) Representative pseudocolor plots of BALF pre-gated on CD45^{+}F4/80^{+} cells depicting CD11c^{high}Siglec-F^{+} alveolar macrophages. (D) Percentage of AM in the total CD45^{+} population. BALF was pre-gated according to FSC/SSC to exclude debris. All CD45^{+} cells were gated and the percentage of CD11c^{high}Siglec-F^{+} cells within the total CD45^{+} population was analyzed. WT, *Csf2rb*$^{-/-}$ and Lv.GFP n=3, Lv.Csf2rb and CD45.1 n=4. Statistical analysis was carried out by one-way ANOVA with Tukey's multiple comparison testing comparing all samples to untreated *Csf2rb*$^{-/-}$ mice; ns: not significant; $^{**}P<0.01$; $^{****}P<0.0001$. (E) Representative pseudocolor plot of BALF showing GFP and CD131 expression in total CD45^{+} population. (F) Vector copy number (VCN) in bone marrow (BM), peripheral blood (PB), and BALF of *Csf2rb*$^{-/-}$ mice transplanted with Lv.Csf2rb-transduced cells twelve weeks after HSC-GT in two independent experiments (n=5). Circles belong to the first experiment, squares to the second experiment; symbols of individual mice are the same as used in Figure 2C and D.

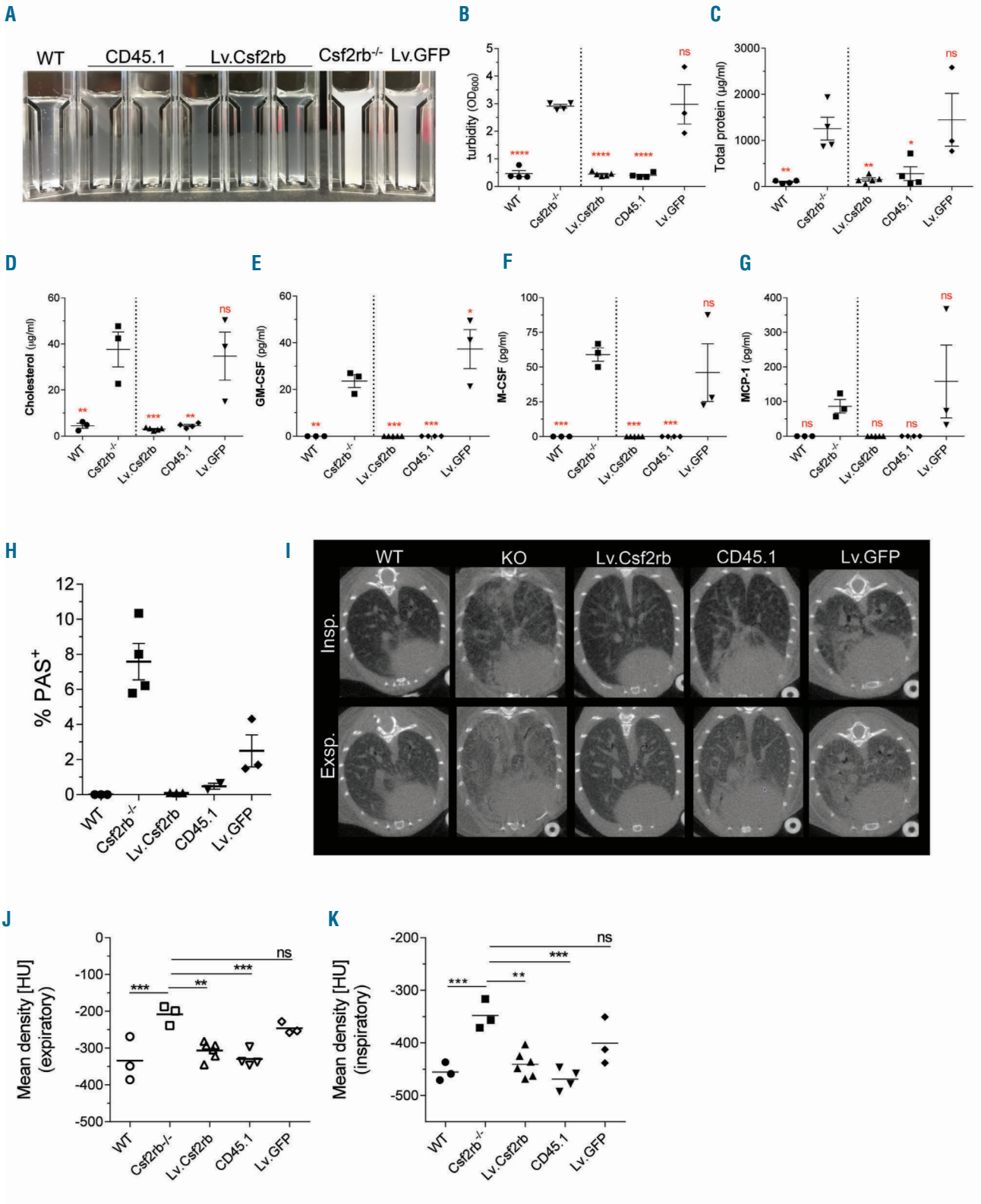

Figure 4. Significant improvement of disease-related parameters twelve weeks after Lv.Csf2rb hematopoietic stem cell-based gene therapy (HSC-GT). (A) Representative picture of bronchoalveolar lavage fluid (BALF) presenting clear and see-through fluid in untreated wild-type (WT) and *Csf2rb*$^{-/-}$ mice transplanted with healthy CD45.1 or Lv.Csf2rb-transduced cells, while *Csf2rb*$^{-/-}$ mice either untreated or transplanted with Lv.GFP-transduced cells present a hereditary pulmonary alveolar proteinosis (herPAP) characteristic milky and turbid fluid. (B) BALF turbidity measured as optical density at 600 nm (OD600). Lv.Csf2rb n=5, Lv.GFP n=3, others n=4 in two independent experiments. (C) Total protein concentration (µg/mL) in BALF. Lv.Csf2rb n=5, Lv.GFP n=3, others n=4 in two independent experiments. Cholesterol (µg/mL) (D), granulocyte/macrophage-colony-stimulating factor (GM-CSF) (pg/mL) (E), macrophage colony-stimulating factor (M-CSF) (pg/mL) (F), and monocyte chemoattractant protein-1 (MCP-1) (pg/mL) (G) levels in BALF. Lv.Csf2rb n=5, CD45.1 n=4, others n=3 in two independent experiments. (H) Quantification of Periodic Acid-Schiff (PAS) positive (PAS$^+$) areas in lung slices. Lv.Csf2rb, Lv.GFP and WT n=3, CD45.1 n=2, *Csf2rb*$^{-/-}$ n= 4. Lines indicate mean±standard error of mean. (I) Representative computed tomography scans during inspiratory (Insp.) and expiratory (Exsp.) phase. (J and K) Quantification of mean lung density in Hounsfield units (HU) measured in computed tomography scans in expiratory (J) and inspiratory (K) phase. Lv.Csf2rb n=6, WT, *Csf2rb*$^{-/-}$ and Lv.GFP n=3, CD45.1 n=4 in two independent experiments. Lines indicate means. All statistical analysis was carried out by one-way ANOVA with Dunnett's multiple comparison testing comparing all samples to untreated *Csf2rb*$^{-/-}$ mice; ns: not significant; **P*<0.05; ***P*<0.01; ****P*<0.001; *****P*<0.0001.

CD45$^+$ cells in BALF (*Online Supplementary Figure S4A and B*), which was accompanied by decreased turbidity, total protein, cholesterol, GM-CSF, M-CSF and MCP-1 in BALF of these mice nine months after HSC-GT (*Online Supplementary Figure S4C-I*).

Thus, Lv.Csf2rb HSC-GT can reverse the herPAP disease phenotype and provide a long-term cure.

Rapid restoration of functional alveolar macrophages following hematopoietic stem cell transplantation

Given the efficient seeding of the lung with transplanted cells and the marked improvements in disease phenotype present already three months after HSC-GT, we next aimed to thoroughly characterize and better understand the early phases of pulmonary cell engraftment and its association with disease parameters. For these studies, lin$^-$ HSPC derived from healthy CD45.1$^+$ were utilized and transplanted intravenously into lethally irradiated *Csf2rb*$^{-/-}$ mice. The fate of CD45.1$^+$ donor cells was analyzed in PB, BM, lungs and BALF one, two, four and eight weeks after HSCT (Figure 6A). Substantial contribution of CD45.1$^+$ donor cells to the total hematopoietic pool of CD45$^+$ cells was observed for the BM already one week after HSCT and increased to >90% at the 4-week time point. However, donor cells were low in the PB (4.3±0.8%) and virtually absent in the BALF and lungs at one week, and only increased moderately at the two week time point. The contribution of donor cells to overall blood cells rapidly increased to 53±14% in the PB, 39±5% in BALF, and 41±15% in lungs at four weeks and reached 64±10% in blood, 73±5% in BALF and 67±5% in lungs eight weeks after HSCT. A more detailed characterization of these donor-derived cells in the BALF using AM typical CD11c/Siglec-F marker combination revealed that the few

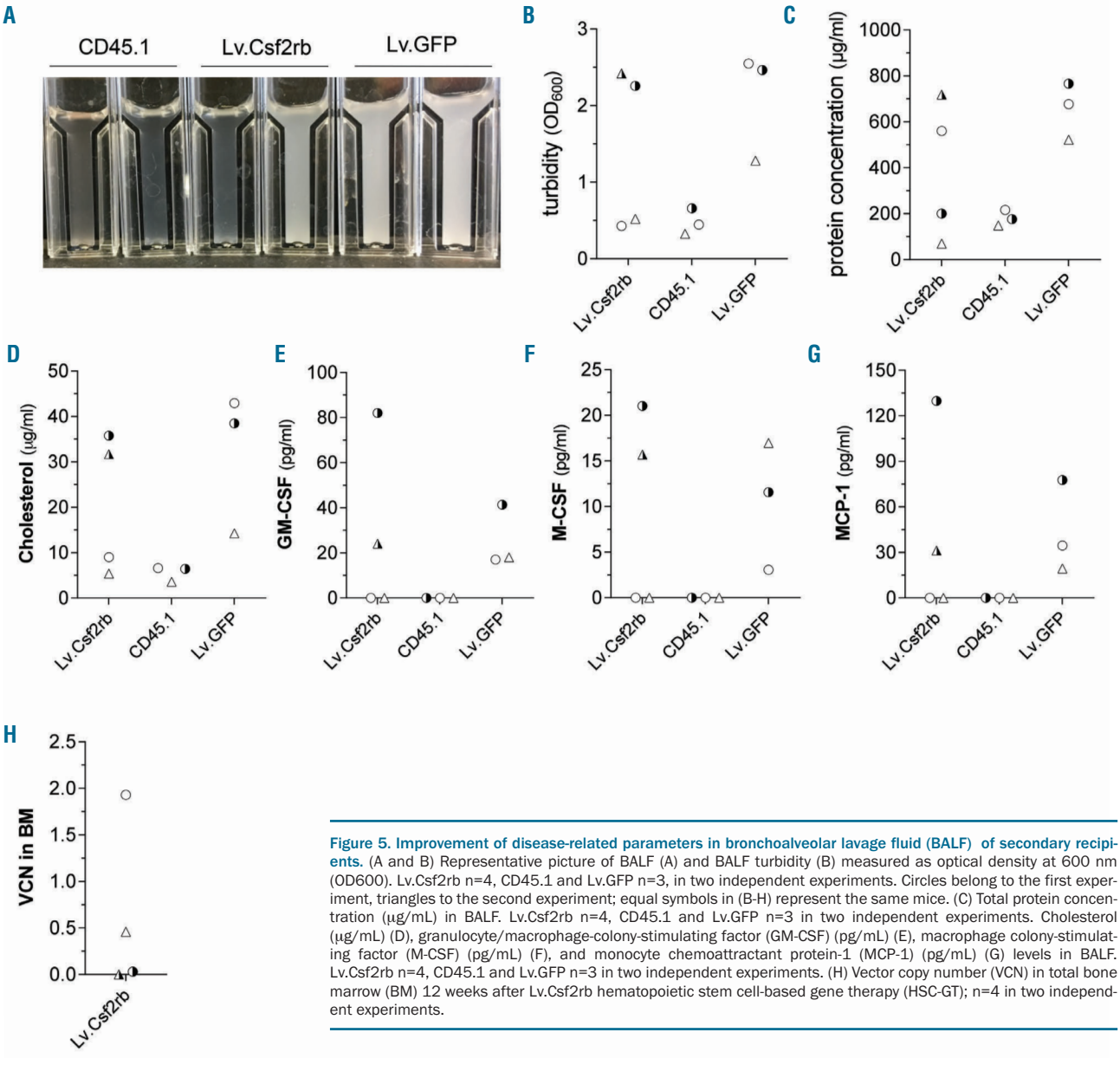

Figure 5. Improvement of disease-related parameters in bronchoalveolar lavage fluid (BALF) of secondary recipients. (A and B) Representative picture of BALF (A) and BALF turbidity (B) measured as optical density at 600 nm (OD600). Lv.Csf2rb n=4, CD45.1 and Lv.GFP n=3, in two independent experiments. Circles belong to the first experiment, triangles to the second experiment; equal symbols in (B-H) represent the same mice. (C) Total protein concentration (µg/mL) in BALF. Lv.Csf2rb n=4, CD45.1 and Lv.GFP n=3 in two independent experiments. Cholesterol (µg/mL) (D), granulocyte/macrophage-colony-stimulating factor (GM-CSF) (pg/mL) (E), macrophage colony-stimulating factor (M-CSF) (pg/mL) (F), and monocyte chemoattractant protein-1 (MCP-1) (pg/mL) (G) levels in BALF. Lv.Csf2rb n=4, CD45.1 and Lv.GFP n=3 in two independent experiments. (H) Vector copy number (VCN) in total bone marrow (BM) 12 weeks after Lv.Csf2rb hematopoietic stem cell-based gene therapy (HSC-GT); n=4 in two independent experiments.

cells present after one week were predominantly Siglec-F$^-$CD11c$^-$ (Figure 6B). At two weeks, gradually a Siglec-F$^+$CD11c$^-$ population evolved, which persisted at week four, but after eight weeks seemed to have matured completely to a Siglec-F$^+$CD11c$^+$ AM population. Thus, eight weeks after HSCT, the mature Siglec-F$^+$CD11c$^+$ AM population was dominant and accounted for 75±2% of all CD45.1$^+$ cells. Correlating these engraftment kinetics with BALF turbidity as a critical marker of disease severity (Figure 6C and D), the occurrence of the Siglec-F$^+$CD11c$^-$ "AM progenitor-like" population two weeks after HSCT was associated with a small, though not yet significant, improvement. The occurrence of Siglec-F$^+$CD11c$^+$ AMs at weeks 4 and 8 was associated with the profound and significant reversal of the herPAP disease phenotype. This stringent correlation between the appearance of AM in the BALF and reversal of disease parameters underlines the importance of reconstitution of the AM population in the alveolar spaces as the critical factor for surfactant breakdown and disease improvements.

Discussion

Utilizing *Csf2rb*$^{-/-}$ mice, a model closely mimicking the human disease phenotype of herPAP, the current work establishes the feasibility and efficacy of an HSC-GT-based approach for the treatment of this disease entity. Two months after HSCT, we demonstrate rapid, robust and long-term seeding of the alveolar spaces with genetically repaired AM, associated with marked improvements in major disease parameters including BALF turbidity, protein content, GM-CSF, M-CSF, and cholesterol levels, pulmonary density on CT scans, alveolar deposition of PAS$^+$ material on lung histology, as well as respiratory mechanics. Concerning BALF parameters, even normalization to the levels of WT control animals was demonstrated. These data are in accordance with earlier reports on retrovirus-based HSC-GT in the *Csf2rb*$^{-/-}$ model.[9] However, these studies not only employed mutagenesis prone, LTR-driven transgene expression and a selection cassette within the vector backbone, but also fell short of a detailed

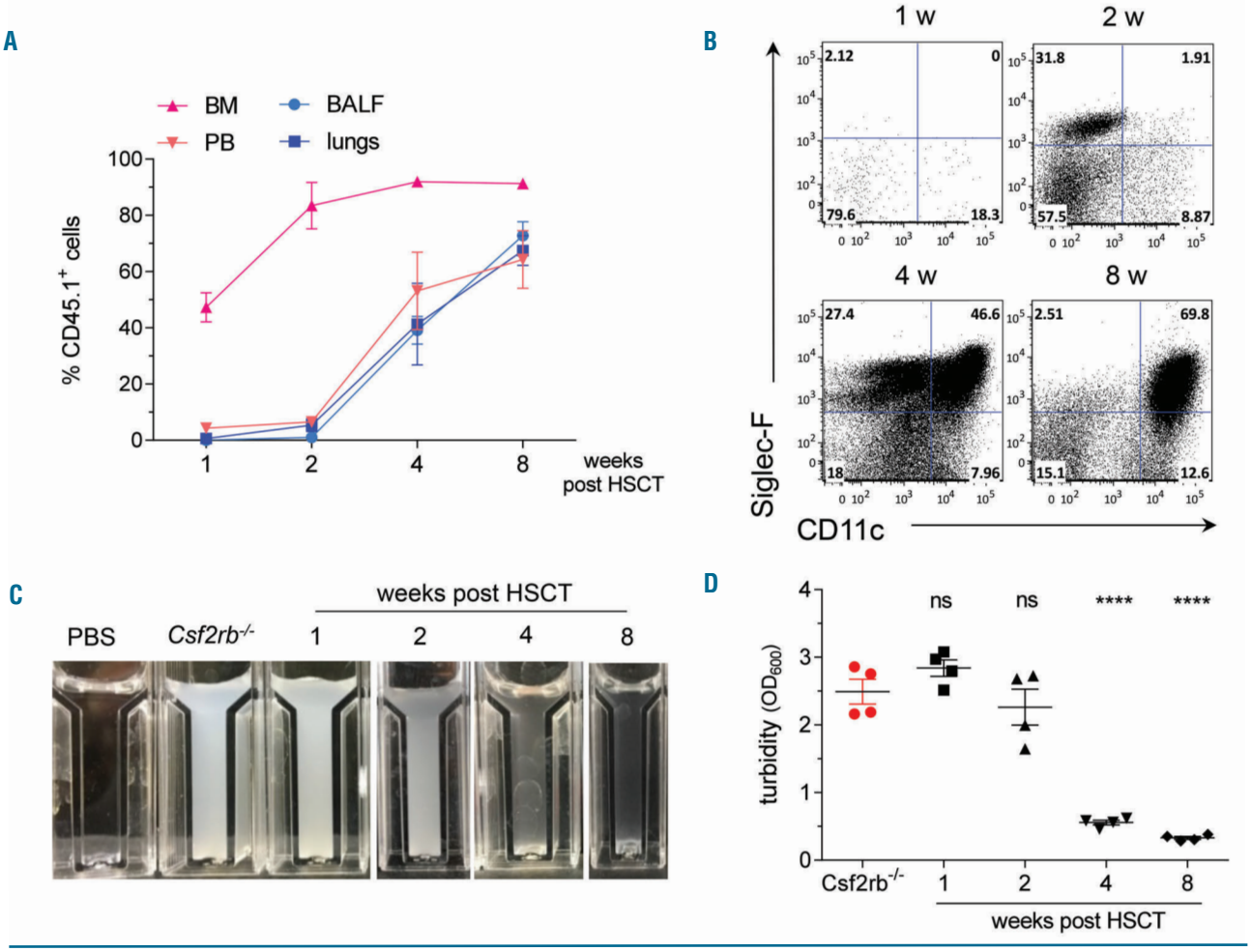

Figure 6. Rapid recovery of functional alveolar macrophages (AM) after hematopoietic stem cell transplantation (HSCT). (A) Engraftment of healthy CD45.1$^+$ donor-derived cells in bone marrow (BM), lungs, bronchoalveolar lavage fluid (BALF), and peripheral blood (PB) of *Csf2rb*$^{-/-}$ recipients one, two, four, and eight weeks (w) after HSCT. Data points indicate mean±standard error of mean (SEM); n=4 in one experiment. (B) Representative dot plots depicting expression of AM markers CD11c and Siglec-F in the CD45$^+$ fraction derived from BALF one, two, four, and eight weeks after HSCT. (C) Representative pictures of BALF derived one, two, four, and eight weeks after HSCT, untreated *Csf2rb*$^{-/-}$ mice and plain phosphate buffer saline (PBS) that was used for lavage. (D) Quantification of BALF turbidity (OD600) one, two, four, and eight weeks after HSCT. Lines and error bars indicate mean±SEM; n=4 in one experiment. Statistical analysis was carried out by one-way ANOVA with Dunnett's multiple comparison testing comparing all samples to untreated *Csf2rb*$^{-/-}$ mice; ns: not significant; **** P<0.0001.

analysis of pulmonary engraftment and the effect on the various disease parameters. Moreover, in the current study, pronounced therapeutic efficacy was shown for prolonged periods employing the 9-month time point or secondary HSCT as read-outs. Thus, our data demonstrate the profound potential of HSC-based therapies for the treatment of herPAP.

These findings have considerable relevance for the future treatment of herPAP patients. So far, therapy of herPAP patients is symptomatic only, and combines vigorous antibiotic prophylaxis and treatment of pulmonary infections with repetitive whole lung lavage, a highly invasive procedure associated with considerable cardiovascular risks.[1,3,5] Importantly, alloHSCT or HSC-GT, which meanwhile represent fairly established therapeutic concepts for other congenital diseases affecting the lymphohematopoietic system, were considered problematic in herPAP patients due to the severe lung phenotype that complicates the preconditioning procedure.[3] On the other hand, reduced-intensity conditioning regimens, improvements in diagnosis, and treatment of bacterial, fungal and viral infections, as well as better HLA-matching, have considerably advanced the field of HSCT, and successful alloHSCT has recently been described in two patients suffering from secondary PAP due to primary immunodeficiencies,[10] as well as in a herPAP patient.[11] Moreover, new therapeutic strategies for herPAP targeting cholesterol homeostasis[19,22] may ameliorate symptoms in PAP patients, and, at least in murine disease models, direct intrapulmonary transplantation of macrophages has been shown to improve substantially (if not cure) herPAP disease.[12-16] Given this, HSCT-based treatment approaches increasingly appear to be a realistic scenario, and in this context, HSC-GT avoids the critical side effects of alloHSCT such as graft-*versus*-host disease or graft rejection, and might also allow for less toxic preconditioning regimens.

In the current study, we have utilized *Csf2rb*-deficient mice primarily based on availability. However, given the almost identical clinical presentation of *CSF2RA*- and *CSF2RB*-deficient herPAP patients,[23] the HSC-GT based treatment approach presented here should apply to both molecular types of herPAP. Of note, recently also *Csf2ra*-deficient mice have been generated, and these are now available for detailed efficacy and safety testing also for *Csf2ra* expression vectors.[24,25]

In our study, we employed a 3rd generation, safety-improved SIN vector design, which is also used in current HSC-GT-based approaches targeting other monogenic diseases affecting the lymphohematopoietic system, such as X-linked- or adenosine deaminase-deficient severe combined immunodeficiency (X-SCID, ADA-SCID),[26,27] Wiskott Aldrich syndrome (WAS),[28] metachromatic leukodystrophy,[29] or hemoglobinopathies such as β-thalassemia and sickle cell disease.[30,31] Importantly, in the past, a number of phase I/II clinical studies using HSC-GT approaches and LTR-driven transgene expression suffered from insertional mutagenesis and leukemia induced by transactivation of oncogenes *via* retroviral enhancer sequences.[32-34] In contrast, modern SIN alpha-, or gamma-retroviral, as well as lentiviral vector constructs, harbor inactivating mutations in their LTR and employ internal promoters usually derived from house-keeping genes for transgene expression. Meanwhile, more than 100 patients have undergone HSC-GT employing safety modified SIN vectors, such as the one used in our study, without a single event of insertional leukemia. This covers observation periods extending up to ten years in individual patients.

In our model, low VCN in BM cells ranging from 0.02 to 0.86 were sufficient to provide pronounced clinical benefit, which represents an additional safety feature as low VCN reduce the risk of insertion-triggered mutagenic events. Moreover, it corroborates data from GM-CSFR-deficient cells where single copy *CSF2RA* expression from an EFS-driven lentiviral construct was sufficient to initiate GM-CSFR downstream signaling.[35] Interestingly, corrected cells with VCN of up to 7.32 were recruited to and enriched in the lungs, where they exerted their therapeutic effects. This observation is most likely due to the increased pulmonary cytokine levels in herPAP and the feedback mechanism by which cytokines, and in particular GM-CSF, regulate the AM pool.[23]

Recovery of the AM pool following injection of HSC occurred rapidly and resulted in an intra-alveolar cell population displaying the AM typical Siglec-F$^+$CD11c$^+$ phenotype 4-8 weeks after transplantation recapitulating the data from other murine HSC transplant models.[36,37] This time course also mimics quite well the clinical situation following alloHSCT, describing the emergence of donor type AM after 6-8 weeks.[11,38] Development of AM from Siglec-F$^-$CD11c$^-$ peripheral blood monocytes to mature Siglec-F$^+$CD11c$^+$ AM, as observed in our model, closely recapitulates the physiological development of AM from fetal monocytes in the early postnatal period. During fetal development, an intermediate pre-AM stage seems to be employed, which is no longer detectable once AM differentiation is completed.[39] Moreover, similar to early postnatal AM development, cytokines such as M-CSF, and particularly GM-CSF, play crucial roles in the generation and maintenance of the AM pool.[23,39,40] In this respect, the profound reduction of bronchoalveolar M-CSF as well as GM-CSF levels observed in our studies reflect the (auto)-regulatory reaction to the successful pulmonary engraftment and differentiation of AM. It remains unknown whether the rapid recovery of the AM compartment in our studies is due to progenitors generated in the murine BM following HSC engraftment or is achieved directly from primitive hematopoietic cells present in the graft.

Thus, in summary, we provide evidence that 3rd generation SIN lentiviral vector-based HSC-GT effectively reverses the GM-CSF-dependent disease pathology and normalizes, or at least significantly improves, critical disease-related parameters in a relevant murine model of herPAP. On these grounds, we would advocate HSC-GT as an effective and cause-directed therapeutic approach for herPAP patients, which in the clinical setting should offer the chance of long-lasting improvement of symptoms, if not a definitive cure for herPAP patients.

Acknowledgments

The authors would like to thank M. Ballmaier (Cell Sorting Facility, Hannover Medical School) for scientific support and D. Lüttge, E. Janosz, J. Mischke (Institute of Experimental Hematology, Hannover Medical School), P. Felsch, S. Eilert, and A. Kanwischer (Department of Nuclear Medicine, Hannover Medical School) for experimental and technical support.

Funding

This work was supported by grants from the Else Kröner-Fresenius-Stiftung (2013_A24 to T.M. and 2015_A92 to NL),

the Eva Luise Köhler Research Award for Rare Diseases (to GH, NL and TM), Deutsche Forschungsgemeinschaft (Cluster of Excellence REBIRTH), the German Ministry for Education and Technology (BMBF, grant 01EK1602A to GH, NL and TM), JSPS KAKENHI 16K21750 (to TS), Astellas Foundation for Research on Metabolic Disorders (to TS) and the NIH R01HL136721 (to TS) R01HL085453 (to BCT), R01HL118342 (to BCT), U54HL127672 (to BCT).

References

1. Suzuki T, Sakagami T, Young LR, et al. Hereditary pulmonary alveolar proteinosis: pathogenesis, presentation, diagnosis, and therapy. Am J Respir Crit Care Med. 2010; 182(10):1292-1304.
2. Suzuki T, Sakagami T, Rubin BK, et al. Familial pulmonary alveolar proteinosis caused by mutations in CSF2RA. J Exp Med. 2008;205(12):2703-2710.
3. Martinez-Moczygemba M, Doan ML, Elidemir O, et al. Pulmonary alveolar proteinosis caused by deletion of the GM-CSFRα gene in the X chromosome pseudoautosomal region 1. J Exp Med. 2008; 205(12):2711-2716.
4. Suzuki T, Maranda B, Sakagami T, et al. Hereditary pulmonary alveolar proteinosis caused by recessive CSF2RB mutations. Eur Respir J. 2011;37(1):201-204.
5. Tanaka T, Motoi N, Tsuchihashi Y, et al. Adult-onset hereditary pulmonary alveolar proteinosis caused by a single-base deletion in CSF2RB. J Med Genet. 2011;48(3):205-209.
6. Kaufmann KB, Buning H, Galy A, Schambach A, Grez M. Gene therapy on the move. EMBO Mol Med. 2013;5(11):1642-1661.
7. Morgan RA, Gray D, Lomova A, Kohn DB. Hematopoietic Stem Cell Gene Therapy: Progress and Lessons Learned. Cell Stem Cell. 2017;21(5):574-590.
8. Nishinakamura R, Wiler R, Dirksen U, et al. The pulmonary alveolar proteinosis in granulocyte macrophage colony-stimulating factor/interleukins 3/5 beta c receptor-deficient mice is reversed by bone marrow transplantation. J Exp Med. 1996;183(6):2657-2662.
9. Kleff V, Sorg UR, Bury C, et al. Gene therapy of beta(c)-deficient pulmonary alveolar proteinosis (beta(c)-PAP): studies in a murine in vivo model. Mol Ther. 2008;16(4):757-764.
10. Tanaka-Kubota M, Shinozaki K, Miyamoto S, et al. Hematopoietic stem cell transplantation for pulmonary alveolar proteinosis associated with primary immunodeficiency disease. Int J Hematol. 2018;107(5):610-614.
11. Fremond ML, Hadchouel A, Schweitzer C, et al. Successful haematopoietic stem cell transplantation in a case of pulmonary alveolar proteinosis due to GM-CSF receptor deficiency. Thorax. 2018;73(6):590-592.
12. Happle C, Lachmann N, Skuljec J, et al. Pulmonary transplantation of macrophage progenitors as effective and long-lasting therapy for hereditary pulmonary alveolar proteinosis. Sci Transl Med. 2014;6(250):250ra113.
13. Happle C, Lachmann N, Ackermann M, et al. Pulmonary transplantation of human Induced pluripotent stem cell-derived macrophages ameliorates pulmonary alveolar proteinosis. Am J Respir Crit Care Med. 2018;198(3):350-360.
14. Mucci A, Lopez-Rodriguez E, Hetzel M, et al. iPSC-Derived Macrophages Effectively Treat Pulmonary Alveolar Proteinosis in Csf2rb-Deficient Mice. Stem Cell Reports. 2018;11(3):696-710.
15. Takata K, Kozaki T, Lee CZW, et al. Induced-Pluripotent-Stem-Cell-Derived Primitive Macrophages Provide a Platform for Modeling Tissue-Resident Macrophage Differentiation and Function. Immunity. 2017;47(1):183-198.e6.
16. Suzuki T, Arumugam P, Sakagami T, et al. Pulmonary macrophage transplantation therapy. Nature. 2014;514(7523):450-454.
17. Nishinakamura R, Nakayama N, Hirabayashi Y, et al. Mice deficient for the IL-3/GM-CSF/IL-5 beta c receptor exhibit lung pathology and impaired immune response, while beta IL3 receptor-deficient mice are normal. Immunity. 1995;2(3):211-222.
18. Mucci A, Kunkiel J, Suzuki T, et al. Murine iPSC-Derived Macrophages as a Tool for Disease Modeling of Hereditary Pulmonary Alveolar Proteinosis due to Csf2rb Deficiency. Stem Cell Reports. 2016; 7(2):292-305.
19. Sallese A, Suzuki T, McCarthy C, et al. Targeting cholesterol homeostasis in lung diseases. Sci Rep. 2017;7(1):10211.
20. Hara T, Miyajima A. Two distinct functional high affinity receptors for mouse interleukin-3 (IL-3). EMBO J. 1992;11(5):1875-1884.
21. Iyonaga K, Suga M, Yamamoto T, Ichiyasu H, Miyakawa H, Ando M. Elevated bronchoalveolar concentrations of MCP-1 in patients with pulmonary alveolar proteinosis. Eur Respir J. 1999;14(2):383-389.
22. McCarthy C, Lee E, Bridges JP, et al. Statin as a novel pharmacotherapy of pulmonary alveolar proteinosis. Nat Commun. 2018; 9(1):3127.
23. Suzuki T, Trapnell BC. Pulmonary Alveolar Proteinosis Syndrome. Clin Chest Med. 2016;37(3):431-440.
24. Schneider C, Nobs SP, Heer AK, et al. Frontline Science: Coincidental null mutation of Csf2ralpha in a colony of PI3Kgamma$^{-/-}$ mice causes alveolar macrophage deficiency and fatal respiratory viral infection. J Leukoc Biol. 2017; 101(2):367-376.
25. Shima K, Suzuki T, Arumugam P, et al. Pulmonary Macrophage Transplantation Therapy in Csf2ra Gene-Ablated Mice: A Novel Model of Hereditary Pulmonary Alveolar Proteinosis in Children. In: B108. CYSTIC FIBROSIS, PRIMARY CILIARY DYSKINESIA, AND ILD. American Thoracic Society; 2017. p. A4857.
26. De Ravin SS, Wu X, Moir S, et al. Lentiviral hematopoietic stem cell gene therapy for X-linked severe combined immunodeficiency. Sci Transl Med. 2016;8(335):335ra57.
27. Gaspar HB, Buckland K, Rivat C, et al. 276. Immunological and metabolic correction after lentiviral vector mediated haematopoietic stem cell gene therapy for ADA deficiency. Molecular Therapy. 2014;22:S106.
28. Aiuti A, Biasco L, Scaramuzza S, et al. Lentiviral hematopoietic stem cell gene therapy in patients with Wiskott-Aldrich syndrome. Science. 2013;341(6148):1233151.
29. Biffi A, Montini E, Lorioli L, et al. Lentiviral hematopoietic stem cell gene therapy benefits metachromatic leukodystrophy. Science. 2013;341(6148):1233158.
30. Cavazzana-Calvo M, Payen E, Negre O, et al. Transfusion independence and HMGA2 activation after gene therapy of human beta-thalassaemia. Nature. 2010;467(7313):318-322.
31. Kanter J, Walters MC, Hsieh M, et al. Interim results from a Phase 1/2 clinical study of lentiglobin gene therapy for severe sickle cell disease. Blood. 2017;130(Suppl 1):527-527.
32. Hacein-Bey-Abina S, Garrigue A, Wang GP, et al. Insertional oncogenesis in 4 patients after retrovirus-mediated gene therapy of SCID-X1. J Clin Invest. 2008;118(9):3132-3142.
33. Hacein-Bey-Abina S, Von Kalle C, Schmidt M, et al. LMO2-associated clonal T cell proliferation in two patients after gene therapy for SCID-X1. Science. 2003;302(5644):415-419.
34. Stein S, Ott MG, Schultze-Strasser S, et al. Genomic instability and myelodysplasia with monosomy 7 consequent to EVI1 activation after gene therapy for chronic granulomatous disease. Nat Med. 2010;16(2):198-204.
35. Hetzel M, Suzuki T, Hashtchin AR, et al. Function and safety of lentivirus-mediated gene transfer for CSF2RA-deficiency. Hum Gene Ther Methods. 2017;28(6):318-329.
36. Matute-Bello G, Lee JS, Frevert CW, et al. Optimal timing to repopulation of resident alveolar macrophages with donor cells following total body irradiation and bone marrow transplantation in mice. J Immunol Methods. 2004;292(1-2):25-34.
37. Murphy J, Summer R, Wilson AA, Kotton DN, Fine A. The prolonged life-span of alveolar macrophages. Am J Respir Cell Mol Biol. 2008;38(4):380-385.
38. Nakata K, Gotoh H, Watanabe J, et al. Augmented proliferation of human alveolar macrophages after allogeneic bone marrow transplantation. Blood. 1999;93(2):667-673.
39. Guilliams M, De Kleer I, Henri S, et al. Alveolar macrophages develop from fetal monocytes that differentiate into long-lived cells in the first week of life via GM-CSF. J Exp Med. 2013;210(10):1977-1992.
40. Hashimoto D, Chow A, Noizat C, et al. Tissue-resident macrophages self-maintain locally throughout adult life with minimal contribution from circulating monocytes. Immunity. 2013;38(4):792-804.

Ferrata Storti Foundation

Haematologica 2020
Volume 105(4):1158-1165

Transition from fresh frozen plasma to solvent/detergent plasma in the Netherlands: comparing clinical use and transfusion reaction risks

Nicholas H. Saadah,[1,2,3] Martin R. Schipperus,[3,4] Johanna C. Wiersum-Osselton,[3,5] Marian G. van Kraaij,[5,6] Camila Caram-Deelder,[1,2] Erik A.M. Beckers,[7] Anja Leyte,[8] Jan M.M. Rondeel,[9] Karen M.K. de Vooght,[10] Floor Weerkamp,[11] Jaap Jan Zwaginga[12] and Johanna G. van der Bom[1,2]

[1]Jon J. van Rood Centre for Clinical Transfusion Research, Sanquin Research, Leiden; [2]Deptartment of Clinical Epidemiology, Leiden University Medical Centre, Leiden; [3]TRIP, National Hemovigilance & Biovigilance Office, Leiden; [4]Haga Teaching Hospital, Department of Haematology, The Hague; [5]Donor Affairs, Sanquin Blood Supply, Leiden; [6]Department of Transfusion Medicine, Sanquin Blood Supply, Amsterdam; [7]Department of Haematology, Maastricht University Medical Centre, Maastricht; [8]Department of Clinical Chemistry, OLVG Location East, Amsterdam; [9]Department of Clinical Chemistry, Isala Clinics, Zwolle; [10]Department of Clinical Chemistry, University Medical Centre Utrecht, Utrecht; [11]Department of Clinical Chemistry, Maasstad Hospital, Rotterdam and [12]Department of Immunohaematology and Blood Transfusion, Leiden University Medical Centre, Leiden, the Netherlands

ABSTRACT

Plasma transfusion is indicated for replenishment of coagulative proteins to stop or prevent bleeding. In 2014, the Netherlands switched from using ~300mL fresh frozen plasma (FFP) units to using 200mL Omniplasma, a solvent/detergent treated pooled plasma (SD plasma), units. We evaluated the effect of the introduction of SD plasma on clinical plasma use, associated bleeding, and transfusion reaction incidences. Using diagnostic data from six Dutch hospitals, national blood bank data, and national hemovigilance data for 2011 to 2017, we compared the plasma/red blood cell (RBC) units ratio (f) and the mean number of plasma and RBC units transfused for FFP (~300mL) and SD plasma (200mL) for various patient groups, and calculated odds ratios comparing their associated transfusion reaction risks. Analyzing 13,910 transfusion episodes, the difference ($\Delta f = f_{SD} - f_{FFP}$) in mean plasma/RBC ratio (f) was negligible ($\Delta f_{entire\_cohort} = 0.01$ [95% confidence interval (CI): -0.02 - 0.05]; *P*=0.48). SD plasma was associated with fewer RBC units transfused per episode in gynecological (difference of mean number of units -1.66 [95% CI: -2.72, -0.61]) and aneurysm (-0.97 [-1.59, -0.35]) patients. SD plasma was further associated with fewer anaphylactic reactions than FFP (odds ratio 0.37 [0.18, 0.77; *P*<0.01]) while the differences for most transfusion reactions were not statistically significant. SD plasma units, despite being one third smaller in volume than FFP units, are not associated with a higher plasma/RBC ratio. SD plasma is associated with fewer anaphylactic reactions than FFP plasma/RBC units ratio.

Correspondence:

JOHANNA G. VAN DER BOM
j.g.van_der_bom@lumc.nl

Received: March 15, 2019.

Accepted: June 26, 2019.

Pre-published: July 4, 2019.

doi:10.3324/haematol.2019.222083

Check the online version for the most updated information on this article, online supplements, and information on authorship & disclosures: www.haematologica.org/content/105/4/1158

Introduction

Plasma transfusion is indicated in a range of medical situations involving replenishment of coagulative proteins to stop or prevent bleeding (e.g. surgery, liver disease), or removal of an insulting entity via plasma exchange (e.g. thrombotic thrombocytopenic purpura, hemolytic-uremic syndrome [TTP/HUS]).[1,2] On January 1, 2014, Sanquin Blood Bank, the National Blood Bank of the Netherlands, replaced quarantined FFP units, with a volume of ~300mL, with SD plasma Omniplasma made by Octapharma from a pool of either ~600 or ~1200 apheresis plasma donations, whose units are exactly 200mL in volume. Omniplasma is made

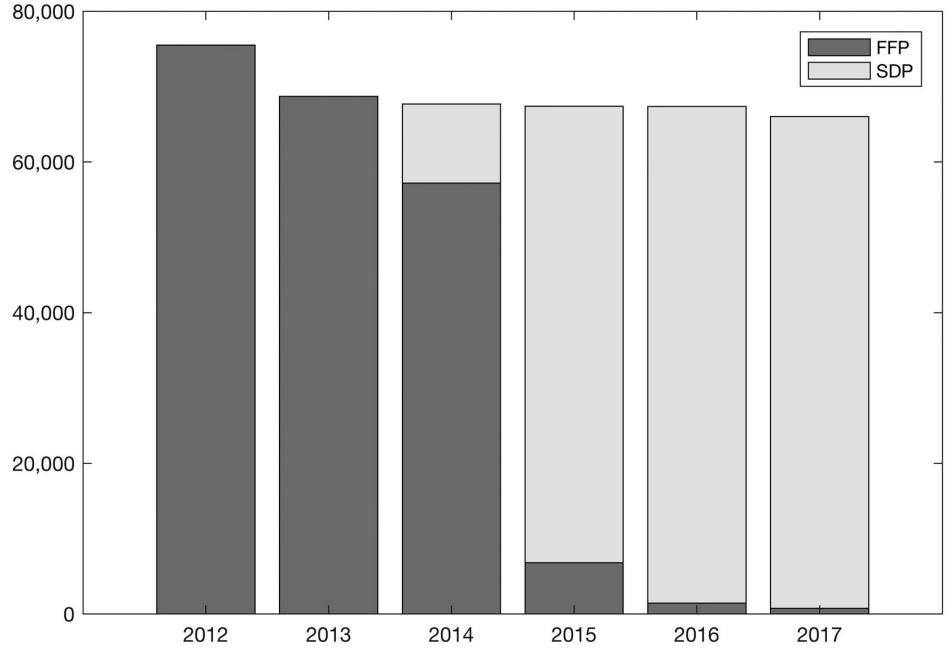

Figure 1. Number and type of plasma units distributed to all Dutch hospitals between 2012 and 2017. The national switch from FFP to SD plasma occurred on January 1, 2014, but FFP units can be stored for up to two years prior to use, hence a gradual transition to SD plasma is observed. Residual amounts of FFP are still transfused in 2016 and 2017 for those few patient groups for which SD plasma is counter-indicated (see background). FFP: fresh frozen plasma; SD plasma: solvent/detergent treated pooled plasma.

from plasma donations of non-remunerated Dutch donors, the same pool as that of FFP, and is functionally equivalent to OctaplasLG.[3] As FFP can be stored for up to 2 years, FFP distribution and use continued in a decreasing fashion during the period from 2014 to 2015. As of 2016, with the exception of a patient groups for which FFP remains indicated (e.g. IgA-deficient patients, protein S deficient patients), SD plasma is the only plasma type available for transfusion in the Netherlands.[4]

Since the purpose of plasma in the surgical setting is to stop active bleeding, the number of RBC units transfused alongside the plasma serves as a measure of effectiveness of plasma transfusion at the population level. Plasma and RBC units are often transfused in fixed ratios in the surgical setting (e.g. two units of plasma for every RBC), however SD plasma units are smaller than FFP units (200 mL *vs.* ~300mL, respectively). Of interest was thus whether this ratio of blood product use changed with the switch from FFP to SD plasma. Further, the switch to SD plasma was expected to result in a reduced risk of TRALI and allergic reactions as well as (theoretically) viral and prion transmission[5] as observed in other countries switching to SD plasma.[6–14]

Analysis objectives

A comparison of the plasma/RBC units ratio, the number of RBC units concurrently transfused, and the transfusion reaction risks for SD plasma and FFP in the Netherlands in the period before and after the national switch to SD plasma on January 1, 2014.

Methods

Data Sources

With approval from the medical ethical committee of the Leiden University Medical Centre (protocol number P13.251), we submitted our study plan to the Dutch National Blood Bank (Sanquin), six Dutch hospitals (which altogether account for roughly 20% of the plasma transfused per annum in the Netherlands), and the Dutch National Hemovigilance and Biovigilance Office (TRIP: Transfusie-en transplantatieReacties In Patiënten). Data from these sources were used to examine change in blood product use (blood bank data and hospital data) and transfusion reaction risk (hemovigilance data) in the years before and after the national switch to SD plasma in 2014. A more detailed description of our methodology and the data collected from each source is found in the *Online Supplementary Materials* and *Methods*.

Grouping of transfusions into transfusion episodes and patient subpopulations

Transfusions were grouped into transfusion episodes, with a transfusion episode defined as a series of consecutive transfusions for which the time interval between transfusions did not exceed 72 hours. In order to be able to perform the comparisons in relatively homogeneous patient groups, transfusion episodes were subdivided based on the ward specified by their diagnostic code(s), the four analyzed wards being (1) cardiothoracic surgery + cardiology (CTsurg+cardio); (2) general surgery (gs); (3) gynaecology (gyn); (4) all others (oth), with this last group including TTP/HUS patients. To create further homogenous groups, within each of the analyzed wards we selected transfusion episodes coded with the most commonly occurring diagnostic codes. Within the cardiothoracic surgery + cardiology group, we selected episodes involving patients undergoing cardio arterial bypass grafting (CABG), valve replacement (VR), or maze procedure. Within the general surgery group, we selected episodes involving patients with any type of aneurysm. Within the gynecological group, we selected obstetric episodes. We analyzed episodes involving plasma exchange for TTP/HUS patients separately.

Blood product use analysis

National plasma use during study period

For visualization of blood product use at the national level, we plotted the number of FFP and SD plasma units distributed by the Dutch Blood Bank (Sanquin) to all hospitals for the period between 2011 and 2017.

Table 1. Blood product details for the different cohorts (episodes involving plasma transfusion).

Episode characteristics	CT surg. + cardiology		general surgery		gynecology		other	TTP/HUS	entire
	all	CABG, VR, maze	all	non-elective aneurysm	all	labor			cohort
transfusion episodes	9,420	4,334	4,249	534	652	478	3,540	79	17,861
median age in years (IQR)	62 (35-73)	68 (57-75)	58 (36-70)	74 (67-79)	34 (29-39)	33 (29-36)	46 (11-65)	53 (43-60)	58 (27-71)
proportion male	0.64	0.68	0.58	0.79	0	0	0.54	0.18	0.59
Transfused blood products:									
FFP									
episodes:	7,232	3,267	3,332	390	506	362	2,917	67	13,987
total units transfused:	31,073	12,156	16,985	2,364	1,795	1,384	14,707	3,211	64,560
mean units per episode (sd):	4.30 (8.0)	3.72 (5.2)	5.10 (9.7)	6.06 (6.2)	3.55 (5.1)	3.82 (5.8)	5.04 (14.0)	47.9 (69.3)	4.62 (9.8)
SD plasma									
episodes:	2,188	1,067	917	144	146	116	623	12	3,874
total units transfused:	10,704	4,256	4,652	748	395	325	3,155	979	18,906
mean units per episode (sd):	4.89 (5.2)	3.99 (3.2)	5.07 (5.0)	5.19 (3.9)	2.71 (1.5)	2.80 (1.6)	5.06 (6.4)	81.6 (37.6)	4.88 (5.3)
RBC									
episodes:	8,115	3,603	3,426	510	603	448	2,181	23	14,325
total units transfused:	50,066	20,229	25,356	4,719	3,094	2,261	10,815	57	89,331
mean units per episode (sd):	6.17 (8.1)	5.61 (6.7)	7.40 (7.5)	9.25 (8.2)	5.13 (4.4)	5.05 (4.2)	4.96 (5.0)	2.48 (1.3)	6.24 (7.4)
Platelets									
episodes:	6,153	3,137	1,634	294	198	155	1,073	3	9,058
total units transfused:	15,489	6,395	5,135	653	549	290	4,521	3	25,694
mean units per episode (sd):	2.52 (4.4)	2.04 (2.1)	3.14 (4.3)	2.22 (1.8)	2.77 (3.6)	1.87 (1.2)	4.21 (6.5)	1.00 (0.2)	2.84 (4.9)

Note that for each blood product, the denominator used for calculation of the average units per episode is the number of episodes involving transfusion of that blood product (indicated). RBC: red bllod cells; avg per ep: average units/episode of given blood product for episodes involving transfusion of that product; CABG: coronary arterial bypass graft; CT surgery: cardiothoracic surgery; FFP: fresh frozen plasma; IQR: interquartile range; maze : maze procedure; sd: standard deviation; SD plasma: solvent/detergent treated pooled plasma; TTP/HUS: thrombocytopenic thrombotic purpura/hemolytic uremic syndrome; VR: valve replacement.

Patient-level blood product use

For each of the analyzed groups, we selected episodes involving transfusion of both plasma and RBC units and calculated the mean plasma units per episode, the mean RBC units per episode, and the mean ratio thereof (plasma/RBC units).

Sensitivity analyses

As a first sensitivity analysis, we repeated the patient-level blood product use analysis described above using only those patients in each analysis cohort receiving ≥5 RBC units during the transfusion episode to additionally compare use in patients experiencing heavy bleeding. As a second sensitivity analysis, to ensure the chosen hierarchy did not affect our results, we re-ran this analysis using two other hierarchies for group selection (see the *Online Supplement Materials and Methods* for the hierarchy description).

Comparison of transfusion reaction risk for FFP and SD plasma

We compared the risk of non-infectious transfusion reactions between the two plasma types. Infectious transfusion reactions are rarely attributed to plasma transfusion, with the few cases reported involving infection with bacteria present in the water baths used to thaw the plasma units.[15]

Results

Comparison of blood product use

National plasma use during the study period

Figure 1 shows plasma use in the Netherlands of the period from 2012 to 2017, with the national switch to SD plasma occurring on January 1, 2014 (the date as of which Sanquin began distributing SD plasma to hospitals as the standard plasma product). As FFP can be stored for up to two years, stocks continued to be distributed and transfused in the Netherlands until the end of 2015. Total plasma units used decreased by 13% in the course of the 6-year study period. This trend was not reversed by the switch to the smaller SD plasma units.

Patient-level plasma use

Figure 2 shows our data flow. From the six participating hospitals, we collected data on 18,053 transfusion episodes involving plasma transfusion. Together, these episodes involved transfusion of 85,768 plasma units (65,160 FFP; 20,608 SD plasma), 91,318 red cell units, and 26,290 platelet units, and were coded by 891 unique diagnostic codes. Following exclusion of 192 episodes involving transfusion of both SD plasma and FFP, blood product details for the remaining 17,861 episodes are provided in Table 1. Comparing average plasma units per episode for FFP and SD plasma across the cohorts shows no systematic increase in plasma units transfused with the switch to SD plasma, excepting for the TTP/HUS cohort where the average number of plasma units transfused was higher for SD plasma than for FFP (81 *vs.* 48 plasma units/episode).

Figure 3 shows the results of our comparison of SD plasma and FFP with regard to (a) mean plasma units transfused, (b) mean RBC units transfused and (c) mean plasma/RBC units ratio for episodes involving transfusion of both RBC and plasma units (13,910 episodes), with

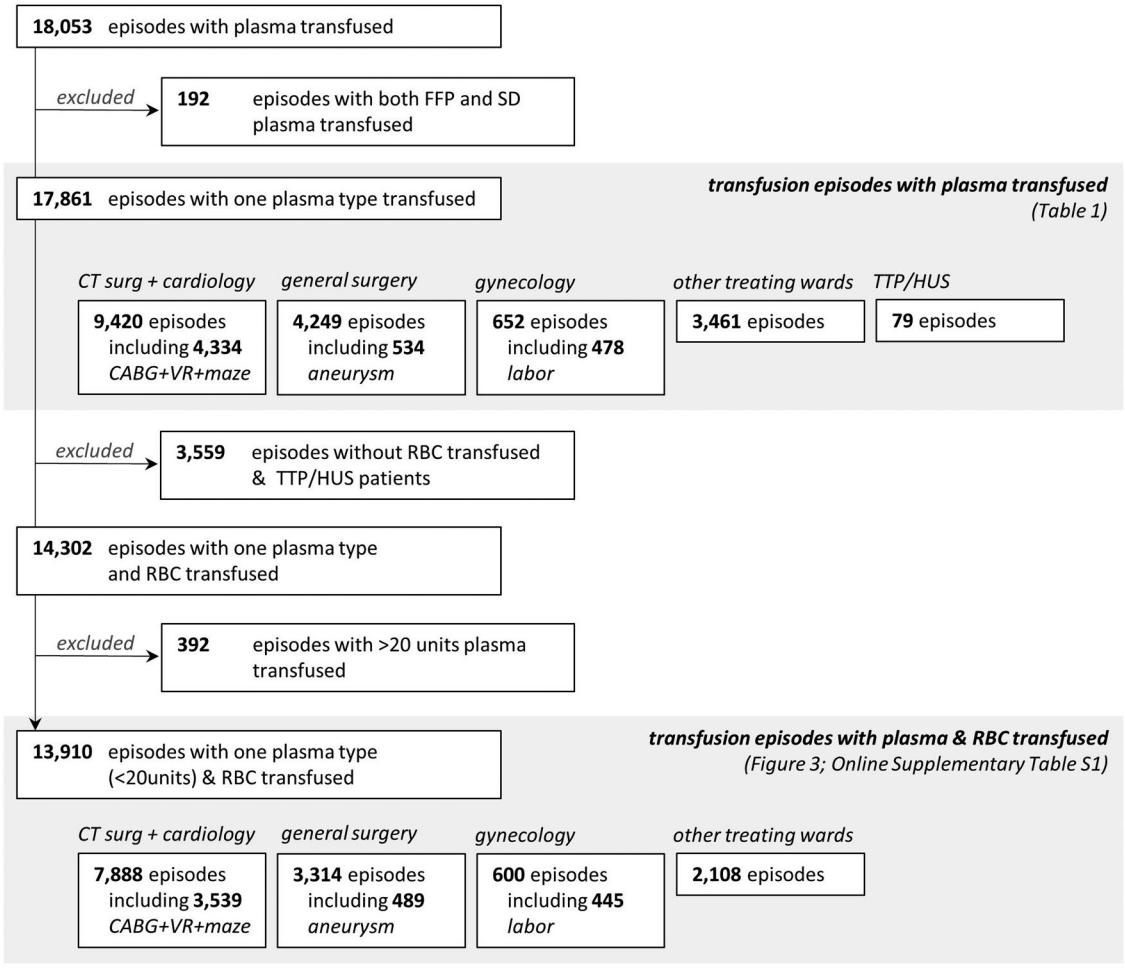

Figure 2. Data flow diagram showing categorization of episodes into sub-cohorts for patients receiving plasma transfusion in (all or part of) 2010 to 2016. CABG+VR+maze: cardio arterial bypass graft + valve replacement + maze procedure; CT surgery: cardiothoracic surgery; FFP: fresh frozen plasma; maze: maze procedure; RBC: red blood cells; SD plasma: solvent/detergent treated pooled plasma; TTP/HUS: thrombotic thrombocytopenic purpura/hemolytic uremic syndrome.

numeric results presented in the *Online Supplementary Table S1*. For all three outcomes (mean plasma units/episode; mean RBC units/episode; mean plasma/RBC units ratio), a positive difference in means indicates a higher mean value for SD plasma. Changes in mean plasma ($\Delta\mu_{Pl} = \mu_{FFP} - \mu_{SD}$) and RBC ($\Delta\mu_{RBCs}=\mu_{RBCs\_pre\text{-}switch} - \mu R_{RBCs\_post\text{-}switch}$) units transfused per episode with the switch were negative for some groups, indicating a decrease with the switch to SD plasma (aneurysm: $\Delta\mu_{Pl(an)}$ = -1.06 [-1.71, -0.41], $\Delta\mu_{RBCs(an)}$ = -1.66 [-2.72, -0.61]; gynecology: $\Delta\mu_{Pl(gyn)}$ = -0.52 [-0.95, -0.08], $\Delta\mu_{RBCs(gyn)}$ = -0.97 [-1.59, -0.35]) and positive for others, indicating an increase (cardiothoracic surgery + cardiology: $\Delta_{\mu Pl(cts)}$ = 0.33 [0.15, 0.51], $\Delta\mu_{RBCs(cts)}$ = 0.36 [0.08, 0.64]). For the group as a whole, the mean number of plasma units transfused per episode increased slightly with the switch to SD plasma ($\Delta\mu_{Pl(cohort)}$ = 0.19 [0.06, 0.32]).

The mean plasma/RBC units ratio (f) for the group as a whole (13,910 episodes) involving transfusion of both plasma and RBC units was 0.86 (95% CI: 0.84 - 0.88) for FFP and 0.87 (0.85-0.91) for SD plasma. The difference in means ($f_{SD} - f_{FFP}$) was 0.01 [-0.02- 0.05]; *P*=0.48 indicating no significant change in the number of plasma units transfused per unit of RBC when SD plasma is transfused. For all wards (cardiothoracic surgery + cardiology, general surgery, gynecology) and diagnoses (CABG+valve replacement+maze procedure, aneurysm, labor), $f_{SD} - f_{FFP}$ remained consistently close to zero with none of the differences being statistically significant at the α=0.05 level.

Sensitivity analyses

The *Online Supplementary Figure S1* shows the results of our first sensitivity analysis, the plasma/RBC units ratio (f) comparison for those episodes involving transfusion of plasma and five or more RBC units. The ratios for both plasma types were lower in this group of massive transfusion patients compared to the patient cohort as a whole: f_{FFP} = 0.56 (0.55 - 0.57); the *Online Supplementary Figure S1* shows the results of our first sensitivity analysis, the plasma/RBC units ratio (f) comparison for those episodes involving transfusion of plasma and five or more RBC units. The ratios for both plasma types were lower in this group of massive transfusion patients compared to the patient cohort as a whole: f_{FFP} = 0.56 (0.55 - 0.57); f_{SD} = 0.57 (0.55 - 0.59); $f_{SD} - f_{FFP}$ 0.02 (-0.01-0.04); *P*=0.19. Here too none of the ward or diagnostic based sub-cohorts returned a statistically significant result for the difference in means

Table 2. Comparison of the number of transfusion reactions and transfusion reaction risk for fresh frozen plasma and solvent/detergent plasma using national hemovigilance data.

Transfusion reaction	FFP (209,681 units)	SD plasma (137,028 units)	Risk Ratio (95% CI) $risk_{SD}/risk_{FFP}$	Significance
allergic (other) reaction	114	14	0.19 [0.11 to 0.33]	$P<0.01$
allergic (anaphylactic) reaction	37	9	0.37 [0.18 to 0.77]	$P<0.01$
non-hemolytic transfusion reaction	9	1	0.17 [0.02 to 1.34]	$P=0.10$
febrile non-hemolytic transfusion reaction	8	1	0.19 [0.02 to 1.53]	$P=0.10$
transfusion associated circulatory overload	2	2	1.53 [0.22 to 10.86]	$P=0.65$
transfusion related acute lung injury	1	1*	1.53 [0.10 to 24.46]	$P=0.71$
other	24	5	0.32 [0.12 to 0.84]	$P=0.01$

**Upon review, the expert panel tasked with evaluating debatable cases could not rule out TACO.* TACO: transfusion associated circulatory overload; FFP: fresh frozen plasma; SD plasma: solvent/detergent treated pooled plasma.

$f_{SD} - f_{FFP}$. In the *Online Supplementary Table S1*, the numeric results of our entire blood product use analysis are shown.

In our second sensitivity analysis, involving use of varying hierarchies for cohort selection, we found changing the hierarchy yielded nearly identical results as only a few transfusion episodes were coded with diagnostic codes from two different treatment wards (*data not shown*).

Comparison of plasma transfusion reaction risk

During the period from 2012 to 2016, Sanquin distributed 209,681 units of FFP and 137,028 units of SD plasma. During the same period, the National Hemovigilance Office received reports of 46 allergic (anaphylactic) reactions, 128 allergic (other) reactions, 10 mild non-hemolytic febrile reactions (mild NHFR), nine non-hemolytic transfusion reactions (NHTR), four cases of transfusion associated circulatory overload (TACO), two cases of transfusion related acute lung injury (TRALI), and 29 'other' plasma transfusion reactions in association with transfusion of one or more plasma units. Table 2 shows risk ratios comparing SD plasma and FFP for the seven plasma transfusion reaction types reported during the study period with an imputability of 'certain', 'probable', or 'possible'. SD plasma was associated with fewer allergic (other) reactions (RR=0.19 [95% CI: 0.11 - 0.34]; $P<0.01$) and allergic (anaphylactic) reactions (RR=0.38 [0.18 - 0.79]; $P<0.01$), as well as fewer 'other' plasma transfusion reactions (RR=0.33 [0.13 - 0.86]; $P=0.02$) than FFP. No bacterial transfusion reactions were attributed to transfusion of either plasma during the study period.

Discussion

We compared the plasma/RBC units ratio, number of RBC units concurrently transfused, and transfusion reaction risks for SD plasma (200 mL) and FFP (~300mL) units in the Netherlands in the years surrounding the Dutch switch to SD plasma in 2014 and compared plasma unit use for transfusion episodes involving the two plasma types for the same period. The mean number of plasma and RBC units transfused per episode decreased significantly in the aneurysm and gynecological groups, and the decrease in overall plasma use continued despite the switch to the smaller SD plasma units. Despite the significantly (one third) smaller volume of SD plasma units, the plasma/RBC units ratio remained constant across all patient cohorts with the switch from FFP to SD plasma units. The risk of most plasma transfusion reactions decreased.

The SD process involves pooling FFP, treating the pool to disrupt lipid-coated viruses, and running the pool through a filter designed to remove prions. This process normalizes coagulation factor levels and dilutes proteins/cytokines from the individual donations, and is thus expected to reduce the incidence of some transfusion reactions (e.g. allergic, FNHTR). However, no aspect of the SD process is expected to increase the product efficiency, suggesting equal volumes of the two would be needed to affect the same reduction in active bleeding. In the Netherlands, a 200 mL unit of SD plasma is smaller than a unit of FFP which typically contains between 300 and 330 mL of plasma,[3] meaning transfusing equal volumes of the two plasma products requires transfusing more units of SD plasma.

At the national level, we observed no such increase in units issued, with the switch to SD plasma not interrupting the downward trend in plasma use over the period. At the transfusion episode level, we observed only a small increase in mean plasma units transfused per episode for the cohort as a whole. Rather than a large increase of SD plasma being transfused – an increase of 50% in the number of transfused units could have been expected - this small increase is likely due to plasma exchange patients who, being exchanged with a specific volume, were transfused with more units of SD plasma (Table 1). The changes in the plasma use for the ward-based patient groups and diagnosis-based sub-cohorts varied, but did not show the trend we expected to see were the number of plasma units transfused systematically different for FFP versus SD plasma. When the changes in mean plasma units per episode did reach the level of statistical significance (*e.g.* cardiothoracic surgery + cardiology group), the effect sizes were in line with those of the other cohorts and the statistical significance resembles the result of the larger size of these cohorts. Given that the change in plasma/RBC ratio (f) was not significant for any of the cohorts, we interpret these results as showing continued transfusion of SD plasma units in the same proportion to RBC units as FFP plasma. We have found no previous studies comparing the plasma/RBC units ratio for FFP and SD plasma. In broad terms, plasma is transfused to replenish plasma proteins during active bleeding (*e.g.* during surgery) or to remove a harmful entity/constituent *via* plasma

exchange (*e.g.* in TTP/HUS patients). By creating cohorts of transfusion episodes involving transfusion of both RBC and plasma units, we aimed to capture episodes where plasma was used in cases of active bleeding. The further stratification of these episodes by ward and diagnosis was intended to create progressively more homogeneous cohorts for comparison. If one plasma type more effectively stopped active bleeding than the other, we might expect to observe a change in the mean number of RBC units transfused per episode with the switch to SD plasma.[16] We observed such a change in the general surgery and gynecological groups, where the number of RBC units transfused alongside plasma was around half a unit (general surgery) and one unit (gynecology) lower for SD plasma than for FFP. Confounding our results, however, is the trend of decreased RBC transfusion within the

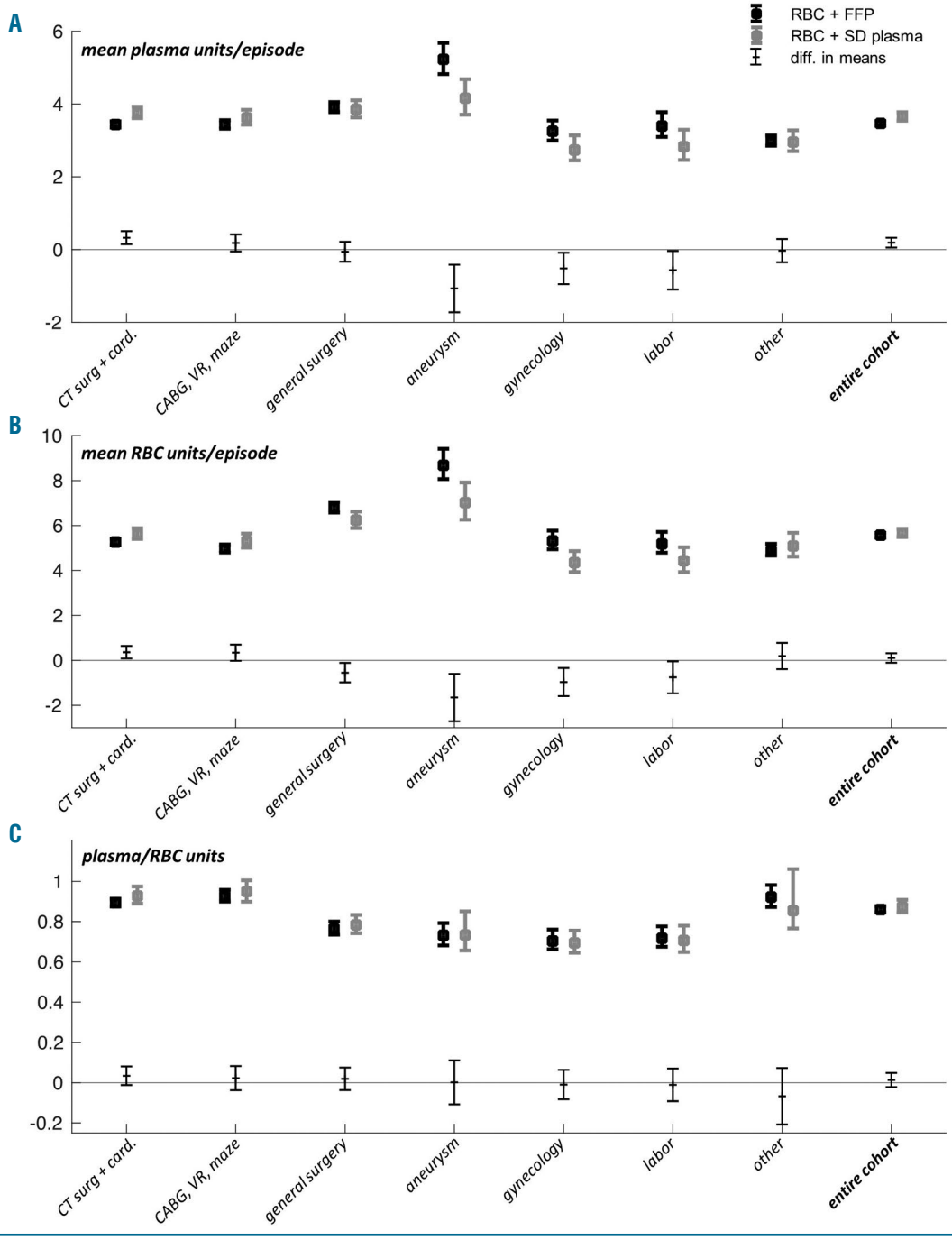

Figure 3. Blood product use prior to versus after the switch from fresh frozen plasma to solvent/detergent treated pooled plasma. (A) mean plasma units, (B) mean RBC units, and (C) mean plasma/RBC units ratio for FFP (thick black) and SD plasma (thick grey) along with mean differences (thin black) for all three values. Note that mean differences are calculated as $mean_{SD}$ - $mean_{FFP}$ such that a positive value indicates a higher value for SD plasma, and *vice versa*. CABG, VR, maze: coronary artery bypass graft, valve replacement, maze procedure; CT surg + card.:cardiothoracic surgery + cardiology; FFP: fresh frozen plasma; RBC: red blood cell; SD plasma: solvent/detergent treated pooled plasma.

Netherlands.[17] Within our analysis, the mean number of concurrently transfused RBC units was generally similar to or lower for SD plasma, transfused after 2014, than for FFP, transfused before 2016 (Figure 3). While we cannot separate the effects of plasma efficiency from those of this trend, our data suggest no differences in effectiveness of stoppage of bleeding between the two plasma types, despite a one third reduction of plasma volume being transfused following the switch to SD plasma.

The results of our transfusion reaction risk analysis, showing a lower incidence of allergic reactions, both anaphylactic and 'other', for SD plasma as compared to FFP, are in line with those of several other studies in which SD plasma was consistently found to lead to fewer transfusion reactions in general.[6–14] While transfusion reaction reporting practices likely changed during the seven years of data collection, the number of transfusion reactions reported to the National Haemovigilance Office has remained fairly constant across all categories in the last five years of FFP use (*data not shown*). This suggests the reporting procedures in use have reached steady-state, meaning a low risk of bias in our comparison due to differences in reporting processes between the periods in which two plasma products were used.

Given the rarity with which they are ascribed to plasma transfusion, our study did not observe enough TACO or TRALI cases to make meaningful conclusions with regards to their relative risks following FFP versus SD plasma transfusion, despite other studies noting a decreased incidence of TRALI with SD plasma.[18] Of note, thus, is the TRALI case associated with transfusion of SD plasma in 2016. The patient, a pediatric stem-cell transplant recipient, was already at an increased risk for respiratory transfusion reactions and had received transfusions of RBC and platelets, in addition to plasma.[19] As a debatable case, this was further evaluated by an expert panel which agreed TRALI was a possibility but could not rule out TACO. As such, it was recorded in the TRIP database as a TRALI with a low imputability of 'possible.'

Relevance and future research

Our study shows that in the Netherlands, reducing the size of plasma units by one third resulted in no change in the number of transfused plasma units. This suggests clinicians continued to transfuse the same number of plasma units, despite the decrease in volume, resulting in a reduction of around one third in the country's total transfused plasma volume. Given the SD process is not reported to increase product efficiency, the fact that the number of transfused RBC units did not concurrently increase at a population level serves as a suggestion, though not the first,[20] that the clinical evidence base for the volume ratio of plasma to RBC transfused to stop bleeding needs re-evaluation. A logical next step would be an observational study exploring mortality in matched patients receiving different plasma/RBC volume ratios, or a trial exploring the effect on mortality of a reduction in transfused plasma volume. A potential general decrease in demand of plasma for transfusion would have obvious benefits to a country's donor population and healthcare costs.

Limitations

In our analysis of blood product use and plasma transfusion safety, around 20% (3,559 of 17,861 episodes – see Figure 1) of the transfusion episodes involved transfusion of only plasma, without concurrent RBC units. This is not in line with current evidence-based indications for plasma transfusion which (if followed) would lead to plasma always being transfused with RBC units except in cases of plasma exchange (plasma exchange episodes comprise less than 1% of the transfusion episodes analyzed in our study).[21] After review of a sample of these patients' transfusion data we confirmed that data were not missing (*i.e.* that only plasma was transfused during these episodes). Previous studies have likewise pointed out a high rate of plasma transfusion outside the context of evidence-based indications.[2,22,23] As an example, in some of the reporting hospitals, plasma is transfused prophylactically prior to biopsy procedures.

The large standard deviations in mean plasma and RBC units transfused (Table 1) demonstrate the extent to which transfusion practice varied among the patients in our study. Further, we matched patients only on ward or diagnosis without correcting for other predictors, as this was not the goal of our analysis. The conclusions are thus to be interpreted at a population level, and not at the level of the individual patient. Finally, given the rare nature of many of the transfusion reactions analyzed, even 6 years of data from a country performing only 60,000 plasma transfusions per year yields datasets too small for solid hemovigilance comparisons. Meta-analyses, large-scale observational trials, or active hemovigilance studies are better equipped to address comparative safety of blood products with regard to rare adverse events.

Conclusions

Using national bood bank and hemovigilance data, as well as transfusion data from six large hospitals in the Netherlands, we compared FFP and SD plasma with regard to blood product use and transfusion reaction risk in the period surrounding the national switch from FFP to SD plasma in 2014. We found some small differences in the average number of RBC units transfused alongside SD plasma *versus* FFP, but no systemic changes in mean RBC transfused or the mean plasma/RBC units ratio when comparing the two products. This suggests the two plasmas were transfused in the same ratio (by units) to RBC and that they do not differ significantly in their effectiveness at stopping bleeding at a unit level, despite the significantly (one third) smaller volume of SD plasma units and their chemical similarity to FFP. SD plasma is associated with fewer allergic (other) and allergic (anaphylactic) transfusion reactions.

Acknowledgments

The authors wish to thank Yavanna van Oostveen and the data management team at Sanquin's Centre for Clinical Transfusion Research (CCTR) for their collection and cleaning of the patient data used within this study and the Scientific Committee of the CCTR for their analytical advice.

References

1. Wong MP, Droubatchevskaia N, Chipperfield KM, Wadsworth LD, Ferguson DJ. Guidelines for frozen plasma transfusion. B C Med J. 2007;49(6):311-319.
2. Tinmouth A, Thompson T, Arnold DM, et al. Utilization of frozen plasma in Ontario: a provincewide audit reveals a high rate of inappropriate transfusions. Transfusion. 2013;53(10):2222-2229.
3. Sanquin Bloed Supply. Vergelijking Q-plasma Omniplasma. https://www.sanquin.org/binaries/content/assets/nl/producten-en-diensten/plasmaproducten/vergelijking_q-plasma-omniplasma.pdf (2014, accessed May 23, 2019).
4. Wiersum-Osselton JC, Middelburg RA, van der Bom JG, Van TA, Zijlker-Jansen PY, Schipperus MR. Effect of using male-only fresh frozen plasma for TRALI prevention in the Netherlands. Vox Sang. 2010; 99(S):457.
5. Wiersum-Osselton JC, Schipperus MR. Transfusiereacties bij patiënten : hemovigilantiemeldingen aan het Landelijk Hemovigilantiebureau over 2003. Ned Tijdschrijft voor Geneeskd. 2005; 149(47):2622-2627.
6. Edel E, Al-Ali HK, Seeger S, Kauschat D, Matthes G. Efficacy and Safety Profile of Solvent/Detergent Plasma in the Treatment of Acute Thrombotic Thrombocytopenic Purpura: A Single-Center Experience. Transfus Med Hemother. 2010;37(1):13-19.
7. Solheim BG, Seghatchian J. Update on pathogen reduction technology for therapeutic plasma: an overview. Transfus Apher Sci. 2006;35(1):83-90.
8. Saadah NH, van der Bom JG, Wiersum-Osselton JC, et al. Comparing transfusion reaction risks for various plasma products - an analysis of 7 years of ISTARE haemovigilance data. Br J Haematol. 2018; 180(5):727-734.
9. Scully M, Longair I, Flynn M, Berryman J, Machin SJ. Cryosupernatant and solvent detergent fresh-frozen plasma (Octaplas) usage at a single centre in acute thrombotic thrombocytopenic purpura. Vox Sang. 2007;93(2):154-158.
10. Mayr WR. Haemovigilance: are there significant differences among plasma products? Transfus Apher Sci. 2010;43(3):407-409.
11. Riedler GF, Haycox R, Duggan K, Dakin H. Cost-effectiveness of solvent/detergent-treated fresh-frozen plasma. Vox Sang. 2003;85(2):88-95.
12. Klein HG, Dodd RY, Dzik WH, et al. Current status of solvent/detergent-treated frozen plasma. Transfusion. 1998; 38(1):102-107.
13. Baudoux E, Margraff U, Coenen A, et al. Hemovigilance: clinical tolerance of solvent-detergent treated plasma. Vox Sang. 1998;74(S1):237-239.
14. Hellstern P, Solheim BG. The Use of Solvent/Detergent Treatment in Pathogen Reduction of Plasma. Transfus Med Hemother. 2011;38(1):65-70.
15. Pandey S, Vyas GN. Adverse effects of plasma transfusion. Transfusion. 2012;52(Suppl 1):65S-79S.
16. Cinqualbre J, Kientz D, Remy E, Huang N, Corash L, Cazenave JP. Comparative effectiveness of plasma prepared with amotosalen-UVA pathogen inactivation and conventional plasma for support of liver transplantation. Transfusion. 2015;55(7):1710-1720.
17. van Hoeven LR, Koopman MM, Koffijberg H, Roes KC, Janssen MP. Historical time trends in red blood cell usage in the Netherlands. Int J Clin Transfus Med. 2016; (4):67-77.
18. Marietta M, Franchini M, Bindi ML, Picardi F, Ruggeri M, De Silvestro G. Is solvent/detergent plasma better than standard fresh-frozen plasma? A systematic review and an expert consensus document. Blood Transfus. 2016;14(4):277-286.
19. TRIP National Hemovigilance and Biovigilance Office. Transfusie- en transplantatiereacties in Patiënten annual report (2016). 10–11. https://www.tripnet.nl/publicaties/rapporten/ (accessed May 23, 2019).
20. Holcomb JB, Tilley BC, Baraniuk S, et al. Transfusion of plasma, platelets, and red blood cells in a 1:1:1 vs a 1:1:2 ratio and mortality in patients with severe trauma: the PROPPR randomized clinical trial. JAMA. 2015;313(5):471-482.
21. Liumbruno GM, Catalano L, Piccinini V, Pupella S, Grazzini G. Reduction of the risk of bacterial contamination of blood components through diversion of the first part of the donation of blood and blood components. Blood Transfus. 2009;7(2):86-93.
22. Iorio A, Basileo M, Marchesini E, et al. Audit of the clinical use of fresh-frozen plasma in Umbria: Study design and results of the pilot phase. Blood Transfus. 2008;6211-6219.
23. Pahuja S, Sethi N, Singh S, Sharma S, Jain M, Kushwaha S. Concurrent audit of fresh frozen plasma: experience of a tertiary care hospital. Hematology. 2012;17(5):306-310.

Pathogenic mutations identified by a multimodality approach in 117 Japanese Fanconi anemia patients

Minako Mori,[1,2] Asuka Hira,[1] Kenichi Yoshida,[3] Hideki Muramatsu,[4] Yusuke Okuno,[4] Yuichi Shiraishi,[5] Michiko Anmae,[6] Jun Yasuda,[7] Shu Tadaka,[7] Kengo Kinoshita,[7,8,9] Tomoo Osumi,[10] Yasushi Noguchi,[11] Souichi Adachi,[12] Ryoji Kobayashi,[13] Hiroshi Kawabata,[14] Kohsuke Imai,[15] Tomohiro Morio,[16] Kazuo Tamura,[6] Akifumi Takaori-Kondo,[2] Masayuki Yamamoto,[7,17] Satoru Miyano,[5] Seiji Kojima,[4] Etsuro Ito,[18] Seishi Ogawa,[3,19] Keitaro Matsuo,[20] Hiromasa Yabe,[21] Miharu Yabe[21] and Minoru Takata[1]

[1]Laboratory of DNA Damage Signaling, Department of Late Effects Studies, Radiation Biology Center, Graduate School of Biostudies, Kyoto University, Kyoto, Japan; [2]Department of Hematology and Oncology, Graduate School of Medicine, Kyoto University, Kyoto, Japan; [3]Department of Pathology and Tumor Biology, Graduate School of Medicine, Kyoto University, Kyoto, Japan; [4]Department of Pediatrics, Nagoya University Graduate School of Medicine, Nagoya, Japan; [5]Laboratory of DNA Information Analysis, Human Genome Center, The Institute of Medical Science, University of Tokyo, Tokyo Japan; [6]Medical Genetics Laboratory, Graduate School of Science and Engineering, Kindai University, Osaka, Japan; [7]Tohoku Medical Megabank Organization, Tohoku University, Sendai, Japan; [8]Department of Applied Information Sciences, Graduate School of Information Sciences, Tohoku University, Sendai, Japan; [9]Institute of Development, Aging, and Cancer, Tohoku University, Sendai, Japan; [10]Children's Cancer Center, National Center for Child Health and Development, Tokyo, Japan; [11]Department of Pediatrics, Japanese Red Cross Narita Hospital, Chiba, Japan; [12]Department of Pediatrics, Kyoto University Graduate School of Medicine, Kyoto, Japan; [13]Department of Pediatrics and Adolescence, Sapporo Hokuyu Hospital, Sapporo, Japan; [14]Department of Hematology and Immunology, Kanazawa Medical University, Uchinada-machi, Japan; [15]Department of Community Pediatrics, Perinatal and Maternal Medicine, Tokyo Medical and Dental University, Tokyo, Japan; [16]Department of Pediatrics and Developmental Biology, Tokyo Medical and Dental University, Tokyo, Japan; [17]Department of Medical Biochemistry, Graduate School of Medicine, Tohoku University, Sendai, Japan; [18]Department of Pediatrics, Hirosaki University Graduate School of Medicine, Hirosaki, Japan; [19]Department of Medicine, Center for Hematology and Regenerative Medicine, Karolinska Institute, Stockholm, Sweden; [20]Division of Molecular and Clinical Epidemiology, Aichi Cancer Center Research Institute, Nagoya, Japan and [21]Department of Innovative Medical Science, Tokai University School of Medicine, Isehara, Kanagawa, Japan

doi:10.3324/haematol.2019.245720

An incorrected version of table 2 appared On October 2019 Issue, page 1967.
The corrected version of table 2 is published on the next page.

Table 2. Clinical phenotype of 10 Japanese Fanconi anemia patients with VACTERL-H association.

Individual	Affected gene	Mutation patterns	VACTERL-H features	FA-features	Family history of FA*	Birth weight SD score	DEB induced chromosome breakage (breaks / cell)	*ALDH2* *** genotype
Case 18-1	*FANCA*	c.2546delC: p.S849FfsX40 c.4042_4043insC: p.I1348TfsX77	C: PDA R: Left renal agenesis L: Bilateral absent thumbs/ Bilateral radial hypoplasia	Short stature	+	-1.9	0.44	AA
Case 30	FANCA	c.2546delC: p.S849FfsX40 c.2546delC: p.S849FfsX40	V: scoliosis C: ASD/Persistent left superior vena E: Esophageal atresia	Skin pigmentation Deafness Right inguinal hernia Bicornuate uterus Short stature (-1.8SD)	–	-2.1	2.06	GG
Case 37	*FANCA*	c.2546delC: p.S849FfsX40 c.3295C>T: p.Q1099X	E: Esophageal atresia R: Right pelvic kidney L: Bilateral thumb hypoplasia	Jejunal atresia Strabismus Short stature (-4SD)	–	-2.3	0.12	GG

continued on the next page

continued from previous page

Case 60	*FANCB*	complete loss of *FANCB* gene (chrX g.14730104-14904216 del)	V: Spina bifida occulta/ Abnormal ribs A: Anal atresia C: PDA R: Right renal agenesis L: Right absent thumb/ Partial loss of left thumb	Skin pigmentation Microphthalmus/ Stenocephaly/Ptosis Duodenal stenosis Annular pancreas/ Hypospadias/ Undescended testis Short stature (-6SD)	–	-4.8	3.8	GG
Case 61	*FANCB*	complete loss of *FANCB* gene (chrX g.14810970-14932973 del)	V: Abnormal ribs/Scoliosis A: Anal atresia C: VSD/PS E: Duodenal atresia** R: Left renal agenesis L: Bilateral absent thumbs H: Hydrocephalus	Skin pigmentation Microphthalmus/ Deafness/ Ear canal stenosis Undescended testis (Short stature (-1SD))	–	-2.8	4.2	GA
Case 64	*FANCC*	c.1154+5G>A: p.S386X c.1154+5G>A: p.S386X	A: Anal atresia C: VSD, PDA E: Esophageal atresia	Skin pigmentation Deafness/Left aural stenosis/ Right aural atresia Cleft palate Short stature (-2SD)	–	-2.53	7.8	GG
Case 69	*FANCG*	c.307+1G>C c.1066C>T: p.Q356X	C: Coarctation complex R: Right renal agenesis/ Left renal cyst L: Bilateral absent thumbs/ Right radial hypoplasia	Skin pigmentation Short stature (-8SD)	–	-1.7	8.54	GA
Case 73-1	*FANCG*	c.307+1G>C c.307+1G>C	C: PDA R: Left renal agenesis L: Right absent thumb/ Bilateral radial hypoplasia	Skin pigmentation Bilateral aural atresia Short stature (-2.7SD)	+	-0.9	3.49	GA
Case 96	*FANCI*	c.158-2A>G:p.S54FfsX5 c.288G>A:p.C56FfsX8	A: Anal atresia C: VSD/PDA R: Right renal agenesis/ Left renal hypoplasia L: Bilateral absent thumb/ Bilateral absent radius H: Hydrocephalus	Skin pigmentation Microphthalmus Hypogenitalia Short stature (-8SD)	–	-3.9	0.52	GA
Case 99-1	*FANCP*	c.343delA: p.S115AfsX11 c.343delA: p.S115AfsX11	C: ASD/VSD/PS R: horseshoe kidney L: Bilateral floating thumbs/ bilateral radial hypoplasia	Intestinal malrotation Duodenal stenosis Short stature (-5.8SD)	+	-2.3	0.91	AA

*Case 18-1, 73-1, and 99-1 had a sibling with Fanconi anemia (FA). ** Duodenal atresia is considered to be a part of the VACTERL association by some reports.[27] ***_ALDH2_ wild type and the inactivating mutation (p.Glu504Lys) allele is referred to as G and A, respectively. ALDH2: aldehyde dehydrogenase-2; ASD: atrial septal defect; BM: bone marrow; DEB: diepoxybutane; PDA: patent ductus arteriosus; PS: pulmonary stenosis; SD: Standard Deviation; VACTERL-H: vertebral anomalies, anal atresia, cardiac anomalies, tracheal-esophageal fistula, esophageal atresia, renal structural abnormalities, limb anomalies, and hypocephalus; VSD: ventricular septal defect.

.

RESEARCH, READ & CONNECT

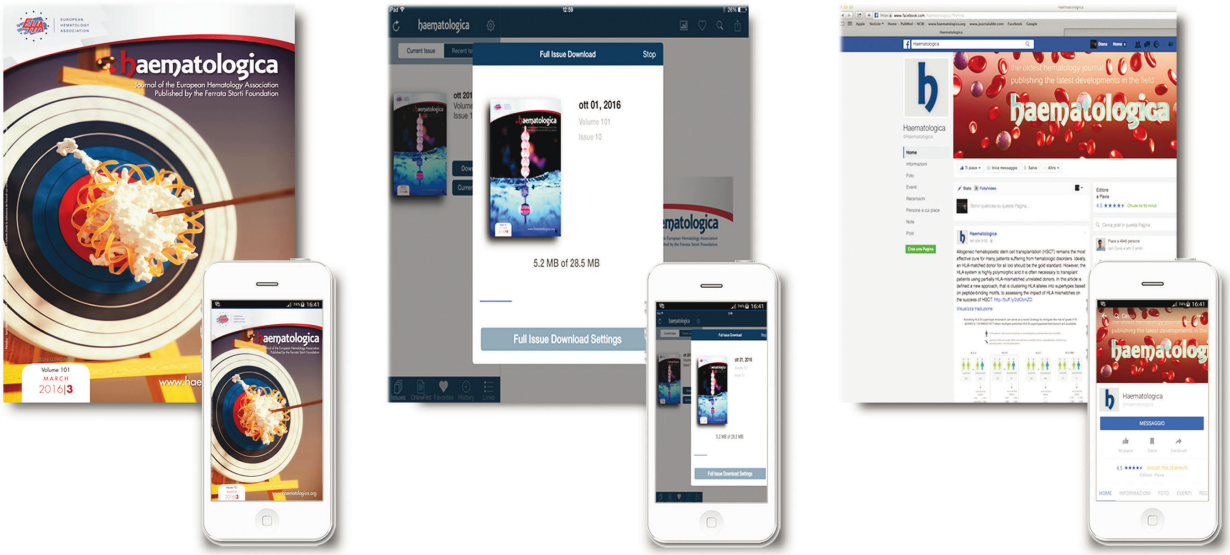

We reach more than
6 hundred thousand readers each year

The first Hematology Journal in Europe

Impressions YTD

9,621,645

Digital Readers

4,431

Total Audience

554,484

Worldwide rank	Impact factor	Total citations
7 th	7.570	16,255

haematologica

Journal of the Ferrata Storti Foundation